frontiers | Research Topics

Biomaterials in asia

Edited by
Mingqiang Li, Jianxun Ding, Yuce Li and Yin Fang

Published in
Frontiers in Bioengineering and Biotechnology
Frontiers in Materials

ISSN 1664-8714
ISBN 978-2-83251-516-7
DOI 10.3389/978-2-83251-516-7

About Frontiers

Frontiers is more than just an open access publisher of scholarly articles: it is a pioneering approach to the world of academia, radically improving the way scholarly research is managed. The grand vision of Frontiers is a world where all people have an equal opportunity to seek, share and generate knowledge. Frontiers provides immediate and permanent online open access to all its publications, but this alone is not enough to realize our grand goals.

Frontiers journal series

The Frontiers journal series is a multi-tier and interdisciplinary set of open-access, online journals, promising a paradigm shift from the current review, selection and dissemination processes in academic publishing. All Frontiers journals are driven by researchers for researchers; therefore, they constitute a service to the scholarly community. At the same time, the *Frontiers journal series* operates on a revolutionary invention, the tiered publishing system, initially addressing specific communities of scholars, and gradually climbing up to broader public understanding, thus serving the interests of the lay society, too.

Dedication to quality

Each Frontiers article is a landmark of the highest quality, thanks to genuinely collaborative interactions between authors and review editors, who include some of the world's best academicians. Research must be certified by peers before entering a stream of knowledge that may eventually reach the public - and shape society; therefore, Frontiers only applies the most rigorous and unbiased reviews. Frontiers revolutionizes research publishing by freely delivering the most outstanding research, evaluated with no bias from both the academic and social point of view. By applying the most advanced information technologies, Frontiers is catapulting scholarly publishing into a new generation.

What are Frontiers Research Topics?

Frontiers Research Topics are very popular trademarks of the *Frontiers journals series*: they are collections of at least ten articles, all centered on a particular subject. With their unique mix of varied contributions from Original Research to Review Articles, Frontiers Research Topics unify the most influential researchers, the latest key findings and historical advances in a hot research area.

Find out more on how to host your own Frontiers Research Topic or contribute to one as an author by contacting the Frontiers editorial office: frontiersin.org/about/contact

Biomaterials in asia

Topic editors

Mingqiang Li — Third Affiliated Hospital of Sun Yat-sen University, China
Jianxun Ding — Changchun Institute of Applied Chemistry, Chinese Academy of Sciences (CAS), China
Yuce Li — Sungkyunkwan University, Republic of Korea
Yin Fang — Nanyang Technological University, Singapore

Citation

Li, M., Ding, J., Li, Y., Fang, Y., eds. (2023). *Biomaterials in asia*. Lausanne: Frontiers Media SA. doi: 10.3389/978-2-83251-516-7

Table of contents

07 Editorial: Biomaterials in Asia
Yuce Li, Yin Fang, Mingqiang Li and Jianxun Ding

10 Immobilization of Glycogen Synthase Kinase-3β Inhibitor on 316L Stainless Steel *via* Polydopamine to Accelerate Endothelialization
Ming Zhang, Xudong Shi, Hai Sun, Donghua Xu, Yang Gao, Xi Wu, Jianqi Zhang and Jichang Zhang

19 Anti-Biofouling Polymers with Special Surface Wettability for Biomedical Applications
Zhoukun He, Xiaochen Yang, Na Wang, Linpeng Mu, Jinyuan Pan, Xiaorong Lan, Hongmei Li and Fei Deng

39 Case Report: A Pseudoaneurysm Involving the Left Common Iliac Artery Secondary to Brucellosis: A Rare Case Report
Qilong Wang, Liang Tang, Yue Qin, Qi Wang, Ping Zhang and Zhihua Cheng

43 Photothermal Detection of MicroRNA Using a Horseradish Peroxidase-Encapsulated DNA Hydrogel With a Portable Thermometer
Xiujuan Liu, Meixiang Zhang, Ze Chen, Jiuqing Cui, Long Yang, Zihe Lu, Fang Qi and Haixia Wang

51 Enhanced Anticancer Efficacy of Chemotherapy by Amphiphilic Y-Shaped Polypeptide Micelles
Cong Hua, Yi Zhang and Yuanhao Liu

59 Ultrasound-Guided Percutaneous Thermal Ablation of Hepatic Focal Nodular Hyperplasia——A Multicenter Retrospective Study
Xuan Yu, Jiandong Chang, Dezhi Zhang, Qiang Lu, Songsong Wu and Kai Li

66 Acitretin-Conjugated Dextran Nanoparticles Ameliorate Psoriasis-like Skin Disease at Low Dosages
Jiajia Lan, Yuce Li, Jingjing Wen, Yu Chen, Jing Yang, Liang Zhao, Yuting Xia, Hongyao Du, Juan Tao, Yan Li and Jintao Zhu

77 Surface Modification of Polycaprolactone Scaffold With Improved Biocompatibility and Controlled Growth Factor Release for Enhanced Stem Cell Differentiation
Xiaoyan Qin, Yixin Wu, Shuang Liu, Lei Yang, Hongxia Yuan, Susu Cai, Julia Flesch, Zehao Li, Yujing Tang, Xiaomin Li, Yi Zhuang, Changjiang You, Chaoyong Liu and Changyuan Yu

91 Hypocapnia Stimuli-Responsive Engineered Exosomes Delivering miR-218 Facilitate Sciatic Nerve Regeneration
Yingshuai Wang, Tao Yu and Feihu Hu

102 Extramedullary Osseointegration—A Novel Design of Percutaneous Osseointegration Prosthesis for Amputees
Yingying Sun, Jinying Xu, Shuang Lv, Ziran Xu, Lisha Li, Yan Li and Yulin Li

116 Biomimetic Redox-Responsive Mesoporous Organosilica Nanoparticles Enhance Cisplatin-Based Chemotherapy
Fangman Chen, Fan Zhang, Yanbin Wang, Jiahui Peng, Lei Cao, Qian Mei, Mingfeng Ge, Li Li, Meiwan Chen, Wen-fei Dong and Zhimin Chang

126 Nanoparticle-Based Drug Delivery Systems for Induction of Tolerance and Treatment of Autoimmune Diseases
He Li, Yong-Guang Yang and Tianmeng Sun

140 PBPK Modeling on Organs-on-Chips: An Overview of Recent Advancements
Yi Yang, Yin Chen, Liang Wang, Shihui Xu, Guoqing Fang, Xilin Guo, Zaozao Chen and Zhongze Gu

153 Tetrandrine Prevents Neomycin-Induced Ototoxicity by Promoting Steroid Biosynthesis
Qilei Zhang, Yunhao Wu, Yan Yu, Yuguang Niu, Qiaojun Fang, Xin Chen, Jieyu Qi, Chen Zhang, Geping Wu, Kaiming Su and Renjie Chai

163 Interaction of Neurovascular Signals in the Degraded Condylar Cartilage
Wenpin Qin, Zibin Zhang, Jianfei Yan, Xiaoxiao Han, Li-Na Niu and Kai Jiao

172 Conductive GelMA/PEDOT: PSS Hybrid Hydrogel as a Neural Stem Cell Niche for Treating Cerebral Ischemia-Reperfusion Injury
Yilei Zhang, Meimei Zhang, Runlin Zhang, Haining Liu, Hui Chen, Xiaofeng Zhang, Chen Li, Qing Zeng, Yunhua Chen and Guozhi Huang

186 Oriented Growth of Neural Stem Cell–Derived Neurons Regulated by Magnetic Nanochains
Lin Xia, Chen Zhang, Kaiming Su, Jiangang Fan, Yuguang Niu, Yafeng Yu and Renjie Chai

193 Copper-Lithium-Doped Nanohydroxyapatite Modulates Mesenchymal Stem Cells Homing to Treat Glucocorticoids-Related Osteonecrosis of the Femoral Head
Qianhao Li, Zhouyuan Yang, Zhun Wei, Donghai Li, Yue Luo and Pengde Kang

205 Recent Advances of Intraocular Lens Materials and Surface Modification in Cataract Surgery
Chenqi Luo, Hanle Wang, Xinyi Chen, Jingjie Xu, Houfa Yin and Ke Yao

223 Graphene Substrates Promote the Differentiation of Inner Ear Lgr5+ Progenitor Cells Into Hair Cells
Xiaoqiong Ding, Yangnan Hu, Hong Cheng, Xiaoli Zhang, Ling Lu, Song Gao, Cheng Cheng, Lifen Wang, Xiaoyun Qian, Chen Zhang, Renjie Chai, Xia Gao and Zhichun Huang

231 Study on the Effect of PDA-PLGA Scaffold Loaded With Islet Cells for Skeletal Muscle Transplantation in the Treatment of Diabetes
Meishuang Zhang, Hongwei Du, Yueqi Guan, Jingyue Liu, Sushan Wang, Haoran Li, Wenyou Zhang, Hao Han, Ming Zhang and Li Chen

243 Intracellular K^+-Responsive Block Copolymer Micelles for Targeted Drug Delivery of Curcumin
Mingyue Jiang, Le Chen, Bo Chen, Qinghua Yu, Xianming Zhang, Weihong Jing, Limei Ma, Tao Deng, Zhangyou Yang and Chao Yu

255 Electroactive shape memory polyurethane composites reinforced with octadecyl isocyanate-functionalized multi-walled carbon nanotubes
Yadong Sun, Jiachi Teng, Yi Kuang, Shengxiang Yang, Jiquan Yang, Hongli Mao and Zhongwei Gu

268 Effect of viscoelastic properties of cellulose nanocrystal/collagen hydrogels on chondrocyte behaviors
Donglei Liu, Hao Zhang, Xufeng Dong, Lin Sang and Min Qi

283 Imitation-mussel fluorescent silicon quantum dots for selective labeling and imaging of bacteria and biofilms
Jiayi Lin, Linlin Xu, Yuling Zheng, Dalin Wu and Jun Yue

294 Fabrication of Ginsenoside-Based Nanodrugs for Enhanced Antitumor Efficacy on Triple-Negative Breast Cancer
Shuting Zuo, Jing Wang, Xianquan An, Zhenyu Wang, Xiao Zheng and Yan Zhang

302 3D-printed collagen/silk fibroin/secretome derived from bFGF-pretreated HUCMSCs scaffolds enhanced therapeutic ability in canines traumatic brain injury model
Xiaoyin Liu, Guijun Zhang, Pan Wei, Lifang Hao, Lin Zhong, Kunhon Zhong, Chang Liu, Peng Liu, Qingbo Feng, Shan Wang, Jianyong Zhang, Rui Tian and Liangxue Zhou

318 Effect of hot etching with HF on the surface topography and bond strength of zirconia
Zhuoran Liang, Yang Liu, Yulin Jiang, Pan Liu, Yannan Zhang, Fanhao Meng, Min Liu, Zhi Cui, Jinbao Ma and Jianfeng Chen

328 Epigallocatechin-3-gallate selenium nanoparticles for neuroprotection by scavenging reactive oxygen species and reducing inflammation
Yiming Wang, Wenqi Luo, Feng Lin, Wanguo Liu and Rui Gu

340 Application of medical imaging methods and artificial intelligence in tissue engineering and organ-on-a-chip
Wanying Gao, Chunyan Wang, Qiwei Li, Xijing Zhang, Jianmin Yuan, Dianfu Li, Yu Sun, Zaozao Chen and Zhongze Gu

363 Hypoxia-pretreated mesenchymal stem cell-derived exosomes-loaded low-temperature extrusion 3D-printed implants for neural regeneration after traumatic brain injury in canines
Xiaoyin Liu, Jingjing Wang, Peng Wang, Lin Zhong, Shan Wang, Qingbo Feng, Xin Wei and Liangxue Zhou

381 Urokinase-loaded cyclic RGD-decorated liposome targeted therapy for *in-situ* thrombus of pulmonary arteriole of pulmonary hypertension
Jingtao Li, Xiaofeng Zhang, Yingying Mo, Tongtong Huang, Huaqing Rao, Zhenyuan Tan, Liuliu Huang, Decai Zeng, Chunlan Jiang, Yanfen Zhong, Yongzhi Cai, Binbin Liang and Ji Wu

396 Application of single and cooperative different delivery systems for the treatment of intervertebral disc degeneration
Zongtai Liu and Changfeng Fu

418 Knowledge domain and hotspots concerning photosensitive hydrogels for tissue engineering applications: A bibliometric and visualized analysis (1996-2022)
Hongxun Fu, Baojun Yu, Hao Wang, Haibin Tong, Lin Jiang, Yupeng Zhang, Guixian Meng, Meiyan Sun and Jieqiong Lin

433 Engineering exosomes for bone defect repair
Shaoyang Ma, Yuchen Zhang, Sijia Li, Ang Li, Ye Li and Dandan Pei

frontiers | Frontiers in Bioengineering and Biotechnology

TYPE Editorial
PUBLISHED 17 January 2023
DOI 10.3389/fbioe.2023.1136139

OPEN ACCESS

EDITED AND REVIEWED BY
Hasan Uludag,
University of Alberta, Canada

*CORRESPONDENCE
Yuce Li,
liyuce@skku.edu
Yin Fang,
yin.fang@ntu.edu.sg
Mingqiang Li,
limq567@mail.sysu.edu.cn
Jianxun Ding,
jxding@ciac.ac.cn

SPECIALTY SECTION
This article was submitted to Biomaterials, a section of the journal Frontiers in Bioengineering and Biotechnology

RECEIVED 02 January 2023
ACCEPTED 09 January 2023
PUBLISHED 17 January 2023

CITATION
Li Y, Fang Y, Li M and Ding J (2023), Editorial: Biomaterials in Asia. *Front. Bioeng. Biotechnol.* 11:1136139. doi: 10.3389/fbioe.2023.1136139

Editorial: Biomaterials in Asia

Yuce Li[1,2]*, Yin Fang[3]*, Mingqiang Li[4]* and Jianxun Ding[5]*

[1]College of Life Science and Health, Wuhan University of Science and Technology (WUST), Wuhan, China, [2]School of Chemical Engineering, College of Engineering, Sungkyunkwan University, Suwon, South Korea, [3]School of Chemistry, Nanyang Technological University, Singapore, Singapore, [4]Laboratory of Biomaterials and Translational Medicine, Center for Nanomedicine, The Third Affiliated Hospital, Sun Yat-sen University, Guangzhou, China, [5]Key Laboratory of Polymer Ecomaterials, Changchun Institute of Applied Chemistry, Chinese Academy of Sciences, Changchun, China

KEYWORDS

biomaterial, drug delivery, tissue engineering, regenerative medicine, disease diagnostics

Editorial on the Research Topic
Biomaterials in Asia

Biomaterials in Asia

Biomaterials have shown significant potential in various biomedical fields, including disease prevention, theranostics, and tissue regeneration by controlled delivery of therapeutics, contrast agents, sensing agents, growth factors, and so forth. In recent years, Asian scientists have contributed more to biomaterials with the increasing support of various funds. Through this Research Topic, we expected to collect several state-of-the-art advances in biomaterial science and engineering research within Asia and disseminate them to the global audience. This Research Topic comprised 35 articles (including 7 reviews, 27 original research articles, and 1 case report) contributed by 263 authors, and it has attracted 54,023 views, 11,892 downloads, and 27 citations by researchers worldwide up to 15 January 2023. Undoubtedly, this Research Topic has won great success in displaying the significant contributions of Asian scientists to the next-generation precision medicine and further clinical translation.

The reviews from this Research Topic have covered the latest progress in several different types of biomaterials for diverse biomedical applications, including intraocular lens materials and their surface modification for cataract surgery (Luo et al.), drug delivery systems for the treatment of autoimmune diseases (Li et al.) and intervertebral disc degeneration (Liu and Fu), and engineering exosomes for bone defect repair (Ma et al.). Also, anti-biofouling polymer materials with special surface wettability and their biomedical applications are summarized (He et al.). Particularly, this Research Topic included two review articles about the recent development of organ-on-a-chips, regarding the application of medical imaging methods and artificial intelligence (Gao et al.) and physiologically based pharmacokinetic (PBPK) modeling (Yang et al.). These well-organized reviews would provide the readers with an overview and constructive perspectives of these specific topics of biomaterials.

The original research articles on this Research Topic have contributed to several critical aspects of biomaterials, including the preparation, characterizations, biological functions/mechanisms, and practical applications in clinic.

Smart biomaterials have shown distinct and adjustable *in vivo* behaviors for the delivery of therapeutic agents, such as small-molecule drugs, genes, and proteins, which is promising to improve the limitations of such therapeutics in clinic, including the low solubility/stability, short circulation, unsatisfactory selectivity on target tissues, and so forth. For example, cancer cell membrane-coated biomimetic mesoporous organosilica nanoparticles improved the anticancer performance and

decreased the *in vivo* system toxicity of cisplatin because it prolonged the circulation time and increased tumor accumulation (Chen et al.). Jiang et al. demonstrated that micelles containing 15-crown-5 selectively released the loaded curcumin in response to the intracellular potassium ion (K^+) by forming the 2:1 "sandwich" host-guest complexes between 15-crown-5 and K^+. Similarly, an amphiphilic micelle comprised of a Y-shaped polypeptide has demonstrated excellent drug loading and release behaviors (Hua et al.). Interestingly, a carrier-free nanomedicine composed of ginsenosides Rg3 and Rb1 has shown better antitumor and antimetastatic effects against triple-negative breast cancer than the direct combination of free drugs (Zuo et al.). In addition, a cyclic Arg-Gly-Asp (cRGD)-decorated liposome loading with urokinase has shown enhanced thrombolytic effects by active targeting delivery of urokinase to the thrombi (Li et al.). Sun et al. developed electroactive shape memory polymers based on polyurethane and carbon nanotube, which would be employed as four-dimensional (4D)-printing materials for potential biomedical applications.

Some biomaterials have shown capacities to manipulate the behaviors of cells. For example, graphene was proven to promote the differentiation of Lgr5+ progenitors into inner ear hair cells (Ding et al.). Besides, copper-lithium-doped nanohydroxyapatite promoted the migration and homing of mesenchymal stem cells (MSCs) by upregulating the hypoxia-inducible factor 1α/stromal cell-derived factor-1 (HIF-1α/SDF-1) pathway (Li et al.). Interestingly, increasing the viscoelastic properties of cellulose nanocrystal/collagen hydrogels promoted the proliferation, alteration of shape, and matrix deposition of chondrocytes and reduced the interleukin-1β (IL-1β) secretion (Liu et al.). Moreover, Xia et al. developed magnetic nano chains, which guided the oriented growth of neural stem cell-derived neurons. Zhang et al. demonstrated that a conductive hybrid hydrogel promoted the development of neural stem cells into neurons. Wang et al. indicated that epigallocatechin-3-gallate selenium nanoparticle scavenged reactive oxygen species (ROS) effectively and thus provided superior neuroprotective effect. Qin et al. demonstrated intimate interactions among innervation, angiogenesis, and inflammation in the condylar cartilage of temporomandibular joint osteoarthritis, which provided promising treatment targets. In addition to developing advanced biomaterials, the surface modification of materials is also a method to obtain biomaterials with specific functions. For example, coating 316L stainless steel with glycogen synthase kinase-3β inhibitor (GSKi) improved the adhesion and proliferation of human coronary artery endothelial cells (Zhang et al.). Such properties of these biomaterials made them promise to treat various diseases, such as sensory hearing loss, osteonecrosis, osteoarthritis, neurodegenerative disorders, cerebral ischemia-reperfusion injury, and cardiovascular diseases.

In the past several decades, tissue engineering and regenerative medicine have emerged as essential branches of biomaterials. Several impressive research articles have provided constructive insights into the current Research Topic. Fu et al. performed a systemic bibliometric and visualized analysis regarding the photosensitive hydrogels for tissue engineering. Qin et al. established a "click" reaction-based method for surface modification of polycaprolactone scaffold, which could be utilized in the long-term controlled release of multiplex signal proteins for tissue engineering. Zhang et al. developed a polydopamine-poly(lactic-*co*-glycolic acid) (PDA-PLGA) scaffold carrying RINm5f islet cells, which supported the growth of islet cells and showed no influence on insulin secretion. When the type I diabetic rats were transplanted with the scaffold in the skeletal muscles, their blood glucose was maintained at a low level for approximately 3 weeks.

As emerging multipotential natural biomaterials, exosomes and secretomes have exhibited bright prospects in regenerative medicine. Particularly, scaffolds containing engineered exosomes derived from adipose-derived mesenchymal stem cells (A-MSCs) under hypocapnia (Wang et al.) and hypoxia-pretreated MSCs (Liu et al.) or secretomes derived from basic fibroblast growth factor (bFGF)-pretreated human umbilical cord blood-derived mesenchymal stem cells (hUCB-MSCs) (Liu et al.) have significantly facilitated the neural regeneration, which demonstrated great promise in the treatment of traumatic brain injury and the functional recovery after surgical treatment.

Biomaterials are also developed as sensitive detectors or contrast agents for disease diagnostics and identification of microbes/biomolecules. For example, Lin et al. reported polydopamine-coated silicon quantum dots as fluorescent probes of bacteria and their biofilms. Selective labeling of Gram-positive and Gram-negative bacteria was achieved by altering the surface functionalization groups. Besides, Liu et al. developed a visual and temperature-sensitive probe to detect microRNA, which could be biomarkers of diverse diseases like cancer. This biosensor enables point-of-care detection of biomolecules with low cost, ease of operation, and high sensitivity.

Clinical translations and applications are the terminal goals of development of biomaterials. The unique or modified biomaterials and biotechnologies should benefit more patients only when they pass the reliability assessment and model validation. Sun et al. provided an updated design of percutaneously osseointegrated prostheses for amputees, in which new bone formation at the bone-implant-skin opening area and distal bone canal was observed. For dental materials, Liang et al. demonstrated that the hot etching of zirconia with hydrofluoric acid (HF) induced a more uniform and dense porous morphology, greater roughness, and provided the highest shear bond strength. In addition, a multicenter retrospective study has demonstrated the high efficiency of ultrasound-guided percutaneous thermal ablation in the clinical treatment of hepatic focal nodular hyperplasia (Yu et al.).

Notably, the severe side effects of some medicines have limited their broad applications, although they are approved for clinical use. This Research Topic also reports strategies to reduce the side effects of clinically used therapeutics. Lan et al. developed acitretin-conjugated dextran nanoparticle (ACT-Dex NP), which achieved a similar therapeutic effect on psoriasis-like skin disease at a significantly lower dosage compared to neat acitretin. This low dosage is promising to avoid acitretin's well-known teratogenicity on fetuses. Moreover, Zhang et al. demonstrated that the neomycin-induced ototoxicity would be prevented by combination with tetrandrine (a bioactive bisbenzylisoquinoline alkaloid derived from *Stephania tetrandra*) by promoting the steroid biosynthesis.

This Research Topic also included a rare case report in clinic (Wang et al.). The authors reported a patient with an uncommon pseudoaneurysm, involving the left common iliac artery because of brucellosis. A favorable therapeutic effect and well prognosis were obtained with a combination treatment of long-term multi-course antibacterial therapy with combination antibiotics. This report would provide a paradigm for the clinical treatment of such diseases.

In summary, this Research Topic encompasses a proportion of critical contributions made by Asian researchers in the biomaterial field in recent years. This regionalized Research Topic showed the rapid

development of biomaterials in Asia, and it is foreseeable that Asian scientists will play a more significant role in this field in the future.

Author contributions

All authors listed have made a substantial, direct, and intellectual contribution to the work, and approved it for publication.

Acknowledgments

The editors appreciate the contributions of all authors to this Research Topic, the constructive comments of all the reviewers, and the editorial support from Frontiers throughout the publication process.

Conflict of interest

The authors declare that the research was conducted in the absence of any commercial or financial relationships that could be construed as a potential conflict of interest.

Publisher's note

frontiers in Bioengineering and Biotechnology

ORIGINAL RESEARCH
published: 22 November 2021
doi: 10.3389/fbioe.2021.806151

Immobilization of Glycogen Synthase Kinase-3β Inhibitor on 316L Stainless Steel *via* Polydopamine to Accelerate Endothelialization

*Ming Zhang[1†], Xudong Shi[2,3†], Hai Sun[2,3], Donghua Xu[4], Yang Gao[1], Xi Wu[1], Jianqi Zhang[1] and Jichang Zhang[1]**

[1]Cardiology Department, The Second Hospital of Jilin University, Jilin University, Changchun, China, [2]Key Laboratory of Polymer Ecomaterials, Changchun Institute of Applied Chemistry, Chinese Academy of Sciences, Changchun, China, [3]Jilin Biomedical Polymers Engineering Laboratory, Changchun, China, [4]State Key Laboratory of Polymer Physics and Chemistry, Changchun Institute of Applied Chemistry, Chinese Academy of Sciences, Changchun, China

OPEN ACCESS

Edited by:
Mingqiang Li,
Sun Yat-sen University, China

Reviewed by:
Haiqing Li,
Nanjing Tech University, China
Zhenbo Ning,
Beijing University of Chemical Technology, China
Kun Zhang,
Zhengzhou University, China

***Correspondence:**
Jichang Zhang
jichang@jlu.edu.cn

†These authors have contributed equally to this work and share first authorship

Specialty section:
This article was submitted to Biomaterials, a section of the journal Frontiers in Bioengineering and Biotechnology

Received: *31 October 2021*
Accepted: *04 November 2021*
Published: *22 November 2021*

Citation:
Zhang M, Shi X, Sun H, Xu D, Gao Y, Wu X, Zhang J and Zhang J (2021) Immobilization of Glycogen Synthase Kinase-3β Inhibitor on 316L Stainless Steel via Polydopamine to Accelerate Endothelialization. Front. Bioeng. Biotechnol. 9:806151. doi: 10.3389/fbioe.2021.806151

The coverage of stents with healthy endothelium is crucial to the success of cardiovascular stent implantation. Immobilizing bioactive molecules on stents is an effective strategy to generate such stents. Glycogen synthase kinase-3β inhibitor (GSKi) is a bioactive molecule that can effectively accelerate vascular endothelialization. In this work, GSKi was covalently conjugated on 316L stainless steel through polydopamine to develop a stable bioactive surface. Fourier transform infrared spectroscopy (FTIR), scanning electron microscopy (SEM) and water contact angle results revealed the successful introduction of GSKi onto 316L stainless steel. The GSKi coating did not obviously affect the hemocompatibility of plates. The adhesion and proliferation of human coronary artery endothelial cells (HCAECs) on stainless steel was significantly promoted by the addition of GSKi. In summary, this work provides a universal and stable strategy of immobilizing GSKi on the stent surface. This method has the potential for widespread application in the modification of vascular stents.

Keywords: glycogen synthase kinase-3β inhibitor (GSKi), polydopamine, 316L stainless steel, endothelialization, human coronary artery endothelial cells

1 INTRODUCTION

Coronary artery disease (CAD), especially myocardial infarction, is becoming a major cause of death worldwide and is responsible for more than 17.5 million deaths annually (Cui et al., 2018). Drug-eluting stents (DESs) have been successfully used in the treatment of CAD. Despite the success of DESs, a previous study demonstrated that in-stent restenosis (ISR) and late stent thrombosis (LST) represent obstacles to long-term application in the clinic (Otsuka et al., 2012; Liang et al., 2016). It was soon realized that the occurrences of ISR and LST are ultimately due to endothelial injury or the re-endothelialization delay of the stents (Kakinoki et al., 2018). A functionally intact vessel endothelium not only prevents thrombosis but also mediates intimal hyperplasia. As a result, re-endothelialization on the stent effectively prevents ISR and LST (Woods and Marks, 2004). Considerable efforts in the surface modification of stents have been made to improve their ability to rapidly re-endothelialize (Avci-Adali et al., 2010; Qi et al., 2014; Pang et al., 2015). However, the selection of appropriate bioactive molecules and the strategy of immobilizing molecules on stents still need to be investigated.

Glycogen synthase kinase-3β (GSK3β) acts as a nodal point of converging signaling pathways in endothelial cells to adjust vessel growth. It is a pro-apoptotic kinase given that it's overexpression makes cells sensitive to apoptosis. The inhibitor of GSK3β (GSKi) increases the expression of β-catenin in endothelial cells and promote the expression of vascular endothelial growth factor (VEGF) (Doble and Woodgett, 2003; Skurk et al., 2005; Choi et al., 2007), which is an important regulatory molecule of endothelial cells and plays an important role in vascular development (Ferrara et al., 2003; Eichmann and Simons, 2012). Zhang et al. found that GSKi had a protective effect on endothelial cells by phosphorylating inactivated GSK3β and inhibiting endothelial cell apoptosis (Zhang et al., 2004). Benjamin Hibbert et al. treated endothelial progenitor cells with GSKi to promote the secretion of VEGF and then injected them into immunocompromised mice. They found that GSKi promoted re-endothelialization and reduced neointimal formation after arterial injury (Hibbert et al., 2009). These exciting results indicated that GSKi can be used to accelerate vascular endothelialization after coronary stent implantation. However, the clinical feasibility of transplantation in operant cells *in vitro* may be limited given that the process is labor intensive and impractical.

To date, only a few studies have reported on GSKi-modified stents. Ma et al. coated stents with a mixture of lubricating jelly and active compounds [GSKi and rapamycin (a key DES agent)]. The experimental results revealed that GSKi-coated stents enhance the adhesion of endothelial progenitor cells and efficiently ameliorate the vascular response to stent implantation. Furthermore, GSKi-coated stents can redeem the deleterious endothelial effects of rapamycin-coated stents (Ma et al., 2010). However, this method of coating stents may lead to weak adhesion between the coating and stents and the rapid loss of active compounds caused by simple blending.

In recent years, mussel-inspired polydopamine coatings have attracted researchers' attention because they have outstanding ability to bind strongly to almost all types of substrates (Lee et al., 2006; Lee et al., 2007a; Lee et al., 2007b; Luo et al., 2013; Zhang et al., 2014; Wu et al., 2016; Zhang et al., 2016; Zhang et al., 2019). Polydopamine coatings can be realized through the simple dip-coating step of the substrates in the aqueous solution of dopamine and provides secondary reactivity for conjugating bioactive molecules. The reaction conditions are mild and easy to perform (Madhurakkat Perikamana et al., 2015; Yang et al., 2015). The bioactive molecules are connected on the material surface by a stable covalent bond between the sulydryl/amine groups of the molecule and the phenolic hydroxyl/quinone groups of polydopamine (Lynge et al., 2011; Qi et al., 2014).

In this study, GSKi was immobilized onto 316L stainless steel plates (316L-SS) by polydopamine coating. The surfaces of the modified 316L-SS were observed by SEM and water contact angle. The hemocompatibility of the modified 316L-SS was studied by blood clotting time tests and platelet adhesion. The viability, adhesion, proliferation and morphology of human coronary artery endothelial cells (HCAECs) on the modified plates were examined using *in vitro* cell experiments.

2 EXPERIMENTS

2.1 Preparation of Functionalized Surfaces

The 316L-SS substrates were ultrasonically washed with acetone, ethanol and distilled water for 5 min. The preparation procedure of functionalized surfaces was as follows: 316L-SS was immersed in a 2 mg/L dopamine hydrochloride (Aladdin, United States) solution (dissolved in 10 mM Tris buffer, pH 8.5) for 24 h at room temperature and then rinsed with 10 mM Tris buffer (pH 8.5) thrice to remove the poorly bound polydopamine. The obtained polydopamine-modified stainless steel plates were air-dried and labeled PDAM-SS.

Then, 2 ml GSKi (CHIR-98014, Abmole, United States) solution (2.5 mg/ml DMSO solution) was added to 48 ml distilled water to obtain the supersaturated aqueous solution of GSKi. Then, PDAM-SS was placed into a culture plate and incubated with the supersaturated aqueous solution of GSKi at room temperature for 24 h. Finally, the GSKi-modified samples were rinsed thrice with distilled water and air-dried (labeled GSKi-SS).

2.2 Surface Characterization

2.2.1 Fourier Transform Infrared Spectroscopy

Fourier transform infrared spectroscopy (FTIR) (Bruker ALPHA) with the diffuse reflectance mode was used to determine the chemical structure of 316L-SS, PDAM-SS and GSKi-SS.

2.2.2 SEM

The surface morphologies of 316L-SS, PDAM-SS and GSKi-SS were observed using a Gemini 300/VP field emission scanning electron microscope (Zeiss, Germany).

2.2.3 Water Contact Angle

The wettability studies were performed using a contact angle analyzer (DSA10-MK2, Krüss, Germany). The measurement was performed at five different points on each stainless steel plate to obtain the average contact angle.

2.3 Hemocompatibility

2.3.1 Activated Partial Thromboplastin Time (APTT)

Platelet-poor plasma (PPP) was obtained by centrifuging fresh human whole blood at 3,000 rpm for 15 min. The samples were incubated with 500 μL PPP in a 24-well plate for 30 min at 37°C. The dotting time of incubated PPP was detected using a coagulometer (ACL TOP 500, Werfen, United States).

2.3.2 Platelet Adhesion

Fresh peripheral blood was obtained from a healthy human volunteer. Platelet-rich plasma (PRP) was obtained by centrifugation of whole blood at 1,500 rpm for 15 min. The samples were placed in a 24-well plate, and 100 μL PRP was added to each sample surface. After incubation at 37°C for 2 h, the PRP on the sample was absorbed and rinsed with PBS thrice. The

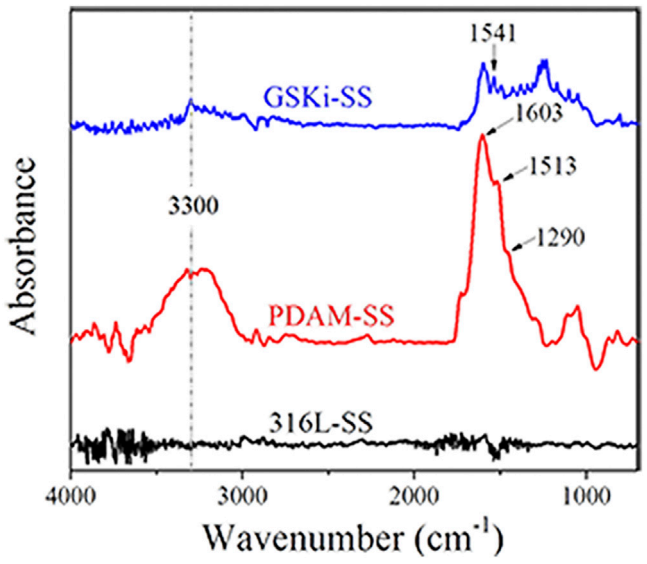

FIGURE 1 | FTIR spectra of 316L-SS, PDAM-SS and GSKi-SS.

rinsed samples were then fixed in 2.5% glutaraldehyde for 2 h, rinsed again with PBS thrice, and dehydrated in graded ethanol solution (50, 75, 90, and 100%). Finally, the samples were dried and observed by SEM (Gemini 300/VP field emission scanning electron microscope, Zeiss, Germany).

2.4 Cell Experiments

2.4.1 Cell Viability

Complete DMEM was incubated with different samples in a 24-well plate for 24 h to obtain conditioned media, and media without substrate was used as a control. HCAECs were cultured at a density of 3,000 cells per well in a 96-well plate and cultured with normal DMEM complete media overnight. The next day, the media was changed to conditioned media and cultured for 24 h. Then, cell viability was detected using the Cell Counting Kit-8 (CCK-8, Dojindo) assay.

2.4.2 Cell Adhesion and Proliferation

HCAECs were seeded onto different samples at a density of 15,000 cells per well in a 24-well plate. After 2 h of incubation, the cells were fixed in 4% paraformaldehyde for 20 min and blocked with PBS containing 5% BSA for 30 min. Then, 4′,6-diamidino-2-phenylindole (DAPI, 1 μg/ml, Sigma) was used to stain nuclei for 5 min. Then, the adhesion of cells was observed by a confocal laser microscope (LSM 780, Zeiss, Germany). Six images in each channel were obtained for each sample. Image-Pro Plus software was used to calculate the number of cells.

A CCK-8 assay was performed to investigate cell proliferation in different samples. After 24 or 48 h of incubation, 50 μL CCK8 was added to 500 μL culture media and incubated with cells for 1 h at 37°C. One hundred microliters of supernatant was transferred to a 96-well plate, and the optical density was measured with a microplate reader at 450 nm wavelength after the instrument was blanked with PBS solution. Three replicates were prepared for each sample.

2.4.3 Cell Morphology

Cell morphology was determined by DAPI and fluorescein isothiocyanate (FITC)-labeled phalloidin (Sigma) staining. These fluorescent dyes are indicators of the cell nucleus and skeleton. Briefly, HCAECs were incubated on different samples for 2 or 24 h. Then, samples were fixed in 4% paraformaldehyde and blocked with PBS containing 5% BSA for 20 and 30 min, respectively. The cytoskeleton was labeled with 300 nM FITC-labeled phalloidin for 30 min followed by washing with PBS containing 0.1% Tween 20 thrice. DAPI (1 μg/ml) was used to stain nuclei for 5 min. Then, the cells were mounted on slides in glycerol with cover slips and observed with a confocal laser microscope.

2.5 Statistical Analysis

All numerical data are presented as the mean ± SD ($n \geq 3$). Statistical analysis was performed using one-way ANOVA. If the p-value was less than 0.05 ($^*p < 0.05$), the differences were considered statistically significant.

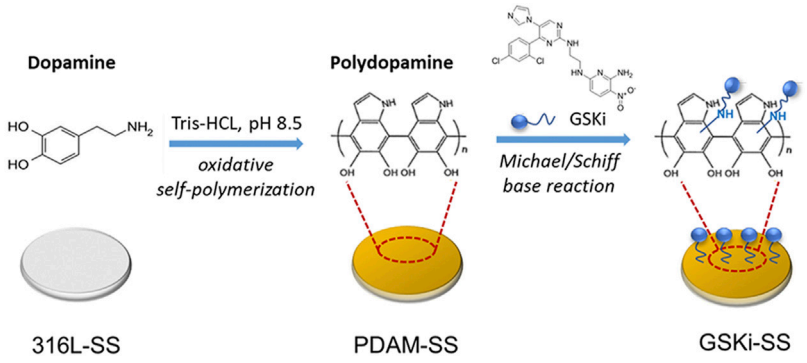

FIGURE 2 | Schematic diagram of the surface modification of 316L-SS.

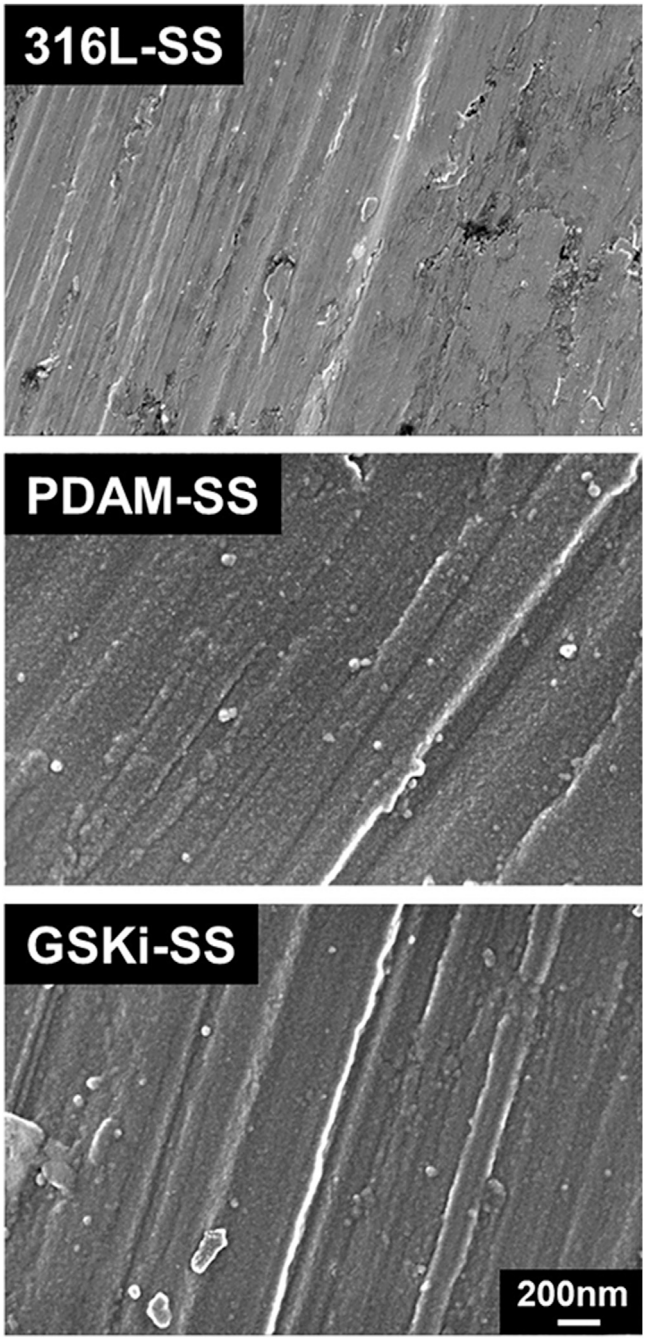

FIGURE 3 | SEM images of 316L-SS, PDAM-SS and GSKi-SS.

3 RESULTS AND DISCUSSION

3.1 Characterization of Surfaces

The FTIR results in **Figure 1** show that 316L-SS has no obvious absorption peak. The characteristic adsorption peaks of PDAM-SS at ~3,300 cm^{-1} (stretching vibration of phenolic O-H and N-H), 1,603 cm^{-1} (superposition of N-H bending vibration and stretching vibration of aromatic ring), 1,513 cm^{-1} (N-H shearing vibration), and 1,290 cm^{-1} (C-O stretching vibration) proved the existence of polydopamine layer on 316L stainless steel. Compared with PDAM-SS, GSKi-SS exhibits many changes in the FTIR spectrum. The peak at 1,541 cm^{-1} was assigned to amide II (N-H bending vibration), which indicated that GSKi was successfully immobilized on PDAM-SS. The catecholic groups in polydopamine coating offered the active sites to immobilize GSKi molecules.

A schematic diagram of the surface modification procedure of 316L-SS is shown in **Figure 2**. After 24 h of immersion in dopamine solution, the 31-SS substrates turned light brown in our experiments. The color of PDAM-SS did not change much after immersion in GSKi solution for an additional 24 h. Under weakly alkaline conditions, dopamine self-polymerized and formed a light brown polydopamine coating on the 316L-SS surface. The polydopamine layer is rich in catechol groups. These groups are easily oxidized to phenolic hydroxyl/quinone groups and undergo a Schiff base reaction or a Michael addition reaction with the primary amino group (-NH2) or secondary amino group (–NH) of GSKi (Yang et al., 2014; Madhurakkat Perikamana et al., 2015). Then, GSKi was covalently immobilized on the PDAM-SS surface through polydopamine coating.

The SEM results of 31-SS, PDAM-SS and GSKi-SS are shown in **Figure 3**. First, the stripes left on the surface of the original 316L-SS were caused by the polishing process. After 24 h of polydopamine coating, the surface morphology of 316L-SS changed significantly. Some nanoscale aggregation was observed on the PDAM-SS surface. However, the surface morphology changed slightly after GSKi was immobilized on the surface of PDAM-SS.

Dopamine is polymerized under weakly alkaline conditions (pH 8.5), and polymerized dopamine can be spontaneously deposited on many types of substrates, such as metals and polymers (Lee et al., 2007a; Yang et al., 2015). After the long-term coating process, polymerized dopamine changed the surface morphology of 316L-SS. It formed a thin adhesive layer and even

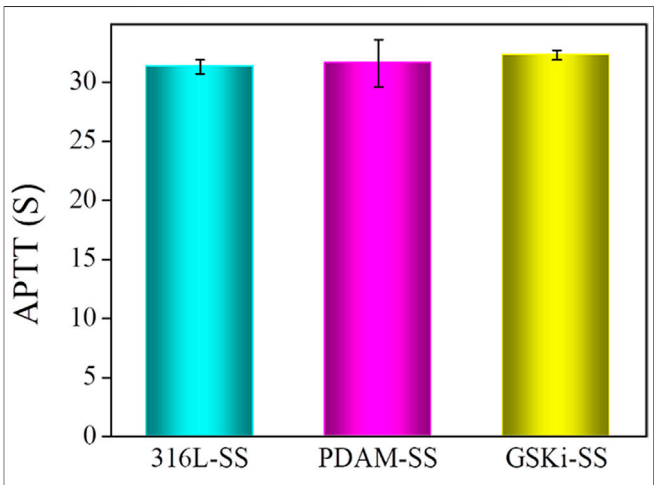

FIGURE 4 | APTT evaluation of 316L-SS, PDAM-SS and GSKi-SS (mean ± SD, $N = 3$).

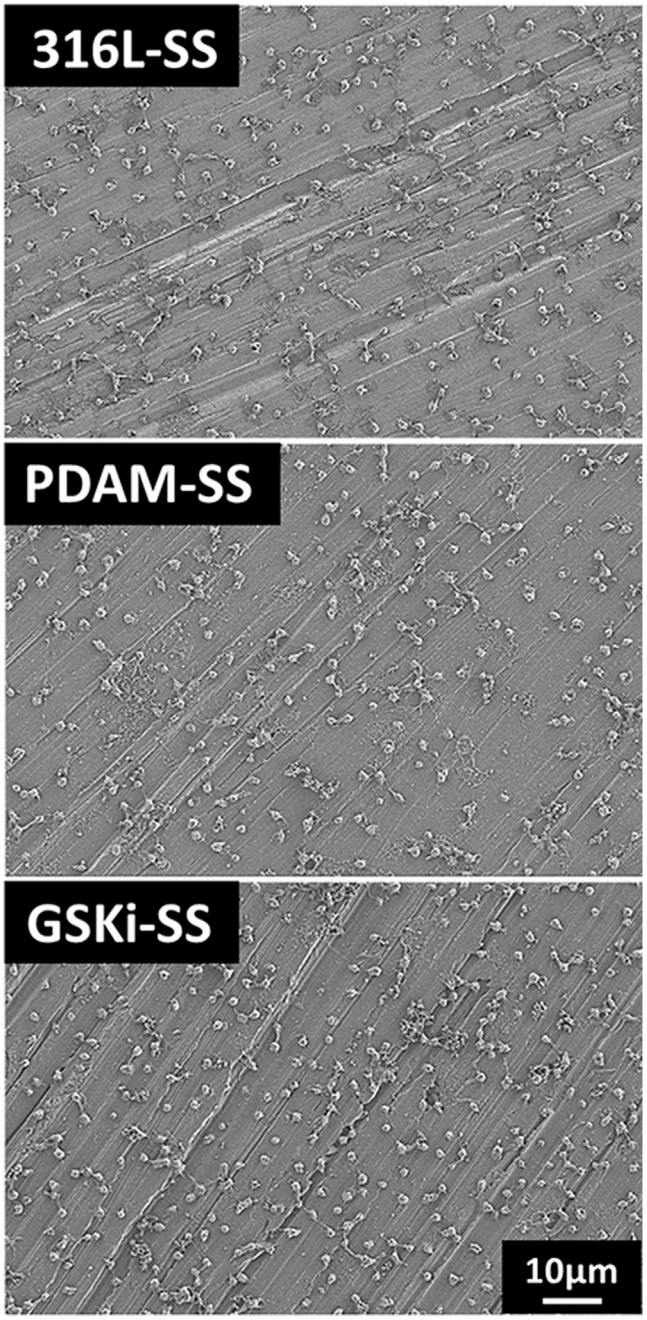

FIGURE 5 | Platelet adhesion on 316L-SS, PDAM-SS and GSKi-SS after contact with PRP for 2 h.

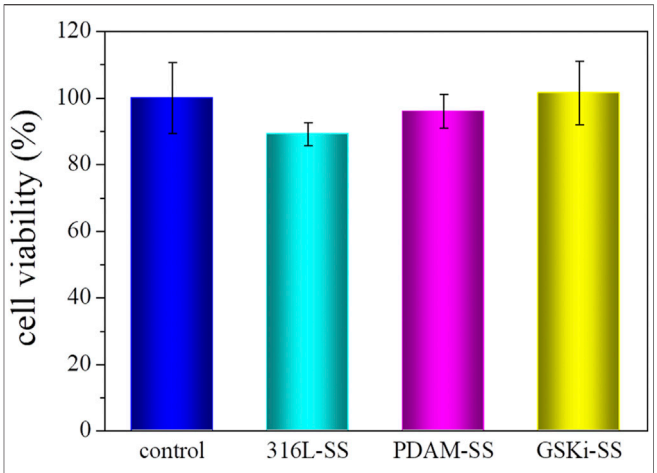

FIGURE 6 | HCAEC viability after incubation with 316L-SS, PDAM-SS and GSKi-SS for 24 h.

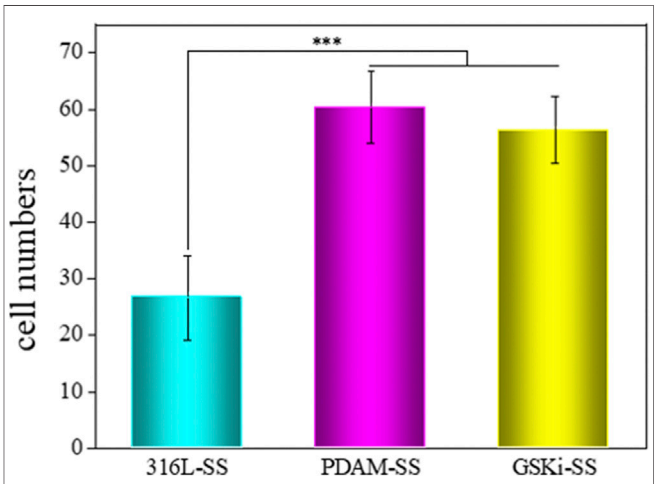

FIGURE 7 | Cell adhesion numbers on various samples after 2 h of incubation (mean ± SD, ***$p < 0.001$).

appeared as nanoaggregates or clumps on the surface of stainless steel plates, which was also reported in other studies (Yang et al., 2012b; Hong et al., 2013; Yang et al., 2015).

The surface hydrophobicity was evaluated by measuring the water contact angle of each sample. The results of 316L-SS, PDAM-SS and GSKi-SS are 53.9 ± 7.4°, 6.4 ± 1.1° and 40.7 ± 2.3°, respectively. The addition of polydopamine obviously improved the surface hydrophilicity of stainless steel plates. GSKi-SS is more hydrophobic than PDAM-SS.

The large amount of hydrophilic functional groups, such as phenolic hydroxyl groups and amino groups of the polydopamine coating, are potentially responsible for the improved hydrophilicity of PDAM-SS (Yang et al., 2010; Ding et al., 2014). The increased hydrophobicity of GSKi-SS may be due to the connection of GSKi with the phenolic hydroxyl group of the polydopamine coating, which resulted in a significant reduction of the hydrophilic group. The change in contact angle of the three samples indirectly demonstrated the successful coating of polydopamine and GSKi on the 316L-SS surface.

3.2 Hemocompatibility

For cardiovascular implant devices, improperly modified materials can trigger thrombus cascade reactions, which lead

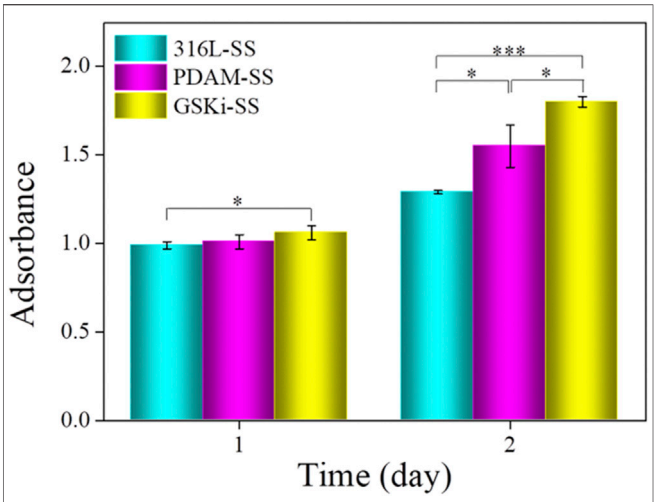

FIGURE 8 | Proliferation of HCAECs on various samples under serum condition (mean ± SD, $*p < 0.05$, $***p < 0.001$).

to implantation failure. APTT is a simple and highly reliable assay for the evaluation of the anticoagulant capacity of material surfaces (Lu et al., 2012). When stents with poor blood compatibility are implanted, the coagulation factor will bind to the stent surface to initiate the endogenous coagulation reaction, and the clotting time will be reduced during APTT detection (Basmadjian et al., 1997). The APTT results of 316L-SS, PDAM-SS, and GSKi-SS are shown in **Figure 4**. Compared with 316L-SS (31.33 ± 0.55 s), the values of PDAM-SS (31.63 ± 1.95 s) and GSKi-SS (32.3 ± 0.44 s) were not drastically altered. No significant difference was noted among the three groups ($p > 0.05$), indicating that these groups have similar anticoagulant properties. Therefore, the polydopamine and GSKi coating on 316L-SS did not obviously activate the endogenous coagulation system.

As a key step of thrombosis, platelet adhesion has been widely used to characterize the thrombogenic ability of materials. The adhesion morphology of platelets on materials can be divided into five grades: discoid, dendritic, partially spreading, spreading and aggregation (Goodman et al., 1989). To study the thrombogenic properties of PDAM- and GSKi-modified 316L stainless steel, platelets adhered to these sample surfaces were observed by SEM (as shown in **Figure 5**). The amount and morphology of platelets were similar in the three groups. All platelets showed discoid or partial dendritic morphology. This SEM result indicated that 316L-SS, PDAM-SS and GSKi-SS had similar anticoagulant properties, which was consistent with the results of the APTT test. Therefore, the polydopamine and GSKi coating on 316L-SS did not obviously activate the endogenous coagulation system.

3.3 Cellular Responses

To explore the neovascularization ability of modified stainless steel plates, it is necessary to study the growth behaviors of HCAECs in the three groups. **Figure 6** shows the cell cytotoxicity of 316L-SS, PDAM-SS and GSKi-SS after 24 h of cell culture. The tissue culture plate served as a control. The cell viability of each sample was not significantly different from that of the control group and was greater than 85%. This finding indicated that 316L-SS, PDAM-SS and GSKi-SS had good biocompatibility. The polydopamine and GSKi coating of 316L-SS did not lead to obvious cell cytotoxicity.

The adhesion and proliferation of endothelial cells on stent surfaces is necessary for the re-endothelialization of stents. **Figure 7** shows the number of cells attached to different stainless steel samples after 2 h of incubation. The cell

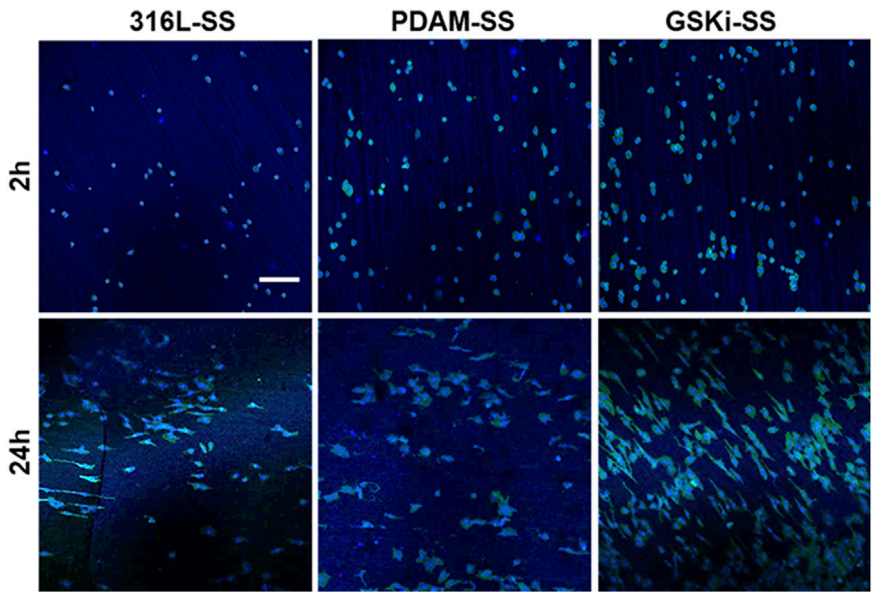

FIGURE 9 | Fluorescence images of HCAECs cultured on different samples for 2 and 24 h; the scale bar is 200 μm.

adhesion numbers for PDAM-SS and GSKi-SS were significantly greater than that of 316L-SS. No significant difference was noted between PDAM-SS and GSKi-SS. The surface properties of materials, such as topography, wettability and functional groups, play important roles in regulating cell behaviors (Flemming et al., 1999; Alves et al., 2010; Yuan et al., 2018; Amani et al., 2019; Shi et al., 2019). In this study, nanopolydopamine dots that appeared on the surface of PDAM-SS and GSKi-SS were thought to contribute to improving the adhesion of HCAECs. The strong protein adsorption capacity of the polydopamine coating also promoted the adhesion of cells on PDAM-SS (Ku et al., 2010; Yang et al., 2012b). Ma et al. reported that GSKi increases the attachment of endothelial progenitor cells to GSKi-coated stents (Ma et al., 2010). In our experiments, the HCAEC attachment efficiency of GSKi-SS was similar to that of PDAM-SS when cells were cultured for 2 h. The cell adhesion results indicated that PDAM-SS and GSKi-SS provided a more suitable microenvironment for the adhesion of HCAECs than 316L-SS.

The cell proliferation results of different samples are shown in **Figure 8**. Compared with 316L-SS, PDAM-SS did not obviously promote HCAEC proliferation until 48 h of culture. For the GSKi-SS group, cell proliferation increased after incubation for 24 h and was further significantly enhanced after 48 h. These results showed that both polydopamine and GSKi coating on stainless steel plates can promote HCAEC proliferation. GSKi more effectively improves cell proliferation than PDAM. GSKi protects endothelial cells by phosphorylating inactivated GSK3β, resulting in the accumulation of β-catenin in the endothelial nucleus, activating the Wnt signaling pathway and inhibiting endothelial cell apoptosis (Zhang et al., 2004). Choi et al. reported that GSKi stimulates VEGF expression in endothelial cells (Choi et al., 2004). *In vitro* studies we found that VEGF-immobilized surfaces accelerate endothelialization by increasing the adhesion, proliferation and migration of endothelial cells (Shin et al., 2012). Therefore, GSKi-SS yields better cell proliferation results than 316L-SS and PDAM-SS.

The morphology of HCAECs on different samples is shown in **Figure 9**. After culturing for 2 h, only a few cells adhered to 316L-SS. The number of adherent cells on PDAM-SS and GSKi-SS was significantly increased. Cells on PDAM-SS and GSKi-SS began to spread and showed similar morphological features. After 24 h of culture, the cell numbers obviously increased, and the cells completely spread on all three samples. GSKi-SS showed a significant increase in cell coverage and proliferation compared with PDAM-SS and 316L-SS.

The nano and microscale architecture of material surfaces can modulate endothelial cell structure and function (Leclech et al., 2020). Cells on along the microgrooves on the stainless steel surface in the GSKi-SS samples exhibited a more elongated, unidirectional and polarized morphology than those in the 316L-SS and PDAM-SS groups. These slender HCAECs were thought to not only have stronger proliferative capacity and extracellular matrix secretion but also have a faster migration rate than fully spread cells (Yang et al., 2012a). This fluorescence result was consistent with the cell adhesion and proliferation results shown in **Figure 8**.

4 CONCLUSION

In this study, GSKi was successfully introduced on the surface of 316L stainless steel through polydopamine to form a stable bioactive coating. Blood compatibility tests indicated that the addition of GSKi did not obviously affect the hemocompatibility of 316L-SS. Cell experiments revealed that the GSKi coating significantly promoted the adhesion and proliferation of HCAECs on stainless steel surfaces. Compared with 316L-SS and PDAM-SS, cells on GSKi-SS exhibited a more elongated, unidirectional and polarized morphology along the microgrooves on the stainless steel surface. These results suggested that this surface modification strategy of stable GSKi coating has potential application in the modification of cardiovascular stents.

DATA AVAILABILITY STATEMENT

The original contributions presented in the study are included in the article/Supplementary Material, further inquiries can be directed to the corresponding author.

AUTHOR CONTRIBUTIONS

Writing—original draft preparation, MZ; writing—review and editing, XS; investigation, HS; methodology, DX; software, YG; data curation, XW and JQZ; conceptualization—review and editing, JCZ; All authors have read and agreed to the published version of the manuscript. All authors contributed to manuscript revision and read and approved the submitted version.

FUNDING

This project was supported by the National Key Research and Development Program of China (2016YFC1100701), the Capital Construction Funds within the Provincial Budget (2019C045-6), the Natural Science Foundation of Jilin Province (20200201381JC), the Science Foundation of Jilin Education Department (JJKH20201097KJ), and the Graduate Innovation Fund of Jilin University (101832018C072).

REFERENCES

Alves, N. M., Pashkuleva, I., Reis, R. L., and Mano, J. F. (2010). Controlling Cell Behavior through the Design of Polymer Surfaces. *Small* 6 (20), 2208–2220. doi:10.1002/smll.201000233

Amani, H., Arzaghi, H., Bayandori, M., Dezfuli, A. S., Pazoki-Toroudi, H., Shafiee, A., et al. (2019). Controlling Cell Behavior through the Design of Biomaterial Surfaces: A Focus on Surface Modification Techniques. *Adv. Mater. Inter.* 6 (13), 1900572. doi:10.1002/admi.201900572

Avci-Adali, M., Ziemer, G., and Wendel, H. P. (2010). Induction of EPC Homing on Biofunctionalized Vascular Grafts for Rapid *In Vivo* Self-Endothelialization - A Review of Current Strategies. *Biotechnol. Adv.* 28 (1), 119–129. doi:10.1016/j.biotechadv.2009.10.005

Basmadjian, D., Sefton, M. V., and Baldwin, S. A. (1997). Coagulation on Biomaterials in Flowing Blood: Some Theoretical Considerations. *Biomaterials* 18 (23), 1511–1522. doi:10.1016/s0142-9612(97)80002-6

Choi, J.-H., Hur, J., Yoon, C.-H., Kim, J.-H., Lee, C.-S., Youn, S.-W., et al. (2004). Augmentation of Therapeutic Angiogenesis Using Genetically Modified Human Endothelial Progenitor Cells with Altered Glycogen Synthase Kinase-3β Activity. *J. Biol. Chem.* 279 (47), 49430–49438. doi:10.1074/jbc.M402088200

Choi, S.-E., Kang, Y., Jang, H.-J., Shin, H.-C., Kim, H.-E., Kim, H.-S., et al. (2007). Involvement of Glycogen Synthase Kinase-3β in Palmitate-Induced Human Umbilical Vein Endothelial Cell Apoptosis. *J. Vasc. Res.* 44 (5), 365–374. doi:10.1159/000102321

Cui, Y., Zhou, F., Wei, L., Song, Q., Tan, J., Zeng, Z., et al. (2018). *In Situ* Endothelialization Promoted by SEMA4D and CXCL12 for Titanium-Based Biomaterials. *Semin. Thromb. Hemost.* 44 (1), 070–080. doi:10.1055/s-0037-1605569

Ding, Y., Yang, Z., Bi, C. W. C., Yang, M., Xu, S. L., Lu, X., et al. (2014). Directing Vascular Cell Selectivity and Hemocompatibility on Patterned Platforms Featuring Variable Topographic Geometry and Size. *ACS Appl. Mater. Inter.* 6 (15), 12062–12070. doi:10.1021/am502692k

Doble, B. W., and Woodgett, J. R. (2003). GSK-3: Tricks of the Trade for a Multi-Tasking Kinase. *J. Cel. Sci.* 116, 1175–1186. doi:10.1242/jcs.00384

Eichmann, A., and Simons, M. (2012). VEGF Signaling inside Vascular Endothelial Cells and beyond. *Curr. Opin. Cel. Biol.* 24 (2), 188–193. doi:10.1016/j.ceb.2012.02.002

Ferrara, N., Gerber, H.-P., and LeCouter, J. (2003). The Biology of VEGF and its Receptors. *Nat. Med.* 9 (6), 669–676. doi:10.1038/nm0603-669

Flemming, R. G., Murphy, C. J., Abrams, G. A., Goodman, S. L., and Nealey, P. F. (1999). Effects of Synthetic Micro- and Nano-Structured Surfaces on Cell Behavior. *Biomaterials* 20 (6), 573–588. doi:10.1016/s0142-9612(98)00209-9

Goodman, S. L., Grasel, T. G., Cooper, S. L., and Albrecht, R. M. (1989). Platelet Shape Change and Cytoskeletal Reorganization on Polyurethaneureas. *J. Biomed. Mater. Res.* 23 (1), 105–123. doi:10.1002/jbm.820230109

Hibbert, B., Ma, X., Pourdjabbar, A., Holm, E., Rayner, K., Chen, Y.-X., et al. (2009). Inhibition of Endothelial Progenitor Cell Glycogen Synthase Kinase-3β Results in Attenuated Neointima Formation and Enhanced Re-endothelialization after Arterial Injury. *Cardiovasc. Res.* 83 (1), 16–23. doi:10.1093/cvr/cvp156

Hong, S., Kim, J., Na, Y. S., Park, J., Kim, S., Singha, K., et al. (2013). Poly(norepinephrine): Ultrasmooth Material-independent Surface Chemistry and Nanodepot for Nitric Oxide. *Angew. Chem. Int. Ed.* 52 (35), 9187–9191. doi:10.1002/anie.201301646

Kakinoki, S., Takasaki, K., Mahara, A., Ehashi, T., Hirano, Y., and Yamaoka, T. (2018). Direct Surface Modification of Metallic Biomaterials via Tyrosine Oxidation Aiming to Accelerate the Re-endothelialization of Vascular Stents. *J. Biomed. Mater. Res.* 106 (2), 491–499. doi:10.1002/jbm.a.36258

Ku, S. H., Ryu, J., Hong, S. K., Lee, H., and Park, C. B. (2010). General Functionalization Route for Cell Adhesion on Non-wetting Surfaces. *Biomaterials* 31 (9), 2535–2541. doi:10.1016/j.biomaterials.2009.12.020

Leclech, C., Natale, C. F., and Barakat, A. I. (2020). The Basement Membrane as a Structured Surface - Role in Vascular Health and Disease. *J. Cel. Sci.* 133 (18), jcs239889. doi:10.1242/jcs.239889

Lee, H., Dellatore, S. M., Miller, W. M., and Messersmith, P. B. (2007a). Mussel-inspired Surface Chemistry for Multifunctional Coatings. *Science* 318 (5849), 426–430. doi:10.1126/science.1147241

Lee, H., Lee, B. P., and Messersmith, P. B. (2007b). A Reversible Wet/dry Adhesive Inspired by Mussels and Geckos. *Nature* 448 (7151), 338–341. doi:10.1038/nature05968

Lee, H., Scherer, N. F., and Messersmith, P. B. (2006). Single-molecule Mechanics of Mussel Adhesion. *Proc. Natl. Acad. Sci.* 103 (35), 12999–13003. doi:10.1073/pnas.0605552103

Liang, C., Hu, Y., Wang, H., Xia, D., Li, Q., Zhang, J., et al. (2016). Biomimetic Cardiovascular Stents for *In Vivo* Re-endothelialization. *Biomaterials* 103, 170–182. doi:10.1016/j.biomaterials.2016.06.042

Lu, L., Li, Q.-L., Maitz, M. F., Chen, J.-L., and Huang, N. (2012). Immobilization of the Direct Thrombin Inhibitor-Bivalirudin on 316L Stainless Steel via Polydopamine and the Resulting Effects on Hemocompatibility *In Vitro*. *J. Biomed. Mater. Res.* 100 (9), 2421. doi:10.1002/jbm.a.34143

Luo, R., Tang, L., Zhong, S., Yang, Z., Wang, J., Weng, Y., et al. (2013). *In Vitro* investigation of Enhanced Hemocompatibility and Endothelial Cell Proliferation Associated with Quinone-Rich Polydopamine Coating. *ACS Appl. Mater. Inter.* 5 (5), 1704–1714. doi:10.1021/am3027635

Lynge, M. E., van der Westen, R., Postma, A., and Städler, B. (2011). Polydopamine-a Nature-Inspired Polymer Coating for Biomedical Science. *Nanoscale* 3 (12), 4916–4928. doi:10.1039/c1nr10969c

Ma, X., Hibbert, B., Dhaliwal, B., Seibert, T., Chen, Y.-X., Zhao, X., et al. (2010). Delayed Re-endothelialization with Rapamycin-Coated Stents Is Rescued by the Addition of a Glycogen Synthase Kinase-3β Inhibitor. *Cardiovasc. Res.* 86 (2), 338–345. doi:10.1093/cvr/cvq047

Madhurakkat Perikamana, S. K., Lee, J., Lee, Y. B., Shin, Y. M., Lee, E. J., Mikos, A. G., et al. (2015). Materials from Mussel-Inspired Chemistry for Cell and Tissue Engineering Applications. *Biomacromolecules* 16 (9), 2541–2555. doi:10.1021/acs.biomac.5b00852

Otsuka, F., Finn, A. V., Yazdani, S. K., Nakano, M., Kolodgie, F. D., and Virmani, R. (2012). The Importance of the Endothelium in Atherothrombosis and Coronary Stenting. *Nat. Rev. Cardiol.* 9 (8), 439–453. doi:10.1038/nrcardio.2012.64

Pang, J. H., Farhatnia, Y., Godarzi, F., Tan, A., Rajadas, J., Cousins, B. G., et al. (2015). *In Situ* Endothelialization: Bioengineering Considerations to Translation. *Small* 11 (47), 6248–6264. doi:10.1002/smll.201402579

Qi, P., Chen, S., Liu, T., Chen, J., Yang, Z., Weng, Y., et al. (2014). New Strategies for Developing Cardiovascular Stent Surfaces with Novel Functions (Review). *Biointerphases* 9 (2), 029017. doi:10.1116/1.4878719

Shi, X., Cui, L., Sun, H., Jiang, N., Heng, L., Zhuang, X., et al. (2019). Promoting Cell Growth on Porous PLA Microspheres through Simple Degradation Methods. *Polym. Degrad. Stab.* 161, 319–325. doi:10.1016/j.polymdegradstab.2019.01.003

Shin, Y. M., Lee, Y. B., Kim, S. J., Kang, J. K., Park, J.-C., Jang, W., et al. (2012). Mussel-inspired Immobilization of Vascular Endothelial Growth Factor (VEGF) for Enhanced Endothelialization of Vascular Grafts. *Biomacromolecules* 13 (7), 2020–2028. doi:10.1021/bm300194b

Skurk, C., Maatz, H., Rocnik, E., Bialik, A., Force, T., and Walsh, K. (2005). Glycogen-Synthase Kinase3β/β-Catenin Axis Promotes Angiogenesis through Activation of Vascular Endothelial Growth Factor Signaling in Endothelial Cells. *Circ. Res.* 96 (3), 308–318. doi:10.1161/01.RES.0000156273.30274.f7

Woods, T. C., and Marks, A. R. (2004). Drug-eluting Stents. *Annu. Rev. Med.* 55, 169–178. doi:10.1146/annurev.med.55.091902.105243

Wu, F., Li, J., Zhang, K., He, Z., Yang, P., Zou, D., et al. (2016). Multifunctional Coating Based on Hyaluronic Acid and Dopamine Conjugate for Potential Application on Surface Modification of Cardiovascular Implanted Devices. *ACS Appl. Mater. Inter.* 8 (1), 109–121. doi:10.1021/acsami.5b07427

Yang, Y., Qi, P., Ding, Y., Maitz, M. F., Yang, Z., Tu, Q., et al. (2015). A Biocompatible and Functional Adhesive Amine-Rich Coating Based on Dopamine Polymerization. *J. Mater. Chem. B* 3 (1), 72–81. doi:10.1039/c4tb01236d

Yang, Y., Qi, P., Wen, F., Li, X., Xia, Q., Maitz, M. F., et al. (2014). Mussel-Inspired One-step Adherent Coating Rich in Amine Groups for Covalent Immobilization of Heparin: Hemocompatibility, Growth Behaviors of Vascular Cells, and Tissue Response. *ACS Appl. Mater. Inter.* 6 (16), 14608–14620. doi:10.1021/am503925r

Yang, Z., Tu, Q., Wang, J., and Huang, N. (2012a). The Role of Heparin Binding Surfaces in the Direction of Endothelial and Smooth Muscle Cell Fate and Re-endothelialization. *Biomaterials* 33 (28), 6615–6625. doi:10.1016/j.biomaterials.2012.06.055

Yang, Z., Tu, Q., Zhu, Y., Luo, R., Li, X., Xie, Y., et al. (2012b). Mussel-inspired Coating of Polydopamine Directs Endothelial and Smooth Muscle Cell Fate for Re-endothelialization of Vascular Devices. *Adv. Healthc. Mater.* 1 (5), 548–559. doi:10.1002/adhm.201200073

Yang, Z., Wang, J., Luo, R., Maitz, M. F., Jing, F., Sun, H., et al. (2010). The Covalent Immobilization of Heparin to Pulsed-Plasma Polymeric Allylamine Films on 316L Stainless Steel and the Resulting Effects on Hemocompatibility. *Biomaterials* 31 (8), 2072–2083. doi:10.1016/j.biomaterials.2009.11.091

Yuan, Y., Shi, X., Gan, Z., and Wang, F. (2018). Modification of Porous PLGA Microspheres by Poly-L-Lysine for Use as Tissue Engineering Scaffolds. *Colloids Surf. B: Biointerfaces* 161, 162–168. doi:10.1016/j.colsurfb.2017.10.044

Zhang, F., Cheng, J., Hackett, N. R., Lam, G., Shido, K., Pergolizzi, R., et al. (2004). Adenovirus E4 Gene Promotes Selective Endothelial Cell Survival and Angiogenesis via Activation of the Vascular Endothelial-cadherin/Akt Signaling Pathway. *J. Biol. Chem.* 279 (12), 11760–11766. doi:10.1074/jbc.M312221200

Zhang, F., Zhang, Q., Li, X., Huang, N., Zhao, X., and Yang, Z. (2019). Mussel-inspired Dopamine-CuII Coatings for Sustained *In Situ* Generation of Nitric Oxide for Prevention of Stent Thrombosis and Restenosis. *Biomaterials* 194, 117–129. doi:10.1016/j.biomaterials.2018.12.020

Zhang, H., Xie, L., Deng, J., Zhuang, W., Luo, R., Wang, J., et al. (2016). Stability Research on Polydopamine and Immobilized Albumin on 316L Stainless Steel. *Regen. Biomater.* 3 (5), 277–284. doi:10.1093/rb/rbw030

Zhang, S., Zhang, Y., Bi, G., Liu, J., Wang, Z., Xu, Q., et al. (2014). Mussel-inspired Polydopamine Biopolymer Decorated with Magnetic Nanoparticles for Multiple Pollutants Removal. *J. Hazard. Mater.* 270, 27–34. doi:10.1016/j.jhazmat.2014.01.039

Conflict of Interest: The authors declare that the research was conducted in the absence of any commercial or financial relationships that could be construed as a potential conflict of interest.

Publisher's Note: All claims expressed in this article are solely those of the authors and do not necessarily represent those of their affiliated organizations, or those of the publisher, the editors and the reviewers. Any product that may be evaluated in this article, or claim that may be made by its manufacturer, is not guaranteed or endorsed by the publisher.

frontiers in Bioengineering and Biotechnology

REVIEW
published: 07 December 2021
doi: 10.3389/fbioe.2021.807357

Anti-Biofouling Polymers with Special Surface Wettability for Biomedical Applications

Zhoukun He[1], Xiaochen Yang[1,2], Na Wang[1,2], Linpeng Mu[1,2], Jinyuan Pan[1,2], Xiaorong Lan[3], Hongmei Li[4] and Fei Deng[5,6]**

[1]Institute for Advanced Study, Research Center of Composites and Surface and Interface Engineering, Chengdu University, Chengdu, China, [2]School of Mechanical Engineering, Chengdu University, Chengdu, China, [3]National Engineering Research Center for Biomaterials, Sichuan University, Chengdu, China, [4]School of Food and Biological Engineering, Chengdu University, Chengdu, China, [5]Department of Nephrology, Jinniu Hospital of Sichuan Provincial People's Hospital and Chengdu Jinniu District People's Hospital, Chengdu, China, [6]Department of Nephrology, Sichuan Academy of Medical Sciences and Sichuan Provincial People's Hospital, University of Electronic Science and Technology of China, Chengdu, China

OPEN ACCESS

Edited by:
Jianxun Ding,
Chinese Academy of Sciences, China

Reviewed by:
Jindan Wu,
Zhejiang Sci-Tech University, China
Shuaishuai Yuan,
Qingdao University of Science and Technology, China

***Correspondence:**
Xiaorong Lan
xiaoronglancdm@163.com
Fei Deng
dengfei_here@163.com

Specialty section:
This article was submitted to Biomaterials, a section of the journal Frontiers in Bioengineering and Biotechnology

Received: 02 November 2021
Accepted: 22 November 2021
Published: 07 December 2021

Citation:
He Z, Yang X, Wang N, Mu L, Pan J, Lan X, Li H and Deng F (2021) Anti-Biofouling Polymers with Special Surface Wettability for Biomedical Applications. Front. Bioeng. Biotechnol. 9:807357. doi: 10.3389/fbioe.2021.807357

The use of anti-biofouling polymers has widespread potential for counteracting marine, medical, and industrial biofouling. The anti-biofouling action is usually related to the degree of surface wettability. This review is focusing on anti-biofouling polymers with special surface wettability, and it will provide a new perspective to promote the development of anti-biofouling polymers for biomedical applications. Firstly, current anti-biofouling strategies are discussed followed by a comprehensive review of anti-biofouling polymers with specific types of surface wettability, including superhydrophilicity, hydrophilicity, and hydrophobicity. We then summarize the applications of anti-biofouling polymers with specific surface wettability in typical biomedical fields both *in vivo* and *in vitro*, such as cardiology, ophthalmology, and nephrology. Finally, the challenges and directions of the development of anti-biofouling polymers with special surface wettability are discussed. It is helpful for future researchers to choose suitable anti-biofouling polymers with special surface wettability for specific biomedical applications.

Keywords: anti-biofouling, antifouling, superhydrophilic, hydrophilic, hydrophobic

Abbreviations: BSA, bovine serum albumin; CLs, contact lens; E. coli, *escherichia coli*; FITC-BSA, fluorescein isothiocyanate conjugate-bovine serum albumin; FITC-HSA, fluorescein isothiocyanate conjugate-human serum albumin; IgG, immunoglobulin G; IOL, intraocular lens; MI-dPG, mussel-inspired dendritic polyglycerol; MPDSAH, (3-(methacryloylamino)propyl)-dimethyl (3-sulfopropyl) ammonium hydroxide inner salt; PAA, poly(acrylic acid); PCBAA, poly(carboxybetaine acrylamide); PCBMA, poly(carboxybetaine methacrylate); PCL, polycaprolactide; PDMS, poly(dimethyl siloxane); PEG, poly(ethylene glycol); PEGDA, poly(ethylene glycol) diacrylate; PEO, poly(ethylene oxide); PES, poly(ether sulfone); PHEMA, poly(2-hydroxyethyl methacrylate); PLA, poly(lactic acid); PMMA, poly(methyl methacrylate); PPGL, homopolymer grafts from α-tert-butoxy-ω-vinylbenzyl-polyglycidol; PSBMA, poly(sulfobetaine methacrylate); PSF, polysulfone; PU, polyurethanes; PVA, poly(vinyl alcohol); PVP, poly(N-vinyl pyrrolidone); S. aureus, *staphylococcus aureus*; SEM, scanning electron microscopy; S. epidermidis, staphylococcus epidermidis; WCA, water contact angle.

INTRODUCTION

The first known documentation of fouling is a papyrus dating from 412 BCE (1). To date, many kinds of fouling, such as dust, ice, crude oil, barnacles, bacteria, and blood, have been described and researched. Fouling has serious impacts on human life, as it degrades material surfaces, increases drag resistance in ships, and promotes infection in hospitals (1, (Almeida et al., 2007; He et al., 2021)). Our previous review defined four categories of foulant, namely, organic, inorganic, biofouling, and composite fouling (He et al., 2021). Biofouling is a persistent and widespread problem, the consequence of the aggregation of undesirable and often pathogenic organisms on surfaces, comprising biofilm produced by microorganisms and macroscale biofouling (macrofouling) resulting from foulants such as bacteria, cells, and proteins. As shown in **Figure 1**, biofouling usually begins with a surface film formed by organic molecules, to which different foulants attach, resulting in mixed communities that may undergo long-term changes over long periods of time (Rosenhahn et al., 2010). The presence of biofouling has significant impacts in various fields, including ships' hulls, water pipes, biosensors, filters, and in the biomedical field where it contaminates applications such as surgical products, sutures, and dressings (Liu et al., 2020a).

Biofouling has been divided into three categories: marine, industrial, and medical (Callow and Callow, 2011; Bixler et al., 2014). In marine and freshwater environments, biofouling involves the undesirable attachment of organisms to artificial surfaces, such as ceramic, metal, or plastic (Dobretsov et al., 2013; Mieszkin et al., 2013; Hu et al., 2020). In the medical field, microorganisms may attach to devices and biosensors, resulting in the infection of patients (Jorge et al., 2012; Ammons and Copié, 2013; Leslie et al., 2014; Gaw et al., 2017). In industrial situations, microorganisms may feed and proliferate using nutrients in membranes, eventually blocking the pores (Bixler and Bhushan, 2012). Biofouling of microbes and viruses to surfaces, especially for medical biofouling, still remains an urgent problem to be solved owing to their crucial roles in medical implants, CLs, catheters, hemodialyzers, biosensors, and respirators (Jorge et al., 2012; Ammons and Copié, 2013; Leslie et al., 2014; Gaw et al., 2017). For example, the COVID-19 emergency lasted nearly 2 years but there is still no sign of it disappearing. The COVID-19 virus as a new kind of biofoulant is probably inhibited to fouling the materials with an anti-biofouling ability. Suhas S. Joshi and coauthors reported that fullerene-coated anti-biofouling surfaces could be a possible solution to decrease the adhesion of the COVID-19 virus on the surface, as they will be hydrophobic and toxic to the virus envelope (Siddiquie et al., 2020a).

The use of chemical coatings based on biocides or enzymes is the initial strategy in the prevention of fouling (Lejars et al., 2012). Although these strategies are effective in fouling prevention, they may be toxic to animals and plants in terrestrial and marine environments if there are some harmful materials in the coatings (Yebra et al., 2004), such as organotin, copper, etc. Because of this, there are restrictions and even prohibitions on the use of such materials. A following developed strategy is the use of self-polishing coatings. These rely on the hydrolysis of side-chains or degradation of the main polymer chain (Zhang and Chiao, 2015; Yang et al., 2020). Nevertheless, these coatings still have adverse environmental. Thus, the traditionally used chemical and self-polishing coatings are not adequate for the complex conditions present in the world today (Zhang et al., 2016). In biomedical situations, it has been proposed to use materials that either prevent the attachment of microorganisms to devices or destroy them in the vicinity of the device. These materials include coatings that repel or prevent attachment or kill the microorganisms in the vicinity. A variety of polymers have been developed to counteract or reduce biofilm (Carr et al., 2011; Jorge et al., 2012; He et al., 2021), including: *1*) cationic or peptide-mimicking polymers, or composites that can retain and release bioactive compounds; and *2*) systems that can prevent microbial attachment by either physical or chemical means. Antifouling and antimicrobial coating may be differentiated by ability of the former to repel microbes or modify the structure of biofilm, while the latter have either bacteriostatic or bactericidal activities. Antifouling coatings use steric repulsion or nanoscale rough topography to prevent microbial attachment, while antimicrobial materials interact directly, resulting in microbial death through physical contact or the release of bactericidal compounds (Zheng et al., 2021). In general, environmentally safe and non-toxic antifouling polymer coating materials thus require specific attributes of surface chemical compositions and physical structures, which both significantly affect the surface wettability that can be quantified as the water droplets contact angle (WCA, 0–180°) on the surface (Zhu et al., 2012; He et al., 2013; Tian et al., 2014; Yu et al., 2015; Kuang et al., 2016; Martin et al., 2017; Yu et al., 2018; Li et al., 2019a; Zhu et al., 2019). As defined by Young's equation (Young, 1805), the Wenzel model (Wenzel, 1936), and the Cassie-Baxter model (Cassie and Baxter, 1944), the surface wettability can be described as superhydrophilic (WCA <10°), hydrophilic (WCA <90°), hydrophobic (WCA ≥90°), and superhydrophobic (WCA ≥150°), as shown in **Figure 2**.

Since the surface wettability and antifouling action of coatings are dependent on the properties, both chemical compositions and physical structures, of the surfaces (Maan et al., 2020), there should be some relationship between the surface wettability and antifouling ability of materials. Actually, many organisms with antifouling ability such as Lotus Leaf, Rice Leaf, and Shark Skin have a natural special surface wettability. After the design principle of materials with special surface wettability has been proposed by Lei Jiang et al. (Su et al., 2016), alterations in surface wettability allow the fine-tuning of bionic antifouling coatings and such techniques have attracted much attention over the past decade (He et al., 2021). The fluoro- and silicone-based hydrophobic polymers used in traditional antifouling materials reduce the attachment of the fouling substances to the surface (Lejars et al., 2012; Dobretsov and Thomason, 2011; Liang et al., 2020; Carl et al., 2012). Together with the chemical composition

[1]http://corrosion-doctors.org/Seawater/Fouling.htm

[1]http://corrosion-doctors.org/Seawater/Fouling.htm

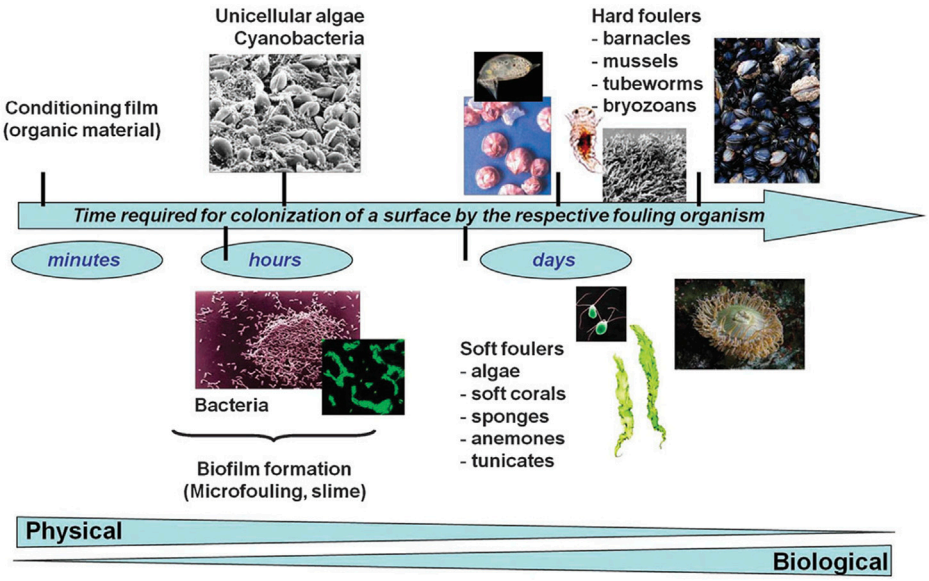

FIGURE 1 | Surface colonization by a fouling organism. Reprinted with permission from Ref. (Rosenhahn et al., 2010). Copyright 2010, Royal Society of Chemistry.

of the material, physical properties including the "Lotus Leaf," "Rice Leaf," and "Shark Skin" effects also influence the antifouling action (Zhang et al., 2016; Zhao and Liu, 2016; Shi et al., 2015; Lee and Yong, 2015; Roach et al., 2008; Pan et al., 2019; Jiang et al., 2015; Ball, 1999; Pu et al., 2016; Azemar et al., 2015; Kang et al., 2013; Bixler and Bhushan, 2013; Zhu et al., 2010; Bixler and Bhushan, 2014; Wu et al., 2011; Lee et al., 2013; Xia and Jiang, 2008). Engineered micro-topographical structures together with specific chemicals are commonly used for bionic implementation (Scardino and de Nys, 2011; Zarghami et al., 2019). Jie Zheng and coauthors have reviewed hydrophilic non-fouling materials and emphasized the importance of using strongly hydrated groups with optimal physical attributes on the material surface, concluding that, together with methods for coating surfaces, are critical for the development of stable and successful non-fouling materials for use in biomedical devices and applications (Chen et al., 2010). As shown in **Figure 3**, we have comprehensively reviewed the antifouling strategies for the four types of fouling according to different super-phobic surfaces, namely, superhydrophobicity in air (He et al., 2011; Martin and Bhushan, 2017), superoleophobicity in air (Chen et al., 2019; Li et al., 2020), superhemophobicity in air (Movafaghi et al., 2017; Galante et al., 2020), and underwater superoleophobicity (Du et al., 2017; Su et al., 2018).

In this review, we will focus on the anti-biofouling strategies, because the removal of fouling resulting from the deposition of organic or inorganic material is usually easier than eliminating biofouling. Superhydrophobic or superoleophobic surfaces are often able to prevent and release inorganic fouling, while superoleophobic surfaces or surfaces with underwater superoleophobicity are suitable for organic contaminants. Biofouling, however, usually involves a variety of foulants, and the solution is not simple. The most effective method, in terms of both cost and efficacy, is the use of surface wettability to counteract the attachment of foulants. Actually, an anti-biofouling surface can be achieved by tuning its surface wettability (Krishnan et al., 2008; He et al., 2021). For instance, anti-biofouling measures directed against bacteria

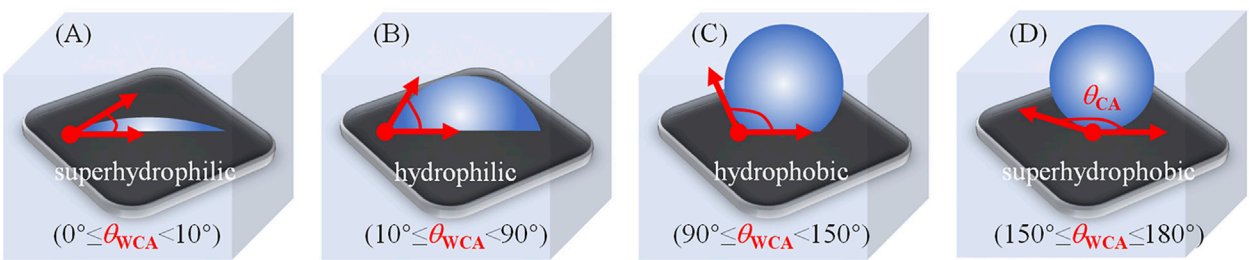

FIGURE 2 | Diagrams of the degree of WCA (θ_{WCA}) and water droplets on the four surface types in air. Reprinted with permission from Ref from Ref. (He et al., 2021). Copyright 2021, Elsevier B.V.

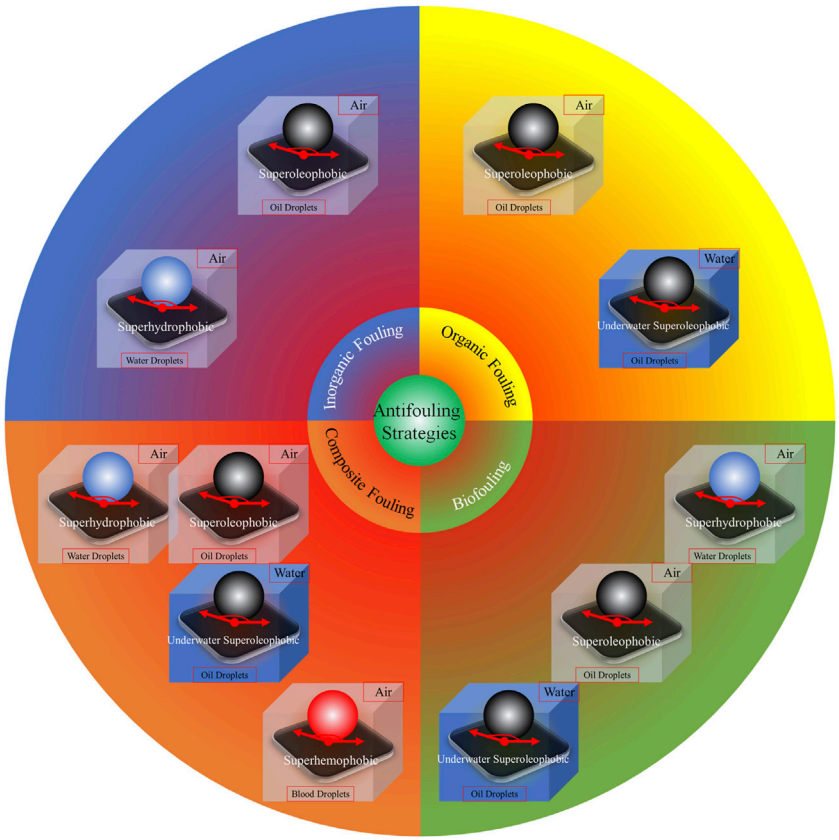

FIGURE 3 | Antifouling strategies based on various super-phobic surfaces. Reprinted with permission from Ref. (He et al., 2021). Copyright 2021, Elsevier B.V.

rely on hydrophilic or superhydrophobic effects (Liu et al., 2020b). In addition, surfaces with superhydrophobicity, usually containing a layer of air that blocks contact between the foulant and the surface (Simovich et al., 2020), are effective against fouling, as shown in **Figure 3**.

Biofouling extensively exists in biomedical applications both *in vivo* and *in vitro*, such as cardiology, ophthalmology, nephrology, and various surgical equipment. Bacteria, cells, and proteins usually adhere to and forming dense collagenous capsule around the biomedical implants, which would induce inflammatory responses, and may give rise to infection and/or implant rejection (Chan et al., 2020). Thus, in view of the necessity for anti-biofouling in biomedical applications, we will focus on the anti-biofouling strategies based on polymers with special surface wettability such as superhydrophilicity, hydrophilicity and hydrophobicity but excluding superhydrophobicity which can be found in our previous review (He et al., 2021). Meanwhile, we just focus on the biomedical applications in cardiology, ophthalmology, and nephrology. Moreover, biofoulants mentioned in this review are focused on the usual bacteria, cells, and proteins. Although there are some reviews about antifouling polymers (Lejars et al., 2012; Wu et al., 2019; Maan et al., 2020), our review is focusing on anti-biofouling polymers with special surface wettability, and it will provide a new perspective to promote the development of anti-biofouling polymers. Meanwhile, the anti-biofouling strategies reviewed in this manuscript will offer help for future researchers to choose suitable polymers for specific anti-biofouling applications.

ANTI-BIOFOULING POLYMERS WITH SPECIAL SURFACE WETTABILITY

Anti-biofouling polymers are attractive as they can avoid the introduction of drugs to achieve anti-biofouling but their efficacy is determined by the polymer and foulant species (Francolini et al., 2015). As summarized in **Table 1**, numerous proposals with various surface wettability have been reported to generate anti-biofouling ability. The various types of polymers and biofoulants are also listed in **Table 1**, which clearly reveals the relationship between the polymers and foulants (bacteria, cells, proteins, etc.).

Superhydrophilicity

Surfaces that prevent both microbial attachment and non-specific protein adsorption are required in the biomedical sphere. These should be hydrophilic as the polymer surface should bind water in preference to microorganisms. Wetting is thus an important consideration (Chen et al., 2010). According to these criteria, a number of anti-biofouling polymers have been developed that

TABLE 1 | A summary of polymers with different surface wettability and the relevant types of foulants for anti-biofouling applications (sorted in alphabetical order of the description of the typical polymers for each special surface wettability).

Strategy based on surface wettability	WCA(°)	Typical polymers	Foulants	Ref
Superhydro-philicity	0	MI-dPG	(a) Bacteria: *E. coli*, *S. aureus*	Li et al. (2019b)
	<5	PCBAA	(a) Cells: GLC-82 cells (b) Proteins: FITC-BSA, FITC-HSA (c) Blood: Blood cells, Blood proteins	Xu et al. (2017)
	0	Pluronic® F127	(a) Cells: L929 (b) Proteins: Fibrinogen, BSA.	Zheng et al. (2010)
	0	PPGL	(a) Proteins: Anti-BSA, Anti-myoglobin	Gam-Derouich et al. (2011)
	6	Sulfobetaine silane	(a) Bacteria: *P. aeruginosa*, *S. epidermidis* (b) Proteins: BSA, Mucin, Lysozyme, Liposomes	Yeh et al. (2014)
	10	Zwitterionic bottlebrush polymers	(a) Bacteria: *E. coli* (b) Proteins: BSA, Lysozyme, β-Lactoglobulin	Xia et al. (2019)
	7	Zwitterionic hydrogels	(a) Bacteria: *S. aureus*, *E. coli* (b) Cells: Human primary dermal fibroblasts, Red blood cells (c) Proteins: BSA (d) Blood: Platelets	Chan et al. (2020)
Hydrophilicity	28	PAA	(a) Proteins: BSA (b) Cells: L929 cells (c) Blood: Blood erythrocytes	Lei et al. (2021)
	27	PCBAA	(a) Bacteria: *E. coli*, *S. aureus* (b) Cells: L929 (c) Protein: BSA, HRP-conjugated anti-IgG	Wang et al. (2018); Zhang et al. (2021a)
	26–74	PEG	(a) Bacteria: *S. epidermidis*, *S. aureus*, *P. aeruginosa* (b) Cells: Human corneal epithelial cells (c) Proteins: BSA, Lysozyme (d) Fungi: C. albicans, F. solani	Cheng et al. (2015); Wang and He, (2019)
	41	PEGDA	(a) Blood: Platelet-rich-plasma	Guo et al. (2019)
	41	PEGylated	(a) Cells: NIH 3T3 cells (b) Protein: BSA.	Chen et al. (2015a)
	58	PEO	(a) Bacteria: *S. aureus*	Martínez-Gómez et al. (2015)
	60	PHEMA	(a) Protein: BSA (b) Blood: Platelet.	Zhu et al. (2015)
	25	Pluronic® F127	(a) Cells: L929 (b) Proteins: Fibrinogen, BSA.	Zheng et al. (2010)
	72	Poloxamers 338	(a) Bacteria: *E. coli*	Stirpe et al. (2020)
	17	Poly(carboxylbetaine-co-dopamine methacrylamide) copolymer	(a) Bacteria: *E. coli*, *P. aeruginosa*, *S. aureus* (b) Fungi: C. albicans	Liu et al. (2020c)
	56	Poly (citric acid)	(a) Proteins: BSA	Abidin et al. (2016)
	36	Poly(p-phenylene terephthalamide)	(a) Bacteria: *E. coli* (b) Proteins: BSA	Chen et al. (2018)
	12–38	PSBMA	(a) Bacteria: *E. coli*, *S. epidermidis* (b) Cells: Human MG63 osteoblast, HT1080 fibroblast, L929 (c) Blood: Plasma protein, Blood platelets, Blood erythrocytes, Blood leukocytes	Chen et al. (2012); Sin et al. (2014); Li et al. (2017); Zhang et al. (2021b)
	63	PVA	(a) Proteins: BSA (b) Cells: L929 cells	Lan et al. (2021)
	20–60	PVP	(a) Bacteria: *S. aureus*, *E. coli* (b) Cells: L929 cells (c) Proteins: FITC-BSA, Fibrinogen, IgG, Lysozyme (d) Blood: Platelets	Telford et al. (2010); Ran et al. (2011); Wu et al. (2012); Jiang et al. (2013); Liu et al. (2013); Zhu et al. (2017)

(Continued on following page)

TABLE 1 | (*Continued*) A summary of polymers with different surface wettability and the relevant types of foulants for anti-biofouling applications (sorted in alphabetical order of the description of the typical polymers for each special surface wettability).

Strategy based on surface wettability	WCA(°)	Typical polymers	Foulants	Ref
	85	Segmented PU with -SO_3H	(a) Bacteria: *S. epidermidis*	Francolini et al. (2012)
	25–80	Others	(a) Bacteria: *S. aureus*, *E. coli* (b) Cells: L929 cells, Bovine aortic endothelial cells (c) Proteins: BSA, Fibrinogen, Lysozyme (d) Blood: Platelet-rich plasma, Platelet-poor plasma	Huang et al. (2011); Seo et al. (2011); Chen et al. (2014); Li et al. (2014); Xie et al. (2015); Yin et al. (2015); Wang et al. (2016); Valencia et al. (2018); Xie et al. (2018); Ji et al. (2019); Ye et al. (2019)
Hydrophobicity	125	2-perfluorooctylethyl methacrylate	(a) Proteins: FITC-BSA, Fibrinogen	Wang et al. (2015)
	100–147	PDMS, PU, silicone oil	(a) Bacteria: *E. coli*	Siddiquie et al. (2020b)
	101	Poly(siloxane-urethane)	(a) Proteins: BSA.	Santiago et al. (2016)
	106	Others	(a) Bacteria: *S. aureus*, *E. coli* (b) Proteins: BSA, Lysozyme	Kim et al. (2016); Wang et al. (2017)

effectively prevent the adhesion of proteins, cells, and bacteria. These include hydrophilic polymers (Epstein et al., 2012; Keefe et al., 2012; Chen et al., 2015a; Mohan et al., 2015; Zhu et al., 2015; Guo et al., 2019; Jiang et al., 2020), e.g., PEG, PEGylated polymers, PHEMA, polysaccharides, and zwitterionic polymers (Carr et al., 2011; Chen et al., 2012; Sin et al., 2014; He et al., 2016; Kang et al., 2016; Wang et al., 2018; He et al., 2019; Liu et al., 2020c; Erathodiyil et al., 2020; Su et al., 2020; Zhang et al., 2020; Zhang et al., 2021a; Zhang et al., 2021b; Zhou et al., 2021), e.g., PSBMA, PCBMA, and PCBAA. Although these polymers differ in their structures and chemistry, they are all able to bind strongly to water, resulting in the presence of a layer of water that reduces interaction and attachment between the surface and the foulant. Effective surface hydration is achieved through hydrogen bonding in the case of hydrophilic polymers, and ionic solvation in the case of zwitterionic materials (Liu et al., 2020a). In addition, some papers have been published on the synthesis and application of polyglycidol and its derivatives with various morphologies. For example, the PPGL with a WCA near zero showed a superhydrophilic character and good anti-biofouling ability tested in anti-BSA and anti-myoglobin experiments (Gam-Derouich et al., 2011).

Superhydrophilic anti-biofouling zwitterionic polymers show great potential for biomedical applications (Chan et al., 2020; Xu et al., 2017; Xia et al., 2019). Rongxin Su and coauthors reported an anti-biofouling three-block polymer with zwitterionic chains on the bottlebrush polymers that showed high stability in high-saline solutions and over an extensive pH range (Xia et al., 2019). The anti-biofouling properties benefited from a low WCA near 10° as demonstrated by serum albumin and lysozyme adsorption with ultralow fouling properties of lower than 0.2 ng cm^{-2} (Xia et al., 2019). Jackie Y. Ying and coauthors produced a novel superhydrophilic anti-biofouling, biocompatible hydrogel formed by the crosslinking of polymers with calcium and monomers of methacryloyl-L-lysine (MLL), a zwitterionic amino acid (Chan et al., 2020). The resultant hydrogel containing 30% MLL was found to be strongly porous with a high degree of water encapsulation. The WCA on a glass slide with hydrogel coating decreased to 7.6° and the superhydrophilic hydrogel was effective in preventing bacterial, cell, and protein adhesion. The anti-biofouling hydrogel did not form capsules when subcutaneously implanted in mice over 2 months (Chan et al., 2020). Lei Zhang and coauthors reported an efficient and simple strategy (**Figure 4A**) to modify hydrophobic electrospun meshes with zwitterionic PCBAA hydrogels to obtain superhydrophilic anti-biofouling meshes with WCAs of less than 5° (**Figures 4B,C**) (Xu et al., 2017). The coated superhydrophilic mesh resisted attachment of FITC-BSA, FITC-HSA proteins, and GLC-82 cells (**Figures 4D–4K**). Furthermore, the hydrogel structure retained its stability under physiological conditions for a minimum of 3 months. This report demonstrates an effective technique for modulating hydrophilic surfaces on different fibrous structures, and may have widespread biomedical applications.

Hydrophilicity

Among hydrophilic polymers, PEG-based polymers are probably the most investigated for biomedical applications, as PEG is both non-immunogenic and anti-thrombogenic, as well as being largely resistant to protein adsorption. The anti-biofouling action of PEG-based polymers is the result of both steric and hydration effects and is dependent on the size, branching, and surface-packing density of the specific PEG molecule (Francolini et al., 2015). A high degree of hydration on the surfaces of the polymers is necessary for effective anti-biofouling actions, although the molecular mechanisms and details involved are not fully understood. Jie Zheng and coauthors conducted a computational investigation of the properties of four poly(N-hydroxyalkyl acrylamide) (PAMs) brushes with different carbon spacer lengths (CSLs = 1, 2, 3, and 5) using molecular mechanics (MM), Monte Carlo (MC), and molecular dynamics (MD) simulations (Liu et al., 2020a). MM assessed the type of packing structure of the brushes, while MC simulations were used to evaluate the interaction between the brushes and a lysozyme, and MD was utilized for examining the interactions between the brushes, proteins, and water molecules. The results showed that minor variations in the CSL structure are able to influence both the surface hydration and antifouling properties of

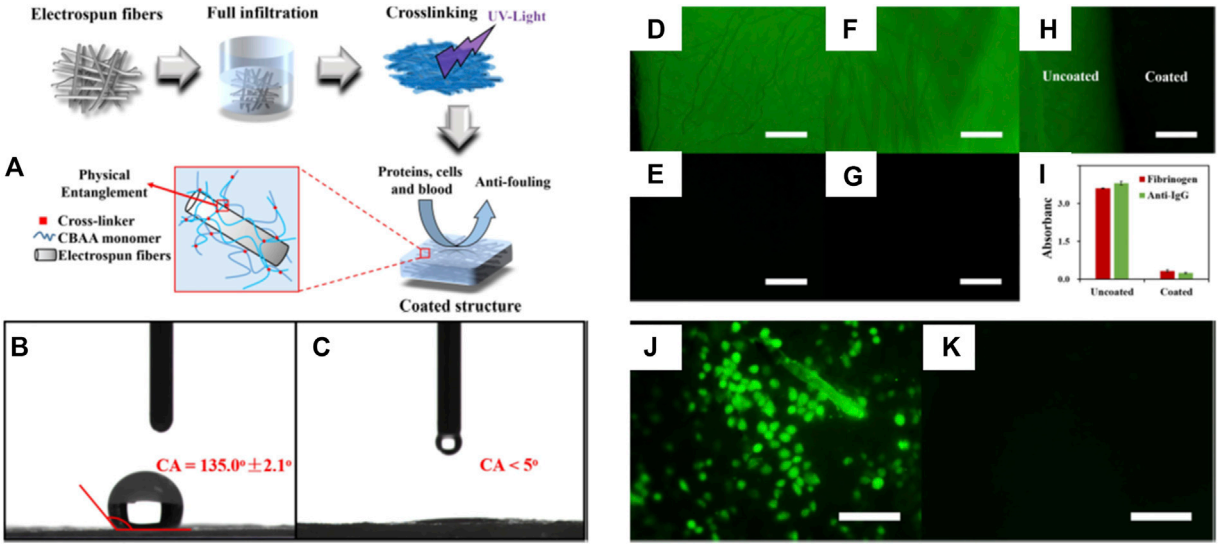

FIGURE 4 | The process of preparing anti-biofouling zwitterionic hydrogels **(A)**. WCA on uncoated mesh **(B)** and coated superhydrophilic mesh **(C)**. Fluorescence micrographs of FITC-BSA **(D,E)** and FITC-HSA **(F,G)** adsorption on uncoated **(D,F)** and coated structures **(E,G)**, respectively. Merge of uncoated and coated materials after FITC-BSA adsorption **(H)**, and the enzyme-linked immunosorbent assay (ELISA) results **(I)**. Fluorescence micrographs of cell adhesion test on uncoated mesh **(J)** and coated superhydrophilic mesh **(K)**. Scale bar = 100 μm. Reprinted with permission from Ref. (Xu et al., 2017). Copyright 2018, IOP Publishing, Ltd.

the surface, confirming experimental findings using surface plasmon resonance and sum frequency generation vibrational spectroscopy, as well as measurements of contact angles. These results promote improved understanding of PAM brushes and their properties in relation to anti-biofouling materials and surfaces (Liu et al., 2020a).

Polyurethane (PU) is a commonly used biocompatible polymer, being used in numerous biomedical engineering applications, including dressings, joints, and catheters. Adsorption of proteins to its surface frequently occurs in biological and medical situations, with consequent deleterious effects. Thus, investigation of PU-protein interactions is critical. Both the chemical constituents of the material and its physical topography influence adsorption, and these factors have been extensively investigated over the past few decades. These studies have demonstrated the efficacy of tethering hydrophilic polymers, such as PEO, to the surface. Surfaces modified in this way are strongly resistant to nonspecific protein adsorption, with both the lengths and densities of the PEO chains playing significant roles (Zheng et al., 2010).

In their investigation of suitable materials for preventing the complications of infection and thrombosis in devices making contact with the blood, Francolini and coauthors designed and synthesized a heparin-mimetic segmented PU (Francolini et al., 2012). This introduced sulfate and sulfamate moieties that are responsible for the anticoagulant activity of heparin onto PU. It was found that the modified PU was more hydrophilic than the parent compound. These polymers also reduced the degree of bacterial attachment, measured as colony-forming units (CFUs) found per cm^2 of polymer (**Figure 5A**). These observations were confirmed by SEM (**Figures 5B,C**), which demonstrated bacterial colonization and aggregation on surfaces lacking the -SO_3H groups (**Figure 5B**), and no accumulation of bacteria on surfaces with the -SO_3H groups (**Figure 5C**). These results show that increasing the hydrophilicity of the polymer as well as the addition of -SO_3H groups affected the antifouling action of the surface (Francolini et al., 2012).

Hydrophobicity

Hydrophilic anti-biofouling polymers tend to swell, resulting in lower space for interaction and thus reduced attachments (Rosenhahn et al., 2010; Eshet et al., 2011). The use of hydrophobic polymers can evade this issue. Hybrid poly(siloxane-urethane) copolymers were developed by Lourdes Irusta and coauthors using isophorone diisocyanate trimers, polycaprolactone triols, and hydroxy-terminated PDMS (Santiago et al., 2016). The authors then used quartz crystal microbalance with dissipation monitoring to measure BSA adsorption, observing that the protein was adsorbed in a conformation that did not allow water retention. This indicates that the increased surface hydrophobicity produced by the PDMS was responsible for the improved antifouling action of these copolymers (Santiago et al., 2016). Xinping Wang et al. described the preparation of acrylate block polymer brushes with two 2-perfluorooctylethyl methacrylate units at the brush end on an Au substrate with a "grafting to" method (Wang et al., 2015). It was found that the amount of fibrinogen adsorbed to the surface was reduced in proportion to the hydrophobicity of the perfluoroalkyl chains (Wang et al., 2015).

Suhas S. Joshi and coauthors investigated the effects of introducing femtosecond laser-induced submicron physical structures onto PDMS and PU surfaces for biomedical applications, as shown in **Figure 6** (Siddiquie et al., 2020b). Highly regular and single scale submicron laser-induced periodic surface structures (LIPSS), and multiscale structures (MS) containing both submicron- and micron-scale features were obtained by femtosecond laser processing on

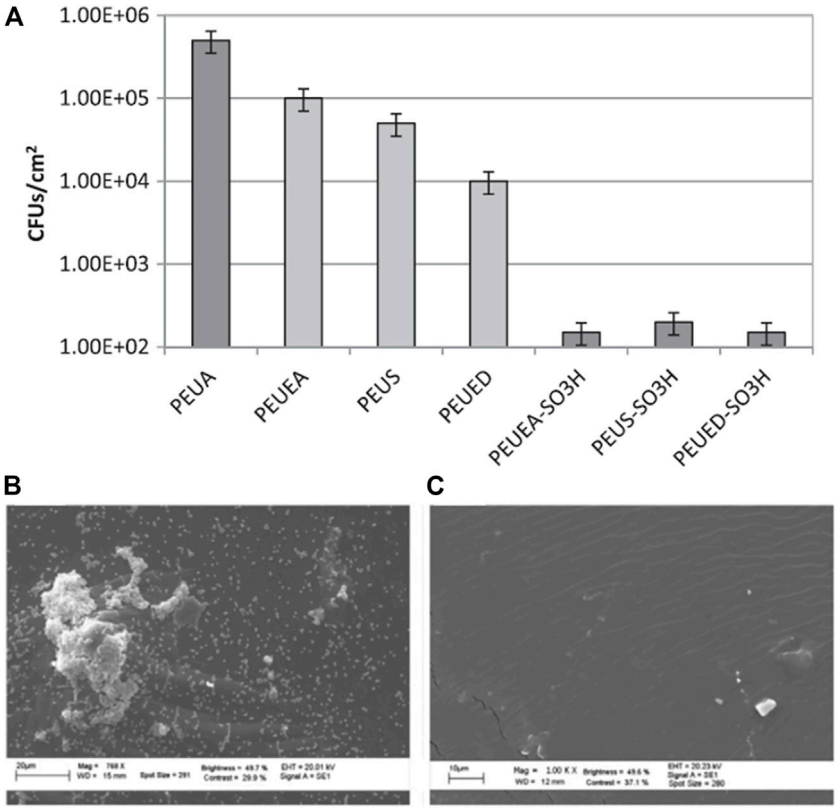

FIGURE 5 | *S. epidermidis* colony-forming units per cm^2 of PEUA (control), amidated, and -SO_3H group-containing polymers **(A)**. SEM results showing the aggregates of bacterial on the PEUA surface **(B)** and the absence of aggregates on the PEUEA–SO_3H surface **(C)** after 24 h of exposure. Reprinted with permission from Ref. (Francolini et al., 2012). Copyright 2012, Elsevier B.V.

stainless-steel (SS) substrates and following replicate processing with PDMS and PU elastomers. Surface hydrophobicity was enhanced on LIPSS and MSs surfaces (**Figure 6A**). It was observed that the hydrophobic submicron-textured PDMS and PU surfaces were stable and performed well for up to 100 h when immersed (**Figure 6B**). *E. coli* attachment was significantly reduced (>89%) on both LIPSS- and MS-modified surfaces (**Figures 6C,D**).

ANTI-BIOFOULING POLYMERS WITH SPECIAL SURFACE WETTABILITY FOR BIOMEDICAL APPLICATIONS

As discussed in **Section 2** above, various strategies to achieve different surface wettability can produce anti-biofouling ability for different biomedical applications with extensive alternative schemes. In this section, we will review the applications of anti-biofouling polymers with special surface wettability in typical biomedical fields both *in vivo* and *in vitro*, including cardiology, ophthalmology, and nephrology.

Heart Valves in Cardiology

Although the bioprosthetic heart valve (BHV) has been used in clinical applications, there are still some complications, including calcification and thrombosis, which will shorten the service life of BHV. Hydrophilic polymers such as PAA are usually utilized to enhance the anti-biofouling actions of materials (Zhang et al., 2021c). Our previous article proposed a strategy to fabricate a hydrophilic-coated anti-biofouling BHV using PAA and PDMS in the inner and outer valves (Lei et al., 2021). We evaluated the anti-biofouling properties, including anti-coagulation, anti-cell adhesion, anti-calcification, and ability to resist BSA adsorption, both *in vivo* and *in vitro* (**Figure 7**). The anti-biofouling-coated sample (PHIL) was significantly better than the GLUT-treated control sample in various tests, including attachment of L929 cells, whole blood, FITC-BSA, and calcification. These results indicate the effectiveness of this method to produce hemocompatible biomedical materials with good anti-biofouling abilities.

Polymeric heart valves have attracted much attention (Bezuidenhout et al., 2015; Guo et al., 2019; Kambe et al., 2019). Xing Zhang and coauthors reported that a composition of PEGDA hydrogels and polyethylene terephthalate/polyamide6 (PET-PA6) fabric (PEGDA/PET-PA6) was fabricated to form artificial heart valve leaflets (Guo et al., 2019). The WCA on the PET-PA6 fabric was about 129° (**Figure 8A**) but it decreased to about 41° (**Figures 8B,C**) after the introduction of PEGDA

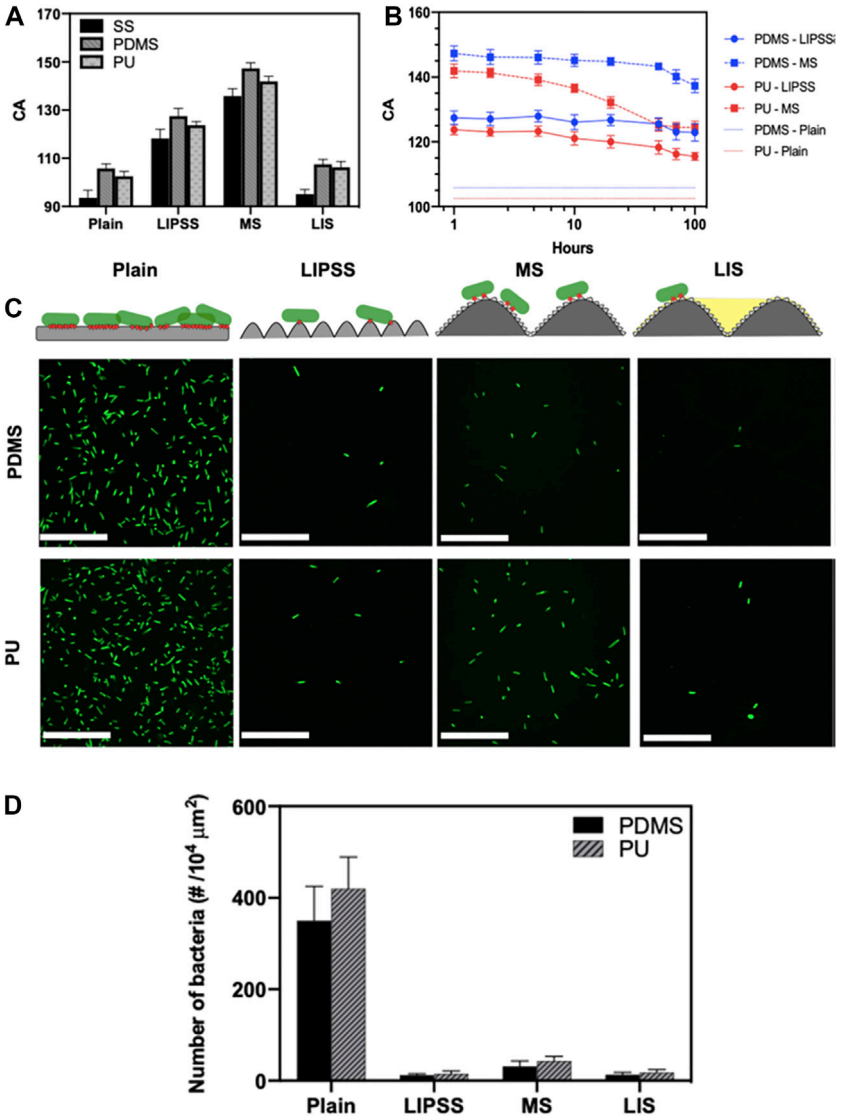

FIGURE 6 | Static WCA on unmodified, LIPSS-, and MSs-modified SS, PDMS, and PU surfaces **(A)**. Differences in water CA with different immersion times **(B)**. Bacteria on the different surfaces (**C**, above). Bacterial contacts on the surfaces are shown in red, and fluorescence micrographs indicate bacterial attachment to different PDMS and PU surfaces (below). Numbers of attached bacteria in relation to topography **(D)**. Reprinted with permission from Ref. (Siddiquie et al., 2020b). Copyright 2020, American Chemical Society.

hydrogels, showing an obvious increase of surface hydrophilicity. After porcine platelet-rich plasma was cultivated for 2 h, a few platelets were seen on the PET-PA6 material (**Figures 8D,E**), while none were visible on the PEGDA/PET-PA6 composite (**Figures 8F,G**). Therefore, the increased hydrophilicity from the PEGDA hydrogels could enhance the anti-biofouling ability of the composite artificial heart valve leaflets with a low thrombogenic risk when interacting with blood.

IOLs and CLs in Ophthalmology

Biofoulant adhesion, including the attachment of bacteria, cells, or proteins, to devices such as IOLs can result in the failure of the implant. We fabricated a simple and economical PVA coating with or without the introduction of a "bridge." The "bridge" comprised an intermediate adhesive layer (AL) to augment the interaction between the coating and the IOL material (**Figure 9A**) (Lan et al., 2021). Cell proliferation on the material was measured using CCK-8 assays (**Figure 9B**) and the adhesion of L929 cells measured by CLSM is shown in **Figure 9C**. The fluorescent protein adsorption performance and the fluorescence intensity of FITC-BSA on different samples were shown in **Figure 9D**. Increasing the PVA coating time to 10 s resulted in a reduction in the WCA to approximately 63°, in conjunction with augmented hydrophilicity and anti-biofouling action against both L929

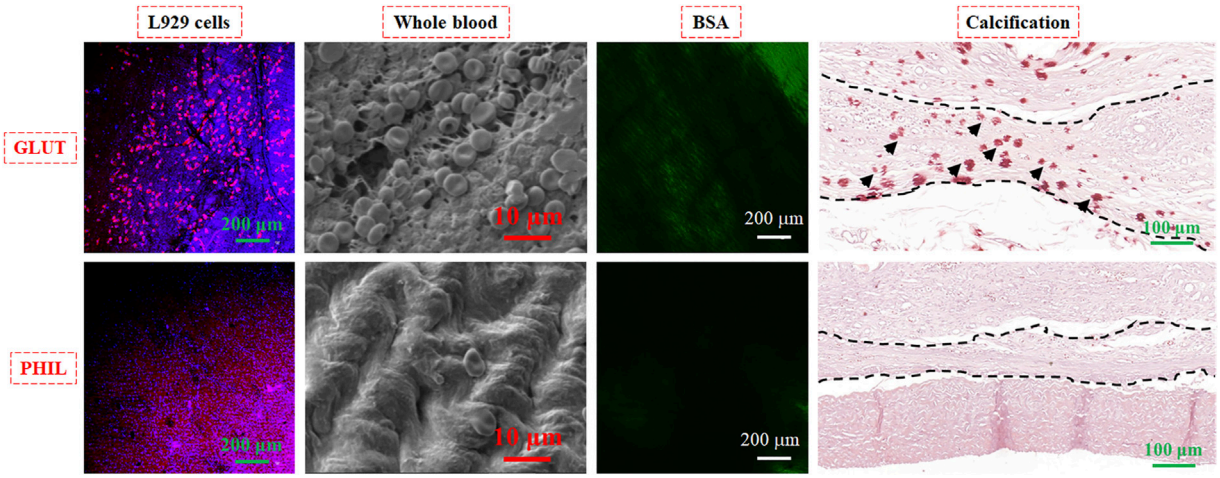

FIGURE 7 | Anti-biofouling behavior of L929 cells, whole blood, FITC-labeled BSA, and calcification experiments on pristine BHV treated with GLUT and the sample treated with anti-biofouling coating (PHIL). Reprinted with permission from Ref. (Lei et al., 2021).

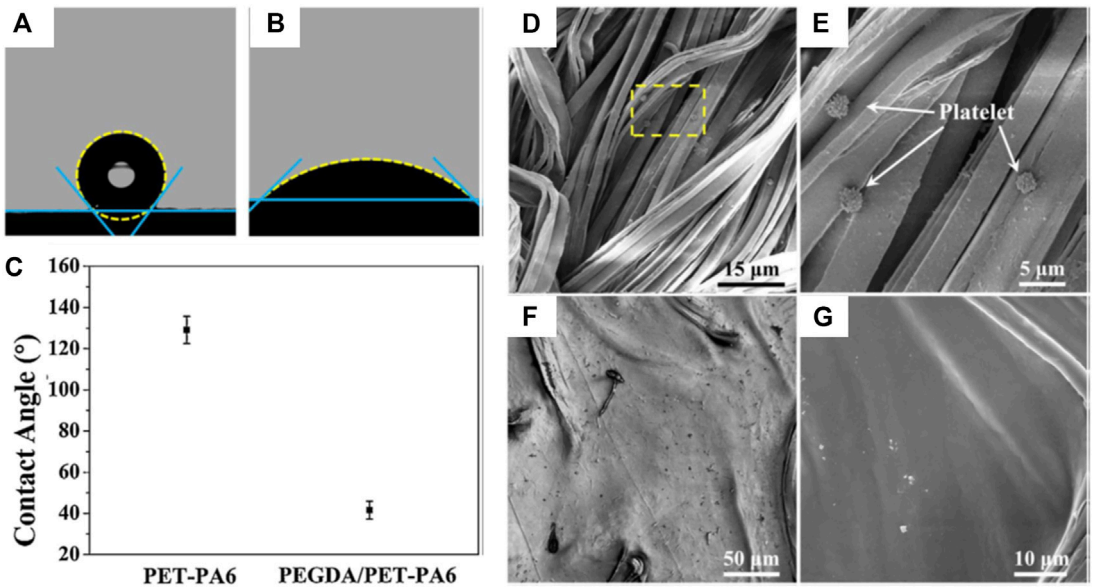

FIGURE 8 | Profiles of water droplets on PET-PA6 fabric **(A)** and PEGDA/PET-PA6 composite **(B)**, and WCA results of the samples **(C)**. SEM micrographs showing platelet adherence on the PET-PA6 fabric **(D,E)** and PEGDA/PET-PA6 composites **(F,G)**. Reprinted with permission from Ref. (Guo et al., 2019). Copyright 2019, Elsevier B.V.

cells and BSA. The coating prepared by AL "bridge" could greatly improve the mechanical stability of PVA coating on PMMA IOL surface to extend the lifetime of anti-biofouling ability, which could provide a new means of preparing a transparent hydrophilic anti-biofouling PVA coating applicable to IOLs.

Besides the IOL, CLs are a common application in ophthalmology and the development of anti-biofouling CLs would ensure safety. Gongyan Liu and coauthors introduced the zwitterionic anti-biofouling carboxybetaine groups onto the surface of CLs to significantly increase their wettability and reduce their adsorption of bacteria and proteins (Liu et al., 2020c). Yiyan Yang and coauthors reported a series of polymers that were conjugated with adhesive catechol, anti-biofouling PEG, and hydrophobic urea/ethyl onto branched poly(ethylenimine). The CLs were coated by immersing in aqueous solutions of the modified polymers, and the coating was found to tolerate autoclaving, remaining on the device for its lifetime of approximately 7 days (Cheng et al., 2015). Silicone is widely utilized in biomedical devices, and the most commonly used silicone is PDMS as it is transparent, inert, inflammable, and non-toxic. Chun-Jen Huang and

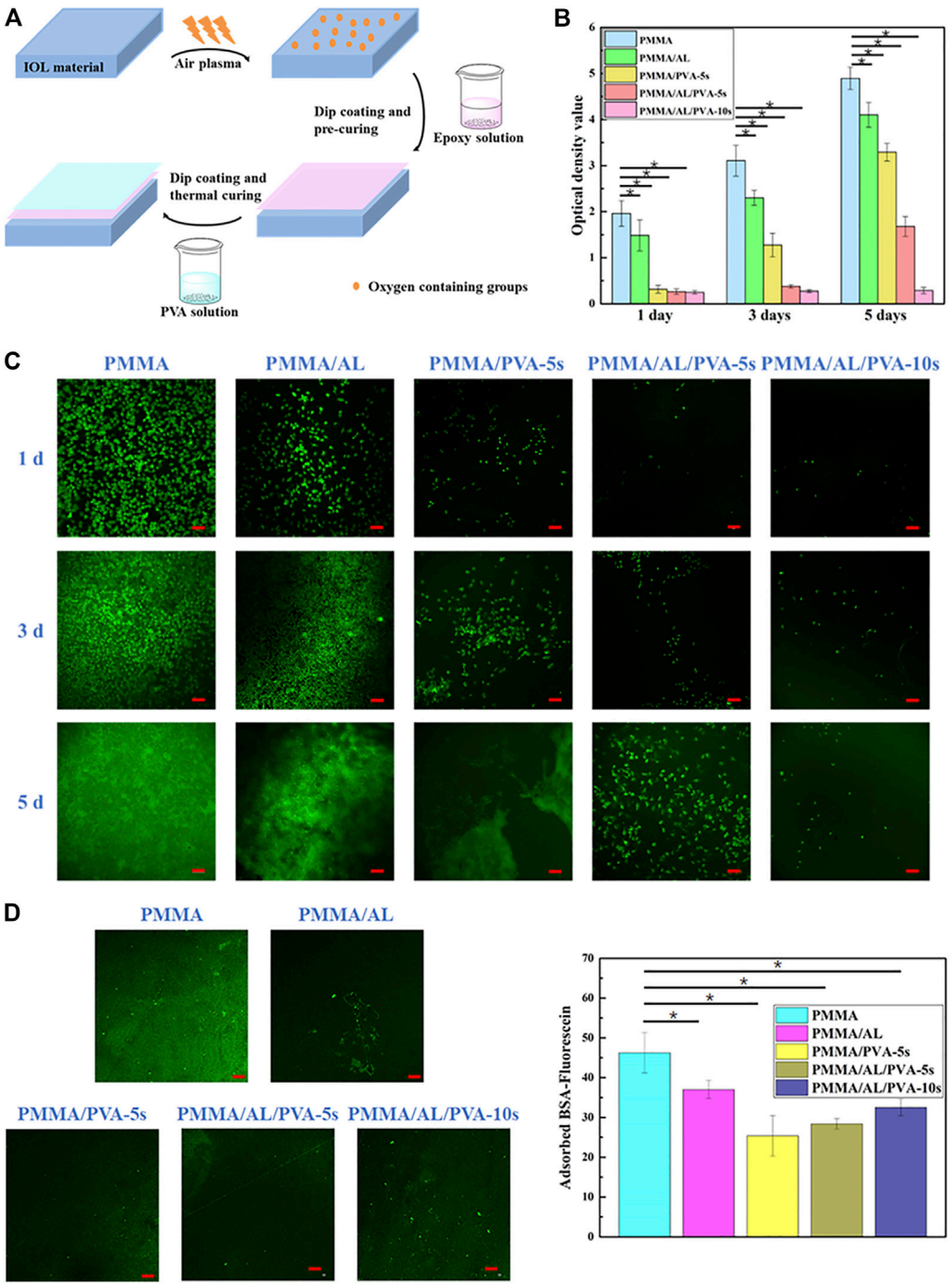

FIGURE 9 | Fabrication process of hydrophilic PVA with an intermediate AL on PMMA IOL surface **(A)**. Cell proliferation measured by CCK-8 assay **(B)** and proliferation at 1, 3, and 5 days pre- and post-modification **(C)**. Fluorescent protein absorbance **(D, left)** and the fluorescence intensity **(D, right)** of FITC-BSA in different samples. Reprinted with permission from Ref. (Lan et al., 2021). Copyright 2021, Royal Society of Chemistry.

coauthors developed a stable superhydrophilic zwitterionic interface on PDMS by covalent silanization of sulfobetaine silane (SBSi) (Yeh et al., 2014). This was effective against biofouling by both *Pseudomonas aeruginosa* and *S. epidermidis* even after storage for 30 days at room temperature (**Figures 10A–C**), and the SBSi-modified commercially available silicone hydrogel CLs showed similar excellent anti-biofouling ability. Meanwhile, the adsorption of BSA, mucin, lysozyme (**Figures 10D–F**) and sulforhodamine B sodium (SRB)-encapsulated liposomes (**Figures 10G,H**) on SBSi-tailored PDMS showed an obvious decrease compared with that on pure PDMS.

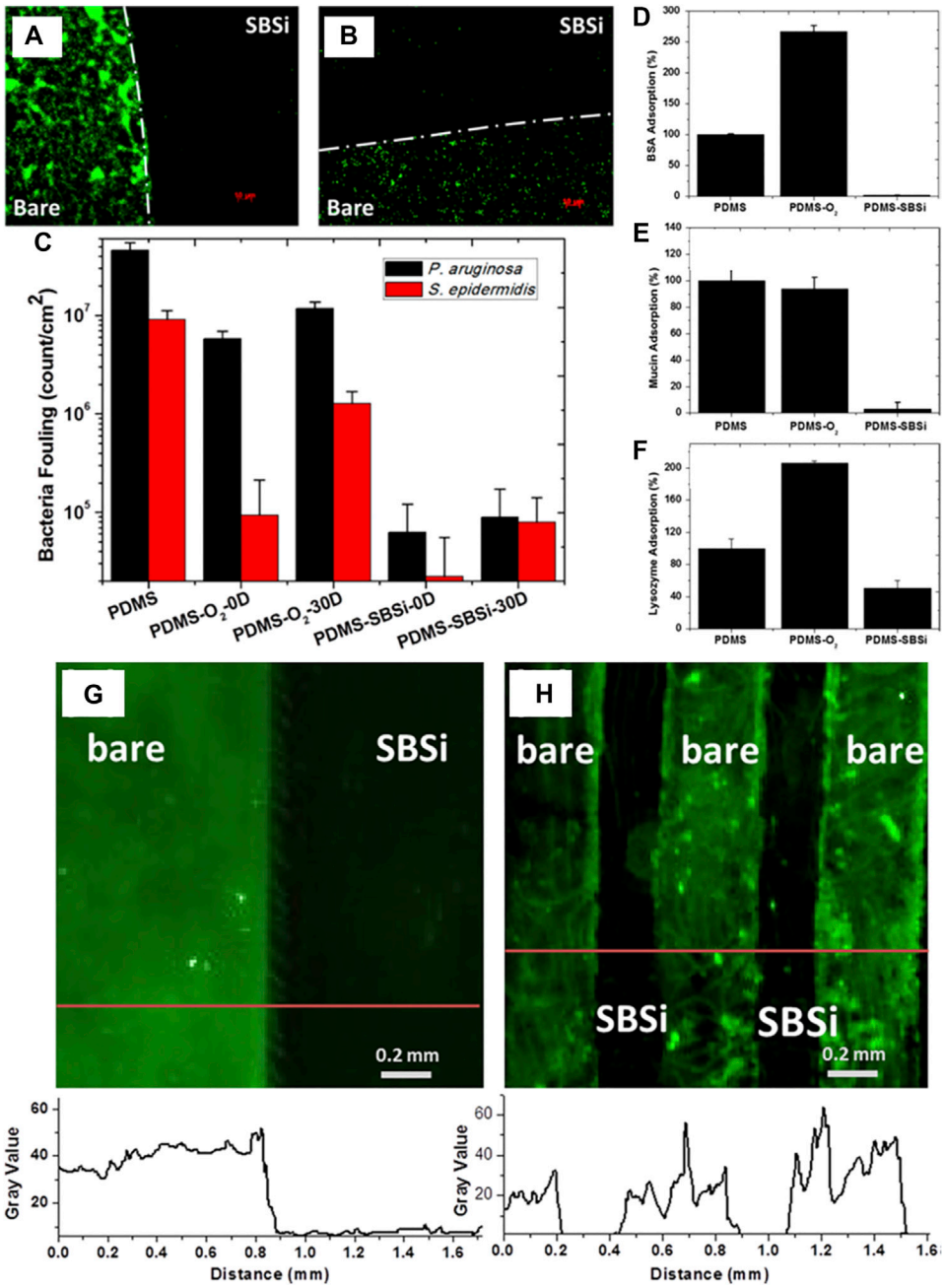

FIGURE 10 | Fluorescence micrographs showing *P. aeruginosa* **(A)** and *S. epidermidis* **(B)** adsorption to partially modified PDMS. Quantification of adsorption on PDMS samples as a function of treatment and time **(C)**. Enzyme-linked immunosorbent assay (ELISA) measurements for adsorption of BSA **(D)**, mucin **(E)**, and lysozyme **(F)** on samples of PDMS, PDMS-O_2, and PDMS-SBSi. Adsorption of SRB-encapsulated liposomes on SBSi-patterned PDMS samples prepared by elastomeric stencil **(G)** and microchannels **(H)**. Fluorescence intensities are indicated by red lines below the images. Reprinted with permission from Ref. (Yeh et al., 2014). Copyright 2014, American Chemical Society.

Urinary Catheters and Hemodialysis Membranes in Nephrology

Urinary catheters and hemodialysis membranes are the typical polymer materials used in nephrology. Various strategies to prevent bacterial adhesion and growth on medical devices have been developed. Poloxamers are nontoxic hydrophilic copolymers and Poloxamer 338 (P388) can be used to prevent the formation of biofilm and consequent infection. The anti-biofouling behavior was investigated by the adhesion of Ec5FSL and Ec9FSL *E. coli* on a segment of a hydrophilic P388-adsorbed silicone urinary catheter compared to an uncoated segment. Neither *E. coli* isolate was detected on the former due to the

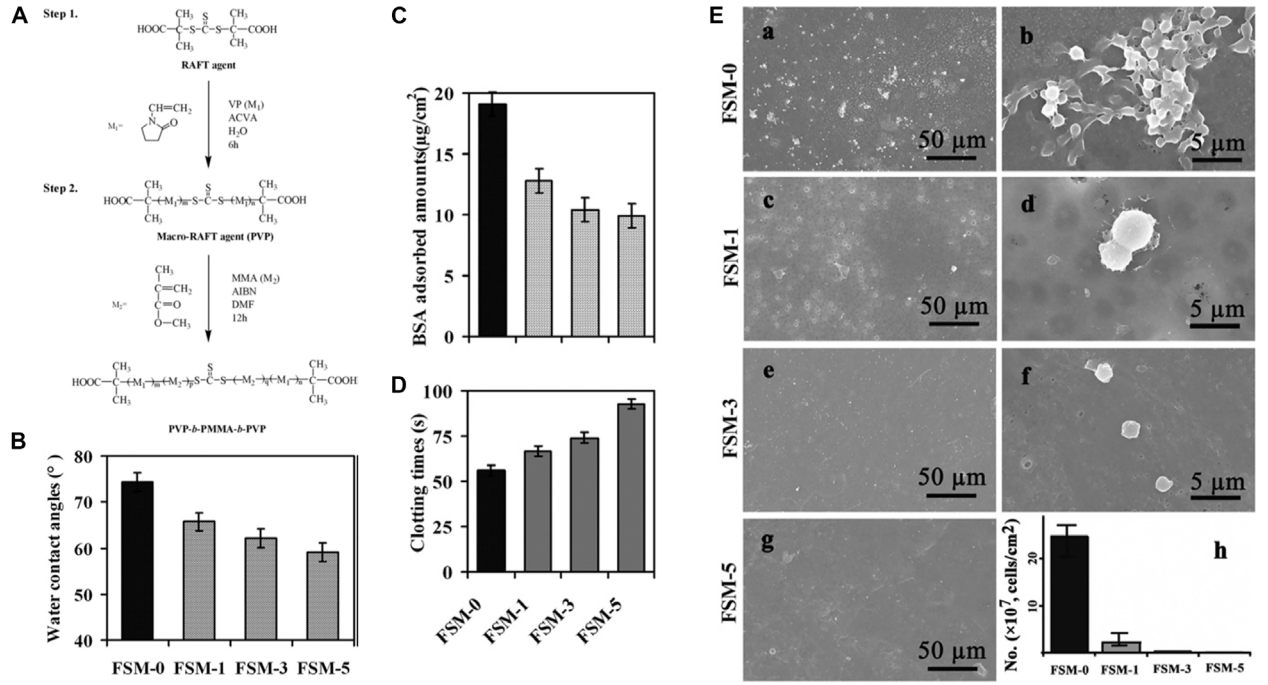

FIGURE 11 | Synthesis of the PVP-*b*-PMMA-*b*-PVP block copolymer **(A)**. WCA of the modified membranes **(B)**. BSA adsorption **(C)**. Activated partial thromboplastin time **(D)**. SEM micrographs showing platelet adhesion (**E**, h, number of the adherent platelets on the membranes adsorbed from platelet-rich plasma estimated from the SEM pictures). Reprinted with permission from Ref. (Ran et al., 2011). Copyright 2011, Elsevier B.V.

excellent anti-biofouling ability of hydrophilic P388 (Stirpe et al., 2020).

Hemodialysis membrane is another typical example of a nephrological application. PSF is frequently used for ultrafiltration membranes due to its stability under various conditions (Xie et al., 2015; Yin et al., 2015). A variety of surface modifications for ultrafiltration membranes have been investigated to combat biofouling. A novel zwitterionic molecule, MPDSAH, was grafted onto PSF membranes using benzophenone to increase their anti-biofouling actions (Yu et al., 2009). Measurement of WCA indicated the enhancement of membrane hydrophilicity by this modification. The passage of water was somewhat reduced by the modification, while adsorption of BSA was significantly reduced. The increase in anti-biofouling action was shown to be related to increased surface hydrophilicity (Yu et al., 2009). The immobilization of heparin on PSF allowed use of the membrane for dialysis. The higher the heparin density, the lower WCA and the platelet adherence. The flux of the heparin-modified membrane also recovered well after BSA filtration, indicating the improved anti-biofouling action of the heparin-modified membrane (Huang et al., 2011).

PES is a typical PSF and is frequently used for hemodialysis membranes. Poly (citric acid)-grafted-MWCNT (PCA-g-MWCNT) was included as a nanofiller in PES to generate a hemodialysis mixed-matrix membrane (MMM) with improved hydrophilicity (from 77° to 56°) and anti-biofouling ability (Abidin et al., 2016). The passage of pure water and the resistance to BSA were increased as a result of the presence of numerous hydrophilic groups derived from PCA-*g*-MWCNT (Abidin et al., 2016). Changsheng Zhao and coauthors synthesized a hydrophilic triblock copolymer of PVP-*b*-PMMA-*b*-PVP *via* reversible addition-fragmentation chain transfer polymerization (**Figure 11A**) (Ran et al., 2011). After the introduction of the copolymer, the membranes showed a lower WCA (**Figure 11B**), lower BSA adsorption (**Figure 11C**), prolonged blood coagulation times (**Figure 11D**), and reduced platelet adhesion (**Figure 11E**). These results suggested that modifying the surface hydrophilicity of PES improves their anti-biofouling action, allowing the membranes to be used for blood purification, including hemodialysis (Ran et al., 2011).

PHEMA, the simplest hydroxylated polymethacrylate, can impart an anti-biofouling character to surfaces. Lixin Xue and coauthors reported another hemodialysis membrane based on biobased and biodegradable PLA and PHEMA (Zhu et al., 2015). Anti-biofouling and hemocompatible PLA membranes were developed using different concentrations of PLA-PHEMA copolymers as the blending additive (M0 indicates pure PLA membrane, and M20 indicates 20 wt% copolymer). The results showed that PLA/PLA-PHEMA membranes with high PLA-PHEMA concentrations showed augmented hydrophilicity (WCA decreased from 75° for M0 to 60° for M20), water permeability, anti-biofouling (decreased BSA adsorption and platelet adhesion, **Figures 2**, **12A,C,D**) and

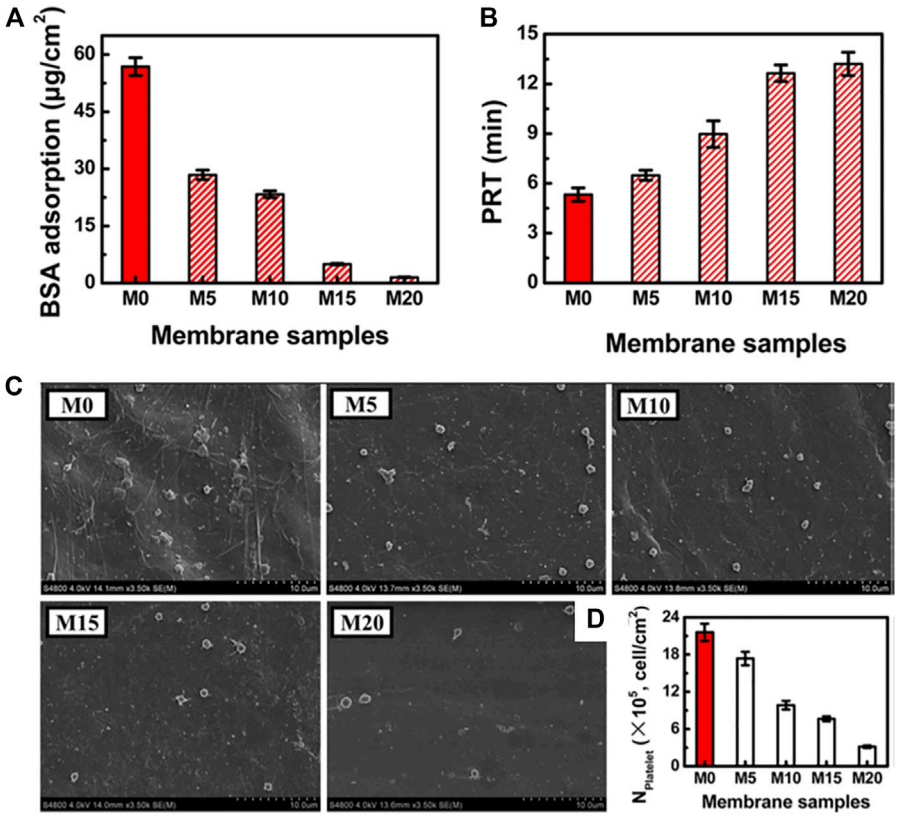

FIGURE 12 | Hemocompatibility of M0 and PLA/PLA–PHEMA membranes (M5, M10, M15, and M20). Adsorption of BSA to membranes **(A)**. Plasma recalcification times for membranes **(B)**. SEM micrograph **(C)** and the number **(D)** of adherent platelets on the membrane surfaces. Reprinted with permission from Ref. (Zhu et al., 2015). Copyright 2015, American Chemical Society.

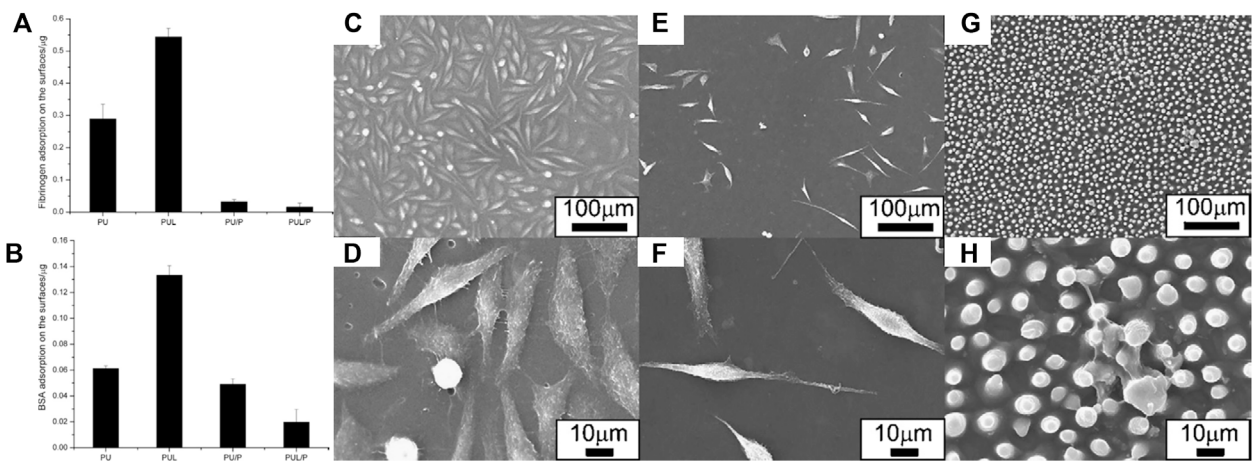

FIGURE 13 | Adsorbed fibrinogen **(A)** and BSA **(B)** on PU, PU/P, PUL and PUL/P. SEM micrograph showing cell morphologies on PU **(C**,**D)**, PU/P **(E**,**F)**, and PUL/P **(G**,**H)**. Reprinted with permission from Ref. (Zheng et al., 2010). Copyright 2010, Elsevier B.V.

hemocompatibility (increased plasma recalcification time (PRT), **Figure 12B**). These findings indicate that PLA-PHEMA copolymers were effective in optimizing PLA membranes for hemodialysis applications (Zhu et al., 2015).

CONCLUSION AND OUTLOOK

The ability of polymers to combat biofouling can be enhanced by the regulation of special surface wettability, including

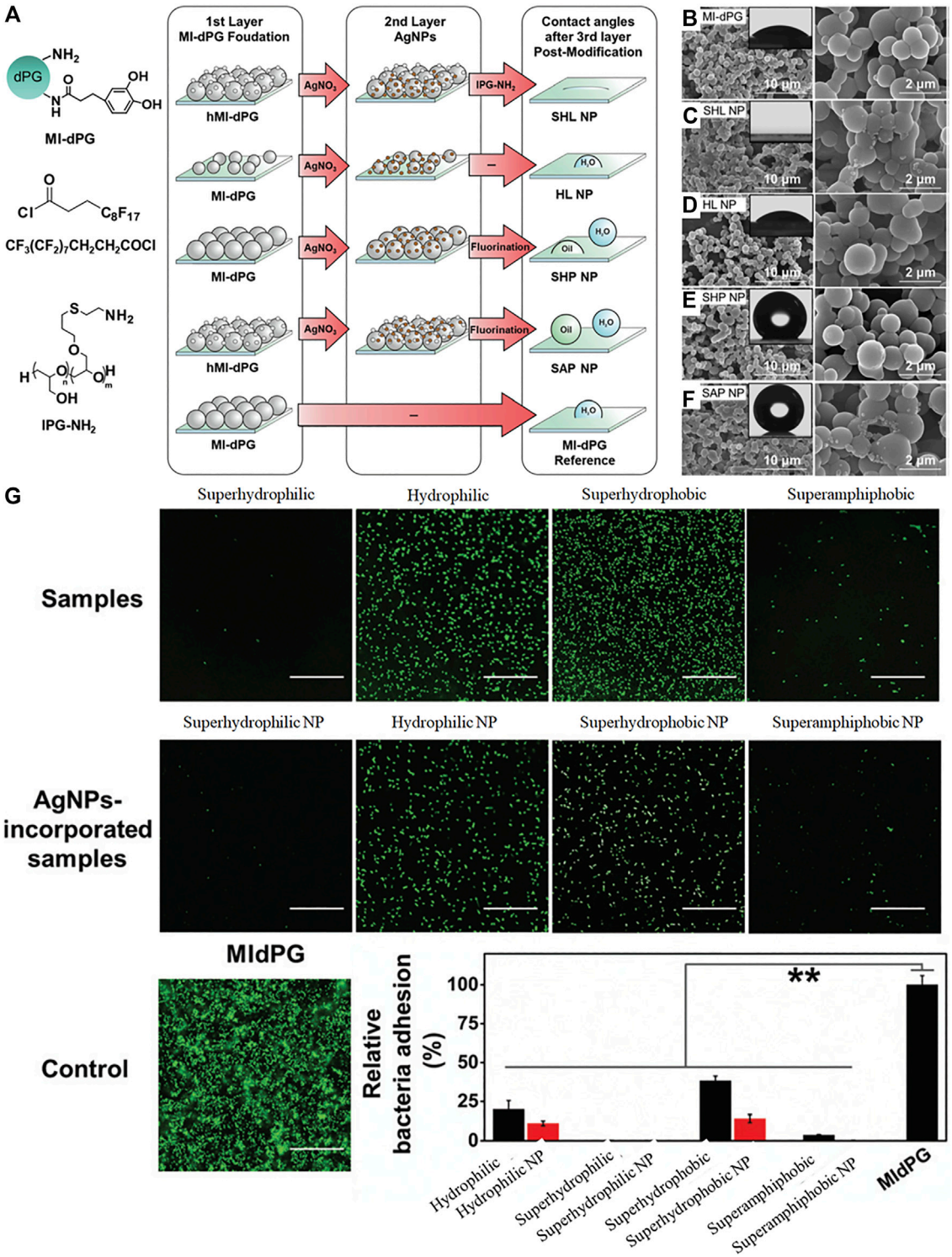

FIGURE 14 | Fabrication process **(A)** of MI-dPG based coatings with different wettability characteristics and physical structures, MI-dPG **(B)**, superhydrophilic NP **(C)**, hydrophilic NP **(D)**, superhydrophobic NP **(E)**, superamphiphobic NP **(F)**. Quantification of bacterial attachment and their corresponding micrographs **(G)**. Reprinted with permission from Ref. (Li et al., 2019b). Copyright 2019, Royal Society of Chemistry.

superhydrophilicity, hydrophilicity, hydrophobicity, and superhydrophobicity. In this review, we focus on the anti-biofouling polymers with superhydrophilicity, hydrophilicity and hydrophobicity but excluding superhydrophobicity which can be found in our previous review (He et al., 2021). Meanwhile, we just focus on the biomedical applications in cardiology, ophthalmology, and nephrology. Moreover, biofoulants mentioned in this review are focused on the usual bacteria, cells, and proteins. This review will provide a new perspective to promote the development of anti-biofouling polymers. Meanwhile, the anti-biofouling strategies reviewed in this manuscript will offer help for future researchers to choose suitable polymers for specific anti-biofouling applications. Considering the biomedical applications of anti-biofouling polymers, most research has focused on materials with superhydrophilicity or hydrophilicity which may be more achievable than hydrophobicity or superhydrophobicity. However, there is still some research that obtained excellent anti-biofouling polymers by hydrophobic manipulation. Therefore, exploring more anti-biofouling polymers with hydrophobic or superhydrophobic properties should be a research priority in the future to avoid the drawbacks of anti-biofouling polymers with hydrophilic properties. Meanwhile, there are some issues that should be paid more attention, that are discussed below.

Exploring the Inherent Correlation Between the Anti-Biofouling and Surface Wettability

Protein adsorption depends not only on the hydrophilic or hydrophobic properties of materials, but also on topographical features, including surface curvature, roughness, and geometrical characteristics. There is research focusing on the effects of surface micro- or nano-typography on adsorption. In 1964, Curtis and Varde described the effects of surrounding topography on cells. It is generally accepted that both the topography and chemical characteristics of surfaces can influence the growth and properties of cells (Zheng et al., 2010). Hong Chen and coauthors fabricated lotus leaf-like polyurethane/Pluronic® F-127 surface (PUL/P) by replica molding using a lotus leaf as the template (Zheng et al., 2010). When water droplets touched the superhydrophilic PUL/P surface, the drop spread rapidly with a WCA near zero, suggesting enhancement of the surface by the adoption of the lotus leaf-like structure compared to those without (PU/P). Adsorption of both BSA and fibrinogen was significantly lower on the PU/P surface (**Figures 13A,B**). Further reductions in adsorption were observed on the superhydrophilic PUL/P surface (**Figures 13A,B**). Experiments with L929 cells showed that cells adhered less to PU/P surfaces (**Figures 13C–F**). Meanwhile, cell adhesion to the superhydrophilic PUL/P was reduced with cells showing spherical shapes and diminished viability (**Figures 13G,H**). The superhydrophilic PUL/P thus appears to resist non-specific protein adsorption and cell attachment, with these effects deriving from both topographical and chemical structures. However, adsorption and adhesion to the hydrophobic lotus leaf-like polyurethane surface (PUL) were obviously enhanced compared with the hydrophilic PU, in apparent contradiction of the anti-biofouling strategies based on hydrophobic polymers discussed in **section 2.3**. Biofoulants adsorption and adhesion may be increased or decreased with the increased hydrophobicity. Therefore, the inherent correlation between the anti-biofouling and surface wettability was still non-uniform, and in-depth research should be applied. A comprehensive consideration and more quantitative research of the influence of chemical compositions and physical structures on the anti-biofouling ability should be under consideration.

Design and Fabrication of Surfaces

Both chemical and physical properties influence the resistance of surfaces to biofoulants. This is borne out in natural antifouling materials (Magin et al., 2010). Rainer Haag and coauthors reported the effect of extreme wettability ranging from superhydrophilicity to superhydrophobicity on the antibacterial efficiency of an MI-dPG and silver nanoparticle (AgNPs) coating (Li et al., 2019b). As shown in **Figure 14A**, MI-dPG or hierarchical micro- and nanometer roughed MI-dPG (hMI-dPG) was formed by controlling surface polymerization and subsequent modification by AgNPs, linear polyglycerol (lPG-NH_2) or fluorination. Different surface wetting properties containing superhydrophilic, hydrophilic, superhydrophobic, and even superamphiphobic wettability were achieved by different post-functionalization without obvious physical structural changes, demonstrated by WCA and SEM (**Figures 14B–F**). The resulting superhydrophilic polymer coatings were effective in repelling both *E. coli* and *S. aureus,* and the coating properties in relation to their antibacterial activities are shown in **Figure 14G**. The results indicated that the polymer coatings with superhydrophilic or superamphiphobic properties had good anti-biofouling ability but those with hydrophilic and superhydrophobic character showed less anti-biofouling ability.

Therefore, it is necessary to develop surfaces with quantifiable physical structures for optimization of anti-biofouling action. We previously reported a simple and mold-free technique for fabricating surfaces by 3D printing (He et al., 2017), which may assist in the precise design and manufacture of physical surfaces to combat biofouling (Mazinani et al., 2019).

Anti-biofouling Polymers With Good Biocompatibility

Biocompatibility is defined as the ability of a material to perform with an appropriate host response in a specific application (Grainger, 1999; Barrère et al., 2008). It is an important issue for the chosen of anti-biofouling polymer types especially when these materials will be used in biomedical fields. If anti-biofouling polymers used *in vivo* are not biocompatible, they will elicit pernicious local or systemic inflammatory responses and induce the biomedical implants failed. Therefore, good biocompatibility should be paid more attention in the future researches of anti-biofouling polymers with special surface wettability.

Long-Term Anti-Biofouling Polymers

Anti-biofouling surfaces are easily damaged by scratching, degradation, and rough handling. This damage destroys the surface characteristics leading to a loss of anti-biofouling

activity. The development of robust and long-lasting anti-biofouling polymers remains a major challenge (Wu et al., 2019). Investigation of self-repairing materials, inspired by the repair mechanisms seen in natural organisms (Cai et al., 2014) would be advantageous to maintain and restore the properties of surfaces. This is a promising strategy for obtaining long-term and robust anti-biofouling surfaces (Wang et al., 2011; Chen et al., 2015a; Chen et al., 2015b; Chen et al., 2016; Liu and Guo, 2018; Wang et al., 2020).

AUTHOR CONTRIBUTIONS

ZH, XL, and FD conceived and designed this review paper; ZH and XL wrote this review paper; XY, NW, LM, JP, HL, and FD revised this review paper.

FUNDING

The authors would like to acknowledge the financial support from the National Natural Science Foundation of China (grant numbers 51873240, 51703142), the Sichuan Science and Technology Program (2019YJ0658, 2019YFH0069), the Talent Introduction Program of Chengdu University (2081920001), Sichuan Medical Research Project (S20014), and Chengdu Medical Research Project (2020208).

SUPPLEMENTARY MATERIAL

The Supplementary Material for this article can be found online at: https://www.frontiersin.org/articles/10.3389/fbioe.2021.807357/full#supplementary-material

REFERENCES

Abidin, M. N. Z., Goh, P. S., Ismail, A. F., Othman, M. H. D., Hasbullah, H., Said, N., et al. (2016). Antifouling Polyethersulfone Hemodialysis Membranes Incorporated with Poly (Citric Acid) Polymerized Multi-Walled Carbon Nanotubes. *Mater. Sci. Eng. C* 68, 540–550. doi:10.1016/j.msec.2016.06.039

Almeida, E., Diamantino, T. C., and de Sousa, O. (2007). Marine Paints: The Particular Case of Antifouling Paints. *Prog. Org. Coat.* 59 (1), 2–20. doi:10.1016/j.porgcoat.2007.01.017

Ammons, M. C., and Copié, V. (2013). Mini-review: Lactoferrin: A Bioinspired, Anti-biofilm Therapeutic. *Biofouling* 29 (4), 443–455. doi:10.1080/08927014.2013.773317

Azemar, F., Faÿ, F., Réhel, K., and Linossier, I. (2015). Development of Hybrid Antifouling Paints. *Prog. Org. Coat.* 87, 10–19. doi:10.1016/j.porgcoat.2015.04.007

Ball, P. (1999). Engineering Shark Skin and Other Solutions. *Nature* 400 (6744), 507–509. doi:10.1038/22883

Barrère, F., Mahmood, T. A., de Groot, K., and van Blitterswijk, C. A. (2008). Advanced Biomaterials for Skeletal Tissue Regeneration: Instructive and Smart Functions. *Mater. Sci. Eng. R: Rep.* 59 (1), 38–71. doi:10.1016/j.mser.2007.12.001

Bezuidenhout, D., Williams, D. F., and Zilla, P. (2015). Polymeric Heart Valves for Surgical Implantation, Catheter-Based Technologies and Heart Assist Devices. *Biomaterials* 36, 6–25. doi:10.1016/j.biomaterials.2014.09.013

Bixler, G. D., and Bhushan, B. (2012). Biofouling: Lessons from Nature. *Phil. Trans. R. Soc. A.* 370, 2381–2417. doi:10.1098/rsta.2011.0502

Bixler, G. D., and Bhushan, B. (2013). Fluid Drag Reduction and Efficient Self-Cleaning with Rice Leaf and Butterfly Wing Bioinspired Surfaces. *Nanoscale* 5 (17), 7685–7710. doi:10.1039/c3nr01710a

Bixler, G. D., and Bhushan, B. (2014). Rice- and Butterfly-wing Effect Inspired Self-Cleaning and Low Drag Micro/nanopatterned Surfaces in Water, Oil, and Air Flow. *Nanoscale* 6 (1), 76–96. doi:10.1039/c3nr04755e

Bixler, G. D., Theiss, A., Bhushan, B., and Lee, S. C. (2014). Anti-fouling Properties of Microstructured Surfaces Bio-Inspired by Rice Leaves and Butterfly Wings. *J. Colloid Interf. Sci.* 419, 114–133. doi:10.1016/j.jcis.2013.12.019

Cai, Y., Lin, L., Xue, Z., Liu, M., Wang, S., and Jiang, L. (2014). Filefish-Inspired Surface Design for Anisotropic Underwater Oleophobicity. *Adv. Funct. Mater.* 24 (6), 809–816. doi:10.1002/adfm.201302034

Callow, J. A., and Callow, M. E. (2011). Trends in the Development of Environmentally Friendly Fouling-Resistant Marine Coatings. *Nat. Commun.* 2, 244. doi:10.1038/ncomms1251

Carl, C., Poole, A. J., Sexton, B. A., Glenn, F. L., Vucko, M. J., Williams, M. R., et al. (2012). Enhancing the Settlement and Attachment Strength of Pediveligers ofMytilus Galloprovincialisbychanging Surface Wettability and Microtopography. *Biofouling* 28 (2), 175–186. doi:10.1080/08927014.2012.662676

Carr, L. R., Zhou, Y., Krause, J. E., Xue, H., and Jiang, S. (2011). Uniform Zwitterionic Polymer Hydrogels with a Nonfouling and Functionalizable Crosslinker Using Photopolymerization. *Biomaterials* 32 (29), 6893–6899. doi:10.1016/j.biomaterials.2011.06.006

Cassie, A. B. D., and Baxter, S. (1944). Wettability of Porous Surfaces. *Trans. Faraday Soc.* 40, 546–551. doi:10.1039/tf9444000546

Chan, H.-M., Erathodiyil, N., Wu, H., Lu, H., Zheng, Y., and Ying, J. Y. (2020). Calcium Cross-Linked Zwitterionic Hydrogels as Antifouling Materials. *Mater. Today Commun.* 23, 100950. doi:10.1016/j.mtcomm.2020.100950

Chen, D., Wu, M., Li, B., Ren, K., Cheng, Z., Ji, J., et al. (2015). Layer-by-Layer-Assembled Healable Antifouling Films. *Adv. Mater.* 27 (39), 5882–5888. doi:10.1002/adma.201501726

Chen, H., Zhang, M., Yang, J., Zhao, C., Hu, R., Chen, Q., et al. (2014). Synthesis and Characterization of Antifouling poly(N-Acryloylaminoethoxyethanol) with Ultralow Protein Adsorption and Cell Attachment. *Langmuir* 30 (34), 10398–10409. doi:10.1021/la502136q

Chen, J., Liu, Z., Wen, X., Xu, S., Wang, F., and Pi, P. (2019). Two-Step Approach for Fabrication of Durable Superamphiphobic Fabrics for Self-Cleaning, Antifouling, and On-Demand Oil/Water Separation. *Ind. Eng. Chem. Res.* 58 (14), 5490–5500. doi:10.1021/acs.iecr.9b00049

Chen, K., Zhou, S., and Wu, L. (2016). Self-Healing Underwater Superoleophobic and Antibiofouling Coatings Based on the Assembly of Hierarchical Microgel Spheres. *ACS Nano* 10 (1), 1386–1394. doi:10.1021/acsnano.5b06816

Chen, K., Zhou, S., Yang, S., and Wu, L. (2015). Fabrication of All-Water-Based Self-Repairing Superhydrophobic Coatings Based on UV-Responsive Microcapsules. *Adv. Funct. Mater.* 25 (7), 1035–1041. doi:10.1002/adfm.201403496

Chen, S.-H., Chang, Y., Lee, K.-R., Wei, T.-C., Higuchi, A., Ho, F.-M., et al. (2012). Hemocompatible Control of Sulfobetaine-Grafted Polypropylene Fibrous Membranes in Human Whole Blood via Plasma-Induced Surface Zwitterionization. *Langmuir* 28 (51), 17733–17742. doi:10.1021/la3036902

Chen, S., Li, L., Zhao, C., and Zheng, J. (2010). Surface Hydration: Principles and Applications Toward Low-Fouling/nonfouling Biomaterials. *Polymer* 51 (23), 5283–5293. doi:10.1016/j.polymer.2010.08.022

Chen, Z., Du, X.-a., Liu, Y., Ju, Y., Song, S., and Dong, L. (2018). A High-Efficiency Ultrafiltration Nanofibrous Membrane with Remarkable Antifouling and Antibacterial Ability. *J. Mater. Chem. A.* 6 (31), 15191–15199. doi:10.1039/c8ta02649a

Cheng, W., Yang, C., Ding, X., Engler, A. C., Hedrick, J. L., and Yang, Y. Y. (2015). Broad-Spectrum Antimicrobial/Antifouling Soft Material Coatings Using Poly(ethylenimine) as a Tailorable Scaffold. *Biomacromolecules* 16 (7), 1967–1977. doi:10.1021/acs.biomac.5b00359

Dobretsov, S., Abed, R. M. M., and Teplitski, M. (2013). Mini-review: Inhibition of Biofouling by Marine Microorganisms. *Biofouling* 29 (4), 423–441. doi:10.1080/08927014.2013.776042

Dobretsov, S., and Thomason, J. C. (2011). The Development of Marine Biofilms on Two Commercial Non-biocidal Coatings: A Comparison Between Silicone and Fluoropolymer Technologies. *Biofouling* 27 (8), 869–880. doi:10.1080/08927014.2011.607233

Du, T., Ma, S., Pei, X., Wang, S., and Zhou, F. (2017). Bio-Inspired Design and Fabrication of Micro/Nano-Brush Dual Structural Surfaces for Switchable Oil Adhesion and Antifouling. *Small* 13 (4), 1602020. doi:10.1002/smll.201602020

Epstein, A. K., Wong, T.-S., Belisle, R. A., Boggs, E. M., and Aizenberg, J. (2012). Liquid-infused Structured Surfaces with Exceptional Anti-biofouling

Performance. *Proc. Natl. Acad. Sci.* 109 (33), 13182–13187. doi:10.1073/pnas.1201973109

Erathodiyil, N., Chan, H.-M., Wu, H., and Ying, J. Y. (2020). Zwitterionic Polymers and Hydrogels for Antibiofouling Applications in Implantable Devices. *Mater. Today* 38, 84–98. doi:10.1016/j.mattod.2020.03.024

Eshet, I., Freger, V., Kasher, R., Herzberg, M., Lei, J., and Ulbricht, M. (2011). Chemical and Physical Factors in Design of Antibiofouling Polymer Coatings. *Biomacromolecules* 12 (7), 2681–2685. doi:10.1021/bm200476g

Francolini, I., Crisante, F., Martinelli, A., D'Ilario, L., and Piozzi, A. (2012). Synthesis of Biomimetic Segmented Polyurethanes as Antifouling Biomaterials. *Acta Biomater.* 8 (2), 549–558. doi:10.1016/j.actbio.2011.10.024

Francolini, I., Donelli, G., Crisante, F., Taresco, V., and Piozzi, A. (2015). "Antimicrobial Polymers for Anti-biofilm Medical Devices: State-Of-Art and Perspectives," in *Biofilm-based Healthcare-Associated Infections: Volume II*. Editor G. Donelli (New York, NY: Springer International Publishing, Cham), 93–117. doi:10.1007/978-3-319-09782-4_7

Galante, A. J., Haghanifar, S., Romanowski, E. G., Shanks, R. M. Q., and Leu, P. W. (2020). Superhemophobic and Antivirofouling Coating for Mechanically Durable and Wash-Stable Medical Textiles. *ACS Appl. Mater. Inter.* 12 (19), 22120–22128. doi:10.1021/acsami.9b23058

Gam-Derouich, S., Gosecka, M., Lepinay, S., Turmine, M., Carbonnier, B., Basinska, T., et al. (2011). Highly Hydrophilic Surfaces from Polyglycidol Grafts with Dual Antifouling and Specific Protein Recognition Properties. *Langmuir* 27 (15), 9285–9294. doi:10.1021/la200290k

Gaw, S. L., Sarkar, S., Nir, S., Schnell, Y., Mandler, D., Xu, Z. J., et al. (2017). Electrochemical Approach for Effective Antifouling and Antimicrobial Surfaces. *ACS Appl. Mater. Inter.* 9 (31), 26503–26509. doi:10.1021/acsami.7b03761

Grainger, D. W. (1999). The Williams Dictionary of Biomaterials. *Mater. Today* 2 (3), 29. doi:10.1016/S1369-7021(99)80066-2

Guo, F., Jiao, K., Bai, Y., Guo, J., Chen, Q., Yang, R., et al. (2019). Novel Transcatheter Aortic Heart Valves Exhibiting Excellent Hemodynamic Performance and Low-Fouling Property. *J. Mater. Sci. Technol.* 35 (1), 207–215. doi:10.1016/j.jmst.2018.09.026

He, H., Xuan, X., Zhang, C., Song, Y., Chen, S., Gong, X., et al. (2019). Simple Thermal Pretreatment Strategy to Tune Mechanical and Antifouling Properties of Zwitterionic Hydrogels. *Langmuir* 35 (5), 1828–1836. doi:10.1021/acs.langmuir.8b01755

He, M., Gao, K., Zhou, L., Jiao, Z., Wu, M., Cao, J., et al. (2016). Zwitterionic Materials for Antifouling Membrane Surface Construction. *Acta Biomater.* 40, 142–152. doi:10.1016/j.actbio.2016.03.038

He, Z., Chen, Y., Yang, J., Tang, C., Lv, J., Liu, Y., et al. (2017). Fabrication of Polydimethylsiloxane Films with Special Surface Wettability by 3D Printing. *Composites B: Eng.* 129, 58–65. doi:10.1016/j.compositesb.2017.07.025

He, Z., Lan, X., Chen, F., Wang, K., Deng, H., Zhang, Q., et al. (2013). Effect of Surface Wettability on Transparency in Different Water Conditions. *J. Coat. Technol. Res.* 10 (5), 641–647. doi:10.1007/s11998-013-9490-6

He, Z., Lan, X., Hu, Q., Li, H., Li, L., and Mao, J. (2021). Antifouling Strategies Based on Super-phobic Polymer Materials. *Prog. Org. Coat.* 157, 106285. doi:10.1016/j.porgcoat.2021.106285

He, Z., Ma, M., Lan, X., Chen, F., Wang, K., Deng, H., et al. (2011). Fabrication of a Transparent Superamphiphobic Coating with Improved Stability. *Soft Matter* 7 (14), 6435–6443. doi:10.1039/c1sm05574g

Hu, P., Xie, Q., Ma, C., and Zhang, G. (2020). Silicone-Based Fouling-Release Coatings for Marine Antifouling. *Langmuir* 36 (9), 2170–2183. doi:10.1021/acs.langmuir.9b03926

Huang, X.-J., Guduru, D., Xu, Z.-K., Vienken, J., and Groth, T. (2011). Blood Compatibility and Permeability of Heparin-Modified Polysulfone as Potential Membrane for Simultaneous Hemodialysis and LDL Removal. *Macromol. Biosci.* 11 (1), 131–140. doi:10.1002/mabi.201000278

Ji, H.-F., He, C., Wang, R., Fan, X., Xiong, L., Zhao, W.-F., et al. (2019). Multifunctionalized Polyethersulfone Membranes with Networked Submicrogels to Improve Antifouling Property, Antibacterial Adhesion and Blood Compatibility. *Mater. Sci. Eng. C* 96, 402–411. doi:10.1016/j.msec.2018.11.047

Jiang, C., Wang, G., Hein, R., Liu, N., Luo, X., and Davis, J. J. (2020). Antifouling Strategies for Selective In Vitro and In Vivo Sensing. *Chem. Rev.* 120 (8), 3852–3889. doi:10.1021/acs.chemrev.9b00739

Jiang, J., Zhu, L., Zhu, L., Zhang, H., Zhu, B., and Xu, Y. (2013). Antifouling and Antimicrobial Polymer Membranes Based on Bioinspired Polydopamine and Strong Hydrogen-Bonded poly(N-Vinyl Pyrrolidone). *ACS Appl. Mater. Inter.* 5 (24), 12895–12904. doi:10.1021/am403405c

Jiang, T., Guo, Z., and Liu, W. (2015). Biomimetic Superoleophobic Surfaces: Focusing on Their Fabrication and Applications. *J. Mater. Chem. A.* 3 (5), 1811–1827. doi:10.1039/C4TA05582A

Jorge, P., Lourenço, A., and Pereira, M. O. (2012). New Trends in Peptide-Based Anti-biofilm Strategies: A Review of Recent Achievements and Bioinformatic Approaches. *Biofouling* 28 (10), 1033–1061. doi:10.1080/08927014.2012.728210

Kambe, Y., Mahara, A., Tanaka, H., Kakinoki, S., Fukazawa, K., Liu, Y., et al. (2019). Short-term Evaluation of Thromboresistance of a Poly(ether Ether Ketone) (PEEK) Mechanical Heart Valve with Poly(2-methacryloyloxyethyl Phosphorylcholine) (PMPC)-grafted Surface in a Porcine Aortic Valve Replacement Model. *J. Biomed. Mater. Res.* 107 (5), 1052–1063. doi:10.1002/jbm.a.36628

Kang, S., Lee, M., Kang, M., Noh, M., Jeon, J., Lee, Y., et al. (2016). Development of Anti-biofouling Interface on Hydroxyapatite Surface by Coating Zwitterionic MPC Polymer Containing Calcium-Binding Moieties to Prevent Oral Bacterial Adhesion. *Acta Biomater.* 40, 70–77. doi:10.1016/j.actbio.2016.03.006

Kang, S. M., Lee, C., Kim, H. N., Lee, B. J., Lee, J. E., Kwak, M. K., et al. (2013). Directional Oil Sliding Surfaces with Hierarchical Anisotropic Groove Microstructures. *Adv. Mater.* 25 (40), 5756–5761. doi:10.1002/adma.201302083

Keefe, A. J., Brault, N. D., and Jiang, S. (2012). Suppressing Surface Reconstruction of Superhydrophobic PDMS Using a Superhydrophilic Zwitterionic Polymer. *Biomacromolecules* 13 (5), 1683–1687. doi:10.1021/bm300399s

Kim, S.-E., Zhang, C., Advincula, A. A., Baer, E., and Pokorski, J. K. (2016). Protein and Bacterial Antifouling Behavior of Melt-Coextruded Nanofiber Mats. *ACS Appl. Mater. Inter.* 8 (14), 8928–8938. doi:10.1021/acsami.6b00093

Krishnan, S., Weinman, C. J., and Ober, C. K. (2008). Advances in Polymers for Anti-biofouling Surfaces. *J. Mater. Chem.* 18 (29), 3405–3413. doi:10.1039/B801491D

Kuang, M., Wang, J., and Jiang, L. (2016). Bio-inspired Photonic Crystals with Superwettability. *Chem. Soc. Rev.* 45 (24), 6833–6854. doi:10.1039/c6cs00562d

Lan, X., Lei, Y., He, Z., Yin, A., Li, L., Tang, Z., et al. (2021). A Transparent Hydrophilic Anti-biofouling Coating for Intraocular Lens Materials Prepared by "bridging" of the Intermediate Adhesive Layer. *J. Mater. Chem. B* 9 (17), 3696–3704. doi:10.1039/d1tb00065a

Lee, J., and Yong, K. (2015). Combining the Lotus Leaf Effect with Artificial Photosynthesis: Regeneration of Underwater Superhydrophobicity of Hierarchical ZnO/Si Surfaces by Solar Water Splitting. *NPG Asia Mater.* 7 (7), e201. doi:10.1038/am.2015.74

Lee, S. G., Lim, H. S., Lee, D. Y., Kwak, D., and Cho, K. (2013). Tunable Anisotropic Wettability of Rice Leaf-like Wavy Surfaces. *Adv. Funct. Mater.* 23 (5), 547–553. doi:10.1002/adfm.201201541

Lei, Y., Lan, X., He, Z., Yin, A., Jin, W., Hu, Q., et al. (2021). Multifarious Anti-biofouling Bioprosthetic Heart Valve Materials with the Formation of Interpenetrating Polymer Network Structures. *Mater. Des.* 206, 109803. doi:10.1016/j.matdes.2021.109803

Lejars, M., Margaillan, A., and Bressy, C. (2012). Fouling Release Coatings: A Nontoxic Alternative to Biocidal Antifouling Coatings. *Chem. Rev.* 112 (8), 4347–4390. doi:10.1021/cr200350v

Leslie, D. C., Waterhouse, A., Berthet, J. B., Valentin, T. M., Watters, A. L., Jain, A., et al. (2014). A Bioinspired Omniphobic Surface Coating on Medical Devices Prevents Thrombosis and Biofouling. *Nat. Biotechnol.* 32, 1134–1140. doi:10.1038/nbt.3020

Li, D., Fan, Y., Han, G., and Guo, Z. (2020). Superomniphobic Silk Fibroin/Ag Nanowires Membrane for Flexible and Transparent Electronic Sensor. *ACS Appl. Mater. Inter.* 12 (8), 10039–10049. doi:10.1021/acsami.9b23378

Li, M., Schlaich, C., Willem Kulka, M., Donskyi, I. S., Schwerdtle, T., Unger, W. E. S., et al. (2019). Mussel-inspired Coatings with Tunable Wettability, for Enhanced Antibacterial Efficiency and Reduced Bacterial Adhesion. *J. Mater. Chem. B* 7 (21), 3438–3445. doi:10.1039/C9TB00534J

Li, Q., Lin, H.-H., and Wang, X.-L. (2014). Preparation of Sulfobetaine-Grafted PVDF Hollow Fiber Membranes with a Stably Anti-protein-fouling Performance. *Membranes* 4 (2), 181–199. doi:10.3390/membranes4020181

Li, X., Hu, X., and Cai, T. (2017). Construction of Hierarchical Fouling Resistance Surfaces onto Poly(vinylidene Fluoride) Membranes for Combating Membrane Biofouling. *Langmuir* 33 (18), 4477–4489. doi:10.1021/acs.langmuir.7b00191

Li, X., Zhao, S., Hu, W., Zhang, X., Pei, L., and Wang, Z. (2019). Robust Superhydrophobic Surface with Excellent Adhesive Properties Based on Benzoxazine/epoxy/mesoporous SiO2. *Appl. Surf. Sci.* 481, 374–378. doi:10.1016/j.apsusc.2019.03.114

Liang, Y., Kim, S., Yang, E., and Choi, H. (2020). Omni-Directional Protected Nanofiber Membranes by Surface Segregation of PDMS-Terminated Triblock Copolymer for High-Efficiency Oil/Water Emulsion Separation. *ACS Appl. Mater. Inter.* 12 (22), 25324–25333. doi:10.1021/acsami.0c05559

Liu, G., Li, K., Wang, H., Ma, L., Yu, L., and Nie, Y. (2020). Stable Fabrication of Zwitterionic Coating Based on Copper-Phenolic Networks on Contact Lens with Improved Surface Wettability and Broad-Spectrum Antimicrobial Activity. *ACS Appl. Mater. Inter.* 12 (14), 16125–16136. doi:10.1021/acsami.0c02143

Liu, S., and Guo, W. (2018). Anti-Biofouling and Healable Materials: Preparation, Mechanisms, and Biomedical Applications. *Adv. Funct. Mater.* 28 (41), 1800596. doi:10.1002/adfm.201800596

Liu, S., Zheng, J., Hao, L., Yegin, Y., Bae, M., Ulugun, B., et al. (2020). Dual-Functional, Superhydrophobic Coatings with Bacterial Anticontact and Antimicrobial Characteristics. *ACS Appl. Mater. Inter.* 12 (19), 21311–21321. doi:10.1021/acsami.9b18928

Liu, X., Tong, W., Wu, Z., and Jiang, W. (2013). Poly(N-vinylpyrrolidone)-grafted Poly(dimethylsiloxane) Surfaces with Tunable Microtopography and Anti-biofouling Properties. *RSC Adv.* 3 (14), 4716–4722. doi:10.1039/C3RA23069D

Liu, Y., Zhang, D., Ren, B., Gong, X., Liu, A., Chang, Y., et al. (2020). Computational Investigation of Antifouling Property of Polyacrylamide Brushes. *Langmuir* 36 (11), 2757–2766. doi:10.1021/acs.langmuir.0c00165

Maan, A. M. C., Hofman, A. H., Vos, W. M., and Kamperman, M. (2020). Recent Developments and Practical Feasibility of Polymer-Based Antifouling Coatings. *Adv. Funct. Mater.* 30 (32), 2000936. doi:10.1002/adfm.202000936

Magin, C. M., Cooper, S. P., and Brennan, A. B. (2010). Non-toxic Antifouling Strategies. *Mater. Today* 13 (4), 36–44. doi:10.1016/s1369-7021(10)70058-4

Martin, S., and Bhushan, B. (2017). Transparent, Wear-Resistant, Superhydrophobic and Superoleophobic Poly(dimethylsiloxane) (PDMS) Surfaces. *J. Colloid Interf. Sci.* 488, 118–126. doi:10.1016/j.jcis.2016.10.094

Martin, S., Brown, P. S., and Bhushan, B. (2017). Fabrication Techniques for Bioinspired, Mechanically-Durable, Superliquiphobic Surfaces for Water, Oil, and Surfactant Repellency. *Adv. Colloid Interf. Sci.* 241, 1–23. doi:10.1016/j.cis.2017.01.004

Martínez-Gómez, A., Alvarez, C., de Abajo, J., del Campo, A., Cortajarena, A. L., and Rodriguez-Hernandez, J. (2015). Poly(ethylene Oxide) Functionalized Polyimide-Based Microporous Films to Prevent Bacterial Adhesion. *ACS Appl. Mater. Inter.* 7 (18), 9716–9724. doi:10.1021/acsami.5b01525

Mazinani, S., Al-Shimmery, A., Chew, Y. M. J., and Mattia, D. (2019). 3D Printed Fouling-Resistant Composite Membranes. *ACS Appl. Mater. Inter.* 11 (29), 26373–26383. doi:10.1021/acsami.9b07764

Mieszkin, S., Callow, M. E., and Callow, J. A. (2013). Interactions Between Microbial Biofilms and Marine Fouling Algae: A Mini Review. *Biofouling* 29 (9), 1097–1113. doi:10.1080/08927014.2013.828712

Mohan, T., Kargl, R., Tradt, K. E., Kulterer, M. R., Bračić, M., Hribernik, S., et al. (2015). Antifouling Coating of Cellulose Acetate Thin Films with Polysaccharide Multilayers. *Carbohydr. Polym.* 116, 149–158. doi:10.1016/j.carbpol.2014.04.068

Movafaghi, S., Leszczak, V., Wang, W., Sorkin, J. A., Dasi, L. P., Popat, K. C., et al. (2017). Hemocompatibility of Superhemophobic Titania Surfaces. *Adv. Healthc. Mater.* 6 (4), 1600717. doi:10.1002/adhm.201600717

Pan, S., Guo, R., Richardson, J. J., Berry, J. D., Besford, Q. A., Björnmalm, M., et al. (2019). Ricocheting Droplets Moving on Super-Repellent Surfaces. *Adv. Sci.* 6 (21), 1901846. doi:10.1002/advs.201901846

Pu, X., Li, G., and Huang, H. (2016). Preparation, Anti-biofouling and Drag-Reduction Properties of a Biomimetic Shark Skin Surface. *Biol. Open* 5 (4), 389–396. doi:10.1242/bio.016899

Ran, F., Nie, S., Zhao, W., Li, J., Su, B., Sun, S., et al. (2011). Biocompatibility of Modified Polyethersulfone Membranes by Blending an Amphiphilic Triblock Co-polymer of Poly(vinyl Pyrrolidone)-B-Poly(methyl Methacrylate)-B-Poly(vinyl Pyrrolidone). *Acta Biomater.* 7 (9), 3370–3381. doi:10.1016/j.actbio.2011.05.026

Roach, P., Shirtcliffe, N. J., and Newton, M. I. (2008). Progess in Superhydrophobic Surface Development. *Soft Matter* 4 (2), 224–240. doi:10.1039/b712575p

Rosenhahn, A., Schilp, S., Kreuzer, H. J., and Grunze, M. (2010). The Role of "inert" Surface Chemistry in Marine Biofouling Prevention. *Phys. Chem. Chem. Phys.* 12 (17), 4275–4286. doi:10.1039/c001968m

Santiago, A., Irusta, L., Schäfer, T., Corres, A., Martin, L., and González, A. (2016). Resistance to Protein Sorption as a Model of Antifouling Performance of Poly(siloxane-Urethane) Coatings Exhibiting Phase Separated Morphologies. *Prog. Org. Coat.* 99, 110–116. doi:10.1016/j.porgcoat.2016.05.011

Scardino, A. J., and de Nys, R. (2011). Mini Review: Biomimetic Models and Bioinspired Surfaces for Fouling Control. *Biofouling* 27 (1), 73–86. doi:10.1080/08927014.2010.536837

Seo, J.-H., Shibayama, T., Takai, M., and Ishihara, K. (2011). Quick and Simple Modification of a Poly(dimethylsiloxane) Surface by Optimized Molecular Design of the Anti-biofouling Phospholipid Copolymer. *Soft Matter* 7 (6), 2968–2976. doi:10.1039/C0SM01292K

Shi, X., Dou, R., Ma, T., Liu, W., Lu, X., Shea, K. J., et al. (2015). Bioinspired Lotus-like Self-Illuminous Coating. *ACS Appl. Mater. Inter.* 7 (33), 18424–18428. doi:10.1021/acsami.5b04499

Siddiquie, R. Y., Agrawal, A., and Joshi, S. S. (2020). Surface Alterations to Impart Antiviral Properties to Combat COVID-19 Transmission. *Trans. Indian Natl. Acad. Eng.* 5 (2), 343–347. doi:10.1007/s41403-020-00096-9

Siddiquie, R. Y., Gaddam, A., Agrawal, A., Dimov, S. S., and Joshi, S. S. (2020). Anti-Biofouling Properties of Femtosecond Laser-Induced Submicron Topographies on Elastomeric Surfaces. *Langmuir* 36 (19), 5349–5358. doi:10.1021/acs.langmuir.0c00753

Simovich, T., Rosenhahn, A., and Lamb, R. N. (2020). Thermoregeneration of Plastrons on Superhydrophobic Coatings for Sustained Antifouling Properties. *Adv. Eng. Mater.* 22 (3), 1900806. doi:10.1002/adem.201900806

Sin, M.-C., Sun, Y.-M., and Chang, Y. (2014). Zwitterionic-based Stainless Steel with Well-Defined Polysulfobetaine Brushes for General Bioadhesive Control. *ACS Appl. Mater. Inter.* 6 (2), 861–873. doi:10.1021/am4041256

Stirpe, M., Brugnoli, B., Donelli, G., Francolini, I., and Vuotto, C. (2020). Poloxamer 338 Affects Cell Adhesion and Biofilm Formation in *Escherichia coli*: Potential Applications in the Management of Catheter-Associated Urinary Tract Infections. *Pathogens* 9 (11), 885. doi:10.3390/pathogens9110885

Su, B., Tian, Y., and Jiang, L. (2016). Bioinspired Interfaces with Superwettability: From Materials to Chemistry. *J. Am. Chem. Soc.* 138 (6), 1727–1748. doi:10.1021/jacs.5b12728

Su, M., Liu, Y., Zhang, Y., Wang, Z., Li, Y., and He, P. (2018). Robust and Underwater Superoleophobic Coating with Excellent Corrosion and Biofouling Resistance in Harsh Environments. *Appl. Surf. Sci.* 436, 152–161. doi:10.1016/j.apsusc.2017.11.215

Su, X., Hao, D., Xu, X., Guo, X., Li, Z., and Jiang, L. (2020). Hydrophilic/Hydrophobic Heterogeneity Anti-biofouling Hydrogels with Well-Regulated Rehydration. *ACS Appl. Mater. Inter.* 12 (22), 25316–25323. doi:10.1021/acsami.0c05406

Telford, A. M., James, M., Meagher, L., and Neto, C. (2010). Thermally Cross-Linked PNVP Films as Antifouling Coatings for Biomedical Applications. *ACS Appl. Mater. Inter.* 2 (8), 2399–2408. doi:10.1021/am100406j

Tian, Y., Su, B., and Jiang, L. (2014). Interfacial Material System Exhibiting Superwettability. *Adv. Mater.* 26 (40), 6872–6897. doi:10.1002/adma.201400883

Valencia, L., Kumar, S., Jalvo, B., Mautner, A., Salazar-Alvarez, G., and Mathew, A. P. (2018). Fully Bio-Based Zwitterionic Membranes with Superior Antifouling and Antibacterial Properties Prepared via Surface-Initiated Free-Radical Polymerization of Poly(cysteine Methacrylate). *J. Mater. Chem. A.* 6 (34), 16361–16370. doi:10.1039/c8ta06095a

Wang, B., Ye, Z., Tang, Y., Han, Y., Lin, Q., Liu, H., et al. (2016). Fabrication of Nonfouling, Bactericidal, and Bacteria Corpse Release Multifunctional Surface Through Surface-Initiated RAFT Polymerization. *Ijn* Vol. 12, 111–125. doi:10.2147/ijn.S107472

Wang, H., Jasensky, J., Ulrich, N. W., Cheng, J., Huang, H., Chen, Z., et al. (2017). Capsaicin-Inspired Thiol-Ene Terpolymer Networks Designed for Antibiofouling Coatings. *Langmuir* 33 (47), 13689–13698. doi:10.1021/acs.langmuir.7b03098

Wang, H., Wu, Y., Cui, C., Yang, J., and Liu, W. (2018). Antifouling Super Water Absorbent Supramolecular Polymer Hydrogel as an Artificial Vitreous Body. *Adv. Sci.* 5 (11), 1800711. doi:10.1002/advs.201800711

Wang, J., and He, C. (2019). Photopolymerized Biomimetic Self-Adhesive Polydimethylsiloxane-Based Amphiphilic Cross-Linked Coating for Anti-biofouling. *Appl. Surf. Sci.* 463, 1097–1106. doi:10.1016/j.apsusc.2018.08.214

Wang, L., Chen, X., Cao, X., Xu, J., Zuo, B., Zhang, L., et al. (2015). Fabrication of Polymer brush Surfaces with Highly-Ordered Perfluoroalkyl Side Groups at the Brush End and Their Antibiofouling Properties. *J. Mater. Chem. B* 3 (21), 4388–4400. doi:10.1039/C5TB00210A

Wang, X., Liu, X., Zhou, F., and Liu, W. (2011). Self-healing Superamphiphobicity. *Chem. Commun.* 47 (8), 2324–2326. doi:10.1039/c0cc04066e

Wang, Z., Scheres, L., Xia, H., and Zuilhof, H. (2020). Developments and Challenges in Self-Healing Antifouling Materials. *Adv. Funct. Mater.* 30 (26), 1908098. doi:10.1002/adfm.201908098

Wenzel, R. N. (1936). Resistance of Solid Surfaces to Wetting by Water. *Ind. Eng. Chem.* 28, 988–994. doi:10.1021/ie50320a024

Wu, D., Wang, J.-N., Wu, S.-Z., Chen, Q.-D., Zhao, S., Zhang, H., et al. (2011). Three-Level Biomimetic Rice-Leaf Surfaces with Controllable Anisotropic Sliding. *Adv. Funct. Mater.* 21 (15), 2927–2932. doi:10.1002/adfm.201002733

Wu, J.-G., Chen, J.-H., Liu, K.-T., and Luo, S.-C. (2019). Engineering Antifouling Conducting Polymers for Modern Biomedical Applications. *ACS Appl. Mater. Inter.* 11 (24), 21294–21307. doi:10.1021/acsami.9b04924

Wu, Z., Tong, W., Jiang, W., Liu, X., Wang, Y., and Chen, H. (2012). Poly(N-vinylpyrrolidone)-modified Poly(dimethylsiloxane) Elastomers as Anti-biofouling Materials. *Colloids Surf. B: Biointerfaces* 96, 37–43. doi:10.1016/j.colsurfb.2012.03.016

Xia, F., and Jiang, L. (2008). Bio-inspired, Smart, Multiscale Interfacial Materials. *Adv. Mater.* 20 (15), 2842–2858. doi:10.1002/adma.200800836

Xia, Y., Adibnia, V., Huang, R., Murschel, F., Faivre, J., Xie, G., et al. (2019). Biomimetic Bottlebrush Polymer Coatings for Fabrication of Ultralow Fouling Surfaces. *Angew. Chem. Int. Ed.* 58 (5), 1308–1314. doi:10.1002/anie.201808987

Xie, Q., Xie, Q., Pan, J., Ma, C., and Zhang, G. (2018). Biodegradable Polymer with Hydrolysis-Induced Zwitterions for Antibiofouling. *ACS Appl. Mater. Inter.* 10 (13), 11213–11220. doi:10.1021/acsami.8b00962

Xie, Y., Li, S.-S., Jiang, X., Xiang, T., Wang, R., and Zhao, C.-S. (2015). Zwitterionic Glycosyl Modified Polyethersulfone Membranes with Enhanced Anti-fouling Property and Blood Compatibility. *J. Colloid Interf. Sci.* 443, 36–44. doi:10.1016/j.jcis.2014.11.053

Xu, T., Yang, J., Zhang, J., Zhu, Y., Li, Q., Pan, C., et al. (2017). Facile Modification of Electrospun Fibrous Structures with Antifouling Zwitterionic Hydrogels. *Biomed. Mater.* 13 (1), 015021. doi:10.1088/1748-605X/aa89b2

Yang, H., Chang, H., Zhang, Q., Song, Y., Jiang, L., Jiang, Q., et al. (2020). Highly Branched Copolymers with Degradable Bridges for Antifouling Coatings. *ACS Appl. Mater. Inter.* 12 (14), 16849–16855. doi:10.1021/acsami.9b22748

Ye, Q., He, B., Zhang, Y., Zhang, J., Liu, S., and Zhou, F. (2019). Grafting Robust Thick Zwitterionic Polymer Brushes via Subsurface-Initiated Ring-Opening Metathesis Polymerization for Antimicrobial and Anti-biofouling. *ACS Appl. Mater. Inter.* 11 (42), 39171–39178. doi:10.1021/acsami.9b11946

Yebra, D. M., Kiil, S., and Dam-Johansen, K. (2004). Antifouling Technology-Past, Present and Future Steps Towards Efficient and Environmentally Friendly Antifouling Coatings. *Prog. Org. Coat.* 50 (2), 75–104. doi:10.1016/j.porgcoat.2003.06.001

Yeh, S.-B., Chen, C.-S., Chen, W.-Y., and Huang, C.-J. (2014). Modification of Silicone Elastomer with Zwitterionic Silane for Durable Antifouling Properties. *Langmuir* 30 (38), 11386–11393. doi:10.1021/la502486e

Yin, Z., Cheng, C., Qin, H., Nie, C., He, C., and Zhao, C. (2015). Hemocompatible Polyethersulfone/polyurethane Composite Membrane for High-Performance Antifouling and Antithrombotic Dialyzer. *J. Biomed. Mater. Res.* 103 (1), 97–105. doi:10.1002/jbm.b.33177

Young, T. (1805). III. An Essay on the Cohesion of Fluids. *Phil. Trans. R. Soc.* 95 (0), 65–87. doi:10.1098/rstl.1805.0005

Yu, H., Cao, Y., Kang, G., Liu, J., Li, M., and Yuan, Q. (2009). Enhancing Antifouling Property of Polysulfone Ultrafiltration Membrane by Grafting Zwitterionic Copolymer via UV-Initiated Polymerization. *J. Membr. Sci.* 342 (1-2), 6–13. doi:10.1016/j.memsci.2009.05.041

Yu, S., Guo, Z., and Liu, W. (2015). Biomimetic Transparent and Superhydrophobic Coatings: From Nature and Beyond Nature. *Chem. Commun.* 51 (10), 1775–1794. doi:10.1039/C4CC06868H

Yu, Y., Shao, H., He, Z., Tang, C., Yang, J., Li, Y., et al. (2018). Patternable Poly(chloro-P-Xylylene) Film with Tunable Surface Wettability Prepared by Temperature and Humidity Treatment on a Polydimethylsiloxane/Silica Coating. *Materials* 11 (4), 486. doi:10.3390/ma11040486

Zarghami, S., Mohammadi, T., Sadrzadeh, M., and Van der Bruggen, B. (2019). Superhydrophilic and Underwater Superoleophobic Membranes - A Review of Synthesis Methods. *Prog. Polym. Sci.* 98, 101166. doi:10.1016/j.progpolymsci.2019.101166

Zhang, D., Ren, B., Zhang, Y., Liu, Y., Chen, H., Xiao, S., et al. (2020). Micro- and Macroscopically Structured Zwitterionic Polymers with Ultralow Fouling Property. *J. Colloid Interf. Sci.* 578, 242–253. doi:10.1016/j.jcis.2020.05.122

Zhang, H., and Chiao, M. (2015). Anti-fouling Coatings of Poly(dimethylsiloxane) Devices for Biological and Biomedical Applications. *J. Med. Biol. Eng.* 35 (2), 143–155. doi:10.1007/s40846-015-0029-4

Zhang, J., Chen, L., Chen, L., Qian, S., Mou, X., and Feng, J. (2021). Highly Antifouling, Biocompatible and Tough Double Network Hydrogel Based on Carboxybetaine-type Zwitterionic Polymer and Alginate. *Carbohydr. Polym.* 257, 117627. doi:10.1016/j.carbpol.2021.117627

Zhang, J., Qian, S., Chen, L., Chen, L., Zhao, L., and Feng, J. (2021). Highly Antifouling Double Network Hydrogel Based on Poly(sulfobetaine Methacrylate) and Sodium Alginate with Great Toughness. *J. Mater. Sci. Technol.* 85, 235–244. doi:10.1016/j.jmst.2021.01.012

Zhang, J., Wang, G., Zhang, J., Xu, Z., Zhao, Y., Wang, Y., et al. (2021). Substrate-Independent, Regenerable Anti-biofouling Coating for Polymeric Membranes. *Membranes* 11 (3), 205. doi:10.3390/membranes11030205

Zhang, P., Lin, L., Zang, D., Guo, X., and Liu, M. (2016). Designing Bioinspired Anti-biofouling Surfaces Based on a Superwettability Strategy. *Small* 13 (4), 1503334. doi:10.1002/smll.201503334

Zhao, X., and Liu, C. (2016). One-step Fabricated Bionic PVDF Ultrafiltration Membranes Exhibiting Innovative Antifouling Ability to the Cake Fouling. *J. Membr. Sci.* 515, 29–35. doi:10.1016/j.memsci.2016.05.025

Zheng, J., Song, W., Huang, H., and Chen, H. (2010). Protein Adsorption and Cell Adhesion on Polyurethane/Pluronic Surface with Lotus Leaf-like Topography. *Colloids Surf. B: Biointerfaces* 77 (2), 234–239. doi:10.1016/j.colsurfb.2010.01.032

Zheng, S., Bawazir, M., Dhall, A., Kim, H.-E., He, L., Heo, J., et al. (2021). Implication of Surface Properties, Bacterial Motility, and Hydrodynamic Conditions on Bacterial Surface Sensing and Their Initial Adhesion. *Front. Bioeng. Biotechnol.* 9 (82), 643722. doi:10.3389/fbioe.2021.643722

Zhou, J., Lin, Y., Wang, L., Zhou, L., Yu, B., Zou, X., et al. (2021). Poly(carboxybetaine Methacrylate) Grafted on PVA Hydrogel via a Novel Surface Modification Method Under Near-Infrared Light for Enhancement of Antifouling Properties. *Colloids Surf. A: Physicochemical Eng. Aspects* 617, 126369. doi:10.1016/j.colsurfa.2021.126369

Zhu, D., Li, X., Zhang, G., Zhang, X., Zhang, X., Wang, T., et al. (2010). Mimicking the Rice Leaf-From Ordered Binary Structures to Anisotropic Wettability. *Langmuir* 26 (17), 14276–14283. doi:10.1021/la102243c

Zhu, H., Hu, W., Xu, Y., Wang, B., Zheng, D., Fu, Y., et al. (2019). Gradient Structure Based Dual-Robust Superhydrophobic Surfaces with High-Adhesive Force. *Appl. Surf. Sci.* 463, 427–434. doi:10.1016/j.apsusc.2018.08.241

Zhu, L., Liu, F., Yu, X., and Xue, L. (2015). Poly(Lactic Acid) Hemodialysis Membranes with Poly(Lactic Acid)-Block-Poly(2-Hydroxyethyl Methacrylate) Copolymer as Additive: Preparation, Characterization, and Performance. *ACS Appl. Mater. Inter.* 7 (32), 17748–17755. doi:10.1021/acsami.5b03951

Zhu, L., Song, H., Wang, J., and Xue, L. (2017). Polysulfone Hemodiafiltration Membranes with Enhanced Anti-fouling and Hemocompatibility Modified by Poly(vinyl Pyrrolidone) via In Situ Cross-Linked Polymerization. *Mater. Sci. Eng. C* 74, 159–166. doi:10.1016/j.msec.2017.02.019

Zhu, X., Zhang, Z., Ren, G., Yang, J., Wang, K., Xu, X., et al. (2012). A Novel Superhydrophobic Bulk Material. *J. Mater. Chem.* 22 (38), 20146–20148. doi:10.1039/C2JM33769J

Conflict of Interest: The authors declare that the research was conducted in the absence of any commercial or financial relationships that could be construed as a potential conflict of interest.

Publisher's Note: All claims expressed in this article are solely those of the authors and do not necessarily represent those of their affiliated organizations, or those of the publisher, the editors and the reviewers. Any product that may be evaluated in this article, or claim that may be made by its manufacturer, is not guaranteed or endorsed by the publisher.

frontiers in Bioengineering and Biotechnology

CASE REPORT
published: 13 December 2021
doi: 10.3389/fbioe.2021.811229

Case Report: A Pseudoaneurysm Involving the Left Common Iliac Artery Secondary to Brucellosis: A Rare Case Report

Qilong Wang[1], Liang Tang[2], Yue Qin[1], Qi Wang[1], Ping Zhang[3] and Zhihua Cheng[1]**

[1]Department of Vascular Surgery, The First Bethune Hospital of Jilin University, Changchun, China, [2]Department of Neurology, Songyuan Jilin Oilfield Hospital, Songyuan, China, [3]Department of Hepatopancreatobiliary Surgery, The First Bethune Hospital of Jilin University, Changchun, China

OPEN ACCESS

Edited by:
Mingqiang Li,
Sun Yat-sen University, China

Reviewed by:
Zilun Li,
The First Affiliated Hospital of Sun Yat-sen University, China
Guandou Yuan,
Guangxi Medical University, China
Yuchen Jing,
The First Affiliated Hospital of China Medical University, China

***Correspondence:**
Ping Zhang
z_ping@jlu.edu.cn
Zhihua Cheng
chengzh@jlu.edu.cn

Specialty section:
This article was submitted to Biomaterials, a section of the journal Frontiers in Bioengineering and Biotechnology

Received: *08 November 2021*
Accepted: *30 November 2021*
Published: *13 December 2021*

Citation:
Wang Q, Tang L, Qin Y, Wang Q, Zhang P and Cheng Z (2021) Case Report: A Pseudoaneurysm Involving the Left Common Iliac Artery Secondary to Brucellosis: A Rare Case Report. Front. Bioeng. Biotechnol. 9:811229. doi: 10.3389/fbioe.2021.811229

Pseudoaneurysms of the common iliac artery caused by Brucellosis are exceedingly uncommon. Infected common iliac artery pseudoaneurysms, particularly those caused by brucellosis, are more difficult to diagnose and cure than general pseudoaneurysms. The risk of mortality is significantly high in this condition. Nonsurgical treatment of a brucellosis-induced common iliac artery pseudoaneurysm is futile, and it should be operated on as soon as feasible. Long-term and multi-course antibacterial therapy with combination antibiotics is required. For the treatment of *Brucella*-infected pseudoaneurysms, endovascular surgery can be both effective and safe.

Keywords: brucellosis, common iliac artery, pseudoaneurysm, endovascular surgery, case report

INTRODUCTION

Brucellosis is a zoonotic infection caused by bacteria of the genus *Brucella* (Wang et al., 2017; Amjadi et al., 2019; Bagheri Nejad et al., 2020; Iqbal et al., 2020). Fever, hyperhidrosis, fatigue, joint soreness, and lymphadenopathy (Jia et al., 2017; Liang et al., 2018; Alkahtani et al., 2020) are some of the clinical manifestations of the condition. Infection is spread mostly through infected animals and their products (Zhang et al., 2018; Willems et al., 2021). *Brucella* infection in humans is typically transmitted by direct contact with the skin and mucous membranes (Haque et al., 2011). However, on occasion, food-borne diseases are transferred through the digestive tract and infections are transmitted through the respiratory tract via inhalation of contaminated droplets and dust; humans are generally susceptible to *Brucella*. Additionally, brucellosis can have a detrimental effect on the respiratory, circulatory, digestive, and nervous systems. Endocarditis and pericarditis are the most prevalent disease symptoms of the circulatory system, while pseudoaneurysms involving the left common iliac artery are extremely rare. A pseudoaneurysm involving the common iliac artery that is infected is unstable. In medicine, it is frequently referred to as an "untimed bomb" implanted in the body that is likely to "explode" at any time, referring to aneurysm rupture and hemorrhage. Severe bleeding can result in hemorrhagic shock and lead to death. Herein, we report a rare instance of pseudoaneurysm affecting the left common iliac artery due to brucellosis and detail the treatment of this patient.

CASE PRESENTATION

A 67-year-old man, a local farmer specializing in sheep and swine production, was admitted to the Department of Vascular Surgery of the First Bethune Hospital of Jilin University in July 2019 after

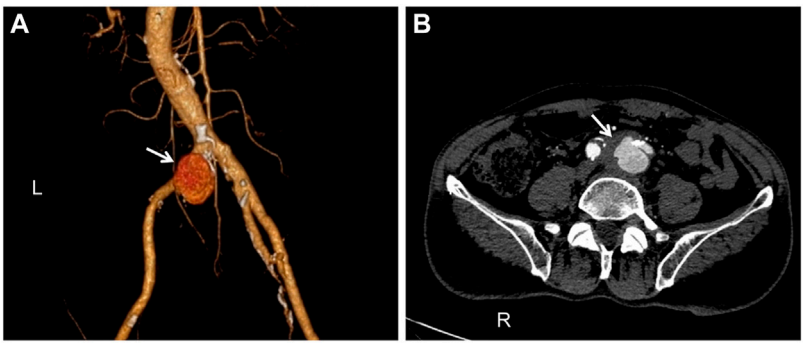

FIGURE 1 | Computed tomography angiography (CTA): **(A)**. The pseudoaneurysm has a maximum diameter of 33 mm and is placed near the commencement of the left common iliac artery (white arrow). **(B)**. A breach is visible in the arterial wall, and there is an overflow of contrast agents (white arrow).

experiencing back pain for 3 days. For 1 month, the patient developed a fever with a maximum temperature of 39°C, which was alleviated with non-steroidal anti-inflammatory medicines (NSAIDs). The course of the disease was accompanied by fatigue and hyperhidrosis, but there was no joint discomfort. Medical and family history were unremarkable. The skin and sclera of the patient were not yellowish, nor were his abdominal muscles tense, tender, or creating rebound pain. The patient's liver and spleen were not palpable beneath the ribs, nor was the entire abdomen. Percussion and auscultation in the abdomen were normal. Physical examination revealed a temperature of 36.3°C, heart rate of 78/min, respiratory rate of 18/min, and blood pressure of 146/80 mmHg. Laboratory examination showed the following results: C-reactive protein, 8.19 mg/L; erythrocyte sedimentation rate, 29 mm/1 h; white blood cell count, 5.95×10^9/L; and hemoglobin, 127 g/L. All other laboratory tests were within normal limits. The *Brucella* tube agglutination test showed a titer of 1:400, and a solid and accurate diagnosis was made by isolating *Brucella* in the blood culture. We found pseudoaneurysm formation using computed tomography angiography (CTA) (**Figures 1A,B**). Accordingly, the patient was diagnosed with a brucellosis-related left common iliac artery pseudoaneurysm. The patient had no pseudoaneurysms elsewhere. To our knowledge, no previous report of a left common iliac artery pseudoaneurysm owing to brucellosis has been reported. Nonsurgical treatment of a common iliac artery pseudoaneurysm caused by brucellosis is ineffective, and it should be operated on as soon as possible. However, the patient underwent surgery while being infected systemically and then faced the possibility of reoperation and death following implant infection. Hence, a long-term and multi-course antibiotic treatment with combined antibacterial agents was required. Our patient was first treated for 6 weeks with doxycycline and rifampicin while preparing for emergency surgery at any time. After 6 weeks, the *Brucella* tube agglutination test was positive, and the blood culture of *Brucella* was negative. It represents a previous infection with *Brucella*. Endovascular aneurysm repair (EVAR) was performed under general anesthesia after the patient's infection was controlled to prevent mortality and further complications from the left common iliac artery pseudoaneurysm. A TAG-covered stent graft (W. L. Gore & Associates, Inc., Flagstaff, AE, United States) was used to isolate the pseudoaneurysm. A 6F sheath (Terumo Corporation, Japan) was retrogradely inserted into the left common femoral artery intraoperatively. On digital subtraction angiography with a pigtail catheter, a pseudoaneurysm was identified (**Figure 2A**). Then, with the help of a Lunderquist® Extra-Stiff Wire Guide (Cook Medical Inc., Denmark), a 22F sheath (W. L. Gore & Associates, Inc., Flagstaff, AE, United States) was introduced and a 26 mm × 12 mm × 18 cm TAG-coated stent-graft and a 16 mm × 12 mm × 12 cm endoprosthesis contralateral leg (W. L. Gore & Associates, Inc., Flagstaff, AE, United States) were implanted to isolate the pseudoaneurysm. In the final angiography, no endoleaks were identified. The contrast agent went smoothly through the left common iliac artery without leakage (**Figure 2B**). The anti-brucellosis medication was maintained following surgery due to possible recurrence, and the patient's painful symptoms progressively subsided after 3 days. After surgery, the patient was discharged from the hospital. There were no reports of relapse in the 1-month, 6-months, 1-year, and 2-years follow-up assessments. The patient had no other endovascular complications.

DISCUSSION

Brucellosis is a zoonotic disease that is frequently transmitted from animals to humans, but is only rarely passed between humans (Colomba et al., 2012). Vascular pathological symptoms of brucellosis are infrequent (Willems et al., 2021). After bacterial colonization of the arterial wall (Amirghofran et al., 2011), the artery's structure is damaged, which may result in life-threatening bleeding. Once ruptured, it can also be wrapped by surrounding soft tissues, resulting in the formation of pseudoaneurysms. Pseudoaneurysms produced by brucellosis are uncommon in clinical practice. Diagnosing and treating infected common iliac artery pseudoaneurysms, particularly those produced by *Brucella*, is more challenging than general pseudoaneurysms (Chiyoya et al., 2019). The incidence of

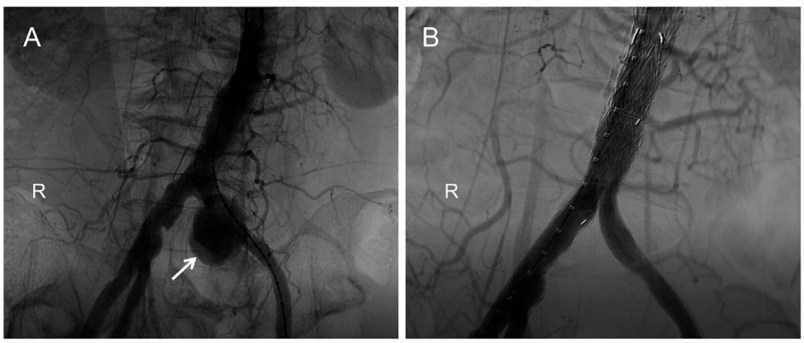

FIGURE 2 | Digital subtraction angiography (DSA): **(A)**. The pseudoaneurysm was observed by contrast-medium overflow (white arrow). **(B)**. Postoperatively, angiography showed no contrast-agent spillage in the left common iliac artery.

positive blood cultures (particularly following antibiotic therapy) is clinically insignificant, and markers such as erythrocyte sedimentation rate, C-reactive protein (al-Kassab et al., 1991), and procalcitonin are not specific for infected pseudoaneurysms (Kayaaslan et al., 2016; Liu and Zhao, 2017). The signs and symptoms of the patient were not specific (Harman et al., 2004). Patients in some cases were asymptomatic. Owing to the fact that *Brucella* reproduces primarily in the cells of the human reticuloendothelial system, it is difficult to treat and relapses often. If pseudoaneurysms are not treated promptly, they might rupture at any time. As a result, it must be operated upon as soon as possible. Traditionally, aneurysmectomy, local debridement, and graft replacement have been used to treat this condition (Chakfé et al., 2020). Under general anesthesia, the patient had a major incision to reveal and excise the pseudoaneurysm and replace it with an artificial blood vessel. Pseudoaneurysms lack a full wall, making surgery challenging, posing a high risk of rupture, resulting in significant surgical stress and a protracted postoperative recovery time. While endovascular repair involves minimal trauma, has a low complication rate, and allows for rapid postoperative recovery (Willems et al., 2021), it has stringent criteria for correct stent placement and sealing. Primary treatment, in our opinion, should always be the first option in endovascular surgery. Because endovascular repair does not require anatomical or arterial incision, it significantly streamlines the surgery process. This method results in less bleeding and trauma; is well tolerated by the patient and is safe and effective; results in fewer problems; has a quicker recovery; and has other benefits that traditional surgery cannot match (Goodney et al., 2011). The primary advantage of endovascular repair for an infected left common iliac artery pseudoaneurysm is that it minimizes the risk of infection spreading. If endovascular repair is unsuccessful, conventional surgery to remove the iliac artery and rebuild arterial access can be undertaken. However, endograft infection and difficulty with secondary intervention are common issues for both intracavitary and open conventional surgery. Infected endografts are very difficult to treat, and often have poor prognosis (Laohapensang et al., 2017). Therefore, surgical therapy should begin as soon as the existing infection is managed. As a result, antibiotics must be used in combination. The World Health Organization recommends a 6-weeks course of doxycycline (100 mg, bid) and rifampicin (600–900 mg/d) (Fillmore and Valentine, 2003). Reasonable and standardized application of antibiotics can play a key role in the effective control of *Brucella*, thereby reducing the possibility of pseudoaneurysms in other blood vessels. Once the pseudoaneurysm appears, it should be treated as soon as possible to avoid aggravation. Therefore, regular physical examinations are necessary. To assess if a patient can wait for surgery following infection management, we consider two factors: 1) repeat CT to detect whether the pseudoaneurysm body has increased further; and 2) determine whether the patient's symptoms such as back pain and fever have deteriorated. Following a repeat CT examination, our patient's pseudoaneurysm body did not expand, and the patient's symptoms progressively improved with anti-infective medication. In preparation for emergency surgery, we make every effort to complete an adequate antibiotic course. No bacterial growth was seen in blood cultures. After the patient's infection was managed, EVAR was conducted. Antibiotic therapy was continued for 6 weeks following surgery. We recommend CT examination every 6 months. Although endovascular therapy has established itself as a safe and successful alternative to open surgery in the treatment of pseudoaneurysms, there is still a dearth of experience in this area. Simultaneously, medication therapy for brucellosis is crucial. Thus, we presented this case report to increase awareness of the condition, decrease the rate of missed diagnoses and misdiagnoses, and promote active and successful treatment and improve prognosis. Therefore, in individuals with a history of contact with cattle and sheep, long-term unexplained fever, and back and abdominal pain, *Brucella*-infection induced common iliac artery pseudoaneurysm should be considered in the differential diagnosis, and timely blood culture, antibody testing, and CTA, as well as other related checks should be performed to avoid life-threatening delays in treatment.

DATA AVAILABILITY STATEMENT

The original contributions presented in the study are included in the article/Supplementary Material, further inquiries can be directed to the corresponding authors.

ETHICS STATEMENT

The studies involving human participants were reviewed and approved by the First Bethune Hospital of Jilin University. The patients/participants provided their written informed consent to participate in this study. Written informed consent was obtained from the individual(s) for the publication of any potentially identifiable images or data included in this article.

AUTHOR CONTRIBUTIONS

QW evaluated the patient and initiated the case report and reviewed the literature and drafted the manuscript; LT, ZC, QW, and PZ consulted the relevant literature and contributed to the diagnosis and treatment of the patient; YQ and PZ were responsible for formulating the patient's treatment plan and revising the manuscript. All authors issued final approval for the version to be submitted.

FUNDING

This study was financially supported by the Natural Science Foundation of Jilin Province, China: No. 20200201353JC, No. 20210204157YY, and No. 20210101276JC.

REFERENCES

al-Kassab, A. S., Nur, M. A., and Malik, J. M. (1991). Evaluation of Serum C-Reactive Protein in the Diagnosis of Arthritic and Non-arthritic Brucellosis. *J. Trop. Med. Hyg.* 94, 92–96.

Alkahtani, A. M., Assiry, M. M., Chandramoorthy, H. C., Al-Hakami, A. M., and Hamid, M. E. (2020). Sero-prevalence and Risk Factors of Brucellosis Among Suspected Febrile Patients Attending a Referral Hospital in Southern Saudi Arabia (2014-2018). *BMC Infect. Dis.* 20, 26. doi:10.1186/s12879-020-4763-z

Amirghofran, A. A., Karimi, A., Emaminia, A., Sharifkazemi, M. B., and Salaminia, S. (2011). Brucellosis Relapse Causing Prosthetic Valve Endocarditis and Aortic Root Infective Pseudoaneurysm. *Ann. Thorac. Surg.* 92, e77–e79. doi:10.1016/j.athoracsur.2011.03.144

Amjadi, O., Rafiei, A., Mardani, M., Zafari, P., and Zarifian, A. (2019). A Review of the Immunopathogenesis of Brucellosis. *Infect. Dis.* 51, 321–333. doi:10.1080/23744235.2019.1568545

Bagheri Nejad, R., Krecek, R. C., Khalaf, O. H., Hailat, N., and Arenas-Gamboa, A. M. (2020). Brucellosis in the Middle East: Current Situation and a Pathway Forward. *Plos Negl. Trop. Dis.* 14, e0008071. doi:10.1371/journal.pntd.0008071

Chakfé, N., Diener, H., Lejay, A., Assadian, O., Berard, X., Caillon, J., et al. (2020). Editor's Choice - European Society for Vascular Surgery (ESVS) 2020 Clinical Practice Guidelines on the Management of Vascular Graft and Endograft Infections. *Eur. J. Vasc. Endovascular Surg.* 59, 339–384. doi:10.1016/j.ejvs.2019.10.016

Chiyoya, M., Kondo, N., Taniguchi, S., and Fukuda, I. (2019). Endovascular Treatment for a Perforated Superficial Femoral Vein Graft for an Infected Abdominal Aortic Aneurysm. *Ann. Vasc. Dis.* 12, 91–94. doi:10.3400/avd.cr.18-00095

Colomba, C., Siracusa, L., Rubino, R., Trizzino, M., Scarlata, F., Imburgia, C., et al. (2012). A Case ofBrucellaEndocarditis in Association with Subclavian Artery Thrombosis. *Case Rep. Infect. Dis.* 2012, 1–3. doi:10.1155/2012/581489

Fillmore, A. J., and Valentine, R. J. (2003). Surgical Mortality in Patients with Infected Aortic Aneurysms. *J. Am. Coll. Surgeons* 196, 435–441. doi:10.1016/s1072-7515(02)01607-1

Goodney, P. P., Travis, L., Lucas, F. L., Fillinger, M. F., Goodman, D. C., Cronenwett, J. L., et al. (2011). Survival after Open versus Endovascular Thoracic Aortic Aneurysm Repair in an Observational Study of the Medicare Population. *Circulation* 124, 2661–2669. doi:10.1161/circulationaha.111.033944

Haque, N., Bari, M. S., Hossain, M. A., Muhammad, N., Ahmed, S., Rahman, A., et al. (2011). An Overview of Brucellosis. *Mymensingh Med. J.* 20, 742–747.

Harman, M., Irmak, H., Arslan, H., Arslan, n., and Kayan, M. (2004). Popliteal Artery Pseudoaneurysm: a Rare Complication of Brucellosis. *J. Clin. Ultrasound* 32, 33–36. doi:10.1002/jcu.10217

Iqbal, M., Fatmi, Z., and Khan, M. (2020). Brucellosis in Pakistan: a Neglected Zoonotic Disease. *J. Pak Med. Assoc.* 70, 1625–1626. doi:10.5455/jpma.24139

Jia, B., Zhang, F., Lu, Y., Zhang, W., Li, J., Zhang, Y., et al. (2017). The Clinical Features of 590 Patients with Brucellosis in Xinjiang, China with the Emphasis on the Treatment of Complications. *Plos Negl. Trop. Dis.* 11, e0005577. doi:10.1371/journal.pntd.0005577

Kayaaslan, B., Bastug, A., Aydin, E., Akinci, E., But, A., Aslaner, H., et al. (2016). A Long-Term Survey of Brucellosis: Is There Any Marker to Predict the Complicated Cases? *Infect. Dis.* 48, 215–221. doi:10.3109/23744235.2015.1107187

Laohapensang, K., Arworn, S., Orrapin, S., Reanpang, T., and Orrapin, S. (2017). Management of the Infected Aortic Endograft. *Semin. Vasc. Surg.* 30, 91–94. doi:10.1053/j.semvascsurg.2017.11.001

Liang, C., Wei, W., Liang, X. W., Wang, L. J., Peng, L., and De, E. J. (2018). Occupational Characteristics and Clinical Manifestations of 245 Cases of Occupational Brucellosis. *Zhonghua Lao Dong Wei Sheng Zhi Ye Bing Za Zhi* 36, 755–758. doi:10.3760/cma.j.issn.1001-9391.2018.10.009

Liu, J., and Zhao, X. (2017). Clinical Features and Serum Profile of Inflammatory Biomarkers in Patients with Brucellosis. *J. Infect. Dev. Ctries* 11, 840–846. doi:10.3855/jidc.8872

Wang, S., Wang, Q., Liu, H., Sun, S., Sun, X., Zhang, Y., et al. (2017). Endovascular Treatment of Thoracic Aortic Pseudoaneurysm Due to Brucellosis: a Rare Case Report. *BMC Infect. Dis.* 17, 387. doi:10.1186/s12879-017-2485-7

Willems, S. A., Buntinx, M., Gelinck, L. B. S., van Schaik, J., and Eefting, D. (2021). Ruptured Aneurysm of the Common Iliac Artery Caused by Brucella Melitensis: A Case Report. *EJVES Vasc. Forum* 52, 26–29. doi:10.1016/j.ejvsvf.2021.06.011

Zhang, N., Huang, D., Wu, W., Liu, J., Liang, F., Zhou, B., et al. (2018). Animal Brucellosis Control or Eradication Programs Worldwide: A Systematic Review of Experiences and Lessons Learned. *Prev. Vet. Med.* 160, 105–115. doi:10.1016/j.prevetmed.2018.10.002

Conflict of Interest: The authors declare that the research was conducted in the absence of any commercial or financial relationships that could be construed as a potential conflict of interest.

Publisher's Note: All claims expressed in this article are solely those of the authors and do not necessarily represent those of their affiliated organizations, or those of the publisher, the editors and the reviewers. Any product that may be evaluated in this article, or claim that may be made by its manufacturer, is not guaranteed or endorsed by the publisher.

frontiers in Bioengineering and Biotechnology

ORIGINAL RESEARCH
published: 13 December 2021
doi: 10.3389/fbioe.2021.799370

Photothermal Detection of MicroRNA Using a Horseradish Peroxidase-Encapsulated DNA Hydrogel With a Portable Thermometer

Xiujuan Liu[1], Meixiang Zhang[1], Ze Chen[1], Jiuqing Cui[2], Long Yang[1], Zihe Lu[3], Fang Qi[1] and Haixia Wang[1]*

[1]Department of Intensive Care Unit, The First Hospital of Qinhuangdao, Qinhuangdao, China, [2]Department of Intensive Care Unit, Hebei Petrochina Central Hospital, Langfang, China, [3]Department of Intensive Care Unit, Chengde Medical University, Chengde, China

OPEN ACCESS

Edited by:
Jianxun Ding,
Changchun Institute of Applied Chemistry (CAS), China

Reviewed by:
Rui Liu,
Sichuan University, China
Shun Duan,
Beijing University of Chemical Technology, China
Xiao Gong,
Wuhan University of Technology, China
Cheng Du,
Sun Yat-sen University, China

***Correspondence:**
Xiujuan Liu
xiujuanliu1965@163.com

Specialty section:
This article was submitted to Biomaterials, a section of the journal Frontiers in Bioengineering and Biotechnology

Received: 21 October 2021
Accepted: 29 November 2021
Published: 13 December 2021

Citation:
Liu X, Zhang M, Chen Z, Cui J, Yang L, Lu Z, Qi F and Wang H (2021) Photothermal Detection of MicroRNA Using a Horseradish Peroxidase-Encapsulated DNA Hydrogel With a Portable Thermometer. Front. Bioeng. Biotechnol. 9:799370. doi: 10.3389/fbioe.2021.799370

MicroRNA (miRNA) detection has attracted widespread interest as a tumor detection marker. In this work, a miRNA-responsive visual and temperature sensitive probe composed of a horseradish peroxidase (HRP)-encapsulated DNA hydrogel was designed and synthesized. The biosensor converted the miRNA hybridization signal to a photothermal effect which was measured using a digital thermometer. The substrate DNA linker strand of the hydrogel hybridizes with different sequences of miRNA resulting in the collapse of the hydrogel and the release of HRP. HRP oxidizes 3,3′,5,5′-tetramethylbenzidine (TMB) resulting in a color change and a strong photothermal effect was observed after shining near-infrared light on the oxidized product. The thermometer-based readout method has a wide linear range (0.5–4.0 μM) and a limit of detection limit of 7.8 nM which is comparable with traditional UV-vis absorption spectrometry detection and quantitative real time polymerase chain reaction methods. The low cost, ease of operation, and high sensitivity shows that this biosensor has potential for point-of-care biomolecular detection and biomedical applications.

Keywords: detection of MicroRNAs, photothermal detection, biosensor, hydrogel, tumor detection marker

INTRODUCTION

MicroRNAs (miRNAs) are endogenous non-coding RNAs and post-transcriptional gene regulators which are closely related to tumor occurrence and development (Wightman et al., 1993; Bartel, 2009; Lin and Gregory, 2015; Das and Ghosal, 2018). Deregulated miRNAs exist in the plasma and serum of many cancer patients (Lin and Gregory, 2015; Armand-Labit and Pradines, 2017; Ji and Guo, 2019; Si et al., 2020). Increased miRNA expression is correlated with cancer cells or the presence of tumorous tissues and high levels are also found in the peripheral blood (Mitchell et al., 2008; Boeri et al., 2011; Kelly et al., 2013). Thus, elevated miRNA levels are tumor markers and their detection has attracted widespread interest. Detection of miRNA levels over the past decade has included northern blotting, real-time quantitative polymerase chain reaction (qRT-PCR), flow cytometry, microarray, and enzyme-catalyzed amplification technology (Calin et al., 2004; Guo et al., 2009; Git et al., 2010; Pritchard et al., 2012; Porichis et al., 2014). However, high-efficiency and sensitive

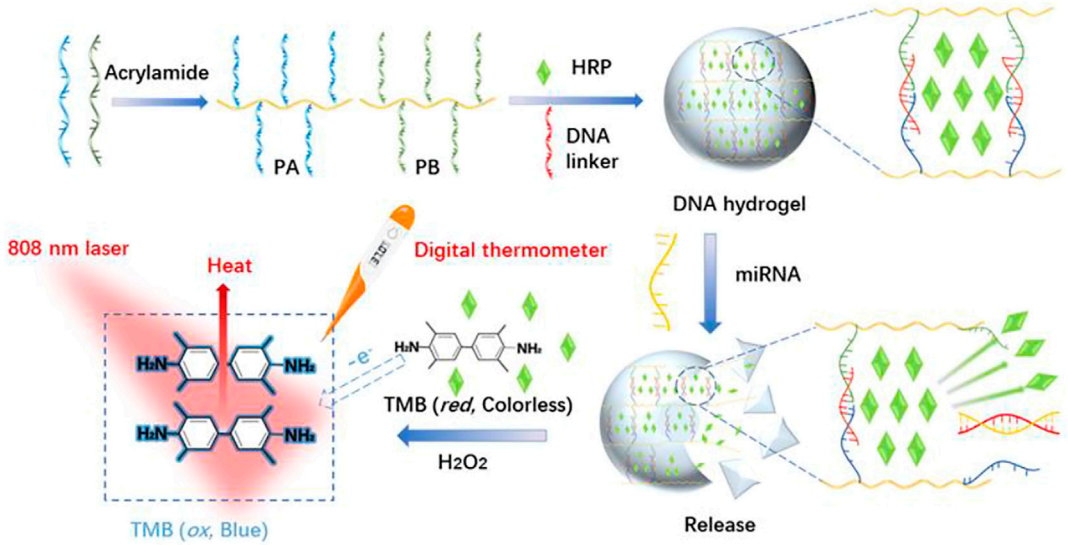

SCHEME 1 | Schematic illustration of the synthesis of stimuli-response DNA hydrogels and photothermal sensing detection of miRNAs based on HRP-Mediated TMB-H_2O_2 colorimetric system.

detection of miRNAs is challenging because they have low abundance, readily degraded, require accurate temperature control, and involve complex processes and expensive equipment (Li et al., 2016). The current gold standard method for detecting miRNA by northern blotting is time consuming, has low sensitivity, is at risk of degradation by RNases, and involves the use of carcinogenic chemicals (ethidium bromide and formaldehyde). Meanwhile, qRT-PCR exhibits highly sensitive detection but it suffers from poor selectivity and low specificity (Li et al., 2020). Alternatively, biosensors based on fluorescence, electrochemistry, photoelectrochemistry, and chemiluminescence are promising analytical technologies with high selectivity and sensitivity compared with conventional miRNA detection methods (Zheng et al., 2019a; Wang et al., 2020; Jin et al., 2021). Biosensing detection based on visual recognition and quantitation through a portable readout is potentially an ideal detection approach because output signals are obtained by simple portable analytical instruments or the naked eye which overcomes the limitations of assay readout methods dependent on complex, expensive, and bulky analytical equipment (Qu et al., 2011; Fu et al., 2016; Zheng et al., 2019b; Zhao et al., 2019; Xu et al., 2020; Xu et al., 2021).

The horseradish peroxidase (HRP)-3,3′,5,5′-tetramethylbenzidine (TMB)-H_2O_2 system (HRP-TMB- H_2O_2) has been explored as a classical system for portable qualitative detection. HRP catalyzes the one-electron oxidation of TMB to generate a blue colored charge-transfer complex of oxidized TMB (oxTMB) with an absorbance maximum of 652 nm. OxTMB also exhibits a strong near infrared (NIR) laser-driven photothermal effect which could be used as a highly sensitive photothermal probe (Fu et al., 2016). However, HRP is easily affected by the detecting environment. Hydrogel is a type of cross-linked hydrophilic polymer and a large amount of water can be absorbed. Hydrophilic polymers can be dissolved in water without a defined shape, however, after cross-links, the solid-like three-dimensional structures are formed, which bring a uid-like properties (Guan et al., 2020; Wei et al., 2020). Stimulus-responsive (or target-responsive) DNA hydrogels composed of multifunctional polymers as the backbone and functional DNA as the cross-linker are potential colorimetric sensors carrying enzymes because of their biocompatibility, encapsulation and release capability, flexibility, and mechanical stability (Xiang and Lu, 2012; Kahn et al., 2017; Amalfitano et al., 2021; Liu et al., 2021). They are widely used for the determination of various targets including ions, small molecules, nucleic acids, and proteins (Zhu et al., 2010; Lin et al., 2011; Yan et al., 2013).

Herein, a target-responsive DNA hydrogel-based biosensor was generated and applied for visual recognition and portable photothermal quantification of miRNAs using a common thermometer readout (**Scheme 1**). PA and PB were synthesized by copolymerization of acrylic DNA and acrylamide monomers, cross-linked with a substrate DNA linker strand containing partial complementary sequences with PA and PB, and complete complementary sequence of miRNA to form a hydrogel with encapsulated HRP. In the presence of miRNA, the substrate DNA linker strand hybridized with miRNA which led to the collapse of the hydrogel and HRP release. Then, released HRP oxidized TMB-H_2O_2 and formed a blue colored product. Laser NIR irradiation of oxidized TMB at 808 nm exhibited a strong photothermal effect resulting in the conversion of the miRNA hybridization signal to heat. A digital thermometer detected the signal with a linear detection range from 0.5 to 4.0 μM and a limit of detection of 7.8 nM. Therefore, this strategy achieved visual recognition and portable photothermal quantitation of miRNAs.

MATERIALS AND METHODS

Materials and Reagents

Acrylamide, ammonium persulfate (APS), and H_2O_2 (30%) were obtained from Sinopharm Chemical Reagent (Shanghai, China). 3,3′,5,5′-tetramethylbenzidine (TMB), N,N,N′,N′-tetramethylethylenediamine (TEMED), tris(hydroxymethyl) aminomethane (Tris), Dulbecco's modified Eagle's medium (DMEM), fetal bovine serum (FBS), and penicillin-streptomycin were obtained from Sigma-Aldrich (St. Louis, MO, USA). HRP was purchased from J&K Scientific Ltd. (Beijing, China). TRIzol solution, acrylic-DNA and all other oligonucleotides used in this study (**Supplementary Table S1**) were synthesized by Sangon Biotech Co., Ltd. (Shanghai, China). Other reagents were purchased from Damao Chemical Reagent Factory (Tianjin, China). HeLa cells were obtained from Sangon Biotech Co., Ltd.

Synthesis of the DNA Functional Linear Polyacrylamide Chains

A typical synthesis involved mixing 10 μL acrylamide (25% w/v) with 20 μL Tris-HCl pH 8.0 (10 mM), followed by the addition of 16 μL acrydite-DNA solution (10 μM SA or SB in **Supplementary Table S1**). The mixture was kept in a N_2 atmosphere at 20°C for 10 min to remove air. Next, 2 μL of APS (4% w/v) and 2 μL TEMED (5% v/v) were added, and the solution was incubated in a N_2 atmosphere for a further 15 min. The resulting functional DNA linear polyacrylamide chains (PA and PB) were stored at 4°C for subsequent use.

Preparation of the HRP -Encapsulated Stimulus-Responsive Hydrogel

10 μL (10 μM) DNA functional linear polyacrylamide solution, PA and PB, were mixed at room, and then 40 ng HRP (10 μL 4 μg/ml) was added to them. 10 μL (10 μM) DNA (L1) was added into the above mixture was incubated at 37°C for 30 min. After being washed three times with 10 μL wash buffer (containing Tris-HCl (10 mM), NaCl (50 mM), and $MgCl_2$ (10 mM), pH 8.0) and followed by lyophilization the HRP-encapsulated stimulus-responsive hydrogel was obtained.

Detection of miRNA

For the target miRNA assay, 5 μL H_2O_2 (0.4 mM) and 10 μL of TMB (0.4 mM) were added to a 0.5 ml tube at room temperature and incubated until the solution was separated into two colorless layers. Then, 10 μL miRNA target with different concentrations was added into the hydrogel-containing tube and incubated for 15 min at 37°C to ensure the complete disassociation reaction. A series of blue solutions was obtained. 5 μL of this solution was taken to measure the absorbance at 650 nm with a UV spectrophotometer. Another 5 μL was taken to investigate the photothermal effect by recording the temperature using a common digital thermometer [Sangon Biotech Co., Ltd. (Shanghai, China)] under 808 nm laser at a power density of 5.26 W cm^{-2} for 300 s.

miRNA Extraction From HeLa Cells

HeLa cells, were cultured in Dulbecco's modified Eagle's medium (DMEM) supplemented with 10% fetal bovine serum (FBS), penicillin (100 units/mL), and streptomycin (100 μg/ml) in an incubator containing (5% CO_2, 37°C). After the cells were all over the bottom of the bottle, the target miRNA was extracted using TRIzol solution following the instructions and was analyzed by above photothermal biosensor. Moreover, the results were verified by qRT-PCR method.

RESULTS AND DISCUSSION

Characterization of the HRP -Encapsulated Stimulus-Responsive Hydrogel

PA and PB synthesized by copolymerization of acrylic DNA and acrylamide monomers were validated by polyacrylamide gel electrophoresis (PAGE, **Supplementary Figure S1**). The substrate DNA linker strand containing partial complementary sequences with both PA and PB, and complete complementary sequence of miRNA cross-linked with PA and PB formed the HRP-encapsulated stimulus-responsive hydrogel (**Figure 1A**) which formed a porous, three-dimensional network structure observed by SEM (**Figure 1B**). A vial inversion test was adopted to show hydrogel formation as **Supplementary Figure S2**. The element mapping images demonstrated the distribution of Fe, P, and N (**Supplementary Figure S3**) which provided direct evidence that HRP was trapped in the hydrogels and DNA strands participated in the construction of HRP-encapsulated hydrogels. TEM images indicated that the functional linear DNA polyacrylamide chains were interconnected in HRP-encapsulated hydrogels (**Figure 1C**). The surface area was calculated as 15.9 $m^2 g^{-1}$ (**Figure 1D**) by Brunauer-Emmett-Teller (BET) model (Naderi and Tarleton, 2015).

Principle and Feasibility of Visual Recognition and Photothermal Quantitation of MicroRNAs Based on Target-Responsive DNA Hydrogels

In the absence of miRNA, HRP was stably trapped inside the hydrogel and physically separated from TMB-H_2O_2 which was in the solution outside the hydrogel. After the addition of target miRNA, hybridization of the substrate linker strand with miRNA led to the collapse of the hydrogel and the release of HRP. HRP oxidized TMB-H_2O_2 with the one-electron transfer generated in TMB forming the blue-colored, charged, oxidized TMB (oxTMB) complex which generated heat following NIR laser irradiation at 808 nm (Fu et al., 2018). Hence the hybridization signal of miRNA was converted into a photothermal effect.

The intensity of the 650 nm absorption peak representing oxTMB was used to determine the encapsulation and release of HRP in hydrogels (**Figure 2A**). Weak oxTMB absorption was observed in the presence of crosslinking DNA (L1) and in the absence of miRNA (R1) indicating that most of the HRP was trapped inside the DNA hydrogel. When the crosslinking DNA

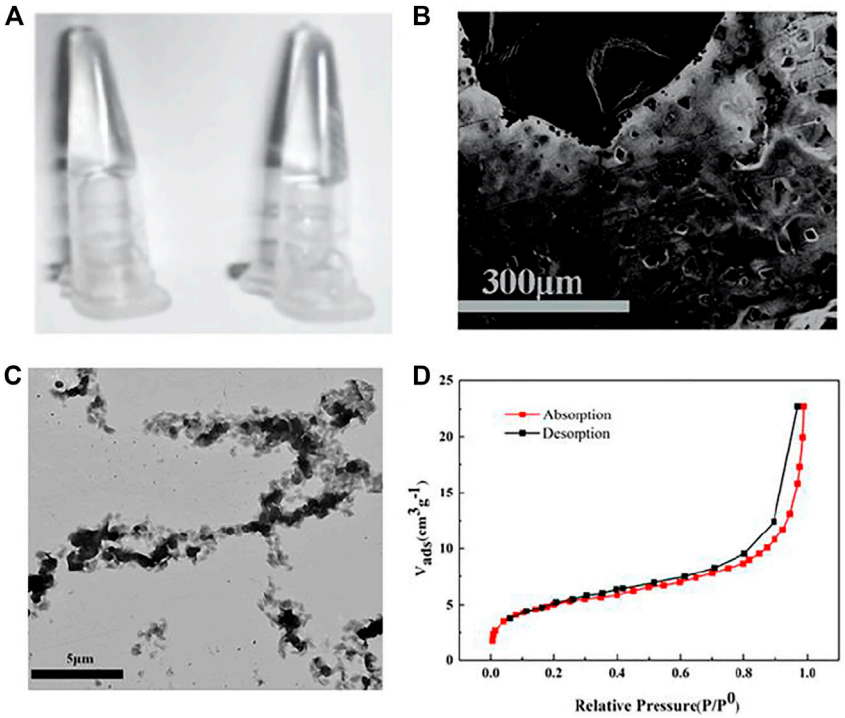

FIGURE 1 | (A) Digital photographs, SEM image **(B)**, TEM image **(C)**, N_2 physisorption isotherm **(D)** of HRP -encapsulated stimulus-responsive hydrogel.

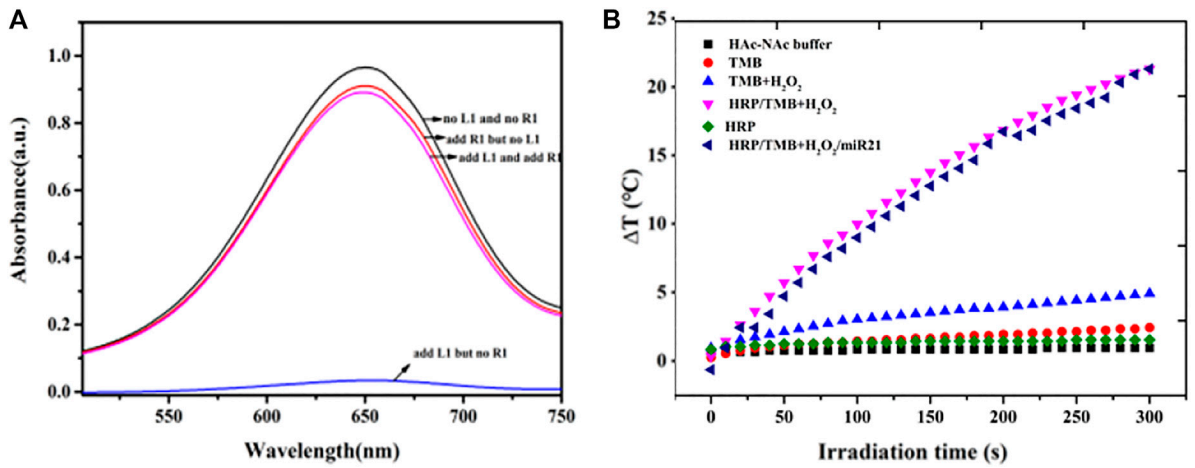

FIGURE 2 | (A) Feasibility test of the release of HRP in hydrogels based on the intensity of absorption peak of oxTMB at 650 nm **(B)** Photothermal evolution of different components including HAc-NaAc buffer, TMB, TMB-H_2O_2, HRP, HRP-TMB-H_2O_2 under 808 nm laser at a power density of 5.26 W cm^{-2} for 300 s.

(L1) and target miRNA (R1) were absent, a stronger absorption peak appeared after TMB-H_2O_2 was added (black line) indicating that PA and PB did not trap HRP in the DNA hydrogel. When miRNA (R1) was added, the absorption peak of oxTMB slightly increased (red line) indicating that crosslinking DNA is required to trap HRP inside the DNA hydrogel. This was confirmed by the addition of crosslinking DNA (L1) resulting in decreased absorption indicating that the DNA hydrogel was constructed and some HRP was encapsulated. The addition of TMB-H_2O_2 resulted in little absorbance change showing that there were only trace amounts of free HRP in the supernatant. Subsequent addition of target miRNA resulted in a gradual increase in the oxTMB absorption peak demonstrating that HRP was released from the hydrogel (purple line).

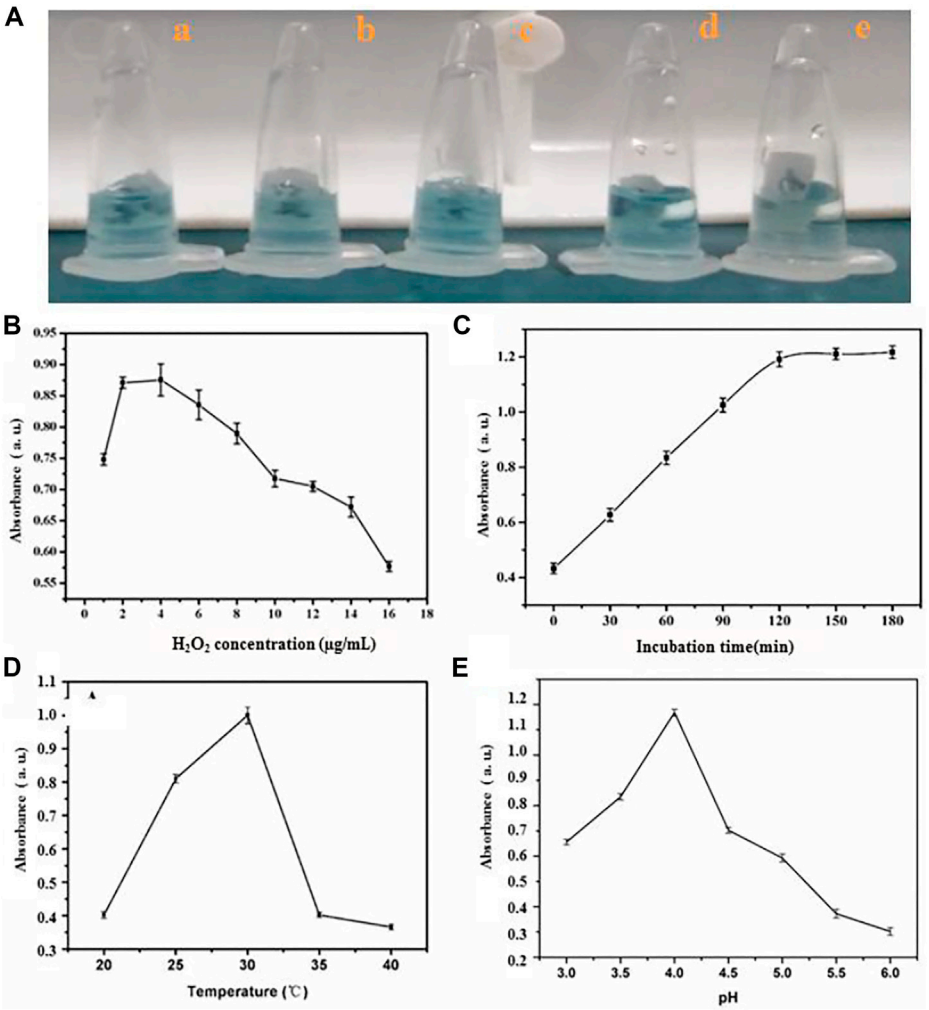

FIGURE 3 | The influence of **(A)** amount of HRP (a) 4 μg/ml (b) 6 μg/ml (c) 8 μg/ml (d) 9 μg/ml (e)10 μg/ml, **(B)** quantity of H_2O_2 **(C)** incubating time **(D)** temperature and **(E)** pH value for sensing system.

The photothermal properties of HAc-NaAc buffer, TMB, TMB-H_2O_2, HRP, and HRP-TMB-H_2O_2 were determined under 808 nm laser at a power density of 5.26 W cm^{-2} for 300 s to investigate the feasibility of the HRP-catalyzed TMB-H_2O_2 system for photothermal conversion (**Figure 2B**). A dramatic temperature increase appeared in the HRP-TMB-H_2O_2 system, while no apparent temperature increases were exhibited in all other cases. Therefore, the HRP-TMB-H_2O_2 system based on target-responsive DNA hydrogels is a suitable biosensor to detect miRNA using a thermometer.

Optimization of Assay Condition for Visual Recognition and Photothermal Quantitation of MicroRNAs

The optimal incubation time, temperature, amount of HRP and H_2O_2 was tested to achieve sensitive detection of miRNA using the HRP-encapsulated DNA hydrogel/TMB-H_2O_2 probe (**Figure 3**). 4 μg/ml HRP was chosen as the optimal loading concentration, since higher concentrations would result in the leakage of enzyme, which would bring the false positives of investigation (**Figure 3A**). The intensity of oxTMB absorption increased from 1 to 4 nM H_2O_2 however, the intensity of the absorption peak sharply decreased beyond 4 nM demonstrating that inhibition of the catalytic reaction occurred (**Figure 3B**). Therefore, 4 nM H_2O_2 was chosen as the optimal concentration for miRNA detection.

The absorption intensity of oxTMB plateaued at 120 min incubation time (**Figure 3C**) demonstrating that the hybridization process of substrate linker strand with miRNA was complete. Therefore, 120 min was chosen as the optimal incubation time. OxTMB absorption intensity increased from 20°C to 30°C, then stabilized up to 40°C (**Figure 3D**). Therefore, 30°C was taken as the optimal assay temperature. Finally, a pH of 4.0 was chosen as the ideal condition for maximal oxTMB absorption intensity (**Figure 3E**).

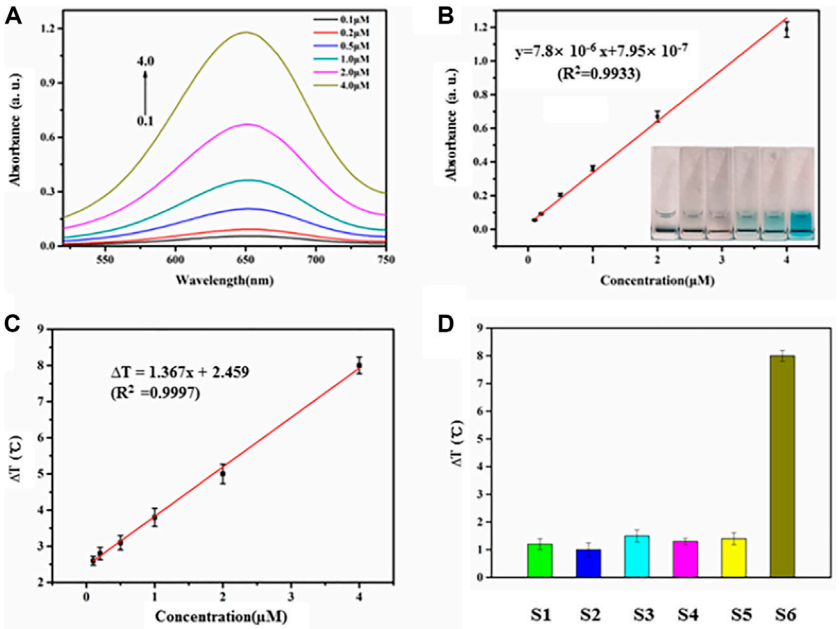

FIGURE 4 | (A) Absorbance intensities at 650 nm were obtained upon addition of miR21 with different concentrations (0.1, 0.2, 0.5, 1.0,2.0, 4.0 μM). **(B)** The relationship of absorbance intensities and miRNA concentration. The range of miR21 concentration is from 0 to 4.0 μM. **(C)** The relationship of temperature evolution and miRNA concentration from 0.5 to 4.0 μM. **(D)** Investigation of the selectivity of the miRNA-responsive HRP encapsulated DNA hydrogels/TMB- H_2O_2 (S1, miR18; S2, miR205; S3, miR141; S4, miR25; S5, miR183; S6, miR21).

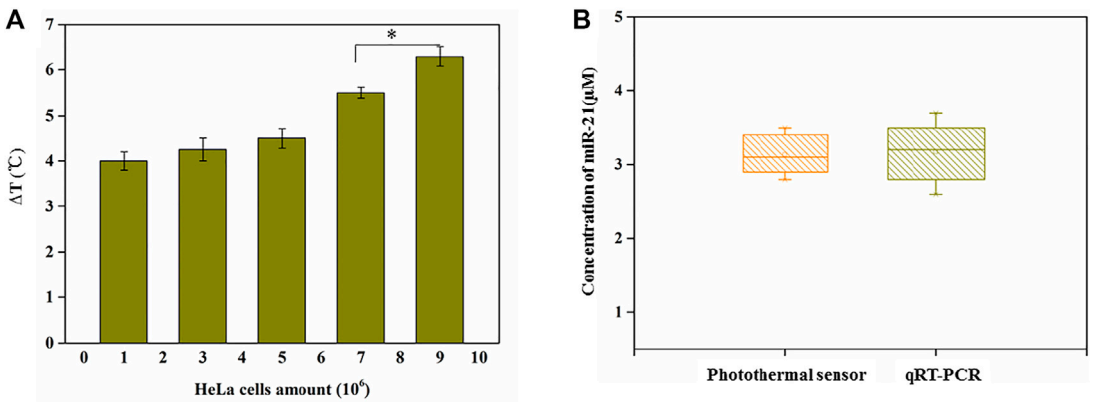

FIGURE 5 | (A) Temperature changes with the endogenous miR21 extracted from different amounts of HeLa cells. An asterisk indicates a statistically significant difference (*$p < 0.05$). **(B)** Detection of miR-21 using current photothermal sensor and qRT-PCR from HeLa cells (concentration: 9 × 10^6).

Performance of Biosensor Based on HRP Encapsulated DNA Hydrogels/TMB- H_2O_2 System for miRNA Determination

The biosensor exhibited a concentration-dependent effect following the addition of increasing amounts of miR-21 extracted from HeLa cells under the optimized conditions (**Figure 4A**). The transition from colorless to blue (**Figure 4B**, inset) is easily distinguished by the naked eye. There is a linear relationship between the intensity of the absorption peaks at 650 nm and miRNA concentration between 0 and 4 μM (**Figure 4B**). The regression equation is $y = 7.8 \times 10^{-6} x + 7.95 \times 10^{-7}$ ($R^2 = 0.9933$), where x is miR-21 concentration; y is the intensity of absorption peaks at 650 nm; R^2 is the correlation coefficient. The detection limit was approximately 10 nM (signal-to-noise ratio = 3). Similarly, the temperature increase following NIR illumination was linearly proportional to the miR21 concentration between 0.5–4.0 μM when the irradiation time was 90 s (**Figure 4C**, **Supplementary Figure S4**). The regression equation was $\Delta T = 1.367x + 2.459$ ($R^2 = 0.9997$), where x is the miRNA concentration, ΔT is the temperature increase, and R^2 is the correlation coefficient. The detection limit

was approximately 7.8 nM (signal-to-noise ratio = 3). Six experiments were carried out at 2 ng ml^{-1} miR-21, and the relative standard deviation was 5.2% over a 5-week period showing that the biosensor results were stable and reproducible. Moreover, other miRNAs with different sequences were similarly detected by the biosensor due to the precise base pairing (**Figure 4D**).

Detection of miRNA in Cell Lysates

As the detection for miRNA above, the proposed photothermal sensor based on thermometer-based readout composed of miRNA -responsive HRP encapsulated DNA hydrogels/TMB-H_2O_2 showed high selectivity, sensitivity and reproducibility. We detected miR-21, which was extracted from HeLa cells using TRIzol, through this biosensor to further evaluate its feasibility in real biological samples. As we expected, as the amount of HeLa cells increased as **Figure 5A** shown in, the temperature increased accordingly. Moreover, when the detection of miR-21 in cell lysates of HeLa was performed through this photothermal biosensor, a standard qRT-PCR detection was also carried out simultaneously to verify this. No obvious difference in detecting miR-21 in them as shown in **Figure 5B** which indicated the effectiveness of this biosensor using for miRNA detection in real biological samples.

CONCLUSION

In summary, we designed and synthesized a novel and simple photothermal detection method of miRNA using a common thermometer based on a target-responsive HRP encapsulated DNA hydrogel/TMB-H_2O_2 biosensor. The dissociation of the hydrogel was directly controlled by miRNA, and the released HRP catalyzed the TMB-H_2O_2 system to form oxTMB which exhibited photothermal properties under 808 nm laser irradiation. The resulting temperature evolution was proportional to the miRNA concentration. The limit of detection was 7.8 nM and the linear range was between 0.5–4.0 μM. Moreover, compared with traditional spectrophotometric or RT-qPCR methods, this method exhibited the distinct advantage including no need for specialized equipment and reagents, high selectivity and specificity of ease of use and greatly reduced cost since there is no need for specialized equipment and reagents. This biosensor method which showed great potential for point-of-care miRNA detection and biomedical applications.

DATA AVAILABILITY STATEMENT

The original contributions presented in the study are included in the article/**Supplementary Material**, further inquiries can be directed to the corresponding author.

AUTHOR CONTRIBUTIONS

Conceptualization, XL; methodology, MZ; formal analysis, ZC; investigation, FQ and HW; writing-original draft preparation, LY; writing-review and editing, JC; project administration, ZL; All authors have read and agreed to the published version of the manuscript.

SUPPLEMENTARY MATERIAL

The Supplementary Material for this article can be found online at: https://www.frontiersin.org/articles/10.3389/fbioe.2021.799370/full#supplementary-material

REFERENCES

Amalfitano, E., Karlikow, M., Norouzi, M., Jaenes, K., Cicek, S., Masum, F., et al. (2021). A Glucose Meter Interface for point-of-care Gene Circuit-Based Diagnostics. *Nat. Commun.* 12 (1), 724. doi:10.1038/s41467-020-20639-6

Armand-Labit, V., and Pradines, A. (2017). Circulating Cell-free microRNAs as Clinical Cancer Biomarkers. *Biomol. Concepts* 8 (2), 61–81. doi:10.1515/bmc-2017-0002

Bartel, D. P. (2009). MicroRNAs: Target Recognition and Regulatory Functions. *Cell* 136 (2), 215–233. doi:10.1016/j.cell.2009.01.002

Boeri, M., Verri, C., Conte, D., Roz, L., Modena, P., Facchinetti, F., et al. (2011). MicroRNA Signatures in Tissues and Plasma Predict Development and Prognosis of Computed Tomography Detected Lung Cancer. *Proc. Natl. Acad. Sci. USA* 108 (9), 3713–3718. doi:10.1073/pnas.1100048108

Calin, G. A., Sevignani, C., Dumitru, C. D., Hyslop, T., Noch, E., Yendamuri, S., et al. (2004). Human microRNA Genes Are Frequently Located at Fragile Sites and Genomic Regions Involved in Cancers. *Proc. Natl. Acad. Sci.* 101 (9), 2999–3004. doi:10.1073/pnas.0307323101

Das, S., and Ghosal, S. (2018). "Alteration of MicroRNA Biogenesis Pathways in Cancers - ScienceDirect," in *Cancer and Noncoding RNAs* (Bethesda, MD, United States: National Institute of Health), 47–58. doi:10.1016/b978-0-12-811022-5.00003-6

Fu, G., Sanjay, S. T., Dou, M., and Li, X. (2016). Nanoparticle-mediated Photothermal Effect Enables a New Method for Quantitative Biochemical Analysis Using a Thermometer. *Nanoscale* 8 (10), 5422–5427. doi:10.1039/C5NR09051B

Fu, G., Sanjay, S. T., Zhou, W., Brekken, R. A., Kirken, R. A., and Li, X. (2018). Exploration of Nanoparticle-Mediated Photothermal Effect of TMB-H2o2 Colorimetric System and its Application in a Visual Quantitative Photothermal Immunoassay. *Anal. Chem.* 90 (9), 5930–5937. doi:10.1021/acs.analchem.8b00842

Git, A., Dvinge, H., Salmon-Divon, M., Osborne, M., Kutter, C., Hadfield, J., et al. (2010). Systematic Comparison of Microarray Profiling, Real-Time PCR, and Next-Generation Sequencing Technologies for Measuring Differential microRNA Expression. *Rna* 16 (5), 991–1006. doi:10.1261/rna.1947110

Guan, F., Song, Z., Xin, F., Wang, H., Yu, D., Li, G., et al. (2020). Preparation of Hydrophobic Transparent Paper via Using Polydimethylsiloxane as Transparent Agent. *J. Bioresources Bioproducts* 5 (1), 37–43. doi:10.1016/j.jobab.2020.03.004

Guo, C.-J., Pan, Q., Li, D.-G., Sun, H., and Liu, B.-W. (2009). miR-15b and miR-16 Are Implicated in Activation of the Rat Hepatic Stellate Cell: An Essential Role for Apoptosis. *J. Hepatol.* 50 (4), 766–778. doi:10.1016/j.jhep.2008.11.025

Ji, C., and Guo, X. (2019). The Clinical Potential of Circulating microRNAs in Obesity. *Nat. Rev. Endocrinol.* 15 (12), 731–743. doi:10.1038/s41574-019-0260-0

Jin, P., Ma, D., Gao, Y., Wang, L., Gao, Z., Zhang, Y., et al. (2021). Determination of Cisplatin Cross-Linked Hyaluronic Acid (CPHA) Hydrogel and DNA Using the Fluorescent Response from Mercaptopropionic Acid (MPA) Capped Cadmium Telluride Quantum Dots (CdTe QDs). *Anal. Lett.* 54, 2411–2422. doi:10.1080/00032719.2020.1869979

Kahn, J. S., Hu, Y., and Willner, I. (2017). Stimuli-Responsive DNA-Based Hydrogels: From Basic Principles to Applications. *Acc. Chem. Res.* 50 (4), 680–690. doi:10.1021/acs.accounts.6b00542

Kelly, B. D., Miller, N., Healy, N. A., Walsh, K., and Kerin, M. J. (2013). A Review of Expression Profiling of Circulating microRNAs in Men with Prostate Cancer. *BJU Int.* 111 (1), 17–21. doi:10.1111/j.1464-410X.2012.11244.x

Li, F., Zhou, Y., Yin, H., and Ai, S. (2020). Recent Advances on Signal Amplification Strategies in Photoelectrochemical Sensing of microRNAs. *Biosens. Bioelectron.* 166, 112476. doi:10.1016/j.bios.2020.112476

Li, S., Xu, L., Ma, W., Wu, X., Sun, M., Kuang, H., et al. (2016). Dual-Mode Ultrasensitive Quantification of MicroRNA in Living Cells by Chiroplasmonic Nanopyramids Self-Assembled from Gold and Upconversion Nanoparticles. *J. Am. Chem. Soc.* 138 (1), 306–312. doi:10.1021/jacs.5b10309

Lin, H., Zou, Y., Huang, Y., Chen, J., Zhang, W. Y., Zhuang, Z., et al. (2011). DNAzyme Crosslinked Hydrogel: a New Platform for Visual Detection of Metal Ions. *Chem. Commun.* 47 (33), 9312–9314. doi:10.1039/C1CC12290H

Lin, S., and Gregory, R. I. (2015). MicroRNA Biogenesis Pathways in Cancer. *Nat. Rev. Cancer* 15 (6), 321–333. doi:10.1038/nrc3932

Liu, C., Morimoto, N., Jiang, L., Kawahara, S., Noritomi, T., Yokoyama, H., et al. (2021). Tough Hydrogels with Rapid Self-Reinforcement. *Science* 372 (6546), 1078–1081. doi:10.1126/science.aaz6694

Mitchell, P. S., Parkin, R. K., Kroh, E. M., Fritz, B. R., Wyman, S. K., Pogosova-Agadjanyan, E. L., et al. (2008). Circulating microRNAs as Stable Blood-Based Markers for Cancer Detection. *Proc. Natl. Acad. Sci. United States America* 105 (30), 10513–10518. doi:10.1073/pnas.0804549105

Naderi, M. (2015). "Surface Area," in *Progress in Filtration and Separation*. Editor S. Tarleton (Oxford: Academic Press), 585–608. doi:10.1016/B978-0-12-384746-1.00014-8

Porichis, F., Hart, M. G., Griesbeck, M., Everett, H. L., Hassan, M., Baxter, A. E., et al. (2014). High-throughput Detection of miRNAs and Gene-specific mRNA at the Single-Cell Level by Flow Cytometry. *Nat. Commun.* 5 (1), 5641. doi:10.1038/ncomms6641

Pritchard, C. C., Cheng, H. H., and Tewari, M. (2012). MicroRNA Profiling: Approaches and Considerations. *Nat. Rev. Genet.* 13 (5), 358–369. doi:10.1038/nrg3198

Qu, W., Liu, Y., Liu, D., Wang, Z., and Jiang, X. (2011). Copper-mediated Amplification Allows Readout of Immunoassays by the Naked Eye. *Angew. Chem. Int. Ed.* 50 (15), 3442–3445. doi:10.1002/anie.201006025

Si, Y., Xu, L., Wang, N., Zheng, J., Yang, R., and Li, J. (2020). Target MicroRNA-Responsive DNA Hydrogel-Based Surface-Enhanced Raman Scattering Sensor Arrays for MicroRNA-Marked Cancer Screening. *Anal. Chem.* 92 (3), 2649–2655. doi:10.1021/acs.analchem.9b04606

Wang, J., Gao, Z., He, S., Jin, P., Ma, D., Gao, Y., et al. (2020). A Universal Growth Strategy for DNA-Programmed Quantum Dots on Graphene Oxide Surfaces. *Nanotechnology* 31, 24LT02. doi:10.1088/1361-6528/ab7c42

Wei, D. W., Wei, H., Gauthier, A. C., Song, J., Jin, Y., and Xiao, H. (2020). Superhydrophobic Modification of Cellulose and Cotton Textiles: Methodologies and Applications. *J. Bioresources Bioproducts* 5 (1), 1–15. doi:10.1016/j.jobab.2020.03.001

Wightman, B., Ha, I., and Ruvkun, G. (1993). Posttranscriptional Regulation of the Heterochronic Gene Lin-14 by Lin-4 Mediates Temporal Pattern Formation in *C. elegans*. *Cell* 75 (5), 855–862. doi:10.1016/0092-8674(93)90530-4

Xiang, Y., and Lu, Y. (2012). Using Commercially Available Personal Glucose Meters for Portable Quantification of DNA. *Anal. Chem.* 84 (4), 1975–1980. doi:10.1021/ac203014s

Xu, J., Tao, J., Su, L., Wang, J., and Jiao, T. (2021). A Critical Review of Carbon Quantum Dots: From Synthesis toward Applications in Electrochemical Biosensors for the Determination of a Depression-Related Neurotransmitter. *Materials* 14 (14), 3987. doi:10.3390/ma14143987

Xu, J., Tao, J., and Wang, J. (2020). Design and Application in Delivery System of Intranasal Antidepressants. *Front. Bioeng. Biotechnol.* 8, 626882. doi:10.3389/fbioe.2020.626882

Yan, L., Zhu, Z., Zou, Y., Huang, Y., Liu, D., Jia, S., et al. (2013). Target-Responsive "Sweet" Hydrogel with Glucometer Readout for Portable and Quantitative Detection of Non-glucose Targets. *J. Am. Chem. Soc.* 135 (10), 3748–3751. doi:10.1021/ja3114714

Zhao, M., Yu, H., and He, Y. (2019). A Dynamic Multichannel Colorimetric Sensor Array for Highly Effective Discrimination of Ten Explosives. *Sensors Actuators B: Chem.* 283, 329–333. doi:10.1016/j.snb.2018.12.061

Zheng, L., Cai, G., Wang, S., Liao, M., Li, Y., and Lin, J. (2019). A Microfluidic Colorimetric Biosensor for Rapid Detection of *Escherichia coli* O157:H7 Using Gold Nanoparticle Aggregation and Smart Phone Imaging. *Biosens. Bioelectron.* 124-125, 143–149. doi:10.1016/j.bios.2018.10.006

Zheng, Y., Wang, X., He, S., Gao, Z., Di, Y., Lu, K., et al. (2019). Aptamer-DNA Concatamer-Quantum Dots Based Electrochemical Biosensing Strategy for green and Ultrasensitive Detection of Tumor Cells via Mercury-free Anodic Stripping Voltammetry. *Biosens. Bioelectron.* 126, 261–268. doi:10.1016/j.bios.2018.09.076

Zhu, Z., Wu, C., Liu, H., Zou, Y., Zhang, X., Kang, H., et al. (2010). An Aptamer Cross-Linked Hydrogel as a Colorimetric Platform for Visual Detection. *Angew. Chem. Int. Ed.* 49 (6), 1052–1056. doi:10.1002/anie.200905570

Conflict of Interest: The authors declare that the research was conducted in the absence of any commercial or financial relationships that could be construed as a potential conflict of interest.

Publisher's Note: All claims expressed in this article are solely those of the authors and do not necessarily represent those of their affiliated organizations, or those of the publisher, the editors and the reviewers. Any product that may be evaluated in this article, or claim that may be made by its manufacturer, is not guaranteed or endorsed by the publisher.

frontiers in Bioengineering and Biotechnology

ORIGINAL RESEARCH
published: 31 December 2021
doi: 10.3389/fbioe.2021.817143

Enhanced Anticancer Efficacy of Chemotherapy by Amphiphilic Y-Shaped Polypeptide Micelles

Cong Hua, Yi Zhang and Yuanhao Liu*

Department of Neurosurgery, The First Hospital of Jilin University, Changchun, China

Although the treatment modalities of cancers are developing rapidly, chemotherapy is still the primary treatment strategy for most solid cancers. The progress in nanotechnology provides an opportunity to upregulate the tumor suppression efficacy and decreases the systemic toxicities. As a promising nanoplatform, the polymer micelles are fascinating nanocarriers for the encapsulation and delivery of chemotherapeutic agents. The chemical and physical properties of amphiphilic co-polymers could significantly regulate the performances of the micellar self-assembly and affect the behaviors of controlled release of drugs. Herein, two amphiphilic Y-shaped polypeptides are prepared by the ring-opening polymerization of cyclic monomer L-leucine *N*-carboxyanhydride (L-Leu NCA) initiated by a dual-amino-ended macroinitiator poly(ethylene glycol) [mPEG-$(NH_2)_2$]. The block co-polypeptides with $PLeu_8$ and $PLeu_{16}$ segments could form spontaneously into micelles in an aqueous solution with hydrodynamic radii of 80.0 ± 6.0 and 69.1 ± 4.8 nm, respectively. The developed doxorubicin (DOX)-loaded micelles could release the payload in a sustained pattern and inhibit the growth of xenografted human HepG2 hepatocellular carcinoma with decreased systemic toxicity. The results demonstrated the great potential of polypeptide micellar formulations in cancer therapy clinically.

Keywords: polypeptide, polymer topology, micelle, controlled drug delivery, cancer therapy

OPEN ACCESS

Edited by:
Yuce Li,
Sungkyunkwan University, South Korea

Reviewed by:
Jun Yue,
Sun Yat-sen University, China
Ruogu Qi,
Nanjing University of Chinese Medicine, China
Kewa Gao,
University of California, Davis, United States
Chao Zhao,
University of Alabama, United States

****Correspondence:***
Cong Hua
huacong@jlu.edu.cn

Specialty section:
This article was submitted to Biomaterials, a section of the journal Frontiers in Bioengineering and Biotechnology

Received: *17 November 2021*
Accepted: *30 November 2021*
Published: *31 December 2021*

Citation:
Hua C, Zhang Y and Liu Y (2021) Enhanced Anticancer Efficacy of Chemotherapy by Amphiphilic Y-Shaped Polypeptide Micelles. Front. Bioeng. Biotechnol. 9:817143. doi: 10.3389/fbioe.2021.817143

INTRODUCTION

Chemotherapy is still an essential modality for the treatments of most solid cancers, although a variety of emerging strategies have been developed in the past few decades (Neoptolemos et al., 2018; Bukowski et al., 2020; Lu et al., 2020; Zheng et al., 2020; Zhao et al., 2021). However, the low water solubility, instability, short circulation period, and poor selectivity to tumor tissue of the mainstream small-molecule chemotherapeutic drugs in the clinic restrict the applicable diseases, reduce the anticancer efficacy, and even induce severe side effects (Steinbrueck et al., 2020; Zheng et al., 2021). The development of nanotechnology and the preparation of various organic and inorganic nanoparticles provide a robust tool for the controlled delivery of small-molecule chemotherapeutic drugs (Jiang et al., 2019; Sun et al., 2019; Jiang et al., 2020; Kim et al., 2020; Thomas et al., 2020; Zhang et al., 2020). Among them, the micelles self-assembled from the amphiphilic polymers are attracting increasing attention in the controlled delivery of chemotherapeutic drugs because of their controlled sizes, morphologies, stability, stimulus responsiveness, high drug loading efficiency, and targeted drug delivery behaviors (Zeinali et al., 2020; Bai et al., 2021; Rajes et al., 2021; Wei et al., 2021).

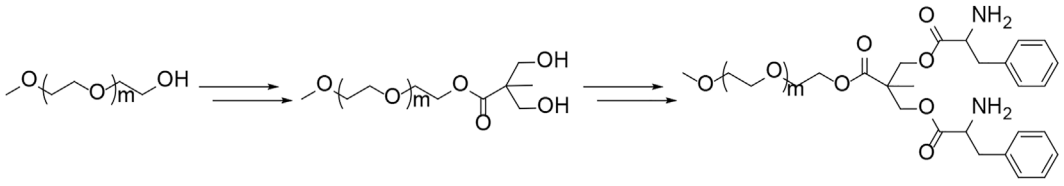

SCHEME 1 | Synthesis route of mPEG-$(NH_2)_2$.

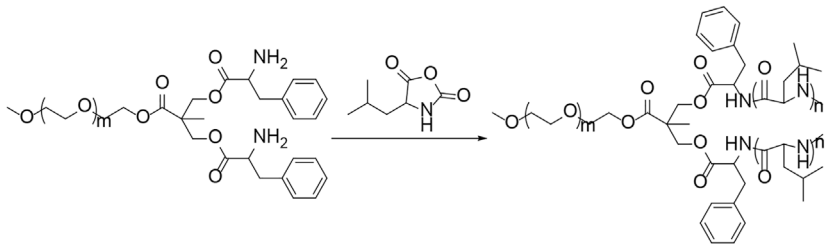

SCHEME 2 | Synthesis pathway of mPEG-$(PLeu)_2$.

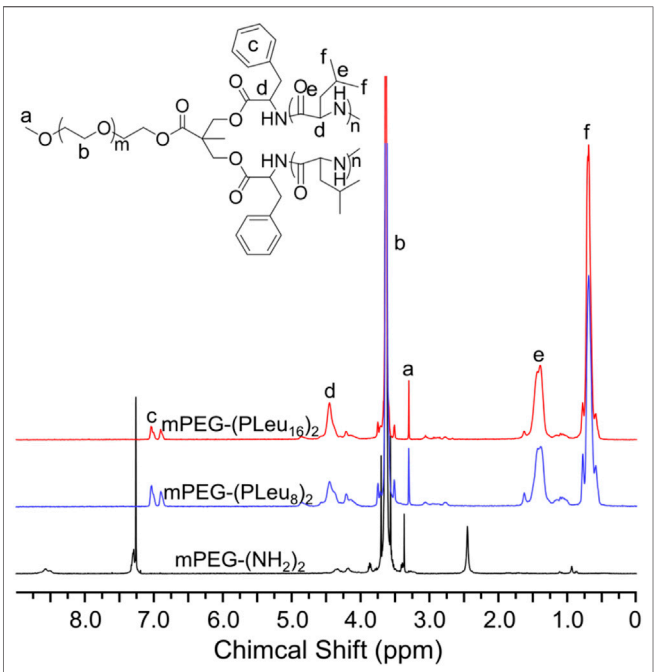

FIGURE 1 | ^{1}H NMR spectra of mPEG-$(NH_2)_2$, mPEG-$(PLeu_8)_2$, and mPEG-$(PLeu_{16})_2$.

The chemical structures and physical properties of amphiphilic polymers could always significantly regulate the behavior of self-assembly and the performances of obtained micelles (Danafar et al., 2018; Saravanakumar et al., 2018; Brega et al., 2019). The length of hydrophilic and hydrophobic blocks and their ratio are the main factors regulating the sizes, shape, and stability of the polymer micelles and even significantly influence their drug loading properties (Li et al., 2013; Zhang et al., 2013). Typically, longer hydrophobic polymer moieties correspond to smaller sizes, more compact cores, upregulated drug loading capability, and more constant drug release (Hussein and Youssry, 2018).

In addition, the topology of polymers is another critical factor for changing the behavior of self-assembly of polymers and properties of micelles (Li et al., 2013; Yang et al., 2017). The nonlinear amphiphilic polymers, including the graft, Y-shaped, dumbbell-shaped, and even star ones, always induce more stable self-assembled micellar nanoparticles compared with the linear amphiphilic polymers with the same components (Ding et al., 2011; Li et al., 2012; Li et al., 2013; Yang et al., 2021). Therefore, the micelles based on the nonlinear amphiphilic polymers exhibited more promising applications in controlled drug delivery for cancer therapy (Shi et al., 2018; Perin et al., 2021).

In this study, a kind of Y-shaped amphiphilic block co-polymers of methoxy poly(ethylene glycol) (mPEG) and poly(L-leucine) (PLeu) was developed to form spontaneously into micelles and deliver chemotherapeutic agent doxorubicin (DOX) in a controlled manner. PLeu was used as a typical polypeptide segment in this study, and other hydrophobic polypeptides, such as polyglycine, polyvaline, and polyphenylalanine, could also be used as components of amphiphilic block co-polymers for effective drug loading and controlled release. The block co-polypeptides were prepared by the ring-opening polymerization (ROP) of L-leucine *N*-carboxyanhydride (L-Leu NCA) initiated by a dual-amino-ended macroinitiator poly(ethylene glycol) [mPEG-$(NH_2)_2$] (Wang et al., 2019b; Song et al., 2019; Liu et al., 2020). The co-polymer could form into spherical micellar nanoparticles, which exhibited excellent drug encapsulation and release behaviors. The loaded polypeptide micelles showed fascinating tumor growth inhibition efficacy,

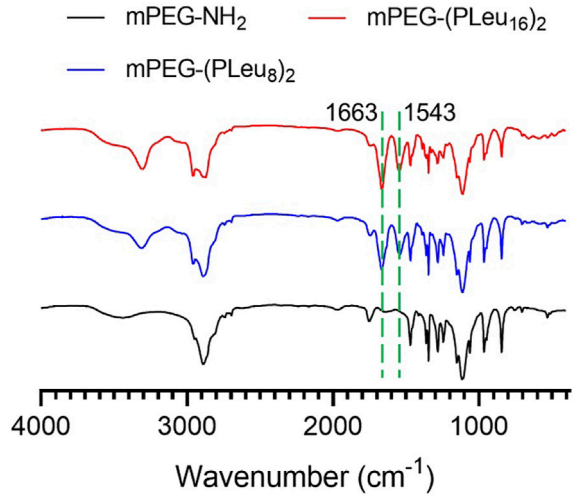

FIGURE 2 | FT-IR spectra of mPEG-$(NH_2)_2$, mPEG-$(PLeu_8)_2$, and mPEG-$(PLeu_{16})_2$. FT-IR, Fourier transform IR.

indicating their great potential for anticancer application clinically (Deng et al., 2020; Zheng et al., 2021).

MATERIALS AND METHODS

The materials, synthesis of methoxy poly(ethylene glycol)-(poly(L-leucine))$_2$; characterizations, preparation, and characterization of DOX-loaded co-polypeptide micelles; and DOX release *in vitro* are described in the **Supplementary Material** in detail.

In Vitro Biocompatibility Toward L929 Cells and Cytotoxicity Toward HepG2 Cells

The biocompatibility of mPEG-$(PLeu)_2$ against mouse fibroblast L929 cells and the cytotoxicity of mPEG-$(PLeu)_2$/DOX toward human hepatocellular carcinoma HepG2 cells were assessed by a typical methyl thiazolyl tetrazolium (MTT) technique *in vitro*. The selected cells were inoculated into tissue culture plates (TCPs) with 96 wells, with 7,000 cells in a well and dispersed in 200.0 μl of Dulbecco's modified Eagle's medium (DMEM) with fetal bovine serum (FBS) and antibiotics. At 24 h post-inoculation, the original incubation DMEM was removed, and the solutions of mPEG-$(PLeu)_2$ micelles at a concentration from 1.6 to 100.0 μg ml^{-1} or mPEG-$(PLeu)_2$/DOX at a concentration from 0.16 to 10.0 μg ml^{-1} in DMEM was supplemented. In 72 h post-co-incubation, the cell viability was determined by an MTT technique. The absorbances of the MTT co-incubated cell solutions in dimethyl sulfoxide (DMSO) were tested at 490 nm on a microplate reader (Bio-Rad 680, Bio-Rad Laboratories, Hercules, CA, USA). The cell viability is assessed in **Eq. 1**.

$$\text{Cell viability } (\%) = \frac{A_{Sample}}{A_{Control}} \times 100\% \quad (1)$$

In **Eq. 1**, A_{Sample} and A_{Control} represent the absorbances of the corresponding groups.

In Vivo Tumor Suppression

The BALB/c nude mice (female, 6 weeks old) were bought from Beijing Vital River Laboratory Animal Technology Co., Ltd. (Beijing, China). The suppression efficacy of tumor growth by various DOX formulations was evaluated toward the human HepG2 hepatocellular carcinoma-xenografted BALB/c node mice (Zhao et al., 2013; Wang et al., 2019a). The tumor-bearing mouse model was prepared by injecting subcutaneously 1.0 × 10^6 HepG2 cells dispersed with 100.0 μl of 0.01 M of phosphate-buffered saline (PBS) to the right anterior limb's armpit in BALB/c nude mice (5 weeks old, ~25 g). When the tumor volume reached about 72 mm^3, the mice were stochastically separated into four groups (n = 6). The control of PBS or various formulations of model chemotherapeutic agent DOX, including free DOX, mPEG-$(PLeu_8)_2$/DOX, or mPEG-$(PLeu_{16})_2$/DOX, were administrated by the tail-vein injection to treat the tumor-bearing mice. The equivalent DOX dosage was set as 5.0 mg for every kg body weight [mg (kg BW)$^{-1}$]. The chemotherapy was given every 4 days. The tumor volume was assessed every 2 days, and the body weight was detected at the same frequency.

The tumor volume could be assessed according to **Eq. 2**.

$$\text{Tumor volume } (mm^3) = \frac{L \times W^2}{2} \quad (2)$$

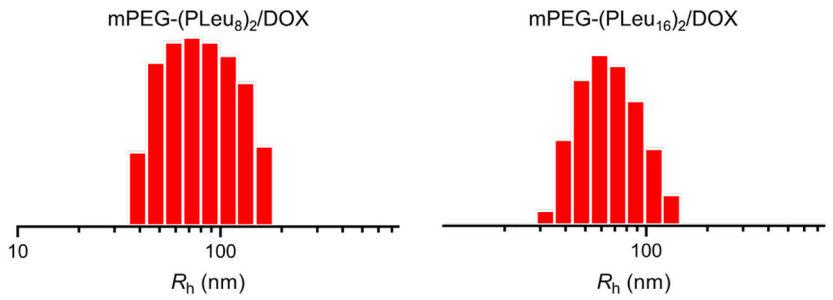

FIGURE 3 | R_hs of mPEG-$(PLeu_8)_2$/DOX and mPEG-$(PLeu_{16})_2$/DOX. DOX, doxorubicin.

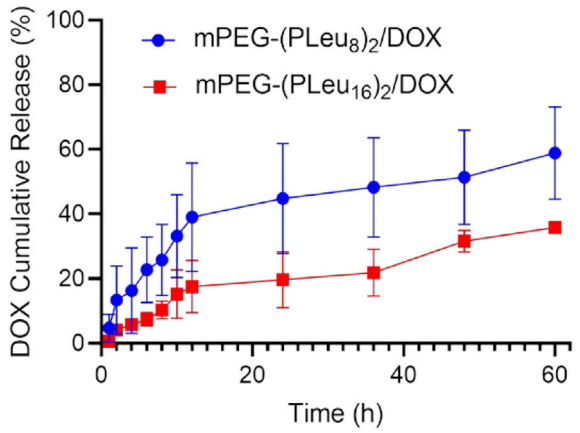

FIGURE 4 | Cumulative DOX release from mPEG-$(PLeu_8)_2$/DOX and mPEG-$(PLeu_{16})_2$/DOX in release medium of PBS at pH 7.4. DOX, doxorubicin; PBS, phosphate-buffered saline.

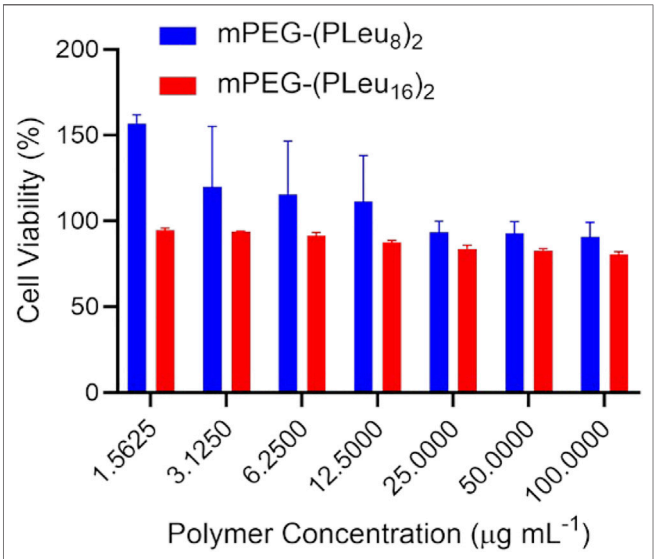

FIGURE 5 | Cytotoxicity of Y-shaped polypeptide micelle toward L929 cells.

The tumor growth rate was calculated according to **Eq. 3**.

$$\text{Tumor growth rate} = \frac{\text{Tumor volume}_t}{\text{Tumor volume}_0} \quad (3)$$

RESULTS AND DISCUSSION

Synthesis and Characterizations of Methoxy Poly(ethylene glycol)–(Poly(L-leucine))$_2$

Polypeptides could be prepared by the ROP of amino acid NCA monomers in a controlled manner (Liu et al., 2020; Lv et al., 2020; Vrijsen et al., 2020). In this study, the Y-shaped co-polypeptide mPEG-$(PLeu)_2$ was prepared by the ROP of L-Leu NCA with the dual-amino-ended mPEG-$(NH_2)_2$ as a macroinitiator, as shown in **Schemes 1** and **2**. The successful synthesis of macroinitiator mPEG-$(NH_2)_2$ and the co-polypeptide mPEG-$(PLeu)_2$ was demonstrated through the spectrum results of ^{1}H NMR and Fourier transform IR (FT-IR). As demonstrated by the results of **Figure 1**, the appearance of the peaks at 4.45 ppm is attributed to the backbone proton (d, –NHC*H*C(O)–$(CH_2$–)), 1.41 ppm is attributed to the methylene protons in the side segment (e, –CH_2C*H*$(CH_3)_2$), and 0.71 ppm belonged to the protons of side methyl groups (f, –CH_2CH$(CH_3)_2$), which proved the successful preparation of mPEG-$(PLeu)_2$. The degrees of polymerization (DPs) of PLeu segments were detected to be 8 and 16 based on the area ratios between the resonance peak at 1.41 ppm and that at 3.64 ppm assigned to the protons in methylene segment in the backbone of mPEG (b, –CH_2CH_2O–). Moreover, the successful preparation of mPEG-$(PLeu)_2$ was further confirmed by the results of FT-IR, as depicted in **Figure 2**. The wavenumbers at 1,543 and 1,663 cm^{-1} should be attributed to the stretching vibration of C(O)–NH ($\nu_{C(O)-NH}$) and C=O ($\nu_{C=O}$), respectively, revealing the formation of the amide bond and the synthesis of PLeu. Moreover, the stretching vibration signal of C–O–C (ν_{C-O-C}) demonstrated the appearance of mPEG in the co-polypeptides. Therefore, the results proved the successful synthesis of mPEG-$(PLeu_8)_2$ and mPEG-$(PLeu_{16})_2$.

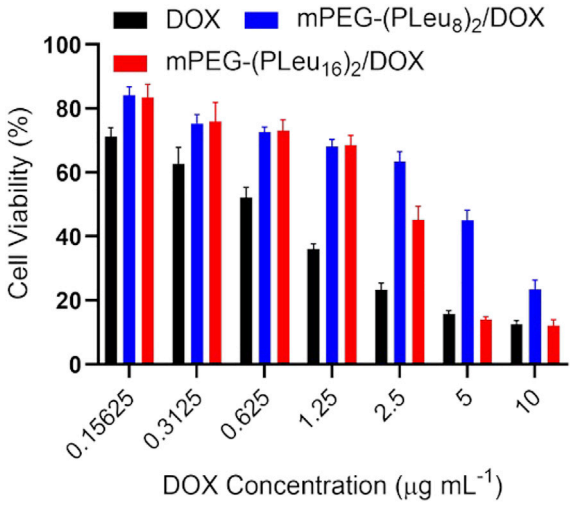

FIGURE 6 | Cell proliferation inhibition efficacy of free DOX, mPEG-$(PLeu_8)_2$/DOX, and mPEG-$(PLeu_{16})_2$/DOX toward HepG2 cells. DOX, doxorubicin.

Preparation and Detection of Doxorubicin-Loaded Co-Polypeptide Micelles *In Vitro*

The micelles from various amphiphilic polymers or co-polymers could be effective nanocarriers for the controlled delivery of anticancer drugs (Ray et al., 2018; Pinyakit et al., 2020). In

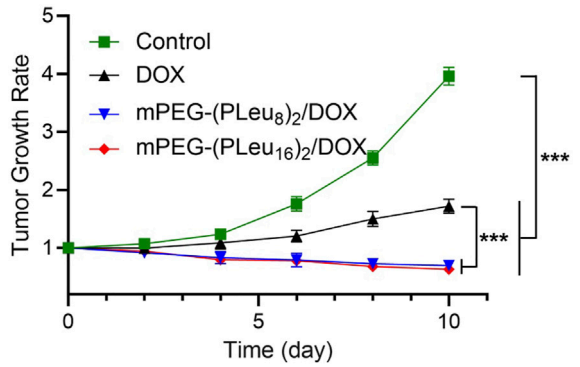

FIGURE 7 | Tumor growth rate of human HepG2 hepatocellular carcinoma-xenografted BALB/c node mice during treatment with PBS as control, free DOX, mPEG-$(PLeu_8)_2$/DOX, or mPEG-$(PLeu_{16})_2$/DOX. The data are represented as mean ± SD (n = 6; ***p < 0.001). PBS, phosphate-buffered saline; DOX, doxorubicin.

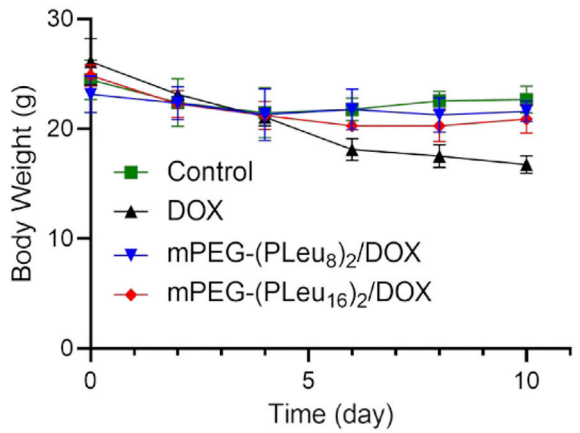

FIGURE 8 | Body weight change of human HepG2 hepatocellular carcinoma-xenografted BALB/c node mouse model during treatment with PBS as control, free DOX, mPEG-$(PLeu_8)_2$/DOX, or mPEG-$(PLeu_{16})_2$/DOX. PBS, phosphate-buffered saline; DOX, doxorubicin.

this work, the chemotherapeutic agent DOX was encapsulated to the cores of micelles of mPEG-$(PLeu_8)_2$ and mPEG-$(PLeu_{16})_2$ through nanoprecipitation. The contents of DOX in the micelles were tested by high-performance liquid chromatography (HPLC), and the drug-loading content (DLC) of mPEG-$(PLeu_8)_2$, and mPEG-$(PLeu_{16})_2$ micelles were calculated to be 8.75 and 12.94 wt%. The drug-loading efficiency (DLE) of the above micelles were assessed to be 47.95 and 74.32 wt%, respectively. The higher DLC and DLE of mPEG-$(PLeu_{16})_2$ micelle resulted from the more hydrophobic property of a longer PLeu block (Chen et al., 2018; Lübtow et al., 2019). As shown in **Figure 3**, the hydrophobic radii (R_hs) of DOX-loaded co-polypeptide micelles mPEG-$(PLeu_8)_2$/DOX and mPEG-$(PLeu_{16})_2$/DOX were detected to be 80.0 ± 6.0 and 69.1 ± 4.8 nm, respectively. The smaller size of mPEG-$(PLeu_{16})_2$/DOX also should be assigned to the more hydrophobic performance of $PLeu_{16}$ (Hussein and Youssry, 2018).

The release behaviors of micelles always affected the therapeutic efficacy of loaded micelles (Wang et al., 2019c). The sustained drug release profiles of mPEG-$(PLeu_8)_2$/DOX and mPEG-$(PLeu_{16})_2$/DOX were detected. As depicted in **Figure 4**, mPEG-$(PLeu_8)_2$/DOX released 58.88% of loaded DOX in the detected 60 h, while mPEG-$(PLeu_{16})_2$/DOX released 35.89%. The more compact and hydrophobic core of the micelle always induces a higher drug loading capability and more sustained drug release behavior.

The biocompatibility of materials is a critical factor for biomedical applications (Ding et al., 2013; Abbina et al., 2017; Reina et al., 2017). This study detected the biocompatibility of the prepared co-polypeptide micelles of mPEG-$(PLeu_8)_2$ and mPEG-$(PLeu_{16})_2$ by an MTT protocol toward L929 cells. As depicted in **Figure 5**, both the micelles showed excellent biocompatibility at the concentration of 100.0 μg ml^{-1}, which was revealed by the high cell viability at above 80%.

An MTT technique detected the antitumor efficacy of various DOX formulations toward HepG2 cells *in vitro*. As demonstrated by **Figure 6**, free DOX showed the best inhibition efficiency of cell proliferation as a benefit of its fastest cell entry speed through dispersion. The slightly weaker anticancer effect of DOX-loaded co-polypeptide micelles could be assigned to the slower endocytosis speed by HepG2 cells. In addition, the better anticancer effect of mPEG-$(PLeu_{16})_2$ should be attributed to the more sustained release profile of the chemotherapeutic agent in the cells.

Anticancer Efficacy of Doxorubicin-Loaded Co-Polypeptide Micelles *In Vivo*

The excellent anticancer efficacy of nanoformulations of chemotherapeutic drugs is one of the essential properties for potential clinical application (Ghosh et al., 2021; Zheng et al., 2021). Herein, the anticancer efficacy of PBS as control, free DOX, mPEG-$(PLeu_8)_2$/DOX, and mPEG-$(PLeu_{16})_2$/DOX were detected toward human HepG2 hepatocellular carcinoma-xenografted BALB/c node murine model.

The tumor-bearing mice were constructed by inoculating 1.0×10^6 HepG2 cells dispersed in 100.0 μl of PBS into the right anterior limb's armpit in a BALB/c nude mouse. As the tumor grew to ~72 mm^3 in volume, the model animals were divided into four groups (n = 6). On days 1, 4, and 8, the human HepG2 hepatocellular carcinoma-xenografted mice were treated with PBS as control, free DOX, mPEG-$(PLeu_8)_2$/DOX, or mPEG-$(PLeu_{16})_2$/DOX three times. The dosage of DOX was set at 5.0 mg (kg BW)$^{-1}$. The tumor volume was monitored every other day. As shown in **Figure 7**, the tumor growth rates calculated based on the data of tumor volumes decreased to some extent in the groups of mPEG-$(PLeu_8)_2$/DOX and mPEG-$(PLeu_{16})_2$/DOX, while it increased to about 3.96 and 1.72 in the PBS as control and free DOX groups, respectively. The best anticancer efficacy should be assigned to the target release of DOX by the micelles of Y-shaped co-polypeptides.

The safety of nanoformulations of chemotherapeutic drugs is another critical factor influencing their potential application in a clinic (Zheng et al., 2021). In this work, the safety of free DOX and DOX-loaded Y-shaped co-polypeptide micelles was revealed by the change of body weight of human HepG2 hepatocellular carcinoma-xenografted mice in the process of treatment. As shown in **Figure 8**, the body weight decreased significantly after the treatment with free DOX, indicating the toxicity of free DOX *in vivo*. Fortunately, the body weight of mPEG-$(PLeu_8)_2$/DOX and mPEG-$(PLeu_{16})_2$/DOX groups was similar to the body weight of the control group, demonstrating their excellent safety *in vivo*. Therefore, the findings confirmed that the Y-shaped polypeptide micelles exhibited great potential for controlled delivery of chemotherapeutic drugs *in vivo*, which benefited the improved anticancer efficacy and reduced systemic toxicity.

CONCLUSION

Chemotherapy is still the primary treatment modality for most solid tumors. To overcome the disadvantages of small-molecule drugs, including low water solubility, short circulation time, and low targeting *in vivo*, a variety of nanocarriers were developed. In this study, two Y-shaped co-polypeptides were prepared by the ROP of L-Leu NCA. mPEG-$(PLeu)_2$ could self-assemble into micelle and effectively encapsulate and release the model chemotherapeutic drug DOX in a sustained manner. The DOX-loaded Y-shaped co-polypeptide micelles could significantly suppress the growth of HepG2 hepatocellular carcinoma *in vitro* and *in vivo* with reduced systemic toxicity. The results indicated the great potential of the micelles from nonlinear amphiphilic polymers or co-polymers in cancer therapy clinically.

In this study, the human HepG2 hepatocellular carcinoma and DOX are just models to characterize and confirm the advantages of micelles from nonlinear amphiphilic polymers or co-polymers. The developed advanced micelles could be used for the controlled delivery of other therapeutic agents to treat different kinds of cancers and even other diseases.

DATA AVAILABILITY STATEMENT

The original contributions presented in the study are included in the article/**Supplementary Material**. Further inquiries can be directed to the corresponding author.

ETHICS STATEMENT

The animal study was reviewed and approved by the Institutional Animal Care and Use Committee of Jilin University.

AUTHOR CONTRIBUTIONS

CH provided the idea of this study and supersized the experiment implementation and data analysis. CH, YZ, and YL designed and performed all the experiments and analyzed all the obtained results. CH and YZ prepared the draft article, and all authors carefully revised it. All authors have read and agreed to the published version of the article.

ACKNOWLEDGMENTS

The authors appreciated the assistance from Changchun Institute of Applied Chemistry, Chinese Academy of Sciences, Changchun, P. R. China, for the polymer synthesis and characterizations.

SUPPLEMENTARY MATERIAL

The Supplementary Material for this article can be found online at: https://www.frontiersin.org/articles/10.3389/fbioe.2021.817143/full#supplementary-material

REFERENCES

Abbina, S., Vappala, S., Kumar, P., Siren, E. M. J., La, C. C., Abbasi, U., et al. (2017). Hyperbranched Polyglycerols: Recent Advances in Synthesis, Biocompatibility and Biomedical Applications. *J. Mater. Chem. B* 5, 9249–9277. doi:10.1039/c7tb02515g

Bai, S., Jia, D., Ma, X., Liang, M., Xue, P., Kang, Y., et al. (2021). Cylindrical Polymer Brushes-Anisotropic Unimolecular Micelle Drug Delivery System for Enhancing the Effectiveness of Chemotherapy. *Bioactive Mater.* 6, 2894–2904. doi:10.1016/j.bioactmat.2021.02.011

Brega, V., Scaletti, F., Zhang, X., Wang, L.-S., Li, P., Xu, Q., et al. (2019). Polymer Amphiphiles for Photoregulated Anticancer Drug Delivery. *ACS Appl. Mater. Inter.* 11, 2814–2820. doi:10.1021/acsami.8b18099

Bukowski, K., Kciuk, M., and Kontek, R. (2020). Mechanisms of Multidrug Resistance in Cancer Chemotherapy. *Ijms* 21, 3233. doi:10.3390/ijms21093233

Chen, W., Zhou, S., Ge, L., Wu, W., and Jiang, X. (2018). Translatable High Drug Loading Drug Delivery Systems Based on Biocompatible Polymer Nanocarriers. *Biomacromolecules* 19, 1732–1745. doi:10.1021/acs.biomac.8b00218

Danafar, H., Rostamizadeh, K., and Hamidi, M. (2018). Polylactide/poly(ethylene Glycol)/polylactide Triblock Copolymer Micelles as Carrier for Delivery of Hydrophilic and Hydrophobic Drugs: a Comparison Study. *J. Pharm. Investig.* 48, 381–391. doi:10.1007/s40005-017-0334-8

Deng, C., Zhang, Q., Guo, J., Zhao, X., and Zhong, Z. (2020). Robust and Smart Polypeptide-Based Nanomedicines for Targeted Tumor Therapy. *Adv. Drug Deliv. Rev.* 160, 199–211. doi:10.1016/j.addr.2020.10.019

Ding, J., Chen, J., Li, D., Xiao, C., Zhang, J., He, C., et al. (2013). Biocompatible Reduction-Responsive Polypeptide Micelles as Nanocarriers for Enhanced Chemotherapy Efficacy *In Vitro*. *J. Mater. Chem. B* 1, 69–81. doi:10.1039/c2tb00063f

Ding, J., Shi, F., Xiao, C., Lin, L., Chen, L., He, C., et al. (2011). One-step Preparation of Reduction-Responsive Poly(ethylene Glycol)-Poly(amino Acid)s Nanogels as Efficient Intracellular Drug Delivery Platforms. *Polym. Chem.* 2, 2857–2864. doi:10.1039/c1py00360g

Ghosh, S., Javia, A., Shetty, S., Bardoliwala, D., Maiti, K., Banerjee, S., et al. (2021). Triple Negative Breast Cancer and Non-small Cell Lung Cancer: Clinical Challenges and Nano-Formulation Approaches. *J. Controlled Release* 337, 27–58. doi:10.1016/j.jconrel.2021.07.014

Hussein, Y. H. A., and Youssry, M. (2018). Polymeric Micelles of Biodegradable Diblock Copolymers: Enhanced Encapsulation of Hydrophobic Drugs. *Materials (Basel)* 11, 688. doi:10.3390/ma11050688

Jiang, Z.-Y., Feng, X.-R., Xu, W.-G., Zhuang, X.-L., Ding, J.-X., and Chen, X.-S. (2020). Calcium Phosphate-Cured Nanocluster of Poly(L-Glutamic Acid)-Cisplatin and Arsenic Trioxide for Synergistic Chemotherapy of Peritoneal Metastasis of Ovarian Cancer. *Acta Polymerica Sinica* 51, 901–910. doi:10.11777/j.issn1000-3304.2020.20053

Jiang, Z., Liu, Y., Feng, X., and Ding, J. (2019). Functional Polypeptide Nanogels. *J. Funct. Polym.* 32, 13–27. doi:10.14133/j.cnki.1008-9357.20180612001

Kim, S., Im, S., Park, E.-Y., Lee, J., Kim, C., Kim, T.-I., et al. (2020). Biology, and MedicineDrug-Loaded Titanium Dioxide Nanoparticle Coated with Tumor Targeting Polymer as a Sonodynamic Chemotherapeutic Agent for Anti-cancer Therapy. *Nanomedicine: Nanotechnology, Biol. Med.* 24, 102110. doi:10.1016/j.nano.2019.102110

Li, D., Ding, J. X., Tang, Z. H., Sun, H., Zhuang, X. L., Xu, J. Z., et al. (2012). *In Vitro* evaluation of Anticancer Nanomedicines Based on Doxorubicin and Amphiphilic Y-Shaped Copolymers. *Int. J. Nanomedicine* 7, 2687–2697. doi:10.2147/IJN.S30687

Li, D., Sun, H., Ding, J., Tang, Z., Zhang, Y., Xu, W., et al. (2013). Polymeric Topology and Composition Constrained Polyether-Polyester Micelles for Directional Antitumor Drug Delivery. *Acta Biomater.* 9, 8875–8884. doi:10.1016/j.actbio.2013.06.041

Liu, Y., Li, D., Ding, J., and Chen, X. (2020). Controlled Synthesis of Polypeptides. *Chin. Chem. Lett.* 31, 3001–3014. doi:10.1016/j.cclet.2020.04.029

Lu, Z., Peng, Z., Liu, C., Wang, Z., Wang, Y., Jiao, X., et al. (2020). Current Status and Future Perspective of Immunotherapy in Gastrointestinal Cancers. *The Innovation* 1, 100041. doi:10.1016/j.xinn.2020.100041

Lübtow, M. M., Haider, M. S., Kirsch, M., Klisch, S., and Luxenhofer, R. (2019). Like Dissolves like? A Comprehensive Evaluation of Partial Solubility Parameters to Predict Polymer-Drug Compatibility in Ultrahigh Drug-Loaded Polymer Micelles. *Biomacromolecules* 20, 3041–3056. doi:10.1021/acs.biomac.9b00618

Lv, S., Kim, H., Song, Z., Feng, L., Yang, Y., Baumgartner, R., et al. (2020). Unimolecular Polypeptide Micelles via Ultrafast Polymerization of N-Carboxyanhydrides. *J. Am. Chem. Soc.* 142, 8570–8574. doi:10.1021/jacs.0c01173

Neoptolemos, J. P., Kleeff, J., Michl, P., Costello, E., Greenhalf, W., and Palmer, D. H. (2018). Therapeutic Developments in Pancreatic Cancer: Current and Future Perspectives. *Nat. Rev. Gastroenterol. Hepatol.* 15, 333–348. doi:10.1038/s41575-018-0005-x

Perin, F., Motta, A., and Maniglio, D. (2021). Amphiphilic Copolymers in Biomedical Applications: Synthesis Routes and Property Control. *Mater. Sci. Eng. C* 123, 111952. doi:10.1016/j.msec.2021.111952

Pinyakit, Y., Palaga, T., Kiatkamjornwong, S., and Hoven, V. P. (2020). Sequential post-polymerization Modification of a Pentafluorophenyl Ester-Containing Homopolymer: a Convenient Route to Effective pH-Responsive Nanocarriers for Anticancer Drugs. *J. Mater. Chem. B* 8, 454–464. doi:10.1039/c9tb01533g

Rajes, K., Walker, K. A., Hadam, S., Zabihi, F., Ibrahim-Bacha, J., Germer, G., et al. (2021). Oxidation-Sensitive Core-Multishell Nanocarriers for the Controlled Delivery of Hydrophobic Drugs. *ACS Biomater. Sci. Eng.* 7, 2485–2495. doi:10.1021/acsbiomaterials.0c01771

Ray, S., Li, Z., Hsu, C.-H., Hwang, L.-P., Lin, Y.-C., Chou, P.-T., et al. (2018). Dendrimer- and Copolymer-Based Nanoparticles for Magnetic Resonance Cancer Theranostics. *Theranostics* 8, 6322–6349. doi:10.7150/thno.27828

Reina, G., González-Domínguez, J. M., Criado, A., Vázquez, E., Bianco, A., and Prato, M. (2017). Promises, Facts and Challenges for Graphene in Biomedical Applications. *Chem. Soc. Rev.* 46, 4400–4416. doi:10.1039/c7cs00363c

Saravanakumar, G., Park, H., Kim, J., Park, D., Pramanick, S., Kim, D. H., et al. (2018). Miktoarm Amphiphilic Block Copolymer with Singlet Oxygen-Labile Stereospecific β-Aminoacrylate Junction: Synthesis, Self-Assembly, and Photodynamically Triggered Drug Release. *Biomacromolecules* 19, 2202–2213. doi:10.1021/acs.biomac.8b00290

Shi, X., Bai, S., Yang, C., Ma, X., Hou, M., Chen, J., et al. (2018). Improving the Carrier Stability and Drug Loading of Unimolecular Micelle-Based Nanotherapeutics for Acid-Activated Drug Delivery and Enhanced Antitumor Therapy. *J. Mater. Chem. B* 6, 5549–5561. doi:10.1039/c8tb01384e

Song, Z., Tan, Z., and Cheng, J. (2019). Recent Advances and Future Perspectives of Synthetic Polypeptides from N-Carboxyanhydrides. *Macromolecules* 52, 8521–8539. doi:10.1021/acs.macromol.9b01450

Steinbrueck, A., Sedgwick, A. C., Brewster, J. T., Yan, K.-C., Shang, Y., Knoll, D. M., et al. (2020). Transition Metal Chelators, Pro-chelators, and Ionophores as Small Molecule Cancer Chemotherapeutic Agents. *Chem. Soc. Rev.* 49, 3726–3747. doi:10.1039/c9cs00373h

Sun, Y., Shan, H., Wang, J., Wang, X., Yang, X., and Ding, J. (2019). Laden Nanofiber Capsules for Local Malignancy Chemotherapy. *J Biomed. Nanotechnol* 15, 939–950. doi:10.1166/jbn.2019.2745

Thomas, R. G., Surendran, S. P., and Jeong, Y. Y. (2020). Tumor Microenvironment-Stimuli Responsive Nanoparticles for Anticancer Therapy. *Front. Mol. Biosciences* 7, 414. doi:10.3389/fmolb.2020.610533

Vrijsen, J. H., Rasines Mazo, A., Junkers, T., and Qiao, G. G. (2020). Accelerated Polypeptide Synthesis via N -Carboxyanhydride Ring Opening Polymerization in Continuous Flow. *Macromol. Rapid Commun.* 41, 2000071. doi:10.1002/marc.202000071

Wang, Q., Zhang, P., Li, Z., Feng, X., Lv, C., Zhang, H., et al. (2019a). Evaluation of Polymer Nanoformulations in Hepatoma Therapy by Established Rodent Models. *Theranostics* 9, 1426–1452. doi:10.7150/thno.31683

Wang, Y., Jiang, Z., Xu, W., Yang, Y., Zhuang, X., Ding, J., et al. (2019b). Chiral Polypeptide Thermogels Induce Controlled Inflammatory Response as Potential Immunoadjuvants. *ACS Appl. Mater. Inter.* 11, 8725–8730. doi:10.1021/acsami.9b01872

Wang, Y., Wang, X., Zhang, J., Wang, L., Ou, C., Shu, Y., et al. (2019c). Gambogic Acid-Encapsulated Polymeric Micelles Improved Therapeutic Effects on Pancreatic Cancer. *Chin. Chem. Lett.* 30, 885–888. doi:10.1016/j.cclet.2019.02.018

Wei, L., Chen, J., and Ding, J. (2021). Sequentially Stimuli-Responsive Anticancer Nanomedicines. *Nanomedicine* 16, 261–264. doi:10.2217/nnm-2021-0019

Yang, D.-P., Oo, M. N. N. L., Deen, G. R., Li, Z., and Loh, X. J. (2017). Nano-Star-Shaped Polymers for Drug Delivery Applications. *Macromol. Rapid Commun.* 38, 1700410. doi:10.1002/marc.201700410

Yang, J.-Z., Zou, H.-Y., Ding, J.-X., and Chen, X.-S. (2021). Controlled Synthesis and Biomedical Applications of Cystine-Based Polypeptide Nanomaterials. *Acta Polymerica Sinica* 52, 960–977. doi:10.11777/j.issn1000-3304.2021.21115

Zeinali, M., Abbaspour-Ravasjani, S., Ghorbani, M., Babazadeh, A., Soltanfam, T., Santos, A. C., et al. (2020). Nanovehicles for Co-delivery of Anticancer Agents. *Drug Discov. Today* 25 (8), 1416–1430. doi:10.1016/j.drudis.2020.06.027

Zhang, H., Dong, S., Li, Z., Feng, X., Xu, W., Tulinao, C. M. S., et al. (2020). Biointerface Engineering Nanoplatforms for Cancer-Targeted Drug Delivery. *Asian J. Pharm. Sci.* 15, 397–415. doi:10.1016/j.ajps.2019.11.004

Zhang, Z., Qu, Q., Li, J., and Zhou, S. (2013). The Effect of the Hydrophilic/Hydrophobic Ratio of Polymeric Micelles on Their Endocytosis Pathways into Cells. *Macromol. Biosci.* 13, 789–798. doi:10.1002/mabi.201300037

Zhao, D., Huang, X., Zhang, Z., Ding, J., Cui, Y., and Chen, X. (2021). Engineered Nanomedicines for Tumor Vasculature Blockade Therapy. *Wiley Interdiscip. Rev. Nanomed Nanobiotechnol* 13, e1691. doi:10.1002/wnan.1691

Zhao, L., Ding, J., Xiao, C., He, P., Tang, Z., and Chen, X. (2013). Phenylboronic Acid Functionalized Polypeptide Micelles for

Glucose-Responsive Insulin Release at Physiological pH. *J. Controlled Release* 172, E110. doi:10.1016/j.jconrel.2013.08.267

Zheng, C., Li, M., and Ding, J. (2021). Challenges and Opportunities of Nanomedicines in Clinical Translation. *BIO Integration* 2, 57–60. doi:10.15212/bioi-2021-0016

Zheng, P., Liu, Y., Chen, J., Xu, W., Li, G., and Ding, J. (2020). Targeted pH-Responsive Polyion Complex Micelle for Controlled Intracellular Drug Delivery. *Chin. Chem. Lett.* 31, 1178–1182. doi:10.1016/j.cclet.2019.12.001

Conflict of Interest: The authors declare that the research was conducted in the absence of any commercial or financial relationships that could be construed as a potential conflict of interest.

Publisher's Note: All claims expressed in this article are solely those of the authors and do not necessarily represent those of their affiliated organizations, or those of the publisher, the editors, and the reviewers. Any product that may be evaluated in this article, or claim that may be made by its manufacturer, is not guaranteed or endorsed by the publisher.

frontiers in Bioengineering and Biotechnology

ORIGINAL RESEARCH
published: 06 January 2022
doi: 10.3389/fbioe.2021.826926

Ultrasound-Guided Percutaneous Thermal Ablation of Hepatic Focal Nodular Hyperplasia——A Multicenter Retrospective Study

Xuan Yu[1†], Jiandong Chang[2†], Dezhi Zhang[3†], Qiang Lu[4†], Songsong Wu[5] and Kai Li[1]**

[1]Department of Medical Ultrasonics, The Third Affiliated Hospital of Sun Yat-sen University, Guangdong, China, [2]Department of Ultrasound, Xiamen Chinese Medical Hospital, Fujian, China, [3]Department of Ultrasound, The First Hospital of Jilin University, Jilin, China, [4]Department of Ultrasound, West China Hospital, Sichuan, China, [5]Department of Ultrasonography, Shengli Clinical Medical College of Fujian Medical University, Fujian, China

OPEN ACCESS

Edited by:
Yuce Li,
Sungkyunkwan University,
South Korea

Reviewed by:
Shixian Lv,
Peking University, China
Junchao Wei,
Nanchang University, China
Jinjin Chen,
Tufts University, United States

***Correspondence:**
Kai Li
likai@mail.sysu.edu.cn
Songsong Wu
465269898@qq.com

†These authors have contributed equally to this work and share first authorship

Specialty section:
This article was submitted to Biomaterials, a section of the journal Frontiers in Bioengineering and Biotechnology

Received: 01 December 2021
Accepted: 20 December 2021
Published: 06 January 2022

Citation:
Yu X, Chang J, Zhang D, Lu Q, Wu S and Li K (2022) Ultrasound-Guided Percutaneous Thermal Ablation of Hepatic Focal Nodular Hyperplasia——A Multicenter Retrospective Study. Front. Bioeng. Biotechnol. 9:826926. doi: 10.3389/fbioe.2021.826926

Background and Aim: To evaluate the clinical effect of ultrasound (US)-guided percutaneous thermal ablation of hepatic focal nodular hyperplasia (FNH).

Methods: A retrospective analysis of the clinical data of patients undergoing US-guided percutaneous thermal ablation of FNH from November 2008 to August 2021 at five medical centers in China was conducted.

Results: A total of 53 patients were included (26 males and 27 females). The mean age was 35.1 ± 10.8 years. Sixty-five lesions (46 solitary cases and 7 cases with multiple lesions) were included, 70.8% (46/65) of which were located in the right liver lobe. The mean tumor length was 2.9 ± 1.5 cm. All patients successfully completed the ablation treatment. Immediate postoperative imaging showed that the primary technical success rate was 94.3% (50/53). Two patients underwent ablation 3 and 6 months after the primary ablation, and the secondary technical success rate was 100% (2/2). The incidence of complications was 3.8% (2/53). Imaging follow-up was conducted regularly after ablation, and no residual lesion enlargement or tumor recurrence was observed during the follow-up period. The technique efficacy rate was 98.1% (52/53).

Conclusion: US-guided percutaneous thermal ablation is a safe and effective treatment for FNH of the liver.

Keywords: focal nodular hyperplasia, ultrasonography, radiofrequency ablation, microwave ablation, thermal ablation

INTRODUCTION

Focal nodular hyperplasia (FNH) is the second most common benign liver tumor in adults, with a prevalence of 0.3–3% in the general population (Oldhafer et al., 2020; Zhu et al., 2021). The exact mechanism of FNH is still unclear, but most scholars agree that nonneoplastic hyperplasia of hepatic parenchyma, which can be caused by anomalous aortic vascularization, secondary thrombosis, reactive hyperplasia after hepatocellular injury caused by vasculitis, or abnormal blood perfusion, may develop into FNH (Towbin et al., 2011; Franchi-Abella et al., 2013; Zarfati et al., 2020; Yao et al., 2021). Since FNH is usually asymptomatic and there have been no reports of malignant progression of this disease, conservative

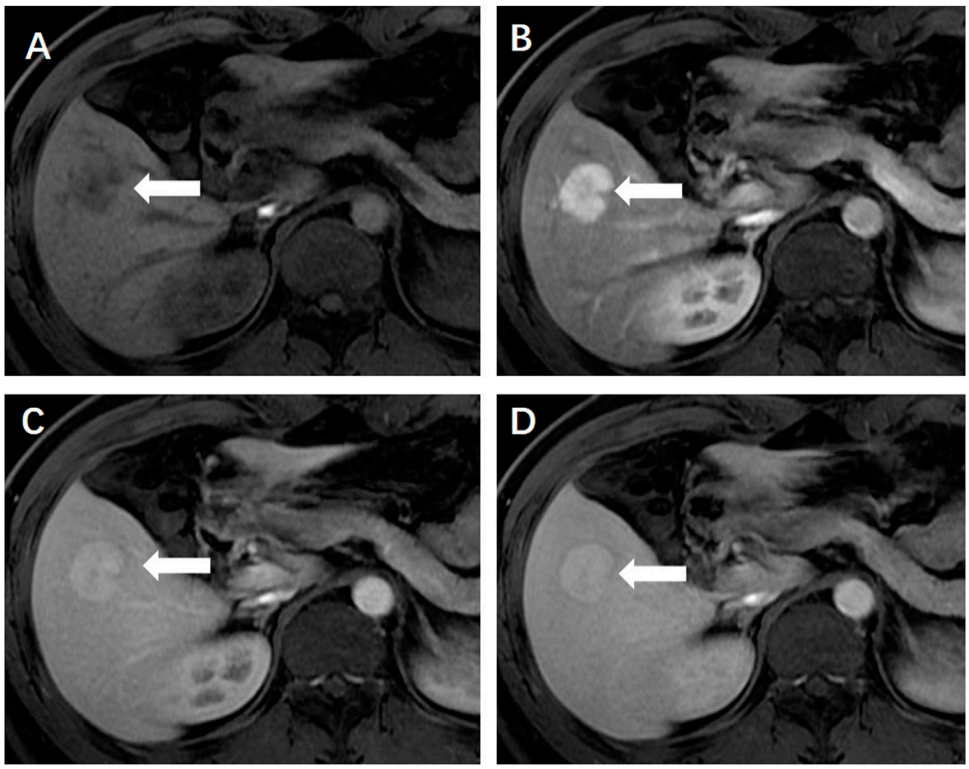

FIGURE 1 | (A) Enhanced magnetic resonance imaging revealed a solid focal liver lesion (←) which showed hyperenhancement in the arterial phase **(B)** and isointensity in the portal venous **(C)** and delayed phase **(D)**.

observation should be considered first. However, clinical treatment should be considered if the diagnosis is unclear, the patient has symptoms or the lesion becomes enlarged during follow-up (Perrakis et al., 2017; Jung et al., 2019).

Surgical resection and transarterial embolization (TAE) are the common treatment methods for FNH. Surgical resection has consistently been considered the preferred treatment, but it may cause greater damage and has a moderate incidence of complications and postoperative mortality (Virgilio and Cavallini, 2018), which may cause concerns for some patients. TAE can be applied to patients who are ineligible for resection and in cases where it is desirable to preserve the normal liver parenchyma. It is also commonly used to reduce the volume of lesions and control pain before surgery (Amesur et al., 2009; Arts et al., 2010; Virgilio and Cavallini, 2018), but TAE also has the risk of residual (Zhang et al., 2017) and increased radiation exposure.

Thermal ablation, a minimally invasive approach, has been widely applied in the treatment of small hepatocellular carcinoma and other solid tumors. Its advantage lies in its curative effect, minimal invasion and lighter economic burden. Theoretically, thermal ablation can also induce curative effects in FNH patients, but there have been few reports (Hedayati et al., 2010; Yao et al., 2021) about using ablation for treating FNH patients.

Therefore, this study aims to analyze the efficacy of US-guided thermal ablation for FNH by assessing clinical data of FNH patients from five medical centers.

MATERIALS AND METHODS

Patients

The study was approved by the Ethical Review Board of the Third Affiliated Hospital of Sun Yat-sen University. We performed a retrospective analysis of patient data using uniform data tables in five medical centers in China. The inclusion criteria for the study were as follows: 1) a diagnosis of FNH confirmed by pathological biopsy, or typical imaging characteristics (**Figures 1**–**3**) shown by contrast-enhanced ultrasound (CEUS) and hepatic magnetic resonance imaging (MRI); and 2) application of US-guided percutaneous thermal ablation (**Figure 4A**). The exclusion criteria were as follows: 1) application of thermal ablation combined with other treatments, such as surgical resection or TAE, on lesions diagnosed as FNH; and 2) lack of postoperative follow-up. The basic information included age, sex, and the number, location, and size of the lesions, and biopsy results, and information related to the ablation procedure was collected.

Assessment of Therapeutic Efficacy and Follow-Up

The efficacy of thermal ablation was evaluated by US, computed tomography (CT) or MRI. Technical success was

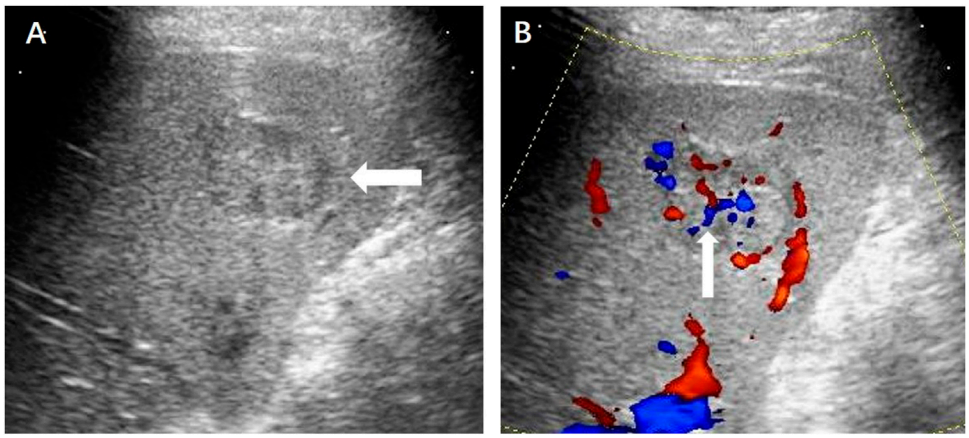

FIGURE 2 | (A) Ultrasound revealed a hypoechoic hepatic lesion (←). **(B)** The lesion had a characteristic radiant blood flow (↑) shown by Color Doppler ultrasound.

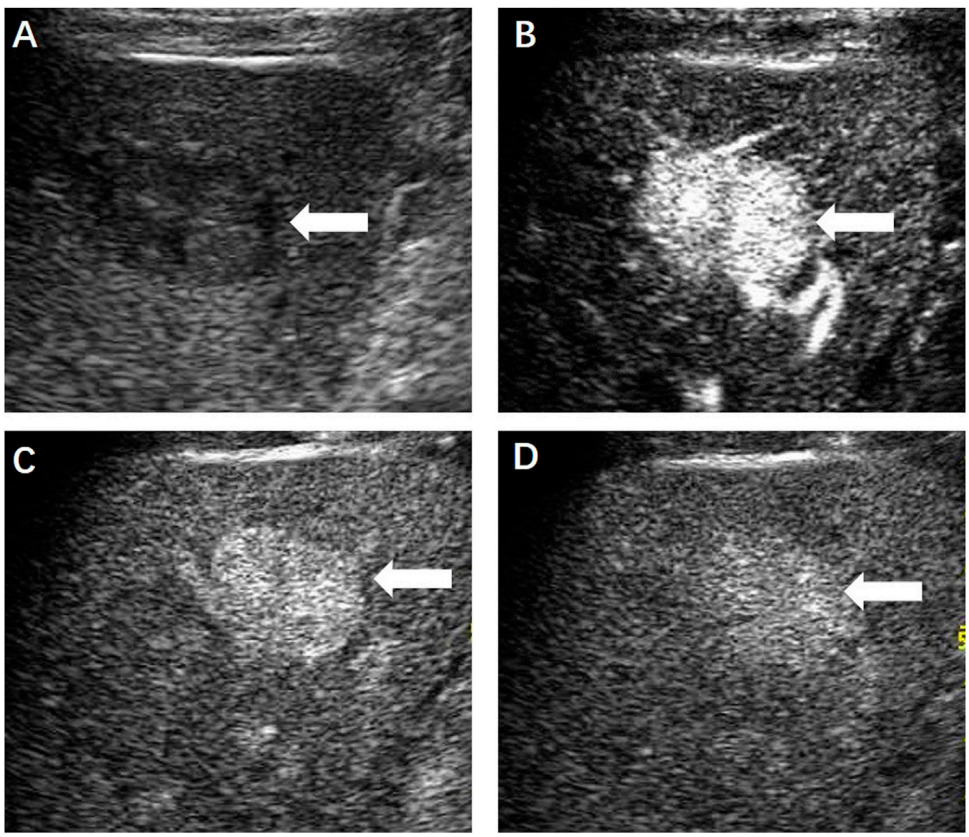

FIGURE 3 | (A) Contrast-enhanced ultrasound displayed a hypoechoic hepatic lesion (←) which showed obvious hyperenhancement in the arterial phase **(B)** and slightly enhancement in the portal **(C)** and delayed phase **(D)**.

defined as the absence of blood supply in the ablation zone assessed by CEUS immediately after the treatment (**Figure 4B**) and the first postoperative day. After discharge, imaging follow-up was conducted regularly among all the patients until September 2021. Technique efficacy was defined based on a lack of enhancements of the primary lesion seen on enhanced-CT or MRI (**Figure 5**) at least 1 month after ablation.

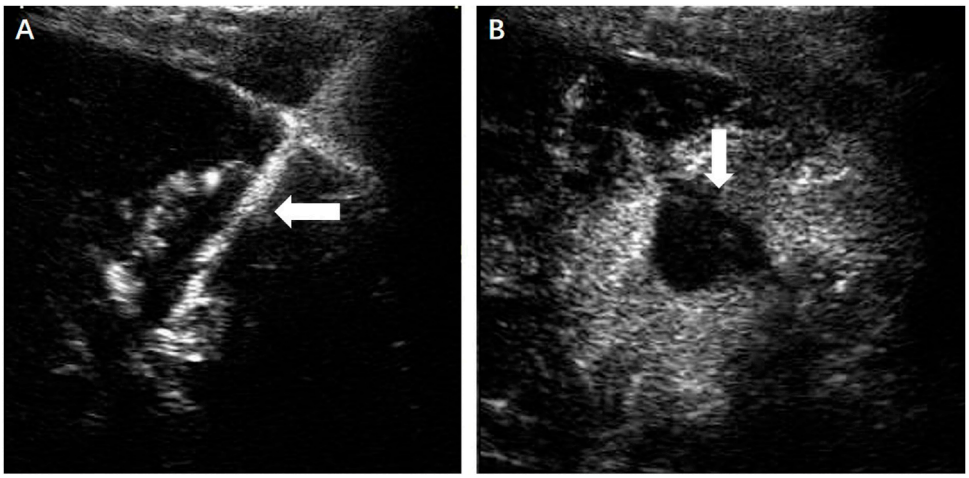

FIGURE 4 | (A) Under the guidance of contrast-enhanced ultrasound, the microwave antenna (←) was inserted directly to the lesion. **(B)** No enhancement of the ablation zone (↓) could be seen in the arterial phase.

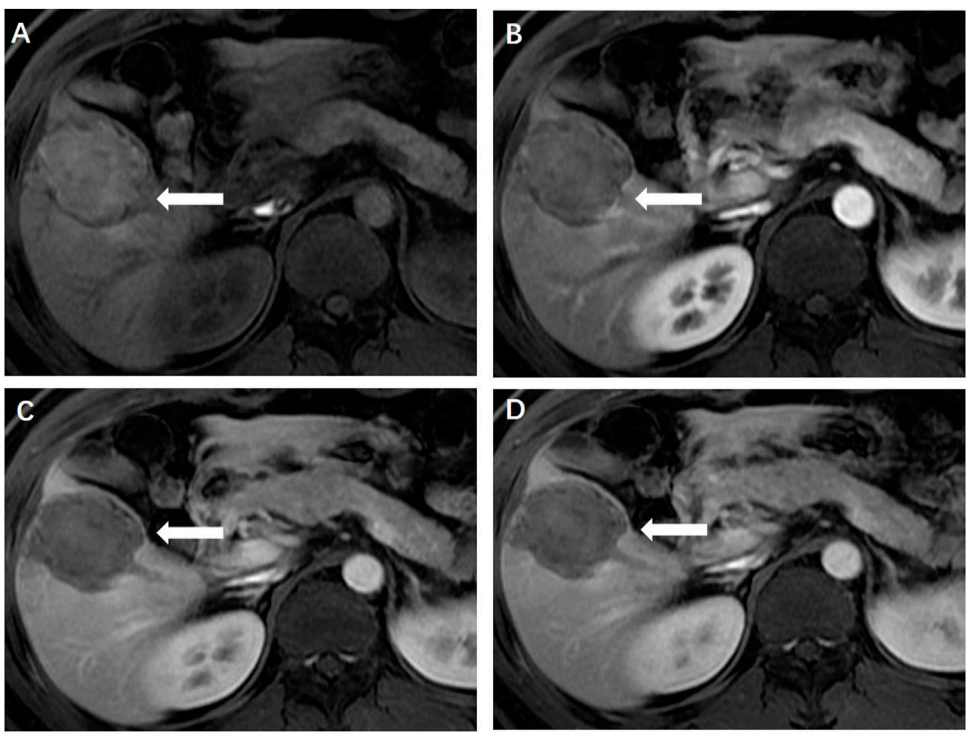

FIGURE 5 | (A) Magnetic resonance imaging 1 month later showed the ablation zone was isointensity (←) and had no enhancement in the arterial **(B)**, portal venous **(C)** and delayed phase **(D)**, indicating completely ablation of the lesion.

RESULTS

Patient Profiles

A total of 53 patients were enrolled between November 2008 and August 2021. The baseline characteristics of the patients are presented in **Table 1**.

Operation and Outcomes

All the patients underwent US-guided percutaneous thermal ablation, including 31 patients who received microwave ablation (MWA), 20 patients who received radiofrequency ablation (RFA) and two patients who received RFA combined with MWA. Artificial ascites (15/53), one-lung ventilation (2/53)

TABLE 1 | Baseline patient and lesion characteristics.

Variables	Numbers
patients	53
Age (years)	35.1 ± 10.8 (18–63)
Gender	
Male	26 (49.1%)
Female	27 (50.9%)
Lesions	
Solitary	46 (86.8%)
Multiple total	7 (13.2%)
Total	65
Tumor location	
Left	19 (29.2%)
Right	46 (70.8%)
Tumor size (cm)	2.9 ± 1.5 (0.6–6.6)
Biopsy	
Yes	39 (73.6%)
No	14 (26.4%)

Data are presented as the mean ± SD (range) or n (%).

and laparoscopy (3/53) were used for assistance. All patients completed the ablation treatment successfully. Immediate postoperative CEUS showed that the ablation zone covered the initial lesions in 50 cases, which indicated that the primary technical success rate was 94.3% (50/53). Partial residual lesions were seen in three patients, two of whom underwent secondary ablation 3 and 6 months after the first procedure. The secondary technical success rate was 100% (2/2).

Complications

The incidence of complications was 3.8% (2/53). One patient had intraoperative needle tract bleeding, which could be controlled by ablation. The other patient developed acute renal failure. After proper specialized treatment, the patient was discharged 1 month later. The rest of the patients did not experience severe complications. Some of the patients (24.5%, 13/53) had minor adverse reactions such as pain, slightly elevated aminotransferase levels and discomfort in the abdomen after ablation, which spontaneously resolved in a short time.

Follow-Up

After ablation, all the patients were regularly followed up with imaging tests including US, CT or MRI. The residual part of the lesion in one patient showed no obvious changes on 1-month CEUS and 3-month MRI, so the patient did not undergo secondary ablation. The rest of the patients showed no evident residual lesions or tumor recurrence during the follow-up period. The technique efficacy rate was 98.1% (52/53). Furthermore, long-term complications related to ablation did not occur in any patient.

DISCUSSION

Thermal ablation, including RFA and MWA, is a major radical method for hepatocellular carcinoma and liver metastasis. A retrospective cohort study (Wang et al., 2016) of 221 patients analyzed the efficacy of MWA for liver cancer, with 90.95% of patients achieving initial complete ablation at the technical evaluation 1 month after surgery. You et al. used thermal ablation to treat 85 liver tumors, and the technical success rate was 100% (You et al., 2021). One instance of a residual lesion was found by CECT/CEMRI 1 month after surgery, and the technique efficacy rate was 98.8%. Technically successful ablation can provide 50–70% 5-year overall survival for very early and early HCC patients (Meloni et al., 2021). FNH is characterized as benign in nature but has abundant arterial blood supply, compared with liver cancer. Technically, thermal ablation can also be considered when clinical treatment is indicated in FNH patients. Hedayati et al. reported the first case of FNH treated with RFA in 2010 (Hedayati et al., 2010). The patient was a 21-year-old female with a history of progressive right upper abdominal pain. The size of the lesion was 2.2 cm and RFA was completed under the guidance of CT. Although a small nodular area of rim enhancement was noted on the follow-up CT 2 months later, the patient's symptoms were significantly relieved. Overall, the treatment was considered successful. In our study, all patients were treated with US-guided percutaneous thermal ablation with a primary technical success rate of 93.9%, and two patients also achieved technical success after secondary ablation. Only one patient decided not to undergo secondary ablation. Most lesions were discovered accidentally, and only a few patients had obvious symptoms, which were significantly relieved after thermal ablation. During the follow-up period, there were no clear residual lesions or tumor recurrence in any patients except in one patient who did not achieve technical success after the first ablation. The overall technique efficacy rate was 98.1% (52/53). Our results suggest that, similar to the situation in liver cancer, thermal ablation for FNH can also achieve curative effects. In addition, our study is the first retrospective analysis of multicenter US-guided thermal ablation for FNH patients, and the results also provide a theoretical basis for prospective studies in the future.

For patients with unresectable lesions or who are ineligible for surgery, TAE is an alternative treatment. In 2013, Birn et al. reported a total of 17 lesions in 12 patients with FNH treated with TAE (Birn et al., 2013). The symptoms were completely relieved in seven patients and partially relieved in five patients after embolization. Only five of the 17 lesions were completely embolized based on a comparison with the lesion appearance on preoperative imaging. Virgilio et al. summarized 17 studies on the use of TAE in the treatment of FNH (Virgilio and Cavallini, 2018). A total of 128 patients received effective treatment, and each patient received TAE at least once. Local recurrence was found in only one of the treated patients during 54 months of follow-up. Although TAE is an effective treatment for FNH, there is a risk of increased radiation exposure in some specific patients, such as children. Our team reported a case of a 9-year-old girl who was diagnosed with FNH and treated by thermal ablation (Yao et al., 2021). The maximum diameter of the lesion was 2.9 cm, and it was treated by US-guided microwave ablation. Both the immediate postoperative CEUS and 1-month MRI after ablation showed that the lesion had been completely ablated.

Similarly, in this study, 97.9% of the patients achieved complete remission of symptoms after one or two ablations and no recurrence of lesions was found during the current follow-up period. These findings indicated that thermal ablation, which is also a minimally invasive technique, can achieve therapeutic effects comparable to TAE and a lower residual lesion rate. Moreover, US-guided percutaneous thermal ablation has the advantage of no radiation exposure and may be more suitable for children or patients who want to reduce the risk of radiation exposure.

In terms of safety, complications of surgical resection mainly include intraoperative and postoperative bleeding, biliary fistula, intestinal obstruction, etc., with a mortality rate of approximately 2%. Although it is currently the preferred treatment for FNH, some scholars (Virgilio and Cavallini, 2018) believe that surgical resection-related complications and mortality are serious and unacceptable for the treatment of benign diseases. The common complications of thermal ablation for liver cancer mainly include subcapsular hematoma, abdominal skin burn and pleural effusion (Spiliotis et al., 2021). These complications may also occur during FNH treatment. However, in this study, only two patients had complications. One patient was found to have needle tract bleeding during the operation, and timely treatment with ablation stopped the bleeding. The other patient developed acute renal failure after surgery, which was relieved by specialized treatment. The rest of the patients did not develop severe complications. Some patients had postoperative adverse reactions, such as wound pain, mildly elevated aminotransferase levels, and discomfort in the upper abdomen, but these symptoms spontaneously resolved in a short time. Similar to thermal ablation, TAE is a relatively safe treatment. Postembolization syndrome, which is characterized by fever, loss of appetite, abdominal pain, low-grade fever, or nausea, is a common complication of TAE, but the symptoms are transient and self-limited (Virgilio and Cavallini, 2018). There is no literature comparing the safety of TAE and thermal ablation. The results of this study indicate that thermal ablation is a safe treatment with less trauma and a lower complication rate than surgical resection. Compared with that of TAE, the safety of thermal ablation is not significantly lower.

However, there are some limitations in this study. 1) Our study is a retrospective study, and only 53 cases were included. If thermal ablation is to be widely applied in the clinical treatment of FNH patients, more cases are needed to prove its effectiveness and safety. 2) This study only included patients treated with thermal ablation and failed to compare them with patients treated with surgical resection or TAE; as such, the results are not sufficiently convincing.

In general, US-guided percutaneous thermal ablation is an effective and safe treatment, and can be used as a radical treatment for FNH patients with appropriate treatment indications.

DATA AVAILABILITY STATEMENT

The original contributions presented in the study are included in the article/Supplementary Material, further inquiries can be directed to the corresponding authors.

AUTHOR CONTRIBUTIONS

SW and KL were responsible for design of the study. XY and KL drafted, interpretated and reviewed the manuscript. JC, QL, DZ and SW performed the data analysis. All authors read and approved the final manuscript.

REFERENCES

Amesur, N., Hammond, J. S., Zajko, A. B., Geller, D. A., and Gamblin, T. C. (2009). Management of Unresectable Symptomatic Focal Nodular Hyperplasia with Arterial Embolization. *J. Vasc. Interv. Radiol.* 20 (4), 543–547. doi:10.1016/j.jvir.2009.01.001

Arts, C. H. P., van Hillegersberg, R., de Kort, G. A. P., and Moll, F. L. (2010). Inferior Caval Vein Thrombosis Owing to Compression of Focal Nodular Hyperplasia: Surgical Resection after Shrinkage by Hepatic Artery Embolization. *Vascular* 18 (1), 53–58. doi:10.2310/6670.2009.00030

Birn, J., Williams, T. R., Croteau, D., Schwartz, S., Sturza, S., and Getzen, T. (2013). Transarterial Embolization of Symptomatic Focal Nodular Hyperplasia. *J. Vasc. Interv. Radiol.* 24 (11), 1647–1655. doi:10.1016/j.jvir.2013.07.012

Franchi-Abella, S., Branchereau, S., Paulette, B., and Bioulac-Sage, P. (2013). Benign Hepatocellular Tumors in Children: Focal Nodular Hyperplasia and Hepatocellular Adenoma. *Int. J. Hepatol.* 2013, 215064–215111. doi:10.1155/2013/215064

Hedayati, P., VanSonnenberg, E., Shamos, R., Gillespie, T., and McMullen, W. (2010). Treatment of Symptomatic Focal Nodular Hyperplasia with Percutaneous Radiofrequency Ablation. *J. Vasc. Interv. Radiol.* 21 (4), 582–585. doi:10.1016/j.jvir.2009.12.385

Jung, J.-M., Hwang, S., Kim, K.-H., Ahn, C.-S., Moon, D.-B., Ha, T.-Y., et al. (2019). Surgical Indications for Focal Nodular Hyperplasia of the Liver: Single-Center Experience of 48 Adult Cases. *Ann. Hepatobiliary Pancreat. Surg.* 23 (1), 8. doi:10.14701/ahbps.2019.23.1.8

Meloni, M. F., Francica, G., Chiang, J., Coltorti, A., Danzi, R., and Laeseke, P. F. (2021). Use of Contrast-Enhanced Ultrasound in Ablation Therapy of HCC: Planning, Guiding, and Assessing Treatment Response. *J. Ultrasound Med.* 40 (5), 879–894. doi:10.1002/jum.15471

Oldhafer, K. J., Habbel, V., Horling, K., Makridis, G., and Wagner, K. C. (2020). Benign Liver Tumors. *Visc. Med.* 36 (4), 292–303. doi:10.1159/000509145

Perrakis, A., Vassos, N., Grützmann, R., and Croner, R. S. (2017). What Is Changing in Indications and Treatment of Focal Nodular Hyperplasia of the Liver. Is There Any Place for Surgery? *Ann. Hepatol.* 16 (3), 333–341. doi:10.5604/16652681.1235475

Spiliotis, A. E., Gäbelein, G., Holländer, S., Scherber, P., Glanemann, M., and Patel, B. (2021). Microwave Ablation Compared with Radiofrequency Ablation for the Treatment of Liver Cancer: A Systematic Review and Meta-Analysis. *Radiol. Oncol.* 55 (3), 247–258. doi:10.2478/raon-2021-0030

Towbin, A. J., Luo, G. G., Yin, H., and Mo, J. Q. (2011). Focal Nodular Hyperplasia in Children, Adolescents, and Young Adults. *Pediatr. Radiol.* 41 (3), 341–349. doi:10.1007/s00247-010-1839-8

Virgilio, E., and Cavallini, M. (2018). Managing Focal Nodular Hyperplasia of the Liver: Surgery or Minimally-Invasive Approaches? A Review of the Preferable Treatment Options. *Anticancer Res.* 38 (1), 33–36. doi:10.21873/anticanres.12188

Wang, T., Lu, X., Chi, J., Ding, M., Zhang, Y., Tang, X., et al. (2016). Microwave Ablation of Hepatocellular Carcinoma as First-Line Treatment: Long Term Outcomes and Prognostic Factors in 221 Patients. *Sci. Rep-Uk* 6 (1). doi:10.1038/srep32728

Yao, Z., Zeng, Q., Yu, X., Lin, S., Jiang, S., Ma, D., et al. (2021). Case Report: Ultrasound-Guided Percutaneous Microwave Ablation of Focal Nodular Hyperplasia in a 9-Year-Old Girl. *Front. Pediatr.* 9, 710779. doi:10.3389/fped.2021.710779

You, Y., Zhang, M., Li, K., Zeng, Q., Luo, L., Long, Y., et al. (2021). Feasibility of 3D US/CEUS-US/CEUS Fusion Imaging-Based Ablation Planning in Liver Tumors: a Retrospective Study. *Abdom. Radiol.* 46 (6), 2865–2874. doi:10.1007/s00261-020-02909-5

Zarfati, A., Chambers, G., Pio, L., Guerin, F., Fouquet, V., Franchi-Abella, S., et al. (2020). Management of Focal Nodular Hyperplasia of the Liver: Experience of 50 Pediatric Patients in a Tertiary Center. *J. Pediatr. Surg.* 55 (9), 1885–1891. doi:10.1016/j.jpedsurg.2020.01.009

Zhang, G., Wang, M., Duan, F., Yuan, K., Li, K., Yan, J., et al. (2017). Transarterial Embolization with Bleomycin for Symptomatic Hepatic Focal Nodular Hyperplasia. *Diagn. Interv. Radiol.* 23 (1), 66–70. doi:10.5152/dir.2016.16061

Zhu, M., Li, H., Wang, C., Yang, B., Wang, X., Hou, F., et al. (2021). Focal Nodular Hyperplasia Mimicking Hepatocellular Adenoma and Carcinoma in Two Cases. *Dd&T* 15 (2), 112–117. doi:10.5582/ddt.2021.01033

Conflict of Interest: The authors declare that the research was conducted in the absence of any commercial or financial relationships that could be construed as a potential conflict of interest.

Publisher's Note: All claims expressed in this article are solely those of the authors and do not necessarily represent those of their affiliated organizations, or those of the publisher, the editors, and the reviewers. Any product that may be evaluated in this article, or claim that may be made by its manufacturer, is not guaranteed or endorsed by the publisher.

frontiers in Bioengineering and Biotechnology

ORIGINAL RESEARCH
published: 07 January 2022
doi: 10.3389/fbioe.2021.816757

Acitretin-Conjugated Dextran Nanoparticles Ameliorate Psoriasis-like Skin Disease at Low Dosages

Jiajia Lan[1,2†], Yuce Li[3,4†], Jingjing Wen[1,2], Yu Chen[3,4], Jing Yang[1,2], Liang Zhao[1,2], Yuting Xia[1,2], Hongyao Du[1,2], Juan Tao[1,2], Yan Li[1,2] and Jintao Zhu[3,4*]*

[1]*Department of Dermatology and Venereology, Union Hospital, Tongji Medical College, Huazhong University of Science and Technology (HUST), Wuhan, China,* [2]*Hubei Engineering Research Center of Skin Disease Theranostics and Health, Huazhong University of Science and Technology (HUST), Wuhan, China,* [3]*Hubei Engineering Research Center for Biomaterials and Medical Protective Materials, School of Chemistry and Chemical Engineering, Huazhong University of Science and Technology (HUST), Wuhan, China,* [4]*State Key Laboratory of Materials Processing and Mold Technology, School of Chemistry and Chemical Engineering, Huazhong University of Science and Technology (HUST), Wuhan, China*

OPEN ACCESS

Edited by:
Jae Hyung Park, Sungkyunkwan University, South Korea

Reviewed by:
Honglin Jin, Huazhong University of Science and Technology, China
Bhang Suk Ho, Sungkyunkwan University, South Korea
Hamidreza Montazeri Aliabadi, Chapman University, United States

***Correspondence:**
Jintao Zhu
jtzhu@mail.hust.edu.cn
Yan Li
littleagong@163.com

[†]These authors have contributed equally to this work

Specialty section:
This article was submitted to Biomaterials, a section of the journal Frontiers in Bioengineering and Biotechnology

Received: *17 November 2021*
Accepted: *17 December 2021*
Published: *07 January 2022*

Citation:
Lan J, Li Y, Wen J, Chen Y, Yang J, Zhao L, Xia Y, Du H, Tao J, Li Y and Zhu J (2022) Acitretin-Conjugated Dextran Nanoparticles Ameliorate Psoriasis-like Skin Disease at Low Dosages. Front. Bioeng. Biotechnol. 9:816757. doi: 10.3389/fbioe.2021.816757

Psoriasis is a common chronic inflammatory skin disease mainly characterized by keratinocyte hyperproliferation and massive infiltration of inflammatory immune cells. Acitretin (ACT), an FDA-approved first-line systemic drug for psoriasis treatment, could suppress the proliferation of keratinocytes and downregulate the expression of inflammatory cytokines by modulating signal transducer and activator of transcription (STAT) signaling pathways. However, dose-dependent side effects of ACT limit its long-term administration in the clinic. Therefore, improving the therapeutic efficacy of ACT to reduce clinical dosage will benefit the patients. Here, we develop ACT-conjugated dextran nanoparticles (ACT-Dex NPs) and evaluated the potential for psoriasis treatment. Our results indicate that ACT-Dex NPs ameliorate psoriasis-like skin disease significantly at a low dosage which does not cause side effects, while neat ACT drugs at an equivalent dosage provide much less benefit. Moreover, we demonstrate that ACT-Dex NPs suppress keratinocyte proliferation more efficiently than neat ACT by enhancing the inhibitory effect on STAT3 phosphorylation. Thus, the proposed ACT-Dex NPs provide an effective and safe option for psoriasis treatment.

Keywords: acitretin, nanoparticles, low dosage, stat3, psoriasis

1 INTRODUCTION

Psoriasis has affected ~ 2% of people worldwide. The quality of life of psoriatic patients was negatively impacted due to the repetitive relapsing and remitting during their lifetime. (Parisi et al., 2013; Boehncke and Schön, 2015; Michalek et al., 2017) The characteristics of psoriasis are epidermis thickening and an inflammatory infiltrate of dermal and epidermal immune cells. The crosstalk between keratinocytes and immune cells through pro-inflammatory cytokines leads to feedforward amplification of psoriasis inflammation. (Lowes et al., 2014)

Acitretin (ACT), as the active metabolic product of etretinate, has been developed as a first-line systemic drug for treating moderate-to-severe psoriasis. (Carretero et al., 2013; Nast et al., 2015; Chiricozzi et al., 2017) It could modulate the signaling pathways related to the signal

transducer and activator of transcription (STAT), thus suppressing the keratinocyte proliferation and downregulating the inflammatory cytokine expression). (Niu et al., 2012; An et al., 2017; Qin et al., 2017) Clinically, ACT could benefit patients with psoriasis at proper doses, which should not be lower than 25 mg/day. (Goldfarb et al., 1988; Gupta et al., 1989; Katz et al., 1999; Chularojanamontri et al., 2019) However, clinicians face a dilemma when setting the doses because both the therapeutic effects and side effects of ACT are dose-dependent; *i.e.*, lower doses result in less efficacy, while higher doses result in significant side effects. These side effects include mucocutaneous effects (e.g., dry skin, skin peeling, cheilitis, alopecia, or rhinitis), hyperlipidemia, hepatotoxicity, ophthalmologic effects, and teratogenicity. Thus, long-term administration of ACT is limited in the clinic. (Katz et al., 1999; Lee and Koo, 2005) A few endeavors have been targeted toward improving the therapeutic efficacy of ACT at lower doses. For example, the combination of low-dose ACT and methotrexate remitted psoriasis-like skin lesions more effectively than monotherapy. (An et al., 2017) However, combined therapies may increase the frequency of adverse effects, and the administration is complicated which could reduce patient compliance. Several studies have developed ACT-loaded nanogel through nanostructured lipid carriers (NLCs), star-shaped polymethacrylic conjugates, chitin-based systems, or niosome-based systems for topical ACT delivery. (Agrawal et al., 2010; Divya et al., 2016; Abu et al., 2018; Mielanczyk et al., 2020) Unfortunately, the development of topical delivery systems may not be the optimum of ACT modification considering the indication of ACT that involves systemic organs in severe psoriasis. (Heath et al., 2018) Therefore, there is an urgent demand for novel delivery systems of ACT with better therapeutic efficacy and safety.

Nanomaterials have attracted much interest for biomedical applications due to their chemical and size-dependent physical properties. (Chen et al., 2021; Dutta et al., 2021) Nanoparticle (NP)-based drug delivery systems could improve the therapeutic efficacy of various drugs due to multiple advantages, including better targeting capacity. (Mitchell et al., 2021) Among the NP-based drug carriers, polysaccharides are the most experimented materials due to their unique physicochemical properties. (Liu et al., 2008) As an FDA-approved homo polysaccharide of glucose, dextran (Dex) exhibits high biodegradability, excellent biocompatibility, wide availability, low cost and easy modifiability. Thus, Dex has been used as a drug delivery vehicle for a variety of drugs. (Almeida et al., 2013; Anirudhan and Binusreejayan, 2016; Raveendran et al., 2016)

In this work, we developed ACT-conjugated dextran NPs (ACT-Dex NPs) for the controlled delivery of ACT and systemic treatment of psoriasis. The NPs were prepared by ultrasonic emulsification, followed by solvent evaporation. We showed that ACT-Dex NPs could ameliorate psoriasis-like skin disease significantly at a low dosage which does not cause side effects, while neat ACT drugs at an equivalent dosage provided much less benefit. Moreover, we demonstrated that ACT-Dex NPs suppressed keratinocyte proliferation more efficiently than neat ACT drugs by enhancing the inhibitory effect on STAT3 phosphorylation.

2 MATERIAL AND METHODS

2.1 Materials

ACT was obtained from Meilunbio (Dalian, China). Poly (vinyl alcohol) (PVA, hydrolyzation rate 87%–89%, 13–23 kDa), dextran (10 kDa), 1-ethyl-3-(3-(dimethylamino)propyl)-carbodiimide hydrochloride (EDC·HCl), and 4-dimethylaminopyridine (DMAP) was purchased from Sigma-Aldrich (St. Louis, MO, USA.). ACT and dextran were esterified to obtain ACT-conjugated dextran (ACT-Dex). Briefly, ACT (0.5 g) and dextran (0.5 g) were dissolved in dimethylsulfoxide (DMSO, 20 ml), followed by adding an excess amount of EDC (0.73 g) and DMAP (0.26 g). After 48 h of reaction at room temperature, the resultant ACT-Dex was precipitated in water and purified with water 3 times. The final product was a bright yellow powder after lyophilization. 1H NMR spectra were obtained from an NMR spectrometer (Bruker AV400, Billerica, MA, U.S.A.). δ (DMSO-d6, ppm): 2.06 (s, 3H), 2.08 (s, 3H), 2.18 (s, 3H), 2.25 (s, 3H), 2.29 (s, 3H), 5.79 (s, 1H), 6.24–6.33 (m, 2H), 6.4 (d, 1H), 6.69 (s, 1H), 6.73 (d, 1H), 7.02–7.10 (dd, 1H), 3.05–4.70 (m). The ACT content in ACT-Dex was determined by a standard curve method using a UV–vis spectrometer (Shimadzu 1800, Tokyo, Japan).

2.2 Preparation of ACT-Dex NPs

ACT-Dex NPs were prepared as reported previously. (Li et al., 2021) Briefly, a solution of ACT-Dex (50 mg) in chloroform (5 ml) was mixed with 50 ml of an aqueous solution of PVA (3 mg/ml). Subsequently, the mixture was sonicated for 5 min to obtain a uniform emulsion using a probe sonicator (settings: 25% power; (10 s)-(5 s) on-off program). After thorough evaporation of chloroform, the ACT-Dex NPs were obtained by repetitive centrifuge and redispersion. The morphology, hydrodynamic diameter (D_h), and size distribution of ACT-Dex NPs were obtained using a Hitachi TM4000Plus transmission electron microscope (TEM, Tokyo, Japan, 100 kV) and a Malvern Nano-ZS90 zetasizer (Malvern, United Kingdom).

2.3 *In Vitro* Drug Release

The *in vitro* ACT release was determined by a dialysis method. A solution of ACT-Dex NPs in phosphate-buffered saline (PBS, 2 ml) was dialyzed against 18 ml of PBS containing 0.02% Tween 80 at 37°C. At each certain time point, 2 ml of solution were collected, and 2 ml of fresh PBS was supplied. The concentrations of released ACT were determined through UV-vis spectra.

2.4 Cell Culture

HaCaT cells (Human keratinocytes) were provided by China Center for Type Culture Collection and were cultured in

Dulbecco's modified Eagle medium (Gibco, Grand Island, NY, USA) supplied with 10% fetal bovine serum (Gibco) and penicillin/streptomycin (Gibco, 100 U/mL) under 100% humidity containing 5% CO_2 at 37°C.

2.5 Cell Uptake of ACT-Dex NPs

To test cellular uptake of NPs, flow cytometry and confocal laser scanning microscope (CLSM) were performed using phycoerythrin (PE)-labeled ACT-Dex NPs. HaCaT cells were treated with PE-labeled ACT-Dex NPs with different concentrations for various time courses. The cells were gently washed with PBS to remove free ACT-Dex NPs. The intracellular fluorescence intensity of different concentrations (for 4 h) and different hours (with 10 μg/ml) were acquired by flow cytometry (LSR II; BD Bioscience, San Jose, USA). CLSM was performed to confirm the intracellular delivery of ACT-Dex NPs. HaCaT cells were seeded and treated with PE-labeled ACT-Dex (10 μg/ml) for 2 and 4 h individually. The cells were washed with PBS, followed by fixed with 4% paraformaldehyde (PFA). The fixed cells were stained with 4′,6-diamidino-2-phenylindole (DAPI, Beyotime, China). Intracellular fluorescence intensity and localization were observed and analyzed using CLSM (Olympus FV500, Tokyo, Japan).

2.6 Cell Viability Assay

Cell viability was evaluated using a Cell Counting Kit-8 assay kit (CCK-8, Beyotime, China). Briefly, HaCaT cells were incubated in a 96-well plate overnight. Cells were then treated with PBS, Dextran, or different concentrations of ACT-Dex NPs for 24 h. Next, 10 μL of CCK-8 reagent was added to each well. The absorbance at 450 nm was measured using a microplate reader (TECAN Infinite F50, Switzerland) two tours later.

2.7 Measurement of STAT3 Expression *In Vitro*

Western blot analysis was performed to determine STAT3 expression *in vitro*. HaCaT cells were treated with PBS, Dextran (20 μg/ml), ACT (20 μg/ml)or ACT-Dex NPs (20 μg ACT equiv./mL) for 12 h. Subsequently, the cells were further stimulated using recombinant IL-22 (PeproTech; 50 ng/ml) for an additional 1 h, and the cell lysate was prepared. After electrophoresis, proteins were electroeluted onto a polyvinylidenedifluoride (PVDF) membrane (Invitrogen, Carlsbad, USA). Antibodies: anti-pSTAT3 (Tyr705) (Cell Signaling, Beverly, USA), STAT3 (Cell Signaling), and anti-actin (Abcam, Cambridge, United Kingdom). For the visualization of the immunoreactive proteins, an enhanced chemiluminescence assay kit and a chemiluminescence imaging system (ChemiScope 6200T, ClinX, Shanghai, China) were used.

2.8 *In Vivo* Effect Studies of ACT-Dex NPs

2.8.1 IMQ-Induced Psoriasis-like Murine Model and *In Vivo* Treatment

Wild-type Balb/c female mice (6–8 weeks) were provided by the Institute of Laboratory Animal Science (Beijing, China). The animal experiments were approved by the Animal Experimentation Ethics Committee of HUST and performed according to the protocols from the Hubei Provincial Animal Care and Use Committee. Mice received daily topical treatment of IMQ (62.5 mg of commercially available IMQ cream) on their back skin for 6 consecutive days to fabricate the psoriasis model. 2 hours after IMQ cream application, mice were treated with an intraperitoneal injection of Dex (20 μg), ACT (20 μg), ACT-Dex NPs (20 μg ACT equiv.), or PBS for 6 consecutive days.

2.8.2 Psoriasis-like Lesion Evaluation

Disease severity was assessed with a clinical scoring system based on the Psoriasis Area and Severity Index (PASI) scores as previously reported.(van der Fits et al., 2009) The severity of inflammation was reflected by the cumulative score of scaling, erythema, and thickness (0–4). The back skinfold thickness was measured daily in triplicate using a vernier caliper before treatment. Data were presented as the percentage change from baseline.

2.8.3 Histological and Immunohistochemical Analysis

The full-thickness skin samples on the region of interest were obtained, fixed with 4% PFA, and embedded with paraffin on day 7th once the mice were sacrificed. Then, the sections (thickness: 5 μm) of these tissues were stained with hematoxylin and eosin (H&E) and observed and photographed under a microscope. Epidermal thickness was measured using ImageJ software (National Institutes of Health, USA). Immunohistochemical studies were performed to detect the expression of Ki67 and pSTAT3 proteins on skin sections. Briefly, the sections were prepared by dewaxing and hydration, antigen retrieval, blocking, incubation with anti-ki67 antibody (1:1000; Abcam) or anti-pSTAT3 (Tyr705) antibody (1:1000; Abcam) and HRP-coupled secondary antibody (1:1000; Proteintech; China), diaminobenzidine (DAB) development, and H&E staining, respectively. Finally, the slides were observed and photographed under a microscope. Protein expression was quantified using Image J software.

2.8.4 Body Weight and Spleen Weight

Body weights of the mice were recorded on day 1st and day 7th when they were sacrificed. Their spleens were then removed and weighed. Spleen index was calculated by the weight ratio between spleen and body.

2.8.5 Hematological and Organ Toxicity Studies

Blood samples of all groups were obtained on day 7th before being sacrificed. Afterward, blood cell counts, aspartate aminotransferase (AST), serum levels of alanine aminotransferase (ALT), creatinine (CREA), and blood urea nitrogen (BUN) were measured following standard protocol. Major organs including livers, lungs, kidneys, and hearts were also harvested and fixed. H&E staining was performed as described above. Nikon Ni-E (Nikon, Tokyo, Japan) was used to image the H&E sections.

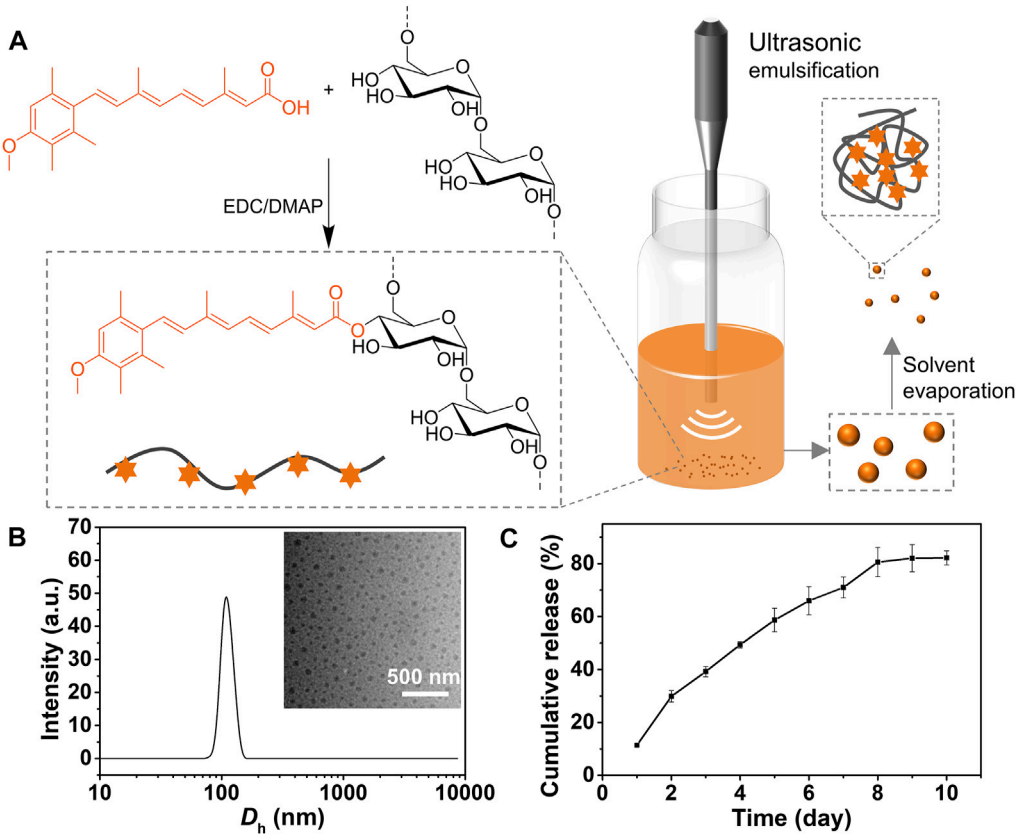

FIGURE 1 | Synthesis, characterization of ACT-Dex NPs. **(A)** Schematic illustration of the synthesis of ACT-Dex conjugate and preparation of ACT-Dex NPs. **(B)** Hydrodynamic diameter (D_h) and representative TEM image (inset) of ACT-Dex NPs. **(C)** *In vitro* ACT release from the NPs. Data were presented as mean ± standard deviation of three independent experiments.

2.9 Statistical Analysis

Data were shown as means ± standard deviation unless otherwise noted. The statistical significance between different groups was analyzed by unpaired Student's *t*-test and one-way ANOVA. Statistical significance was confirmed when $p < 0.05$.

3 RESULTS AND DISCUSSION

3.1 Preparation and Characterization of ACT-Dex NPs

The ACT-Dex conjugate was synthesized by an EDC/DMAP-catalyzed esterification between ACT and dextran (**Figure 1A**). 1H NMR was performed to confirm the structure of the resultant ACT-Dex (**Supplementary Figure S1**). All characteristic peaks were well assigned, indicating the successful conjugation of ACT to dextran. It was quite challenging to quantify the amount of ACT in this conjugate by NMR integrations because the ACT-Dex conjugate formed self-assembled structures even in organic solvents. The reason can be ascribed to the formation of hydrogen bonds and the unfavorable solubility of both dextran and ACT moieties in organic solvents after esterification. Since the UV-vis absorption of ACT at 360 nm displayed a linear relationship with the concentration (**Supplementary Figure S1**), UV-vis spectroscopy was employed to confirm and quantify the amount of ACT in ACT-Dex. The ACT content in ACT-Dex was calculated to be 52.9%, indicating that 1.79 repeat units of dextran on average were conjugated with one molecule of ACT.

The ACT-Dex NPs were prepared as we reported previously (**Figure 1A**). (Li et al., 2021) The aqueous solution of ACT-Dex NPs showed a clear and yellow color appearance. The morphology and size distribution of ACT-Dex NPs were determined by TEM and dynamic laser scattering (DLS) (**Figure 1B**). Clearly, the ACT-Dex NPs displayed an average hydrodynamic diameter (D_h) of ~ 100 nm with narrow size distribution. The NPs showed round-shape, well-dispersed, and no aggregation in the TEM image, indicating the good stability of the NPs.

Since the drug release behavior is usually related to the pharmacokinetics of a drug, we evaluated the drug release of ACT from ACT-Dex NPs **(Figure 1C)**. Due to the slow hydrolysis of ester bonds, ACT was continuously released

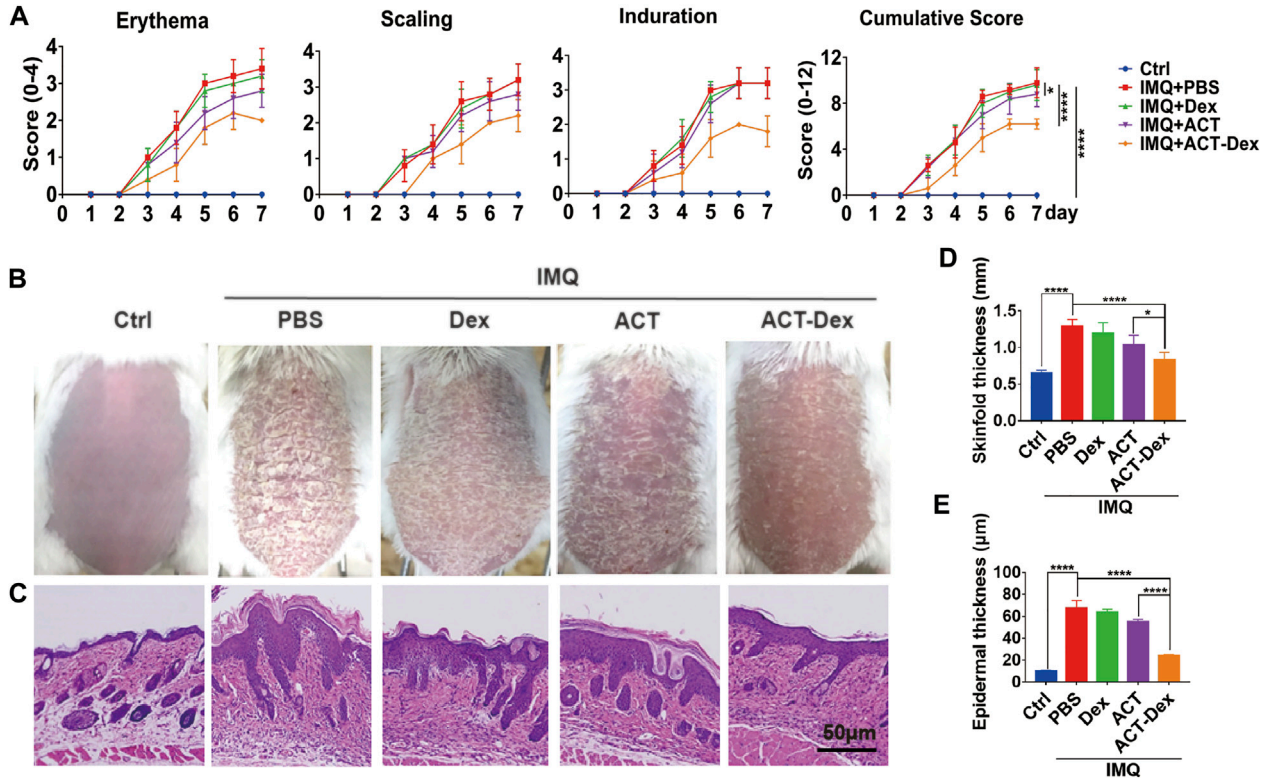

FIGURE 2 | Therapeutic effects of different treatments. **(A)** Psoriasis area and severity index (PASI) scores of skin lesions in IMQ-induced psoriatic mice following different treatments. **(B)** Representative photographs and **(C)** H&E staining of the back skin derived from mice in different groups on day 7th. **(D)** Skinfold thickness and **(E)** epidermal thickness of the back skin derived from mice in different groups. Data were presented as mean ± standard deviation of three independent experiments. (*$p < 0.05$, ****$p < 0.0001$, two-tailed Student's *t*-tests). The scale bar in the bottom right figure of **(C)** applies to the others.

from the ACT-Dex NPs within 8 days and reached a platform thereafter, with a terminal cumulative release ratio of ~ 80%. This sustained-release behavior may benefit the patients by reducing the administration frequency.

3.2 Superior Amelioration of Psoriasis-Like Skin Disease by ACT-Dex NPs

We next investigated whether ACT-Dex NPs could exhibit better therapeutic effects on psoriasis-like skin disease than neat ACT drugs *in vivo*. Generally, the therapeutic effect of ACT is dose-dependent and significantly reduced at a lower dosage. A previous study showed that the psoriasis-like murine skin lesions were improved when intragastrically administrated ACT at a dosage of 168 mg/day, which is obviously a high dosage. (Pang et al., 2018) An *et al.* injected intraperitoneally a combination of low-dose ACT and methotrexate, which is at 20 μg/day, into a psoriatic murine model. (An et al., 2017) Therefore, we administrated neat ACT drugs at 20 μg/day and ACT-Dex NPs at 20 μg ACT equiv./day and compared the therapeutic efficacy of them at an equivalent low dosage. Disease severity was evaluated daily using PASI scores. We found the ACT-Dex NPs group showed a significant impact on alleviating the severity of clinical symptoms on day 3rd, including erythema, scaling, and induration, while neat ACT drugs showed a weak therapeutic effect from day 5th (**Figure 2A**). Consistent with PASI scores, the lesions of mice in the Dex group were similar to the PBS group. In contrast, conditions were slightly improved in the ACT group and significantly improved in the ACT-Dex NPs group (**Figure 2B**). The thickness of IMQ-treated skin increased to 1.296 ± 0.04 mm, while it was repressed to 1.038 ± 0.06 mm by ACT and 0.834 ± 0.04 mm by ACT-Dex NPs. The difference between the ACT group and ACT-Dex NPs group was significant ($p < 0.05$) (**Figure 2C**). Furthermore, the histological analyses of the back-skin lesions were performed by H&E staining. Compared to other treatment groups, treatment with ACT-Dex NPs resulted in decreased epidermal thickness and inflammatory cell infiltration, indicating the superior therapeutic effects of ACT-Dex NPs (**Figure 2D**). The epidermal layer of IMQ-treated skin was thickened to 67.55 ± 3.46 μm, while the epidermal thickness of ACT and ACT-Dex NPs groups were only 55.2 ± 0.93 μm and 24.21 ± 0.53 μm ($p < 0.0001$), respectively (**Figure 2E**).

Generally, the keratinocytes are excessively proliferated in psoriatic skin lesions, and the inflammatory cascade in lesions

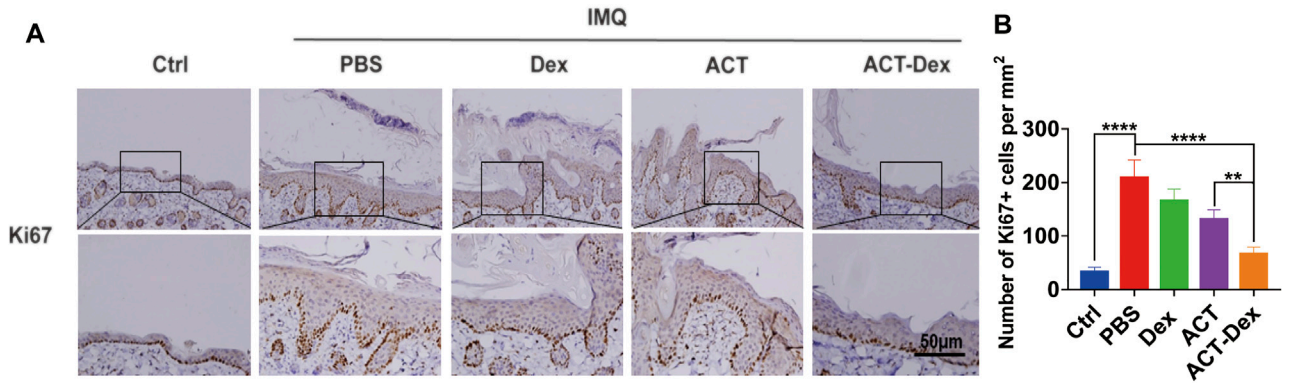

FIGURE 3 | *In vivo* Ki67 expression in different treatments.**(A)** Representative Ki67 IHC staining images of the skin sections in theIMQ-induced psoriatic mice following different treatments. **(B)** The number of Ki67 + cells per square millimeter. (**$p < 0.01$, ****$p < 0.0001$, two-tailed Student's t-tests). The scale bar in the bottom right figure of **(A)** applies to the others.

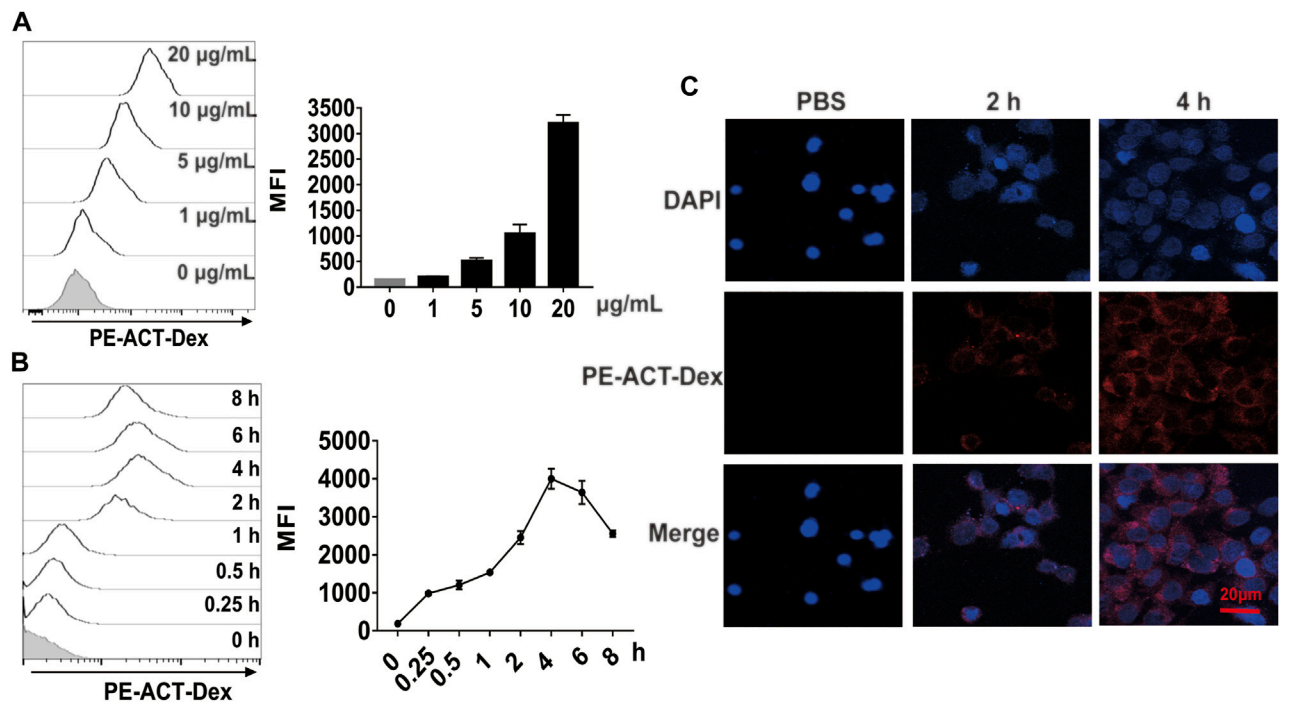

FIGURE 4 | Uptake performance of ACT-Dex NPs by keratinocytes. **(A,B)** Representative flow cytometry histograms and mean fluorescence intensity (MFI) of intracellular uptake of PE-labeled ACT-Dex NPs into HaCaT cells. HaCaT cells were incubated with the indicated concentrations of PE-labeled ACT-Dex NPs for 4 h or with 10 μg/mL PE-labeled ACT-Dex NPs for the indicated times. **(C)** CLSM images of HaCaT cells internalized PE-labeled ACT-Dex NPs for various time.

is critically dependent on keratinocytes. (Garzorz-Stark and Eyerich, 2019; Moos et al., 2019) We thus analyzed the expression of Ki67, a marker of the proliferation of keratinocytes, in the epidermis by Ki67 IHC staining. (Ramezani et al., 2019) We found a remarkable Ki67 upregulation in the PBS and Dex groups, whereas it was slightly inhibited in the ACT group and profoundly inhibited by the ACT-Dex NPs (**Figures 3A,B**, **Supplementary Figure S2A**). These findings suggested that ACT-Dex NPs were more efficient in ameliorating psoriasis-like murine skin disease than neat ACT drugs at an equivalent low dosage.

3.3 Efficient Uptake of ACT-Dex NPs by Keratinocytes

The efficacy of ACT on the proliferation of keratinocytes is contingent on the internalization level of ACT by the target cells. (Pang et al., 2008; Ormerod et al., 2010) Therefore, we

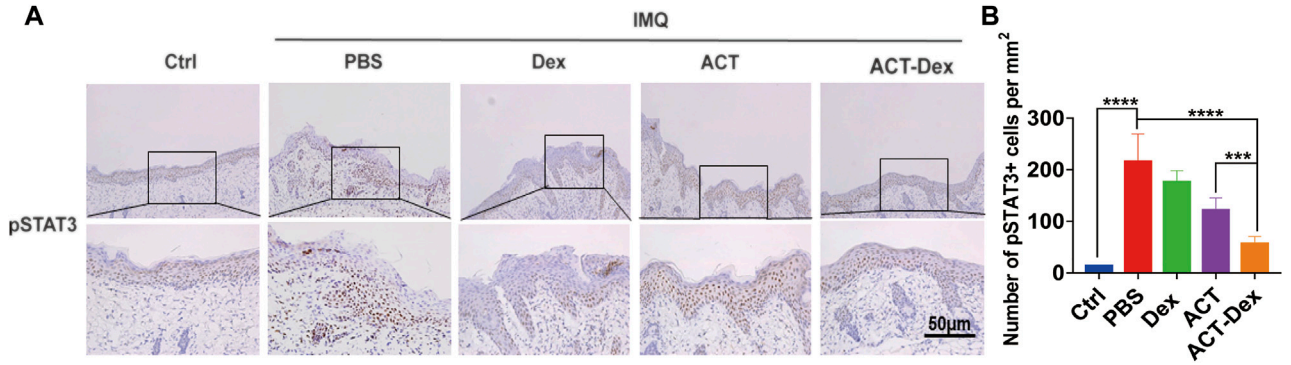

FIGURE 5 | *In vivo* pSTAT3 expression in different treatments. **(A)** Representative pSTAT3 IHC staining images of the skin sections in the imiquimod-induced psoriatic mouse model from different groups. **(B)** The number of pSTAT3+ cells per square millimeter. pSTAT3, phosphorylated STAT3. (***$p < 0.001$, ****$p < 0.0001$, two-tailed Student's t-tests). The scale bar in the bottom right figure of **(A)** applies to the others.

investigated the cellular uptake level of PE-labeled ACT-Dex NPs in HaCaT cells. HaCaT cells were incubated with different dosages of PE-labeled ACT-Dex NPs for various durations, and flow cytometry was used to analyze the intracellular fluorescence intensity. We found that there was a gradual increase in the intensity of intracellular fluorescence with the increased concentration of ACT-Dex NPs (**Figure 4A**) and reached the maximum at 4 h (**Figure 4B**). CLSM also indicated similar results (**Figure 4C**). These findings suggested that ACT-Dex NPs could be internalized into keratinocytes efficiently.

3.4 Better Suppression Effects of ACT-Dex NPs on Psoriatic Keratinocyte Proliferation by Enhanced Inhibition of STAT3 Phosphorylation

ACT could ameliorate psoriasis *via* suppressing keratinocyte proliferation, while the molecular mechanism of it remains unclear. Previous studies indicated that ACT could bind with intracellular retinoic acid-binding protein (CRABP) to translocate to nucleus, then formed RAR and RXR heterodimer complexes which could regulate the expression of over 500 genes after binding to the gene promoter region. (Balmer and Blomhoff, 2002; Larange and Cheroutre, 2016)

STAT3, a member of the STAT family, is vital for cell survival, proliferation, differentiation, and immune responses. (Levy and Darnell, 2002; Yu et al., 2007; Miklossy et al., 2013) Previous studies showed that the constitutive activation of STAT3 was observed in the epidermis of psoriatic skin lesions. (Sano et al., 2005) Also, the activation of STAT3 in keratinocytes in a murine model could develop a skin phenotype closely resembling psoriasis. (Miyoshi et al., 2011; Calautti et al., 2018) These results indicated that activated STAT3 in keratinocytes played a critical role in psoriasis development. Accordingly, we explored the influence of ACT-Dex NPs on STAT3 in comparison with neat ACT.

We first analyzed the skin lesions of psoriasis-like murine models treated by different drugs by phosphorylated STAT3 (pSTAT3) IHC staining. As expected, the expressions of pSTAT3 in the epidermis were strongly enhanced in PBS and Dex groups, while it was slightly inhibited in the ACT group and significantly inhibited in the ACT-Dex NPs group (**Figures 5A,B**, **Supplementary Figure S2B**).

We next conducted *in vitro* experiments to explore the influence of ACT-Dex NPs on the proliferation of STAT3-activated keratinocytes and compare it to neat ACT drugs. Considering IL-22 plays an important role in the pathogenesis of psoriasis and is a major activator of STAT3 signaling. We thus stimulated HaCaT cells with IL-22 to simulate the abnormal keratinocytes in psoriasis, followed by treating with ACT-Dex NPs. (Sestito et al., 2011; Johnston and Gudjonsson, 2014; Nikamo et al., 2014; Tohyama et al., 2018) Cell proliferation detected by CCK8 assay showed that ACT-Dex NPs caused a dose-dependent inhibition of proliferation in IL-22-stimulated HaCaT cells (**Figure 6A**). We next compared the suppressing effects on HaCaT cells by ACT-Dex NPs and neat ACT drugs. IL-22-stimulated HaCaT cells were treated with PBS, Dex (20 μg/ml), ACT (20 μg/ml) and ACT-Dex NPs (20 μg ACT equiv./mL). Surprisingly, we found that ACT-Dex NPs inhibited the proliferation of IL-22-stimulated HaCaT cells by 58.22%, and the inhibitory effect was significantly stronger than that of neat ACT drugs (38.23%) (**Figure 6B**). Correspondingly, ACT-Dex NPs treatment caused a dose-dependent inhibition of STAT3 phosphorylation in IL-22-stimulated HaCaT cells, as shown by western blot analysis (**Figure 6C**). And activating phosphorylation of STAT3 was blocked by ACT-Dex NPs more significantly than neat ACT drugs (**Figure 6D**). Therefore, these results suggested

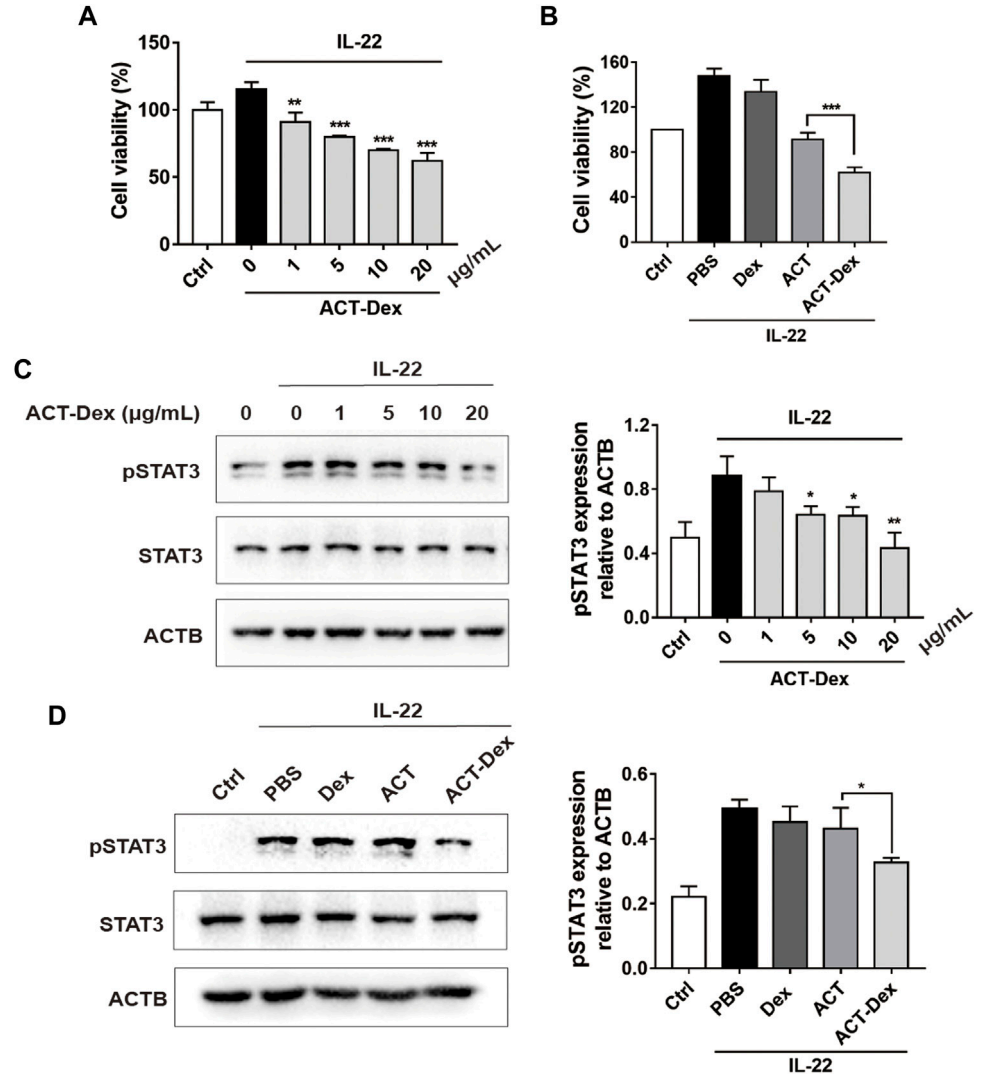

FIGURE 6 | Inhibitory effects of ACT-Dex NPs on keratinocytes. **(A)** Viability of IL-22-stimulated HaCaT cells by treating with ACT-Dex NPs at the indicated concentrations and **(B)** by treating with PBS, Dex, ACT, or ACT-Dex NPs. **(C,D)** Western blot images and densitometric measurements of the expression level of pSTAT3 in IL-22-stimulated HaCaT cells by treating with ACT-Dex NPs (20 μg/ml) at the indicated concentrations and by treating with PBS, Dex (20 μg/ml), ACT (20 μg/ml), or ACT-Dex NPs (20 μg ACT equiv./mL) for 12 h pSTAT3, phosphorylated STAT3. Data are means ± standard deviation of three independent experiments. (**$p < 0.01$, and ***$p < 0.001$, two-tailed Student's *t*-tests).

that ACT-Dex NPs ameliorate psoriasis-like skin disease more efficiently than neat ACT by an enhanced inhibitory effect on STAT3 phosphorylation of psoriatic keratinocytes.

3.5 Systemic Impacts and Safety of ACT-Dex NPs

The systemic impacts and safety of ACT-Dex NPs were evaluated. At the end of 7-days treatments, the body weights of any IMQ-treated groups remained above 90% of original values and no significant difference among these groups was observed (**Supplementary Figure S3A**). The increase in the spleen/body weight ratio could be caused by the increase of cell population in the spleen. (Cesta, 2006) As expected, the spleen/body weight ratio significantly increased in IMQ treated mice, but there was no significant decrease in other treatment groups. This indicated that the influence of low-dose ACT on the systemic immune system was not obvious (**Supplementary Figures S3B,C**).

The counts of white blood cells (WBC), neutrophils, monocytes, and lymphocytes were evaluated. No significant differences between all groups were observed, suggesting that the administration of 20.0 μg ACT or ACT-Dex NPs did not affect the hematopoietic system of the psoriatic mice (**Figure 7A**). Besides, negligible chage in the serum levels of ALT, AST, CREA, and BUN in all groups was observed, indicating that no acute liver or renal toxicities were

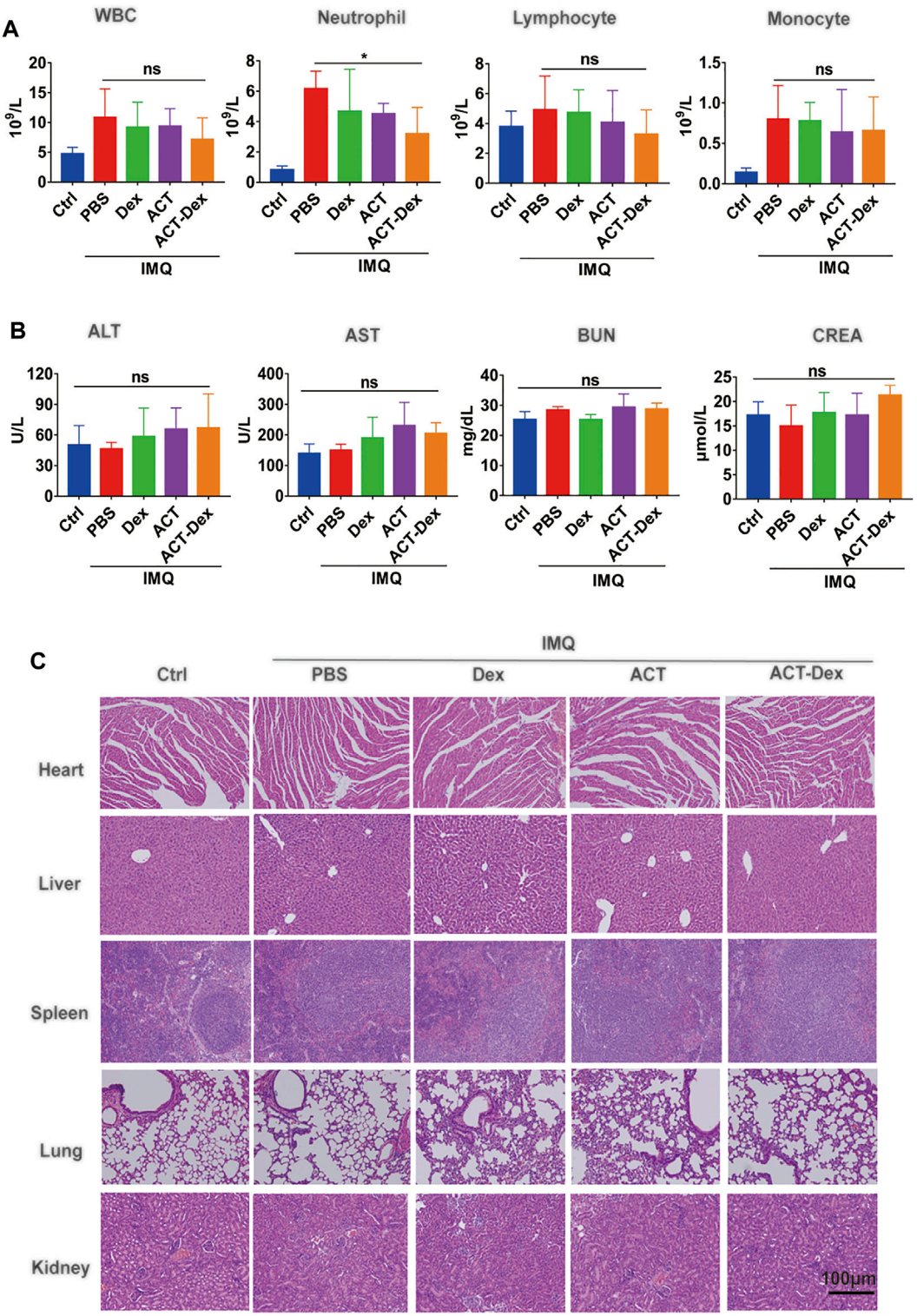

FIGURE 7 | Biocompatibility of ACT-Dex NPs in mice. **(A)** Blood cell counts and **(B)** blood biochemistry of mice in different groups at day 7th. **(C)** Representative images of H&E staining of the heart, lung, liver, spleen and kidney derived from mice in different groups at day 7th. The scale bar in the last image of **(C)** applies to the others. (ns: not significance; $^{*}p < 0.05$; two-tailed Student's *t*-tests.

induced at the dosage of this study (**Figure 7B**). As the H&E staining of major organs, no detectable tissue damage was observed in all groups (**Figure 7C**), suggesting that the administration of 20.0 μg ACT or ACT-Dex NPs did not cause histopathological abnormities. The above results indicate the superior biocompatibility and safety of ACT-Dex NPs for *in vivo* psoriasis treatment.

4 CONCLUSION

In summary, ACT-Dex NPs were developed and proved to ameliorate psoriasis more effectively than neat ACT drugs at an equivalent low dosage. The low-dose (1 mg/kg/day) administration did not cause any adverse systemic events. Moreover, we demonstrated that ACT-Dex NPs inhibited keratinocyte proliferation more efficiently than neat ACT drugs by enhancing the inhibitory effect on STAT3 phosphorylation. This study indicated that ACT-Dex NPs could be a new candidate for psoriasis with higher efficacy and safety.

DATA AVAILABILITY STATEMENT

The original contributions presented in the study are included in the article/**Supplementary Material**, further inquiries can be directed to the corresponding authors.

ETHICS STATEMENT

The animal study was reviewed and approved by the Animal Experimentation Ethics Committee of Huazhong University of Science and Technology.

AUTHOR CONTRIBUTIONS

Conception and design: YL, JZ, JL, and YLi; Methodology: JL, YLi, JW, and YC; Data analysis: JL, YLi, JW,and YC; Writing: JL and YLi; Administrative, technical, or material support: JT, JY, LZ, YX, and HD; Final approval of manuscript: JT, YLi, JZ, and YL.

FUNDING

This work was supported by the National Natural Science Foundation of China (82130089, 82103730, 82071844, and 51703074), and the Innovation Capacity Construction Program for Hubei Engineering Research Center of Skin Disease Theranostics and Health (2020-420103-84-03-072248).

SUPPLEMENTARY MATERIAL

The Supplementary Material for this article can be found online at: https://www.frontiersin.org/articles/10.3389/fbioe.2021.816757/full#supplementary-material

REFERENCES

Abu, I. H., II, Abo El-Magd, N., El-Sheakh, A., Hamed, M., and Abd El-Gawad, A. E-G. (2018). Pivotal Role of Acitretin Nanovesicular Gel for Effective Treatment of Psoriasis: Ex Vivo–In Vivo Evaluation Study. *Int. J. Nanomedicine* 13, 1059–1079. doi:10.2147/IJN.S156412

Agrawal, Y., Petkar, K. C., and Sawant, K. K. (2010). Development, Evaluation and Clinical Studies of Acitretin Loaded Nanostructured Lipid Carriers for Topical Treatment of Psoriasis. *Int. J. Pharmaceutics* 401 (1-2), 93–102. doi:10.1016/j.ijpharm.2010.09.007

Almeida, J. F., Ferreira, P., Alves, P., Lopes, A., and Gil, M. H. (2013). Synthesis of a Dextran Based Thermo-Sensitive Drug Delivery System by Gamma Irradiation. *Int. J. Biol. Macromolecules* 61, 150–155. doi:10.1016/j.ijbiomac.2013.07.002

An, J., Zhang, D., Wu, J., Li, J., Teng, X., Gao, X., et al. (2017). The Acitretin and Methotrexate Combination Therapy for Psoriasis Vulgaris Achieves Higher Effectiveness and Less Liver Fibrosis. *Pharmacol. Res.* 121, 158–168. doi:10.1016/j.phrs.2017.04.014

Anirudhan, T. S., and Binusreejayan (2016). Dextran Based Nanosized Carrier for the Controlled and Targeted Delivery of Curcumin to Liver Cancer Cells. *Int. J. Biol. Macromolecules* 88, 222–235. doi:10.1016/j.ijbiomac.2016.03.040

Balmer, J. E., and Blomhoff, R. (2002). Gene Expression Regulation by Retinoic Acid. *J. Lipid Res.* 43 (11), 1773–1808. doi:10.1194/jlr.r100015-jlr200

Boehncke, W.-H., and Schön, M. P. (2015). Psoriasis. *The Lancet* 386 (9997), 983–994. doi:10.1016/s0140-6736(14)61909-7

Calautti, E., Avalle, L., and Poli, V. (2018). Psoriasis: A STAT3-Centric View. *Int. J. Mol. Sci.* 19 (1), 171. doi:10.3390/ijms19010171

Carretero, G., Ribera, M., Belinchón, I., Carrascosa, J. M., Puig, L., Ferrandiz, C., et al. (2013). Guidelines for the Use of Acitretin in Psoriasis. *Actas Dermo-Sifiliográficas (English Edition)* 104 (7), 598–616. doi:10.1016/j.adengl.2013.01.001

Cesta, M. F. (2006). Normal Structure, Function, and Histology of the Spleen. *Toxicol. Pathol.* 34 (5), 455–465. doi:10.1080/01926230600867743

Chen, J., Zhang, X., Millican, R., Sherwood, J., Martin, S., Jo, H., et al. (2021). Recent Advances in Nanomaterials for Therapy and Diagnosis for Atherosclerosis. *Adv. Drug Deliv. Rev.* 170, 142–199. doi:10.1016/j.addr.2021.01.005

Chiricozzi, A., Panduri, S., Dini, V., Tonini, A., Gualtieri, B., and Romanelli, M. (2017). Optimizing Acitretin Use in Patients with Plaque Psoriasis. *Dermatol. Ther.* 30 (2), e12453. doi:10.1111/dth.12453

Chularojanamontri, L., Silpa-archa, N., Wongpraparut, C., and Limphoka, P. (2019). Long-term Safety and Drug Survival of Acitretin in Psoriasis: a Retrospective Observational Study. *Int. J. Dermatol.* 58 (5), 593–599. doi:10.1111/ijd.14349

Divya, G., Panonnummal, R., Gupta, S., Jayakumar, R., and Sabitha, M. (2016). Acitretin and Aloe-Emodin Loaded Chitin Nanogel for the Treatment of Psoriasis. *Eur. J. Pharmaceutics Biopharmaceutics* 107, 97–109. doi:10.1016/j.ejpb.2016.06.019

Dutta, B., Barick, K. C., and Hassan, P. A. (2021). Recent Advances in Active Targeting of Nanomaterials for Anticancer Drug Delivery. *Adv. Colloid Interf. Sci.* 296, 102509. doi:10.1016/j.cis.2021.102509

Garzorz-Stark, N., and Eyerich, K. (2019). Psoriasis Pathogenesis: Keratinocytes Are Back in the Spotlight. *J. Invest. Dermatol.* 139 (5), 995–996. doi:10.1016/j.jid.2019.01.026

Goldfarb, M. T., Ellis, C. N., Gupta, A. K., Tincoff, T., Hamilton, T. A., and Voorhees, J. J. (1988). Acitretin Improves Psoriasis in a Dose-dependent Fashion. *J. Am. Acad. Dermatol.* 18 (4), 655–662. doi:10.1016/s0190-9622(88)70086-9

Gupta, A. K., Goldfarb, M. T., Ellis, C. N., and Voorhees, J. J. (1989). Side-effect Profile of Acitretin Therapy in Psoriasis. *J. Am. Acad. Dermatol.* 20 (6), 1088–1093. doi:10.1016/s0190-9622(89)70138-9

Heath, M. S., Sahni, D. R., Curry, Z. A., and Feldman, S. R. (2018). Pharmacokinetics of Tazarotene and Acitretin in Psoriasis. *Expert Opin. Drug Metab. Toxicol.* 14 (9), 919–927. doi:10.1080/17425255.2018.1515198

Johnston, A., and Gudjonsson, J. E. (2014). 22 Again: IL-22 as a Risk Gene and Important Mediator in Psoriasis. *J. Invest. Dermatol.* 134 (6), 1501–1503. doi:10.1038/jid.2014.81

Katz, H. I., Waalen, J., and Leach, E. E. (1999). Acitretin in Psoriasis: An Overview of Adverse Effects. *J. Am. Acad. Dermatol.* 41, S7–S12. doi:10.1016/s0190-9622(99)70359-2

Larange, A., and Cheroutre, H. (2016). Retinoic Acid and Retinoic Acid Receptors as Pleiotropic Modulators of the Immune System. *Annu. Rev. Immunol.* 34, 369–394. doi:10.1146/annurev-immunol-041015-055427

Lee, C. S., and Koo, J. (2005). A Review of Acitretin, a Systemic Retinoid for the Treatment of Psoriasis. *Expert Opin. Pharmacother.* 6 (10), 1725–1734. doi:10.1517/14656566.6.10.1725

Levy, D. E., and Darnell, J. E., Jr. (2002). Stats: Transcriptional Control and Biological Impact. *Nat. Rev. Mol. Cel Biol* 3 (9), 651–662. doi:10.1038/nrm909

Li, Y., Lou, Y., Chen, Y., Yang, J., Li, D., Jiang, B., et al. (2021). Polysaccharide Mycophenolate-Based Nanoparticles for Enhanced Immunosuppression and Treatment of Immune-Mediated Inflammatory Diseases. *Theranostics* 11 (8), 3694–3709. doi:10.7150/thno.52891

Liu, Z., Jiao, Y., Wang, Y., Zhou, C., and Zhang, Z. (2008). Polysaccharides-based Nanoparticles as Drug Delivery Systems. *Adv. Drug Deliv. Rev.* 60 (15), 1650–1662. doi:10.1016/j.addr.2008.09.001

Lowes, M. A., Suárez-Fariñas, M., and Krueger, J. G. (2014). Immunology of Psoriasis. *Annu. Rev. Immunol.* 32, 227–255. doi:10.1146/annurev-immunol-032713-120225

Michalek, I. M., Loring, B., and John, S. M. (2017). A Systematic Review of Worldwide Epidemiology of Psoriasis. *J. Eur. Acad. Dermatol. Venereol.* 31 (2), 205–212. doi:10.1111/jdv.13854

Mielanczyk, A., Mrowiec, K., Kupczak, M., Mielanczyk, Ł., Scieglinska, D., Gogler-Piglowska, A., et al. (2020). Synthesis and *In Vitro* Cytotoxicity Evaluation of star-shaped Polymethacrylic Conjugates with Methotrexate or Acitretin as Potential Antipsoriatic Prodrugs. *Eur. J. Pharmacol.* 866, 172804. doi:10.1016/j.ejphar.2019.172804

Miklossy, G., Hilliard, T. S., and Turkson, J. (2013). Therapeutic Modulators of STAT Signalling for Human Diseases. *Nat. Rev. Drug Discov.* 12 (8), 611–629. doi:10.1038/nrd4088

Mitchell, M. J., Billingsley, M. M., Haley, R. M., Wechsler, M. E., Peppas, N. A., and Langer, R. (2021). Engineering Precision Nanoparticles for Drug Delivery. *Nat. Rev. Drug Discov.* 20 (2), 101–124. doi:10.1038/s41573-020-0090-8

Miyoshi, K., Takaishi, M., Nakajima, K., Ikeda, M., Kanda, T., Tarutani, M., et al. (2011). Stat3 as a Therapeutic Target for the Treatment of Psoriasis: a Clinical Feasibility Study with STA-21, a Stat3 Inhibitor. *J. Invest. Dermatol.* 131 (1), 108–117. doi:10.1038/jid.2010.255

Moos, S., Mohebiany, A. N., Waisman, A., and Kurschus, F. C. (2019). Imiquimod-Induced Psoriasis in Mice Depends on the IL-17 Signaling of Keratinocytes. *J. Invest. Dermatol.* 139 (5), 1110–1117. doi:10.1016/j.jid.2019.01.006

Nast, A., Gisondi, P., Ormerod, A. D., Saiag, P., Smith, C., Spuls, P. I., et al. (2015). European S3-Guidelines on the Systemic Treatment of Psoriasis Vulgaris - Update 2015 - Short Version - EDF in Cooperation with EADV and IPC. *J. Eur. Acad. Dermatol. Venereol.* 29 (12), 2277–2294. doi:10.1111/jdv.13354

Nikamo, P., Cheuk, S., Lysell, J., Enerbäck, C., Bergh, K., Xu Landén, N., et al. (2014). Genetic Variants of the IL22 Promoter Associate to Onset of Psoriasis before Puberty and Increased IL-22 Production in T Cells. *J. Invest. Dermatol.* 134 (6), 1535–1541. doi:10.1038/jid.2014.5

Niu, X., Cao, W., Ma, H., Feng, J., Li, X., and Zhang, X. (2012). Acitretin Exerted a Greater Influence on T-Helper (Th)1 and Th17 Than on Th2 Cells in Treatment of Psoriasis Vulgaris. *J. Dermatol.* 39 (11), 916–921. doi:10.1111/j.1346-8138.2012.01637.x

Ormerod, A. D., Campalani, E., Goodfield, M. J. D., and Unit, B. A. D. C. S. (2010). British Association of Dermatologists Guidelines on the Efficacy and Use of Acitretin in Dermatology. *Br. J. Dermatol.* 162 (5), 952–963. doi:10.1111/j.1365-2133.2010.09755.x

Pang, M.-L., Murase, J. E., and Koo, J. (2008). An Updated Review of Acitretin - a Systemic Retinoid for the Treatment of Psoriasis. *Expert Opin. Drug Metab. Toxicol.* 4 (7), 953–964. doi:10.1517/17425255.4.7.953

Pang, X., Zhang, K., Huang, J., Wang, H., Gao, L., Wang, T., et al. (2018). Decryption of Active Constituents and Action Mechanism of the Traditional Uighur Prescription (BXXTR) Alleviating IMQ-Induced Psoriasis-Like Skin Inflammation in BALB/c Mice. *Int. J. Mol. Sci.* 19 (7), 1822. doi:10.3390/ijms19071822

Parisi, R., Symmons, D. P. M., Griffiths, C. E. M., and Ashcroft, D. M. (2013). Global Epidemiology of Psoriasis: a Systematic Review of Incidence and Prevalence. *J. Invest. Dermatol.* 133 (2), 377–385. doi:10.1038/jid.2012.339

Qin, X., Chen, C., Zhang, Y., Zhang, L., Mei, Y., Long, X., et al. (2017). Acitretin Modulates HaCaT Cells Proliferation through STAT1- and STAT3-dependent Signaling. *Saudi Pharm. J.* 25 (4), 620–624. doi:10.1016/j.jsps.2017.04.034

Ramezani, M., Shamshiri, A., Zavattaro, E., Khazaei, S., Rezaei, M., Mahmoodi, R., et al. (2019). Immunohistochemical Expression of P53, Ki-67, and CD34 in Psoriasis and Psoriasiform Dermatitis. *BioMedicine* 9 (4), 26. doi:10.1051/bmdcn/2019090426

Raveendran, R., Bhuvaneshwar, G. S., and Sharma, C. P. (2016). Hemocompatible Curcumin-Dextran Micelles as pH Sensitive Pro-drugs for Enhanced Therapeutic Efficacy in Cancer Cells. *Carbohydr. Polym.* 137, 497–507. doi:10.1016/j.carbpol.2015.11.017

Sano, S., Chan, K. S., Carbajal, S., Clifford, J., Peavey, M., Kiguchi, K., et al. (2005). Stat3 Links Activated Keratinocytes and Immunocytes Required for Development of Psoriasis in a Novel Transgenic Mouse Model. *Nat. Med.* 11 (1), 43–49. doi:10.1038/nm1162

Sestito, R., Madonna, S., Scarponi, C., Cianfarani, F., Failla, C. M., Cavani, A., et al. (2011). STAT3-dependent Effects of IL-22 in Human Keratinocytes Are Counterregulated by Sirtuin 1 through a Direct Inhibition of STAT3 Acetylation. *FASEB j.* 25 (3), 916–927. doi:10.1096/fj.10-172288

Tohyama, M., Shirakata, Y., Hanakawa, Y., Dai, X., Shiraishi, K., Murakami, M., et al. (2018). Bcl-3 Induced by IL-22 via STAT3 Activation Acts as a Potentiator of Psoriasis-Related Gene Expression in Epidermal Keratinocytes. *Eur. J. Immunol.* 48 (1), 168–179. doi:10.1002/eji.201747017

Van der Fits, L., Mourits, S., Voerman, J. S. A., Kant, M., Boon, L., Laman, J. D., et al. (2009). Imiquimod-induced Psoriasis-like Skin Inflammation in Mice Is Mediated via the IL-23/IL-17 axis. *J. Immunol.* 182 (9), 5836–5845. doi:10.4049/jimmunol.0802999

Yu, H., Kortylewski, M., and Pardoll, D. (2007). Crosstalk between Cancer and Immune Cells: Role of STAT3 in the Tumour Microenvironment. *Nat. Rev. Immunol.* 7 (1), 41–51. doi:10.1038/nri1995

Conflict of Interest: The authors declare that the research was conducted in the absence of any commercial or financial relationships that could be construed as a potential conflict of interest.

The reviewer HJ declared a shared affiliation, with no collaboration, with all of the authors to the handling editor at the time of the review.

frontiers in Bioengineering and Biotechnology

ORIGINAL RESEARCH
published: 07 January 2022
doi: 10.3389/fbioe.2021.802311

Surface Modification of Polycaprolactone Scaffold With Improved Biocompatibility and Controlled Growth Factor Release for Enhanced Stem Cell Differentiation

Xiaoyan Qin[1†], Yixin Wu[1†], Shuang Liu[1], Lei Yang[2], Hongxia Yuan[1], Susu Cai[1], Julia Flesch[3,4], Zehao Li[1], Yujing Tang[5], Xiaomin Li[5], Yi Zhuang[6], Changjiang You[3,4], Chaoyong Liu[1]* and Changyuan Yu[1]**

[1]College of Life Sciences and Technology, Beijing University of Chemical Technology, Beijing, China, [2]Department of Spine Surgery, The First Affiliated Hospital, Shenzhen University, Shenzhen Second People's Hospital, Shenzhen, China, [3]Department of Biology/Chemistry, University of Osnabrück, Osnabrück, Germany, [4]Center of Cellular Nanoanalytics (CellNanOs), Osnabrück, Germany, [5]SINOPEC, Beijing Research Institute of Chemical Industry, Beijing, China, [6]Science and Technology Department China Petrochemical Corporation, Beijing, China

Polycaprolactone (PCL) has been widely used as a scaffold material for tissue engineering. Reliable applications of the PCL scaffolds require overcoming their native hydrophobicity and obtaining the sustained release of signaling factors to modulate cell growth and differentiation. Here, we report a surface modification strategy for electrospun PCL nanofibers using an azide-terminated amphiphilic graft polymer. With multiple alkylation and pegylation on the side chains of poly-L-lysine, stable coating of the graft polymer on the PCL nanofibers was achieved in one step. Using the azide-alkyne "click chemistry", we functionalized the azide-pegylated PCL nanofibers with dibenzocyclooctyne-modified nanocapsules containing growth factor, which rendered the nanofiber scaffold with satisfied cell adhesion and growth property. Moreover, by specific immobilization of pH-responsive nanocapsules containing bone morphogenetic protein 2 (BMP-2), controlled release of active BMP-2 from the PCL nanofibers was achieved within 21 days. When bone mesenchyme stem cells were cultured on this nanofiber scaffold, enhanced ossification was observed in correlation with the time-dependent release of BMP-2. The established surface modification can be extended as a generic approach to hydrophobic nanomaterials for longtime sustainable release of multiplex signaling proteins for tissue engineering.

Keywords: surface modification, polycaprolactone scaffold, controlled release, cell differentiation, growth factor

OPEN ACCESS

Edited by:
Jianxun Ding,
Changchun Institute of Applied Chemistry (CAS), China

Reviewed by:
Zhen Geng,
Shanghai University, China
Fengxuan Han,
Soochow University, China
Yuan Xue,
Stony Brook University, United States

***Correspondence:**
Changjiang You
cyou@uni-osnabrueck.de
Chaoyong Liu
chaoyongliu@mail.buct.edu.cn
Changyuan Yu
yucy@mail.buct.edu.cn

†These authors have contributed equally to this work

Specialty section:
This article was submitted to Biomaterials, a section of the journal Frontiers in Bioengineering and Biotechnology

Received: *26 October 2021*
Accepted: *15 November 2021*
Published: *07 January 2022*

Citation:
Qin X, Wu Y, Liu S, Yang L, Yuan H, Cai S, Flesch J, Li Z, Tang Y, Li X, Zhuang Y, You C, Liu C and Yu C (2022) Surface Modification of Polycaprolactone Scaffold With Improved Biocompatibility and Controlled Growth Factor Release for Enhanced Stem Cell Differentiation. Front. Bioeng. Biotechnol. 9:802311. doi: 10.3389/fbioe.2021.802311

INTRODUCTION

Ever since the definition of "tissue engineering" appears in the 1990s, polycaprolactone (PCL) nanofibers have been used as scaffold materials for tissue repair and regeneration due to their high stability, low cost, and biodegradability (Stafiej et al., 2017; Qi et al., 2021a; Qi et al., 2021b). By tuning the molecular weight of PCL, the physical and chemical properties, degradation efficiency, and mechanical strength are adjustable. PCL scaffold materials are therefore used to mimic the

extracellular matrix (ECM), which provides mechanic support and cell signaling cues for cell proliferation and differentiation. Since the interactions between cells and scaffold materials occur at the scaffold surface, the ability of cells to undergo basic cellular processes (such as cell adhesion, migration, proliferation, and differentiation) at the scaffold interface is critical (Yang et al., 2019; Zhao et al., 2021). However, the high hydrophobicity of PCL seriously affects the adhesion and growth of cells on the material. Improving the biocompatibility of PCL is a demanding prerequisite for its application in tissue engineering.

Extensive efforts have been employed to modify the PCL scaffold surface with increased hydrophilicity, mainly including covalent chemical conjugation and non-covalent physical adsorption methods (Madhurakkat Perikamana et al., 2015; Zhang et al., 2018; Chuang et al., 2019). Chemical conjugation *via* the coupling of carboxylic acid group (COOH), amino group (NH_2), alcohol group (OH), or alkynyl-azide "click chemistry" coupling, and sulfhydryl-maleimide coupling are often used to covalently attach hydrophilic functional groups to the surface of nanomaterial (Grafahrend et al., 2011; Lancuski et al., 2012; Lu et al., 2012; Han et al., 2014; Wade et al., 2015; Zhang et al., 2016). Oxygen plasma treatment, chemical etching, or γ-ray irradiation are also used to introduce biomolecules such as proteins, peptides, or growth factors on the surface (Chen et al., 2009; Boccafoschi et al., 2012; Levato et al., 2015). The covalent chemical conjugation methods ensure stable surface modification; however, they always require stringent reaction conditions and laborious multi-step procedures, and the risk of toxic by-products during the reaction. As for physisorption *via* van der Waals interactions, adhesion proteins such as fibrogenic protein, serum albumin, and other ECM proteins are commonly used to obtain the hydrophilic surfaces. However, these methods always suffer from long-term stability due to reverse dissociation of the bound proteins. Coating exogenous proteins also brings the risk of immune response and unwanted cell signal stimulation, leading to uncontrolled stem cell differentiation (Lin et al., 2006; Zhu et al., 2020; Geng et al., 2021b).

To establish reliable stem cell culture and differentiation, the scaffold not only needs to replicate the stiffness and biocompatibility of the ECM environments but also requires to comprise signaling ingredients in ECM and mimic their spatiotemporal regulations (Silva and Mooney, 2004; Jhala and Vasita, 2015). Growth factors are signaling substances that play essential roles for cell proliferation, which together with other stimulations jointly induce cell response to differentiate into the desired lineage (Chen et al., 2020; Liu et al., 2020). As tissue regeneration and repair often take a long time, controlled release of growth factors over weeks is crucial for tissue engineering of ossification (Geng et al., 2021a). Particularly, morphogens, such as the Wnt family members (Clevers and Nusse, 2012) and bone morphologic proteins (BMPs) (Mueller and Nickel, 2012), are tightly regulated within the stem cell niche for stem cell proliferation and differentiation. The BMPs form dimers (Ehrlich et al., 2011) in physiological conditions, which show a short-range effect by their abundant positive surface charges (Matsuda et al., 2016). Spatiotemporal control of BMP signal has been observed in different organs such as the intestine and hair follicle and play a determinant role in ossification (Rompolas et al., 2013; Carulli et al., 2014; Date and Sato, 2015). To protect the growth factors from environmental degradation and maintain their biological activity over a long time, hydrogel encapsulation has been used (Holland et al., 2005; Lee and Shin, 2007; Park et al., 2007; Morrell et al., 2008; Wan et al., 2008; Shachar et al., 2011; Yue et al., 2015). Controlling the release time of growth factors can be achieved by tuning the degree of cross-linking. However, a similar dilemma occurs as the physical encapsulation of signaling factors causes short-term release, while the chemical encapsulation may damage the activity by covalent bonding at the active sites of signaling proteins (Khan et al., 2014; Marchioli et al., 2016).

To obtain fully functional release, elegant designs of nanocarriers such as liposomes and micelles have been introduced to encapsulate growth factors and BMPs (Morrell et al., 2008; Ratanavaraporn et al., 2012). We previously developed a nanocapsule-based growth factor delivery platform by caging the proteins with a degradable polymer network. Different from liposomes and micelles that formed by non-covalent self-assembly of packing molecules, the polymer network can form a protecting layer around the internal growth factor and can be degraded to release the growth factor cargos over a long time. The rate of protein release can be controlled by adjusting the ratio of monomer to cross-linker (Tian et al., 2016; Xu et al., 2019).

Here, we report a surface modification strategy for hydrophobic PCL scaffold using an azide-terminated amphiphilic polymer (**Scheme 1A**), which can be further functionalized with dibenzocyclooctyne (DBCO)-modified growth factor nanocapsules through the azide-alkyne "click chemistry". The amphiphilic polymer was synthesized by grafting α-Carboxyl-ω-azido Poly (ethylene Glycol) (HOOC-PEG-N3, Mw 5,000 Da) and oleic acid to the side chains of poly-L-lysine (PLL, Mw 30–70 kDa) (**Supplementary Figure S1A**). The growth factor nanocapsules with controlled-release capability were synthesized using the methods as previously described where BMP-2 was used as a model growth factor. As shown in **Scheme 1B**, the synthesis was achieved through *in situ* polymerization of N-(3-aminopropyl) methacrylamide (APm), acrylamide (AAm), and glycerol dimethacrylate (GDMA, degradable cross-linker) and Poly (DL–lactide)–b–poly (ethylene glycol)–b–Poly (DL–lactide) diacrylate (PLA-PEG-PLA dimetharylate, degradable cross-linker) around the growth factors. Then, the BMP-2 nanocapsules [denoted as n(BMP-2)] were modified with DBCO-PEG-NHS for further conjugation with the azide group, which is denoted as DBCO-n(BMP-2). Controlled degradation of GDMA and PLA-PEG-PLA diacrylate under a neutral pH environment breaks the shells and enables the controlled release of BMP-2. With multivalent alkylation and PEGylation on the side chains, coating of the graft polymer on the PCL scaffold was achieved through the non-covalent interaction between the OA and PCL in one step (Step I), which is denoted as OA-PLL-PEG-N_3 herein and after (**Scheme 1C**). The DBCO-n(BMP-2) was further conjugated with OA-PLL-PEG-N_3 *via* click reaction (Step II). The pH-sensitive polymer network of the nanocapsules allows the controlled release of the growth factor and induces the differentiation of stem cells (Step III).

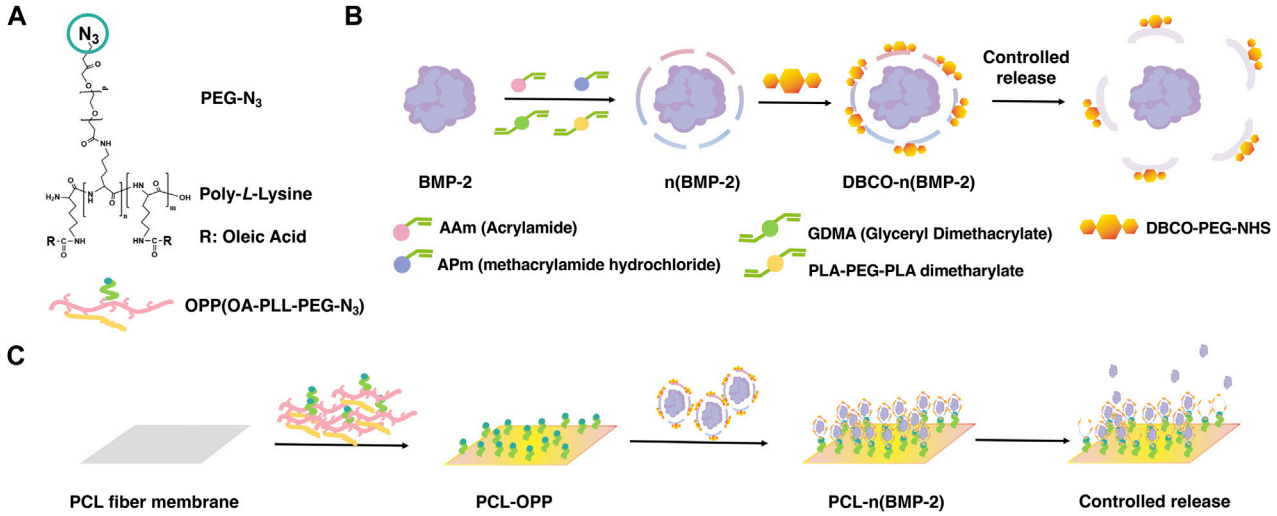

SCHEME 1 | (A) Chemical structure of OA-PLL-PEG-N3 graft polymer. **(B)** Schematic illustration of the synthesis of BMP-2 nanocapsules and DBCO-modified BMP-2 nanocapsules. **(C)** Schematic illustration of surface modification of polycaprolactone scaffold with improved biocompatibility and controlled growth factor release. **(I)** Stable coating of hydrophobic polycaprolactone scaffold by OA-PLL-PEG-N_3 graft polymer in one step. **(II)** Biofunctionalization of PLL-PEG-azide-coated scaffold with DBCO modified growth factor nanocapsules *via* click reaction. **(III)** Controlled release of growth factors from the nanocapsules-immobilized scaffold for inducing stem cell differentiation.

Through surface modification, the PCL is rendered biocompatible for cell adhesion and proliferation. Furthermore, the BMP-2 is protected by the pH-sensitive polymer network and immobilized on the modified PCL surface, allowing preserved activity on the scaffold and controlled release for differentiation of stem cells. As a proof of concept, BMP-2 was used in this work as a model growth factor to verify the effectiveness of our strategy for enhancing the ossification of bone mesenchyme stem cells (BMSCs). The results showed that quantitatively controlled release of active BMP-2 was achieved within 21 days. When BMSCs were cultured on the cell signaling nano fabric scaffold, enhanced ossification was observed correlating with the time-dependent release of BMP-2.

MATERIALS AND METHODS

Reagents

Bone morphogenetic protein 2 (BMP-2) was obtained from Shanghai Ruibang Biomaterials Co., Ltd. (Shanghai China). PCL was purchased from Qingdao Nuokang Environmental Technology Co., Ltd. (Qingdao, China). PLL was obtained from Source leaf (Shanghai, China). Oleic acid was purchased from Sigma Aldrich (St. Louis, MO). HOOC-PEG-N_3 (95%) was obtained from 3A Chemicals (Shanghai, China). DBCO-PEG-NHS N/A was purchased from Xi'an Ruixi Biotech (Xian, China). Deuterated methanol (99.8%) was purchased from Cambridge Isotope Laboratories (Ohio, United States). AAm was obtained from Aladdin, (Shanghai, China). N-(3-aminopropyl) methacrylamide hydrochloride (APm) was purchased from HEOWNS (Tianjin, China). N,N-methylenebisacrylamide (BIS) and ammonium persulfate (APS) were obtained from FuChen (Tianjin, China). N,N,N′,N′-tetramethylethylenediamine (TEMED) and Glyceryl Dimethacrylate (GDMA) were purchased from Sangon Biotech (Shanghai, China). Poly (DL–lactide)–b–poly (ethylene glycol)–b–Poly (DL–lactide) diacrylate (PLA–diacrylate, PLA: PEG:PLA = 2:24:2) was purchased from PolySciTech (West Lafayette, IN). Bovine serum albumin (BSA), BCA protein concentration determination kit, fluorescein isothiocyanate (FITC), dexamethasone, ascorbic acid, sodium β-glycerophosphate, Alizarin Red S Staining Solution, 4% paraformaldehyde solution, and 25% glutaraldehyde solution were obtained from solarbio (Beijing, China). α-MEM medium, penicillin/streptomycin (P/S, 1%), and fetal bovine serum (FBS) were purchased from gibico (Australia). Human BMP-2 ELISA Kit was obtained from Xinbosheng (Beijing, China). BCIP/NBT alkaline phosphatase (ALP) color development kit and CCK-8 kit were purchased from Biyuntian (Shanghai, China). ALP test kit was obtained from Jiancheng Biotechnology (Nanjing, China). Ultrapure water with a resistivity of 18.2 MΩ cm was used throughout.

Instruments

Transmission electron microscopy (TEM) images were acquired on Tecnai T12 Cryo–electron microscope (FEI) operating with an acceleration voltage of 120 kV. Dynamic light scattering (DLS) measurements were performed on a Zetasizer Nano instrument (Malvern) with a 10-mW helium-neon laser and thermoelectric temperature controller. TMS was used as internal standard, and 1H nuclear magnetic resonance (NMR) spectra were recorded on a 500-MHz Bruker AV400 spectrometer. FTIR measurements were performed using an FTIR spectrometer (Nicolet 6700,

Thermo). X-ray photoelectron spectroscopy measurements were performed using an x-ray photoelectron spectroscopy (ESCALAB 250Thermo). Fluorescence intensity imaging was performed using an Automatic multi-function imaging analysis system (OI600-MF-Touch). Cell adhesion on the surface of the material was observed by SEM (CarlZeiss SMT, Germany) imaging. Fluorescence intensity was measured with microplate reader Multiskan GO (Thermo). Fluorescently stained cells were imaged with an OLYMPUS upright fluorescence microscope (Japan). UV absorption measurement was used by NANODROP (Thermo).

Cell Culture

Bone marrow mesenchymal stem cells (BMSCs) isolated from Sprague–Dawley (SD) rats were used to evaluate the *in vitro* cytocompatibility of the materials. The use of animals was performed in compliance with the ethical requirements of experimental animals. Bone marrow mesenchymal stem cells (BMSCs) was cultured on 25 cm^2 tissue culture flasks and maintained by α-MEM, supplemented with 10% FBS and 1% P/S.

Synthesis of the Amphiphilic Graft Polymer

The amphiphilic graft polymer was synthesized by conjugating HOOC-PEG-N_3 and oleic acid to the side chain of PLL (Mw 30–70 kDa). Briefly, 90 mg of HOOC-PEG-N_3, 6.4 μl of oleic acid, 12.8 mg of EDC, and 8.46 mg of sulfo-NHS were dissolved in 2 ml of DMF/$NaHCO_3$ mixed solvent (volume ratio = 1:1) in sequence, and magnetically stirred for 1 h. Next, 7.5 g of PLL was added to the solution and continued to react for 24 h, followed by extensive dialysis against 30% ethanol solution using cellulose membrane (14 kDa) at room temperature for 48 h. Finally, OA-PLL-PEG-N_3 (denoted as was OPP) was obtained by freeze-drying using a freeze dryer (FD-1A-50, Hangzhou Chuanyi). In this experiment, to explore the effect of buffer pH on the grafting efficiency, the volume ratio of the DMF:$NaHCO_3$ mixed solution was adjusted to 3:1 (pH: 7.5–8.0), and the other experimental steps remained unchanged, to obtain OA-PLL-PEG-N_3 IV (denoted as OPP Ⅳ).

Characterization of the Amphiphilic Graft Polymer

To characterize the conjugation of OA to the PLL, the fluorescence spectroscopy was used to identify the presence of hydrophobic area in OPP. Briefly, different Nile Red solutions and 2 mg/ml OPP solutions were mixed and incubated at 4°C for 2 h. Then, the fluorescence of each solution was measured with a fluorescence spectrometer under the following conditions: an excitation wavelength of 500 and an emission wavelength of 800. To confirm the successful conjugation HOOC-PEG-N_3, PLL the OPP, and PLL were mixed and compressed with potassium bromide, respectively, and then, they were detected by an FTIR spectrometer (Nicolet 6700, Thermo) at a wavelength of 400–4000 cm^{-1} to further determine the presence of PEG-N3 on OPP. Through a nuclear magnetic resonance spectrometer (AVANCE III, Brooke), at 500 MHz frequency, with TMS as internal standard and deuterated methanol as solvent, the NMR spectrum of OPP was obtained.

Modification of the PCL Scaffold With Amphiphilic Graft Polymer

OPP was dissolved in 20% ethanol PBS solution at a final concentration of 2 mg/ml. The PCL scaffold was cut into a square with a side length of 1 cm firstly. Next, the PCL surface was rinsed with PBS and soaked in 1 ml of OPP solution, followed by incubation at 37°C for 3 h. Then, the PCL was taken out, rinsed with PBS three times, and placed in a vacuum oven at 37°C for 72 h.

Synthesis of the Non-degradable BSA Nanocapsules

The non-degradable BSA nanocapsules, denoted as n$(BSA)^{ND}$, were synthesized as previously reported (**Supplementary Figure S2A**). Briefly, 240 μl of BSA (6 mg/ml), 40 μl of acrylamide (AAm, 20% m/v), 12 μl of APm (20% m/v), and 1.7 μl of BIS (10% m/v) were thoroughly mixed in a 10 mM pH 7.00 PBS buffer. Free-radical polymerization was initiated by adding 11 μl of APS (10% m/v) and 3 μl of TEMED (10% m/v). The reaction was allowed to proceed for 2 h at 4°C and then was extensively dialyzed against 10 mM pH 7.0 PBS buffer using a cellulose membrane (MWCO 10 kDa) to remove unreacted monomers and initiators.

Synthesis of the Degradable BSA Nanocapsules

The degradable BSA nanocapsules, denoted as n(BSA), were synthesized with a similar method to that of n$(BSA)^{ND}$. Instead of using non-degradable cross-linkers, GDMA and Poly (DL–lactide)–b–poly (ethylene glycol)–b–Poly (DL–lactide) diacrylate (denoted as PLA-PEG-PLA diacrylate) were employed as the degradable cross-linker in the polymerization reaction. The rest of the steps are the same as n$(BSA)^{ND}$.

Synthesis of DBCO-Modified BSA Nanocapsules

The modification of n$(BSA)^{ND}$ or n(BSA) was achieved by the reaction of the amine groups on the surface of the nanocapsules with DBCO-PEG-NHS. Briefly, BSA nanocapsules and DBCO-PEG-NHS were mixed thoroughly at a molar ratio of 1:25 (BSA to DBCO-PEG-NHS) and incubated at room temperature for 2 h. Then, the mixture was extensively dialyzed against 10 mM pH 7.0 PBS buffer using a cellulose membrane (MWCO 10 kDa) to remove any unreacted DBCO-PEG-NHS. The yielded DBCO-modified BSA nanocapsules were stored at −80°C for future use.

Synthesis of the Fluorescence-Labeled BSA and Fluorescence-Labeled BSA Nanocapsules

For imaging purposes, BSA was fluorescently labeled with FITC (Ex 490 nm, Em 525 nm). Briefly, BSA and FITC are mixed at a molar

ratio of 1:5 (BSA to FITC) and incubated at room temperature for 48 h under dark. Then, the mixture was extensively dialyzed against 10 mM pH 7.0 PBS buffer using a cellulose membrane (MWCO 10 kDa) to remove unreacted FITC and finally obtain the FITC-labeled BSA (denoted as BSA-FITC). Fluorescence-labeled BSA nanocapsules and fluorescence-labeled DBCO-modified BSA nanocapsules were synthesized according to the methods described above using BSA-FITC as the protein core.

Synthesis of the DBCO-Modified Degradable BMP-2 Nanocapsules

The synthesis methods of degradable BMP-2 nanocapsules [denoted as n(BMP-2)] and DBCO-modified degradable BMP-2 nanocapsules [denoted as DBCO-n(BMP-2)] are the same as those of degradable n(BSA) and degradable DBCO-n(BSA) except BMP-2 was used as the protein core.

Determination of the Protein Concentrations

The protein concentration of native protein and protein nanocapsules were determined by bicinchoninic acid (BCA) colorimetric protein assay according to the manufacturer's protocol. Briefly, a tartrate buffer (pH 11.25) containing 25 mM BCA, 3.2 mM $CuSO_4$, and protein/nanocapsule samples was incubated at 60°C for 30 min. After the reaction was cooled to room temperature, the absorbance reading at 562 nm was determined with a UV/Vis spectrometer. The measured protein was used as a standard.

Characterizations of the Protein Nanocapsules

The particle size distribution of $n(BSA)^{ND}$ and n(BMP-2) was obtained by measuring suspension using dynamic laser scattering (DLS, ZS90, Malvern, United Kingdom). The morphology of $n(BSA)^{ND}$ and n(BMP-2) was evaluated by a transmission electron microscope (TEM, JZM-2100, Japan). In the TEM observation, the specimens were prepared by dropping a drop of 0.1% $n(BSA)^{ND}$ and n(BMP-2) on a copper and observed at an acceleration voltage of 120 kV. The numbers of the DBCO groups in the DBCO-modified nanocapsules were determined by measuring the adsorption at 309 nm using an ultraviolet spectrophotometer (NAODROP Thermo) at a protein concentration of 0.5 mg/ml. The numbers of DBCO in DBCO-modified nanocapsules was calculated based on the Beer-Lambert law as:

$$Number\ DBCO\ Per\left(DBCO-\ nanocapsules\right) = \frac{A309}{\varepsilon 309 \times Concentration\ of\ DBCO-\ nanocapsules}$$

Wherein A309 is the absorbance of DBCO-modified nanocapsules at 309 nm; ε309 represents the extinction coefficient of DBCO at 309 nm (ε309 = 12,000 M^{-1} cm^{-1}).

Preparation of PCL-OPP Modified With Protein Nanocapsules

To prepare PCL modified with protein nanocapsules, PCL-OPP was firstly soaked in BSA solution (30 mg/ml) and incubated at 37°C for 2 h to block non-specific adsorption. Next, the surface of PCL-OPP was rinsed with PBS, and then incubated with 1 ml of $n(BSA)^{ND}$, DBCO-$n(BSA)^{ND}$, DBCO-n(BSA), or DBCO-n(BMP-2) solution at a concentration of 2 mg/ml, respectively. After reacting overnight at 4°C, the surface was rinsed gently with PBS buffer, and placed in a 37°C vacuum oven (DZF-6021, Shanghai Yiheng) to allow vacuum drying for 72 h to obtain PCL modified with protein nanocapsules, which was denoted as PCL-$n(BSA)^{ND}$, PCL-n(BSA), or PCL-n(BMP-2), respectively.

Characterizations of PCL, PCL-OPP, and PCL-$n(BSA)^{ND}$

To confirm that the OPP was successfully coated onto the PCL, x-ray photoelectron spectroscopy (59 ESCALAB 220i, Thermo Fisher Scientific, Inc., Waltham, MA, United States) was used to determine the chemical composition of PCL and PCL-OPP, and a scanning electron microscope (CarlZeiss SMT, Germany) was used to observe the morphology changes. Optical imaging was used to confirm the specific conjugation of fluorescence-labeled $n(BSA)^{ND}$ to the PCL-OPP using an automatic multifunctional imaging analysis system (OI-600MF-Touch, Guangzhou Guangyi Biology).

Water Contact Angle Assay

Water contact angle assay was used to test the hydrophilicity of the PCL, PCL-OPP, and PCL-$n(BSA)^{ND}$ using the sessile drop method on a contact angle goniometer (DSA100, Dataphysics Instruments GmbH, Filderstadt, Germany). Briefly, the material was placed on the stage and raised so that the material to be tested will make contact with the water droplets of the injector. Then, the stage was lowered to take the water drop away. Finally, a picture of the water droplets was taken after a pause of 10 s. The five-point fitting method was used to measure the static water contact angle.

Protein Adsorption Assay

The PCL and PCL-OPP were cut into 1-cm squares and respectively immersed in 1 ml (0.3 mg/ml) of BSA-FITC solution. After incubation at 37°C for 2 h, the surface of PCL and PCL-OPP was rinsed with 1 × PBS gently, and then the fully automatic multifunctional imaging analysis system (OI-600MF-Touch, Guangzhou Guangyi Biology) was carried out for fluorescence detection. The results were quantified by a Gel-Pro Analyzer.

Protein Release Assays of the PCL-n(BSA) and PCL-n(BMP-2)

To quantify the BSA released from PCL-n(BSA), the square of PCL-n(BSA-FITC) was placed in 500 μl of 1 × PBS (pH 7.0)

solution and incubated in a constant temperature water bath at 37°C. The solution was replaced with 500 μl of 1 × PBS (pH 7.0) solution every 24 h for 4 days. The fluorescence intensity of each collected sample was detected by a fluorescence microplate reader (Multiskan GO, Thermo). The release curve of BSA-FITC was calculated based on the time-dependent fluorescence intensity changes. For quantifying the release kinetics of BMP-2, 1 × 1 cm^2 PCL-n(BMP-2) was placed in 400 μl of 1 × PBS (pH 7.0) solution. The 400 μl of PBS buffer was taken out at 1, 2, 3, 4, 5, 7, 10, 15, and 21 days for analysis using the BMP-2 Elisa kit according to the manufacturer's protocol. Sample O.D. values at 450 nm were recorded by the microplate reader for calculating the release curve of BMP-2.

Cytotoxicity Assays

BMSCs were extracted from newborn SD rats and then cultured with α-MEM (minimum essential medium eagle—alpha modification) with 10% FBS. Fourth-generation BMSCs were used to study the interaction between cells and nanocapsule shells. The BMSCs were allowed to adhere at a density of 5×10^3 cells per well and incubated for 24 h. Then, 100 μl of $n(BSA)^{ND}$ solution (20, 50, 150, 200, and 250 ng/ml), which were diluted with the serum-free medium in advance, were added. After the incubation for 24 h, 10 μl of cck8 was added to each well and the absorbance at 450 nm was measured by a multifunctional microplate reader (EnSpire PerkinElmer). Taking the cell viability of the absorbance value at the blank unmedicated hole as 100%, the relative cell viability of the transformed experimental group.

Osteogenic Differentiation Assay of BMSCs

Second-generation BMSCs were used to study the interaction between cells and n(BMP-2). The BMSCs were seeded to adhere at a density of 2.5×10^4 cells per well and cultured in a carbon dioxide cell incubator (311 Thermo) for 24 h to allow the cells to attach. On the basis of the conventional culture medium, the osteogenic induction medium containing 0.1 μM dexamethasone, 0.05 mg/ml ascorbic acid, and 10 mM sodium glycerophosphate aqueous solution was prepared for subsequent culture. The concentration of n(BSA) and n(BMP-2) in each well of the control or experimental group was maintained at 500 ng/ml per well, and nothing was added to the blank control group. The liquid was changed every 3 days. Then, the cells were stained with the BCIP/NBT ALP staining kit on the third day and stained with Alizarin Red on the 21st day subsequently. All the staining results were observed under an optical microscope and quantitatively analyzed by Image-Pro software.

Adhesion and Proliferation Assay of BMSCs on PCL, PCL-OPP, and PCL-n(BSA)ND

Fourth-generation BMSCs were used to study the cell adhesion and proliferation on PCL, PCL-OPP, and PCL-$n(BSA)^{ND}$. The PCL and PCL and PCL-OPP were disinfected in 75% ethanol for 2 h and rinsed three times with sterile PBS. PCL-$n(BSA)^{ND}$ was obtained from the above sterile PCL-OPP and DBCO-$n(BSA)^{ND}$ according to the method described above and equilibrated it in a culture medium for 2 h. The BMSCs were allowed to adhere to the material's films for 4 h at a density of 2.5×10^5 cells per well. After 8 h, the films were washed three times with PBS to remove any loosely attached cells, 0.5 ml of culture medium containing 10% CCK-8 was added, and the optical densities at 450 nm were measured. The CCK-8 assay was also carried out at 2 and 4 days. On the third day, the medium was aspirated from each well and fixed with 2.5% glutaraldehyde for 15 min. The cell adhesion on the surface of the material was observed by SEM (CarlZeiss SMT, Germany) imaging, and the cell adhesion area was quantified using ImageJ software. The adhesive of BMSCs to the PCL, PCL-OPP, and PCL-$n(BSA)^{ND}$ was observed at different time intervals using fluorescence imaging (OLYMPUS, Japan). Cells were stained by live and dead, and the number of live cells was stained to determine the number of adherent cells.

Osteogenic Differentiation Assay of BMSCs Cultured on PCL, PCL-OPP, PCL-n(BSA), and PCL-n(BMP-2)

BMSCs were cultured on PCL, PCL-OPP, PCL-n(BSA) and PCL-n(BMP-2) with osteogenesis-inducing supplements for 21 days. Firstly, the cells were lysed by 0.2% Triton X-100 v/v for 30 min and then pipette all the lysate was pipetted. Cell homogenate to be tested was added into each well of the 96-well plate, 30 μl of water was added to the blank group, and 30 μl of phenol standard solution (0.02 mg/ml) was prepared for the standard group. After stopping the reaction, the microplate reader (Multiskan GO Thermo) detected the value of OD520. In addition, part of the homogenized cell homogenate was used to determine the total cell protein concentration by the BCA method, and the ALP activity was calculated according to the following formula (King's unit/gprot):

$$AKP\ viability\ in\ cultured\ cell\left(King's\ unit/gprot\right) = \frac{OD1 - OD2}{OD3 - OD1} \times Phenol\ standard\ concentration \div Total\ portein\ concentration$$

Wherein OD1 represents the absorbance value of the measuring hole, OD2 represents the absorbance value of the blank hole, and OD1 represents the absorbance value of the standard.

Alizarin Red Staining Assay of BMSCs Cultured on PCL, PCL-OPP, PCL-n(BSA), and PCL-n(BMP-2)

The mineralization of BMSCs was assessed at day 21 using an Alizarin Red Staining (ARS) assay. The BMSCs were rinsed three times with PBS and fixed with 4% of paraformaldehyde solution for 15 min, subsequently stained with alizarin red for 30 min, and then rinsed with ultrapure water three times. The calcium deposition was observed using Biological Scanning Electron Microscope (SU8010 Thermo).

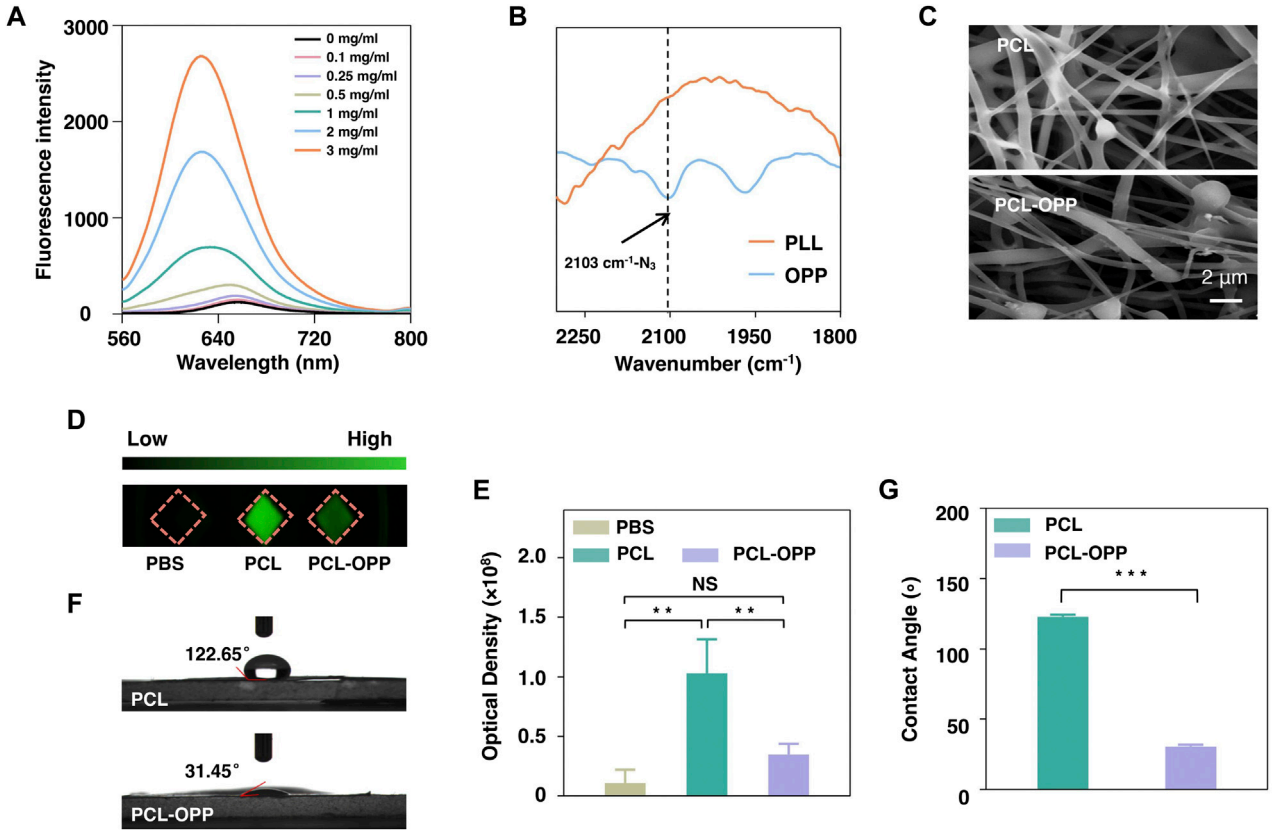

FIGURE 1 | Characterization of PCL and PCL-OPP. **(A)** Fluorescence spectra of Nile Red after incubation with different concentrations of OA-PLL-PEG-N_3(OPP). **(B)** FT-IR spectra of PLL and OA-PLL-PEG-N_3(OPP). **(C)** SEM image of PCL and PCL-OPP. **(D)** FITC-labeled BSA protein adsorption. (E) Quantitative fluorescence density analysis of the BSA-FITC protein adsorption using Image-Pro software. **(F, G)** The water contact angle of PCL and PCL-OPP. (n = 3). p value: *p < 0.05, **p < 0.01, ***p < 0.001 and ****p < 0.0001. ns means not significant.

Statistical Analysis

All results are presented as the mean ± standard error of the mean (s.e.m.) as indicated. Two-way ANOVA was used for multiple comparisons. All statistical analyses were conducted with Prism Software (Prism 8.0.1).

RESULTS AND DISCUSSIONS

Synthesis and Characterization of the Amphiphilic Graft Polymer

Biocompatibility and robust mechanical strength both are the fundamental concerns for nano fabric scaffolds used in tissue engineering. For scaffolds made of hydrophobic polymers, such as commonly used polyesters and polyethylene derivatives, surface biofunctionalization is an efficient method to enhance biocompatibility without compromising the mechanical property. In this work, we synthesized an amphiphilic graft polymer based on fully biodegradable PLL. The graft PLL polymer was designed to contain a 50% molar ratio of oleic acid as the hydrophobic moieties for interaction with nanofibers. The remaining 50% of side chains are left for conjugation with poly(ethylene glycol) terminally modified with azide group (PEG-N_3) (**Supplementary Figure S1A**). For stable coating of the hydrophobic scaffold, PLL with 240 repeat units was chosen (Average Mw: 50 kDa of the PLL hydrobromide). The polymer main chain could thus provide theoretically 120 alkyl chains for multiple van der Waals interactions and 120 PEG-N_3 for multivalent biofunctionalization, respectively.

By optimizing the coupling reaction mediated by 1-ethyl-3-carbodiimide, two batches of graft copolymer OA-PLL-PEG-N_3 III and OA-PLL-PEG-N_3 IV were obtained. The products were characterized by ^{1}H-NMR, showing characteristic chemical shifts of CH_2 groups from PEG, PLL, and the double bond of oleic acid (OA) (**Supplementary Figures S1B, C**). For the product OA-PLL-PEG-N_3 IV, the integral of these corresponding chemical shifts corresponded to 36% of OA and 20% of PEG conjugation on the PLL side chains. Therefore, OA-PLL-PEG-N_3 IV with the highest proportion of oleic acid was selected for the following experiments, denoted as OPP. Fluorescence emission spectroscopy shows enhanced solubility of hydrophobic Nile Red dye by mixing with the grafted polymers, indicating the formation of amphiphilic polymer micelles by successfully coupling oleic acids to PLL-PEG (**Figure 1A**). Fourier transform infrared spectroscopy (FT-IR) of the graft polymer showed a new absorption at 2,103 cm^{-1} for the

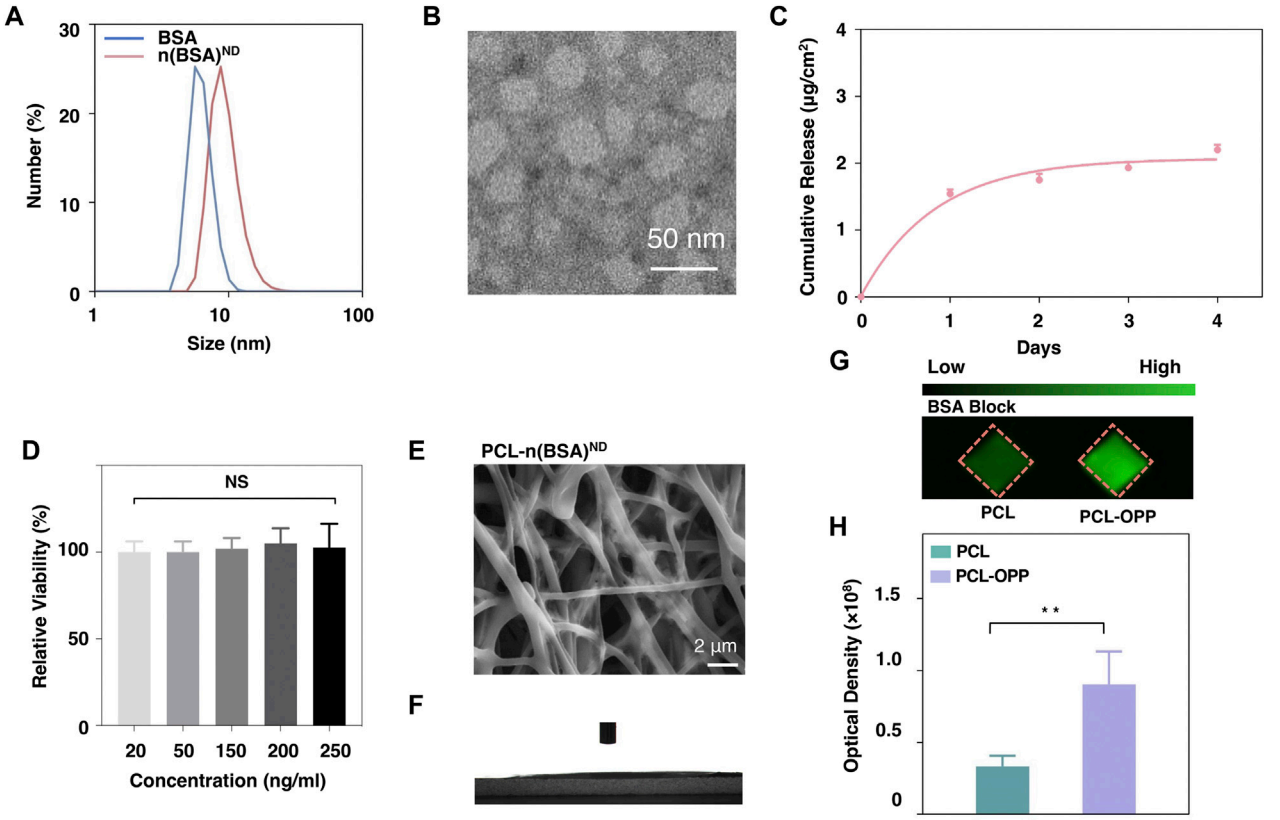

FIGURE 2 | Characterization of n(BSA)ND, DBCO-n(BSA), and PCL-n(BSA)ND. **(A)** The size of BSA and n(BSA)ND. **(B)** Representative TEM image of negatively stained n(BSA)ND. **(C)** The release rate of the BSA cargo from DBCO-degradable n(BSA). **(D)** Cell viability on different concentrations of n(BSA)ND. **(E)** SEM image and **(F)** Water contact angle of PCL-n(BSA)ND. **(G)** Imaging of the PCL and PCL-OPP after incubation with DBCO-n(BSA-FITC)ND. **(H)** Quantification of the fluorescence density analyzed using Image-Pro software (n = 3, NS means no significant difference, $^{*}p < 0.05$, $^{**}p < 0.01$, $^{***}p < 0.001$).

asymmetric stretch vibration of the azide group (**Figure 1B**). X-ray photon spectroscopy further proves the presence of azide groups in the complex (**Supplementary Figure S1D**), which were absent for PLL polymer before the coupling reaction. The results therefore unambitiously confirmed the successful synthesis of OA-PLL-PEG-N_3, where the azide group could be used for click reaction for further bioconjugations.

Preparation and Characterization of Surface-Modified PCL Scaffold

Next, we used the obtained amphiphilic graft polymer to coat the hydrophobic scaffold *via* dip-coating. For this purpose, PCL nanofiber membrane was first to cut into pieces of 1 × 1 cm^2 for dipping into 2 mg/ml OA-PLL-PEG-N_3 (hereafter denoted as OPP for short) PBS solution. Scanning electron microscopy (SEM) results showed that the fiber surface of the PCL-OPP had become rough with particles attached (**Figure 1C**). BSA-FITC was further used to study the protein adsorption capacity of PCL before and after modification. **Figure 1D** shows the fluorescence images of the PCL and PCL-OPP after incubation with BSA-FITC at 37°C for 2 h. The green fluorescence on PCL-OPP is weaker than that of PCL (**Figure 1D**), indicating a lower protein adsorption capacity of PCL-OPP. Quantitative analysis shows that the non-specific protein adsorption capacity of the PCL-OPP scaffold is 3-fold lower than that of the pure PCL scaffold (**Figure 1E**). This result indicates successful functionalization of OPP on PCL nanofiber membranes, which introduces a PEG layer on the PCL surface to inhibit non-specific protein adsorption. In agreement with this result, a significant decrease of the water contact angle was determined on PCL-OPP (31.45°) versus PCL of 122.65° (**Figure 1F, G**), corroborating the fact that the coating of OPP renders the PCL surface highly hydrophilic.

Synthesis and Characterizations of BSA Nanocapsules

To investigate whether the as-obtained PCL-OPP could be further functionalized *via* the azide group on the PEG side chain and demonstrate the synthesis of the nanocapsules with sustained-release capability, we prepared dibenzocyclooctyne (DBCO)-modified protein nanocapsules using BSA as the model protein nanocapsules and explored their coupling efficiencies on PCL-OPP. The synthesis of the model protein nanocapsules [denoted as n(BSA)] can be achieved by *in situ*

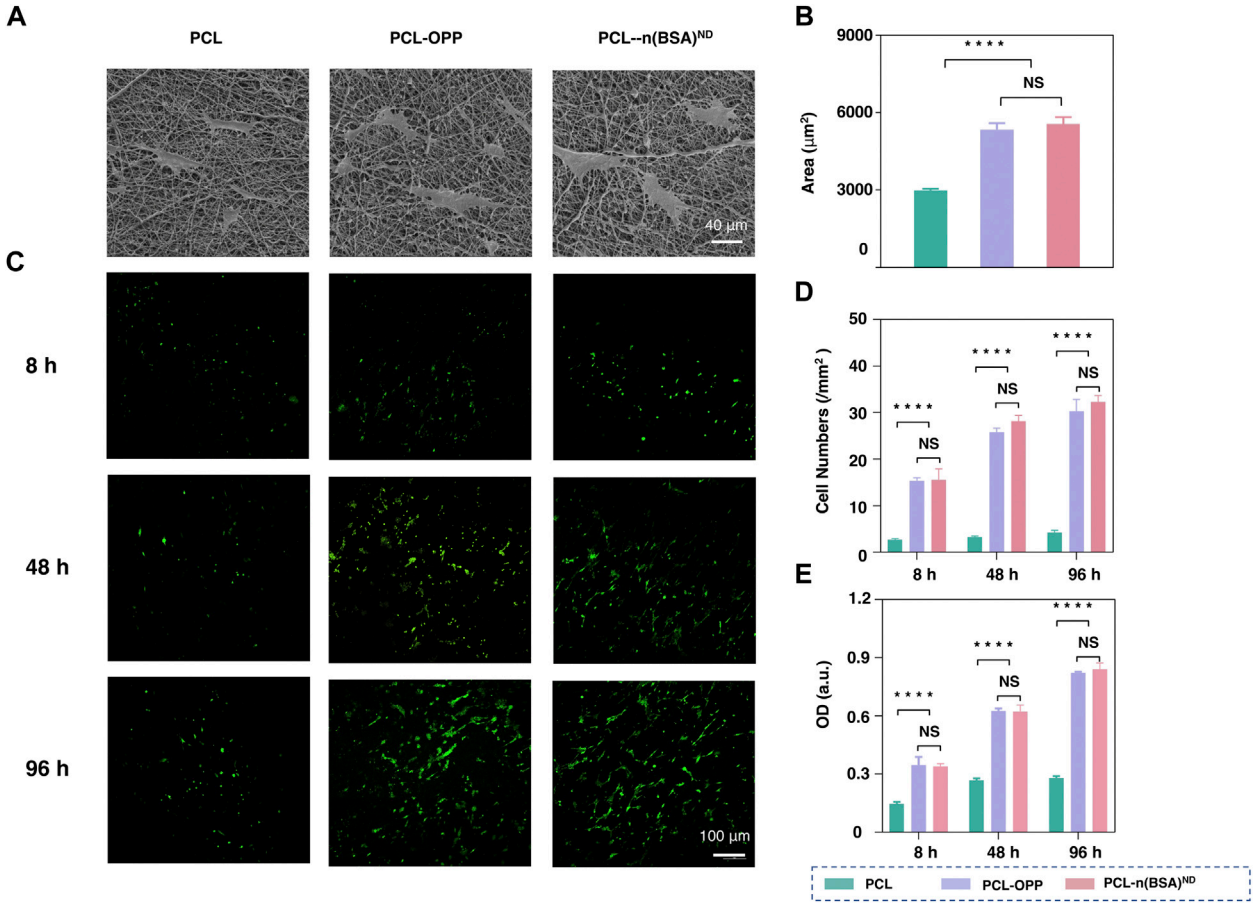

FIGURE 3 | The adhesion and cell proliferation of BMSCs on PCL-n(BSA)ND. **(A)** SEM images of BMSCs adhered to the surfaces of PCL, PCL-OPP, and PCL-n(BSA)ND films on the third day. **(B)** Quantitative analysis of cell area adhered to the surfaces of PCL, PCL-OPP, and PCL-n(BSA)ND using ImageJ software. **(C)** The fluorescence images of BMSCs adhered to the surfaces of PCL, PCL-OPP, and PCL-n(BSA)ND films at different time points. **(D)** Quantitative analysis of the cell numbers adhered to the surfaces of PCL, PCL-OPP, and PCL-n(BSA)ND using ImageJ software. **(E)** Profiles of BMSC proliferation obtained by CCK-8 assay (n = 3, NS means no significant difference, ****p < 0.0001).

polymerization at 4°C (**Supplementary Figures S2A,B**). DLS results showed that the hydrodynamic radius of BSA was 6.242 nm (**Figure 2A**), while the hydrodynamic radius of n(BSA)ND reached 9.544 nm (**Figure 2A**), indicating that the AAm, APm monomers, and GDMA cross-linkers incubated with BSA had formed a thin layer of polymer network around the protein through free radical polymerization, leading to the formation of n(BSA). This was consistent with the TEM image showing that n(BSA)ND had a spherical morphology with an average diameter of about 20 nm (**Figure 2B**). These results collectively suggested the successful synthesis of n(BSA)ND.

Surface Modification of PCL-OPP With BSA Nanocapsules

Next, in order to explore the immobilization of nanocapsules on the surface of PCL-OPP material, DBCO-PEG-NHS ester was used to modify the primary amino groups (-NH_2) on the surface of n(BSA) to form DBCO-n(BSA)ND. From the full-band scanning absorption peak of the UV spectrophotometer, it can be seen that there are obvious absorption peaks at 309 nm (**Supplementary Figure S2C**), indicating that DBCO was successfully grafted to the n(BSA)ND surface. As-obtained DBCO-n(BSA)ND can be specifically immobilized on the surface of PCL-OPP by reacting with the azide group on PCL-OPP ("Click Chemistry" reaction), which is denoted as PCL-n(BSA)ND. **Figure 2E** shows the SEM image of the PCL-n(BSA)ND. Compared with the surface of PCL-OPP, the surface of PCL-n(BSA)ND has a relatively rough fiber structure. Moreover, the water contact angle of PCL-n(BSA)ND is significantly lower than that of PCL-OPP (**Figure 2F**), so that the angle cannot be displayed. To further confirm that the DBCO-n(BSA)ND was covalently conjugated rather than absorbed to the scaffold, the PCL and PCL-OPP were pre-incubated with BSA for block and further incubated with DBCO-n(BSA)ND, respectively. **Figures 2G,H** shows that the amount of specific immobilized protein on PCL-OPP is about twice that of

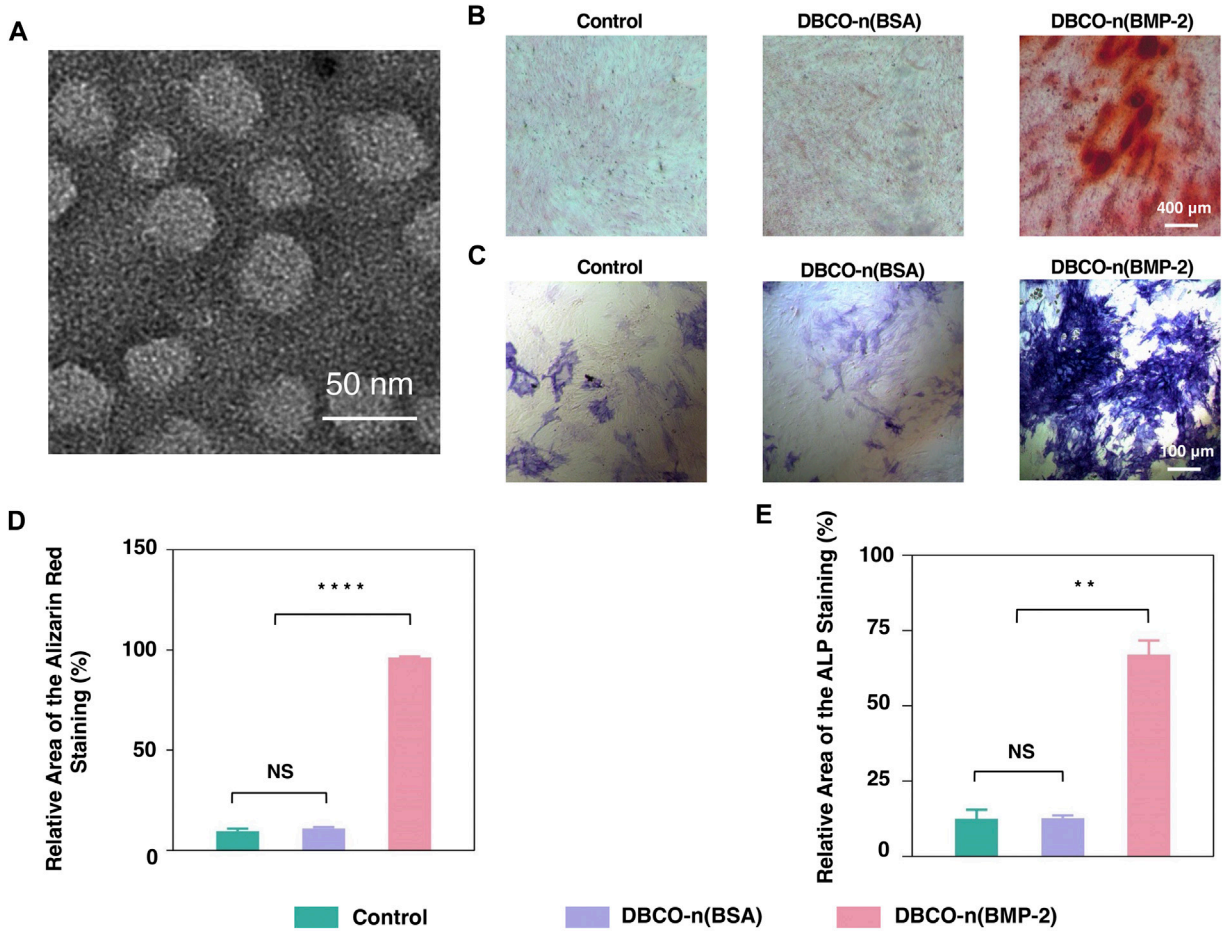

FIGURE 4 | Osteogenic differentiation of BMSCs by n(BMP-2). **(A)** Representative TEM image of negatively stained degradable n(BMP-2). **(B)** Alizarin Red Staining of induced BMSCs for 10 days. **(C)** The ALP staining of induced BMSCs. **(D)** Quantitative analysis of Alizarin Red Staining images using ImageJ software. **(E)** Quantitative analysis of ALP staining images was analyzed using ImageJ software (n = 3, NS means no significant difference, $^{**}p < 0.01$, $^{****}p < 0.0001$).

PCL. **Supplementary Figure S4** also proves that PCL-OPP performs specific immobilization rather than specific adsorption on DBCO-n(BSA)ND, and the protein immobilization capacity of the DBCO-n(BSA-FITC)ND is about twice the non-specific adsorption capacity of the n(BSA-FITC)ND, suggesting that DBCO-n(BSA) efficiently and specifically immobilized on the PCL-OPP.

Under the psychological environment, the ester bonds in the cross-linkers in nanocapsules were gradually cleaved, leading to the dissociation of the polymer shells and the release of the protein cargo. The polymer shell composition can be readily altered to finely tune the degradation kinetics. We monitored the BSA concentration in PBS buffer (pH 7.0) over days from a PCL-n(BSA-FITC) nanofiber membrane leading to the controllable release. Through the BSA release curve, one can see that n(BSA) had sustainable release capability (**Figure 2C**) to avoid the sudden release of protein. Through the cytotoxicity test of different concentrations (20–250 ng/ml) of n(BSA)ND, the nanocapsule shell has no obvious cytotoxicity (**Figure 2D**), which is beneficial for the *in vivo* application of nanocapsules.

BMSCs Adhesion and Proliferation on PCLn(BSA)ND Scaffold

To test the biocompatibility of PCL-n(BSA)ND of cell culture, BMSCs were chosen to study the effect of surface-modified PCL membrane on cell behaviors such as cell adhesion and proliferation. Scanning electron microscope images were used to observe the adhesion areas of BMSCs on the PCL, PCL-OPP, and PCL-n(BSA)ND film surfaces on the third day (**Figure 3A**). The area of cell adhesion on PCL-OPP and PCL-n(BSA)ND materials is much larger than that of the PCL group, which is about twice that of the unmodified PCL nanofiber membrane (**Figure 3B**).

Fluorescence microscopy images were used to observe the adhesion and growth of BMSCs on the PCL, PCL-OPP, and PCL-n(BSA)ND membranes. As shown in **Figure 3C**, after 8 h of adhesion, only a few BMSCs adhered to the PCL membrane, and the

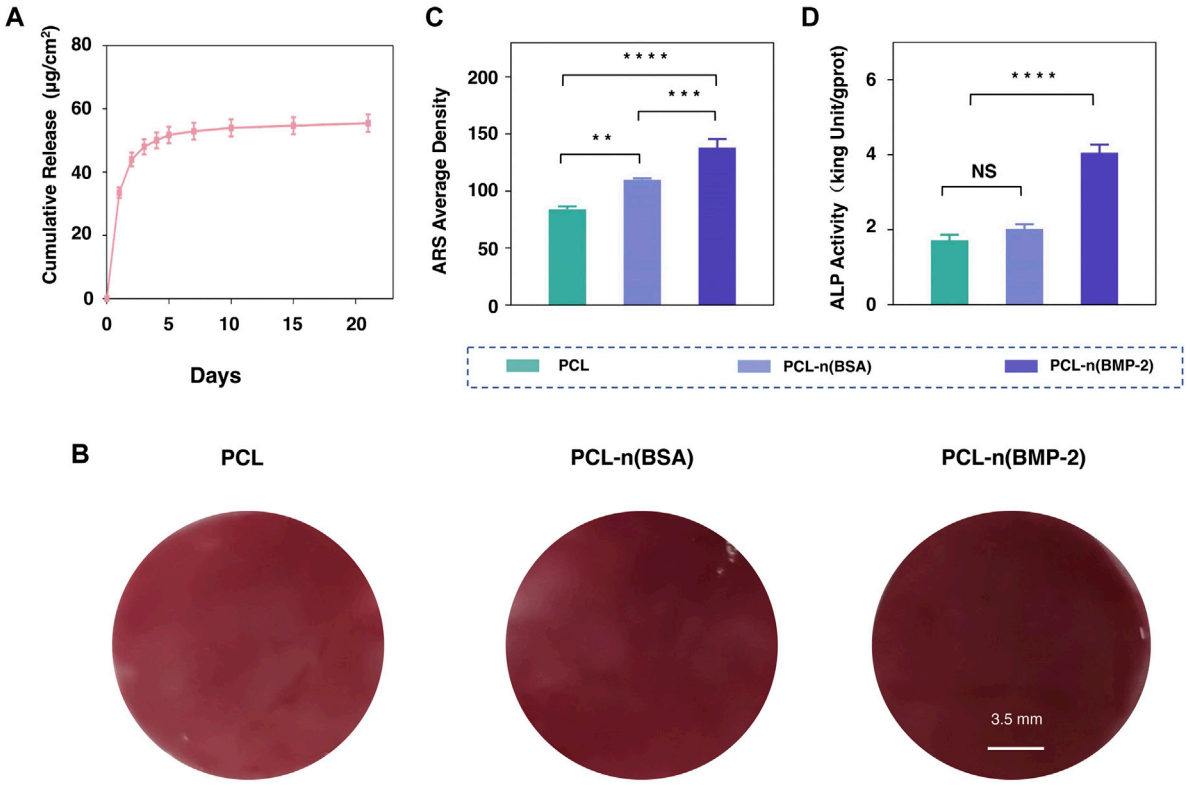

FIGURE 5 | Osteogenic differentiation of BMSCs on PCL-n(BMP-2). **(A)** Release rate of the BMP-2 cargo from PCL-n(BMP-2). **(B)** Alizarin red staining assay of cultured BMSCs on PCL, PCL-n(BSA/BMP-2) at day 21. **(C)** The average density of Alizarin red staining was analyzed by ImageJ software for the quantification. **(D)** ALP activity of cultured BMSCs on PCL, PCL-n(BSA/BMP-2) osteogenic differentiation at day 3 (n = 3, NS means no significant difference, $^{**}p < 0.01$, $^{***}p < 0.001$, $^{****}p < 0.0001$).

number of cells that adhered to the PCL-OPP and PCL-n(BSA)ND membranes was several times higher than that of the PCL group. As the culture time increases, not only does the number of cells on the surface of the PCL-OPP and PCL-n(BSA)ND films increase but also the cells show good morphology for a spreading growth. In contrast, the number of cells on the surface of the PCL membrane only increased slightly compared to the 8 h. Since the number of cells adhering to the surface of the PCL membrane was too small in the first 8 h, even though the culture time was as long as 4 days, the number of cells on the PCL film surface was still several times lower than the PCL-OPP and PCL-n(BSA)ND groups. Quantitative data on the number of adherent cells also verified this trend (**Figure 3D**).

The Cell Counting Kit-8 (CCK-8) test was used to further test the adhesion and proliferation of BMSCs on PCL, PCL-OPP, and PCL-n(BSA)ND membranes. As shown in **Figure 3C**, the optical density (OD) values of the PCL-OPP and PCL-n(BSA)ND groups in each period were significantly higher than those of the PCL group. No significant difference was found between the PCL-OPP and PCL-n(BSA)ND groups. The CCK-8 assays were further used to test the adhesion and proliferation of BMSCs on the PCL, PCL-OPP, and PCL-n(BSA)ND films. As seen in **Figure 3E**, the OD values of the PCL-OPP and PCL-n(BSA)ND groups in each period were significantly higher than that of the pristine PCL group, and there was no significant difference between the PCL-OPP and PCL-n(BSA)ND groups in all the above data. All results proved that the modification of PCL surface with OPP had improved the adhesion and proliferation ability of BMSCs on the material, which was consistent with the previous conclusion that PCL-OPP was significantly more hydrophilic than PCL. The results showed that immobilized nanocapsules did not affect the adhesion and proliferation of BMSCs on PCL-OPP, which pave the way for further application of PCL-OPP material loaded with functional growth factor nanocapsules.

Synthesis and Characterizations of BMP-2 Nanocapsules

Inspired by the successful preparation of the PCL-n(BSA) nanofiber scaffold, n(BMP-2) was synthesized with a similar method to n(BSA). A purified sample was analyzed by SDS-PAGE, in which the bands of product are stacked at the junction of the concentrated gel and the separating gel (**Supplementary Figure S3A**). By the formation of a polymer shell on n(BMP-2), the molecular weight increased greatly, and it could not migrate in the gel as easily as BMP-2. To the end, no obvious BMP-2 band was found after purification of n(BMP-2) (**Supplementary Figure S3A**). DLS results showed that the diameter of n(BMP-2) reached 19.28 nm (**Supplementary Figure S3B**), which was consistent with the result provided by the TEM image, showing a spherical shape with an

average diameter of about 20 nm (**Figure 4A**). Together, the above results confirmed the successful synthesis of n(BMP-2).

Effect of BMP-2 Nanocapsules on BMSC Osteogenic Differentiation

ALP is a specific marker in the early stage of osteogenic differentiation. Meanwhile, calcium deposition is one of the important signs of late osteogenic differentiation, which can be specifically read out by ARS. To quantify the effect of BMP-2 nanocapsules on osteogenic differentiation, ALP and ARS staining were carried out to BMSCs cultivated with osteogenic induction medium alone, with n(BSA) or n(BMP-2) in induction medium for 21 days, respectively. **Figures 4B,C** showed ALP staining with blue-purple and ARS staining of calcium deposits in red. By quantifying the staining area of ALP and ARS (**Figures 4D,E**), it can be seen that although the BMSC culture always contains the induction medium, the percentage of ALP-stained area for the control group and the n(BSA) added group were about 12%, and the proportion of the ARS-stained area was only about 10%. In contrast, the ALP staining area of the experimental group added (BMP-2) accounted for 67.02%, and the ARS staining area accounted for 96.31%, which were both significantly higher than the n(BSA) group and the control group. These results collectively suggested that n(BMP-2) had excellent differentiation osteogenic differentiation ability.

To obtain the sustained release of BMP-2 on biocompatible PCL scaffold, DBCO-n(BMP-2) was immobilized to PCL-OPP according to the abovementioned method and denoted as PCL-n (BMP-2). The effect of BMSC osteogenic differentiation on PCL-n(BMP-2) was evaluated by the above-established ALP and ARS staining. The release kinetics of BMP-2 from PCL-n(BMP-2) incubated in PBS at 37°C were monitored using a BMP-2 ELISA kit. According to this assay, the release of BMP-2 was increased gradually within 10 days. The release amount began to be steadily slow down after the first 10 days and continued until the 21st day as the end of the experiments (**Figure 5A**). The long-term controlled release of BMP-2 showed a cumulative release amount of 53.6 μg/cm^2, which was sufficient to induce the osteogenic differentiation of BMSCs.

For evaluating ossification at the early differentiation stage, the ALP activity was detected on the third day after culturing BMSCs with PCL, PCL-n(BSA), and PCL-n(BMP-2). ARS assay was used to evaluate the synthesis of extracellular mineralized substances on day 21 for the late stage of differentiation. As shown in **Figure 5B**, although the material itself has a certain thickness, the calcium nodules can be detected through the microscope, the results showed that intensity of redness of ARS on PCL-n(BMP-2) was the strongest, followed by a sequence of PCL-n(BSA), and 1.8-fold higher than PCL (**Figure 5C**). Interestingly, the ALP activity results on day 3 showed the highest ALP activity of the PCL-n(BMP-2) group, which was twice that of the PCL and PCL-n(BSA) group (**Figure 5D**). These results are in a good correlation of the release curve of BMP-2, showing a stronger differentiation effect of BMP-2 in the early stage supported by the fast BMP-2 release. In line with the continuous release until day 21, the highest ARS at day 21 of the PCL-n(BMP-2) group highlights the importance of the long-time release of BMP-2 for the sustained ossification. In general, it furthermore illustrates the necessity of specific immobilization of functional signaling nanocapsules on PCL-OPP scaffold for applications in tissue engineering.

CONCLUSION

In summary, we have demonstrated a general approach to surface modification of PCL scaffold with improved biocompatibility and controlled growth factor release for enhanced stem cell differentiation. Compared with PCL, the hydrophilicity of PCL-OPP has been significantly improved, thus providing improved biocompatibility, as well as better cell adhesion, and growth. In addition, through specific immobilization of BMP-2 nanocapsules onto the PCL-OPP, sustained release of BMP-2 enhanced osteogenic differentiation of BMSC. Moreover, as a general method, our strategy could be extended for bioactive functionalization of other hydrophobic scaffold materials with other therapeutic proteins in a variety of clinical applications.

DATA AVAILABILITY STATEMENT

The original contributions presented in the study are included in the article/**Supplementary Material**. Further inquiries can be directed to the corresponding authors.

AUTHOR CONTRIBUTIONS

CYo, CL, and CYu conceived or designed this study. XQ, YW, SL, HY, and SC conducted the experiments. XQ, YW, and SL analyzed the data and performed the statistical analysis. XQ, YW, CYo, CL, and CYu co-wrote the manuscript. All authors discussed the results and commented on the manuscript.

FUNDING

This work was supported by the National Key Research and Development Program of China (No. 2019YFA0903801), the National Natural Science Foundation of China (Grant Nos. 8217453, 52073015, and 31870976), the Shenzhen Science and Technology Projects (Grant No. GJHZ20200731095608025), and SINOPEC project (#421029).

SUPPLEMENTARY MATERIAL

The Supplementary Material for this article can be found online at: https://www.frontiersin.org/articles/10.3389/fbioe.2021.802311/full#supplementary-material

REFERENCES

Boccafoschi, F., Fusaro, L., Mosca, C., Bosetti, M., Chevallier, P., Mantovani, D., et al. (2012). The Biological Response of poly(L-Lactide) Films Modified by Different Biomolecules: Role of the Coating Strategy. *J. Biomed. Mater. Res. A.* 100, 2373–2381. doi:10.1002/jbm.a.34180

Carulli, A. J., Samuelson, L. C., and Schnell, S. (2014). Unraveling Intestinal Stem Cell Behavior with Models of Crypt Dynamics. *Integr. Biol.* 6, 243–257. doi:10.1039/c3ib40163d

Chen, F.-M., Chen, R., Wang, X.-J., Sun, H.-H., and Wu, Z.-F. (2009). *In Vitro* cellular Responses to Scaffolds Containing Two Microencapulated Growth Factors. *Biomaterials* 30, 5215–5224. doi:10.1016/j.biomaterials.2009.06.009

Chen, L., Liu, J., Guan, M., Zhou, T., Duan, X., and Xiang, Z. (2020). Growth Factor and its Polymer Scaffold-Based Delivery System for Cartilage Tissue Engineering. *Ijn* Vol. 15, 6097–6111. doi:10.2147/ijn.s249829

Chuang, Y.-C., Yu, Y., Wei, M.-T., Chang, C.-C., Ricotta, V., Feng, K.-C., et al. (2019). Regulating Substrate Mechanics to Achieve Odontogenic Differentiation for Dental Pulp Stem Cells on TiO2 Filled and Unfilled Polyisoprene. *Acta Biomater.* 89, 60–72. doi:10.1016/j.actbio.2019.02.040

Clevers, H., and Nusse, R. (2012). Wnt/β-Catenin Signaling and Disease. *Cell* 149, 1192–1205. doi:10.1016/j.cell.2012.05.012

Date, S., and Sato, T. (2015). Mini-Gut Organoids: Reconstitution of the Stem Cell Niche. *Annu. Rev. Cel Dev. Biol.* 31, 269–289. doi:10.1146/annurev-cellbio-100814-125218

Ehrlich, M., Horbelt, D., Marom, B., Knaus, P., and Henis, Y. I. (2011). Homomeric and Heteromeric Complexes Among TGF-β and BMP Receptors and Their Roles in Signaling. *Cell Signal.* 23, 1424–1432. doi:10.1016/j.cellsig.2011.04.004

Geng, Z., Ji, L., Li, Z., Wang, J., He, H., Cui, Z., et al. (2021a). Nano-needle Strontium-Substituted Apatite Coating Enhances Osteoporotic Osseointegration through Promoting Osteogenesis and Inhibiting Osteoclastogenesis. *Bioactive Mater.* 6, 905–915. doi:10.1016/j.bioactmat.2020.09.024

Geng, Z., Li, X., Ji, L., Li, Z., Zhu, S., Cui, Z., et al. (2021b). A Novel Snail-Inspired Bionic Design of Titanium with Strontium-Substituted Hydroxyapatite Coating for Promoting Osseointegration. *J. Mater. Sci. Tech.* 79, 35–45. doi:10.1016/j.jmst.2020.11.041

Grafahrend, D., Heffels, K.-H., Beer, M. V., Gasteier, P., Möller, M., Boehm, G., et al. (2011). Degradable Polyester Scaffolds with Controlled Surface Chemistry Combining Minimal Protein Adsorption with Specific Bioactivation. *Nat. Mater* 10, 67–73. doi:10.1038/nmat2904

Han, L.-H., Tong, X., and Yang, F. (2014). Photo-crosslinkable PEG-Based Microribbons for Forming 3D Macroporous Scaffolds with Decoupled Niche Properties. *Adv. Mater.* 26, 1757–1762. doi:10.1002/adma.201304805

Holland, T. A., Tabata, Y., and Mikos, A. G. (2005). Dual Growth Factor Delivery from Degradable Oligo(poly(ethylene Glycol) Fumarate) Hydrogel Scaffolds for Cartilage Tissue Engineering. *J. Controlled Release* 101, 111–125. doi:10.1016/j.jconrel.2004.07.004

Jhala, D., and Vasita, R. (2015). A Review on Extracellular Matrix Mimicking Strategies for an Artificial Stem Cell Niche. *Polym. Rev.* 55, 561–595. doi:10.1080/15583724.2015.1040552

Khan, R. S., Martinez, M. D., Sy, J. C., Pendergrass, K. D., Che, P.-l., Brown, M. E., et al. (2014). Targeting Extracellular DNA to Deliver IGF-1 to the Injured Heart. *Sci. Rep.* 4, 4257. doi:10.1038/srep04257

Lancuski, A., Fort, S., and Bossard, F. (2012). Electrospun Azido-PCL Nanofibers for Enhanced Surface Functionalization by Click Chemistry. *ACS Appl. Mater. Inter.* 4, 6499–6504.

Lee, S.-H., and Shin, H. (2007). Matrices and Scaffolds for Delivery of Bioactive Molecules in Bone and Cartilage Tissue Engineering. *Adv. Drug Deliv. Rev.* 59, 339–359. doi:10.1016/j.addr.2007.03.016

Levato, R., Planell, J. A., Mateos-Timoneda, M. A., and Engel, E. (2015). Role of ECM/peptide Coatings on SDF-1α Triggered Mesenchymal Stromal Cell Migration from Microcarriers for Cell Therapy. *Acta Biomater.* 18, 59–67. doi:10.1016/j.actbio.2015.02.008

Lin, Y., Wang, L., Zhang, P., Wang, X., Chen, X., Jing, X., et al. (2006). Surface Modification of Poly(l-Lactic Acid) to Improve its Cytocompatibility via Assembly of Polyelectrolytes and Gelatin. *Acta Biomater.* 2, 155–164. doi:10.1016/j.actbio.2005.10.002

Liu, Y., Li, D., Ding, J., and Chen, X. (2020). Controlled Synthesis of Polypeptides. *Chin. Chem. Lett.* 31, 3001–3014. doi:10.1016/j.cclet.2020.04.029

Lu, H., Hoshiba, T., Kawazoe, N., and Chen, G. (2012). Comparison of Decellularization Techniques for Preparation of Extracellular Matrix Scaffolds Derived from Three-Dimensional Cell Culture. *J. Biomed. Mater. Res. A.* 100, 2507–2516. doi:10.1002/jbm.a.34150

Madhurakkat Perikamana, S. K., Lee, J., Lee, Y. B., Shin, Y. M., Lee, E. J., Mikos, A. G., et al. (2015). Materials from Mussel-Inspired Chemistry for Cell and Tissue Engineering Applications. *Biomacromolecules* 16, 2541–2555. doi:10.1021/acs.biomac.5b00852

Marchioli, G., Luca, A. D., De Koning, E., Engelse, M., Van Blitterswijk, C. A., Karperien, M., et al. (2016). Hybrid Polycaprolactone/Alginate Scaffolds Functionalized with VEGF to Promote De Novo Vessel Formation for the Transplantation of Islets of Langerhans. *Adv. Healthc. Mater.* 5, 1606–1616. doi:10.1002/adhm.201600058

Matsuda, S., Harmansa, S., and Affolter, M. (2016). BMP Morphogen Gradients in Flies. *Cytokine Growth Factor. Rev.* 27, 119–127. doi:10.1016/j.cytogfr.2015.11.003

Morrell, N. T., Leucht, P., Zhao, L., Kim, J.-B., Ten Berge, D., Ponnusamy, K., et al. (2008). Liposomal Packaging Generates Wnt Protein with *In Vivo* Biological Activity. *PloS one* 3, e2930. doi:10.1371/journal.pone.0002930

Mueller, T. D., and Nickel, J. (2012). Promiscuity and Specificity in BMP Receptor Activation. *FEBS Lett.* 586, 1846–1859. doi:10.1016/j.febslet.2012.02.043

Park, H., Temenoff, J. S., Tabata, Y., Caplan, A. I., and Mikos, A. G. (2007). Injectable Biodegradable Hydrogel Composites for Rabbit Marrow Mesenchymal Stem Cell and Growth Factor Delivery for Cartilage Tissue Engineering. *Biomaterials* 28, 3217–3227. doi:10.1016/j.biomaterials.2007.03.030

Qi, H., Shan, P., Wang, Y., Li, P., Wang, K., and Yang, L. (2021a). Nanomedicines for the Efficient Treatment of Intracellular Bacteria: The "ART" Principle. *Front. Chem.* 9, 775682. doi:10.3389/fchem.2021.775682

Qi, H., Wang, Y., Fa, S., Yuan, C., and Yang, L. (2021b). Extracellular Vesicles as Natural Delivery Carriers Regulate Oxidative Stress under Pathological Conditions. *Front. Bioeng. Biotechnol.* 9, 752019. doi:10.3389/fbioe.2021.752019

Ratanavaraporn, J., Furuya, H., and Tabata, Y. (2012). Local Suppression of Pro-inflammatory Cytokines and the Effects in BMP-2-Induced Bone Regeneration. *Biomaterials* 33, 304–316. doi:10.1016/j.biomaterials.2011.09.050

Rompolas, P., Mesa, K. R., and Greco, V. (2013). Spatial Organization within a Niche as a Determinant of Stem-Cell Fate. *Nature* 502, 513–518. doi:10.1038/nature12602

Shachar, M., Tsur-Gang, O., Dvir, T., Leor, J., and Cohen, S. (2011). The Effect of Immobilized RGD Peptide in Alginate Scaffolds on Cardiac Tissue Engineering. *Acta Biomater.* 7, 152–162. doi:10.1016/j.actbio.2010.07.034

Silva, E. A., and Mooney, D. J. (2004). Synthetic Extracellular Matrices for Tissue Engineering and Regeneration. *Curr. Top. Dev. Biol.* 64, 181–205. doi:10.1016/s0070-2153(04)64008-7

Stafiej, P., Küng, F., Thieme, D., Czugala, M., Kruse, F. E., Schubert, D. W., et al. (2017). Adhesion and Metabolic Activity of Human Corneal Cells on PCL Based Nanofiber Matrices. *Mater. Sci. Eng. C* 71, 764–770. doi:10.1016/j.msec.2016.10.058

Tian, H., Du, J., Wen, J., Liu, Y., Montgomery, S. R., Scott, T. P., et al. (2016). Growth-Factor Nanocapsules that Enable Tunable Controlled Release for Bone Regeneration. *ACS Nano* 10, 7362–7369. doi:10.1021/acsnano.5b07950

Wade, R. J., Bassin, E. J., Gramlich, W. M., and Burdick, J. A. (2015). Nanofibrous Hydrogels with Spatially Patterned Biochemical Signals to Control Cell Behavior. *Adv. Mater.* 27, 1356–1362. doi:10.1002/adma.201404993

Wan, L. Q., Jiang, J., Arnold, D. E., Guo, X. E., Lu, H. H., and Mow, V. C. (2008). Calcium Concentration Effects on the Mechanical and Biochemical Properties of Chondrocyte-Alginate Constructs. *Cel. Mol. Bioeng.* 1, 93–102. doi:10.1007/s12195-008-0014-x

Xu, D., Wu, D., Qin, M., Nih, L. R., Liu, C., Cao, Z., et al. (2019). Efficient Delivery of Nerve Growth Factors to the Central Nervous System for Neural Regeneration. *Adv. Mater.* 31, e1900727. doi:10.1002/adma.201900727

Yang, L., Han, D., Zhan, Q., Li, X., Shan, P., Hu, Y., et al. (2019). Blood TfR+ Exosomes Separated by a pH-Responsive Method Deliver Chemotherapeutics for Tumor Therapy. *Theranostics* 9, 7680–7696. doi:10.7150/thno.37220

Yue, K., Trujillo-De Santiago, G., Alvarez, M. M., Tamayol, A., Annabi, N., and Khademhosseini, A. (2015). Synthesis, Properties, and Biomedical Applications of Gelatin Methacryloyl (GelMA) Hydrogels. *Biomaterials* 73, 254–271. doi:10.1016/j.biomaterials.2015.08.045

Zhang, L., Yu, Y., Feng, K.-C., Chuang, Y.-C., Zuo, X., Zhou, Y., et al. (2018). Templated Dentin Formation by Dental Pulp Stem Cells on Banded Collagen Bundles Nucleated on Electrospun Poly (4-vinyl Pyridine) Fibers *In Vitro*. *Acta Biomater.* 76, 80–88. doi:10.1016/j.actbio.2018.06.028

Zhang, L., Yu, Y., Joubert, C., Bruder, G., Liu, Y., Chang, C.-C., et al. (2016). Differentiation of Dental Pulp Stem Cells on Gutta-Percha Scaffolds. *Polymers* 8, 193. doi:10.3390/polym8050193

Zhao, D., Zhu, T., Li, J., Cui, L., Zhang, Z., Zhuang, X., et al. (2021). Poly(lactic-co-glycolic Acid)-Based Composite Bone-Substitute Materials. *Bioactive Mater.* 6, 346–360. doi:10.1016/j.bioactmat.2020.08.016

Zhu, T., Cui, Y., Zhang, M., Zhao, D., Liu, G., and Ding, J. (2020). Engineered Three-Dimensional Scaffolds for Enhanced Bone Regeneration in Osteonecrosis. *Bioactive Mater.* 5, 584–601. doi:10.1016/j.bioactmat.2020.04.008

Conflict of Interest: Authors YT and XL are employed by Beijing Research Institute of Chemical Industry, and author YZ is employed by Science and Technology Department, China Petrochemical Corporation.

The remaining authors declare that the research was conducted in the absence of any commercial or financial relationships that could be construed as a potential conflict of interest.

frontiers in Bioengineering and Biotechnology

ORIGINAL RESEARCH
published: 08 February 2022
doi: 10.3389/fbioe.2022.825146

Hypocapnia Stimuli-Responsive Engineered Exosomes Delivering miR-218 Facilitate Sciatic Nerve Regeneration

Yingshuai Wang[†], *Tao Yu*[†] *and Feihu Hu*[*]

School of Lifescience and Technology, Weifang Medical University, Weifang, China

Therapeutic strategies of microRNAs (miRNAs) and exosomes have been systematically explored as an enhancing application by paracrine and modulating cellular activity after internalization of recipient cells *in vitro*, and progressively developed to meet the requirements of peripheral nerve regeneration *in vivo*. However, how to obtain exosomes with superior properties and effectively deliver miRNAs becomes a key challenge. Hypocapnia environment might play unexpected outcomes in strengthening exosome function when culturing adipose-derived stem cells (ASCs). Previously, we discovered the intensive regulation of miR-218 on the differentiation of ASCs. In the present study, we analyzed the functional differences of secreted exosomes in response to hypocapnia stimulation, and explored the application in combination with miR-218 to facilitate sciatic nerve regeneration. Our results indicated that the delivery system of engineered exosomes derived from ASCs remarkably loads upregulated miR-218 and promotes cellular activity in the recipient cells (PC12 cells), and hypocapnia stimuli-responsive exosomes exhibit strengthening properties. Furthermore, in a sciatic nerve injury model, exosomes delivering miR-218 combined with engineered scaffold facilitated the regeneration of injured sciatic nerves. In the hypocapnia-stimulated exosome group, more encouraging promotion was revealed on the regeneration of motor and nerve fibers. Hypoc-miR-218-ASC exosomes are suggested as a promising cell-free strategy for peripheral nerve repair.

Keywords: peripheral nerve regeneration, hypocapnia environment, engineered exosomes, delivering miR-218, nerve tissue engineering

OPEN ACCESS

Edited by:
Mingqiang Li,
Sun Yat-sen University, China

Reviewed by:
Yingfeng Tu,
Southern Medical University, China
Lulu Cai,
University of Electronic Science and Technology of China, China

***Correspondence:**
Feihu Hu
hufh@wfmc.edu.cn

[†]*These authors have contributed equally to this work and share first authorship*

Specialty section:
This article was submitted to Biomaterials, a section of the journal Frontiers in Bioengineering and Biotechnology

Received: *30 November 2021*
Accepted: *17 January 2022*
Published: *08 February 2022*

Citation:
Wang Y, Yu T and Hu F (2022) Hypocapnia Stimuli-Responsive Engineered Exosomes Delivering miR-218 Facilitate Sciatic Nerve Regeneration. Front. Bioeng. Biotechnol. 10:825146. doi: 10.3389/fbioe.2022.825146

INTRODUCTION

Peripheral nerves have a limited capacity to self-repair, and repair of severe damage or serious defects is often clinically unsatisfactory, with less than 50% of patients regaining full functional recovery after surgical treatment (Kehoe et al., 2012). Although end-to-end anastomosis or bridge-gap grafts can be the gold standard for curative reconstruction, many novel therapeutic approaches including microRNA (miRNA) strategies are currently being developed and explored in basic, preclinical, and clinical trials. MiRNAs are acknowledged to be key regulators of various cellular processes by interfering with protein expression and mRNA degradation. Existing studies confirm the notable differences in miRNA profiles between autologous repair and tissue engineering-assisted regeneration. The intrinsic mechanisms and molecular targets have been extensively delved

(Yousefi et al., 2019). For example, in the initial period of nerve injury, the expressions of miR-204, miR-27a, and miR-29b were continuously down-regulated, while those of miR-182, miR-221/222, and miR-27a were reversed. MiR-30a, miR-124, miR-9, and miR-132 were wavily expressed during scaffold, facilitating the Schwann cells' migration, axonal regeneration, and myelination (Yu et al., 2015; Tang and Sun, 2020). In our previous studies, miR-218 could promote the differentiation of mesenchymal stem cells (MSCs) to neuronal cells by spatiotemporal induction, and cell-engineered grafts facilitated peripheral nerve regeneration in combination with tissue engineering scaffolds (Hu et al., 2017b; Hu et al., 2017c).

Additionally, the delivery and release of exogenous miRNAs can maximize the application and effectiveness of this therapeutic approach, and serve as an alternative strategy for peripheral nerve regeneration. As a novel and exciting delivery vehicle, exosomes therein have garnered widespread attention. Exosomes are extracellular vehicles and natural nanocarriers derived from various cell types, and can load bimolecular cargoes such as bioactive proteins, mRNAs, and miRNAs to mediate cell-to-cell communication. The intrinsic bioactivity helps to traverse the biological barrier and improve the steadiness in bloodstream. In comparison with artificial nanocarriers, the longer circulation time prolongs their absorption potential and medicinal effectiveness on targeted tissues and cells *in vitro* and *in vivo*. The wide sources, stable storage, easy modification, negligible rejection, and lower risk of tumorigenesis support the exosome delivery system as a new mode of cell-free therapy (Tian et al., 2014; Zhou et al., 2017; Huang et al., 2021; Park and Seo, 2021; Shafiei et al., 2021).

Inspired by this, specific miRNAs can be encapsulated into exosomes and transported to the site of lesion and injury. Exosomes delivering miR-126 promoted angiogenesis and reduced apoptosis after spinal cord injury (Huang et al., 2020). The microglial exosomal miR-124-3p inhibited neuronal inflammation in scratch-injured neurons (Yang et al., 2019). As a cargo, miR-17-92 cluster down-regulated protein kinase B and glycogen synthase kinase 3β, and accelerated myelin remodeling after delivery by exosomes of MSCs (Xin et al., 2017a).

It is noteworthy that the characteristics of exosomes vary with the conditions of their production. Lower gas environment enriched Zeb2/Axin2 to exosomes, and further alleviated axonal demise and promoted synaptic proliferation *in vitro* (Wei et al., 2021). Under the same conditions, the release of exosomes loaded with miR-133b was significantly increased, and the intra-arterially injection additionally enhanced neurons' elongation and brain plasticity in a cultured cortical embryonic rat (Xin et al., 2017b).

Due to this apparent discrepancy, in this study, we focused on the characteristic differences of exosomes derived from ASCs while culturing secretory cells in a low CO_2 environment (3% CO_2 conditions) and in the general environment (5% CO_2 conditions), and assessed the delivery ability of miR-218. We aimed to reveal the properties of stimuli-responsive exosomes upon transfer from ASCs to PC12 cells. The exploration of phagocytosis, migration, and proliferation helps to characterize the facilitation of cellular activity by exosomes.

In combination with injected exosomes, we fabricated a cell-free poly(3-hydroxybutyrate-co-3-hydroxyvalerate) (PHBV) nanofiber scaffold and transplanted it into a sciatic nerve injury model. The efficacy on injured neural tissue was exposed by motor functional restoration and histological assays. Our encouraging results help to explore the application of exosomes *in vivo*, especially hypocapnia environmental stimuli-responsive engineered exosomes. This study provides a promising cell-free approach for future clinical miRNA therapeutic strategies.

MATERIALS AND METHOD

Cell Culture

ASCs were extracted from adipose tissue as previously described (Zuk et al., 2002). The animal study was reviewed and approved by the Medical Ethics Committee of Weifang Medical University in China (no. 2019141). Briefly, the inguinal subcutaneous fat tissue was isolated from Sprague–Dawley (SD) rats. After digestion with 0.1% collagenase I and II (Sigma-Aldrich, United States) for 2 h, the cells were centrifuged and cultured with Dulbecco's modified Eagle medium (DMEM; Thermo Fisher Scientific, United States) with 5% fetal bovine serum (FBS; Thermo Fisher Scientific, United States) at 37°C in a 5% CO_2 environment. The medium was changed every 3 days, and cells were passaged for subsequent studies until 80% confluence was reached.

Isolation and Characterization of Exosomes

Herein, to remove the interference of FBS, ASCs were cultured in a specially treated basal medium (added FBS was vesicle-depleted by an overnight ultracentrifugation at 110,000 g), and exosomes were purified by ultracentrifugation (Liang et al., 2011). The hypocapnia stimuli-responsive exosomes were achieved as follows: ASCs were cultured in a hypocapnia environment (3% CO_2 conditions) for 48 h, and the first culture medium was harvested. The fresh basal medium was subsequently added and maintained for 48 h to form a second culture medium. All mediums were collected for the isolation of exosomes. Meanwhile, the medium of ASCs cultured in the general environment (5% CO_2 condition) was served as control. The mediums were centrifuged at 300 × g for 5 min to eliminate cells, and 10,000 × g for 30 min for removing debris of cells. Finally, the supernatant was centrifuged at 100,000 × g (ultracentrifugation) for 8 h twice for purification of exosomes by L-100 XP ultracentrifuge (Beckman Coulter, United States) (**Figure 1**). The purified exosomes (Hypoc-ASCs-Exo group and ASCs-Exo group) were resuspended into PBS and stored at −80°C.

The morphology of exosomes was observed by transmission electron microscopy (TEM). Exosomes were transferred onto a carbon-coated grid, kept at room temperature for 20 min, and then visualized under TEM (JEM-2100, JEOL, Japan). The vesicle size distribution was characterized by dynamic light scattering (DLS, Zetasizer Nano ZS, United Kingdom). The specific markers were confirmed as **Supplementary Figure S1**.

Construction of miR-218 Plasmids and Exosomes Delivering miR-218

MiR-218 plasmids were designed as shown in **Figure 3**. The multiple cloning site of pPG-eGFP-miR plasmid was inserted with miR-218 objective genes (sense strand), loop, and antisense strand. Enhanced green fluorescence protein (eGFP) was used for a reporter. ASCs were seeded onto 35 mm dish and incubated until 80% confluence, and 10 μl Superfectin Transfection Reagent (Qiagen, Canada) and miR-218 or miR-NC plasmids were added to the medium for transfection. After 24 and 48 h, positive expressions of eGFP were assayed by microscopic fluorescence to identify transfection efficiency (Ti-U Nikon, Japan).

ASCs of highly expressed miR-218 were cultured in hypocapnia and general environments, and the specific exosomes delivering miRNAs were isolated as described above. Expression levels of miR-218 were measured by quantitative real-time PCR in untreated ASCs (Control group), miR-218-transfected ASCs (miR-218-ASCs group), isolated exosomes from generally cultured miR-218-transfected ASCs (miR-218-ASCs-Exo group), and isolated exosomes from hypocapnia-cultured miR-218-transfected ASCs (Hypoc-miR-218-ASCs-Exo group).

PC12 Cells Activity After Internalizing the Exosomes Delivering miR-218

Cellular uptake and distribution of exosomes in PC12 cells were visualized by labeling of fluorescent dye 3,3′-dioctadecyloxacarbocyanine perchlorate (DiO, beyotime, China) under a microscope. Samples (miR-218-ASCs-Exo and Hypoc-miR-218-ASCs-Exo) were incubated with 5 μM DiO at 37°C for 20 min. After two cycles of washing-centrifugation, exosomes were resuspended in PBS. As a widely neural model, PC12 cells were used to expose the deliverable function of exosomes (Westerink and Ewing, 2008). The distribution of DiO-labeled exosomes was analyzed as follows: PC12 cells were seeded onto 35 mm dish and incubated until 80% confluence. Cells were then incubated with the basal culture medium supplemented with 5 μg/ml DiO-labeled exosomes for 24 h. Next, cell nuclei were stained with Hoechst 33342 (Shanghai Shenggong Co., Ltd., China), and fluorescence images were recorded by the confocal fluorescence microscope (Zeiss LSM710, Germany).

The scratch assay was applied to expose the migratory characteristics of PC12 cells' response to two exosomes (miR-218-ASCs-Exo and Hypoc-miR-218-ASCs-Exo groups) as follows: PC12 cells were seeded onto 35 mm dish and incubated until 80% confluence, and a wound maker scratched across to form a physical gap. The two groups of exosomes of 5 μg/ml were added to the scratched cell medium. After 24 h, the scratched images of PC12 cells were microscopically recorded. The transwell assay further assessed the cytotaxis of PC12 cells. Briefly, the PC12 cells placed on the upper layer could be driven across the cell-permeable membrane (8 μm aperture) by the exosomes in the lower layer. After 48 h, the cells were stained by Hoechst 33342 and counted in a view field. Furthermore, the mediums with different contents and sources exosomes (the miR-218-ASCs-Exo and Hypoc-miR-218-ASCs-Exo of 5 μg/ml, 10 μg/ml, and 20 μg/ml) were used to culture PC12 cells (the untreated cells were served as a control), and cell viability was evaluated by the Cell Counting Kit-8 method (Dojindo, Kumamoto, Japan) at 24 and 48 h.

Quantitative Real-Time PCR

The expression levels of miR-218 and targeted genes (*Robo 1*, *Robo 2*, *Sfrp 2*, and *Dkk 2*) were examined by qRT-PCR. The RNA was isolated from un-treated PC12 cells (Control group), PC12 cells transfected miR-218 (miR-218 group), and PC12 cells treated by two kinds of exosomes (miR-218-ASCs-Exo and Hypoc-miR-218-ASCs-Exo groups). According to the M-MLV reverse transcriptase instructions, RNA was converted to cDNA. The PCR reactions were performed using One-step 2 × SG Green qRT-PCR Mix (TaKaRa, China) on the ABI 7500 system (Application Biosystems, United States). The *U6* and *Gapdh* were used as housekeeping genes.

Preparation of Nanofibrous Scaffold and Animal Surgical Procedures

Herein, the PHBV nano-fiber films were obtained *via* the electrospinning technique as previously described (Hu et al., 2017a). In brief, PHBV (no. 403121, Sigma-Aldrich, Germany) was dissolved in TFE (2,2,2-trifluoroethanol, Guangzhou Darui Company, China) to form a 2% (w/v) solution. The nano-fiber films were fabricated by the TL-01 type electrospinning apparatus (Shenzhen TongliWeina Technology Company, China). The biocompatibility were detected as **Supplementary Figures S2, S3**.

PHBV nanofibrous scaffolds were gifted to a rat sciatic nerve injury model *in vivo*. First, the films were rolled into a hollow tubular structure. In surgical procedures, SD rats were anesthetized, and sciatic nerves were exposed and truncated. The ends of segment were inserted into the lumen of conduit, and the incision was closed with silk sutures. Animals were fed *ad libitum* and kept in a standard environment. After 2 days, rats (n = 15) were randomly divided into three groups. Intravenous injections of 2 mg exosomes were performed for each rat *via* tail vein every 3 days continuously for 4 weeks (PHBV-miR-218-ASCs-Exo group and PHBV-Hypoc-miR-218-ASCs-Exo group). Rats of PHBV group were injected with PBS.

Sciatic Function Index and Gastrocnemius Muscle Analysis

The recovery of motor function was analyzed by the sciatic function index (SFI) (Bain et al., 1989). The lengths of the third toe to heel (PL), the first to fifth toe (TS), and the second to fourth toe (IT) were measured on the experimental side (E) and contralateral normal side (N) in each rat. The SFI value was calculated by the following formula: SFI = 109.5*(E'TS−N'TS)/N'TS+13.3*(E'IT−N'IT)/N'IT−38.8*(E'PL−N'PL)/N'PL−8.8. The 0 value represents normal nerve function, and around −100 value represents total dysfunction. At weeks 4 and 8, three groups of rats were allowed to walk across a 100-cm long

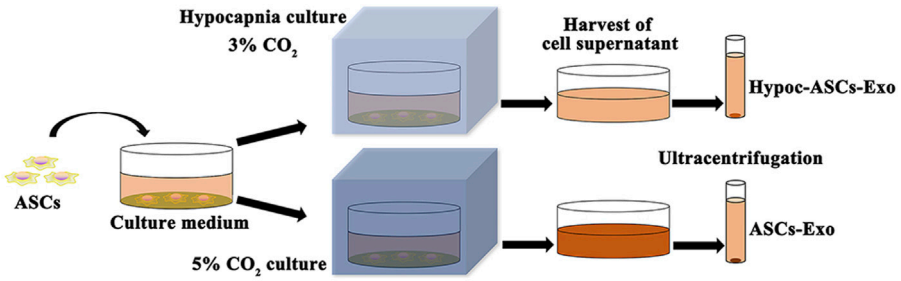

FIGURE 1 | Schematic representations of exosomes isolated from two cultured environments.

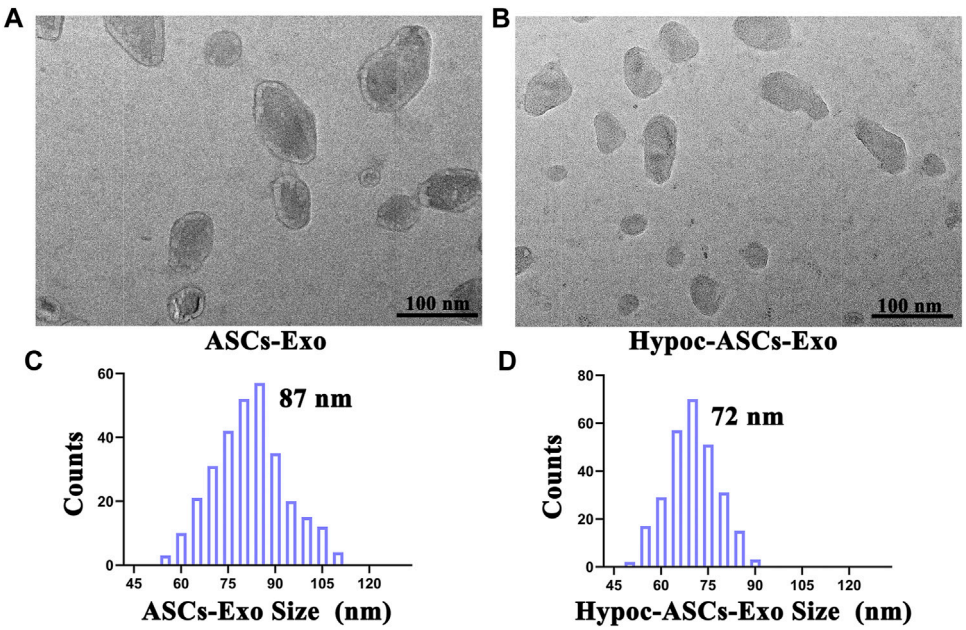

FIGURE 2 | Morphology and diameter distribution of ASCs-Exo and Hypoc-ASCs-Exo. **(A,B)** Morphology of exosomes were assessed by TEM (scale bars = 100 nm). **(C,D)** Diameter of the exosomes was assessed by dynamic laser scattering (DLS).

channel in order to record footprints along the way. At the end of research, the gastrocnemius muscle of three groups was dissected and weighed on an electronic balance (while still wet). The atrophy of gastrocnemius muscle was calculated by wet weight of injured limb and control (100% ratio).

Histological Examination

Gastrocnemius muscle and regenerated nerve were stained and analyzed to evaluate the recovery of muscle, nerve fiber, and myelin sheath. Muscles and central segment nerves were fixed in 10% buffered formalin for 48 h. Samples were dehydrated through a graded ethanol series, cleared in xylene, and cut into 5-μm-thick sections after paraffin embedding. Transverse sections of gastrocnemius muscle were stained with Masson trichrome, and nerve samples were stained with hematoxylin and eosin (H&E) and observed by microscope.

Statistical Analysis

The results were expressed as the mean ± SD. Statistical analysis was performed using GraphPad Prism software.

RESULTS

Characterization of ASCs-Exo

Exosomes were isolated from cell supernatant by ultracentrifugation and characterized using TEM and DLS (**Figures 2A–D**). Photographs revealed that the ASCs-Exo group has a typical saucer-like bilayer membrane structure with an average diameter of 87 nm. Notably, TEM images indicated a few moderate morphological differences compared to hypocapnia environment-derived products, such as slightly smaller average diameter (72 nm) in the Hypoc-ASCs-Exo group. DLS assays were consistent with

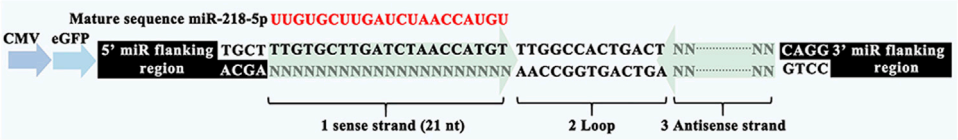

FIGURE 3 | Design and construction of miR-218-5p plasmid.

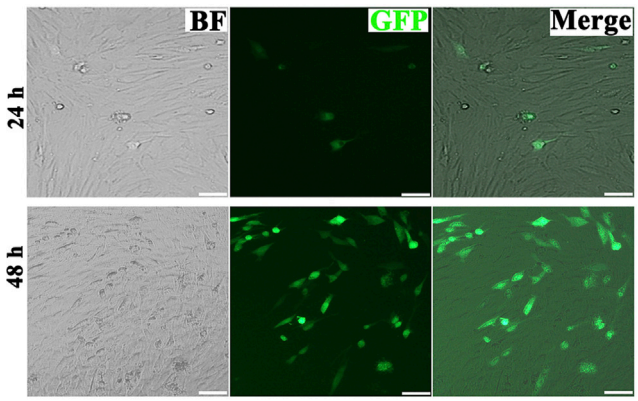

FIGURE 4 | Micrographs of fluorescent, bright field, and merged images of transfected ASCs after 24 and 48 h (scale bars = 20 μm).

TEM morphology in terms of size distribution. The morphologies and size distribution supported that the hypocapnia environment can also stimulate ASCs to secrete exosomes with noteworthy differences of physical size from those obtained in the general environment.

Construction and Validation of miR-218-ASCs-Exo

To verify whether exosomes can concentrate and deliver miR-218, and evaluate the miR-218-regulative strategy, we constructed an expressed plasmid of miR-218 *in vitro* (**Figure 3**). The appearance and increase of eGFP-positive cells proved the successful expression of miR-218 plasmid in ASCs (**Figure 4**). qRT-PCR measured the expression levels of miR-218 in four groups. Compared to the baseline of the miR-218 expressed level in untreated ASCs (Control group), ASCs transfected with miRNA plasmid had 27.2-fold upregulation. As cytoplasmic secretion products, exosomes of two groups highly packed the mature miR-218 (7.8-fold in miR-218-ASCs-Exo group and 9.4-fold in Hypoc-miR-218-ASCs-Exo group) (**Figure 5**). Next, the phagocytosis of PC12 cells was used to analyze the delivery properties of exosomes between different cells. The clear and perinuclear dotted staining confirmed that exosomes isolated from ASCs are successfully transported to the cytoplasm of PC12 cells as expected, highlighting similarities regardless of miR-218-ASCs-Exo or Hypoc-miR-218-ASCs-Exo groups (**Figure 6**).

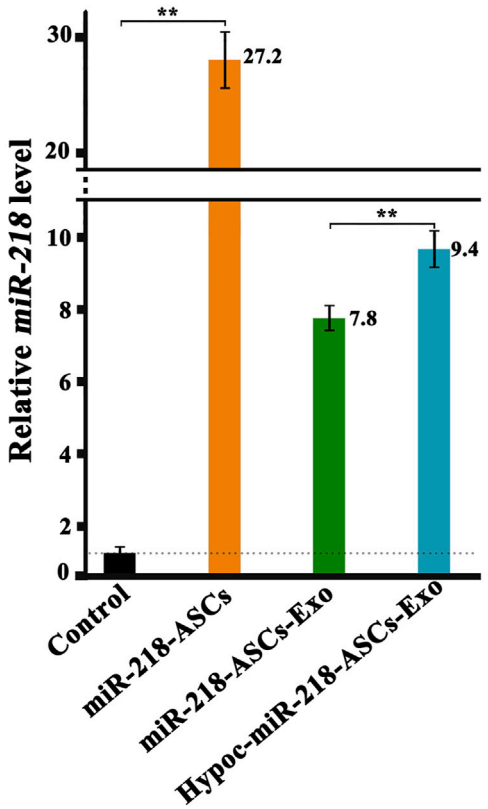

FIGURE 5 | Expression levels of miR-218 in untreated ASCs (normalization and served as the Control group, C group), transfected ASCs (miR-218-ASCs group), exosomes isolated from general environment cultured the transfected ASCs, and exosomes isolated from hypocapnia environment cultured the transfected ASCs.

Enhancement of PC12 Cells Viability by Internalized miR-218-ASCs-Exo and Hypoc-miR-218-ASCs-Exo

The wound-healing approach exposed the migration characteristics of PC12 cells after internalizing exosomes. After 24 h, compared to group of non-exosomes added to the medium (control group), quantitative analysis of scratched distance exhibited a statistically significant shrinkage in the Hypoc-miR-218-ASCs-Exo and miR-218-ASCs-Exo treatment groups (**Figures 7A,B**). In the transwell tests, the Hypoc-miR-218-ASCs-Exo group showed a higher number of nuclei stained with 111 cells than 87 cells in a view field (**Figures 8A,B**). The above results confirmed that Hypoc-miR-218-ASCs-Exo increases PC12

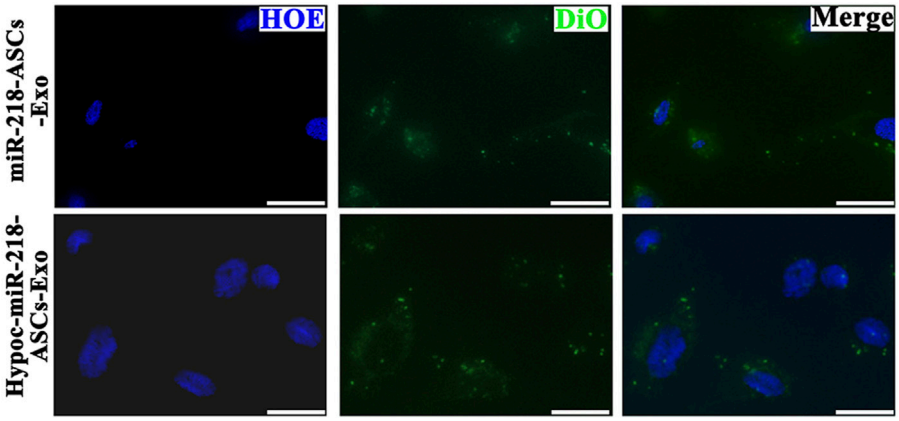

FIGURE 6 | Confocal images of DiO-labeled exosomes (green) and nuclei (blue) were monitored by microscope in two groups (scale bars = 10 μm).

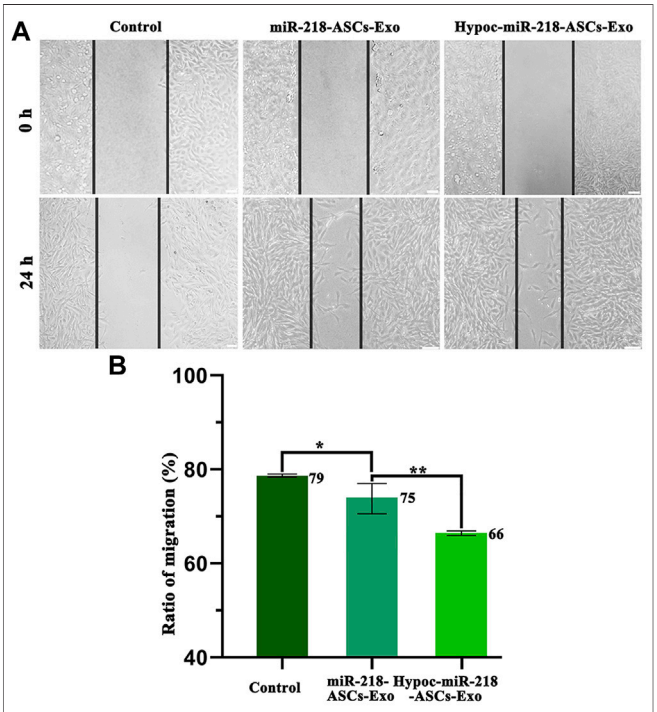

FIGURE 7 | Scratch assay and ratio of migration. **(A)** Images of control (untreated PC12 cells' group), miR-218-ASCs-Exo (miR-218-ASCs-Exo-treated PC12 cells' group), and Hypoc-miR-218-ASCs-Exo (Hypoc-miR-218-ASCs-Exo-treated PC12 cells' group) at 0 and 24 h. **(B)** Ratio of migration (%) was calculated in three groups, respectively, at 24 h.

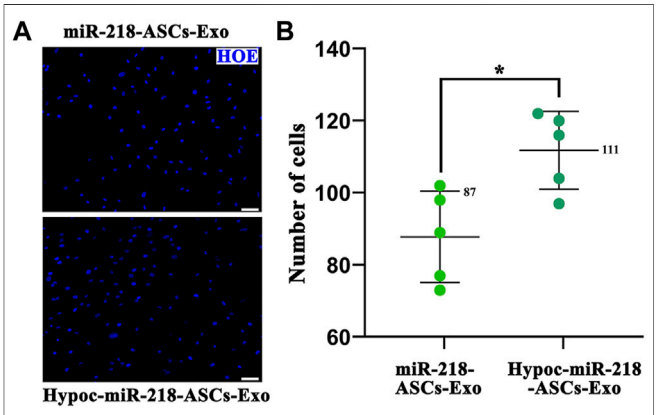

FIGURE 8 | Transwell assay. **(A)** Nuclei of the cell across the membrane were stained by Hoechst 33342 (blue) (scale bars = 50 μm). **(B)** Cell number in a view field was counted, respectively, in two groups.

viability and promotes migration after the internalization of exosomes. Furthermore, cell proliferation results observed that the addition of exosomes may inhibit cell division and proliferation, and with the increase of dose and duration, the differences between groups are continuously widened in a dose-dependent manner. The Hypoc-miR-218-ASCs-Exo-treated PC12 cells performed differential property *versus* the miR-218-ASCs-Exo group (**Figure 9**).

Targeting of miR-218 Delivered by Exosomes

The levels of miR-218 target genes (*robo1* and *robo2*) and Wnt signaling antagonist genes (*sfrp 2* and *dkk2*) were validated by qRT-PCR. In comparison with untreated PC12 cells (Control group), exosomes of miR-218-ASCs-Exo or Hypoc-miR-218-ASCs-Exo groups could deliver miRNA to PC12 cells and suppress the expression levels of target genes (**Figure 10**), although with profound discrepancies to the directly transfected group (miR-218 group).

Facilitation of Exosomes With PHBV Scaffold on Sciatic Nerve Recovery

We fabricated PHBV nanofibrous scaffold to facilitate the application of exosomes for the repair of sciatic nerve injury *in vivo*. After 4 and 8 weeks of surgery, the SFI values of PHBV-miR-218-ASCs-Exo and PHBV-Hypoc-miR-218-ASCs-Exo groups were significantly higher than the PHBV group (−41

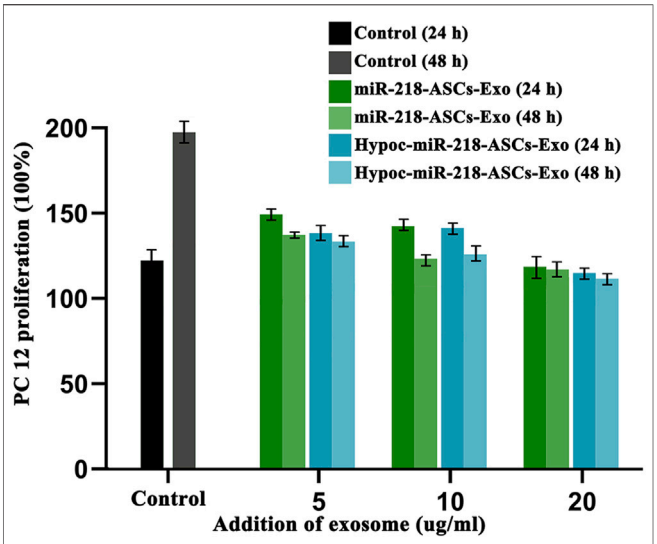

FIGURE 9 | PC12 proliferation was tested after the cultured medium was added to 5 μg/ml, 10 μg/ml, and 20 μg/ml exosomes. Untreated PC12 cells served as the Control group. Expression levels of miR-218 targeted genes (*Robo 1*, *Robo 2*, *Sfrp 2*, and *Dkk 2*) were examined by qRT-PCR in untreated PC12 cells (Control group), PC12 cells of transfected miR-218 plasmid, and two exosomes groups.

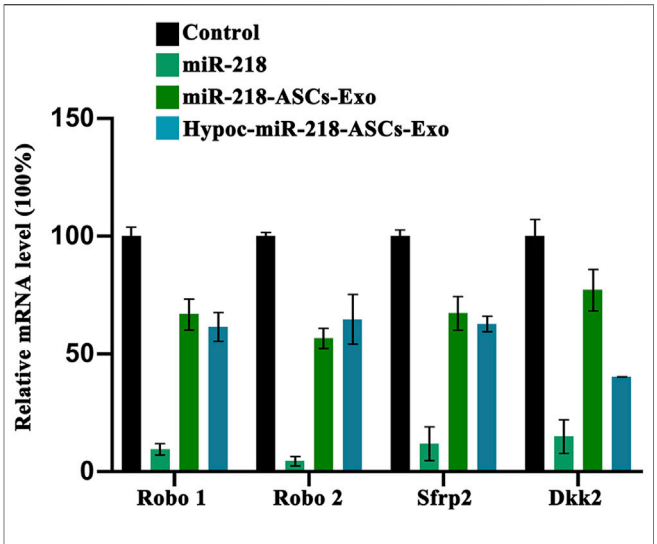

FIGURE 10 | Expression levels of miR-218 targeted genes (*Robo 1*, *Robo 2*, *Sfrp 2*, and *Dkk 2*) were examined by qRT-PCR in untreated PC12 cells (Control group), PC12 cells of transfected miR-218 plasmid, and two exosomes groups.

and −53 compared to −70, and −18 and −27 compared to −61) (**Figures 11A,B**). The wet weight ratio of gastrocnemius muscle in the PHBV-Hypoc-miR-218-ASCs-Exo group was approximated to the PHBV-miR-218-ASCs-Exo group, showing difference with the Control group (PHBV group, 86 and 85% compared to 79%) (**Figures 12A,B**).

The morphology of gastrocnemius muscles was similar to that of the normal muscles and showed slight atrophy of fibers in three groups (**Figures 13A,B**). However, the fibers area results supported the statistical difference in three groups (115 and 112% compared to 100%). In the regional enlarged drawing (**Figure 14**), histological examination of regenerated nerve fibers showed a dense structure with no significant difference in axon diameter or myelin thickness (green arrows). Conversely, more SC nuclei (blue arrows) were found in the PHBV-miR-218-ASCs-Exo group, especially in the PHBV-Hypoc-miR-218-ASCs-Exo group. Encouraging regenerated neural tissues supported that unite PHBV scaffold, the intravenous injections of exosomes, can promote nerve regeneration, and the exosomes stimulated and acquired by hypocapnia further adequately facilitate sciatic nerve recovery.

DISCUSSION

Tissue engineering therapies, including functional cell implants and cell-free physically engineered scaffolds, have been proven effective in promoting nerve regeneration. During repair, a variety of secreted factors are delivered to the injury sites and positively affect the survival and reproduction of neural cells, and a part of the agents is found to be enriched in exosomes. Significant discrepancies are observed in cellular exosomes from different sources, including the type and content of mRNAs, miRNAs, and proteins. This is an unavoidable obstacle in the clinical application of exosomes, and also provides opportunities for the preparation of personalized vectors. In the present study, we set out to investigate the application of miRNA therapy based on exosomes delivering miR-218 in sciatic nerve repair and systematically dissected the differential characteristics of exosomes when the secretory cells (ASCs) were cultured in a lower CO_2 environment.

First, photographs indicated the successful isolation of exosomes. A slightly narrower size was noticed in Hypoc-ASCs-Exo. Regarding these alterations, we speculated that it was a consequence of hypocapnia environment, as all other procedures used to purify exosomes were identical. In our subsequent findings, it was further demonstrated that the smaller sizes in the Hyoc-ASCs-Exo group are more conducive to deliver miR-218, and assist miRNAs to perform a stronger regulatory function. Essentially, the physical properties of exosomes could influence the intercellular communication (Van Deun et al., 2014). Caponnetto et al. (2017) proved that the therapeutic use of exosomes can be enhanced by using size as a parameter to select functionally different sub-populations. Compared to the 81 nm, a smaller particle size distribution (43 nm) was more preferentially and rapidly absorbed by A172 human glioblastoma cells, triggering a stronger cellular motility response.

While exosomes loaded miRNAs, the selected cargoes were orchestrated. Green fluorescence confirmed the success of transfection even as primary culture cells, and ASCs undergo readily clonal distribution to resist transfection reagents. High levels of miR-218 in two groups distinctly indicated miR-218 are

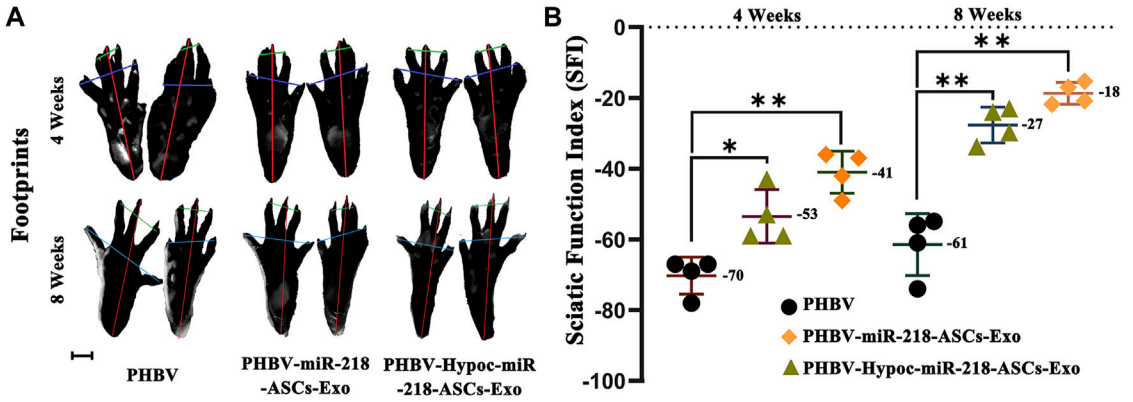

FIGURE 11 | SFI of sole PHBV scaffold (PHBV group), scaffold combined with miR-218-ASCs exosomes (PHBV-miR-218-ASCs-Exo group), and scaffold combined with Hypoc-miR-218-ASCs exosomes (PHBV-Hypoc-miR-218-ASCs-Exo group) were tested after animal surgical procedures. **(A)** Footprints of three groups (scale bars = 2 mm). **(B)** SFI values of three groups.

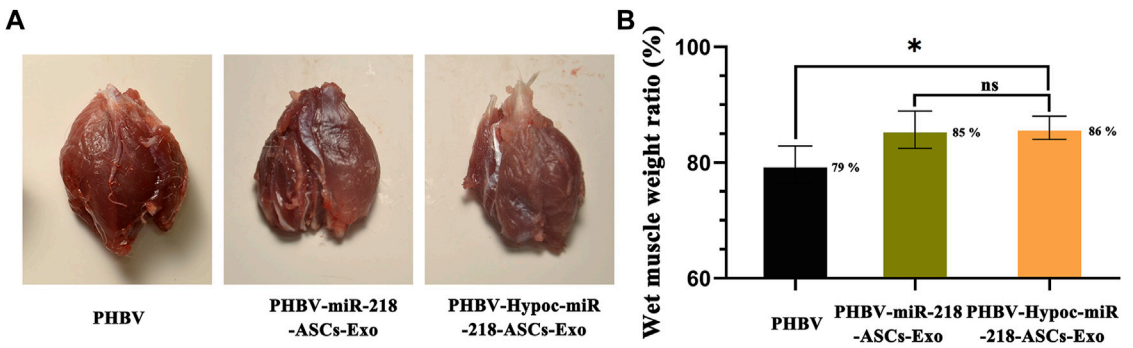

FIGURE 12 | Wet weight of gastrocnemius muscles was tested after animal surgical procedures. **(A)** Images of gastrocnemius muscles of three groups. **(B)** Atrophy of gastrocnemius muscle was calculated by wet weight of injured limb and Control group in three groups.

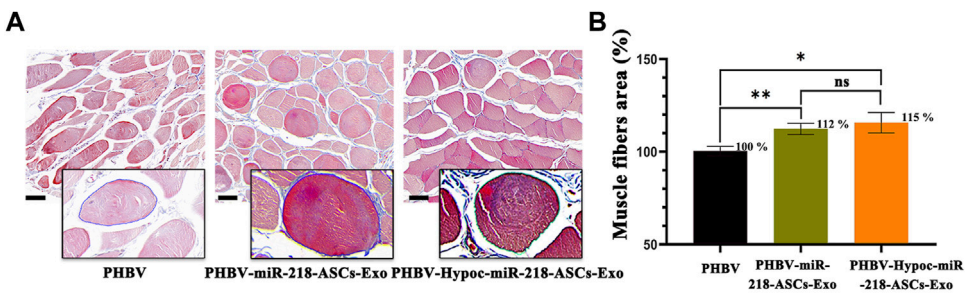

FIGURE 13 | Masson trichrome staining of three gastrocnemius muscles groups. **(A)** Image of masson trichrome staining of three groups (scale bars = 40 μm). **(B)** Muscles fibers area was calculated.

internalized and transferred from cytoplasm to the exocytosed exosomes. In tumors, cancer cells with high migration and activity are usually accompanied by high expression of miR-218, and upregulation inhibits the migratory ability (Zhu et al., 2016; Sun et al., 2021). In contrast, in the differentiation of MSCs, angiogenesis, hair regrowth, *etc.*, upregulated miR-218 plays positive stimulators on cellular activity. These contradictory properties of miR-218 deserve attention. The almost filled gaps and higher numbers revealed that miR-218 seemingly promotes the activity of PC12. However, our proliferation assays performed the opposite indication. Combined with existing studies, a reasonable explanation was that upregulated or delivered miR-

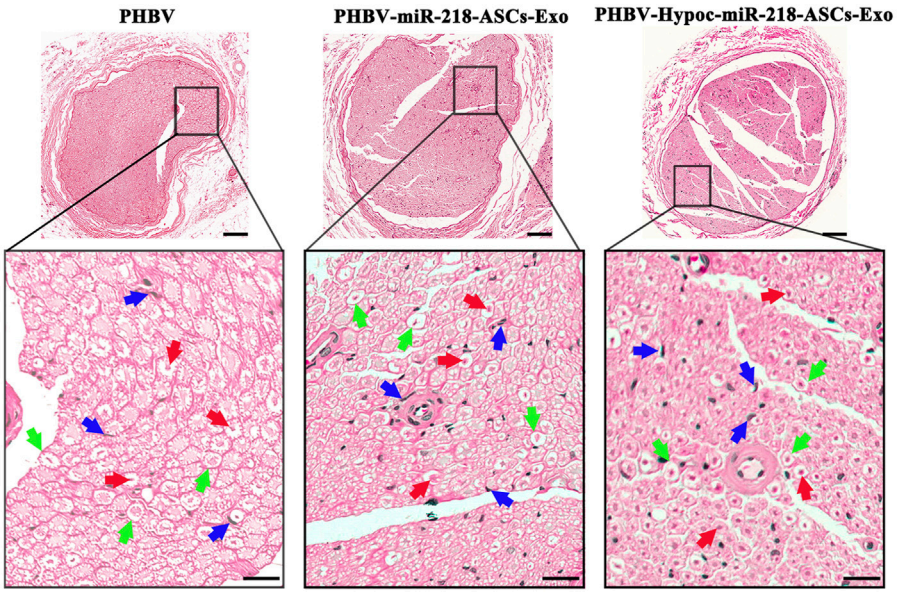

FIGURE 14 | H&E staining of regenerated nerve tissue (scale bars = 100 μm), and red arrows pointed out axon, blue arrows pointed out SCs nucleus, and green arrows pointed out myelin sheath in regional enlarged drawing (scale bars = 20 μm).

218 strengthens cellular activity and enhances the migration ability of PC12 cells rather than proliferation.

The exosomes delivering miR-218 suppressed the target gene (including the *Sfrp 2* and *Dkk 2*) in PC12 cells. The results were a hallmark of positive expression of Wnt signaling pathways. In the growth of hair shafts, the *β-Catenin* and T-cell-specific factor transcriptional activity were activated by miR-218 and targeted *Sfrp 2* (Hu et al., 2020). Melnik et al. exposed the dynamic governor of miR-218 and Wnt signaling on the hypertrophic degeneration of cartilage tissue after ectopic transplantation (Melnik et al., 2020). The abovementioned results suggested that exosomes delivering miR-218 (including Hypoc-miR-218-ASCs-Exo group) may have an enhanced role in the development and regeneration of nerve fibers *in vivo*.

At present, PHBV nano-fiber scaffold has been used as a support construction for cell growth in reconstructing damaged tissues or organs. In this study, the manufactured PHBV scaffold and injection of exosomes adequately helped sciatic nerve regeneration by a cell-free tissue engineering. Existing evidence discovered that during peripheral nerve repair, wound healing and nerve fiber re-extension and re-attachment are established on the physical elastic support and myelin wrap around the axons (Han et al., 2019). All processes might depend on the secretion of collagen, whereas they were exactly the target of miR-218. In gastric cancer, the expressions of collagen type I were correlated with miR-218 (Zhang et al., 2016). In Guo et al.'s research, overexpression of miR-218 suppressed the degradation of collagen type I and IV to overcome the homeostasis loss of connective tissue (Guo et al., 2019). Notably, facilitation of regeneration and recovery was distinctly accelerated, especially in the motorial function. The generation of motor neuron has been attributed to the interacted action of transcription factors such as *Olig2*, *Isl1*, and *Irx3*. The efficient trigger of *Isl1-Lhx3* in a temporal approach could induce motor neuron, and miR-218 was discovered as a downstream effector (Thiebes et al., 2015).

In addition, myelination of SCs is pivotal in neural repair, and our results showed a greater presence of SCs nuclei in PHBV-miR-218-ASCs-Exo and PHBV-Hypoc-miR-218-ASCs-Exo groups. Herein, we suggested that ASC-secreted exosomes may deliver myelin-promoting factors along with delivering miR-218. Bucan et al. noted that ASC exosomes can be internalized by SCs and significantly increase the proliferation. They first demonstrated that ASC exosomes are enriched with multiple neurotrophic factors, such as glial cell-derived neurotrophic factor (GDNF), fibroblast growth factor-1 (FGF1), brain-derived neurotrophic factor (BDNF), insulin-like growth factor-1 (IGF1), and nerve growth factor (NGF). The beneficial effects triggered by exosomes are closely related to the shuttling of these neurotrophic factors (Bucan et al., 2019). Thus, bioactive molecules related to nerve repair and exosomes delivering high-level miR-218 provide profound support on the axonal outgrowth, SC myelination, and nerve fiber regeneration. In the Hypoc-miR-218-ASCs-Exo group, higher encouraging regeneration was attributed to the lack of sufficient CO_2 supply, resulting in a modest change of pH-stimulated cell secretion. ASCs were forced to undergo adaptive alterations and enhanced exosome inclusion and loading capacity, and in this context, the concentrated miR-218 and exosomes finally promoted neural repair *in vivo*. Taken together, this study provides new insights into the hypocapnic environment stimulating the secretion of exosomes. Nevertheless, potential manipulatory mechanisms of specific miR-218 from Hypoc-miR-218-ASCs exosomes on the regeneration of neuronal cells or SCs and combinatorial

effectiveness of exosomes with other unclarified activators need further exploration.

CONCLUSION

The hypocapnia environment could stimulate ASCs to secrete exosomes of smaller size. These exosomes more effectively concentrated the intracellular miR-218 and delivered to recipient cells. As exogenously elements, the special exosomes played as regulators in promoting migratory activity rather than proliferation. *In vivo*, Hypoc-miR-218-ASCs-Exo further accelerated the healing of sciatic nerve injury and promoted the tissue regeneration and motor functional recovery by enhancing myelination. Satisfactory outcomes suggested that environmental modulation becomes an effective treatment of manipulating exosome secretion and function, and the combination of scaffold and exosomes can be novel strategies in peripheral nerve regeneration.

DATA AVAILABILITY STATEMENT

The original contributions presented in the study are included in the article/**Supplementary Material**; further inquiries can be directed to the corresponding author.

ETHICS STATEMENT

The animal study was reviewed and approved by the Medical Ethics Committee of Weifang Medical University in China.

AUTHOR CONTRIBUTIONS

YW and TY designed the work and performed all the experiments. FH wrote the manuscript. TY and FH contributed to the manuscript overview and correction.

FUNDING

This work was supported by the Natural Science Foundation of Shandong Province (ZR2018BC025) and the National Natural Science Foundation of China (81802905).

SUPPLEMENTARY MATERIAL

The Supplementary Material for this article can be found online at: https://www.frontiersin.org/articles/10.3389/fbioe.2022.825146/full#supplementary-material

REFERENCES

Bain, J. R., Mackinnon, S. E., and Hunter, D. A. (1989). Functional Evaluation of Complete Sciatic, Peroneal, and Posterior Tibial Nerve Lesions in the Rat. *Plast. Reconstr. Surg.* 83 (1), 129–136. doi:10.1097/00006534-198901000-00024

Bucan, V., Vaslaitis, D., Peck, C.-T., Strauss, S., Vogt, P. M., and Radtke, C. (2019). Effect of Exosomes from Rat Adipose-Derived Mesenchymal Stem Cells on Neurite Outgrowth and Sciatic Nerve Regeneration after Crush Injury. *Mol. Neurobiol.* 56 (3), 1812–1824. doi:10.1007/s12035-018-1172-z

Caponnetto, F., Manini, I., Skrap, M., Palmai-Pallag, T., Di Loreto, C., Beltrami, A. P., et al. (2017). Size-dependent Cellular Uptake of Exosomes. *Nanomedicine: Nanotechnology, Biol. Med.* 13 (3), 1011–1020. doi:10.1016/j.nano.2016.12.009

Guo, J., Zeng, X., Miao, J., Liu, C., Wei, F., Liu, D., et al. (2019). Expression of Concern: MiRNA-218 Regulates Osteoclast Differentiation and Inflammation Response in Periodontitis Rats through Mmp9. *Cell Microbiol.* 21 (4), 13. doi:10.1111/cmi.12979

Han, Y., Li, X., Zhang, Y., Han, Y., Chang, F., and Ding, J. (2019). Mesenchymal Stem Cells for Regenerative Medicine. *Cells* 8 (8), 886. doi:10.3390/cells8080886

Hu, F., Chen, T., and Wang, W. (2017a). Effects of Polyethylene Oxide and Poly(3-Hydroxybutyrate-Co-3-Hydroxyvalerate) Nanofibrous Substrate on Omental Adipose-Derived Mesenchymal Stem Cell Neuronal Differentiation and Peripheral Nerve Regeneration. *RSC Adv.* 7 (68), 42833–42844. doi:10.1039/c7ra08008e

Hu, F., Sun, B., Xu, P., Zhu, Y., Meng, X., Teng, G., et al. (2017b). MiR-218 Induces Neuronal Differentiation of ASCs in a Temporally Sequential Manner with Fibroblast Growth Factor by Regulation of the Wnt Signaling Pathway. *Sci. Rep.* 7, 39427. doi:10.1038/srep39427

Hu, F., Zhang, X., Liu, H., Xu, P., Doulathunnisa, Teng, G., et al. (2017c). Neuronally Differentiated Adipose-Derived Stem Cells and Aligned PHBV Nanofiber Nerve Scaffolds Promote Sciatic Nerve Regeneration. *Biochem. Biophysical Res. Commun.* 489 (2), 171–178. doi:10.1016/j.bbrc.2017.05.119

Hu, S., Li, Z., Lutz, H., Huang, K., Su, T., Cores, J., et al. (2020). Dermal Exosomes Containing miR-218-5p Promote Hair Regeneration by Regulating β-catenin Signaling. *Sci. Adv.* 6 (30), 11. doi:10.1126/sciadv.aba1685

Huang, J.-H., Xu, Y., Yin, X.-M., and Lin, F.-Y. (2020). Exosomes Derived from miR-126-Modified MSCs Promote Angiogenesis and Neurogenesis and Attenuate Apoptosis after Spinal Cord Injury in Rats. *Neuroscience* 424, 133–145. doi:10.1016/j.neuroscience.2019.10.043

Huang, J., Xiong, J., Yang, L., Zhang, J., Sun, S., and Liang, Y. (2021). Cell-free Exosome-Laden Scaffolds for Tissue Repair. *Nanoscale* 13 (19), 8740–8750. doi:10.1039/d1nr01314a

Kehoe, S., Zhang, X. F., and Boyd, D. (2012). FDA Approved Guidance Conduits and Wraps for Peripheral Nerve Injury: A Review of Materials and Efficacy. *Injury* 43 (5), 553–572. doi:10.1016/j.injury.2010.12.030

Liang, G. F., Zhu, Y. L., Sun, B., Hu, F. H., Tian, T., Li, S. C., et al. (2011). PLGA-based Gene Delivering Nanoparticle Enhance Suppression Effect of miRNA in HePG2 Cells. *Nanoscale Res. Lett.* 6, 447. doi:10.1186/1556-276x-6-447

Melnik, S., Gabler, J., Dreher, S. I., Hecht, N., Hofmann, N., Grossner, T., et al. (2020). MiR-218 Affects Hypertrophic Differentiation of Human Mesenchymal Stromal Cells during Chondrogenesis via Targeting RUNX2, MEF2C, and COL10A1. *Stem Cell Res Ther* 11 (1), 18. doi:10.1186/s13287-020-02026-6

Park, D. J., and Seo, Y. J. (2021). Engineering of Extracellular Vesicles Based on Payload Changes for Tissue Regeneration. *Tissue Eng. Regen. Med.* 18 (4), 485–497. doi:10.1007/s13770-021-00349-w

Shafiei, M., Ansari, M. N. M., Razak, S. I. A., and Aslam Khan, M. U. (2021). A Comprehensive Review on the Applications of Exosomes and Liposomes in Regenerative Medicine and Tissue Engineering. *Polymers* 13 (15), 2529. doi:10.3390/polym13152529

Sun, J.-X., Dou, G.-R., Yang, Z.-Y., Liang, L., Duan, J.-L., Ruan, B., et al. (2021). Notch Activation Promotes Endothelial Quiescence by Repressing MYC Expression via miR-218. *Mol. Ther. - Nucleic Acids* 25, 554–566. doi:10.1016/j.omtn.2021.07.023

Tang, X., and Sun, C. (2020). The Roles of MicroRNAs in Neural Regenerative Medicine. *Exp. Neurol.* 332, 113394. doi:10.1016/j.expneurol.2020.113394

Thiebes, K. P., Nam, H., Cambronne, X. A., Shen, R., Glasgow, S. M., Cho, H.-H., et al. (2015). miR-218 Is Essential to Establish Motor Neuron Fate as a Downstream Effector of Isl1-Lhx3. *Nat. Commun.* 6, 7718. doi:10.1038/ncomms8718

Tian, T., Zhu, Y.-L., Zhou, Y.-Y., Liang, G.-F., Wang, Y.-Y., Hu, F.-H., et al. (2014). Exosome Uptake through Clathrin-Mediated Endocytosis and Macropinocytosis and Mediating miR-21 Delivery. *J. Biol. Chem.* 289 (32), 22258–22267. doi:10.1074/jbc.M114.588046

Van Deun, J., Mestdagh, P., SormunenVermaelen, R., Cocquyt, V., Vermaelen, K., Vandesompele, J., et al. (2014). The Impact of Disparate Isolation Methods for Extracellular Vesicles on Downstream RNA Profiling. *J. Extracellular Vesicles* 3, 24858. doi:10.3402/jev.v3.24858

Wei, R., Zhang, L., Hu, W., Shang, X., He, Y., and Zhang, W. (2021). Zeb2/Axin2-Enriched BMSC-Derived Exosomes Promote Post-Stroke Functional Recovery by Enhancing Neurogenesis and Neural Plasticity. *J. Mol. Neurosci.* 72, 69–81. doi:10.1007/s12031-021-01887-7

Westerink, R. H. S., and Ewing, A. G. (2008). The PC12 Cell as Model for Neurosecretion. *Acta Physiol.* 192 (2), 273–285. doi:10.1111/j.1748-1716.2007.01805.x

Xin, H., Katakowski, M., Wang, F., Qian, J.-Y., Liu, X. S., Ali, M. M., et al. (2017a). MicroRNA-17-92 Cluster in Exosomes Enhance Neuroplasticity and Functional Recovery after Stroke in Rats. *Stroke* 48 (3), 747–753. doi:10.1161/strokeaha.116.015204

Xin, H., Wang, F., Li, Y., Lu, Q.-E., Cheung, W. L., Zhang, Y., et al. (2017b). Secondary Release of Exosomes from Astrocytes Contributes to the Increase in Neural Plasticity and Improvement of Functional Recovery after Stroke in Rats Treated with Exosomes Harvested from MicroRNA 133b-Overexpressing Multipotent Mesenchymal Stromal Cells. *Cell Transpl.* 26 (2), 243–257. doi:10.3727/096368916x693031

Yang, Y., Ye, Y., Kong, C., Su, X., Zhang, X., Bai, W., et al. (2019). MiR-124 Enriched Exosomes Promoted the M2 Polarization of Microglia and Enhanced Hippocampus Neurogenesis after Traumatic Brain Injury by Inhibiting TLR4 Pathway. *Neurochem. Res.* 44 (4), 811–828. doi:10.1007/s11064-018-02714-z

Yousefi, F., Lavi Arab, F., Nikkhah, K., Amiri, H., and Mahmoudi, M. (2019). Novel Approaches Using Mesenchymal Stem Cells for Curing Peripheral Nerve Injuries. *Life Sci.* 221, 99–108. doi:10.1016/j.lfs.2019.01.052

Yu, B., Zhou, S., Yi, S., and Gu, X. (2015). The Regulatory Roles of Non-coding RNAs in Nerve Injury and Regeneration. *Prog. Neurobiol.* 134, 122–139. doi:10.1016/j.pneurobio.2015.09.006

Zhang, Y., Peng, Z., and Chen, L. (2016). Co-regulation of miR-143, miR-218 and miR-338-3pin Inhibits Gastric Cancer Migration and Invasion by Targeting Collagen Type I. *Int. J. Clin. Exp. Pathol.* 9 (6), 6127–6135.

Zhou, Y., Tian, T., Zhu, Y., Ali, D. J., Hu, F., Qi, Y., et al. (2017). Exosomes Transfer Among Different Species Cells and Mediating miRNAs Delivery. *J. Cell. Biochem.* 118 (12), 4267–4274. doi:10.1002/jcb.26077

Zhu, K., Ding, H., Wang, W., Liao, Z., Fu, Z., Hong, Y., et al. (2016). Tumor-suppressive miR-218-5p Inhibits Cancer Cell Proliferation and Migration via EGFR in Non-small Cell Lung Cancer. *Oncotarget* 7 (19), 28075–28085. doi:10.18632/oncotarget.8576

Zuk, P. A., Zhu, M., Ashjian, P., De Ugarte, D. A., Huang, J. I., Mizuno, H., et al. (2002). Human Adipose Tissue Is a Source of Multipotent Stem Cells. *MBoC* 13 (12), 4279–4295. doi:10.1091/mbc.E02-02-0105

Conflict of Interest: The authors declare that the research was conducted in the absence of any commercial or financial relationships that could be construed as a potential conflict of interest.

Publisher's Note: All claims expressed in this article are solely those of the authors and do not necessarily represent those of their affiliated organizations, or those of the publisher, the editors, and the reviewers. Any product that may be evaluated in this article, or claim that may be made by its manufacturer, is not guaranteed or endorsed by the publisher.

frontiers in Bioengineering and Biotechnology

ORIGINAL RESEARCH
published: 10 February 2022
doi: 10.3389/fbioe.2022.811128

Extramedullary Osseointegration—A Novel Design of Percutaneous Osseointegration Prosthesis for Amputees

Yingying Sun[1,2], Jinying Xu[1], Shuang Lv[1], Ziran Xu[1], Lisha Li[1†], Yan Li[3*†] and Yulin Li[1*†]*

[1]The Key Laboratory of Pathobiology, Ministry of Education, College of Basic Medical Sciences, Jilin University, Changchun, China, [2]Department of Stomatology, the First Hospital of Jilin University, Changchun, China, [3]Division of Orthopedics and Biotechnology, Department for Clinical Intervention and Technology (CLINTEC), Karolinska Institutet, Stockholm, Sweden

OPEN ACCESS

Edited by:
Jianxun Ding,
Changchun Institute of Applied Chemistry (CAS), China

Reviewed by:
Munjed Al Muderis,
Macquarie University Hospital, Australia
Junlei Chang,
Shenzhen Institutes of Advanced Technology (CAS), China

***Correspondence:**
Lisha Li
lilisha@jlu.edu.cn
Yan Li
Yan.Li@ki.se
Yulin Li
ylli@jlu.edu.cn

[†]These authors have contributed equally to this work

Specialty section:
This article was submitted to Biomaterials, a section of the journal Frontiers in Bioengineering and Biotechnology

Received: 08 November 2021
Accepted: 13 January 2022
Published: 10 February 2022

Citation:
Sun Y, Xu J, Lv S, Xu Z, Li L, Li Y and Li Y (2022) Extramedullary Osseointegration—A Novel Design of Percutaneous Osseointegration Prosthesis for Amputees. Front. Bioeng. Biotechnol. 10:811128. doi: 10.3389/fbioe.2022.811128

The percutaneous osseointegrated (OI) prostheses have greatly improved the overall quality of life for amputees. However, the long-term maintenance of the OI prostheses is still challenging. A major problem is bone resorption around the bone-implant-skin interface, which might cause implant loosening or osteomyelitis. Another problem is the breakage of connecting components between the intramedullary implant and external prosthesis due to excessive stress. We designed a novel osseointegration implant by changing the bone-implant contact from the inner cortex to the outer surface of cortical bone. In the current study, we compared the extramedullary cap-shaped implants with the intramedullary screw-type implants in rabbits. Osteointegration was confirmed at the interface of bone to implant contact (BIC) in both implant types. The external implant induced intramedullary bone regeneration in the medullary canal and increased the cortical bone density at the end of the stump. This study provides a new perspective on the design of osseointegration implants which might prevent the currently reported complications of the intramedullary OI systems.

Keywords: amputation, implant, osseointegration, prosthesis, endoprosthesis, cortical bone, cancellous bone tissue, rehabilitation

INTRODUCTION

The clinical application of osseointegration (OI) prosthesis for amputees started in Sweden in the 1990s with screw-type implants (OPRA system) and emerged as a rapidly developing area in orthopedic surgery (Lenneras et al., 2017; Li and Brånemark, 2017). With OI surgery, a screw-shape or press-fit implant is inserted intramedullary into the bone stump (Pendegrass et al., 2006). The implant is then connected by transdermal components to the external prosthesis to provide a weight-bearing function (Holt et al., 2013). This technology avoids soft-tissue problems associated with traditional socket prosthesis and provides physiological weight bearing to skeleton. It also preserves a range of motion of the proximal joint under prosthetic usage and provides sensory feedback. All the above advantages contribute to the dramatic improvement in quality of life for amputees (Staubach and Grundei, 2001; Kang et al., 2010; Mastinu et al., 2019; Kim et al., 2020; Souza et al., 2020; Shevtsov et al., 2021).

The OI systems continually evolved during the past 30 years. A major breakthrough was the introduction of press-fit Endo-Exo- Prosthesis (EEPs) by Hans Grundei et al. who applied porous

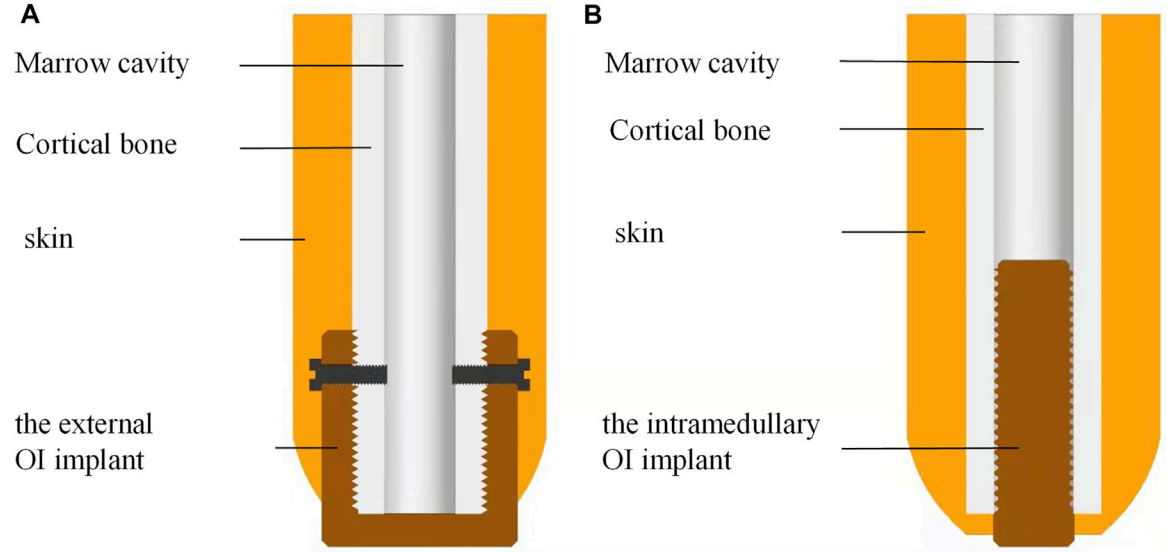

FIGURE 1 | A schematic diagram of the novel external cap implant and the internal columnar implant. **(A)** Novel design of the extramedullary cap-shaped OI implant; **(B)** Current design of the intramedullary implanted columnar implant.

cobalt chromium metal stem as the intramedullary implant (Mittelmeier et al., 1997). Dr. Al Muderis and co-workers later developed the Osseointegrated Prosthetic Limb (OPL) system, in which the implant material was changed from cobalt-chromium to titanium (Thomson et al., 2019). The press-fit systems shortened the time for surgery and rehabilitation, becoming favorable choices for patients and surgeons in recent years (Hoellwarth et al., 2020).

Both screw-type and press-fit implants are inserted in the bone intermedullary canal. When the implant is performing a weight-bearing function, the surrounding bone cortex distal to the BIC will lack sufficient stress stimulation, resulting in bone resorption (osteolysis) around the bone-implant-skin interface (known as a stress-shielding effect) (Atsuta et al., 2016). The colonized bacteria from the skin opening might penetrate through the osteolytic bone and cause implant loosening and osteomyelitis (Chavrier and Couble, 1999; Rompen et al., 2006; Tillander et al., 2017). In the 5-year follow-up of the 51 patients with OPRA implants, 70 superinfections occurred in 34 patients (67%) and 14 deep infections occurred in 11 patients (22%) (Branemark et al., 2019). The results are similar to the 5-years retrospective study on 39 patients using the press-fit implants, in which thirty patients (77%) presented with 156 events of superficial infections in total, with eight events (5%) in 4 patients being classified as deep infections (Reetz et al., 2020).

Mechanical failures of the transdermal components are also of concern for the OI prostheses. In the OPRA cohort, the abutment and/or abutment screw fractures occurred in 15 of the 51 patients (29%) within 5 years (Branemark et al., 2019). Among the 39 patients using the ILP system, nine patients (23%) got 12 dual-adaptor breakages in 5 years (Reetz et al., 2020). A long-term follow-up of 111 patients using the OPRA system indicates that mechanical complications dramatically increased after 8 years of OPRA usage. There is also a positive relationship between a higher activity grade and the number of mechanical complications (Hagberg et al., 2020).

Unlike intraoral and craniofacial osseointegration, the functional structure of the limb stump provides the possibility of inducing osseointegration around the periosteum. Theoretically, the externally applied implant directly closed the bone canal. The implant itself is used as a connecting component to the external prosthesis, which potentially reduced the risk of connecting component breakage. In this study, the design of geometric shape of the external OI implants and the surgical approaches are described. The osseointegration at the bone-implant interface was analyzed and compared with the screw-type intermedullary systems. The process of differentiation of mesenchymal stem cells (MSCs) toward osteogenesis was also explored.

MATERIAL AND METHODS

Implant Design and Mechanical Processing

We designed the extramedullary cap-shaped OI implant (**Figure 1A**) and the intramedullary thread type implant, which mimic the OPRA systems as control (**Figure 1B**). Two types of implants were both 10 mm in length at the BIC with self-tapping screw threads.

The implant sizes were determined according to the geometric characters of the rabbit tibia. **Figure 2A** shows the 3D mechanical processing diagram, and **Figure 2B** shows the model diagram of the inner morphology of the external OI implant. According to the X-ray measurements of the rabbit tibia, the outer and inner diameters of the bone marrow cavities ranged from 7–8 mm and from 3–4 mm, respectively; therefore, the internal diameters of

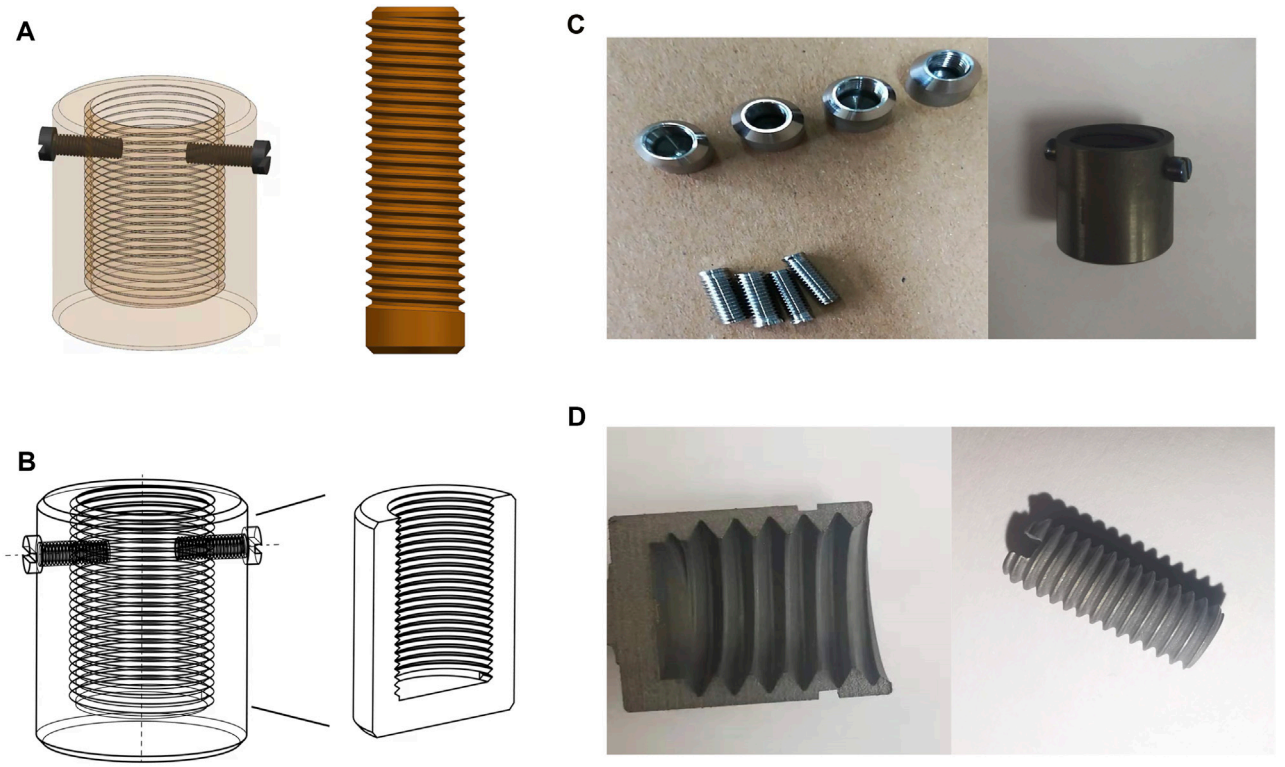

FIGURE 2 | Three-dimensional model diagram and mechanical processing of implants. **(A)** 3D mechanical processing diagram of the external cap implant and the internal column implant; **(B)** the model diagram of the inner morphology of the external cap implant; **(C)** samples of mechanically processed external cap implant and internal columnar implant; **(D)** implant appearance with surface treatment by sandblasting acid etching.

the external OI implant were set as three types: 7, 8, and 9 mm, and the outer diameters of the screw-type implant were 3, 4, and 5 mm. The screw threads of the surface in contact with the bone were designed with a standard M8 coarse pitch with a uniform length of 10 mm, and the bottom thickness of the external implant was 1 mm.

UG NX 10.0 software was used to draw the design draft in three dimensions. The implants were mechanically processed with the computer numerical control machine (JFMT360, Jinan, China). A titanium rod with the corresponding diameter and length was selected according to the designed parameters. The implant surface in contact with the bone was treated with sand blasting and acid etching. The sandblasting treatment was performed by using Al2O3 (110 μm) under 0.6 MPa at 10 mm distance and a 45° angle for 15 s. Hydrofluoric acid (40%) was applied for 60 s. After that, the implants were cleaned ultrasonically in anhydrous ethanol and deionized water for 20 min, dried, sealed in bags, and sterilized using high-temperature steam (120°C, 40 min).

Three-Dimensional Finite Element Analysis of Implants

To evaluate the mechanical properties of the implants under loading, these two types of implants were analyzed under simulated stress *in vivo* using a three-dimensional (3D) finite element method. The 3D mechanical drawing software Pro/E Wildfire (Parametric Technology Corporation, Needham, MC, United States) was used to establish a 3D solid model of the titanium implant and generate a finite element mesh. Then, the software ANSYS Workbench17.0 (SAS IP, Inc., Cary, United States) was used to generate the finite element model and import the material parameters of titanium alloy (elastic modulus 110GPa, Poisson's ratio 0.3) (Neumeister et al., 2017).

TABLE 1 | The material parameters in the three-dimensional (3D) finite element analysis.

Material parameter	Density	Poisson's ratio	E-Modulus
Cortical bone	1228 kg/m^3	0.3	1.7 E + 10 Pa
Implants	4620 kg/m^3	0.36	9.6 E + 10 Pa

To simulate the force and deformation of the implant when the rabbit was walking under its body weight, a fixed support was applied around the bone. According to the body weight of the rabbit, 50 N perpendicular to the surface was applied to the bottom surface of the implants and 20 N was applied on the side of the implants. The parts subjected to the maximum stress were more likely to undergo deformation, but could not be damaged if the loading force does not exceed the maximum stress value. The material parameters were shown in **Table 1**.

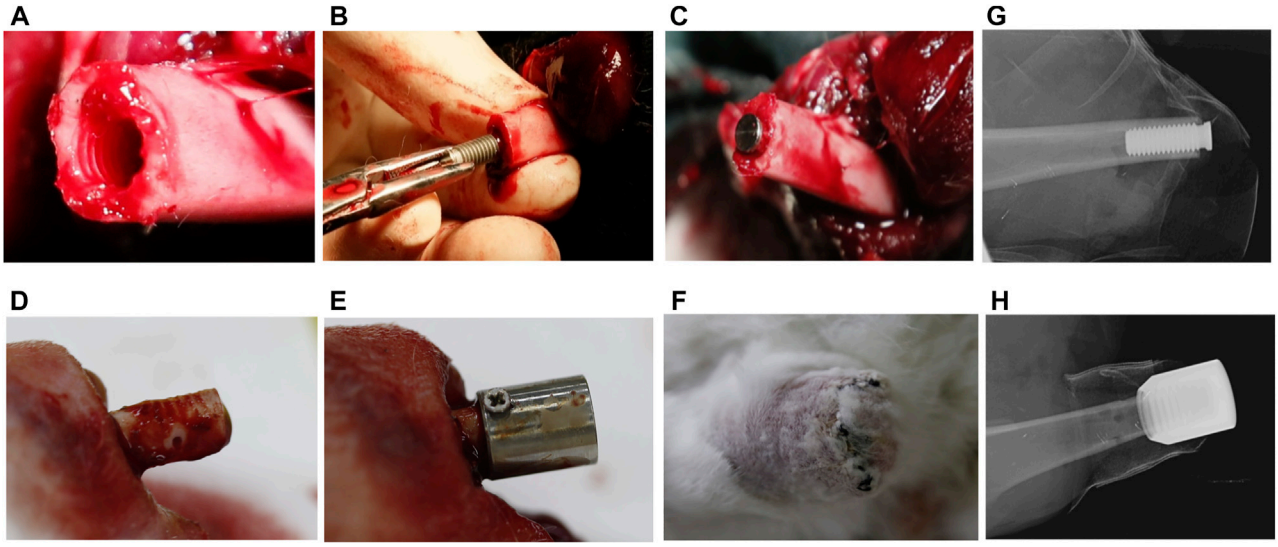

FIGURE 3 | The surgical procedure of implantation in New Zealand Rabbits. **(A)** Preparation of the transplant bed before implantation of internal columnar implants; **(B)** the internal columnar implant was successfully implanted; **(C)** the columnar implant inside the medullary cavity; **(D)** preparation of transplant bed before implantation of external cap implants, with drilling holes on the cortical bone; **(E)** the external cap implants outside the medullary cavity; **(F)** the external cap implant was successfully implanted; **(G,H)** X-ray examination after surgery.

Surgical Procedures With New Zealand Rabbits

Twenty tibial amputation models of ten New Zealand white rabbits (6 months, 2, 5 kg) were established and divided into two groups, implanted either type of the implants, with 10 samples in each group. Adequate procedures were conducted to minimize pain and discomfort in the animals. All animal trials were approved by the Ethics Committee of Experimental Animal Welfare of Jilin University [license number SCXK (Ji)-2016-0004] and were carried out in accordance with the regulations.

During surgery, sodium pentobarbital (3%) was slowly injected into the ear vein to anesthetize the rabbits. After shaving and cleaning (chlorhexidine 0.5 mg/ml) the recipient's leg, the distal aspect of the tibia was exposed through a skin incision. The blood vessels were ligated and cut first, the muscle tissue and nerve were then annularly dissected to expose the central portion of the tibia where osteotomy was done with bone saw.

For the control group, the thread tap with a length of 10 mm was used to prepare the internal side of cortical bone (**Figure 3A**). The screw-type implant was then threaded into the bone canal until stability was achieved (**Figures 1B**, **3B**).

For the external OI group, the periosteum and soft tissue were removed from the bone stump of 10 mm from the end of the amputation, and the screw threads were created on the outer cortical bone surface by thread tap (**Figure 1A**). Three to four holes were randomly drilled in the cortical bone to stimulate blood supply (**Figure 3D**). Titanium screws can be added on both sides of the proximal part of the implant to increase initial stability (**Figure 3E**). The periosteum was reclosed by suture as far as possible.

For both groups, the muscle endings were attached to periosteum and the implant/bone endings were buried under the skin (**Figure 3F**). Before the animals recovered from anesthesia, the implant sites of the stump were photographed using oral X-ray equipment (**Figures 3G**,H). Intramuscular injection of penicillin sodium was administered daily for 3 days, and the implants remained *in situ* for 3 weeks. Wound sites were checked daily in case of inflammation, infection, and implant loosening. All the wounds healed well without signs of infection.

Micro-CT Scan

Twenty-one days after the operation, the experimental animals were euthanized with an excess of 3% sodium pentobarbital. The implants and tibial bone blocks with a length of approximately 20 mm were removed and placed in 4% paraformaldehyde solution for fixation. The specimen was fixed on the micro-CT fixing plate, the orientation was adjusted, and the specimen was placed in a micro-CT machine for scanning. The parameters were a scanning voltage of 80 kV, a current of 50 μA, and a layer thickness of 40 μm. The area of interest was set to a 0.5 mm circumferential volume range around the bone-implant interface. The original data were copied on micro-CT, and the image was processed using Mimics software. The bone mass at the bone-implant interface was calculated according to the CT value of 300–600.

Histological Analyses

To examine new bone formation and osseointegration around the implants, bone blocks with implants were retrieved, and the surrounding bone was processed for histological analyses. The retrieved bone samples were placed in 70% ethanol for fixation and dehydration. Subsequently, the samples were infiltrated with 2-hydroxyethyl methacrylate light-curing resin (Technovit 7200 VLC; Heraeus Kulzer, Wehrheim, Germany), and were finally embedded in the same resin. Non-decalcified sections were then cut with an

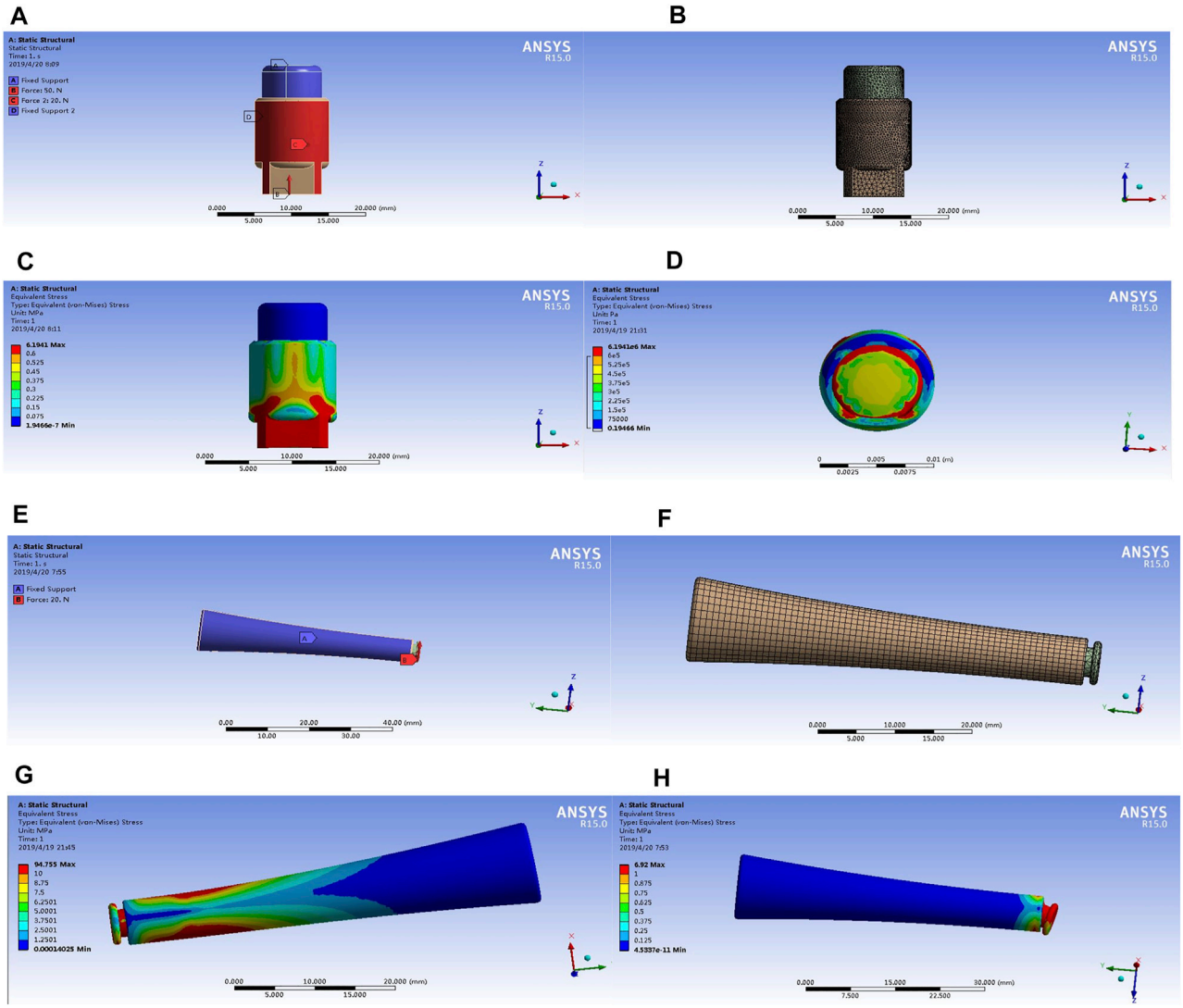

FIGURE 4 | The stress analysis results of the implants with the three-dimensional finite element analysis. The results of the external cap implant were shown in **Figures 3A–D**; the results of the internal cap implant were shown in **Figures 3E–H**. Different colors in the color scale represent different stress values. The blue area represents the part with the minimum stress value, and the red area represents the part with the maximum stress.

Exakt saw (Exakt Apparatebau, Norderstedt, Germany) parallel to the long axis of the implant and ground down to a thickness between 30 and 10 μm following the cutting-grinding technique. The sections were stained with toluidine blue–pyronin and hematoxylin-eosin (HE) dye, and then observed under a light microscope (Eclipse ME600; Nikon, Tokyo, Japan).

Immunohistochemical staining was performed using an anti-AP antibody (ab108337, Abcam) and an anti-Runx2 antibody (ab23981, Abcam). To expose the epitopes, the specimens were treated thrice with xylene, 2-Methosyethyl acetate, and acetone. To remove the superficial layers of methylmethacrylate, the specimens were rinsed with distilled water and incubated with TE or TR buffer (Dako). Before immunostaining, endogenous peroxidase and host immunoglobulin G (IgG) were blocked using peroxidase blocking reagent (Dako) and rodent block R (Biocare). The blocking reagents were removed, and primary antibodies were applied. Specimens were incubated overnight and rinsed with TTBS buffer and antibody detection rabbit-on-rodent HRP-Polymer (Biocare) for AP detection, as well as secondary anti-rabbit IgG (Dako) for Runx2 detection. After 60 min of incubation, immunohistochemical detection was performed using DAB Chromogen Systems (Dako). The samples were rinsed, counterstained with HE, and stored after dehydration. Isotype controls were performed with rabbit-on-rodent HRP-polymer or secondary anti-rabbit IgG only.

RESULTS

The Implants and Three-Dimensional Finite Element Analysis

The implants were processed in accordance with the 3D structure drawn using UG NX 10.0 (**Figures 2A,B**). They

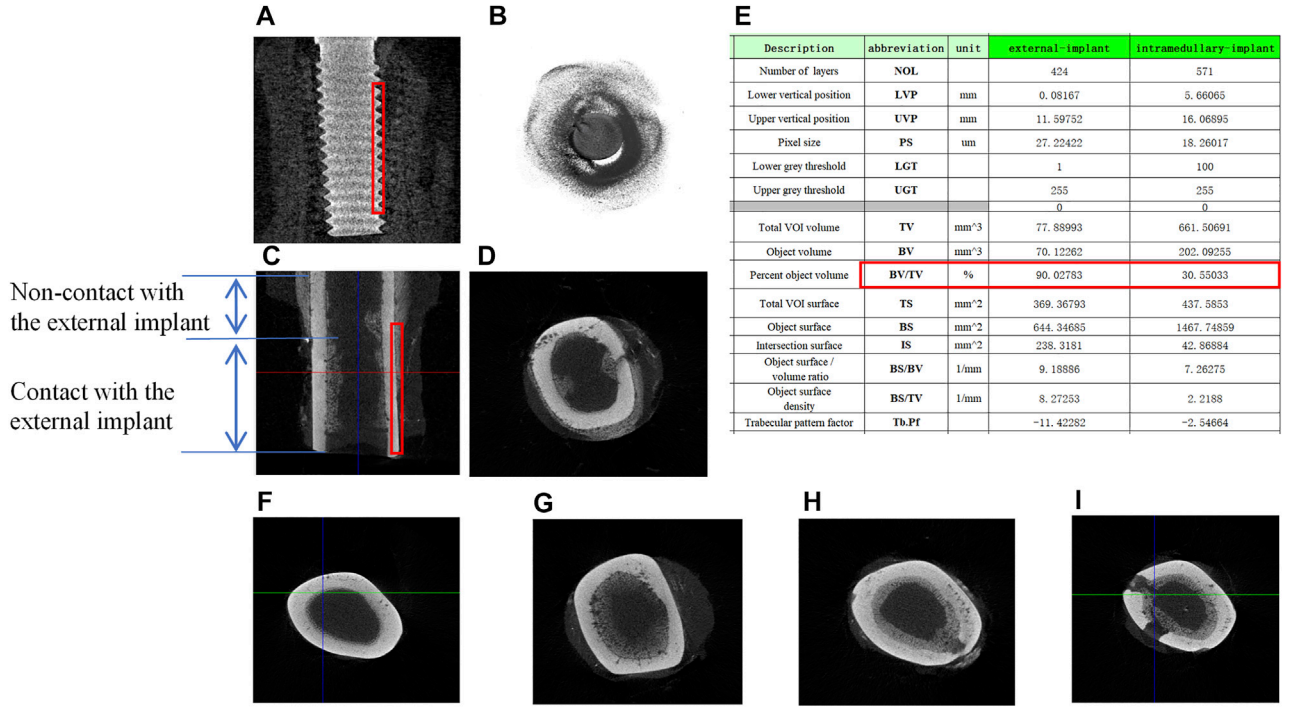

Description	abbreviation	unit	external-implant	intramedullary-implant
Number of layers	NOL		424	571
Lower vertical position	LVP	mm	0.08167	5.66065
Upper vertical position	UVP	mm	11.59752	16.06895
Pixel size	PS	um	27.22422	18.26017
Lower grey threshold	LGT		1	100
Upper grey threshold	UGT		255	255
			0	0
Total VOI volume	TV	mm^3	77.88993	661.50691
Object volume	BV	mm^3	70.12262	202.09255
Percent object volume	BV/TV	%	90.02783	30.55033
Total VOI surface	TS	mm^2	369.36793	437.5853
Object surface	BS	mm^2	644.34685	1467.74859
Intersection surface	IS	mm^2	238.3181	42.86884
Object surface / volume ratio	BS/BV	1/mm	9.18886	7.26275
Object surface density	BS/TV	1/mm	8.27253	2.2188
Trabecular pattern factor	Tb.Pf		-11.42282	-2.54664

FIGURE 5 | Micro-CT scan and the description of bone tissue after implantation. **(A)** Longitudinal scan of samples around internal columnar implants, the red boxes indicate the total VOI volume; **(B)** transverse scan of samples around internal columnar implants; **(C)** longitudinal scan of samples around external cap implants; **(D)** transverse scan of samples around external cap implants; **(E)** the description of Micro-CT scan results; **(F)** transverse scan of the normal rabbit tibia; **(G–I)** new bone regeneration in the marrow cavity surrounded by the external implant.

had smooth surface after mechanical processing and appeared to be dark and coarse after classic sandblasting and acid etching (**Figures 2C,D**). After ultrasonic washing, the implants were dried and sterilized in a sealed bag.

The stress analysis results of the implants were shown in **Figure 4**, the color indicator scale on the left of the figure indicated that the tested part suffered an increasingly load stress, the red area indicated the maximum stress. The implant was prone to deform if a load exceeds this stress. For the external OI implant, the maximum stress concentration appeared at the implant-bone junction, which functioned as a mechanical transmission part and located at the skin opening (**Figures 4A–D**). For the screw-type implant (**Figures 4E–H**), the maximum stress concentration lies proximal to the intramedullary implant in contact with the medial surface of the cortical bone, and the connecting rod where the implant was connected to the external prosthesis, as shown in **Figure 4G**. In addition, the connecting rod of the implant was prone to deformation and fracture under the action of high stress concentration (shown as **Figure 4H**). This result is in accordance with the clinical reports that mechanical failures mostly occurred at the connecting components to the external prosthesis (Li and Fellander-Tsai, 2021). It is also in accordance with the proximal buttressing and distal bone resorption signs as often shown by X-ray analysis for patients who are using the bone-anchored prostheses (Tsikandylakis et al., 2014).

Micro-CT Scan and Description After Implantation

Micro-CT scan was performed to observe osseointegration (OI) at the implant-bone interface. For the screw-type implant, a close contact with the internal bone cortex was seen by both longitudinal and transverse tomography (**Figures 5A,B**). For the external OI implant, besides bone formation close to the external bone cortex, the new bone was also formed in the end of bone marrow cavity (**Figures 5C,D**). In addition, proximal to the BIC surface, sub-periosteum osteogenesis occurred onto the external surface of the cortical bone, but there was no new bone formation inside the marrow cavity (**Figures 5C,D**). From a transverse sectional view of the bone, **Figure 5F** showed the normal tibial canal without any bone hyperplasia. **Figures 5G–I** showed a significant new bone formation at the BIC outside the cortical bone, or inside the marrow cavity, including the pores prepared on the cortical bone.

The red box in **Figures 5A,C** showed the volume-of-interest (VOI) of the samples in 3D volume of the 0.5 mm radius ring around the implants. Micro-CT software was used to analyze bone regeneration in the VOI, and the average data were shown in

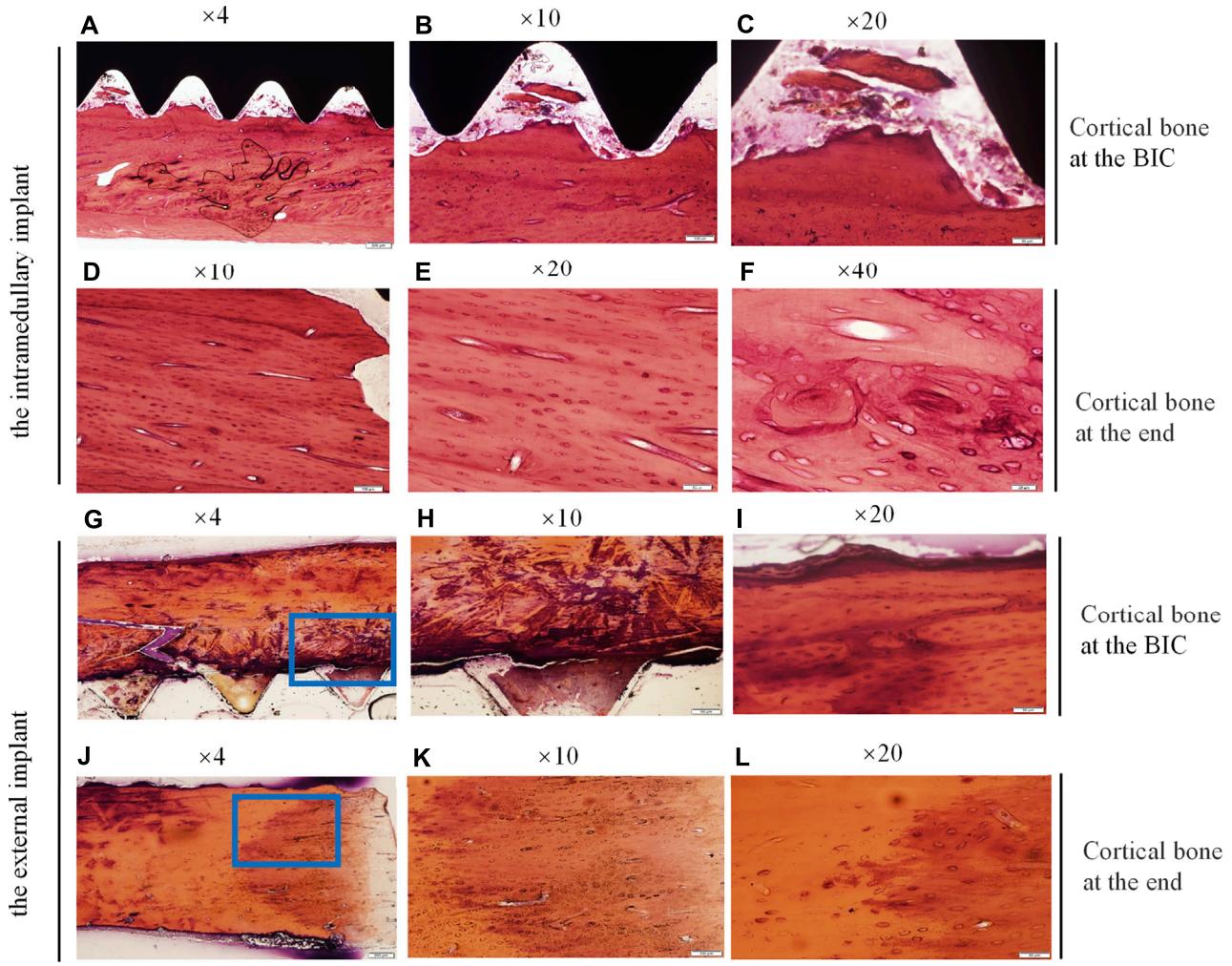

FIGURE 6 | Histological sections and HE staining of the undecalcified bone samples around the implants, observed using a histological microscope. (magnification ×10, ×20, ×40). **(A–C,G–I)** New bone formation within the threads of both implants at the BIC; **(D–F,J–L)** the cortical bone at the end of the stump. Osteocyte lacunae was visible.

Figure 5E. Among the important description obtained, the relative bone volume fraction (BV/TV) reflects the relative bone volume in the region of interest, which was positively correlated with the volume of the new bone. In the VOI of the bone with intramedullary implant, the value of BV/TV obtained was 90.02%, while that of the bone with extramedullary implant was 30.55%, indicating that the volume of the new bone at the BIC was less than that of the traditional intramedullary implants.

Histological Analysis of Bone Tissue Around Implants

HE Staining of Undecalcified Bone Tissue Around the Implants

Bone samples were obtained 21 days after the intramedullary implant and the external cap implant grafted, undecalcified tissue sections and HE staining were performed on both samples around the implants. The results were shown in **Figure 6**. Histological images gradually magnified were shown from left to right, and titanium implants were shown in black or removed. **Figures 6A–C** and **Figures 6G–I** represent the observation areas at the BIC interface. **Figures 6D–F** and **Figures 6J–L** showed the cortical bone at the end of the bone stump.

Figures 6A–C showed the interface between the implant and bone, depicting the newly mineralized bone matrix in the threads, indicating successful osseointegration at the BIC interface. **Figures 6G–I** showed the interface between the inner thread surface of the external implant and bone, indicating that the new bone matrix in the thread was not obvious, which may not provide the best binding interface in the section. **Figures 6G–I** showed the increase of osteocytes in cortical bone and the appearance of vascular structures under high magnification. **Figures 6D–F** and **Figures 6J–L** showed the cortical bone tissue at the end of the stump. The area in contact with the bottom of the external implant was shown in **Figures 6J–L**. There were a large mass of bone cells and new bone trabeculae in this

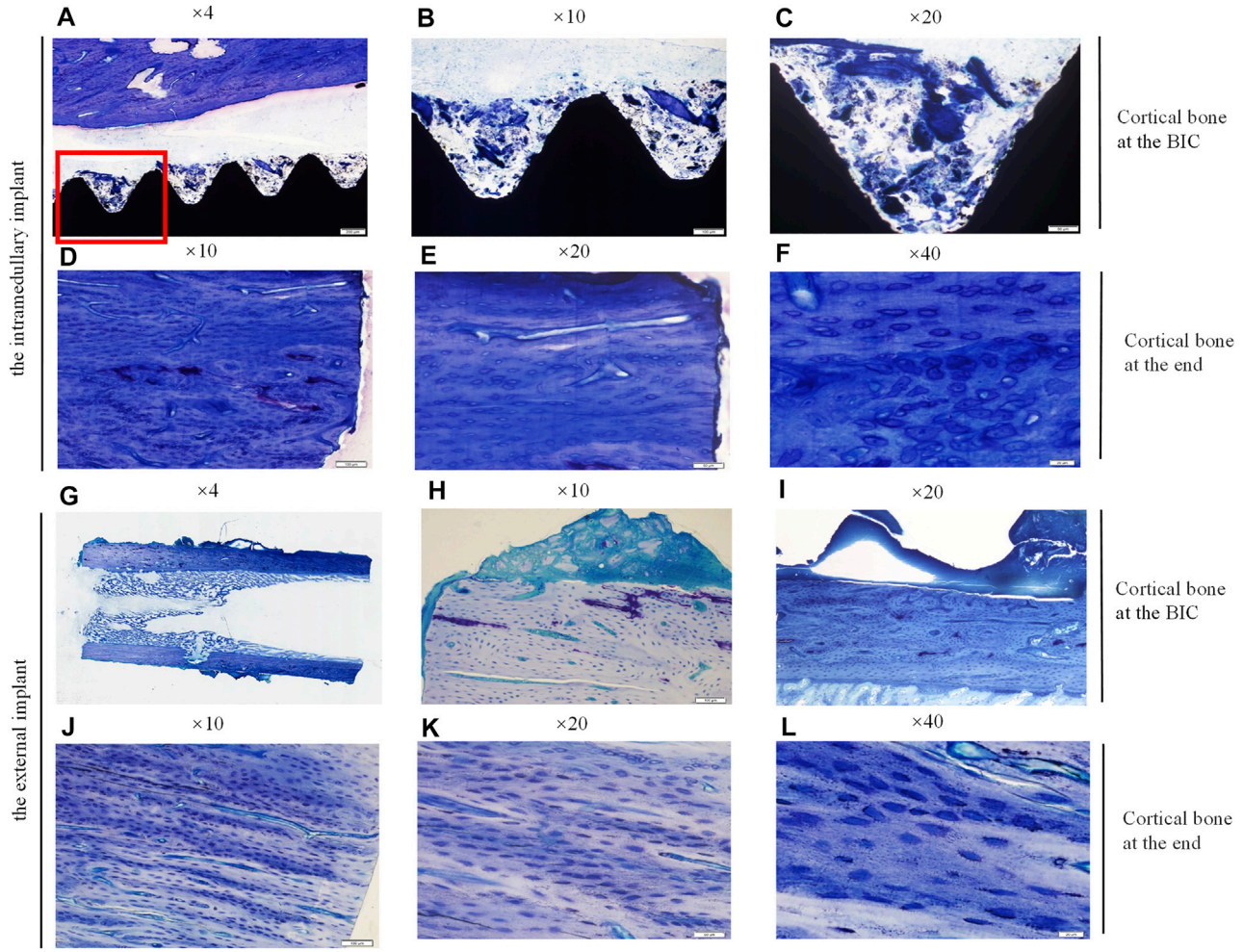

FIGURE 7 | Histological sections and toruidine blue staining of the undecalcified bone samples around the implants, observed using a Histological microscope (magnification ×4, ×10, ×20, ×40). **(A–C,G–I)** New bone formation within the threads of both implants at the BIC; **(D–F,J–L)** the cortical bone with more dense osteocytes at the end of the stump. Osteocyte lacunae was visible.

area, and the bone density was significantly increased. This increase in bone density was consistent with the direction of stress distribution at the implant. These results indicated that there was lower osseointegration at the BIC interface of the external implant as compared with the internal implant. However, the external implant might promote hyperplasia of proximal bone tissue without distal bone resorption.

Toluidine Blue Staining of Undecalcified Bone Tissue Around the Implants

Similarly, the bone samples around the implants were treated with undecalcified ground sections, and then stained with toluidine blue. The results were shown in **Figure 7**. Histological images at ×4, ×10, and ×20 magnification were shown from left to right, and the honeycomb tissue with blue staining was mineralized bone matrix. The results of the toluidine blue staining were consistent with those of HE staining. The results showed that cortical bone density increased, and bone regeneration occurred in the bone marrow cavity of the residual limb corresponding to the external implant. However, bone integration rates at the BIC interface were lower.

Undecalcified sections and toluidine blue staining were performed on the bone blocks after implant removing (**Figure 8**). The blue-stained honeycomb tissue was the mineralized bone matrix. **Figure 8G** showed the overall histological morphology of the bone surrounded by the external implant. A large amount of bone regeneration was observed in the marrow cavity which externally attached to the implant. However, there was no osteogenesis in the bone marrow cavity far away from the implant, but there was considerable bone overgrowth outside the cortical bone.

Figures 8A–F showed the histological morphology of different regions at high magnification, showing the formation of new bone within the marrow cavity. The histological morphology was consistent with the results of the micro-CT.

HE Staining of the Decalcified Paraffin Sections

HE staining of the decalcified paraffin sections showed obvious bone neogenesis with mineralized bone matrix, bone trabeculae,

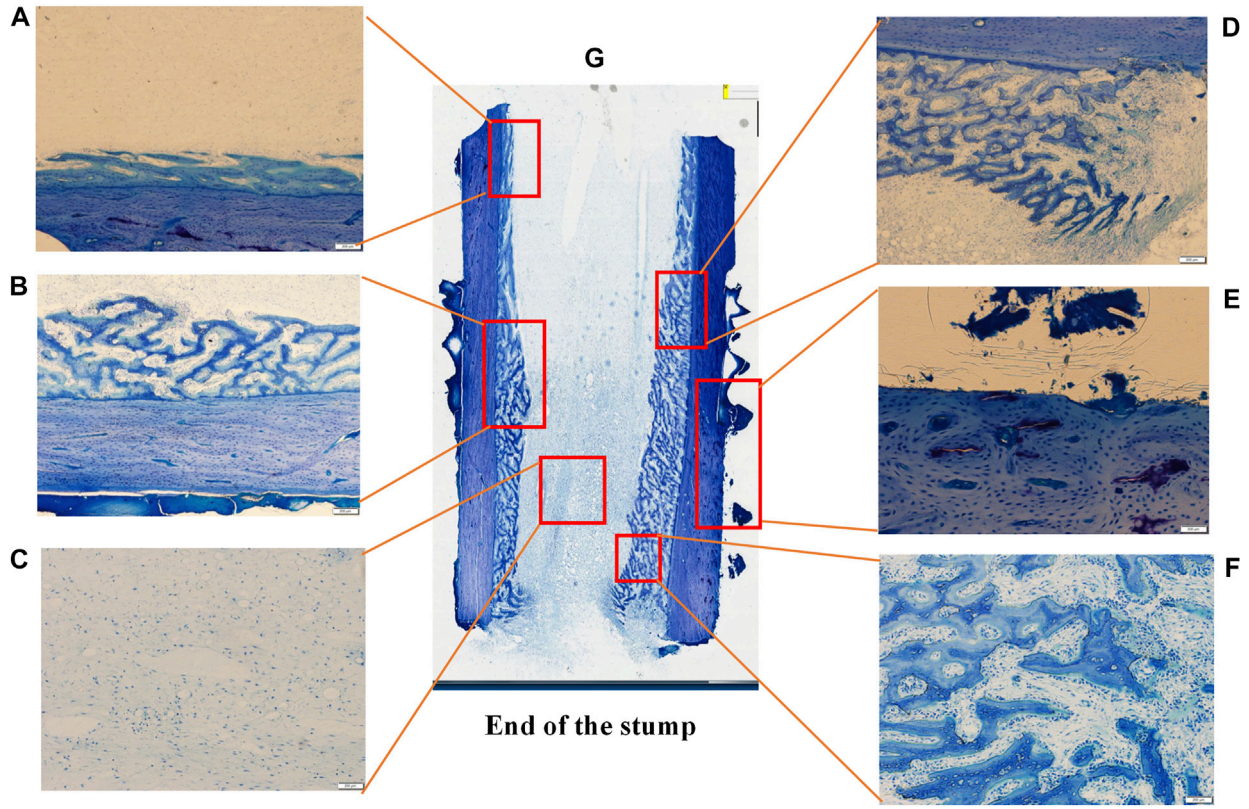

FIGURE 8 | Histological sections and toruidine blue staining of the undecalcified bone sample after the external cap implant removed, observed using a Histological microscope (magnification ×4). Images **(A F)** were the magnification of the areas in the red box in image **(G)**, showed the bone formation in different areas.

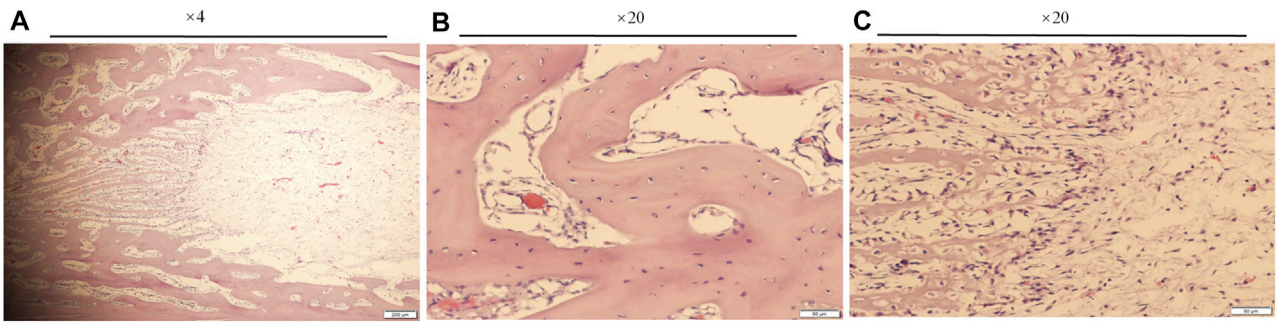

FIGURE 9 | The paraffin sections and HE staining of the bone sample 21 days after the external cap implant grafted, observed using a Histological microscope (magnification ×4, ×20). These images from **(A–C)** were different areas of a sample from the distal to the proximal, at different magnifications gradually.

and osteocytes around the endosteum of bone enveloped by the external implant (**Figure 9**). These images from A to B, to C are different regions of a sample from the distal to the proximal, at different magnifications gradually. Bone regeneration in the bone marrow cavity near the end of the stump was obvious, and the bone cortex proximal to the bone-implant junction was significantly denser (**Figure 9A**). At high magnification (**Figure 9B**), a mass of honeycomb bone trabeculae can be clearly seen in the marrow cavity. Regions in the bone marrow cavity gradually away from the end of the stump showed less significant new bone regeneration (**Figure 9C**).

Immunohistochemical Staining of the Decalcified Paraffin Sections

To further confirm the osteogenic differentiation around the external implants, the expression of osteogenic markers, including osteoprotegerin (OPG) and osteocalcin (OC), was detected by immunohistochemical staining. The results were shown in

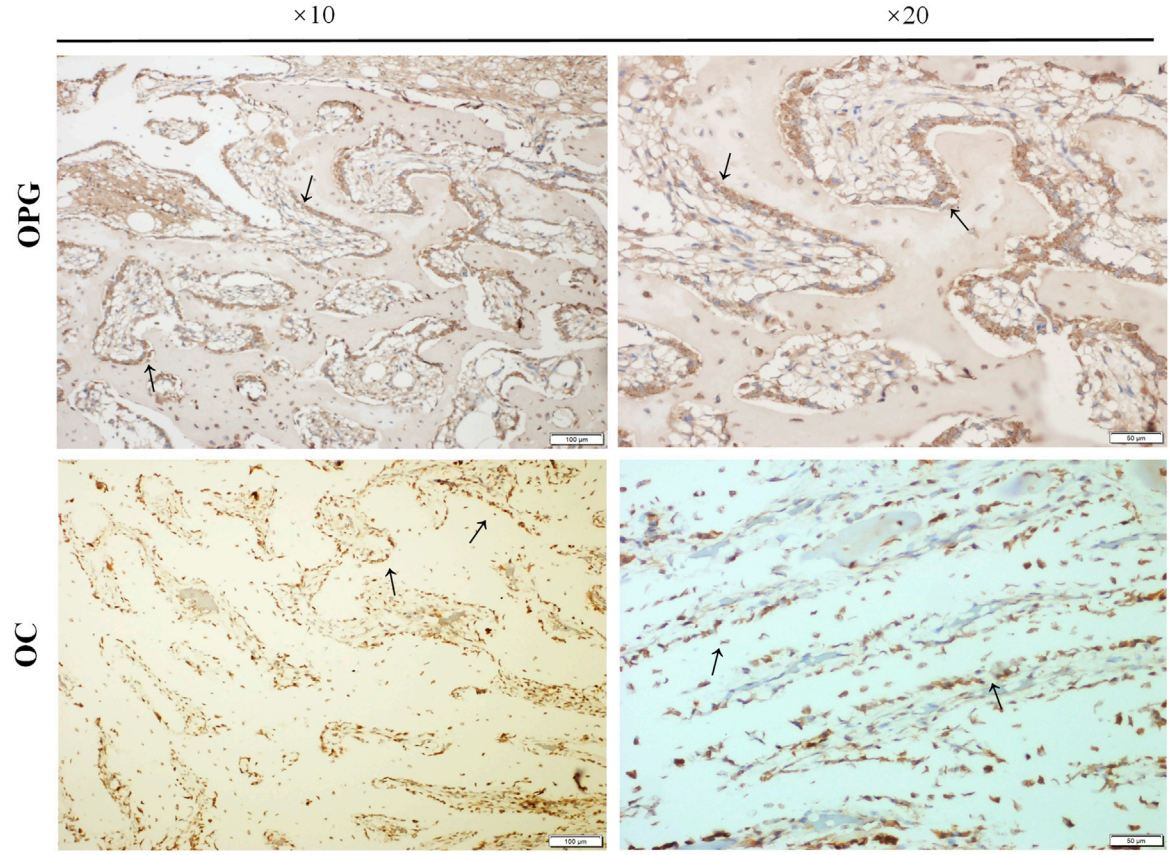

FIGURE 10 | The expressions of osteogenic markers. Paraffin sections of bone samples 21 days after the external cap implant grafted, and the expressions of osteogenic markers including Osteoprotegerin (OPG) and Osteocalcin (OC) were detected by immunohistochemical staining. The black arrows indicated positive expression in the columnar osteoblasts arranged in a palisade.

Figure 10. The black arrow represented positive expression of OPG and OC, new bone was observed in the marrow cavity surrounded by the implant, and columnar arrangement osteoblasts were found. .

Immunohistochemical staining was used to detect the expression of Bone Marrow Stromal Cells (BMSCs) markers CD45 and CD90 and their chemokine CXCR4 in the bone tissue surrounded by the external implants, as shown in **Figure 11**. The red arrow indicated the endosteum in the medullary cavity at the implant contact area. The expression of CD45 was negative, CD90 was positive, and CXCR4 was positively expressed. The black arrows indicated positive expression in bone stroma.

Immunohistochemical staining was used to detect the expression of integrin β1 in the bone tissue surrounded by the external implants, as shown in **Figure 12**. The brown-yellow particles indicated positive expression of integrin β1.

DISCUSSION

Design Concept of the External OI Implant and Surgical Method

The long-term maintenance of the bone-anchored prostheses is challenging due to the risk of mechanical failures and deep infections (Li and Fellander-Tsai 2021). Previous efforts were mainly focused on improving the osseointegration efficiency by the modification of implant surface morphology, changing of implant materials, or improving surgical methods (Overmann and Forsberg 2020). Our 3D finite element analysis revealed that the two maximal stress areas in the screw-type implant system located proximally to the BIC and the connecting rod to external prostheses. Such a biomechanical profile well explained the frequently reported complications such as distal bone resorption around the bone-implant-skin opening and the deformity/fractures at the connecting components for the currently used OI systems (**Figures 4E–H**).

Unlike the intraoral and craniofacial osseointegration, the structure characters of the residual limb make the application of OI implant surrounding the bone ending possible. Our 3D finite element analysis indicated that the external application of implant not only closed the bone canal but also changed the stress-loading character of the system. The maximal stress was around the proximal bone-implant junction where the skin opening located (**Figure 4C**). We suppose that the local stress might induce bone hypertrophy at the implant-bone-skin interface, in favor of bacteria prevention under long-term prosthetic usage. However, it is unclear whether this stress

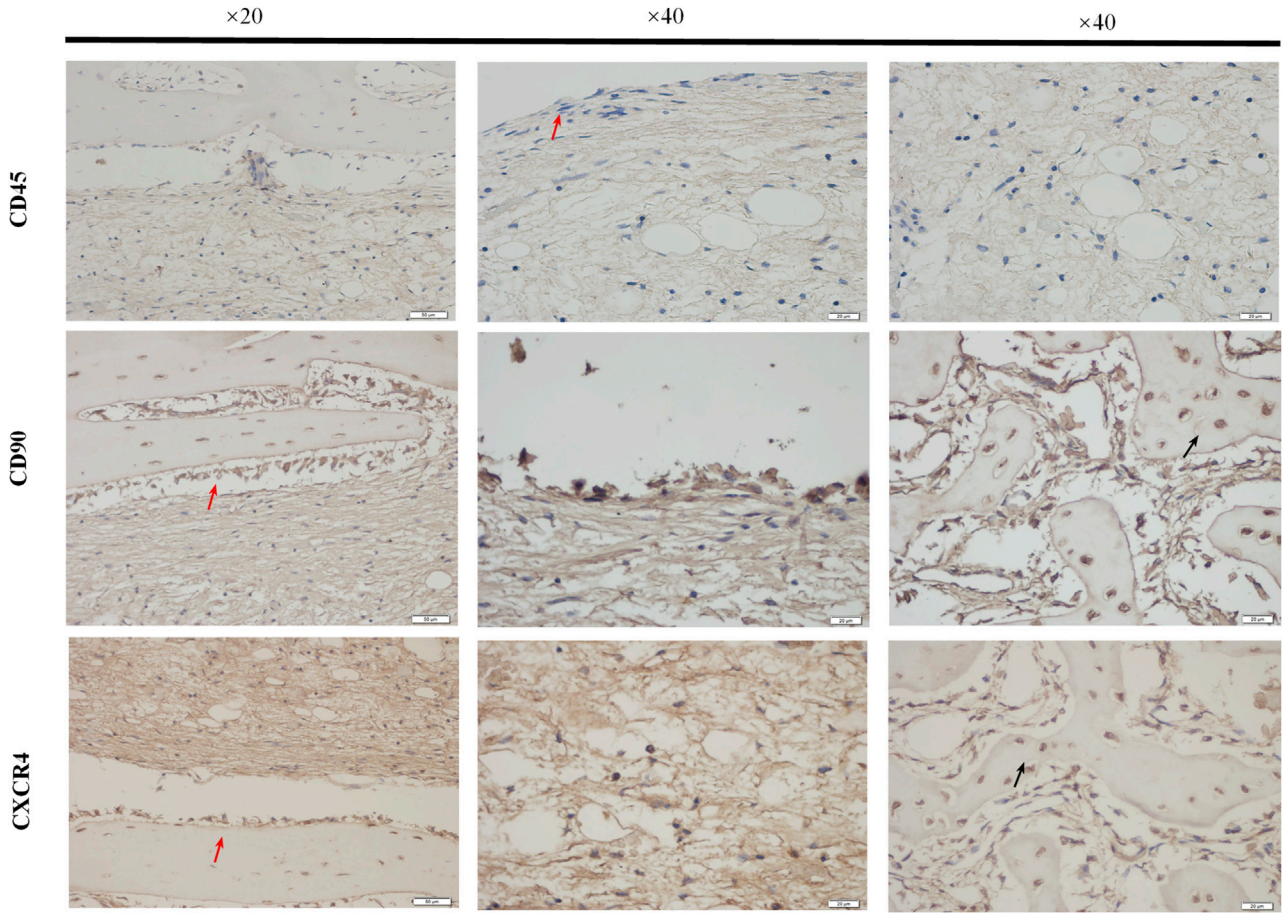

FIGURE 11 | The expressions of BMSCs markers. The paraffin sections of bone samples 21 days after the external cap implant grafted, and the expressions of BMSCs markers (CD45, CD90) chemokines CXCR4 were detected by immunohistochemical staining. The brown-yellow particles indicated the positive expression. The expression of CD45 was negative and that of CD90 was positive, while the expressions of BMSCs chemokines CXCR4 were also positively expressed.

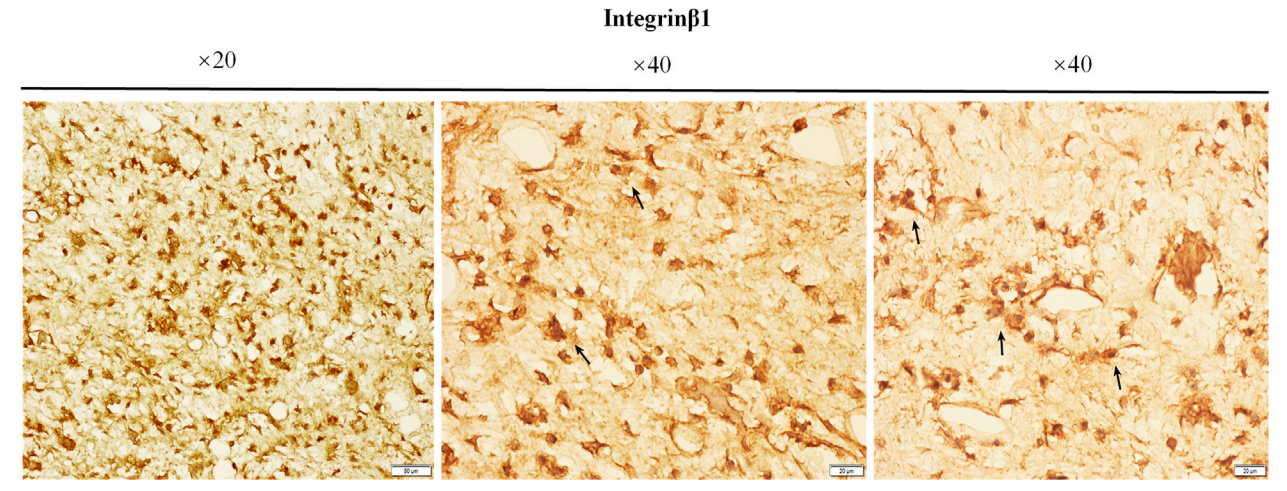

FIGURE 12 | The expressions of integrin β1. The paraffin sections of bone samples 21 days after the external cap implants grafted, and the expression of integrin β1 was detected by immunohistochemical staining. The brown-yellow particles indicated the positive expression of integrin β1.

pattern might also increase fracture risk around the bone-implant junction.

As shown in our study, the diameters of the external implants were significantly larger than the internal implants (7, 8, and 9 mm for the external implants and 3, 4, and 5 mm for the internal implants). With the same implant length, the external implant had therefore larger BIC surface for osseointegration and might contribute to implant stability. The external OI implant can also be directly connected to the external prostheses, which avoid the usage of connecting components and the related complications.

Single-stage surgery reduced the operating time, intraoperative bleeding, hospital stay, and overall costs for the osseointegration treatment. Application of single-stage surgery using intramedullary implant is controversial due to concern of bacteria penetration through the bone-implant-skin opening into the medullar cavity. The external OI implant induces osseointegration on the external part of bone cortex and thus avoids the bacteria penetration in bone cavity, reducing the concern for single-stage surgery.

Osseointegration at the BIC and Bone Remodeling in the Medullary Cavity

Osseointegration is a dynamic status maintained by bone remodeling. The periosteum and endosteum are both layers of connective tissue on the surface of bone matrix, which is composed of osteoblasts and undifferentiated cells. They both have strong ability for bone regeneration and participate in bone remodeling. The blood supply to the surgical site is another prerequisite for Osseointegration and bone regeneration. Neovascularization can maintain the surrounding cells with the necessary oxygen and nutrients to promote their proliferation and differentiation (Abshagen et al., 2009). The arterial blood supply of long bones comes from three main sources: the nourishing arteries branch off to the periosteum, and the epiphyseal and metaphyseal arteries supply both ends and anastomose to the branch of the trophoblast arteries. However, the vessels in the periosteum are transverse, supplying the superficial layers of the cortical bone and usually do not penetrate into the deep layers (Strachan et al., 1990). The existing OI implants are fixed in the intramedullary canal, which occupies in the bone canal and damages bone marrow tissue and endosteum while blood supply to the periosteum is preserved (Greksa et al., 2012). In external implantation, the periosteum is stripped and direct blood supply to the BIC surface from the periosteum is blocked by the implant. Whether osseointegration can occur in this incapsulated environment is largely unclear.

The micro-CT images showed new bone formation at the BIC interface of both implant types. However, the VOI (0.5 mm around the implant) analysis showed that the BIC interface of the intramedullary implant is associated with larger amount of newly formed bone tissue and higher relative bone volume fraction BV/TV (A common index for the evaluation of bone mass of cortical bone and cancellous bone, often used for the evaluation of the bone interface bonding of the implant) (Meakin et al., 2017). This result indicates that the extramedullary osseointegration, although indeed occurred, was less efficient as the intramedullary osseointegration in our experiments. The reason might lie in the over-stripping of periosteum during operating procedures, which devoid large amount of bone progenitors or the blockage of blood supply from the periosteum. However, we found that for areas where direct bone-implant contact occurred, the formation of new bone at the BIC was as good as the internal implants. This result indicates that the blood supply from the penetrating vessels from the marrow cavity or bore holes might be sufficient for implant osseointegration. The major reason for the low BV/TA volume fraction lied probably in the geometric feature of the rabbit tibia. As in humans, the shaft of tibia in a rabbit is an oblate or triangle form. The contact between the implant and the outer surface of the cortical bone was not complete and significant gaps remained (**Figure 5D**). We suppose that the application of the external OI implant to femur, which is relatively round at the outer surface, might increase the BV/TV volume fraction. Further studies in larger animals are therefore needed for femur external osseointegration.

A favorable finding in this study is the new bone formation in the distal part of the intermedullary canal, which is encapsulated by the external implants (**Figure 5C**). This is a unique feature for the external implant system and we suppose that the intramedullary bone regeneration might increase the mechanical strength of the implant system during longer term of prosthetic usage.

Titanium Stimulates Osteoblastic Differentiation of BMSCs to Achieve Osseointegration

To understand the cellular and molecular mechanism for intramedullary bone regeneration and extra cortical osseointegration around the external OI implant we performed a series of histological studies.

Consistent with the micro CT findings, histological analysis showed that the external OI implant not only avoided bone resorption at the implant-bone junction but can also promoted bone regeneration in the end of marrow cavity (**Figures 6**, **7**). Osteoprotegerin (OPG) and osteocalcin (OC) were significantly positive, confirming an active bone regeneration process inside the medullary cavity (**Figure 10**). The mice and human-derived BMSCs expressed CD44, CD90, and CD105, and did not express CD45, CD34 (Koppula et al., 2010; Yan et al., 2019). In this study, $CD90^{+}$ and $CD45^{-}$ were selected as identification markers of BMMCs. To prove whether the implant recruits the BMSCs, we evaluated the expression of a major chemotactic receptor for BMSCs recruitment, the (C) C-X-C chemokine receptor type 4 (CXCR4) (Matsuura et al., 2010; Karazisis et al., 2017). As shown in **Figure 11**, BMSCs were recruited and differentiated into osteoblastic progenitor cells *in vivo*. The above immunohistochemistry results indicated that various factors, including chemokines secreted by osteoblasts adhering to the surface of the material, mobilized the surrounding mesenchymal cells and osteoprogenitor cells to participate in bone regeneration.

The areas with intramedullary bone regeneration had very limited contact with the external implant (only at the end or through the bore holes on cortex). Further studies were done to understand whether this type of distal osteogenesis was natural tissue reaction following amputation or it was induced by the titanium implant, which might provide spatial scaffold for the growth of blood vessels and the formation of new bone.

Integrin β1 is usually expressed in the cell membranes of bone marrow mesenchymal stem cells and osteoprogenitor cells (Du et al., 2011) and has been shown to be crucial in osteoblast adhesion (Gronthos et al., 1997) (Keung et al., 2011). Our results showed that the expression of integrin β1 was higher in the bone marrow cavity of the implant contact region, suggesting that integrin β1 plays a key role in active bone regeneration in this region (**Figure 12**). Contact with titanium surface probably induced osteoblastic differentiation of BMSCs by increased expression of integrin β1 the process of osseointegration and new bone formation in the medullary cavity.

In summary, our study for the first time evaluated the possibility for external osseointegration in animal amputation models. The results for new bone formation at the bone-implant-skin opening area and the distal bone canal were promising. However, the efficiency of the external osseointegration was not as satisfied as internal systems. Studies using larger animals with prosthetic bearing and long-term follow-ups are needed to further evaluate this novel concept for bone-anchored prosthesis.

DATA AVAILABILITY STATEMENT

Datasets are available on request: The raw data supporting the conclusions of this article will be made available by the authors, without undue reservation. Requests to access the datasets should be directed to sunyingying@jlu.edu.cn.

ETHICS STATEMENT

The animal study was reviewed and approved by the Ethics Committee of Experimental Animal Welfare of Jilin University and were carried out in accordance with the regulations.

AUTHOR CONTRIBUTIONS

The project was started, directed, and sponsored by YuL, the experiments were designed by YaL, LL, and YS. YS conducted all the experiments and analysis. YS and YaL drafted the manuscripts. All the authors in research group participated in the discussions of the results and revision of the manuscript.

FUNDING

This work was supported by the National Natural Science Foundation of China (Grant Nos. 81970547, 81572139, 31201052) and CIMED foundation of the Karolinska Institutet, Sweden.

REFERENCES

Abshagen, K., Schrodi, I., Gerber, T., and Vollmar, B. (2009). In Vivoanalysis of Biocompatibility and Vascularization of the Synthetic Bone Grafting Substitute NanoBone. *J. Biomed. Mater. Res.* 91A (2), 557–566. doi:10.1002/jbm.a.32237

Atsuta, I., Ayukawa, Y., Kondo, R., Oshiro, W., Matsuura, Y., Furuhashi, A., et al. (2016). Soft Tissue Sealing Around Dental Implants Based on Histological Interpretation. *J. prosthodontic Res.* 60 (1), 3–11. doi:10.1016/j.jpor.2015.07.001

Brånemark, R. P., Hagberg, K., Kulbacka-Ortiz, K., Berlin, Ö., and Rydevik, B. (2019). Osseointegrated Percutaneous Prosthetic System for the Treatment of Patients with Transfemoral Amputation. *J. Am. Acad. Orthopaedic Surgeons* 27 (16), e743–e751. doi:10.5435/jaaos-d-17-00621

Chavrier, C. A., and Couble, M. L. (1999). Ultrastructural Immunohistochemical Study of Interstitial Collagenous Components of the Healthy Human Keratinized Mucosa Surrounding Implants. *Int. J. Oral Maxillofac. Implants* 14 (1), 108–112.

Du, J., Chen, X., Liang, X., Zhang, G., Xu, J., He, L., et al. (2011). Integrin Activation and Internalization on Soft ECM as a Mechanism of Induction of Stem Cell Differentiation by ECM Elasticity. *Proc. Natl. Acad. Sci.* 108 (23), 9466–9471. doi:10.1073/pnas.1106467108

Greksa, F., Tóth, K., Boros, M., and Szabó, A. (2012). Periosteal Microvascular Reorganization after Tibial Reaming and Intramedullary Nailing in Rats. *J. Orthopaedic Sci.* 17 (4), 477–483. doi:10.1007/s00776-012-0222-z

Gronthos, S., Stewart, K., Graves, S. E., Hay, S., and Simmons, P. J. (1997). Integrin Expression and Function on Human Osteoblast-Like Cells. *J. Bone Miner. Res.* 12 (8), 1189–1197.

Hagberg, K., Ghassemi Jahani, S.-A., Kulbacka-Ortiz, K., Thomsen, P., Malchau, H., and Reinholdt, C. (2020). A 15-year Follow-Up of Transfemoral Amputees with Bone-Anchored Transcutaneous Prostheses. *Bone Jt. J.* 102-B (1), 55–63. doi:10.1302/0301-620x.102b1.bjj-2019-0611.r1

Hoellwarth, J. S., Tetsworth, K., Rozbruch, S. R., Handal, M. B., Coughlan, A., and Al Muderis, M. (2020). Osseointegration for Amputees. *JBJS Rev.* 8 (3), e0043. doi:10.2106/jbjs.rvw.19.00043

Holt, B. M., Bachus, K. N., Beck, J. P., Bloebaum, R. D., and Jeyapalina, S. (2013). Immediate post-implantation Skin Immobilization Decreases Skin Regression Around Percutaneous Osseointegrated Prosthetic Implant Systems. *J. Biomed. Mater. Res.* 101A (7), 2075–2082. doi:10.1002/jbm.a.34510

Kang, N. V., Pendegrass, C., Marks, L., and Blunn, G. (2010). Osseocutaneous Integration of an Intraosseous Transcutaneous Amputation Prosthesis Implant Used for Reconstruction of a Transhumeral Amputee: Case Report. *J. Hand Surg.* 35 (7), 1130–1134. doi:10.1016/j.jhsa.2010.03.037

Karazisis, D., Petronis, S., Agheli, H., Emanuelsson, L., Norlindh, B., Johansson, A., et al. (2017). The Influence of Controlled Surface Nanotopography on the Early Biological Events of Osseointegration. *Acta Biomater.* 53, 559–571. doi:10.1016/j.actbio.2017.02.026

Keung, A. J., de Juan-Pardo, E. M., Schaffer, D. V., and Kumar, S. (2011). Rho GTPases Mediate the Mechanosensitive Lineage Commitment of Neural Stem Cells. *Stem Cells* 29 (11), 1886–1897. doi:10.1002/stem.746

Kim, J.-H., Kim, Y.-S., Park, I., Lee, H.-J., Han, S.-Y., Jung, S., et al. (2020). A Comparison of Open-Construct PEEK Suture Anchor and Non-vented Biocomposite Suture Anchor in Arthroscopic Rotator Cuff Repair: A Prospective Randomized Clinical Trial. *Arthrosc. J. Arthroscopic Relat. Surg.* 36 (2), 389–396. doi:10.1016/j.arthro.2019.08.049

Koppula, P., Polisetti, N., and Vemuganti, G. K. (2010). Unstimulated Diagnostic Marrow Tap - a Minimally Invasive and Reliable Source for Mesenchymal Stem Cells. *Cell. Biol. Int.* 34 (3), 275–281. doi:10.1042/cbi20090142

Lennerås, M., Tsikandylakis, G., Trobos, M., Omar, O., Vazirisani, F., Palmquist, A., et al. (2017). The Clinical, Radiological, Microbiological, and Molecular Profile of the Skin-Penetration Site of Transfemoral Amputees Treated with Bone-Anchored Prostheses. *J. Biomed. Mater. Res.* 105 (2), 578–589. doi:10.1002/jbm.a.35935

Li, Y., and Brånemark, R. (2017). Osseointegrated Prostheses for Rehabilitation Following Amputation. *Unfallchirurg* 120 (4), 285–292. doi:10.1007/s00113-017-0331-4

Li, Y., and Felländer-Tsai, L. (2021). The Bone Anchored Prostheses for Amputees - Historical Development, Current Status, and Future Aspects. *Biomaterials* 273, 120836. doi:10.1016/j.biomaterials.2021.120836

Mastinu, E., Clemente, F., Sassu, P., Aszmann, O., Brånemark, R., Håkansson, B., et al. (2019). Grip Control and Motor Coordination with Implanted and Surface

Electrodes while Grasping with an Osseointegrated Prosthetic Hand. *J. Neuroengineering Rehabil.* 16 (1), 49. doi:10.1186/s12984-019-0511-2

Matsuura, J., Sakanaka, M., Sato, N., Ichikawa, A., and Tanaka, S. (2010). Suppression of CXCR4 Expression in Mast Cells upon IgE-Mediated Antigen Stimulation. *Inflamm. Res.* 59 (2), 123–127. doi:10.1007/s00011-009-0078-7

Meakin, L. B., Todd, H., Delisser, P. J., Galea, G. L., Moustafa, A., Lanyon, L. E., et al. (2017). Parathyroid Hormone's Enhancement of Bones' Osteogenic Response to Loading Is Affected by Ageing in a Dose- and Time-dependent Manner. *Bone* 98, 59–67. doi:10.1016/j.bone.2017.02.009

Mittelmeier, W., Grunwald, I., Schäfer, R., Grundei, H., and Gradinger, R. (1997). Cement-free Incorporation of Endoprotheses by Means of Trabecular, Three-Dimensional Interconnected Surface Structures. *Orthopäde* 26 (2), 117–124. doi:10.1007/s001320050076

Neumeister, A., Schulz, L., and Glodecki, C. (2017). Investigations on the Accuracy of 3D-Printed Drill Guides for Dental Implantology. *Int. J. Comput. Dent* 20 (1), 35–51.

Overmann, A. L., and Forsberg, J. A. (2020). The State of the Art of Osseointegration for Limb Prosthesis. *Biomed. Eng. Lett.* 10 (1), 5–16. doi:10.1007/s13534-019-00133-9

Pendegrass, C. J., Goodship, A. E., and Blunn, G. W. (2006). Development of a Soft Tissue Seal Around Bone-Anchored Transcutaneous Amputation Prostheses. *Biomaterials* 27 (23), 4183–4191. doi:10.1016/j.biomaterials.2006.03.041

Reetz, D., Atallah, R., Mohamed, J., van de Meent, H., Frölke, J. P. M., and Leijendekkers, R. (2020). Safety and Performance of Bone-Anchored Prostheses in Persons with a Transfemoral Amputation. *J. Bone Jt. Surg Am* 102 (15), 1329–1335. doi:10.2106/jbjs.19.01169

Rompen, E., Domken, O., Degidi, M., Farias Pontes, A. E., and Piattelli, A. (2006). The Effect of Material Characteristics, of Surface Topography and of Implant Components and Connections on Soft Tissue Integration: a Literature Review. *Clin. Oral Implants Res.* 17, 55–67. doi:10.1111/j.1600-0501.2006.01367.x

Shevtsov, M., Gavrilov, D., Yudintceva, N., Zemtsova, E., Arbenin, A., Smirnov, V., et al. (2021). Protecting the Skin-implant Interface with Transcutaneous Silver-coated Skin-and-bone-integrated Pylon in Pig and Rabbit Dorsum Models. *J. Biomed. Mater. Res.* 109 (4), 584–595. doi:10.1002/jbm.b.34725

Souza, J. M., Mioton, L. M., Harrington, C. J., Potter, B. K., and Forsberg, J. A. (2020). Osseointegration of Extremity Prostheses: A Primer for the Plastic Surgeon. *Plast. Reconstr. Surg.* 146 (6), 1394–1403. doi:10.1097/prs.0000000000007364

Staubach, K.-H., and Gründei, H. (2001). Die erste osteointegrierte perkutane Prothesenverankerung für Oberschenkel-Amputierte - The First Osseointegrated Percutaneous Anchor for an Exoprosthesis, for Routine Use in Above-knee Amputees. *Biomed. Eng.* 46 (12), 355–361. doi:10.1515/bmte.2001.46.12.355

Strachan, R., McCarthy, I., Fleming, R., and Hughes, S. (1990). The Role of the Tibial Nutrient Artery. Microsphere Estimation of Blood Flow in the Osteotomised Canine Tibia. *J. Bone Jt. Surg. Br.* 72-B (3), 391–394. doi:10.1302/0301-620x.72b3.2341434

Thomson, S., Thomson, A., Tetsworth, K., Lu, W., Zreiqat, H., and Al Muderis, M. (2019). Radiographic Evaluation of Bone Remodeling Around Osseointegration Implants Among Transfemoral Amputees. *J. Orthop. Trauma* 33 (8), e303–e308. doi:10.1097/bot.0000000000001488

Tillander, J., Hagberg, K., Berlin, Ö., Hagberg, L., and Brånemark, R. (2017). Osteomyelitis Risk in Patients with Transfemoral Amputations Treated with Osseointegration Prostheses. *Clin. Orthop. Relat. Res.* 475 (12), 3100–3108. doi:10.1007/s11999-017-5507-2

Tsikandylakis, G., Berlin, Ö., and Brånemark, R. (2014). Implant Survival, Adverse Events, and Bone Remodeling of Osseointegrated Percutaneous Implants for Transhumeral Amputees. *Clin. Orthop. Relat. Res.* 472 (10), 2947–2956. doi:10.1007/s11999-014-3695-6

Yan, D., Tang, B., Yan, L., Zhang, L., Miao, M., Chen, X., et al. (2019). Sodium Selenite Improves the Therapeutic Effect of BMSCs via Promoting the Proliferation and Differentiation, Thereby Promoting the Hematopoietic Factors. *Ott* 12, 9685–9696. doi:10.2147/ott.s209937

Conflict of Interest: The authors declare that the research was conducted in the absence of any commercial or financial relationships that could be construed as a potential conflict of interest.

Publisher's Note: All claims expressed in this article are solely those of the authors and do not necessarily represent those of their affiliated organizations, or those of the publisher, the editors and the reviewers. Any product that may be evaluated in this article, or claim that may be made by its manufacturer, is not guaranteed or endorsed by the publisher.

frontiers in Bioengineering and Biotechnology

ORIGINAL RESEARCH
published: 16 March 2022
doi: 10.3389/fbioe.2022.860949

Biomimetic Redox-Responsive Mesoporous Organosilica Nanoparticles Enhance Cisplatin-Based Chemotherapy

Fangman Chen[1,2], Fan Zhang[2], Yanbin Wang[3], Jiahui Peng[1,2], Lei Cao[1,2], Qian Mei[2], Mingfeng Ge[2], Li Li[2], Meiwan Chen[4], Wen-fei Dong[1,2] and Zhimin Chang[2]**

[1]School of Biomedical Engineering (Suzhou), Division of Life Sciences and Medicine, University of Science and Technology of China, Hefei, China, [2]CAS Key Laboratory of Bio Medical Diagnostics, Suzhou Institute of Biomedical Engineering and Technology Chinese Academy of Sciences, Suzhou, China, [3]Nephrology Department of the Fourth Affiliated Hospital of XinJiang Medical University, Macau, China, [4]State Key Laboratory of Quality Research in Chinese Medicine, Institute of Chinese Medical Sciences, University of Macau, Macau, China

OPEN ACCESS

Edited by:
Yuce Li,
Sungkyunkwan University, South Korea

Reviewed by:
Pengfei Wei,
Binzhou Medical University, China
Wen Wu,
Chongqing University, China
Shixian Lv,
Peking University, China

***Correspondence:**
Wen-fei Dong
wenfeidong@sibet.ac.cn
Zhimin Chang
changzm@sibet.ac.cn

Specialty section:
This article was submitted to Biomaterials, a section of the journal Frontiers in Bioengineering and Biotechnology

Received: *24 January 2022*
Accepted: *10 February 2022*
Published: *16 March 2022*

Citation:
Chen F, Zhang F, Wang Y, Peng J, Cao L, Mei Q, Ge M, Li L, Chen M, Dong W-f and Chang Z (2022) Biomimetic Redox-Responsive Mesoporous Organosilica Nanoparticles Enhance Cisplatin-Based Chemotherapy. Front. Bioeng. Biotechnol. 10:860949. doi: 10.3389/fbioe.2022.860949

Cisplatin-based chemotherapy is dominated in several cancers; however, insufficient therapeutic outcomes and systemic toxicity hamper their clinical applications. Controlled release of cisplatin and reducing inactivation remains an urgent challenge to overcome. Herein, diselenide-bridged mesoporous organosilica nanoparticles (MON) coated with biomimetic cancer cell membrane were tailored for coordination responsive controlled cisplatin delivery and GSH depletion to strengthen Pt-based chemotherapy. Cisplatin-loaded MON (MON-Pt) showed high loading capacity due to robust coordination between selenium and platinum atoms and preventing premature leakage in normal tissue. MON-Pt exhibited a controlled release of activated cisplatin in response to the redox tumor microenvironment. Meanwhile, MON-Pt containing redox-responsive diselenide bonds could efficiently scavenge intracellular inactivation agents, such as GSH, to enhance Pt-based chemotherapy. 4T1 breast cancer cell membranes cloaked MON-Pt (MON-Pt@CM) performed efficient anticancer performance and low *in vivo* system toxicity due to long blood circulation time and high tumor accumulation benefiting from the tumor targeting and immune-invasion properties of the homologic cancer cell membrane. These results suggest a biomimetic nanocarrier to control release and reduce the inactivation of cisplatin for efficient and safe Pt-based chemotherapy by responding and regulating the tumor microenvironment.

Keywords: cisplatin, mesoporous silica nanoparticles, glutathione depletion, biomimetic nanocarrier, degradation

INTRODUCTION

Cancer has become the leading cause of mortality worldwide (Ferlay et al., 2021). Chemotherapy is an essential tool for fighting against cancer (Darge et al., 2021; Wang et al., 2021). Since cisplatin was approved in 1978 by the FDA, platinum-based chemotherapy, including oxaliplatin and carboplatin, is approved commonly for treating numerous cancers that occur in breast, cervix, colon, ovaries, and lung (He et al., 2019; Lin et al., 2020; Chen et al., 2021). The outcome of clinical cisplatin-based chemotherapy becomes inefficient in patients because of serum albumin in blood deactivating cisplatin, inefficient cellular uptake by cancer cells, and easy inactivation by intracellular

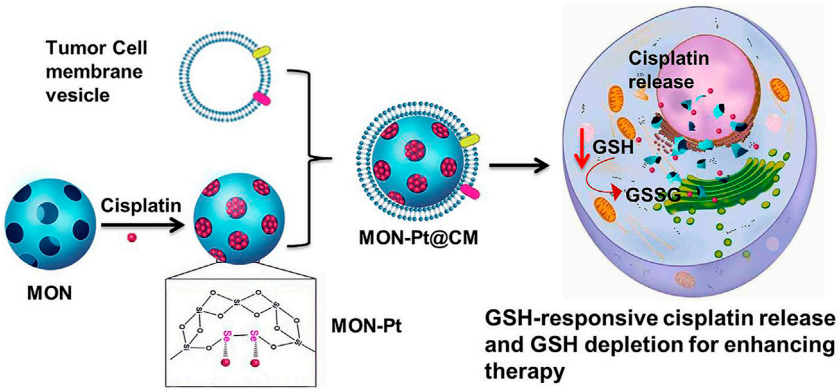

SCHEME 1 | Schematic of synthesis of diselenide bond-bridged MON for redox-responsive cisplatin delivery and GSH depletion for efficient and safe Pt-based chemotherapy.

metallothionein (MT) and glutathione (GSH) (Han et al., 2018; Lan et al., 2018; Kawahara et al., 2019; Zeng et al., 2020). Moreover, cisplatin kills cancer cells and affects normal cells due to lack of selectivity (Davidi et al., 2018; Huang et al., 2018). Consequently, cisplatin inevitably causes severe side effects such as nephrotoxicity and neurotoxicity as well as toxicity to the gastrointestinal tract (Davidi et al., 2018; Huang et al., 2018; Fujishiro et al., 2021; Sun et al., 2021). Cisplatin-based chemotherapy is dominated in several cancers; however, poor therapeutic outcomes and systemic toxicity hamper their clinical applications (Fujishiro et al., 2021; Kuo et al., 2021). It is imperative to design an elaborate drug delivery system to overcome unwanted side effects and deactivation of cisplatin-based chemotherapy.

Drug delivery carriers could endow a controlled and on-demand drug release manner in response to a different stimulus such as pH, redox, light, and magnetic fields (Shao et al., 2018b; Cai et al., 2019; Wang H. et al., 2020; Wang Y. et al., 2020; Chen et al., 2020; Shao et al., 2020). Acid-sensitive nanocarriers, such as polymer micelles and inorganic particles, are widely employed to deliver Pt-based therapeutic agents. However, the encapsulation of cisplatin through charge interaction results in low loading capacity (Wright et al., 2019; Khan et al., 2020). To improve the loading capacity, the coordination coupling of the carboxyl group and cisplatin are developed to achieve high loading capacity (10–20 wt%) and tumor microenvironment-responsive release of cisplatin. Such a coordination binding avoids premature cisplatin leakage in complicated physiological environmental conditions (He et al., 2014; Liu et al., 2021a). Although these nanocarriers show high drug loading capacity and an on-demand drug release manner, it is difficult to prevent the inactivation of cisplatin in high redox tumor microenvironments. There is increasing evidence that cisplatin is quickly deactivated by intracellular metallothionein (MT) and glutathione (GSH) (Han et al., 2018; Lan et al., 2018; Zeng et al., 2020). The intracellular GSH (10 mM) in cancer tissue is 100- to 1000-fold higher than normal tissue (Yin et al., 2018), limiting the performance of cisplatin-based chemotherapy (Ling et al., 2018; Xu et al., 2019). Thus, it poses a challenge for cisplatin delivery to integrate high loading capacity, controlled drug release, and reversion of deactivation into one of the simplified nanocarriers.

Selenium (Se) as an essential element participates in number of critical biological processes, including maintaining the redox homeostasis in humans (Liu et al., 2021b). Selenium-containing materials have attracted much attention for multiresponsive drug delivery and anticancer activities (Sun et al., 2020; Birhan and Tsai, 2021). We recently developed a diselenide-bridged MONs that showed great potential as redox-responsive drug-delivery vehicles for controlled drug release in special tumor environments (Shao et al., 2018a; Chengxin Shi, 2022; Peng et al., 2022; Yang et al., 2022). Diselenide-bridged MONs achieved biodegradation in a high concentration of reductive GSH solution while scavenging; meanwhile, scavenged intracellular GSH. Besides its unique redox properties, selenium exhibits robust coordination with transition metals elements (Lee et al., 2018; Dias et al., 2020). Currently, selenium-containing polymers are used to deliver metal-based chemotherapeutics (e.g., platinum and ruthenium compounds) utilizing their coordination properties. With these findings in mind, we propose that diselenide-bridged MONs could be an ideal carrier for cisplatin delivery to achieve high loading capacity, controlled drug release, and sufficient reversion of deactivation.

Herein, we prepared diselenide-bridged MONs to deliver cisplatin for highly efficient and safe chemotherapy. The diselenide-bridged MONs achieved a high loading capacity of cisplatin (MON-Pt) by coordination binding between active cisplatin and selenium-atom in MONs (**Scheme 1**). MON-Pt exhibited a controlled manner of cisplatin release in response to the redox tumor microenvironment, and coordination binding avoided the premature leakage of cisplatin in normal tissue. Meanwhile, MON-Pt could efficiently achieve GSH depletion in the responsive release of cisplatin. To improve targeting tumor and immune-invasion, biomimetic nanocarrier (MON-Pt@CM) was constructed via coating MON-Pt with the cancer cell membrane (CM), exhibiting long blood circulation time and high tumor accumulation. The *in vitro* and *in vivo* results

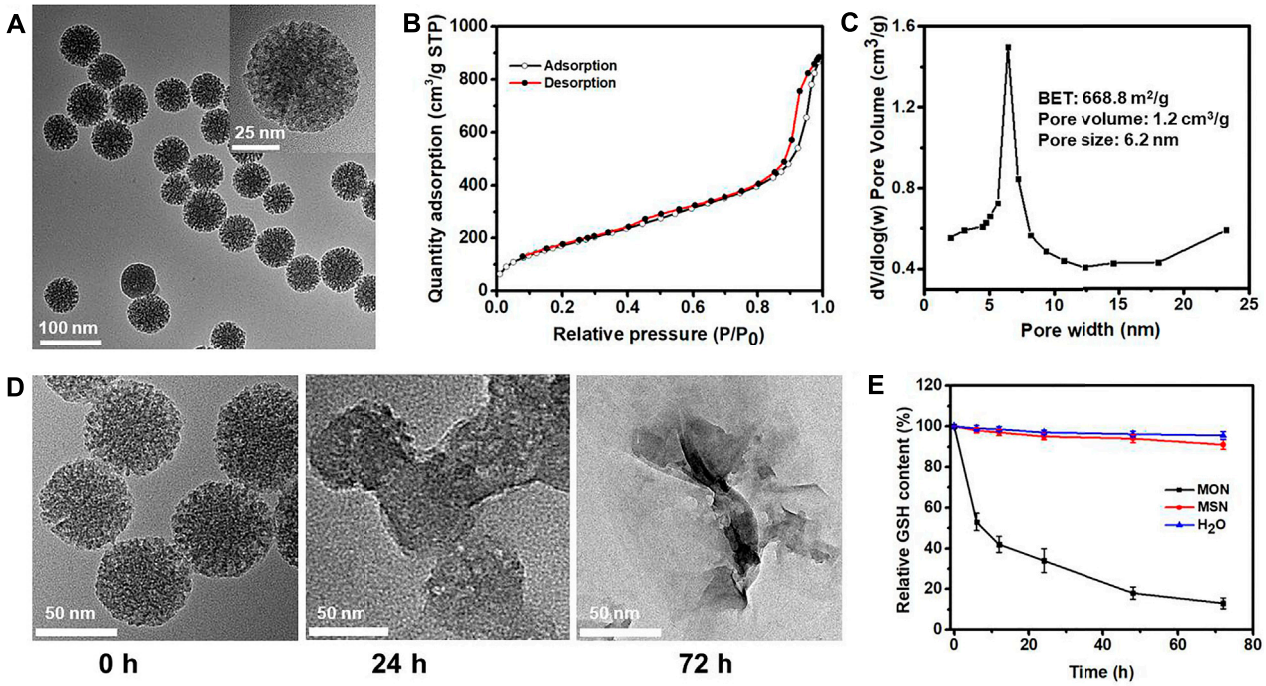

FIGURE 1 | Preparation and characterization of MON. **(A)** TEM, **(B)** N_2 adsorption isotherm,**(C)** pore size distribution of MON. **(D)** TEM images of MONs showing degradation at 0, 24 and 72 h under 10 mM GSH. **(E)** GSH depletion of MON.

have validated the advantages of this biomimetic MON-Pt@CM that reduced server-side effects and improved therapeutic potency.

MATERIALS AND METHODS

Chemicals and Reagents

Chemicals and characterization method was details in Supporting information.

Preparation of MON

According to our previous reports, a designed diselenide-bridged MON was synthesized (Shao et al., 2018a). Briefly, 0.6 g cetyltrimethylammonium tosylate (CTAT), and 0.15 g triethanolamine (TEA) were added into 40 ml deionized water. After stirring at 80°C for 30 min, a mixture of 4.0 g TEOS, 1.0 g Bis [3-(triethoxysilyl)propyl]diselenide (BTESePD) and 3 ml ethanol was added dropwise. The mixture was a continuous reaction for another 4 h. The PEG-silane (3 g) was added dropwise into the mixture after cooling to room temperature, and the mixture was stirred overnight. Then, the mixture was stirred for another 4 h at 80°C. The products were collected, washed thrice, and extracted with a solution of NH_4NO_3 (0.7% w/v) in ethanol for 12 h. FITC-labeled MON was obtained for cellular internalization tracking as our previous works (Shao et al., 2018b). The nonbiodegradable MSN was prepared according to the above mothed except TEOS (5 g) as the only silica source.

Preparation of Activated Cisplatin

The activated cisplatin was prepared as described in the literature (Sood et al., 2006). Cisplatin (400 mg, 1.33 mmol) and $AgNO_3$ (406 mg, 2.39 mmol) were added into 10 ml H_2O. Subsequently, a diluted HNO_3 solution was used to tune pH value to 2. The suspension was stirred at 70°C overnight in the dark. The mixture was cooled at 4°C overnight. The mixture was filtrated through a 0.22 μm syringe filter to obtain activated cisplatin.

Cisplatin Loading and GSH-Responsive Drug Release

A 20 mg MON (or MSN) was mixed with 8 mg active cisplatin in 10 ml solution under sonication, and the resulting mixture was stirred at 500 rpm at 37°C overnight to obtain MON-Pt. The amount of platinum was analyzed by inductively coupled plasma atomic emission spectrometry (ICP-OES). The drug-loading content was calculated as in the equation, Drug loading content (%) = mass of cisplatin in MON-Pt/mass of MON-Pt. For drug release analysis, MON-Pt (5 mg) was dispersed in 10 ml PBS with/without 10 mM GSH has shaken at 100 rpm. The amount of cisplatin release in the supernatant was measured.

Cancer Cell Membrane Derivation and MON-Pt@CM Preparation

The cancer cell membrane–derived vesicles were prepared as described previously (Zhang et al., 2021). 4T1 cells were collected, lysed, and collected via centrifugation. Cell membrane fragments

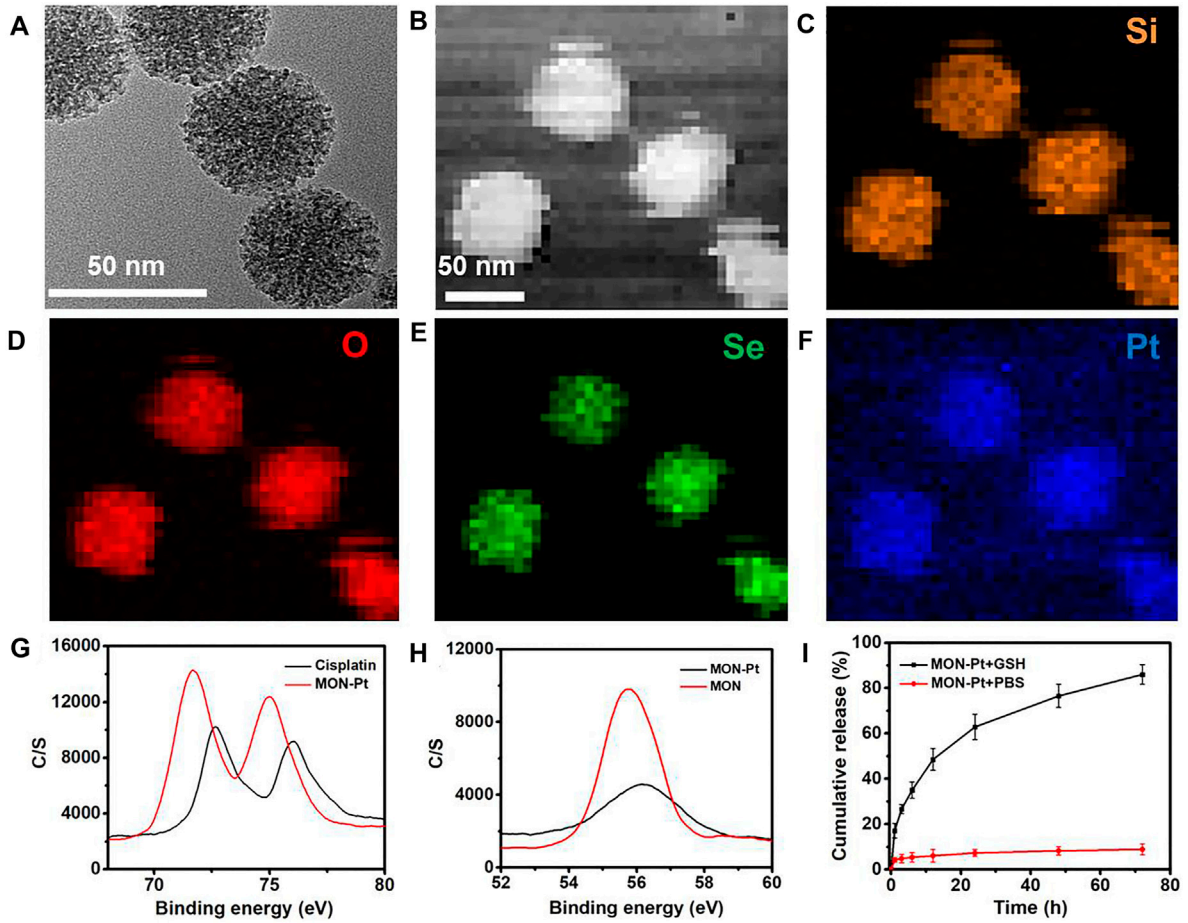

FIGURE 2 | Preparation and characterization of MON-Pt. **(A)** TEM of MON-Pt. **(B–F)** Mapping images of MON-Pt. XPS spectrum of **(G)** platinum and **(H)** selenium of MON-Pt. **(I)** Cisplatin release profiles of MON@Pt in the presence or absence of 10 mM GSH. All data are mean ± SD (n = 3).

were obtained by extrusion and sonication. The final CM vesicles were extruded serially through 1-μm, 400-nm, and 200-nm polycarbonate membranes (Whatman) with an Avanti Mini-Extruder (Avanti Polar Lipids). The 4-chlorobenzenesulfonate salt (DiD) dye-labeled CM vesicles were prepared by staining 4T1 cancer cells before hypotonic lysing. The obtained CM mixed with MON-Pt, sonicated for 5 min to obtain cancer cell membrane-coated MON-Pt (MON-Pt@CM). The obtained MON-Pt@CM was stored at 4°C. SDS-PAGE was used to analyze the protein component of MON-Pt@CM. The marker protein CD47 of 4T1 cells in 4T1 cell membranes and MON-Pt@CM was identified by Western blot.

Extracellular GSH Depletion Assay

The MON was mixed with GSH (10 mM) in a 10 ml solution. The mixtures were shaken overnight at room temperature, and the GSH concentration of the supernatant was analyzed by Ellman's reagent.

Cell Viability

The cell viability was determined by 3-(4,5-dimethylthiazole-2-yl)-2,5-diphenyl tetrazolium bromide (MTT) assay. Briefly, 4T1 cells (5×10^3 cells/well) were inoculated overnight in a 96-well plate. The next day, cells were treated with different formulations. After treatment for 48 h, cell cytotoxicity was analyzed.

Intracellular GSH Depletion Assay

4T1 cells (3×10^4 cells/well) were cultured in 24-well culture plate overnight. After treating with formulations for 24 h, cells were washed, and intracellular glutathione content was analyzed by the Micro Reduced Glutathione (GSH) Assay Kit (BC1175, Solarbio, Beijing, China), following the manufacturer's protocol.

Cellular Uptake and Homogenous Targeting Effects

Homogenous targeting capacity of cisplatin, MON-Pt or MON-Pt@CM (30 μg/ml based on cisplatin) was measured. 4T1, MCF-10A, and RAW264.7 cells (2×10^5 cells/well) were inoculated in a six-well plate for quantifying analysis of endocytosis. After being inoculated overnight, cells were treated with formulations for another 5 h. The cells were digested and collected. The cellular

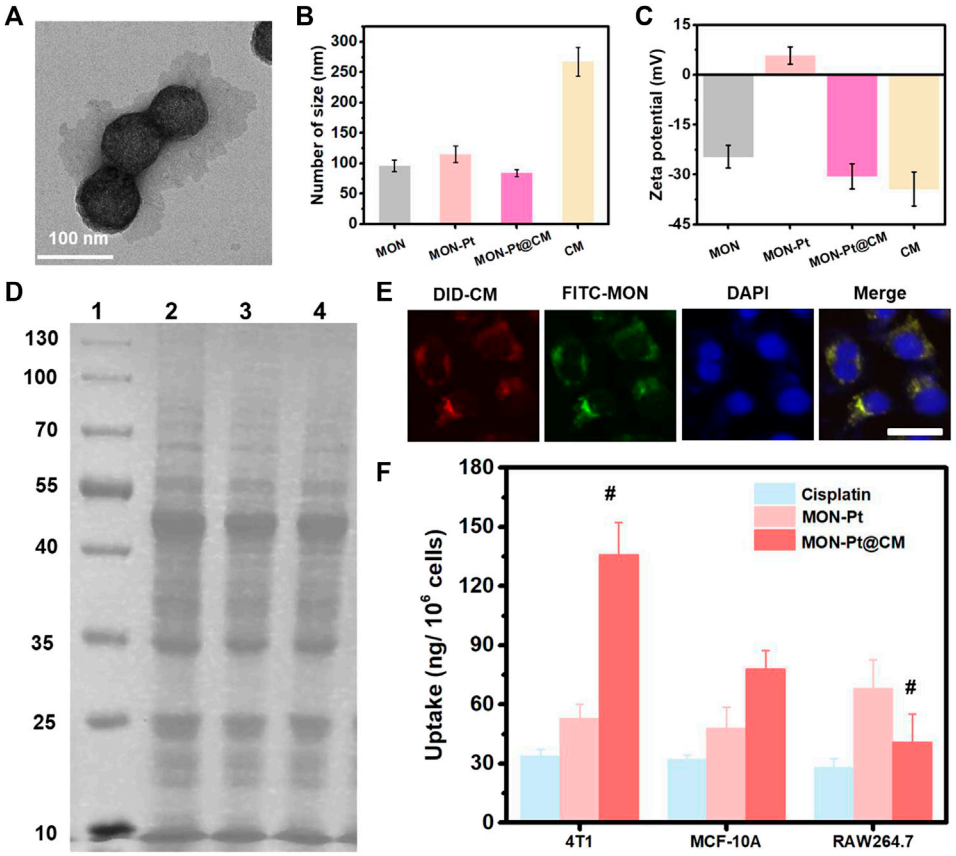

FIGURE 3 | Preparation and characterization of MON-Pt@CM. **(A)** TEM, **(B)** size, **(C)** zeta potential of MON-Pt@CM. **(D)** SDS-PAGE protein analysis. 1-well: marker, 10–130 kDa; 2-well: cell lysate; 3-well: CM vesicle; 4-well: MON-Pt@CM. **(E)** intracellular colocalization of DiD-labeled CM vesicles (red) and FITC-labeled MON (green) of FITC-MON-Pt@DID-CM in 4T1 cells after incubation for 1 h. Scale bars indicate 5 μm. **(F)** Selective uptake of MON-Pt@KP1339 in 4T1, MCF-10A, and RAW264.7 cells after incubation for 6 h $^{\#}p < .05$ compared with MON-Pt group.

uptake of MON-Pt@CM was measured by analysis of platinum content using ICP-OES.

4T1 cells (3×10^4 cells/well) were inoculated overnight in a 24-well culture plate to analyze the colocalization of the cancer cell membranes and MON cores. After incubation with FITC-MON@CM-DiD (30 μg/ml) for 3 h, 4T1 cells were washed and stained with DAPI. The cell imaging was observed under a fluorescence microscope.

Pharmacokinetics and Biodistribution *in vivo*

The ethical committee approved all experimental animal protocols, according to the Suzhou Institute of Biomedical Engineering and Technology recommendations, the Chinese Academy of Sciences Laboratory Animal Center. 4T1 tumor model was established by subcutaneous injection of 4T1 cells (5×10^5 cells) into the left flank of the BALB/C mice (18–20 g, 4–5 weeks). Animals were cultivated in specific pathogen-free (SPF) conditions. To investigate the pharmacokinetics and biodistribution, 4T1 tumor-bearing mice were injected with free cisplatin, MON-Pt, or MON-Pt@CM solution (2 mg/kg based on cisplatin). ICP-OES measured the platinum content in the blood. Major organs and tumor were harvested to investigate the organ distribution after administration of 24 h. ICP-OES measured the platinum content in each sample.

In vivo Chemotherapy

The 4T1 tumor model was established. When the tumor volume was grown to 100 mm^3, the mice were administered with PBS, cisplatin, MON-Pt, MON-Pt@CM, MSN-Pt@CM (2 mg/kg based on cisplatin) once every 3 days. All of the mice had recorded tumor volume and body weight. After treatment for 21 days, the mice were sacrificed and recorded tumor weight. The main organs (liver, spleen, kidneys, heart, and lungs) were stained with Hematoxylin and eosin (H&E) to analyze pathophysiology. Biochemical parameters indexes were also analyzed.

RESULTS AND DISCUSSION

Preparation and GSH Depletion of MON

Mesoporous organosilica nanoparticles with high biocompatibility, porous structure, tunable morphology, highly efficient drug loading capacity, and facile surface-functionalization are widely used to deliver anticancer drugs and perform controlled drug release in response to the tumor microenvironment (Chen et al., 2018; Omar et al., 2018; Yu et al., 2018; Zhang et al., 2020). According to previous reports, diselenide-bridged MON were fabricated via the sol-gel method (Shao et al., 2020; Zhang et al., 2021). The morphology and pore structures of MON were characterized by transmission electron microscope (TEM) and scanning electron microscope (SEM). It was shown that parent MON exhibited uniform spherical particles with an average diameter of 60 ± 5 nm (**Figure 1A**, and **Supplementary Figure S1**). The MON showed worm-like mesoporous channels. The characteristic type-IV of N_2 adsorption–desorption isotherms indicate a mesoporous structure (**Figure 1B**), and the average pore size was 6.2 nm according to the BJH pore size distribution (**Figure 1C**). The MON showed a high surface area (668.8 m^2/g) and cumulative pore volume (1.2 cm^3/g), beneficial for drug loading.

Energy-dispersive X-ray spectroscopy (EDS) revealed a strong signature for the Se element in the MON (**Supplementary Figure S2**). This agrees with the high Se element content (12.4%) in diselenide-bond-bridged MON determined by ICP-OES. The high hybrid of diselenide bond in MON confers sensitive matrix-degradation in response to redox conditions. The degradation of MON was investigated in the media mimicking the tumor microenvironment (10 mM GSH). We observed that MON underwent rapid degradation after 1 day of incubation (**Figure 1D**). The structure of MON disintegrated into small fragments after 3 days of exposure to GSH solution. However, MON was stable in normal physiological conditions (**Supplementary Figure S3**). Our previous research reveals the degradation mechanism attributed to the diselenide bond cleavage under reductive conditions. We further confirmed the mechanisms by determining the residual content of GSH in the mimicking media. As shown in **Figure 1E**, the content of reductive GSH was rapidly decreased to 13.5% after 72 h, indicating excellent GSH depletion. As a control, nondegradable mesoporous silica nanoparticles (MSN) were prepared and exhibited a stable structure in GSH solution (**Supplementary Figure S4**) and did not cause consumption of GSH (**Figure 1E**). These results verify that diselenide-bond-bridged MON has a special GSH scavenge, which may avoid the deactivation of cisplatin-based chemotherapy in the tumor microenvironment.

Preparation and Control Release of MON-Pt

It is well-established that cisplatin exists as an equilibrium of "neutral" or "cationic" structure in an aqueous solution (Liu et al., 2021a). The "neutral" structure is dominant in extracellular high Cl^- ion concentration (≈150 mM). The cationic structure is pharmaceutically active cisplatin due to Cl^- ion concentration (≈30 mM), which induced nuclear DNA crosslinking. This activated cisplatin was easily deactivated by a high intracellular concentration of GSH in tumor cells. Meanwhile, there are also some advantages of cationic cisplatin with coordination capacity for high drug loading and controllable delivery. These findings inspired us to consider loading cationic, activated cisplatin into diselenide-bond-bridged MON for controllable delivery and scavenging intracellular GSH to enhance Pt-based chemotherapy.

The active cisplatin was synthesized by silver nitrate and collected through centrifugation and filtration. The high hybrid of selenium atom in MON provided an abundant coordination site. MON loading cisplatin (MON-Pt) was prepared via mixing with active cisplatin, resulting in 16.1% ± 0.7% of the loading capacity of cisplatin. The morphology of MON-Pt was consistent with parent MON (**Figure 2A**). The elemental mapping of MON-Pt revealed a strong signal of Pt and Se elements (**Figures 2B–F**). In addition, the binding energy of selenium and platinum atoms was characterized by X-ray photoelectron spectroscopy (XPS). After loading with cisplatin, the binding energy of selenium 3 days in MON-Pt shifted upward from 55.7 to 56.2 eV (**Figure 2G**). Meanwhile, the binding energy of platinum 3p in MON-Pt shifted downward from 75.9 to 72.3 to 74.9 and 71.7 eV, respectively (**Figure 2H**). The results of the binding energy analysis supported that coordination bonds between selenium and platinum atom in MON-Pt were formed. The GSH-responsive degradation of MON-Pt inducing controlled drug release was further investigated. The rapid release of cisplatin (>70% after 12 h) was observed in 10 mM GSH solution mimicking the tumor microenvironment (**Figure 2I**). In PBS solution without GSH, less than 10% of cisplatin is released in 96 h. To further demonstrate the advantages of diselenide-bridged MON for controllable cisplatin delivery, mesoporous silica nanoparticles loading cisplatin (MSN-Pt) were prepared as a comparison (**Supplementary Figure S4**). The cisplatin loading capacity of MSN (MSN-Pt) was about 4.3% determined by ICP-OES. Compared with MON-Pt, nondegradable MSN-Pt exhibited a slower cisplatin release manner in 10 mM GSH solution (**Figure 2I** and **Supplementary Figure S5**), but increased a high degree of premature leakage (40%) after incubation in PBS solution over 48 h (**Supplementary Figure S5**). These results verify that the coordination bind between selenium and platinum atoms prevented premature drug leakage, facilitating the controlled on-demand release of cisplatin in response to the tumor microenvironment.

Preparation and Characterization of MON-Pt@CM

Besides on-demand release, targeted drug delivery of cisplatin is another important pathway to overcome unwanted side effects (Shao et al., 2018b; Shao et al., 2020; Kuo et al., 2021). Breast cancer cell membrane (CM) coating nanocarriers could realize homologous tumor-targeted and immune-evasive drugs delivery. 4T1 breast cancer cell membrane (CM) was used to coat MON-Pt according to our previous work (Shao et al., 2018a; Zhang et al., 2021). The biomimetic CM-coated MON-Pt (MON-Pt@CM)

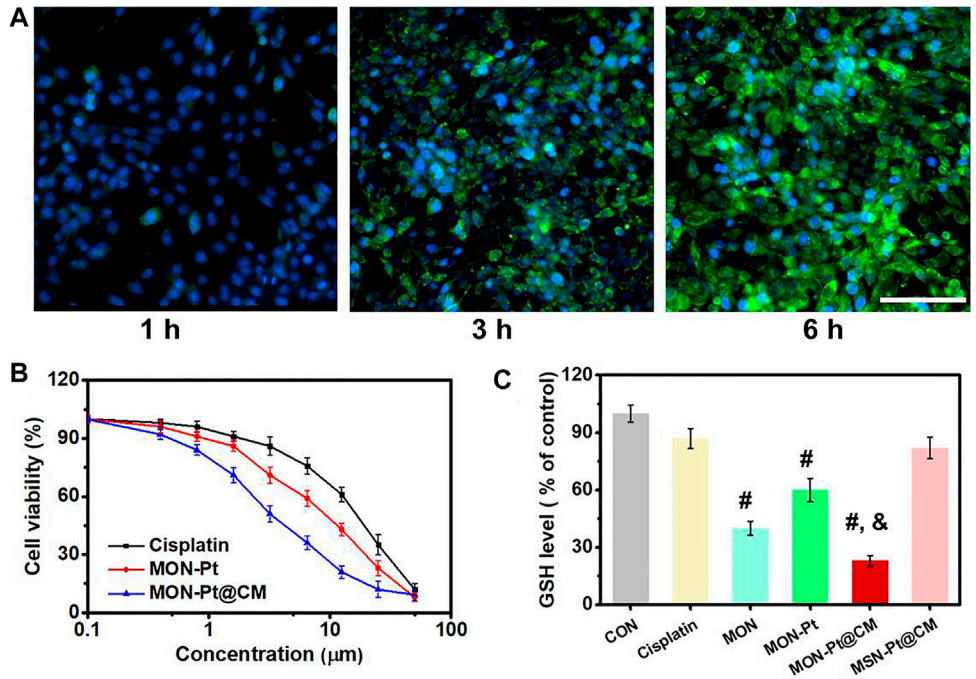

FIGURE 4 | MON-Pt@CM antitumor and GSH depletion *in vitro*. **(A)** Uptake of 4T1 cells incubated with FITC-MON-Pt@CM. Scale bars indicate 50 μm. **(B)** Cytotoxicity of MON-Pt@CM. **(C)** GSH depletion of MON-Pt@CM in 4T1 cells. $^{\#,\,\&}$ $p < .05$ compared with cisplatin group ($^{\#}$) and MSN-Pt@CM group ($^{\&}$).

exhibited a spherical structure with a thin, smooth membrane shell (**Figure 3A**). The hydrodynamic diameter of MON-Pt@CM was slightly decreased than MON-Pt (**Figure 3B**) due to the CM coating facilitating the stability while the surface charge property was decreased dramatically and similar to the CM vesicles (**Figure 3C**). These results confirm that we successfully constructed a CM-coated MON-Pt. The MON-Pt@CM showed excellent colloidal stability incubating in 10% fetal bovine serum-containing medium over 7 days, and MON-Pt showed significant aggregation (**Supplementary Figure S6**). These results indicate that CM coating promoted colloidal stability. Protein electrophoresis analysis further suggests that the membrane proteins from 4T1 CM proteins could be well retained on the MON-Pt@CM (**Figure 3D**). 4T1 breast cells incubated with dye-labeled FITC-MON-Pt@ DiD-CM for 3 h. A high degree of intracellular colocalization indicated the structural integrity of CM-cloaked MON-Pt during the delivery process (**Figure 3E**), which benefited from keeping homologous tumor-targeted and immune-evasive from CM. Higher internalization of MON-Pt@CM was observed in 4T1 cells than in MCF-10A or RAW264.7 macrophages (**Figure 3F**). The facts suggest that biomimetic MON-Pt@CM have homologous targeting ability and immune system evasion advantages. MON-Pt@CM anti-tumor and GSH depletion *in vitro*.

After 4T1 cells incubated with FITC-labeled, intracellular fluorescence became stronger along with prolonged incubation time (**Figure 4A**). It implies that MON-Pt@CM could have efficient uptake by 4T1 cells. Given the selective and efficient cellular uptake capacity, the cytotoxicity of MON-Pt@CM against 4T1 cells was subsequently examined by MTT assay. As shown in **Figure 4B**, free cisplatin, MON-Pt, and MON-Pt@CM all displayed dose-dependent cytotoxicity. It is worth noting that the IC_{50} (the half-maximal inhibitory concentration of drug) of free cisplatin, MON-Pt, and MON-Pt@CM was 15.95, 10.72, and 4.59 μM, respectively. Cell-membrane coating MON-Pt@CM exhibited a stronger antitumor ability. A different mechanism may cause improved cytotoxicity. As expected, biomimetic structure facilitated uptake of cisplatin (**Figure 3F**). In addition, the cellular concentration of GSH was determined to be obviously reduced after MON-Pt and MON-Pt@CM treatment (**Figure 4C**). MON was functional modification of PEG on the surface, which could be more stable than MON-Pt in culture medium. The high dispersity may facilitate the uptake of MON to scavenge intracellular GSH. When 4T1 cells were cultured in 5 mM GSH containing medium, the cytotoxicity of cisplatin against 4T1 cells was obvious deactivation. Diselenide bonds containing the MON-Pt@CM nanosystem could reduce the deactivation cisplatin, and enhance antitumor efficiency (**Supplementary Figure S7**). The results further prove that biomimetic MON-Pt@CM containing the diselenide bond could enhance cisplatin-based chemotherapy. MON-Pt@CM mediated chemotherapy *in vivo*.

A challenge in cisplatin-based chemotherapy is that cisplatin drugs achieve a long blood circulation time and tumor-targeted delivery. To investigate the role of cancer cell camouflaging on cisplatin delivery, we measured pharmacokinetic profiles and

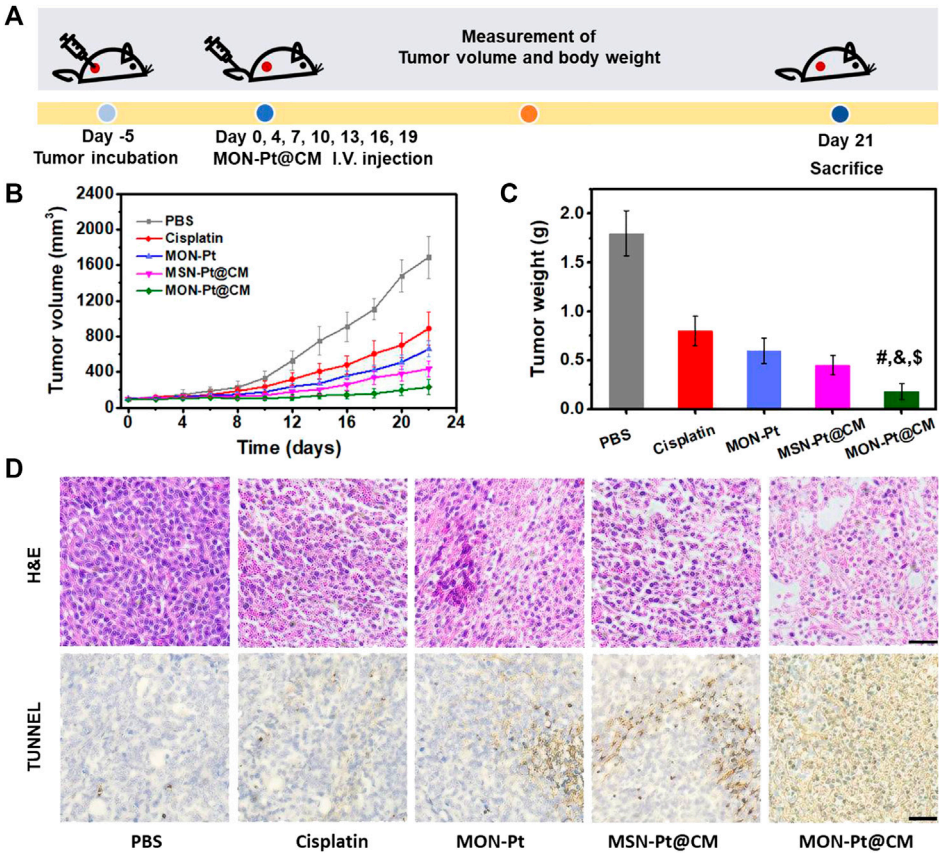

FIGURE 5 | MON-Pt@CM mediated chemotherapy *in vivo*. **(A)** Schematic of treatment schedule in 4T1 bearing tumor model. **(B)** Tumor volume and **(C)** tumor weight. **(D)** H&E stain and TUNEL positive cells of the tumor. Scale bars indicate 50 μm $^{\#,\,\&,\,\$}p < .05$ compared with PBS group ($^{\$}$), cisplatin group ($^{\#}$), and MSN-Pt@CM group ($^{\&}$).

biodistribution in mice. The biomimetic MON-Pt@CM exhibited a prolonged elimination half-life (18.4 h) than that of MON-Pt (6.6 h) and free cisplatin (3.7 h) as shown in **Supplementary Figure S8**. The extended blood circulation time suggests that CM coating conferred colloidal stability and the immune-evasive ability. We examined the biodistribution by determining the platinum content of tumor tissue and major organs (**Supplementary Figure S9**). Compared with MON-Pt, MON-Pt@CM dramatically reduced liver and spleen retention, indicating that cancer-cell-membrane camouflaging promoted immune cell evasion *in vivo*. Moreover, the biomimetic cancer-cell-membrane of MON-Pt@CM referred homologous targeting capacity, dramatically enhancing tumor accumulation.

Encouraged by *in vitro* and *in vivo* results, we next evaluated the therapeutic efficacy on mice bearing 4T1 heterotopic mammary tumor (**Figure 5A**). All mice treated with cisplatin or cisplatin-based formulations showed reduced tumor volumes and tumor weights compared with the control group after treatment (**Figures 5B,C**, and **Supplementary Figure S10**). As envisioned, CM coating MON-Pt@CM significantly enhanced the anticancer effect more than MON-Pt, indicating the advantages of homogeneous tumor targeting. To reveal the advantages of diselenide-bridged MON in the delivery of cisplatin, we prepared CM coating MSN-Pt (MSN-Pt@CM), which serves as a control. MON-Pt@CM exhibits a more pleasing anticancer effect than that of MSN-Pt@CM. This phenomenon could be explained by the GSH-responsive release and intracellular GSH deletion to reduce the deactivation of cisplatin. Terminal deoxynucleotidyl transferase dUTP nick end labeling (TUNEL) staining and hematoxylin-eosin (H&E) staining of the tumor sections further revealed the highest apoptosis and necrosis of the tumor cells in MON-Pt@CM groups (**Figure 5D**).

The safety of cisplatin-based chemotherapy is a significant consideration. None of the mice show apparent weight loss (**Supplementary Figure S11**). The systemic toxicity was further evaluated by serum biochemical parameters, and no abnormal changes were observed (**Supplementary Figure S11**). Moreover, H&E staining demonstrated that all treatment groups have no significant pathological changes in the heart, liver,

spleen, lung, and kidney (**Supplementary Figure S12**). Overall, the cancer-cell-membrane-cloaked MON-Pt@CM displayed low systemic toxicity *in vivo*.

In summary, we developed a facile and effective cisplatin drug delivery by diselenide-bond-bridged MONs nanocarrier for safe and efficient chemotherapy. Biodegradable MON was used for activated cisplatin loading by coordination attachment to prevent premature leakage in normal tissue and to achieve degradation-controlled cisplatin release in response to the tumor microenvironment. Besides this, diselenide-bond-bridged MON could consume excess abundant intracellular GSH in the degradation process, which avoids cisplatin deactivation to enhance the chemotherapy effect. MON-Pt coating with cancer CM achieved better tumor targeting and immune system evasion, combined with controlled cisplatin release in response to the tumor microenvironment, to reduce the unwanted side effects. After systemic administration, the MON-Pt@CM exhibited long time in blood circulation and targeting tumor accumulation, leading to remarkable tumor growth inhibition without systematic toxicity. Collectively, this work suggests a biomimetic and biodegradable nanocarrier and offers great promise in enhancing the efficacy and safety of cisplatin-based chemotherapy.

DATA AVAILABILITY STATEMENT

The original contributions presented in the study are included in the article/**Supplementary Material**, further inquiries can be directed to the corresponding authors.

ETHICS STATEMENT

The animal study was reviewed and approved by the Suzhou Institute of Biomedical Engineering and Technology recommendations, the Chinese Academy of Sciences Laboratory Animal Center.

AUTHOR CONTRIBUTIONS

FC, WD, and ZC designed the research. FC, JP, FZ, YW, MG, and LL performed the research. LC, QM, MC and ZC analyzed the data. FC, WD, and ZC wrote the manuscript.

FUNDING

This study was supported by the National Key R&D Program of China (Grand No. 2020YFC2004500), the National Natural Science Foundation of China (Grand No. 81771982, 21803075, 91959112, and 81902166), the Natural Science Foundation of Jiangsu Province (BK20181236 and BK20170389), the Primary Research & Development Plan of Jiangsu Province (BE2019683) and the Science and Technology Department of Jinan City (2018GXRC016).

SUPPLEMENTARY MATERIAL

The Supplementary Material for this article can be found online at: https://www.frontiersin.org/articles/10.3389/fbioe.2022.860949/full#supplementary-material

REFERENCES

Birhan, Y. S., and Tsai, H.-C. (2021). Recent Developments in Selenium-Containing Polymeric Micelles: Prospective Stimuli, Drug-Release Behaviors, and Intrinsic Anticancer Activity. *J. Mater. Chem. B* 9 (34), 6770–6801. doi:10.1039/d1tb01253c

Cai, W., Wang, J., Chu, C., Chen, W., Wu, C., and Liu, G. (2019). Metal-Organic Framework-Based Stimuli-Responsive Systems for Drug Delivery. *Adv. Sci.* 6 (1), 1801526. doi:10.1002/Advs.201801526

Chen, F. M., Zhang, F., Shao, D., Zhang, W. B., Zheng, L. Q., Wang, W., et al. (2020). Bioreducible and Traceable Ru(III) Prodrug-Loaded Mesoporous Silica Nanoparticles for Sequentially Targeted Nonsmall Cell Lung Cancer Chemotherapy. *Appl. Mater. Today* 19. doi:10.1016/J.Apmt.2019.100558

Chen, F., Xiao, F., Zhang, W., Lin, C., and Wu, Y. (2018). Highly Stable and NIR Luminescent Ru-Lpmsn Hybrid Materials for Sensitive Detection of Cu2+ *In Vivo*. *ACS Appl. Mater. Inter.* 10 (32), 26964–26971. doi:10.1021/acsami.8b08887

Chen, H., Wang, Y., Liu, Y., Tang, L., Mu, Q., Yin, X., et al. (2021). Delivery of Cationic Platinum Prodrugs via Reduction Sensitive Polymer for Improved Chemotherapy. *Small* 17 (45), 2101804. doi:10.1002/Smll.202101804

Davidi, E. S., Dreifuss, T., Motiei, M., Shai, E., Bragilovski, D., Lubimov, L., et al. (2018). Cisplatin-conjugated Gold Nanoparticles as a Theranostic Agent for Head and Neck Cancer. *Head & Neck* 40 (1), 70–78. doi:10.1002/hed.24935

Dias, R. d. S., Cervo, R., Siqueira, F. d. S., Campos, M. M. A., Lang, E. S., Tirloni, B., et al. (2020). Synthesis and Antimicrobial Evaluation of Coordination Compounds Containing 2,2′-bis(3-aminopyridyl) Diselenide as Ligand. *Appl. Organomet. Chem.* 34 (9). doi:10.1002/Aoc.5750

Fentahun Darge, H., Yibru Hanurry, E., Simegniew Birhan, Y., Worku Mekonnen, T., Tizazu Andrgie, A., Chou, H.-Y., et al. (2021). Multifunctional Drug-Loaded Micelles Encapsulated in Thermo-Sensitive Hydrogel for *In Vivo* Local Cancer Treatment: Synergistic Effects of Anti-vascular and Immuno-Chemotherapy. *Chem. Eng. J.* 406, 126879. doi:10.1016/J.Cej.2020.126879

Ferlay, J., Colombet, M., Soerjomataram, I., Parkin, D. M., Piñeros, M., Znaor, A., et al. (2021). Cancer Statistics for the Year 2020: An Overview. *Int. J. Cancer* 149 (4), 778–789. doi:10.1002/ijc.33588

Fujishiro, H., Taguchi, H., Hamao, S., Sumi, D., and Himeno, S. (2021). Comparisons of Segment-specific Toxicity of Platinum-Based Agents and Cadmium Using S1, S2, and S3 Cells Derived from Mouse Kidney Proximal Tubules. *Toxicol. Vitro* 75, 105179. doi:10.1016/J.Tiv.2021.105179

Han, Y., Yin, W., Li, J., Zhao, H., Zha, Z., Ke, W., et al. (2018). Intracellular Glutathione-Depleting Polymeric Micelles for Cisplatin Prodrug Delivery to Overcome Cisplatin Resistance of Cancers. *J. Controlled Release* 273, 30–39. doi:10.1016/j.jconrel.2018.01.019

He, H., Xiao, H., Kuang, H., Xie, Z., Chen, X., Jing, X., et al. (2014). Synthesis of Mesoporous Silica Nanoparticle-Oxaliplatin Conjugates for Improved Anticancer Drug Delivery. *Colloids Surf. B: Biointerfaces* 117, 75–81. doi:10.1016/j.colsurfb.2014.02.014

He, L., Sun, M., Cheng, X., Xu, Y., Lv, X., Wang, X., et al. (2019). pH/Redox Dual-Sensitive Platinum (IV)-based Micelles with Greatly Enhanced Antitumor Effect for Combination Chemotherapy. *J. Colloid Interf. Sci.* 541, 30–41. doi:10.1016/j.jcis.2019.01.076

Huang, X., Shen, Q.-K., Zhang, H.-J., Li, J.-L., Tian, Y.-S., and Quan, Z.-S. (2018). Design and Synthesis of Novel Dehydroepiandrosterone Analogues as Potent Antiproliferative Agents. *Molecules* 23 (9), 2243. doi:10.3390/Molecules23092243

Kawahara, B., Ramadoss, S., Chaudhuri, G., Janzen, C., Sen, S., and Mascharak, P. K. (2019). Carbon Monoxide Sensitizes Cisplatin-Resistant Ovarian Cancer Cell Lines toward Cisplatin via Attenuation of Levels of Glutathione and Nuclear Metallothionein. *J. Inorg. Biochem.* 191, 29–39. doi:10.1016/j.jinorgbio.2018.11.003

Khan, M. M., Madni, A., Tahir, N., Parveen, F., Khan, S., Jan, N., et al. (2020). Co-Delivery of Curcumin and Cisplatin to Enhance Cytotoxicity of Cisplatin Using Lipid-Chitosan Hybrid Nanoparticles. *Ijn* Vol. 15, 2207–2217. doi:10.2147/Ijn.S247893

Kuo, M. T., Huang, Y.-F., Chou, C.-Y., and Chen, H. H. W. (2021). Targeting the Copper Transport System to Improve Treatment Efficacies of Platinum-Containing Drugs in Cancer Chemotherapy. *Pharmaceuticals* 14 (6), 549. doi:10.3390/Ph14060549

Lan, D., Wang, L., He, R., Ma, J., Bin, Y., Chi, X., et al. (2018). Exogenous Glutathione Contributes to Cisplatin Resistance in Lung Cancer A549 Cells. *Am. J. Transl Res.* 10 (5), 1295–1309.

Lee, S. M., Heard, P. J., and Tiekink, E. R. T. (2018). Molecular and Supramolecular Chemistry of Mono- and Di-selenium Analogues of Metal Dithiocarbamates. *Coord. Chem. Rev.* 375, 410–423. doi:10.1016/j.ccr.2018.03.001

Lin, J. J., Schoenfeld, A. J., Zhu, V. W., Yeap, B. Y., Chin, E., Rooney, M., et al. (2020). Efficacy of Platinum/Pemetrexed Combination Chemotherapy in ALK-Positive NSCLC Refractory to Second-Generation ALK Inhibitors. *J. Thorac. Oncol.* 15 (2), 258–265. doi:10.1016/j.jtho.2019.10.014

Ling, X., Chen, X., Riddell, I. A., Tao, W., Wang, J., Hollett, G., et al. (2018). Glutathione-Scavenging Poly(disulfide Amide) Nanoparticles for the Effective Delivery of Pt(IV) Prodrugs and Reversal of Cisplatin Resistance. *Nano Lett.* 18 (7), 4618–4625. doi:10.1021/acs.nanolett.8b01924

Liu, X., Jiang, J., Chang, C. H., Liao, Y. P., Lodico, J. J., Tang, I., et al. (2021a). Development of Facile and Versatile Platinum Drug Delivering Silicasome Nanocarriers for Efficient Pancreatic Cancer Chemo-Immunotherapy. *Small* 17 (14), 2005993. doi:10.1002/smll.202005993

Liu, X., Yuan, Z., Tang, Z., Chen, Q., Huang, J., He, L., et al. (2021b). Selenium-driven Enhancement of Synergistic Cancer Chemo-/radiotherapy by Targeting Nanotherapeutics. *Biomater. Sci.* 9 (13), 4691–4700. doi:10.1039/d1bm00348h

Omar, H., Moosa, B., Alamoudi, K., Anjum, D. H., Emwas, A.-H., El Tall, O., et al. (2018). Impact of Pore-Walls Ligand Assembly on the Biodegradation of Mesoporous Organosilica Nanoparticles for Controlled Drug Delivery. *Acs Omega* 3 (5), 5195–5201. doi:10.1021/acsomega.8b00418

Peng, J., Chen, F., Liu, Y., Zhang, F., Cao, L., You, Q., et al. (2022). A Light-Driven Dual-Nanotransformer with Deep Tumor Penetration for Efficient Chemo-Immunotherapy. *Theranostics* 12 (4), 1756–1768. doi:10.7150/thno.68756

Shao, D., Li, M., Wang, Z., Zheng, X., Lao, Y.-H., Chang, Z., et al. (2018a). Bioinspired Diselenide-Bridged Mesoporous Silica Nanoparticles for Dual-Responsive Protein Delivery. *Adv. Mater.* 30, 1801198. doi:10.1002/adma.201801198

Shao, D., Li, M., Wang, Z., Zheng, X., Lao, Y.-H., Chang, Z., et al. (2018b). Bioinspired Diselenide-Bridged Mesoporous Silica Nanoparticles for Dual-Responsive Protein Delivery. *Adv. Mater.* 30 (29), 1801198. doi:10.1002/Adma.201801198

Shao, D., Zhang, F., Chen, F., Zheng, X., Hu, H., Yang, C., et al. (2020). Biomimetic Diselenide-Bridged Mesoporous Organosilica Nanoparticles as an X-ray-Responsive Biodegradable Carrier for Chemo-Immunotherapy. *Adv. Mater.* 32 (50), 2004385. doi:10.1002/Adma.202004385

Shi, C., Dawulieti, J., Shi, F., Yang, C., Qin, Q., Shi, T., et al. (2022). A Nanoparticulate Dual Scavenger for Targeted Therapy of Inflammatory Bowel Disease. *Sci. Adv.* 8 (4), eabj2372. doi:10.1126/sciadv.abj2372

Sood, P., Thurmond, K. B., Jacob, J. E., Waller, L. K., Silva, G. O., Stewart, D. R., et al. (2006). Synthesis and Characterization of AP5346, a Novel Polymer-Linked Diaminocyclohexyl Platinum Chemotherapeutic Agent. *Bioconjug. Chem.* 17 (5), 1270–1279. doi:10.1021/bc0600517

Sun, C., Wang, J., Hu, J., Lu, W., Song, Z., and Zhang, Y. (2020). Facile Synthesis of a Well-Defined Heteroatom-Containing Main Chain Polycarbonate for Activated Intracellular Drug Release. *Mater. Chem. Front.* 4 (8), 2443–2451. doi:10.1039/c9qm00778d

Sun, T., Zhang, G., Ning, T., Chen, Q., Chu, Y., Luo, Y., et al. (2021). A Versatile Theranostic Platform for Colorectal Cancer Peritoneal Metastases: Real-Time Tumor-Tracking and Photothermal-Enhanced Chemotherapy. *Adv. Sci.* 8 (20), 2102256. doi:10.1002/Advs.202102256

Wang, H., Yang, J., Cao, P., Guo, N., Li, Y., Zhao, Y., et al. (2020a). Functionalization of Bismuth Sulfide Nanomaterials for Their Application in Cancer Theranostics. *Chin. Chem. Lett.* 31 (12), 3015–3026. doi:10.1016/j.cclet.2020.05.003

Wang, J., Lu, S., Yu, X., Hu, Y., Sun, Y., Wang, Z., et al. (2021). Tislelizumab Plus Chemotherapy vs Chemotherapy Alone as First-Line Treatment for Advanced Squamous Non-small-cell Lung Cancer. *JAMA Oncol.* 7 (5), 709–717. doi:10.1001/jamaoncol.2021.0366

Wang, Y., Yan, J., Wen, N., Xiong, H., Cai, S., He, Q., et al. (2020b). Metal-organic Frameworks for Stimuli-Responsive Drug Delivery. *Biomaterials* 230, 119619. doi:10.1016/j.biomaterials.2019.119619

Wright, D. B., Proetto, M. T., Touve, M. A., and Gianneschi, N. C. (2019). Ring-opening Metathesis Polymerization-Induced Self-Assembly (ROMPISA) of a Cisplatin Analogue for High Drug-Loaded Nanoparticles. *Polym. Chem.* 10 (23), 2996–3000. doi:10.1039/c8py01539b

Xu, Y., Han, X., Li, Y., Min, H., Zhao, X., Zhang, Y., et al. (2019). Sulforaphane Mediates Glutathione Depletion via Polymeric Nanoparticles to Restore Cisplatin Chemosensitivity. *Acs Nano* 13 (11), 13445–13455. doi:10.1021/acsnano.9b07032

Yang, Y., Chen, F., Xu, N., Yao, Q., Wang, R., Xie, X., et al. (2022). Red-light-triggered Self-Destructive Mesoporous Silica Nanoparticles for cascade-amplifying Chemo-Photodynamic Therapy Favoring Antitumor Immune Responses. *Biomaterials* 281, 121368. doi:10.1016/j.biomaterials.2022.121368

Yin, C., Tang, Y., Li, X., Yang, Z., Li, J., Li, X., et al. (2018). A Single Composition Architecture-Based Nanoprobe for Ratiometric Photoacoustic Imaging of Glutathione (GSH) in Living Mice. *Small* 14 (11), 1703400. doi:10.1002/Smll.201703400

Yu, L., Chen, Y., Lin, H., Du, W., Chen, H., and Shi, J. (2018). Ultrasmall Mesoporous Organosilica Nanoparticles: Morphology Modulations and Redox-Responsive Biodegradability for Tumor-specific Drug Delivery. *Biomaterials* 161, 292–305. doi:10.1016/j.biomaterials.2018.01.046

Zeng, X., Wang, Y., Han, J., Sun, W., Butt, H. J., Liang, X. J., et al. (2020). Fighting against Drug-Resistant Tumors Using a Dual-Responsive Pt(IV)/Ru(II) Bimetallic Polymer. *Adv. Mater.* 32 (43), 2004766. doi:10.1002/Adma.202004766

Zhang, F., Chen, F., Yang, C., Wang, L., Hu, H., Li, X., et al. (2021). Coordination and Redox Dual-Responsive Mesoporous Organosilica Nanoparticles Amplify Immunogenic Cell Death for Cancer Chemoimmunotherapy. *Small* 17 (26), 2100006. doi:10.1002/Smll.202100006

Zhang, T., Lu, Z., Zhang, L., Li, Y., Yang, J., Shen, J., et al. (2020). Preparation of Hollow Mesoporous Silica Nanorods for Encapsulating and Slowly Releasing Eugenol. *Chin. Chem. Lett.* 31 (12), 3135–3138. doi:10.1016/j.cclet.2020.07.010

Conflict of Interest: The authors declare that the research was conducted in the absence of any commercial or financial relationships that could be construed as a potential conflict of interest.

Publisher's Note: All claims expressed in this article are solely those of the authors and do not necessarily represent those of their affiliated organizations, or those of the publisher, the editors and the reviewers. Any product that may be evaluated in this article, or claim that may be made by its manufacturer, is not guaranteed or endorsed by the publisher.

frontiers | Frontiers in Bioengineering and Biotechnology

REVIEW
published: 06 April 2022
doi: 10.3389/fbioe.2022.889291

Nanoparticle-Based Drug Delivery Systems for Induction of Tolerance and Treatment of Autoimmune Diseases

He Li[1,2,3], *Yong-Guang Yang*[1,2,4] *and Tianmeng Sun*[1,2,4]*

[1]Key Laboratory of Organ Regeneration and Transplantation of Ministry of Education, Institute of Immunology, The First Hospital, Jilin University, Changchun, China, [2]National-local Joint Engineering Laboratory of Animal Models for Human Diseases, Changchun, China, [3]Department of Rehabilitation Medicine, The First Hospital, Jilin University, Changchun, China, [4]International Center of Future Science, Jilin University, Changchun, China

Autoimmune disease is a chronic inflammatory disease caused by disorders of immune regulation. Antigen-specific immunotherapy has the potential to inhibit the autoreactivity of inflammatory T cells and induce antigen-specific immune suppression without impairing normal immune function, offering an ideal strategy for autoimmune disease treatment. Tolerogenic dendritic cells (Tol DCs) with immunoregulatory functions play important roles in inducing immune tolerance. However, the effective generation of tolerogenic DCs *in vivo* remains a great challenge. The application of nanoparticle-based drug delivery systems in autoimmune disease treatment can increase the efficiency of inducing antigen-specific tolerance *in vivo*. In this review, we discuss multiple nanoparticles, with a focus on their potential in treatment of autoimmune diseases. We also discuss how the physical properties of nanoparticles influence their therapeutic efficacy.

Keywords: Antigen-specific tolerance, autoimmune diseases, nanoparticle, tolerogenic DC, drug delivery system

OPEN ACCESS

Edited by:
Mingqiang Li,
Third Affiliated Hospital of Sun Yat-sen University, China

Reviewed by:
Liangzhu Feng,
Soochow University, China
Yuanyu Huang,
Beijing Institute of Technology, China
Chunsheng Xiao,
Changchun Institute of Applied Chemistry (CAS), China

***Correspondence:**
Tianmeng Sun
tsun41@jlu.edu.cn

Specialty section:
This article was submitted to Biomaterials, a section of the journal Frontiers in Bioengineering and Biotechnology

Received: *04 March 2022*
Accepted: *10 March 2022*
Published: *06 April 2022*

Citation:
Li H, Yang Y-G and Sun T (2022) Nanoparticle-Based Drug Delivery Systems for Induction of Tolerance and Treatment of Autoimmune Diseases. Front. Bioeng. Biotechnol. 10:889291. doi: 10.3389/fbioe.2022.889291

1 INTRODUCTION

Autoimmune diseases result from genetic factors, viral or bacterial infections, and other causes such as abnormal activation of immune cells in the body, which result in the immune destruction of host tissues or organs. According to statistics published online by the American Autoimmune Diseases Association, more than 100 autoimmune diseases affect approximately 24 million people in America (80% are women). Furthermore, approximately 5–10% of the U.S. population has one or more autoimmune diseases. Abnormal activation of T lymphocytes and autoantibodies are often detected in patients, affecting particular organs. These diseases include Hashimoto's thyroiditis (thyroid gland), pernicious anemia (stomach), Addison's disease (adrenal glands), and type 1 diabetes (pancreas). These diseases can also involve multiple organs and tissues, such as rheumatoid arthritis, systemic lupus erythematosus (SLE), and dermatomyositis. Autoimmune disease is often repeated with chronic delay. Most patients often display tissue destruction and residual complications during clinical diagnosis. The current treatment for autoimmune diseases involves the administration of broad-spectrum, nonspecific, anti-inflammatory, or immunosuppressive drugs (such as cyclosporine, tacrolimus, or corticosteroids). These treatments mainly reduce the proliferation of inflammatory cells and inhibit the immune reactions in the body, which can alleviate clinical symptoms but cannot fundamentally cure the disease and eliminate complications. Moreover, long-term and extensive

use of immunosuppressants and cytotoxic drugs will reduce the body's normal immune response and increase the potential risk for developing cancer and infections (Chandrashekara, 2012; https://autoimmune.org/resource-center/about-autoimmunity/; Wikins, 2012; Yu et al., 2018; Angum et al., 2020). In recent decades, efforts have been made to focus on developing therapies that can specifically suppress immunity without impairing normal immune function, with the ultimate goal of restoring immune homeostasis (Yang and Santamaria, 2021).

Compared with other immunosuppressive treatments, tolerogenic dendritic cells (Tol DCs) with immunoregulatory functions have attracted much attention to treat autoimmune diseases as they play important roles in inducing and maintaining immune tolerance (Castenmiller et al., 2021). Currently, it is expensive to obtain autologous tolerogenic DC *in vitro,* and there is a possibility of failure *in vivo* after transfusion (Lehmann et al., 2016). Furthermore, *in vitro* tolerogenic DCs provide nonspecific immunosuppression. However, generating tolerogenic DCs to target-specific autoimmune cells requires loading these DCs with disease-specific autoantigens (Stabler et al., 2019; Cifuentes-Rius et al., 2021). Antigen-specific immunotherapy is ideal for treating autoimmune diseases and allergies and preventing allograft rejection (especially executing the modification *in situ*). The advantage of antigen-specific immunotherapy is the inhibition of autoreactive inflammatory T cells and induction of antigen-specific immune suppression without impairing normal immune function. A feasibility strategy *in vivo* focuses on recognizing and internalizing antigens through surface receptors of DCs such as DEC205 and C-type lectin receptors family (macrophage galactose type C-type lectin and MGL), dendritic cell-specific intercellular adhesion molecule-3-grabbing nonintegrin (DC-SIGN), and mannose receptor (MR) (Zizzari et al., 2015; Castenmiller et al., 2021) which lead to immune tolerance. These receptors can trigger different signaling pathways that affect APC functions and determine the polarization of T cells (Geijtenbeek and Gringhuis, 2009). While the activation status of the DCs controls the induction of tolerogenic DCs with receptors, the acquired tolerogenic effect disappears in the presence of pro-inflammatory modulators (Hawiger et al., 2004; Takenaka and Quintana, 2017) and other immune cells expressing similar receptors as those being targeted (Castenmiller et al., 2021). Another reprogramming DC approach is based on nanoparticle administration *in vivo*. The nanoparticle is a new carrier system designed to target the innate immune cells at a specific size, charge, and chemical modification as required, significantly improving drug loading capacity and bioavailability. In particular, the natural affinity of phagocytes for nanoparticles makes them a powerful tool for initiating and modulating immune responses (Kishimoto and Maldonado, 2018). The intervention of autoimmune response based on nanoparticles is mainly focused on following two aspects: 1) tolerance is induced by targeting antigen-presenting cells (Liu et al., 2019) and 2) tolerance is induced by directly targeting autoreactive lymphocytes (Feldmann and Steinman, 2005; Umeshappa et al., 2019; Umeshappa et al., 2020). The ultimate goal of all these methods is to induce tolerance through various mechanisms, including autoreactive T cell anergy, apoptosis, and the induction of Tregs or Bregs that can be used in tolerant immunotherapies (**Figure 1**) (Prosperi et al., 2017). Antigen-specific immunotherapy based on nano-delivery strategies targeted auto-reacting lymphocytes and antigen-presenting cells such as macrophages (Montes-Cobos et al., 2017), dendritic cells (Lewis et al., 2019), B cells (Stensland et al., 2021), monocytes (Casella et al., 2020), and neutrophils (Sherr et al., 2008). They co-loaded a specific amount of pathogenic antigen through covalent binding, biological coupling, and electrostatic adsorption or co-delivered some immunomodulatory substances that contributed to tolerance simultaneously, thus performing DC reprogramming *in situ*. This article reviews the recent progress of nanotechnology in inducing antigen-specific tolerance *in vivo*. Here, we examine how properties of nanoparticles affect immune tolerance and common strategies for nanoparticles to induce immune tolerance.

2 ANTIGEN-PRESENTING CELLS PLAY AN ESSENTIAL ROLE IN IMMUNE TOLERANCE

Immune tolerance is primarily maintained through coordination between central and peripheral immune tolerance. In central tolerance, most of the autoreactive T and B lymphocytes are cleared during the early stages of thymus and bone marrow development. This process is also known as "negative selection." Thymic DC plays an essential role in central tolerance, such as clone deletion, clone transfer, and clone diversion. Although central tolerance mechanisms are efficient, they cannot eliminate all self-reactive lymphocyte, partly because not all self-antigens are expressed at the primary site of lymphocyte development (**Figure 2**). Therefore, peripheral tolerance mechanisms exist, and these are crucial for controlling the tolerance of lymphocytes that first encounter their cognate self-antigens at the periphery (Xing and Hogquist, 2012).

Peripheral DCs are the inducers of immune responses and the crucial regulators of tolerance induction and maintenance. Many studies have focused on isolating and reprogramming dendritic cells (DCs) to generate tolerogenic DCs and maintain the immune tolerance environment. Tolerogenic DCs are mainly induced by various immunosuppressant drugs such as rapamycin (Macedo e al., 2012; Sukhbaatar et al., 2016), dexamethasone (Lee et al., 2017), and vitamin D (Xie et al., 2017; Kim et al., 2018) or inhibitory cytokines such as IL-10 (Boks et al., 2012; Kryczanowsky et al., 2016) and TGF-β (Rabinovich et al., 2007; Hasegawa and Matsumoto, 2018) to cultivate dendritic cells *in vitro* and then transfuse them back into the body to treat autoimmune diseases. Tolerogenic dendritic cells (Tol DCs) are characterized by reduced

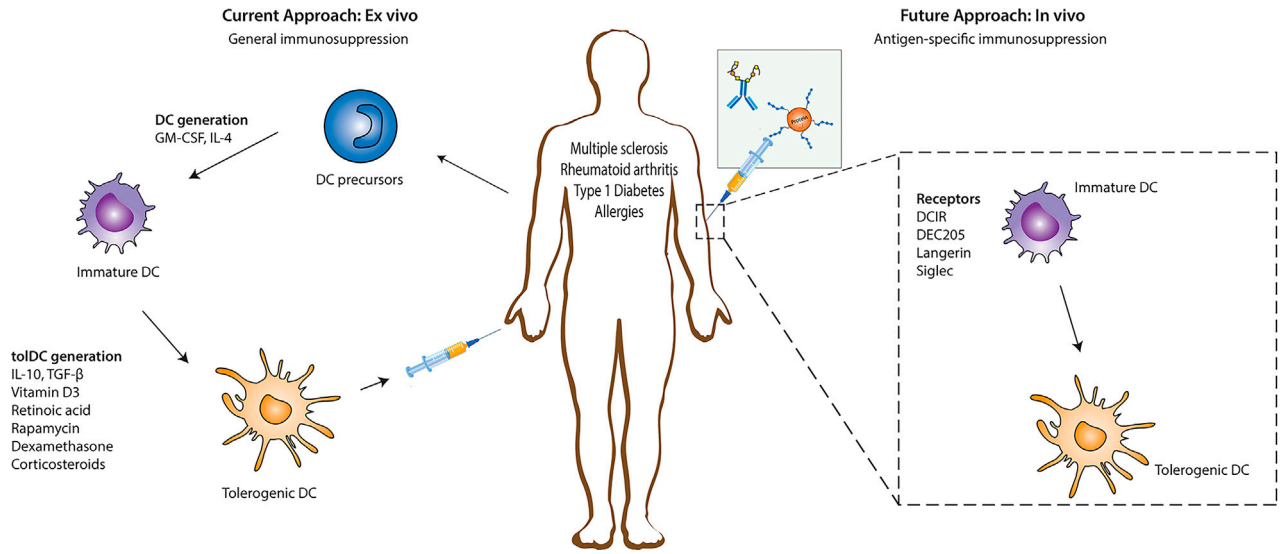

FIGURE 1 | Immune regulation strategy based on DC. Reprogramming DC to induce a tolerogenic phenotype to treat autoimmune diseases. Tolerogenic DC is mainly induced *in vitro*. First, DC precursor cells were isolated from bone marrow and stimulated to differentiate into immature DC (imDC). Then, immunomodulatory agents (such as vitamin D3, rapamycin, retinoic acid, and specific cytokines) were added to induce the differentiation of imDC into tolerogenic DC. Subsequently, reinjecting into patients to suppress inflammation. Another strategy for inducing tolerogenic DC is directly targeting receptors on the DC surface (such as DEC205, langerin, and Siglec receptors). Reproduced with permission from (Castenmiller et al., 2021).

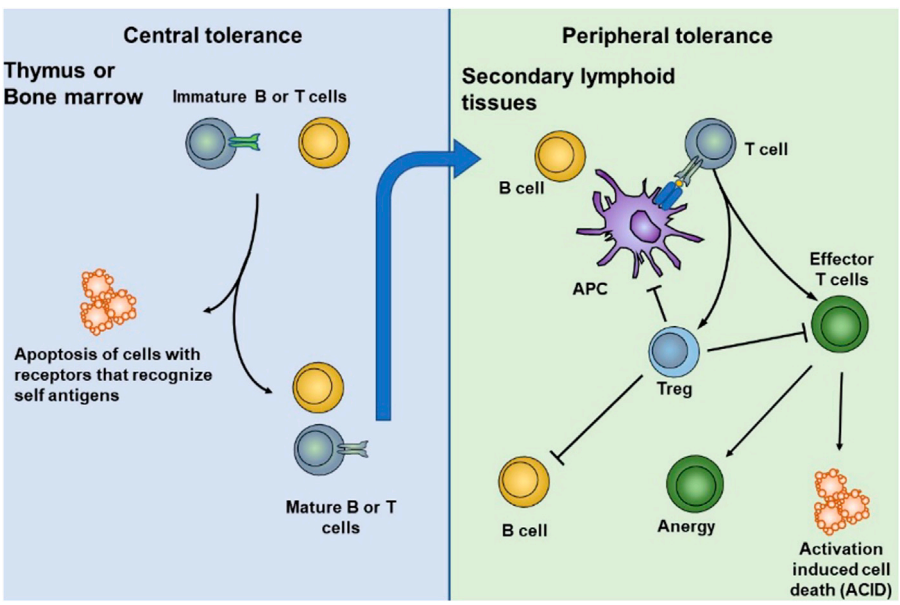

FIGURE 2 | DCs play an essential role in central and peripheral immune tolerance. In central tolerance, most of the autoreactive T and B lymphocytes are cleared during the early stages of thymus and bone marrow development. Some self-reactive lymphocytes that escape central tolerance are cleared, anergized, deleted, or differentiated into normal T cells in peripheral tolerance. Reproduced with permission from (Yu et al., 2018).

expression of costimulatory molecules and MHC class molecules, decreased ability to induce T-cell proliferation, and/or increased differentiation to regulatory T cells (Tregs) (Lee et al., 2017). Despite initial indications of therapeutic efficacy in some trials, the widespread treatment of Tol DCs remains challenging because the Tol DC induced *in vitro* is nonspecific, expensive, and maybe off-target after transfer *in vivo* (Cifuentes-Rius et al., 2021). Moreover, inducing disease,

specifically immune suppression without impairing normal immune function, requires loading these DCs with disease-specific autoantigens (Stabler et al., 2019). Therefore, it is necessary to induce Tol DC to inhibit abnormal cytotoxicity and inflammatory responses in an antigen-specific manner, providing a precise approach for treating autoimmune diseases *in situ* (Gallucci et al., 1999).

Significantly due to the special tolerogenic environment of the liver, there are many research studies on the treatment of autoimmune diseases by targeting antigen-presenting cells in the liver. The liver is a well-known tolerogenic organ, which is constantly exposed to a mass of harmless gut-derived bacterial or commensal antigens from the gastrointestinal tract (Racanelli and Rehermann, 2006; Thomson and Knolle, 2010). The maintenance of hepatic tolerance is mediated by a series of liver-resident antigen-presenting cells, including dendritic cells, Kupffer cells (KCs.), and liver sinusoidal endothelial cells (LSECs) (Carambia et al., 2015; Doherty, 2016).

Many nanoparticles were enriched in the liver after administration *in vivo*. Some of them were internalized by KCs, which play a vital role in antigen presentation and tolerance induction (Horst et al., 2016). As the liver-resident macrophages, they phagocytose pathogens, dead-cell debris, and other alien invaders, such as nanoparticles at about 500 nm in size range. Heymann demonstrated that KCs induced hepatic tolerance protected mice from kidney inflammation in T cell-mediated glomerulonephritis, mainly by mediating T cell arrest and Treg expansion (Heymann et al., 2015). LSECs are special microvascular endothelial cells that are the second type of scavenger cells in the liver. LSECs mainly phagocytose particles at about 200 nm in size range by clathrin-mediated endocytosis (Sorensen et al., 2012), such as small particles and soluble macromolecules, which are mainly from circulation or processing by splenic cells (Thomson and Knolle, 2010; Carambia et al., 2015). LSECs can efficiently suppress inflammatory T cells response (Limmer et al., 2000; Klugewitz et al., 2002) and induce Tregs (Carambia et al., 2014). Carambia showed that targeting LSECs with polymer-coated MBP-coupled NPs administration injection protected mice from $CD4^+$T cell-driven EAE by inducing $Foxp3^+$ Treg cells (Carambia et al., 2015). This team then used SIINFEKL peptide-loaded nanoparticles, which are high selectively, internalized by LSECs *in vivo* and prevent CD8 T-cell driven autoimmune cholangitis (Carambia et al., 2021). Qi Liu et al. used biodegradable PLGA polymers to encapsulate OVA, targeting LSECs to induce antigen-specific immune tolerance in allergic airway disease. LSEC-targeting NPs dramatically suppress airway allergic inflammation by tissue infiltrating Tregs, promoting anti-inflammatory cytokines (Liu et al., 2019).

In general, nanomedicine offers a new way to overcome the above problems by loading a certain amount of pathogenic antigen onto DC *in vivo*, codelivery of some immunomodulatory substances that contribute to tolerance and performing DC reprogramming *in situ* (Cifuentes-Rius et al., 2021). This approach allows tolerogenic DC to be widely used in the clinic and easily applied to many different autoimmune diseases. However, nanoparticles also have many problems affecting their function as carriers.

3 OPTIMIZING NANOPARTICLE'S PROPERTIES

Nanoparticles (NPs) have significant potential as a tolerance delivery vehicle with several benefits to autoimmune disease, allergy, and transplantation rejection immunotherapy. Some primary objectives should be designed to induce tolerance to a specific direction and avoid unnecessary immunosuppression (Liu et al., 2021). A certain amount of peptide is processed by DC, and presented as pMHC multimer to T cell, inducing lymphocyte activation. Interfere with one or multiple progress in lymphocyte reaction could induce apoptosis of autoactivated T cells or differentiation toward regulatory T cells (Yu et al., 2018). In this process, an ideal carrier: 1) should be able to protect the peptide cargo from the degradation of the internal environment *in vivo*, 2) can deliver cargo antigen to specific cells, such as DC (Lewis et al., 2019), macrophage (Montes-Cobos et al., 2017), 3) requires non-toxicity and biodegradability, and does not have apparent characteristics of inducing inflammatory activation. Moreover, NPs can decrease drug dosage and adverse reactions to organisms (**Figure 3**) (Urbanavicius et al., 2018; Cifuentes-Rius et al., 2021). Immune tolerance can be affected by the physicochemical characteristics of NPs, such as the size of the particles that can determine their internalization and biological distribution *in vivo*. The shape plays a role in the particle circulation time, biodistribution, and immune targeting (Thorp et al., 2020). The surface charge influences solubility, uptake by APCs, and DC maturation (Jazayeri et al., 2021; Lu et al., 2021).

3.1 Material Composition of Nanocarriers

At present, there are many biomaterials used for DC stimulation to suppress or activate immune responses. To achieve targeted delivery, nanoparticles are prepared based on design principles. The materials selected as vehicles should meet the main requirements, such as biocompatibility, non-toxic, easy to manipulate in size, and chemical properties (Urbanavicius et al., 2018). Some high immune stimulation materials, such as aluminum salt adjuvants, are unsuitable for inducing tolerance (Huang et al., 2020). Among all the materials used for nanoparticle design, synthetic polyester-based polymers, including polylactic acid (PLA) and poly (lactic-co-glycolic acid) (PLGA), are the most widely used materials for the preparation of nanoparticles. The advantages of these types of polymer materials for nanoparticles are their long shelf life and the ease of synthesis that allows for the encapsulation of various hydrophobic and hydrophilic compounds as well as proteins (Devulapally et al., 2016; Bee et al., 2018). Moreover, these polymers are biocompatible and biodegradable and cause slight immune reactions. Its metabolites are mainly carbon dioxide and water, therefore having low toxicity (Amini et al., 2017; Elmowafy et al., 2019). These PLGA degradation products are lactic acid and glycolic acid, which reduces the environmental

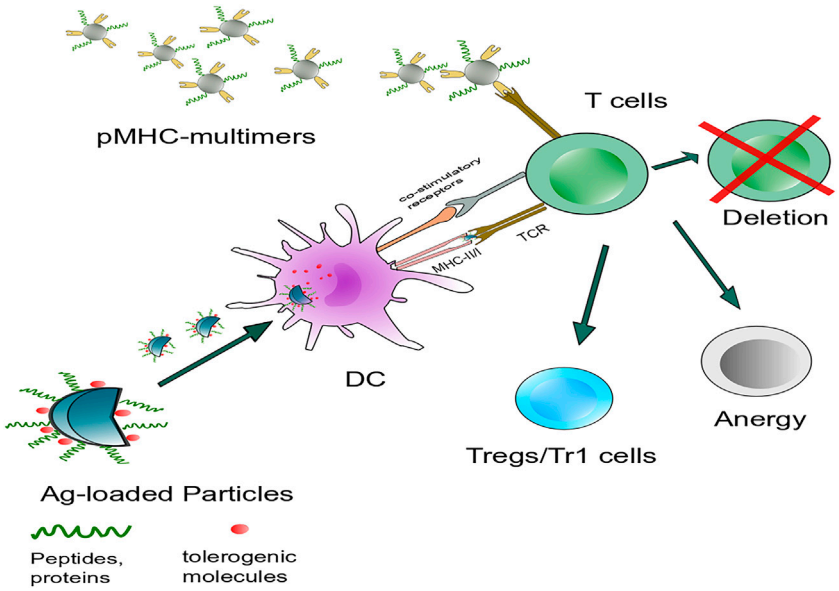

FIGURE 3 | Intervention of antigen-specific autoimmunity is mainly concerned with two aspects: Targeting DCs or autoreactive lymphocytes to induce immune tolerance. Nanoparticles carry specific autoantigens with or without tolerogenic molecules that target antigen-presenting cells such as DCs *in vivo* and interfere with autoreactive T cells, including autoreactive T cell anergy and apoptosis and the induction of Tregs or Tr1 cells. Another strategy is systemic delivery of NPs. Coated with disease-relevant pMHC multimers targeting cognate autoantigen-experienced T-cell directly, leading to the formation and expansion of cognate TR1 cells.

pH value and induce the body to produce an immune tolerance environment (Allen et al., 2018; Bee et al., 2018). The underlying mechanism is related to the interference of the inflammatory signal by lactic acid. Lactic acid (LA) accumulates under inflammatory conditions and may influence a variety of signal pathways, such as NF-κB signal (Samuvel et al., 2009) and the PI3K/AKT pathway (Mendler et al., 2012). Peter considered that LA delayed the phosphorylation of protein kinase B (AKT) and the degradation of IκBα. Consistently, the LPS-induced genes delayed, and diminished NF-κB nuclear accumulation on monocytes and effector protein TNF-α, IL-23 which might contribute to immune suppress (Peter et al., 2015).

The liposome is another common drug carrier similar to the natural composition of cell membranes, which has a high degree of biocompatibility and lower entry barriers. Liposomes are amphiphilic lipid bilayer vesicles composed of phospholipids such as phosphatidylcholine, phosphatidylethanolamine, phosphatidylserine, and phosphatidylglycerol, and a stabilizer, such as cholesterol (Knudsen et al., 2015; Bulbake et al., 2017; Cong et al., 2020; Guo et al., 2021). Compared with polymeric or synthetic nanoparticles, liposomes have natural advantages as tolerogenic materials, partly because lipids are natural components of cell membranes and therefore are less likely to induce inflammatory reactions (Knudsen et al., 2015; Bulbake et al., 2017). Liposome-based platforms have been successfully employed as anti-tumor drug delivery in clinical applications, such as Doxil®, the first FDA-approved PEGylated liposome-based drug delivery (Dai et al., 2019). Many lipid nano-carries have been developed to treat anti-inflammatory (Serhan et al., 2008; Serhan and Petasis, 2011) or induce tolerogenic immune response (Basomba et al., 2002; Nielen et al., 2004; Nouri et al., 2015). Studies have shown that negatively charged lipids, (phosphatidylserine, PS) can induce tolerance *in vivo*. The mechanism may be that these particles can mimic the effects of apoptotic bodies, and inhibit DC maturation (Shi et al., 2007; Benne et al., 2016). Dongmei Shi et al. demonstrated that PS could induce tolerogenic DCs and suppressed $CD4^+$T cell proliferation and IFN-γ production (Shi et al., 2007). Another study also found that PS-liposome phagocytosis resulted in phenotypic and functional changes in human DCs, which were accountable for tolerance induction (Rodriguez-Fernandez et al., 2018). Another mechanism by which liposomes induced tolerance was immunosuppression through the NF-κB signaling pathway (Chambers et al., 2018; Svajger and Rozman, 2020). Compared with free corticosteroids, the liposomal drug delivery system effectively inhibited arthritis, indicating promising therapeutic effects in autoimmune diseases (Meka et al., 2019). In some experimental arthritis models, liposomes-loaded with glucocorticoids and cytotoxic drugs showed a persistent anti-inflammatory effect, low dosage, and minor adverse reactions compared with free drug (A.S. Williams, 2001; Metselaar et al., 2003; Rauchhaus et al., 2009).

Polysaccharides are another frequently designed vaccine delivery system because of their biocompatibility, biodegradability, and low toxicity. Natural polysaccharides may be neutral (amyloglucan), or charged (hyaluronic acid and chitosan), and mainly are bio-adhesive to mucous membranes and the epithelium (Serrano-Sevilla et al., 2019). They are diverse in structure and size, often load various immunosuppressive drugs and antigens through electrostatic

adsorption and selectively deliver immunosuppressive cargos to specific targets. Nanoparticle-mediated hyaluronic acid (HA) preferentially targets inflammatory tissues (for example, collagen-induced arthritis mice), which inhibits the expression of inflammatory cells such as macrophages, lymphocytes, and pro-inflammatory cytokines, ultimately reducing joint use inflammation and destruction (Shin et al., 2014), (Aguero et al., 2017; Barclay et al., 2019). Chitosan is a biopolymer derived from the deacetylation of chitin (Ding et al., 2014). Chitosan is extensively used to deliver nucleic acids because of its cationic nature through electrostatic interaction with the negatively-charged nucleic acid (Mikusova and Mikus, 2021).

Other nanomaterials, such as Au (Niikura et al., 2013; Sun et al., 2019) and pSi (Tieu et al., 2018; Kim B. et al., 2019), are also designed to target DCs and form immune tolerance because of their physical and chemical properties and surface chemical structures. However, nanomaterials themselves are only one parameter to be considered when designing nanomaterials. Nanoparticle size and shape also affect biological function and immune distribution.

3.2 Effect of Size and Shape on Nanoparticles

The size of nanoparticles mainly affects their circulation, internalization, and biological distribution *in vivo*. In terms of particle size alone, particles smaller than 5 nm were mainly cleared in the kidney (Choi et al., 2007), while particles larger than 1 μm would be internalized by macrophages after entering circulation before reaching target tissues and organs (Bachmann and Jennings, 2010). Generally speaking, according to hemodynamic studies, the smaller the particle, the longer it is in the circulation and the more it accumulates in the cells (Thorp et al., 2020). The long tissue residence time prolongs the particle's action time and means higher toxicity to the internal cells (Lovric et al., 2005; Huang et al., 2011; Wozniak et al., 2017). Nanoparticles with diameter smaller than 10 nm exhibited toxicity secondary to inefficient cellular clearance and prolonged cellular accumulation *in vivo* (Huang et al., 2011). Although large-sized particles usually mean high drug load potential, there are many problems associated with large-sized particles, such as blocked small vessels and pulmonary embolism (>1 μm). Those problems make them rarely used to induce immune tolerance by intravenous injection (Decuzzi et al., 2010) or more easily cleared by phagocytic cells in the bloodstream before reaching the target organ (Thorp et al., 2020).

Since particles are internalized by antigen-presenting cells after entering the circulation, particle size also affects the type of internalization. Studies among a series of cell lines and different nanoparticles show the ideal size for nanoparticles uptake relevant to the cell type (Shang et al., 2014). For some non-phagocytic cells (such as the B16 cell line, etc.), particles smaller than 200 nm in diameter are most taken up by clathrin-mediated processes (Zuhorn et al., 2002), larger particles (200 nm–1 μm) enter cells preferentially along the pathway of caveolae-mediated endocytosis(Rejman et al., 2004; Gratton et al., 2008). After internalization, about particles of around 200 nm accumulate in late endosomal or lysosomal compartments, through the late intracellular endosomal receptors, engaging both adaptive and innate immune process, which is considered beneficial for immunomodulation (Gleeson, 2014).

While in professional antigen-presenting cells, the size of nanoparticle may be only one parameter besides charge, shape, and the route of administration, as nanomaterials ranging from under 5 nm to more than 1 μm could be internalized by DCs successfully (Bachmann and Jennings, 2010). In general, nanoparticles administered intravenously are mainly internalized by macrophages in the reticuloendothelial system (for example, liver, spleen) (Patel et al., 2010; Wang et al., 2012) or captured by DCs in the blood and peripheral organs (Jia et al., 2018). Therefore, the ideal size of particle-induced tolerance is related to the target location. The larger particles (about 500 nm) are more likely to attract macrophages from the liver and spleen to initiate phagocytosis. There was much researches focused on the peptide coupled-PLGA/PLG/PS nanoparticle platform, which targets $MARCO^+$ APCs in the marginal zone (Getts et al., 2012; Hunter et al., 2014; Hlavaty et al., 2016; Pearson et al., 2019; Freitag et al., 2020). Getts et al. speculated that MARCO played an important role in cell uptake of peptide-linked particles, macrophage antigen presentation, and/or antigen transfer to local dendritic cells (Getts et al., 2012). In addition, MARCO showed the effects in inhibiting inflammatory responses through inhibiting DC migration (Arredouani et al., 2007).

Nanoparticles at about 200 nm in diameter often rely on nonspecific internalization pathways, such as pinocytosis, microtubules, and clathrin (Getts et al., 2015; Behzadi et al., 2017). These particles predominantly accumulated in the red pulp of spleen (Ernsting et al., 2013; Serra and Santamaria, 2015) and LSECs in liver (Carambia et al., 2015), which allowed them to preferentially interact with immune cells at that location and made them ideal for inducing tolerance. At about 100–200 nm, the particles tend to circulate in the bloodstream for several hours and then enter the local draining lymph nodes, where resident DC captures them in the lymph nodes and induces early T cell immune responses. Nanoparticles larger than 200 nm circulate longer circulation life and enter lymph nodes mainly through migrating DC (Manolova et al., 2008; Rincon-Restrepo et al., 2017) and/or remain at the injection site (Engman et al., 2015; Rincon-Restrepo et al., 2017; Lewis et al., 2019). Nanoparticles with larger particle sizes are more likely to be accumulated in barrier cells before entering lymphatic vessels, making them relatively less targeted (Thorp et al., 2020). Therefore, the conclusion on ideal diameters for inducing tolerance remains widely divergent in the different findings.

The nanoparticles could be prepared in a variety of shapes. The biodistribution, cytotoxicity, circulation time, and immunogenicity of nanoparticles can be affected by their morphologies (Gratton et al., 2008). When designing nanoparticles, shape is often taken into account along with size (Firestein, 2003). Spherical nanoparticles have a lower tendency to marginate in the bloodstream and a longer circulation time than non-spherical nanoparticles, such as cubic, rod, and needle nanoparticles (Decuzzi et al., 2010). Spherical nanoparticles tend to be distributed homogeneously

in most tissues and organs, especially preferential accumulation in liver, spleen, and lung (Gratton et al., 2008). The non-spherical nanoparticles usually have a higher surface area (cylinders, rods), which makes them more likely to be internalized by phagocytes, such as liver macrophages and circulating phagocytes (Gratton et al., 2008; Decuzzi et al., 2010; Huang et al., 2011). While the nonspherical nanoparticles tend to be more rigid, and are more likely to damage membrane during cell uptake, they may also cause further activation of the inflammasome in immune cells (Zhao et al., 2013; Wozniak et al., 2017).

3.3 Surface Properties of Nanocarrier

3.3.1 Charge of the Particles

The nanoparticle charge is another critical character parameter that affects particle internalization and subsequent immune response. Generally, high charge (>30 mV), whether positive or negative, are generally more stable because of electrostatic repulsion (Yan et al., 2008; Hunter et al., 2014; Sun et al., 2014; Hlavaty et al., 2016; Saito et al., 2019a; Saito et al., 2019b). While charge is a dynamic physicochemical parameter, in biological microenvironment, proteins can adsorb to surface of particles, forming protein coronas which can lead to aggregation, macrophage uptake, and rapid clearance (Cifuentes-Rius et al., 2013). In general, cationic nanoparticles are more easily internalized by cells (Fytianos et al., 2015). Compared with anionic particles, cationic nanoparticles appear to be internalized rapidly by interacting with negatively charged cell membranes (He et al., 2010) or *via* the clathrin-mediated pathway (Harush-Frenkel et al., 2007) and are more suitable for inducing inflammatory responses (Yan et al., 2008; Saito et al., 2019b). Furthermore, positively particles tend to be taken up by DCs, which stimulates Th1 immune response consequently (Koppolu and Zaharoff, 2013; Fromen et al., 2015). Antigen encapsulated cationic NPs could induce elevated IgG2a titers and IFN-γ secretion by DCs after mucosal or intradermal vaccination, resulting in Th1 immune responses (Gursel et al., 2001; Bal et al., 2011; Getts et al., 2015).

On the other hand, negatively charged NPs show an inferior rate of internalization, and rarely through the clathrin-mediated pathway (Harush-Frenkel et al., 2007). Some studies show negatively charged particles have the effect of ameliorating inflammation in autoimmune diseases and chronic injury (Allen et al., 2018; Saito et al., 2019b). The underlying mechanism is that the particles were intravenously injected, targeting inflammatory cells in circulation directly, disturbing their migration to CNS (Fromen et al., 2017; Saito et al., 2019b) or phagocytosed by monocytes and neutrophils, inducing apoptosis, then sequestered in the spleen or liver for elimination, delayed infiltration into the CNS. What is more, it has been proved that nanoparticles with a charge below −30 mV have anti-inflammatory efficacy (Hunter et al., 2014; Hlavaty et al., 2016; Saito et al., 2019a). Some studies have shown peptide coupled nanoparticles (500 nm range) with negatively charge ranging from −40 to −70 mV could target phagocytes cells expressed MARCO receptors in the spleen or liver in an opsonin-independent manner, inducing antigen-specific tolerance (Getts et al., 2012; Hunter et al., 2014; Hlavaty et al., 2016; Pearson et al., 2019; Freitag et al., 2020).

However, the rate of internalization of a particle is not necessarily related to its ultimate potency. Studies on intestinal epithelial cells have found that cationic nanoparticles internalize rapidly, but their vesicular trans-monolayer transport is slow. In contrast, anionic nanoparticles have the opposite properties, which make them more efficient in cortical transport (Bannunah et al., 2014). In summary, surface charge influences particle internalization, transmembrane transport, and biological functions. However, it is only one parameter of surface properties in particles. Further surface modification is necessary to control the complex interactions between nanoparticles and cells.

3.3.2 Surface Modification of Nanoparticles

Sometimes, it is necessary to modify the surface to prolong their circulation time, delivering to specific targets (Fan et al., 2020) or designing for desired therapeutic effects (Rieger et al., 2009). The clearance of nanoparticles by the reticuloendothelial system (RES) is the main obstacle to the delivery efficiency of nanocarriers. Many methods have been adopted to increase the half-life of nanoparticles. A commonly used means is coating particles with polymeric ethylene glycol (PEG). PEG-modified nanoparticles can increase the hydrophilic protective layer around the nanoparticles making it difficult to be adsorbed or collected by hemoglobin, thus prolonging the circulation time of particles in the blood (Gref et al., 2000; Casals et al., 2010). Previous studies have suggested that liposome particles with a slightly negative charge, modified with PEG (10%; 5 kDa), can prolong the circulation time *in vivo* and have better joint targeting, improving the therapeutic effect of RA (Hirai et al., 2007; Meka et al., 2018). PEO (polyethylene oxide) is the low molecular weight derivative of PEG, which forms a "mushroom-brush" or "brush" configuration on particles, avoiding clearance by scavenger cells. Unlike PEG, PEO may change activation from the C1q-dependent complement pathway to the lectin pathway. Meantime, PEO can also reduce the level of complement activation products (Hamad et al., 2010). When NPs are administrated by vein, some plasma protein (such as immunoglobulin G, complement factors, and fibrinogen), rapidly bind to NPs to form a protein corona, inducing macrophage recognition and phagocytosis (Gao and He, 2014; Shen et al., 2018) which is called particle opsonization. By contrast, replacing these proteins with to some serum albumins or lipoproteins could reduce the internalization and prolong circulation times. Another strategy to minimize recognition and phagocytosis is codelivery of a "self-marker," such as CD47 molecules, with the NPs to prevent endocytosis. CD47 may interact with SIRPα expressed on phagocytes, and suppress endocytosis (Pei et al., 2018).

3.3.3 Codelivery of Tolerant Payloads

Targeting DC to induce immune tolerance has been studied widely, including immune tolerance by mimicking apoptotic

cell death (Turley and Miller, 2007; Luo et al., 2008; Kontos et al., 2013; Pozsgay et al., 2016; Clough et al., 2020), allowing antigens to utilize the immune tolerance environment of the body (Carambia et al., 2015; Park et al., 2016; Liu et al., 2019), or inducing tolerance by simultaneous coupling of some tolerant drugs or small molecules targeting DC (Yu et al., 2018). The mainly co-delivered tolerance cargo includes glucocorticoids, nucleic acids, and small molecule immunosuppressants.

Glucocorticoids are the most commonly used immunosuppressive drugs in the clinic, and their main pharmacological action is to dissolve active immune cells and block cell differentiation. They are characterized by non-specificity and are broad immunosuppressants. Some studies used PLGA-loaded glucocorticoids to treat multiple sclerosis, autoreactive arthritis, and ulcerative colitis, both of which achieved ideal target therapeutic effects, durable anti-inflammatory effects, and lower adverse reactions, such as metabolic syndrome disorder, hyperglycemia, hyperlipidemia, and hypertension (Nakase et al., 2003; Higaki et al., 2005; Montes-Cobos et al., 2017; Kim S.-H. et al., 2019).

Gene therapy is a great potential treatment for autoimmune disease; however, few clinically available options are available. There are several reasons for limiting the clinical use of nucleic acids, such as high molecular weight, instability in natural environments, enzymatic degradation, and inability to transport across the cell membrane (Lostalé-Seijo and Montenegro, 2018). A nanoparticle can protect siRNA (Guo et al., 2021), mRNA, microRNA, and plasmid DNA from a series of barriers. Currently, the most utilized nucleic acid nanocarrier delivery modules are cationic lipids and synthetic polymers. In addition, a chitosan nanoparticle loaded with Lingo-1 siRNA (a protein suppressing myelination and axonal regeneration) in the mouse model of demyelination showed neuroprotection and remyelination effects (Youssef et al., 2019). A PLGA microsphere codelivery peptide and an antisense oligonucleotide of costimulatory molecules can reverse the hyperglycemia in type 1 diabetic mice (Engman et al., 2015). Similar research used short interfering RNA (siRNA) to explicitly generate tolerogenic DCs by knockdown of CD40, CD80, and CD86 at the same time after injection the arthritogenic antigen collagen II [setting up the collagen-induced arthritis (CIA) model], which could effectively suppress the onset of collagen-induced arthritis. The results support using siRNA to generate tailor-made tolerogenic vaccines for treating autoimmunity (Zheng et al., 2010).

Small molecule compounds have advantages in pharmaceutical technology, stability, and safety compared with nucleic acids and some protein drugs. Small molecule immunomodulators, including vitamin D3 (Agmon-Levin et al., 2013; Keijzer et al., 2013), mycophenolic acid (Look et al., 2013), and rapamycin (Stabler et al., 2019), have been shown to effectively induce tolerance through various mechanisms, including the induction of Tregs or by altering the profile of pathogenic immunity. Codelivery of rapamycin, a natural macrolide compound that acts as an allosteric inhibitor of the mammalian target of rapamycin (mTOR) pathway, has been shown to have tolerogenic properties *in vitro* and *in vivo* (Maldonado et al., 2015; Tostanoski et al., 2016; Zhang et al., 2016). Some research also showed that rapamycin-carrying nanocarriers have potent immunosuppressive activity to inhibit T cell proliferation, and the possible mechanism of rapamycin-carrying nanocarriers is the inhibition of anti-drug antibodies. Takashi et al. evaluated a synthetic, biodegradable, nanoparticle codelivery disease-related peptide, SVP-rapamycin, to induce durable immune tolerance *in vivo* by treating animals in multiple autoimmune disease models such as experimental autoimmune encephalomyelitis (EAE) and rheumatoid arthritis (RA) in different species such as mice, rats, and monkeys. The results demonstrate the ability of SVP-rapamycin co-administered with antigen to induce tolerogenic DCs *in vivo* that can promote antigen-specific Tregs (Kishimoto et al., 2016). Similarly, SJL mice treated with nanoparticles containing rapamycin and pathogenic peptides protected the mice from developing EAE and induced antigen-specific tolerance (LaMothe et al., 2018). Coadministration of protein/pathogenic peptide antigen and the immunosuppressant rapamycin can induce durable and specific resistance to mounting immune responses toward the antigen in animal models of hemophilia A and relapsing-remitting model of experimental autoimmune encephalomyelitis (Maldonado et al., 2015). Sialic acid (SA), a 9-carbon carboxylated monosaccharide, is mainly located on the surface of cell membranes. As the binding ligand of E-selectin receptors, SA can improve transportation and accumulation of micelles in inflammatory cells. Methotrexate loaded SA-dextran-octadecanoic acid micelle (SA-Dex-OA/MTX) to inhibit the inflammatory response, reduce the side effects of methotrexate and enhance the bone repair activities in the treatment of RA (Xu et al., 2018). The aryl hydrocarbon receptor (AhR) is a ligand-activated transcription factor, which is another candidate to target DC because of its modulation in the differentiation of regulatory T cell subsets (Quintana et al., 2010; Takenaka et al., 2019). Nanoliposome-loaded AhR ligand (ITE) and disease-specific peptide antigens were used to induce antigen-specific tolerance and suppress EAE in mouse models of multiple sclerosis (Yeste et al., 2012; Rothhammer et al., 2017).

In the course of the onset or progression of autoimmune diseases, autoreactive T-lymphocytes produce inflammatory cytokines, resulting in inflammatory reactions or organ and tissue damage. Some therapeutic strategies have been proposed to block inflammatory cytokines or increase anti-inflammatory cytokines. Cytokines [such as IL-10 (Cappellano et al., 2014) and TGF-β (Casey et al., 2018)] are often delivered to antigen-presenting cells together with antigens to induce antigen-specific immune tolerance. However, there are still some problems associated with cytokines used as therapies. *In vivo*, a variety of cytokines play a synergistic role, so the effect of the cytokine is often context-dependent. For example, although IL-2 and TGF-β induce Tregs, IL-17 and

TABLE 1 | Some clinical trials on nanoparticle therapies for tolerance induction.

Disease	Properties of nanoparticles	Administration method	Codelivery antigen/drug	Phase	Reference
Type 1 diabetes	Gold	Intradermally	Proinsulin-derived peptide (C19-A3 GNP)	Phase I	https://clinicaltrials.gov/ct2/show/NCT02837094
Plaque psoriasis	Uncoated nanoparticle paclitaxel ointment (SOR007)	External use	Paclitaxel	Phase I	https://clinicaltrials.gov/ct2/show/NCT03004339
RA	Liposomes	Subcutaneous injection	Prednisolone	Phase II	https://clinicaltrials.gov/ct2/show/NCT00241982
RA	PEGylated nanomolecules (Pegsunercept)	Subcutaneous injection	TNFα inhibitor	Phase II	https://clinicaltrials.gov/ct2/show/NCT00111423
RA	PEGylated nanomolecules (Pegsunercept)	Subcutaneous injection	TNFα inhibitor	Phase II	https://clinicaltrials.gov/ct2/show/NCT00037700
RA	Liposome	Subcutaneous injection	NF-kB inhibitor 1,25 hydroxyvitamin D3(calcitriol)	Phase I	2019 ACR/ARP Annual Meeting Archives - ACR Meeting Abstracts (acrabstracts.org)
Coeliac disease	PLG [poly(lactide-co-glycolide)] nanoparticles	Splenic marginal zone macrophages and liver phagocytic cells via scavenger receptors (MARCO)	Gliadin	Phase I	Freitag et al., (2020)

TGF-β induce pro-inflammatory Th17 cells (Horwitz et al., 2019).

4 SUMMARY AND PROSPECTS

Autoimmune diseases are chronic inflammatory diseases involving multiple cells and systems, and traditional systemic immunosuppression cannot meet the requirements of precise treatment. Nanoparticle-mediated delivery-induced tolerance *in vivo* is a promising strategy in autoimmune disease or transplantation. The ability of particles to efficiently deliver antigens and immunomodulators, mainly targeting antigen-presenting cells and lymphocytes, can increase the ability to induce specific tolerance. Targeted delivery of protected antigens directly to immune cells ensures efficient, safe, and nonspecific damage. In addition, there are many strategies to optimize nanoparticles for a better fit for immune tolerance therapy, such as controlling the localization, dose, and kinetics of tolerogenic particles. These studies have resulted in many remarkable results. The first-in-man, open-label, single-center clinical trial in RR and SP (secondary progressive) MS patients (ETIMS trial) involved autologous peripheral blood mononuclear cells chemically coupled with seven myelin peptides in the presence of the chemical cross-linker 1-ethyl-3-(3-dimethylaminopropyl)-carbodiimide (EDC) in MS patients, establishing the feasibility and indicating good tolerability and safety of this therapeutic approach(Lutterotti et al., 2013).

Great efforts have been made to develop nanotechnology-induced tolerance during the last decades. It has been more than 30 years since the first nanotechnology vaccination against tetanus toxoid (Birrenbach and Speiser, 1976). Although it has successful experience in human clinical practice (**Table 1**), it is still difficult to translate this therapy into the clinic, as several factors limit its clinical transformation. First, there are noticeable species differences between animals and humans in genetic inheritance and living environment, so the guidance of animal models for actual diseases is limited. Second, animal models of diseases often adopt a single antigen to simulate disease models. However, most human autoimmune diseases are characterized by antigen heterogeneity and epitope expansion or variation, which results in animal models being unable to accurately simulate clinical disease models. This occurred with the first nano-vaccine that co-delivered seven pathogenic peptides at one time and many more autoimmune disease epitopes that were not clear. In addition, animal experiments used prevention to interfere with the disease process, while human diseases tend to develop insidiously and delay for several years. Patients often were presented with obvious clinical symptoms or sequelae during observation, indicating that their disease is in the progression or sequelae stage, making the treatment more challenging (Pearson et al., 2017). In the long term, antigen-specific immune tolerance based on nanoparticles may be a good focus area for research on autoimmune diseases, but much more effort is still required.

AUTHOR CONTRIBUTIONS

HL wrote the manuscript. Y-GY and TS revised the manuscript. All authors contributed to the article and approved the submitted version.

FUNDING

This work was supported by grants from the National Key Research and Development Program of China (No. 2017YFA0208100), NSFC (Nos. 81871478, 91642208, 81422026, and 32171379), Jilin Scientific and Technological Development Program (Nos 20190201094JC and 20200301007RQ), Interdisciplinary Innovation Project of the First Hospital of Jilin University (No. JDYYJCHX001), and the Fundamental Research Funds for the Central Universities, JLU.

REFERENCES

Agmon-Levin, N., Theodor, E., Segal, R. M., and Shoenfeld, Y. (2013). Vitamin D in Systemic and Organ-specific Autoimmune Diseases. *Clinic Rev. Allerg Immunol.* 45 (2), 256–266. doi:10.1007/s12016-012-8342-y

Agüero, L., Zaldivar-Silva, D., Peña, L., and Dias, M. L. (2017). Alginate Microparticles as Oral colon Drug Delivery Device: A Review. *Carbohydr. Polym.* 168, 32–43. doi:10.1016/j.carbpol.2017.03.033

Allen, R. P., Bolandparvaz, A., Ma, J. A., Manickam, V. A., and Lewis, J. S. (2018). Latent, Immunosuppressive Nature of Poly(lactic-Co-Glycolic Acid) Microparticles. *ACS Biomater. Sci. Eng.* 4 (3), 900–918. doi:10.1021/acsbiomaterials.7b00831

Amini, Y., Amel Jamehdar, S., Sadri, K., Zare, S., Musavi, D., and Tafaghodi, M. (2017). Different Methods to Determine the Encapsulation Efficiency of Protein in PLGA Nanoparticles. *Bme* 28 (6), 613–620. doi:10.3233/BME-171705

Angum, F., Khan, T., Kaler, J., Siddiqui, L., and Hussain, A. (2020). The Prevalence of Autoimmune Disorders in Women: A Narrative Review. *Cureus* 12 (3), e8094. doi:10.7759/cureus.8094

Arredouani, M. S., Franco, F., Imrich, A., Fedulov, A., Lu, X., Perkins, D., et al. (2007). Scavenger Receptors SR-AI/II and MARCO Limit Pulmonary Dendritic Cell Migration and Allergic Airway Inflammation. *J. Immunol.* 178 (9), 5912–5920. doi:10.4049/jimmunol.178.9.5912

Bachmann, M. F., and Jennings, G. T. (2010). Vaccine Delivery: a Matter of Size, Geometry, Kinetics and Molecular Patterns. *Nat. Rev. Immunol.* 10 (11), 787–796. doi:10.1038/nri2868

Bal, S. M., Hortensius, S., Ding, Z., Jiskoot, W., and Bouwstra, J. A. (2011). Co-encapsulation of Antigen and Toll-like Receptor Ligand in Cationic Liposomes Affects the Quality of the Immune Response in Mice after Intradermal Vaccination. *Vaccine* 29 (5), 1045–1052. doi:10.1016/j.vaccine.2010.11.061

Bannunah, A. M., Vllasaliu, D., Lord, J., and Stolnik, S. (2014). Mechanisms of Nanoparticle Internalization and Transport across an Intestinal Epithelial Cell Model: Effect of Size and Surface Charge. *Mol. Pharmaceutics* 11 (12), 4363–4373. doi:10.1021/mp500439c

Barclay, T. G., Day, C. M., Petrovsky, N., and Garg, S. (2019). Review of Polysaccharide Particle-Based Functional Drug Delivery. *Carbohydr. Polym.* 221, 94–112. doi:10.1016/j.carbpol.2019.05.067

Basomba, A., Tabar, A. I., de Rojas, D. H. F., García, B. E., Alamar, R., Olaguíbel, J. M., et al. (2002). Allergen Vaccination with a Liposome-Encapsulated Extract of Dermatophagoides Pteronyssinus : A Randomized, Double-Blind, Placebo-Controlled Trial in Asthmatic Patients. *J. Allergy Clin. Immunol.* 109 (6), 943–948. doi:10.1067/mai.2002.124465

Bee, S.-L., Hamid, Z. A. A., Mariatti, M., Yahaya, B. H., Lim, K., Bee, S.-T., et al. (2018). Approaches to Improve Therapeutic Efficacy of Biodegradable PLA/PLGA Microspheres: A Review. *Polym. Rev.* 58 (3), 495–536. doi:10.1080/15583724.2018.1437547

Behzadi, S., Serpooshan, V., Tao, W., Hamaly, M. A., Alkawareek, M. Y., Dreaden, E. C., et al. (2017). Cellular Uptake of Nanoparticles: Journey inside the Cell. *Chem. Soc. Rev.* 46 (14), 4218–4244. doi:10.1039/c6cs00636a

Benne, N., van Duijn, J., Kuiper, J., Jiskoot, W., and Slütter, B. (2016). Orchestrating Immune Responses: How Size, Shape and Rigidity Affect the Immunogenicity of Particulate Vaccines. *J. Controlled Release* 234, 124–134. doi:10.1016/j.jconrel.2016.05.033

Birrenbach, G., and Speiser, P. P. (1976). Polymerized Micelles and Their Use as Adjuvants in Immunology. *J. Pharm. Sci.* 65 (12), 1763–1766. doi:10.1002/jps.2600651217

Boks, M. A., Kager-Groenland, J. R., Haasjes, M. S. P., Zwaginga, J. J., van Ham, S. M., and ten Brinke, A. (2012). IL-10-generated Tolerogenic Dendritic Cells Are Optimal for Functional Regulatory T Cell Induction - A Comparative Study of Human Clinical-Applicable DC. *Clin. Immunol.* 142 (3), 332–342. doi:10.1016/j.clim.2011.11.011

Bulbake, U., Doppalapudi, S., Kommineni, N., and Khan, W. (2017). Liposomal Formulations in Clinical Use: An Updated Review. *Pharmaceutics* 9 (2), 12. doi:10.3390/pharmaceutics9020012

Cappellano, G., Woldetsadik, A. D., Orilieri, E., Shivakumar, Y., Rizzi, M., Carniato, F., et al. (2014). Subcutaneous Inverse Vaccination with PLGA Particles Loaded with a MOG Peptide and IL-10 Decreases the Severity of Experimental Autoimmune Encephalomyelitis. *Vaccine* 32 (43), 5681–5689. doi:10.1016/j.vaccine.2014.08.016

Carambia, A., Freund, B., Schwinge, D., Bruns, O. T., Salmen, S. C., Ittrich, H., et al. (2015). Nanoparticle-based Autoantigen Delivery to Treg-Inducing Liver Sinusoidal Endothelial Cells Enables Control of Autoimmunity in Mice. *J. Hepatol.* 62 (6), 1349–1356. doi:10.1016/j.jhep.2015.01.006

Carambia, A., Freund, B., Schwinge, D., Heine, M., Laschtowitz, A., Huber, S., et al. (2014). TGF-β-dependent Induction of CD4+CD25+Foxp3+ Tregs by Liver Sinusoidal Endothelial Cells. *J. Hepatol.* 61 (3), 594–599. doi:10.1016/j.jhep.2014.04.027

Carambia, A., Gottwick, C., Schwinge, D., Stein, S., Digigow, R., Şeleci, M., et al. (2021). Nanoparticle-mediated Targeting of Autoantigen Peptide to Cross-presenting Liver Sinusoidal Endothelial Cells Protects from CD8 T-cell-driven Autoimmune Cholangitis. *Immunology* 162 (4), 452–463. doi:10.1111/imm.13298

Casals, E., Pfaller, T., Duschl, A., Oostingh, G. J., and Puntes, V. (2010). Time Evolution of the Nanoparticle Protein corona. *ACS Nano* 4 (7), 3623–3632. doi:10.1021/nn901372t

Casella, G., Rasouli, J., Boehm, A., Zhang, W., Xiao, D., Ishikawa, L. L. W., et al. (2020). Oligodendrocyte-derived Extracellular Vesicles as Antigen-specific Therapy for Autoimmune Neuroinflammation in Mice. *Sci. Transl. Med.* 12 (568). doi:10.1126/scitranslmed.aba0599

Casey, L. M., Pearson, R. M., Hughes, K. R., Liu, J. M. H., Rose, J. A., North, M. G., et al. (2018). Conjugation of Transforming Growth Factor Beta to Antigen-Loaded Poly(lactide-Co-Glycolide) Nanoparticles Enhances Efficiency of Antigen-specific Tolerance. *Bioconjug. Chem.* 29 (3), 813–823. doi:10.1021/acs.bioconjchem.7b00624

Castenmiller, C., Keumatio-Doungtsop, B.-C., van Ree, R., de Jong, E. C., and van Kooyk, Y. (2021). Tolerogenic Immunotherapy: Targeting DC Surface Receptors to Induce Antigen-specific Tolerance. *Front. Immunol.* 12, 643240. doi:10.3389/fimmu.2021.643240

Chambers, E. S., Nanzer, A. M., Pfeffer, P. E., Richards, D. F., Martineau, A. R., Griffiths, C. J., et al. (2018). Dendritic Cell Phenotype in Severe Asthma Reflects Clinical Responsiveness to Glucocorticoids. *Clin. Exp. Allergy* 48 (1), 13–22. doi:10.1111/cea.13061

Chandrashekara, S. (2012). The Treatment Strategies of Autoimmune Disease May Need a Different Approach from Conventional Protocol: A Review. *Indian J. Pharmacol.* 44, 665–671. doi:10.4103/0253-7613.103235DOI

Cifuentes-Rius, A., de Puig, H., Kah, J. C. Y., Borros, S., and Hamad-Schifferli, K. (2013). Optimizing the Properties of the Protein corona Surrounding Nanoparticles for Tuning Payload Release. *ACS Nano* 7 (11), 10066–10074. doi:10.1021/nn404166q

Cifuentes-Rius, A., Desai, A., Yuen, D., Johnston, A. P. R., and Voelcker, N. H. (2021). Inducing Immune Tolerance with Dendritic Cell-Targeting Nanomedicines. *Nat. Nanotechnol.* 16 (1), 37–46. doi:10.1038/s41565-020-00810-2

Clough, D. W., King, J. L., Li, F., and Shea, L. D. (2020). Integration of Islet/Beta-Cell Transplants with Host Tissue Using Biomaterial Platforms. *Endocrinology* 161 (11). doi:10.1210/endocr/bqaa156

Cong, X., Tian, H., Liu, S., Mao, K., Chen, H., Xin, Y., et al. (2020). Cationic Liposome/DNA Complexes Mediate Antitumor Immunotherapy by Promoting Immunogenic Tumor Cell Death and Dendritic Cell Activation. *ACS Appl. Mater. Inter.* 12 (25), 28047–28056. doi:10.1021/acsami.0c08112

Dai, Z., Yu, M., Yi, X., Wu, Z., Tian, F., Miao, Y., et al. (2019). Chain-Length- and Saturation-Tuned Mechanics of Fluid Nanovesicles Direct Tumor Delivery. *ACS Nano* 13 (7), 7676–7689. doi:10.1021/acsnano.9b01181

Decuzzi, P., Godin, B., Tanaka, T., Lee, S.-Y., Chiappini, C., Liu, X., et al. (2010). Size and Shape Effects in the Biodistribution of Intravascularly Injected Particles. *J. Controlled Release* 141 (3), 320–327. doi:10.1016/j.jconrel.2009.10.014

Devulapally, R., Foygel, K., Sekar, T. V., Willmann, J. K., and Paulmurugan, R. (2016). Gemcitabine and Antisense-microRNA Co-encapsulated PLGA-PEG Polymer Nanoparticles for Hepatocellular Carcinoma Therapy. *ACS Appl. Mater. Inter.* 8 (49), 33412–33422. doi:10.1021/acsami.6b08153

Ding, F., Deng, H., Du, Y., Shi, X., and Wang, Q. (2014). Emerging Chitin and Chitosan Nanofibrous Materials for Biomedical Applications. *Nanoscale* 6 (16), 9477–9493. doi:10.1039/c4nr02814g

Doherty, D. G. (2016). Immunity, Tolerance and Autoimmunity in the Liver: A Comprehensive Review. *J. Autoimmun.* 66, 60–75. doi:10.1016/j.jaut.2015.08.020

Elmowafy, E. M., Tiboni, M., and Soliman, M. E. (2019). Biocompatibility, Biodegradation and Biomedical Applications of Poly(lactic Acid)/poly(lactic-Co-Glycolic Acid) Micro and Nanoparticles. *J. Pharm. Investig.* 49 (4), 347–380. doi:10.1007/s40005-019-00439-x

Engman, C., Wen, Y., Meng, W. S., Bottino, R., Trucco, M., and Giannoukakis, N. (2015). Generation of Antigen-specific Foxp3+ Regulatory T-Cells *In Vivo* Following Administration of Diabetes-Reversing Tolerogenic Microspheres Does Not Require Provision of Antigen in the Formulation. *Clin. Immunol.* 160 (1), 103–123. doi:10.1016/j.clim.2015.03.004

Ernsting, M. J., Murakami, M., Roy, A., and Li, S.-D. (2013). Factors Controlling the Pharmacokinetics, Biodistribution and Intratumoral Penetration of Nanoparticles. *J. Controlled Release* 172 (3), 782–794. doi:10.1016/j.jconrel.2013.09.013

Fan, Q.-Q., Zhang, C.-L., Qiao, J.-B., Cui, P.-F., Xing, L., Oh, Y.-K., et al. (2020). Extracellular Matrix-Penetrating Nanodrill Micelles for Liver Fibrosis Therapy. *Biomaterials* 230, 119616. doi:10.1016/j.biomaterials.2019.119616

Feldmann, M., and Steinman, L. (2005). Design of Effective Immunotherapy for Human Autoimmunity. *Nature* 435 (7042), 612–619. doi:10.1038/nature03727

Firestein, G. S. (2003). Evolving Concepts of Rheumatoid Arthritis. *Nature* 423 (6937), 356–361. doi:10.1038/nature01661

Freitag, T. L., Podojil, J. R., Pearson, R. M., Fokta, F. J., Sahl, C., Messing, M., et al. (2020). Gliadin Nanoparticles Induce Immune Tolerance to Gliadin in Mouse Models of Celiac Disease. *Gastroenterology* 158 (6), 1667–1681 e1612. doi:10.1053/j.gastro.2020.01.045

Fromen, C. A., Kelley, W. J., Fish, M. B., Adili, R., Noble, J., Hoenerhoff, M. J., et al. (2017). Neutrophil-Particle Interactions in Blood Circulation Drive Particle Clearance and Alter Neutrophil Responses in Acute Inflammation. *ACS Nano* 11 (11), 10797–10807. doi:10.1021/acsnano.7b03190

Fromen, C. A., Robbins, G. R., Shen, T. W., Kai, M. P., Ting, J. P. Y., and DeSimone, J. M. (2015). Controlled Analysis of Nanoparticle Charge on Mucosal and Systemic Antibody Responses Following Pulmonary Immunization. *Proc. Natl. Acad. Sci. U.S.A.* 112 (2), 488–493. doi:10.1073/pnas.1422923112

Fytianos, K., Rodriguez-Lorenzo, L., Clift, M. J. D., Blank, F., Vanhecke, D., von Garnier, C., et al. (2015). Uptake Efficiency of Surface Modified Gold Nanoparticles Does Not Correlate with Functional Changes and Cytokine Secretion in Human Dendritic Cells *In Vitro*. *Nanomedicine: Nanotechnology, Biol. Med.* 11 (3), 633–644. doi:10.1016/j.nano.2014.11.004

Gallucci, S., Lolkema, M., and Matzinger, P. (1999). Natural Adjuvants: Endogenous Activators of Dendritic Cells. *Nat. Med.* 5 (11), 1249–1255. doi:10.1038/15200

Gao, H., and He, Q. (2014). The Interaction of Nanoparticles with Plasma Proteins and the Consequent Influence on Nanoparticles Behavior. *Expert Opin. Drug Deliv.* 11 (3), 409–420. doi:10.1517/17425247.2014.877442

Geijtenbeek, T. B. H., and Gringhuis, S. I. (2009). Signalling through C-type Lectin Receptors: Shaping Immune Responses. *Nat. Rev. Immunol.* 9 (7), 465–479. doi:10.1038/nri2569

Getts, D. R., Martin, A. J., McCarthy, D. P., Terry, R. L., Hunter, Z. N., Yap, W. T., et al. (2012). Microparticles Bearing Encephalitogenic Peptides Induce T-Cell Tolerance and Ameliorate Experimental Autoimmune Encephalomyelitis. *Nat. Biotechnol.* 30 (12), 1217–1224. doi:10.1038/nbt.2434

Getts, D. R., Shea, L. D., Miller, S. D., and King, N. J. C. (2015). Harnessing Nanoparticles for Immune Modulation. *Trends Immunol.* 36 (7), 419–427. doi:10.1016/j.it.2015.05.007

Gleeson, P. A. (2014). The Role of Endosomes in Innate and Adaptive Immunity. *Semin. Cel Dev. Biol.* 31, 64–72. doi:10.1016/j.semcdb.2014.03.002

Gratton, S. E. A., Ropp, P. A., Pohlhaus, P. D., Luft, J. C., Madden, V. J., Napier, M. E., et al. (2008). The Effect of Particle Design on Cellular Internalization Pathways. *Proc. Natl. Acad. Sci. U.S.A.* 105 (33), 11613–11618. doi:10.1073/pnas.0801763105

Gref, R., Lück, M., Marchand, M., Dellacherie, E., Harnisch, S., et al. (2000). 'Stealth' corona-core Nanoparticles Surface Modified by Polyethylene Glycol (PEG): Influences of the corona (PEG Chain Length and Surface Density) and of the Core Composition on Phagocytic Uptake and Plasma Protein Adsorption. *Colloids Surf. B: Biointerfaces* 18, 301–313. doi:10.1016/s0927-7765(99)00156-3

Guo, S., Li, K., Hu, B., Li, C., Zhang, M., Hussain, A., et al. (2021). Membrane-destabilizing Ionizable Lipid Empowered Imaging-guided siRNA Delivery and Cancer Treatment. *Exploration* 1 (1), 35–49. doi:10.1002/exp.20210008

Gursel, I., Gursel, M., Ishii, K. J., and Klinman, D. M. (2001). Sterically Stabilized Cationic Liposomes Improve the Uptake and Immunostimulatory Activity of CpG Oligonucleotides. *J. Immunol.* 167 (6), 3324–3328. doi:10.4049/jimmunol.167.6.3324

Hamad, I., Al-Hanbali, O., Hunter, A. C., Rutt, K. J., Andresen, T. L., and Moghimi, S. M. (2010). Distinct Polymer Architecture Mediates Switching of Complement Activation Pathways at the Nanosphere–Serum Interface: Implications for Stealth Nanoparticle Engineering. *ACS Nano* 4 (11), 6629–6638. doi:10.1021/nn101990a

Harush-Frenkel, O., Debotton, N., Benita, S., and Altschuler, Y. (2007). Targeting of Nanoparticles to the Clathrin-Mediated Endocytic Pathway. *Biochem. Biophysical Res. Commun.* 353 (1), 26–32. doi:10.1016/j.bbrc.2006.11.135

Hasegawa, H., and Matsumoto, T. (2018). Mechanisms of Tolerance Induction by Dendritic Cells *In Vivo*. *Front. Immunol.* 9, 350. doi:10.3389/fimmu.2018.00350

Hawiger, D., Masilamani, R. F., Bettelli, E., Kuchroo, V. K., and Nussenzweig, M. C. (2004). Immunological Unresponsiveness Characterized by Increased Expression of CD5 on Peripheral T Cells Induced by Dendritic Cells *In Vivo*. *Immunity* 20 (6), 695–705. doi:10.1016/j.immuni.2004.05.002

He, C., Hu, Y., Yin, L., Tang, C., and Yin, C. (2010). Effects of Particle Size and Surface Charge on Cellular Uptake and Biodistribution of Polymeric Nanoparticles. *Biomaterials* 31 (13), 3657–3666. doi:10.1016/j.biomaterials.2010.01.065

Heymann, F., Peusquens, J., Ludwig-Portugall, I., Kohlhepp, M., Ergen, C., Niemietz, P., et al. (2015). Liver Inflammation Abrogates Immunological Tolerance Induced by Kupffer Cells. *Hepatology* 62 (1), 279–291. doi:10.1002/hep.27793

Higaki, M., Ishihara, T., Izumo, N., Takatsu, M., and Mizushima, Y. (2005). Treatment of Experimental Arthritis with poly(D, L-Lactic/glycolic Acid) Nanoparticles Encapsulating Betamethasone Sodium Phosphate. *Ann. Rheum. Dis.* 64 (8), 1132–1136. doi:10.1136/ard.2004.030759

Hirai, M., Minematsu, H., Kondo, N., Oie, K., Igarashi, K., and Yamazaki, N. (2007). Accumulation of Liposome with Sialyl Lewis X to Inflammation and Tumor Region: Application to *In Vivo* Bio-Imaging. *Biochem. Biophysical Res. Commun.* 353 (3), 553–558. doi:10.1016/j.bbrc.2006.12.060

Hlavaty, K. A., McCarthy, D. P., Saito, E., Yap, W. T., Miller, S. D., and Shea, L. D. (2016). Tolerance Induction Using Nanoparticles Bearing HY Peptides in Bone Marrow Transplantation. *Biomaterials* 76, 1–10. doi:10.1016/j.biomaterials.2015.10.041

Horst, A. K., Neumann, K., Diehl, L., and Tiegs, G. (2016). Modulation of Liver Tolerance by Conventional and Nonconventional Antigen-Presenting Cells and Regulatory Immune Cells. *Cell Mol Immunol* 13 (3), 277–292. doi:10.1038/cmi.2015.112

Horwitz, D. A., Fahmy, T. M., Piccirillo, C. A., and La Cava, A. (2019). Rebalancing Immune Homeostasis to Treat Autoimmune Diseases. *Trends Immunol.* 40 (10), 888–908. Available at: https://autoimmune.org/resource-center/about-autoimmunityhttps://autoimmune.org/resource-center/about-autoimmunity. doi:10.1016/j.it.2019.08.003

Huang, F., Zhao, J., Wei, Y., Wen, Z., Zhang, Y., Wang, X., et al. (2020). Anti-Tumor Efficacy of an Adjuvant Built-In Nanovaccine Based on Ubiquitinated Proteins from Tumor Cells. *Ijn* Vol. 15, 1021–1035. doi:10.2147/IJN.S237578

Huang, X., Li, L., Liu, T., Hao, N., Liu, H., Chen, D., et al. (2011). The Shape Effect of Mesoporous Silica Nanoparticles on Biodistribution, Clearance, and Biocompatibility *In Vivo*. *ACS Nano* 5 (7), 5390–5399. doi:10.1021/nn200365a

Hunter, Z., McCarthy, D. P., Yap, W. T., Harp, C. T., Getts, D. R., Shea, L. D., et al. (2014). A Biodegradable Nanoparticle Platform for the Induction of Antigen-specific Immune Tolerance for Treatment of Autoimmune Disease. *ACS Nano* 8 (3), 2148–2160. doi:10.1021/nn405033r

Jazayeri, S. D., Lim, H. X., Shameli, K., Yeap, S. K., and Poh, C. L. (2021). Nano and Microparticles as Potential Oral Vaccine Carriers and Adjuvants against Infectious Diseases. *Front. Pharmacol.* 12, 682286. doi:10.3389/fphar.2021.682286

Jia, J., Zhang, Y., Xin, Y., Jiang, C., Yan, B., and Zhai, S. (2018). Interactions between Nanoparticles and Dendritic Cells: From the Perspective of Cancer Immunotherapy. *Front. Oncol.* 8, 404. doi:10.3389/fonc.2018.00404

Keijzer, C., van der Zee, R., van Eden, W., and Broere, F. (2013). Treg Inducing Adjuvants for Therapeutic Vaccination against Chronic Inflammatory Diseases. *Front. Immunol.* 4, 245. doi:10.3389/fimmu.2013.00245

Kim, B., Sun, S., Varner, J. A., Howell, S. B., Ruoslahti, E., and Sailor, M. J. (2019a). Securing the Payload, Finding the Cell, and Avoiding the Endosome: Peptide-Targeted, Fusogenic Porous Silicon Nanoparticles for Delivery of siRNA. *Adv. Mater.* 31 (35), 1902952. doi:10.1002/adma.201902952

Kim, S.-H., Jung, H.-H., and Lee, C.-K. (2018). Generation, Characteristics and Clinical Trials ofEx VivoGenerated Tolerogenic Dendritic Cells. *Yonsei Med. J.* 59 (7), 807–815. doi:10.3349/ymj.2018.59.7.807

Kim, S.-H., Moon, J.-H., Jeong, S.-U., Jung, H.-H., Park, C.-S., Hwang, B. Y., et al. (2019b). Induction of Antigen-specific Immune Tolerance Using Biodegradable Nanoparticles Containing Antigen and Dexamethasone. *Ijn* Vol. 14, 5229–5242. doi:10.2147/ijn.S210546

Kishimoto, T. K., Ferrari, J. D., LaMothe, R. A., Kolte, P. N., Griset, A. P., O'Neil, C., et al. (2016). Improving the Efficacy and Safety of Biologic Drugs with Tolerogenic Nanoparticles. *Nat. Nanotech* 11 (10), 890–899. doi:10.1038/nnano.2016.135

Kishimoto, T. K., and Maldonado, R. A. (2018). Nanoparticles for the Induction of Antigen-specific Immunological Tolerance. *Front. Immunol.* 9, 230. doi:10.3389/fimmu.2018.00230

Klugewitz, K., Blumenthal-Barby, F., Schrage, A., Knolle, P. A., Hamann, A., and Crispe, I. N. (2002). Immunomodulatory Effects of the Liver: Deletion of Activated CD4+ Effector Cells and Suppression of IFN-γ-Producing Cells after Intravenous Protein Immunization. *J. Immunol.* 169 (5), 2407–2413. doi:10.4049/jimmunol.169.5.2407

Knudsen, K. B., Northeved, H., Kumar Ek, P., Permin, A., Gjetting, T., Andresen, T. L., et al. (2015). *In Vivo* toxicity of Cationic Micelles and Liposomes. *Nanomedicine: Nanotechnology, Biol. Med.* 11 (2), 467–477. doi:10.1016/j.nano.2014.08.004

Kontos, S., Kourtis, I. C., Dane, K. Y., and Hubbell, J. A. (2013). Engineering Antigens for *In Situ* Erythrocyte Binding Induces T-Cell Deletion. *Proc. Natl. Acad. Sci. U.S.A.* 110 (1), E60–E68. doi:10.1073/pnas.1216353110

Koppolu, B., and Zaharoff, D. A. (2013). The Effect of Antigen Encapsulation in Chitosan Particles on Uptake, Activation and Presentation by Antigen Presenting Cells. *Biomaterials* 34 (9), 2359–2369. doi:10.1016/j.biomaterials.2012.11.066

Kryczanowsky, F., Raker, V., Graulich, E., Domogalla, M. P., and Steinbrink, K. (2016). IL-10-Modulated Human Dendritic Cells for Clinical Use: Identification of a Stable and Migratory Subset with Improved Tolerogenic Activity. *J.I.* 197 (9), 3607–3617. doi:10.4049/jimmunol.1501769

LaMothe, R. A., Kolte, P. N., Vo, T., Ferrari, J. D., Gelsinger, T. C., Wong, J., et al. (2018). Tolerogenic Nanoparticles Induce Antigen-specific Regulatory T Cells and Provide Therapeutic Efficacy and Transferrable Tolerance against Experimental Autoimmune Encephalomyelitis. *Front. Immunol.* 9, 281. doi:10.3389/fimmu.2018.00281

Lee, J.-H., Park, C.-S., Jang, S., Kim, J.-W., Kim, S.-H., Song, S., et al. (2017). Tolerogenic Dendritic Cells Are Efficiently Generated Using Minocycline and Dexamethasone. *Sci. Rep.* 7 (1), 15087. doi:10.1038/s41598-017-15569-1

Lehmann, C., Heger, L., Heidkamp, G., Baranska, A., Lühr, J., Hoffmann, A., et al. (2016). Direct Delivery of Antigens to Dendritic Cells via Antibodies Specific for Endocytic Receptors as a Promising Strategy for Future Therapies. *Vaccines* 4 (2), 8. doi:10.3390/vaccines4020008

Lewis, J. S., Stewart, J. M., Marshall, G. P., Carstens, M. R., Zhang, Y., Dolgova, N. V., et al. (2019). Dual-Sized Microparticle System for Generating Suppressive Dendritic Cells Prevents and Reverses Type 1 Diabetes in the Nonobese Diabetic Mouse Model. *ACS Biomater. Sci. Eng.* 5 (5), 2631–2646. doi:10.1021/acsbiomaterials.9b00332

Limmer, A., Ohl, J., Kurts, C., Ljunggren, H.-G., Reiss, Y., Groettrup, M., et al. (2000). Efficient Presentation of Exogenous Antigen by Liver Endothelial Cells to CD8+ T Cells Results in Antigen-specific T-Cell Tolerance. *Nat. Med.* 6 (12), 1348–1354. doi:10.1038/82161

Liu, J., Chen, C., Wei, T., Gayet, O., Loncle, C., Borge, L., et al. (2021). Dendrimeric Nanosystem Consistently Circumvents Heterogeneous Drug Response and Resistance in Pancreatic Cancer. *Exploration* 1 (1), 21–34. doi:10.1002/exp.20210003

Liu, Q., Wang, X., Liu, X., Kumar, S., Gochman, G., Ji, Y., et al. (2019). Use of Polymeric Nanoparticle Platform Targeting the Liver to Induce Treg-Mediated Antigen-specific Immune Tolerance in a Pulmonary Allergen Sensitization Model. *ACS Nano* 13 (4), 4778–4794. doi:10.1021/acsnano.9b01444

Look, M., Stern, E., Wang, Q. A., DiPlacido, L. D., Kashgarian, M., Craft, J., et al. (2013). Nanogel-based Delivery of Mycophenolic Acid Ameliorates Systemic Lupus Erythematosus in Mice. *J. Clin. Invest.* 123 (4), 1741–1749. doi:10.1172/JCI65907

Lostalé-Seijo, I., and Montenegro, J. (2018). Synthetic Materials at the Forefront of Gene Delivery. *Nat. Rev. Chem.* 2 (10), 258–277. doi:10.1038/s41570-018-0039-1

Lovrić, J., Bazzi, H. S., Cuie, Y., Fortin, G. R. A., Winnik, F. M., and Maysinger, D. (2005). Differences in Subcellular Distribution and Toxicity of green and Red Emitting CdTe Quantum Dots. *J. Mol. Med.* 83 (5), 377–385. doi:10.1007/s00109-004-0629-x

Lu, L., Duong, V. T., Shalash, A. O., Skwarczynski, M., and Toth, I. (2021). Chemical Conjugation Strategies for the Development of Protein-Based Subunit Nanovaccines. *Vaccines* 9 (6), 563. doi:10.3390/vaccines9060563

Luo, X., Pothoven, K. L., McCarthy, D., DeGutes, M., Martin, A., Getts, D. R., et al. (2008). ECDI-fixed Allogeneic Splenocytes Induce Donor-specific Tolerance for Long-Term Survival of Islet Transplants via Two Distinct Mechanisms. *Proc. Natl. Acad. Sci. U.S.A.* 105 (38), 14527–14532. doi:10.1073/pnas.0805204105

Lutterotti, A., Yousef, S., Sputtek, A., Stürner, K. H., Stellmann, J.-P., Breiden, P., et al. (2013). Antigen-specific Tolerance by Autologous Myelin Peptide-Coupled Cells: a Phase 1 Trial in Multiple Sclerosis. *Sci. Transl. Med.* 5 (188), 188ra175. doi:10.1126/scitranslmed.3006168

Macedo, C., Turquist, H., Metes, D., and Thomson, Angus. W. (20122012). Immunoregulatory Properties of Rapamycin-Conditioned Monocyte-Derived Dendritic Cells and Their Role in Transplantation. *Transpl. Res* 116, 16–17. doi:10.1186/2047-1440-1-16

Maldonado, R. A., LaMothe, R. A., Ferrari, J. D., Zhang, A.-H., Rossi, R. J., Kolte, P. N., et al. (2015). Polymeric Synthetic Nanoparticles for the Induction of Antigen-specific Immunological Tolerance. *Proc. Natl. Acad. Sci. U.S.A.* 112 (2), E156–E165. doi:10.1073/pnas.1408686111

Manolova, V., Flace, A., Bauer, M., Schwarz, K., Saudan, P., and Bachmann, M. F. (2008). Nanoparticles Target Distinct Dendritic Cell Populations According to Their Size. *Eur. J. Immunol.* 38 (5), 1404–1413. doi:10.1002/eji.200737984

Meka, R. R., Venkatesha, S. H., Acharya, B., and Moudgil, K. D. (2019). Peptide-targeted Liposomal Delivery of Dexamethasone for Arthritis Therapy. *Nanomedicine* 14 (11), 1455–1469. doi:10.2217/nnm-2018-0501

Meka, R. R., Venkatesha, S. H., and Moudgil, K. D. (2018). Peptide-directed Liposomal Delivery Improves the Therapeutic index of an Immunomodulatory Cytokine in Controlling Autoimmune Arthritis. *J. Controlled Release* 286, 279–288. doi:10.1016/j.jconrel.2018.08.007

Mendler, A. N., Hu, B., Prinz, P. U., Kreutz, M., Gottfried, E., and Noessner, E. (2012). Tumor Lactic Acidosis Suppresses CTL Function by Inhibition of P38 and JNK/c-Jun Activation. *Int. J. Cancer* 131 (3), 633–640. doi:10.1002/ijc.26410

Metselaar, J. M., Wauben, M. H. M., Wagenaar-Hilbers, J. P. A., Boerman, O. C., and Storm, G. (2003). Complete Remission of Experimental Arthritis by Joint Targeting of Glucocorticoids with Long-Circulating Liposomes. *Arthritis Rheum.* 48 (7), 2059–2066. doi:10.1002/art.11140

Mikušová, V., and Mikuš, P. (2021). Advances in Chitosan-Based Nanoparticles for Drug Delivery. *Ijms* 22 (17), 9652. doi:10.3390/ijms22179652

Montes-Cobos, E., Ring, S., Fischer, H. J., Heck, J., Strauss, J., Schwaninger, M., et al. (2017). Targeted Delivery of Glucocorticoids to Macrophages in a Mouse Model of Multiple Sclerosis Using Inorganic-Organic Hybrid Nanoparticles. *J. Controlled Release* 245, 157–169. doi:10.1016/j.jconrel.2016.12.003

Nakase, H., Okazaki, K., Tabata, Y., and Chiba, T. (2003). Biodegradable Microspheres Targeting Mucosal Immune-Regulating Cells: New Approach for Treatment of Inflammatory Bowel Disease. *J. Gastroenterol.* 38 Suppl 15 (Suppl. 15), 59–62.

Nielen, M. M. J., van Schaardenburg, D., Reesink, H. W., van de Stadt, R. J., van der Horst-Bruinsma, I. E., de Koning, M. H. M. T., et al. (2004). Specific Autoantibodies Precede the Symptoms of Rheumatoid Arthritis: a Study of Serial Measurements in Blood Donors. *Arthritis Rheum.* 50 (2), 380–386. doi:10.1002/art.20018

Niikura, K., Matsunaga, T., Suzuki, T., Kobayashi, S., Yamaguchi, H., Orba, Y., et al. (2013). Gold Nanoparticles as a Vaccine Platform: Influence of Size and Shape

on Immunological Responses *In Vitro* and *In Vivo*. *ACS Nano* 7 (5), 3926–3938. doi:10.1021/nn3057005

Nouri, H. R., Varasteh, A., Jaafari, M. R., Davies, J. M., and Sankian, M. (2015). Induction of a Th1 Immune Response and Suppression of IgE via Immunotherapy with a Recombinant Hybrid Molecule Encapsulated in Liposome-Protamine-DNA Nanoparticles in a Model of Experimental Allergy. *Immunol. Res.* 62 (3), 280–291. doi:10.1007/s12026-015-8659-8

Park, J.-K., Utsumi, T., Seo, Y.-E., Deng, Y., Satoh, A., Saltzman, W. M., et al. (2016). Cellular Distribution of Injected PLGA-Nanoparticles in the Liver. *Nanomedicine: Nanotechnology, Biol. Med.* 12 (5), 1365–1374. doi:10.1016/j.nano.2016.01.013

Patel, P. C., Giljohann, D. A., Daniel, W. L., Zheng, D., Prigodich, A. E., and Mirkin, C. A. (2010). Scavenger Receptors Mediate Cellular Uptake of Polyvalent Oligonucleotide-Functionalized Gold Nanoparticles. *Bioconjug. Chem.* 21 (12), 2250–2256. doi:10.1021/bc1002423

Pearson, R. M., Casey, L. M., Hughes, K. R., Miller, S. D., and Shea, L. D. (2017). *In Vivo* reprogramming of Immune Cells: Technologies for Induction of Antigen-specific Tolerance. *Adv. Drug Deliv. Rev.* 114, 240–255. doi:10.1016/j.addr.2017.04.005

Pearson, R. M., Podojil, J. R., Shea, L. D., King, N. J. C., Miller, S. D., and Getts, D. R. (2019). Overcoming Challenges in Treating Autoimmuntity: Development of Tolerogenic Immune-Modifying Nanoparticles. *Nanomedicine: Nanotechnology, Biol. Med.* 18, 282–291. doi:10.1016/j.nano.2018.10.001

Pei, W., Wan, X., Shahzad, K. A., Zhang, L., Song, S., Jin, X., et al. (2018). Direct Modulation of Myelin-Autoreactive CD4+ and CD8+ T Cells in EAE Mice by a Tolerogenic Nanoparticle Co-carrying Myelin Peptide-Loaded Major Histocompatibility Complexes, CD47 and Multiple Regulatory Molecules. *Ijn* Vol. 13, 3731–3750. doi:10.2147/IJN.S164500

Peter, K., Rehli, M., Singer, K., Renner-Sattler, K., and Kreutz, M. (2015). Lactic Acid Delays the Inflammatory Response of Human Monocytes. *Biochem. Biophysical Res. Commun.* 457 (3), 412–418. doi:10.1016/j.bbrc.2015.01.005

Pozsgay, J., Babos, F., Uray, K., Magyar, A., Gyulai, G., Kiss, É., et al. (2016). *In Vitro* eradication of Citrullinated Protein Specific B-Lymphocytes of Rheumatoid Arthritis Patients by Targeted Bifunctional Nanoparticles. *Arthritis Res. Ther.* 18, 15. doi:10.1186/s13075-016-0918-0

Prosperi, D., Colombo, M., Zanoni, I., and Granucci, F. (2017). Drug Nanocarriers to Treat Autoimmunity and Chronic Inflammatory Diseases. *Semin. Immunol.* 34, 61–67. doi:10.1016/j.smim.2017.08.010

Quintana, F. J., Murugaiyan, G., Farez, M. F., Mitsdoerffer, M., Tukpah, A.-M., Burns, E. J., et al. (2010). An Endogenous Aryl Hydrocarbon Receptor Ligand Acts on Dendritic Cells and T Cells to Suppress Experimental Autoimmune Encephalomyelitis. *Proc. Natl. Acad. Sci. U.S.A.* 107 (48), 20768–20773. doi:10.1073/pnas.1009201107

Rabinovich, G. A., Gabrilovich, D., and Sotomayor, E. M. (2007). Immunosuppressive Strategies that Are Mediated by Tumor Cells. *Annu. Rev. Immunol.* 25, 267–296. doi:10.1146/annurev.immunol.25.022106.141609

Racanelli, V., and Rehermann, B. (2006). The Liver as an Immunological Organ. *Hepatology* 43 (2 Suppl. 1), S54–S62. doi:10.1002/hep.21060

Rauchhaus, U., Schwaiger, F., and Panzner, S. (2009). Separating Therapeutic Efficacy from Glucocorticoid Side-Effects in Rodent Arthritis Using Novel, Liposomal Delivery of Dexamethasone Phosphate: Long-Term Suppression of Arthritis Facilitates Interval Treatment. *Arthritis Res. Ther.* 11 (6), R190. doi:10.1186/ar2889

Rejman, J., Oberle, V., Zuhorn, I. S., and Hoekstra, D. (2004). Size-dependent Internalization of Particles via the Pathways of Clathrin- and Caveolae-Mediated Endocytosis. *Biochem. J.* 377 (Pt 1), 159–169. doi:10.1042/BJ20031253

Rieger, J., Freichels, H., Imberty, A., Putaux, J.-L., Delair, T., Je´rôme, C., et al. (2009). Polyester Nanoparticles Presenting Mannose Residues: toward the Development of New Vaccine Delivery Systems Combining Biodegradability and Targeting Properties. *Biomacromolecules* 10 (3), 651–657. doi:10.1021/bm801492c

Rincon-Restrepo, M., Mayer, A., Hauert, S., Bonner, D. K., Phelps, E. A., Hubbell, J. A., et al. (2017). Vaccine Nanocarriers: Coupling Intracellular Pathways and Cellular Biodistribution to Control CD4 vs CD8 T Cell Responses. *Biomaterials* 132, 48–58. doi:10.1016/j.biomaterials.2017.03.047

Rodriguez-Fernandez, S., Pujol-Autonell, I., Brianso, F., Perna-Barrull, D., Cano-Sarabia, M., Garcia-Jimeno, S., et al. (2018). Phosphatidylserine-Liposomes Promote Tolerogenic Features on Dendritic Cells in Human Type 1 Diabetes by Apoptotic Mimicry. *Front. Immunol.* 9, 253. doi:10.3389/fimmu.2018.00253

Rothhammer, V., Kenison, J. E., Tjon, E., Takenaka, M. C., de Lima, K. A., Borucki, D. M., et al. (2017). Sphingosine 1-phosphate Receptor Modulation Suppresses Pathogenic Astrocyte Activation and Chronic Progressive CNS Inflammation. *Proc. Natl. Acad. Sci. U.S.A.* 114 (8), 2012–2017. doi:10.1073/pnas.1615413114

Saito, E., Kuo, R., Kramer, K. R., Gohel, N., Giles, D. A., Moore, B. B., et al. (2019a). Design of Biodegradable Nanoparticles to Modulate Phenotypes of Antigen-Presenting Cells for Antigen-specific Treatment of Autoimmune Disease. *Biomaterials* 222, 119432. doi:10.1016/j.biomaterials.2019.119432

Saito, E., Kuo, R., Pearson, R. M., Gohel, N., Cheung, B., King, N. J. C., et al. (2019b). Designing Drug-free Biodegradable Nanoparticles to Modulate Inflammatory Monocytes and Neutrophils for Ameliorating Inflammation. *J. Controlled Release* 300, 185–196. doi:10.1016/j.jconrel.2019.02.025

Samuvel, D. J., Sundararaj, K. P., Nareika, A., Lopes-Virella, M. F., and Huang, Y. (2009). Lactate Boosts TLR4 Signaling and NF-Kb Pathway-Mediated Gene Transcription in Macrophages via Monocarboxylate Transporters and MD-2 Up-Regulation. *J. Immunol.* 182 (4), 2476–2484. doi:10.4049/jimmunol.0802059

Serhan, C. N., and Petasis, N. A. (2011). Resolvins and Protectins in Inflammation Resolution. *Chem. Rev.* 111 (10), 5922–5943. doi:10.1021/cr100396c

Serhan, C. N., Yacoubian, S., and Yang, R. (2008). Anti-inflammatory and Proresolving Lipid Mediators. *Annu. Rev. Pathol. Mech. Dis.* 3, 279–312. doi:10.1146/annurev.pathmechdis.3.121806.151409

Serra, P., and Santamaria, P. (2015). Nanoparticle-based Autoimmune Disease Therapy. *Clin. Immunol.* 160 (1), 3–13. doi:10.1016/j.clim.2015.02.003

Serrano-Sevilla, I., Artiga, Á., Mitchell, S. G., De Matteis, L., and de la Fuente, J. M. (2019). Natural Polysaccharides for siRNA Delivery: Nanocarriers Based on Chitosan, Hyaluronic Acid, and Their Derivatives. *Molecules* 24 (14), 2570. doi:10.3390/molecules24142570

Shang, L., Nienhaus, K., and Nienhaus, G. U. (2014). Engineered Nanoparticles Interacting with Cells: Size Matters. *J. Nanobiotechnol* 12, 5. doi:10.1186/1477-3155-12-5

Shen, L., Tenzer, S., Storck, W., Hobernik, D., Raker, V. K., Fischer, K., et al. (2018). Protein corona-mediated Targeting of Nanocarriers to B Cells Allows Redirection of Allergic Immune Responses. *J. Allergy Clin. Immunol.* 142 (5), 1558–1570. doi:10.1016/j.jaci.2017.08.049

Sherr, J., Sosenko, J., Skyler, J. S., and Herold, K. C. (2008). Prevention of Type 1 Diabetes: the Time Has Come. *Nat. Rev. Endocrinol.* 4 (6), 334–343. doi:10.1038/ncpendmet0832

Shi, D., Fu, M., Fan, P., Li, W., Chen, X., Li, C., et al. (2007). Artificial Phosphatidylserine Liposome Mimics Apoptotic Cells in Inhibiting Maturation and Immunostimulatory Function of Murine Myeloid Dendritic Cells in Response to 1-Chloro-2,4-Dinitrobenze *In Vitro*. *Arch. Dermatol. Res.* 299 (7), 327–336. doi:10.1007/s00403-007-0770-9

Shin, J. M., Kim, S.-H., Thambi, T., You, D. G., Jeon, J., Lee, J. O., et al. (2014). A Hyaluronic Acid-Methotrexate Conjugate for Targeted Therapy of Rheumatoid Arthritis. *Chem. Commun.* 50 (57), 7632–7635. doi:10.1039/c4cc02595d

Soo Choi, H., Liu, W., Misra, P., Tanaka, E., Zimmer, J. P., Itty Ipe, B., et al. (2007). Renal Clearance of Quantum Dots. *Nat. Biotechnol.* 25 (10), 1165–1170. doi:10.1038/nbt1340

Sørensen, K. K., McCourt, P., Berg, T., Crossley, C., Couteur, D. L., Wake, K., et al. (2012). The Scavenger Endothelial Cell: a New Player in Homeostasis and Immunity. *Am. J. Physiology-Regulatory, Integr. Comp. Physiol.* 303 (12), R1217–R1230. doi:10.1152/ajpregu.00686.2011

Stabler, C. L., Li, Y., Stewart, J. M., and Keselowsky, B. G. (2019). Engineering Immunomodulatory Biomaterials for Type 1 Diabetes. *Nat. Rev. Mater.* 4 (6), 429–450. doi:10.1038/s41578-019-0112-5

Stensland, Z. C., Cambier, J. C., and Smith, M. J. (2021). Therapeutic Targeting of Autoreactive B Cells: Why, How, and when? *Biomedicines* 9 (1), 83. doi:10.3390/biomedicines9010083

Sukhbaatar, N., Hengstschläger, M., and Weichhart, T. (2016). mTOR-Mediated Regulation of Dendritic Cell Differentiation and Function. *Trends Immunol.* 37 (11), 778–789. doi:10.1016/j.it.2016.08.009

Sun, T., Zhang, Y. S., Pang, B., Hyun, D. C., Yang, M., and Xia, Y. (2014). Engineered Nanoparticles for Drug Delivery in Cancer Therapy. *Angew. Chem. Int. Ed.* 53 (46), a–n. doi:10.1002/anie.201403036

Sun, X., Gamal, M., Nold, P., Said, A., Chakraborty, I., Pelaz, B., et al. (2019). Tracking Stem Cells and Macrophages with Gold and Iron Oxide Nanoparticles - the Choice of the Best Suited Particles. *Appl. Mater. Today* 15, 267–279. doi:10.1016/j.apmt.2018.12.006

Švajger, U., and Rožman, P. J. (2020). Recent Discoveries in Dendritic Cell Tolerance-Inducing Pharmacological Molecules. *Int. Immunopharmacology* 81, 106275. doi:10.1016/j.intimp.2020.106275

Takenaka, M. C., Gabriely, G., Rothhammer, V., Mascanfroni, I. D., Wheeler, M. A., Chao, C.-C., et al. (2019). Control of Tumor-Associated Macrophages and T Cells in Glioblastoma via AHR and CD39. *Nat. Neurosci.* 22 (5), 729–740. doi:10.1038/s41593-019-0370-y

Takenaka, M. C., and Quintana, F. J. (2017). Tolerogenic Dendritic Cells. *Semin. Immunopathol* 39 (2), 113–120. doi:10.1007/s00281-016-0587-8

Thomson, A. W., and Knolle, P. A. (2010). Antigen-presenting Cell Function in the Tolerogenic Liver Environment. *Nat. Rev. Immunol.* 10 (11), 753–766. doi:10.1038/nri2858

Thorp, E. B., Boada, C., Jarbath, C., and Luo, X. (2020). Nanoparticle Platforms for Antigen-specific Immune Tolerance. *Front. Immunol.* 11, 945. doi:10.3389/fimmu.2020.00945

Tieu, T., Alba, M., Elnathan, R., Cifuentes-Rius, A., and Voelcker, N. H. (2018). Advances in Porous Silicon-Based Nanomaterials for Diagnostic and Therapeutic Applications. *Adv. Therap.* 2 (1), 1800095. doi:10.1002/adtp.201800095

Tostanoski, L. H., Chiu, Y.-C., Gammon, J. M., Simon, T., Andorko, J. I., Bromberg, J. S., et al. (2016). Reprogramming the Local Lymph Node Microenvironment Promotes Tolerance that Is Systemic and Antigen Specific. *Cel Rep.* 16 (11), 2940–2952. doi:10.1016/j.celrep.2016.08.033

Turley, D. M., and Miller, S. D. (2007). Peripheral Tolerance Induction Using Ethylenecarbodiimide-Fixed APCs Uses Both Direct and Indirect Mechanisms of Antigen Presentation for Prevention of Experimental Autoimmune Encephalomyelitis. *J. Immunol.* 178 (4), 2212–2220. doi:10.4049/jimmunol.178.4.2212

Umeshappa, C. S., Mbongue, J., Singha, S., Mohapatra, S., Yamanouchi, J., Lee, J. A., et al. (2020). Ubiquitous Antigen-specific T Regulatory Type 1 Cells Variably Suppress Hepatic and Extrahepatic Autoimmunity. *J. Clin. Invest.* 130 (4), 1823–1829. doi:10.1172/JCI130670

Umeshappa, C. S., Singha, S., Blanco, J., Shao, K., Nanjundappa, R. H., Yamanouchi, J., et al. (2019). Suppression of a Broad Spectrum of Liver Autoimmune Pathologies by Single Peptide-MHC-Based Nanomedicines. *Nat. Commun.* 10 (1), 2150. doi:10.1038/s41467-019-09893-5

Urbanavicius, D., Alvarez, T., Such, G. K., Johnston, A. P. R., and Mintern, J. D. (2018). The Potential of Nanoparticle Vaccines as a Treatment for Cancer. *Mol. Immunol.* 98, 2–7. doi:10.1016/j.molimm.2017.12.022

Wang, H., Wu, L., and Reinhard, B. M. (2012). Scavenger Receptor Mediated Endocytosis of Silver Nanoparticles into J774A.1 Macrophages Is Heterogeneous. *ACS Nano* 6 (8), 7122–7132. doi:10.1021/nn302186n

Wikins, L. W. a. (2012). *Fundamental Immunology*. 6th Edition.

Williams, A. S., Dojcinov, S., Richards, P. J., and Williams, B. D. (2001). Amelioration of Rat Antigen-Induced Arthritis by Liposomally Conjugated Methotrexate Is Accompanied by Down-Regulation of Cytokine mRNA Expression. *Rheumatology* 40, 375–383. doi:10.1093/rheumatology/40.4.375

Woźniak, A., Malankowska, A., Nowaczyk, G., Grześkowiak, B. F., Tuśnio, K., Słomski, R., et al. (2017). Size and Shape-dependent Cytotoxicity Profile of Gold Nanoparticles for Biomedical Applications. *J. Mater. Sci. Mater. Med.* 28 (6), 92. doi:10.1007/s10856-017-5902-y

Xie, Z., Chen, J., Zheng, C., Wu, J., Cheng, Y., Zhu, S., et al. (2017). 1,25-dihydroxyvitamin D3 -induced Dendritic Cells Suppress Experimental Autoimmune Encephalomyelitis by Increasing Proportions of the Regulatory Lymphocytes and Reducing T Helper Type 1 and Type 17 Cells. *Immunology* 152 (3), 414–424. doi:10.1111/imm.12776

Xing, Y., and Hogquist, K. A. (2012). T-cell Tolerance: central and Peripheral. *Cold Spring Harbor Perspect. Biol.* 4 (6), a006957. doi:10.1101/cshperspect.a006957

Xu, X.-L., Li, W.-S., Wang, X.-J., Du, Y.-L., Kang, X.-Q., Hu, J.-B., et al. (2018). Endogenous Sialic Acid-Engineered Micelles: a Multifunctional Platform for On-Demand Methotrexate Delivery and Bone Repair of Rheumatoid Arthritis. *Nanoscale* 10 (6), 2923–2935. doi:10.1039/c7nr08430g

Yan, W., Chen, W., and Huang, L. (2008). Reactive Oxygen Species Play a central Role in the Activity of Cationic Liposome Based Cancer Vaccine. *J. Controlled Release* 130 (1), 22–28. doi:10.1016/j.jconrel.2008.05.005

Yang, Y., and Santamaria, P. (2021). Evolution of Nanomedicines for the Treatment of Autoimmune Disease: From Vehicles for Drug Delivery to Inducers of Bystander Immunoregulation. *Adv. Drug Deliv. Rev.* 176, 113898. doi:10.1016/j.addr.2021.113898

Yeste, A., Nadeau, M., Burns, E. J., Weiner, H. L., and Quintana, F. J. (2012). Nanoparticle-mediated Codelivery of Myelin Antigen and a Tolerogenic Small Molecule Suppresses Experimental Autoimmune Encephalomyelitis. *Proc. Natl. Acad. Sci. U.S.A.* 109 (28), 11270–11275. doi:10.1073/pnas.1120611109

Youssef, A. E. H., Dief, A. E., El Azhary, N. M., Abdelmonsif, D. A., and El-Fetiany, O. S. (2019). LINGO-1 siRNA Nanoparticles Promote central Remyelination in Ethidium Bromide-Induced Demyelination in Rats. *J. Physiol. Biochem.* 75 (1), 89–99. doi:10.1007/s13105-018-00660-6

Yu, C., Xi, J., Li, M., An, M., and Liu, H. (2018). Bioconjugate Strategies for the Induction of Antigen-specific Tolerance in Autoimmune Diseases. *Bioconjug. Chem.* 29 (5), 719–732. doi:10.1021/acs.bioconjchem.7b00632

Zhang, A.-H., Rossi, R. J., Yoon, J., Wang, H., and Scott, D. W. (2016). Tolerogenic Nanoparticles to Induce Immunologic Tolerance: Prevention and Reversal of FVIII Inhibitor Formation. *Cell Immunol.* 301, 74–81. doi:10.1016/j.cellimm.2015.11.004

Zhao, X., Ng, S., Heng, B. C., Guo, J., Ma, L., Tan, T. T. Y., et al. (2013). Cytotoxicity of Hydroxyapatite Nanoparticles Is Shape and Cell Dependent. *Arch. Toxicol.* 87 (6), 1037–1052. doi:10.1007/s00204-012-0827-1

Zheng, X., Suzuki, M., Ichim, T. E., Zhang, X., Sun, H., Zhu, F., et al. (2010). Treatment of Autoimmune Arthritis Using RNA Interference-Modulated Dendritic Cells. *J.I.* 184 (11), 6457–6464. doi:10.4049/jimmunol.0901717

Zizzari, I. G., Napoletano, C., Battisti, F., Rahimi, H., Caponnetto, S., Pierelli, L., et al. (2015). MGL Receptor and Immunity: When the Ligand Can Make the Difference. *J. Immunol. Res.* 2015, 1–8. doi:10.1155/2015/450695

Zuhorn, I. S., Kalicharan, R., and Hoekstra, D. (2002). Lipoplex-mediated Transfection of Mammalian Cells Occurs through the Cholesterol-dependent Clathrin-Mediated Pathway of Endocytosis. *J. Biol. Chem.* 277 (20), 18021–18028. doi:10.1074/jbc.M111257200

Conflict of Interest: The authors declare that the research was conducted in the absence of any commercial or financial relationships that could be construed as a potential conflict of interest.

Publisher's Note: All claims expressed in this article are solely those of the authors and do not necessarily represent those of their affiliated organizations, or those of the publisher, the editors, and the reviewers. Any product that may be evaluated in this article, or claim that may be made by its manufacturer, is not guaranteed or endorsed by the publisher.

frontiers | Frontiers in Bioengineering and Biotechnology

REVIEW
published: 14 April 2022
doi: 10.3389/fbioe.2022.900481

PBPK Modeling on Organs-on-Chips: An Overview of Recent Advancements

Yi Yang[1†], *Yin Chen*[2†], *Liang Wang*[1*], *Shihui Xu*[3], *Guoqing Fang*[3], *Xilin Guo*[2], *Zaozao Chen*[1,3*] *and Zhongze Gu*[1,3*]

[1]State Key Laboratory of Bioelectronics, School of Biological Science & Medical Engineering, Southeast University, Nanjing, China, [2]Jiangsu Provincial Center for Disease Control and Prevention, Key Laboratory of Enteric Pathogenic Microbiology, Ministry Health, Institute of Pathogenic Microbiology Health, Nanjing, China, [3]Institute of Medical Devices (Suzhou), Southeast University, Suzhou, China

Organ-on-a-chip (OoC) is a new and promising technology, which aims to improve the efficiency of drug development and realize personalized medicine by simulating *in vivo* environment *in vitro*. Physiologically based pharmacokinetic (PBPK) modeling is believed to have the advantage of better reflecting the absorption, distribution, metabolism and excretion process of drugs *in vivo* than traditional compartmental or non-compartmental pharmacokinetic models. The combination of PBPK modeling and organ-on-a-chip is believed to provide a strong new tool for new drug development and have the potential to replace animal testing. This article provides the recent development of organ-on-a-chip technology and PBPK modeling including model construction, parameter estimation and validation strategies. Application of PBPK modeling on Organ-on-a-Chip (OoC) has been emphasized, and considerable progress has been made. PBPK modeling on OoC would become an essential part of new drug development, personalized medicine and other fields.

Keywords: PBPK modeling, Organ-on-a-chip, drug development, pharmacokinetic, preclinical trails

OPEN ACCESS

Edited by:
Mingqiang Li,
Third Affiliated Hospital of Sun Yat-sen University, China

Reviewed by:
Huaiqi Jing,
Chinese Center For Disease Control and Prevention, China
Xiaoni Ai,
Peking University, China
Heng Zuo,
Sichuan Normal University, China

***Correspondence:**
Liang Wang
liangwang@seu.edu.cn
Zaozao Chen
zaozaochen@seu.edu.cn
Zhongze Gu
gu@seu.edu.cn

[†]*These authors have contributed equally to this work*

Specialty section:
This article was submitted to Biomaterials, a section of the journal Frontiers in Bioengineering and Biotechnology

Received: *20 March 2022*
Accepted: *29 March 2022*
Published: *14 April 2022*

Citation:
Yang Y, Chen Y, Wang L, Xu S, Fang G, Guo X, Chen Z and Gu Z (2022) PBPK Modeling on Organs-on-Chips: An Overview of Recent Advancements. Front. Bioeng. Biotechnol. 10:900481. doi: 10.3389/fbioe.2022.900481

1 INTRODUCTION

To predict the pharmacokinetic (PK) behaviors of drug absorption, distribution, metabolism and excretion (ADME) in a quantitative manner is of great importance in new drug development. PK modeling uses mathematical principles and methods to study the dynamics behaviors of drugs *in vivo* like ADME. Before conducting clinical trials of the drug, it is necessary to establish an effective PK model to analyze and predict the kinetics of multi-organ interactions, the concentration curve of drug and its metabolites over time to determine the appropriate dose of the drug. Pharmacodynamics (PD) studies the effect of a drug *in vivo*, including efficacy (drug action on tissues or organs), toxicity (side effects), and drug-drug interactions (effects of drug combinations). The combined PK-PD model can be used to predict and analyze the physiological effect of a drug on organs at a given dose. Physiologically based pharmacokinetic (PBPK) model studies the drug pharmacokinetics by viewing human organs as separate compartments and integrating them into a system according to physiological and anatomical knowledge. Compared with the traditional compartmental

Abbreviations: PBPK, physiologically based pharmacokinetic; PD, pharmacodynamics; OoC, Organ-on-a-Chip; MOoCs, Multiple Organs-on-Chips; IVIVE, *in vitro* to *in vivo* extrapolation; IVIVR, *in vitro in vivo* relationship; DDI, Drug-Drug Interaction; ADME, absorption, distribution, metabolism, excretion; PDMS, polydimethylsil.

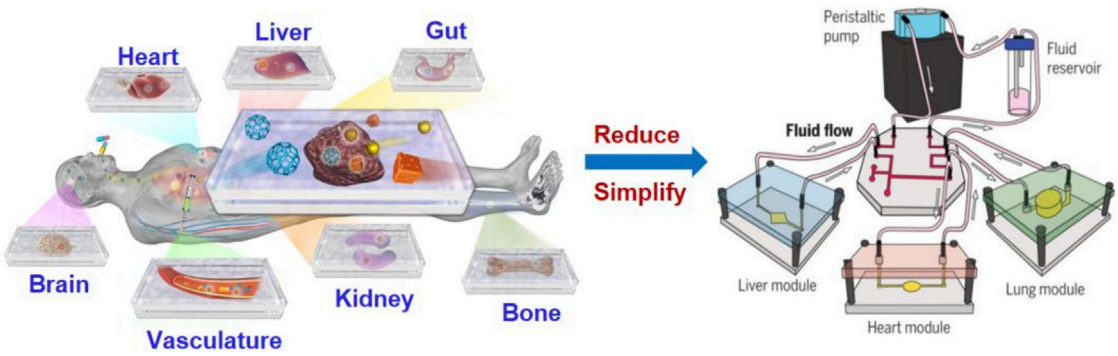

FIGURE 1 | Illustration of organ-on-a-chip technologies to mimic human organs structure and function (Park et al., 2019).

pharmacokinetic model, the compartments and model parameters of PBPK model have physiological meaning. Thus PBPK model is believed to more accurately reflect the ADME process of the drug *in vivo*.

The failure of preclinical cell culture and animal models to predict the efficacy and safety of drugs *in vivo* causes huge amounts waste of time, resources and money each year (Edington et al., 2018). Besides animal experiments are also under increasing ethical pressure. Since proposed in 1959, the 3R principle (i.e., replacement, reduction, refinement) has been incorporated into legislation when conducting animal experiments for scientific purposes [e.g., European Union's 2010/63/EU Directive (D´ıaz et al., 2021)]. Under the guidance of the 3R principle, in 2019, the US Environmental Protection Agency proposed to phase out any experiments on mammals by 2035 (U.S. EPA Holds Inaugural Conference on Reducing Animal Testing for Chemical Safety, 2019). Some scholars recommended using new methods (Fernandes and Pedroso, 2017) to replace animal experiments. These methods include *in vitro* tests (tissues and cells); non-invasive clinical research on human volunteers; the use of species (e.g., shrimp and daphnia larvae) that are not listed as protected animals; computer simulation, etc. The above events have led to a series of emerging technologies that capture complex human physiology *in vitro* outside the human body, including the micro-physiological system (MPS), also known as the organs-on-a-chip (OoC). OoC technology is considered to have the potential to improve the efficiency of drug development and replace animal experiments (Edington et al., 2018; Heringa et al., 2020; Chen et al., 2021; Lee et al., 2021; Yang et al., 2021; Zhang et al., 2021). The combination of OoC technology and PK-PD model provides a new tool for drug development.

2 ORGAN-ON-A-CHIP OVERVIEW

2.1 Organ-on-a-Chip

Organ-on-a-chip (OoC) is a kind of microfluidic cell culture equipment, which reproduces the physiological and pathological characteristics of organs or tissues by reconstructing the structure and function *in vitro* (**Figure 1**). The design and fabrication of an organ-on-a-chip system involves a series of technologies, including microfluidic, material and cell biology which will be introduced in the following subsections.

2.1.1. Microfluidic

Microfluidics refers to the technology for precisely manipulating microscale fluids in tiny structures (usually on the sub-micron scale), also known as lab-on-a-chip. The combination of microfluidic technology and cell culture technology has created OoC technology that is believed to be able to capture complex human physiology *in vitro*. Microfluidics can control the cell culture conditions on the microscopic level (Wikswo et al., 2013b; Jiang et al., 2016), and the geometric design of the organ chip can further control the biochemical phenomena related to the concentration gradient, such as the formation of blood vessels (Zhang et al., 2016). Linda (Edington et al., 2018) reported a programmable microfluidic system that controls the rate of fluid in the organ chip by changing the frequency of compressed air and partial vacuum delivered by the manifold.

2.1.2 Material

Most of the current OoC cell culture devices are made of polydimethylsiloxane (PDMS). However, the adsorption of small hydrophobic molecules by PDMS makes it challenging to accurately predict the results of drug experiments. Ingber (Grant et al., 2021) reported their work on predicting the drug concentration of organ chips through simulation and experimental methods with the molecular adsorption process taken into consideration. In addition, some materials such as polysulfone (PSF) plastic (Edington et al., 2018) are considered to have the potential to replace PDMS for their lower absorption ability of hydrophobic molecules compared with PDMS.

Thin and flexible biopolymer membranes also play an important role in making culture devices for OoC. Such structures can be used to simulate the specific biological characteristics of organs, such as mechanical stretching to simulate the breathing process. Polyurethane membrane (Gabriel et al., 2017) has been reported as a material for fabricating this type of biopolymer membrane.

2.1.3 3D Cell Culture

A specific function of an organ may rely on its specific cell structures. A series of 3D structures (Lee et al., 2019; Oso´rio et al., 2021; Shim et al., 2017) have been proposed to better mimic human physiology. 3D bioprinting is currently one of the most promising technologies for shaping cell structure, and has been successfully applied in the production of artificial organ chips (Ewald et al., 2021).

2.2 Recent Reported Progress on Organ-on-a-Chip Technology

2.2.1 Heart-on-a-Chip

The heart is responsible for providing sufficient blood to other organs and tissues in the human body to supply oxygen and nutrients and take away the metabolic waste in the organs. Zhang (Zhang et al., 2016) proposed a novel hybrid strategy based on 3D bioprinting to fabricate endothelialized myocardium. By using composite bio-ink, the endothelial cells are directly bioprinted in the microfiber hydrogel scaffold to form a layer of confluent endothelium. An aligned myocardium capable of spontaneous and synchronous contraction can be made by seeding cardiomyocytes into the 3D endothelial bed.

2.2.2 Intestine-on-a-Chip

The intestine is an important digestive organ of the human body. Oral drugs must pass through the small intestine to enter the blood. Therefore, research on intestinal chips is essential for preclinical drug experiments using OoC technology. Zhang (Zhang et al., 2016) combined intestinal tissue engineering and OoC technology to establish an *in vitro* biological model of the human duodenum. The intestinal epithelial cells cultured on the chip come from endoscopic biopsy or organ resection. This chip represents the closest model to the living duodenum and captures the key features of the small intestine.

2.2.3 Liver-on-a-Chip

The liver system is the main site of drug metabolism. The liver is composed of a series of complex hepatic lobules (Mccuskey, 2008). Maintaining the long-term physiological function of liver cells is a challenging problem. With the purpose of improving the physiological model of hepatocytes *in vivo*, 3D hepatocyte culture technology is applied (An et al., 2015; Ma et al., 2018) to develop a platform that presented a long-term maintenance of liver-on-a-chip. Yum (Yum et al., 2014) developed a system to study how liver cells affect other cell types. A high-throughput assay was developed to assess the toxicity of hepatocyte drugs. Riahi (Riahi et al., 2016) fabricated a microfluidic electrochemical chip sensor to detect biomarkers produced in the process of liver metabolism. Liver-on-a-Chip has shown great application value in the field of clinical trial. Hou (Hou et al., 2020) developed an integrated biomimetic array chip (iBAC) including a Liver-on-a-Chip and a tumor-on-a-Chip as a screening tool of drug development. Xiao (Xiao et al., 2021) developed an iBAC for establishing extracellular matrix (ECM) based model as a case for systematical prediction of hepatotoxicity.

2.2.4 Pancreas-on-a-Chip

Pancreas-on-a-chip technology is rapidly growing into a platform for complex *in vitro* modeling of pancreatic islet physiology. Advances in microfluidic design through the use of imaging compatible bio-materials and biosensor technology may provide a new future tool for predicting the outcome of islet transplantation. The progress of combining pancreatic islets with other types of tissues provides the possibility to study diabetes intervention in a minimally equivalent *in vitro* environment (Abadpour et al., 2020). With the purpose to investigate the cause of cystic fibrosis, A pancreas-on-a-chip incorporated in an *in vitro* co-culture system was proposed to deepened the understanding of pancreatic function (Shik Mun et al., 2019).

2.2.5 Vascularized Organ-on-a-Chip

The blood vessel itself is a major organ in the human body, which carries nutrients, immune cells, signaling molecules and therapeutic drugs to all other organs. It also plays a key role in inducing and maintaining tissue characteristics and providing a tissue-specific environment (i.e., vascular niche) that supports the survival and function of stem cells through the expression of vascular secretion factors.

Vascularized OoC are currently a promising research direction in the field of organ chips. There are at least three reasons for the application of Vascularized OoC: 1) Replication of vascular secretion signals (Osaki et al., 2018). Growth factors secreted by vascular endothelial cells are considered to be essential in inducing organ regeneration, as well as the maintenance of homeostasis and metabolism; 2) Building of a larger-scale *in vitro* tissues (Mehling and Tay, 2014; Jung et al., 2015), beyond the volume limitation of traditional *in vitro* tissues that rely on diffusion for nutrient delivery and waste elimination; 3) Capture the complex human physiology *in vitro* (Ji et al., 2016; Chen et al., 2018). There are a large number of organ epithelial cells and vascular endothelial cells in the human body with of physiologically relevant tissue-tissue barriers between vascular endothelial cells and parenchymal cells of various organs. These barriers can significantly affect the ADME process *in vivo*.

2.2.6 The Fabrication of Vascularized Organ-on-a-Chip

Capillary-like structures in tissue-engineered organs are generally produced through self-assembled, pre-patterned, and 3D-bioprinted (Rollas, 2008). The self-assembled vascularized OoC platform reproduces the formation of new blood vessels *in vitro*, the pre-patterned and 3D-bioprinted vascularized OoC can form a fully perfusable vascular system with predefined dimensions and control configurations, but the size of the blood vessels is largely limited by the resolution and size of the mold or nozzle.

2.2.7 Advantages of Vascularized Organ-on-a-Chip

There are substantial epithelial cells of organs and endothelial cells of blood vessels in the human body, and physiologically related tissue-tissue barriers exist between the vascular endothelium and the parenchymal cells of each organ. These

			Human		milliHuman(mHu)		microHuman(μHu)		Organ mass ratios	
	Body mass:		60kg		60g		60mg			
Organ	A	B	M,g	Organ/Body	M,g	Organ/Body	M,mg	Organ/Body	M_{mHu}/M_{Hu}	$M_{\mu Hu}/M_{Hu}$
Liver	33.2	0.93	1496	2.5%	2.4	4.0%	3.9	6.6%	1.62E-03	2.63E-06
Brain	85	0.66	1268	2.1%	13	22%	139	232%	1.05E-02	1.10E-04
Lungs	9.7	0.94	455	0.76%	0.69	1.2%	1.0	1.7%	1.51E-03	2.29E-06
Heart	5.2	0.97	276	0.46%	0.34	0.57%	0.42	0.70%	1.23E-03	1.51E-06
Kidney	6.3	0.87	222	0.37%	0.54	0.91%	1.3	2.2%	2.45E-03	6.03E-06
Pancreas	2.0	0.91	83	0.14%	0.15	0.26%	0.29	0.48%	1.86E-03	3.47E-06
Spleen	1.5	0.85	49	0.081%	0.14	0.23%	0.39	0.64%	2.82E-03	7.94E-06
Thyroid	0.15	1.12	15	0.025%	0.0064	0.01%	0.0028	0.0047%	4.37E-04	1.91E-06
Adrenals	0.53	0.7	9.3	0.016%	0.07	0.12%	0.59	0.98%	7.94E-03	6.31E-05
Pituitary	0.03		0.49	0.00081%	0.0044	0.0074%	0.040	0.067%	9.12E-03	8.32E-05

FIGURE 2 | Allometric scaling coefficients and organ masse (Adapted from Wikswo et al., 2013b).

barriers can significantly affect the ADME response. This is essential for simulating PK in a clinically relevant way. Vascularized OoC will be helpful in simulating the complex mechanism of multi-organ cooperation *in vivo*.

2.3 Multiple Organs-on-Chips (Human-on-a-Chip)

Since researchers have made great progress (Grosberg et al., 2011; Mehling and Tay, 2014) on Individual OoC technologies in the last decade, it is still difficult to put these technologies into the use of real drug experiment before multiple organs can be integrated into a single system correctly. Even though our understanding of a multiple coupled OoCs or human-on-a-chip (HoC) is very limited so far, some progress has been achieved by scaling and system biology for multiple OoCs as explored in several studies. An introduction to these studies will be provided.

John (Wikswo et al., 2013b) argues that "To replicate human physiology and drug response with interconnected human OoCs/HoCs, it is critical that each OoC/HoC has the correct relative size." By observing a large number of plants and animals, scientists have discovered formulas that can express the relationship between parts and the whole organism, which is called allometric scaling. Allometric scaling formula has the form $M = AM^B$. M_b represents the mass of an organism and A, B represent coefficients related to Species. M here represents the mass of an organ. It is necessary to establish the relationship between human mass and organ mass before applying this formula into determining micro-organ relative size.

Allometric scaling has been extremely little used in the research of multiple OoCs while it has been studied for more than one century. Stahl (1965) puts it that allometric scaling can be applied to determining the human organs mass according to the human body mass using the statistics collected from primates (Alford et al., 2010). **Figure 2** shows coefficients A and B obtained from primates. These coefficients inform us how the weight of different organs or tissues should be determined based on the allometric scaling law for a multiple-organs-on-chips (MOoCs).

However, there still exists considerably problems in the application of allometric scaling. First, allometric scaling may not give the appropriate organs mass estimation since the coefficients are derived from primates weighed over 10 g. If the mass of a human body is set as 60 mg, the mass of the brain will be 139 mg according to allometric scaling which is obvious not rational. In this situation, the mass of different organs on a chip must be modified by researchers to make sure they have correct relative size and all modifications are based upon the experience of researchers. Second, OoCs may be impossible to conduct drug experiments if its mass is decided by allometric scaling. As Grosberg (Grosberg et al., 2011) puts certain immune cells function at such a low density [3,000 leukocytes per ml of cerebral spinal fluid (CSF)] that the breadth of acquired immune response may not be replicable in a μBrain with a CSF volume around 1 μl that would contain about 3 leukocytes. It is obvious that a brain immune drug experiment cannot be conducted on the brain-on-a-chip since it has too little leukocytes while the mass of the brain is relatively large.

Since the application of allometric scaling in integrating OoCs still remains challenging. researchers attempt to find other solutions to integrate multiple organs into a single system. Grosberg has descripted it as "living histological 'section' of an adult human" (Grosberg et al., 2011). Constructing a single OoC which is relatively big and can reflect the property of a human organ, then put these different single OoC together.

On the condition that the volume for the media of a certain OoC is decided properly, Grosberg (Grosberg et al., 2011) argues that "It is necessary, however, to make the 'section' large enough and sufficiently realistic that the organ functions in a more physiologically realistic manner than a simple monolayer monoculture in a Petri dish or well plate. Building a functional 'section' from an individual human's cells may have advantages over using real ones in that it may be possible to create 'sections' of an individual patient's organs that are not readily available."

While living histological "section" performs well in the experiment on a single OoC, it is complex to integrate two or more OoCs in a system. The size of each section must be modified carefully to achieve a system that can correctly recover the interaction between different organs.

Obviously, it is very difficult to simulate the human body system even from the mass level. The researchers also proposed a method (Alford et al., 2010; Grosberg et al., 2011) which is called functional scaling that does not approximate the human body in every aspect but focuses on the main indicators of each organ chip. For example, we only pay attention to the gas exchange

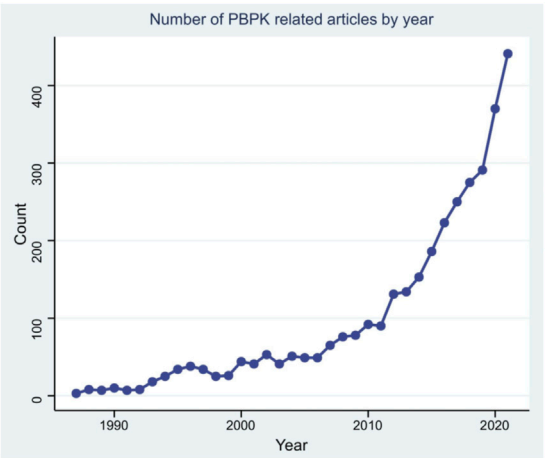

FIGURE 3 | Number of PBPK related articles by year.

ability of a lung (Gas exchange volume per unit time). This method provides a realistic way to integrate multiple OoCs into a coupled system. However, functional scaling may lead to an oversimplification of micro physiology system and increase the difficulty of interpreting experimental results.

The current common practice in establishing the application of human-on-a-chipis as follows: multiple organs on the chip are simultaneously cultured with cells from different organs and tissues. These cells are connected through channels to achieve the integration of multiple organs to establish a system (Palaninathan et al., 2018; Zhao et al., 2019). These methods can be divided into static, semi-static and flexible methods (Rogal et al., 2017). Static multiple organs are integrated into a single connected device. In a semi-static system, organs are connected by a fluid network through a tissue insert based on Transwell® (Rogal et al., 2017). In systems that use flexible methods, individual organ-specific platforms are interconnected using flexible micro-channels. Such a system facilitates the recreation of multiple organs (Rogal et al., 2017). Although the concept of multi-organ chips is still in its infancy, some breakthroughs have been made, including dual-organ (van Midwoud et al., 2010; Tsamandouras et al., 2017), three-organs (Maschmeyer et al., 2015; Skardal et al., 2017), four-organs (Maschmeyer et al., 2015; Oleaga et al., 2016) and ten-organs on-chip (Edington et al., 2018) design.

3 PHYSIOLOGICALLY BASED PHARMACOKINETIC MODELING

3.1 Physiologically Based Pharmacokinetic Models

3.1.1 The Development of PK/PD Model

Although some explorations on ADME process of drugs *in vivo* have been done before 1937 (Widmark and Tandberg, 1924; Paalzow, 1995), the establishment of modern pharmacokinetics is generally attributed to Torsten (Paalzow, 1995) in 1937 for his proposition of two-compartment model. In 1960, Brodie (Brodie et al., 1960) introduced a calculation method of pharmacokinetic model parameter for the first time when studying the drugs entering the cerebrospinal fluid. In 1978, Yamaoka (Yamaoka et al., 1978) applied the statistical moment method to pharmacokinetics research, which was later known as the non-compartmental model of pharmacokinetics. Since then, pharmacokinetics has gone through a period of rapid development, during which the PBPK modeling has been established. To count the relevant data, a PubMed search was conducted using the search terms "PK/PD," "pharmacokinetics" and "pharmacodynamics" within the abstract or title of the manuscript. The results are shown in the **Figure 3**. As our knowledge of human physiology advances, the PBPK model has become more complex and closer to the actual situation of human body. More commercial PBPK modeling software such as Gastroplus® and Simcpy® has emerged to study the ADME behaviors of the drugs. In the future, the PBPK model will be applied to different fields including food safety, and will be more precise and more physiologically sound.

3.1.2 Physiologically Based Pharmacokinetic Models

Physiologically based PK (PBPK) models (Rollas, 2008; Rowland et al., 2011; Sager et al., 2015) have been developed to simulate drugs behavior in complex human body. The PBPK model represents the human body as a network connecting various organs through arterial and venous blood flow (**Figure 4**) (Prantil-Baun et al., 2018). The red arrow indicates the blood flow direction of the artery and the blue arrow indicates the blood flow direction of the vein. **Figure 4B** gives how some key PK parameters can be calculated from drug exposure curves. The graph on the top shows the area under the curve (AUC), which reflects the time dependent exposure in the body to a drug over time, and shows how drug levels vary with administration, as shown by comparing oral and intravenous (IV) dosing. From these curves, one can identify the maximum concentration after initial administration of an IV drug (C0), maximum concentration for orally administered drug (Cmax), and minimum concentration at the end of the elimination phase (Cmin), as well as the time it takes for the plasma concentration to decrease by 50% (t1/2) and the corresponding time (tmax) to reach Cmax after oral administration of the drug. The bottom graph shows the determination of volume of distribution (Vd). Vc represents the volume in which the drug is distributed immediately after IV administration when the drug is limited to the blood and, thus, highly perfused organs. The steady-state volume of distribution (Vss) is achieved when the drug enters tissues. The parameter Varea describes the elimination phase of the drug, whether it is metabolized or cleared from the system, typically by the liver and kidney, where CL represents clearance and k is the elimination rate constant, which describes the rate at which a drug is removed from the system. Some key PK parameters, such as maximum concentration (Cmax), maximum time to reach Cmax (tmax), area under the curve (AUC), bioavailability (F), volume of distribution (Vd), clearance (CL), elimination rate constant (k), and half-life (t1/2) are described briefly here (Benet, 1984; Urso et al., 2002; Rowland and Tozer, 2005; Aungst, 2017).

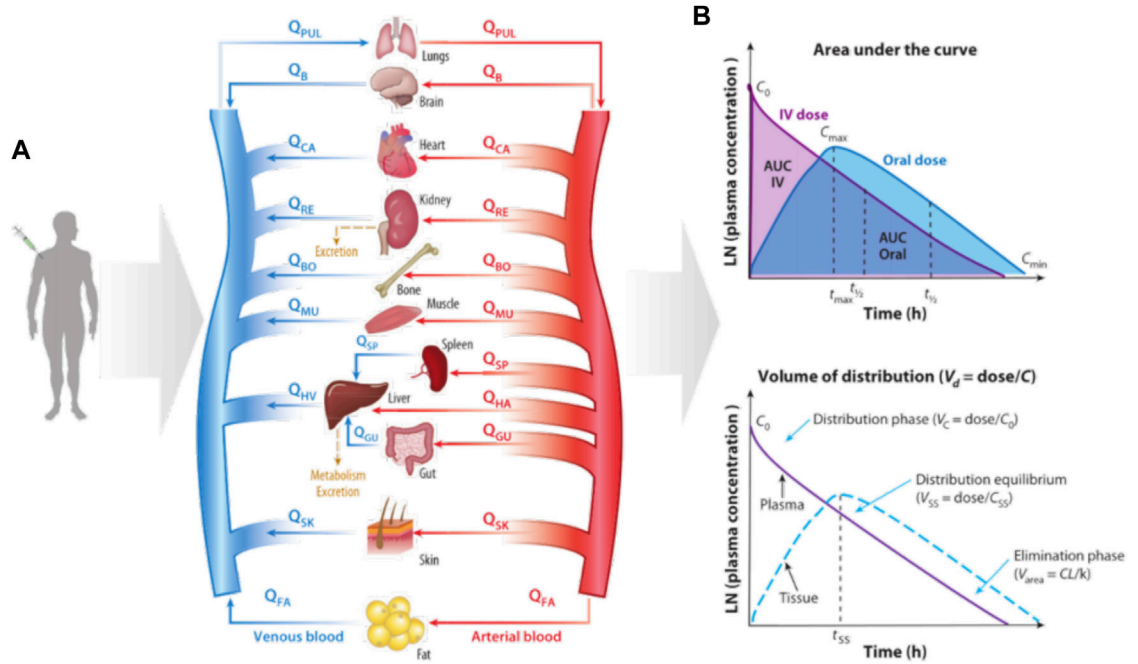

FIGURE 4 | Diagram of how organ size, composition, and blood flows (Q) are used to construct a physiologically based pharmacokinetic (PBPK) model of the whole body and predict the kinetics of drug exposure (Prantil-Baun et al., 2018). **(A)** How a PBPK model can be built based on physiology knowledge; **(B)** The calculation of key PK parameters.

3.2 The Establishment of Physiologically Based Pharmacokinetic Models

PBPK models can be divided into two types: the full model and the minimal model. The full PBPK models mean that all distribution organs and tissues are represented as independent perfused chambers, and the minimum PBPK models lump organs with similar kinetics. The full PBPK models often fit the experimental data better than the minimum model, but too many parameters may lead to overfitting. An advantage of the full PBPK modeling is that it can simulate the exposure of drugs or their metabolites in specific tissues that are not available for clinical sampling. The pharmacological or toxicological effects of some drugs are driven by the concentration in the tissue, which is particularly important. The complete PBPK model is usually used to systematically predict the distribution kinetics to simulate the plasma concentration-time distribution.

As shown in **Figure 5**, the PBPK model consists of system-specific and drug-specific parameters. System- specific parameters include blood flow, organ volume, expression of enzymes and transporters, and plasma protein concentration. Drug-specific parameters include internal clearance, volume of distribution, solubility and physical and chemical parameters, tissue distribution, plasma protein binding affinity and membrane permeability. Drug-related parameters are independent of system-specific parameters, so the *in vitro* bottom-up method can be used to mechanically extrapolate human body dynamics parameters. Drug dependent parameters are independent of system parameters, allowing a bottom-up approach to mechanically extrapolate human pharmacokinetics from *in vitro* and silicon data.

3.3 Physiologically Based Pharmacokinetic Model Validation

There are no clear requirements or guidelines on how to determine the quality of the PBPK model currently. In regulatory guidelines, the criteria for evaluating the effectiveness of a model are usually put forward in the context of whether the model meets the performance requirements for its specific purpose.

As shown in **Figure 6A**, a statistic (Sager et al., 2015) pointed out that 97% of PBPK related articles between 2008 and 2015 will undergo model verification, but only 32% of the data set used for verification (the data set used for validation here generally describes a pharmacokinetic process) were reported to match the simulated age, gender of the models. In addition, only 21% of model validations took into account genotype. Since some PBPK model parameters are related to characteristics such as age, gender, genotype, etc., this may lead to a decrease in the accuracy of the model prediction and the failure of the model verification.

Statistics (Sager et al., 2015) also pointed out that the criteria for determining model performance of PBPK model in related papers published in English from 2008 to 2015 are inconsistent and subjective. As shown in **Figure 6B**, in 56% of the models, the authors did not specify a criterion to determine whether their model was successful; for 7% models, the authors specified that the predicted mean PK parameters were supposed to be within 30% of the observed mean; for 10% of the models, the predicted fold change in the AUC or Cmax between different simulated populations or study conditions had to be within two-fold of the observed fold change; for 4% of the models, the predicted

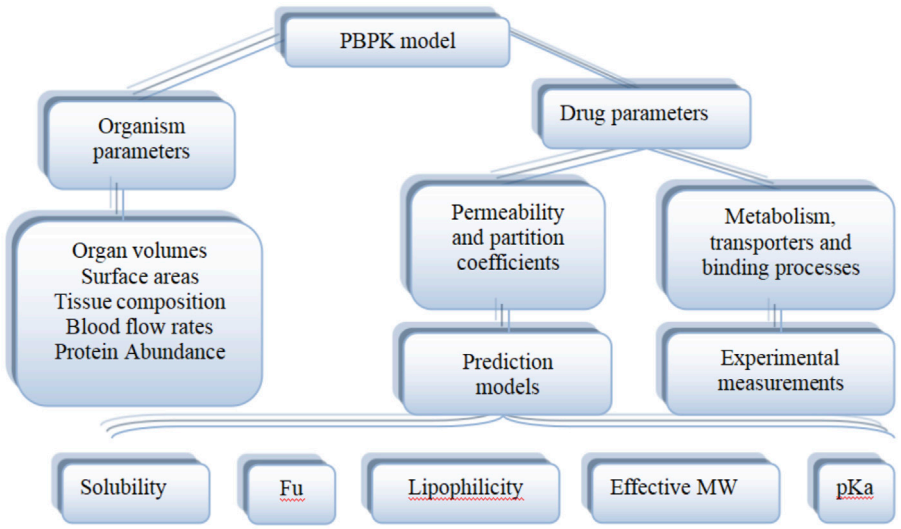

FIGURE 5 | Physiological and drug parameters in PBPK models (Adapted from Kuepfer et al., 2016).

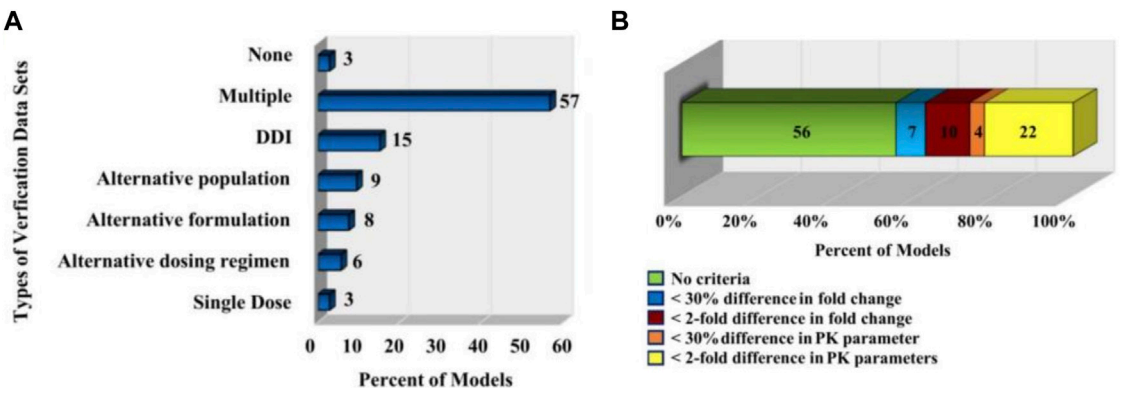

FIGURE 6 | PBPK model validation. **(A)** The types of *in vivo* datasets used to verify the quality of the models (Sager et al., 2015). **(B)** The distribution of the acceptance criteria used in PBPK models (Sager et al., 2015).

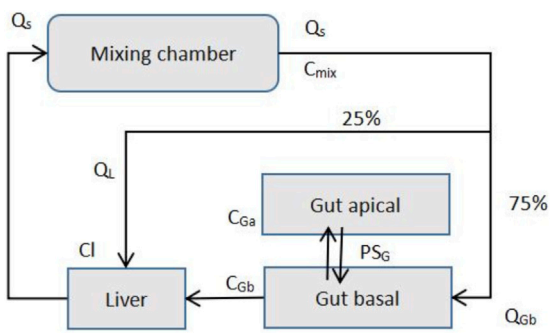

FIGURE 7 | MIT gut-liver MPS Platform (Adapted from Kasendra et al., 2018).

fold change in ADME characteristics (e.g., AUC, Cmax.) in a given population were supposed to be within 30% of the observed fold change; for 22% of the models, the predicted ADME characteristics (e.g., AUC, Cmax.) in a given population were supposed to be within two-fold of the observed value.

3.4 Application of Physiologically Based Pharmacokinetic Model Combined With Organ-on-a-Chip

3.4.1 Models of Drug Pharmacokinetics in Micro-Physiological System

Conventional flat cell culture, due to its simple and limited structure, is often unable to accurately study the ADME process in the human

body. Micro-physiological systems can be used to simulate drug transport and metabolism between human organs. The current MPS calculation model consists of only a few number of organs, usually gut and liver, and other blood supplying organs are represented by mixing pools (Przekwas and Somayaji, 2020).

The PK transport model of the MPS platform can be described by ordinary differential equations just like the simple one-compartment model (Jones and Rowland-Yeo, 2013). Only a few ordinary differential equations are used to describe it. **Figure 7** presents the description of the transport model of MIT's gut-liver MPS platform (Kasendra et al., 2018).

Species mass balance equations in each organ: Gut apical (lumen-enterocytes):

$$V_{Ga}\frac{dC_{Ga}}{dt} = P_G A_G (C_{Gb} - C_{Ga}) - CL_G C_{Ga}$$

Gut basolateral (blood):

$$V_{Ga}\frac{dC_{Gb}}{dt} = Q_{Gb}(C_{mix} - C_{Gb})A_G (G_{Gb} - C_{Ga})$$

Liver:

$$V_L\frac{dC_L}{dt} = Q_{Gb}(G_{Gb} + C_L) + Q_L (G_{mix} - C_L) - CL_L C_L$$

Mixer:

$$V_{mix}\frac{dC_{mix}}{dt} = (Q_{Gb} + G_L)(C_L - C_{mix})$$

C_{Ga}, C_{Gb}, C_L, and C_{mix} are drug concentrations in individual organs, and V_{Ga}, V_{Gb}, V_L, and V_{mix} are the volumes of each organs. AG is the gut barrier exchange area, PG is the gut barrier effective permeability, and CL_G and CL_L are intrinsic drug clearance rates for the gut and liver. Q is the flow rates, which is determined by the total outflow from the mixer.

3.4.2 *In vitro* to *In vivo* Extrapolation Process

The purpose of building the PBPK model based on the OOC device is to convert drug data from *in vitro* experiments to organ-level data, which is the IVIVE process. Existing method requires us to know the scaling factor when estimating the organ-level data using *in vitro* PK results from static cell culture experiments. Scaling factor is the ratio from vitro experiments data to the organ-level data. But this method has defects such as: 1) Absence of *in vivo* aspects of fluid flow and mechanical cues. 2) No multiscale architecture at the biological interfaces, which is essential to emulating certain organ-level functions. The OoC or HoC devices is an ideal alternative.

Some researchers mentioned some future directions: according to the specific drug properties for a given HoC configuration and design to get the scaling factors, such as the vitro system, medium type, cell properties, cell culture conditions, and drug properties (Prantil-Baun et al., 2018).

3.4.3 Drug-Drug Interactions

Organs-on-a-chip technology has been used in the construction of PBPK models in drug development. A team from Tokai University in Japan introduced a study using organs-on-a-chip technology and PKPD models to evaluate drug-drug interactions (DDI) in 2019 (Shinha et al., 2020) as shown in **Figure 8**.

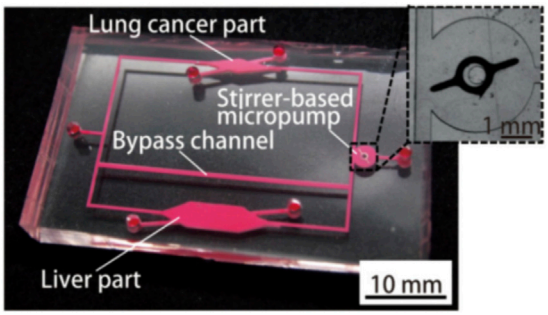

FIGURE 8 | Photograph of the fabricated organs-on-chips with a liver part, a lung cancer part, and other parts connected by micro-channels (Shinha et al., 2020).

Shinha et al. (2020) established a PK-PD model to predict the efficacy of the drug. The change in metabolite concentration can be expressed as:

$$C_M[t] = \frac{E_p \times f_m \times X_\circ}{E_p - E_M} \times \left(e^{-\frac{Q \times E_{M_L}}{V_d}\times} - e^{-\frac{Q \times E_{P_L}}{V_d}\times}\right)$$

The drug efficacy is expressed as:

$$\frac{Celldensity}{Controlcelldensity} = -0.086 \times ln\left(\int_t^0 CM[t]\right) + 0.052$$

where: CL: the clearance in the liver part, V_d: the distribution volume, Q: the flow rate in the liver part, E: the extraction ratio in the liver part, fm: the fraction metabolized (he metabolized rate by each metabolic enzyme). The numerical parameters, V_d, Q, and X0 were determined from the MOoC design and the experimental conditions.

The cells were exposed to CPT-11 dissolved in the culture medium, which was exchanged every 24 h. After exposure for 72 h, the cells were stained and observed using camera installed with a fluorescence microscope. The extraction ratios in the liver part of CPT-11(Irinotecan Hydrochloride Trihydrate) and SN-38 (7-Ethyl-10-hydroxycamptothecin) in the multiple-organs-on-chips (MOoCs) were estimated from the experimental results using the MOoCs with and without bypass channels and our PK-PD model.

For the evaluation of the DDI, they used CPT-11 and simvastatin (SV) or Ritonavir (RTV) for MOoC at the same time, and observed the changes cell densities on the OoC. The effects of DDI were evaluated by comparing the predicted cell density of the PK-PD model with that of the experimental results.

After analyzing the experimental results and the predicted value of the PKPD model, the researchers found that the DDI of inhibitor chemicals were quite similar to the results of previous studies, they used OoC to evaluate the effect of metabolites from experimental results, and estimate drug-specific parameters by combining PKPD and OoC. Their final conclusion is that the DDI evaluation using the PKPD model and OoC is useful.

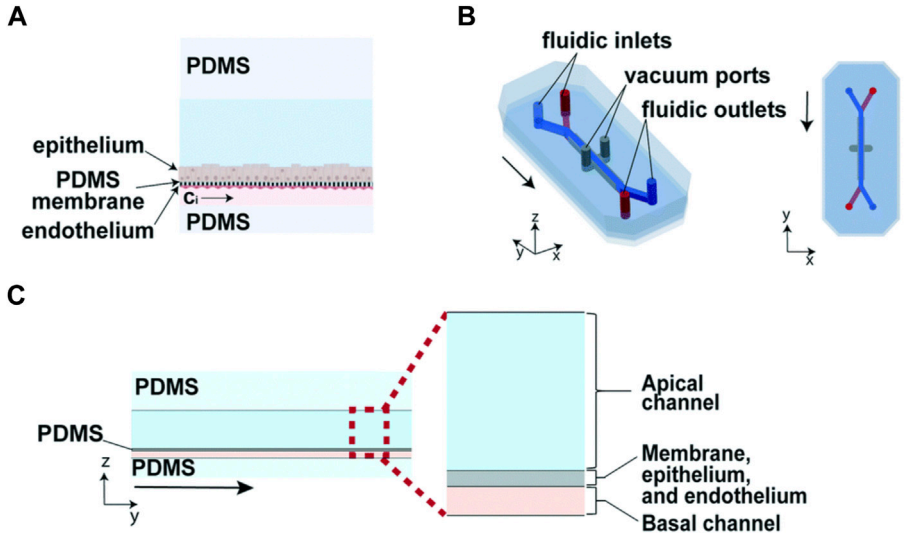

FIGURE 9 | Design of a two-channel human lung airway organ chip. **(A)** reconstruction of the porous PDMS film; **(B)** the illustration of the lung airway organ chip; **(C)** the side view of the construction of organ chip (Grant et al., 2021).

3.4.4 Recent Advances in Physiologically Based Pharmacokinetic Modeling Enabled by Organs-on-Chips

As previously mentioned, PDMS is currently the mainstream material used in the fabrication of OoCs. However, its absorption of hydrophobic small molecules remains as a problem and should be resolved before PDMS-made OoC can be put into the practice of drug experiment. Ingber (Grant et al., 2021) proposed a method that combines experiment and simulation to predict the concentration of drugs in OoCs made of PDMS materials.

As shown in **Figure 9**, the organ chip used is a commercially available PDMS microfluidic culture device, which contains two parallel fluid channels separated by a porous PDMS film.

It is assumed that the drug must be first adsorbed to the wall before it enters into the bulk PDMS. The process of the absorption of a drug from the cell culture medium onto the PDMS wall can be described by the partition coefficient (i.e., P):

$$P = \frac{C_{pdms}}{C_{med}}$$

Where C_{pdms} is the drug concentration in PDMS and C_{med} is the drug concentration in cell culture medium. After the drug is adsorbed to the PDMS wall, it diffuses into the bulk PDMS according to Fick's second law:

$$\rho \frac{\partial c_{med}}{\partial t} - \nabla \left(D_{med} \nabla c_{med} \right) + u \nabla c_{med} = 0$$

$$\rho \frac{\partial c_{pdms}}{\partial t} - \nabla \left(D_{pdms} \nabla c_{pdms} \right) = 0$$

Where D_{med} is the diffusivity of drug in cell culture medium, D_{pdms} is the diffusivity of drug in PDMS.Since D_{pdms} is not easy to measure, an experimental method for the measure of D_{pdms} is proposed.

The drug intended to investigate is amodiaquine, and fluorescein isothiocyanate (FITC) was used as a surrogate compound to amodiaquine because it is similar in molecular weight, structure, and hydrophobicity. In the designed experiment, FITC is absorbed into the bulk PDMS, and fluorescence microscope can be used for quantitative and spatial analysis. The estimated value of D_{pdms} can be obtained by fitting the analytical solution of Fick second law with experimental data. After obtaining the estimated value of D_{pdms}, the estimated value of P can be obtained by fitting experimental data and simulation results. All the parameters needed in the simulation are obtained.

As is shown in **Figure 10**, subsequent simulations revealed the influence of factors such as drug delivery speed on drug concentration, and a more realistic drug concentration curve was obtained. In short, this article describes a strategy that combines experiment and computational method to simulate the spatial and temporal gradients of drugs without obtaining the distribution coefficient of drugs in PDMS in advance.

4 DISCUSSION AND FUTURE PERSPECTIVES

Physiologically based pharmacokinetic (PBPK) model constructs the mathematical models to study pharmacokinetic (PK) behaviors following compartmental modeling approach with relevant human physiology considered. It provided a great way to predict the ADME (absorption, distribution, metabolism and excretion) process of drugs. Organ-on-a-chip, as an emerging technology aimed to simulate the organ structure and function *in vitro*. The combination of the organ-on-a-chip technology and PBPK PD model provides a new tool in new drug development, personalized medicine and other fields.

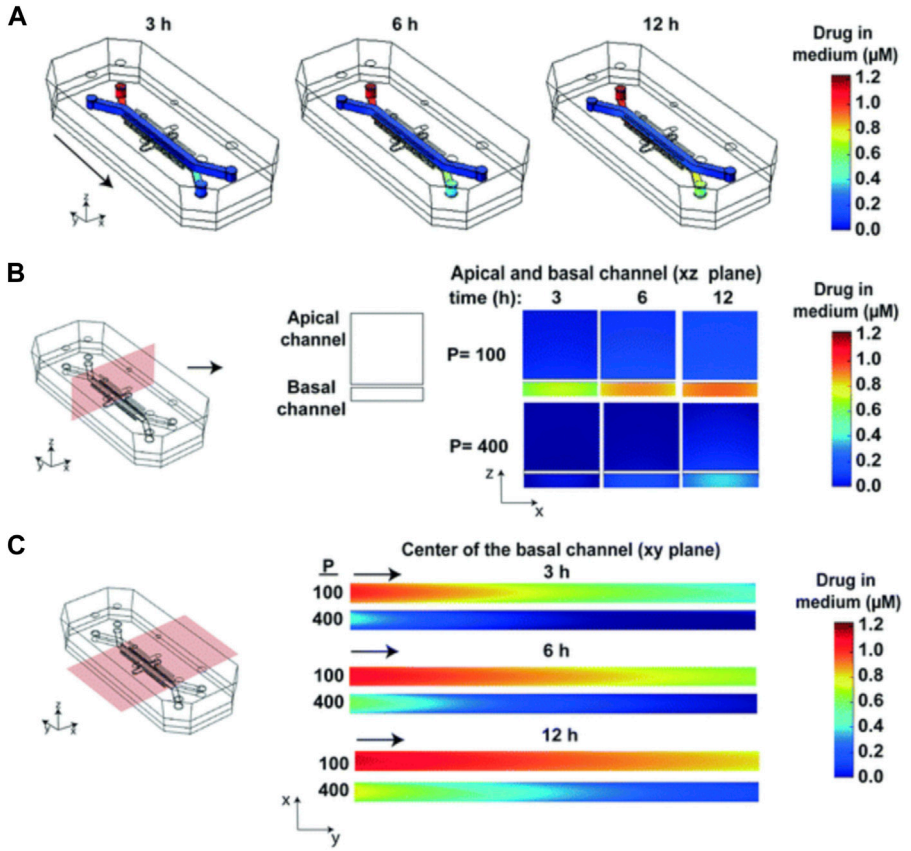

FIGURE 10 | Heat maps of the drug concentration. **(A)** 3D surface heat maps of the concentration of drug in the fluidic channels of the human lung airway chip at 3, 6, and 12 h; **(B)** 2D heat maps of drug concentration through a vertical cross section in the center of the chip; **(C)** 2D heat maps of drug concentration through a horizontal cross section in the center of the basal channel (Grant et al., 2021).

4.1 Considerable Progress of Physiologically Based Pharmacokinetic Modeling on Organ-on-a-Chips

The application of PBPK model in OoC is still an emerging research area while a few works that combine PK model with OoC for drug development have been reported. In 2017, Tsamandouras et al. first introduced a MOoCs system including gut-on-a-chip and liver-on–a-chip described by the PK model, and used this system to study the mechanism of drug transport (Tsamandouras et al., 2017). *In vitro* to *in vivo* extrapolation (IVIVE) of these results are also provided. This work reveals the bright prospects of the combination of the PK model with OoC in drug development. Shinha et al. used the MOoCs system described by the PBPK model to study the inhibitory effect of simvastatin and ritonavir on the metabolism of CPT-11, thereby demonstrating that the combination of PK model and OoC can be used for drug-drug interaction (DDI) prediction (Shinha et al., 2020). Works including the above studies demonstrate the potentially great application prospects of PBPK modeling on OoC.

The ultimate goal of *in vitro* PBPK/PKPD research with OoC is to establish complementary experimental and computational tools that can translate *in vitro* data to the *in vivo* situation (Przekwas and Somayaji, 2020). However, the differences between abstraction and real situation make it difficult to mimic *in vivo* physiological functions and pharmacological responses (Wikswo et al., 2013a). As two key parts of *in vitro* PK-PD modeling, much efforts should be made on improving the OoC technologies and computational models to move forward, and considerable progress has been achieved.

4.2 Current Limitations and Future Improvements

On the OoC side, firstly, due to availability of data on allometric ratios and its simplicity in terms of implementation, allometric scaling has been the most commonly used method. But some researchers have found it difficult in sustaining the allometric ratios upon scale-down (Wikswo et al., 2013b). One example is that some drugs first metabolized by the liver to their active compounds. Under this circumstance, the other organs could not be exposed to realistic levels unless the liver-on-a-chip could provide a physiological conversion of the drug. Likewise, in order to make paracrine signaling between organs replicable, the cytokines produced by each organ should be present in the

blood at physiological concentrations. An alternative is scaling organ-on-chips considering the amount of time that each organ is exposed to a molecule (a.k.a. residence time) (van Midwoud et al., 2010). Considering the extent of reaction in the tissue, residence time-based scaling which is based on the degree of chemical conversion has a great advantage over allometric scaling and may better replicate organ–organ interactions.

Secondly, the current organ-on-a-chip platforms are predominately made of by polydimethylsiloxane (PDMS), which has been proved to be attributable for adsorption of biomolecules (Abaci and Shuler, 2015). With growing effort to address this problem, there are now several encouraging solutions available, including modification of the surface chemistry of PDMS to prevent adsorption, using alternative materials (e.g., polystyrene) to PDMS or adjust the computational model for compensation (Prantil-Baun et al., 2018).

On the computational model side, considering the dynamic process of ADME, microfluidic OoC devices require spatially distributed models that account for convection, diffusion, barrier transport, and reaction phenomena, while the conventional *in vitro* static cell cultures could be represented by simple one compartment well-stirred mathematical models (Przekwas and Somayaji, 2020). So in an attempt to achieve more precise simulation, novel mathematical formulation and multiscale models are necessary.

Owning to the complicated nature of the physiological system, current mathematical models of micro- physiological systems (MPS) use the simplified ordinary differential equation based models. Other than individual OoC models, mathematical modeling of MOoC also involves models of various peripheral devices such as tubing, mixers, and reservoirs. Similar to PBPK, simulation of a multi-organ closed-loop MPS involves the "arterial" medium distribution to "venous" medium, and collection from individual organs (Przekwas and Somayaji, 2020). Furthermore, the reservoir model should account for total medium volume dynamics, sampling, fresh medium resupply, and the *in vitro* "intravenous" drug administration. In contrast, current MPS combine both medium pools into a single "mixer" (Przekwas and Somayaji, 2020).

PBPK modeling on OoC has shown great application prospects and is expected to revolutionize the field of drug development and personalized medicine. In China, some start-ups are trying to combine PBPK modeling with OoC to reduce the time cost and opportunity cost of new drug development, and have achieved initial success.

PBPK modeling on OoC provided great experimental and computational tools to understand the ADME process of drugs *in vitro*. There is no doubt that relevant studies would make significant advance in our understanding therapeutic effects of drugs on human pathophysiology. Considerable progress has been made in the field of preclinical trial and personalized medicine based on PBPK/PD modeling and OoC technology. However, much are needed to be done to guarantee the IVIVE process of the fruitful results. Then PBPK modeling on OoC would become an essential part of new drug development.

AUTHOR CONTRIBUTIONS

ZC, LW, XG, and ZG contributed to conception and design of the review, YY, YC, LW, and ZC wrote the manuscript. LW and XG revised the manuscript.

FUNDING

This study was supported by the National Key R&D Program of China (No. 2017YFA0700500), Experiment Project of China Manned Space Program No. HYZHXM01019, and the Fundamental Research Funds for the Central Universities from Southeast University: No. 3207032101C3.

REFERENCES

Abaci, H. E., and Shuler, M. L. (2015). Human-on-a-chip Design Strategies and Principles for Physiologically Based Pharmacokinetics/pharmacodynamics Modeling. *Integr. Biol.* 7, 383–391. doi:10.1039/c4ib00292j

Abadpour, S., Aizenshtadt, A., Olsen, P. A., Shoji, K., Wilson, S. R., Krauss, S., et al. (2020). Pancreas-on-a-Chip Technology for Transplantation Applications. *Curr. Diab Rep.* 20, 72–13. doi:10.1007/s11892-020-01357-1

Alford, P. W., Feinberg, A. W., Sheehy, S. P., and Parker, K. K. (2010). Biohybrid Thin Films for Measuring Contractility in Engineered Cardiovascular Muscle. *Biomaterials* 31, 3613–3621. doi:10.1016/j.biomaterials.2010.01.079

An, F., Qu, Y., Liu, X., Zhong, R., and Luo, Y. (2015). Organ-on-a-chip: New Platform for Biological Analysis. *Anal. Chem. Insights* 10, 39–45. doi:10.4137/ACI.S28905

Aungst, B. J. (2017). Optimizing Oral Bioavailability in Drug Discovery: an Overview of Design and Testing Strategies and Formulation Options. *J. Pharm. Sci.* 106, 921–929. doi:10.1016/j.xphs.2016.12.002

Benet, L. Z. (1984). Pharmacokinetic Parameters: Which Are Necessary to Define a Drug Substance? *Eur. J. Respir. Dis. Suppl.* 134, 45–61.

Brodie, B. B., Kurz, H., and Schanker, L. S. (1960). The Importance of Dissociaton Constant and Lipid-Solubility in Influencing the Passage of Drugs into the Cerebrospinal Fluid. *J. Pharmacol. Exp. Ther.* 130, 20–25.

Chen, Z., Ma, N., Sun, X., Li, Q., Zeng, Y., Chen, F., et al. (2021). Automated Evaluation of Tumor Spheroid Behavior in 3d Culture Using Deep Learning-Based Recognition. *Biomaterials* 272, 120770. doi:10.1016/j.biomaterials.2021.120770

Chen, Z., Tang, M., Huang, D., Jiang, W., Li, M., Ji, H., et al. (2018). Real-time Observation of Leukocyte-Endothelium Interactions in Tissue-Engineered Blood Vessel. *Lab. Chip* 18, 2047–2054. doi:10.1039/c8lc00202a

Díaz, L., Zambrano-González, E., Flores, M. E., Contreras, M., Crispín, J. C., Alemán, G., et al. (2021). Ethical Considerations in Animal Research: The Principle of 3R's. *Ric* 73, 199–209. doi:10.24875/ric.20000380

Edington, C. D., Chen, W. L. K., Geishecker, E., Kassis, T., Soenksen, L. R., Bhushan, B. M., et al. (2018). Interconnected Microphysiological Systems for Quantitative Biology and Pharmacology Studies. *Sci. Rep.* 8, 1–18. doi:10.1038/s41598-018-22749-0

Ewald, M. L., Chen, Y.-H., Lee, A. P., and Hughes, C. C. W. (2021). Correction: The Vascular Niche in Next Generation Microphysiological Systems. *Lab. Chip* 21, 3615–3616. doi:10.1039/d1lc90093e

Fernandes, M. R., and Pedroso, A. R. (2017). Animal Experimentation: A Look into Ethics, Welfare and Alternative Methods. *Rev. Assoc. Med. Bras.* 63, 923–928. doi:10.1590/1806-9282.63.11.923

Gabriel, L. P., Rodrigues, A. A., Macedo, M., Jardini, A. L., and Maciel Filho, R. (2017). Electrospun Polyurethane Membranes for Tissue Engineering Applications. *Mater. Sci. Eng. C* 72, 113–117. doi:10.1016/j.msec.2016.11.057

Grant, J., Özkan, A., Oh, C., Mahajan, G., Prantil-Baun, R., and Ingber, D. E. (2021). Simulating Drug Concentrations in Pdms Microfluidic Organ Chips. *Lab. Chip* 21, 3509–3519. doi:10.1039/d1lc00348h

Grosberg, A., Alford, P. W., Mccain, M. L., and Parker, K. K. (2011). Ensembles of Engineered Cardiac Tissues for Physiological and Pharmacological Study: Heart on a Chip. *Lab. Chip* 11, 4165–4173. doi:10.1039/C1LC20557A

Heringa, M., Park, M. V., Kienhuis, A. S., and Vandebriel, R. J. (2020). The Value of Organs-On-Chip for Regulatory Safety Assessment. *Altex* 37, 208–222. doi:10.14573/altex.1910111

Hou, Y., Ai, X., Zhao, L., Gao, Z., Wang, Y., Lu, Y., et al. (2020). An Integrated Biomimetic Array Chip for High-Throughput Co-culture of Liver and Tumor Microtissues for Advanced Anticancer Bioactivity Screening. *Lab. Chip* 20 (14), 2482–2494. doi:10.1039/d0lc00288g

Ji, H., Atchison, L., Chen, Z., Chakraborty, S., Jung, Y., Truskey, G. A., et al. (2016). Transdifferentiation of Human Endothelial Progenitors into Smooth Muscle Cells. *Biomaterials* 85, 180–194. doi:10.1016/j.biomaterials.2016.01.066

Jiang, W., Li, M., Chen, Z., and Leong, K. W. (2016). Cell-laden Microfluidic Microgels for Tissue Regeneration. *Lab. Chip* 16, 4482–4506. doi:10.1039/C6LC01193D

Jones, H., and Rowland-Yeo, K. (2013). Basic Concepts in Physiologically Based Pharmacokinetic Modeling in Drug Discovery and Development. *CPT Pharmacometrics Syst. Pharmacol.* 2, e63–12. doi:10.1038/psp.2013.41

Jung, Y., Ji, H., Chen, Z., Fai Chan, H., Atchison, L., Klitzman, B., et al. (2015). Scaffold-Free, Human Mesenchymal Stem Cell-Based Tissue Engineered Blood Vessels. *Sci. Rep.* 5, 1–9. doi:10.1038/srep151

Kasendra, M., Tovaglieri, A., Sontheimer-Phelps, A., Jalili-Firoozinezhad, S., Bein, A., Chalkiadaki, A., et al. (2018). Development of a Primary Human Small Intestine-On-A-Chip Using Biopsy-Derived Organoids. *Sci. Rep.* 8, 1–14. doi:10.1038/s41598-018-21201-7

Kuepfer, L., Niederalt, C., Wendl, T., Schlender, J. F., Willmann, S., Lippert, J., et al. (2016). Applied Concepts in Pbpk Modeling: How to Build a Pbpk/pd Model. *CPT Pharmacometrics Syst. Pharmacol.* 5, 516–531. doi:10.1002/psp4.12134

Lee, H., Chae, S., Kim, J. Y., Han, W., Kim, J., Choi, Y., et al. (2019). Cell-printed 3d Liver-On-A-Chip Possessing a Liver Microenvironment and Biliary System. *Biofabrication* 11, 025001. doi:10.1088/1758-5090/aaf9fa

Lee, J. H., Chen, Z., He, S., Zhou, J. K., Tsai, A., Truskey, G. A., et al. (2021). Emulating Early Atherosclerosis in a Vascular Microphysiological System Using Branched Tissue-Engineered Blood Vessels. *Adv. Biol.* 5, 2000428. doi:10.1002/adbi.202000428

Ma, L.-D., Wang, Y.-T., Wang, J.-R., Wu, J.-L., Meng, X.-S., Hu, P., et al. (2018). Design and Fabrication of a Liver-On-A-Chip Platform for Convenient, Highly Efficient, and Safe *In Situ* Perfusion Culture of 3d Hepatic Spheroids. *Lab. Chip* 18, 2547–2562. doi:10.1039/C8LC00333E

Maschmeyer, I., Lorenz, A. K., Schimek, K., Hasenberg, T., Ramme, A. P., Hübner, J., et al. (2015). A Four-Organ-Chip for Interconnected Long-Term Co-culture of Human Intestine, Liver, Skin and Kidney Equivalents. *Lab. Chip* 15, 2688–2699. doi:10.1039/C5LC00392J

Mccuskey, R. S. (2008). The Hepatic Microvascular System in Health and its Response to Toxicants. *Anat. Rec.* 291, 661–671. doi:10.1002/ar.20663

Mehling, M., and Tay, S. (2014). Microfluidic Cell Culture. *Curr. Opin. Biotechnol.* 25, 95–102. doi:10.1016/j.copbio.2013.10.005

Oleaga, C., Bernabini, C., Smith, A. S. T., Srinivasan, B., Jackson, M., McLamb, W., et al. (2016). Multi-Organ Toxicity Demonstration in a Functional Human *In Vitro* System Composed of Four Organs. *Sci. Rep.* 6, 1–17. doi:10.1038/srep20030

Osaki, T., Sivathanu, V., and Kamm, R. D. (2018). Vascularized Microfluidic Organ-Chips for Drug Screening, Disease Models and Tissue Engineering. *Curr. Opin. Biotechnol.* 52, 116–123. doi:10.1016/j.copbio.2018.03.011

Osório, L. A., Silva, E., and Mackay, R. E. (2021). A Review of Biomaterials and Scaffold Fabrication for Organ-On-A-Chip (Ooac) Systems. *Bioengineering* 8, 113. doi:10.3390/bioengineering8080113

Paalzow, L. K. (1995). Torsten Teorell, the Father of Pharmacokinetics. *Upsala J. Med. Sci.* 100 (1), 41–46. doi:10.3109/03009739509178895

Palaninathan, V., Kumar, V., Maekawa, T., Liepmann, D., Paulmurugan, R., Eswara, J. R., et al. (2018). Multi-organ on a Chip for Personalized Precision Medicine. *MRS Commun.* 8, 652–667. doi:10.1557/mrc.2018.148

Park, S. E., Georgescu, A., and Huh, D. (2019). Organoids-on-a-chip. *Science* 364 (6444), 960–965. doi:10.1126/science.aaw7894

Prantil-Baun, R., Novak, R., Das, D., Somayaji, M. R., Przekwas, A., and Ingber, D. E. (2018). Physiologically Based Pharmacokinetic and Pharmacodynamic Analysis Enabled by Microfluidically Linked Organs-On-Chips. *Annu. Rev. Pharmacol. Toxicol.* 58, 37–64. doi:10.1146/annurev-pharmtox-010716-104748

Przekwas, A., and Somayaji, M. R. (2020). Computational Pharmacokinetic Modeling of Organ-On-Chip Devices and Microphysiological Systems. *Organ-on-a-chip*, 311–361. doi:10.1016/b978-0-12-817202-5.00011-5

Riahi, R., Shaegh, S. A. M., Ghaderi, M., Zhang, Y. S., Shin, S. R., Aleman, J., et al. (2016). Automated Microfluidic Platform of Bead-Based Electrochemical Immunosensor Integrated with Bioreactor for Continual Monitoring of Cell Secreted Biomarkers. *Sci. Rep.* 6, 1–14. doi:10.1038/srep24598

Rogal, J., Probst, C., and Loskill, P. (2017). Integration Concepts for Multi-Organ Chips: How to Maintain Flexibility?!. *Future Sci. OA* 3, FSO180. doi:10.4155/fsoa-2016-0092

Rollas, S. (2008). "Adme and Biopharmaceutical Properties," in *Preclinical Development Handbook*. Editor S. C. Gad (Hoboken, New Jersey, United States: Wiley).

Rowland, M., Peck, C., and Tucker, G. (2011). Physiologically-based Pharmacokinetics in Drug Development and Regulatory Science. *Annu. Rev. Pharmacol. Toxicol.* 51, 45–73. doi:10.1146/annurev-pharmtox-010510-100540

Rowland, M., and Tozer, T. N. (2005). *Clinical Pharmacokinetics/pharmacodynamics*. Gainesville, Philadelphia: Lippincott Williams and Wilkins.

Sager, J. E., Yu, J., Ragueneau-Majlessi, I., and Isoherranen, N. (2015). Physiologically Based Pharmacokinetic (Pbpk) Modeling and Simulation Approaches: a Systematic Review of Published Models, Applications, and Model Verification. *Drug Metab. Dispos* 43, 1823–1837. doi:10.1124/dmd.115.065920

Shik Mun, K., Arora, K., Huang, Y., Yang, F., Yarlagadda, S., Ramananda, Y., et al. (2019). Patient-derived Pancreas-On-A-Chip to Model Cystic Fibrosis-Related Disorders. *Nat. Commun.* 10, 1–12. doi:10.1038/s41467-019-11178-w

Shim, K. Y., Lee, D., Han, J., Nguyen, N. T., Park, S., and Sung, J. H. (2017). Microfluidic Gut-On-A-Chip with Three-Dimensional Villi Structure. *Biomed. Microdevices* 19, 37–10. doi:10.1007/s10544-017-0179-y

Shinha, K., Nihei, W., Ono, T., Nakazato, R., and Kimura, H. (2020). A Pharmacokinetic– Pharmacodynamic Model Based on Multi-Organ-On-A-Chip for Drug–Drug Interaction Studies. *Biomicrofluidics* 14, 044108. doi:10.1063/5.0011545

Skardal, A., Murphy, S. V., Devarasetty, M., Mead, I., Kang, H.-W., Seol, Y.-J., et al. (2017). Multi-tissue Interactions in an Integrated Three-Tissue Organ-On-A-Chip Platform. *Sci. Rep.* 7, 1–16. doi:10.1038/s41598-017-08879-x

Stahl, W. R. (1965). Organ Weights in Primates and Other Mammals. *Science* 150, 1039–1042. doi:10.1126/science.150.3699.1039

Tsamandouras, N., Chen, W. L. K., Edington, C. D., Stokes, C. L., Griffith, L. G., and Cirit, M. (2017). Integrated Gut and Liver Microphysiological Systems for Quantitative *In Vitro* Pharmacokinetic Studies. *Aaps J.* 19, 1499–1512. doi:10.1208/s12248-017-0122-4

Urso, R., Blardi, P., and Giorgi, G. (2002). A Short Introduction to Pharmacokinetics. *Eur. Rev. Med. Pharmacol. Sci.* 6, 33–44.

van Midwoud, P. M., Merema, M. T., Verpoorte, E., and Groothuis, G. M. M. (2010). A Microfluidic Approach for *In Vitro* Assessment of Interorgan Interactions in Drug Metabolism Using Intestinal and Liver Slices. *Lab. Chip* 10, 2778–2786. doi:10.1039/C0LC00043D

Widmark, E., and Tandberg, J. (1924). Uber die bedingungen Fur die akkumulation indifferenter narkoliken theoretische bereckerunger. *Biochem. Z.* 147, 358–369.

Wikswo, J. P., Block, F. E., III, Cliffel, D. E., Goodwin, C. R., Marasco, C. C., Markov, D. A., et al. (2013a). Engineering Challenges for Instrumenting and Controlling Integrated Organ-On-Chip Systems. *IEEE Trans. Biomed. Eng.* 60, 682–690. doi:10.1109/TBME.2013.2244891

Wikswo, J. P., Curtis, E. L., Eagleton, Z. E., Evans, B. C., Kole, A., Hofmeister, L. H., et al. (2013b). Scaling and Systems Biology for Integrating Multiple Organs-On-A-Chip. *Lab. Chip* 13, 3496–3511. doi:10.1039/C3LC50243K

Xiao, R. R., Lv, T., Tu, X., Li, P., Wang, T., Dong, H., et al. (2021). An Integrated Biomimetic Array Chip for Establishment of Collagen-based 3D Primary Human Hepatocyte Model for Prediction of Clinical Drug-induced Liver Injury. *Biotechnol. Bioeng.* 118, 4687–4698. doi:10.1002/bit.27931

Yamaoka, K., Nakagawa, T., and Uno, T. (1978). Statistical Moments in Pharmacokinetics. *J. Pharmacokinet. biopharmaceutics* 6, 547–558. doi:10.1007/BF01062109

Yang, S., Chen, Z., Cheng, Y., Liu, T., Lihong Yin, L., Pu, Y., et al. (2021). Environmental Toxicology Wars: Organ-On-A-Chip for Assessing the Toxicity of Environmental Pollutants. *Environ. Pollut.* 268, 115861. doi:10.1016/j.envpol.2020.115861

Yum, K., Hong, S. G., Healy, K. E., and Lee, L. P. (2014). Physiologically Relevant Organs on Chips. *Biotechnol. J.* 9, 16–27. doi:10.1002/biot.201300187

Zhang, J., Chen, Z., Zhang, Y., Wang, X., Ouyang, J., Zhu, J., et al. (2021). Construction of a High Fidelity Epidermis-On-A-Chip for Scalable *In Vitro* Irritation Evaluation. *Lab. Chip* 21, 3804–3818. doi:10.1039/D1LC00099C

Zhang, Y. S., Arneri, A., Bersini, S., Shin, S.-R., Zhu, K., Goli-Malekabadi, Z., et al. (2016). Bioprinting 3d Microfibrous Scaffolds for Engineering Endothelialized Myocardium and Heart-On-A-Chip. *Biomaterials* 110, 45–59. doi:10.1016/j.biomaterials.2016.09.003

Zhao, Y., Kankala, R., Wang, S.-B., and Chen, A.-Z. (2019). Multi-organs-on-chips: towards Long-Term Biomedical Investigations. *Molecules* 24, 675. doi:10.3390/molecules24040675

Conflict of Interest: The authors declare that the research was conducted in the absence of any commercial or financial relationships that could be construed as a potential conflict of interest.

Publisher's Note: All claims expressed in this article are solely those of the authors and do not necessarily represent those of their affiliated organizations, or those of the publisher, the editors and the reviewers. Any product that may be evaluated in this article, or claim that may be made by its manufacturer, is not guaranteed or endorsed by the publisher.

frontiers | Frontiers in Bioengineering and Biotechnology

ORIGINAL RESEARCH
published: 20 April 2022
doi: 10.3389/fbioe.2022.876237

Tetrandrine Prevents Neomycin-Induced Ototoxicity by Promoting Steroid Biosynthesis

Qilei Zhang[1†], Yunhao Wu[2†], Yan Yu[1†], Yuguang Niu[3†], Qiaojun Fang[2], Xin Chen[2], Jieyu Qi[2], Chen Zhang[4], Geping Wu[1*], Kaiming Su[5*] and Renjie Chai[2,6,7,8,9*]*

[1]The Affiliated Zhangjiagang Hospital of Soochow University, Zhangjiagang, China, [2]State Key Laboratory of Bioelectronics, Department of Otolaryngology Head and Neck Surgery, Zhongda Hospital, School of Life Sciences and Technology, Advanced Institute for Life and Health, Jiangsu Province High-Tech Key Laboratory for Bio-Medical Research, Southeast University, Nanjing, China, [3]Department of Ambulatory Medicine, the First Medical Center of PLA General Hospital, Beijing, China, [4]Department of Neurobiology, School of Basic Medical Sciences, Beijing Key Laboratory of Neural Regeneration and Repair, Advanced Innovation Center for Human Brain Protection, Capital Medical University, Beijing, China, [5]Department of Otolaryngology-Head and Neck Surgery, Shanghai Jiao Tong University Affiliated Sixth People's Hospital, Shanghai, China, [6]Department of Otolaryngology Head and Neck Surgery, Sichuan Provincial People's Hospital, University of Electronic Science and Technology of China, Chengdu, China, [7]Co-Innovation Center of Neuroregeneration, Nantong University, Nantong, China, [8]Institute for Stem Cell and Regeneration, Chinese Academy of Science, Beijing, China, [9]Beijing Key Laboratory of Neural Regeneration and Repair, Capital Medical University, Beijing, China

Aminoglycoside antibiotics are widely used for the treatment of serious acute infections, life-threatening sepsis, and *tuberculosis*, but all aminoglycosides cause side effects, especially irreversible ototoxicity. The mechanisms underlying the ototoxicity of aminoglycosides need further investigation, and there are no effective drugs in the clinic. Here we showed that tetrandrine (TET), a bioactive bisbenzylisoquinoline alkaloid derived from *Stephania tetrandra*, ameliorated neomycin-induced cochlear hair cell injury. In both *in vitro* and *in vivo* experiments we found that TET administration significantly improved auditory function and reduced hair cell damage after neomycin exposure. In addition, we observed that TET could significantly decrease oxidative stress and apoptosis in hair cells after neomycin exposure. Finally, RNA-seq analysis suggested that TET protected against neomycin-induced ototoxicity mainly by promoting steroid biosynthesis. Collectively, our results provide pharmacological evidence showing that TET may be a promising agent in preventing aminoglycosides-induced ototoxicity.

Keywords: tetrandrine, hair cell, apoptosis, oxidative stress, steroid biosynthesis

OPEN ACCESS

Edited by:
Mingqiang Li,
Third Affiliated Hospital of Sun Yat-sen University, China

Reviewed by:
Xiaojun Xu,
China Pharmaceutical University, China
Fang Zhou,
China Pharmaceutical University, China
Shaojun Peng,
Zhuhai People's Hospital, China

***Correspondence:**
Yunhao Wu
yunhaowu0730@outlook.com
Geping Wu
gordon-wu@qq.com
Kaiming Su
021china@sina.com
Renjie Chai
renjiec@seu.edu.cn

[†]*These authors have contributed equally to this work*

Specialty section:
This article was submitted to Biomaterials, a section of the journal Frontiers in Bioengineering and Biotechnology

Received: *15 February 2022*
Accepted: *18 March 2022*
Published: *20 April 2022*

Citation:
Zhang Q, Wu Y, Yu Y, Niu Y, Fang Q, Chen X, Qi J, Zhang C, Wu G, Su K and Chai R (2022) Tetrandrine Prevents Neomycin-Induced Ototoxicity by Promoting Steroid Biosynthesis. Front. Bioeng. Biotechnol. 10:876237. doi: 10.3389/fbioe.2022.876237

INTRODUCTION

Sensorineural hearing loss (SHL), results from degeneration of the sensory hair cells in the organ of Corti, and the loss of the ability to communicate with others severely impacts people's quality of life. Aminoglycoside antibiotics, the most commonly used ototoxic drugs, are one of the leading contributors to SHL (O'Sullivan et al., 2017). Despite this, aminoglycosides are still widely used in the treatment of many diseases due to their special antibacterial activities and physicochemical properties. It is therefore of great clinical significance to explore the molecular mechanisms through which aminoglycosides damage cochlear hair cells and to develop therapeutic drugs for preventing SHL.

Recently, several active ingredients derived from traditional Chinese medicine have shown promising otoprotective effects against SHL and tinnitus (Zhai et al., 2013; Fetoni et al., 2015; Li

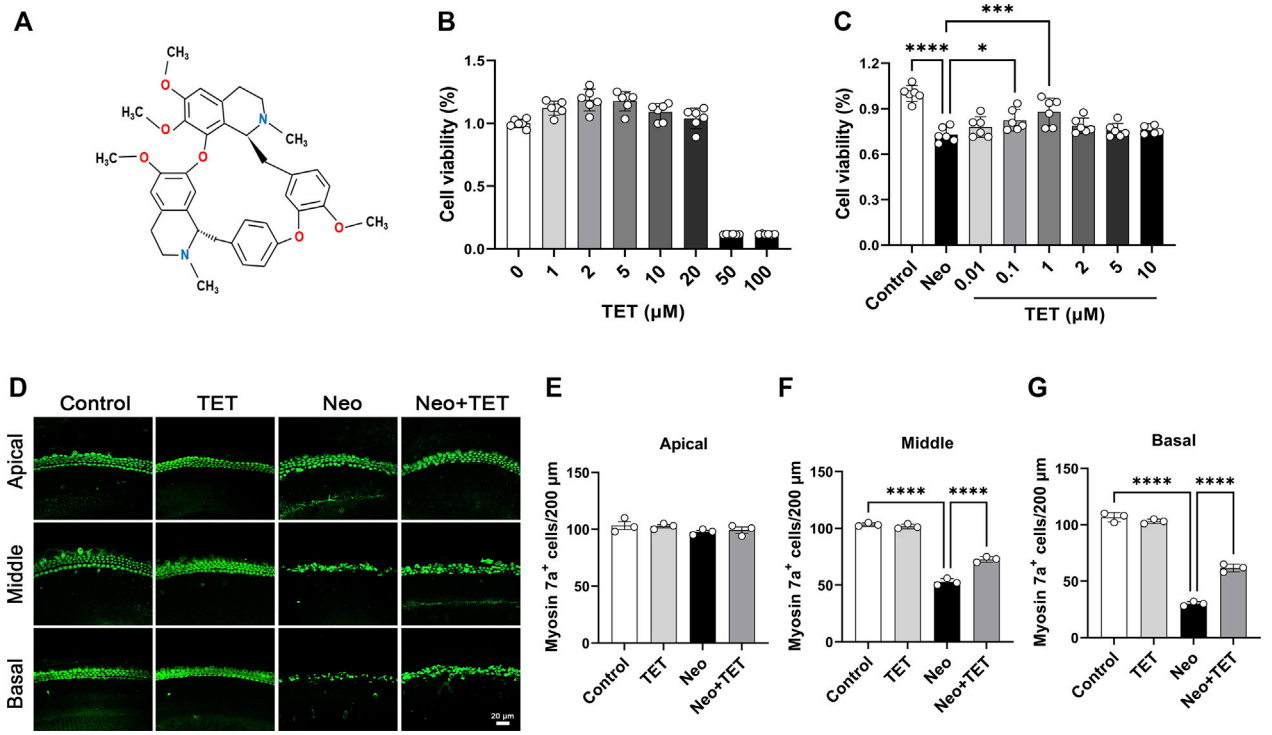

FIGURE 1 | TET increases HEI-OC1 cell viability and promotes cochlear hair cell survival after neomycin exposure **(A)** Structure of TET **(B)** The toxicity of TET at different doses (1, 2, 5, 10, 20, 50, 100 μM) in HEI-OC1 cells was measured by CCK-8 (n = 6) **(C)** CCK-8 results showing the protective effects of TET on HEI-OC1 cells after neomycin treatment (n = 6) **(D)** Immunostaining of hair cells with anti-Myosin 7a antibody in the apical, middle and basal turns of the cochlea. Scale bars: 20 μm **(E-G)** Quantification of the number of cochlear hair cells per 200 μm in the apical, middle and basal turns (n = 3). *$p < 0.05$, ***$p < 0.001$, ****$p < 0.0001$.

et al., 2019; Di et al., 2020). Tetrandrine (TET) (**Figure 1A**) is a natural bisbenzylisoquinoline alkaloid isolated from the roots of *Stephania tetrandra* S. Moore of the Menispermaceae family (Bhagya and Chandrashekar, 2016; Luan et al., 2020). Numerous studies have verified that TET possesses a broad-spectrum of distinct pharmacological activities such as anti-inflammatory (Ren et al., 2021), neuroprotective (Chen et al., 2016), calcium antagonistic (Ding et al., 2021), anti-hypertensive (Huang et al., 2016), and antineoplastic (Zhang et al., 2020) activities. Furthermore, it has been reported that TET has an otoprotective effect against noise-induced hearing loss (Yu et al., 2018). We thus speculated that TET may have great potential in the prevention of aminoglycoside-induced SHL.

In the present study, we aimed to investigate the protective effect of TET on neomycin-induced SHL by establishing *in vitro*, *in vivo*, and whole-organ explant culture models and contributed to the development of preventive and therapeutic drugs that protect against aminoglycosides-induced SHL.

RESULTS

TET Protects Against Neomycin-Induced HEI-OC1 Damage

To determine the appropriate dose of TET in the HEI-OC1 auditory cell line prior to neomycin stimulation, the cells were treated with different concentrations of TET (1, 2, 5, 10, 20, 50 and 100 μM). The CCK8 results indicated that there was no toxicity in the range of 1–20 μM (**Figure 1B**). We then pretreated the HEI-OC1 cells with TET (0.01, 0.1, 1, 2, 5 and 10 μM) for 24 h and then treated the cells with 2 mM neomycin together with TET for another 24 h. We observed that TET significantly enhanced cell viability after neomycin exposure at doses of 0.1 and 1 μM (**Figure 1C**), so we chose 1 μM TET administration for 24 h as the optimum treatment condition. We next investigated the effect of TET on cochlear hair cell loss induced by neomycin in whole-organ explant cultures *in vitro*. The cochlear explants were pre-treated with 1 μM TET for 12 h and then treated with 0.5 mM neomycin for 12 h. Immunostaining results showed that TET markedly prevented neomycin-induced hair cell loss in the middle and basal turns of the cochlear explants (**Figures 1D–G**). Taken together, these results suggest that TET has protective effects against neomycin-induced hair cell damage.

TET Attenuates Neomycin-Induced SHL *in vivo*

To investigate the protective effects of TET on neomycin-induced SHL *in vivo*, we established an acute neomycin damage model as previously reported (He et al., 2020). Postnatal day (P)28 wild type C57 mice were injected with

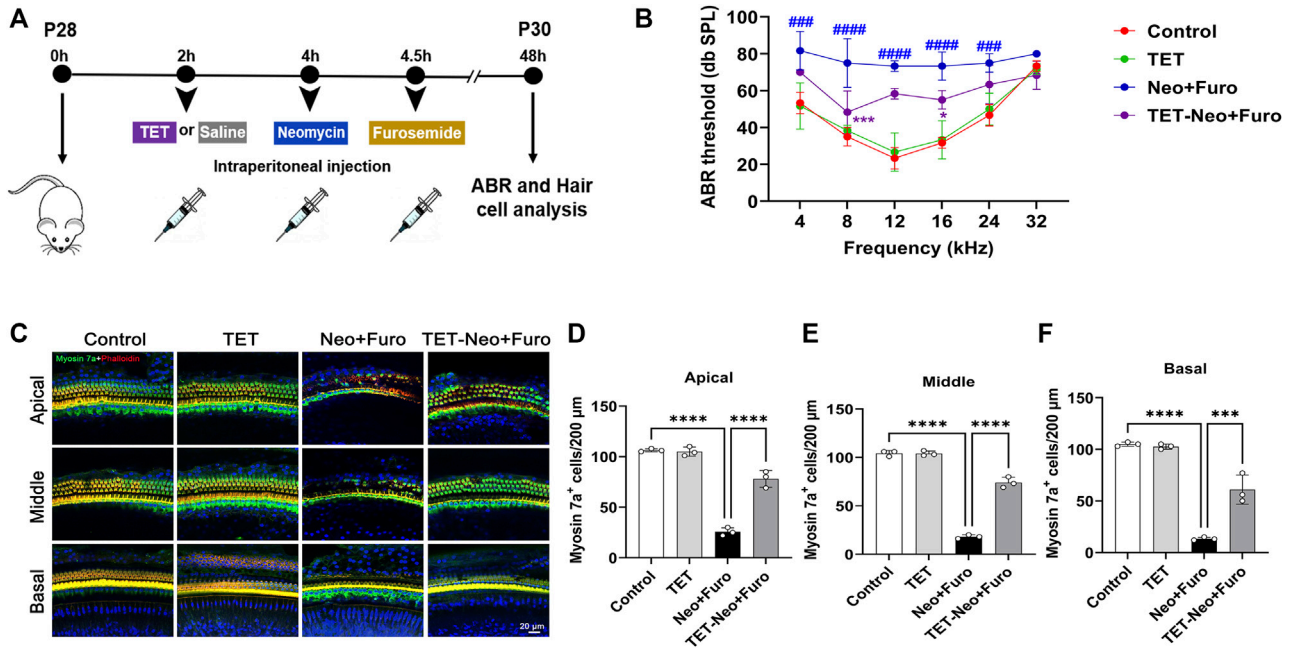

FIGURE 2 | TET improves auditory function and protects against neomycin-induced cochlear hair cell loss **(A)** Schematic illustration of the acute neomycin damage model **(B)** ABR thresholds were analyzed to determine the effect of TET on neomycin-induced hearing loss in mice (n = 6) **(C)** Immunostaining of cochlear hair cells marked by myosin 7a in the apical, middle and basal turns. Scale bars: 20 μm **(D-F)** Quantification of the number of cochlear hair cells per 200 μm in apical, middle and basal turns (n = 3). $^{*}p < 0.05$, $^{***}p < 0.001$, $^{****}p < 0.0001$.

TET (150mg/kg) intraperitoneally, and 2 h later the mice were given neomycin (100 mg/kg) in conjunction with intraperitoneal injection of furosemide (200 mg/kg) (**Figure 2A**). Mice treated with TET alone and saline alone were used as controls. Auditory brainstem response (ABR) analysis showed that TET had a protective effect against neomycin-induced hearing loss and showed significant reduced threshold elevation at 8 and 16 kHz after neomycin treatment (**Figure 2B**). The hair cells in the cochleae were stained with myosin 7a and phalloidin. We observed that neomycin with furosemide led to massive hair cell loss in the apical, middle, and basal turns, while co-administration of TET clearly promoted hair cell survival (**Figure 2C–F**). Together, these results indicate that TET may attenuate neomycin-induced SHL *in vivo*.

TET Alleviates Neomycin-Induced HEI-OC1 Cell Apoptosis

Annexin V-FITC/PI staining was used to study the protective effect of TET on neomycin-induced cell death and apoptosis in HEI-OC1 cells. Cells were pre-treated with 1 μM TET for 24 h followed by neomycin stimulation together with 1 μM TET for another 24 h. The immunofluorescence and flow cytometry analysis showed that neomycin exposure led to significant cell death and apoptosis, while TET treatment showed a remarkable improvement in cell death and apoptosis in HEI-OC1 cells (**Figure 3A–D**). TUNEL and cleaved caspase-3 staining were also used for the detection of apoptosis in HEI-OC1 cells. And we found that there were more TUNEL-positive and cleaved caspase-3-positive cells in the neomycin treatment group compared with the control group and that TET administration significantly reduced the proportions of TUNEL-positive and cleaved caspase-3-positive cells after neomycin treatment (**Figure 3E–H**). Collectively, these results disclosed that TET might prevent HEI-OC1 apoptosis and cell death when challenged by neomycin.

TET Decreases Cochlear Hair Cell Apoptosis Induced by Neomycin

We also investigate the protective effects of TET on neomycin-induced hair cell apoptosis in whole-organ explant cultures *in vitro*. Consistent with the results discussed above, immunofluorescence staining of TUNEL/myosin 7a and cleaved caspase-3/myosin 7a showed that the numbers and proportions of TUNEL/myosin 7a double-positive and cleaved caspase-3/myosin 7a double-positive hair cells per 200 μm cochlear length of the middle turn in the neomycin treatment group were notably greater than the normal control group, while TET pre-treatment dramatically reduced the numbers and proportions of TUNEL/myosin 7a double-positive and cleaved caspase-3/myosin 7a double-positive hair cells compared with the neomycin only group (**Figure 4A–D**). These results indicated that pre-treatment with TET can suppress the apoptotic cascade induced by aminoglycosides.

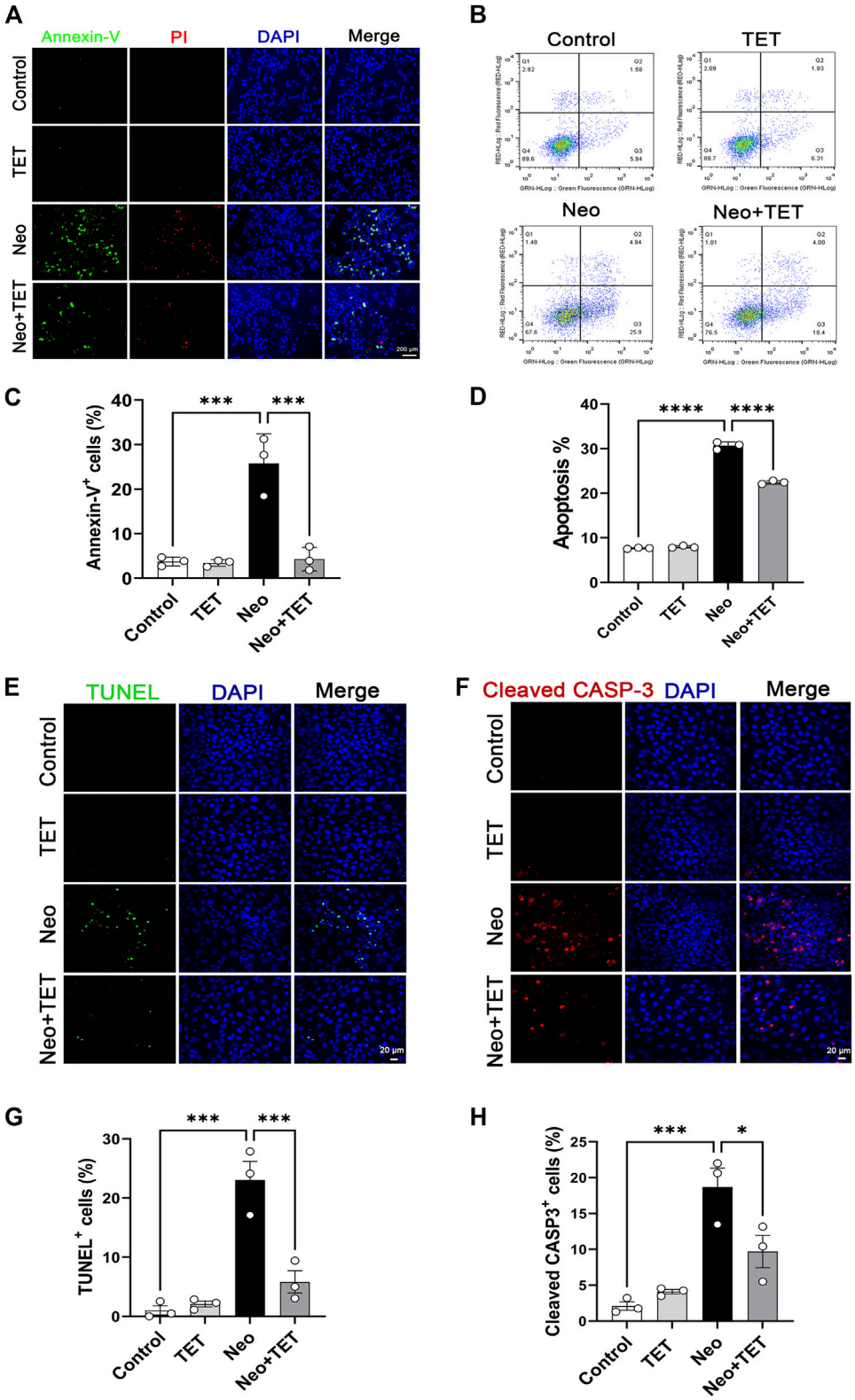

FIGURE 3 | Effects of TET on neomycin-stimulated apoptosis in HEI-OC1 cells **(A)** Annexin-V/PI staining in HEI-OC1 cells after TET treatment followed by neomycin stimulation. Scale bars: 200 μm **(B)** Apoptosis analysis of HEI-OC1 cells by flow cytometry **(C)** Quantification of the numbers of Annexin-V-positive HEI-OC1 cells in **(A)** (n = 3) **(D)** Quantification of the proportions of apoptotic cells (n = 3) **(E,F)** TUNEL and cleaved caspase-3 staining of HEI-OC1 cells after TET administration followed by neomycin exposure. Scale bars: 20 μm **(G,H)** Quantification of the numbers of TUNEL/cleaved caspase-3-positive HEI-OC1 cells in **(E,F)** (n = 3). $^{*}p < 0.05$, $^{***}p < 0.001$, $^{****}p < 0.0001$.

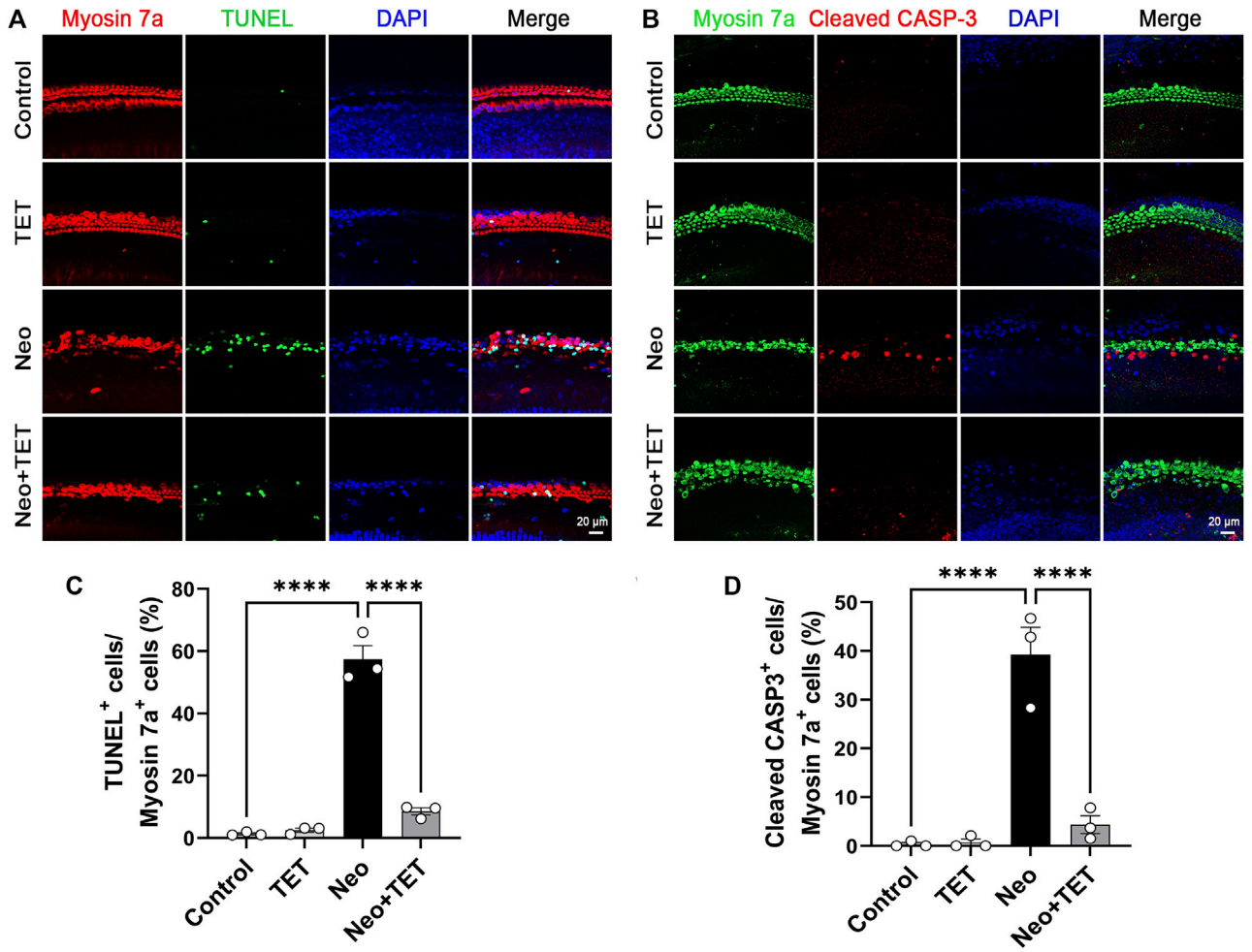

FIGURE 4 | Effects of TET on hair cell apoptosis in the mouse cochlea after neomycin exposure **(A)** Immunofluorescence staining with TUNEL and myosin 7a in cochlear hair cells in the middle turn after TET treatment followed by neomycin exposure. Scale bars: 20 μm **(B)** Immunofluorescence staining with cleaved caspase-3 and myosin 7a in cochlear hair cells in the middle turn after TET treatment followed by neomycin induction. Scale bars: 20 μm **(C)** Quantification of the numbers of TUNEL/myosin 7a double-positive cells in **(A)** (n = 3) **(D)** Quantification of the numbers of cleaved caspase-3/myosin 7a double-positive cells in **(B)** (n = 3). ****$p <$ 0.0001.

TET Decreases Reactive Oxygen Species (ROS) Production After Neomycin Treatment in HEI-OC1 Cells

It has been reported that the accumulation of ROS in mitochondria is the initiating contributor to drugs-induced ototoxicity (Choung et al., 2009; Schacht et al., 2012). We used a Mito-SOX™ Red kit to determine the levels of mitochondrial superoxide in HEI-OC1 cells. Immunostaining analysis showed that there were almost no Mito-SOX Red/ myosin 7a double-positive cells in the normal control group and TET only group, but ROS accumulation was prominently increased after neomycin treatment for 24 h compared to the control group, and this increase was strongly inhibited by TET administration (**Figure 5A**,**B**). In accordance with the immunostaining data, flow cytometry results showed that TET could attenuate neomycin-induced oxidative stress in HEI-OC1 cells (**Figure 5C**,**D**). Together, these results suggest that TET pre-treatment might alleviate neomycin-induced oxidative stress.

TET Prevents Neomycin-Induced Ototoxicity by Promoting Steroid Biosynthesis

To further explore the possible underlying mechanism of TET on neomycin-induced ototoxicity, the extracted RNA of cochlear explants was subjected to RNA sequencing. After TET treatment, there were 492 significantly differentially expressed genes, including 191 up-regulated genes and 301 down-regulated genes (**Figure 6A**,**B**). To identify the pathways involved in TET regulation, we performed pathway enrichment analysis based on the Kyoto Encyclopedia of Genes and Genomes (KEGG) database. Among the top significantly enriched

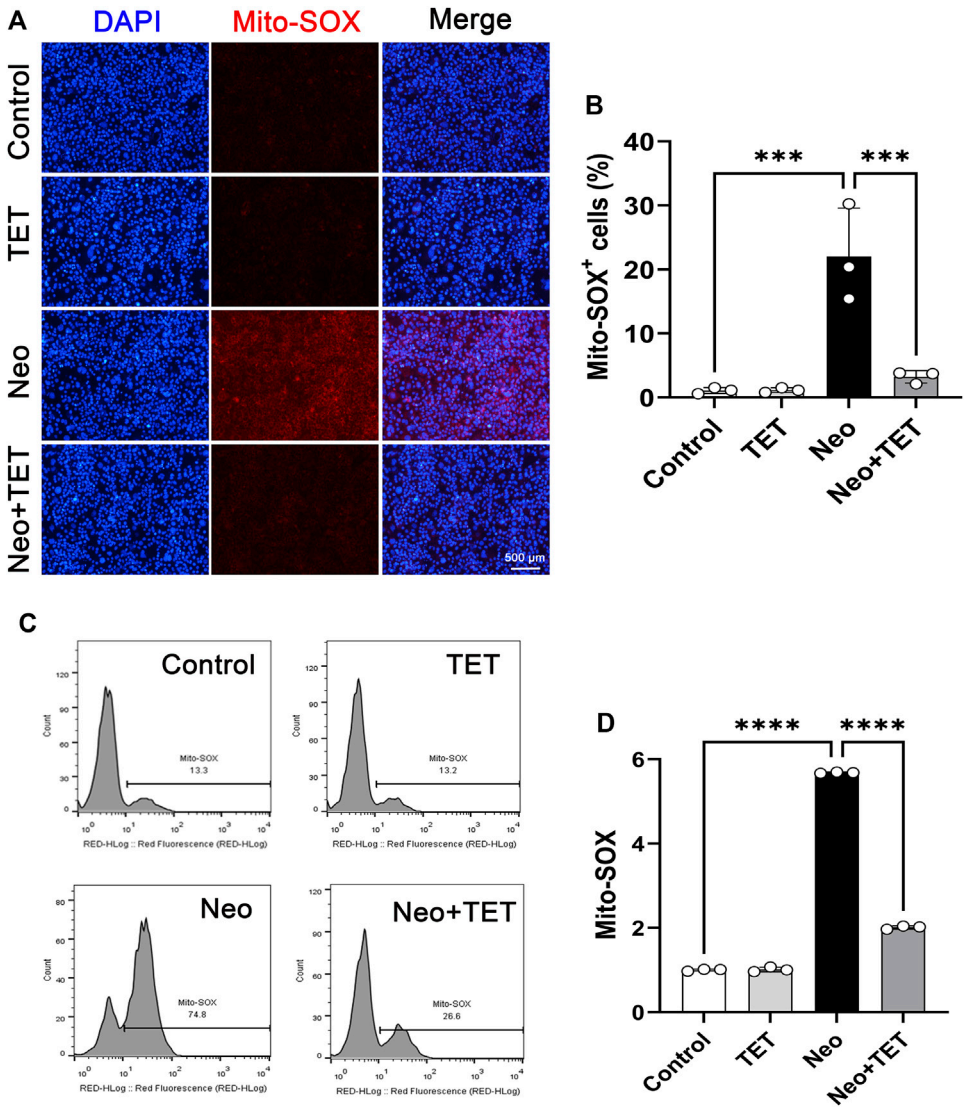

FIGURE 5 | Effects of TET on neomycin-induced oxidative stress in HEI-OC1 cells **(A)** HEI-OC1 cells were labeled with a Mito-SOX staining kit (n = 3). Scale bars: 500 μm **(B)** Quantification of the numbers of Mito-SOX-positive HEI-OC1 cells in **(A)** (n = 3) **(C)** ROS accumulation was further confirmed by flow cytometry (n = 3) **(D)** Quantification of the results of flow cytometry in **(C)**. ***$p < 0.001$, ****$p < 0.0001$.

signaling pathways, steroid biosynthesis was the most significantly enriched functional pathway in the TET treatment group (**Figure 6C**). To further validate our data, gene set enrichment analysis (GSEA) was applied to the differentially expressed genes between the control and TET treatment group. This analysis confirmed that steroid biosynthesis was significantly enriched in the TET treatment group (**Figure 6D**). The significantly changed genes that were enriched in steroid biosynthesis were mainly involved in cholesterol biosynthesis (*Msmo1*, *Lss*, *Fdft1*, *Dhcr24*, *Sc5d*, *Tm7sf2*, and *Hsd17b7*), cholesterol metabolism (*Fdft1*, *Nsdhl*, and *Sqle*), isoprenoid biosynthesis (*Fdft1*) and sterol biosynthesis (*Dhcr7* and *Fdft1*) (**Figure 6E**). By using quantitative real-time PCR, we confirmed that the steroid biosynthesis-related mRNA expression was significantly increased in the TET treatment group compared to the control group (**Figure 6F**). Collectively, these results suggest that TET can prevent neomycin-induced ototoxicity mainly by promoting steroid biosynthesis.

MATERIALS AND METHODS

Animal Experiments

C57BL/6 mice (4 weeks-old) were obtained from Vital River Laboratory Animal Technology (Beijing, China). All animal experiments were carried out according to protocols approved by the Animal Care and Use Committee of Southeast University and were consistent with the National Institutes of Health Guide for the Care and Use of Laboratory Animals.

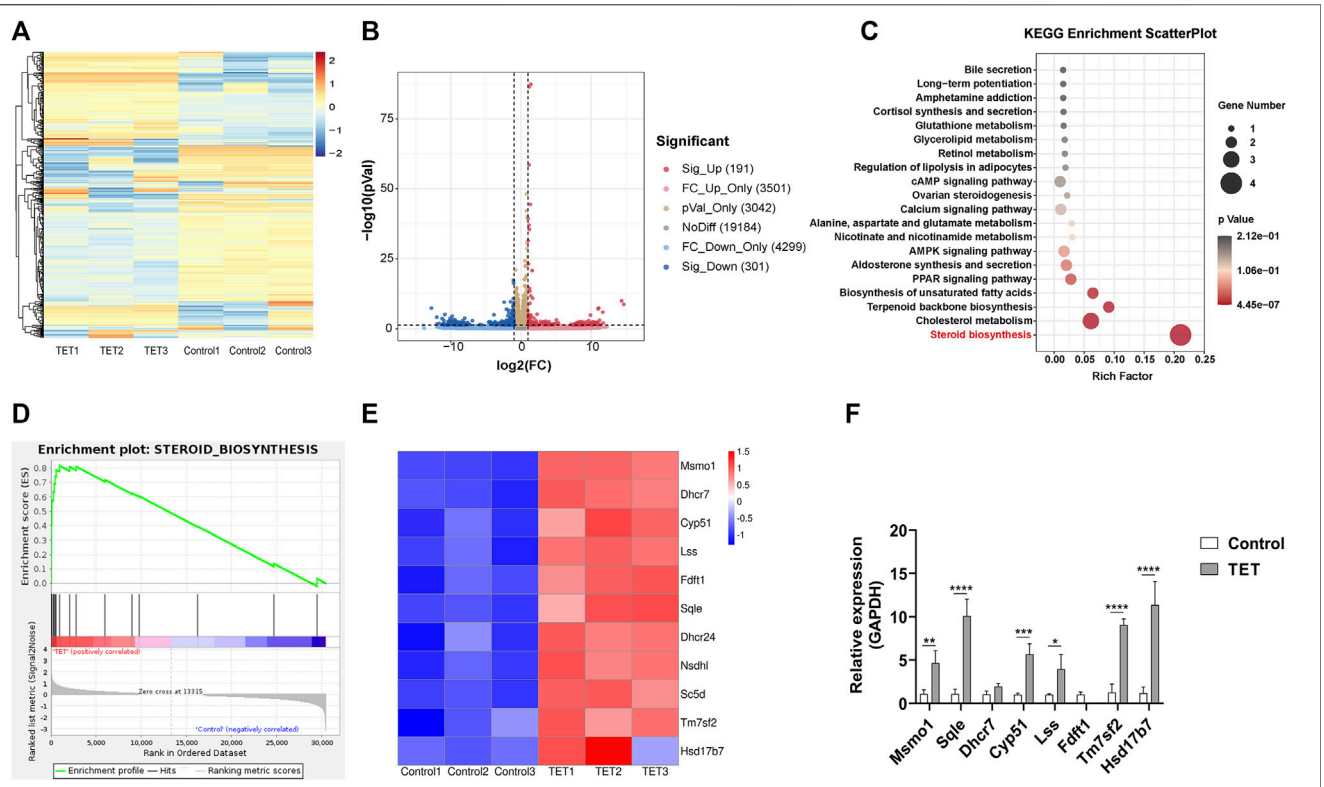

FIGURE 6 | TET promotes steroid biosynthesis in the cochlea **(A)** Heat map representation of significantly differentially expressed genes after TET treatment **(B)** Volcano plot representation of significantly differentially expressed genes after TET treatment **(C)** KEGG pathway enrichment analysis of the most significantly changed pathways after TET treatment **(D)** GSEA of genes related to steroid biosynthesis in the control and TET treatment groups **(E)** Heat map of differentially expressed genes in the steroid biosynthesis pathway **(F)** Real-time PCR analysis of differentially expressed genes related to the steroid biosynthesis pathway (n = 3). $^{*}p < 0.05$, $^{**}p < 0.01$, $^{***}p < 0.001$, $^{****}p < 0.0001$.

Mice at P28 received an intraperitoneal injection of 150 mg/kg TET (Topscience, T2996), and the mice in the control group were injected with the same volume of saline. After 2 h, mice were given 100 mg/kg neomycin (Sigma, N6386) by intraperitoneal injection followed by a single dose of 200 mg/kg furosemide (Sigma, BP547) 0.5 h later. The ABR threshold detection and hair cell counting assay were performed 2 days later.

Immunofluorescence Analysis

The dissected mouse cochleae or cultured HEI-OC1 cells were fixed in 4% paraformaldehyde. After washsing three times with 1% Triton X-100 in PBS (PBST) for 5 min each time, the samples were blocked with 10% donkey serum for 1 h at room temperature, followed by incubation with primary antibody at 4°C overnight. After washing three times with PBST, samples were incubated with secondary antibody with or without phalloidin for 1.5 h at room temperature, then washed three times again for 5 min each time and imaged under a confocal microscope.

The primary antibodies used in the present study were: myosin 7a (*Proteus* Bioscience, 25–6790, 1:1000 dilution) and cleaved caspase-3 (Cell Signaling Technology, #9661, 1:400 dilution). The secondary antibodies were: goat anti-rabbit, Alexa Fluor Plus 488 (Thermo Fisher, A32731, 1:400 dilution); goat anti-mouse, Alexa Fluor Plus 555 (Thermo Fisher, A32727, 1:400 dilution), goat anti-rabbit, Alexa Fluor Plus 555 (Thermo Fisher, A32732, 1:400 dilution), and Alexa FluorTM 594-conjugated phalloidin (Thermo Fisher, A12381, 1:400 dilution).

Cell Treatments

HEI-OC1 cells were seeded into 96-well plates at 6×10^4 cells/well for 24 h. Then the cells were treated with different concentrations of TET (0.01, 0.1, 1, 2, 5 and 10 μM) for 24 h followed by the treatment with neomycin for 24 h. CCK8 solution (10%) was added to the plates for 1 h, the absorbance at 450 nm was detected by a microplate reader.

Cochlear Explant Culture

The cochleae from the inner ear in neonatal (P3) mice were dissected and placed in sterile Hank's Balanced Salt Solution under a microscope. After removing the spiral ligament, stria vascularis and spiral ganglion, the cochleae were placed in a four-well dish covered with Cell-Tak (Corning, 354,240) and cultured in DMEM-F12 medium containing B-27TM (Thermo Fisher, 17504044), N2 (Thermo Fisher, 17502001) and ampicillin (Beyotime, ST008). After incubation at 37°C in a 5% CO_2 cell incubator for 12 h, the cochleae were pre-treated with 1 μM TET for 12 h and then given 0.5 mM neomycin and 1 μM TET for another 12 h.

ABR Audiometry

ABR was used to measure the hearing thresholds of the mice. As has been reported previously (Liu et al., 2019), anesthetized mice were placed on a thermostatic heating pad, and the hearing threshold was evaluated at six frequencies (4, 8, 12, 16, 24, and 32 kHz) on a TDT System three apparatus (Tucker Davies Technologies, Gainesville, FL, United States).

TUNEL Staining

The samples were balanced with 1× equilibration buffer for 20 min at temperature. Then the samples were incubated with 50 μL labeling buffer which including ddH_2O, equilibration buffer, brightgreen labeling mix and recombinant TdT enzyme at 37°C for 60 min. After washed 3 times with PBS, myosin 7a and DAPI were used as counterstain to mark hair cells. Images were obtained using a confocal microscope.

Flow Cytometry

An Annexin V-FITC/PI (BD, 556,419) kit was used to determine the levels of apoptosis and necrosis in HEI-OC1 cells. In brief, HEI-OC1 cells were trypsinized and centrifuged at 300 ×*g* for 5 min. After washing 3 times with cold PBS, cells were incubated with FITC Annexin V in a buffer containing propidium iodide and analyzed by flow cytometry (FACSCanto, BD, San Jose, CA, United States).

A Mito-SOX kit (Thermo Fisher, M36008) was employed to measure the oxidative stress level of HEI-OC1 cells. Cells were trypsinized and collected by centrifugation at 300 *g* for 5 min. The cells were then resuspended in Mito-SOX solution for 10 min, washed three times in PBS, and analyzed by flow cytometry.

Quantitative Real-Time PCR (qRT-PCR)

The total cochlear RNA was extracted using a FastPure Cell/Tissue Total RNA Isolation Kit (Vazyme, RC112-01) and was reversed transcribed to cDNA using a HiScript III first Strand cDNA Synthesis Kit (Vazyme, R312-01). The qRT-PCR was performed on an Applied Biosystems CFX96 real-time PCR system (Bio-Rad, Hercules, CA, United States) using the AceQ universal SYBR qPCR Master Mix (Vazyme, Q511-02). The qRT-PCR conditions were set as follows: 5 min denaturing at 95°C followed by 40 cycles at 95°C for 10 s, 60°C for 30 s, then 95°C for 15 s, 60°C for 60 s and 95°C for 15 s according to the manufacturer's recommendations. GAPDH was used as the control and the results were calculated using the comparative cycle threshold (ΔΔCt) method.

Statistical Analysis

The data are shown as mean ± standard deviation (SD). The GraphPad Prism 9 software was used in the data analysis. Statistical significance was calculated with one-way analysis of variance (ANOVA) followed by the Dunnett's test. Differences were considered statistically significant at p values <0.05.

DISCUSSION

The results of the present study showed a previously unrecognized role for TET in protecting against aminoglycoside-induced ototoxicity, and the possible mechanism was investigated. We found that TET could attenuate neomycin-induced hearing loss *in vivo* and in HEI-OC1 cells and in injured cochlear explants *in vitro*. In addition, TET treatment effectively reversed neomycin-induced ROS accumulation in hair cells and prevented apoptosis in both HEI-OC1 cells and cochlear explants. Furthermore, RNA-seq analysis showed that TET treatment could significantly promote steroid biosynthesis in cochlear hair cells, which might be the main way that TET exerts its protective effects against neomycin-induced ototoxicity.

The clinical use of aminoglycosides is hampered by their ototoxic side effects. It has been reported that aminoglycosides are permeant blockers and that they can enter cochlear hair cells by interacting with several kinds of ion channels such as mechanoelectrical transducer channels (Xie et al., 2011; Kenyon et al., 2017; Kros and Steyger, 2019). Thus aminoglycosides accumulate in hair cells where they inhibit mitochondrial protein synthesis resulting in oxidative stress, and this leads to the initiation of apoptotic signaling cascades in the inner ears (Shulman et al., 2014; Esterberg et al., 2016; Desa et al., 2018). Despite multiple agents having been reported to protect against aminoglycoside-induced SHL, it is a concerning reality that none of the described agents have yet entered clinical trials. Previous research showed that TET could prevent outer hair cell damage and synapse loss after noise exposure (Yu et al., 2018), but there is little information about the effect of TET on neomycin-induced ototoxicity.

In this study we first investigated the protective effect of TET on neomycin-induced cochlear hair cell injury, and we observed that TET significantly promoted HEI-OC1 cell survival and reversed cochlear hair cell loss after neomycin treatment *in vitro* (**Figure 1**). To further evaluate whether TET can protect against neomycin-induced hearing loss *in vivo*, ABR analysis and cochlear hair cell counting by immunostaining were performed. These results indicated that TET had a strong protective effect on low frequency and middle frequency thresholds (8 and 16 kHz) and that it remarkably attenuated neomycin-induced cochlear hair cell loss (**Figure 2**).

An event that is frequently and predominantly involved in the degeneration of cochlear mechanosensory hair cells is the accumulation of toxic levels of ROS after aminoglycosides exposure (Denamur et al., 2011; Ye et al., 2018), and interventions using diverse antioxidants both *in vitro* and *in vivo* have proven to be effective in protecting against the ototoxicity of aminoglycosides (Tokgoz et al., 2011; Polony et al., 2014; Sekulic-Jablanovic et al., 2020). Overproduction of ROS may lead to the activation of caspase 3, which initiates apoptosis in hair cells (Kim et al., 2016; Wen et al., 2018). In the current study, Mito-SOX staining and flow cytometry were used to determine the antioxidative effect of TET in HEI-OC1 cells after neomycin exposure. The results indicated that TET could significantly reduce the oxidative stress level and ameliorate hair cell apoptosis after neomycin exposure (**Figures 3–5**).

To further explore the possible mechanism by which TET protects against neomycin-induced hair cell injury, we performed an RNA-seq analysis of cochlear explants after TET treatment. We observed a total of 191 significantly up-regulated differentially expressed genes and 301 significantly down-regulated differentially expressed genes. KEGG enrichment analysis showed that TET mainly promoted steroid

biosynthesis (**Figure 6**). Steroid therapy is commonly used to treat sudden SHL clinically (Skarżyńska et al., 2018; Kapoor et al., 2020; Song et al., 2021), and it has been reported that steroids including corticosteroids like dexamethasone, neuroactive steroids such as dehydroepiandrosterone, and bile acids like tauroursodeoxycholic acid exert protective effects against aminoglycoside-induced cochlear hair cell damage (Nakamagoe et al., 2011; Bas et al., 2012; Jia et al., 2018). Therefore, we propose that TET attenuates neomycin-induced cochlear hair cell injury by promoting steroid biosynthesis.

CONCLUSION

In summary, our results show that TET exerts a protective effect against neomycin-induced cochlear hair cell damage by reducing ROS accumulation and attenuating cell apoptosis, possibly due to the promotion of steroid biosynthesis. These findings identified an anti-oxidative and anti-apoptotic effect of TET in aminoglycoside-induced ototoxicity, and TET may therefore have clinical potential for the management of aminoglycoside-induced SHL.

DATA AVAILABILITY STATEMENT

The original contributions presented in the study are included in the article/**Supplementary Material**, further inquiries can be directed to the corresponding authors.

ETHICS STATEMENT

The animal study was reviewed and approved by The Animal Care and Use Committee of Southeast University.

AUTHOR CONTRIBUTIONS

RC, KS and GW conceived this project and designed the experiments. YW and QZ performed the experiments and analyzed the data. YW, YN and YY performed the experiments and drafted the manuscript. QF, XC, CZ and JQ performed part of the *in vivo* experiments and revised the manuscript.

FUNDING

This work was supported by grants from the National Basic Research Program of China (2017YFA0105201) and the National Natural Science Foundation of China (No. 81900943 and No. 81974142) and the Science and Technology project of Zhangjiagang City (No. ZKS2127).

SUPPLEMENTARY MATERIAL

The Supplementary Material for this article can be found online at: https://www.frontiersin.org/articles/10.3389/fbioe.2022.876237/full#supplementary-material

REFERENCES

Bas, E., Van De Water, T., Gupta, C., Dinh, J., Vu, L., Martínez-Soriano, F., et al. (2012). Efficacy of Three Drugs for Protecting against Gentamicin-Induced Hair Cell and Hearing Losses. *Br. J. Pharmacol.* 166 (6), 1888–1904. doi:10.1111/j.1476-5381.2012.01890.x

Bhagya, N., and Chandrashekar, K. R. (2016). Tetrandrine - A Molecule of Wide Bioactivity. *Phytochemistry* 125, 5–13. doi:10.1016/j.phytochem.2016.02.005

Chen, L.-x., Lv, Y.-l., Wu, Z.-z., Wu, B.-x., Chen, L.-l., Qin, G.-c., et al. (2016). Neuroprotective Effects of Tetrandrine against Vascular Dementia. *Neural Regen. Res.* 11 (3), 454–459. doi:10.4103/1673-5374.179058

Choung, Y. H., Taura, A., Pak, K., Choi, S. J., Masuda, M., and Ryan, A. F. (2009). Generation of Highly-Reactive Oxygen Species Is Closely Related to Hair Cell Damage in Rat Organ of Corti Treated with Gentamicin. *Neuroscience* 161 (1), 214–226. doi:10.1016/j.neuroscience.2009.02.085

Denamur, S., Tyteca, D., Marchand-Brynaert, J., Van Bambeke, F., Tulkens, P. M., Courtoy, P. J., et al. (2011). Role of Oxidative Stress in Lysosomal Membrane Permeabilization and Apoptosis Induced by Gentamicin, an Aminoglycoside Antibiotic. *Free Radic. Biol. Med.* 51 (9), 1656–1665. doi:10.1016/j.freeradbiomed.2011.07.015

Desa, D. E., Nichols, M. G., and Smith, H. J. (2018). Aminoglycosides Rapidly Inhibit NAD(P)H Metabolism Increasing Reactive Oxygen Species and Cochlear Cell Demise. *J. Biomed. Opt.* 24 (5), 1–14. doi:10.1117/1.JBO.24.5.051403

Di, Y., Xu, T., Tian, Y., Ma, T., Qu, D., Wang, Y., et al. (2020). Ursolic Acid Protects against Cisplatin-induced Ototoxicity by Inhibiting Oxidative Stress and TRPV1 Mediated Ca2+ signaling. *Int. J. Mol. Med.* 46 (2), 806–816. doi:10.3892/ijmm.2020.4633

Ding, Y., Tang, X., Wang, Y., Yu, D., Zhu, C., and Yu, J. (2021). Tetrandrine Alleviates Podocyte Injury via Calcium-dependent Calpain-1 Signaling Blockade. *BMC Complement. Med. Ther.* 21 (1), 296. doi:10.1186/s12906-021-03469-x

Esterberg, R., Linbo, T., Pickett, S. B., Wu, P., Ou, H. C., Rubel, E. W., et al. (2016). Mitochondrial Calcium Uptake Underlies ROS Generation during Aminoglycoside-Induced Hair Cell Death. *J. Clin. Invest.* 126 (9), 3556–3566. doi:10.1172/JCI84939

Fetoni, A. R., Paciello, F., Rolesi, R., Eramo, S. L. M., Mancuso, C., Troiani, D., et al. (2015). Rosmarinic Acid Up-Regulates the Noise-Activated Nrf2/HO-1 Pathway and Protects against Noise-Induced Injury in Rat Cochlea. *Free Radic. Biol. Med.* 85, 269–281. doi:10.1016/j.freeradbiomed.2015.04.021

He, Y., Li, W., Zheng, Z., Zhao, L., Li, W., Wang, Y., et al. (2020). Inhibition of Protein Arginine Methyltransferase 6 Reduces Reactive Oxygen Species Production and Attenuates Aminoglycoside- and Cisplatin-Induced Hair Cell Death. *Theranostics* 10 (1), 133–150. doi:10.7150/thno.37362

Huang, Y.-L., Cui, S.-Y., Cui, X.-Y., Cao, Q., Ding, H., Song, J.-Z., et al. (2016). Tetrandrine, an Alkaloid from S. Tetrandra Exhibits Anti-hypertensive and Sleep-Enhancing Effects in SHR via Different Mechanisms. *Phytomedicine* 23 (14), 1821–1829. doi:10.1016/j.phymed.2016.10.021

Jia, Z., He, Q., Shan, C., and Li, F. (2018). Tauroursodeoxycholic Acid Attenuates Gentamicin-Induced Cochlear Hair Cell Death *In Vitro*. *Toxicol. Lett.* 294, 20–26. doi:10.1016/j.toxlet.2018.05.007

Kapoor, E., Sabetrasekh, P., and Monfared, A. (2020). A Case of Incus Necrosis Following Oral and Intratympanic Steroid Administration for Sensorineural Hearing Loss. *Otol. Neurotol.* 41 (9), 1210–1213. doi:10.1097/MAO.0000000000002799

Kenyon, E. J., Kirkwood, N. K., Kitcher, S. R., O'Reilly, M., Derudas, M., Cantillon, D. M., et al. (2017). Identification of Ion-Channel Modulators that Protect

against Aminoglycoside-Induced Hair Cell Death. *JCI Insight* 2 (24), e96773. doi:10.1172/jci.insight.96773

Kim, Y.-R., Kim, M.-A., Cho, H.-J., Oh, S.-K., Lee, I.-K., Kim, U.-K., et al. (2016). Galangin Prevents Aminoglycoside-Induced Ototoxicity by Decreasing Mitochondrial Production of Reactive Oxygen Species in Mouse Cochlear Cultures. *Toxicol. Lett.* 245, 78–85. doi:10.1016/j.toxlet.2016.01.005

Kros, C. J., and Steyger, P. S. (2019). Aminoglycoside- and Cisplatin-Induced Ototoxicity: Mechanisms and Otoprotective Strategies. *Cold Spring Harb. Perspect. Med.* 9 (11), a033548. doi:10.1101/cshperspect.a033548

Li, J., Wu, G., Qin, C., Chen, W., Chen, G., and Wen, L. (2019). Structure Characterization and Otoprotective Effects of a New Endophytic Exopolysaccharide from Saffron. *Molecules* 24 (4), 749. doi:10.3390/molecules24040749

Liu, Y., Qi, J., Chen, X., Tang, M., Chu, C., Zhu, W., et al. (2019). Critical Role of Spectrin in Hearing Development and Deafness. *Sci. Adv.* 5 (4), eaav7803. doi:10.1126/sciadv.aav7803

Luan, F., He, X., and Zeng, N. (2020). Tetrandrine: a Review of its Anticancer Potentials, Clinical Settings, Pharmacokinetics and Drug Delivery Systems. *J. Pharm. Pharmacol.* 72 (11), 1491–1512. doi:10.1111/jphp.13339

Nakamagoe, M., Tabuchi, K., Nishimura, B., and Hara, A. (2011). Effects of Neuroactive Steroids on Cochlear Hair Cell Death Induced by Gentamicin. *Steroids* 76 (13), 1443–1450. doi:10.1016/j.steroids.2011.07.014

O'Sullivan, M. E., Perez, A., Lin, R., Sajjadi, A., Ricci, A. J., and Cheng, A. G. (2017). Towards the Prevention of Aminoglycoside-Related Hearing Loss. *Front. Cel. Neurosci.* 11, 325. doi:10.3389/fncel.2017.00325

Polony, G., Humli, V., Andó, R., Aller, M., Horváth, T., Harnos, A., et al. (2014). Protective Effect of Rasagiline in Aminoglycoside Ototoxicity. *Neuroscience* 265, 263–273. doi:10.1016/j.neuroscience.2014.01.057

Ren, D., Fu, Y., Wang, L., Liu, J., Zhong, X., Yuan, J., et al. (2021). Tetrandrine Ameliorated Alzheimer's Disease through Suppressing Microglial Inflammatory Activation and Neurotoxicity in the 5XFAD Mouse. *Phytomedicine* 90, 153627. doi:10.1016/j.phymed.2021.153627

Schacht, J., Talaska, A. E., and Rybak, L. P. (2012). Cisplatin and Aminoglycoside Antibiotics: Hearing Loss and its Prevention. *Anat. Rec.* 295 (11), 1837–1850. doi:10.1002/ar.22578

Sekulic-Jablanovic, M., Voronkova, K., Bodmer, D., and Petkovic, V. (2020). Combination of Antioxidants and NFAT (Nuclear Factor of Activated T Cells) Inhibitor Protects Auditory Hair Cells from Ototoxic Insult. *J. Neurochem.* 154 (5), 519–529. doi:10.1111/jnc.14921

Shulman, E., Belakhov, V., Wei, G., Kendall, A., Meyron-Holtz, E. G., Ben-Shachar, D., et al. (2014). Designer Aminoglycosides that Selectively Inhibit Cytoplasmic rather Than Mitochondrial Ribosomes Show Decreased Ototoxicity. *J. Biol. Chem.* 289 (4), 2318–2330. doi:10.1074/jbc.M113.533588

Skarżyńska, M. B., Skarżyński, P. H., Król, B., Kozieł, M., Osińska, K., Gos, E., et al. (2018). Preservation of Hearing Following Cochlear Implantation Using Different Steroid Therapy Regimens: A Prospective Clinical Study. *Med. Sci. Monit.* 24, 2437–2445. doi:10.12659/msm.906210

Song, M. H., Jung, S. Y., Gu, J. W., and Shim, D. B. (2021). Therapeutic Efficacy of Super-high-dose Steroid Therapy in Patients with Profound Sudden Sensorineural Hearing Loss: a Comparison with Conventional Steroid Therapy. *Acta Oto-Laryngol.* 141 (2), 152–157. doi:10.1080/00016489.2020.1842493

Tokgoz, B., Ucar, C., Kocyigit, I., Somdas, M., Unal, A., Vural, A., et al. (2011). Protective Effect of N-Acetylcysteine from Drug-Induced Ototoxicity in Uraemic Patients with CAPD Peritonitis. *Nephrol. Dial. Transplant.* 26 (12), 4073–4078. doi:10.1093/ndt/gfr211

Wen, S.-Y., Tsai, C.-Y., Pai, P.-Y., Chen, Y.-W., Yang, Y.-C., Aneja, R., et al. (2018). Diallyl Trisulfide Suppresses Doxorubicin-Induced Cardiomyocyte Apoptosis by Inhibiting MAPK/NF-κB Signaling through Attenuation of ROS Generation. *Environ. Toxicol.* 33 (1), 93–103. doi:10.1002/tox.22500

Xie, J., Talaska, A. E., and Schacht, J. (2011). New Developments in Aminoglycoside Therapy and Ototoxicity. *Hearing Res.* 281 (1-2), 28–37. doi:10.1016/j.heares.2011.05.008

Ye, J.-z., Su, Y.-b., Lin, X.-m., Lai, S.-s., Li, W.-x., Ali, F., et al. (2018). Alanine Enhances Aminoglycosides-Induced ROS Production as Revealed by Proteomic Analysis. *Front. Microbiol.* 9, 29. doi:10.3389/fmicb.2018.00029

Yu, Y., Hu, B., Bao, J., Mulvany, J., Bielefeld, E., Harrison, R. T., et al. (2018). Otoprotective Effects of Stephania Tetrandra S. Moore Herb Isolate against Acoustic Trauma. *J. Assoc. Res. Otolaryngol.* 19 (6), 653–668. doi:10.1007/s10162-018-00690-3

Zhai, S., Fang, Y., Yang, W., Gu, R., Han, D., and Yang, S. (2013). Clinical Investigation on the Beneficial Effects of the Chinese Medicinal Herb Gushen Pian on Sensorineural Deafness and Tinnitus. *Cell Biochem. Biophys.* 67 (2), 785–793. doi:10.1007/s12013-013-9536-5

Zhang, R.-H., Wang, S., Zhang, H., Lan, J.-J., Xu, G.-B., Zhao, Y.-L., et al. (2020). Discovery of Tetrandrine Derivatives as Tumor Migration, Invasion and Angiogenesis Inhibitors. *Bioorg. Chem.* 101, 104025. doi:10.1016/j.bioorg.2020.104025

Conflict of Interest: The authors declare that the research was conducted in the absence of any commercial or financial relationships that could be construed as a potential conflict of interest.

Publisher's Note: All claims expressed in this article are solely those of the authors and do not necessarily represent those of their affiliated organizations, or those of the publisher, the editors and the reviewers. Any product that may be evaluated in this article, or claim that may be made by its manufacturer, is not guaranteed or endorsed by the publisher.

frontiers | Frontiers in Bioengineering and Biotechnology

ORIGINAL RESEARCH
published: 29 April 2022
doi: 10.3389/fbioe.2022.901749

Interaction of Neurovascular Signals in the Degraded Condylar Cartilage

Wenpin Qin[1†], *Zibin Zhang*[1†], *Jianfei Yan*[1†], *Xiaoxiao Han*[1,2], *Li-Na Niu*[1] *and Kai Jiao*[1*]

[1]State Key Laboratory of Military Stomatology and National Clinical Research Center for Oral Diseases and Shaanxi Key Laboratory of Stomatology, School of Stomatology, The Fourth Military Medical University, Xi'an, China, [2]The College of Life Science, Northwest University, Xi'an, China

Introduction: Degradation of the condylar cartilage during temporomandibular joint osteoarthritis (TMJ-OA) results in the infiltration of nerves, blood vessels and inflammatory cells from the subchondral bone into the cartilage. The interaction among innervation, angiogenesis and inflammation in the condylar cartilage of TMJ-OA remains largely unknown.

Method: In the present study, microarray-based transcriptome analysis was used to detect, and quantitative real-time polymerase chain reaction was used to validate transcriptome changes in the condylar cartilage from a well-established rat TMJ-OA model. Gene ontology (GO), Kyoto encyclopedia of genes and genomes (KEGG) pathway and protein-protein interaction (PPI) analyses were conducted.

Result: There were 1817 differentially expressed genes (DEGs, fold change ≥2, $p < 0.05$) between TMJ-OA and control cartilages, with 553 up-regulated and 1,264 down-regulated genes. Among those genes, representative DEGs with known/suspected roles in innervation, angiogenesis and inflammation were further validated by enriched GO terms and KEGG pathways. The DEGs related to innervation were predominately enriched in the GO terms of neurogenesis, generation of neurons, and KEGG pathways of cholinergic synapse and neurotrophin signaling. Genes related to angiogenesis were enriched in GO terms of vasculature and blood vessel development, and KEGG pathways of hypoxia-inducible factor 1 (HIF-1) pathway and calcium signaling pathway. For inflammation, the DEGs were enriched in the GO terms of immune system process and immune response, and KEGG pathways of Toll-like receptor and transforming growth factor β (TGFβ) signaling. Analysis with PPI indicated that the aforementioned DEGs were highly-interacted. Several hub genes such as v-akt murine thymoma viral oncogene homolog 1 (*Akt1*), glycogen synthase kinase 3β (*Gsk3b*), fibroblast growth factor 2 (*Fgf2*) and nerve growth factor receptor (*Ngfr)* were validated.

Conclusion: The present study demonstrated, for the first time, that intimate interactions exist among innervation, angiogenesis and inflammation in the condylar cartilage of TMJ-OA.

Keywords: angiogenesis, temporomandibular disorders, bioinformatics, growth factor, chondrocyte

OPEN ACCESS

Edited by:
Mingqiang Li,
Third Affiliated Hospital of Sun Yat-sen University, China

Reviewed by:
Changjun Li,
Central South University, China
Xin Chen,
Xi'an Jiaotong University, China
Min Guan,
Chinese Academy of Sciences, China

****Correspondence:***
Kai Jiao
kjiao1@163.com

†These authors have contributed equally to this work

Specialty section:
This article was submitted to Biomaterials, a section of the journal Frontiers in Bioengineering and Biotechnology

Received: *22 March 2022*
Accepted: *01 April 2022*
Published: *29 April 2022*

Citation:
Qin W, Zhang Z, Yan J, Han X, Niu L-N and Jiao K (2022) Interaction of Neurovascular Signals in the Degraded Condylar Cartilage. Front. Bioeng. Biotechnol. 10:901749. doi: 10.3389/fbioe.2022.901749

INTRODUCTION

Temporomandibular joint osteoarthritis (TMJ-OA) is characterized by progressive cartilage degradation, thickening of the calcified cartilage and subchondral bone changes. This condition is one of the most complex temporomandibular disorders (Chen et al., 2020). The osteochondral junction in the TMJ comprises a calcified cartilage layer and a subchondral plate. In normal joints, the terminal blood vessels in the subchondral plate are in direct contact with, or infiltrate the calcified cartilage. These vessels are rarely detected in the non-calcified cartilage beyond the tidemark (i.e., boundary between the calcified and non-calcified cartilage) (Wang et al., 2012). In OA, blood vessels and nerve endings from the subchondral bone can breach the tidemark and cause channels to extend from the subchondral bone into the non-calcified cartilage (Zhu et al., 2019). Pathological neurovascularization within the non-calcified cartilage damages the normal barrier between articular cartilage and subchondral bone. Infiltration of inflammatory cells from the blood vessels disrupts chondrocyte function and degrades the cartilage matrix (Findlay and Kuliwaba, 2016). Pathological neurovascularization is also an essential component of endochondral ossification (Wang et al., 2012). Alteration of the osteochondral junction further aggravates OA progression via direct involvement of innervation, angiogenesis, and inflammation (Jiao et al., 2015; Chen et al., 2020).

Angiogenesis and innervation are closely integrated processes in pathological conditions such as cancer and arthritis (Jin et al., 2020; Hu et al., 2021). In OA, perivascular nerve growth causes the sensory nerves within the cartilage to be exposed to chemical and mechanical stimulation, thereby contributing to osteoarthritic pain. Neuropeptides such as calcitonin gene-related peptide and substance p, in turn, act on specific vascular receptors to regulate blood flow and permeability, as well as stimulating endothelial cell proliferation, migration and tube formation to promote growth of the blood vessels. Sympathetic neuropeptides such as neuropeptide Y are also acute vasoconstrictors that increase blood flow and promote angiogenesis (Mapp and Walsh, 2012). Apart from the contribution of blood vessel growth to inflammation in arthritis, increased infiltration of macrophages also provides a key stimulus for angiogenesis through the production of proangiogenic factors such as vascular endothelial growth factor (VEGF). Nerve growth regulators are also produced by vascular cells and inflammatory cells in the perivascular environment (Marrella et al., 2018; Wan et al., 2021). Although the growth of blood vessels, nerves and the infiltration of inflammatory cells are closely interacting processes that share common regulatory pathways, information on the interactions of these three processes in the TMJ-OA cartilage is scanty (Marrella et al., 2018).

Previous work by the authors demonstrated that OA-like lesions were created by unilateral anterior crossbite (UAC)-induced dysregulated mechanical loading of rodent TMJs (Sun J.-l. et al., 2020; Sun et al., 2020 J. L.). In the present study, pathologic changes in the blood vessels and nerves from the osteochondral junction to condylar cartilage of UAC mice were characterized. Microarray-based transcriptome analysis was used to select target genes involved in innervation, angiogenesis and inflammation in the cartilages of UAC mice and the corresponding control. Enrichment analysis and protein-protein interaction analysis were used to identify differentially expressed genes (DEGs) that were associated with these processes. The hypothesis to be tested was that there is intricate crosstalk among innervation, angiogenesis and inflammation during OA progression.

MATERIALS AND METHODS

Male Sprague-Dawley rats (140–160 g; 6-week-old) were obtained from the animal center of the Air Force Medical University (AFMU), Xi'an, China. Animal experimental protocols were reviewed and approved by the Institutional Animal Care and Use Committee of AFMU, following the National Institute of Health Guidelines for the Care and Use of Laboratory Animals. The procedures complied with ARRIVE 2.0 guidelines. Unilateral anterior crossbite appliances (metal tubes) were fitted to the jaws of the rats to induce osteoarthritic-like changes in their TMJ cartilage (Jiao et al., 2016). In the control group, rats were subjected to the aforementioned procedures except for the bonding of the UAC appliances.

Histochemical and Immunohistochemical Staining

All rats were euthanized with pentobarbital overdose. A 3 × 4 mm tissue block that included the joint capsule and surrounding soft tissue was harvested gently from each rat. For hematoxylin-eosin and Safranin O/Fast Green staining, the tissue blocks were fixed in 4% paraformaldehyde, decalcified in 10% ethylenediamine tetra-acetic acid and embedded in paraffin. The TMJ was sectioned in the sagittal plane. The sections were mounted on poly-L-lysine-coated glass slides and deparaffinized. Half of the sections were stained with hematoxylin and eosin. For Safranin O/Fast Green staining, the sections were stained with 0.02% Fast Green and subsequently with 0.1% safranin O. The central sagittal sections of each TMJ section were used for examination.

For immunofluorescence staining, the specimens were sequentially fixed in 4% paraformaldehyde and 30% sucrose, embedded in optimal cutting temperature compound (Leica, Wetzlar, Germany) and stored at −80 C. After blocked with 1.5% goat serum (MilliporeSigma, Burlington, MA), the sections were incubated with CGRP (ab36001, Abcam, Cambridge, United Kingdom) or CD31 (sc-376764, Santa Cruz Biotechnology, Dallas, TX) primary antibodies and subsequently with secondary antibody (US Everbright Inc., Suzhou, China). The sections were rinsed with phosphate-buffered saline then mounted with Prolong Diamond Antifade Mountant containing 4',6-diamidino-2-phenylindole (DAPI; Invitrogen, San Diego, CA). Images were acquired using laser scanning confocal microscopy (FV1000, Olympus, Tokyo, Japan).

Microarray

Condylar cartilages were ground in liquid nitrogen. Total RNA was extracted using Trizol reagent and purified using a RNAeasy mini kit (Qiagen, Hilden, Germany) according to the manufacturer's instructions. All specimens were treated on-column with DNase. The isolated total RNA was translated into cDNA and labeled with Cy3 using the Quick Amp Labeling kit (Agilent Technologies, Santa Clara, CA). After matched with the same concentration of RNA, the specimens were prepared for Whole Rat Genome Microarray (4 × 44K; Agilent Technologies). The hybridization signal intensities were detected using a microarray scanner (G2505C, Agilent). Signals were read, normalized and analyzed using the Feature Extraction 9.5.3 and GeneSpring GX10 software (Agilent). The DEGs were identified as fold change ≥2 ($p < 0.05$). Analyses with Gene Ontology (GO) terms and Kyoto Encyclopedia of Genes and Genomes (KEGG) pathway (Kanehisa et al., 2019) were undertaken by the Database for Annotation, Visualization and Integrated Discovery (DAVID; Laboratory of Immunopathogenesis and Bioinformatics, SAIC, Frederick, Inc., Frederick, MD). Analysis of protein-protein interaction (PPI) was undertaken by Search Tool for the Retrieval of Interacting Genes/Proteins (STRING; https://string-db.org/) (Szklarczyk et al., 2019) and CytoScape (version 3.9.0, Institute of Systems Biology, Seattle, WA; https://cytoscape.org/) (Shannon et al., 2003).

Quantitative Real-Time Polymerase Chain Reaction

Quantitative real-time polymerase chain reaction (qRT-PCR) was performed as previously reported (Ma et al., 2022). The following genes were used for qRT-PCR: v-akt murine thymoma viral oncogene homolog 1 (*Akt1*), glycogen synthase kinase 3β (*Gsk3b*), fibroblast growth factor 2 (*Fgf2*) and nerve growth factor receptor (*Ngfr*). Glyceraldehyde-3-phosphate dehydrogenase (*Gapdh*) was used as the housekeeping gene for data normalization using the $2^{-\Delta\Delta Ct}$ method. GraphPad Prism 8.0 (GraphPad Software, San Diego, CA) was used to examine if significant difference in fold expressions of the tested genes existed between the UAC group and the control group. The Student's t test was used for statistical analysis. Statistical significance was preset at $\alpha = 0.05$. Because the four genes tested were derived from the same rat genome, the t-tests performed belonged to the same "family" of statistical procedures. The Bonferroni correction was used to control the familywise error rate to reduce the chance of obtaining false-positive conclusions. Accordingly, p values less than 0.05/4 = 0.013 were considered significantly different for comparison of fold changes of the four genes between the UAC and control groups.

RESULTS

Validation of Cartilage Changes in Osteoarthritis

Histochemical and immunohistochemical staining were used to characterize the rat TMJ-OA model (**Figure 1A**). The condylar cartilage appeared normal in the control group, with four intact layers. The cartilage had an overall smooth surface and contained homogenously-distributed chondrocytes. The UAC group manifested OA-like changes such as the loss of cartilage surface integrity, abnormal thickening of the four cartilage layers and cellular derangement. There was no significant difference in the changes within the right and left condylar cartilage in the UAC group. Pathological neurovascularization, in the form of new erythrocyte-containing blood vessels and nerves, infiltrated the osteochondral junction into the non-calcified condylar cartilage in the TMJ-OA rat model.

Differential Gene Expression in the Condylar Cartilage

Of the 4,650 genes detectable using the Whole Rat Genome Microarray, 1817 significant DEGs with fold change ≥2 ($p < 0.05$) were detected in the condylar cartilage of the UAC group. Among the DEGs, 553 genes were up-regulated and 1,264 genes were down-regulated. Specific DEGs related to innervation, angiogenesis and inflammation are depicted in **Supplementary Appendix Table S1–S4**, respectively. The heatmap and bar chart in **Figure 1B** showed the fold changes in selected genes expressed by the condylar cartilage in the UAC group versus the control group.

Enrichment Analysis of Differential Gene Expression

GO term enrichment and KEGG pathway analysis were performed on innervation-related, angiogenesis-related and inflammation-related genes to obtain more detailed information on correlated pathways and their potential functions. The KEGG pathways (**Figure 2**) and GO terms (**Figure 3**) related to innervation, angiogenesis and inflammation are presented in the order of enriched factor. Genes related to innervation were enriched in several classical KEGG pathways such as dopaminergic synapse, cholinergic synapse and neurotrophin signaling pathway (**Figure 2A**). Genes related to angiogenesis were enriched in the AMP-activated protein kinase (AMPK), hypoxia-inducible factor (HIF)-1 and calcium signaling pathways (**Figure 2B**). Genes related to inflammation were enriched in the cationic antimicrobial peptide (cAMP) signaling pathway, Toll-like receptor signaling pathway and inflammatory mediator regulation of transient receptor potential (TRP) channels (**Figure 2C**).

The top three enriched GO terms related to innervation were regulation of synapse structure or activity, negative regulation of neuron death, and regulation of neuron apoptotic process; additional enriched terms are depicted in **Figure 3A**. The top three enriched GO terms related to angiogenesis were positive regulation of vasodilation, VEGF receptor signaling pathway, and VEGF signaling pathway; additional enriched terms are depicted in **Figure 3B**. The top three enriched GO terms related to inflammation were regulation of macroautophagy, activation of innate immune response, and positive regulation of innate

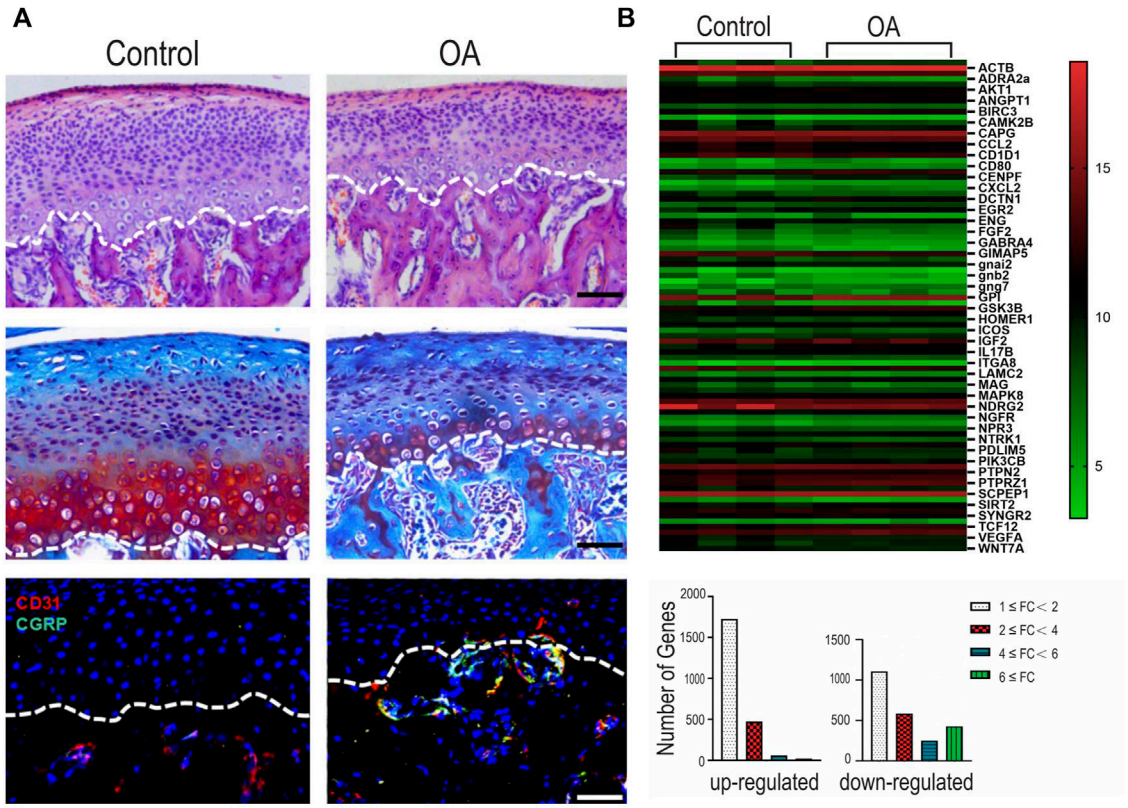

FIGURE 1 | (A) Representative images of hematoxylin-eosin (HE) staining, Safranin O/Fast Green staining and immunofluorescence staining of the mandibular condylar cartilage in the fibrocartilages harvested from the unilateral anterior crossbite (UAC) group versus the control group. Bar = 50 μM. **(B)** Integrated analyses of differentially expressed genes (DEGs). Top: heatmap. The horizontal axis represents cluster analysis of groups. The vertical axis represents cluster analysis of genes. Red represents up-regulated DEGs, green represents down-regulated DEGs, black represents gene expression with no difference. The degree of significant difference in gene expression is indicated by the brightness of the color. Bottom: DEGs were classified according to the differential expression level with a minimum of 1-fold, 2-fold, 4-fold, and 6-fold differences. FC: fold change.

immune response; additional enriched terms are depicted in **Figure 3C**.

Among the 30 GO terms related to innervation, 12 terms were related to synapse and axons, suggesting that neurotransmitters are involved in the extension of neurons into the condylar cartilage. Angiogenesis was not only closely related to the angiogenic factors but was related also to classical signaling pathways including AMPK, MAPK, PI3K-Akt, and NF-kappa B signaling. The enriched GO terms related to inflammation identified a possible role for T cells, based on their frequency of occurrence.

Protein-Protein Interaction (PPI) Network Analysis of DEGs

The STRING database and Cytoscape were to analyze PPI to detect hub genes (i.e., genes with high correlation in candidate modules) among the selected genes. The innervation-related genes (**Figure 4A**), angiogenesis-related genes (**Figure 4B**) and inflammation-related genes (**Figure 4C**) were first analyzed separately. All selected genes were then analyzed together to further validate their interactions (**Figure 4D**). Different colors on the dot represented different functions. Different dot sizes represented closeness (i.e., the larger the point, the closer the relationship). The interrelated genes identified included *Akt1*, *Igf1r*, *Vegfa*, *Pik3cb*, *Ngfr*, *Mapk8*, *Mapk12*, *Actb*, *Fgf2*, *Gsk3b*, *Ccl2,* and *Jun*. Remarkably, *Akt1* and *Gsk3b* participated in all the three processes - innervation, angiogenesis and inflammation. *Akt1*, *Igf1r* and *Vegfa* shared several pathways, including PI3K-Akt signaling pathway, MAPK signaling pathway and HIF-1 signaling pathway. These results revealed the strong interactions among innervation, angiogenesis and inflammation in the TMJ-OA cartilage.

qRT-PCR

To confirm the findings of the microarray analysis, qRT-PCR was conducted on four genes involved in innervation, angiogenesis and inflammation (*Akt1*, *Fgf2*, *Gsk3b*, *Ngfr*). The expression profiles of these genes had a good match for the results obtained by microarray analysis (**Figure 5**). Minor differences were attributed to the heterogeneity of OA between individual animals. The qRT-PCR results validated the accuracy of the microarray data and supported that changes in innervation-related, angiogenesis-related and inflammation-related genes were detected in the condylar cartilage of OA rats.

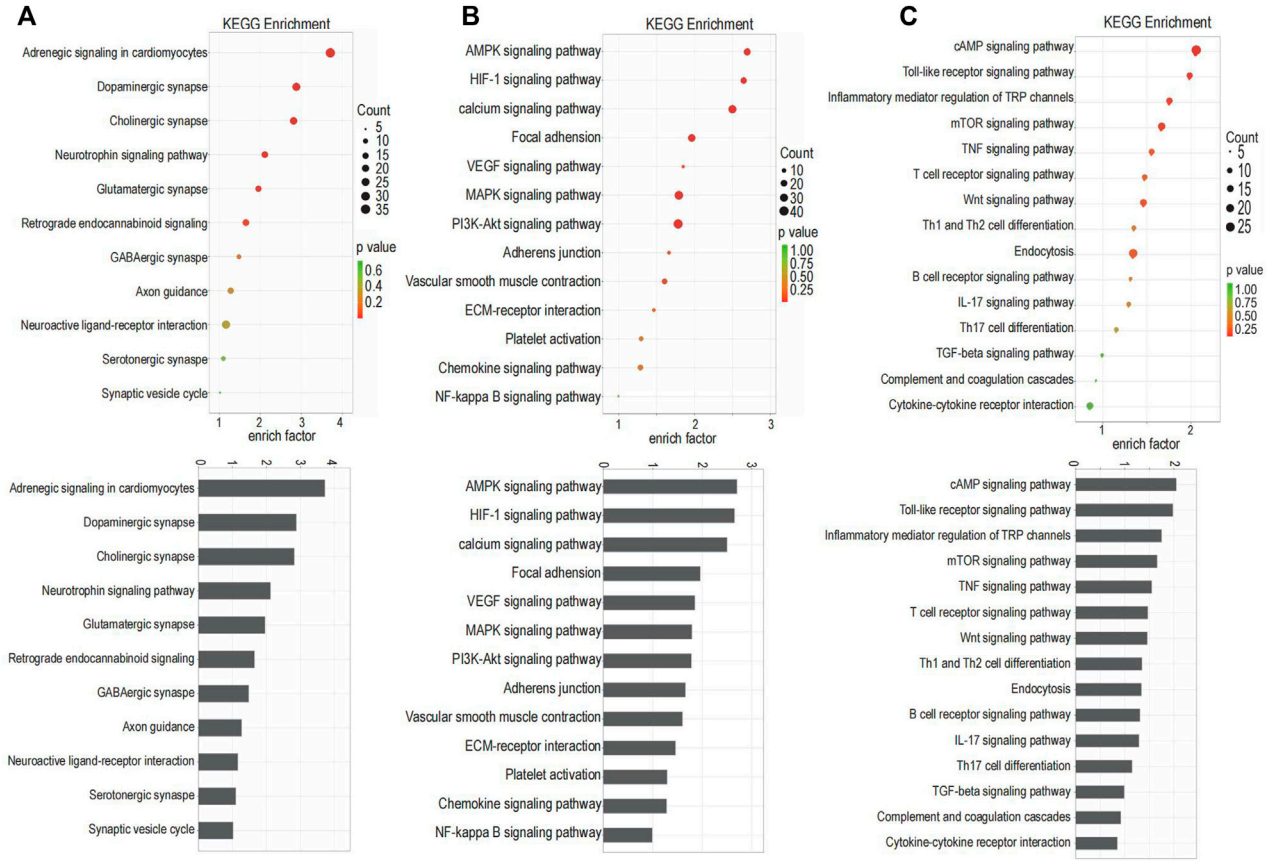

FIGURE 2 | The Kyoto Encyclopedia of Genes and Genomes (KEGG) pathways enriched for the targeted genes. **(A)** The KEGG pathways related to innervation. **(B)** The KEGG pathways related to angiogenesis. **(C)** The KEGG pathways related to inflammation.

DISCUSSION

Neurovascularization within the non-calcified cartilage is a critical pathological change in OA (Mapp and Walsh, 2012; Li B. et al., 2021). In the present study, pathological neurovascularization was validated in TMJ-OA cartilage. Microarray analysis of genes from the condylar cartilage of TMJ identified 1817 significant DEGs between the control and UAC groups. Based on their functions, target genes involved in innervation, angiogenesis and inflammation were selected for further analyses. After enrichment analysis and PPI analysis, the robust interactions among innervation, angiogenesis and inflammation were confirmed in the condylar cartilage of TMJ-OA. Several other microarray analyses about osteoarthritis cartilage also supported our findings. One of which was carried out on IL-1β-stimulated chondrocytes to identify the potential biological processes in the progression of osteoarthritis (Liang et al., 2022). Similarly, they found DEGs were mainly enriched in these terms, including "inflammatory response", "blood vessel morphogenesis", "epithelial cell proliferation" and so on. However, different from our results, the terms about neurogenesis were not included in that research, which may because the subject of our research was cartilage from animal while that of their research was cultured chondrocyte. Another analysis about OA cartilage also found the changes in PI3K/Akt signaling pathway played an important role, which supporting our results (Li S. et al., 2021).

The contribution of angiogenesis to OA progression has been investigated extensively. Osteochondral angiogenesis was observed in mandibular condyles with OA-like changes, with concomitant local up-regulation of VEGF, connective tissue growth factor and matrix metalloprotease-9 (Wang et al., 2012). Growth factors such as Vegfa, Vegfb, Pdgf, and Angpt1 are promoters of angiogenesis (MacDonald et al., 2018); these factors were up-regulated in OA cartilage and down-regulated in the control. Both VEGFa and VEGFb are members of the VEGF family. These angiogenesis regulators act on endothelial cells and pericytes around blood vessels. Platelet-derived growth factor (PDGF), a pro-angiogenic factor derived from preosteoclasts in the subchondral bone, directly induces proliferation of endothelial cells to form type H vessels and stimulates VEGF secretion (Su et al., 2020). Angiopoietin 1 (ANGPT1) is a vascular growth factor that controls endothelial sprouting by regulating vascular stability. It interacts with tyrosine-protein kinase receptor 2 (TIE2) to activate several signaling pathways, including the PI3K/AKT pathway, to ensure endothelial

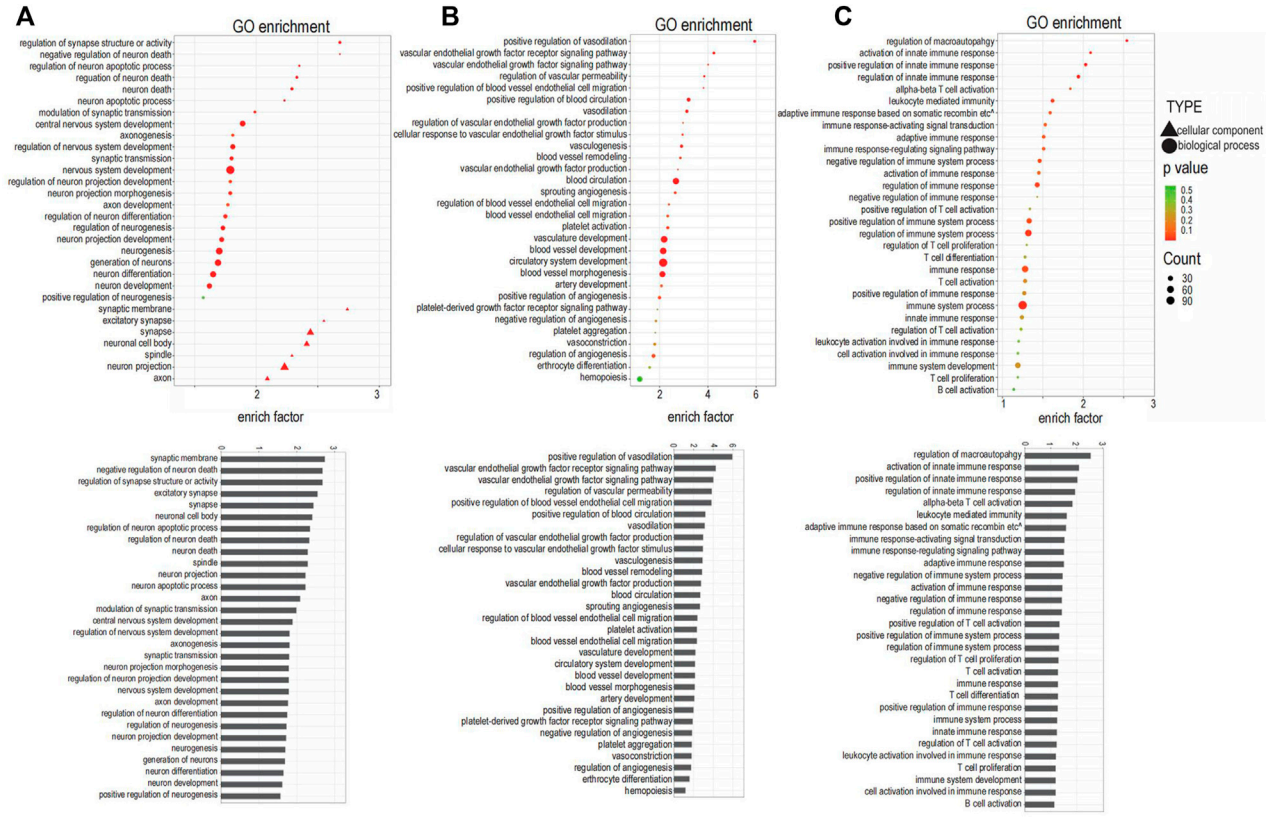

FIGURE 3 | Gene Ontology (GO) analysis enriched for the targeted genes. **(A)** GO terms related to innervation. **(B)** GO terms related to angiogenesis. **(C)** GO terms related to inflammation.

survival and junctional stability (Saharinen et al., 2017). With the use of KEGG analysis, the MAPK, HIF-1 and nuclear factor-kappa B (NF-κB) signaling pathways were significantly enriched in the DEGs. Regulated by the MAPK and NF-κB pathways, HIF-1α upregulates VEGFa expression and promotes type H vessel formation (Fernandez et al., 2017). Hence, the present data confirm that angiogenesis is involved in TMJ-OA progression. Because angiogenesis contributes to synovitis, osteochondral damage, and osteophyte formation in patients with TMJ-OA, inhibition of angiogenesis is potentially useful for treatment of TMJ-OA.

Infiltration of sensory nerves and sympathetic nerves through the osteochondral junction into cartilage occurs after inflammation and angiogenesis in TMJ-OA (Zylinska et al., 2021). Subchondral bone deterioration through increased bone remodeling and nerve sprouting has been identified in the osteochondral junction of osteoarthritic joints and is closely associated with osteoarthritic pain in OA rats (Sun J.-l. et al., 2020). Although the role of sensory nerves and sympathetic nerves in OA has been well demonstrated, pathological innervation in TMJ-OA cartilage requires further studies. The present study demonstrated up-regulation of *Ngfr* in the condylar cartilage of TMJ-OA. This factor induces pain through amplified proliferation of sensory neurons that alter the pain threshold (Jiang et al., 2015). Others reported that gene deletion of NGF produced pain-palliative effects (Zhao et al., 2019). Apart from innervation, NGF/NGFR also stimulates the expression of VEGF and promotes vascular growth. This accounts for the link between angiogenesis and innervation in TMJ-OA. Examination of articular cartilages harvested from healthy and OA patients identified that NGF increased angiogenesis by promoting the expression of FGF2 via PI3K/Akt and ERK/MAPK signaling pathways (Yu et al., 2019). Identification of the up-regulation of *Adrb2* and *Adra2a* genes in the UAC group is indicative of the penetration of sympathetic nerve fibers into the cartilage during TMJ deterioration. Further studies are needed to confirm this finding and clarify the role of pathological innervation in TMJ-OA cartilage.

Because the interactions among innervation, angiogenesis and inflammation contribute to structural damage and pain in TMJ-OA, interception of these interactions offer potential conduits for relieve of symptoms and prevent joint pathology in TMJ-OA. For example, inhibiting inflammation and reducing cartilage innervation produce direct symptomatic benefits for OA patients. Inhibition of angiogenesis reduces pain by moderating each of these pathological processes. Apart from targeting the nervous system, potential nano-therapies that target blood vessels or inflammation also help to relieve pain symptoms (Li X. et al., 2021). Although treatment strategies that individually target angiogenesis (Li et al., 2019; Yajun et al., 2021),

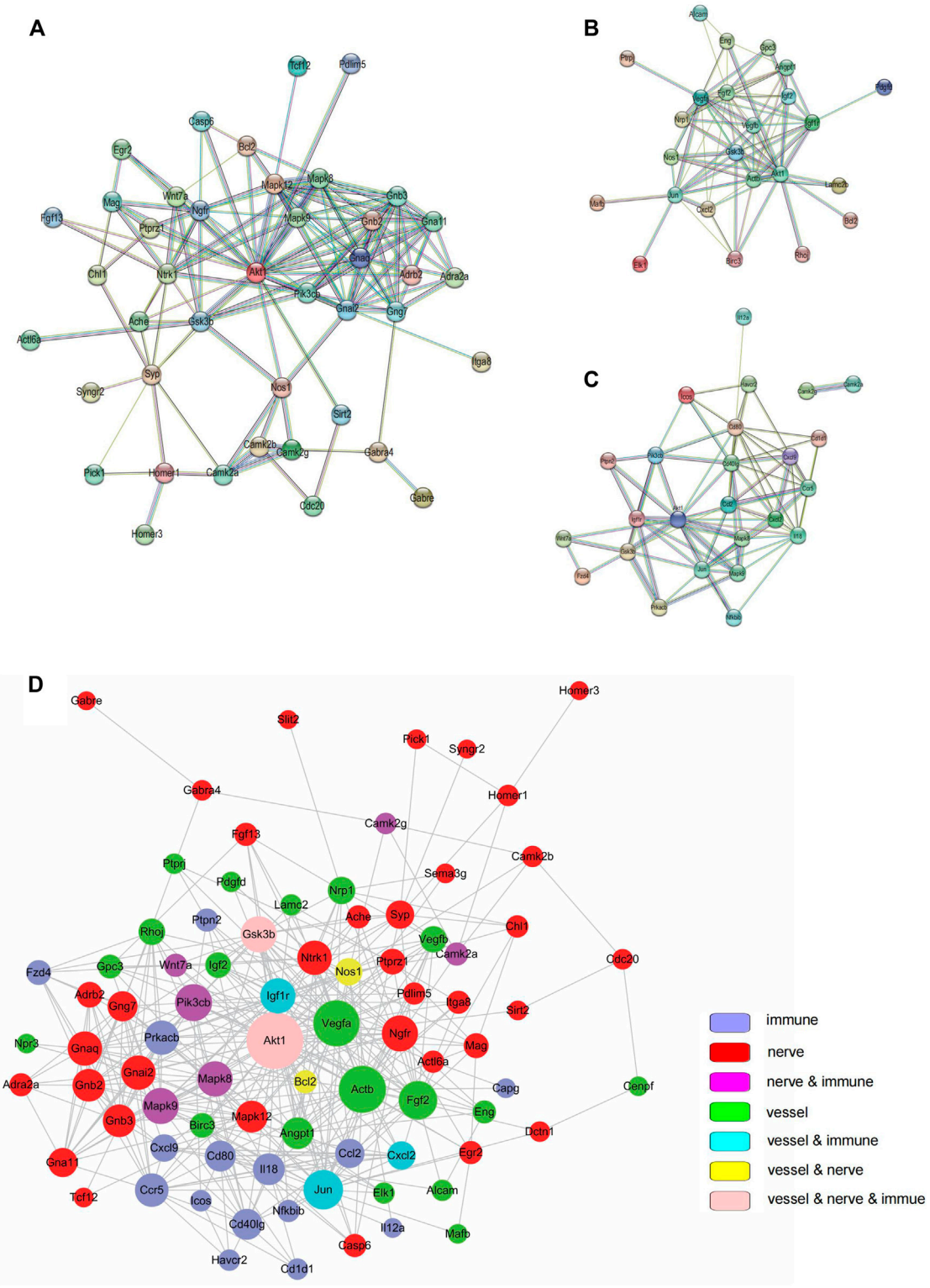

FIGURE 4 | Protein-protein interaction (PPI). **(A)** PPI among genes related to innervation. **(B)** PPI angiogenesis related to angiogenesis. **(C)** PPI among genes related to inflammation. **(D)** PPI among all targeted genes. In **(A–C)**, PPIs were determined with STRING software. In **(D)**, PPI was determined using the Cytoscape software.

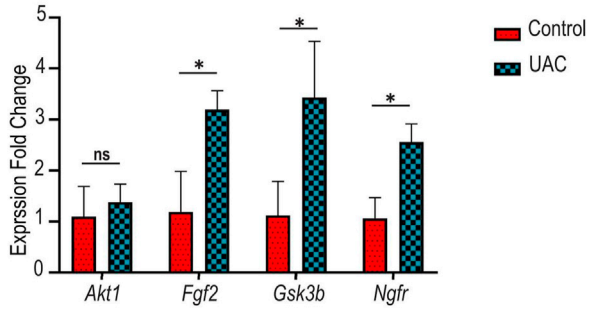

FIGURE 5 | Gene expression patterns of v-akt murine thymoma viral oncogene homolog 1 (*Akt1*), fibroblast growth factor 2 (*Fgf2*), glycogen synthase kinase 3 beta (*Gsk3b*) and nerve growth factor receptor (*Ngfr*). Evaluated was performed with quantitative real-time polymerase chain reaction (qRT-PCR). ns indicates $p > 0.013$ (after Bonferroni correction of familywise error rate, * indicates $p < 0.013$. Analyses were performed using paired t-tests.

pain or inflammation (Lee et al., 2014; Bhalekar et al., 2016) are casually effective in alleviating OA symptoms, therapies that explicitly target the crosstalk among innervation, angiogenesis and inflammation may potentially become the therapeutic target of the future.

The gene expression profiles of TMJ-OA identified in the present study may not completely match those reported by other studies. This may be attributed to the limitations inherent in the present study. These results we obtained were merely based on limited sample size (four in each group), leading to difficulty in excluding false positive. With the development of scientific technology, bulk RNA-sequencing, single-cell RNA-sequencing and spatial transcriptomics have become feasible over the last few years. These timely techniques have become extremely popular assays for transcriptome measurements. In the future, high-throughput sequencing technology should be applied to examine the mechanism of TMJ-OA. It is imperative to mention that differences exist between animal models and human versions of TMJ-OA. Results obtained from animal models should be tested prior to their translation for treatment of human diseases.

In conclusion, the highly interactive crosstalk among innervation, angiogenesis and inflammation in the condylar cartilage is a contributor to disease progression in TMJ-OA. This crosstalk offers possible directions for future research on therapeutics to address TMJ-OA.

DATA AVAILABILITY STATEMENT

The datasets presented in this study can be found in online repositories. The names of the repository/repositories and accession number(s) can be found in the article/ **Supplementary Material**.

ETHICS STATEMENT

The animal study was reviewed and approved by the Institutional Animal Care and Use Committee of Air Force Medical University.

AUTHOR CONTRIBUTIONS

WQ, ZZ and JY contributed equally to conduction of experiments, data acquisition, data analysis and manuscript drafting. WQ, ZZ, XH and JY contributed to conception, design, data acquisition and interpretation, performed statistical analyses. KJ, LN contributed to conception, design and critically revised the manuscript. All authors approved the final version of the manuscript.

FUNDING

The study was supported by National Natural Science Foundation of China to KJ (81870787, 82170978) and Distinguished Young Scientists Funds of Shaanxi Province (2021JC-34).

SUPPLEMENTARY MATERIAL

The Supplementary Material for this article can be found online at: https://www.frontiersin.org/articles/10.3389/fbioe.2022.901749/full#supplementary-material

REFERENCES

Bhalekar, M. R., Upadhaya, P. G., and Madgulkar, A. R. (2016). Fabrication and Efficacy Evaluation of Chloroquine Nanoparticles in CFA-Induced Arthritic Rats Using TNF-α ELISA. *Eur. J. Pharm. Sci.* 84, 1–8. doi:10.1016/j.ejps.2016.01.009

Chen, L., Yao, F., Wang, T., Li, G., Chen, P., Bulsara, M., et al. (2020). Horizontal Fissuring at the Osteochondral Interface: a Novel and Unique Pathological Feature in Patients with Obesity-Related Osteoarthritis. *Ann. Rheum. Dis.* 79 (6), annrheumdis–2020. doi:10.1136/annrheumdis-2020-216942

Fernández, J. T., Zamudio, Y. C., Martínez, G. A. N., and López, A. G. R. (2017). Hypoxia-Inducible Factors (HIFs) in the Articular Cartilage: a Systematic Review. *Eur. Rev. Med. Pharmacol. Sci.* 21 (12), 2800–2810.

Findlay, D. M., and Kuliwaba, J. S. (2016). Bone-cartilage Crosstalk: a Conversation for Understanding Osteoarthritis. *Bone. Res.* 4 (03), 121–132. doi:10.1038/boneres.2016.28

Hu, Y., Chen, X., Wang, S., Jing, Y., and Su, J. (2021). Subchondral Bone Microenvironment in Osteoarthritis and Pain. *Bone. Res.* 9 (1), 20. doi:10.1038/s41413-021-00147-z

Jiang, Y., Hu, C., Yu, S., Yan, J., Peng, H., Ouyang, H. W., et al. (2015). Cartilage Stem/progenitor Cells Are Activated in Osteoarthritis via Interleukin-1β/nerve Growth Factor Signaling. *Arthritis Res. Ther.* 17 (1), 327. doi:10.1186/s13075-015-0840-x

Jiao, K., Niu, L., Xu, X., Liu, Y., Li, X., Tay, F. R., et al. (2015). Norepinephrine Regulates Condylar Bone Loss via Comorbid Factors. *J. Dent. Res.* 94 (6), 813–820. doi:10.1177/0022034515577677

Jiao, K., Zeng, G., Niu, L.-N., Yang, H.-x., Ren, G.-t., Xu, X.-y., et al. (2016). Activation of α2A-adrenergic Signal Transduction in Chondrocytes Promotes

Degenerative Remodelling of Temporomandibular Joint. *Sci. Rep.* 6, 30085. doi:10.1038/srep30085

Jin, T., Wu, D., Liu, X.-M., Xu, J.-T., Ma, B.-J., Ji, Y., et al. (2020). Intra-articular Delivery of Celastrol by Hollow Mesoporous Silica Nanoparticles for pH-Sensitive Anti-inflammatory Therapy against Knee Osteoarthritis. *J. Nanobiotechnol* 18 (1), 94. doi:10.1186/s12951-020-00651-0

Kanehisa, M., Sato, Y., Furumichi, M., Morishima, K., and Tanabe, M. (2019). New Approach for Understanding Genome Variations in KEGG. *Nucleic Acids Res.* 47 (D1), D590–D595. doi:10.1093/nar/gky962

Lee, H., Lee, M.-Y., Bhang, S. H., Kim, B.-S., Kim, Y. S., Ju, J. H., et al. (2014). Hyaluronate-gold Nanoparticle/tocilizumab Complex for the Treatment of Rheumatoid Arthritis. *ACS. Nano.* 8 (5), 4790–4798. doi:10.1021/nn500685h

Li, B., Guan, G., Mei, L., Jiao, K., and Li, H. (2021a). Pathological Mechanism of Chondrocytes and the Surrounding Environment during Osteoarthritis of Temporomandibular Joint. *J. Cel. Mol. Med.* 25 (11), 4902–4911. doi:10.1111/jcmm.16514

Li, S., Wang, H., Zhang, Y., Qiao, R., Xia, P., Kong, Z., et al. (2021c). COL3A1 and MMP9 Serve as Potential Diagnostic Biomarkers of Osteoarthritis and Are Associated with Immune Cell Infiltration. *Front. Genet.* 12, 721258. doi:10.3389/fgene.2021.721258

Li, X., Dai, B., Guo, J., Zheng, L., Guo, Q., Peng, J., et al. (2021b). Nanoparticle-cartilage Interaction: Pathology-Based Intra-articular Drug Delivery for Osteoarthritis Therapy. *Nano-micro Lett.* 13 (1), 149. doi:10.1007/s40820-021-00670-y

Li, Y., Mu, W., Xu, B., Ren, J., Wahafu, T., Wuermanbieke, S., et al. (2019). Artesunate, an Anti-malaria Agent, Attenuates Experimental Osteoarthritis by Inhibiting Bone Resorption and CD31hiEmcnhi Vessel Formation in Subchondral Bone. *Front. Pharmacol.* 10, 685. doi:10.3389/fphar.2019.00685

Liang, F., Peng, L., Ma, Y.-G., Hu, W., Zhang, W.-B., Deng, M., et al. (2022). Bioinformatics Analysis and Experimental Validation of Differentially Expressed Genes in Mouse Articular Chondrocytes Treated with IL-1β U-sing M-icroarray D-ata. *Exp. Ther. Med.* 23 (1), 6. doi:10.3892/etm.2021.10928

Ma, Y.-X., Jiao, K., Wan, Q.-Q., Li, J., Liu, M.-Y., Zhang, Z.-B., et al. (2022). Silicified Collagen Scaffold Induces Semaphorin 3A Secretion by Sensory Nerves to Improve *In-Situ* Bone Regeneration. *Bioactive Mater.* 9, 475–490. doi:10.1016/j.bioactmat.2021.07.016

MacDonald, I., Liu, S.-C., Su, C.-M., Wang, Y.-H., Tsai, C.-H., and Tang, C.-H. (2018). Implications of Angiogenesis Involvement in Arthritis. *Ijms* 19 (7), 2012. doi:10.3390/ijms19072012

Mapp, P. I., and Walsh, D. A. (2012). Mechanisms and Targets of Angiogenesis and Nerve Growth in Osteoarthritis. *Nat. Rev. Rheumatol.* 8 (7), 390–398. doi:10.1038/nrrheum.2012.80

Marrella, A., Lee, T. Y., Lee, D. H., Karuthedom, S., Syla, D., Chawla, A., et al. (2018). Engineering Vascularized and Innervated Bone Biomaterials for Improved Skeletal Tissue Regeneration. *Mater. Today* 21 (4), 362–376. doi:10.1016/j.mattod.2017.10.005

Saharinen, P., Eklund, L., and Alitalo, K. (2017). Therapeutic Targeting of the Angiopoietin-TIE Pathway. *Nat. Rev. Drug Discov.* 16 (9), 635–661. doi:10.1038/nrd.2016.278

Shannon, P., Markiel, A., Ozier, O., Baliga, N. S., Wang, J. T., Ramage, D., et al. (2003). Cytoscape: a Software Environment for Integrated Models of Biomolecular Interaction Networks. *Genome Res.* 13 (11), 2498–2504. doi:10.1101/gr.1239303

Su, W., Liu, G., Liu, X., Zhou, Y., Sun, Q., Zhen, G., et al. (2020). Angiogenesis Stimulated by Elevated PDGF-BB in Subchondral Bone Contributes to Osteoarthritis Development. *JCI. Insight.* 5 (8), e135446. doi:10.1172/jci.insight.135446

Sun, J.-l., Yan, J.-f., Li, J., Wang, W.-r., Yu, S.-b., Zhang, H.-y., et al. (2020a). Conditional Deletion of Adrb2 in Mesenchymal Stem Cells Attenuates Osteoarthritis-like Defects in Temporomandibular Joint. *Bone* 133, 115229. doi:10.1016/j.bone.2020.115229

Sun, J. L., Yan, J. F., Yu, S. B., Zhao, J., Lin, Q. Q., and Jiao, K. (2020b). MicroRNA-29b Promotes Subchondral Bone Loss in TMJ Osteoarthritis. *J. Dent. Res.* 99 (13), 1469–1477. doi:10.1177/0022034520937617

Szklarczyk, D., Gable, A. L., Lyon, D., Junge, A., Wyder, S., Huerta-Cepas, J., et al. (2019). STRING V11: Protein-Protein Association Networks with Increased Coverage, Supporting Functional Discovery in Genome-wide Experimental Datasets. *Nucleic Acids Res.* 47 (D1), D607–d613. doi:10.1093/nar/gky1131

Wan, Q. Q., Qin, W. P., Ma, Y. X., Shen, M. J., Li, J., Zhang, Z. B., et al. (2021). Crosstalk between Bone and Nerves within Bone. *Adv. Sci.* 8 (7), 2003390. doi:10.1002/advs.202003390

Wang, Q.-Y., Dai, J., Kuang, B., Zhang, J., Yu, S.-B., Duan, Y.-Z., et al. (2012). Osteochondral Angiogenesis in Rat Mandibular Condyles with Osteoarthritis-like Changes. *Arch. Oral Biol.* 57 (6), 620–629. doi:10.1016/j.archoralbio.2011.12.006

Yajun, W., Jin, C., Zhengrong, G., Chao, F., Yan, H., Weizong, W., et al. (2021). Betaine Attenuates Osteoarthritis by Inhibiting Osteoclastogenesis and Angiogenesis in Subchondral Bone. *Front. Pharmacol.* 12, 723988. doi:10.3389/fphar.2021.723988

Yu, X., Qi, Y., Zhao, T., Fang, J., Liu, X., Xu, T., et al. (2019). NGF Increases FGF2 Expression and Promotes Endothelial Cell Migration and Tube Formation through PI3K/Akt and ERK/MAPK Pathways in Human Chondrocytes. *Osteoarthritis and Cartilage* 27 (3), 526–534. doi:10.1016/j.joca.2018.12.007

Zhao, L., Huang, J., Fan, Y., Li, J., You, T., He, S., et al. (2019). Exploration of CRISPR/Cas9-based Gene Editing as Therapy for Osteoarthritis. *Ann. Rheum. Dis.* 78 (5), 676–682. doi:10.1136/annrheumdis-2018-214724

Zhu, S., Zhu, J., Zhen, G., Hu, Y., An, S., Li, Y., et al. (2019). Subchondral Bone Osteoclasts Induce Sensory Innervation and Osteoarthritis Pain. *J. Clin. Invest.* 129 (3), 1076–1093. doi:10.1172/JCI121561

Żylińska, B., Sobczyńska-rak, A., Lisiecka, U., Stodolak-Zych, E., Jarosz, Ł., and Szponder, T. (2021). Structure and Pathologies of Articular Cartilage. *In Vivo* 35 (3), 1355–1363. doi:10.21873/invivo.12388

Conflict of Interest: The authors declare that the research was conducted in the absence of any commercial or financial relationships that could be construed as a potential conflict of interest.

Publisher's Note: All claims expressed in this article are solely those of the authors and do not necessarily represent those of their affiliated organizations, or those of the publisher, the editors and the reviewers. Any product that may be evaluated in this article, or claim that may be made by its manufacturer, is not guaranteed or endorsed by the publisher.

frontiers | Frontiers in Materials

ORIGINAL RESEARCH
published: 17 May 2022
doi: 10.3389/fmats.2022.914994

Conductive GelMA/PEDOT: PSS Hybrid Hydrogel as a Neural Stem Cell Niche for Treating Cerebral Ischemia-Reperfusion Injury

Yilei Zhang[1,2,3†], Meimei Zhang[1,2†], Runlin Zhang[4†], Haining Liu[1,2], Hui Chen[1,2], Xiaofeng Zhang[1,2], Chen Li[1,2,5], Qing Zeng[1,2], Yunhua Chen[4*] and Guozhi Huang[1,2*]*

[1]Department of Rehabilitation Medicine, Zhujiang Hospital, Southern Medical University, Guangzhou, China, [2]School of Rehabilitation Medicine, Southern Medical University, Guangzhou, China, [3]Department of Neurorehabilitation Medicine, Xiangya Boai Rehabilitation Hospital, Changsha, China, [4]School of Materials Science and Engineering, South China University of Technology, Guangzhou, China, [5]Department of Rehabilitation Medicine, Hunan Provincial People's Hospital, Hunan Normal University, Changsha, China

OPEN ACCESS

Edited by:
Mingqiang Li,
Third Affiliated Hospital of Sun Yat-sen University, China

Reviewed by:
Gao Liang,
Guangdong University of Technology, China
Wei Wang,
Tianjin University, China
Huanan Wang,
Dalian University of Technology, China

***Correspondence:**
Qing Zeng
zengqingyang203@126.com
Yunhua Chen
msyhchen@scut.edu.cn
Guozhi Huang
drhuang66@163.com

†These authors have contributed equally to this work

Specialty section:
This article was submitted to Biomaterials, a section of the journal Frontiers in Materials

Received: 07 April 2022
Accepted: 21 April 2022
Published: 17 May 2022

Citation:
Zhang Y, Zhang M, Zhang R, Liu H, Chen H, Zhang X, Li C, Zeng Q, Chen Y and Huang G (2022) Conductive GelMA/PEDOT: PSS Hybrid Hydrogel as a Neural Stem Cell Niche for Treating Cerebral Ischemia-Reperfusion Injury. Front. Mater. 9:914994. doi: 10.3389/fmats.2022.914994

Cerebral ischemia and the subsequent cerebral ischemia-reperfusion (I/R) injury usually result in neuronal impairment with serious disabilities. Although neural stem cell (NSC) transplantation can help with functional recovery after stroke, due to the improper cellular milieu after brain injury, direct NSC transplantation will result low cell survival rates and differentiation efficiency into neurons. Here a conductive hybrid hydrogel based on gelatin methacryloyl (GelMA) and poly(3,4-ethylenedioxythiophene): poly (styrene sulfonate) (PEDOT:PSS) was created as a NSC niche for the treatment of cerebral I/R injury. GelMA/PEDOT:PSS hybrid hydrogel promoted the development of NSCs into neurons. GelMA/PEDOT:PSS hydrogel along with NSCs could enhance neuronal activity and minimize apoptosis when co-cultured with oxygen-glucose deprivation/reperfusion (OGD/R) neurons. Furthermore, after 7 days of implantation, GelMA/PEDOT:PSS/NSCs on the infarcted brain of rats subjected to reperfusion injury after middle cerebral artery occlusion (MCAO) was verified to attenuate inflammatory responses. These findings show that the conductive GelMA/PEDOT:PSS hybrid hydrogel could regulate NSC development and act as promising cell niches for the treatment of cerebral I/R injury.

Keywords: conductive hybrid hydrogel, neural stem cells, 3D culture, cell differentiation, cerebral ischemiareperfusion injury

1 INTRODUCTION

Stroke, cerebral ischemia infarction in particular, is rapidly becoming the main global cause of long-term disability and mortality globally (Naghavi et al., 2017; Tuo et al., 2022). Despite its high prevalence, patients with ischemic stroke have limited therapy options. During the acute stroke period, tissue plasminogen activator and rapid recanalization (thrombectomy) are still being used. However, due to the short therapeutic window and significant risk of intracerebral hemorrhage, individuals who have suffered a stroke cannot just rely on these therapies (Fann et al., 2013; Stonesifer et al., 2017). It is generally believed that the ideal treatment for cerebral infarction should involve replacing the damaged neurons and promoting the proliferation and differentiation of neural stem cells (NSCs), thus improving the patient outcomes (Felling and Song 2015).

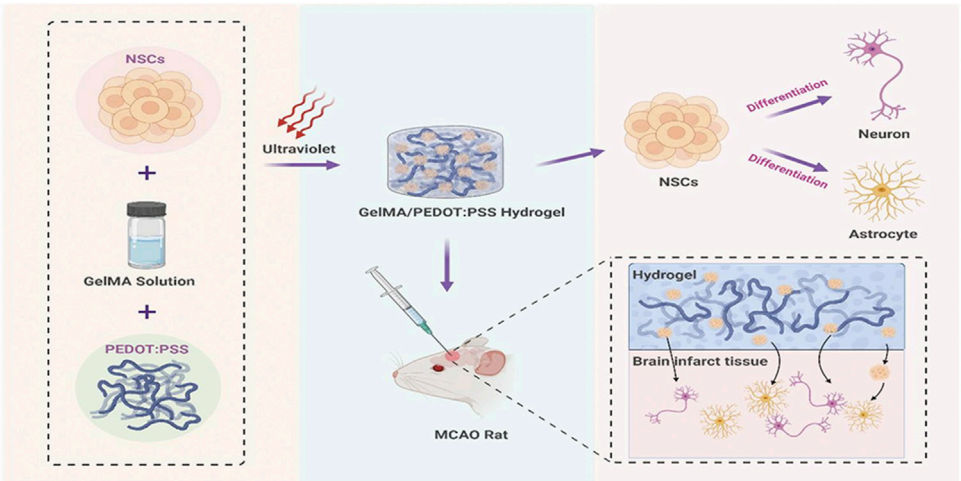

FIGURE 1 | Scheme. Conductive GelMA/PEDOT:PSS hybrid hydrogel to promote NSCs differentiation and treat cerebral I/R injury.

NSC therapy has emerged as a cutting-edge therapeutic technique in recent years. Cell differentiation, cell replacement, immune regulation, neural network repair, and nutritional factor release are mechanisms by which NSC transplantation enhances stroke prognosis (Zhou et al., 2021). NSCs delivery in the early stroke phase attenuates this complex inflammatory signaling cascade (Bacigaluppi et al., 2009; De Feo et al., 2012). NSCs ameliorate ischemic damage by lowering pro-inflammatory mediators including TNF-α, IL-1β, IL-6, MCP-1, and iba-1(Huang and Zhang 2019). However, NSC transplantation has not yet produced the expected therapeutic results (Burns and Quinones-Hinojosa 2021). One possible reason for its low effectiveness of this method can be the limited survival of transplanted NSCs in the damaged cerebral areas. The transplanted cells do not get integrated into the host system and differentiate quickly into neurons (Tang et al., 2015). This could primarily occur owing to an unfavorable environment for transplanted NSCs in the infarcted brain after a stroke (Ju et al., 2014).

Interestingly, various biomaterial scaffolds have been used to support stem cell therapy. Hydrogels were used to help with tissue repair and regeneration in the central nervous system (CNS) (Woerly 1993). For example, the potential of gelatin methacryloyl (GelMA) in facilitating cell adhesion and proliferation, for example, has been established, and it is now considered a suitable biological material for three dimensional (3D) varied cell cultures (Wang et al., 2017; Ning et al., 2020). Conducting polymers, on the other hand, have been used in neural recovery because endogenous bioelectric signals are critical for maintaining neuronal function, neurite growth, and secretion of neurotrophic factors (Lee et al., 2009; Levin et al., 2017). However, the biological application of conductive polymers has been limited due to drawbacks such as low processability, hydrophobicity, and poor degradability. The most common method for overcoming these drawbacks is to combine the benefits of both materials (Balint et al., 2014). Dissolvable inert particles (Yang and Martin 2004) and biodegradable polymer fibers, for example, can be used as a template for conducting polymers (Abidian et al., 2006). Because of its better electrical conductivity and chemical stability, poly(3,4-ethylenedioxythiophene)-poly(styrenesulfonate) (PEDOT: PSS), a derivative of polythiophene, is one of the most promising conductive polymers. PEDOT: PSS in a soft hydrogel matrix has been proven to improve dorsal root ganglion differentiation (Fitria 2019). It would be appealing to combine GelMA and PEDOT: PSS to generate a conductive hydrogel to be used as a NSCs niche to promote its differentiation. However, to the best of our knowledge, there is no such study in this regard. Moreover, the neuroprotective effect of hydrogel in combination with NSCs on oxygen-glucose depribation/reperfusion (OGD/R) neurons as well as on cerebral I/R injury remain unidentified.

In this study, a conductive GelMA/PEDOT: PSS hybrid hydrogel has been developed under photo-initiated polymerization and more importantly utilized as NSCs niche to stimulate neuron development and treat cerebral I/R injury (**Figure 1**). The *in vitro* results demonstrated that the hybrid hydrogel with good biocompatibility might stimulate differentiation in NSCs into neurons. When co-cultured with OGD/R neurons, NSCs embedded in the GelMA/PEDOT:PSS hydrogel showed neuroprotective benefits. Furthermore, following 7 days of implantation, the GelMA/PEDOT:PSS/NSCs significantly reduced inflammatory responses in a rat model of middle cerebral artery occlusion (MCAO), even showed the function of protecting damaged neurons, suggesting that the conductive GelMA/PEDOT:PSS hydrogel could serve as a promising NSC niche for the treatment of cerebral I/R injury.

2 MATERIALS AND METHODS

2.1 Hydrogel Preparation and Characterization

2.1.1 Materials

GelMA was purchased from Yongqin-Quan Intelligent Equipment Co., Ltd. (Suzhou, China). PEDOT:PSS was

provided by Sigma-Aldrich. Lithium Phenyl(2,4,6-trimethylbenzoyl)phosphinate (LAP) has already embed in the GelMA hydrogel by Yongqin-Quan Intelligent Equipment Co., Ltd. Other reagents are of analytical grade and are used as received.

2.1.2 Gelatin Methacryloyl/ Poly(3,4-Ethylenedioxythiophene): Poly (Styrene Sulfonate) Hydrogel Preparation

PEDOT:PSS was ultrasonically dissolved in PBS at varying concentrations (0%, 0.005%, 0.01%, and 0.015% w/v). The mixture (1 ml) was then agitated at 40°C with 60 mg of GelMA. Finally, the GelMA/PEDOT:PSS hydrogels were set for 18 s under Ultraviolet light (UV) light (405 nm). GelMA, GelMA/PEDOT:PSS50, GelMA/PEDOT:PSS100, and GelMA/PEDOT:PSS150 represented hydrogels with PEDOT:PSS concentrations of 0%, 0.005%, 0.01%, and 0.015% w/v.

2.1.3 Gelatin Methacryloyl/ Poly(3,4-Ethylenedioxythiophene): Poly (Styrene Sulfonate) Hydrogel Morphology

Scanning electron microscopy (SEM, FEI Q25) was used to investigate the macroporous structure of lyophilized GelMA/PEDOT: PSS hydrogels. The fracture surface of hydrogels was detected under SEM after gold sputtering.

2.1.4 Compressive Mechanical Properties

Compressive stress-strain of the hydrogels was tested using a dynamic mechanical analyzer (DMA Q800, United States). Compression and compressive cycle tests were performed on cylindrical hydrogel samples (8-mm diameter and 10-mm thickness). Compression testing was conducted in a strain control mode at a linear rate of 50% per minute from 0% to 100%, whereas compression cycle testing was repeated 10 times at a strain rate of 100% per minute in the strain range of 0%–30%.

2.1.5 Conductivity Measurement

A Fluke F17B+ digital multimeter was used to study the electrical conductivity of GelMA/PEDOT: PSS hydrogels (Guangzhou Ruice Electronic Technology Co., Ltd.). The conductivity was computed using the following formula: $\sigma = l/R \times S$, where l is the hydrogels' height, R is the hydrogels' resistance, and S is the hydrogels' contacting area. The hydrogel resistance was determined by calculating the average of three measurements.

2.2 Cell Viability and Proliferation Analysis

As previously stated, NSCs were extracted from the embryonic brains of Sprague-Dawley rats (gestation days 13–15; provided by the Experimental Animal Center of South Medical University in China) (Zhou et al., 2020). NSCs encased in a variety of PEDOT: On day 3, 5, and 7, PSS concentrations of GelMA solution were employed in a CCK-8 assay to determine proliferation. Briefly, a hydrogel precursor comprising 6% GelMA was dissolved in PBS and combined with PEDOT: PSS in varying concentrations (0%, 0.005%, 0.01%, and 0.015% w/v). The absorbance OD value at 450 nm was measured using a microplate reader. Cells planted in GelMA hydrogels were used as conrtols. The viability of NSCs was determined using LIVE/DEAD dyes (Apexbio, Suzhou, China) in accordance with the manufacturer's instructions, and a Leica THUNDER Imager DM18 was used to capture images under a microscope.

2.3 *In Vitro* Immunocytochemistry

Immunocytochemical analysis was performed to examine the differentiation of NSCs encapsulated within the 3D GelMA/PEDOT:PSS hydrogels, as previously described (Wang et al., 2018). Briefly, NSCs (1×10^5) were co-cultured in 24-well plates each well using various GelMA/PEDOT:PSS hydrogels. On day 7, the NSCs in the hydrogels were fixed for 15 min at room temperature with 4% formaldehyde. The cells were incubated in PBS containing 0.1% TritonX-100 for 5 min at room temperature and permeabilized with 10% serum for 1 h at room temperature. The samples were then incubated overnight with MAP2 and GFAP as primary antibodies at 4°C. After three gentle washes with PBS, secondary antibodies were incubated with the sample for 2 h at room temperature in the dark. The cells were finally stained with DAPI after three gentle washes with PBS.

2.4 Gene Expression Analysis

As previously stated, the expression levels of NSCs cultured for 7 days in different hydrogel concentrations were examined using quantitative reverse transcription-polymerase chain reaction (qRT-PCR) (Lu et al., 2018). To release the contained NSCs, the hydrogels were first decomposed in a 0.3 mg/ml GelMA pyrolysis liquid solution (Yongqin-Quan Intelligent Equipment Co., Ltd., China). RNAiso Plus was then used to extract the total RNA from the NSCs (TaKaRa, Japan). A PrimeScript RT reagent Kit with a gDNA Eraser was used to conduct the cDNA reverse transcription reaction (Accurate Biotechnology Co., Ltd.). The SYBR Green Premix Pro Taq HS qPCR Kit was used to perform qPCR (Accurate Biotechnology Co., Ltd.). The primers were manufactured by Sangon Biotech (Shanghai, China), and the NSC primer sequences for β tubulin-III, MAP2, and GFAP are listed in **Table 1**. As an internal control, glyceraldehyde 3-phosphate dehydrogenase (GAPDH) was used.

2.5 Co-Culturing Oxygen-Glucose Deprivation/Reperfusion Neurons and Gelatin Methacryloyl/ Poly(3,4-Ethylenedioxythiophene): Poly (Styrene Sulfonate)/Neural Stem Cell

Based on previous research, primary neurons were extracted from 16 to 18-days old embryonic mouse brains cortex (Lin et al., 2020) and seeded on poly-L-lysine (Sigma–Aldrich)-coated plates (1.0×10^5 cells/mL). To simulate ischemia, the neurons were placed in a glucose-free Dulbecco's modified Eagle medium with 5% CO_2 and 1% O_2 for 2 h at 37°C after 7 days of normal culture (OGD). After OGD, the glucose-free medium was replaced with neurobasal media, and the mice were reintroduced to a normoxic incubator for 24 h to simulate reperfusion. The cells in the control group were cultured in a neurobasal medium and were not exposed to OGD/R (Spencer et al., 2018). To separate the neurons and hydrogel NSCs composites, transwell plates

TABLE 1 | The primer sequences for quantitative reverse transcription-polymerase chain reaction.

Rat Target Genes	Forward primers (5′–3′)	Reverse primers (5′–3′)
MAP2	AACATCCTCCGAGTCACCCTTCC	ATCTAGCATCTCAGGCAGGTCAGG
β-tubulin 3	CATGAAGGAGGTGATGACAGATG	GTTGCCGATGAAGGTGGACGAC
GFAP	CAGACCTCACAGACGTTGCTTCC	AGTTGGCGGCGATAGTCATTAGC
GAPDH	GGCACAGTCAAGGCTGAGAATG	ATGGTGGTGAAGACGCCAGTA

(Corning, United States) were used for co-culture. Primary cultured neurons were grown in the lower compartment. Following OGD/R or control treatment, NSCs (1×10^5 cells/ml), NSCs with GelMA, or NSCs with GelMA/PEDOT:PSS100 were co-cultured with neurons in the upper chamber. The neurons were harvested after 7 days of co-culture.

2.6 Hoechst 33342/Propidium Iodide Double Staining

The procedure of staining with Hoechst 33342 and propidium iodide (PI) was previously reported (Wang et al., 2018). Hoechst 33342 (Apexbio, Houston, TX, United States) was used to treat neurons, followed by PI (Apexbio, Houston, TX, United States) staining at 37°C for 15 min. Images were taken using an inverted fluorescent microscope (NIKON ECLIPSE Ti2-E), and the proportion of PI-positive cells was determined.

2.7 Histocompatibility of the Gelatin Methacryloyl/ Poly(3,4-Ethylenedioxythiophene): Poly (Styrene Sulfonate) Hybrid Hydrogel

An intraperitoneal dose of 1% pentobarbital sodium (30 mg/kg) was used to anesthetize normal Sprague-Dawley rats. The rats were shaved using a shaving knife after inducing anesthesia. The cerebral stereo positioning injection equipment was used to fix the sedated rats, and the ear rod was softly pushed into the external auditory canal. The top jaw was then fixed by inserting the upper front teeth of rats into the groove of the upper tooth fastening plate and tightening the screws. By measuring the placement needle, the anterior and posterior fontanelles are adjusted on the same sagittal line, and the anterior fontanelle (Bregma) and posterior fontanelle (Lambda) is maintained as horizontal as possible. To avoid infection, the head is disinfected with 75% alcohol. To corrode the meninges, cut 1.5 cm of the skin between the ears were cut using scissors and use 3% hydrogen peroxide was used. 20 μl of PBS, GelMA, GelMA/PEDOT:PSS100 (n = 4) subjecting to UV irradiation for 18 s, were then injected using microsyringes at the rate of 1 μl/min, respectively. A syringe with a 26 G needle was used to inject 10 μl into two distinct locations in the brain: AP + 2.3 mm, ML-3.0 mm, DV-2.3 mm and AP 0 mm, ML-3.0 mm, DV-2.3 mm (Tuladhar et al., 2020). The microsyringe was removed 5 min after the injection. After the rats were awakened, the skin incisions were cleansed using iodine and sutured; the animals were then returned to the feeding chamber. The biocompatibility of the conductive hydrogel injected into the brain was evaluated by hematoxylin and eosin (HE) staining of the brain tissue at 3 and 14 days following the injection. The samples were embedded in paraffin after paraformaldehyde cardiac perfusion fixing and dehydration. As per a previous study, the samples were sliced into 4-μm-thin cross-sections for HE staining (Ying et al., 2020).

2.8 Establishment of Middle Cerebral Artery Occlusion Model in Rats

The Southern Medical University Zhujiang Hospital Ethics Committee approved all procedures involving animals in this investigation. In a rat model of MCAO, male Sprague-Dawley rats (starting weight 250–280 g, Southern Medical University animal facility) were used, as previously described (Zhao et al., 2013). The neck hair was shaved after anesthesia, and the limbs were secured to the surgical table. Disinfect the neck skin and use scissors to make a 2 cm incision. To expose the common carotid artery and the bifurcation of the common carotid artery, the tissue surrounding the incision was torn bluntly. A suture thread was placed in a dead knot at the proximal end of the common carotid artery and a loose knot was used at the distal end of the common carotid artery to fix the threaded plug. Spring scissors were used to make an incision at the proximal end of the heart, tweezers were used to insert the threaded plug from the incision, and the external carotid artery was gently constricted using tweezers to protect the line plug. The thread plug was stopped when the black mark on the threaded plug reached the bifurcation of the common carotid artery. Indwelled sutures were used to secure the threaded plug. The body temperature was maintained by using the thermal insulation pads, and the suture plug was removed 90 min later and the surgical incision was sutured. Inclusion criteria for the MCAO model are as follows: After the rats were awake, the Longa score (She et al., 2019) was evaluated, and those with a score of 1–3 were chosen for the rest of the experiment.

2.9 Immunohistochemical Staining

After successfully establishing the MCAO rat model for 5 days, the rats were intraperitoneally with anesthetized using pentobarbital (30 mg/kg) and then mounted on a stereotaxic frame and injected with hydrogel (Liu et al., 2014). The rats were then injected with NSCs (5.0×10^6 cells/ml), NSCs mixed with GelMA/PEDOT:PSS100 hydrogels, or GelMA hydrogels, whereas the MCAO rats were treated with PBS (n = 4). The hydrogels and NSCs were fixed, mounted, flash-frozen, and sectioned after 7 days of implanting (Basara et al., 2021). Immunofluorescence labeling was performed on brain cryosections (10 μm thick) (Li et al., 2019). The primary antibodies were GFAP and iba1 (both from Abcam, Boston, MA, United States). The secondary antibodies were incubated

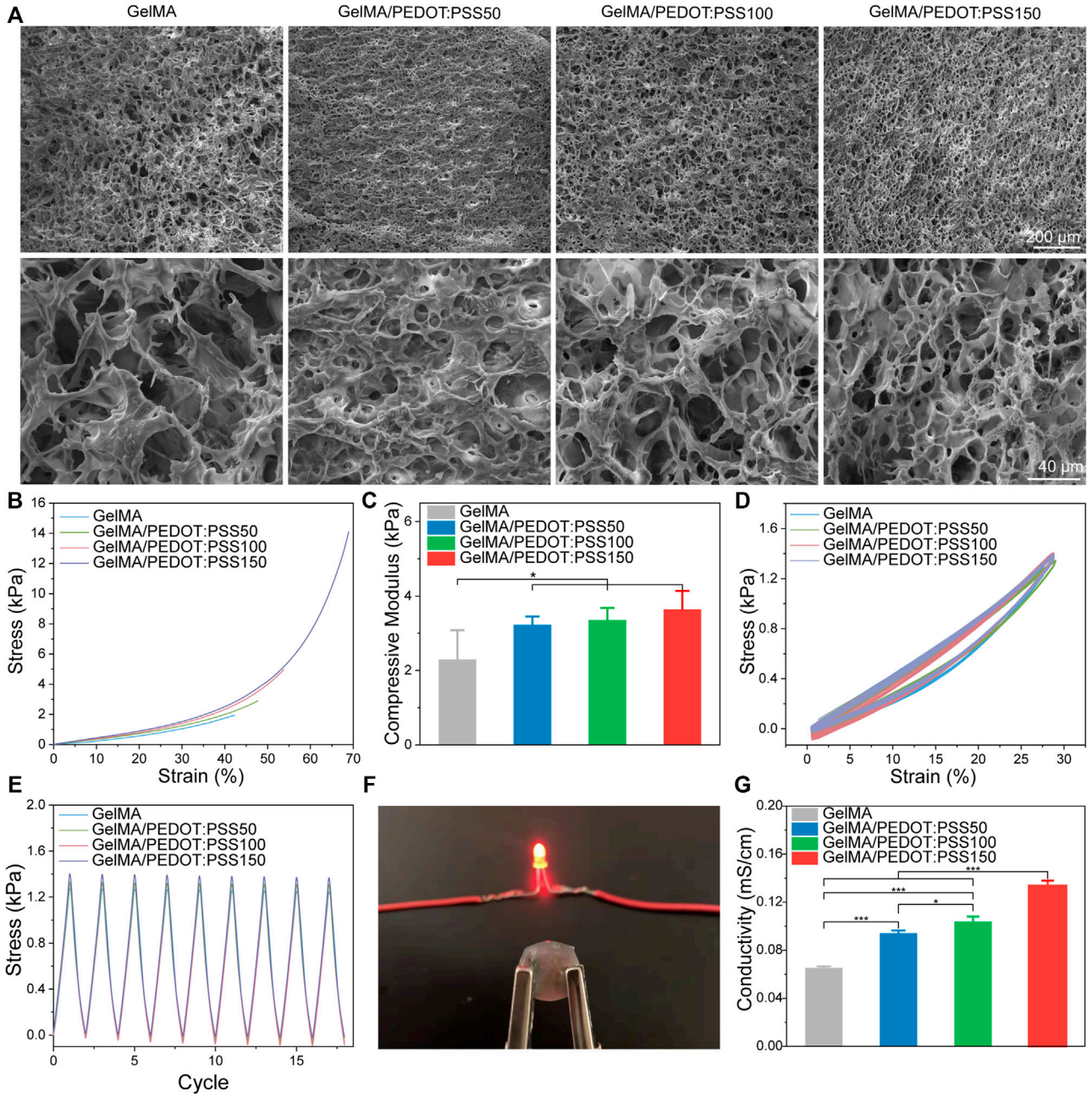

FIGURE 2 | Structural characterization and physical properties of GelMA/PEDOT: PSS hydrogels. **(A)** Internal porous morphology of GelMA/PEDOT:PSS hydrogels. **(B)** Representative compressive stress-strain curves. **(C)** Compressive moduli of GelMA/PEDOT: PSS hydrogels. **(D)** Loading-unloading curves of GelMA/PEDOT: PSS hydrogels at a strain of 30%. **(E)** Compressive stress was recovered to the initial state after repeated compression. **(F)** An LED bulb and GelMA/PEDOT: PSS100 hydrogel formed a closed circuit. **(G)** The conductivity of GelMA/PEDOT: PSS hydrogels. The data are expressed as mean ± standard deviation. $^{*}p < 0.05$, $^{**}p < 0.01$, $^{***}p < 0.001$.

with the sections for 2 h in the dark at room temperature before being gently washed three times. The nuclei were dyed for 10 min with DAPI (Solarbio, China) and then gently rinsed three times. A fluorescence microscope was used to image the slices (NIKON ECLIPSE Ti2-E). The number of regions with positive cells was counted using the ImageJ software.

2.10 Statistical Analyses

For statistical analysis, Graph Pad Prism software (version 8.0, CA) was used. All quantitative data were expressed as mean and ± standard deviation (SD). The findings were analyzed using one-way ANOVA, followed by Tukey's HSD post hoc test (for multiple groups).

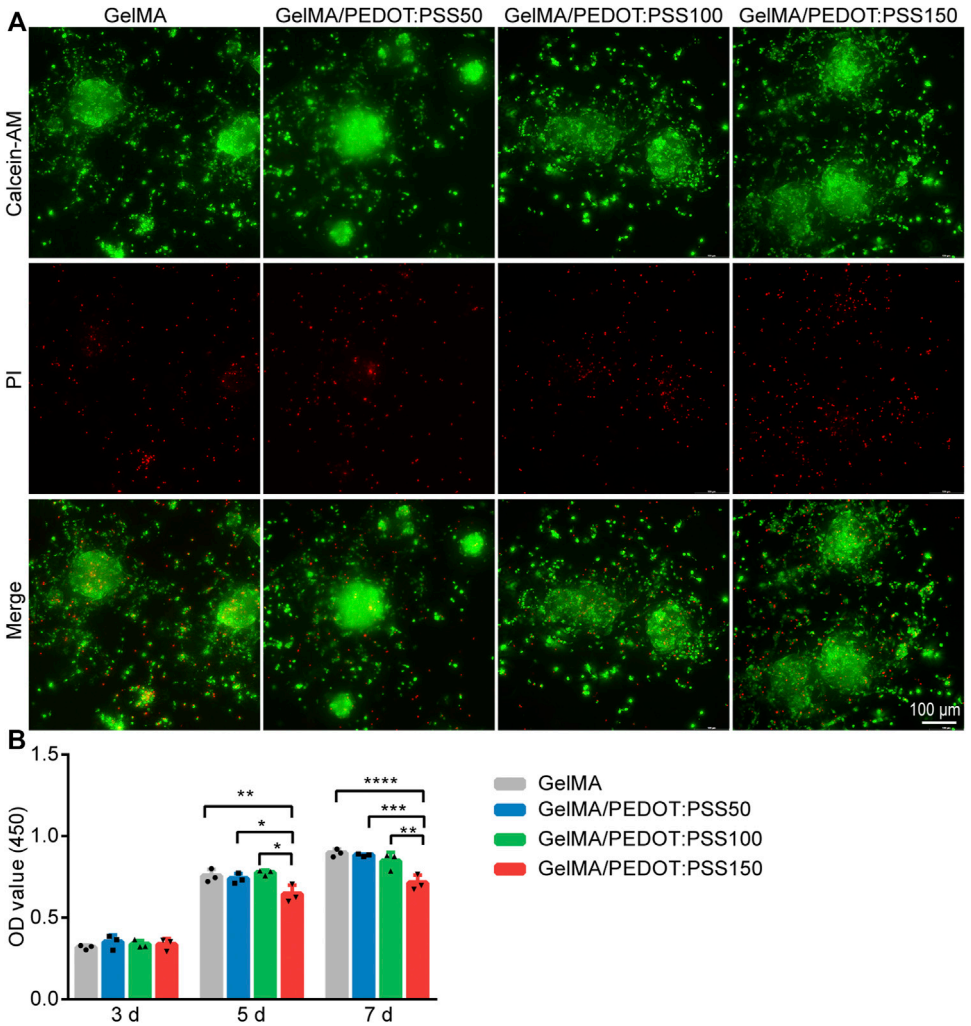

FIGURE 3 | NSC viability in the conductive GelMA/PEDOT: PSS hybrid hydrogels. **(A)** LIVE (green)/DEAD (red) NSC staining using Calcein-AM/PI staining after 7 days of culture. **(B)** Assessment of cell proliferation by the CCK-8 assay (n = 3), $^{*}p < 0.05$ $^{**}p < 0.01$ $^{***}p < 0.001$, and $^{****}p < 0.0001$.

3 RESULTS

3.1 Characterization of Conductive Gelatin Methacryloyl/ Poly(3,4-Ethylenedioxythiophene): Poly (Styrene Sulfonate) Hydrogels

GelMA/PEDOT:PSS hybrid hydrogels were facilely prepared by photo-initiation polymerization. **Figure 2A** presents the SEM images of the porous structure of GelMA/PEDOT:PSS hydrogels. The incorporation of PEDOT:PSS into the hydrogel matrices did not significantly affect the macroporous morphology of the lyophilized hydrogels. **Figure 2B** reveals how PEDOT: PSS increased the compressive stress and maximum strain of GelMA/PEDOT:PSS hydrogels. GelMA/PEDOT:PSS150 hydrogels showed a compressive stress of 14.1 kPa and a maximum strain of 68.9%, whereas GelMA hydrogels without PEDOT: PSS had compressive stress of 1.92 kPa and a maximum strain of 42.2%. **Figure 2C** shows that the compressive modulus of PSS150 and GelMA hydrogels was 3.64 and 2.30 kPa, respectively. Furthermore, the mechanical recovery of GelMA/ PEDOT: PSS hydrogels was studied during compressive cycle testing. After 10 compressive cycles, all hydrogels in **Figures 2D,E** immediately recovered to their initial stress levels. PEDOT:PSS showed considerably improved compressive strength and mechanical reversibility under cyclic compression, according to these findings. An LED bulb and GelMA/PEDOT:PSS100 hydrogel formed a closed circuit in **Figure 2F**. As demonstrated in **Figure 2G**, increasing the concentration of PEDOT:PSS enhanced the conductivity of the GelMA/PEDOT: PSS hydrogel. The conductivity of GelMA/PEDOT:PSS150 hydrogels increased substantially compared with GelMA hydrogels (0.065 ± 0.001 mS/cm) and even reached 0.134 ± 0.004 mS/cm.

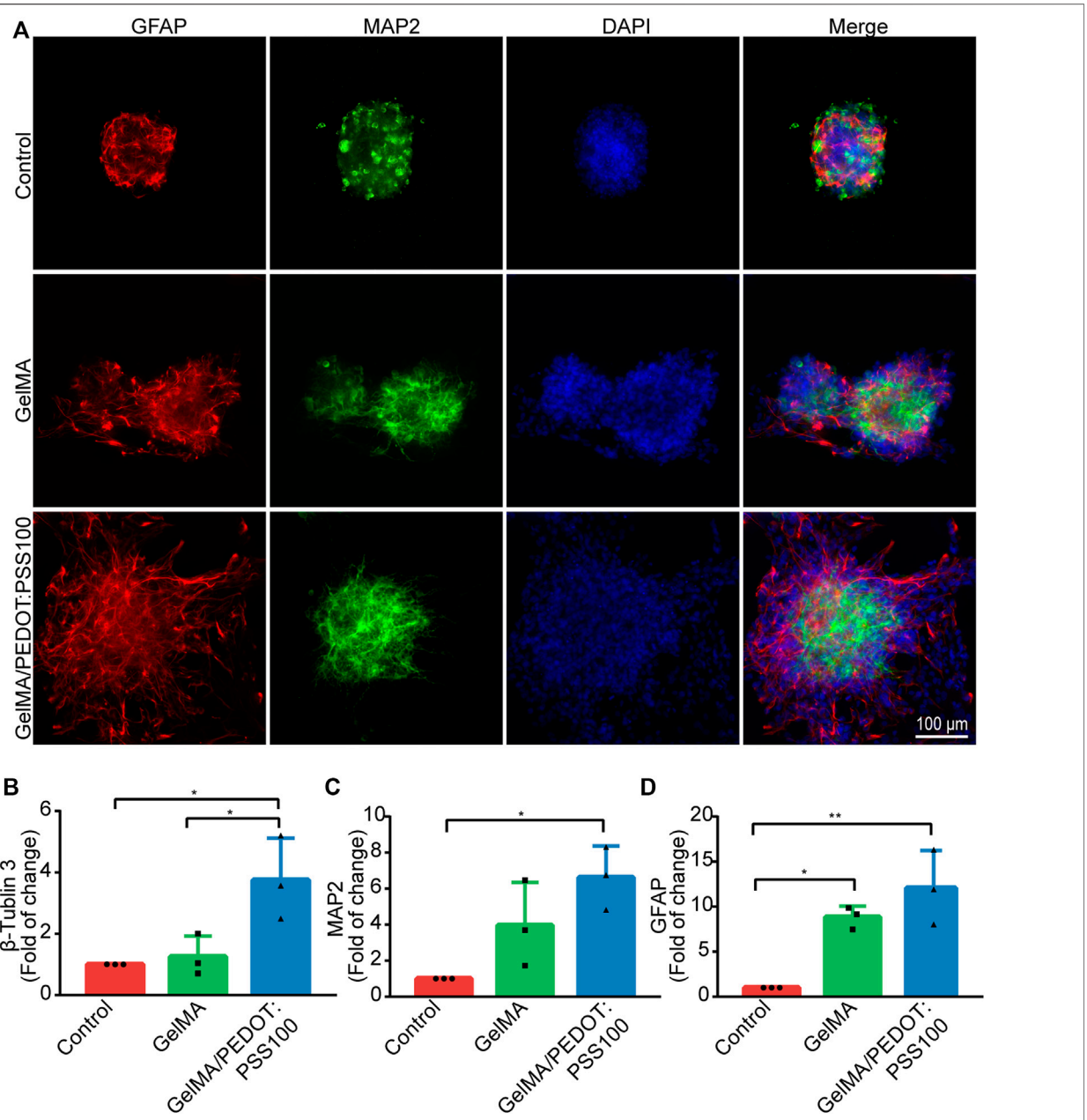

FIGURE 4 | *In vitro* immunostaining of NSCs and gene expression level of NSCs. **(A)** NSCs immunostaining images. **(B)** β-Tubulin 3, **(C)** MAP2, and **(D)** GFAP gene expression levels (n = 3). The data are expressed as mean ± standard deviation. $^{*}p < 0.05$ and $^{**}p < 0.01$.

3.2 Neural Stem Cell Viability in Conductive Gelatin Methacryloyl/ Poly(3,4-Ethylenedioxythiophene): Poly (Styrene Sulfonate) Hydrogels

Immunofluorescence staining was used to identify NSCs and their ability to differentiate into various nerve cells (**Supplementary Figure S1**). The LIVE/DEAD staining was used to determine the cytotoxicity of conductive hydrogels on day 7 (**Figure 3A**), and a CCK-8 assay was used to determine viability on day 3, 5, and 7 (**Figure 3B**). According to our findings, 6% of GelMA hydrogel-encapsulated NSCs still had spherical shapes, which is consistent with the findings of other studies (C. Li et al., 2021). The LIVE/DEAD assay revealed that the density of dead cells steadily increased as PEDOT:PSS concentrations increased.This pattern matched that of the CCK-8 assay, which showed a high level of cell viability, indicating that the GelMA hydrogel inclusion of PEDOT:PSS50/100/150 had no significant effect on cell viability on day 3 compared with the control samples without PEDOT:PSS. On day 5 and 7, however, in addition to NSC proliferation, the addition of PEDOT:PSS150

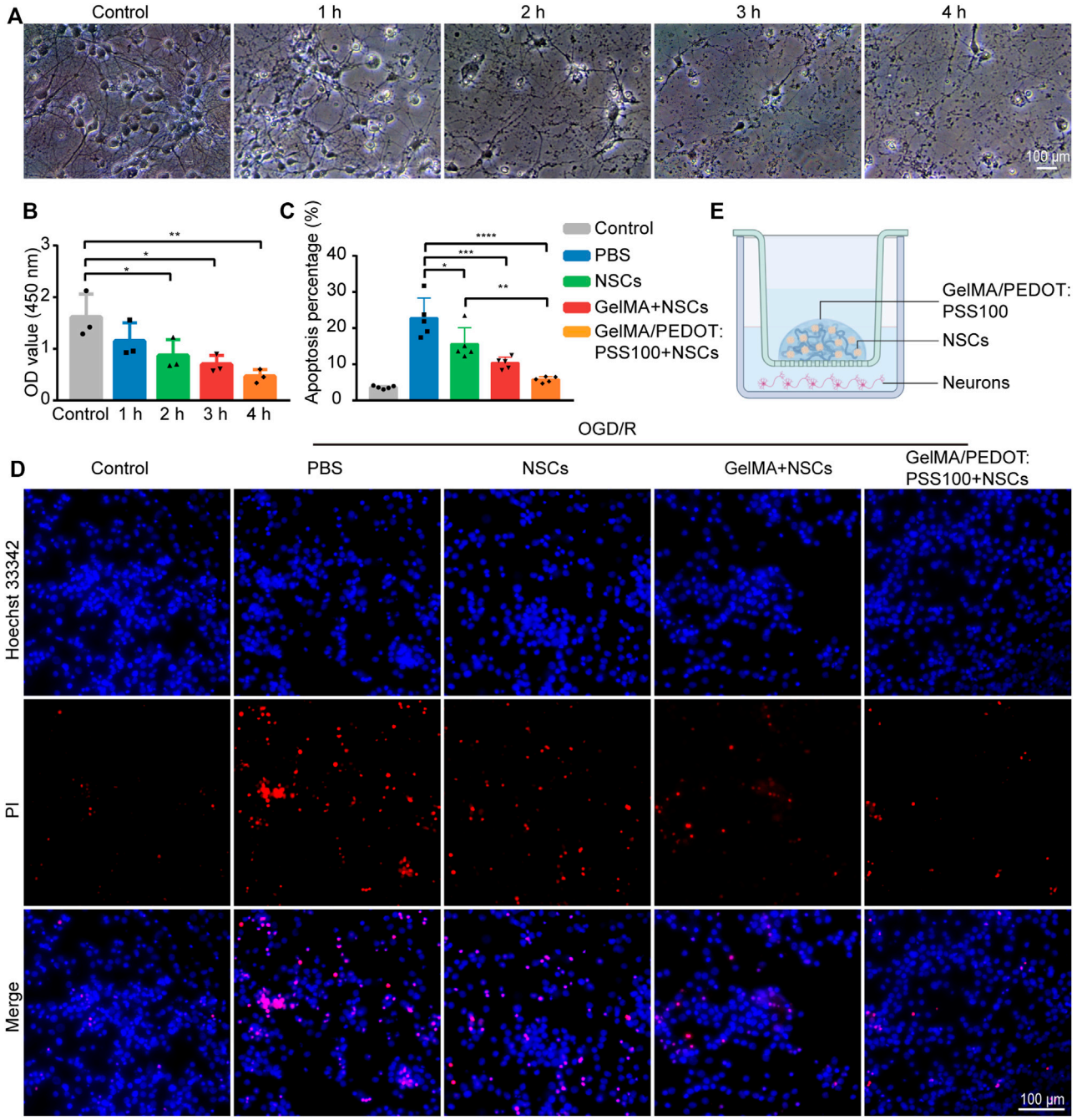

FIGURE 5 | Repairing effects on OGD/R-injured neurons. **(A)** Neuronal morphology of OGD/R-injured neurons after 1–4 h. **(B)** The cell viability was determined by the CCK-8 assay of OGD/R-injured neurons. **(C)** Analysis of the percentage of the apoptotic cells in the different OGD/R treatment groups. **(D)** Fluorescent microscopic analysis of apoptotic cells stained with PI and Hoechst 33342 in the different OGD/R treatment groups. **(E)** Diagram of Transwell co-culture system. The data are expressed as mean ± standard deviation. $^{*}p < 0.05$, $^{**}p < 0.01^{***}$, $p < 0.001$, and $^{****}p < 0.0001$.

resulted in reduced cell viability compared with other groups. We choose the optimum PEDOT:PSS concentration to form a conductive hydrogel for our next experiment based on hydrogel conductivity and NSC viability on PEDOT:PSS. GelMA/PEDOT:PSS100 may have conductive qualities as well as the best biocompatibility for NSCs. Compared with GelMA hydrogels, NSC differentiation in this conductive hydrogel was observed for 7 days.

3.3 Neural Stem Cell Differentiation in Conductive Gelatin Methacryloyl/ Poly(3,4-Ethylenedioxythiophene): Poly (Styrene Sulfonate) Hydrogels

NSCs cultured in conductive PEDOT:PSS hydrogels displayed elongated neurite outgrowth, resulting in a thin neural network, as described by Wang et al. (2018). NSCs were stained with antibodies against astrocytes and neuronal markers of GFAP and MAP2 after 7 days of culturing to observe the differentiation. The pluripotency of the NSCs was preserved, allowing them to develop into a variety of neural cell types (**Figure 4A**). The expression levels of differentiation-related genes expression in NSCs were then assessed using qRT-PCR. β Tubulin-III (**Figure 4B**), MAP2 (**Figure 4C**), and GFAP (**Figure 4D**) expression levels were found to be higher in NSCs cultured in the GelMA/PEDOT:PSS100 scaffold than in the control group. Our results showed that the GelMA/PEDOT:PSS hydrogel co-cultured with NSCs facilitated the differentiation of NSCs into astrocytes and neurons, which is comparable to the results of previously reported conductive materials for promoting NSCs differentiation (Wang et al., 2018). This also means there will be lower differentiation rate into other types of neurocytes such as oligodendrocytes.

3.4 Gelatin Methacryloyl/ Poly(3,4-Ethylenedioxythiophene): Poly (Styrene Sulfonate)/Neural Stem Cell Repairing Effect on Oxygen-Glucose Deprivation/Reperfusion-Injured Neurons

Figure 5A shows the neuronal morphology of OGD/R-injured neurons after 1–4 h. **Figure 5B** presents the CCK-8 assay results of OGD/R-injured neurons, which was used to evaluate cell viability. The OD value of neurons in the OGD/R 2 h group was half that of the control group, according to the CCK8 assay results. As a result, we chose the 2 h group for the following experiment, as described in earlier studies (Liu et al., 2014). In **Figure 5E**, we used the Transwell assay to observe the alterations in OGD/R neurons following a 7-days hydrogel intervention. The protective effects of NSCs and NSCs in hydrogels of varying concentrations were evaluated using Hoechst 33342/PI staining on damaged neurons exposed to OGD/R. Compared with the NSCs group, the percentage of apoptotic cells in the GelMA/PEDOT: PSS100/NSCs group markedly decreased dramatically (**Figures 5C,D**). These findings suggested that NSCs cultured in GelMA/PEDOT:PSS100 hydrogels could increase neuroprotective effects more effectively than NSCs alone.

3.5 Conductive Hydrogel Histocompatibility *In Vivo*

The histocompatibility of the hydrogels was determined by transcranial injection of HE staining into the brains of healthy Sprague-Dawley rats before *in vivo* application. PBS injection, GelMA injection, and GelMA/PEDOT:PSS100 injection groups (n = 4) were used in the experiments. Three days after the injection was administered, both groups showed similar amount of inflammation in their cerebral tissue. On day 14, the number of inflammatory cells had gradually decreased, and only a few inflammatory cells remained (**Figures 6A,B**). It can be seen from the HE staining results that the hydrogel group did not cause severe inflammation and tissue necrosis in the surrounding tissue compared with the sterile PBS group, indicating that the hydrogel has no toxicity to brain tissue. It was also found that the injection of PBS caused a mild inflammatory response, which could attribute to the mechanical damage caused by the syringe. However, lesions were formed after cerebral ischemia, and the tissue damage caused by the syringe was negligible. This observation is in line with the earlier report (Yuan et al., 2021). Therefore, the GelMA and GelMA/PEDOT:PSS100 hydrogels all had great biocompatibility and did not cause cerebral inflammation *in vivo*.

3.6 Inflammatory Response of the Conductive Hydrogel in Middle Cerebral Artery Occlusion Rats

The following interference groups were constructed to investigate the anti-inflammatory activity of hydrogel systems in I/R tissues (n = 4): PBS, NSCs, GelMA/NSCs and GelMA/PEDOT: PSS100/ NSCs. Day 7 was presumed to be a critical day for stem cell transplantation (L. Huang and Zhang 2019). To analyze the microglia and astrocyte responses to the implanted materials, immunostaining was performed at the ipsilateral cerebral cortex near the injection site and peri-injection site (approximately 500 μm away from the injection site) (Feig et al., 2021). The fluorescent GFAP (astrocytes) and iba1 (microglia) staining images of the injection and peri-injection locations in the MCAO brain are presented in **Figures 7A,B**. The GelMA/ PEDOT:PSS100/NSCs group had a much lower percent area of GFAP and iba1 fluorescence (**Figures 7C,E**) than the NSCs group. The percent area of GFAP and iba1 at the peri-injection location (**Figures 7D,F**) revealed no significant differences among the four groups. These findings indicated that the inflammatory responses in cerebral I/R tissues were lower than those seen in the PBS, particularly NSCs with GelMA/PEDOT: PSS100 hydrogels.

4 DISCUSSION

A conductive hydrogel scaffold with a high water content and filled with NSCs was designed for the treatment of stroke. This study is based on the complicated electrical conduction excitability and soft mechanical properties of brain tissues. According to characterization of the conductive hydrogels, the storage modulus of the GelMA/PEDOT:PSS hydrogel was affected by the mass ratio of GelMA and PEDOT:PSS,and PSS addition improved the storage modulus of the hydrogel by 1.92–3.64 kPa. It is critical to match the elastic modulus of the hydrogel to that of the rat brain as this allows the hydrogel to endure physical pressure from the surrounding brain tissue, maintain its shape after implantation, and protest the loaded NSCs (Weickenmeier et al., 2018). Our findings suggest that in

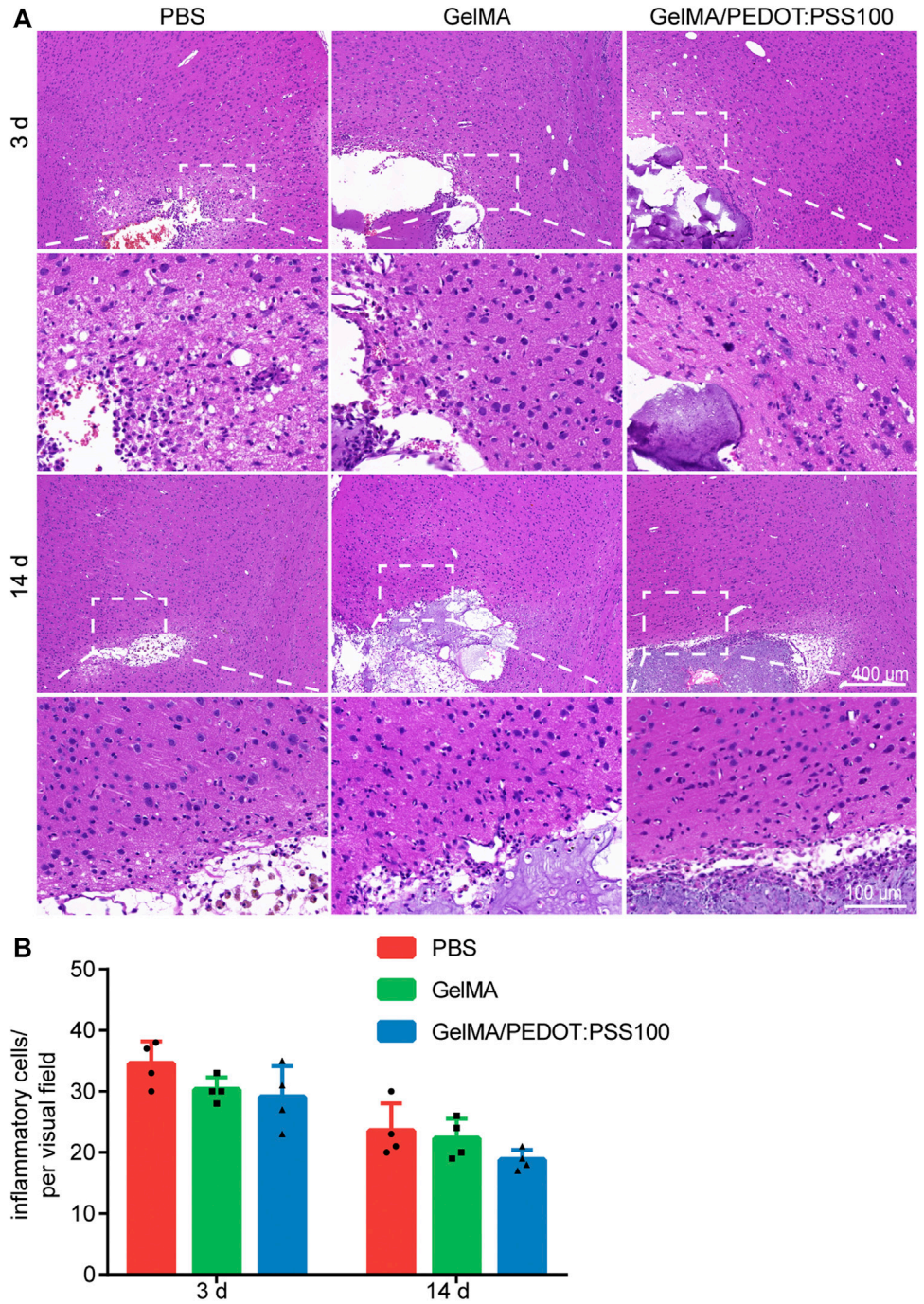

FIGURE 6 | HE staining images of different hydrogel groups 3 and 14 days after implantation. **(A)** HE staining on day 3 and 14. **(B)** Statistics of inflammatory cells. The data are expressed as mean ± SD.

the storage modulus range, GelMA/PEDOT:PSS hydrogels can provide a suitable mechanical microenvironment for nerve cells and tissues. The GelMA/PEDOT:PSS conductive hydrogel exhibits good tensile/compression mechanical capabilities, as indicated by the results of the repeated compression testing. PEDOT/PSS is a polymer that does not affect the regularity of the hydrogel molecular chain; instead, it is doped onto the hydrogel network structure as a conductive component. As a result, there will be minimal change in the tensile characteristics of the hydrogel.

An ideal material used in neural tissue engineering should have a certain electrical conductivity, allowing electrical signals to pass through the material scaffold, regulate cell activity, and stimulate nerve regeneration. According to studies, gels have a

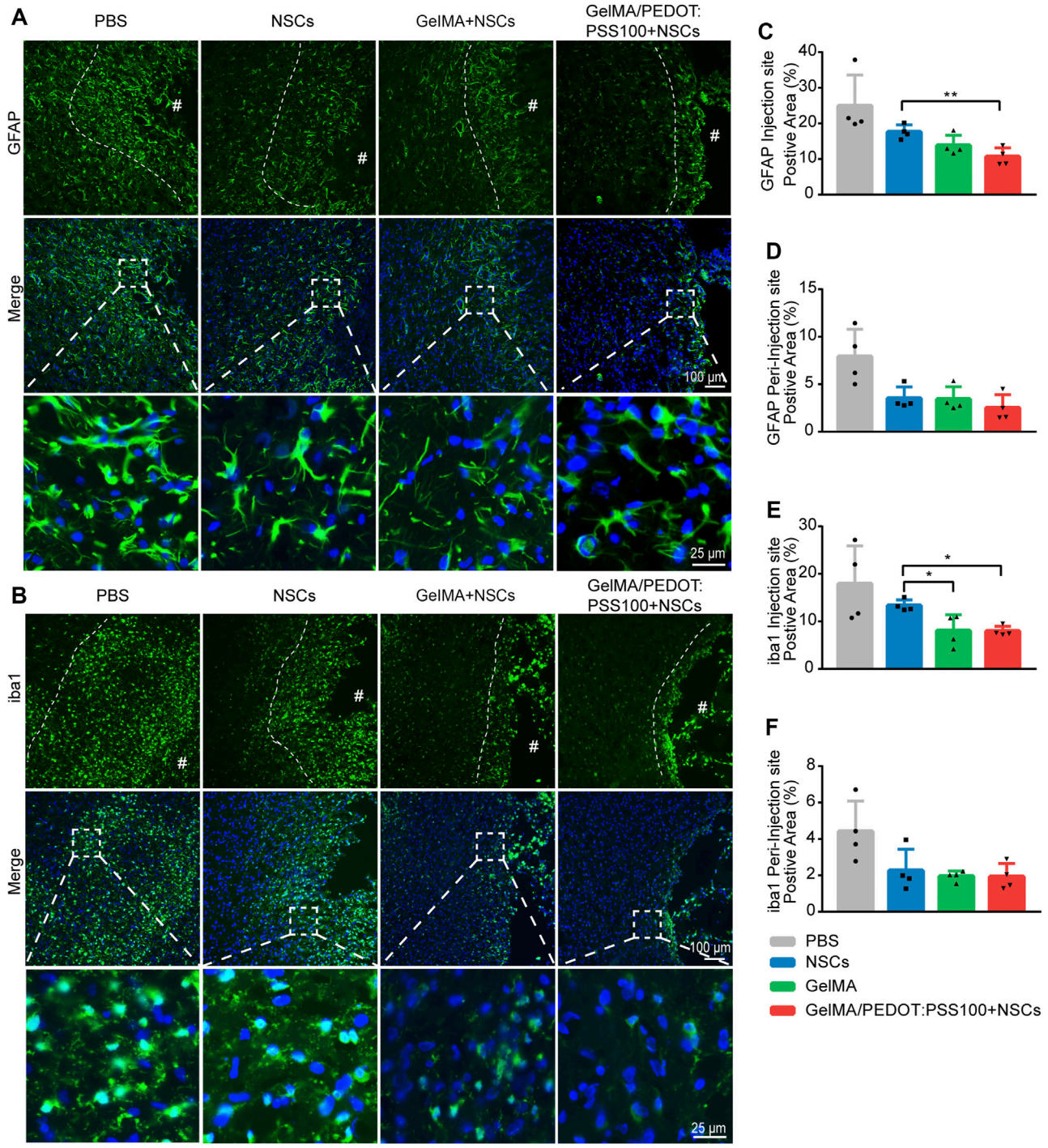

FIGURE 7 | Inflammatory response of the conductive hydrogel-loaded NSCs to cerebral I/R injury. Fluorescent images of **(A)** astrocyte (GFAP) and **(B)** microglia (iba1) staining in rat brain tissues close to the injection and peri-injection sites. The dotted lines indicate the proliferation area of astrocytes and microglia surrounding the site of injection. Quantitative analysis of GFAP positive area at the injection **(C)** and peri-injection **(D)** sites. Quantitative analysis of iba1 positive area at the injection **(E)** and peri-injection **(F)** sites. The data are expressed as mean ± SD. $^{*}p < 0.05$ and $^{**}p < 0.01$.

conductivity of approximately 10^{-7}–10^{-2} S/cm, which can be used to convey electrical signals from an organism to induce cell growth and differentiation (Zarrintaj et al., 2017). Therefore, the GelMA/PEDOT:PSS conductive hydrogel can be used in biomedical applications. The suitable conductivity criteria for conducting materials are yet to be identified. According to certain studies, only stents having an electrical conductivity of higher than 10^{-3} S/cm are viable candidates (Baniasadi et al., 2015).

Some researchers suggest that even if the conductivity is less than 10^{-3} S/cm, the hydrogel can still stimulate neuronal development, which may have no connection with the calcium channel and everything to do with its PEDOT:PSS enhances the electrostatic contact between the matrix material and the cellular anchor protein, which leads to cell differentiation (Da Silva et al., 2018). In the event of non-electrical stimulation, the regulating role of the material is stronger than the ion flow transformation. Non-electrical stimulation was used in our research to check whether the GelMA/PEDOT:PSS hydrogel, which is ideal for loading with NSCs for cerebral I/R injury, can reduce the danger of metabolic residues of conductive polymer materials *in vivo*.

Latest research on PEDOT:PSS hydrogel research was conducted using 2D culture models, which provided a better conductive contact between the cells; however, there remains a gap between the true 3D culture environments *in vivo*. Compared with the 2D culture environment, the 3D culture environment was shown to be associated with reduced cell proliferation levels (Song et al., 2019). In contrast, 3D cell encapsulation simulates the conditions that implanted cells would face *in vivo*. We were pleased to discover that at a specific concentration, PEDOT:PSS could maintain a favorable biological influence on cells and even enhance neuron metamorphosis while enhancing conductivity in a 3D culture environment. This result matched our expectations and was consistent with previous research (Fitria 2019). However, a higher concentrations of PEDOT:PSS resulted in reduced cell vitality, possibly due to the anionic PSS chain limiting cell adhesion (Spencer et al., 2018). Another cause for this could be that PEDOT:PSS is acidic, making it corrosive and poisonous. PSS components have an acidic SO3H (sulfonate acid) group on every benzene ring (Ostrakhovitch et al., 2012). Because NSCs have electrical features that distinguish them from regular adult cells, we hypothesized that they could be more sensitive to the matrix response of conductive materials. As a brain interface material, graphene has also been discovered to influence NSC differentiation by modifying the passive or active bioelectrical properties of NSCs, according to research (Huang et al., 2012). As a result, we hypothesized that NSCs cultured in 3D environments would be more electroactive in PEDOT: PSS and that NSCs would be more sensitive to external electrical ion activities. Next, we'll investigate the role of conductive materials in NSC differentiation.

We also investigated the effect of GelMA/PEDOT:PSS hydrogels loaded with NSCs on OGD/R neurons *in vitro*. It is possible because NSCs in the upper chamber shows a higher rate of development into neurons and glial cells, which secreted more brain trophic substances to impact the environment. We observed that neurospheres cultured in GelMA/PEDOT: PSS100 hydrogels could raise trophic factor transcription levels, possibly leading to an enhanced neuroprotective effect because conductive polymers can regulate trophic factors derived from stem cells, such as brain-derived neurotrophic factor (Oh and George, 2019) (**Supplementary Figure S2**).

GelMA/PEDOT:PSS/NSCs have excellent compatibility with nervous tissues as observed in our *in vivo* investigation. The mechanical damage caused by needle insertion was the primary cause of the early inflammatory reaction after hydrogel injection. After the transcranial injection, all groups in this study had the same level of inflammation level, which could be due to the mechanical damage generated by the transcranial injection. After 14 days, the number of inflammatory cells gradually decreased. Inflammatory cell infiltration into the hydrogels was noticeable, indicating that the hydrogel breakdown and integration with the surrounding tissues. The GelMA/PEDOT:PSS and GelMA hydrogel groups displayed similar inflammatory responses over the 14-days observation period, albeit a longer observation period would be required to evaluate if PEDOT: PSS sediments can cause further alterations.

The damage associated molecular patterns (DAMPs) generated by cerebral I/R injury activate resident microglia and macrophages to differentiate into a pro-inflammatory M1 phenotype. This phenotype secretes tumor necrosis factor-α, interleukin-1β and reactive oxygen species (Xiong et al., 2016). These inflammatory factors can promote the body's inflammatory response, not only changing its own structure and function, but also causing damage to surrounding tissues and indirectly promoting cell apoptosis. Following cerebral I/R injury, brain tissue expressed more proteases and hyaluronidase than normal tissue (Feig et al., 2021); as a result, hydrogels may have experienced more severe disintegration of the inflammatory response than in healthy brain tissue samples. The buildup of conductive material may result in a more severe inflammatory reaction. In contrast to the other studies (Köhler et al., 2015), we discovered that implanted NSCs loaded with GelMA/PTDOT:PSS conductive hydrogels might lower astrocyte and microglia positive areas near the inject site. It is possible that the conductive hydrogel stimulated NSC differentiation and increased neurotrophic factor secretion. In order to further confirm the neuroprotective effect of GelMA/PEDOT:PSS-loaded neural stem cells on damaged neurons, we used brain frozen section on day 7 for staining of neurons (**Supplementary Figure S3**). By observing the number of surviving neurons in the brain tissue around the injection site, it was confirmed that the GelMA/PEDOT:PSS hydrogel had a synergistic protective effect on brain neurons when loaded with neural stem cells.

5 CONCLUSION

A conductive high-water-content hydrogel scaffold filled with NSCs was designed for stroke treatment in this study, based on the complicated electrical conduction excitability and soft mechanical properties of brain tissues. *In vitro* and *in vivo* experiments proved that GelMA/PEDOT:PSS had good compatibility with neural tissue. The differentiation of neural stem cells into neurons can be promoted when 3D cultured in GelMA/PEDOT:PSS hydrogel. This conductive hydrogel loaded with NSCs could not only inhibit the apoptosis of OGD/R damaged neurons, but also improve anti-inflammatory effects of NSCs on cerebral I/R-injured tissues. Therefore, GelMA/ PEDOT: PSS hydrogels have the great potentials of regulating

NSC differentiation and serving as cell niches for cerebral I/R injury treatment.

DATA AVAILABILITY STATEMENT

The original contributions presented in the study are included in the article/**Supplementary Material**, further inquiries can be directed to the corresponding authors.

ETHICS STATEMENT

The animal study was reviewed and approved by The Ethics Committee of Zhujiang Hospital, Southern Medical University approved the Animal Research Program.

AUTHOR CONTRIBUTIONS

Conceptualization, GH, YC, and QZ; Methodology, YZ; Software, MZ; Validation, RZ; Formal analysis, HC; Investigation, XZ, and CL; Resources, HL; Data acculturation, YZ, and MZ; Writing, YZ; Visualization, MZ.; Supervision, QZ; Project administration, YC; Funding acquisition, GH. All authors have read the article carefully and agree to the published version of the manuscript.

FUNDING

This study was supported by the National Natural Science Foundation of China (82072528, 82002380 and 81874032) and Natural Science Foundation of Guangdong Province (2022A1515012460).

ACKNOWLEDGMENTS

We would like to gratefully acknowledge the support of the Animal Central Laboratory of Zhujiang Hospital, Southern Medical University.

SUPPLEMENTARY MATERIAL

The Supplementary Material for this article can be found online at: https://www.frontiersin.org/articles/10.3389/fmats.2022.914994/full#supplementary-material

REFERENCES

Abidian, M. R., Kim, D.-H., and Martin, D. C. (2006). Conducting-polymer Nanotubes for Controlled Drug Release. *Adv. Mat.* 18 (4), 405–409. doi:10.1002/adma.200501726

Bacigaluppi, M., Pluchino, S., Jametti, L. P., Kilic, E., Kilic, Ü., and Salani, G. (2009). Delayed Post-Ischaemic Neuroprotection Following Systemic Neural Stem Cell Transplantation Involves Multiple Mechanisms. *Brain* 132 (8), 2239–2251. doi:10.1093/brain/awp174

Balint, R., Cassidy, N. J., and Cartmell, S. H. (2014). Conductive Polymers: towards a Smart Biomaterial for Tissue Engineering. *Acta Biomater.* 10 (6), 2341–2353. doi:10.1016/j.actbio.2014.02.015

Baniasadi, H., Ramazani S.A., A., and Mashayekhan, S. (2015). Fabrication and Characterization of Conductive Chitosan/gelatin-Based Scaffolds for Nerve Tissue Engineering. *Int. J. Biol. Macromol.* 74, 360–366. doi:10.1016/j.ijbiomac.2014.12.014

Basara, G., Ozcebe, S. G., Ellis, B. W., and Zorlutuna, P. (2021). Tunable Human Myocardium Derived Decellularized Extracellular Matrix for 3d Bioprinting and Cardiac Tissue Engineering. *Gels* 7 (2), 70. doi:10.3390/gels7020070

Burns, T. C., and Quinones-Hinojosa, A. (2021). Regenerative Medicine for Neurological Diseases-Will Regenerative Neurosurgery Deliver? *BMJ* 373, n955. doi:10.1136/bmj.n955

Da Silva, A. C., Semeano, A. T. S., Dourado, A. H. B., Ulrich, H., and Cordoba De Torresi, S. I. (2018). Novel Conducting and Biodegradable Copolymers with Noncytotoxic Properties toward Embryonic Stem Cells. *ACS Omega* 3 (5), 5593–5604. doi:10.1021/acsomega.8b00510

De Feo, D., Merlini, A., Laterza, C., and Martino, G. (2012). Neural Stem Cell Transplantation in Central Nervous System Disorders: From Cell Replacement to Neuroprotection. *Current Opinion in Neurology* 25 (3), 322–333. doi:10.1097/WCO.0b013e328352ec45

Fann, D. Y.-W., Lee, S.-Y., Manzanero, S., Chunduri, P., Sobey, C. G., and Arumugam, T. V. (2013). Pathogenesis of Acute Stroke and the Role of Inflammasomes. *Ageing Res. Rev.* 12 (4), 941–966. doi:10.1016/j.arr.2013.09.004

Feig, V. R., Santhanam, S., McConnell, K. W., Liu, K., Azadian, M., Brunel, L. G., et al. (2021). Conducting Polymer-Based Granular Hydrogels for Injectable 3D Cell Scaffolds. *Adv. Mat. Technol.* 6 (6), 1–10. doi:10.1002/admt.202100162

Felling, R. J., and Song, H. (2015). Epigenetic Mechanisms of Neuroplasticity and the Implications for Stroke Recovery. *Exp. Neurol.* 268, 37–45. doi:10.1016/j.expneurol.2014.09.017

Fitria (2019). Development of 3D Printable Conductive Hydrogel with Crystallized PEDOT:PSS for Neural Tissue Engineering. *J. Chem. Inf. Model.* 53 (9), 1689–1699. doi:10.1016/j.msec.2019.02.008

Huang, L., and Zhang, L. (2019). Neural Stem Cell Therapies and Hypoxic-Ischemic Brain Injury. *Prog. Neurobiol.* 173, 1–17. doi:10.1016/j.pneurobio.2018.05.004

Huang, Y.-J., Wu, H.-C., Tai, N.-H., and Wang, T.-W. (2012). Carbon Nanotube Rope with Electrical Stimulation Promotes the Differentiation and Maturity of Neural Stem Cells. *Small* 8 (18), 2869–2877. doi:10.1002/smll.201200715

Ju, R., Wen, Y., Gou, R., Wang, Y., and Xu, Q. (2014). The Experimental Therapy on Brain Ischemia by Improvement of Local Angiogenesis with Tissue Engineering in the Mouse. *Cell Transpl.* 23 (Suppl. 1), S83–S95. doi:10.3727/096368914X684998

Köhler, P., Wolff, A., Ejserholm, F., Wallman, L., Schouenborg, J., and Linsmeier, C. E. (2015). Influence of Probe Flexibility and Gelatin Embedding on Neuronal Density and Glial Responses to Brain Implants. *PLOS ONE* 10 (3), e0119340. doi:10.1371/journal.pone.0119340

Lee, J. Y., Bashur, C. A., Goldstein, A. S., and Schmidt, C. E. (2009). Polypyrrole-coated Electrospun PLGA Nanofibers for Neural Tissue Applications. *Biomaterials* 30 (26), 4325–4335. doi:10.1016/j.biomaterials.2009.04.042

Levin, M., Pezzulo, G., and Finkelstein, J. M. (2017). Endogenous Bioelectric Signaling Networks: Exploiting Voltage Gradients for Control of Growth and Form. *Annu. Rev. Biomed. Eng.* 19, 353–387. doi:10.1146/annurev-bioeng-071114-040647

Li, C., Kuss, M., Kong, Y., Nie, F., Liu, X., Liu, B., et al. (2021). 3D Printed Hydrogels with Aligned Microchannels to Guide Neural Stem Cell Migration. *ACS Biomater. Sci. Eng.* 7 (2), 690–700. doi:10.1021/acsbiomaterials.0c01619

Li, H., Wang, Y., Sun, X., Tian, W., Xu, J., and Wang, J. (2019). Steady-state Behavior and Endothelialization of a Silk-Based Small-Caliber Scaffold *In Vivo* Transplantation. *Polymers* 11 (8), 1303. doi:10.3390/polym11081303

Lin, C., Li, N., Chang, H., Shen, Y., Li, Z., Wei, W., et al. (2020). Dual Effects of Thyroid Hormone on Neurons and Neurogenesis in Traumatic Brain Injury. *Cell Death Dis.* 11 (8), 671. doi:10.1038/s41419-020-02836-9

Liu, Q., Fan, X., Zhu, J., Xu, G., Li, Y., and Liu, X. (2014). Co-culturing Improves the OGD-Injured Neuron Repairing and NSCs Differentiation via Notch Pathway Activation. *Neurosci. Lett.* 559, 1–6. doi:10.1016/j.neulet.2013.11.027

Lu, J., Shen, X., Sun, X., Yin, H., Yang, S., Lu, C., et al. (2018). Increased Recruitment of Endogenous Stem Cells and Chondrogenic Differentiation by a Composite Scaffold Containing Bone Marrow Homing Peptide for Cartilage Regeneration. *Theranostics* 8 (18), 5039–5058. doi:10.7150/thno.26981

Naghavi, M., Abajobir, A. A., Abbafati, C., Abbas, K. M., Abd-Allah, F., Abera, S. F., et al. (2017). Global, Regional, and National Age-Sex Specific Mortality for 264 Causes of Death, 1980-2016: a Systematic Analysis for the Global Burden of Disease Study 2016. *Lancet* 390 (10100), 1151–1210. doi:10.1016/S0140-6736(17)32152-9

Ning, L., Mehta, R., Cao, C., Theus, A., Tomov, M., Zhu, N., et al. (2020). Embedded 3D Bioprinting of Gelatin Methacryloyl-Based Constructs with Highly Tunable Structural Fidelity. *ACS Appl. Mat. Interfaces* 12 (40), 44563–44577. doi:10.1021/acsami.0c15078

Oh, B., and George, P. (2019). Conductive Polymers to Modulate the Post-stroke Neural Environment. *Brain Res. Bull.* 148, 10–17. doi:10.1016/j.brainresbull.2019.02.015

Ostrakhovitch, E. A., Byers, J. C., O'Neil, K. D., and Semenikhin, O. A. (2012). Directed Differentiation of Embryonic P19 Cells and Neural Stem Cells into Neural Lineage on Conducting PEDOT-PEG and ITO Glass Substrates. *Archives Biochem. Biophysics* 528 (1), 21–31. doi:10.1016/j.abb.2012.08.006

She, Y., Shao, L., Zhang, Y., Hao, Y., Cai, Y., Cheng, Z., et al. (2019). Neuroprotective Effect of Glycosides in Buyang Huanwu Decoction on Pyroptosis Following Cerebral Ischemia-Reperfusion Injury in Rats. *J. Ethnopharmacol.* 242, 112051. doi:10.1016/j.jep.2019.112051

Song, S., Amores, D., Chen, C., McConnell, K., Oh, B., Poon, A., et al. (2019). Controlling Properties of Human Neural Progenitor Cells Using 2D and 3D Conductive Polymer Scaffolds. *Sci. Rep.* 9 (1), 19565. doi:10.1038/s41598-019-56021-w

Spencer, A. R., Primbetova, A., Koppes, A. N., Koppes, R. A., Fenniri, H., and Annabi, N. (2018). Electroconductive Gelatin Methacryloyl-PEDOT:PSS Composite Hydrogels: Design, Synthesis, and Properties. *ACS Biomater. Sci. Eng.* 4 (5), 1558–1567. doi:10.1021/acsbiomaterials.8b00135

Stonesifer, C., Corey, S., Ghanekar, S., Diamandis, Z., Acosta, S. A., and Borlongan, C. V. (2017). Stem Cell Therapy for Abrogating Stroke-Induced Neuroinflammation and Relevant Secondary Cell Death Mechanisms. *Prog. Neurobiol.* 158, 94–131. doi:10.1016/j.pneurobio.2017.07.004

Tang, Y.-H., Ma, Y.-Y., Zhang, Z.-J., Wang, Y.-T., and Yang, G.-Y. (2015). Opportunities and Challenges: Stem Cell-Based Therapy for the Treatment of Ischemic Stroke. *CNS Neurosci. Ther.* 21 (4), 337–347. doi:10.1111/cns.12386

Tuladhar, A., Obermeyer, J. M., Payne, S. L., Siu, R. C. W., Zand, S., Morshead, C. M., et al. (2020). Injectable Hydrogel Enables Local and Sustained Co-delivery to the Brain: Two Clinically Approved Biomolecules, Cyclosporine and Erythropoietin, Accelerate Functional Recovery in Rat Model of Stroke. *Biomaterials* 235, 119794. doi:10.1016/j.biomaterials.2020.119794

Tuo, Q. z., Zhang, S. t., and Lei, P. (2022). Mechanisms of Neuronal Cell Death in Ischemic Stroke and Their Therapeutic Implications. *Med. Res. Rev.* 42 (1), 259–305. doi:10.1002/med.21817

Wang, S., Guan, S., Li, W., Ge, D., Xu, J., Sun, C., et al. (2018). 3D Culture of Neural Stem Cells within Conductive PEDOT Layer-Assembled Chitosan/gelatin Scaffolds for Neural Tissue Engineering. *Mater. Sci. Eng. C* 93, 890–901. doi:10.1016/j.msec.2018.08.054

Wang, S., Guan, S., Zhu, Z., Li, W., Liu, T., and Ma, X. (2017). Hyaluronic Acid Doped-Poly(3,4-Ethylenedioxythiophene)/chitosan/gelatin (PEDOT-HA/Cs/gel) Porous Conductive Scaffold for Nerve Regeneration. *Mater. Sci. Eng. C* 71, 308–316. doi:10.1016/j.msec.2016.10.029

Weickenmeier, J., Kurt, M., Ozkaya, E., Wintermark, M., Pauly, K. B., and Kuhl, E. (2018). Magnetic Resonance Elastography of the Brain: A Comparison between Pigs and Humans. *J. Mech. Behav. Biomed. Mater.* 77, 702–710. doi:10.1016/j.jmbbm.2017.08.029

Woerly, S. (1993). Hydrogels for Neural Tissue Reconstruction and Transplantation. *Biomaterials* 14 (14), 1056–1058. doi:10.1016/0142-9612(93)90205-g

Xiong, X. Y., Liu, L. Y., and Yang, Q. W. (2016). Functions and Mechanisms of Microglia/Macrophages in Neuroinflammation and Neurogenesis After Stroke. *Progress in Neurobiology* 142, 23–44. doi:10.1016/j.pneurobio.2016.05.001

Yang, J., and Martin, D. C. (2004). Microporous Conducting Polymers on Neural Microelectrode Arrays. *Sensors Actuators A Phys.* 113 (2), 204–211. doi:10.1016/j.sna.2004.02.029

Ying, G., Jiang, N., Parra, C., Tang, G., Zhang, J., Wang, H., et al. (2020). Bioprinted Injectable Hierarchically Porous Gelatin Methacryloyl Hydrogel Constructs with Shape-Memory Properties. *Adv. Funct. Mat.* 30 (46), 1–13. doi:10.1002/adfm.202003740

Yuan, Z., Yuan, X., Zhao, Y., Cai, Q., Wang, Y., Luo, R., et al. (2021). Injectable GelMA Cryogel Microspheres for Modularized Cell Delivery and Potential Vascularized Bone Regeneration. *Small* 17 (11), e2006596. doi:10.1002/smll.202006596

Zarrintaj, P., Bakhshandeh, B., Rezaeian, I., Heshmatian, B., and Ganjali, M. R. (2017). A Novel Electroactive Agarose-Aniline Pentamer Platform as a Potential Candidate for Neural Tissue Engineering. *Sci. Rep.* 7 (1), 17187. doi:10.1038/s41598-017-17486-9

Zhao, J., Li, Y. X., Hao, Y. J., Chen, R., Zhang, J. Z., Sun, T., et al. (2013). Effects of Oxysophoridine on Rat Hippocampal Neurons Sustained Oxygen-Glucose Deprivation and Reperfusion. *CNS Neurosci. Ther.* 19 (2), 138–141. doi:10.1111/cns.12047

Zhou, G., Wang, Y., Gao, S., Fu, X., Cao, Y., Peng, Y., et al. (2021). Potential Mechanisms and Perspectives in Ischemic Stroke Treatment Using Stem Cell Therapies. *Front. Cell Dev. Biol.* 9, 646927. doi:10.3389/fcell.2021.646927

Zhou, H., Yang, H., Lu, L., Li, X., Pan, B., Fu, Z., et al. (2020). A Modified Protocol for the Isolation, Culture, and Cryopreservation of Rat Embryonic Neural Stem Cellsfied Protocol for the Isolation, Culture, and Cryopreservation of Rat Embryonic Neural Stem Cells. *Exp. Ther. Med.* 20 (6), 156. doi:10.3892/etm.2020.9285

Conflict of Interest: The authors declare that the research was conducted in the absence of any commercial or financial relationships that could be construed as a potential conflict of interest.

frontiers | Frontiers in Bioengineering and Biotechnology

ORIGINAL RESEARCH
published: 23 May 2022
doi: 10.3389/fbioe.2022.895107

Oriented Growth of Neural Stem Cell–Derived Neurons Regulated by Magnetic Nanochains

Lin Xia[1], Chen Zhang[2], Kaiming Su[3], Jiangang Fan[4], Yuguang Niu[5]*, Yafeng Yu[6]* and Renjie Chai[1,7,8,9,2]**

[1]State Key Laboratory of Bioelectronics, Department of Otolaryngology Head and Neck Surgery, Zhongda Hospital, School of Life Sciences and Technology, Advanced Institute for Life and Health, Jiangsu Province High-Tech Key Laboratory for Bio-Medical Research, Southeast University, Nanjing, China, [2]Beijing Key Laboratory of Neural Regeneration and Repair, Capital Medical University, Beijing, China, [3]Department of Otolaryngology-Head and Neck Surgery, Shanghai Jiao Tong University Affiliated Sixth People's Hospital, Shanghai, China, [4]Department of Otolaryngology Head and Neck Surgery, Sichuan Academy of Medical Science, Sichuan Provincial People's Hospital, Chengdu, China, [5]Department of Ambulatory Medicine, The First Medical Center of PLA General Hospital, Beijing, China, [6]Department of Otolaryngology, First Affiliated Hospital of Soochow University, Suzhou, China, [7]Department of Otolaryngology Head and Neck Surgery, Sichuan Provincial People's Hospital, University of Electronic Science and Technology of China, Chengdu, China, [8]Co-Innovation Center of Neuroregeneration, Nantong University, Nantong, China, [9]Institute for Stem Cell and Regeneration, Chinese Academy of Science, Beijing, China

OPEN ACCESS

Edited by:
Mingqiang Li,
Third Affiliated Hospital of Sun Yat-Sen University, China

Reviewed by:
Xiaowei Yang,
Shanghai Jiao Tong University, China
Yan Liu,
Nanjing Medical University, China
Dan Shao,
South China University of Technology, China

***Correspondence:**
Jiangang Fan
entscfjg@163.com
Yuguang Niu
nygent301@163.com
Yafeng Yu
yfyu1024@163.com
Renjie Chai
101011723@seu.edu.cn

Specialty section:
This article was submitted to Biomaterials, a section of the journal Frontiers in Bioengineering and Biotechnology

Received: *13 March 2022*
Accepted: *11 April 2022*
Published: *23 May 2022*

Citation:
Xia L, Zhang C, Su K, Fan J, Niu Y, Yu Y and Chai R (2022) Oriented Growth of Neural Stem Cell–Derived Neurons Regulated by Magnetic Nanochains. Front. Bioeng. Biotechnol. 10:895107. doi: 10.3389/fbioe.2022.895107

Neural stem cell therapy has become a promising cure in the treatment of neurodegenerative disorders. Owing to the anisotropy of the nervous system, the newly derived neurons need not only the functional integrity but also the oriented growth to contact with the partner cells to establish functional connections. So the oriented growth of the newly derived neurons is a key factor in neural stem cell–based nerve regeneration. Nowadays, various biomaterials have been applied to assist in the oriented growth of neural stem cell–derived neurons. However, among these biomaterials, the magnetic materials applied in guiding the neuronal growth are still fewer than the other materials, such as the fibers. So in this work, we developed the magnetic nanochains to guide the oriented growth of neural stem cell–derived neurons. With the guidance of the magnetic nanochains, the seeded neural stem cells exhibited a good arrangement, and the neural stem cell–derived neurons showed well-oriented growth with the orientation of the nanochains. We anticipated that the magnetic nanochains would have huge potential in stem cell–based nerve regeneration.

Keywords: neural stem cells, magnetic nanochains, oriented growth, newly derived neurons, nerve regeneration

INTRODUCTION

Neurodegenerative disorders are a series of diseases caused by degeneration or loss of neurons in the nervous system, such as the brain (Shariati et al., 2020). Acute neurodegenerations are always caused by the lesioned loss of neurons, triggered by the temporally separate brain hemorrhage. In comparison, chronic neurodegenerations always show a long period of progressive loss of specific or multiple neuronal cells in the brain, brainstem, and spinal cord, such as the Alzheimer's disease (AD), amyotrophic lateral sclerosis (ALS), Parkinson's disease, spinal muscular atrophy (SMA), and Huntington's disease (HD) (Allan and Rothwell, 2001; Shi et al., 2017; Raza et al., 2019). Although these neurodegenerative disorders indicate the same neuronal pathologies, the loss mechanism of neuronal cells is multifaceted, thus hampering the designing of a

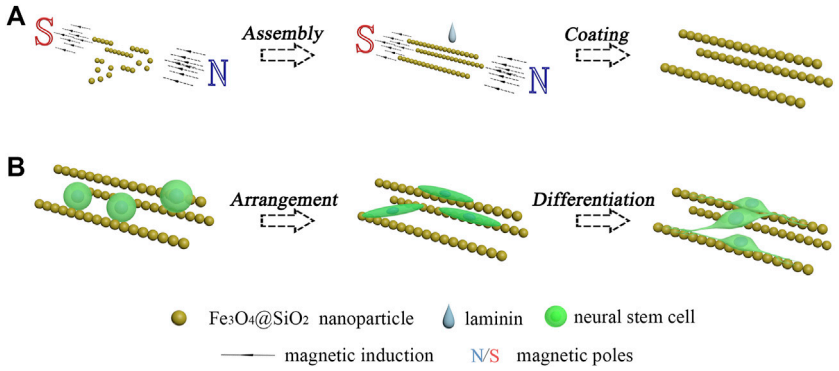

FIGURE 1 | Schematic illustration of the oriented growth of newly derived neurons. **(A)** Assembly of magnetic nanochains. **(B)** Guided oriented growth of the newborn neurons derived from the seeded neural stem cells.

therapeutic approach. Currently, the therapy based on stem cells has attracted cumulative attention toward the cure for neurodegenerative disorders. Stem cells could be classified as various cell types and possess excellent proliferation and differentiation potentials to generate specific cell lineages. This unique property exhibited great importance for regenerative medicine and tissue engineering.

Along with the wide application of stem cell therapy, many biomaterials have been developed to assist the regenerative application of stem cells, such as the scaffolds. He et al. developed a kind of immunoregulatory hydrogel scaffold, which could be applied to promote the spinal cord injury. This immunoregulatory hydrogel scaffold could effectively scavenge the damage-associated molecular patterns and release the anti-inflammatory cytokine 10 (Shen et al., 2022). Qi et al. (2022) reported a dual-drug (cetuximab and FTY720) enhanced hydrogel, which could be introduced by injection. This kind of hydrogel could be integrated with neural stem cells and promote tissue regeneration in a complete transected rat SCI model. Luo et al. (2022) integrated chondroitin sulfate, gelatin, and polypyrrole to fabricate the injective hydrogel with excellent conductivity. After fabrication, the composite hydrogel was applied to promote the traumatic SCI repair. It was found that the composite hydrogel activated the neurogenesis of the endogenous neural stem cells, and the myelinated axon regeneration was also induced through the activation of PI3K/AKT and MEK/ERK pathways. So it could be concluded that biomaterials have been widely applied in nerve regeneration based on stem cell therapy.

Among the various biomaterials that are applied in nerve regeneration, magnetic nanoparticles have attracted much attention. The magnetic nanoparticles possess a large specific surface area, good surficial modification, and excellent supermagnetism. These properties endowed a wide range of applications of the magnetic nanoparticles in biomedicine, such as the use of Fe_3O_4 nanoparticles in magnetic resonance imaging (Gradinaru et al., 2021; Wang et al., 2021; Khani et al., 2022). The good magnetic response makes the magnetic nanoparticles a good assembling property under the magnetic field (Yu et al., 2022). Many kinds of magnetic assemblies have been developed and applied in various fields, including nanochains (Luo et al., 2020; Cai et al., 2022; Qiao et al., 2022), nanosheets (Qin et al., 2021; Huang et al., 2022), and nanocrystals (Pan et al., 2021; Pileni, 2021; Deng et al., 2022). However, the application of magnetic assemblies in nerve regeneration has not been sufficiently studied. In this work, the Fe_3O_4 nanoparticles were coated with a thin layer of silicon dioxide. Then, the dispersed Fe_3O_4@SiO_2 nanoparticles were arranged by the magnetic field to form the magnetic nanochains and immobilized by the coating of laminin. The neural stem cell monodispersed solution was dripped onto the immobilized magnetic nanochains. After adhesion, proliferation and differentiation culturings were sequentially performed. As shown in **Figure 1**, it was found that the adhered neural stem cells exhibited well-oriented arrangement, and the newly derived neurons grew along the orientation of the magnetic nanochains.

RESULTS

Magnetic Material Characterization

In this work, the magnetic nanochains were fabricated by the assembly of the dispersed solution of magnetic nanoparticles induced by the static magnetic field. The magnetic nanoparticles were obtained through hydrothermal synthesis, following with the surficial modification of SiO_2. As shown in **Figure 2**, the Fe_3O_4 cores of the nanoparticles exhibited obvious spherical morphology (**Figure 2A**), and their surfaces presented obvious wrinkles. Then, the Fe_3O_4 nanoparticles were packaged by a SiO_2 layer through surficial modification (**Figure 2B**). The surfaces of the Fe_3O_4@SiO_2 nanoparticles were smooth in comparison with the Fe_3O_4 nanoparticles. After the manufacture of the magnetic nanoparticles, the magnetic nanochains were assembled by inducing of the magnetic field. The magnetic nanoparticles were arranged according to the magnetic induction lines and exhibited good linear topography. A representative single magnetic nanochain was presented in **Figure 2C**, and the magnetic nanochain exhibited good anisotropic morphology. Then, the laminin was applied to coat the assembled magnetic nanochains. The laminin is a kind of adhesion protein derived

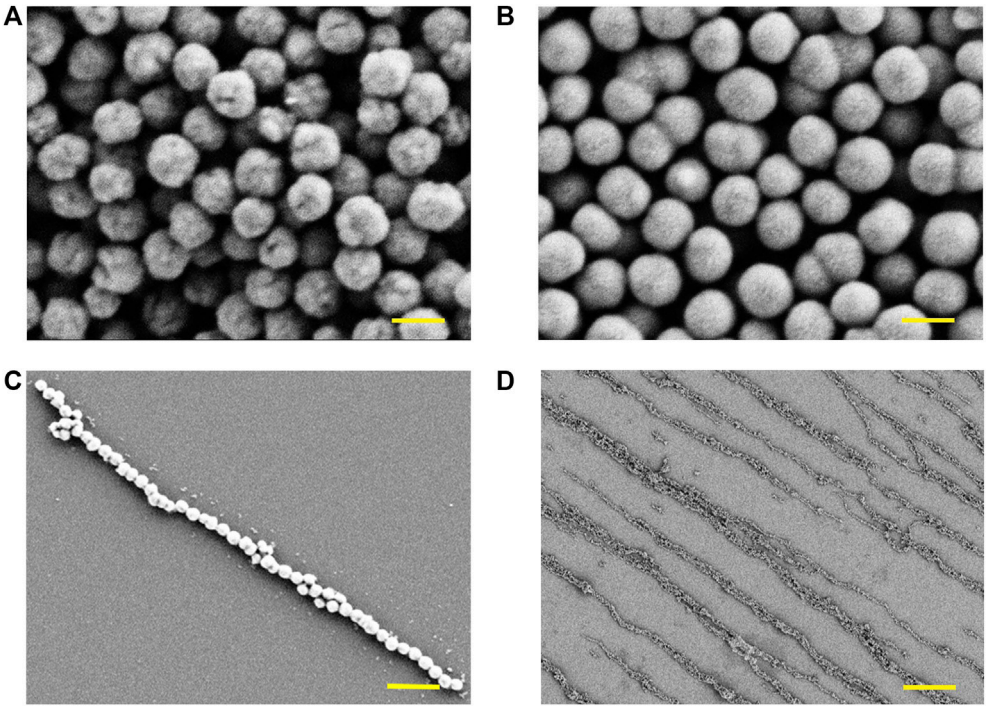

FIGURE 2 | Characterization of magnetic nanomaterials. **(A)** Fe_3O_4 cores of the magnetic nanoparticles observed by SEM, and the scale bar is 200 nm. **(B)** Fe_3O_4@ SiO_2 nanoparticles observed by SEM, and the scale bar is 200 nm. **(C)** Representative single magnetic nanochain observed by SEM, and the scale bar is 1 μm. **(D)** Overview of magnetic nanochains observed by SEM, and the scale bar is 10 μm.

from the basement membrane, which is applied to promote adhesion, migration, and differentiation of cells. With coating, the magnetic nanochains were immobilized, maintaining the anisotropic morphology in the absence of the magnetic field. Moreover, the coating of laminin also improved the biocompatibility of the magnetic nanochains. The overview in **Figure 2D** presented the aligned magnetic nanochains, which possessed good anisotropic topography.

Neural Stem Cells' Oriented Arrangement

To evaluate the guiding effect of the magnetic nanochains, the neural stem cell monodispersed solution was dripped onto the control coverslips and the magnetic nanochain–adhered coverslips. After culturing for 7 days, the neural stem cell activity marker "nestin" was applied to stain the cultured cells, thus visualizing the neural stem cells and evaluating the activity. As shown in **Figure 3**, the schematic illustration described the guidance of the neural stem cells performed by the magnetic nanochains (**Figure 3A**). With the guidance of the magnetic nanochains, the seeded neural stem cells exhibited well-oriented arrangement, according to the orientation of the magnetic nanochains. It could be found that the control neural stem cells were random after 7 days of culturing; in comparison, the nanochain-guided neural stem cells showed well-oriented arrangement to the orientation of the magnetic nanochains after 7 days of culturing (**Figure 3B**). The white arrows in **Figure 3Biv–vi** mark the magnetic nanochains. In the photograph, the magnetic nanochains interacted with the neural stem cells, and their orientations were highly consistent with each other. These results demonstrated a good "contact-guidance" effect of the magnetic nanochains in guiding the neural stem cell–oriented arrangement. In statistics, the nanochain-guided neural stem cells performed more than 70% orientation angles less than 10°. In comparison, the orientation angles of the control group were distributed randomly; there were only 12.7% of neural stem cells with the orientation angles less than 10° (**Figure 3C**). Thus, it could be concluded that the magnetic nanochains with good anisotropic topography showed excellent oriented guidance on the neural stem cell arrangement by the "contact-guidance" effect, while the immunofluorescent results of the activity marker "nestin" also demonstrated that the neural stem cells maintained a good activity at the same time.

Newly Derived Neurons' Oriented Growth

The aforementioned results have demonstrated the good guidance of the magnetic nanochains on the neural stem cell–oriented arrangement. After the arrangement, the differentiation culturing was performed by the replacement of the differentiation medium. Then, the orientation of the growth of the neural stem cell–derived neurons was evaluated. The schematic illustration in **Figure 4A** shows the oriented growth of the neural stem cell–derived neurons, with the guidance of the magnetic nanochains. With differentiation,

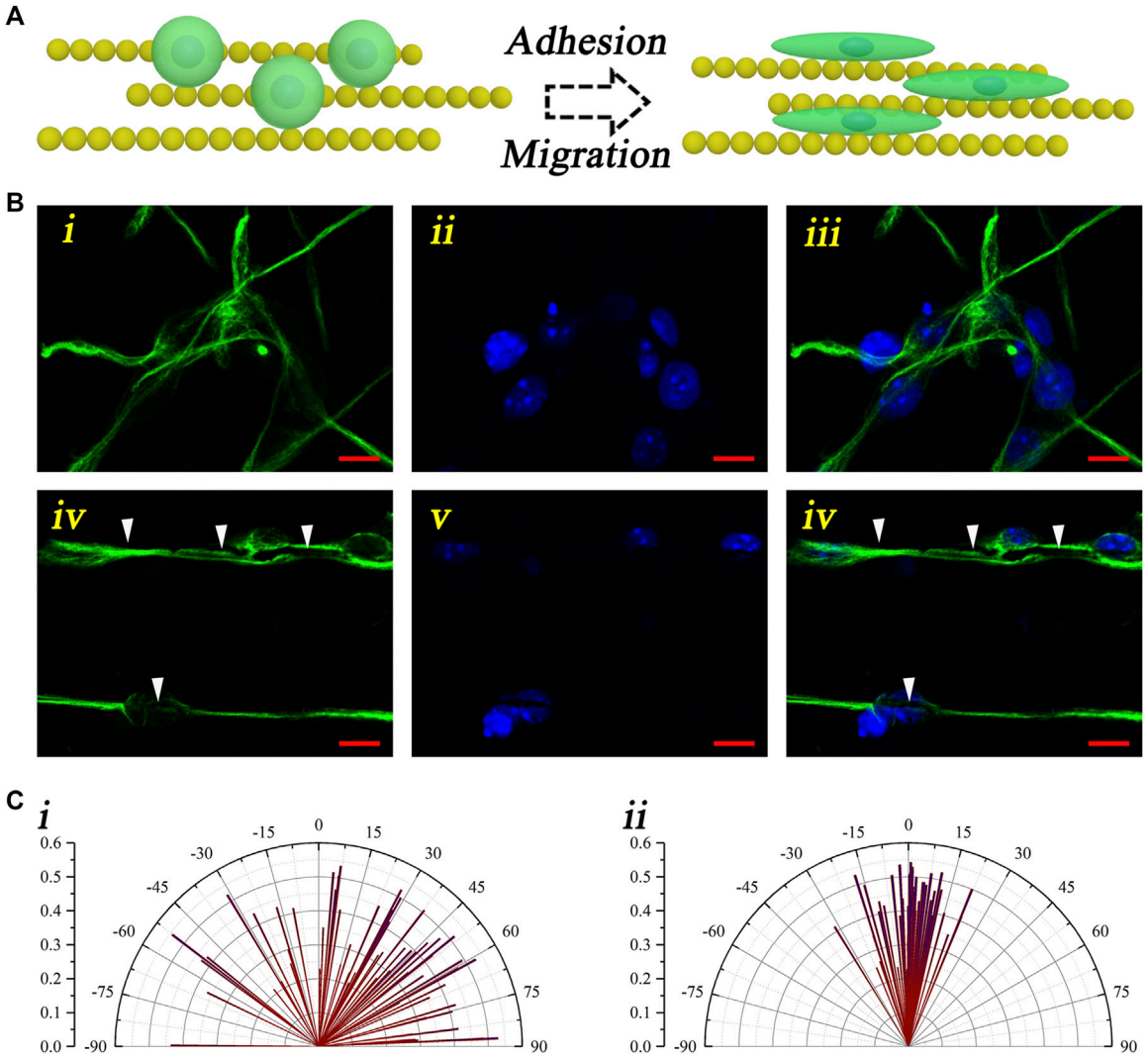

FIGURE 3 | Oriented arrangement of the neural stem cells. **(A)** Schematic illustration of the neural stem cell–oriented arrangement under the guidance of magnetic nanochains. **(B)** Representative fluorescent photographs of neural stem cells both in the control (i–iii) and the nanochain-guided groups (iv–vi) (green: nestin; blue: DAPI), and the scale bars are 10 μm. **(C)** Orientation angle statistic graphs of both the control (i) and the nanochain-guided groups (ii).

the neurites of newly derived neurons outgrew and extended along with the magnetic nanochains, which exhibited well-oriented growth. To visualize the newly derived neurons, the marker of neuron TuJ-1 was applied to stain the differentiated cells, as shown in **Figure 4B**. The fluorescent photographs in **Figure 4Bi–iv** showed the control newly derived neurons, whose orientations were random. In comparison, the fluorescent photographs in **Figure 4Bv–viii** showed the nanochain-guided newly derived neurons. It could be found that the neurites of the newly derived neurons extended well, along with the magnetic nanochains. The white arrows marked the magnetic nanochains. Furthermore, to evaluate the guiding effect of the magnetic nanochains on the newly derived neurons, the orientation angles of the newly derived neurons were calculated both in the control and the nanochain-guided groups. As shown in **Figure 4C**, the statistic graphs showed that the orientation angles of the control newly derived neurons were random; in comparison, the orientation angles of the nanochain-guided newly derived neurons were highly concentrated in distribution. There were more than 50% of newly derived neurons with the orientation angle within 10° to the magnetic nanochains in comparison with 16.8% of the control newly derived neurons. These results demonstrated the good guiding effect of the magnetic nanochains on the oriented growth of the neural stem cell–derived neurons.

DISCUSSION

In this work, we have developed a guiding approach for the oriented growth of newly derived neurons based on magnetic nanochains. During fabrication, the magnetic nanoparticles

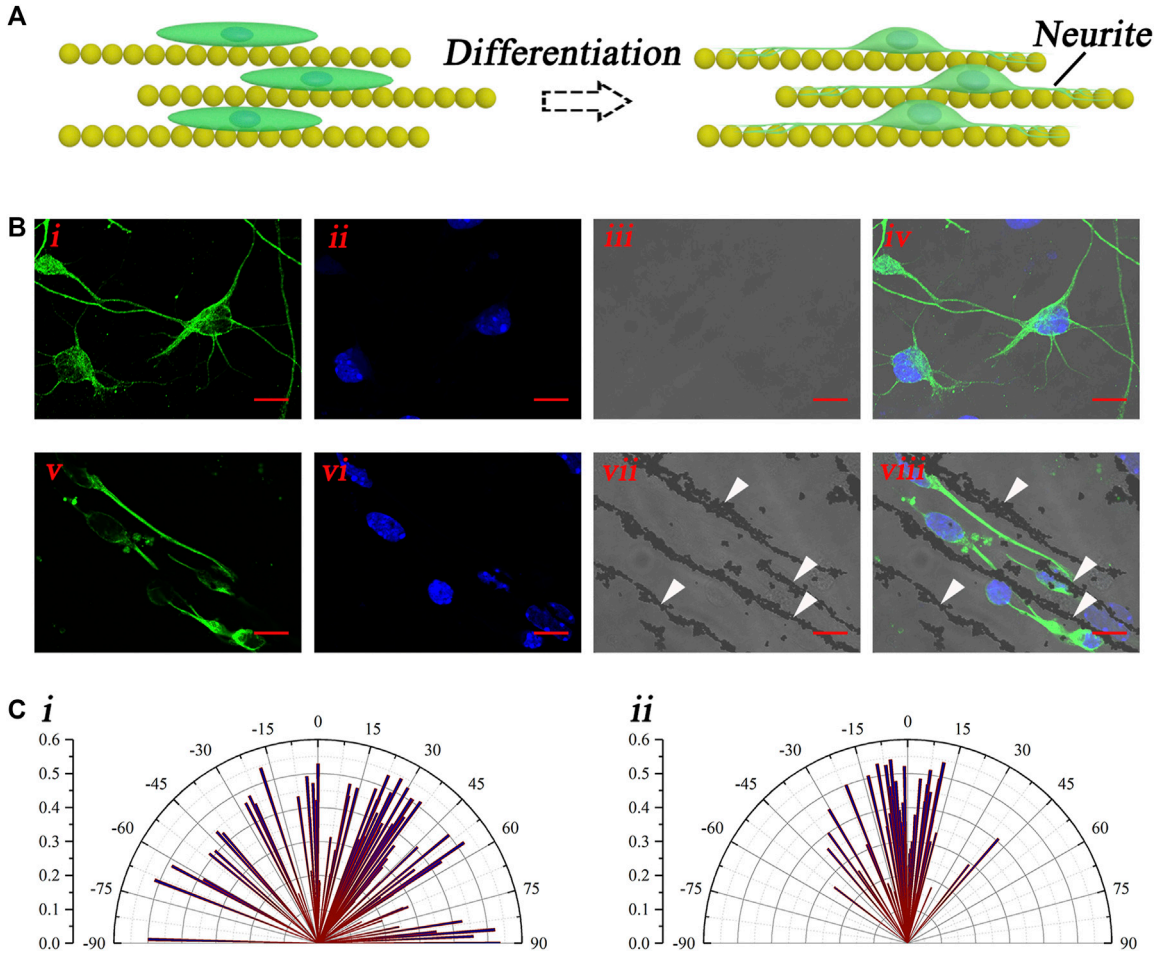

FIGURE 4 | Oriented growth of the newly derived neurons. **(A)** Schematic illustration of the oriented growth of newly derived neurons. **(B)** Representative fluorescent photographs of newly derived neurons of both the control (i–iv) and the nanochain-guided (v–viii) groups, the scale bars are 10 μm. **(C)** Orientation angle statistic graphs of both the control (i) and the nanochain-guided (ii) newly derived neurons.

were assembled into linear nanochains by inducing of the magnetic field. Based on the "contact-guidance" of the magnetic nanochains, the seeded neural stem cells exhibited a linear arrangement in comparison to the control. When aligned, neural stem cells maintained the good activity at the same time. This result demonstrated that the anisotropic topography of the magnetic nanochains possessed an excellent guiding effect in regulating the neural stem cells migration through the "contact-guidance" effect. Following the arrangement, the differentiation culturing of the neural stem cells was performed. With culturing, the neurites of the newly derived neurons extended along with the magnetic nanochains. By immunofluorescence staining, the newly derived neurons showed an obvious orientation in comparison to the control, as confirmed by the statistics. So it could be concluded that the magnetic nanochains also had a good guiding effect on the extension of the neurites of the newly derived neurons. This result exhibited huge potential in various anisotropic regenerative environments.

In addition, the magnetic nanochains were assembled by the Fe_3O_4@SiO_2 magnetic nanoparticles, whose bioeffects and biosafety have been extensively studied and widely applied in biomedicine, such as magnetic resonance imaging (MRI). This property endowed excellent biocompatibility for the magnetic nanochains, which was confirmed by activity marker staining. Moreover, the Fe_3O_4@SiO_2 magnetic nanoparticles possessed good monodispersity, which was very convenient to prepare the monodispersed solution. This monodispersed solution could easily be introduced to the regenerative site, which possessed huge potential in clinical application. Furthermore, the magnetic nanochains could be easily integrated with the other biomaterials, such as the hydrogel, to fabricate the composite materials. During fabrication, the linear topography of the magnetic nanochains could be effectively integrated into the composite biomaterials, thus significantly enhancing the guiding effect of the composite biomaterials. So it could be concluded that the magnetic nanochains would become a versatile platform in biomedical applications.

MATERIALS AND METHODS

Materials

Ethylene glycol, ferric chloride, and sodium acetate were obtained from Aladdin (Shanghai, China). Sodium hydroxide and tetraethoxysilane (TEOS) were obtained from Macklin (Shanghai, China). Laminin and acrylamide were obtained from Sigma-Aldrich (MO, United States). Phosphate buffered saline (PBS), accutase, Hanks' balanced salt solution (HBSS), B-27, and recombinant human epidermal growth factor (EGF) were obtained from Gibco (NY, United States). Recombinant murine FGF-basic (FGF) was obtained from PropTech (NJ, United States). The NeuroCult™ differentiation kit was obtained from STEMCELL Technologies (CA, United States). The nestin marker (Nestin antibody, AN205), TuJ-1 marker (neuronal class III β-tubulin, AT809), and DAPI (C1002) were obtained from Beyotime (Jiangsu, China). Donkey anti-mouse secondary antibody (A21202) was obtained from ThermoFisher (MA, United States).

Fabrication of the Fe_3O_4 Nanoparticles

In detail, 16 ml of ethylene glycol, 0.26 g of ferric chloride, 1.2 g of sodium acetate, 0.4 g of poly (4-styrenesulfonic acid-co-maleic acid) sodium salt, 4.5 mg of acrylamide, and 20–50 μL of deionized water were added into a boiling flask in sequence. Then, the mixed solution was kept for vigorous stirring for 30 min to obtain a solution with uniform yellow under room temperature. Then, 0.24 g sodium hydroxide was added to the uniform yellow solution, maintaining the stirring until the mixed solution became black. The black solution was transferred into a 20-ml stainless steel autoclave lined by Teflon and kept under 190°C for 9 h. After the process, the solution was cooled to room temperature, and the obtained Fe_3O_4 nanoparticles were collected with a magnet. Then, the Fe_3O_4 nanoparticles were sequentially washed by the mixed solution of deionized water and ethanol (1:1) three times and then by deionized water three times. Then, the Fe_3O_4 nanoparticles were dispersed in deionized water in the final step. The manufacturing procedure was according to the hydrothermal synthesis, as elaborated in the literature (Dong et al., 2016; Tang et al., 2018; Zhang et al., 2019).

Fabrication of the Fe_3O_4@SiO_2 Nanoparticles

First, 6 ml of Fe_3O_4 dispersed solution (obtained above) was dissolved in 40 ml ethanol, and then, 2 ml of ammonia hydroxide was added to the solution. It was followed by sonicating the mixed solution for 5 min and transferring the mixed solution into a three-necked flask. It was subjected to stirring for 10 min with the speed of 600 rpm under a 50°C water bath. Then, TEOS was added into the mixed solution at a speed of 200 μL per 20 min. Under constant stirring for 1 h, the manufactured Fe_3O_4@SiO_2 nanoparticles were collected by a magnet, washed with ethanol and deionized water, and then dispersed into deionized water.

Magnetic Nanochain Fabrication

The monodispersed solution of Fe_3O_4@SiO_2 nanoparticles (20 μg/ml) containing 1% laminin was added onto a coverslip within a 20 mT static magnetic field. The whole device was maintained at 37°C with 5% CO_2 overnight. The Fe_3O_4@SiO_2 nanoparticles were arranged in lines, according to the magnetic induction. Then, laminin coating was performed on the aligned magnetic nanochains. After coating, the magnetic nanochains were immobilized without the magnetic field.

Isolation and Proliferation of Neural Stem Cells

The hippocampuses of embryonic rats (16–19 days) were collected into HBSS solution in a Petri dish under 4°C. Then, it was followed by discarding the HBSS solution and dripping the accutase into the collected hippocampuses for digestion. Digestion was allowed for 20 min at 37°C with 5% CO_2. The accutase was discarded. Then, the proliferation medium (DMEM/F12 containing 2% B-27, 20 ng/ml FGF, and 20 ng/ml EGF) was added to the Petri dish, and the hippocampuses were triturated gently to form the monodispersed cell solution. Then, the monodispersed cell solution was cultured in the incubator at 37°C with 5% CO_2.

Differentiation of Neural Stem Cells

The neural stem cell monodispersed solution was dripped onto the laminin-coated magnetic nanochains and cultured for 7 days with the proliferation medium. Then, the medium was displaced by the differentiation medium (NeuroCult™ differentiation kit). The differentiation culturing was maintained for 7 days. The neural lineage cells were stained by immunofluorescence and observed by using a confocal microscope.

DATA AVAILABILITY STATEMENT

The raw data supporting the conclusions of this article will be made available by the authors, without undue reservation.

AUTHOR CONTRIBUTIONS

LX Investigation, Formal analysis, Methodology, Writing-original draft; JGF Validation; KMS Validation; CZ Writing-review and editing; YGN Writing-review and editing; YFY Writing-review and editing; RJC Supervision, Funding acquisition.

FUNDING

This work was supported in finance by the National Basic Research Program of China (award number: 2017YFA0105201), the National Key R&D Program of China (award numbers: 2021YFA1101300 and 2020YFA0112503), the Strategic Priority Research Program

of the Chinese Academy of Science (award number: XDA16010303), the National Natural Science Foundation of China (award numbers: 82030029, 81970882, 81800913, and 81974142), the Natural Science Foundation from Jiangsu Province (award number: BE2019711), the Science and Technology Department of Sichuan Province (award number: 2021YFS0371),the Shenzhen Fundamental Research Program (award numbers: JCYJ20190814093401920 and JCYJ20210324125608022), and the Open Research Fund of the State Key Laboratory of Genetic Engineering, Fudan University (award number: SKLGE-2109).

REFERENCES

Allan, S. M., and Rothwell, N. J. (2001). Cytokines and Acute Neurodegeneration. *Nat. Rev. Neurosci.* 2, 734–744. doi:10.1038/35094583

Cai, J., Luo, W., Pan, J., Li, G., Pu, Y., Si, L., et al. (2022). Glucose-Sensing Photonic Nanochain Probes with Color Change in Seconds. *Adv. Sci.* 9, 2105239. doi:10.1002/advs.202105239

Deng, Y., Xi, X., Xia, Y., Cao, Y., Xue, S., Wan, S., et al. (2022). 2D FeP Nanoframe Superlattices via Space-Confined Topochemical Transformation. *Adv. Mater.* 34, 2109145. doi:10.1002/adma.202109145

Dong, Y., Wen, B., Chen, Y., Cao, P., and Zhang, C. (2016). Autoclave-free Facile Approach to the Synthesis of Highly Tunable Nanocrystal Clusters for Magnetic Responsive Photonic Crystals. *RSC Adv.* 6, 64434–64440. doi:10.1039/c6ra10355c

Gradinaru, L. M., Barbalata Mandru, M., Drobota, M., Aflori, M., Butnaru, M., Spiridon, M., et al. (2021). Composite Materials Based on Iron Oxide Nanoparticles and Polyurethane for Improving the Quality of MRI. *Polymers* 13, 4316. doi:10.3390/polym13244316

Huang, H.-Q., Li, Y.-Y., Chen, S.-H., Liu, Z.-G., Cui, Y.-M., Li, H.-Q., et al. (2022). Noble-metal-free Fe3O4/Co3S4 Nanosheets with Oxygen Vacancies as an Efficient Electrocatalyst for Highly Sensitive Electrochemical Detection of As(III). *Anal. Chim. Acta* 1189, 339208. doi:10.1016/j.aca.2021.339208

Khani, T., Alamzadeh, Z., Sarikhani, A., Mousavi, M., Mirrahimi, M., Tabei, M., et al. (2022). Fe3O4@Au Core-Shell Hybrid Nanocomposite for MRI-Guided Magnetic Targeted Photo-Chemotherapy. *Lasers Med. Sci.* doi:10.1007/s10103-021-03486-9

Luo, W., Cui, Q., Fang, K., Chen, K., Ma, H., and Guan, J. (2020). Responsive Hydrogel-Based Photonic Nanochains for Microenvironment Sensing and Imaging in Real Time and High Resolution. *Nano Lett.* 20, 803–811. doi:10.1021/acs.nanolett.7b04218

Luo, Y., Fan, L., Liu, C., Wen, H., Wang, S., Guan, P., et al. (2022). An Injectable, Self-Healing, Electroconductive Extracellular Matrix-Based Hydrogel for Enhancing Tissue Repair after Traumatic Spinal Cord Injury. *Bioact. Mater.* 7, 98–111. doi:10.1016/j.bioactmat.2021.05.039

Pan, L., Peng, Z., Yu, H., Liang, T., and Cheng, C. (2021). Robust Synthesis of Highly Charged Superparamagnetic Fe3O4 Colloidal Nanocrystal Clusters for Magnetically Responsive Photonic Crystals. *New J. Chem.* 45, 16511–16519. doi:10.1039/d1nj02582a

Pileni, M.-P. (2021). Self-Assemblies of Nanocrystals in Tumor Cells: Controlling the Intracellular Fate, Manipulation, and Photothermal Effects. *J. Phys. Chem. C* 125, 20143–20156. doi:10.1021/acs.jpcc.1c05115

Qi, Z., Zhang, T., Kong, W., Fu, C., Chang, Y., Li, H., et al. (2022). A Dual-Drug Enhanced Injectable Hydrogel Incorporated with Neural Stem Cells for Combination Therapy in Spinal Cord Injury. *Chem. Eng. J.* 427, 130906. doi:10.1016/j.cej.2021.130906

Qiao, M., Tian, Y., Li, J., He, X., Lei, X., Zhang, Q., et al. (2022). Core-shell Fe3O4@SnO2 Nanochains toward the Application of Radar-Infrared-Visible Compatible Stealth. *J. Colloid Interface Sci.* 609, 330–340. doi:10.1016/j.jcis.2021.12.012

Qin, Z., Wang, C., Ma, Y., Sun, Z., Zhong, B., Li, X., et al. (2021). MoS2 Nanoflowers Decorated with Fe3O4/Graphite Nanosheets for Controllable Electromagnetic Wave Absorption. *ACS Appl. Nano Mat.* 4, 3434–3443. doi:10.1021/acsanm.0c03328

Raza, C., Anjum, R., and Shakeel, N. u. A. (2019). Parkinson's Disease: Mechanisms, Translational Models and Management Strategies. *Life Sci.* 226, 77–90. doi:10.1016/j.lfs.2019.03.057

Shariati, A., Nemati, R., Sadeghipour, Y., Yaghoubi, Y., Baghbani, R., Javidi, K., et al. (2020). Mesenchymal Stromal Cells (MSCs) for Neurodegenerative Disease: A Promising Frontier. *Eur. J. Cell Biol.* 99, 151097. doi:10.1016/j.ejcb.2020.151097

Shen, H., Xu, B., Yang, C., Xue, W., You, Z., Wu, X., et al. (2022). A DAMP-Scavenging, IL-10-releasing Hydrogel Promotes Neural Regeneration and Motor Function Recovery after Spinal Cord Injury. *Biomaterials* 280, 121279. Biomaterials 280. doi:10.1016/j.biomaterials.2021.121279

Shi, L., Du, X., Jiang, H., and Xie, J. (2017). Ghrelin and Neurodegenerative Disorders-A Review. *Mol. Neurobiol.* 54, 1144–1155. doi:10.1007/s12035-016-9729-1

Tang, S., Wang, C., Liu, N., Li, Y., Han, P., and Lu, Q. (2018). Instantaneous Magnetically Assembled and Hydrophilic Photonic Crystals with Controlled Diffraction Colors. *J. Phys. Chem. C* 122, 18021–18028. doi:10.1021/acs.jpcc.8b05967

Wang, K., Xu, X., Li, Y., Rong, M., Wang, L., Lu, L., et al. (2021). Preparation Fe3O4@chitosan-Graphene Quantum Dots Nanocomposites for Fluorescence and Magnetic Resonance Imaging. *Chem. Phys. Lett.* 783, 139060. doi:10.1016/j.cplett.2021.139060

Yu, L., Liu, M., Zhang, Y., Ni, Y., Wu, S., and Liu, R. (2022). Magnetically Induced Self-Assembly DNAzyme Electrochemical Biosensor Based on Gold-Modified α-Fe2O3/Fe3O4 Heterogeneous Nanoparticles for Sensitive Detection of Ni2+. *Nanotechnology* 33, 095601. doi:10.1088/1361-6528/ac3b0e

Zhang, Y., Wang, Y., Wang, H., Yu, Y., Zhong, Q., and Zhao, Y. (2019). Super-Elastic Magnetic Structural Color Hydrogels. *Small* 15, 1902198. doi:10.1002/smll.201902198

Conflict of Interest: The authors declare that the research was conducted in the absence of any commercial or financial relationships that could be construed as a potential conflict of interest.

The reviewer XY declared a shared affiliation with the author KS to the handling editor at the time of review.

Publisher's Note: All claims expressed in this article are solely those of the authors and do not necessarily represent those of their affiliated organizations, or those of the publisher, the editors, and the reviewers. Any product that may be evaluated in this article, or claim that may be made by its manufacturer, is not guaranteed or endorsed by the publisher.

frontiers | Frontiers in Bioengineering and Biotechnology

ORIGINAL RESEARCH
published: 02 June 2022
doi: 10.3389/fbioe.2022.916562

Copper-Lithium-Doped Nanohydroxyapatite Modulates Mesenchymal Stem Cells Homing to Treat Glucocorticoids-Related Osteonecrosis of the Femoral Head

*Qianhao Li†, Zhouyuan Yang†, Zhun Wei, Donghai Li, Yue Luo and Pengde Kang**

Orthopedic Research Institute, Department of Orthopedics, West China Hospital, Sichuan University, Chengdu, China

OPEN ACCESS

Edited by:
Jianxun Ding,
Changchun Institute of Applied Chemistry (CAS), China

Reviewed by:
Tairong Kuang,
Zhejiang University of Technology, China
Jun Wu,
Sun Yat-sen University, China
Yong Sun,
Sichuan University, China

***Correspondence:**
Pengde Kang
kangpengde69@126.com

†These authors have contributed equally to this work and share first authorship

Specialty section:
This article was submitted to Biomaterials, a section of the journal Frontiers in Bioengineering and Biotechnology

Received: *09 April 2022*
Accepted: *18 May 2022*
Published: *02 June 2022*

Citation:
Li Q, Yang Z, Wei Z, Li D, Luo Y and Kang P (2022) Copper-Lithium-Doped Nanohydroxyapatite Modulates Mesenchymal Stem Cells Homing to Treat Glucocorticoids-Related Osteonecrosis of the Femoral Head. Front. Bioeng. Biotechnol. 10:916562. doi: 10.3389/fbioe.2022.916562

In situ tissue regeneration has been demonstrated to promote bone repair. To identify a better approach for treating osteonecrosis of the femoral head (ONFH), we prepared scaffolds using copper-lithium-doped nanohydroxyapatite (Cu-Li-nHA), which has the potential to modulate mesenchymal stem cells (MSCs) homing. The scaffold was fabricated using the gas foaming method and the migration, angiogenesis, and osteogenesis activities of MSCs were detected using Transwell assays, tube formation assays, alkaline phosphatase and alizarin red S staining, respectively. We then implanted the Cu-Li-nHA scaffold into the femoral heads of ONFH rabbits, and CFSE labeled exogenous MSCs were injected intravenously to verify cell homing. The repair effect was subsequently examined using micro-CT and histological analysis *in vivo*. The results showed that Cu-Li-nHA significantly promoted MSCs migration and homing by upregulating the HIF-1α/SDF-1 pathway. The Cu-Li-nHA group showed optimal osteogenesis and angiogenesis and greater improvements in new bone formation in ONFH rabbits. To summarize, Cu-Li-nHA promoted homing and induced the osteogenic differentiation of MSCs, thereby enhancing bone regeneration during ONFH repair. Thus, Cu-Li-nHA implantation may serve as a potential therapeutic strategy for ONFH in the future.

Keywords: copper-lithium-doped nanohydroxyapatite, osteonecrosis of the femoral head, mesenchymal stem cells, cell homing, *in situ* tissue regeneration

INTRODUCTION

The excessive long-term use of glucocorticoids (GCs) is one of the major etiologies of osteonecrosis of the femoral head (ONFH), a condition that decreases a patient's quality of life (Chughtai et al., 2017; Mont et al., 2020). Moreover, most patients who experience a collapse of the femoral head need to undergo total hip arthroplasty (THA) (Moya-Angeler et al., 2015). Unfortunately, the mechanisms underlying GCs-ONFH remain unclear, although, abnormal differentiation of bone marrow stem cells (BMSCs), apoptosis of osteocytes, and tissue ischemia may play important roles in its pathogenesis (Zhun et al., 2018; Chang et al., 2020). Studies have demonstrated that BMSCs derived from patients with GCs-ONFH exhibit poorer osteogenic differentiation activity than those derived from healthy individuals (Houdek et al., 2016). High-dose GCs can inhibit the Wnt/β-

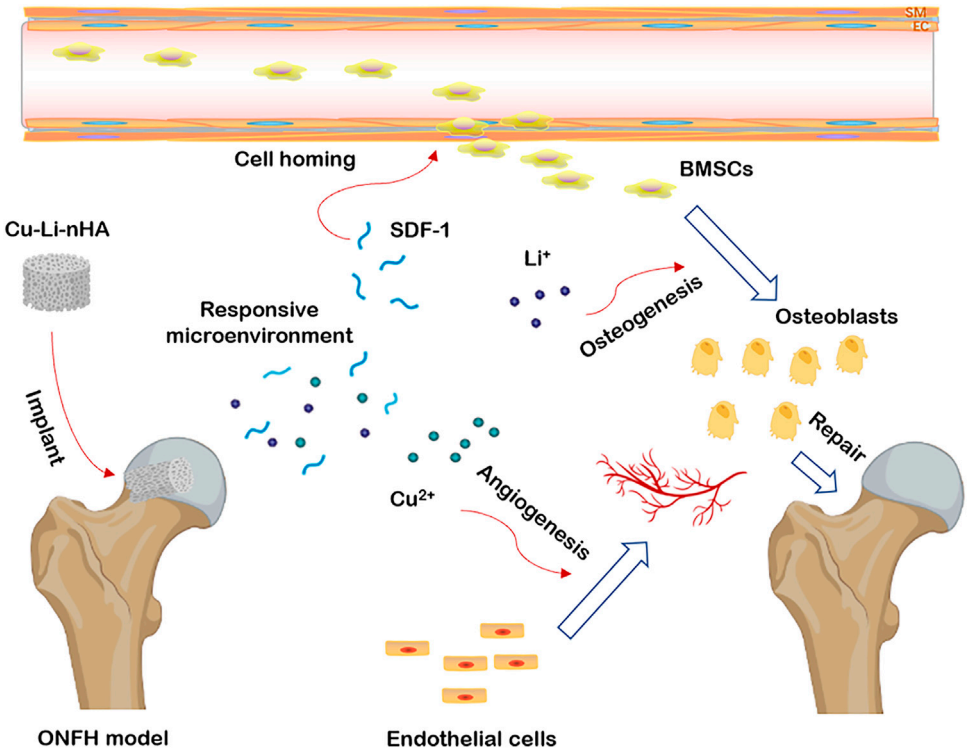

FIGURE 1 | The graphical abstract of the study. Cu-Li-nHA implantation could stimulate adjacent tissue and build an optimal microenvironment *via* releasing Li^{+} and Cu^{2+}, and promote cell homing, osteogenesis and angiogenesis to repair ONFH.

catenin pathway by upregulating the expression of DKK-1, which prevents the differentiation of BMSCs into osteoblasts and induces adipogenesis (Kato et al., 2018; Zhun et al., 2018). In recent years, biomaterials that promote osteogenesis have made great progress in the treatment of ONFH (Zhao and Ma, 2020; Zhu et al., 2020; Zhu et al., 2022).

Nanohydroxyapatite (nHA) has been widely used in clinical applications, especially for bone defect repair, owing to its excellent biocompatibility and osteoconductivity (Winkler et al., 2018). However, their insufficient osteoinductivity limits the use. Considerable efforts have been made to improve the osteogenesis of nHA by doping metal ions (such as strontium and lithium) into it, which could effectively contribute to the osteoblast differentiation of BMSCs (Ge et al., 2018; Li et al., 2018a). Lithium (Li), a common psychotropic drug, has been shown to enhance bone regeneration by activating the Wnt/GSK-3β pathway (Li et al., 2011). Lithium-doped nanohydroxyapatite (Li-nHA) scaffolds have better osteoinductivity than nHA for repairing bone defects (Li et al., 2018a). However, although Li-nHA improves the cell adherence and differentiation of BMSCs, it cannot help recruit more BMSCs to necrotic areas. Mesenchymal stem cells (MSCs) therapies have been widely studied for the treatment of various diseases (Wang Z. et al., 2022). Although researchers have implanted BMSCs into the femoral head to improve osteogenesis, the complex process of implantation and low survival rate of BMSCs limit the extensive use of this method (Kang et al., 2018; Zhou et al., 2021). An approach known as *in situ* tissue regeneration has been introduced, which can mobilize host endogenous stem cells to target tissues (Ko et al., 2013). Therefore, a scaffold that can modulate the host microenvironment to recruit MSCs to the damaged regions of ONFH is required.

Copper (Cu) ions can stabilize the expression of hypoxia-inducible factor-1α (HIF-1α) and upregulate vascular endothelial growth factor (VEGF) to induce neovascularization (Feng et al., 2009; Li et al., 2021). Angiogenesis also promotes bone development (Hu and Olsen, 2016; Wang L. et al., 2022). After co-culture with BMSCs, Cu-containing bioactive glass scaffolds increased the expression of VEGF and osteocalcin (OCN) simultaneously (Wu et al., 2013). Interestingly, studies have indicated that Cu has the potential to induce cell homing (Meng et al., 2015). After implanting Cu-containing microbubbles in the ischemic infarct area of the heart, BMSCs migrate to this area for regeneration. Cu may elevate the levels of localized stromal cell-derived factor-1 (SDF-1), thus, leading to the recruitment of BMSCs *via* chemotactic attraction (Lau and Wang, 2011; Zhu et al., 2018). Here, according to the *in situ* tissue regeneration concept, we have developed a copper-lithium-doped nanohydroxyapatite (Cu-Li-nHA) composite scaffold that releases Cu ions by upregulating SDF-1 expression, promotes MSCs homing to the necrotic zone, and induces the differentiation of recruited MSCs *via* osteoblastogenesis through Wnt/β-catenin signaling activation. Finally, these

synergistic effects contribute to bone repair in patients with ONFH (**Figure 1**).

MATERIALS AND METHODS

Synthesis and Characterization of Cu-Li-nHA

Cu-nHA and Li-nHA were synthesized by liquid-phase coprecipitation and were mixed to prepare Cu-Li-nHA using the gas foaming method. The doped copper had a molar ratio of 0.25%, and a lithium content of 1.5% (Li et al., 2018b; Li et al., 2021). The synthesis was performed as follows: 1) $(NH_4)_2HPO_4$ (Sinopharm, China) solution was added dropwise to the $Ca(NO_3)_2{\cdot}4H_2O$ (Sinopharm, China) solution containing $LiNO_3$ or $Cu(NO_3)_2$ (Sigma, United States), and then colloidal fluid was separated by a standing and layering process and the precipitate was rinsed and sintered at 1,000°C for 2 h in a muffle furnace to obtain Cu-nHA and Li-nHA powders; 2) 0.25% Cu-nHA and 1.5% Li-nHA powders (1:1 mass) were mixed using a planetary ball mill with a rotating speed of 45 Hz for 10 min to obtain Cu-Li-nHA powders; and 3) The slurry was prepared using a mixture of 5% polyvinyl alcohol, followed by the addition of 10 ml of H_2O_2, and the mixture was then stirred and heated repeatedly until a slurry was filled with foam. Finally, the slurry was dried and the scaffold precursors were sintered at 1,150°C for 4 h to form porous scaffolds.

The materials were characterized using X-ray diffraction (XRD, Shimadzu, Japan) and Fourier-transform infrared spectroscopy (FTIR, Thermo, United States). Transmission electron microscopy (TEM, FEI, United States) was used to observe the particle size, and scanning electron microscopy (SEM, JEOL, Japan) was used to observe the scaffold structure. The porosity was analyzed using mercury intrusion (Micromeritics, United States), and the compressive performance was measured using an electronic universal testing machine (Shimadzu, Japan).

Effects of Cu-Li-nHA on the Differentiation and Migration of BMSCs

BMSCs were isolated from newborn New Zealand white rabbit pups and identified using a previously published method (shown in the **Supplementary Material**) (Li et al., 2018a). BMSCs were co-cultured with Cu-Li-nHA, Li-nHA and nHA (Cu-Li-nHA + BMSCs, Li-nHA + BMSCs, nHA + BMSCs) in an incubator at 37°C, 5% CO_2 for 7 days. Cell adhesion was observed using SEM. In addition, BMSCs were inoculated into 6-well plates containing extract solutions of different materials per well at a density of 5×10^4/ml. Alkaline phosphatase and alizarin red S staining assays were performed to test the osteogenic differentiation of BMSCs at 2 weeks.

Tube formation assays were performed to evaluate neovascularization. Starvation-treated human umbilical vein endothelial cells were inoculated in 48-well plates at a density of 2×10^4/ml. The groups were set as follows: 1) Cu-Li-nHA group: Cu-Li-nHA + BMSCs co-culture medium, 2) Li-nHA group: Li-nHA + BMSCs co-culture medium, 3) nHA group: nHA + BMSCs co-culture medium, 4) positive group: complete medium +50 ng/ml recombinant VEGF protein (SinoBiological, China), and 5) negative group: complete medium. Closed lumens were observed using an inverted microscope (Olympus, Japan).

TABLE 1 | RNA primer sequence.

RNA	Primer sequence
RUNX2	F: 5′GGACGAGGCAAGAGTTTCACTT3′
	R: 5′CTGTCTGTGCCTTCTTGGTTCC3′
β-catenin	F: 5′TCTGCTATTGTACGCACCAT3′
	R: 5′CTGCCATTTTAGCTCCTTCT3′
HIF-1α	F: 5′TCGAAGTAGTGCTGACCCTG3′
	R: 5′ACTGGTAGGCTCAGGTGAAC3′
VEGF	F: 5′TCTACCTCCACCATGCCAAG3′
	R: 5′CACGCACTCCAGGCTTTCAT3′
SDF-1	F: 5′GCTCTGCATCAGTGACGGTA3′
	R: 5′TAATTTCGGGTCAA-TGCACA3′
β-actin	F: 5′CGTCTTCCCCTCCATCGTG3′
	R: 5′GGGTACTTGAGCGTCAGGAT3′

Transwell assays were performed to detect migration of BMSCs. BMSCs and scaffolds were co-cultured for 7 days to prepare the conditioned medium. Conditioned or complete medium was added to the lower chamber of a 24-well Transwell plate for the following five groups: 1) Cu-Li-nHA, 2) Li-nHA, 3) nHA, 4) SDF-1 (complete medium +100 ng/ml recombinant protein of SDF-1) (SinoBiological, China), and 5) negative (complete medium). One milliliter of the CFSE-labeled BMSCs suspension (5×10^4/ml) was dropped into the upper chamber. Transwell plates were incubated for 8 h in an incubator at 37°C and 5% CO_2 and were finally observed by fluorescence microscopy (Olympus, Japan).

The expression levels of Runx2, β-catenin, HIF-1α, VEGF, and SDF-1 were verified using reverse transcription-polymerase chain reaction (RT-PCR) and western blotting. 1) RT-PCR: RNA was isolated from BMSCs using TRIzol reagent (Invitrogen, United States). Primer sequences for each gene are shown in **Table 1**. PCR amplification was performed using real-time PCR (QuantStudio 3, ABI, United States). The pre-reaction was at 95°C for 10 min, and 40 reaction cycles were performed. The parameters were set as follows: 95°C for 15 s, 55°C for 30 s, and 72°C for 30 s. 2) Western blotting: The total protein concentration was determined using the BCA method (Epizyme, China). Proteins were separated by electrophoresis (BioRad, United States) and then diluted primary antibodies (1:1,000) were added and the membranes were incubated at 4°C overnight. The membranes were then incubated with secondary antibodies (1:5,000) at 37°C for 60 min. The bands were obtained using an imaging system (BioRad, United States).

Establishment of the ONFH Model and Material Implantations

The animal study protocol was reviewed and approved by the Animal Care and Use Committee of Sichuan University

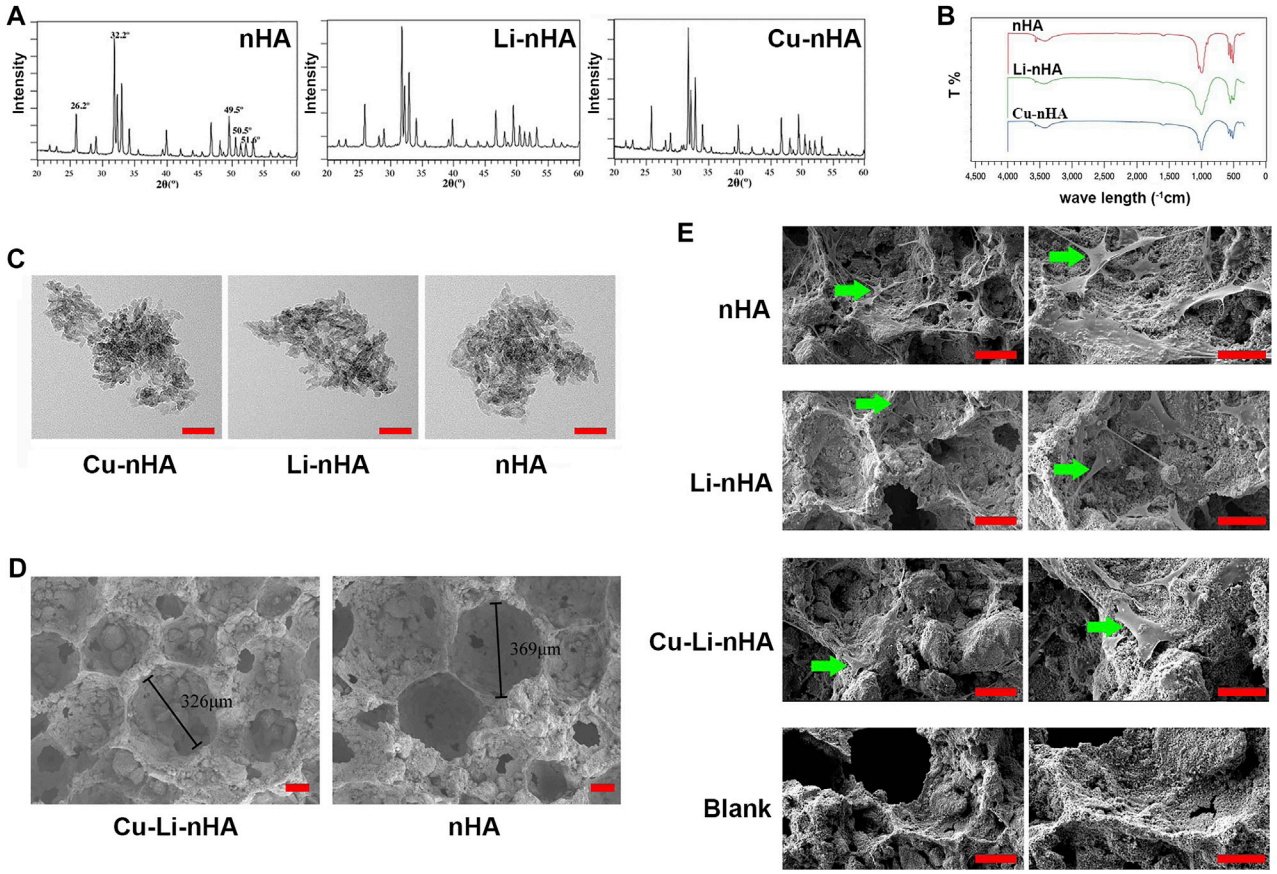

FIGURE 2 | (A) XRD spectrum. **(B)** FITR spectrum. **(C)** TEM observation for particle size. Scale bar in the bottom right-hand corner of each image (red): 50 nm. **(D)** SEM observation for porous scaffold structure. Pore size is shown in each image. Scale bar in the bottom right-hand corner of each image (red): 100 μm. **(E)** SEM observation for BMSCs adhesion to scaffolds. Blank Group: nHA without BMSCs co-culture. Green arrow: adherent BMSCs. Scale bar in the bottom right-hand corner of each image in the left column (red): 100 μm; Scale bar in the bottom right-hand corner of each image in the right column (red): 50 μm.

(2020091A). Thirty New Zealand white rabbits (male, aged 28–32 weeks, weight 2.5–3.2 kg, one per cage) were housed at the animal center of our institution and maintained on a standard laboratory diet and water. The rabbit model of ONFH was established by intramuscular injection of lipopolysaccharide (10 μg/kg, Sigma, United States) combined with intramuscular injection of methylprednisolone (20 mg/kg, Sigma, United States) for the following 3 days (Li et al., 2022).

All animals were labeled with an implantable RFID chip tag and then randomly grouped (six for each) using SPSS software as follows: 1) nHA group, 2) Li-nHA group, 3) Cu-Li-nHA group, 4) negative group (only surgically drilled), and 5) blank group. Drilling and material implantation were performed using the posterior-lateral approach 2 weeks after ONFH modeling in groups 1–4. Materials were implanted after drilling a tunnel (diameter, 3.5 mm) below the junction of the femoral head and neck and 1 cm in depth along the axial direction of the femoral neck (**Supplementary Figures S4, S5**).

In Vivo Evaluation of BMSCs Homing by Cu-Li-nHA

Four weeks after surgery, all groups except for group 4 were injected with 1 ml of exogenous BMSCs (5×10^6/ml) labeled with fluorescent CFSE *via* ear margin veins. Two weeks later, two rabbits in each group were sacrificed to perform immunofluorescence assays to verify cell homing.

Femoral head samples were obtained at 6 and 12 weeks after surgery. The following tests were performed to detect implanted materials and new bone reconstruction: 1) Micro-CT and bone volume (BV)/total volume (TV) analysis; 2) HE and Goldner staining; and 3) immunohistochemistry of OCN, Runx2, GSK-3β, β-catenin, VEGF, and SDF-1 (Abcam, United States).

After fixing with 10% neutral formaldehyde for 7 days, the samples were scanned by micro-CT (Quantum GX II, Perkin Elmer, United States) at a voltage of 90 kV, a current of 88 A, and a voxel size of 50 μm. Then, the samples were decalcified in 20% EDTA for 14 days and then embedded in paraffin. Coronally sections were sliced at a thickness of 3 μm,

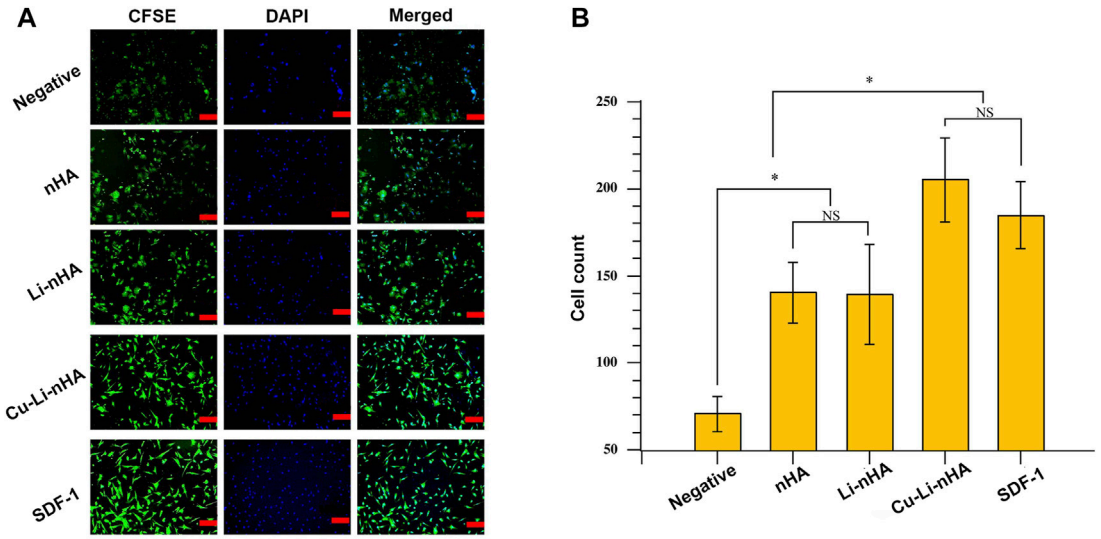

FIGURE 3 | (A) Immunofluorescence assays of BMSCs migration using Transwell device. BMSCs were labeled by CFSE (green) and DAPI (blue). Scale bar in the bottom right-hand corner of each image (red): 100 μm. **(B)** The number of migrated cells under the membrane among different groups. Negative Group: complete medium; SDF-1 Group: SDF-1 + complete medium. Statistical analysis was conducted using a one-way analysis of variance with post-hoc Bonferroni's multiple comparisons test. NS: $p > 0.05$, $^*p < 0.05$.

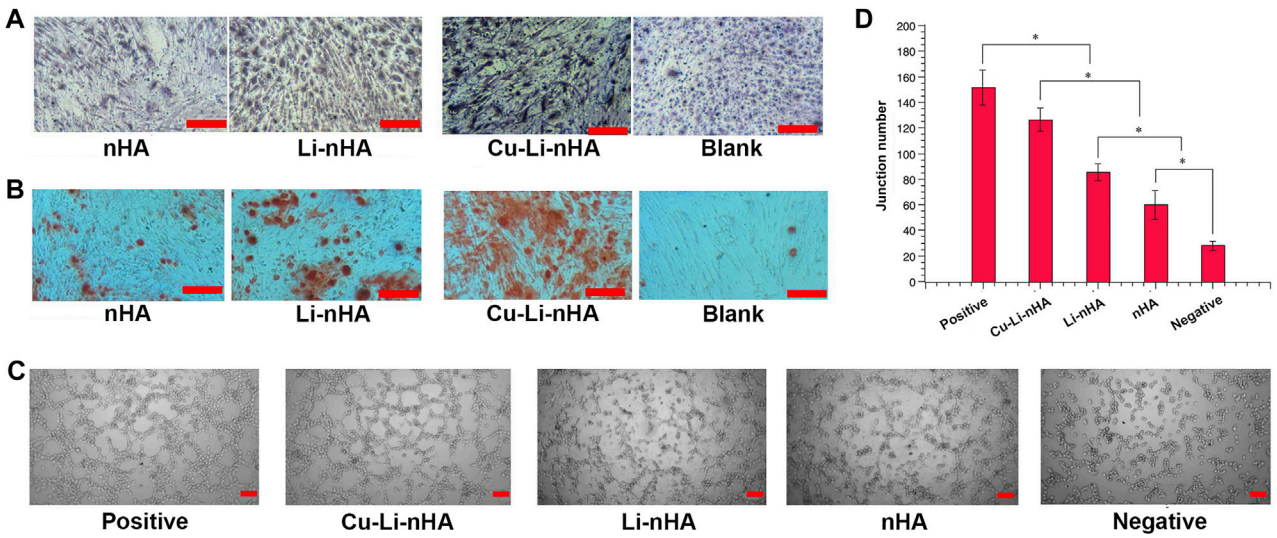

FIGURE 4 | (A,B) Osteogenic differentiation tests. **(A)** Alkaline phosphatase staining among groups. Light or dark purple staining cells represent positive cells. **(B)** Alizarin red S staining among groups. The red areas or dots represent calcium nodules or deposits. Blank Group: complete medium. Scale bar in the bottom right-hand corner of each image (red): 200 μm. **(C,D)** Tube formation assays for angiogenesis test. **(C)** Tube-like structure represents newly formed vessel. Scale bar in the bottom right-hand corner of each image (red): 200 μm. **(D)** The number of tube-like structures among different groups. Positive Group: VEGF + complete medium; Negative Group: complete medium. Statistical analysis was conducted using a one-way analysis of variance with post-hoc Bonferroni's multiple comparisons test. $^*p < 0.05$.

dewaxed in xylene, and hydrated with graded ethanol series before staining with the HE reagent kit (Beyotime, China). To analyze the area of mineralized bone, Goldner staining was performed sequentially following the protocols of the stain kit (Solarbio, China) using Weigert iron hematoxylin solution, Ponceau solution, Orange G solution, and Light Green solution. The sections for detecting cell homing were incubated with the diluted primary antibody of Collagen I (1:200), and then labeled with the secondary antibody of Cy5. DAPI (1 μg/ml) counterstained sections were observed under the confocal microscope (Nikon, Japan). Immunohistochemistry was

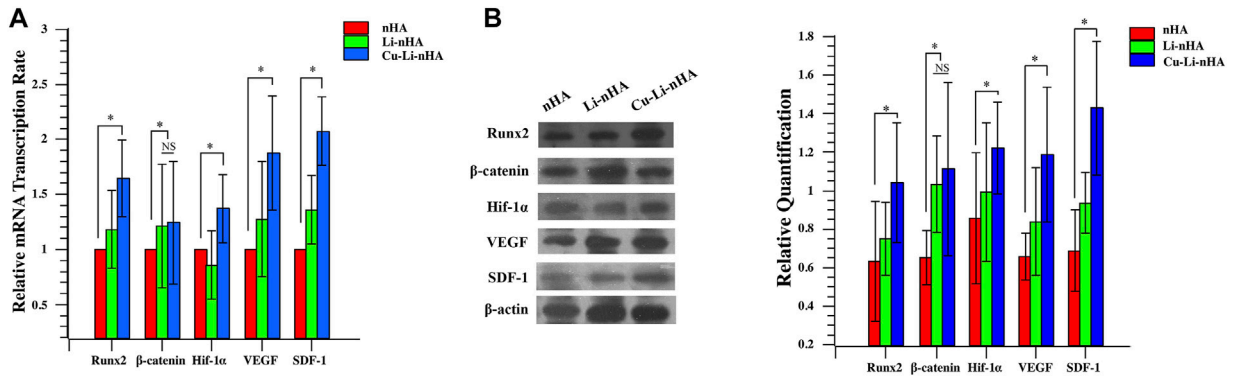

FIGURE 5 | (A) RT-PCR and **(B)** Western-blotting of RUNX2, β-catenin, HIF-1α, VEGF and SDF-1 in BMSCs. Statistical analysis was conducted using a one-way analysis of variance with post-hoc Bonferroni's multiple comparisons test. NS: $p > 0.05$, $^*p < 0.05$.

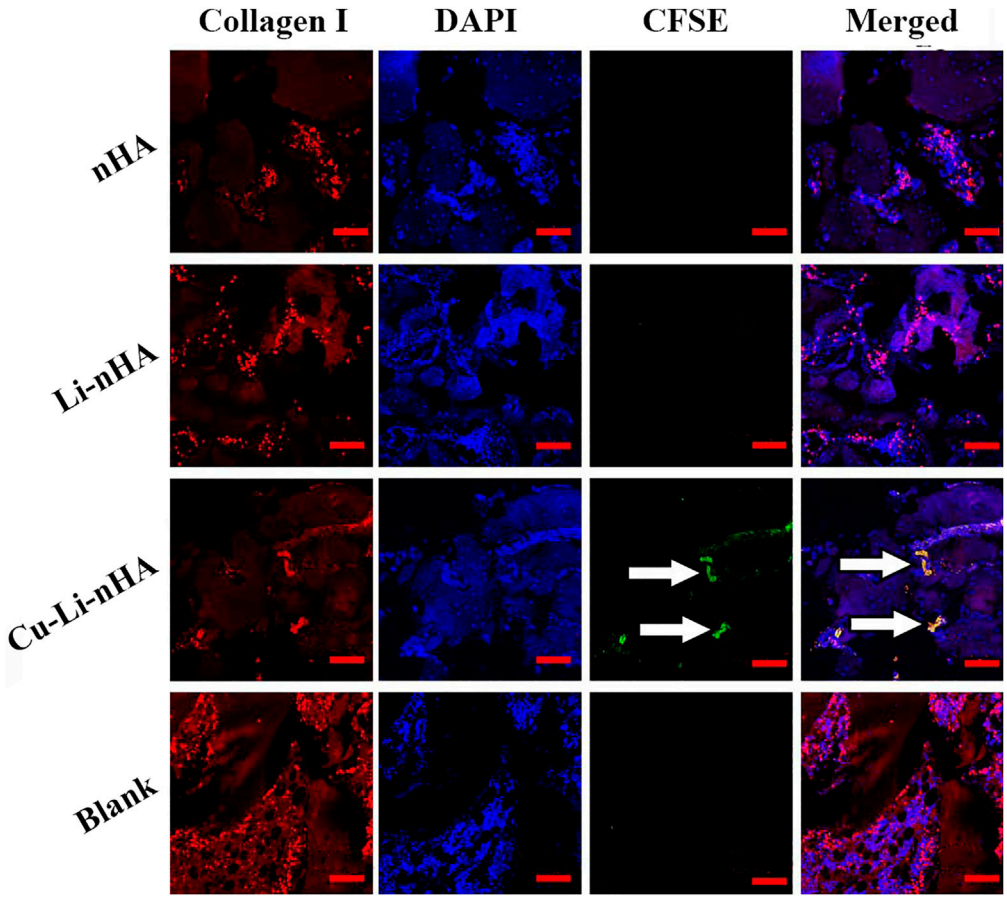

FIGURE 6 | Immunofluorescence assays to verify BMSCs homing 2 weeks after injecting with exogenous CFSE-labeled BMSCs. BMSCs in the implanted regions were shown under the Collagen I signal (red), and homing BMSCs were shown under the CFSE signal (green). White arrow: CFSE-labeled BMSCs. Scale bar in the bottom right-hand corner of each image (red): 200 μm.

conducted with diluted primary antibodies (1:200) at 4°C overnight and visualized with a secondary antibody. Immunohistochemical proteins were analyzed using the positive staining area ratio.

Statistical Analysis

For the semi-quantitative analysis above, three researchers blinded to the group allocation used ImageJ software (National Institutes of Health, United States) to analyze each sample, and

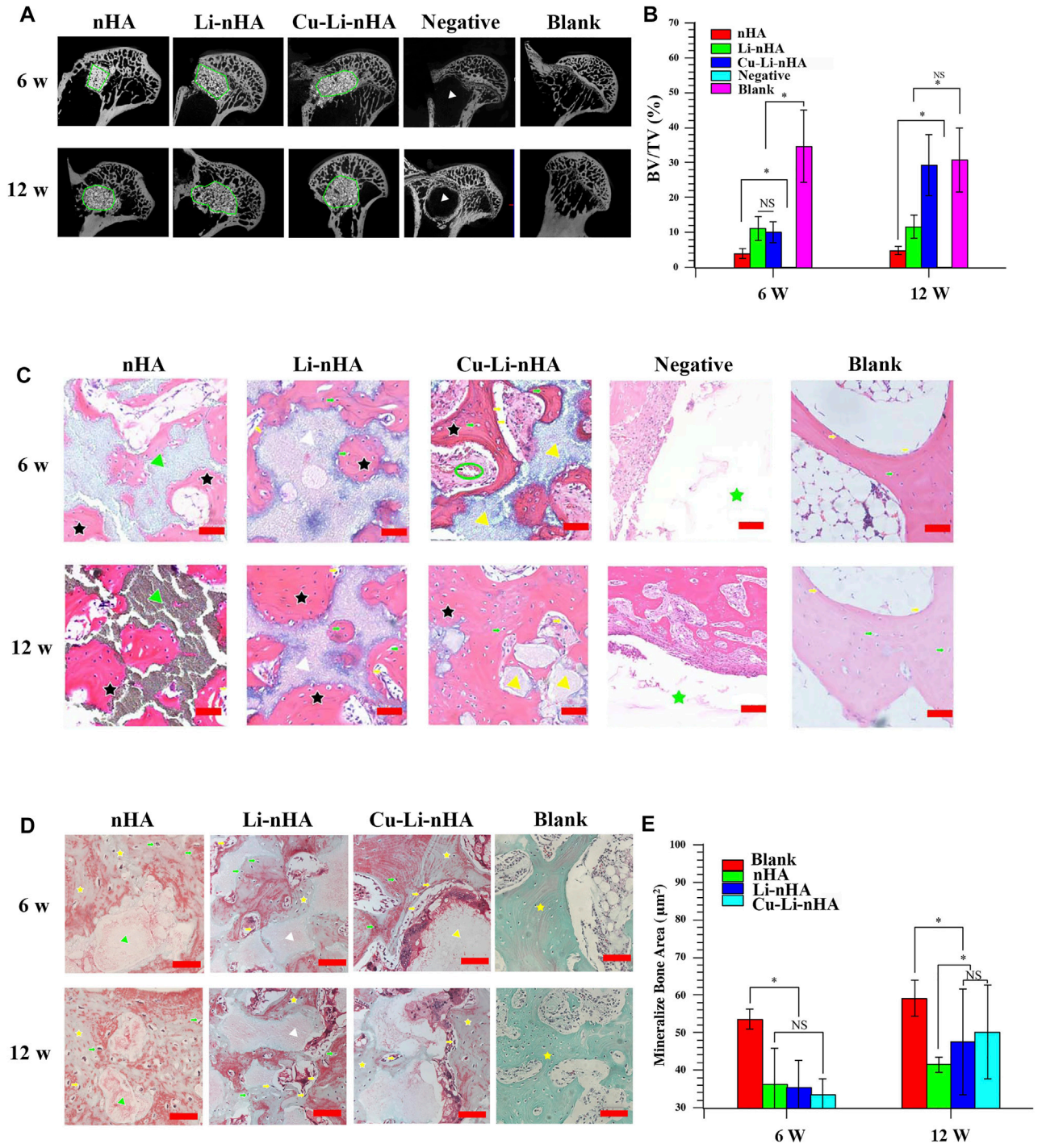

FIGURE 7 | (A,B) Micro-CT observation and BV/TV values in the bone defect area. The regions within the green circle were implanted with scaffolds. Materials showed high density and new trabecular bone showed medium density. Negative Group: only drilling tunnels. Blank Group: without ONFH modeling and scaffold-implantation operation. White triangle: region of drilling. **(C)** HE staining. Black asterisk: trabecular bone. Green asterisk: drilling region. Yellow arrow: lining cell. Green arrow: osteocyte. Green triangle: nHA scaffold. White triangle: Li-nHA scaffold. Yellow triangle: Cu-Li-nHA scaffold. Green circle: neovascularization. Negative Group: only drilling tunnels. Blank Group: without ONFH modeling and scaffold-implantation operation. Scale bar in the bottom right-hand corner of each image (red): 100 μm. **(D,E)** Goldner staining and mineralize bone area analysis. Mineralized bone was stained in green, and osteoid was in red. Yellow asterisk: mineralized trabecular bone. Yellow arrow: lining cell. Green arrow: osteocyte. Green triangle: nHA scaffold. White triangle: Li-nHA scaffold. Yellow triangle: Cu-Li-nHA scaffold. Blank Group: without ONFH modeling and scaffold-implantation operation. Scale bar in the bottom right-hand corner of each image (red): 50 μm. Statistical analysis was conducted using a one-way analysis of variance with post-hoc Bonferroni's multiple comparisons test. NS: $p > 0.05$, $^{*}p < 0.05$.

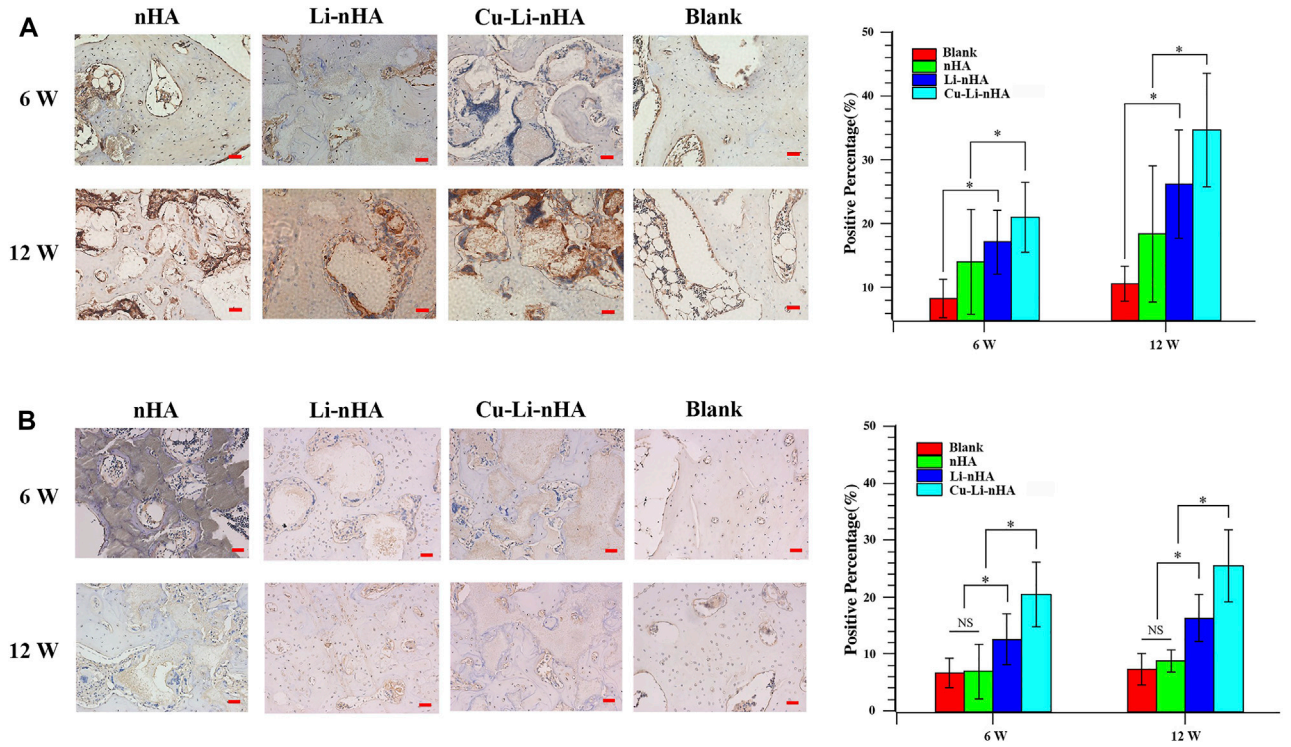

FIGURE 8 | Immunohistochemistry and positive ratio analysis of OCN **(A)**, Runx2 **(B)**. Blank Group: without ONFH modeling and scaffold-implantation operation. Scale bar in the bottom right-hand corner of each image (red): 100 μm. Statistical analysis was conducted using a one-way analysis of variance with post-hoc Bonferroni's multiple comparisons test. NS: $p > 0.05$, $^{*}p < 0.05$.

the average results were determined after three repeated measurements.

SPSS 22.0 (SPSS Inc., Chicago) was used to perform statistical analysis, and significant differences were defined at $p < 0.05$. All continuous variables are expressed as the mean ± standard deviation (mean ± SD). The results were analyzed using a one-way analysis of variance with post-hoc Bonferroni's multiple comparisons test.

RESULTS

Characterization of Cu-Li-nHA

The characteristic peaks of Li-nHA or Cu-nHA were detected at 26.2°, 32.2°, 49.5°, 50.5° and 51.6°, and these findings are consistent with the spectrum of the standard nHA (**Figure 2A**). The FTIR results also showed a similar spectrum for the three groups. The peak at the wave length near 3,500 cm^{-1} was the absorption peak of hydroxyl groups (O-H), while the peaks at the wave length near 1,000 cm^{-1} and 600 to 500 cm^{-1} were the absorption peaks of phosphate (PO_4^{3-}) (**Figure 2B**). TEM showed that each particle was composed of several needle- or rod-like structures with long diameter less than 50 nm, thus, confirming the sizes of Cu-nHA and Li-nHA were at the nanometer level (**Figure 2C**). The SEM analysis showed that the gas foaming method could prepare a Cu-Li-nHA three-dimensional porous scaffold with see-through pores between macropores and the interconnections of pores (**Figure 2D**). Cu-Li-nHA and nHA had no significant differences in porosity (74.65 ± 11.33% vs. 71.59 ± 11.09%, $p > 0.05$) or compressive strength (4.79 ± 0.92 MPa vs. 4.82 ± 0.85 MPa, $p > 0.05$).

Cu-Li-nHA Promoted BMSCs Migration, Osteogenesis, and Angiogenesis

Cu-Li-nHA had the advantage of cell compatibility in that fibroblast-like BMSCs adhered to the pore wall (**Figure 2E**). The number of migrated cells in the Cu-Li-nHA group was the highest ($p < 0.05$), but there was no significant difference between the Cu-Li-nHA and the SDF-1 groups ($p > 0.05$) (**Figures 3A,B**). The number of migrated BMSCs in the nHA and Li-nHA groups was clearly less than that in the SDF-1 group ($p < 0.05$). Alkaline phosphatase expression in the Cu-Li-nHA group was significantly higher than that in the nHA and Li-nHA groups. The number of calcium deposits was also visibly higher in the Cu-Li-nHA group than in the nHA and Li-nHA groups (**Figures 4A,B**). As shown in **Figures 4C,D**, the number of vascular-like structures in the Cu-Li-nHA group was the highest among the three scaffold groups ($p < 0.05$), but less than that in the positive group ($p < 0.05$). The expression levels of Runx2, HIF-1α, VEGF, and SDF-1 in BMSCs were significantly higher

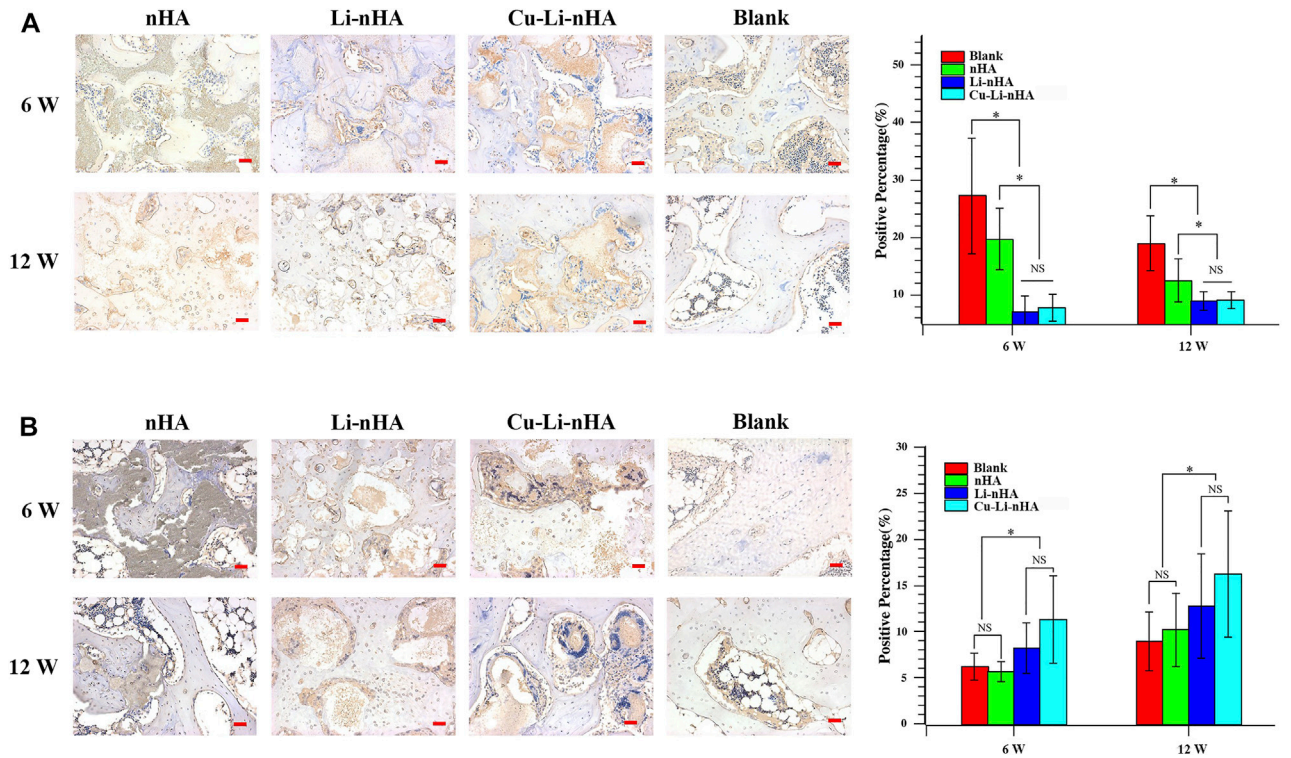

FIGURE 9 | Immunohistochemistry and positive ratio analysis of GSK-3β **(A)**, β-catenin **(B)**. Blank Group: without ONFH modeling and scaffold-implantation operation. Scale bar in the bottom right-hand corner of each image (red): 100 μm. Statistical analysis was conducted using a one-way analysis of variance with post-hoc Bonferroni's multiple comparisons test. NS: $p > 0.05$, $^{*}p < 0.05$.

in the Cu-Li-nHA group than in the other groups (**Figures 5A,B**).

Cu-Li-nHA Modulated BMSCs Homing for Treating ONFH *in Vivo*

Cells *in situ* were observed in all groups, whereas CFSE-labeled cells were observed only in the Cu-Li-nHA group (**Figure 6**). The materials showed high density in the bone defect area under micro-CT, whereas the new trabecular bone showed medium density (**Figure 7A**). A greater medium-density area could be observed in the Li-nHA and Cu-Li-nHA groups than in the nHA group after 6 weeks, and the density of the implanted region in the Cu-Li-nHA group was close to that in the blank group after 12 weeks. BV/TV showed similar trends after 6 (Cu-Li-nHA vs. nHA, $p < 0.05$) and 12 weeks (Cu-Li-nHA vs. Li-nHA, $p < 0.05$) (**Figure 7B**).

HE staining showed new trabecular bone formation in the nHA, Li-nHA, and Cu-Li-nHA groups, and the shape of the trabecular bone in the Cu-Li-nHA group was intact. Abundant neovascularization was also observed in the Cu-Li-nHA group (**Figure 7C**). Goldner staining showed that trabecular bone mineralization in the Cu-Li-nHA and Li-nHA groups was higher than that in the nHA group ($p < 0.05$), but lower than that in the blank group (without ONFH modeling and scaffold-implantation operation) ($p < 0.05$) (**Figures 7D,E**). The expression levels of OCN, Runx2, β-catenin, VEGF, and SDF-1 in the Cu-Li-nHA group were higher than those in the other groups ($p < 0.05$) (**Figures 8**, **9**, **10**). In addition, the expression levels of GSK-3β in the Cu-Li-nHA and Li-nHA groups were significantly lower ($p < 0.05$).

DISCUSSION

In current study, we evaluated the Cu-Li-nHA porous composite scaffold for GCs-ONFH repair and we interestingly found that Cu-Li-nHA with biocompatibility and osteoconductivity, enabled MSCs recruitment to the target region and induced osteogenesis. The results indicated that Cu-Li-nHA promoted MSCs homing and enhanced bone regeneration in ONFH.

Surgical reconstruction usually requires tissue transplantation to restore normal structure and function (Zhao et al., 2021). However, autografts and allografts both present certain issues problems, such as additional surgical procedures and immune rejection (Dimitriou et al., 2011). Repair for ONFH is also faced with such challenges. To overcome these limitations, *in situ* tissue regeneration technology has been designed, which utilizes the implantation of bioactive scaffolds to recruit host progenitor cells, and simultaneously provides optimal microenvironment, contributing to proliferation and differentiation of recruited cells, finally promoting tissue regeneration (Lutolf et al., 2009;

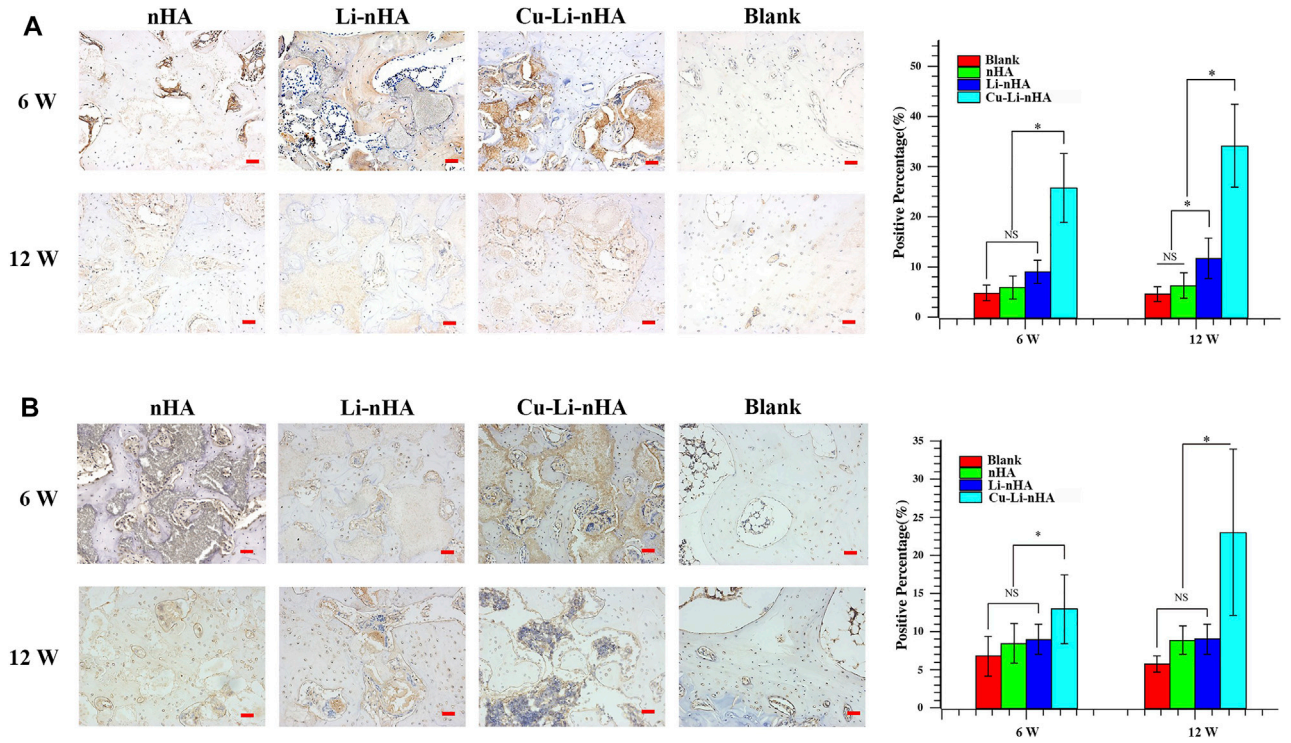

FIGURE 10 | Immunohistochemistry and positive ratio analysis of VEGF **(A)**, SDF-1 **(B)**. Blank Group: without ONFH modeling and scaffold-implantation operation. Scale bar in the bottom right-hand corner of each image (red): 100 μm. Statistical analysis was conducted using a one-way analysis of variance with post-hoc Bonferroni's multiple comparisons test. NS: $p > 0.05$, $^{*}p < 0.05$.

Ko et al., 2013). Several studies have confirmed the superiority of MSCs homing in improving the quantity and efficacy of regeneration of different tissues (Karp and Leng Teo, 2009; Xiang et al., 2020; Chen et al., 2021). For instance, Wang succeeded in BMSCs recruitment and osteogenic differentiation by loading hydroxyapatite/polyacrylonitrile scaffolds with SDF-1 (Wang et al., 2019). Moreover, patients with GCs-ONFH present a decreased number of BMSCs in the lesion area (Hernigou et al., 1999). Chronic abuse of GCs results in the differentiation of BMSCs into adipose tissue and cartilage, thereby reducing the reserve of stem cells (Cui et al., 1997; Houdek et al., 2016). Thus, a well-designed material must be fabricated to recruit MSCs and provide an osteogenic microenvironment for GCs-ONFH reconstruction.

SDF-1 is one of the factors that induce the directional migration of cells (Lau and Wang, 2011). Scaffolds composite with SDF-1 are efficient in repairing organ defects by stimulating BMSCs homing (Chen et al., 2015; Chen et al., 2019). SDF-1 in local tissues not only mobilizes adjacent BMSCs, but also recruits MSCs from the peripheral blood (Ceradini and Gurtner, 2005). HIF-1α regulates SDF-1 expression, and theoretically, Cu also upregulates HIF-1α to increase SDF-1 levels indirectly. Chen found that Cu increased BMSCs motility and recruitment through Rnd3 pathway-dependent cytoskeletal remodeling (Chen et al., 2020). Hence, we designed a composite scaffold by doping Cu into Li-nHA to enhance tissue regeneration potential through the MSCs homing. We successfully developed a Cu-Li-nHA scaffold with a three-dimensional porous structure and good compressive strength. In an *in vitro* chemotaxis experiment, Cu-Li-nHA promoted the directional migration of BMSCs. Moreover, the effect of Cu-Li-nHA on chemotaxis was not inferior to that of SDF-1. Cu-Li-nHA also induced exogenous BMSCs homing to the scaffold site *in vivo* and highly expressed SDF-1. Thus, Cu-Li-nHA mobilized the intrinsic reserves of MSCs to repair the damaged region of ONFH.

Li-nHA has been reported to enhance osteogenic differentiation of BMSCs *via* the Wnt pathway (Li et al., 2018a; Luo et al., 2018). Our results are consistent with the findings of previous studies. In addition, the angiogenesis of Cu-Li-nHA was explored. Neovascularization increases local blood supply in osteonecrosis, which benefits new bone ingrowth for reconstruction (Zhao et al., 2016). VEGF plays an important role in this process. Kim found that VEGF-loaded biomaterials provided an appropriate environment for accelerated osteogenesis (Kim et al., 2021). Similarly, our study indicated that Cu doping in the composite scaffold also increased vascular-like structures and promoted trabecular bone formation, largely because Cu can activate VEGF by inhibiting the degradation of HIF-1α (Feng et al., 2009). Cu-Li-nHA improved the microcirculation of ONFH to create more conducive conditions for MSCs differentiation.

This study also has several limitations. First, we did not include a Cu-nHA group in the study. Previous studies have demonstrated that Li-nHA has osteogenic properties but Li with limited ability of cell homing (Li et al., 2018a). Therefore, we

doped Cu into Li-nHA to improve tissue regeneration potential *via* Cu modulating MSCs homing for promoting the repair of ONFH, instead of verifying role of Cu in MSCs mobilization alone. Second, we had not set relevant experiments by regulating HIF-1α/SDF-1 pathway for further validation. Third, further research should be conducted using other animal models of ONFH to confirm the reconstruction effect of Cu-Li-nHA.

The current study demonstrated that the Cu-Li-nHA composite scaffold could induce MSCs homing and improve osteogenesis and angiogenesis, consequently promoting GCs-ONFH repair. Thus, Cu-Li-nHA implantation may serve as a potential therapeutic strategy for ONFH in the future.

DATA AVAILABILITY STATEMENT

The original contributions presented in the study are included in the article/**Supplementary Material**, further inquiries can be directed to the corresponding author.

ETHICS STATEMENT

The animal study was reviewed and approved by the Animal Care and Use Committee of Sichuan University (2020091A).

AUTHOR CONTRIBUTIONS

QL, ZW, and PK contributed to conception and design of the study. ZY organized the database. DL performed the statistical analysis. QL and ZY wrote the first draft of the manuscript. QL, ZY, ZW, DL, YL, and PK wrote sections of the manuscript. All authors contributed to manuscript revision, read, and approved the submitted version.

FUNDING

This work was supported by the 1.3.5 project for disciplines of excellence, West China Hospital, Sichuan University (No. ZYJC18040), the National Key Research and Development Program of China (No. 2020YFC2004900), and the Science and technology program of Sichuan Province (No. 2019YFS0123).

ACKNOWLEDGMENTS

We are grateful to all the colleague who have offered us invaluable help about *in vitro* experiments and histology evaluation of this study, especially Hongying Chen, Yi Zhang, Mengli Zhu, and Wanli Zhang, in the Center of Research Core Facility of West China Hospital, Sichuan University.

SUPPLEMENTARY MATERIAL

The Supplementary Material for this article can be found online at: https://www.frontiersin.org/articles/10.3389/fbioe.2022.916562/full#supplementary-material

REFERENCES

Ceradini, D. J., and Gurtner, G. C. (2005). Homing to Hypoxia: HIF-1 as a Mediator of Progenitor Cell Recruitment to Injured Tissue. *Trends Cardiovasc. Med.* 15 (2), 57–63. doi:10.1016/j.tcm.2005.02.002

Chang, C., Greenspan, A., and Gershwin, M. E. (2020). The Pathogenesis, Diagnosis and Clinical Manifestations of Steroid-Induced Osteonecrosis. *J. Autoimmun.* 110, 102460. doi:10.1016/j.jaut.2020.102460

Chen, P., Tao, J., Zhu, S., Cai, Y., Mao, Q., Yu, D., et al. (2015). Radially Oriented Collagen Scaffold with SDF-1 Promotes Osteochondral Repair by Facilitating Cell Homing. *Biomaterials* 39, 114–123. doi:10.1016/j.biomaterials.2014.10.049

Chen, Y., Wu, T., Huang, S., Suen, C.-W. W., Cheng, X., Li, J., et al. (2019). Sustained Release SDF-1α/tgf-B1-Loaded Silk Fibroin-Porous Gelatin Scaffold Promotes Cartilage Repair. *ACS Appl. Mat. Interfaces* 11 (16), 14608–14618. doi:10.1021/acsami.9b01532

Chen, X., Hu, J. G., Huang, Y. Z., Li, S., Li, S. F., Wang, M., et al. (2020). Copper Promotes the Migration of Bone Marrow Mesenchymal Stem Cells via Rnd3-dependent Cytoskeleton Remodeling. *J. Cell Physiol.* 235 (1), 221–231. doi:10.1002/jcp.28961

Chen, L., Luo, W., Wang, Y., Song, X., Li, S., Wu, J., et al. (2021). Directional Homing of Glycosylation-Modified Bone Marrow Mesenchymal Stem Cells for Bone Defect Repair. *J. Nanobiotechnol.* 19 (1), 228. doi:10.1186/s12951-021-00969-3

Chughtai, M., Piuzzi, N. S., Khlopas, A., Jones, L. C., Goodman, S. B., and Mont, M. A. (2017). An Evidence-Based Guide to the Treatment of Osteonecrosis of the Femoral Head. *Bone Joint. J.* 99-b (10), 1267–1279. doi:10.1302/0301-620x.99b10.Bjj-2017-0233.R2

Cui, Q., Wang, G.-J., and Balian, G. (1997). Steroid-Induced Adipogenesis in a Pluripotential Cell Line from Bone Marrow*. *J. Bone Joint. Surg. Am.* 79 (7), 1054–1063. doi:10.2106/00004623-199707000-00012

Dimitriou, R., Jones, E., McGonagle, D., and Giannoudis, P. V. (2011). Bone Regeneration: Current Concepts and Future Directions. *BMC Med.* 9, 66. doi:10.1186/1741-7015-9-66

Feng, W., Ye, F., Xue, W., Zhou, Z., and Kang, Y. J. (2009). Copper Regulation of Hypoxia-Inducible Factor-1 Activity. *Mol. Pharmacol.* 75 (1), 174–182. doi:10.1124/mol.108.051516

Ge, M., Ge, K., Gao, F., Yan, W., Liu, H., Xue, L., et al. (2018). Biomimetic Mineralized Strontium-Doped Hydroxyapatite on Porous Poly(l-Lactic Acid) Scaffolds for Bone Defect Repair. *Int. J. Nanomed.* 13, 1707–1721. doi:10.2147/ijn.S154605

Hernigou, P., Beaujean, F., and Lambotte, J. C. (1999). Decrease in the Mesenchymal Stem-Cell Pool in the Proximal Femur in Corticosteroid-Induced Osteonecrosis. *J. Bone Jt. Surg. Br.* 81-B (2), 349–355. doi:10.1302/0301-620x.81b2.881810.1302/0301-620x.81b2.0810349

Houdek, M. T., Wyles, C. C., Packard, B. D., Terzic, A., Behfar, A., and Sierra, R. J. (2016). Decreased Osteogenic Activity of Mesenchymal Stem Cells in Patients with Corticosteroid-Induced Osteonecrosis of the Femoral Head. *J. Arthroplasty* 31 (4), 893–898. doi:10.1016/j.arth.2015.08.017

Hu, K., and Olsen, B. R. (2016). Osteoblast-derived VEGF Regulates Osteoblast Differentiation and Bone Formation during Bone Repair. *J. Clin. Invest.* 126 (2), 509–526. doi:10.1172/jci82585

Kang, J. S., Suh, Y. J., Moon, K. H., Park, J. S., Roh, T. H., Park, M. H., et al. (2018). Clinical Efficiency of Bone Marrow Mesenchymal Stem Cell Implantation for Osteonecrosis of the Femoral Head: a Matched Pair Control Study with Simple Core Decompression. *Stem Cell Res. Ther.* 9 (1), 274. doi:10.1186/s13287-018-1030-y

Karp, J. M., and Leng Teo, G. S. (2009). Mesenchymal Stem Cell Homing: the Devil Is in the Details. *Cell Stem Cell* 4 (3), 206–216. doi:10.1016/j.stem.2009.02.001

Kato, T., Khanh, V. C., Sato, K., Kimura, K., Yamashita, T., Sugaya, H., et al. (2018). Elevated Expression of Dkk-1 by Glucocorticoid Treatment Impairs Bone Regenerative Capacity of Adipose Tissue-Derived Mesenchymal Stem Cells. *Stem Cells Dev.* 27 (2), 85–99. doi:10.1089/scd.2017.0199

Kim, H. Y., Park, J.-H., Kim, M. J., Lee, J. H., Oh, S. H., and Byun, J.-H. (2021). The Effects of VEGF-Centered Biomimetic Delivery of Growth Factors on Bone Regeneration. *Biomater. Sci.* 9 (10), 3675–3691. doi:10.1039/d1bm00245g

Ko, I. K., Lee, S. J., Atala, A., and Yoo, J. J. (2013). *In Situ* tissue Regeneration through Host Stem Cell Recruitment. *Exp. Mol. Med.* 45 (11), e57. doi:10.1038/emm.2013.118

Lau, T. T., and Wang, D.-A. (2011). Stromal Cell-Derived Factor-1 (SDF-1): Homing Factor for Engineered Regenerative Medicine. *Expert Opin. Biol. Ther.* 11 (2), 189–197. doi:10.1517/14712598.2011.546338

Li, J., Khavandgar, Z., Lin, S.-H., and Murshed, M. (2011). Lithium Chloride Attenuates BMP-2 Signaling and Inhibits Osteogenic Differentiation through a Novel WNT/GSK3- Independent Mechanism. *Bone* 48 (2), 321–331. doi:10.1016/j.bone.2010.09.033

Li, D., Huifang, L., Zhao, J., Yang, Z., Xie, X., Wei, Z., et al. (2018a). Porous Lithium-Doped Hydroxyapatite Scaffold Seeded with Hypoxia-Preconditioned Bone-Marrow Mesenchymal Stem Cells for Bone-Tissue Regeneration. *Biomed. Mat.* 13 (5), 055002. doi:10.1088/1748-605X/aac627

Li, D., Xie, X., Yang, Z., Wang, C., Wei, Z., and Kang, P. (2018b). Enhanced Bone Defect Repairing Effects in Glucocorticoid-Induced Osteonecrosis of the Femoral Head Using a Porous Nano-Lithium-Hydroxyapatite/gelatin Microsphere/erythropoietin Composite Scaffold. *Biomater. Sci.* 6 (3), 519–537. doi:10.1039/c7bm00975e

Li, B., Lei, Y., Hu, Q., Li, D., Zhao, H., and Kang, P. (2021). Porous Copper- and Lithium-Doped Nano-Hydroxyapatite Composite Scaffold Promotes Angiogenesis and Bone Regeneration in the Repair of Glucocorticoids-Induced Osteonecrosis of the Femoral Head. *Biomed. Mat.* 16 (6), 065012. doi:10.1088/1748-605X/ac246e

Li, D., Yang, Z., Luo, Y., Zhao, X., Tian, M., and Kang, P. (2022). Delivery of MiR335-5p-Pendant Tetrahedron DNA Nanostructures Using an Injectable Heparin Lithium Hydrogel for Challenging Bone Defects in Steroid-Associated Osteonecrosis. *Adv. Healthc. Mater.* 11 (1), 2101412. doi:10.1002/adhm.202101412

Luo, Y., Li, D., Zhao, J., Yang, Z., and Kang, P. (2018). *In Vivo* Evaluation of Porous Lithium-Doped Hydroxyapatite Scaffolds for the Treatment of Bone Defect. *Biomed. Mater. Eng.* 29 (6), 699–721. doi:10.3233/bme-181018

Lutolf, M. P., Gilbert, P. M., and Blau, H. M. (2009). Designing Materials to Direct Stem-Cell Fate. *Nature* 462 (7272), 433–441. doi:10.1038/nature08602

Meng, L., Sun, W., Sun, X., Bai, L., Wang, H., Wang, N., et al. (2015). GW26-e5347 Recovery of Mesenchymal Stem Cells Homing to Rabbit Myocardial Ischemic Infarct Area by Cu-Microbubble Treatment. *J. Am. Coll. Cardiol.* 66 (16), C76. doi:10.1016/j.jacc.2015.06.303

Mont, M. A., Salem, H. S., Piuzzi, N. S., Goodman, S. B., and Jones, L. C. (2020). Nontraumatic Osteonecrosis of the Femoral Head: Where Do We Stand Today? *J. Bone Jt. Surg. Am.* 102 (12), 1084–1099. doi:10.2106/jbjs.19.01271

Moya-Angeler, J., Gianakos, A. L., Villa, J. C., Ni, A., and Lane, J. M. (2015). Current Concepts on Osteonecrosis of the Femoral Head. *World J. Orthop.* 6 (8), 590–601. doi:10.5312/wjo.v6.i8.590

Wang, J., Li, J., Lu, Y., Yang, H., Hong, N., Jin, L., et al. (2019). Incorporation of Stromal Cell-Derived Factor-1α in Three-Dimensional Hydroxyapatite/Polyacrylonitrile Composite Scaffolds for Bone Regeneration. *ACS Biomater. Sci. Eng.* 5 (2), 911–921. doi:10.1021/acsbiomaterials.8b01146

Wang, L., Chen, L., Wang, J., Wang, L., Gao, C., Li, B., et al. (2022). Bioactive Gelatin Cryogels with BMP-2 Biomimetic Peptide and VEGF: A Potential Scaffold for Synergistically Induced Osteogenesis. *Chin. Chem. Lett.* 33 (4), 1956–1962. doi:10.1016/j.cclet.2021.10.070

Wang, Z., Le, H., Wang, Y., Liu, H., Li, Z., Yang, X., et al. (2022). Instructive Cartilage Regeneration Modalities with Advanced Therapeutic Implantations under Abnormal Conditions. *Bioact. Mater.* 11, 317–338. doi:10.1016/j.bioactmat.2021.10.002

Winkler, T., Sass, F. A., Duda, G. N., and Schmidt-Bleek, K. (2018). A Review of Biomaterials in Bone Defect Healing, Remaining Shortcomings and Future Opportunities for Bone Tissue Engineering. *Bone Jt. Res.* 7 (3), 232–243. doi:10.1302/2046-3758.73.Bjr-2017-0270.R1

Wu, C., Zhou, Y., Xu, M., Han, P., Chen, L., Chang, J., et al. (2013). Copper-Containing Mesoporous Bioactive Glass Scaffolds with Multifunctional Properties of Angiogenesis Capacity, Osteostimulation and Antibacterial Activity. *Biomaterials* 34 (2), 422–433. doi:10.1016/j.biomaterials.2012.09.066

Xiang, X., Liu, H., Wang, L., Zhu, B., Ma, L., Du, F., et al. (2020). Ultrasound Combined with SDF-1α Chemotactic Microbubbles Promotes Stem Cell Homing in an Osteoarthritis Model. *J. Cell Mol. Med.* 24 (18), 10816–10829. doi:10.1111/jcmm.15706

Zhao, D., and Ma, Z. (2020). Application of Biomaterials for the Repair and Treatment of Osteonecrosis of the Femoral Head. *Regen. Biomater.* 7 (1), 1–8. doi:10.1093/rb/rbz048

Zhao, D., Huang, S., Lu, F., Wang, B., Yang, L., Qin, L., et al. (2016). Vascularized Bone Grafting Fixed by Biodegradable Magnesium Screw for Treating Osteonecrosis of the Femoral Head. *Biomaterials* 81, 84–92. doi:10.1016/j.biomaterials.2015.11.038

Zhao, D., Zhu, T., Li, J., Cui, L., Zhang, Z., Zhuang, X., et al. (2021). Poly(lactic-co-glycolic Acid)-Based Composite Bone-Substitute Materials. *Bioact. Mater.* 6 (2), 346–360. doi:10.1016/j.bioactmat.2020.08.016

Zhou, M., Xi, J., Cheng, Y., Sun, D., Shu, P., Chi, S., et al. (2021). Reprogrammed Mesenchymal Stem Cells Derived from iPSCs Promote Bone Repair in Steroid-Associated Osteonecrosis of the Femoral Head. *Stem Cell Res. Ther.* 12 (1), 175. doi:10.1186/s13287-021-02249-1

Zhu, H., Wang, X., Han, Y., Zhang, W., Xin, W., Zheng, X., et al. (2018). Icariin Promotes the Migration of Bone Marrow Stromal Cells via the SDF-1α/HIF-1α/CXCR4 Pathway. *Drug Des. Dev. Ther.* 12, 4023–4031. doi:10.2147/dddt.S179989

Zhu, T., Cui, Y., Zhang, M., Zhao, D., Liu, G., and Ding, J. (2020). Engineered Three-Dimensional Scaffolds for Enhanced Bone Regeneration in Osteonecrosis. *Bioact. Mater.* 5 (3), 584–601. doi:10.1016/j.bioactmat.2020.04.008

Zhu, T., Jiang, M., Zhang, M., Cui, L., Yang, X., Wang, X., et al. (2022). Biofunctionalized Composite Scaffold to Potentiate Osteoconduction, Angiogenesis, and Favorable Metabolic Microenvironment for Osteonecrosis Therapy. *Bioact. Mater.* 9, 446–460. doi:10.1016/j.bioactmat.2021.08.005

Zhun, W., Donghai, L., Zhouyuan, Y., Haiyan, Z., and Pengde, K. (2018). Efficiency of Cell Therapy to GC-Induced ONFH: BMSCs with Dkk-1 Interference Is Not Superior to Unmodified BMSCs. *Stem Cells Int.* 2018, 1–9. doi:10.1155/2018/1340252

Conflict of Interest: The authors declare that the research was conducted in the absence of any commercial or financial relationships that could be construed as a potential conflict of interest.

The reviewer YS declared a shared parent affiliation with the authors to the handling editor at the time of review.

frontiers | Frontiers in Bioengineering and Biotechnology

REVIEW
published: 08 June 2022
doi: 10.3389/fbioe.2022.913383

Recent Advances of Intraocular Lens Materials and Surface Modification in Cataract Surgery

*Chenqi Luo, Hanle Wang†, Xinyi Chen†, Jingjie Xu†, Houfa Yin and Ke Yao**

Eye Center of the Second Affiliated Hospital, Medical College of Zhejiang University, Hangzhou, China

Advances in cataract surgery have increased the demand for intraocular lens (IOL) materials. At present, the progress of IOL materials mainly contains further improving biocompatibility, providing better visual quality and adjustable ability, reducing surgical incision, as well as dealing with complications such as posterior capsular opacification (PCO) and ophthalmitis. The purpose of this review is to describe the research progress of relevant IOL materials classified according to different clinical purposes. The innovation of IOL materials is often based on the common IOL materials on the market, such as silicon and acrylate. Special properties and functions are obtained by adding extra polymers or surface modification. Most of these studies have not yet been commercialized, which requires a large number of clinical trials. But they provide valuable thoughts for the optimization of the IOL function.

Keywords: biomaterials, intraocular lens, surface modification, biocompatibility, posterior capsular opacification

OPEN ACCESS

Edited by:
Jianxun Ding,
Changchun Institute of Applied Chemistry (CAS), China

Reviewed by:
Di Huang,
Massachusetts Eye and Ear Infirmary and Harvard Medical School, United States
Liangju Kuang,
Harvard Medical School, United States
Quankui Lin,
Wenzhou Medical University, China

****Correspondence:***
Ke Yao
xlren@zju.edu.cn

†These authors have contributed equally to this work and share first authorship

Specialty section:
This article was submitted to Biomaterials, a section of the journal Frontiers in Bioengineering and Biotechnology

Received: *05 April 2022*
Accepted: *23 May 2022*
Published: *08 June 2022*

Citation:
Luo C, Wang H, Chen X, Xu J, Yin H and Yao K (2022) Recent Advances of Intraocular Lens Materials and Surface Modification in Cataract Surgery. Front. Bioeng. Biotechnol. 10:913383. doi: 10.3389/fbioe.2022.913383

INTRODUCTION

Biomaterials are used extensively in medicine nowadays, such as artificial organs, regenerative medicine, wound repair and bioimaging fields (Karayilan et al., 2021). Ophthalmology is also an important application area of biomaterials (Han H. et al., 2020; Wang K. et al., 2021). They are widely involved in retinal regeneration (Abedin Zadeh et al., 2019), vitreous replacement (Wang T. et al., 2021), contact lenses (Xiao et al., 2018; Ma et al., 2022), and intraocular lenses (IOL) (Čanović et al., 2019). The lens is an important transparent, biconvex-shaped structure for optical functions in the eye. It adjusts the refractive power by changing the diopter so that objects at different distances are imaged on the retina (Fisher, 1977; Hejtmancik and Shiels, 2015). Protein denaturation reduces the transparency of the lens and is caused by the increase of age or the influence of other factors such as trauma, genetics, and metabolic diseases (Bloemendal et al., 2004). This pathological condition is called a cataract. It is the leading cause of blindness in elderly patients (Chen et al., 2021). The cataract surgery removes the opacity lens and replaces it with an artificial, transparent, disc-shaped IOL with certain refractive power. About 15.2 million patients can be cured by replacing IOL through cataract surgery every year (Steinmetz et al., 2021).

IOL are used to substitute the preliminary lens. Since its first application in 1949, IOL had experienced more than 70 years of development. In the beginning, people tried to find materials that were safe, stable and had desirable optical properties. Gradually, with the proposing of specific and personalized demands, materials and techniques are continuously updating (Dick and Gerste, 2021). Advances in IOL include materials and structural designs. In the design of the optical structure, the multiple focal points were accomplished through refraction, diffraction, or two combined surface structures to obtain clear imaging at multiple distances (Alio et al., 2017b); Extended Depth of Focus

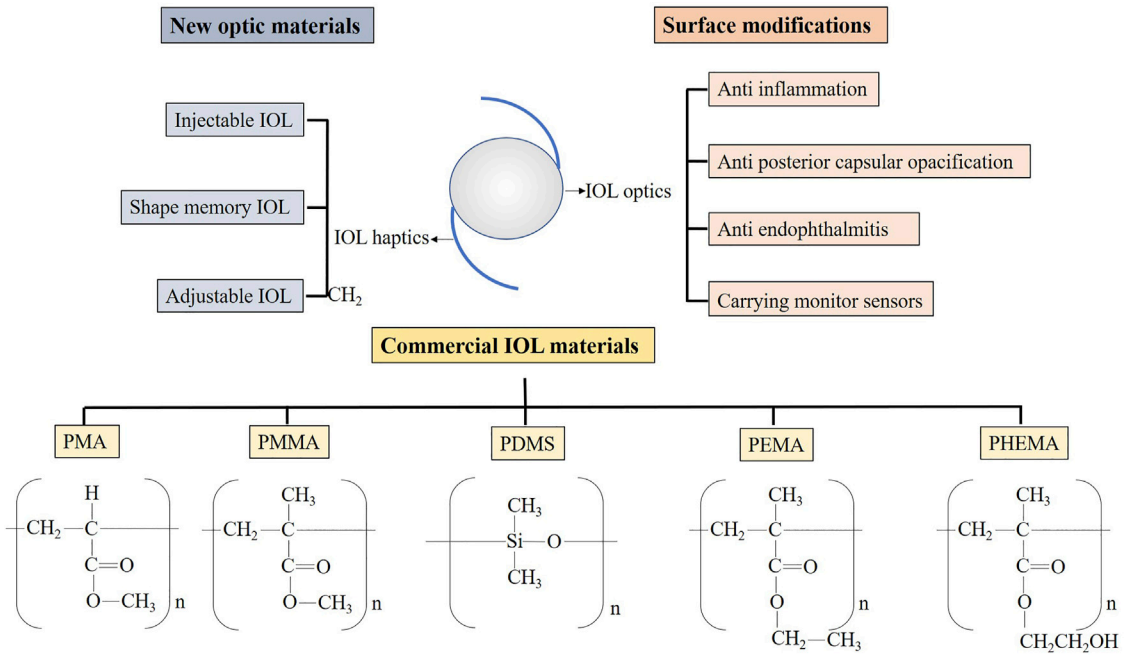

FIGURE 1 | The main outline of this review. PMA, polymethylacrylate; PMMA, polymethylmethacrylate; PDMS, polydimethylsiloxane; PEMA, polyethyl methacrylate; PHEMA, poly2-hydroxyethylmethacrylate.

(EDOF) IOL (Rampat and Gatinel, 2021), toric IOL (Kessel et al., 2016), and Aspheric IOL (Schuster et al., 2013) are designed to improve visual quality. In terms of the non-optical part, the square-edge IOL have been shown to effectively inhibit cell proliferation and reduce postoperative adverse reactions (Maddula et al., 2011). Meanwhile, there are many advances in materials. IOL have gone through a transition from rigid materials to foldable soft materials, and commercially available IOL nowadays are mainly composed of different types of acrylic (Werner, 2021). There will be an overview of them in the next section. Materials are improved to reduce IOL size, prevent adverse effects after IOL implantation and surgery (Topete et al., 2021b), improve biocompatibility (Werner, 2008), provide accommodation ability (Alio et al., 2017a), and filter specific light (Downes, 2016). It is hoped that in the future, the IOL will be able to more closely resemble the original lens, in particular, obtain continuous refractive power modulation. Moreover, IOL with additional therapeutic capabilities are also expected (Toffoletto et al., 2020). There is currently no IOL that fits all needs. Thus, in different conditions, various materials are being studied to improve the IOL on the market.

There were many reviews of IOL published over the years. They usually focused on innovations in structural design, in which case there are more commercialized IOL (Čanović et al., 2019; Dick and Gerste, 2021; Werner, 2021). There were also some reviews on the application of polymer materials in ophthalmology (Kirchhof et al., 2015; Karayilan et al., 2021). They introduced the applications of polymeric materials not only in IOL but also in other ophthalmic fields, such as contact lenses and vitreous replacement. The innovations of IOL with a specific function were other aspects (Huang et al., 2016; Pepose et al., 2017; Toffoletto et al., 2020; Topete et al., 2021b). They tend to focus on advances in IOL for carrying drugs or for therapeutic use and for surface modification to improve biocompatibility. The above types of reviews all discussed the progress of IOL materials, but they often covered only a specific part. In this review, we introduced the material development of IOL from the progress in the aspects of the main optic material and the surface modification. The advances were categorized for different design purposes (**Figure 1**). In considering that some of them had a very long research history and related reviews had been published already, we mainly discussed studies carried out in the last ten years.

MATERIALS ON THE MARKET FOR THE MANUFACTURE OF INTRAOCULAR LENSES

The materials in ophthalmic applications should meet the basic requirements, including lasting optical transparency, high resolution, chemical stability, high histocompatibility, and be sterilizable (Allarakhia et al., 1987). The properties of common IOL materials on the market are summarized in **Table 1**. Polymethylmethacrylate (PMMA) was first introduced in 1949 (Ridley, 1952) as the chemical material to replace the preliminary lens by Ridley. He noticed some injured pilots with plexiglass shards in their eyes. These substances remained in the eye tissue for long periods without much adverse impact (Ridley, 1976). Although PMMA was very hard, difficult to change in shape, and

TABLE 1 | Properties of common IOL materials.

Materials	Foldable/ unfoldable	Biocompatibility	Advantages	Disadvantages
PMMA	Unfoldable (rigid)	Low rate of inflammatory cell accumulation High rate of PCO*	Low cost Low aqueous flare High visual quality	5–6 mm incision to insert
PDMS	Foldable (soft)	Low rate of inflammatory cell accumulation Fibrotic reaction of lens surface	Small incision	Tissue injury during expanding in capsular Opacification of surface after contacting with intravitreal air
Hydrophilic acrylic	Foldable (soft)	Low rate of inflammatory cell accumulation High rate of PCO calcification	Low aqueous flare Easy to handle	Limitation in shape design Long-term IOL opacification
Hydrophobic acrylic	Foldable (soft)	Low rate of PCO High rate of inflammatory cell accumulation	Good visual quality Compatible with a sharp-edged design	High aqueous flare Tacky surface High RI*

**PCO, posterior capsular opacification; RI, refractive index.*

cannot withstand high temperature and pressure, it has been used as an intraocular lens (IOL) without a suitable replacement for decades (Apple et al., 1984). Due to the lack of flexibility, a large incision (5–7 mm) was required to implant the PMMA IOL (Čanović et al., 2019). The advances of phacoemulsification cataract surgery enabling smaller surgical incisions had spurred research into soft, foldable IOL.

The very first foldable IOL used *in vivo* was in 1976 (Allarakhia et al., 1987). In the following period, soft IOL had been extensively studied and applied. One of the soft IOL is made of polydimethylsiloxane (PDMS). Silicone materials are in various structures with a refractive index of 1.41–1.46, higher than that of PMMA (Kapoor and Gupta, 2020). It means that under the same refractive power, the IOL of the silicone material are thinner than PMMA (Čanović et al., 2019). Grafting carbazole on the side chain of polysiloxane has been proved to increase the refractive index of the silicone hydrogel material (Xu et al., 2015). Silicon has been reported to have relatively low biocompatibility and easily adhere to silicone oil and particles when contacting with intravitreal air (Ozyol et al., 2017). This negatively affects the transparency of IOL forwards. In addition, the silicone IOL unfolds very fast after insertion into the eye, and it is likely to injure the capsular bag (Čanović et al., 2019).

The most widely used IOL materials nowadays are acrylic (Olson et al., 2003). They are polymer or copolymer formed by methyl acrylate, methyl methacrylate (MMA), ethyl methacrylate (EMA), and 2-hydroxyethyl methacrylate (HEMA). In the polymerization process, carbon-carbon double bonds open to link molecules and form various structures (Tetz and Jorgensen, 2015). They are less elastic than silicone and take about 3–5 s to fully unfold, making them safer during surgery. Acrylic IOL are mainly divided into hydrophilic and hydrophobic. The water content of hydrophobic IOL is generally 0.5%–1%, while that of hydrophilic IOL is usually 18%–38% (Werner, 2021). The difference is mainly contributed to the content of HEMA in the copolymer, and it is temperature related (Miyata and Yaguchi, 2004).

Hydrophilic IOL can be adapted to smaller surgical incisions (less than 2 mm) by dehydration, thus ideal for microincision cataract surgery (Kohnen and Klaproth, 2010). They are in good compatibility with biological tissues due to high water content (Ozyol et al., 2017) and are reported to be less prone to aggregation of inflammatory cells on the surface (Abela-Formanek et al., 2011). However, studies have found that hydrophilic IOL has a high probability of posterior capsule opacification (PCO) as the hydrophilic surface makes it easier for lens epithelial cells to grow (Ozyol et al., 2017). And calcification has been reported likely to occur in hypertonic hydrophilic surface which allows intraocular metabolites to enter (Werner et al., 2006). In addition, the high-water content can also limit the shape design of the IOL.

Hydrophobic acrylic IOL are more widely used on the market nowadays (Werner, 2021). They can be made thinner with a high refractive index (1.44–1.55) (Čanović et al., 2019). The tacky surface of hydrophobic IOL allows the lens to adhere tightly to the capsule, reducing the proliferation of lens epithelial cells (Katayama et al., 2007), hence decreasing the PCO. Furthermore, a sharp-edged design is more feasible to implement on hydrophobic IOL, which prevent migration of lens epithelial cells to the IOL (Nibourg et al., 2015). The main drawback of hydrophobic IOL is glare caused by a high refractive index (Čanović et al., 2019). Glistening was also found to be more likely to occur in hydrophobic IOL (Tetz et al., 2009). It is because that water that collects in hydrophobic polymers forms pockets that grow as temperature changes. Therefore, properly increasing the water content of the material can be a solution to this problem (Tetz and Jorgensen, 2015).

ADVANCES IN INTRAOCULAR LENS OPTICAL MATERIALS

Material Inserted Through Smaller Incisions

Up to now, phacoemulsification requires an incision within 2 mm (Li et al., 2018). Smaller surgical incisions bring faster

postoperative vision recovery, fewer complications, and less postoperative astigmatism (Rao et al., 2018). This puts forward requirements for the development of IOL. The IOL needs to be implanted in the eye through a small incision, with a 6.0 mm optic portion diameter is sufficient size (Werner, 2021). Furthermore, the accommodative function might remain if the lens capsular bag was preserved. Commonly used IOL reduce the size by folding Seward (1997), but some new materials are also developed through shape memory or injection of liquid IOL, which may further reduce the IOL size.

Injectable Intraocular Lens

The fluid has no fixed shape, so it can enter the capsular bag through a small surgical incision. The ideal injectable IOL is in a liquid state during the implantation procedure and subsequently forms a stable solid or remains in liquid form. Liquid materials for injectable IOL need to meet the basic conditions: good biocompatibility, non-toxicity, ability to maintain a transparent state, and sufficient refractive power (Karayilan et al., 2021). The process of turning liquid materials into solids *in vivo* may involve some external stimulation, which is preferably non-invasive. In addition, due to the fluidity of the liquid, the filling material may flow out of the incision. Thus, a suitable method of filling the incision is required. Kessler was the first to propose the use of liquid to replace the lens in 1960 (Kessler, 1964). He mainly introduced the surgical method of injecting liquid materials such as silicon fluid and oil immersion through a small incision and observed that the silicon and catalyst were solidified after 30 min *in vivo*.

In the following decades, liquid materials and hardening methods have been tried, mainly focused on silicone and hydrogels (de Groot et al., 2001; Koopmans et al., 2003). Hardening methods include light, heat, enzymatic reaction, etc., Meanwhile, inappropriate external stimuli can also cause indeterminate damage to eye tissue. A polysiloxane macromonomer was used by Hughes Hao et al. (2010) to make injectable IOL. Under the attendance of Karstedt's catalyst and blue light (70 mW/cm^2) and a photoinitiator, it would turn into a gel state after about 5 min with a refractive index of 1.47 and good light transmittance. Subsequently, they introduced phenyl to make an adjustable refractive index. But its biological toxicity was uncertain, and the transparency was reported to decrease over time (Hao et al., 2012).

Niu et al. (2010) synthesized the thiol-ene photopolymerization by ultraviolet irradiation. The compounds of three polymers: diacrylate, poly (ethylene glycol) (PEG), and pentaerythritol tetrakis (3-mercapto propionate), were hardened under the radiation of ultraviolet light (4.5 mW/cm^2) with the presence of a photoinitiator. It was proved to reduce the amount of ultraviolet light required when photopolymerizing, compared to the previous studies (Han et al., 2003), thus decreasing the damage of ultraviolet rays to the eyes. Nonetheless, heat release was observed during the polymerization reaction, resulting in a significant local temperature rise, posing a risk of thermal injury to the eye. Moreover, unreacted polymers might be toxic to cells.

In addition to photopolymer materials, heat-sensitive materials were also developing. In 2012 (Annaka et al., 2012), Annaka reported A modified PEG with silica nanoparticles that solidifies into a gel at physiological body temperature. The injection needed to be done at 45°C when it appeared to be in the form of liquid. It had ideal transparency and refractive index, while the biocompatibility was unclear. Its limitation lies in the temperature requirements at the time of surgical injection. Furthermore, enzymatic crosslink reaction was used to solidify hydrogels by 4-PPO/PEO block copolymer [4-arm poly (propylene oxide)-poly (ethylene oxide)] later in 2014 (Lee et al., 2014). The catalysts were horseradish peroxidase (HRP) and hydrogen peroxide (H_2O_2). The gel had young's modulus similar to that of the initial lens, and no tissue damage was found during the injection and coagulation procedure. More importantly, it was observed with high biocompatibility, especially that the PCO rate was significantly lower than other materials.

Except for coagulating the copolymer in the eye, some studies had attempted to keep it in the capsular bag as a liquid. In this way, the liquid IOL could obtain the ability to alter the shape, thus processing the effect of adjusting the refractive power, which was also called accommodation IOL. The relative research in this area is brought by Deboer et al. (2015). They introduced a deformable PDMS lens shell filled with a transparent liquid. Experiments had found that the liquid in this device did not leak out and maintained good light transmittance. The elastic modulus of the IOL shell was close to that of the native lens, so it could achieve the effect of adjusting the refractive power. Other studies on the combination of elastic membrane and optical fluids designed to manufacture accommodation IOL have also been proposed later (Liang et al., 2015; Liang et al., 2019) (**Figure 2**).

In conclusion, research progress in injectable intraocular lenses has been relatively slow. Curing methods currently used mainly include light, heat, and catalysts, all of which can cause eye damage to a certain extent. While injecting fluids with maintaining devices will be safer methods. Further exploration is needed to ensure the safety of the materials and inserting process.

Shape Memory Intraocular Lens

External stimuli (light, temperature, PH, etc.) cause some polymers to change in shape. When the shape change is irreversible, they are called shape memory polymers (SMPs), and the phenomenon is known as the shape memory effect (SME) (Sun et al., 2019). The use of SMPs material allows the IOL to be pre-deformed to a very small size, requiring only a small surgical incision to pass through. After inserting in the eye, when the environmental conditions change, the IOL will revert to memory. Song et al. (2011) introduced a type of methacrylate SMPs that could be applied in IOL. Ethylene glycol phenyl ether acrylate (EGPEA), ethylene glycol phenyl ether methacrylate (EGPEMA), and long alkyl chain formed the basic structure of SMP. The solid SMP was scrimped to a small size *in vitro* by heating and expanded to a full-size IOL when it reached the body temperature and remained stable. The experiment found that the transition temperature is positively correlated with the concentration of methacrylate. The refractive index of the copolymer was also changed by the concentration of EGPEA

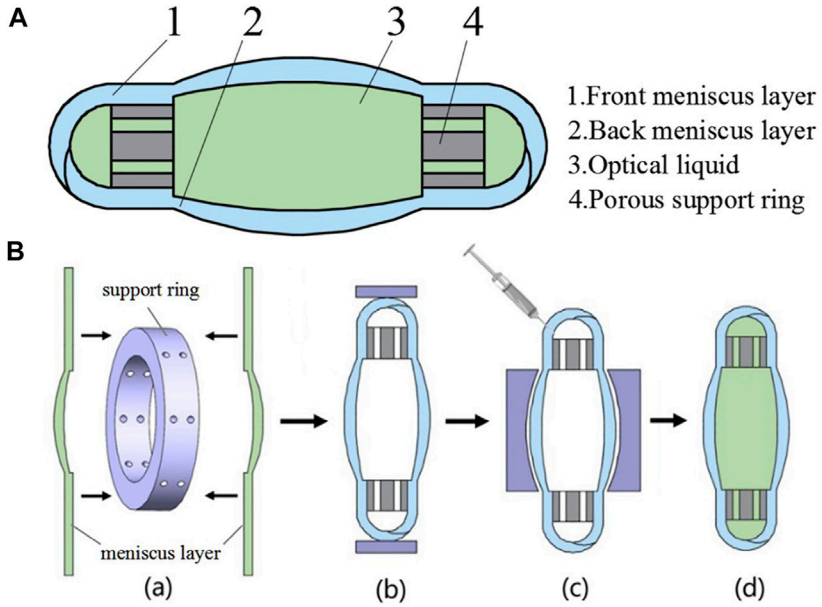

FIGURE 2 | (A) The structure diagram of IOL. **(B)** The assembling process of the designed IOL from Liang et al. (2019), with the permission of Elsevier.

and EGPEMA and was reported 1.514–1.499. And the cytocompatibility was proved to be good.

Recently, a series of poly (dimethyl acrylamide-co-stearyl acrylate and/or lauryl acrylate) (PDMAAm-co-SA and/or LA) was synthesized by 3D printing technology (Shiblee et al., 2018). 3D printing technology, rather than traditional mold production, provides the possibility for the customization of personalized IOL. The PDMAAm-co-SA and/or LA thermal set material was proved to have a refractive index of 1.41–1.47, comparable to traditional IOL materials. However, its young's modulus varies widely and could be high for IOL, and biocompatibility remained unclear.

Adjustable Intraocular Lens Materials

Failure to achieve target diopter after IOL replacement is a very common problem after cataract surgery for patients (Chee et al., 2015). A recent European survey showed that more than 27% of patients had postoperative refractive power, not within ±0.5 diopter (D) of the target (Lundstrom et al., 2018). In the past, postoperative ametropia often required a second invasive surgery, such as keratorefractive surgery, for correction (Ford et al., 2014). Adjustable IOL were hence designed to avoid secondary surgery.

A light-adjustable lens (LAL), produced by Calhoun Vision, Inc., has been officially approved for commercial use for years (Chang, 2019). This LAL was synthesized based on silicon and mainly contained ultraviolet absorbers, photoinitiators, and photosensitive macromolecules. When exposed to ultraviolet light, macromolecules were promoted to polymerize by photoinitiators Dick and Gerste (2021). The macromer that did not participate in the polymerization subsequently diffused into the treated or exposed areas, leading to a change in the shape of the LAL, which ultimately resulted in an alteration in refractive power. Clinical trials had proved that this LAL had the ideal ability to correct visual acuity after cataract surgery, including patients with long or short axial lengths and patients undergoing corneal refractive surgery. It was reported to have modulation capabilities up to 2D (Hengerer et al., 2011; Villegas et al., 2014). However, since the process of adjusting refractive power required the eye to be exposed to ultraviolet light, its negative effects on the retina are concerned. An update to LAL was reported that ultraviolet-absorbing groups were added to reduce eye exposure (Chang, 2019). However, light exposure depleted the number of monomers in the material. Hence the polymerization of macromonomers in LAL was irreversible. Once the diopter of LAL was fixed, it could not be changed anymore.

(Kim et al., 2003; Trager et al., 2008), Schraub and Hampp (2011) proposed a silicon-coumarin polymer-based IOL design that can repeatedly adjust the diopter. Modulation of diopter was accomplished by photoreaction of coumarin side groups, the dimerization of coumarin to form cyclobutane led to a decrease in refractive power *via* crosslinking. On the contrary, its rupture allowed the refractive power to increase. It was proven to achieve a 2.5D adjustment range. With optimization, this process could be achieved by visible light two-photon absorption or ultraviolet single-photon absorption. This represents better protection for the eyes. On this basis, Jellali et al. (2017) synthesized a silicone-coumarin phototunable intraocular lens and tested the photosensitivity and biocompatibility. Ultraviolet-visible light spectroscopy showed that irradiation above 300 nm occurred crosslinking, and the process was reversed under light below 245 nm. It was able to be implanted in the eye in a crosslinked state and did not require special protection of the patient's eyes from the light (**Figure 3**).

A thermoplastic material, soft polysiloxane-urea-elastomers (PSUs), was synthesized by Riehle for accommodation IOL Riehle et al. (2018). Amino-propyl-terminated polydimethylsiloxanes,

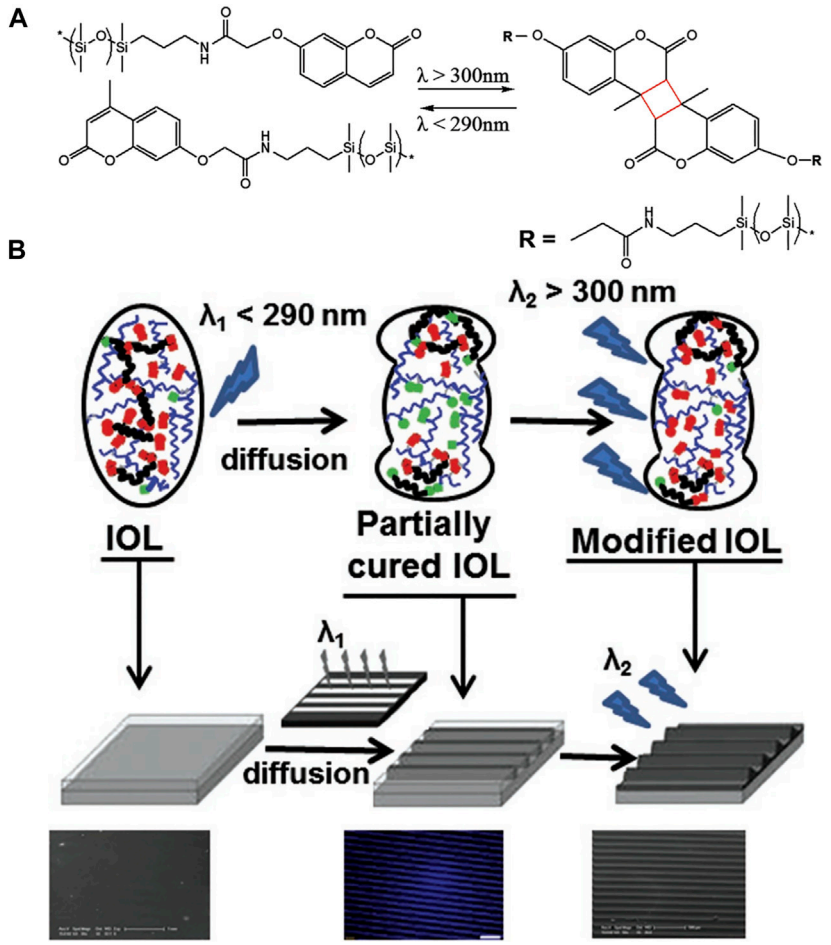

FIGURE 3 | (A) Schematic of photoreversible crosslinking of PDSM-coumarin polymer. **(B)** Schematic of designed IOL from Jellali et al. (2017), with the permission of Wiley.

4,4′-methylenebis (cyclohexylisocyanate), and 1,3-Bis (3-aminopropyl)-1,1,3,3-tetramethyldisiloxane were involved in the synthesis of this material. The material was verified to withstand a mechanical stretch of 5% (1 mm), equivalent to an 8D refractive index change. The transparency and refractive index are desirable for IOL, and it has been proved to have no apparent cytotoxicity. The elastic material avoids light injury to the eyes, but how to stretch the material through the ciliary muscle still needs further research.

Femtosecond lasers are now a widely used assistive technology for cataract surgery. Research has found that femtosecond lasers may affect the properties of polymers. Ding et al. (2006) induced a 0.06 refractive index change in the polymer of the hydrogel under femtosecond laser treatment. This phenomenon was called "laser-induced refractive index change (LIRIC)." Changes in the refractive index of IOL materials were thought to be caused by thermal or alternation in hydrophilicity (Bille et al., 2017). Scientists tried to apply it to produce new tunable IOL, possibly shortly.

In addition, overall material optimization was also designed to improve biocompatibility, which will be introduced in detail in the next section. Based on the previous research (Kannan et al., 2005), Wang et al. (2014) proposed a method to synthesize poly (hedral oligomeric silsesquioxane-co-methyl methacrylate) (allyl POSS-PMMA) polymer and applied it as an IOL material. It had a regular structure, forming a better surface morphology. And it was more hydrophobic than PMMA material. But more animal experiments need to be carried out to verify its biocompatibility.

INTRAOCULAR LENS SURFACE MODIFICATION MATERIALS

Materials to Improve Biocompatibility

Biocompatibility refers to the ability of a material to fuse with the surrounding tissue. Amon described biocompatibility of the IOL as uveal and capsular biocompatibility Amon (2001). The implantation of allogeneic IOL materials will promote the leakage of proteins and macrophages in the vascular of the uvea. They may adhere to the surface of the IOL and promote inflammatory response (Titiyal et al., 2020). The extent of the inflammatory response induced by IOL is indicative of uveal

TABLE 2 | The studies on materials reducing inflammation.

Surface modification	IOL optic materials	Technique	Article
HEP*	PMMA PMMA, Silicon Hydrophobic acrylic PMMA		Larsson et al. (1989) Arthur et al. (2001) Krall et al. (2014) Rønbeck and Kugelberg, (2014)
PEG*	Hydrophobic acrylic	APGD*	Lin et al. (2010)
NVP*	Hydrophobic acrylic		Wang et al. (2013)
MPC*	Hydrophobic acrylic Silicon	Ultraviolt irradiation SI-RAFT*	Huang et al. (2017) Han et al. (2017)
MPC-MAA*	Hydrophobic acrylic	Plasma	Tan et al. (2017)
Recombinant hirudin anticoagulant	Hydrophobic acrylic	Ammonia plasma	Zheng et al. (2016)

**HEP, heparin; PEG, poly (Ethylene Glycol); NVP, N-vinyl pyrrolidone; MPC, 2-methacryloyloxyethyl phosphorylcholine; MAA, methyl acrylic acid; APGD, atmospheric pressure glow discharge; SI-RAFT, surface-initiated reversible addition-fragmentation chain transfer.*

compatibility. As for capsular biocompatibility, it often manifests as anterior capsular opacity (ACO), PCO, and capsular bag contraction (Trivedi et al., 2002). They are mainly related to the growth of LECs. In addition, the residual LECs on the capsular bag may grow to the surface of the IOL and lead to calcification (Grzybowski et al., 2021).

Improving biocompatibility helps reduce adverse effects after cataract surgery, such as inflammatory reactions, PCO, ACO, etc., And optimizing IOL materials is considered a promising approach to improve IOL biocompatibility. In addition to altering the IOL material, surface modification is also seen as an effective method. It includes layer-by-layer (LBL) self-assembly, plasma surface modification, surface coating, surface grafted, photochemical immobilization, etc., (Huang et al., 2016) Moreover, drugs or chemical molecules are modified on the surface of the material to reduce negative reactions (Topete et al., 2021b).

The polymer with good light transmittance is considered preferentially, and the step of surface modification should also minimize the change to the surface structure of IOL. These reduce the impact on the optical properties of the IOL. In addition, the coating thickness, refractive index, transmittance, swelling capacity and wettability before and after modification also need to be proved to be close by experiments. Different modifications affect the hydrophilicity or hydrophobicity of the IOL surface and this may be the same or opposite to the IOL bulk material. Since hydrophilic and hydrophobic IOL surfaces have their own advantages and disadvantages, the choice needs to be based on actual needs. Some modifications occurred in the non-optical region of the IOL surface, so that its change to the optical properties of the IOL did not affect the IOL function.

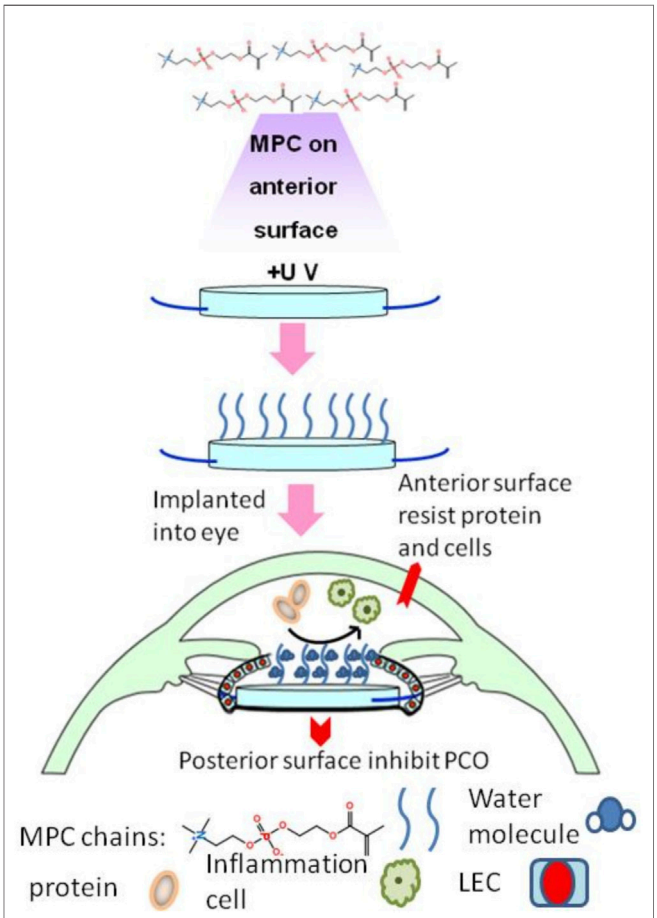

FIGURE 4 | The modified IOL from Huang et al. (2017), with the permission of Elsevier. MPC, 2-methacryloyloxyethyl phosphorylcholine.

Materials to Reduce Inflammation

As previously introduced, the improvement of uveal biocompatibility is mainly manifested in the reduction of postoperative inflammation. Research in this area has been ongoing for decades, and heparin-surface-modified (HSM) IOL have been proven reliable and applied in clinical use. At present, the main research direction in this field is grafting hydrophilic or anti-adhesion groups to the IOL surface. The articles involved are listed in **Table 2**.

HSM IOL had been designed for decades and successfully commercialized. It was first synthesized with the initiation of Ce^{4+} ions (Boffa et al., 1979). Heparin and PMMA were polymerized by oxidation reaction. HSM was gradually applied to the surface of various IOL materials, such as PMMA (Larsson et al., 1989) and silicon (Arthur et al., 2001). Heparin provides higher hydrophilicity to the surface of the IOL. It had been proved by experiments those materials with high hydrophilicity cause less postoperative inflammatory reactions due to reduced adhesion of surface cells and proteins (Roesel et al., 2008). Therefore, HSM was thought to improve the uveal biocompatibility of the material, which had also been demonstrated in many clinical trials, especially for patients with preoperative uveitis (Krall et al., 2014; Zhang et al., 2017). Unfortunately, HSM has not shown a special effect on the prevention of PCO (Ronbeck and Kugelberg, 2014) through long-term observation.

Plasma surface modification was applied to change the surface of the silicon IOL by adding 2-methacryloyloxyethyl phosphorylcholine (MPC) (Wang and Liu, 2011). Not only did MPC-IOL exhibit a repulsive effect on proteins, but it had also been shown to reduce the adhesion of silicone oil, which was an important defect of silicon IOL (Huang X.-D. et al., 2013). Similarly, MPCs were grafted onto hydrophobic acrylate IOL together with methyl acrylic acid (MAA) by air plasma treatment in 2017 (Tan et al., 2017). This MPC-MMA IOL had been reported to significantly reduce protein absorption and inflammatory responses than previous MPC IOL.

The flaw is that plasma technology requires vacuum equipment and takes a long time to accomplish. Huang then tried to graft MPC onto hydrophobic acrylate to construct a hydrophilic interior surface by ultraviolet irradiation (Huang et al., 2017) (**Figure 4**). This method grafted MPC on the surface of IOL more efficiently. *In vitro* experiments showed that macrophage attachment was inhibited, but LEC migration was found to be increased. This meant that the hydrophilic surface helped reduce anterior inflammatory response but had no promotion of capsular compatibility. From this, they designed IOL in which the front surface links hydrophilic MPCs, while the back surface remains hydrophobic, which was able to control inflammation reaction without causing severe PCO. Han introduced poly MPC brushes to hydrophobic IOL surfaces by surface-initiated reversible addition-fragmentation chain transfer (SI-RAFT) (Han et al., 2017). It allows a wide range of functionalities in the monomers and solvents, including aqueous solutions. Therefore, it is a versatile method of modification. The disadvantages are the complicated preparation process and toxic, colored substances may be involved. Different from previous studies, the incidence of PCO has also been shown *in vivo* to be lower than that with bare IOL.

Other hydrophilic groups, such as PEG and N-vinyl pyrrolidone (NVP), have also been used to modify the IOL surface (Lin et al., 2010; Wang et al., 2013). Few platelets and macrophages were found to adhere postoperatively, proving their good uveal compatibility. And the modified IOL exhibited less corneal edema and exudation in rabbit experiments. In addition, the recombinant hirudin-modified IOL surfaces were reported. The hydrophilicity was mainly provided by -OH. It worked by resisting nonspecific absorption of inflammatory cells and proteins, similar to MPC (Zheng et al., 2016).

Materials to Prevent Posterior Capsule Opacification

PCO is caused by the migration and growth of LECs on the posterior capsule and is a major complication after cataract surgery. The incidence of PCO is an important manifestation of capsular compatibility (Awasthi et al., 2009). It has been a hot spot for IOL materials in recent years. Plenty of innovative IOL material modifications provides new ideas for PCO prevention (Han et al., 2018). They mainly focused on inhibiting LECs growing, migrating, and killing LECs. The articles involved are listed in **Table 3**.

Drug-Loading Modification

Many drugs are used to stop PCO from happening. The traditional method of soaking IOL in the solution can only carry limited drugs and is quickly eluted and metabolized after implantation in the eye (Liu et al., 2013). In this way, the drug works for a short period and cannot meet the long-term effect demands. Therefore, combining drugs with chemical materials on the IOL surface to increase the drug loading and reduce the release rate has been widely studied.

Cell apoptotic drug doxorubicin (DOX) is most commonly carried in drug-loaded materials. Attaching DOX to the IOL surface was thought to influence the growth of LECs. Han et al. (2019) developed an anti-proliferative drug-loaded coating doxorubicin-chitosan-tripolyphosphate (DOX-CHI-TPP, CTDNP). CTDNP nanoparticles were used to make polyelectrolyte multilayer (HEP/CTDNP) n together with heparin by LBL technique. LBL is a solution processing technique for generating multilayer films and coatings with nanoscale thickness control of the overall films and of the hierarchical material composition. Its reaction conditions are mild and its preparation is simple. But it takes a long time and the stability of modification is relatively poor. And drug release was still detected one week after implantation. The migration experiments of LECs *in vitro* demonstrated that the modified IOL had an inhibitory impact on cell proliferation and migration, and the effect was positively related to the number of layers. Another method of loading DOX drugs was proposed by Liu et al. (2021) in 2021. First, a polydopamine (PDA) coating was formed on the surface of the IOL through the self-polymerization of PDA, and the drug loading of DOX on this coating was significantly improved. The hydrophilic MPC was then grafted onto the surface of the drug-loaded coating. The PDA (DOX)-MPC multifunctional coating had good hydrophilicity released drugs slowly and long-term lasting over 3 weeks. It had been proved to suppress the proliferation of LEC by *in vivo* and *in vitro* experiments.

Modified materials not only serve as tools for carrying drugs but may also have additional therapeutic effects. Qin et al. (2021) used cationic dendrimer to improve the therapeutic effect of DOX. DOX-encapsulated polyaminoamide (PAMAM) and heparin were

TABLE 3 | The studies on materials reducing PCO.

	Surface modification	IOL optic materials	Technique	Article
Drug loading modification	DOX*-CHI*-sodium TPP*/HEP*	Hydrophobic acrylic	LBL* assembly	Han et al. (2019)
	PDA*-DOX-MPC*	Hydrophobic acrylic	Immersion	Liu et al. (2021)
	DOX-PAMAM*/HEP		LBL assembly	Chen et al. (2021)
	PEGMA*-s-peptide-DOX	Hydrophobic acrylic	SI-RAFT	Han et al. (2020a)
	DOX-PEGMA-co-GMA*	Hydrophobic acrylic	Immersion	Xia et al. (2021)
	DOX-exosomes	Hydrophobic acrylic	Electroporation	Zhu et al. (2022)
	MTX*	Hydrophobic acrylic	Supercritical fluid	Ongkasin et al. (2020)
	MTX-PLGA*	Hydrophobic acrylic hydrophilic acrylic	Spray coating	Kassumeh et al. (2018)
	CsA*-PLGA		Spin coating	Lu et al. (2022)
	Y27632-PLGA	Hydrophobic acrylic		Lin et al. (2019)
	PEI*-(anti-T/PLL*)4-(anti-T)	Hydrophobic acrylic	LBL assembly	Sun et al. (2014)
	PLGA-bromfenac	Hhydrophobic acrylic	Ultrasonic spray	Zhang et al. (2022)
	HA*-Pac*/CHI	Silicon	LBL assembly	Huang et al. (2021)
	5-Fu-CHI	PMMA	Immersion	Huang et al. (2013b)
	5-Fu-PPGC*	Hydrophobic acrylic	Immersion	Xia et al. (2022)
	GOD*-HRP*-MSNs*	Silicon	Immersion	Huang et al. (2022)
Photodynamic modification	ICG*-PLGA	Immersion		Zhang et al. (2016)
	α-CD-Ce6*-PPEGMA* brush	Hydrophobic acrylic	Supramolecular interaction	Tang et al. (2021)
	Carboxylated CuInS/ZnS quantum dots		Facial activation-immersion	Mao et al. (2020)
	PDA/PEI-PMMA	Hydrophobic acrylic	Immersion	Xu et al. (2021)
	PDA	Hydrophobic acrylic	Immersion	Qie et al. (2022)
Hydrophobic modification	RGD	Hydrophilic acrylic	Plasma	Huang et al. (2014)
Hydrophilic modification	PSBMA* brush coating		SI-RAFT	Wang et al. (2021c)
	PEG* brush		SI-RAFT	Lin et al. (2010)
	HA-CHI	Silicon	LBL assembly	Lin et al. (2015)
	PEG	Hydrogel	Grafting	Bozukova et al. (2007)
	PEG	Hydrophobic acrylic	Plasma	Xu et al. (2016)
	EGPEMA*-co-EA*	Hydrophobic acrylic		Liu et al. (2021)

**DOX, doxorubicin; CHI, chitosan; TPP, tripolyphosphate; HEP, heparin; PDA, polydopamine; MPC, 2-methacryloyloxyethyl phosphorylcholine; PAMAM, polyaminoamide; PEGMA, poly (ethylene glycol) methacrylate; GMA, glycidyl methacrylate; MTX, methotrexate; PLGA, poly (lactic-co-glycolic) acid; CsA, cyclosporine A; PEI, polyethylenimine; PLL, poly-L-lysine; HA, hyaluronic acid; Pac, paclitaxel; ICG, indocyanine green; PPGC, poly (polyethylene glycol methacrylate-co-glycidyl methacrylate-co-coumarin methacrylate); GOD, glucose oxidase; HRP, horseradish peroxidase; MSNs, mesoporous silica nanoparticles; α-CD-Ce6, chlorin e6 grafted α-cyclodextrin; PPEGMA, poly (poly (ethylene glycol) methacrylate); PSBMA, poly (sulfobetaine methacrylate); PEG, poly (Ethylene Glycol); LBL, layer-by-layer; EGPEMA, ethylene glycol phenyl ether methacrylate; EA, 2-(2-ethoxyethoxy) ethyl acrylate.*

assembled to the IOL surface by the LBL technique. The material itself enhanced the medical effect. Animal experiments found that this modification showed a better prevention effect of PCO than free DOX. This might be due to the ability of cationic dendrimer to enhance cell penetration and autophagy. Han Y. et al. (2020) carried DOX with poly (ethylene glycol) methacrylate (PEGMA) and grafted it to the IOL surface *via* MMP-2-sensitive peptide linkage. In addition to the pharmacological effects of DOX, this modification increased sensitivity to metalloproteinases (MMPs), a protein found to be up-regulated during LEC proliferation. The hydrophilicity of PEGMA itself was also applied by Xia et al. (2021) to work with DOX to further inhibit PCO. Zhu et al. (2022) used exosomes extracted from LECs to carry DOX. They found that the drug was absorbed more effective by the cells and thought this might be due to the targeting ability of the exosomes.

Ongkasin et al. (2020) modified anti-metabolic drug methotrexate (MTX) onto the IOL surface *via* supercritical impregnations. During this process, supercritical CO_2 was used to dissolve and carry the drug, and ethanol was added to increase drug dissolution. By adjusting the conditions, 8 Mpa, 4 h impregnation achieved 80 days drug-release. Experiments in an *in vitro* model showed that it might contribute to the prevention of PCO in the clinic by inhibiting epithelial-mesenchymal transformation. Kassumeh et al. (2018) sprayed the solution containing MTX, poly (lactic-co-glycolic) acid (PLGA), and isopropanol on the IOL surface to obtain a drug-loaded coating. The drug-loaded coating material, compared to the control group without the drugs, significantly suppressed cell growth and migration. Interestingly, the authors found that modified hydrophilic IOL released more drugs than hydrophobic IOL.

There were other drugs used to manifest PCO, carried by PLGA, which was proved to be a safe and feasible drug carrier (Loureiro and Pereira, 2020). PLGA can effectively protect drugs from degradation and unrestrained release. Solutions of PLGA and cyclosporine A (CsA) were used to modify the IOL surface by Lu et al. (2022). The spin coating method was applied to construct the centrifuging concentric circles drug-loaded coating on the IOL surface. Rotation speed and spin time were adjusted to determine the most appropriate drug release profile. The immunosuppressive drug CsA effectively inhibited the growth of LECs *in vitro* investigations and was thought to control cell apoptosis through autophagic effects. Animal experiments also convinced it. Lin et al.

TABLE 4 | The studies on materials reducing endophthalmitis.

Drug	Surface modification	IOL optic materials	Technique	Article
MXF*	AMPS*/SBMA*	Hydrophilic acrylic	Plasma grafting	Pimenta et al. (2017)
	PHEMA coating	Hydrophilic acrylic	Argon plasma-assisted grafting	Vieira et al. (2017)
AMP*	PSS*-PEI	PMMA	LBL assembly	Manju and Kunnatheeri, (2010)
Vancomycin	Poly 2/polyanion/vancomycin/polyanion		LBL assembly	Shukla et al. (2011)
NFX*	Octadecyl isocyanate	Hydrophilic acrylic	Grafting	Anderson et al. (2009)
Gentamycin	PPPE* IOL-PDA	Hydrophobic acrylic		Yang et al. (2021)
No antibiotics	p (DMAEMA*-CO-MPC) brush	Silicon	SI-RAFT	Wang et al. (2017)
	p (VBC-CO-DMAEMA)		Chemical vapor deposition	Choi et al. (2020)
	HA*-CHI*	Silicon	Polyelectrolyte deposition	Lin et al. (2017a)

**MXF, moxifloxacin; AMP, ampicillin; NFX, norfloxacin; AMPS, 2-acrylamido-2-methylpropane sulfonic acid; SBMA, (2-(methacryloyloxy)ethyl) dimethyl-(3-sulfopropyl) ammonium hydroxide; PSS, poly (sodium 4-styrenesulfonate); PPPE, poly (2-phenoxyethyl methacrylate-co-2-phenoxyethyl acrylate-co-2-ethylhexyl methacrylate); DMAEMA, 2-(dimethylamino)-ethyl methacrylate; HA, hyaluronic acid; CHI, chitosan polyelectrolyte.*

(2019) proposed a PLGA carried, ROCK pathway inhibitor Y27632, to suppress LEC growth. They demonstrated the mechanism by which the ROCK pathway promoted LEC proliferation. And they confirmed that LEC proliferation was reduced when the ROCK pathway was inhibited. Subsequently, modified IOL carrying ROCK pathway inhibitors were also shown to significantly inhibit PCO *in vivo* experiments.

TGF-β is an important factor in promoting lens epithelial-mesenchymal transformation (EMT), which is one of the steps in the occurrence of PCO. It exists in the fluid tissue of the eye and promotes the development of PCO. Sun et al. (2014) firstly applied APGD to create a negatively charged surface on hydrophobic IOL. APGD is an environmentally friendly and energy efficient technique, which has relatively little impact on the bulk material. Then, polyethyleneimine was deposited on the surface. Thirdly, anti-TGF-β2 (anti-T) antibody and poly-L-lysine were placed on the modified surface using the LBL technique for four cycles. The structure could be maintained for three months without difference in optical and physical properties. *In vitro* experiments demonstrated that LEC migration and EMT were greatly suppressed, but proliferation and adhesion were not inhibited significantly. The inhibitory effect of bromfenac on TGF-β was also applied to the modified IOL surface. PLGA-modified extended-release bromfenac was proved effective in preventing PCO (Zhang et al., 2022).

The anti-proliferative drug paclitaxel (Pac) is also thought to possibly inhibit the occurrence of PCO. Huang et al. (2021) made the multilayer coating of hyaluronic acid (HA), CHI, and Pac through the LBL technique. The coating was proven to have good sustained release and biocompatibility. LEC proliferation on the surface of the material was also found to be significantly reduced. 5-fluorouracil chitosan nanoparticles (5-Fu-CSNP) were introduced to effectively suppress PCO (Huang X. et al., 2013). The drug could be continuously released for four days *in vitro* and effectively promoted apoptosis. Subsequently, a light-controlled drug-releasing coating was used to carry 5-Fu (Xia et al., 2022). This modification finely controlled drug release through illumination based on the photo reactivity of coumarin.

In addition to conventional drugs, special chemical reactions were also considered to kill LECs. Horseradish peroxidase (HRP) and glucose oxidase (GOD) were used to catalyse the production of reactive oxygen species, resulting in cell apoptosis. Huang et al. (2022) immobilized GOD and HRP on IOL surface *via* mesoporous silica nanoparticles (MSNs) and obtained positive results.

Photodynamic Coating Modification

Using photodynamic therapy-effect coatings instead of carrying drugs may further simplify the production techniques. Due to its exogenous excitation, the effect is more controllable (Han et al., 2016). In 2015, Zhang et al. (2016) had tried laser-activated indocyanine green (ICG) to inhibit LEC proliferation and migration. And PLGA was used to cover the ICG coating to prolong the residence time of the drug. *In vivo* pharmacodynamic experiments demonstrated that the ICG-IOL could successfully inhibit PCO. Moreover, both the ICG and PLGA were easily metabolized, indicating little harm to the human body.

Another photodynamic coating was presented to control PCO (Tang et al., 2021). The poly [poly (ethylene glycol) methacrylate] (PPEGMA) brush was firstly established on the surface of IOL by SI-RAFT. The chlorin e6 grafted α-cyclodextrin (α-CD-Ce6) then was attached to the PPEGMA brush as a photosensitizer. When exposed to light, α-CD-Ce6 induced apoptosis by producing reactive oxygen species (ROS). Illumination has been shown to not influence the optical properties and biocompatibility of the material. And the effectiveness was also proved in animal experiments. CuInS/ZnS quantum dots (ZCIS QDs) was synthesized and carboxylated by Mao et al. (2021). And it was modified onto the non-optical surface of IOL by the facial activation-immersion method. ZCIS QDs inhibited LEC growth by releasing localized heat under mild near-infrared light irradiation. But its biocompatibility was not known due to the lack of *in vivo* experiments.

Xu et al. (2021) introduced a photothermal IOL (PT-IOL) with a mussel-inspired coating. Dopamine hydrochloride was dissolved with $CuSO_4$ $5H_2O$ and H_2O_2 (30%) for PDA deposition. Hydrophobic acrylic IOL were immersed respectively in PDA and polyethyleneimine (PEI) solutions to form the coating on the non-optical surface. It was found that the thickness of the coating was positively related to the soaking time, and 40 min immersion obtained the most appropriate coating. The irradiation of NIR was converted to thermal energy through this material, and elevated temperature around the PT-IOL proved to be effective in killing LECs. Biological experiments, as well, proved the preventive effect on PCO. Another PDA surface modification was introduced by Qie and proved to be effective in blocking PCO Qie et al. (2022). Its

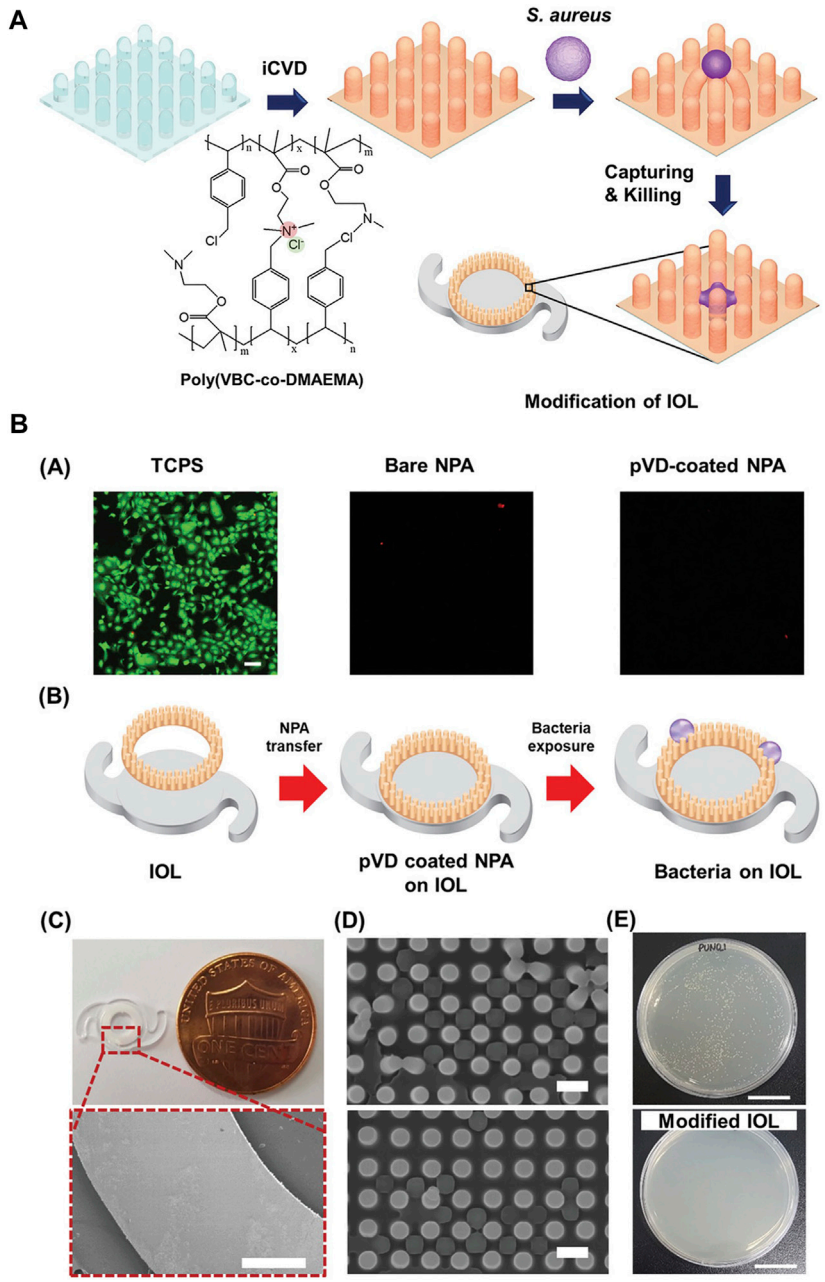

FIGURE 5 | (A) Schematic of the ionic polymer-coated NPA. **(B)**. **(A)** Live/dead staining and adhesion test of corneal endothelial cells on each NPA after a 1 day culture. There were no usable and adhered cells on the NPA due to the dimension of the NPA structure. The scale bar is 100 μm. **(B–E)** Modification of IOL with pVD-coated NPA for the antibacterial property. **(B)** Schematic of the monolithic integration strategy of pVD-coated NPA onto the IOL. **(C)** Photographic image of the modified IOL and SEM images of the modified IOL edge. Scale bars are 500 μm. **(D)** SEM images of the NPA after exposure to *S. aureus*. Scale bars is 1 μm. **(E)** Representative images after colony-counting assay with control and modified IOL. The scale bars are 1 cm. Reprinted from Choi et al. (2020), with the permission of Wiley. NPA, polymeric nanopillar array; pVD, crosslinked ionic polymer thin film.

mechanism was thought to induce apoptosis through reactive oxygen species.

Hydrophobic Modification

Hydrophilic materials are generally considered to be more likely to cause severe PCO than hydrophobic materials. The sticky surface of the hydrophobic material largely prevents the migration of LECs. LECs rapidly fibrosis, degenerate, and even die around the hydrophobic edges, which do not cover the center of IOL. However, hydrophilic materials are more suitable for LECs growth. It will block the optical part, seriously affecting the vision (Bertrand et al., 2014). A cell adhesion

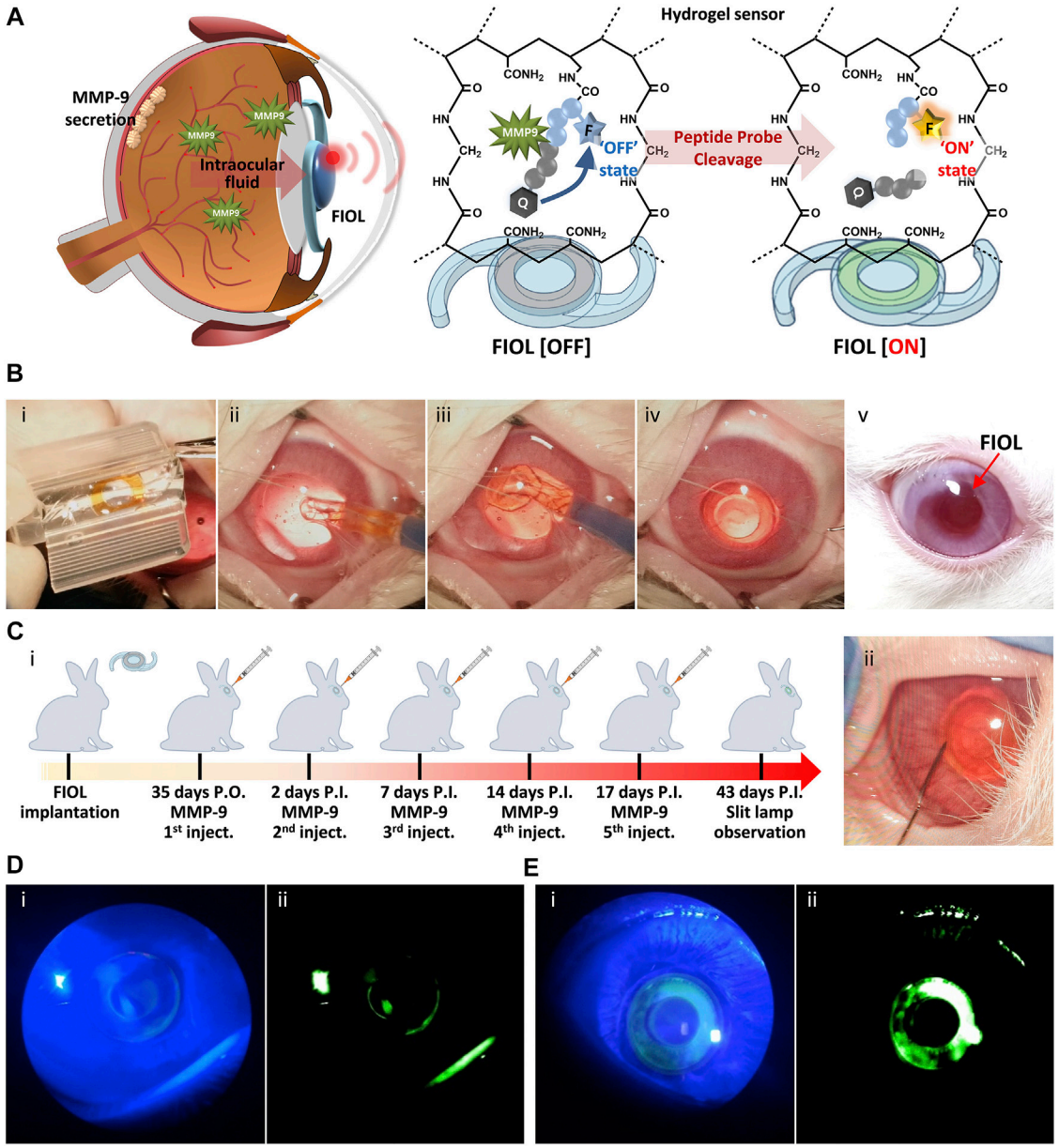

FIGURE 6 | *In vivo* monitoring of MMP-9 using FIOL. **(A)** Schematic illustration of the reaction mechanism of FIOL implanted inside the eye. **(B)** Representative photographs of the process of FIOL implantation during *in vivo* rabbit cataract surgery: **(i)** Loading of FIOL into the cartridge of the injector, **(ii,iii)** Insertion of FIOL into the posterior chamber of the eye and **(iv)** final implantation status of FIOL in the eye. **(v)** FIOL implanted in the eye maintained proper position without any adverse response, including immune reactions, over 7 weeks postoperatively. **(C) (i)** Schematic illustration of *in vivo* testing for MMP-9 sensing of FIOL inside the eye and **(ii)** representative photograph of intraocular MMP-9 injection after FIOL implantation. Slit-lamp photographs of FIOL inside the eye after **(D)** 2 days P.I. and **(E)** 43 days P.I., with **(i)** cobalt blue filtered light and **(ii)** green filtered images, respectively. Reprinted from Shin et al. (2020), with the permission of Elsevier.

molecule (RGD peptide) that can be recognized by a variety of integrins to adhere to many cells was used to compensate for the defects of hydrophilic materials (Huang et al., 2014). Oxygen plasma was involved in the surface modification process. The modified material is highly hydrophilic but exhibits significant LEC adhesion. It meant that RGD might play a role in inhibiting PCO.

Hydrophilic Modification

On the contrary, Wang R. et al. (2021) tried to modify the surface of hydrophobic IOL with hydrophilic polymer poly (sulfobetaine methacrylate) (PSBMA); some of researches (Bozukova et al., 2007; Xu et al., 2016; Lin Q. et al., 2017) modified IOL surface with PEG. PSBMA and PEG brushes were coated on to IOL surface by the SI-RAFT technique. Cellular experiments showed

that initial LEC adhesion to IOL surfaces was reduced. Recently, bulk modification was used to graft EGPEMA-co-2-(2-ethoxyethoxy) ethyl acrylate (EA) polymer onto IOL surfaces. And it was believed to be easier and more efficient to produce compared to other surface modifications. However, previous studies had suggested that hydrophilic materials were more suitable for cell growth due to their high water content. This seems to contradict their results. Thus, further research is expected to verify the specific impact of hydrophilic materials on the development of PCO.

Antibacterial Surface Modification

Postoperative endophthalmitis is caused by bacteria, of which more than 95% are Gram-positive, entering the eye with the instrument or IOL during surgery (Garg et al., 2017). The probability of postoperative endophthalmitis is very low. But once endophthalmitis occurs, it can be serious and even lead to blindness (Durand, 2017; Fan et al., 2021). To prevent endophthalmitis, the surgeons use antibiotic eye drops (Friling et al., 2013). Drug-carrying IOL have also been of concern. Some studies carried multiple drugs, giving IOLs the effect of preventing multiple complications (Topete et al., 2020). This requires the innovation of IOL materials to meet the needs of carrying antibiotics and sustained release. The articles involved are listed in **Table 4**.

Moxifloxacin (MXF), a type of broad-spectrum antibacterial fluoroquinolone, is often used to prevent endophthalmitis after cataract surgery. Pimenta et al. (2017) grafted [2-(methacryloyloxy)ethyl] dimethyl-(3-sulfopropyl) ammonium hydroxide (SBMA) or 2-acrylamido-2-methylpropane sulfonic acid (AMPS) onto the surface of IOL through argon plasma-assisted copolymerization. AMPS showed higher MXF carrying capacity and longer drug release time with 21 days. The modified drug-loaded materials were stored 30 days after sterilization. Released MXF remained effective against *S. aureus* and Staphylococcus epidermidis after 12 days, consistent with the recommended duration of antibiotic therapy after surgery. Vieira et al. (2017) used poly HEMA modified IOL to load MXF. Argon exposure for 3 min appeared higher hydrophilicity. Controlled experiments compared the status of drug loading under different conditions, 15 h at 37°C, with 100 rpm proved to be the best loading condition.

Adjusting the bulk material can further extend the duration of maintenance. Topete et al. (2021a) added functional monomers in hydrogels to regulate the release of MXF. They tried acrylic acid (AA), methacrylic acid (MAA), 4-vinylpiridine (4-VP), and MAA+4-VP, as well as molecular imprinting techniques. The addition of MMA functional monomers alone was considered the best way to carry MXF. The physical properties and transparency of the modified IOL material were not affected. Antimicrobial tests showed that released MFX remained active against *S. aureus*.

Other types of antibiotics were applied to prevent endophthalmitis. Manju and Kunnatheeri (2010) created a multilayer coating IOL to load ampicillin (AMP). LBL technique was applied. IOL was sunk alternatively in a solution of PEI and another of poly (sodium 4-styrenesulfonate) (PSS) after being immersed in an ammonia solution. The drug release was observed to reach 91% of the total after 4 days, with a plateau in approximately 5 days. Shukla et al. (2011) used the same technique to carry vancomycin. Likewise, the modified IOL material exhibits good drug loading capacity. Octadecyl isocyanate worked as a hydrophobic barrier to limit drug release, exhibiting a sustained-release effect (Anderson et al., 2009). Norfloxacin (NFX) was dissolved in the solution to modify PHEMA hydrogels, and a significant bacteriostatic effect was demonstrated. Yang (Xiang et al., 2021) grafted PDA and gentamicin on the hydrophobic acrylate IOL synthesized of poly (2-phenoxyethyl methacrylate-co-2-phenoxyethyl acrylate-co-2-ethylhexyl methacrylate) (PPPE). It was proven to be effective against bacteria and reduce PCO. For different types of antibacterial drugs, there are the most suitable modification conditions, respectively. Therefore, it is necessary to develop more drug-loaded modifications.

The modified materials can also exert antibacterial effects. Wang et al. (2017) grafted 2-(dimethylamino)-ethyl methacrylate-co-2-methacryloyloxyethyl phosphorylcholine p (DMAEMA-co-MPC) brushes on PDMS, which was one of the commonly used IOL materials. SI-RAFT was involved in this procedure. 1-bromoheptane (25 v/v%) was applied to quaternize the polymer, and meanwhile, invest the antibacterial function. Shake-flask culture and live/dead staining confirmed the suppression of *S. aureus*. Furthermore, p (DMAEMA-co-MPC) increased surface hydrophilicity. The modified IOL was proved to be able to reduce bacterial adhesion and biofilm formation on the surface. Likewise, a polymeric nanopillar array surface modification was engineered to disrupt bacterial membranes (Choi et al., 2020). 4-vinylbenzyl chloride (VBC) and DMAEMA were deposited onto the IOL surface to form p (VBC-co-DMAEMA) modification. In addition to being antibacterial, it has also been shown to be somewhat resistant to PCO (**Figure 5**). HA/CHI modification have also been proved to inhibit bacterial growth (Lin Q. K. et al., 2017). This was attributed to the ability of reducing bacterial adhesion. And similar to LECs, HA/CHI modification inhibit the cells to grow on the surface of IOL, thus preventing the PCO (Lin et al., 2015).

Surface Modification as Sensors

In recent years, attempts have been made to impose additional uses for IOL. The development of biosensing technology makes it possible for IOL to be used as a sensing device to detect special biomolecules or the environment in the eye (Yang et al., 2021). And some biosensing devices also involve material development. Shin et al. (2020) developed a fluorescent IOL (FIOL) based on diacrylamide-group-modified PEG diacrylamide (PEGDAAm) hydrogels. Specific peptide probes were attached to IOL to detect the concentration of MMP-9 in aqueous humor, which is a biomarker reflecting neurological diseases (**Figure 6**). Other sensors for monitoring intraocular pressure (Narasimhan et al., 2018) and glucose concentration (Yang et al., 2018) are also being developed, but they are not well

integrated with intraocular lens materials. We expect more research in related fields in the future.

CONCLUSION

The commonly used materials for commercialized IOL today are silicon, hydrophilic and hydrophobic acrylates. Liquid and shape-memory materials have been developed to insert through smaller surgical incisions, and even if an intact capsular bag can be maintained, the ability to accommodate is preserved. Light-reactive molecules are used to make IOL that can adjust the refractive power. Usually, surface modification of polymer materials is considered to improve biocompatibility, involving LPL, plasma, grafting, coating, and other methods. A variety of molecules are modified to the surface of the IOL material to complement specific effects by changing the properties of the surface. Carrying drugs on the surface of the IOL prevents postoperative complications, such as intraocular infections and PCO, which is also an indicator of capsular biocompatibility.

AUTHOR CONTRIBUTIONS

KY conceptualized this review. The first draft of this paper was conceived by CL and HW; XC and JX critically revised the draft to yield the final manuscript; supervision and revision over the article was accomplished by HY and KY; KY acquihired the funding. All authors have read and agreed to the published version of the manuscript.

FUNDING

This review was funded by the National Natural Science Foundation of China (Grant Nos. 82070939 and 81870641), the National Key Research and Development Program of China (Grant No. 2018YFC1106104), Key Research and Development Project of Zhejiang Province (Grant No. 2020C03035), Zhejiang Provincial Natural Science Foundation of China (Grant No. LQ19H120011) and the Program of Zhejiang Medical Technology (Grant No. 2019RC178).

REFERENCES

Abedin zadeh, M., Khoder, M., AL-Kinani, A. A., Younes, H. M., and Alany, R. G. (2019). Retinal Cell Regeneration Using Tissue Engineered Polymeric Scaffolds. *Drug Discov. Today* 24, 1669–1678. doi:10.1016/j.drudis.2019.04.009

Abela-formanek, C., Amon, M., Kahraman, G., Schauersberger, J., and Dunavoelgyi, R. (2011). Biocompatibility of Hydrophilic Acrylic, Hydrophobic Acrylic, and Silicone Intraocular Lenses in Eyes with Uveitis Having Cataract Surgery: Long-Term Follow-Up. *J. Cataract. Refract Surg.* 37, 104–112. doi:10.1016/j.jcrs.2010.07.038

Alió, J. L., Alió del Barrio, J. L., and Vega-Estrada, A. (2017a). Accommodative Intraocular Lenses: where Are We and where We Are Going. *Eye Vis* 4, 16. doi:10.1186/s40662-017-0077-7

Alio, J. L., Plaza-Puche, A. B., Férnandez-Buenaga, R., Pikkel, J., and Maldonado, M. (2017b). Multifocal Intraocular Lenses: An Overview. *Surv. Ophthalmol.* 62, 611–634. doi:10.1016/j.survophthal.2017.03.005

Allarakhia, L., Knoll, R. L., and Lindstrom, R. L. (1987). Soft Intraocular Lenses. *J. Cataract. Refract Surg.* 13, 607–620. doi:10.1016/s0886-3350(87)80149-9

Amon, M. (2001). Biocompatibility of Intraocular Lenses. *J. Cataract. Refract Surg.* 27, 178–179. doi:10.1016/s0886-3350(01)00742-8

Anderson, E. M., Noble, M. L., Garty, S., Ma, H., Bryers, J. D., Shen, T. T., et al. (2009). Sustained Release of Antibiotic from Poly(2-Hydroxyethyl Methacrylate) to Prevent Blinding Infections after Cataract Surgery. *Biomaterials* 30, 5675–5681. doi:10.1016/j.biomaterials.2009.06.047

Annaka, M., Mortensen, K., Matsuura, T., Ito, M., Nochioka, K., and Ogata, N. (2012). Organic-inorganic Nanocomposite Gels as an *In Situ* Gelation Biomaterial for Injectable Accommodative Intraocular Lens. *Soft Matter* 8, 7185–7196. doi:10.1039/c2sm25534k

Apple, D. J., Mamalis, N., Loftfield, K., Googe, J. M., Novak, L. C., Kavka-VAN Norman, D., et al. (1984). Complications of Intraocular Lenses. A Historical and Histopathological Review. *Surv. Ophthalmol.* 29, 1–54. doi:10.1016/0039-6257(84)90113-9

Arthur, S. N., Peng, Q., Apple, D. J., Escobar-Gomez, M., Bianchi, R., Pandey, S. K., et al. (2001). Effect of Heparin Surface Modification in Reducing Silicone Oil Adherence to Various Intraocular Lenses. *J. Cataract. Refract Surg.* 27, 1662–1669. doi:10.1016/s0886-3350(01)00891-4

Awasthi, N., Guo, S., and Wagner, B. (2009). Posterior Capsular Opacification. *Arch. Ophthalmol.* 127, 555–562. doi:10.1001/archophthalmol.2009.3

Bertrand, V., Bozukova, D., Lanero, T. S., Huang, Y.-S., Schol, D., Rosière, N., et al. (2014). Biointerface Multiparametric Study of Intraocular Lens Acrylic Materials. *J. Cataract. Refract Surg.* 40, 1536–1544. doi:10.1016/j.jcrs.2014.01.035

Bille, J. F., Engelhardt, J., Volpp, H.-R., Laghouissa, A., Motzkus, M., Jiang, Z., et al. (2017). Chemical Basis for Alteration of an Intraocular Lens Using a Femtosecond Laser. *Biomed. Opt. Express* 8, 1390–1404. doi:10.1364/boe.8.001390

BloemendaL, H., DE Jong, W., Jaenicke, R., Lubsen, N. H., Slingsby, C., and Tardieu, A. (2004). Ageing and Vision: Structure, Stability and Function of Lens Crystallins. *Prog. Biophysics Mol. Biol.* 86, 407–485. doi:10.1016/j.pbiomolbio.2003.11.012

Boffa, M. C., Labarre, D., Jozefowicz, M., and Boffa, G. A. (1979). Interactions between Human Plasma Proteins and Heparin-Poly(methyl Methacrylate) Copolymer. *Thromb. Haemost.* 41, 346–356. doi:10.1055/s-0038-1646784

Bozukova, D., Pagnoulle, C., DE Pauw-Gillet, M.-C., Desbief, S., Lazzaroni, R., Ruth, N., et al. (2007). Improved Performances of Intraocular Lenses by Poly(ethylene Glycol) Chemical Coatings. *Biomacromolecules* 8, 2379–2387. doi:10.1021/bm0701649

Čanović, S., Konjevoda, S., Pavičić, A. D., and Stanić, R. (2019). *Intraocular Lens (IOL) Materials*. London, United Kingdom: Intraocular Lens. IntechOpen.

Chang, D. F. (2019). Disruptive Innovation and Refractive IOLs: How the Game Will Change with Adjustable IOLs. *Asia-Pacific J. Ophthalmol.* 8, 432–435. doi:10.1097/apo.0000000000000266

Chee, S.-P., Yang, Y., and Ti, S.-E. (2015). Clinical Outcomes in the First Two Years of Femtosecond Laser-Assisted Cataract Surgery. *Am. J. Ophthalmol.* 159, 714–719. doi:10.1016/j.ajo.2015.01.016

Chen, X., Xu, J., Chen, X., and Yao, K. (2021). Cataract: Advances in Surgery and whether Surgery Remains the Only Treatment in Future. *Adv. Ophthalmol. Pract. Res.* 1, 100008. doi:10.1016/j.aopr.2021.100008

Choi, G., Song, Y., Lim, H., Lee, S. H., Lee, H. K., Lee, E., et al. (2020). Antibacterial Nanopillar Array for an Implantable Intraocular Lens. *Adv. Healthc. Mater* 9, e2000447. doi:10.1002/adhm.202000447

De groot, J. H., VAN Beijma, F. J., Haitjema, H. J., Dillingham, K. A., Hodd, K. A., Koopmans, S. A., et al. (2001). Injectable Intraocular Lens Materials Based upon Hydrogels. *Biomacromolecules* 2, 628–634. doi:10.1021/bm005622r

Deboer, C. M., Lee, J. K., Wheelan, B. P., Cable, C., Shi, W., Tai, Y. C., et al. (2016). Biomimetic Accommodating Intraocular Lens Using a Valved Deformable Liquid Balloon. *IEEE Trans. Biomed. Eng.* 63, 1129–1135. doi:10.1109/TBME.2015.2484379

Dick, H. B., and Gerste, R. D. (2021). Future Intraocular Lens Technologies. *Ophthalmology* 128, e206–e213. doi:10.1016/j.ophtha.2020.12.025

Ding, L., Blackwell, R., Kunzler, J. F., and Knox, W. H. (2006). Large Refractive Index Change in Silicone-Based and Non-silicone-based Hydrogel Polymers

Induced by Femtosecond Laser Micro-machining. *Opt. Express* 14, 11901–11909. doi:10.1364/oe.14.011901

Downes, S. M. (2016). Ultraviolet or Blue-Filtering Intraocular Lenses: what Is the Evidence? *Eye* 30, 215–221. doi:10.1038/eye.2015.267

Durand, M. L. (2017). Bacterial and Fungal Endophthalmitis. *Clin. Microbiol. Rev.* 30, 597–613. doi:10.1128/cmr.00113-16

Fan, W., Han, H., Chen, Y., Zhang, X., Gao, Y., Li, S., et al. (2021). Antimicrobial Nanomedicine for Ocular Bacterial and Fungal Infection. *Drug Deliv. Transl. Res.* 11, 1352–1375. doi:10.1007/s13346-021-00966-x

Fisher, R. F. (1977). The Force of Contraction of the Human Ciliary Muscle during Accommodation. *J. Physiol.* 270, 51–74. doi:10.1113/jphysiol.1977.sp011938

Ford, J., Werner, L., and Mamalis, N. (2014). Adjustable Intraocular Lens Power Technology. *J. Cataract. Refract Surg.* 40, 1205–1223. doi:10.1016/j.jcrs.2014.05.005

Friling, E., Lundström, M., Stenevi, U., and Montan, P. (2013). Six-year Incidence of Endophthalmitis after Cataract Surgery: Swedish National Study. *J. Cataract. Refract Surg.* 39, 15–21. doi:10.1016/j.jcrs.2012.10.037

Garg, P., Roy, A., and Sharma, S. (2017). Endophthalmitis after Cataract Surgery. *Curr. Opin. Ophthalmol.* 28, 67–72. doi:10.1097/icu.0000000000000326

Grzybowski, A., Zemaitiene, R., Markeviciute, A., and Tuuminen, R. (2021). Should We Abandon Hydrophilic Intraocular Lenses? *Am. J. Ophthalmol.* 237, 139–145. doi:10.1016/j.ajo.2021.11.021

Han, H., Gao, Y., Chai, M., Zhang, X., Liu, S., Huang, Y., et al. (2020a). Biofilm Microenvironment Activated Supramolecular Nanoparticles for Enhanced Photodynamic Therapy of Bacterial Keratitis. *J. Control. Release* 327, 676–687. doi:10.1016/j.jconrel.2020.09.014

Han, H., Jin, Q., Wang, H., Teng, W., Wu, J., Tong, H., et al. (2016). Intracellular Dual Fluorescent Lightup Bioprobes for Image-Guided Photodynamic Cancer Therapy. *Small* 12, 3870–3878. doi:10.1002/smll.201600950

Han, Y., Xu, X., Tang, J., Shen, C., Lin, Q., and Chen, H. (2017). Bottom-up Fabrication of Zwitterionic Polymer Brushes on Intraocular Lens for Improved Biocompatibility. *Int. J. Nanomedicine* 12, 127–135. doi:10.2147/IJN.S107491

Han, Y. K., Kwon, J. W., Kim, J. S., Cho, C. S., Wee, W. R., and Lee, J. H. (2003). *In Vitro* and *In Vivo* Study of Lens Refilling with Poloxamer Hydrogel. *Br. J. Ophthalmol.* 87, 1399–1402. doi:10.1136/bjo.87.11.1399

Han, Y., Tang, J., Liu, S., Zhao, X., Wang, R., Xia, J., et al. (2020b). Cellular Microenvironment-Sensitive Drug Eluting Coating on Intraocular Lens for Enhanced Posterior Capsular Opacification Prevention and *In Vivo* Biocompatibility. *ACS Appl. Bio Mat.* 3, 3582–3593. doi:10.1021/acsabm.0c00331

Han, Y., Tang, J., Xia, J., Wang, R., Qin, C., Liu, S., et al. (2019). Anti-Adhesive and Antiproliferative Synergistic Surface Modification of Intraocular Lens for Reduced Posterior Capsular Opacification. *Ijn* 14, 9047–9061. doi:10.2147/ijn.s215802

Han, Y., Xu, X., Wang, Y., Liu, S., Zhao, X., Chen, H., et al. (2018). Drug Eluting Intraocular Lens Surface Modification for PCO Prevention. *Colloids Interface Sci. Commun.* 24, 40–41. doi:10.1016/j.colcom.2018.03.007

Hao, X., Jeffery, J. L., LE, T. P. T., Mcfarland, G., Johnson, G., Mulder, R. J., et al. (2012). High Refractive Index Polysiloxane as Injectable, *In Situ* Curable Accommodating Intraocular Lens. *Biomaterials* 33, 5659–5671. doi:10.1016/j.biomaterials.2012.04.052

Hao, X., Jeffery, J. L., Wilkie, J. S., Meijs, G. F., Clayton, A. B., Watling, J. D., et al. (2010). Functionalised Polysiloxanes as Injectable, *In Situ* Curable Accommodating Intraocular Lenses. *Biomaterials* 31, 8153–8163. doi:10.1016/j.biomaterials.2010.07.065

Hejtmancik, J. F., and Shiels, A. (2015). Overview of the Lens. *Prog. Mol. Biol. Transl. Sci.* 134, 119–127. doi:10.1016/bs.pmbts.2015.04.006

Hengerer, F. H., Dick, H. B., and Conrad-Hengerer, I. (2011). Clinical Evaluation of an Ultraviolet Light Adjustable Intraocular Lens Implanted after Cataract Removal. *Ophthalmology* 118, 2382–2388. doi:10.1016/j.ophtha.2011.05.030

Huang, H., Zhu, S., Han, Y., Liu, D., Liu, S., Lu, D., et al. (2022). Cascade Catalytic Platform Modified Intraocular Lens for High-Efficient Posterior Capsule Opacification Prevention. *Chem. Eng. J.* 427, 13155. doi:10.1016/j.cej.2021.131553

Huang, H., Zhu, S., Liu, D., Wen, S., and Lin, Q. (2021). Antiproliferative Drug-Loaded Multi-Functionalized Intraocular Lens for Reducing Posterior Capsular Opacification. *J. Biomaterials Sci. Polym. Ed.* 32, 735–748. doi:10.1080/09205063.2020.1865691

Huang, Q., Cheng, G. P.-M., Chiu, K., and Wang, G.-Q. (2016). Surface Modification of Intraocular Lenses. *Chin. Med. J. Engl.* 129, 206–214. doi:10.4103/0366-6999.173496

Huang, X.-D., Li, H.-Y., Lin, L., and Yao, K. (2013b). Reduced Silicone Oil Adherence to Silicone Intraocular Lens by Surface Modification with 2-methacryloyloxyethyl Phosphoryl-Choline. *Curr. Eye Res.* 38, 91–96. doi:10.3109/02713683.2012.704477

Huang, X., Luo, C., Lin, L., Zhang, L., Li, H., Yao, K., et al. (2017). UV-assisted Treatment on Hydrophobic Acrylic IOLs Anterior Surface with Methacryloyloxyethyl Phosphorylcholine: Reducing Inflammation and Maintaining Low Posterior Capsular Opacification Properties. *Mater. Sci. Eng. C* 75, 1289–1298. doi:10.1016/j.msec.2017.03.029

Huang, X., Wang, Y., Cai, J.-P., Ma, X.-Y., Li, Y., Cheng, J.-W., et al. (2013a). Sustained Release of 5-fluorouracil from Chitosan Nanoparticles Surface Modified Intra Ocular Lens to Prevent Posterior Capsule Opacification: an *In Vitro* and *In Vivo* Study. *J. Ocular Pharmacol. Ther.* 29, 208–215. doi:10.1089/jop.2012.0184

Huang, Y.-S., Bertrand, V., Bozukova, D., Pagnoulle, C., Labrugère, C., DE Pauw, E., et al. (2014). RGD Surface Functionalization of the Hydrophilic Acrylic Intraocular Lens Material to Control Posterior Capsular Opacification. *PLoS One* 9, e114973. doi:10.1371/journal.pone.0114973

Jellali, R., Bertrand, V., Alexandre, M., Rosière, N., Grauwels, M., DE Pauw-Gillet, M. C., et al. (2017). Photoreversibility and Biocompatibility of Polydimethylsiloxane-Coumarin as Adjustable Intraocular Lens Material. *Macromol. Biosci.* 17. doi:10.1002/mabi.201600495

Kannan, R. Y., Salacinski, H. J., Butler, P. E., and Seifalian, A. M. (2005). Polyhedral Oligomeric Silsesquioxane Nanocomposites: the Next Generation Material for Biomedical Applications. *Acc. Chem. Res.* 38, 879–884. doi:10.1021/ar050055b

Kapoor, S., and Gupta, S. (2020). *Basic Science of Intraocular Lens Materials*. London, United Kingdom: Intraocular LensIntechOpen.

Karayilan, M., Clamen, L., and Becker, M. L. (2021). Polymeric Materials for Eye Surface and Intraocular Applications. *Biomacromolecules* 22, 223–261. doi:10.1021/acs.biomac.0c01525

Kassumeh, S. A., Wertheimer, C. M., VON Studnitz, A., Hillenmayer, A., Priglinger, C., Wolf, A., et al. (2018). Poly(lactic-co-glycolic) Acid as a Slow-Release Drug-Carrying Matrix for Methotrexate Coated onto Intraocular Lenses to Conquer Posterior Capsule Opacification. *Curr. Eye Res.* 43, 702–708. doi:10.1080/02713683.2018.1437455

Katayama, Y., Kobayakawa, S., Yanagawa, H., and Tochikubo, T. (2007). The Relationship between the Adhesion Characteristics of Acrylic Intraocular Lens Materials and Posterior Capsule Opacification. *Ophthalmic Res.* 39, 276–281. doi:10.1159/000108121

Kessel, L., Andresen, J., Tendal, B., Erngaard, D., Flesner, P., and Hjortdal, J. (2016). Toric Intraocular Lenses in the Correction of Astigmatism during Cataract Surgery. *Ophthalmology* 123, 275–286. doi:10.1016/j.ophtha.2015.10.002

Kessler, J. (1964). Experiments in Refilling the Lens. *Archives Ophthalmol.* 71, 412–417. doi:10.1001/archopht.1964.00970010428021

Kim, H.-C., Kreiling, S., Greiner, A., and Hampp, N. (2003). Two-photon-induced Cycloreversion Reaction of Coumarin Photodimers. *Chem. Phys. Lett.* 372, 899–903. doi:10.1016/s0009-2614(03)00535-9

Kirchhof, S., Goepferich, A. M., and Brandl, F. P. (2015). Hydrogels in Ophthalmic Applications. *Eur. J. Pharm. Biopharm.* 95, 227–238. doi:10.1016/j.ejpb.2015.05.016

Kohnen, T., and Klaproth, O. K. (2010). Intraokularlinsen für die mikroinzisionale Kataraktchirurgie. *Ophthalmologe* 107, 127–135. doi:10.1007/s00347-009-1978-1

Koopmans, S. A., Terwee, T., Barkhof, J., Haitjema, H. J., and Kooijman, A. C. (2003). Polymer Refilling of Presbyopic Human Lenses *In Vitro* Restores the Ability to Undergo Accommodative Changes. *Invest. Ophthalmol. Vis. Sci.* 44, 250–257. doi:10.1167/iovs.02-0256

Krall, E. M., Arlt, E. M., Jell, G., Strohmaier, C., Bachernegg, A., Emesz, M., et al. (2014). Intraindividual Aqueous Flare Comparison after Implantation of Hydrophobic Intraocular Lenses with or without a Heparin-Coated Surface. *J. Cataract. Refract Surg.* 40, 1363–1370. doi:10.1016/j.jcrs.2013.11.043

Larsson, R., Selen, G., Bjorklund, H., and Fagerholm, P. (1989). Intraocular PMMA Lenses Modified with Surface-Immobilized Heparin: Evaluation of Biocompatibility *In Vitro* and *In Vivo*. *Biomaterials* 10, 511–516. doi:10.1016/0142-9612(89)90055-0

Lee, H., Oh, H. J., Yoon, K. C., Tae, G., and Kim, Y. H. (2014). Fast *In Situ* Enzymatic Gelation of PPO-PEO Block Copolymer for Injectable Intraocular Lens *In Vivo*. *J. Biomater. Appl.* 28, 1247–1263. doi:10.1177/0885328213505247

Li, S. S., Misra, S. L., Wallace, H. B., and Mckelvie, J. (2018). Effect of Phacoemulsification Incision Size on Incision Repair and Remodeling: Optical Coherence Tomography Assessment. *J. Cataract. Refract Surg.* 44, 1336–1343. doi:10.1016/j.jcrs.2018.07.025

Liang, D., Liang, D. T., and Li, P. (2019). Fabrication and Analyses of Bionic Intraocular Lens with Meniscus Polymer Layer and Porous Structure. *Opt. Commun.* 430, 204–209. doi:10.1016/j.optcom.2018.08.050

Liang, D., Wang, X.-Y., DU, J.-W., and Xiang, K. (2015). Bionic Intraocular Lens with Variable Focus and Integrated Structure. *Opt. Eng.* 54, 105106. doi:10.1117/1.oe.54.10.105106

Lin, L., Lin, Q., Li, J., Han, Y., Chang, P., Lu, F., et al. (2019). ROCK Inhibitor Modified Intraocular Lens as an Approach for Inhibiting the Proliferation and Migration of Lens Epithelial Cells and Posterior Capsule Opacification. *Biomater. Sci.* 7, 4208–4217. doi:10.1039/c9bm00787c

Lin, L., Wang, Y., Huang, X.-D., Xu, Z.-K., and Yao, K. (2010). Modification of Hydrophobic Acrylic Intraocular Lens with Poly(ethylene Glycol) by Atmospheric Pressure Glow Discharge: A Facile Approach. *Appl. Surf. Sci.* 256, 7354–7364. doi:10.1016/j.apsusc.2010.05.068

Lin, Q. K., Xu, X., Wang, Y., Wang, B., and Chen, H. (2017b). *Antiadhesive and Antibacterial Polysaccharide Multilayer as IOL Coating for Prevention of Postoperative Infectious Endophthalmitis*. Taylor & Francis.

Lin, Q., Tang, J., Han, Y., Xu, X., Hao, X., and Chen, H. (2017a). Hydrophilic Modification of Intraocular Lens via Surface Initiated Reversible Addition-Fragmentation Chain Transfer Polymerization for Reduced Posterior Capsular Opacification. *Colloids Surfaces B Biointerfaces* 151, 271–279. doi:10.1016/j.colsurfb.2016.12.028

Lin, Q., Xu, X., Wang, B., Shen, C., Tang, J., Han, Y., et al. (2015). *Hydrated Polysaccharide Multilayer as an Intraocular Lens Surface Coating for Biocompatibility Improvements*. London, United Kingdom: Royal Society of Chemistry.

Liu, S., Zhao, X., Tang, J., Han, Y., and Lin, Q. (2021). Drug-Eluting Hydrophilic Coating Modification of Intraocular Lens via Facile Dopamine Self-Polymerization for Posterior Capsular Opacification Prevention. *ACS Biomater. Sci. Eng.* 7, 1065–1073. doi:10.1021/acsbiomaterials.0c01705

Liu, Y.-C., Wong, T. T., and Mehta, J. S. (2013). Intraocular Lens as a Drug Delivery Reservoir. *Curr. Opin. Ophthalmol.* 24, 53–59. doi:10.1097/icu.0b013e32835a93fc

Loureiro, J. A., and Pereira, M. C. (2020). *PLGA Based Drug Carrier and Pharmaceutical Applications: The Most Recent Advances*. Basel, Switzerland: Multidisciplinary Digital Publishing Institute.

Lu, D., Han, Y., Liu, D., Chen, S., Qie, J., Qu, J., et al. (2022). Centrifugally Concentric Ring-Patterned Drug-Loaded Polymeric Coating as an Intraocular Lens Surface Modification for Efficient Prevention of Posterior Capsular Opacification. *Acta Biomater.* 138, 327–341. doi:10.1016/j.actbio.2021.11.018

Lundström, M., Dickman, M., Henry, Y., Manning, S., Rosen, P., Tassignon, M.-J., et al. (2018). Risk Factors for Refractive Error after Cataract Surgery: Analysis of 282 811 Cataract Extractions Reported to the European Registry of Quality Outcomes for Cataract and Refractive Surgery. *J. Cataract. Refract Surg.* 44, 447–452. doi:10.1016/j.jcrs.2018.01.031

Ma, L., Li, K., Xia, J., Chen, C., Liu, Y., Lang, S., et al. (2022). Commercial Soft Contact Lenses Engineered with Zwitterionic Silver Nanoparticles for Effectively Treating Microbial Keratitis. *J. Colloid Interface Sci.* 610, 923–933. doi:10.1016/j.jcis.2021.11.145

Maddula, S., Werner, L., Ness, P. J., Davis, D., Zaugg, B., Stringham, J., et al. (2011). Pathology of 157 Human Cadaver Eyes with Round-Edged or Modern Square-Edged Silicone Intraocular Lenses: Analyses of Capsule Bag Opacification. *J. Cataract. Refract Surg.* 37, 740–748. doi:10.1016/j.jcrs.2010.10.058

Manju, S., and Kunnatheeri, S. (2010). Layer-by-Layer Modification of Poly (Methyl Methacrylate) Intra Ocular Lens: Drug Delivery Applications. *Pharm. Dev. Technol.* 15, 379–385. doi:10.3109/10837450903262025

Mao, Y., Yu, S., Kang, Y., Zhang, D., Wu, S., Zhang, J., et al. (2021). CuInS/ZnS Quantum Dots Modified Intraocular Lens for Photothermal Therapy of Posterior Capsule Opacification. *Exp. Eye Res.* 202, 108282. doi:10.1016/j.exer.2020.108282

Miyata, A., and Yaguchi, S. (2004). Equilibrium Water Content and Glistenings in Acrylic Intraocular Lenses. *J. Cataract. Refract Surg.* 30, 1768–1772. doi:10.1016/j.jcrs.2003.12.038

Narasimhan, V., Siddique, R. H., Lee, J. O., Kumar, S., Ndjamen, B., DU, J., et al. (2018). Multifunctional Biophotonic Nanostructures Inspired by the Longtail Glasswing Butterfly for Medical Devices. *Nat. Nanotech* 13, 512–519. doi:10.1038/s41565-018-0111-5

Nibourg, L. M., Gelens, E., Kuijer, R., Hooymans, J. M. M., VAN Kooten, T. G., and Koopmans, S. A. (2015). Prevention of Posterior Capsular Opacification. *Exp. Eye Res.* 136, 100–115. doi:10.1016/j.exer.2015.03.011

Niu, G., Song, L., Zhang, H., Cui, X., Kashima, M., Yang, Z., et al. (2010). Application of Thiol-ene Photopolymerization for Injectable Intraocular Lenses: A Preliminary Study. *Polym. Eng. Sci.* 50, 174–182. doi:10.1002/pen.21465

Olson, R. J., Mamalis, N., Werner, L., and Apple, D. J. (2003). Cataract Treatment in the Beginning of the 21st Century. *Am. J. Ophthalmol.* 136, 146–154. doi:10.1016/s0002-9394(03)00226-5

Ongkasin, K., Masmoudi, Y., Wertheimer, C. M., Hillenmayer, A., Eibl-Lindner, K. H., and Badens, E. (2020). Supercritical Fluid Technology for the Development of Innovative Ophthalmic Medical Devices: Drug Loaded Intraocular Lenses to Mitigate Posterior Capsule Opacification. *Eur. J. Pharm. Biopharm.* 149, 248–256. doi:10.1016/j.ejpb.2020.02.011

Ozyol, P., Ozyol, E., and Karel, F. (2017). Biocompatibility of Intraocular Lenses. *Turk J. Ophthalmol.* 47, 221–225. doi:10.4274/tjo.10437

Pepose, J. S., Burke, J. S., and Qazi, M. A. (2017). Accommodating Intraocular Lenses. *Asia-Pacific J. Ophthalmol.* 6, 350–357. doi:10.1097/ICU.0000000000000323

Pimenta, A. F. R., Vieira, A. P., Colaco, R., Saramago, B., Gil, M. H., Coimbra, P., et al. (2017). Controlled Release of Moxifloxacin from Intraocular Lenses Modified by Ar Plasma-Assisted Grafting with AMPS or SBMA: An *In Vitro* Study. *Colloids Surf. B Biointerfaces* 156, 95–103. doi:10.1016/j.colsurfb.2017.04.060

Qie, J., Wen, S., Han, Y., Liu, S., Shen, L., Chen, H., et al. (2022). A Polydopamine-Based Photodynamic Coating on the Intraocular Lens Surface for Safer Posterior Capsule Opacification Conquering. *Biomater. Sci.* 10, 2188–2197. doi:10.1039/d2bm00038e

Qin, C., Liu, S., Wen, S., Han, Y., Chen, S., Qie, J., et al. (2021). Enhanced PCO Prevention of Drug Eluting IOLs via Endocytosis and Autophagy Effects of a PAMAM Dendrimer. *J. Mater Chem. B* 9, 793–800. doi:10.1039/d0tb02530e

Rampat, R., and Gatinel, D. (2021). Multifocal and Extended Depth-Of-Focus Intraocular Lenses in 2020. *Ophthalmology* 128, e164–e185. doi:10.1016/j.ophtha.2020.09.026

Rao, A., Padhy, D., Das, G., and Sarangi, S. (2018). Viscoless Manual Small Incision Cataract Surgery with Trabeculectomy. *Semin. Ophthalmol.* 33, 552–559. doi:10.1080/08820538.2017.1339092

Ridley, H. (1952). Intra-ocular Acrylic Lenses; a Recent Development in the Surgery of Cataract. *Br. J. Ophthalmol.* 36, 113–122. doi:10.1136/bjo.36.3.113

Ridley, H. (1976). The Origin and Objectives of Intraocular Lenticular Implants. *Trans. Sect. Ophthalmol. Am. Acad. Ophthalmol. Otolaryngol.* 81, OP65–6.

Riehle, N., Thude, S., GöTZ, T., Kandelbauer, A., Thanos, S., Tovar, G. E., et al. (2018). Influence of PDMS Molecular Weight on Transparency and Mechanical Properties of Soft Polysiloxane-Urea-Elastomers for Intraocular Lens Application. *Eur. Polym. J.* 101, 190–201. doi:10.1016/j.eurpolymj.2018.02.029

Roesel, M., Heinz, C., Heimes, B., Koch, J. M., and Heiligenhaus, A. (2008). Uveal and Capsular Biocompatibility of Two Foldable Acrylic Intraocular Lenses in Patients with Endogenous Uveitis-Aa Prospective Randomized Study. *Graefes Arch. Clin. Exp. Ophthalmol.* 246, 1609–1615. doi:10.1007/s00417-008-0886-4

Ronbeck, M., and Kugelberg, M. (2014). Posterior Capsule Opacification with 3 Intraocular Lenses: 12-year Prospective Study. *J. Cataract. Refract Surg.* 40, 70–76. doi:10.1016/j.jcrs.2013.07.039

Schraub, M., and Hampp, N. (2011). Smart Polymers Containing Substituted Coumarin Side Groups Enable Photo-Induced Tuning of Focal Length of Intraocular Lenses. *Ophthalmic Technol. XXI* 7885, 78851Z. doi:10.1117/12.873814

Schuster, A. K., Tesarz, J., and Vossmerbaeumer, U. (2013). The Impact on Vision of Aspheric to Spherical Monofocal Intraocular Lenses in Cataract Surgery: a

Systematic Review with Meta-Analysis. *Ophthalmology* 120, 2166–2175. doi:10.1016/j.ophtha.2013.04.011

Seward, H. C. (1997). Folding Intraocular Lenses: Materials and Methods. *Br. J. Ophthalmol.* 81, 340–341. doi:10.1136/bjo.81.5.340

Shiblee, M. N. I., Ahmed, K., Khosla, A., Kawakami, M., and Furukawa, H. (2018). 3D Printing of Shape Memory Hydrogels with Tunable Mechanical Properties. *Soft Matter* 14, 7809–7817. doi:10.1039/c8sm01156g

Shin, M. K., Ji, Y. W., Moon, C. E., Lee, H., Kang, B., Jinn, W. S., et al. (2020). Matrix Metalloproteinase 9-activatable Peptide-Conjugated Hydrogel-Based Fluorogenic Intraocular-Lens Sensor. *Biosens. Bioelectron.* 162, 112254. doi:10.1016/j.bios.2020.112254

Shukla, A., Fuller, R. C., and Hammond, P. T. (2011). Design of Multi-Drug Release Coatings Targeting Infection and Inflammation. *J. Control Release* 155, 159–166. doi:10.1016/j.jconrel.2011.06.011

Song, L., Hu, W., Wang, G., Zhang, H., Niu, G., Cao, H., et al. (2011). Synthesis and Characterization of Shape Memory (Meth)Acrylate Co-polymers and Their Cytocompatibility *In Vitro*. *J. Biomater. Sci. Polym. Ed.* 22, 1–17. doi:10.1163/092050609x12567412849136

Steinmetz, J. D., Bourne, R. R., Briant, P. S., Flaxman, S. R., Taylor, H. R., Jonas, J. B., et al. (2021). Causes of Blindness and Vision Impairment in 2020 and Trends over 30 years, and Prevalence of Avoidable Blindness in Relation to VISION 2020: the Right to Sight: an Analysis for the Global Burden of Disease Study. *Lancet Glob. Health* 9, e144–e160.

Sun, C. B., Teng, W. Q., Cui, J. T., Huang, X. J., and Yao, K. (2014). The Effect of Anti-TGF-beta2 Antibody Functionalized Intraocular Lens on Lens Epithelial Cell Migration and Epithelial-Mesenchymal Transition. *Colloids Surf. B Biointerfaces* 113, 33–42. doi:10.1016/j.colsurfb.2013.08.024

Sun, L., Wang, T. X., Chen, H. M., Salvekar, A. V., Naveen, B. S., Xu, Q., et al. (2019). A Brief Review of the Shape Memory Phenomena in Polymers and Their Typical Sensor Applications. *Polym. (Basel)* 11, 1049. doi:10.3390/polym11061049

Tan, X., Zhan, J., Zhu, Y., Cao, J., Wang, L., Liu, S., et al. (2017). Improvement of Uveal and Capsular Biocompatibility of Hydrophobic Acrylic Intraocular Lens by Surface Grafting with 2-Methacryloyloxyethyl Phosphorylcholine-Methacrylic Acid Copolymer. *Sci. Rep.* 7, 40462. doi:10.1038/srep40462

Tang, J., Liu, S., Han, Y., Wang, R., Xia, J., Chen, H., et al. (2021). Surface Modification of Intraocular Lenses via Photodynamic Coating for Safe and Effective PCO Prevention. *J. Mater Chem. B* 9, 1546–1556. doi:10.1039/d0tb02802a

Tetz, M., and Jorgensen, M. R. (2015). New Hydrophobic IOL Materials and Understanding the Science of Glistenings. *Curr. Eye Res.* 40, 969–981. doi:10.3109/02713683.2014.978476

Tetz, M., Werner, L., Schwahn-Bendig, S., and Batlle, J. (2009). *Prospective Clinical Study to Quantify Glistenings in New Hydrophobic Acrylic IOLASCRS Symposium on Cataract*. San Francisco, California, USA: IOL and Refractive Surgery.

Titiyal, J. S., Kaur, M., Shaikh, F., and Rawat, J. (2020). Resurgence of Inflammatory Giant-Cell Deposits in Modern Surface-Modified Intraocular Lenses. *J. Cataract. Refract Surg.* 46, 149–151. doi:10.1097/j.jcrs.0000000000000003

Toffoletto, N., Saramago, B., and Serro, A. P. (2020). Therapeutic Ophthalmic Lenses: A Review. *Pharmaceutics* 13. doi:10.3390/pharmaceutics13010036

Topete, A., Barahona, I., Santos, L. F., Pinto, C. A., Saraiva, J. A., Paula Serro, A., et al. (2021a). The Effects of Addition of Functional Monomers and Molecular Imprinting on Dual Drug Release from Intraocular Lens Material. *Int. J. Pharm.* 600, 120513. doi:10.1016/j.ijpharm.2021.120513

Topete, A., Saramago, B., and Serro, A. P. (2021b). Intraocular Lenses as Drug Delivery Devices. *Int. J. Pharm.* 602, 120613. doi:10.1016/j.ijpharm.2021.120613

Topete, A., Tang, J., Ding, X., Filipe, H. P., Saraiva, J. A., Serro, A. P., et al. (2020). Dual Drug Delivery from Hydrophobic and Hydrophilic Intraocular Lenses: In-Vitro and In-Vivo Studies. *J. Control. Release* 326, 245–255. doi:10.1016/j.jconrel.2020.07.020

Trager, J., Heinzer, J., Kim, H. C., and Hampp, N. (2008). Polymers for *In Vivo* Tuning of Refractive Properties in Intraocular Lenses. *Macromol. Biosci.* 8, 177–183. doi:10.1002/mabi.200700155

Trivedi, R. H., Werner, L., Apple, D. J., Pandey, S. K., and Izak, A. M. (2002). Post Cataract-Intraocular Lens (IOL) Surgery Opacification. *Eye (Lond)* 16, 217–241. doi:10.1038/sj.eye.6700066

Vieira, A. P., Pimenta, A. F. R., Silva, D., Gil, M. H., Alves, P., Coimbra, P., et al. (2017). Surface Modification of an Intraocular Lens Material by Plasma-Assisted Grafting with 2-hydroxyethyl Methacrylate (HEMA), for Controlled Release of Moxifloxacin. *Eur. J. Pharm. Biopharm.* 120, 52–62. doi:10.1016/j.ejpb.2017.08.006

Villegas, E. A., Alcon, E., Rubio, E., Marin, J. M., and Artal, P. (2014). Refractive Accuracy with Light-Adjustable Intraocular Lenses. *J. Cataract. Refract Surg.* 40, 1075–1084 e2. doi:10.1016/j.jcrs.2013.10.046

Wang, B., Lin, Q., Shen, C., Tang, J., Han, Y., and Chen, H. (2014). Hydrophobic Modification of Polymethyl Methacrylate as Intraocular Lenses Material to Improve the Cytocompatibility. *J. Colloid Interface Sci.* 431, 1–7. doi:10.1016/j.jcis.2014.05.056

Wang, B., Ye, Z., Tang, Y., Han, Y., Lin, Q., Liu, H., et al. (2017). Fabrication of Nonfouling, Bactericidal, and Bacteria Corpse Release Multifunctional Surface through Surface-Initiated RAFT Polymerization. *Int. J. Nanomedicine* 12, 111–125. doi:10.2147/IJN.S107472

Wang, G., Cao, L., Li, N., Peng, X., Tang, H., Wan, R., et al. (2013). *In Vivo* implantation of Hydrophobic Acrylic Intraocular Lenses with Surface Modification. *Eye Sci.* 28, 176–179.

Wang, J. J., and Liu, F. (2011). Photoinduced Graft Polymerization of 2-methacryloyloxyethyl Phosphorylcholine on Silicone Hydrogels for Reducing Protein Adsorption. *J. Mater Sci. Mater Med.* 22, 2651–2657. doi:10.1007/s10856-011-4452-y

Wang, K., Jiang, L., Zhong, Y., Zhang, Y., Yin, Q., Li, S., et al. (2021a). Ferrostatin-1-loaded Liposome for Treatment of Corneal Alkali Burn via Targeting Ferroptosis. *Bioeng. Transl. Med.*, e10276. doi:10.1002/btm2.10276

Wang, R., Xia, J., Tang, J., Liu, D., Zhu, S., Wen, S., et al. (2021b). Surface Modification of Intraocular Lens with Hydrophilic Poly(Sulfobetaine Methacrylate) Brush for Posterior Capsular Opacification Prevention. *J. Ocul. Pharmacol. Ther.* 37, 172–180. doi:10.1089/jop.2020.0134

Wang, T., Ran, R., Ma, Y., and Zhang, M. (2021c). Polymeric Hydrogel as a Vitreous Substitute: Current Research, Challenges, and Future Directions. *Biomed. Mater.* 16, 4. doi:10.1088/1748-605x/ac058e

Werner, L. (2008). Biocompatibility of Intraocular Lens Materials. *Curr. Opin. Ophthalmol.* 19, 41–49. doi:10.1097/icu.0b013e3282f20132

Werner, L., Hunter, B., Stevens, S., Chew, J. J., and Mamalis, N. (2006). Role of Silicon Contamination on Calcification of Hydrophilic Acrylic Intraocular Lenses. *Am. J. Ophthalmol.* 141, 35–43. doi:10.1016/j.ajo.2005.08.045

Werner, L. (2021). Intraocular Lenses: Overview of Designs, Materials, and Pathophysiologic Features. *Ophthalmology* 128, e74–e93. doi:10.1016/j.ophtha.2020.06.055

Xia, J., Han, Y., Shen, L., Wang, R., Wen, S., Zhu, S., et al. (2022). Photo-responsive Intraocular Lens with on Demand Drug Release for Posterior Capsule Opacification Prevention and Improved Biosafety. *Chem. Eng. J.* 430, 132716. doi:10.1016/j.cej.2021.132716

Xia, J., Lu, D., Han, Y., Wang, J., Hong, Y., Zhao, P., et al. (2021). Facile Multifunctional IOL Surface Modification via Poly (PEGMA-Co-GMA) Grafting for Posterior Capsular Opacification Inhibition. *RSC Adv.* 11, 9840–9848. doi:10.1039/D1RA00201E

Xiang, Y., Jin, R., Zhang, Y., Li, K., Liu, G., Song, X., et al. (2021). Foldable Glistening-free Acrylic Intraocular Lens Biomaterials with Dual-Side Heterogeneous Surface Modification for Postoperative Endophthalmitis and Posterior Capsule Opacification Prophylaxis. *Biomacromolecules* 22, 3510–3521. doi:10.1021/acs.biomac.1c00582

Xiao, A., Dhand, C., Leung, C. M., Beuerman, R. W., Ramakrishna, S., and Lakshminarayanan, R. (2018). Strategies to Design Antimicrobial Contact Lenses and Contact Lens Cases. *J. Mater Chem. B* 6, 2171–2186. doi:10.1039/c7tb03136j

Xu, J. W., Li, H. N., Hu, D. F., Zhang, X. B., Wang, W., Ji, J., et al. (2021). Intraocular Lens with Mussel-Inspired Coating for Preventing Posterior Capsule Opacification via Photothermal Effect. *ACS Appl. Bio Mater* 4, 3579–3586. doi:10.1021/acsabm.1c00089

Xu, J., Zhu, W., Jiang, L., Xu, J., Zhang, Y., and Cui, Y. (2015). Carbazole-grafted Silicone Hydrogel with a High Refractive Index for Intraocular Lens. *RSC Adv.* 5, 72736–72744. doi:10.1039/c5ra10614a

Xu, X., Tang, J.-M., Han, Y.-M., Wang, W., Chen, H., and Lin, Q.-K. (2016). *Surface PEGylation of Intraocular Lens for PCO Prevention: An* in Vivo *Evaluation*. London, England: SAGE Publications Sage UK.

Yang, C., Huang, X., Li, X., Yang, C., Zhang, T., Wu, Q., et al. (2021). Wearable and Implantable Intraocular Pressure Biosensors: Recent Progress and Future Prospects. *Adv. Sci. (Weinh)* 8, 2002971. doi:10.1002/advs.202002971

Yang, D., Afroosheh, S., Lee, J. O., Cho, H., Kumar, S., Siddique, R. H., et al. (2018). Glucose Sensing Using Surface-Enhanced Raman-Mode Constraining. *Anal. Chem.* 90, 14269–14278. doi:10.1021/acs.analchem.8b03420

Zhang, X., Lai, K., Li, S., Wang, J., Li, J., Wang, W., et al. (2022). Drug-eluting Intraocular Lens with Sustained Bromfenac Release for Conquering Posterior Capsular Opacification. *Bioact. Mater* 9, 343–357. doi:10.1016/j.bioactmat.2021.07.015

Zhang, Y., Zhu, X., He, W., Jiang, Y., and Lu, Y. (2017). Efficacy of Cataract Surgery in Patients with Uveitis: A STROBE-Compliant Article. *Med. Baltim.* 96, e7353. doi:10.1097/md.0000000000007353

Zhang, Z., Huang, W., Lei, M., He, Y., Yan, M., Zhang, X., et al. (2016). Laser-triggered Intraocular Implant to Induce Photodynamic Therapy for Posterior Capsule Opacification Prevention. *Int. J. Pharm.* 498, 1–11. doi:10.1016/j.ijpharm.2015.10.006

Zheng, Z., Wang, Y., Jiao, Y., and Zhai, Z. (2016). Biological Performance of Functionalized Biomedical Polymers for Potential Applications as Intraocular Lens. *J. Biomed. Mater Res. A* 104, 1961–1967. doi:10.1002/jbm.a.35727

Zhu, S., Huang, H., Liu, D., Wen, S., Shen, L., and Lin, Q. (2022). Augmented Cellular Uptake and Homologous Targeting of Exosome-Based Drug Loaded IOL for Posterior Capsular Opacification Prevention and Biosafety Improvement. *Bioact. Mater* 15, 469–481. doi:10.1016/j.bioactmat.2022.02.019

Conflict of Interest: The authors declare that the research was conducted in the absence of any commercial or financial relationships that could be construed as a potential conflict of interest.

frontiers | Frontiers in Bioengineering and Biotechnology

ORIGINAL RESEARCH
published: 22 June 2022
doi: 10.3389/fbioe.2022.927248

Graphene Substrates Promote the Differentiation of Inner Ear Lgr5+ Progenitor Cells Into Hair Cells

Xiaoqiong Ding[1,2†], Yangnan Hu[3†], Hong Cheng[3†], Xiaoli Zhang[4], Ling Lu[4], Song Gao[4], Cheng Cheng[4], Lifen Wang[2], Xiaoyun Qian[4], Chen Zhang[5], Renjie Chai[2,3,4,5,6,7,8‡], Xia Gao[1*‡] and Zhichun Huang[2*‡]*

[1]Department of Otorhinolaryngology-Head and Neck Surgery, Nanjing Drum Tower Hospital, Drum Tower Clinical College of Nanjing Medical University, Nanjing, China, [2]Department of Otorhinolaryngology-Head and Neck Surgery, Zhongda Hospital, Southeast University, Nanjing, China, [3]State Key Laboratory of Bioelectronics, Jiangsu Province High-Tech Key Laboratory for Bio-Medical Research, School of Life Sciences and Technology, Advanced Institute for Life and Health, Southeast University, Nanjing, China, [4]Department of Otorhinolaryngology-Head and Neck Surgery, Affiliated Drum Tower Hospital of Nanjing University Medical School, Nanjing, China, [5]Beijing Key Laboratory of Neural Regeneration and Repair, Capital Medical University, Beijing, China, [6]Department of Otolaryngology Head and Neck Surgery, Sichuan Provincial People's Hospital, University of Electronic Science and Technology of China, Chengdu, China, [7]Co-Innovation Center of Neuroregeneration, Nantong University, Nantong, China, [8]Institute for Stem Cell and Regeneration, Chinese Academy of Science, Beijing, China

The ideal treatment for sensory hearing loss is to regenerate inner ear hair cells (HCs) through stem cell therapy, thereby restoring the function and structure of the cochlea. Previous studies have found that Lgr5+ supporting cells (SCs) in the inner ear can regenerate HCs, thus being considered inner ear progenitor cells. In addition to traditional biochemical factors, physical factors such as electrical conductivity also play a crucial role in the regulation of stem cell proliferation and differentiation. In this study, the graphene substrates were used to culture Lgr5+ progenitor cells and investigated their regulatory effects on cells. It was demonstrated that the graphene substrates displayed great cytocompatibility for Lgr5+ progenitors and promoted their sphere-forming ability. Moreover, more Myosin7a+ cells were found on the graphene substrates compared with tissue culture polystyrene (TCPS). These results suggest that graphene is an efficient interface that can promote the differentiation of Lgr5+ progenitors into HCs, which is great significance for its future application in combination with Lgr5+ cells to regenerate HCs in the inner ear.

Keywords: graphene, sensorineural hearing loss, hair cell regeneration, proliferation, differentiation

OPEN ACCESS

Edited by:
Mingqiang Li,
Third Affiliated Hospital of Sun Yat-sen University, China

Reviewed by:
Wenguo Cui,
Shanghai Jiao Tong University, China
Xiaowei Yang,
Shanghai Jiao Tong University, China

****Correspondence:***
Renjie Chai
renjiec@seu.edu.cn
Xia Gao
xiagaogao@hotmail.com
Zhichun Huang
huang193618@sohu.com

[†]These authors share first authorship

[‡]These authors have contributed equally to this work

Specialty section:
This article was submitted to Biomaterials, a section of the journal Frontiers in Bioengineering and Biotechnology

Received: *24 April 2022*
Accepted: *03 June 2022*
Published: *22 June 2022*

Citation:
Ding X, Hu Y, Cheng H, Zhang X, Lu L, Gao S, Cheng C, Wang L, Qian X, Zhang C, Chai R, Gao X and Huang Z (2022) Graphene Substrates Promote the Differentiation of Inner Ear Lgr5+ Progenitor Cells Into Hair Cells. Front. Bioeng. Biotechnol. 10:927248. doi: 10.3389/fbioe.2022.927248

INTRODUCTION

Inner ear sensory hair cells (HCs) mainly function for transduction of mechanical stimuli into electrical signals and are mechanoreceptors for sound recognition (Li et al., 2018; Liu et al., 2019; Zhang et al., 2019). Aging, ototoxic drugs, trauma, inflammation, and other factors can all contribute to hair cell damage, resulting in sensorineural hearing loss (Liu et al., 2016; Zhou et al., 2020). Sensorineural hearing loss is a common sensory disease caused by damage or loss of HCs, affecting millions of people worldwide. Supporting cells (SCs) in the auditory and vestibular systems of birds and fish have been reported to have the capability to regenerate HCs in response to the damage to HCs (Corwin and Cotanche, 1988; Balak et al., 1990; Warchol, 2011). However, studies have shown that HC damage in adult mammals is irreparable, which lead to permanent hearing loss (Rubel et al., 2013). Recently, several studies reported that Lgr5+ SCs in the inner ear can regenerate HCs and considered inner ear

progenitor cells, which bringing new possibilities for the regeneration of HCs in adult mammals (Bermingham-McDonogh and Reh, 2011; Chai et al., 2011; Chai et al., 2012; Shi et al., 2013; Bramhall et al., 2014; Waqas et al., 2016).

The most ideal treatment for sensory hearing loss is to regenerate inner ear HCs to restore the structure and function of the cochlea (Wang et al., 2015). The behaviors of cochlear of progenitor cells including proliferation and differentiation are regulated by numerous biochemical and physical factors. Investigating the regulatory strategies that promote the differentiation of cochlear progenitor cells into mature HCs is critical for HC regeneration and hearing reconstruction. Several studies have shown that some conductive materials such as graphene and MXenes can regulate the behavior of stem cells, including proliferation and differentiation (Guo et al., 2016; Farokhi et al., 2021; Yao et al., 2021; Guo et al., 2022). Lgr5+ progenitors have characteristics similar to adult stem cells. The detailed regulatory effects of these conductive materials on Lgr5+ progenitors' behavior and their potential in the treatment of sensorineural hearing loss have not been investigated.

Herein, in this work, we fabricated graphene substrates and studied their regulatory effects on the proliferation and differentiation. Graphene has been reported to significantly promote neuronal differentiation of neural stem cells (NSCs). Several studies have reported their potential for applications in the biomedical field, including drug delivery (Song et al., 2020; Sattari et al., 2021), photothermal therapy (de Melo-Diogo et al., 2019; Palmieri et al., 2020; Wang et al., 2020), and nerve regeneration (Aydin et al., 2018; Grijalvo and Díaz, 2021). Therefore, the current study focus on the effects of graphene substrate on the survival, proliferation and differentiation into HCs in Lgr5+ progenitors, which is of great significance for the combined therapy of physical stimulation and stem cell transplantation for the treatment of sensorineural hearing loss.

MATERIALS AND METHODS

Animals

Lgr5-EGFP-IRES-creERT2 mice (stock no. 008875) were purchased from The Jackson Laboratory. All animal experiments were performed in accordance with protocols that were approved by the Animal Care and Use Committee of Southeast University (Approved No. 20200402025) and the National Institute of Health's Guide for the Care and Use of Laboratory Animals. All efforts were made to minimize the number of animals used and to prevent their suffering.

Genotyping PCR

For genotyping of transgenic mice, the tail tips were first collected, and genomic DNA was obtained by adding 180 uL 50 mM NaOH and incubating at 98°C for 1 h, followed by adding 20 uL 1 M Tris-HCl (pH 7.0). The tube was then vortexed vigorously for 1 min for complete tissue dispersion. The primers used for genotyping are as follows; wild-type (R) ATA CCC CAT CCC TTT TGA GC; Lgr5: (F) CTG CTC TCT GCT CCC AGT CT; mutant (R) GAA CTT CAG GGT CAG CTT GC.

Preparation and Characterization of Graphene Substrates

The graphene substrates were purchased from Nanjing MKNANO Tech. Co., Ltd. Specifically, the graphene was prepared by chemical vapor deposition (CVD) and then transferred to the surface of coverslips to obtain a graphene substrate. For cell culture, the graphene substrates were immersed in 75% alcohol for 1 h, then washed three times with sterilized water and irradiated under ultraviolet light overnight.

The surface of graphene substrates was observed by Scanning Electron Microscope (SEM) (Zeiss, Ultra Plus). The graphene substrates were then characterized by a Raman microscopy (Renishaw inVia) and an X-ray diffractometer (XRD) (PANalytical Empyrean).

Isolation of Lgr5+ Cels by Flow Cytometry

The cochleae of Lgr5-EGFP-creERT2 mice (postnatal day 1–3, P1-3) were dissected out and collected in a tube. Subsequently, the collected cochleae were digested by trypsin (0.125%, Invitrogen) at 37°C for 8 min, followed by adding equal volume of soybean trypsin inhibitor (Worthington Biochem) to terminate the digestion. Cochleae tissue were dissociated into single cell suspensions by blunt tips (Eppendorf) and then filtered with a 40 μm cell strainer (BD Biosciences). Finally, the obtained single cells were sorted by a BD FACS Aria III (BD Biosciences) through GFP channel. Finally, the sorted cells were cultured on graphene substrates and tissue culture polystyrene (TCPS), respectively.

Sphere-Forming Assay and Differentiation Assay

The cells sorted by FAC were cultured in DMEM/F12 medium supplemented with N2 (1%, Invitrogen), B27 (2% dilution, Invitrogen), EGF (20 ng/ml, Sigma), bFGF (10 ng/ml, Sigma), and IGF-1 (50 ng/ml, Sigma), heparin sulfate (50 ng/ml, Sigma) (full medium), and ampicillin (0.1%, Beyotime). For sphere-forming assay, the sorted cells were seeded on TCPS or graphene substrates with 200 cells per well for 5 days. Subsequently, we measured the number and diameter of the formed spheres to evaluate their proliferation capacity. For differentiation assay, the sorted single cells and formed spheres were differentiated separately. The cells or spheres were cultured in a 4-well dish for 10 days, and immunofluorescence staining was then applied to analyze the differentiation of Lgr5+ cells. As described in previous reports, cell aggregation with more than 5 cells were considered a sphere or colony.

Immunostaining and Image Acquisition

After culture, the cells grown on different substrates were fixed with 4% paraformaldehyde for 1 h at room temperature and then washed with PBS containing 0.1% Triton X-100 (PBST). The cells were then blocked with PBS containing 1% BSA for 1 h at room temperature. Afterwards, the primary antibody anti-Myosin7a (Proteus Bioscience) was diluted and incubated with these cells at 4°C overnight. After that, the cells were washed with PBST and then incubated with secondary antibody along with 2-(4-

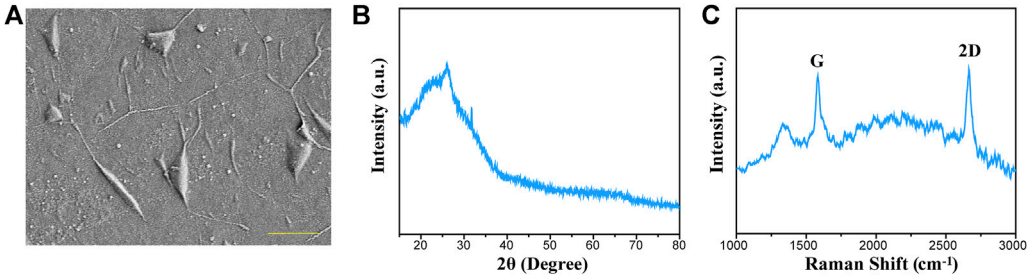

FIGURE 1 | Characterization of graphene substrates prepared by the CVD method. **(A)** Representative SEM image of the graphene substrates. **(B)** XRD spectra for graphene substrates. **(C)** Raman spectra for graphene substrates.

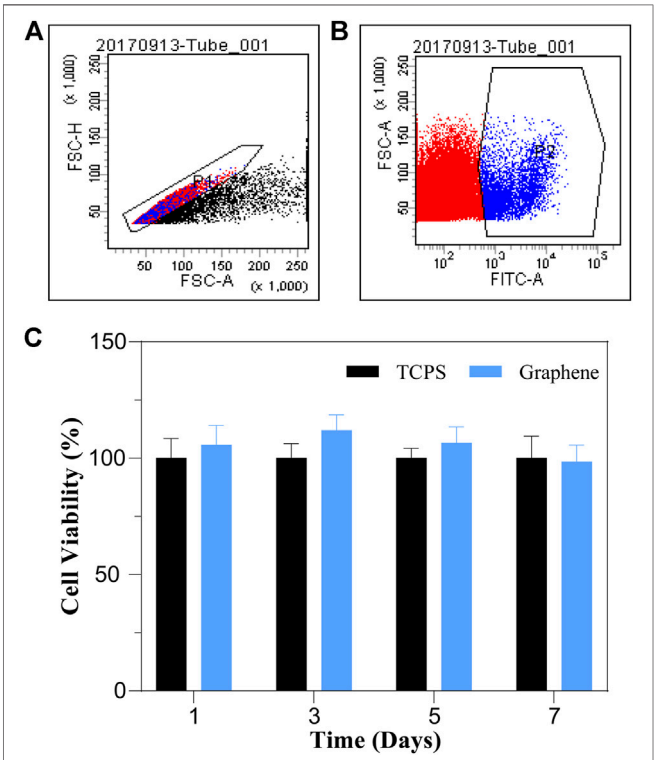

FIGURE 2 | FAC sorting plots and the effects of graphene substrates on the cell viability of Lgr5+ progenitors. **(A,B)** FAC sorting plots. **(C)** Cell viability results from CCK-8 assay.

Amidinophenyl)-6-indolecarbamidine dihydrochloride (DAPI) for 1 h at room temperature. Finally, the cells cultured on different substrates were washed and then covered with coverslips in fluorescence mounting medium (DAKO). The cells were observed and captured with a laser scanning confocal microscope (Zeiss, LSM 700).

Statistical Analysis

All data were analyzed with GraphPad Prism6 software and presented as mean ± SD. Two-tailed, unpaired Student's t-tests were used to determine statistical significance when comparing two groups, and a value of $p < 0.05$ was considered statistically significant. At least three individual experiments were conducted for all experiments.

RESULTS

Characterization of Graphene

Graphene substrates used in our work were fabricated by a CVD method and then transferred to the surface of coverslips. The morphology of the graphene substrates was observed from the SEM image (**Figure 1A**). **Figure 1B** displays the XRD pattern of graphene substrates. It was suggested that the graphene has a distinct peak at 27.5°, which can be indexed to (002) diffraction plane. The Raman spectra displayed the characteristic peaks of 2D and G bands, and the intensity ratio indicated that the graphene substrates composed of a few layers of graphene sheets (**Figure 1C**).

Graphene Substrates Have No Effects on the Viability of Lgr5+ Cells

To evaluate the cytocompatibility of graphene substrates, we isolated Lgr5+ cells from Lgr5-EGFP- CreERT2 mice by FAC sorting and cultured the sorted cells on graphene substrates and TCPS for different times. The flow cytometry plots displayed that about 5.8% of the whole cochlear cell population were Lgr5+ progenitors (**Figures 2A,B**). After culture, a CCK-8 assay was conducted to analyze the influence of graphene substrates on the viability of Lgr5+ cells (**Figure 2C**). It was suggested that cells cultured on graphene substrates for different times had similar viability to cells cultured on TCPS, indicating our prepared graphene substrates are nontoxic and cytocompatible. Therefore, we further investigated the effects of graphene substrates on the proliferation and differentiation of Lgr5+ progenitors.

Lgr5+ Progenitors Cultured on Graphene Substrates Have Higher Sphere-Forming Ability Than Those Cultured on TCPS

The capacity of self-renew is an important characteristic of stem cells and progenitor cells. Therefore, we cultured the sorted cells on graphene substrates and TCPS for 5 days to form spheres,

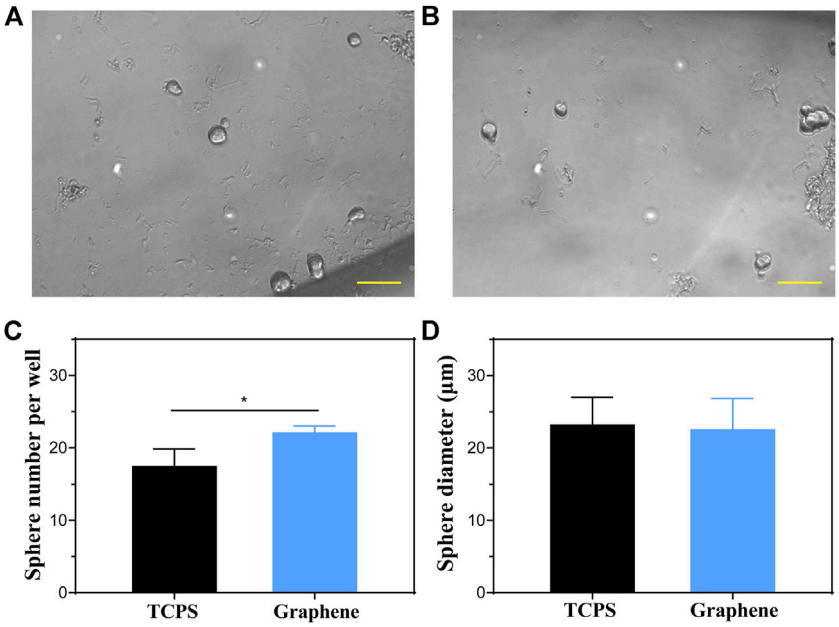

FIGURE 3 | Sphere-forming assay of Lgr5+ progenitors. **(A,B)** The spheres formed by Lgr5+ progenitors cultured on TCPS **(A)** and graphene substrates **(B)**. **(C,D)** The sphere number **(C)** and diameter **(D)** of Lgr5+ spheres cultured on different substrates. The scale bars are 50 μm in **(A,B)**.

respectively, to determine their proliferation capacity. **Figures 3A,B** showed images of spheres formed from Lgr5+ progenitors cultured on different substrates. It was suggested that the Lgr5+ progenitors cultured on graphene substrates formed more spheres than those cultured on TCPS (**Figure 3C**). However, there was no significant difference in the diameter of the formed spheres (**Figure 3D**). These results demonstrated that our prepared graphene substrates could promote the sphere-forming ability of Lgr5+ progenitors.

Lgr5+ Progenitors Cultured on Graphene Substrates Generate More HCs Compared to Those Cultured on TCPS

To investigate the HC regeneration capability of the formed spheres on different substrates, we performed differentiation assay for 10 days after 5 days of sphere-forming assay, as shown in **Figure 4A**. After differentiation, the spheres were stained with HC marker Myosin7a (**Figures 4B,C**). Subsequently, we counted the number of Myosin7a+ cells generated from each sphere and total Myosin7a+ cells per well. It was suggested that each sphere cultured on graphene generated more Myosin7a+ HCs than sphere cultured on TCPS (**Figure 4D**), and the total spheres on graphene also generated more Myosin7a+ HCs than those cultured on TCPS (**Figure 4E**).

To further explore the HC regeneration capability, we cultured the sorted Lgr5+ cells on laminin-coated graphene or TCPS substrates for 10 days of differentiation (**Figure 5A**). The cells were next stained with Myosin7a after 10 days of differentiation (**Figures 5B,C**). The results demonstrated that the cells cultured on graphene substrates formed significantly more Myosin7a+ colonies and total colonies than those cultured on TCPS (**Figure 5D**). It is worth noting that the Myosin7a+ cells inside the colony are mitotically regenerated HCs, and those outside the colony are directly differentiated HCs. The Myosin7a+ cells both inside and outside the colony were both counted. and the results suggested that the Lgr5+ progenitors cultured on graphene substrates differentiated more Myosin7a+ HCs both inside and outside the colony than those cultured on TCPS (**Figure 5E**). Overall, our findings suggest that graphene could promote the differentiation of Lgr5+ progenitors into HCs.

DISCUSSION

HCs in the mammalian cochlea mainly function for transduction of mechanical stimuli into electrical signals, thus play an important role in sound recognition. Irreversible damage or loss of HCs due to aging, ototoxic drugs, trauma, inflammation and other stress can lead to permanent hearing loss. In recent years, great progress has been made in HC regeneration, many studies have successfully induced embryonic stem cells and pluripotent stem cells to differentiate into hair cell-like cells *in vitro* (Roccio et al., 2018). Recently, several studies have reported that Lgr5+ SCs in the inner ear maintain the ability to generate HCs and SCs, and thereby considered inner ear progenitor cells. Lgr5 is a target gene of Wnt and is considered a stem cell marker in a variety of adult tissues (Barker et al., 2007; Jaks et al., 2008).

Recently, Smith-Cortinez et al. reported the long-term presence of Lgr5+ SCs in the adult mouse cochlea (Smith-

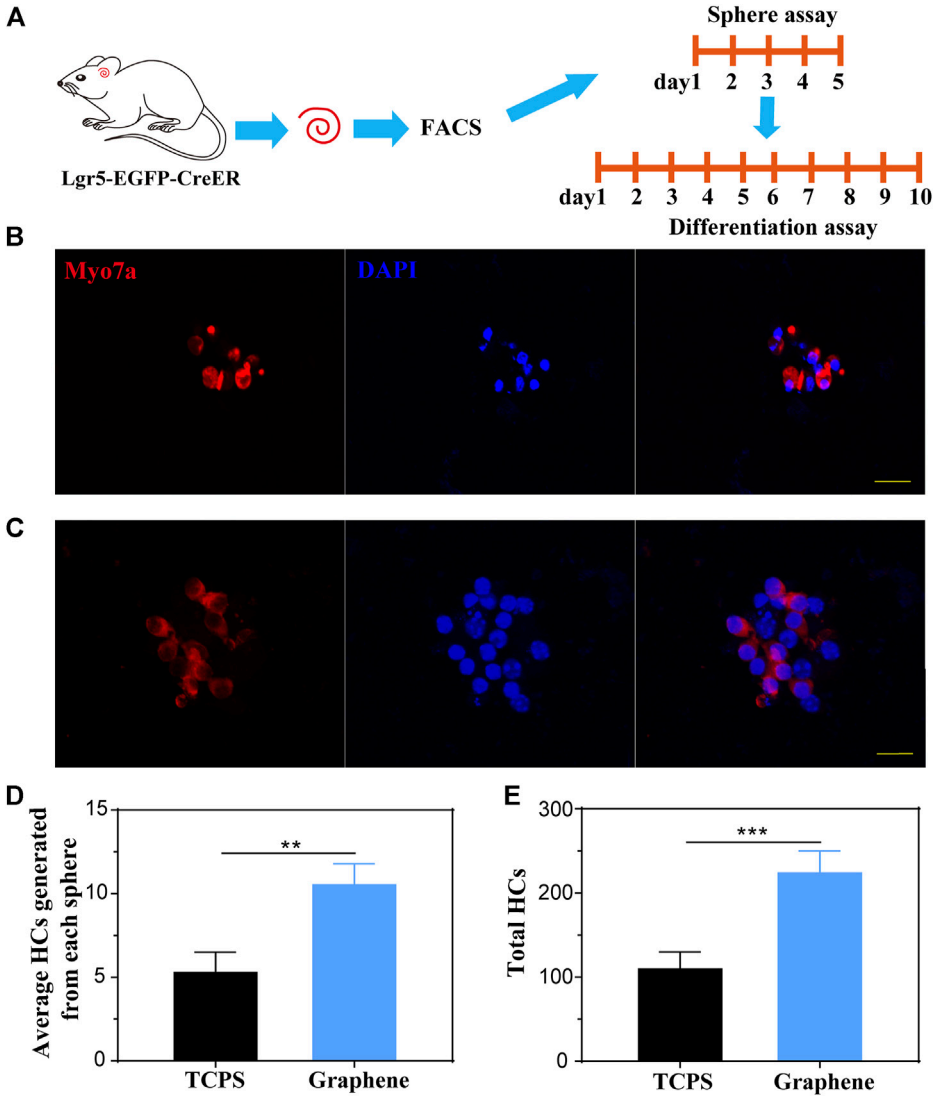

FIGURE 4 | Lgr5+ spheres cultured on graphene substrates generate more HCs compared to those on TCPS. **(A)** Lgr5+ progenitors were cultured on different substrates for 5 days of sphere assay and 10 days of differentiation assay. **(B,C)** An Lgr5+ sphere cultured on TCPS **(B)** and graphene substrates **(C)** stained with the Myosin7a (red) and DAPI (blue). **(D)** Quantification of the average number of HCs differentiated from each sphere. **(E)** Quantification of the total number of HCs differentiated from Lgr5+ progenitors per well. The scale bars are 20 μm in **(B,C)**.

Cortinez et al., 2021). These inner ear progenitor cells are able to survive in the cochlea even after severe ototoxic injury. Therefore, they have great potential in the treatment of sensorineural hearing loss caused by HC damage or loss. However, the efficiency of proliferation and regenerating HCs from Lgr5+ progenitors are low. Many studies have focused on the regulation of the proliferation and differentiation capacity of inner ear progenitor cells by different methods. With the development of tissue engineering technology, several novel therapeutic systems combining biomaterials with stem cells have been widely studied (Tong et al., 2015; Kim et al., 2018). In this work, we introduced graphene as a cell culture substrate to investigate its regulation on the behaviors of inner ear Lgr5+ progenitors, including proliferation and differentiation.

Graphene substrates have been shown to have great cytocompatibility and electrical conductivity, and have been extensively studied in the biomedical field. Various studies have suggested that graphene substrates could support cell culture and regulate the proliferation and differentiation of different types of stem cells (Park et al., 2011; Guo et al., 2016; Kenry et al., 2018). The regulation of stem cell differentiation by graphene opens a new horizon for its applications in regenerative medicine. However, its potential in the field of auditory field is remain exploring. Therefore, in this work, we investigated the *in vitro* regulation of graphene on inner ear progenitors, especially their proliferation and differentiation.

The sphere-forming assay suggested that Lgr5+ progenitors cultured on graphene substrates generated more spheres than

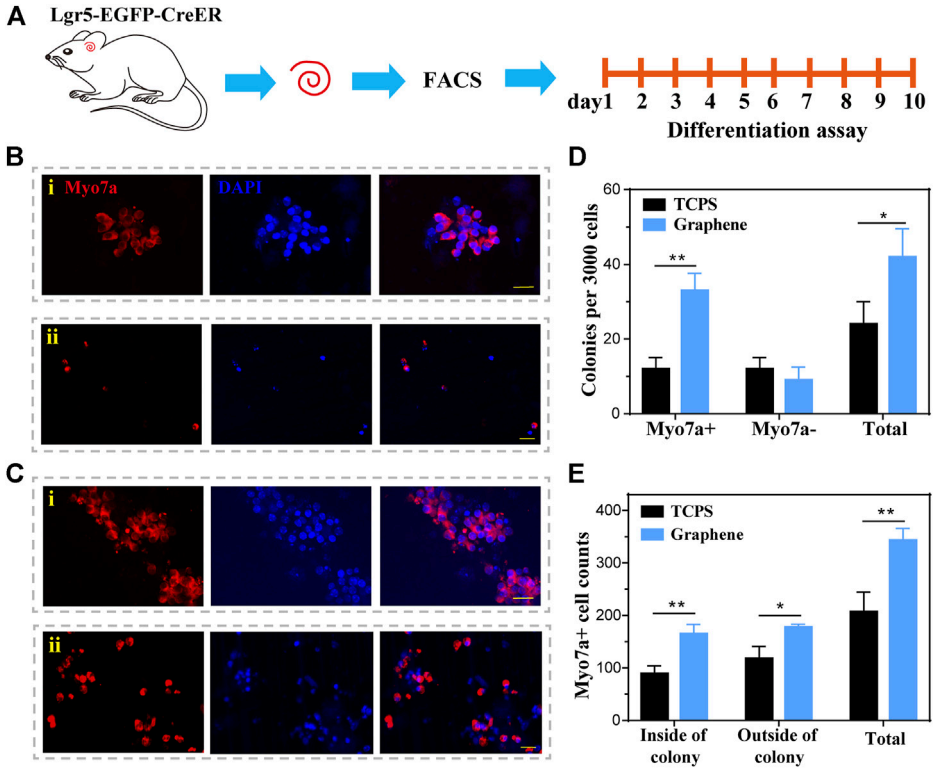

FIGURE 5 | The differentiation of Lgr5+ progenitors. **(A)** The Lgr5+ progenitors were cultured on graphene or TCPS for 10 days of differentiation. **(B)** Immunofluorescence images of Lgr5+ progenitors cultured on TCPS after 10 days of differentiation, both inside (i) and outside (ii) the colony. **(C)** Immunofluorescence images of Lgr5+ progenitors cultured on graphene substrates after 10 days of differentiation, both inside (i) and outside (ii) the colony. **(D)** The number of colonies per 3,000 cells. **(E)** Quantification of Myosin7a+ cells. The scale bars are 20 μm in **(B,C)**.

those cultured on TCPS *in vitro*. However, there was no statistical difference in the diameter of the formed spheres. The results indicate that graphene can promote the sphere-forming ability of Lgr5+ progenitors. The results of differentiation assay suggested that Lgr5+ progenitors could differentiate into Myosin7a+ cells, and the number of Myosin7a+ cells on graphene was larger than TCPS, indicating that our prepared graphene substrates could promote the generation of HCs from Lgr5+ progenitors. Recent studies have found that the regeneration of HCs from inner ear progenitors were regulated by several genes, including Pou4f3, Atoh1, Cdh23, Jag2, Skp2 (Waqas et al., 2016). We speculate that graphene substrates may promote the differentiation of Lgr5+ progenitors into HCs by regulating the expression of related genes. We will carry out in-depth research on the underlying mechanism in the future. What's important, we will develop more graphene-based 3D scaffolds with superior properties and combine them with stem cell transplantation for the regeneration of inner ear HCs.

In summary, we prepared graphene substrates by depositing graphene onto coverslips. We found that the graphene substrates promoted the sphere-forming and HC regeneration capabilities of cochlea Lgr5+ progenitors. The results suggest that graphene is an efficient interface that can promote the differentiation of Lgr5+ progenitor cells into HCs, which is essential for its future application in combination with Lgr5+ cells to regenerate HCs in the inner ear. In future work, we will continue to explore better graphene-based scaffolds to advance the application of graphene in stem cell therapy. In addition, we plan to further explore the specific mechanism by which graphene substrates regulate cell proliferation and differentiation. Understanding the specific mechanism of the interaction between graphene and inner ear Lgr5+ progenitors may provide more information for promoting HC regeneration through tissue engineering approaches.

DATA AVAILABILITY STATEMENT

The raw data supporting the conclusion of this article will be made available by the authors, without undue reservation.

ETHICS STATEMENT

The animal study was reviewed and approved by animal care and welfare committee of Southeast University.

AUTHOR CONTRIBUTIONS

XD, YH, and HC carried out the studies, participated in collecting data, and drafted the manuscript. XZ, LL, and SG performed the

statistical analysis. CC, LW, XQ, and CZ participated in its design. RC, XG, and ZH designed the study and helped to draft the manuscript. All authors read and approved the final manuscript.

FUNDING

This work was supported by grants from the National Basic Research Program of China (2017YFA0105201), the National Natural Science Foundation of China (Nos. 81771019, 81970884, 82071059, 81900944, 81900941).

SUPPLEMENTARY MATERIAL

The Supplementary Material for this article can be found online at: https://www.frontiersin.org/articles/10.3389/fbioe.2022.927248/full#supplementary-material

REFERENCES

Aydin, T., Gurcan, C., Taheri, H., and Yilmazer, A. (2018). Graphene Based Materials in Neural Tissue Regeneration. *Adv. Exp. Med. Biol.* 1107, 129–142. doi:10.1007/5584_2018_221

Balak, K., Corwin, J., and Jones, J. (1990). Regenerated Hair Cells Can Originate from Supporting Cell Progeny: Evidence from Phototoxicity and Laser Ablation Experiments in the Lateral Line System. *J. Neurosci.* 10 (8), 2502–2512. doi:10.1523/jneurosci.10-08-02502.1990

Barker, N., van Es, J. H., Kuipers, J., Kujala, P., van den Born, M., Cozijnsen, M., et al. (2007). Identification of Stem Cells in Small Intestine and Colon by Marker Gene Lgr5. *Nature* 449 (7165), 1003–1007. doi:10.1038/nature06196

Bermingham-McDonogh, O., and Reh, T. A. (2011). Regulated Reprogramming in the Regeneration of Sensory Receptor Cells. *Neuron* 71 (3), 389–405. doi:10.1016/j.neuron.2011.07.015

Bramhall, N. F., Shi, F., Arnold, K., Hochedlinger, K., and Edge, A. S. B. (2014). Lgr5-positive Supporting Cells Generate New Hair Cells in the Postnatal Cochlea. *Stem Cell. Rep.* 2 (3), 311–322. doi:10.1016/j.stemcr.2014.01.008

Chai, R., Kuo, B., Wang, T., Liaw, E. J., Xia, A., Jan, T. A., et al. (2012). Wnt Signaling Induces Proliferation of Sensory Precursors in the Postnatal Mouse Cochlea. *Proc. Natl. Acad. Sci. U.S.A.* 109 (21), 8167–8172. doi:10.1073/pnas.1202774109

Chai, R., Xia, A., Wang, T., Jan, T. A., Hayashi, T., Bermingham-McDonogh, O., et al. (2011). Dynamic Expression of Lgr5, a Wnt Target Gene, in the Developing and Mature Mouse Cochlea. *Jaro* 12 (4), 455–469. doi:10.1007/s10162-011-0267-2

Corwin, J. T., and Cotanche, D. A. (1988). Regeneration of Sensory Hair Cells after Acoustic Trauma. *Science* 240 (4860), 1772–1774. doi:10.1126/science.3381100

de Melo-Diogo, D., Lima-Sousa, R., Alves, C. G., and Correia, I. J. (2019). Graphene Family Nanomaterials for Application in Cancer Combination Photothermal Therapy. *Biomater. Sci.* 7 (9), 3534–3551. doi:10.1039/c9bm00577c

Farokhi, M., Mottaghitalab, F., Saeb, M. R., Shojaei, S., Zarrin, N. K., Thomas, S., et al. (2021). Conductive Biomaterials as Substrates for Neural Stem Cells Differentiation towards Neuronal Lineage Cells. *Macromol. Biosci.* 21 (1), 2000123. doi:10.1002/mabi.202000123

Grijalvo, S., and Díaz, D. D. (2021). Graphene-based Hybrid Materials as Promising Scaffolds for Peripheral Nerve Regeneration. *Neurochem. Int.* 147, 105005. doi:10.1016/j.neuint.2021.105005

Guo, R., Xiao, M., Zhao, W., Zhou, S., Hu, Y., Liao, M., et al. (2022). 2D Ti3C2TxMXene Couples Electrical Stimulation to Promote Proliferation and Neural Differentiation of Neural Stem Cells. *Acta Biomater.* 139, 105–117. doi:10.1016/j.actbio.2020.12.035

Guo, R., Zhang, S., Xiao, M., Qian, F., He, Z., Li, D., et al. (2016). Accelerating Bioelectric Functional Development of Neural Stem Cells by Graphene Coupling: Implications for Neural Interfacing with Conductive Materials. *Biomaterials* 106, 193–204. doi:10.1016/j.biomaterials.2016.08.019

Jaks, V., Barker, N., Kasper, M., van Es, J. H., Snippert, H. J., Clevers, H., et al. (2008). Lgr5 Marks Cycling, yet Long-Lived, Hair Follicle Stem Cells. *Nat. Genet.* 40 (11), 1291–1299. doi:10.1038/ng.239

Kenry, Lee, W. C., Loh, K. P., and Lim, C. T. (2018). When Stem Cells Meet Graphene: Opportunities and Challenges in Regenerative Medicine. *Biomaterials* 155, 236–250. doi:10.1016/j.biomaterials.2017.10.004

Kim, H., Kim, S.-H. L., Choi, Y.-H., Ahn, Y.-H., and Hwang, N. S. (2018). Biomaterials for Stem Cell Therapy for Cardiac Disease. *Adv. Exp. Med. Biol.* 1064, 181–193. doi:10.1007/978-981-13-0445-3_11

Li, A., You, D., Li, W., Cui, Y., He, Y., Li, W., et al. (2018). Novel Compounds Protect Auditory Hair Cells against Gentamycin-Induced Apoptosis by Maintaining the Expression Level of H3K4me2. *Drug Deliv.* 25 (1), 1033–1043. doi:10.1080/10717544.2018.1461277

Liu, L., Chen, Y., Qi, J., Zhang, Y., He, Y., Ni, W., et al. (2016). Wnt Activation Protects against Neomycin-Induced Hair Cell Damage in the Mouse Cochlea. *Cell. Death Dis.* 7 (3)–e2136. doi:10.1038/cddis.2016.35

Liu, Y., Qi, J., Chen, X., Tang, M., Chu, C., Zhu, W., et al. (2019). Critical Role of Spectrin in Hearing Development and Deafness. *Sci. Adv.* 5 (4), eaav7803. doi:10.1126/sciadv.aav7803

Palmieri, V., Spirito, M. D., and Papi, M. (2020). Graphene-based Scaffolds for Tissue Engineering and Photothermal Therapy. *Nanomedicine* 15 (14), 1411–1417. doi:10.2217/nnm-2020-0050

Park, S. Y., Park, J., Sim, S. H., Sung, M. G., Kim, K. S., Hong, B. H., et al. (2011). Enhanced Differentiation of Human Neural Stem Cells into Neurons on Graphene. *Adv. Mat.* 23 (36), H263–H267. doi:10.1002/adma.201101503

Roccio, M., Perny, M., Ealy, M., Widmer, H. R., Heller, S., and Senn, P. (2018). Molecular Characterization and Prospective Isolation of Human Fetal Cochlear Hair Cell Progenitors. *Nat. Commun.* 9 (1), 4027. doi:10.1038/s41467-018-06334-7

Rubel, E. W., Furrer, S. A., and Stone, J. S. (2013). A Brief History of Hair Cell Regeneration Research and Speculations on the Future. *Hear. Res.* 297, 42–51. doi:10.1016/j.heares.2012.12.014

Sattari, S., Adeli, M., Beyranvand, S., and Nemati, M. (2021). Functionalized Graphene Platforms for Anticancer Drug Delivery. *Ijn* Vol. 16, 5955–5980. doi:10.2147/ijn.S249712

Shi, F., Hu, L., and Edge, A. S. B. (2013). Generation of Hair Cells in Neonatal Mice by β-catenin Overexpression in Lgr5-Positive Cochlear Progenitors. *Proc. Natl. Acad. Sci. U.S.A.* 110 (34), 13851–13856. doi:10.1073/pnas.1219952110

Smith-Cortinez, N., Yadak, R., Hendriksen, F. G. J., Sanders, E., Ramekers, D., Stokroos, R. J., et al. (2021). LGR5-Positive Supporting Cells Survive Ototoxic Trauma in the Adult Mouse Cochlea. *Front. Mol. Neurosci.* 14, 729625. doi:10.3389/fnmol.2021.729625

Song, S., Shen, H., Wang, Y., Chu, X., Xie, J., Zhou, N., et al. (2020). Biomedical Application of Graphene: From Drug Delivery, Tumor Therapy, to Theranostics. *Colloids Surfaces B Biointerfaces* 185, 110596. doi:10.1016/j.colsurfb.2019.110596

Tong, Z., Solanki, A., Hamilos, A., Levy, O., Wen, K., Yin, X., et al. (2015). Application of Biomaterials to Advance Induced Pluripotent Stem Cell Research and Therapy. *Embo J.* 34 (8), 987–1008. doi:10.15252/embj.201490756

Wang, C., Wang, X., Chen, Y., and Fang, Z. (2020). In-vitro Photothermal Therapy Using Plant Extract Polyphenols Functionalized Graphene Sheets for Treatment of Lung Cancer. *J. Photochem. Photobiol. B Biol.* 204, 111587. doi:10.1016/j.jphotobiol.2019.111587

Wang, T., Chai, R., Kim, G. S., Pham, N., Jansson, L., Nguyen, D.-H., et al. (2015). Lgr5+ Cells Regenerate Hair Cells via Proliferation and Direct Transdifferentiation in Damaged Neonatal Mouse Utricle. *Nat. Commun.* 6, 6613. doi:10.1038/ncomms7613

Waqas, M., Guo, L., Zhang, S., Chen, Y., Zhang, X., Wang, L., et al. (2016). Characterization of Lgr5+ Progenitor Cell Transcriptomes in the Apical and

Basal Turns of the Mouse Cochlea. *Oncotarget* 7 (27), 41123–41141. doi:10.18632/oncotarget.8636

Warchol, M. E. (2011). Sensory Regeneration in the Vertebrate Inner Ear: Differences at the Levels of Cells and Species. *Hear. Res.* 273 (1-2), 72–79. doi:10.1016/j.heares.2010.05.004

Yao, X., Yan, Z., Wang, X., Jiang, H., Qian, Y., and Fan, C. (2021). The Influence of Reduced Graphene Oxide on Stem Cells: a Perspective in Peripheral Nerve Regeneration. *Regen. Biomater.* 8 (4), rbab032. doi:10.1093/rb/rbab032

Zhang, Y., Li, W., He, Z., Wang, Y., Shao, B., Cheng, C., et al. (2019). Pre-treatment with Fasudil Prevents Neomycin-Induced Hair Cell Damage by Reducing the Accumulation of Reactive Oxygen Species. *Front. Mol. Neurosci.* 12, 264. doi:10.3389/fnmol.2019.00264

Zhou, H., Qian, X., Xu, N., Zhang, S., Zhu, G., Zhang, Y., et al. (2020). Disruption of Atg7-dependent Autophagy Causes Electromotility Disturbances, Outer Hair Cell Loss, and Deafness in Mice. *Cell. Death Dis.* 11 (10), 913. doi:10.1038/s41419-020-03110-8

Conflict of Interest: The authors declare that the research was conducted in the absence of any commercial or financial relationships that could be construed as a potential conflict of interest.

frontiers | Frontiers in Bioengineering and Biotechnology

ORIGINAL RESEARCH
published: 30 June 2022
doi: 10.3389/fbioe.2022.927348

Study on the Effect of PDA-PLGA Scaffold Loaded With Islet Cells for Skeletal Muscle Transplantation in the Treatment of Diabetes

Meishuang Zhang[1†], Hongwei Du[2†], Yueqi Guan[1], Jingyue Liu[1], Sushan Wang[1], Haoran Li[1], Wenyou Zhang[1], Hao Han[1], Ming Zhang[1] and Li Chen[1*]*

[1]Department of Pharmacology, College of Basic Medical Sciences, School of Nursing, Jilin University, Changchun, China, [2]Research Institution of Paediatrics, Department of Pediatric Endocrinology, The First Clinical Hospital Affiliated to Jilin University, Changchun, China

OPEN ACCESS

Edited by:
Mingqiang Li,
Third Affiliated Hospital of Sun Yat-sen University, China

Reviewed by:
Dongshi Chen,
University of Southern California, United States
Sun Jiaming,
Changchun University of Chinese Medicine, China
He Shen,
Suzhou Institute of Nano-tech and Nano-bionics (CAS), China

***Correspondence:**
Ming Zhang
zhangming99@jlu.edu.cn
Li Chen
chenl@jlu.edu.cn

[†]These authors have contributed equally to this work

Specialty section:
This article was submitted to Biomaterials, a section of the journal Frontiers in Bioengineering and Biotechnology

Received: 24 April 2022
Accepted: 10 June 2022
Published: 30 June 2022

Citation:
Zhang M, Du H, Guan Y, Liu J, Wang S, Li H, Zhang W, Han H, Zhang M and Chen L (2022) Study on the Effect of PDA-PLGA Scaffold Loaded With Islet Cells for Skeletal Muscle Transplantation in the Treatment of Diabetes. Front. Bioeng. Biotechnol. 10:927348. doi: 10.3389/fbioe.2022.927348

At present, islet cells transplantation was limited by the way in which islet cells are implanted into the body, their ability to adapt to the microenvironment and the maintenance time for relieving diabetic symptoms. In order to solve this problem, we made PDA-PLGA scaffold loaded with islet cells and used it for skeletal muscle transplantation to investigate its therapeutic effect in the treatment of diabetes. The PLGA scaffold was prepared by the electrospinning method, and modified by polydopamine coating. A rat diabetic model was established to evaluate the efficacy of PDA-PLGA scaffold loaded with RINm5f islet cells through skeletal muscle transplantation. The results showed that the PDA-PLGA scaffold has good biosafety performance. At the same time, transplantation of the stent to the skeletal muscle site had little effect on the serum biochemical indicators of rats, which was conducive to angiogenesis. The PDA-PLGA scaffold had no effect on the secretory function of pancreatic islet cells. The PDA-PLGA scaffold carrying RINm5f cells was transplanted into the skeletal muscle of type I diabetic rats. 1 week after the transplantation of the PDA-PLGA cell scaffold complex, the blood glucose of the treatment group was significantly lower than that of the model group ($p < 0.001$) and lasted for approximately 3 weeks, which further indicated the skeletal muscle transplantation site was a new choice for islet cell transplantation in the future.

Keywords: electrospinning, PDA-PLGA scaffold, biocompatibility, type I diabetes, transplantation in skeletal muscle

INTRODUCTION

Diabetes is a complex disorder of glucose and lipid metabolism, with an increasing incidence (Roden, 2016). Islet β-cell failure is the decisive factor in type I diabetes and the late stage of type II diabetes. At present, drugs for the treatment of diabetes do not induce islet β-cell regeneration and cannot fundamentally cure the disease. With the development of tissue engineering technology, a series of

Abbreviations: PLGA, Lactic acid-glycolic acid copolymer; PDA-PLGA, Lactic acid-glycolic acid copolymer scaffold was modified by polydopamine coating; STZ, Streptozotocin; AST, Aspartate aminotransferase; ALT, Alanine aminotransferase; TP, Total Protein; ALB, Serum albumin; ALP, Alkaline phosphatase; BUN, Blood urea nitrogen; Cr, Creatinine; UA, Uric acid; TNF-α, Tumor necrosis factor-α; IL-4, Interleukin.

various types of scaffolds apply to improvement and treatment of diseases (Shen et al., 2022), islet cell transplantation provides a new method for the treatment of diabetes (Rengifo et al., 2014; Frei et al., 2018; Perez-Basterrechea et al., 2018). However, its clinical application is limited by the way in which islet cells are implanted into the body, their ability to adapt to the microenvironment and the maintenance time for relieving diabetic symptoms.

Poly (lactic acid-glycolic acid) copolymer (PLGA), as the most widely used polymer material in the biomedical field, has a suitable degradation rate and is nontoxic and harmless, and functional modification of the surface can improve the surface hydrophilicity and histocompatibility (Middleton and Tipton, 2000; Qian et al., 2014). Polydopamine (PDA) is widely used in surface functional modification. It can significantly improve the hydrophilicity and mechanical properties of materials, is nontoxic and biodegradable and has excellent applicability for cell adhesion and proliferation (Lee et al., 2007; Hong et al., 2011; Zhao et al., 2017). There are many studies showing the enhanced biocompatibility effect of polydopamine coat on scaffolds (also on PLGA in bone tissue engineering scaffolds) (Zhao et al., 2017; Yang et al., 2020). Materials can also be designed to prevent adhesive interactions of leukocytes and endothelial cells that ameliorate the microenvironment (Tu et al., 2022).

The selection of the transplantation site is the key to the success of islet cell transplantation. At present, the common transplantation sites mainly include subcutaneous sites, the portal vein and skeletal muscle (Rajab, 2010; Salazar-Bañuelos et al., 2010; Perez et al., 2011). Subcutaneous transplantation cannot meet the requirements of islet cells for the microenvironment because it is insensitive to changes in glucose levels (Cantarelli et al., 2009; Vlahos et al., 2017). Portal vein islet transplantation is prone to immediate blood-mediated inflammation (Bennet et al., 2000). Skeletal muscle, as the key target organ of glucose utilization, can stimulate islet cells in the transplantation site to release insulin over time according to the glucose content. Therefore, skeletal muscle is the preferred site for islet cell transplantation (Christoffersson et al., 2011). However, there is no report on the related research of PDA-PLGA scaffold loaded with islet cells in skeletal muscle transplantation to treat diabetes.

In this study, PLGA scaffolds were prepared by electrospinning and modified by polydopamine coating on the surfaces. The morphology and properties of the scaffolds were identified, and the safety of the scaffolds was evaluated; then, they were cocultured with islet cells to detect the effect of the scaffolds on the morphology and function of islet cells. Furthermore, PDA-PLGA scaffold loaded with islet cells were transplanted into the skeletal muscle of type I diabetic rats to explore the therapeutic effect of islet cells and the PDA-PLGA scaffold complex on diabetes mellitus.

MATERIALS AND METHODS

Synthesis of the PLGA and PDA-PLGA Scaffolds

First, the solid polymer PLGA particles, which are the main bodies used for electrospinning, were dissolved in a mixed solution of $CHCL_3$ and C_3H_6O (v/v = 3:1) and stirred at 25°C for 1 h until completely dissolved, and an electrospinning solution with a mass fraction of 10%–15% was prepared. The electrospinning solution was added to a 5 ml syringe. The front end is connected with the electrospinning machine through a 17G flat head metal spinneret, and the syringe is fixed on the injection pump. The inner diameter of the metal spinneret is 1.12 mm. The distance between the metal receiving plate and the spinneret is adjusted to determine the receiving distance of 15 cm. During the spinning process, the high electrostatic voltage between the metal spinneret and the receiving plate was 15 kV, the flow rate of the electrospinning solution was controlled by an injection pump at 1.5 ml/h for 3 h, and the prepared material was lowered and dried overnight in a ventilator to obtain the PLGA scaffolds.

To generate a polydopamine-coated PDA-PLGA scaffold, a 10 mM Tris-HCl buffer solution of with a pH of 8.5 was prepared, and 20 mg dopamine hydrochloride was dissolved in 10 ml Tris-HCl buffer solution to prepare a weakly alkaline 2 mg/ml dopamine solution. The PLGA scaffold was immersed in a weak alkaline solution of dopamine and kept in aerobic conditions. The dopamine self-polymerized on the surface of the material and was fully shaken to synthesize the polydopamine (PDA) coating. During the self-polymerization of PDA, it was observed that the solution colour changed from light brown to black. After 24 h, the scaffold was removed and washed with distilled water 3 times to remove the unadhered polydopamine molecules. The PDA-PLGA scaffold was obtained by drying the material in a ventilator overnight.

Structure and Surface Characterization

The surface topography of the PLGA and PDA-PLGA scaffolds was characterized using a field emission scanning electron microscope (FE-SEM; JSM-7401F, JEOL Ltd. Japan), and the surface functional groups were measured by Fourier transform infrared (FTIR) spectroscopy. The contact angles of the samples were investigated using a contact angle metre (SL200B, Solon Technology Science, Shanghai, China) as described previously (Vlahos et al., 2017).

Mechanical Properties

Rectangular (10 mm × 30 mm) samples with an average thickness of 0.10 mm were tested for tensile strength and the elastic modulus using an electronic universal testing machine (INSTRON 5948, United States). During measurement, the square clamping position of 1 cm × 1 cm was set aside at each end, and sand paper was used to clamp both ends of the samples to prevent slipping during the testing. The crosshead speed was set at 1 mm/min. The yield point value of the stress-strain curve was determined as the tensile strength, and the elasticity modulus was calculated by the slope of the linear portion of the curve.

Detection of Degradation Behaviour *in vitro*

The prepared PLGA and PDA-PLGA scaffolds were cut into 2.5 × 2.5 cm^2 squares, and the thickness was measured with a Vernier calliper at four random points on each membrane; the average value was considered the thickness (≈0.1 mm), and the fibre scaffold was placed into a 50 ml centrifuge tube and immersed in 40 ml aseptic PBS buffer solution. It was incubated at 37°C, and the lactic acid level was detected in the solution every week.

Cell Culture and Proliferation

HUVECs and RAW264.7 cells were cultured in RPMI 1640 medium (Gibco, United States) and 10% foetal bovine serum (Gibco, United States) in an atmosphere of 5% CO_2 at 37°C. ADSCs, C2C12 and RINm5f cells were cultured in Dulbecco's modified Eagle's medium (DMEM) and 10% foetal bovine serum (Gibco, United States) in an atmosphere of 5% CO_2 at 37°C. MTT (Sigma, United States) was used for the cell proliferation study.

Cell Morphology and Cell Adhesion

Cells (2×10^4) were seeded onto 14 mm scaffolds (average thickness of 0.10 mm) and cultured in 24-well plates in an atmosphere of 5% CO_2 at 37°C for 24 h. After 24 h, the scaffolds carrying the cells were washed with PBS once and fixed with 4% paraformaldehyde at room temperature for 30 min. The sample was washed with PBS 3 times after fixation. Then, the cells were permeated with 0.1% Triton X-100 for 3 min and washed with PBS 3 times after osmosis. Then, 200 μL of phalloidin-iFluor488 reagent (diluted 1:1,000) was added to each well, incubated at room temperature without light for 40 min, and washed with PBS 3 times to remove excess dye. The adhesion morphology of cells on the scaffold was observed by positive fluorescence microscopy (CarlZeiss, Axio Imager Z2). Cells cultured without scaffolds were defined as the control group (Con), cells cocultured with PLGA scaffolds were defined as the PLGA group (PLGA), cells cocultured with PDA-PLGA scaffolds were defined as the PDA-PLGA group (PDA-PLGA).

Determination of Glucose Consumption and Glucose Uptake in C2C12 Cells

Differentiated C2C12 cells were incubated with conditioned medium obtained from the RINm5f cells seeded onto the PDA-PLGA scaffolds for 24 h. Cells were then cultured in FBS-free DMEM (15 mM D-glucose) supplemented with 0.2% BSA for 48 h. The media glucose concentration was determined as described above. Glucose consumption was calculated based on the difference between the initial glucose concentration and the residual glucose concentration of the culture medium. For glucose uptake determination, cells were washed three times with KRB and incubated with conditioned medium or normal medium for 10 min, and 100 μM 2-NBDG (Invitrogen, United States) was added to the medium for 30 min. The medium was removed, and the cells were then washed twice with ice-cold PBS. The fluorescence intensity in each well was then measured at 485 nm/535 nm (excitation wavelength/emission wavelength) using an Epoch fluorescence microplate reader (Biotek, United States). Cells cultured without conditioned medium were defined as the control group (Con), cells cocultured with conditioned medium were defined as the RINm5f group (RINm5f).

Determination of Glucose-Stimulated Insulin Secretion

When the RINm5f cells were seeded onto the 14 mm scaffolds (average thickness of 0.10 mm) and inoculated in a 24-well plate until the cell fusion degree reached approximately 80%, the cells were incubated with glucose-free KRB buffer for 90 min, and then the cells were treated according to their respective groupings. KRB buffers containing different concentrations of glucose were added to stimulate the cells for 2 h. After stimulation, the supernatant was collected immediately to terminate the incubation, and the detection of insulin in the supernatant was performed with an ELISA kit.

Experimental Animals

One hundred and two male 5-6-week-old Wistar rats were purchased from Beijing HFK Bioscience Co., Ltd. [SCXK (Jing) 2019–0008]. They were free fed individually in a room (15–25°C) with a 12 h day-night cycle. After adaptive feeding for 1 week, seventy-two male rats were used to evaluate the safety of the PDA-PLGA scaffold *in vivo*. They were randomly divided into three groups (24 rats in each group were divided into four groups according to different time points, with six rats in each group). Animals without PDA-PLGA scaffold transplantation were defined as control group. PDA-PLGA scaffold was transplanted intraperitoneally (Ip), into skeletal muscle (Mus) and subcutaneously (Sub). Some of the rats were sacrificed on the 3rd, 7th, 14th, and 28th days after transplantation, and related tests were performed.

The remaining thirty rats were used to establish type I diabetes models to further detect the therapeutic effect of skeletal muscle transplantation of the PDA-PLGA scaffold loaded with islet cells. After 1 week of acclimation with free access to regular rodent chow and water, the rats were randomly divided into three groups: Group 1 (n = 6, normal control [Con]), Group 2 (n = 6, diabetic model [DM]) and Group 3 (n = 18, treatment group [PDA-PLGA]). After fasting for more than 12 h and injection of high-dose STZ (65 mg/kg) in Group 2 and Group 3, Group 1 was injected with the citrate buffer vehicle. One week after STZ injection, the rats in Group 2 and Group 3 had an FBG level ≥11.1 mmol/L. After the successful establishment of the model, skeletal muscle transplantation of the PDA-PLGA scaffold loaded with islet cells was performed in Group 3, and the fasting blood glucose was detected weekly. After 4 weeks, blood samples obtained from the abdominal aorta were collected in EDTA tubes and placed on ice. The main organs and pancreatic tissues were preserved and stored at −80°C. In this manuscript, the ARRIVE guidelines have been followed. All animal experimental procedures were approved by the Ethics Committee for the Use of Experimental Animals of Jilin University [SYXK (Ji) 2018–0001].

Biochemical Indicator Detection

At the end of the experimental period, AST, ALT, TP, ALB, ALP, BUN, CR, UA, TNF-α, and IL-4 in the blood and lactic acid levels in the blood and tissue from transplantation sites in rats were measured by ELISA.

Histopathology

Tissue from the heart, liver, spleen, lung, kidney, and the transplant site were obtained for histopathological examination. Four percent formaldehyde fixation, paraffin embedding, HE staining and Masson trichrome staining were performed.

Immunofluorescence

Paraffin tissue sections were prepared and incubated with a primary antibody mixture of insulin (1:150, Abcam) at 4°C overnight. Then, the slides were protected from light, and a secondary antibody mixture was used that included anti-mouse IgG FITC (1:100, Sungene) for 1 h at room temperature. Counterstaining was followed by staining with DAPI for 10 min in an aluminium foil-covered box. Finally, the slides were covered with anti-fade mounting medium (P0128, Beyotime Biotechnology) for imaging.

Statistical Analysis

All the data are presented as the mean ± SD. Student's t-test or one-way ANOVA was used for the determination of statistical significance. The level of significance was defined as $p < 0.05$.

RESULTS

The Characterization and Properties of the PLGA and PDA-PLGA Scaffold

The PDA coating adheres to the surface of the material but does not change the chemical properties of PLGA through the infrared spectra of the scaffolds (**Supplementary FigureS1A**). Through SEM observation, we found that the PDA coating changes the surface properties of the PLGA scaffold. Topographic stimulation caused by the increase in scaffold surface roughness may enhance cell adhesion and proliferation on the scaffold (**Supplementary Figure S1B**). As shown in **Supplementary Figure S1C**, the hydrophilicity of the PLGA scaffold before and after modification with the PDA coating was significantly different ($p < 0.001$), showing good hydrophilicity, and the tensile strength and elastic modulus of the PLGA scaffolds were significantly different before and after PDA coating modification (**Supplementary Figures 1D,E**). The results about degradation behaviour of the PDA-PLGA scaffold *in vitro* was show that the PDA coating improves the stability of the PLGA scaffold and can be used in more fields of medicine and materials.

Effects of the Scaffolds on the Proliferation and Morphology of Various Cell Lines

To evaluate the biosafety of our PDA-PLGA scaffold, we first tested its safety *in vitro*. The effects of the PDA-PLGA scaffold on the proliferation of HUVECs, RAW264.7 cells, ADSCs, C2C12 cells and RINm5f cells were detected by the MTT method. The results showed that the scaffold had no adverse effect on cell proliferation and growth when coincubated with different cells (**Figure 1**). To evaluate the effect of PDA-PLGA scaffold on cell morphology and adhesion, the adhesion morphology of different kinds of cells on PLGA cell scaffolds was observed by fluorescence microscopy. The results showed that the cells could adhere to the cell scaffold, and a slender pseudopod was observed extending into the 3D cell scaffold nanofibre structure. Cells attach to the surface through extended filamentous pseudopodia and tend to grow along polymer nanofibres on their surfaces (**Figure 2**).

Effect of the PDA-PLGA Scaffold on Biochemical Indexes in the Serum and Tissue of Rats

After transplantation of the PDA-PLGA scaffold at three different sites, the rats recovered well, the incision healed well, and there was no infection (data not shown). As shown in **Figure 3A–H**, the AST, ALP, ALT, and other indexes fluctuated obviously in the early stage of transplantation. On the 3rd day, the contents of ALT, ALB, ALP, and BUN in the subcutaneous transplantation group decreased significantly, while the content of Cr increased in the subcutaneous transplantation group, while the ALT, AST, and ALP contents decreased in the intraperitoneal transplantation group. On the 7th day after transplantation, except for the decrease in ALT, ALB, and ALP contents in the intraperitoneal transplantation group, there was no difference in details between the other groups and the control group. On the 14th day of transplantation, except for the level of AST in the subcutaneous transplantation group and the intraperitoneal transplantation group, which increased, the other indexes were at the normal level. On the 28th day, the level of Cr in the intraperitoneal transplantation group increased, and all the indexes in the other groups were at the normal level. Except for the decrease in AST levels on the 3rd day in the skeletal muscle transplantation group, there was no significant difference in all indexes between the skeletal muscle transplantation group and the control group at other time points. The above results showed that the PDA-PLGA scaffold affected all the indexes of the rat body at the initial stage of transplantation but basically returned to normal after 14 days, and transplantation in the skeletal muscle site had the least effect on the liver function and kidney function of rats.

Compared with the Con group, the level of TNF-α in the transplanted rats increased significantly, indicating that the transplanted fibrous scaffold as a foreign body caused a certain inflammatory response. Although the content of TNF-α decreased with the extension of time, it was still higher than the normal level, while the content of IL-4 only decreased in the early stage of the subcutaneous transplantation group, and there was no significant difference between the other time points and the control group (**Figures 3I,J**). The contents of lactic acid in the serum and tissue of rats were detected at each time point after transplantation. As shown in **Figures 3K,L**, the content of lactic acid in serum increased in each group on the 3rd day of transplantation but decreased significantly compared with the control group in tissue. Then, the content of serum lactic acid gradually returned to normal. The content of lactic acid in the skeletal muscle transplantation group increased on the 7th and 28th days, which may be due to the degradation of scaffold materials and the increase in lactic acid produced by muscle.

Effects of the PDA-PLGA Scaffold on Tissues and Organs of Rats

On the 3rd, 7th, 14th and 28th days, some rats were killed, the main organs were observed with the naked eye, and no changes, such as hyperaemia and necrosis, were found. As shown in

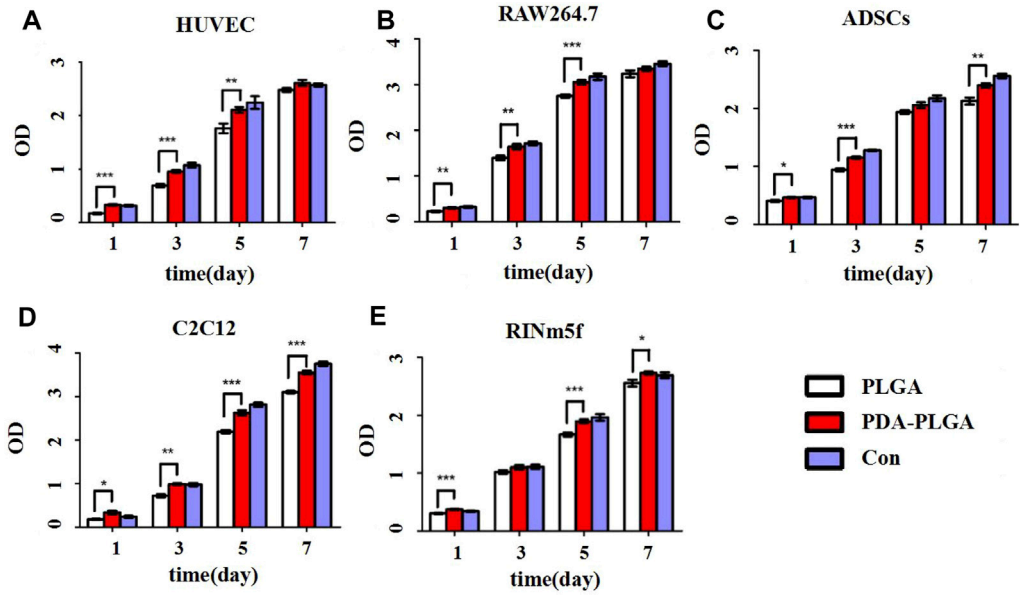

FIGURE 1 | Proliferation of different cell types on the PDA-PLGA scaffold. **(A)** HUVECs. **(B)**: RAW264.7 cells. **(C)** ADSCs. **(D)** C2C12 cells. **(E)** RINm5f cells. Con: control group, PLGA: cell and PLGA scaffold coculture group, PDA-PLGA: cell and PDA-PLGA scaffold coculture group. $n = 3$, $^{*}p < 0.05$, $^{**}p < 0.01$ and $^{***}p < 0.001$ compared to the PLGA group.

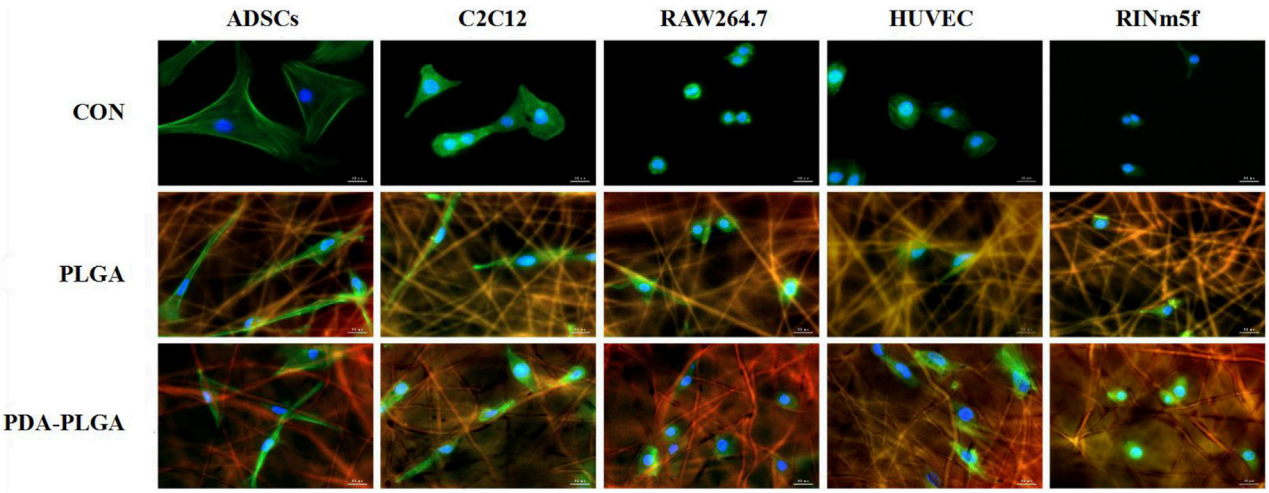

FIGURE 2 | The adhesion morphology of different types of cells on the PDA-PLGA scaffold. Con: control group, PLGA: cell and PLGA scaffold coculture group, PDA-PLGA: cell and PDA-PLGA scaffold coculture group. Cells were stained for F-actin (green), nuclei (blue), and fibre scaffolds (red) with fluorescent dyes. Scale bars = 20 μm.

Figures 4, **5**, obvious cell infiltration and orientation formed by material curling could be observed at the transplantation site after transplantation. Inflammatory cells were mainly attached to the surface of the material, and cell affinity was conducive to blood vessel growth. Red blood cells were found in the subcutaneous transplantation group and skeletal muscle transplantation group from the 7th day, and small blood vessels gradually formed, which was beneficial to the survival of the graft. Masson staining showed that the trend of cell infiltration and neovascularization was similar to that of HE staining, and the collagen fibres were mainly concentrated on the surface of the material and gradually increased with time. As shown in **Figure 6**, the main organs of the rats 28 days after transplantation were compared with those of the control group, and there was no obvious abnormality. In summary, no pathological changes caused by the PDA-PLGA scaffold was found by histopathological examination and the PDA-PLGA scaffold had good biological safety.

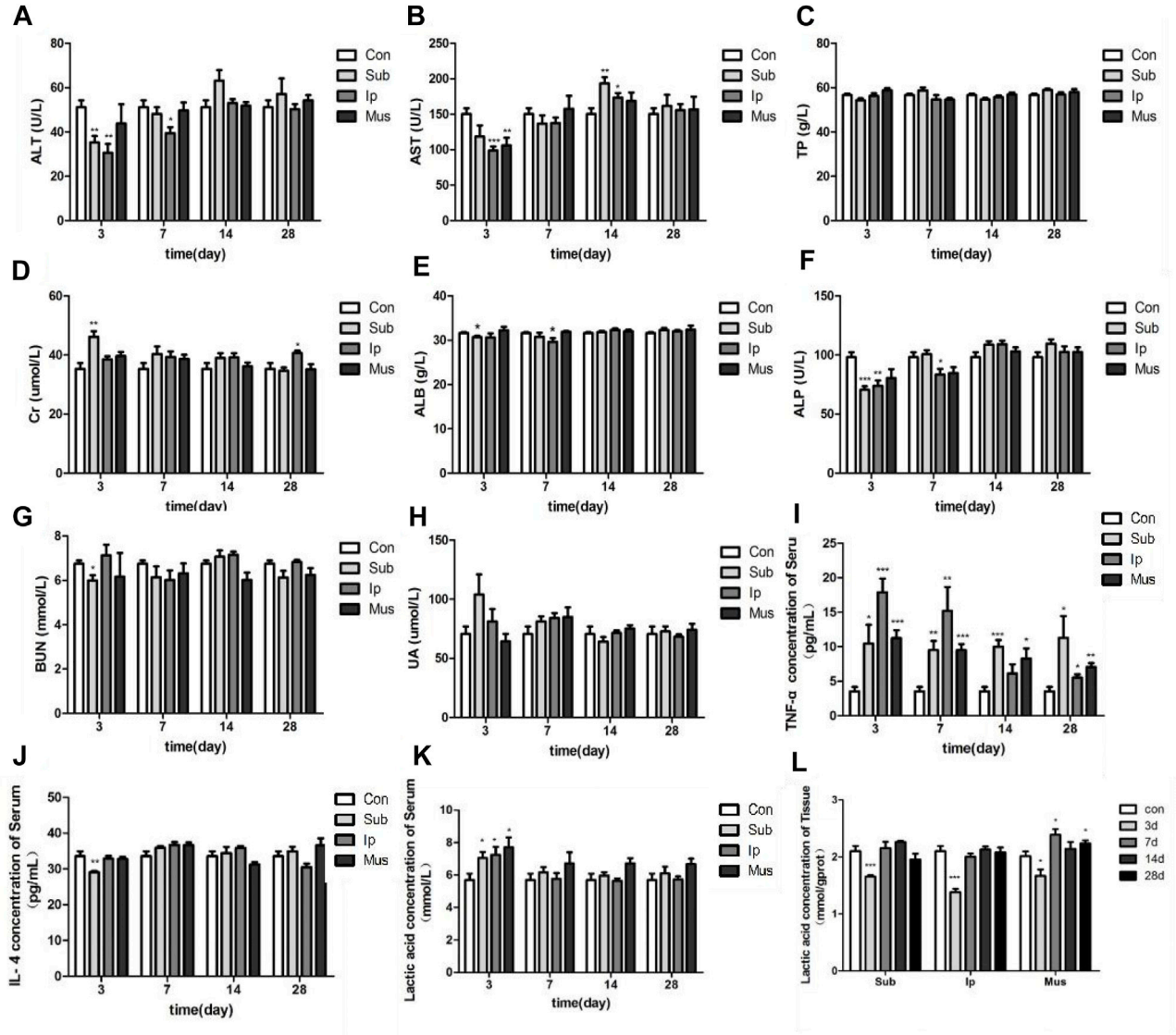

FIGURE 3 | Changes in serum biochemical indexes and tissue lactic acid levels in rats at different locations and at various time points after PDA-PLGA transplantation. **(A)** ALT level. **(B)** AST level. **(C)** TP level. **(D)** Cr level. **(E)** ALB level. **(F)** ALP level. **(G)** BUN level. **(H)** UA level. **(I)** TNF-α level. **(J)** IL-4 level. **(K)** Blood lactic acid level. **(L)**: Tissue lactic acid level. Con: control group, Sub: subcutaneous transplantation group, Ip: intraperitoneally transplanted group, Mus: skeletal muscle transplantation group. $n = 6$, $^{*}p < 0.05$, $^{**}p < 0.01$ and $^{***}p < 0.001$ compared to the Con group.

Effects of the PDA-PLGA Scaffold Loaded With RINm5f Cells on Insulin Secretion

The insulin secretion of islet cells under different concentrations of glucose stimulation was detected by GSIS when islet cells were cocultured with the PDA-PLGA scaffold. As shown in **Figure 7A**, when RINm5f cells were cocultured with the PDA-PLGA scaffold, the secretion function was normal, and the amount of insulin secretion increased with increasing glucose concentration, showing an obvious dose-effect relationship. The results show that the PDA-PLGA scaffold had no effect on the secretory function of islet cells and can be used as a carrier for islet cell transplantation.

Effects of the PDA-PLGA Scaffold Loaded With RINm5f Cells on Glucose Uptake and Consumption by C2C12 Cells

In view of the fact that skeletal muscle is the key target organ of glucose metabolism, we chose skeletal muscle as the transplantation site of islet cells. To verify whether insulin secreted by RINm5f cells in PDA-PLGA scaffold can promote glucose uptake and glucose consumption in skeletal muscle cells and achieve hypoglycaemia, we coincubated C2C12 cells with the supernatant of RINm5f cells to detect their effects on glucose consumption and glucose uptake in skeletal muscle C2C12 cells. The results of cellular glucose uptake and glucose consumption are shown in **Figures 7B,C**. After

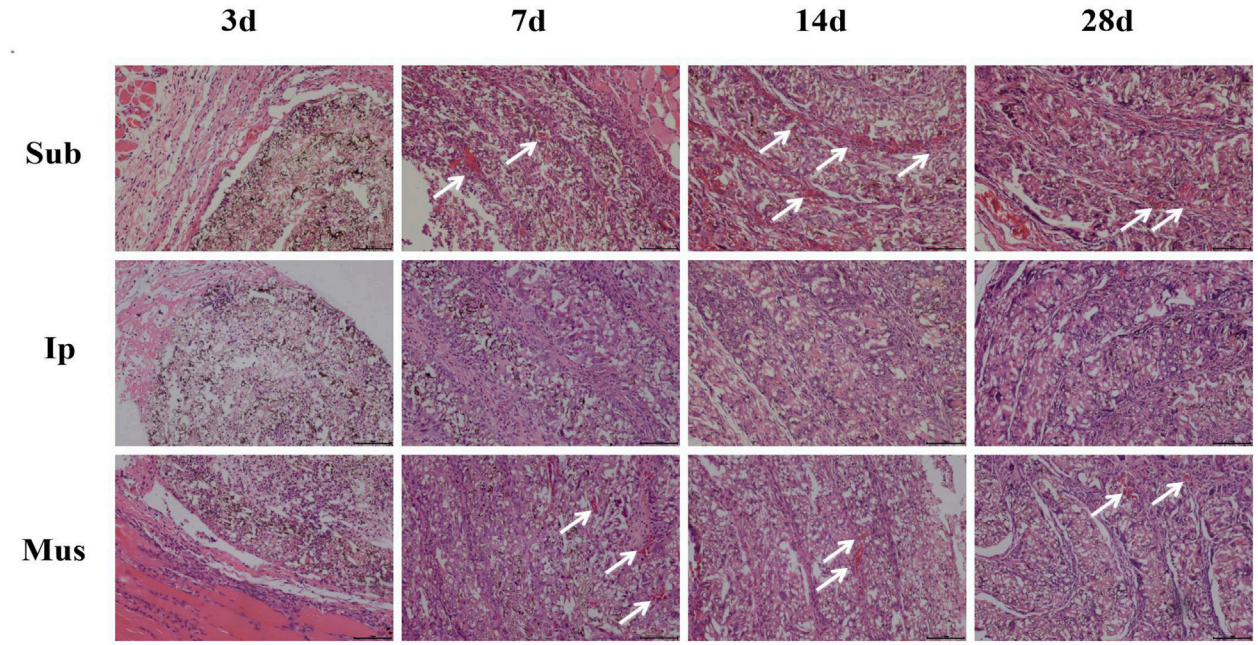

FIGURE 4 | HE staining of the PDA-PLGA scaffold at the rat transplantation site (100×). Sub: subcutaneous transplantation group, Ip: intraperitoneally transplanted group, Mus: skeletal muscle transplantation group.

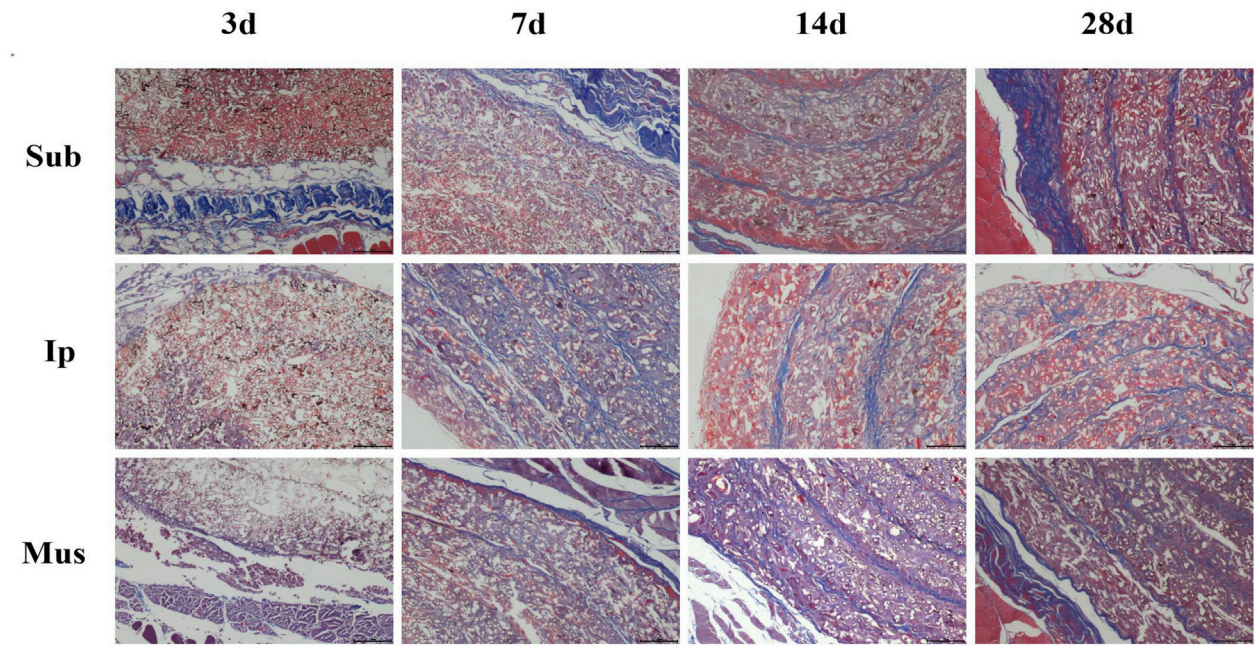

FIGURE 5 | Masson trichrome staining of the PDA-PLGA scaffold at the rat transplantation site (100×). Sub: subcutaneous transplantation group, Ip: intraperitoneally transplanted group, Mus: skeletal muscle transplantation group.

treatment with RINm5f cell supernatant, the basal metabolic glucose uptake of skeletal muscle cells was significantly higher than that of the control group ($p < 0.001$), and the glucose consumption increased significantly ($p < 0.001$). The results showed that insulin secreted by RINm5f can enhance skeletal muscle glucose uptake and consumption. At the cellular level, islet cell transplantation in skeletal muscle is expected to reduce blood glucose and achieve the purpose of treating diabetes.

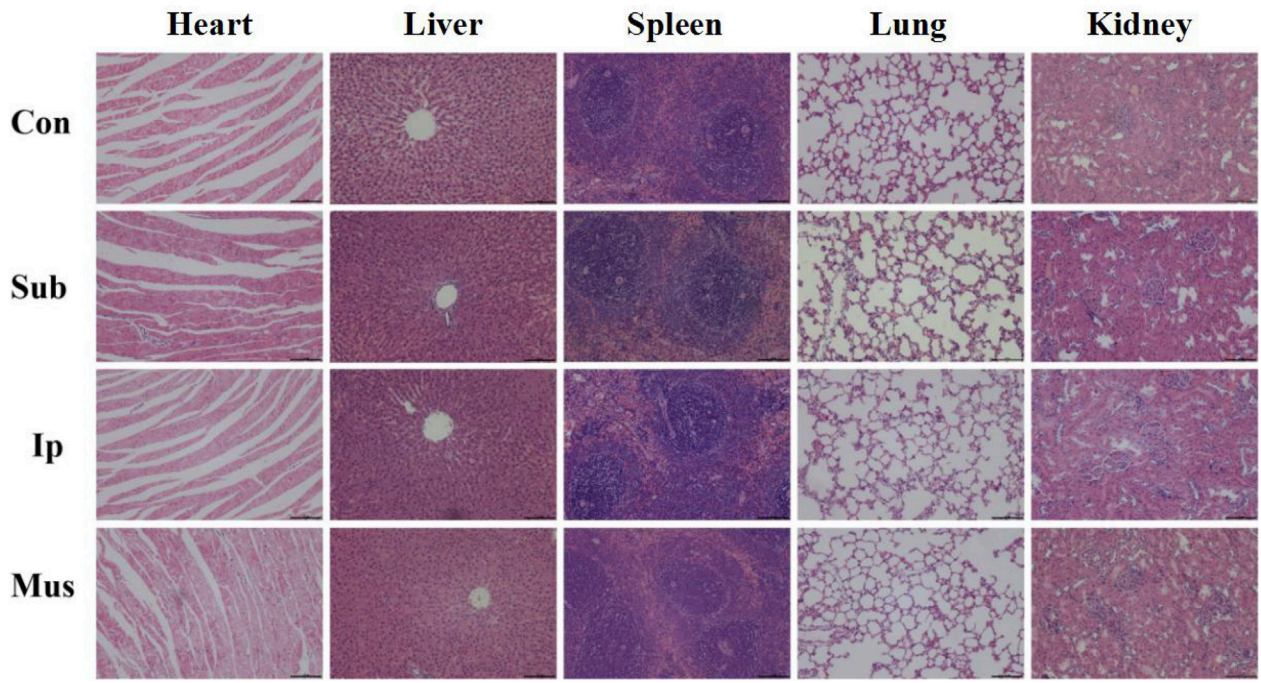

FIGURE 6 | Representative images of H&E staining of the main organs, including the heart, liver, spleen, lungs and kidneys, from rats after transplantation for 28 days. The scale bars represent 100 μm.

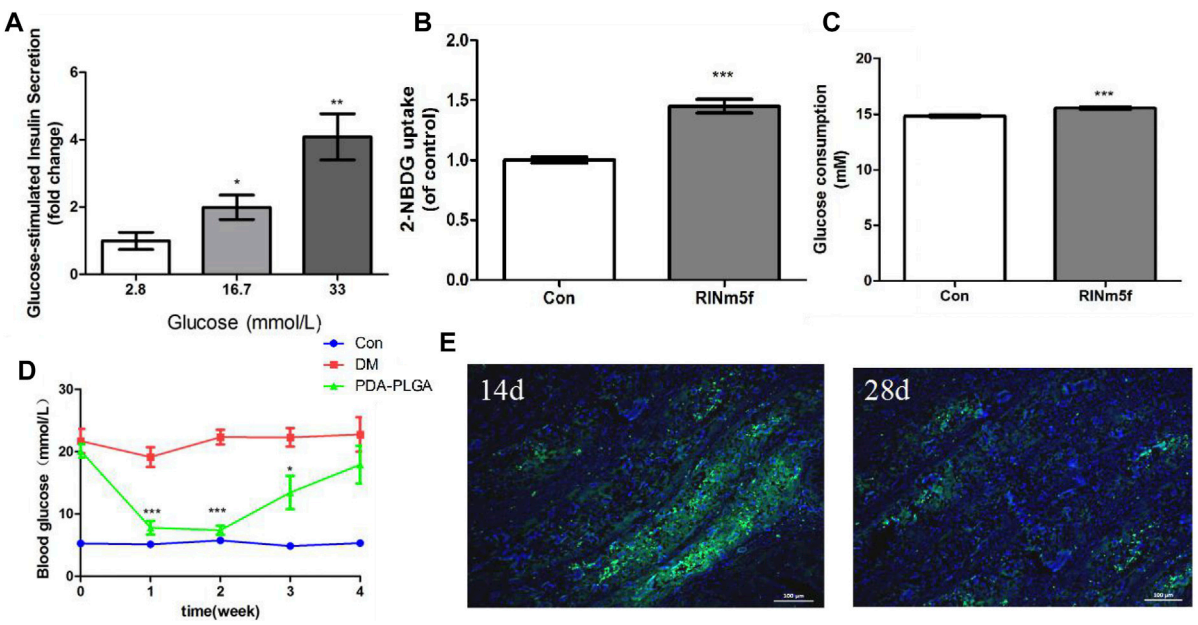

FIGURE 7 | Therapeutic effect of the PDA-PLGA scaffold with islet cell skeletal muscle transplantation on the treatment of type 1 diabetic rats. **(A)**: Insulin secretion in RINm5f cells seeded onto the PDA-PLGA scaffolds stimulated by glucose, $n = 3$, $^{*}p < 0.05$ and $^{**}p < 0.01$ compared to the corresponding basal group with 2.8 mM glucose. **(B,C)**: Effect of RINm5f cell supernatant on skeletal muscle glucose uptake and consumption. Con: control group, RINm5f: RINm5f cell supernatant treatment group, $n = 3$, $^{***}p < 0.001$ compared to the Con group. **(D)**: Fasting blood glucose levels of rats after transplantation of RINm5f cells and PDA-PLGA cell scaffold complex, Con: control group, DM: diabetes model group, PDA-PLGA: islet cell transplantation treatment group, $n = 6$, $^{***}p < 0.001$ and $^{*}p < 0.05$ compared to the DM group. **(E)**: RINm5f and PDA-PLGA cell scaffold complex skeletal muscle transplantation insulin immunofluorescence results at different times. Cells were stained for nuclei (blue) and insulin (green) with fluorescent dyes. Scale bars = 100 μm.

Therapeutic Effect of PDA-PLGA Scaffold Skeletal Muscle Transplantation Loaded With Islet Cells on Type 1 Diabetic Rats

Compared with the control group, the fasting blood glucose of rats in the treatment group and model group increased significantly after STZ ($p < 0.001$), and the fasting blood glucose was ≥11.1 mmoL. One week after the transplantation of islet cells and the PDA-PLGA scaffold complex, the blood glucose of the treatment group was significantly lower than that of the model group ($p < 0.001$). It was proven that the transplanted islet cells played a role, secreted insulin and decreased the blood glucose of rats, but approximately 4 weeks after transplantation, the blood glucose of the treatment group increased, which was no different from that of the model group. It is speculated that the inflammatory reaction may be caused by foreign bodies. The complex microenvironment in the body led to the gradual death of islet cells and the disappearance of the hypoglycaemic effect (**Figure 7D**).

To verify the therapeutic effect of RINm5f cells and the PDA-PLGA scaffold complex on type I diabetic rats, fixed sections of muscle and grafts were obtained for insulin immunofluorescence detection, and the survival and insulin secretion of RINm5f cells were observed. The results of insulin immunofluorescence are shown in **Figure 7E**. In the treatment group, insulin green fluorescence was obvious on the 14th day, insulin secretion was large, and the hypoglycaemic effect was significant; on the 28th day, insulin green fluorescence was obviously weakened, and islet cells basically died. In summary, the transplantation of islet cells in skeletal muscle with the PDA-PLGA scaffold has a certain therapeutic effect on type I diabetes, but the transplanted islet cells are still allotransplanted, which is easily affected by rejection and mechanical pressure caused by skeletal muscle movement, resulting in cell death, so they still need to be further improved.

DISCUSSION

The functional damage of islet β cells is the core link in the pathogenesis of diabetes. The regeneration and transplantation of islet β cells and the reconstruction of insulin secretion function have become new strategies for curing diabetes, but the donor and site of transplantation and the selection of transplantation carriers are the key to this strategy. In this study, PDA-PLGA scaffold was prepared by electrospinning and polydopamine coating techniques, and their safety was evaluated by coculture of cells with scaffolds and *in vivo* transplantation of PDA-PLGA scaffold at different parts. On this basis, islet cells were inoculated into the PDA-PLGA scaffold to construct a cell-scaffold complex for *in vivo* transplantation in diabetic rats. After a preliminary study of its therapeutic effect on diabetes, the following important findings were obtained: 1) The PDA-PLGA scaffold had better biological safety, in which skeletal muscle stent transplantation has less impact on various indexes of the body and is conducive to angiogenesis, which also shows that skeletal muscle as a transplant site has a certain development potential. 2) The transplantation of islet cells in the skeletal muscle of diabetic rats with the PDA-PLGA scaffold could treat diabetes and lasts for approximately 3 weeks.

Biological scaffolds play a fundamental role in tissue engineering, which can provide mechanical and structural support for cell adhesion and tissue development, act as extracellular matrix, and create an environment for cell proliferation and differentiation (Hendow et al., 2016). As the main body of scaffolds, polymer materials such as PLGA, which have been used in the study of some diseases (Lin et al., 2014; Niu et al., 2014; Uma Maheshwari et al., 2014; Zheng et al., 2014; Sidney et al., 2015; Ebrahimi et al., 2016). Qian et al. (Qian et al., 2016) found that the hydrophilicity and mechanical properties of PLGA/PCL blended fibre scaffolds modified by PDA coating were significantly improved. In the experiment, we prepared PLGA fibre scaffold and treated with PDA coating. The results show that after PDA coating, the water contact angle of the scaffold decreases obviously, the hydrophilicity increases, the elastic modulus and tensile strength increase significantly, and the degradation rate can be slowed down, which is basically consistent with the conclusions of other researchers.

Biosafety is an important prerequisite for the clinical application of scaffolds. Rim et al. (Rim et al., 2012) showed that the surface modification of a PLA scaffold with a PDA coating could enhance the adhesion of mesenchymal stem cells to the fibre surface. Jeong et al. (Wang et al., 2011) used PDA to modify the surface of polymethyl methacrylate (PMMA) and found that it improved the biological binding of the material and promoted the proliferation of corneal epithelial cells and corneal stromal cells. We selected inflammatory cells, vascular endothelial cells, skeletal muscle cells, islet cells, adipose mesenchymal stem cells and other different cell lines for *in vitro* experiments, and the study shows that the cells can adhere to the fibre surface of the stent well. At present, research on PDA is mainly focused on the cellular level, but there are few experimental studies on *in vivo* transplantation, and there are no studies evaluating its safety *in vivo*. New nanomedicine strategy shown to be effective in improving tissue inflammation in diseases (Shi et al., 2022). We selected three different sites of rats to evaluate the safety of different transplantation sites. By comparison, skeletal muscle transplantation had the least effect on serum biochemical indexes, although the transplanted PDA-PLGA scaffold caused certain inflammatory reactions as a foreign body. The level of TNF-α increased, but with the extension of time, the level of inflammatory factors decreased gradually. Obvious cell infiltration and collagen accumulation could be found on the surface of the transplanted materials by HE and Masson staining. Angiogenesis could be found in the subcutaneous transplantation group and skeletal muscle transplantation group from the 7th day. Early angiogenesis was important for the survival of the grafts. The sections of the main organs of each group were stained with HE, and compared with the control group, no significant difference was found. In summary, the PDA-PLGA scaffold prepared in this study showed good biological safety in preclinical *in vivo* and *in vitro* experiments. Skeletal muscle as a stent transplantation site has less impact on various indicators of the body and is conducive to angiogenesis, so it may be a good site for cell transplantation.

Islet cell transplantation, as a promising alternative to total pancreatic transplantation, has been greatly developed in the past few years. However, this therapy also faces a number of challenges: for example, the function of the transplanted islet cells continues to decline due to the maladaptive nature of the implantation site (Brusko et al., 2021). A major technical obstacle in the cell transplantation process is the difficulty of islet β-cells surviving in the patient. Some studies have pointed out that more than half of the injected islets are acutely damaged after transplantation, liver islet injections can also lead to islet cell death and substantial loss due to severe inflammatory reactions and inadequate islet haemodialysis (Moberg et al., 2002; Augsornworawat et al., 2020). However, unlike whole-tissue transplantation, the location selection and implantation parameters of β-cell transplantation are highly flexible. Therefore, in order to improve the survival rate after β-cell transplantation, researchers need breakthroughs in the following two main directions: first, to find more suitable transplantation sites. Second, material-based adjuvants.

Studies have shown that in the field of islet transplantation, sodium alginate has been used for islet cell transplantation through microcapsules and giant capsules (Dang et al., 2013; Khanna et al., 2013; Chen et al., 2015; Llacua et al., 2016). In addition, Kim JS et al. (Kim et al., 2019) implanted a flake PLGA scaffold coated with hypo-MSCs (mesenchymal stem cells cultured in hypoxia) subcutaneously with islet cells in mice, which also confirmed its therapeutic effect on diabetes. At present, there is no study on the use of PDA-PLGA scaffold in the treatment of islet cell transplantation. To explore whether the PDA-PLGA scaffold can be used as a carrier to carry islet cells for *in vivo* transplantation for the treatment of diabetes, we cocultured PDA-PLGA scaffold with RINm5f cells to construct the transplantation complex and, according to previous experimental results, determined the site of skeletal muscle as the treatment site of diabetic cell transplantation. Some studies have shown that skeletal muscle, as a key target organ for glucose utilization, shows high blood oxygen tension, meets the requirements of islet cells for the microenvironment and is an ideal islet implantation site (Wolf-Van Buerck et al., 2015). In this study, we found that the PDA-PLGA scaffold had no effect on islet cell secretion, and could promote glucose consumption and glucose uptake in C2C12. At the animal level, the cell-scaffold complex was transplanting into the skeletal muscle of diabetic rats. The results showed that the fasting blood glucose of the rats in the transplantation group decreased significantly, and the therapeutic effect disappeared on the 28th day after transplantation. It is speculated that the transplanted islet cells are affected by rejection, tissue mechanical pressure and fibrosis, resulting in cell death gradually, so it still needs to be improved to further prolong the cell survival time. We will try to combine scaffolds with hydrogel, matrix glue and other materials to enhance the mechanical strength of the scaffold, reduce the effect of inflammatory cell affinity on the growth of islet cells, and prolong the survival time of islet cells.

CONCLUSION

In this study, we prepared polydopamine-coated nanofibre scaffolds (PDA-PLGA). In the follow-up experiment, we cocultured islet cells with scaffolds and transplanted them into the skeletal muscle of diabetic rats. The results showed that the skeletal muscle as the transplantation site for PDA-PLGA cell scaffold could reduce the blood glucose in diabetic rats successfully and lasted for approximately 3 weeks, which further indicated the skeletal muscle transplantation site was a new choice for islet cell transplantation in the future.

DATA AVAILABILITY STATEMENT

The original contributions presented in the study are included in the article/**Supplementary Material**, further inquiries can be directed to the corresponding authors.

ETHICS STATEMENT

The animal study was reviewed and approved by the Ethics Committee for the Use of Experimental Animals of Jilin University [SYXK (Ji) 2018-0001].

AUTHOR CONTRIBUTIONS

MSZ, LC, and MZ have made contributions to conception and design; MSZ, HWD, YQG, and WYZ collected data, MSZ, JYL, SSW, and HRL analysed and interpreted data; MSZ and HH have been involved in drafting the manuscript and revising it critically for important intellectual content.

FUNDING

This work was supported by funds from Science and Technology Development Projects of Jilin Province (20180201025YY) and Talent Special Project of Jilin Province (JLSWSRCZX 2020-019). Interdisciplinary Integration and Innovation Project of JLU (JLUXKJC2021ZZ06), the Science and Technology Development Projects of Changchun (21ZY18), the Scientific Research Project of Jilin Provincial Department of Education (JJKH20221104KJ).

SUPPLEMENTARY MATERIAL

The Supplementary Material for this article can be found online at: https://www.frontiersin.org/articles/10.3389/fbioe.2022.927348/full#supplementary-material

REFERENCES

Augsornworawat, P., Maxwell, K. G., Velazco-Cruz, L., and Millman, J. R. (2020). Single-Cell Transcriptome Profiling Reveals β Cell Maturation in Stem Cell-Derived Islets after Transplantation. *Cell Rep.* 32 (8), 108067. doi:10.1016/j.celrep.2020.108067

Bennet, W., Groth, C.-G., Larsson, R., Nilsson, B., and Korsgren, O. (2000). Isolated Human Islets Trigger an Instant Blood Mediated Inflammatory Reaction: Implications for Intraportal Islet Transplantation as a Treatment for Patients with Type 1 Diabetes. *Upsala J. Med. Sci.* 105 (2), 125–133. doi:10.1517/03009734000000059

Brusko, T. M., Russ, H. A., and Stabler, C. L. (2021). Strategies for Durable β Cell Replacement in Type 1 Diabetes. *Science* 373 (6554), 516–522. doi:10.1126/science.abh1657

Cantarelli, E., Melzi, R., Mercalli, A., Sordi, V., Ferrari, G., Lederer, C. W., et al. (2009). Bone Marrow as an Alternative Site for Islet Transplantation. *Blood* 114 (20), 4566–4574. doi:10.1182/blood-2009-03-209973

Chen, T., Yuan, J., Duncanson, S., Hibert, M. L., Kodish, B. C., Mylavaganam, G., et al. (2015). Alginate Encapsulant Incorporating CXCL12 Supports Long-Term Allo- and Xenoislet Transplantation without Systemic Immune Suppression. *Am. J. Transpl.* 15 (3), 618–627. doi:10.1111/ajt.13049

Christoffersson, G., Carlsson, P.-O., and Phillipson, M. (2011). Intramuscular Islet Transplantation Promotes Restored Islet Vascularity. *Islets* 3 (2), 69–71. doi:10.4161/isl.3.2.14997

Dang, T. T., Thai, A. V., Cohen, J., Slosberg, J. E., Siniakowicz, K., Doloff, J. C., et al. (2013). Enhanced Function of Immuno-Isolated Islets in Diabetes Therapy by Co-Encapsulation with an Anti-inflammatory Drug. *Biomaterials* 34 (23), 5792–5801. doi:10.1016/j.biomaterials.2013.04.016

Ebrahimi, E., Akbarzadeh, A., Abbasi, E., Khandaghi, A. A., Abasalizadeh, F., and Davaran, S. (2016). Novel Drug Delivery System Based on Doxorubicin-Encapsulated Magnetic Nanoparticles Modified with PLGA-PEG1000 Copolymer. *Artif. Cells, Nanomed. Biotechnol.* 44 (1), 290–297. doi:10.3109/21691401.2014.944646

Frei, A. W., Li, Y., Jiang, K., Buchwald, P., and Stabler, C. L. (2018). Local Delivery of Fingolimod from Three-Dimensional Scaffolds Impacts Islet Graft Efficacy and Microenvironment in a Murine Diabetic Model. *J. Tissue Eng. Regen. Med.* 12 (2), 393–404. doi:10.1002/term.2464

Hendow, E. K., Guhmann, P., Wright, B., Sofokleous, P., Parmar, N., and Day, R. M. (2016). Biomaterials for Hollow Organ Tissue Engineering. *Fibrogenes. Tissue Repair* 9 (1), 3. doi:10.1186/s13069-016-0040-6

Hong, S., Kim, K. Y., Wook, H. J., Park, S. Y., Lee, K. D., Lee, D. Y., et al. (2011). Attenuation of the *In Vivo* Toxicity of Biomaterials by Polydopamine Surface Modification. *Nanomedicine* 6 (5), 793–801. doi:10.2217/nnm.11.76

Khanna, O., Huang, J.-J., Moya, M. L., Wu, C.-W., Cheng, M.-H., Opara, E. C., et al. (2013). FGF-1 Delivery from Multilayer Alginate Microbeads Stimulates a Rapid and Persistent Increase in Vascular Density. *Microvasc. Res.* 90, 23–29. doi:10.1016/j.mvr.2013.08.006

Kim, J. S., Jung, Y., Kim, S. H., Shin, J. S., Kim, S. H., and Park, C. G. (2019). Vascularization of PLGA-Based Bio-Artificial Beds by Hypoxia-Preconditioned Mesenchymal Stem Cells for Subcutaneous Xenogeneic Islet Transplantation. *Xenotransplantation* 26 (1), e12441. doi:10.1111/xen.12441

Lee, H., Dellatore, S. M., Miller, W. M., and Messersmith, P. B. (2007). Mussel-Inspired Surface Chemistry for Multifunctional Coatings. *Science* 318 (5849), 426–430. doi:10.1126/science.1147241

Lin, C.-C., Fu, S.-J., Lin, Y.-C., Yang, I.-K., and Gu, Y. (2014). Chitosan-coated Electrospun PLA Fibers for Rapid Mineralization of Calcium Phosphate. *Int. J. Biol. Macromol.* 68, 39–47. doi:10.1016/j.ijbiomac.2014.04.039

Llacua, A., de Haan, B. J., Smink, S. A., and de Vos, P. (2016). Extracellular Matrix Components Supporting Human Islet Function in Alginate-Based Immunoprotective Microcapsules for Treatment of Diabetes. *J. Biomed. Mater. Res.* 104 (7), 1788–1796. doi:10.1002/jbm.a.35706

Middleton, J. C., and Tipton, A. J. (2000). Synthetic Biodegradable Polymers as Orthopedic Devices. *Biomaterials* 21 (23), 2335–2346. doi:10.1016/s0142-9612(00)00101-0

Moberg, L., Johansson, H., Lukinius, A., Berne, C., Foss, A., Källen, R., et al. (2002). Production of Tissue Factor by Pancreatic Islet Cells as a Trigger of Detrimental Thrombotic Reactions in Clinical Islet Transplantation. *Lancet* 360 (9350), 2039–2045. doi:10.1016/s0140-6736(02)12020-4

Niu, Y., Chen, K. C., He, T., Yu, W., Huang, S., and Xu, K. (2014). Scaffolds from Block Polyurethanes Based on Poly(ε-Caprolactone) (PCL) and Poly (Ethylene Glycol) (PEG) for Peripheral Nerve Regeneration. *Biomaterials* 35 (14), 4266–4277. doi:10.1016/j.biomaterials.2014.02.013

Perez, V. L., Caicedo, A., Berman, D. M., Arrieta, E., Abdulreda, M. H., Rodriguez-Diaz, R., et al. (2011). The Anterior Chamber of the Eye as a Clinical Transplantation Site for the Treatment of Diabetes: a Study in a Baboon Model of Diabetes. *Diabetologia* 54 (5), 1121–1126. doi:10.1007/s00125-011-2091-y

Perez-Basterrechea, M., Esteban, M. M., Vega, J. A., and Obaya, A. J. (2018). Tissue-engineering Approaches in Pancreatic Islet Transplantation. *Biotechnol. Bioeng.* 115 (12), 3009–3029. doi:10.1002/bit.26821

Qian, J., Xu, W., Yong, X., Jin, X., and Zhang, W. (2014). Fabrication and *In Vitro* Biocompatibility of Biomorphic PLGA/nHA Composite Scaffolds for Bone Tissue Engineering. *Mater. Sci. Eng. C* 36, 95–101. doi:10.1016/j.msec.2013.11.047

Qian, Y., Chen, H., Xu, Y., Yang, J., Zhou, X., Zhang, F., et al. (2016). The Preosteoblast Response of Electrospinning PLGA/PCL Nanofibers: Effects of Biomimetic Architecture and Collagen I. *Int. J. Nanomed.* 11, 4157–4171. doi:10.2147/IJN.S110577

Rajab, A. (2010). Islet Transplantation: Alternative Sites. *Curr. Diab Rep.* 10 (5), 332–337. doi:10.1007/s11892-010-0130-6

Rengifo, H. R., Giraldo, J. A., Labrada, I., and Stabler, C. L. (2014). Long-Term Survival of Allograft Murine Islets Coated via Covalently Stabilized Polymers. *Adv. Healthc. Mater.* 3 (7), 1061–1070. doi:10.1002/adhm.201300573

Rim, N. G., Kim, S. J., Shin, Y. M., Jun, I., Lim, D. W., Park, J. H., et al. (2012). Mussel-inspired Surface Modification of Poly(l-Lactide) Electrospun Fibers for Modulation of Osteogenic Differentiation of Human Mesenchymal Stem Cells. *Colloids Surfaces B Biointerfaces* 91, 189–197. doi:10.1016/j.colsurfb.2011.10.057

Roden, M. (2016). Diabetes Mellitus: Definition, Classification and Diagnosis. *Wien Klin. Wochenschr* 128 Suppl 2 (2), S37–S40. doi:10.1007/s00508-015-0931-3

Salazar-Bañuelos, A., Benitez-Bribiesca, L., Sigalet, D. L., Korbutt, G., and Wright, J. R. (2010). Bone Marrow as a Site for Pancreatic Islet Transplantation. *Blood* 115 (17), 3643–3644. doi:10.1182/blood-2009-12-256826

Shen, H., Xu, B., Yang, C., Xue, W., You, Z., Wu, X., et al. (2022). A DAMP-Scavenging, IL-10-releasing Hydrogel Promotes Neural Regeneration and Motor Function Recovery after Spinal Cord Injury. *Biomaterials* 280, 121279. doi:10.1016/j.biomaterials.2021.121279

Shi, C., Dawulieti, J., Shi, F., Yang, C., Qin, Q., Shi, T., et al. (2022). A Nanoparticulate Dual Scavenger for Targeted Therapy of Inflammatory Bowel Disease. *Sci. Adv.* 8 (4), eabj2372. doi:10.1126/sciadv.abj2372

Sidney, L. E., Heathman, T. R., Britchford, E. R., Abed, A., Rahman, C. V., and Buttery, L. D. (2015). Investigation of Localized Delivery of Diclofenac Sodium from Poly (D, L-Lactic Acid-Co-Glycolic Acid)/Poly (Ethylene Glycol) Scaffolds Using an *In Vitro* Osteoblast Inflammation Model. *Tissue Eng. Part A* 21 (1), 362–373. doi:10.1089/ten.TEA.2014.0100

Tu, Z., Zhong, Y., Hu, H., Shao, D., Haag, R., Schirner, M., et al. (2022). Design of Therapeutic Biomaterials to Control Inflammation. *Nat. Rev. Mater* 28, 1–18. doi:10.1038/s41578-022-00426-z

Uma Maheshwari, S., Samuel, V. K., and Nagiah, N. (2014). Fabrication and Evaluation of (PVA/HAp/PCL) Bilayer Composites as Potential Scaffolds for Bone Tissue Regeneration Application. *Ceram. Int.* 40 (6), 8469–8477. doi:10.1016/j.ceramint.2014.01.058

Vlahos, A. E., Cober, N., and Sefton, M. V. (2017). Modular Tissue Engineering for the Vascularization of Subcutaneously Transplanted Pancreatic Islets. *Proc. Natl. Acad. Sci. U.S.A.* 114 (35), 9337–9342. doi:10.1073/pnas.1619216114

Wang, L., Jeong, K. J., Chiang, H. H., Zurakowski, D., Behlau, I., Chodosh, J., et al. (2011). Hydroxyapatite for Keratoprosthesis Biointegration. *Invest. Ophthalmol. Vis. Sci.* 52 (10), 7392–7399. doi:10.1167/iovs.11-7601

Wolf-Van Buerck, L., Schuster, M., Baehr, A., Mayr, T., Guethoff, S., Abicht, J., et al. (2015). Engraftment and Reversal of Diabetes after Intramuscular Transplantation of Neonatal Porcine Islet-like Clusters. *Xenotransplantation* 22 (6), 443–450. doi:10.1111/xen.12201

Yang, X., Zhan, P., Wang, X., Zhang, Q., Zhang, Y., Fan, H., et al. (2020). Polydopamine-assisted PDGF-BB Immobilization on PLGA Fibrous Substrate Enhances Wound

Healing via Regulating Anti-inflammatory and Cytokine Secretion. *PLoS One* 15 (9), e0239366. doi:10.1371/journal.pone.0239366

Zhao, X., Han, Y., Li, J., Cai, B., Gao, H., Feng, W., et al. (2017). BMP-2 Immobilized PLGA/hydroxyapatite Fibrous Scaffold via Polydopamine Stimulates Osteoblast Growth. *Mater. Sci. Eng. C* 78, 658–666. doi:10.1016/j.msec.2017.03.186

Zheng, R., Duan, H., Xue, J., Liu, Y., Feng, B., Zhao, S., et al. (2014). The Influence of Gelatin/PCL Ratio and 3-D Construct Shape of Electrospun Membranes on Cartilage Regeneration. *Biomaterials* 35 (1), 152–164. doi:10.1016/j.biomaterials.2013.09.082

Conflict of Interest: The authors declare that the research was conducted in the absence of any commercial or financial relationships that could be construed as a potential conflict of interest.

Publisher's Note: All claims expressed in this article are solely those of the authors and do not necessarily represent those of their affiliated organizations, or those of the publisher, the editors and the reviewers. Any product that may be evaluated in this article, or claim that may be made by its manufacturer, is not guaranteed or endorsed by the publisher.

frontiers | Frontiers in Bioengineering and Biotechnology

ORIGINAL RESEARCH
published: 30 June 2022
doi: 10.3389/fbioe.2022.919189

Intracellular K^+-Responsive Block Copolymer Micelles for Targeted Drug Delivery of Curcumin

*Mingyue Jiang[1,2], Le Chen[1,3], Bo Chen[1], Qinghua Yu[1,2], Xianming Zhang[1,2], Weihong Jing[1,2], Limei Ma[1,3], Tao Deng[1,2], Zhangyou Yang[1,2] and Chao Yu[1,2,3]**

[1]Chongqing Key Laboratory for Pharmaceutical Metabolism Research, College of Pharmacy, Chongqing Medical University, Chongqing, China, [2]Research Center of Pharmaceutical Preparations and Nanomedicine, College of Pharmacy, Chongqing Medical University, Chongqing, China, [3]Chongqing Pharmacodynamic Evaluation Engineering Technology Research Center, College of Pharmacy, Chongqing Medical University, Chongqing, China

Curcumin (CUR) is a natural bioactive compound that has attracted attention as a "golden molecule" due to its therapeutic properties against several types of tumors. Nonetheless, the antitumor application of CUR is hampered due to its extremely low aqueous solubility and chemical instability. Herein, a novel type of CUR-loaded polymeric micelles with intracellular K^+-responsive controlled-release properties is designed and developed. The polymeric micelles are self-assembled by poly (*N*-isopropylacrylamide-*co*-acryloylamidobenzo-15-crown-5-*co*-*N*, *N*-dimethylacrylamide)-b-DSPE (PNDB-b-DSPE) block copolymers, and CUR. CUR is successfully loaded into the micelles with a CUR loading content of 6.26 wt%. The proposed CUR-PNDB-DSPE polymeric micelles exhibit a significant CUR release in simulated intracellular fluid due to the formation of 2 : 1 ''sandwich'' host–guest complexes of 15-crown-5 and K^+, which lead to the hydrophilic outer shell of micelles to collapse and the drug to rapidly migrate out of the micelles. *In vitro*, the B16F10 cell experiment indicates that CUR-PNDB-DSPE micelles exhibit a high cellular uptake and excellent intracellular drug release in response to the intracellular K^+ concentration. Moreover, CUR-PNDB-DSPE micelles show high cytotoxicity to B16F10 cells compared to free CUR and CUR-PEG-DSPE micelles. The polymeric micelles with intracellular K^+-responsive controlled release properties proposed in this study provide a new strategy for designing novel targeted drug delivery systems for CUR delivery for cancer treatment.

Keywords: curcumin, polymer micelles, K^+ -triggered drug release, responsive host–guest system, anticancer

OPEN ACCESS

Edited by:
Mingqiang Li,
Third Affiliated Hospital of Sun Yat-Sen University, China

Reviewed by:
Dan Shao,
South China University of Technology, China
Yingshuai Wang,
Weifang Medical University, China
Jie Tang,
The University of Queensland, Australia

****Correspondence:***
Chao Yu
yuchao@cqmu.edu.cn

Specialty section:
This article was submitted to Biomaterials, a section of the journal Frontiers in Bioengineering and Biotechnology

Received: *13 April 2022*
Accepted: *20 May 2022*
Published: *30 June 2022*

Citation:
Jiang M, Chen L, Chen B, Yu Q, Zhang X, Jing W, Ma L, Deng T, Yang Z and Yu C (2022) Intracellular K^+-Responsive Block Copolymer Micelles for Targeted Drug Delivery of Curcumin. Front. Bioeng. Biotechnol. 10:919189. doi: 10.3389/fbioe.2022.919189

INTRODUCTION

Curcumin (CUR) is a natural bioactive compound found in turmeric that has attracted attention as a "golden molecule" due to its therapeutic properties against several types of tumors (Sharma et al., 2005; Fan et al., 2013; Zoi et al., 2021). Nonetheless, the antitumor application of CUR is hampered because of its extremely low aqueous solubility and chemical instability, resulting in low bioavailability and fast metabolism (Siviero et al., 2015; Nelson et al., 2017). Nano-based drug delivery systems have been exploited to improve CUR solubility, protect CUR against hydrolysis and enzymatic reduction, and facilitate targeted accumulation in tumor tissues (Naksuriya et al., 2014; D'Angelo et al., 2021; Tu et al., 2022). Polymeric micelles, able to encapsulate hydrophobic drugs in

the micelle core, have gathered significant interest as nano-based drug delivery systems to deliver CUR because of their good biocompatibility, prolonged blood circulation, and modified release pattern (Yadav et al., 2020; Machtakova et al., 2022). Moreover, to achieve site-specific release at targeting regions, stimuli-responsive polymeric micelles have been designed to respond to environmental stimuli such as tumor extracellular and/or intracellular microenvironment (Wang et al., 2016; Cabral et al., 2018; Shao et al., 2020; Shi et al., 2022). Particularly, stimuli-responsive polymeric micelles that could achieve controlled intracellular release of drugs exert significant therapeutic effects for reducing the leakage of the drug in the systemic circulation and maximizing the drug release to the targeted tumor cells. Potassium ion (K^+) plays an important role in biological systems, where the normal serum K^+ level in the human body is in the range of 3.5–5.5 mM, while the value of the intracellular K^+ concentration is about 30 times that of the extracellular K^+ concentration (Kuo et al., 2001; Armstrong, 2003). Therefore, the design and preparation of stimuli-responsive polymeric micelles that can recognize the signal of intracellular K^+ concentration for controlled intracellular release of CUR are of great significance in cancer treatment.

To date, a lot of investigations have been carried out on stimuli-responsive polymeric micelles loaded with CUR for cancer treatment, in which most polymeric micelles are designed in response to endogenous stimuli including variations in pH (Yu et al., 2014; Cai et al., 2016), redox potential (Li et al., 2018; Zhao et al., 2020), and enzyme concentration (Li et al., 2017). For instance, polymeric micelles designed to respond to pH changes, acidic interstitial pH (pH 6.5–7.2), or endosomal/lysosomal pH (pH 6.5–4.5) are usually equipped with ionizable groups or pH-cleavable linkages and can release CUR intratumorally or intracellularly (Bae et al., 2003; Mura et al., 2013). However, it is difficult to achieve satisfactory pH-responsive release in response to such subtle pH variation. Redox-sensitive polymeric micelles can be modified with disulfide bonds for drug conjugation or cross-linking, which are cleaved by elevated glutathione in the cytosol (2–10 mM), which is 1000-fold higher than the levels at the extracellular fluid (Kuppusamy et al., 2002; Lopez-Mirabal and Winther, 2008). Moreover, enzyme-sensitive micelles can be prepared by introducing moieties in the building segments which are selectively recognized and degraded by enzymes overexpressed in interstitial or intracellular environments (Andresen et al., 2010). Nevertheless, the core-shell structure of polymeric micelles may limit the access of bulky enzymes to the enzyme-cleavable moieties within the core, thus reducing the drug release rate. In addition, as aforementioned, there is an obvious variation in K^+ concentration between extracellular (3.5–5.5 mM) and intracellular fluid (140–150 mM). However, until now, K^+-responsive polymeric micelles encapsulating CUR with controlled-release behaviors have not been reported yet. It has been reported that crown ether 15-crown-5 can selectively recognize and capture K^+ by forming stable 2 : 1 "sandwich-type" host–guest complexes (Yu et al., 2013; Jiang et al., 2014; Jiang et al., 2016). K^+-responsive micelles self-assembled by poly (ethylene glycol)-b-poly (*N*-isopropylacry-lamide-*co*-benzo-18-crown-6-acrylamide) (PEG-b-P(NIPAM-*co*-B18C6Am)) block copolymers have been reported to load prednisolone acetate (Yan et al., 2017). However, the therapeutic properties of the micelles are not studied, and these micelles should be stored in solution at 45 °C, which limits their further use. Therefore, the design and preparation of the K^+-responsive micelles loaded with CUR that can recognize intracellular K^+ signals and achieve adjustable controlled release characteristics are of great importance for treating cancer.

In this study, we develop a novel type of CUR-loaded polymeric micelles with intracellular K^+-responsive drug-release properties. Poly (*N*-isopropylacrylamide-*co*-acryloylamidobenzo-15-crown-5-*co*-*N*, *N*-dimethylacrylamide) (PNDB) copolymers with 15-crown-5 as the K^+ sensor are used as the hydrophilic block, which presents an obvious K^+-responsive hydrophilic/hydrophobic phase transition. Inspired by *N*-(carbonyl-methoxypolyethylene glycol)-1,2-distearoyl-sn-glycero-3-phosphoethanolamine (mPEG-DSPE), which has been approved by the FDA for medical applications, DSPE is used as the hydrophobic block. As illustrated in **Scheme 1**, when the environmental K^+ concentration is low, PNDB copolymers present a hydrophilic and swollen state at normal physiological temperature (37°C). The micelles are self-assembled by PNDB-b-DSPE block copolymers and CUR. The hydrophobic DSPE segments in the copolymers form the micellar core that acts as a reservoir for CUR, while the hydrophilic and swollen PNDB copolymers form the micellar shell that can maintain colloidal stability. After isothermally transferring into the intracellular fluid, where the environmental K^+ concentration is significantly increased, the adjacent 15-crown-5 receptors capture K^+ to form stable 2 : 1 "sandwich-type" host–guest complexes, which would disrupt the hydrogen bonding between the oxygen atoms in 15-crown-5 and the hydrogen atoms of water, resulting in the hydrophobic and shrunken state of PNDB copolymers. Therefore, the hydrophilic outer shell collapses, and the drug can migrate out of the micelles in intracellular fluid, and thus micelles exhibit a fast release of CUR. CUR-PNDB-DSPE micelles demonstrate an obvious cellular uptake and excellent intracellular drug release in the B16F10 cell study. Moreover, CUR-PNDB-DSPE micelles show high cytotoxicity to B16F10 cells compared to that of free CUR and CUR-PEG-DSPE micelles. The results in this study provide valuable guidance for designing novel targeted drug delivery systems serving as a delivery vehicle for CUR with intracellular K^+-responsive controlled release properties.

MATERIALS AND METHODS

Materials

N-isopropylacrylamide (NIPAM, purchased from Rhawn) is purified by recrystallization with a hexane/acetone mixture (v/v, 50/50). Benzo-15-crown-5-acrylamide (B15C5Am) is synthesized from 4′-nitro-benzo-15-crown-5 (NB15C5, TCI) according to previously reported procedures (Mi et al., 2008; Mi et al., 2010). *N*, *N*-dimethylacrylamide (DMAm, Sigma-Aldrich) is passed through a previously washed prepacked column of inhibitor removers (Aldrich). 2,2′-

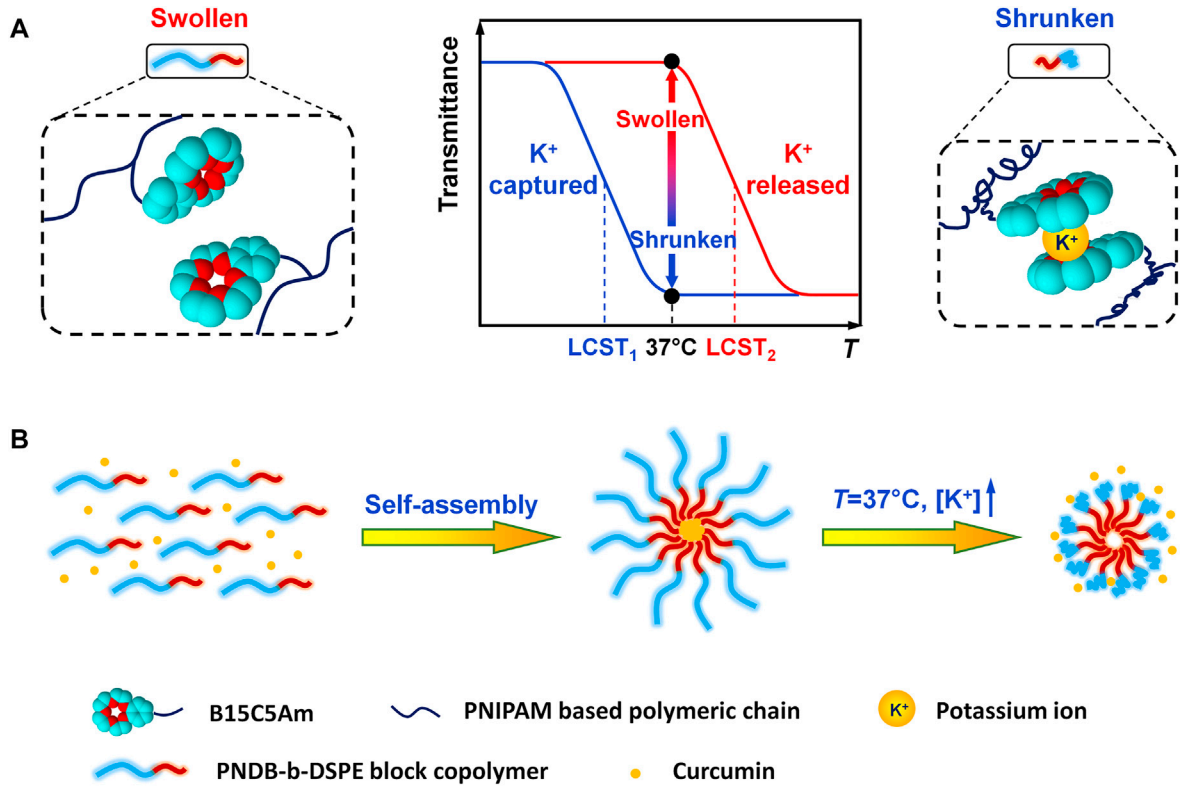

SCHEME 1 | Schematic illustration of K^+-responsive behavior of CUR-PNDB-DSPE micelles. **(A)** Different states of block copolymers responding to K^+. **(B)** Self-assembly of block copolymers to form micelles and K^+-responsive drug release of micelles.

azoisobutyronitrile (AIBN, Aladdin) is used after recrystallization with ethanol. 2-(dodecylthiocarbonothioylthio)-2-methylpropanoic acid (DDMAT, Adamas), 1, 2-distearoyl-sn-glycero-3-phosphoethanolamine (DSPE, Aladdin), 1-(3-dimethylaminopropyl)-3-ethyl carbodiimide hydrochloride (EDC, Rhawn), *N*-hydroxysuccinimide (NHS, Rhawn), curcumin (Macklin), and mPEG-DSPE (2000Da, Macklin) are used without further purification. All solvents and other chemicals are of analytical grade and used as received. Deionized water (18.2 MΩ, 25°C) from a water purification system (Research Water Purification Technology Co., Ltd, China) is used throughout this study.

Synthesis of Block Copolymers

The proposed PNDB-b-DSPE copolymers are prepared by a two-step reaction method combining the reversible addition-fragmentation chain transfer polymerization (RAFT) method and condensation reaction. The detailed synthesis route is illustrated in **Supplementary Scheme S1**. First, carboxyl-terminated PNDB copolymers are prepared by thermally initiated RAFT of NIPAM, B15C5Am, and DMAm comonomers in 1,4-dioxane with DDMAT as the transfer agent and AIBN as the initiator. The concentration of total monomers (NIPAM, B15C5Am, and DMAm) is 0.3 mol·L^{-1}, and the molar ratios of B15C5Am, AIBN, and DDMAT to the total comonomers are kept constant at 20 mol%, 1 mol%, and 0.8 mol%, respectively. The reaction solution is bubbled with N_2 gas for 20 min to remove dissolved oxygen and then is heated to 70 °C to initiate the copolymerization. The copolymerization is carried out at 70 °C for 4 h under an N_2 atmosphere. The obtained PNDB copolymers solution is diluted with tetrahydrofuran and purified three times by reprecipitation with excess of methyl tert-butyl ether from tetrahydrofuran to thoroughly remove the unreacted monomers and impurities and then dried under vacuum. The lower critical solution temperature (LCST) of copolymers can be flexibly controlled by adjusting the molar ratios of the DMAm monomer during the synthesis process, and the theoretical feeding molar ratios of DMAm to the total monomers are designed as 50, 60, and 70 mol%, which are labeled as PNDB1, PNDB2, and PNDB3, respectively.

Next, PNDB-b-DSPE block copolymers are synthesized by the condensation reaction of carboxyl-terminated PNDB and DSPE by using EDC and NHS as dehydration catalysts. Briefly, the dispersion of carboxyl-terminated PNDB copolymers in chloroform that mixed with EDC and NHS is stirred below 4°C for 20 min under an N_2 atmosphere. DSPE dissolved in chloroform with a small amount of triethylamine is then added dropwise to the mixed solution, and the reaction is carried out for 24 h. Then, the synthesized copolymers are purified by dialysis (cutoff 1,000 Da) against deionized water. The prepared PNDB-b-DSPE block copolymers are obtained by freeze-drying. Three kinds of PNDB-b-DSPE block copolymers with different mole

ratios of DMAm are synthesized and labeled as PNDB-b-DSPE1, PNDB-b-DSPE2, and PNDB-b-DSPE3.

Compositional Characterizations of Block Copolymers

The chemical compositions of carboxyl-terminated PNDB and PNDB-b-DSPE copolymers are confirmed by Fourier transform infrared spectroscopy (FT-IR, Nicolet iS5, Thermo Fisher Scientific) by using the KBr disc technique. The compositions of the copolymers are determined by nuclear magnetic resonance spectrometry (^{1}H NMR, Bruker, America). The weighted average molecular weight of PNDB-b-DSPE is determined by gel permeation chromatography (GPC, Waters-2410, Waters) using tetrahydrofuran as the mobile phase and polystyrene as the standard. The critical micelle concentration (CMC) values of PNDB-b-DSPE block copolymers are determined using a fluorescence spectrometer (RF-5301PC, Shimadzu), and pyrene is used as a fluorescent probe.

Characterization of K^+-Responsive Behaviors of Block Copolymers

The K^+-responsive behaviors of carboxyl-terminated PNDB and PNDB-b-DSPE copolymers with different contents of DMAm units are comprehensively investigated by measuring their corresponding LCST values in aqueous solutions containing K^+ ions with different concentrations. An aqueous solution with K^+ concentration of 5 mM and Na^+ concentration of 150 mM is regarded as the simulated extracellular fluid, and the aqueous solution with K^+ concentration of 150 mM and Na^+ concentration of 5 mM is regarded as the simulated intracellular fluid. The LCST values of the copolymers are evaluated by measuring the optical transmittance of the copolymer aqueous solutions at 500 nm as a function of temperature using a UV–Vis spectrophotometer (UV-2600, Shimadzu) equipped with a temperature-controlled cell (TCC-100, Shimadzu). The LCST value is defined as the temperature at which the optical transmittance decreases to half of the initial value. To minimize salting-out effects, nitrates are chosen as the model salts (Inomata et al., 1992; Zhang et al., 2005). The concentrations of the block copolymers in different aqueous solutions are all fixed at 0.5 wt%.

Preparation of Micelles

CUR-loaded micelles are prepared by a thin-film hydration method. Briefly, PNDB-b-DSPE copolymers and CUR (mass ratio, 10:1) are dissolved in methanol. The organic solvent is removed by rotary evaporation at 37°C, and the thin film is hydrated with PBS at 37°C for 1 h. The micelle solution (CUR-PNDB-DSPE micelles) is filtered through a 0.22-μm syringe filter (Jinteng, China) to remove free curcumin, lyophilized, and stored at 4°C for further use. Blank micelles are synthesized by using the same procedure without encapsulation of CUR. In addition, CUR-loaded micelles self-assembled by mPEG-DSPE copolymers and CUR (CUR-PEG-DSPE micelles) served as the control group.

Characterization of Micelles

The hydrodynamic diameters and zeta potentials of micelles are measured by dynamic light scattering (DLS, ZEN3690, Malvern) with highly diluted micelle dispersions in aqueous solutions. Moreover, the hydrodynamic diameters of CUR-PNDB-DSPE micelles in serum (10%, v/v) are monitored for 24 h. The size and morphology of micelles are observed by a transmission electron microscope (TEM, JEM-1200EX, JEOL). The micelles are diluted with distilled water and dropped on a copper grid covered with nitrocellulose. All specimens for TEM measurements are dried at room temperature and negatively stained with 2% phosphotungstic acid before observation. Encapsulation efficiency (EE) and loading content (LC) of CUR are detected by UV–Vis spectrophotometer (UV-2600, Shimadzu). EE is calculated by using the mass ratio of their loaded drug to the initially fed drug, while LC is calculated by using the mass ratio of their loaded drug to the drug-loaded micelles.

Characterization of K^+-Responsive Controlled-Release Behaviors of Micelles

In vitro drug release behavior of micelles is performed by dialysis in simulated extracellular fluid or simulated intracellular fluid with 0.5 wt% Tween 80. The molecular weight cutoff size of the dialysis membrane is 3,000 Da. Briefly, 5 ml of CUR-PNDB-DSPE micelles and CUR-PEG-DSPE micelle solution are placed into a dialysis bag, sealed on both ends, and immersed in the dissolution medium (50 ml) under 100 rpm stirring at 37°C. At the predetermined time intervals, 1 ml of the solution is withdrawn from the release medium and replaced by an equal volume of fresh medium. With suitable dilution, the concentrations of CUR in the release medium are determined by a UV–Vis spectrophotometer at 426 nm.

Cell Culture

Metastatic murine melanoma cells (B16F10) are incubated in Dulbecco's modified Eagle's medium nutrient mixture F12 (DMEM/F12, Gibco) containing 10% fetal bovine serum (FBS, Bio-Channel) and 1% antibiotic (penicillin/streptomycin/amphotericin B, Beyotime) solution in a humidified atmosphere with 5% CO_2 at 37°C.

Cellular Uptake and Intracellular Drug Release

The cellular uptake and intracellular drug release of CUR-loaded micelles are evaluated by using a fluorescence microscope. B16F10 cells are seeded into a 24-well plate with 1×10^5 cells per well on sterile coverslips and incubated for 24 h. Subsequently, the medium is replaced, and then the cells are incubated with free CUR, CUR-PNDB-DSPE micelles, or CUR-PEG-DSPE micelles, with the same concentration of CUR at 20 μg mL^{-1}, for 1, 4, and 8 h, respectively. Free CUR solutions are prepared by using DMSO to improve the solubility, and the final concentration of DMSO in the culture medium is 0.2% (v/v). After incubation, the cells are washed with ice-cold PBS and fixed with 4% polyoxymethylene for 20 min. Then, the samples are

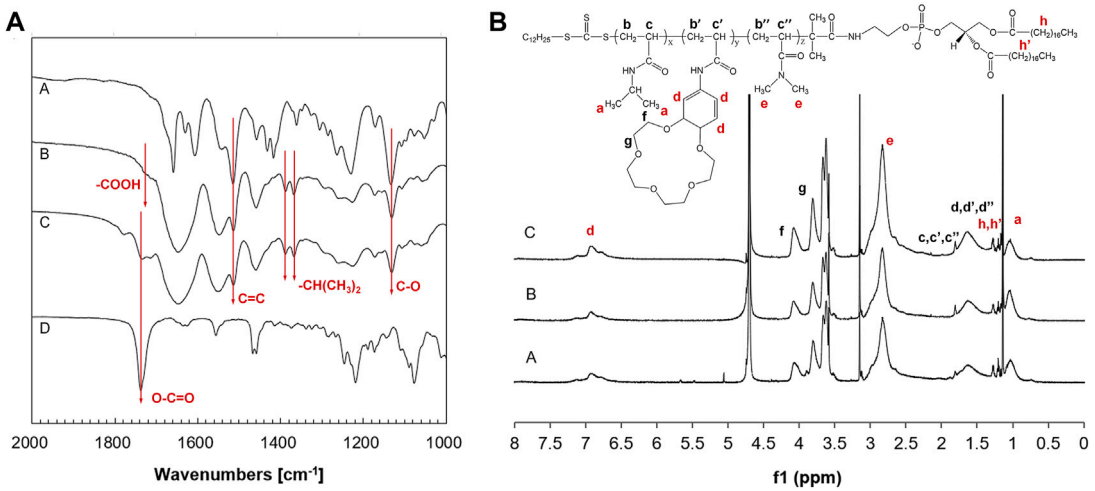

FIGURE 1 | (A) FT-IR spectra of B15C5Am (Curve A), PNDB (Curve B), PNDB-b-DSPE (Curve C), and DSPE (Curve D). **(B)** 1H NMR spectra of PNDB-b-DSPE1 (Curve A), PNDB-b-DSPE2 (Curve B), and PNDB-b-DSPE3 (Curve C) block copolymers.

washed with PBS three times followed by staining with DAPI in a dark environment. Finally, the prepared samples are observed using a laser scanning confocal microscope (CLSM, Leica, Germany).

Cytotoxicity Assays

B16F10 cells are seeded in 96-well plates at a density of 1×10^4 cells per well and cultured for 24 h. After that, the culture medium is replaced by free CUR, CUR-PNDB-DSPE micelles, and CUR-PEG-DSPE micelles at concentrations of CUR equivalents ranging from 0.078–20 μg mL^{-1}. Blank PNDB-DSPE micelles without encapsulation of CUR are used as vehicle control, with concentrations of PNDB-DSPE copolymers ranging from 20–400 μg mL^{-1}. The cells are incubated for 24 and 48 h. Afterward, in the dark, fresh culture medium (100 μL) containing CCK-8 solution (10 μL, 5 mg/ml in PBS) is added and incubated for 2 h. Then, the absorbance at 450 nm is measured by using a Varioskan LUX microplate reader (Thermo Fisher Scientific, United States). Cell viability is calculated according to the absorbance values.

RESULTS AND DISCUSSION

Compositional Characterizations of Block Copolymers

FT-IR spectra of carboxyl-terminated PNDB and PNDB-b-DSPE copolymers are shown in **Figure 1A**. From the FT-IR spectra, successful fabrications of carboxyl-terminated PNDB and PNDB-b-DSPE copolymers are confirmed. Specifically, the characteristic bands of a benzo-15-crown-5 group of B15C5Am (Curve A), including a strong peak at 1,513 cm^{-1} (shoulder peak) for C=C skeletal stretching vibration in the phenyl ring, a peak at 1,130 cm^{-1} for C–O asymmetric stretching vibration in R–O–R', and double peaks at 1,386 cm^{-1} and 1,367 cm^{-1} for isopropyl group of NIPAM, are both found in the FT-IR spectra of carboxyl-terminated PNDB (Curve B) and PNDB-b-DSPE copolymers (Curve C). Furthermore, the weak characteristic peak at 1718 cm^{-1} for the carboxylic group in the FT-IR spectrum of carboxyl-terminated PNDB (Curve B) disappears in the FT-IR spectrum of PNDB-b-DSPE copolymers (Curve C), and the characteristic peak at 1737 cm^{-1} for the ester group of DSPE (Curve D) is found in the FT-IR spectrum of PNDB-b-DSPE copolymers (Curve C), which indicates the successful chemical modification of DSPE on the carboxyl-terminated PNDB.

^{1}H NMR spectra are used to further confirm the chemical structure of the block copolymers as shown in **Figure 1B**. The ^{1}H chemical shifts at around 1, 7, and 2.8 ppm are the characteristic peaks of protons on the isopropyl, benzene ring, and methyl groups, respectively. Calculated from the ^{1}H NMR results, the molar ratio of DMAm to total monomers of PNDB1, PNDB2, and PNDB3 is 56.93, 60.23, and 65.58%, respectively, which is similar with corresponding theoretical feeding molar ratios. In addition, the molecular weights of copolymers are also measured by the GPC method shown in **Supplementary Figure S1**, and the number of average molecular weights (M_n) of PNDB-b-DSPE1, PNDB-b-DSPE2, and PNDB-b-DSPE3 is 2,300, 2,510, and 2,550, respectively. Thus, mPEG-DSPE with molecular weights of 2000 is used to prepare micelles as a control group for further study.

K+-Responsive Behaviors of Block Copolymers

The effects of different cations on the stability of micelles result from the hydrophilic–hydrophobic states of the block copolymers. The effects of K^+, Na^+, Mg^{2+}, and Ca^{2+} ions, which are the main cations in the human body, on the phase transition behaviors of PNB copolymers have been systematically investigated in the reported study (Yu et al., 2013). The results indicate that PNB copolymers only show good selectivity and sensitivity toward K^+ among those cations, which is mainly caused by the formation of stable 2:1 (ligand/ion) "sandwich-type" host–guest complexes between 15-crown-5 units and K^+

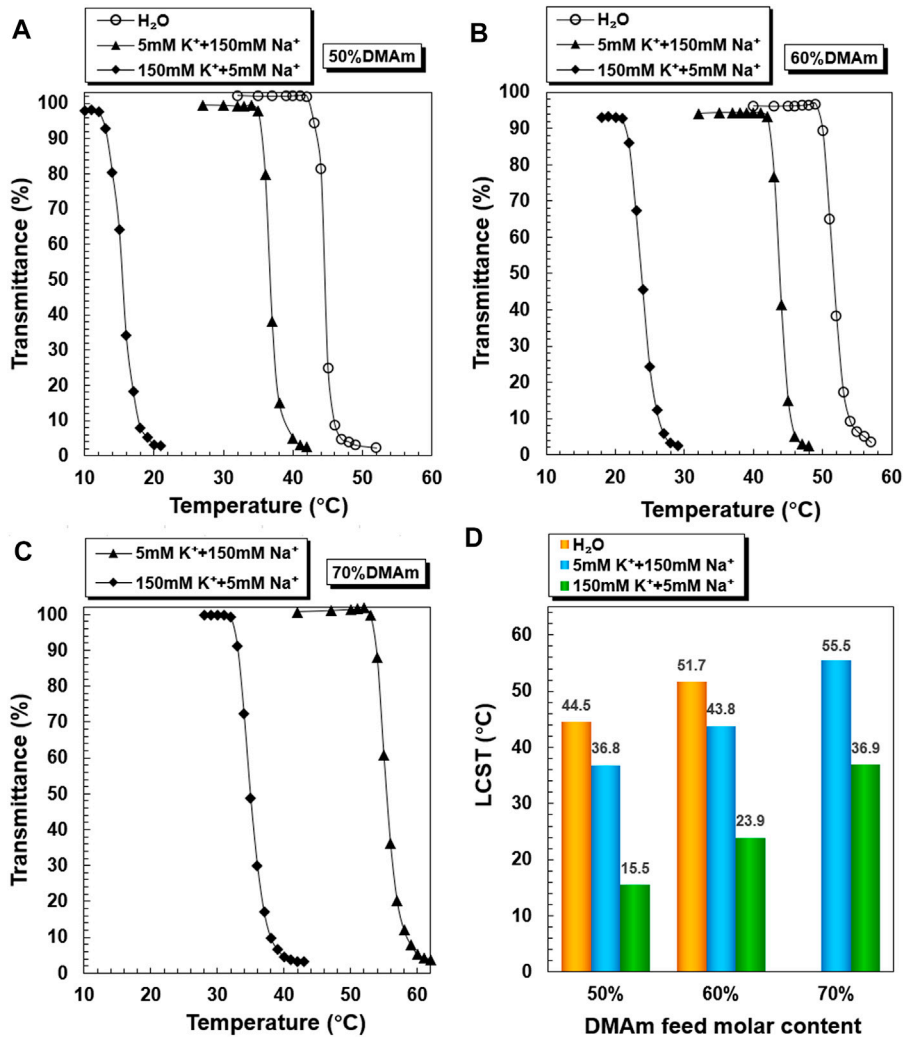

FIGURE 2 | K^+-responsive behaviors of PNDB copolymers. Temperature-dependent phase transition behaviors of PNDB1 **(A)**, PNDB2 **(B)**, and PNDB3 **(C)** copolymer solutions with different K^+ concentration levels. LCST values of PNDB1, PNDB2, and PNDB3 copolymer solutions with different K^+ concentration levels **(D)**.

ions, which leads to the contraction of copolymers. However, other cations cannot form stable 2:1 host–guest complexes with 15-crown-5 units. Therefore, only the effects of K^+ concentrations on the LCST values of the PNDB-b-DSPE block copolymers are investigated.

The temperature-dependent transmittance changes of PNDB1, PNDB2, and PNDB3 copolymer solutions with different K^+ concentrations are shown in **Figures 2A–C**. As expected, by increasing the temperature, PNDB1, PNDB2, and PNDB3 copolymer solutions with different K^+ concentrations all undergo a rapid optical transmittance change when the environmental temperature varies across a corresponding temperature region due to the excellent thermoresponsive property of the PNIPAM chain, while with introducing crown ether 15-crown-5 units in the copolymers, the LCST of PNDB1, PNDB2, and PNDB3 copolymers exhibits an obvious negative shift in K^+ solution compared with that of deionized water. Such a distinct change in the phase transition temperature results from the formation of stable 2:1 "sandwich" host–guest complexes of 15-crown-5 with K^+, whereas the phase transition behaviors of PNDB3 copolymers with a 70% DMAm feeding ratio in water, with relatively high LCSTs, are not presented since it is beyond the detection limit of the instrument. With increasing K^+ concentration from 5 to 150 mM, the negative shift degree of LCST is increased due to the formation of more 2:1 "sandwich" host–guest complexes. For PNDB1, PNDB2, and PNDB3, the LCST values are 36.8, 43.8, and 55.5°C in the simulated extracellular fluid and dramatically decrease to 15.5, 23.9, and 36.9°C, respectively, in the simulated intracellular fluid (**Figure 2D**). As indicated, the LCST values in simulated extracellular and intracellular fluids of PNDB copolymers increase with increasing molar ratio of DMAm in PNDB copolymers (Katsumoto et al., 2005). It is reported that, on the one hand, an increased molar ratio of DMAm in NIPAM-based copolymers leads to fewer hydrogen donors for intramolecular hydrogen bonding, and on the other hand, more thermal energy is

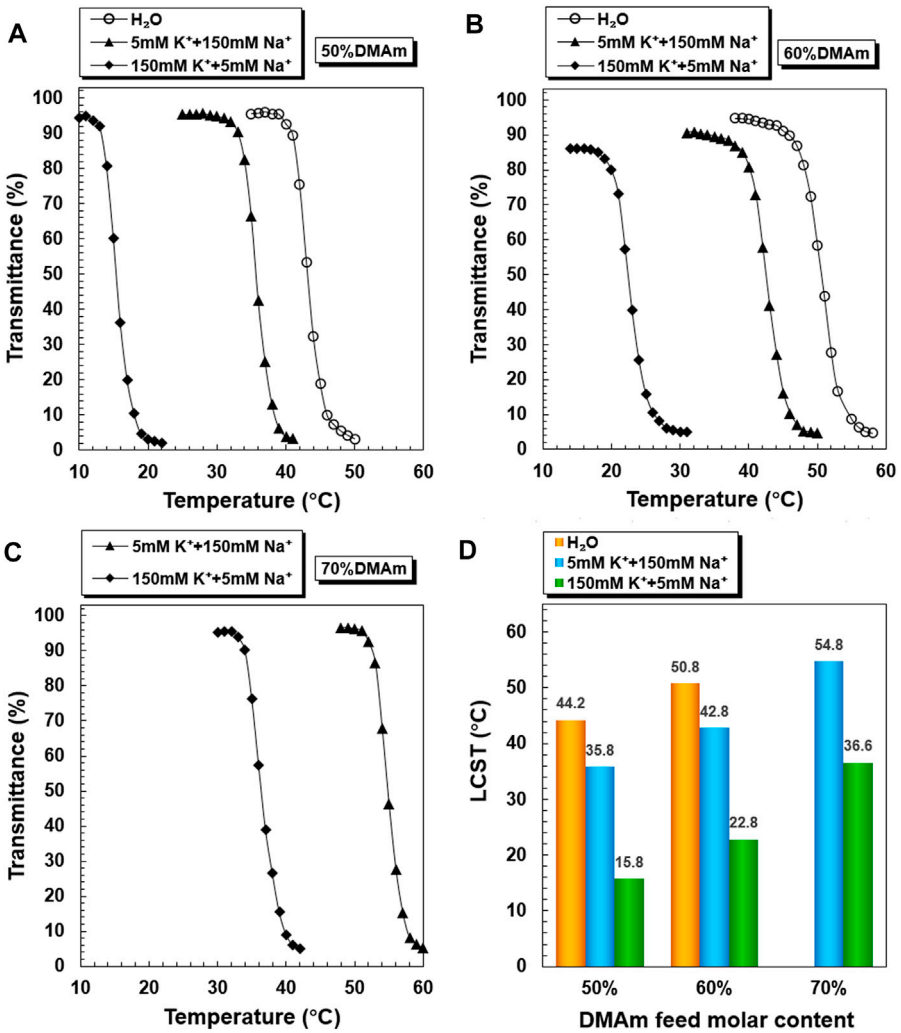

FIGURE 3 | K^+-responsive behaviors of PNDB-b-DSPE block copolymers. Temperature-dependent phase transition behaviors of PNDB-b-DSPE1 **(A)**, PNDB-b-DSPE2 **(B)**, and PNDB-b-DSPE3 **(C)** copolymer solutions with different K^+ concentration levels. LCST values of PNDB-b-DSPE1, PNDB-b-DSPE2, and PNDB-b-DSPE3 copolymer solutions with different K^+ concentration levels.

required for dehydrating the C=O groups of DMAm and increasing the strength of intramolecular hydrogen bonding among neighboring units for DMAm. Thus, an increased molar ratio of DMAm could improve the hydrophilicity of the PNDB copolymers and increase the corresponding LCST values.

PNDB-b-DSPE1, PNDB-b-DSPE2, and PNDB-b-DSPE3 solutions with different K^+ concentrations exhibit similar LCST shifts (**Figure 3**). The LCST values of PNDB-b-DSPE1, PNDB-b-DSPE2, and PNDB-b-DSPE3 block copolymers in simulated extracellular and intracellular fluids are almost the same as those of the corresponding PNDB1, PNDB2, and PNDB3 copolymers. That is, the combination of a DSPE block barely affects the K^+-responsive behaviors of PNDB copolymers. When the ambient temperature is set at a certain temperature between the two LCSTs of PNDB-DSPE block copolymers in simulated extracellular and intracellular solution, block copolymers can change from a hydrophilic state to a hydrophobic state. In this study, normal physiological temperature (37°C) is chosen as the certain temperature. Herein, to achieve a successful intracellular drug release, the LCST values of PNDB-b-DSPE block copolymers need to be lower than 37°C in the simulated extracellular fluid and higher than 37°C in the simulated intracellular fluid. Therefore, PNDB-b-DSPE2 is chosen in this study to prepare micelles for subsequent experiments due to its appropriate LCST values in simulated intracellular and extracellular fluids and the large LCST shift values. In addition, the CMC value of PNDB-b-DSPE2 is 12 mg L^{-1} (**Supplementary Figure S2**).

Characterization of Micelles

The prepared micelles are self-assembled by PNDB-b-DSPE2 copolymers and CUR. The morphology and size distribution of the micelles are characterized by TEM and DLS, respectively. As shown in **Figure 4**, blank PNDB-DSPE micelles and CUR-PNDB-DSPE micelles disperse well and exhibit good spherical shapes and fine monodispersity. The average diameters of dried blank PNDB-DSPE micelles and CUR-PNDB-DSPE micelles are about 60 and

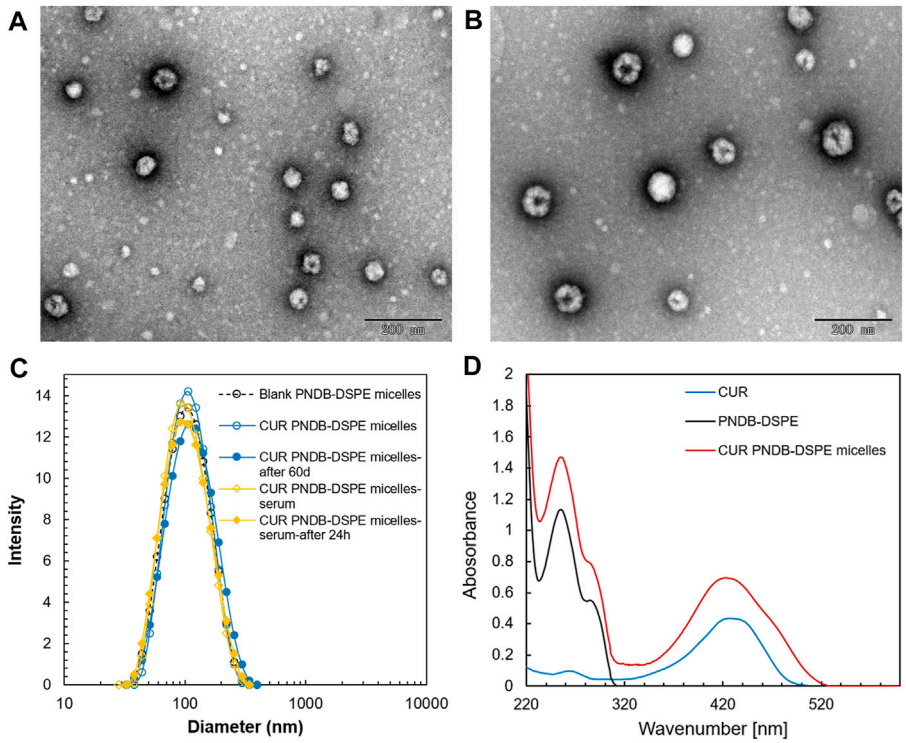

FIGURE 4 | TEM images of blank PNDB-DSPE micelles **(A)** and CUR-PNDB-DSPE micelles **(B)**. Hydrodynamic size distributions of blank PNDB-DSPE micelles and CUR-PNDB-DSPE micelles **(C)**. The UV–Vis analysis of free CUR, blank PNDB-DSPE micelles, and CUR-PNDB-DSPE micelles **(D)**.

80 nm, respectively. The hydrodynamic diameters of blank PNDB-DSPE micelles and CUR-PNDB-DSPE micelles are about 95 and 100 nm, respectively, with polydispersity index (PDI) values of 0.141 and 0.129, respectively. Moreover, their size distribution nearly remains the same even after 60 days in storage, indicating the good stability of the prepared micelles. Moreover, the hydrodynamic diameter of CUR-PNDB-DSPE micelles in serum is monitored, and significant variation of diameter after 24 h incubation in serum is not observed, which indicates that the stability of CUR-PNDB-DSPE micelles is not influenced by serum. The zeta potential of blank PNDB-DSPE micelles and CUR-PNDB-DSPE micelles is −4.84 and −11.73 mV, respectively. For the UV–Vis analysis, the absorption spectra of CUR-PNDB-DSPE micelles display absorption peaks at approximately 255 and 426 nm, which attribute to PNDB-b-DSPE copolymers and CUR, respectively, and thus confirm the successful synthesis of micelles. Moreover, CUR-loading content (LC) and encapsulation efficiency (EE) of CUR-loaded micelles are 6.62 and 58.27%, respectively.

K^+-Responsive Controlled-Release Behaviors of Micelles

Figure 5 shows the *in vitro* release profiles of CUR from the CUR-PEG-DSPE micelles and CUR-PNDB-DSPE micelles at 37°C in simulated extracellular and intracellular fluids, respectively. As shown in **Figure 5A**, the release behaviors of CUR from CUR-PEG-DSPE micelles in simulated extracellular and intracellular fluids are almost the same, where both exhibit a burst release followed by a sustained slow release, reaching 23.75 and 24.87% at 37°C within 72 h, respectively. That is, the variation of K^+ concentration nearly does not affect the drug release behaviors of CUR-PEG-DSPE micelles, which indicates that the CUR-PEG-DSPE micelles do not have K^+-responsive controlled-release properties. In contrast, CUR-PNDB-DSPE micelles yield a much faster release in simulated intracellular fluids, while the same slow release is observed in simulated extracellular fluids and reaches 78.30 and 27.73% at 37°C within 72 h (**Figure 5B**). The results indicate that the drug release behavior of the CUR-PNDB-DSPE micelles is greatly affected by the environmental K^+ concentration. Such K^+-responsive controlled release properties of CUR-PNDB-DSPE micelles are achieved by altering the stability of the core-shell structure of micelles in response to the change in K^+ concentration. The core-shell structure of CUR-PNDB-DSPE micelles could keep stable when the K^+ concentration is about 5 mM, and CUR-PNDB-DSPE micelles demonstrate a slow drug release rate. When the K^+ concentration is increased to 150 mM, the hydrophilic outer shell collapses due to the formation of 2 : 1 "sandwich" host–guest complexes of 15-crown-5 and K^+, and the drug can migrate out of the micelles, and thus CUR-PNDB-DSPE micelles exhibit a fast release (Fleige et al., 2012).

Thus, CUR-PNDB-DSPE micelles are stable in simulated extracellular fluids while unstable in simulated intracellular fluids. Neither the early release of drug in a normal physiological environment nor the incapable drug release in the tumor sites

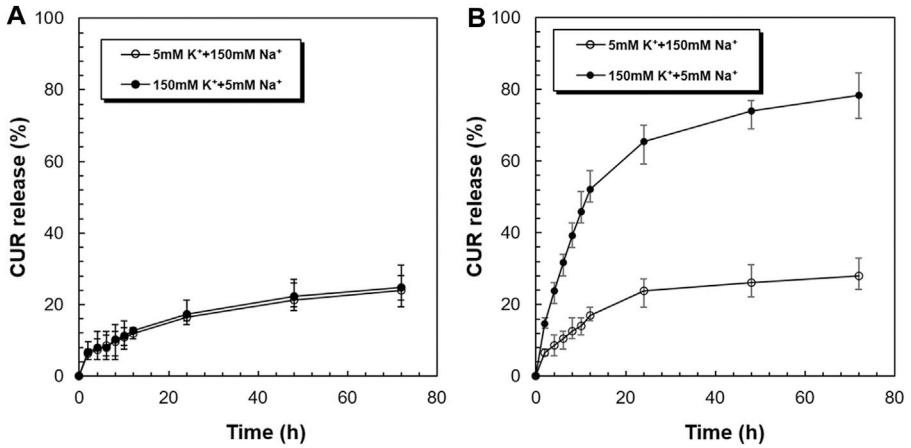

FIGURE 5 | K^+-responsive controlled-release behaviors of CUR from CUR-PEG-DSPE micelles **(A)** and CUR-PNDB-DSPE micelles **(B)** in simulated extracellular and intracellular fluids.

can achieve a satisfactory therapeutic effect on solid tumors. Since the CUR-PNDB-DSPE micelles remain stable in a normal physiological environment and exhibit rapid drug release in intracellular fluid, these micelles are expected to be an appropriate candidate to deliver anticancer drugs for cancer therapy.

Cellular Uptake and Intracellular Drug Release

CUR has been reported to show anticancer activity against several types of tumors including melanoma, which is discussed herein, and B16F10 cells are used in further study. B16F10 cells are incubated with free CUR, CUR-PEG-DSPE micelles, and CUR-PNDB-DSPE micelles at an equal CUR concentration of 20 μg mL^{-1} for 1, 4, and 8 h, respectively, and then visualized under a fluorescence microscope to assess cellular uptake and intracellular drug release behaviors of the nanocarriers (**Figure 6**). The results demonstrate that these micelles are actively taken up by B16F10 cells as seen by green fluorescence within the cells. CUR-PNDB-DSPE micelles could rapidly accumulate in the cytosol of cells in 1 h revealed by bright green fluorescence compared to the cells treated with free CUR and CUR-PEG-DSPE micelles, which resulted in less intense fluorescence in the cytosol, indicating that CUR-PNDB-DSPE micelles exhibit a much higher cellular uptake. Furthermore, the intensity of green fluorescence in the cytosol after micelle treatment is much brighter after 4 h than in the 1 h treatment. Interestingly, comparing green fluorescence intensity in the cytosol after incubation for 8 h with 4 h, it is almost the same for cells treated with CUR-PNDB-DSPE micelles, while cells treated with free CUR and CUR-PEG-DSPE micelles all exhibit increased fluorescence intensity by increasing incubation time. The results demonstrate successful CUR release of CUR-PNDB-DSPE micelles due to the degradation of micelles in response to the high intracellular K^+ concentration in the cells, and the release behaviors of CUR-PNDB-DSPE micelles can almost be completed within 4 h. Thus, the prepared CUR-PNDB-DSPE micelles have great potential as drug nanocarriers for excellent intracellular drug release in response to the intracellular K^+ concentration.

Cytotoxicity Assays

To further evaluate the therapeutic efficacy of various CUR formulations, B16F10 cells are incubated with free CUR, CUR-PEG-DSPE micelles, and CUR-PNDB-DSPE micelles at CUR concentrations ranging from 3.125 to 25 μg mL^{-1} for 24 and 48 h. The results of cell viabilities are shown in **Figure 7**. After 24 h incubation, there is no significant cytotoxicity for free CUR and CUR formulations at low concentrations as 3.125 μg mL^{-1}, and then the cell viability decreases with increasing CUR concentrations of free CUR and CUR formulations. When the concentrations exceed 6.25 μg mL^{-1}, the toxicity of CUR-PNDB-DSPE micelles increases rapidly and is higher than that of CUR-PEG-DSPE micelles. When at the same CUR concentration, such as 12.5 μg mL^{-1}, the toxicity of CUR-PNDB-DSPE micelles (33.6%) is significantly greater than that of CUR-PEG-DSPE micelles (46.7%). The results are consistent with the cellular uptake results. That is, CUR-PNDB-DSPE micelles could exhibit a high cellular uptake and excellent intracellular drug release in response to the intracellular K^+ concentration and thus lead to increased cytotoxicity when compared to CUR-PEG-DSPE micelles. To verify whether the increased cytotoxicity of the CUR-PNDB-DSPE micelles is caused by the copolymers, a cytotoxicity assay of blank PNDB-DSPE micelles is performed, which shows good cell compatibility (**Supplementary Figure S3**). Moreover, free CUR also exhibits an obvious cytotoxicity property, which could be attributed to DMSO used to improve the solubility of CUR, which is toxic and could induce cell damage (Hanslick et al., 2009; Pal et al., 2011). Compared with incubation for 24 h, the cytotoxicity of free CUR and CUR formulations at various CUR concentrations is all increased after incubation for 48 h. For instance, when CUR concentration is 25 μg mL^{-1}, the toxicity of free CUR, CUR-PEG-DSPE micelles, and CUR-PNDB-DSPE

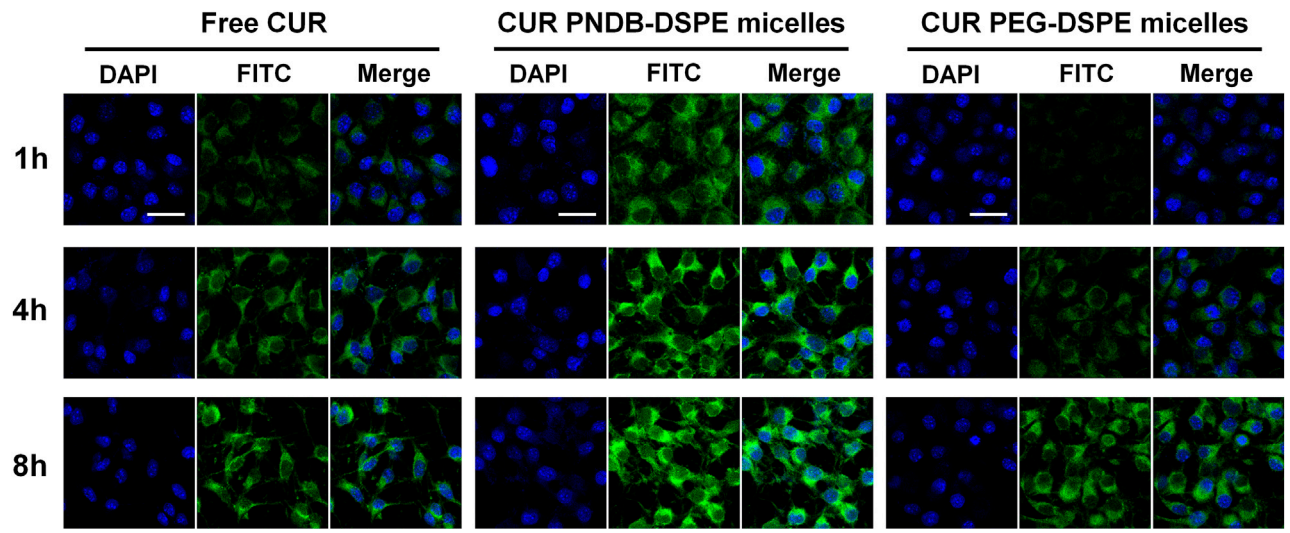

FIGURE 6 | Confocal images of B16F10 cells incubated with free CUR, CUR-PEG-DSPE micelles, and CUR-PNDB-DSPE micelles for 1, 4, and 8 h at an equal CUR concentration of 20 μg mL^{-1}; bars indicate 25 μm.

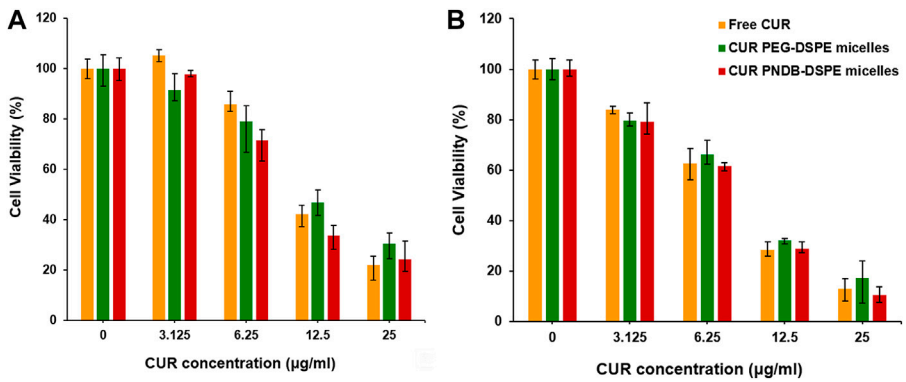

FIGURE 7 | Cytotoxicity evaluation of B16F10 cells incubated with free CUR, CUR-PEG-DSPE micelles, and CUR-PNDB-DSPE micelles for 24 h **(A)** and 48 h **(B)** at different CUR concentration levels ranging from 3.125 to 20 μg mL^{-1}.

micelles after incubation for 24 and 48 h is 21.8%, 30.4%, and 24.3% and 12.8%, 17.3%, and 10.4%, respectively. The results indicate that CUR-PNDB-DSPE micelles show a high cytotoxicity to B16F10 cells and are expected to be an appropriate candidate for melanoma treatment.

CONCLUSION

A novel type of polymeric micelles with intracellular K^+-responsive controlled-release properties based on the responsive host–guest system has been successfully developed for delivering CUR. The polymeric micelles are self-assembled by PNDB-b-DSPE block copolymers and CUR, and the hydrophobic DSPE segments in the copolymers form the micellar core that acts as a reservoir for CUR, while the PNDB copolymers form the micellar shell with an obvious K^+-responsive hydrophilic/hydrophobic phase transition behavior. The proposed CUR-PNDB-DSPE polymeric micelles exhibit good spherical shapes and fine monodispersity. When the environmental K^+ concentration is significantly increased as the simulating intracellular fluid, the adjacent 15-crown-5 receptors in PNDB copolymers capture K^+ to form stable 2 : 1 "sandwich-type" host–guest complexes, resulting in the hydrophilic outer shell to collapse and micelles to exhibit a fast release of CUR. CUR-PNDB-DSPE micelles demonstrate a high cellular uptake and excellent intracellular drug release in response to the intracellular K^+ concentration of B16F10 cells. Moreover, CUR-PNDB-DSPE micelles show significant cytotoxicity to B16F10 cells compared to free CUR and CUR-PEG-DSPE micelles. The results in this study provide valuable guidance for designing and developing novel polymeric micelles with intracellular K^+-responsive

controlled release properties for delivering CUR for melanoma treatment.

DATA AVAILABILITY STATEMENT

The original contributions presented in the study are included in the article/**Supplementary Material**; further inquiries can be directed to the corresponding author.

AUTHOR CONTRIBUTIONS

MJ and CY designed the research. MJ, LC, BC, QY, XZ, and WJ performed the research. MJ, LM, TD, ZY, and CY analyzed the data. MJ and CY wrote the manuscript.

FUNDING

The authors gratefully acknowledge support from the Natural Science Foundation of Chongqing (cstc2021jcyj-msxmX0246), the Special Postdoctoral Foundation of Chongqing (2010010005416933), and the Postdoctoral Foundation of Chongqing Medical University (YXY2019BSH1).

SUPPLEMENTARY MATERIAL

The Supplementary Material for this article can be found online at: https://www.frontiersin.org/articles/10.3389/fbioe.2022.919189/full#supplementary-material

REFERENCES

Andresen, T. L., Thompson, D. H., and Kaasgaard, T. (2010). Enzyme-Triggered Nanomedicine: Drug Release Strategies in Cancer Therapy. *Mol. Membr. Biol.* 27 (7), 353–363. doi:10.3109/09687688.2010.515950

Armstrong, C. M. (2003). The Na/K Pump, Cl Ion, and Osmotic Stabilization of Cells. *Proc. Natl. Acad. Sci. U. S. A.* 100 (10), 6257–6262. doi:10.1073/pnas.0931278100

Bae, Y., Fukushima, S., Harada, A., and Kataoka, K. (2003). Design of Environment-Sensitive Supramolecular Assemblies for Intracellular Drug Delivery: Polymeric Micelles that are Responsive to Intracellular Ph Change. *Angew. Chem. Int. Ed.* 42 (38), 4640–4643. doi:10.1002/anie.200250653

Cabral, H., Miyata, K., Osada, K., and Kataoka, K. (2018). Block Copolymer Micelles in Nanomedicine Applications. *Chem. Rev.* 118 (14), 6844–6892. doi:10.1021/acs.chemrev.8b00199

Cai, X., Liu, M., Zhang, C., Sun, D., and Zhai, G. (2016). pH-Responsive Copolymers Based on Pluronic P123-Poly(β-Amino Ester): Synthesis, Characterization and Application of Copolymer Micelles. *Colloids Surfaces B Biointerfaces* 142, 114–122. doi:10.1016/j.colsurfb.2016.02.033

D'Angelo, N. A., Noronha, M. A., Kurnik, I. S., Câmara, M. C. C., Vieira, J. M., Abrunhosa, L., et al. (2021). Curcumin Encapsulation in Nanostructures for Cancer Therapy: A 10-Year Overview. *Int. J. Pharm.* 604, 120534. doi:10.1016/j.ijpharm.2021.120534

Fan, X., Zhang, C., Liu, D.-b., Yan, J., and Liang, H.-p. (2013). The Clinical Applications of Curcumin: Current State and the Future. *Curr. Pharm. Des.* 19 (11), 2011–2031. doi:10.2174/1381612811319110005

Fleige, E., Quadir, M. A., and Haag, R. (2012). Stimuli-Responsive Polymeric Nanocarriers for the Controlled Transport of Active Compounds: Concepts and Applications. *Adv. Drug Del. Rev.* 64 (9), 866–884. doi:10.1016/j.addr.2012.01.020

Hanslick, J. L., Lau, K., Noguchi, K. K., Olney, J. W., Zorumski, C. F., Mennerick, S., et al. (2009). Dimethyl Sulfoxide (Dmso) Produces Widespread Apoptosis in the Developing Central Nervous System. *Neurobiol. Dis.* 34 (1), 1–10. doi:10.1016/j.nbd.2008.11.006

Inomata, H., Goto, S., Otake, K., and Saito, S. (1992). Effect of Additives on Phase Transition of N-Isopropylacrylamide Gels. *Langmuir* 8 (2), 687–690. doi:10.1021/la00038a064

Jiang, M.-Y., Ju, X.-J., Deng, K., Fan, X.-X., He, X.-H., Wu, F., et al. (2016). The Microfluidic Synthesis of Composite Hollow Microfibers for K+-Responsive Controlled Release Based on a Host-Guest System. *J. Mat. Chem. B* 4 (22), 3925–3935. doi:10.1039/c6tb00333h

Jiang, M.-Y., Ju, X.-J., Fang, L., Liu, Z., Yu, H.-R., Jiang, L., et al. (2014). A Novel, Smart Microsphere with K(+)-Induced Shrinking and Aggregating Properties Based on a Responsive Host-Guest System. *ACS Appl. Mat. Interfaces* 6 (21), 19405–19415. doi:10.1021/am505506v

Katsumoto, Y., Tanaka, T., and Ozaki, Y. (2005). Molecular Interpretation for the Solvation of Poly(Acrylamide)S. I. Solvent-Dependent Changes in the Co Stretching Band Region of Poly(N,N-Dialkylacrylamide)S. *J. Phys. Chem. B* 109 (44), 20690–20696. doi:10.1021/jp052263r

Kuo, H.-C., Cheng, C.-F., Clark, R. B., Lin, J. J.-C., Lin, J. L.-C., Hoshijima, M., et al. (2001). A Defect in the Kv Channel-Interacting Protein 2 (Kchip2) Gene Leads to a Complete Loss of I-to and Confers Susceptibility to Ventricular Tachycardia. *Cell* 107 (6), 801–813. doi:10.1016/S0092-8674(01)00588-8

Kuppusamy, P., Li, H., Ilangovan, G., Cardounel, A. J., Zweier, J. L., Yamada, K., et al. (2002). Noninvasive Imaging of Tumor Redox Status and its Modification by Tissue Glutathione Levels. *Cancer Res.* 62 (1), 307–312.

Li, Y., Li, W., Bao, W., Liu, B., Li, D., Jiang, Y., et al. (2017). Bioinspired Peptosomes with Programmed Stimuli-Responses for Sequential Drug Release and High-Performance Anticancer Therapy. *Nanoscale* 9 (27), 9317–9324. doi:10.1039/c7nr00598a

Li, Y., Zou, Q., Yuan, C., Li, S., Xing, R., and Yan, X. (2018). Amino Acid Coordination Driven Self-Assembly for Enhancing Both the Biological Stability and Tumor Accumulation of Curcumin. *Angew. Chem. Int. Ed.* 57 (52), 17084–17088. doi:10.1002/anie.201810087

Lopez-Mirabal, H. R., and Winther, J. R. (2008). Redox Characteristics of the Eukaryotic Cytosol. *Biochim. Biophys. Acta* 1783 (4), 629–640. doi:10.1016/j.bbamcr.2007.10.013

Machtakova, M., Thérien-Aubin, H., and Landfester, K. (2022). Polymer Nano-Systems for the Encapsulation and Delivery of Active Biomacromolecular Therapeutic Agents. *Chem. Soc. Rev.* 51 (1), 128–152. doi:10.1039/d1cs00686j

Mi, P., Chu, L.-Y., Ju, X.-J., and Niu, C. H. (2008). A Smart Polymer with Ion-Induced Negative Shift of the Lower Critical Solution Temperature for Phase Transition. *Macromol. Rapid Commun.* 29 (1), 27–32. doi:10.1002/marc.200700546

Mi, P., Ju, X.-J., Xie, R., Wu, H.-G., Ma, J., and Chu, L.-Y. (2010). A Novel Stimuli-Responsive Hydrogel for K+-Induced Controlled-Release. *Polymer* 51 (7), 1648–1653. doi:10.1016/j.polymer.2010.02.018

Mura, S., Nicolas, J., and Couvreur, P. (2013). Stimuli-Responsive Nanocarriers for Drug Delivery. *Nat. Mat.* 12 (11), 991–1003. doi:10.1038/nmat3776

Naksuriya, O., Okonogi, S., Schiffelers, R. M., and Hennink, W. E. (2014). Curcumin Nanoformulations: A Review of Pharmaceutical Properties and Preclinical Studies and Clinical Data Related to Cancer Treatment. *Biomaterials* 35 (10), 3365–3383. doi:10.1016/j.biomaterials.2013.12.090

Nelson, K. M., Dahlin, J. L., Bisson, J., Graham, J., Pauli, G. F., and Walters, M. A. (2017). The Essential Medicinal Chemistry of Curcumin. *J. Med. Chem.* 60 (5), 1620–1637. doi:10.1021/acs.jmedchem.6b00975

Pal, R., Mamidi, M. K., Das, A. K., and Bhonde, R. (2011). Diverse Effects of Dimethyl Sulfoxide (Dmso) on the Differentiation Potential of Human Embryonic Stem Cells. *Arch. Toxicol.* 86, 651–661. doi:10.1007/s00204-011-0782-2

Shao, D., Zhang, F., Chen, F., Zheng, X., Hu, H., Yang, C., et al. (2020). Biomimetic Diselenide-Bridged Mesoporous Organosilica Nanoparticles as an X-Ray-

Responsive Biodegradable Carrier for Chemo-Immunotherapy. *Adv. Mat.* 32 (50), e2004385. doi:10.1002/adma.202004385

Sharma, R. A., Gescher, A. J., and Steward, W. P. (2005). Curcumin: The Story So Far. *Eur. J. Cancer* 41 (13), 1955–1968. doi:10.1016/j.ejca.2005.05.009

Shi, C., Dawulieti, J., Shi, F., Yang, C., Qin, Q., Shi, T., et al. (2022). A Nanoparticulate Dual Scavenger for Targeted Therapy of Inflammatory Bowel Disease. *Sci. Adv.* 8 (4), eabj2372. doi:10.1126/sciadv.abj2372

Siviero, A., Gallo, E., Maggini, V., Gori, L., Mugelli, A., Firenzuoli, F., et al. (2015). Curcumin, a Golden Spice with a Low Bioavailability. *J. Herb. Med.* 5 (2), 57–70. doi:10.1016/j.hermed.2015.03.001

Tu, Z., Zhong, Y., Hu, H., Shao, D., Haag, R., Schirner, M., et al. (2022). Design of Therapeutic Biomaterials to Control Inflammation. *Nat. Rev. Mat.* doi:10.1038/s41578-022-00426-z

Wang, S., Huang, P., and Chen, X. (2016). Stimuli-Responsive Programmed Specific Targeting in Nanomedicine. *ACS Nano* 10 (3), 2991–2994. doi:10.1021/acsnano.6b00870

Yadav, S., Sharma, A. K., and Kumar, P. (2020). Nanoscale Self-Assembly for Therapeutic Delivery. *Front. Bioeng. Biotechnol.* 8, 127. doi:10.3389/fbioe.2020.00127

Yan, S., Wan, L.-Y., Ju, X.-J., Wu, J.-F., Zhang, L., Li, M., et al. (2017). K(+) -Responsive Block Copolymer Micelles for Targeted Intracellular Drug Delivery. *Macromol. Biosci.* 17 (9), 1700143. doi:10.1002/mabi.201700143

Yu, H.-R., Ju, X.-J., Xie, R., Wang, W., Zhang, B., and Chu, L.-Y. (2013). Portable Diagnosis Method of Hyperkalemia Using Potassium-Recognizable Poly(N-Isopropylacrylamide-Co-Benzo-15-Crown-5-Acrylamide) Copolymers. *Anal. Chem.* 85 (13), 6477–6484. doi:10.1021/ac401028a

Yu, Y., Zhang, X., and Qiu, L. (2014). The Anti-Tumor Efficacy of Curcumin When Delivered by Size/Charge-Changing Multistage Polymeric Micelles Based on Amphiphilic Poly(Beta-Amino Ester) Derivates. *Biomaterials* 35 (10), 3467–3479. doi:10.1016/j.biomaterials.2013.12.096

Zhang, Y., Furyk, S., Bergbreiter, D. E., and Cremer, P. S. (2005). Specific Ion Effects on the Water Solubility of Macromolecules: Pnipam and the Hofmeister Series. *J. Am. Chem. Soc.* 127 (41), 14505–14510. doi:10.1021/ja0546424

Zhao, G., Sun, Y., and Dong, X. (2020). Zwitterionic Polymer Micelles with Dual Conjugation of Doxorubicin and Curcumin: Synergistically Enhanced Efficacy against Multidrug-Resistant Tumor Cells. *Langmuir* 36 (9), 2383–2395. doi:10.1021/acs.langmuir.9b03722

Zoi, V., Galani, V., Lianos, G. D., Voulgaris, S., Kyritsis, A. P., and Alexiou, G. A. (2021). The Role of Curcumin in Cancer Treatment. *Biomedicines* 9 (9), 1086. doi:10.3390/biomedicines9091086

Conflict of Interest: The authors declare that the research was conducted in the absence of any commercial or financial relationships that could be construed as a potential conflict of interest.

Publisher's Note: All claims expressed in this article are solely those of the authors and do not necessarily represent those of their affiliated organizations, or those of the publisher, the editors, and the reviewers. Any product that may be evaluated in this article, or claim that may be made by its manufacturer, is not guaranteed or endorsed by the publisher.

frontiers | Frontiers in Bioengineering and Biotechnology

TYPE Original Research
PUBLISHED 15 July 2022
DOI 10.3389/fbioe.2022.964080

OPEN ACCESS

EDITED BY
Jianxun Ding,
Changchun Institute of Applied Chemistry (CAS), China

REVIEWED BY
Haoyu Tang,
Soochow University, China
Liu Tong,
Zhejiang University of Technology, China
Xiaomeng Li,
Zhengzhou University, China

*CORRESPONDENCE
Hongli Mao,
h.mao@njtech.edu.cn

†These authors have contributed equally to this work and share first authorship

SPECIALTY SECTION
This article was submitted to Biomaterials, a section of the journal Frontiers in Bioengineering and Biotechnology

RECEIVED 08 June 2022
ACCEPTED 28 June 2022
PUBLISHED 15 July 2022

CITATION
Sun Y, Teng J, Kuang Y, Yang S, Yang J, Mao H and Gu Z (2022), Electroactive shape memory polyurethane composites reinforced with octadecyl isocyanate-functionalized multi-walled carbon nanotubes.
Front. Bioeng. Biotechnol. 10:964080.
doi: 10.3389/fbioe.2022.964080

Electroactive shape memory polyurethane composites reinforced with octadecyl isocyanate-functionalized multi-walled carbon nanotubes

Yadong Sun[1†], Jiachi Teng[1†], Yi Kuang[2†], Shengxiang Yang[2], Jiquan Yang[3], Hongli Mao[1,4*] and Zhongwei Gu[1,4]

[1]Research Institute for Biomaterials, Tech Institute for Advanced Materials, College of Materials Science and Engineering, Nanjing Tech University, Nanjing, China, [2]College of Chemical and Materials Engineering, Zhejiang A&F University, Lin'an, China, [3]Nanjing Industry Institute for Advanced Intelligent Equipment, Nanjing, China, [4]NJTech-BARTY Joint Research Center for Innovative Medical Technology, Nanjing, China

Shape memory polymers (SMPs) have a wide range of potential applications in many fields. In particular, electrically driven SMPs have attracted increasing attention due to their unique electrical deformation behaviors. Carbon nanotubes (CNTs) are often used as SMP conductive fillers because of their excellent electrical conductivities. However, raw CNTs do not disperse into the polymer matrix well. This strictly limits their use. In this study, to improve their dispersion performance characteristics in the polymer matrix, hydroxylated multi-walled carbon nanotubes (MWCNT-OHs) were functionalized with octadecyl isocyanate (i-MWCNTs). Polyurethane with shape memory properties (SMPU) was synthesized using polycaprolactone diol (PCL-diol), hexamethylene diisocyanate (HDI), and 1,4-butanediol (BDO) at a 1:5:4 ratio. Then, electroactive shape memory composites were developed by blending SMPU with i-MWCNTs to produce SMPU/i-MWCNTs. The functionalized i-MWCNTs exhibited better dispersibility characteristics in organic solvents and SMPU composites than the MWCNT-OHs. The addition of i-MWCNTs reduced the crystallinity of SMPU without affecting the original chemical structure. In addition, the hydrogen bond index and melting temperature of the SMPU soft segment decreased significantly, and the thermal decomposition temperatures of the composites increased. The SMPU/i-MWCNT composites exhibited conductivity when the i-MWCNT content was 0.5 wt%. This conductivity increased with the i-MWCNT content. In addition, when the i-MWCNT content exceeded 1 wt%, the composite temperature could increase beyond 60°C within 140 s and the temporary structure could be restored to its initial state within 120 s using a voltage of 30 eV. Therefore, the functionalized CNTs exhibit excellent potential for use in the development of electroactive shape memory composites, which may be used in flexible electronics and other fields.

KEYWORDS

shape memory polyurethane, multi-walled carbon nanotubes, octadecyl isocyanate, functionalization, electroactive

Introduction

Because of their designable shape fixation and recovery properties, shape memory materials have attracted extensive attention in recent years (Behl and Lendlein, 2007; Hager et al., 2015). Shape memory polymers (SMPs) are low cost and lightweight, and offer the advantages of easy manufacturability, a wide range of shape memory designs, and responsiveness to multiple stimuli (including temperature, current, magnetic field, pH change, solvent, etc.). These properties make SMPs more advantageous than shape memory alloys and shape memory ceramics (Leng et al., 2011; Hu et al., 2012; Hardy et al., 2016; Kim et al., 2021; Du et al., 2022). SMPs are used widely in aerospace, biomedicine, flexible electronics, textile manufacturing and other fields (Gao et al., 2019; Sun et al., 2020; Xia et al., 2021; Sun et al., 2022).

One of the most used SMPs, shape memory polyurethane (SMPU) is usually composed of a hard segment with a high glass transition temperature (T_g) and a soft segment with a low glass transition temperature (Laza et al., 2020; Liu et al., 2021). The segmented structures are thermodynamically incompatible and exhibit microphase separation on the molecular scale. The hard segment is used as the stationary phase and provides strength to ensure the shape recovery of the material, whereas the soft segment is a reversible phase that serves to deform the material and fix its shape temporarily (Zhu et al., 2008; Liu et al., 2017; Park et al., 2021). However, traditional SMPU produces shape memory effects only when stimulated directly using heat. This often limits its applications. Therefore, stimulation method development studies have been performed. By introducing azobenzene side-chain groups into the SMPU network, Wen et al. achieved shape-reversible bending and straightening of SMPU under light irradiation (Wen et al., 2018). Reza et al. doped nanographene sheets into SMPU to produce conductive composites and demonstrated the ability to restore a temporary SMPU structure to its original shape gradually using stimulation from an external current (Sofla et al., 2019). Among the various stimuli used to drive SMPUs, light driving must be performed in a highly controlled environment and thermal driving requires direct heating (Ur Rehman et al., 2018; Xie et al., 2018). Since its inherent conductivity can cause itself to become joule heated and produce remote control effects, SMPU that responds to electrical stimulation offers substantial advantages (Umair et al., 2019). The simplest way to produce such materials is to introduce highly conductive particles (e.g., graphene, carbon black, carbon nanotubes) into the shape memory polymer matrix (Zhang et al., 2017; Xu et al., 2018; Zheng et al., 2020; Raza et al., 2021). Although graphene has higher thermal conductivity, the conductivity of its composites is still worse than that of carbon nanotube composites at the same particle content (Galindo et al., 2016; Ke et al., 2018). For carbon black, more additives are needed in the composites in order to obtain conductive effect (Rosales et al., 2018).

As a promising class of nanomaterials with excellent mechanical, thermal, and electrical properties, carbon nanotubes (CNTs) are uniquely superior in the context of electroactive SMPU preparation (Mahapatra et al., 2014; Ren et al., 2019; Qu et al., 2022). However, to obtain ideal CNT-polymer composites, one must achieve a uniform CNT dispersion in the polymer matrix and sufficient interfacial adhesion. Both of these are challenging requirements. Because of the strong van der Waals forces between carbon nanotubes, they prefer to entangle or agglomerate into bundles, and fail to transfer loads from the polymer matrix (Sahoo et al., 2010; Rahmat et al., 2011; Chazot and Hart, 2019). To overcome this problem, it is crucial to modify the CNT surfaces such that they do not aggregate in the polymer matrix (Kim et al., 2009; Zahedi and Amraee, 2018).

In this study, octadecyl isocyanate that can react with hydroxyl or carboxyl groups on CNT surfaces to form carbamate bonds without complex reaction conditions was used to functionalize hydroxylated multi-walled carbon nanotubes (MWCNT-OH) and the dispersion properties of the modified i-MWCNTs were analyzed in various solvents. Then, SMPU/i-MWCNT composites with various i-MWCNT contents were prepared via solution casting. The physicochemical properties and electrically driven shape memory performance characteristics of the resulting materials were then studied in detail.

Experimental

Materials

Polycaprolactone-diol (PCL-diol, Mn = 4,000 g/mol) was purchased from Shenzhen Guanghuaweiye Co. Ltd (China). 1,4-butanediol (BDO, purity ≥ 98%), hexamethylene diisocyanate (HDI, purity ≥ 99%), toluene (purity ≥ 99%), dimethylformamide (DMF, purity ≥ 99%), stannous octoate ($Sn(Oct)_2$, purity ≥ 96%), and hydroxylated multi-walled carbon nanotubes (MWCNT-OH, Length: 20–30 nm) were supplied by Aladdin (China). Octadecyl isocyanate was purchased from Aldrich (United States). Dichloromethane (DCM, purity ≥ 99%) and tetrahydrofuran (THF, purity ≥ 99%) were obtained from 3A Chem (China).

Synthesis of i-MWCNTs

First, 1.00 g of MWCNT-OH was dispersed in 40 ml of anhydrous DMF solution via ultrasonic dispersion. Then, 40 ml of anhydrous DMF solution with 3.00 g of octadecyl

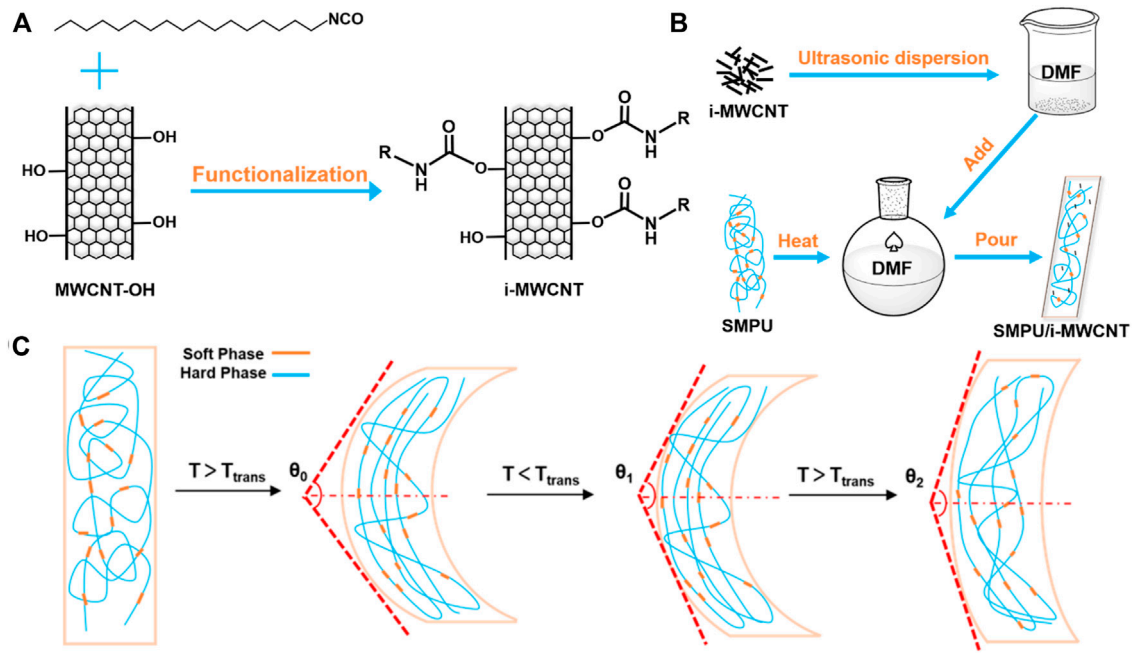

FIGURE 1
(A) Synthesis of i-MWCNT. **(B)** Preparation of SMPU/i-MWCNT composites. **(C)** Schematic illustration of the shape memory behavior test.

isocyanate dissolved in it was mixed with the MWCNT-OH solution and stirred at room temperature (RT) for 8 h under nitrogen. The -OH groups on the MWCNT-OH surfaces reacted with the -NCO groups within octadecyl isocyanate to form urethane linkages (Figure 1A). The product was dried under vacuum at 80°C after being centrifuged and washed with dichloromethane three times.

Synthesis of shape memory polyurethane

SMPU was synthesized gradually via pre-polymerization using a PCL:HDI:BDO molar ratio of 1:5:4. First, 10.00 g of PCL was placed in a three-port flask and dried under vacuum at 100°C for 4 h. When the temperature decreased to RT, 35 ml of anhydrous toluene was injected into the flask, which was then heated to 65°C and stirred for 30 min until the PCL was dissolved completely in the anhydrous toluene. Then, 2.10 g of HDI and two drops of stannous octanoate (0.1 wt% of PCL) were added to the flask. The mixture was heated to 90°C and stirred under nitrogen for 2.5 h. Finally, 1.80 g of BDO was added to the reaction mixture to enable chain extension and thus increase the molecular weight of the polymer. The resulting mixture was stirred quickly for 20 min. The product was transferred into a vacuum drying oven and dried at 80°C for 1 d. The hard segment content of the prepared SMPU was 23% (Nejad et al., 2019; Nouri et al., 2020).

Preparation of SMPU/i-MWCNT composites

Polyurethane matrix composites that contained various quantities of functionalized carbon nanotubes (0 wt%, 0.1 wt%, 0.5 wt%, 1 wt%, and 2 wt%) were prepared via the solution mixed casting method. The resulting materials were named PU, PU-0.1, PU-0.5, PU-1, and PU-2, respectively (Figure 1B). Briefly, 4.00 g of SMPU was dissolved in 40 ml of DMF and stirred at 85°C to produce a transparent polymer solution. Separately, i-MWCNTs were dispersed in DMF via ultrasonic dispersion for 2 h and then mixed with the SMPU solution, stirred for 20 min, and dried quickly for 30 min. The resulting SMPU/i-MWCNT composites were poured into PTFE molds and dried under vacuum at 80°C for 24 h. The SMPU/MWCNT-OH composite with a raw MWCNT-OH content of 1 wt% was used as a negative control.

Characterization

Fourier transform infrared spectroscopy (FT-IR)

The infrared spectra of the samples were measured using a Fourier infrared spectrometer (Nicolet iS5, Thermo Scientific). Each sample was scanned 32 times in the 500–4,000 cm^{-1} range. The hydrogen bonding indexes of the C=O functional groups ($HBI_{(C=O)}$, %) within SMPU and SMPU/i-MWCNT composites with different i-MWCNT contents were determined using the

method and equation (Eq. 1) mentioned in previous studies (Babaie et al., 2019).

$$HBI_{(C=O)}\frac{A^{b}_{(C=O)}}{A^{b}_{(C=O)}+A^{nb}_{(C=O)}}\times 100\% \quad (1)$$

where $A^{b}_{(C=O)}$ and $A^{nb}_{(C=O)}$ are the areas of the free and hydrogen-bonded carbonyl functional bands.

X-ray diffraction

An X-ray diffractometer (Smartlab 9 kW, Japan) equipped with a scintillation counter, CuK α radiation (λ = 0.1540 nm) with an accelerating voltage of 40 kV, and a current of 40 mA was used to record the XRD patterns of the samples. The crystal size and crystallinity equations used with SMPU and SMPU/i-MWCNT composites with various i-MWCNT contents are Eqs. 2, 3, respectively (Eyvazzadeh Kalajahi et al., 2017).

$$L_{hkl}=\frac{K\lambda}{\beta_{hkl}\times cos\theta_{hkl}} \quad (2)$$

where L_{hkl}, β_{hkl}, and θ_{hkl} represent the crystal size, diffraction full-width at half-maximum (FWHM), and (hkl) plane Bragg angle, respectively. λ and K are the X-ray wavelength (0.1540 nm) and Scherrer constant (0.9), respectively.

$$X_c=\frac{A_{110}+A_{111}+A_{200}}{A_{110}+A_{111}+A_{200}+A_{ah}}\times 100\% \quad (3)$$

where A_{110}, A_{111}, and A_{200} represent the areas of the crystalline diffraction peaks and A_{ah} is attributed to the amorphous halo noted in the XRD patterns.

Laser confocal Raman spectroscopy

The i-MWCNT structural order was characterized using a laser confocal Raman spectrometer (Horiba Evolution, Japan) with a laser wavelength of 632.8 nm and a resolution of 3 cm^{-1}. C, N, and O in the i-MWCNT were analyzed using a k-alpha photoelectron spectrometer (Thermo Scientific).

Differential scanning calorimetry

The DSC curves of PCL, SMPU, and several SMPU/i-MWCNT composites with various i-MWCNT contents were obtained under nitrogen using a differential scanning calorimeter (DSC 200-F3, Netzsch). First, each sample was heated to 200°C at a heating rate of 15°C/min and maintained at a constant temperature for 2 min to eliminate the its thermal history of the sample. Then, each sample was cooled to −80 °C at a cooling rate of 15°C/min and maintained at a constant temperature for 2 min. Finally, each sample was heated to 200°C again at a heating rate of 15°C/min. The degree of sample crystallinity, melting temperature, and glass transition temperature were evaluated using data from the first cooling and the second heating cycles. The soft segment crystallinity was calculated as shown in equation Eq. 4 (Nouri et al., 2020).

$$X_c=\frac{\Delta H_{ss}}{136\times 1-G-HS}\times 100\% \quad (4)$$

where 136 and ΔH_{ss} are the heat of fusion of 100% crystalline PCL-diol and the soft segments in the relevant samples. G and HS represent the masses of graphene nanosheets and hard segments in the composites.

Scanning electron microscopy

The fractured surface micromorphologies of SMPU and SMPU/i-MWCNT composites with various i-MWCNT contents after tensile fracture were analyzed using a scanning electron microscope (JSM-IT200). Before scanning, the specimen sections were sprayed with gold at a voltage of 2.5 kV.

Thermal stability

The thermal stability characteristics of i-MWCNT, SMPU, and SMPU/i-MWCNT composites with various i-MWCNT contents were tested using a synchronous thermal analyzer (STA 449-F3, Germany). Briefly, the samples were dried and their weight loss was determined using a heading rate of 10°C/min under nitrogen.

Electrical conductivity

The electrical conductivities of the SMPU and SMPU/i-MWCNT composites with various i-MWCNT contents were measured via a four-probe technique using a surface resistance detector (RHA-FT-331, China). A voltage of 30 V was applied to the samples using two electrodes located 10 mm apart and the surface temperature of the specimen was recorded via a laser digital infrared thermometer.

Mechanical properties

A universal tensile testing machine (Instron 5,943, United States) was used to test the tensile strengths of SMPU and several SMPU/i-MWCNT composites with various i-MWCNT contents at RT. The gauge length of the extensometer was 25 mm and the tensile rate was 10 mm/min.

Each sample was tested three times and the average value was recorded.

Shape memory properties

A prepared rectangular spline was used to test the shape memory fixation (R_f) and recovery (R_r) rates. As shown in Figure 1C, the test process followed a sequence that included heating deformation, cooling fixation, and heating recovery. First, the spline was placed in 60°C water for 10 min. Then, the spline was bent at an angle of θ_0 using an external force, and placed in ice water for 5 min. Next, the angle was measured again and recorded as θ_1. Finally, the spline was heated in 60°C water for 10 min, and the resulting angle was recorded as θ_2. The R_f and R_r of the specimen were calculated using Eqs. 5, 6 (Moghim et al., 2018).

$$R_f = \frac{180 - \theta_1}{180 - \theta_2} \times 100\% \quad (5)$$

$$R_r = \frac{\theta_2 - \theta_1}{180 - \theta_1} \times 100\% \quad (6)$$

Results and discussion

i-MWCNT preparation and characterization

Figure 2A shows the FT-IR spectra of the hydroxylated MWCNTs (MWCNT-OHs) and the octadecyl isocyanate-functionalized MWCNTs (i-MWCNTs). In the MWCNT-OH spectrum, the characteristic peak at 3,450 cm^{-1} belongs to the -OH stretching vibration. In the i-MWCNT spectrum, the absorption peaks at 3,340 cm^{-1}, 1,614 cm^{-1}, 1,575 cm^{-1}, and 1,220 cm^{-1} correspond to the N-H stretching vibration, the NH-CO stretching vibration, the N-H bending vibration, and the C-N stretching vibration, respectively. The disappearance of the characteristic hydroxyl peak and emergence of a characteristic carbamate group peak, as well as the absence of octadecyl ester characteristic peaks at 2,271 cm^{-1} and 1,354 cm^{-1} in the i-MWCNT spectrum, combine to indicate that octadecyl isocyanate is successfully grafted onto the MWCNT-OH surface (Zhao et al., 2004; Deng et al., 2007; Lopes et al., 2017; Salam and Burk, 2017).

The MWCNT-OH and i-MWCNT XRD patterns are shown in Figure 2B. Two of the diffraction peaks present are characteristic of carbon nanotubes: the (002) diffraction peak (the strongest carbon peak with $2\theta = 26^\circ$ and d = 0.45 nm) and the (100) diffraction peak (the secondary carbon diffraction peak with $2\theta = 42.6^\circ$ and d = 0.21 nm) appear at the same positions in the two curves. This suggests that the MWCNT-OH structure does not change upon modification with octadecyl isocyanate. Thus, the functional modification process does not destroy the original MWCNT crystal structure (Bi et al., 2020).

To analyze the interactions on the octadecyl isocyanate-modified nanotube surface further, the structure and morphology of MWCNT-OH and i-MWCNT were analyzed via Raman spectroscopy. Figure 2C shows that both MWCNT-OH and i-MWCNT exhibit two D and G peaks. This indicates that the overall structure of the nanotubes does not change upon modification. The I_D/I_G value for MWCNT-OH (1.52) is greater than that for i-MWCNT (1.34). This suggests an increase in the average size of the C-C sp^3 domain after functionalization. This may be because modification with octadecyl isocyanate introduces long aliphatic chains on the nanotube surface (Tamore et al., 2019).

Figure 2D(i) shows XPS wide-scan spectra of MWCNT-OH and i-MWCNT. The full i-MWCNT XPS spectrum exhibits not only C1s and O1s optoelectronic spectra, but also a new N1s optoelectronic peak at 401.2 eV, that is, not present in the corresponding MWCNT-OH spectrum. After peak splitting fitting, new C-N and O=C-N optoelectronic peaks appear at 285.3 and 287.2 eV, respectively, in the C1s XPS spectrum of i-MWCNT (Figure 2D(ii)). Two new photoelectric peaks at 400.1 and 400.9 eV in the N1s XPS spectrum correspond to the characteristic peaks of -NH- and C-N, respectively (Figure 2D(iii)). Two optoelectronic peaks from C=O (522.3 eV) and C-O (533.3 eV) are observed in the N1s XPS spectrum of i-MWCNT (Figure 2D(iv)). The results indicate the presence of amide (-CO-NH-) and carbamate (-NH-COO-) groups in i-MWCNT. This further demonstrates that octadecyl isocyanate is grafted onto the i-MWCNT surface (Zhao et al., 2004; Lopes et al., 2017; Bi et al., 2020).

Figure 2E shows photos of MWCNT-OH and i-MWCNT samples dispersed via ultrasound in various solvents after standing for 1 d. The MWCNT-OH sample exhibits poor dispersion in four solvents, while i-MWCNT functionalized with octadecyl isocyanate exhibits a perfect dispersion effect in the organic solvents. The i-MWCNT surface is grafted with long-chain molecules that can effectively prevent direct contact between carbon nanotube skeletons and weaken the van der Waals force between the carbon nanotubes. Moreover, -NCO reacts with the -OH groups on the MWCNT-OH surface to form urethane linkages. Therefore, i-MWCNTs can disperse well in organic reagents (Kim et al., 2009; Salam and Burk, 2017).

A TGA test was performed to investigate the thermal stability of i-MWCNT. TG and DTG curves were obtained for i-MWCNT (Figure 2F). The i-MWCNTs decompose as the temperature increases, reaching their maximum decomposition rate at 285°C. The boiling point of octadecyl isocyanate is 173°C. If octadecyl isocyanate is only adsorbed onto the carbon nanotube surface, it is expected to volatilize. Therefore, the peak in the DTG curve corresponds to the decomposition of long alkyl chains grafted onto the i-MWCNT surface. After this point, the decomposition

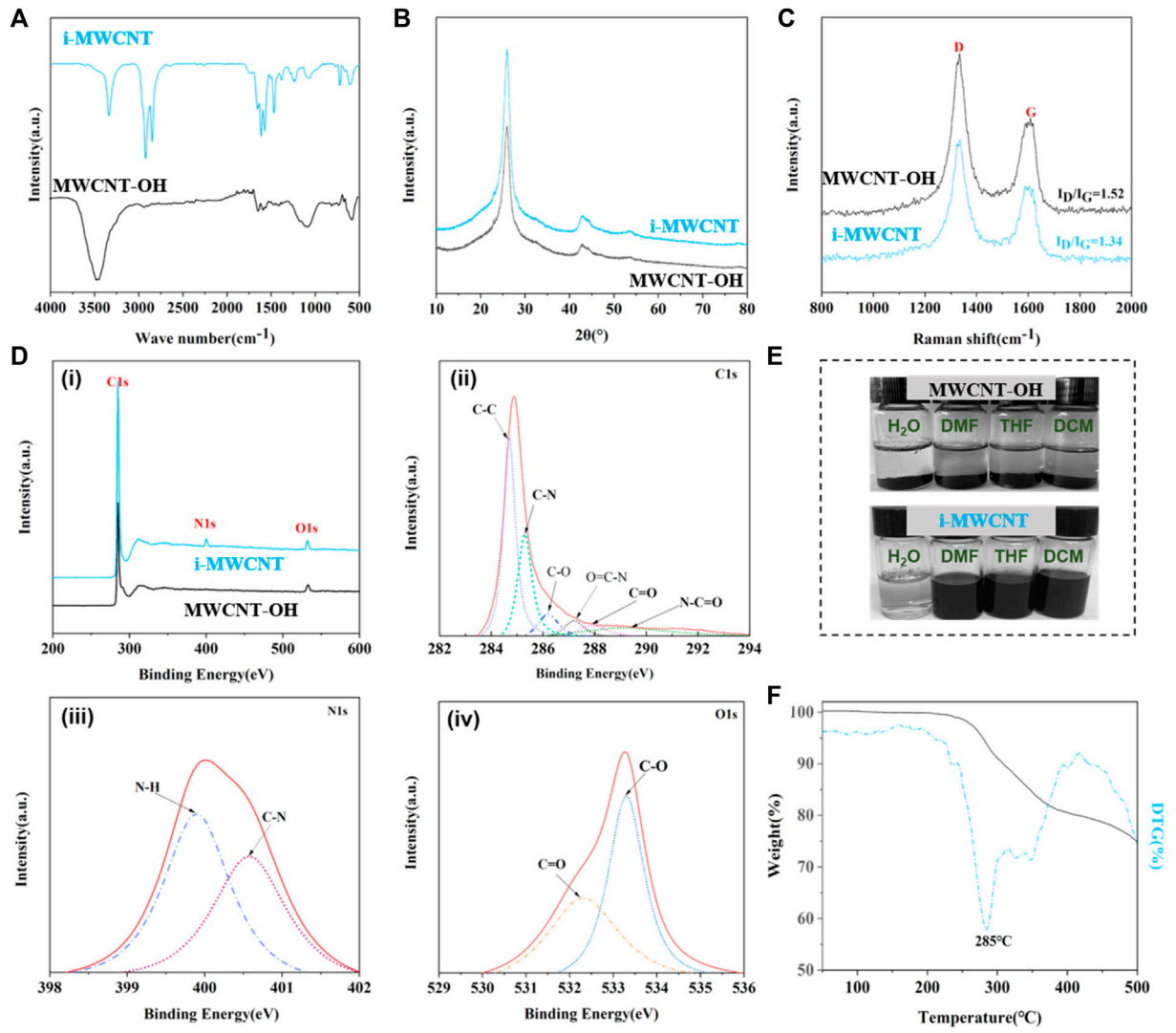

FIGURE 2
(A) FT-IR, **(B)** XRD, and **(C)** Raman spectra of MWCNT-OH and i-MWCNT. **(D)** XPS wide-scan spectra of MWCNT-OH and i-MWCNT (i: high-resolution elements, ii: C1s, iii: O1s, iv: N1s). **(E)** Photos of MWCNT-OH and i-MWCNT dispersed in various solvents. **(F)** i-MWCNT TG-DTG curves.

rate decreases gradually, indicating that oxygen-containing groups on the i-MWCNT surface also begin to decompose gradually (Zhao et al., 2004; Deng et al., 2007; Lopes et al., 2017).

Preparation of SMPU/i-MWCNT composites

The FT-IR spectra of PCL, SMPU, and SMPU/i-MWCNT composites with various i-MWCNT contents are shown in Figure 3A. The relatively wide absorption band at 3,350 cm^{-1} in the PCL spectrum corresponds to the -OH group. The absorption peaks at 2,945 cm^{-1}, 2,864 cm^{-1}, 1,236 cm^{-1}, and 962 cm^{-1} are C-H vibration peaks from methylene groups within PCL. The strong absorption peak at 1720 cm^{-1} is attributed to the characteristic absorption peak of the non-hydrogen bonded esoteric group (C=O). Moreover, since PCL-diol lacks proton donor groups, no peak is observed at 1,680 cm^{-1}.

In the spectrum of pure SMPU, the absorption peaks at 3,319 cm^{-1} and 1,539 cm^{-1} correspond to the N-H stretching vibration peak and the bending vibration peak from the urethane linkage, respectively. The N-H absorption peak that indicates a lack of involvement in hydrogen bond formation does not appear at 3,378–3,400 cm^{-1}. This indicates that all N-H groups are involved in the formation of hydrogen bonds with C=O. This may be caused by the presence of proton acceptor groups (C=O) in both the hard and soft polyurethane segments. The absorption

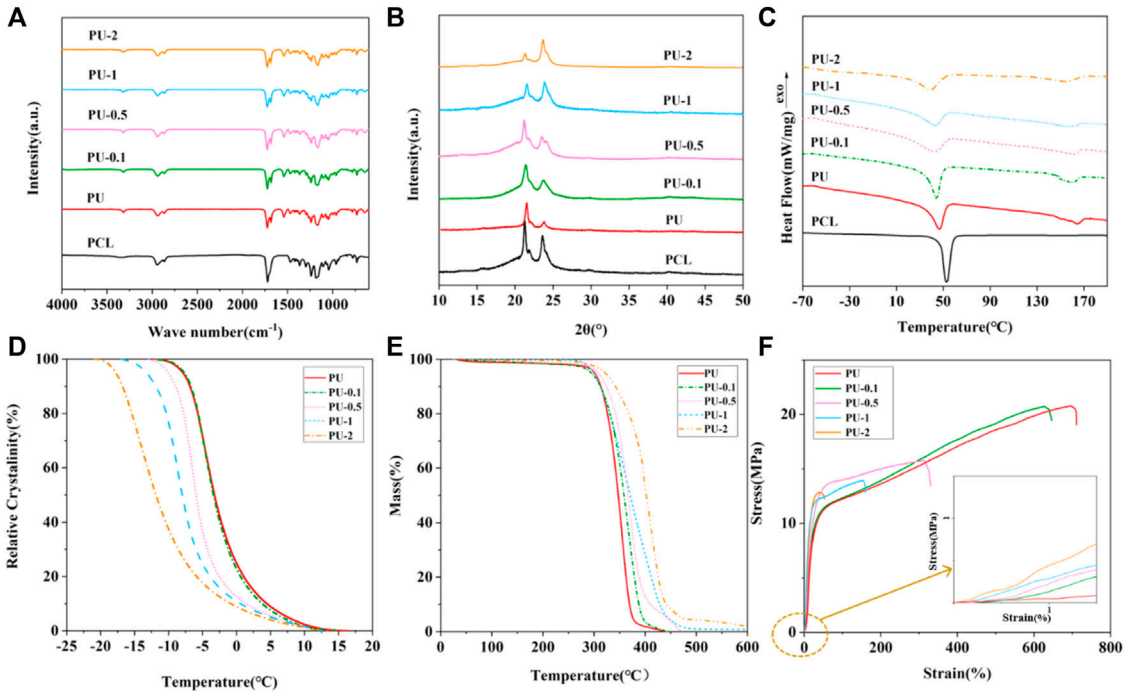

FIGURE 3
(A) FT-IR, **(B)** XRD, and **(C)** DSC curves of PCL, SMPU, and SMPU/i-MWCNT composites with various i-MWCNT contents. **(D)** Relative crystallinity evolution versus temperature, **(E)** TG curves, and **(F)** stress-strain behaviors of SMPU and SMPU/i-MWCNT composites with various i-MWCNT contents at RT.

peaks from non hydrogen-bonded free C=O and C=O, that is, hydrogen bonded with N-H appear at 1725 cm^{-1} and 1,684 cm^{-1}, respectively. Two absorption peaks are observed for the C-O in the soft segment at 1,156 cm^{-1} and 1,064 cm^{-1}. These are the absorption peaks from C-O without and with hydrogen bonding. The disappearance of the -OH contraction vibration peak at 3,450 cm^{-1} and the contraction vibration peak from the isocyanate group (N=C=O) at 2,250–2,274 cm^{-1} indicate the successful synthesis of polyurethane (Sofla et al., 2019; Ren et al., 2019; Nejad et al., 2019).

The SMPU and SMPU/i-MWCNT composite wave peak positions do not change. This indicates that infiltration of i-MWCNTs into SMPU does not change its structure. However, the presence of i-MWCNT has some influence on the hydrogen-bonding group content of SMPU. The hydrogen bond carbonyl index ($HBI_{(C=O)}$, %) of the samples is shown in Table 1. The results indicate that the addition of i-MWCNT reduces the $HBI_{(C=O)}$ contents of the SMPU composites (Sofla et al., 2019; Nejad et al., 2019). It may be owing to the formation of hydrogen bonds between the polyurethane bonds formed in the modified i-MWCNTs and the hard segments of the polyurethane. The carbonyl groups within the carbamate groups in SMPU can form intermolecular hydrogen bonds with amino groups. To verify the accuracy of the calculation results, an ideal polyurethane chain with a PCL:HDI:BDO ratio of 1:5:4 was analyzed statistically. The molecular weight of PCL is 4,000 g/mol, and the molecular weight of its repeat unit is 114 g/mol. Thus, each PCL segment contains approximately 34 carbonyl bases. HDI and BDO form nine carbonyl groups in SMPU. Ideally, the polyurethane chain should contain 43 carbonyl groups. The FT-IR spectrum shows that all such groups are involved in the reaction. Therefore, the $HBI_{(C=O)}$ content in the ideal SMPU is 21.0%, which is consistent with the calculation results in Table 1 (Nouri et al., 2020).

The crystal structures of the samples were calculated via the XRD method, and the results are shown in Figure 3B. PCL-diol has three main diffraction peaks at $2\theta = 21.6^{\circ}$, 22.2°, and 24.0°. The same peaks also appear in the XRD spectra of the SMPU and SMPU/i-MWCNT composites. This indicates that the crystal structures of the SMPU and SMPU/i-MWCNT composites are caused by the PCL soft segment. The crystal sizes and crystallinities of the samples are calculated and the results are shown in Table 2. Different from the structure of PCL-diol, the anchoring effects and the presence of hard segments led to the formation of smaller crystals in the SMPU structure. Sample crystallinity decreases as the i-MWCNT content increases. This was because the addition of i-MWCNT may hinder the orderly

TABLE 1 The hydrogen bonding indexes $HBI_{(C=O)}$, crystal sizes of planes (110) and (200) (L_{110} and L_{200}), and crystallinity contents [Xc (%)] of PCL, SMPU, and SMPU/i-MWCNT composites with various i-MWCNT contents.

Sample	$A^{b}_{(C=O)}$	$A^{nb}_{(C=O)}$	$HBI_{(C=O)}$ (%)	L_{110} (nm)	L_{200} (nm)	X_c (%)
PCL	—	—	—	34.12	27.54	56.36
PU	4.25	13.40	24.08	19.86	24.34	31.56
PU-0.1	3.55	12.18	22.57	27.38	22.81	30.24
PU-0.5	3.22	12.07	21.06	26.56	15.52	22.18
PU-1	3.18	11.65	21.44	25.89	16.31	21.81
PU-2	3.45	12.37	21.81	25.95	15.41	20.73

TABLE 2 The degree of crystallinity (X_c,%); and melting (T_{ms}) and glass transition (T_g,°C) temperatures of the soft segments. The melting temperatures (T_{mh},°C) of the hard segments. Crystallization onset temperatures (T_{onset}, °C).

Sample	X_c (%)	T_{ms} (°C)	T_{mh} (°C)	T_g (°C)	T_{onset} (°C)
PCL	69.76	53.2	-	−65.6	30.8
PU	31.35	49.1	162.3	−56.8	22.3
PU-0.1	35.17	48.9	163.6	−56.4	20.2
PU-0.5	29.56	47.2	168.7	−55.9	19.4
PU-1	28.86	44.9	171.6	−55.4	12.9
PU-2	25.18	42.4	172.7	−55.1	12.5

arrangement of PU segments during crystallization (Hashmi et al., 2015).

Thermal and mechanical properties of SMPU/i-MWCNT composites

Figure 3C shows DSC curves of PCL, SMPU, and SMPU/i-MWCNT composites with various i-MWCNT contents. The results are also shown in Table 2. A PCL crystal melting peak is observed at approximately 50°C in all groups. In addition, an absorption peak is detected from SMPU and the SMPU/i-MWCNT composites at approximately 170°C. This peak appears because of melting of hard-segment crystals or long-range ordered dissociation of the hard segment amorphous state (Sofla et al., 2019; Ren et al., 2019). As the i-MWCNT content increases, the glass transition (T_g) temperatures of the SMPU/i-MWCNT composites increase, the crystallinity (X_c) of the soft segment and the crystallization onset temperatures (T_{onset}) are reduced. This may be attributed to the limiting effect of nanoparticles on soft-segment fluidity. The decrease in crystallinity shows that i-MWCNTs can inhibit SMPU crystallization rather than nucleation, and thus may lead to a decrease in the initial SMPU crystallization temperature. Due to the appearance of nanoparticles, the crystals within the hard segment in SMPU are imperfect and the thicknesses of the crystal flakes are reduced. This reduces the melting temperature of the soft segment (T_{ms}). The melting temperature (T_{mh}) and crystallization enthalpy of the hard segment increase because the addition of i-MWCNTs reduces the degree of microphase separation of PU and they can interact with hard-segment formation (Hashmi et al., 2015; Nouri et al., 2020).

The first cooling step of the DSC test was used to study the crystallization behaviors of the SMPU and SMPU/i-MWCNT composites. The relative crystallinities of the samples shift to lower temperatures as the i-MWCNT content increases (Figure 3D). This indicates that i-MWCNT cannot be used as nucleating agent and that steric hindrance delays crystal formation (Kim et al., 2015; Sofla et al., 2019; Gorbunova et al., 2020). The TG curves of the SMPU and SMPU/i-MWCNT composites are shown in Figure 3E. The improved thermal stability characteristics of the SMPU/i-MWCNT composites relative to pure SMPU can be attributed to the good compatibility of i-MWCNT. The thermal decomposition temperature of SMPU/i-MWCNT increases with the i-MWCNT content because the interactions between i-MWCNT and the hard segment increase. This may promote crystallization of the hard-segment phase (Song et al., 2009; Mogha and Kaushik, 2021).

To study the effects of i-MWCNT addition on the mechanical properties of SMPU, tensile tests were performed on SMPU and SMPU/i-MWCNT composites with various i-MWCNT contents (Figure 3F). Because of weak interfacial interactions between i-MWCNT and the polyurethane chains, the elongation at break decreases gradually as the i-MWCNT content increases. The elongation at break drops sharply when the i-MWCNT content exceeds 0.1 wt%. High i-MWCNT contents may lead to partial agglomeration in the samples, resulting in internal stress defects and easy fracture during stretching. However, by analyzing the tensile strength under low strain, one can find that the tensile strengths of SMPU/i-MWCNT composites increase with the i-MWCNT content. This is because the load from an external force can be transferred from the matrix to the nanofiller effectively, reducing the load on the polymer chains. Thus, the i-MWCNTs play a reinforcing role (Mahapatra et al., 2014; Hashmi et al., 2015; Sofla et al., 2019).

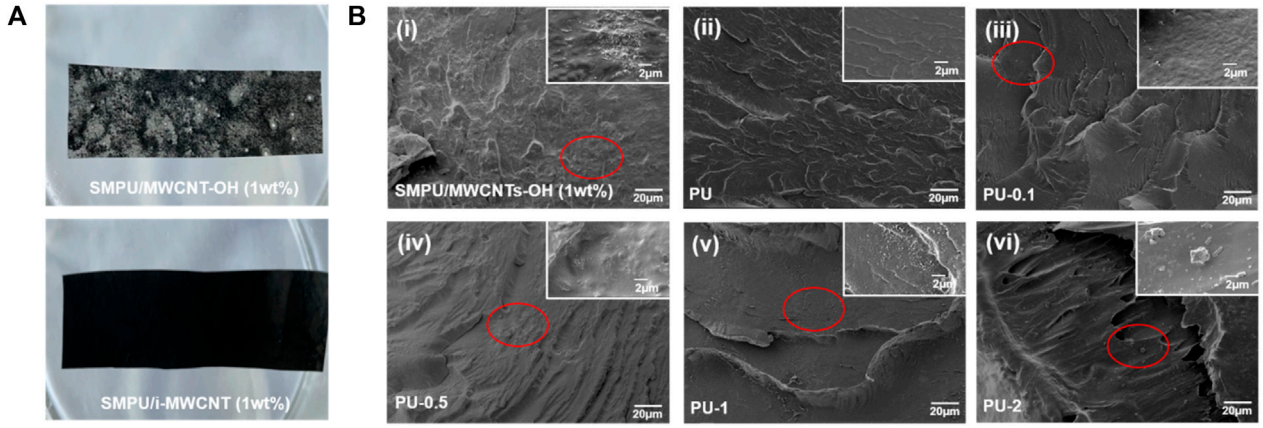

FIGURE 4
(A) The gross appearances of SMPU/MWCNT-OH and SMPU/i-MWCNT composites with MWCNT-OH or i-MWCNT contents of 1 wt%. **(B)** SEM images of **(I)** SMPU/MWCNT-OH (with 1 wt% MWCNT-OH) and SMPU/i-MWCNT composites with (i)-MWCNT contents of (ii) 0%, (iii) 0.1%, (iv) 0.5%, (v) 1%, and (vi) 2%.

Figure 4A shows the typical gross appearances of the SMPU/MWCNT-OH and SMPU/i-MWCNT composites. Unmodified MWCNT-OH exhibits poor dispersibility in the polymer matrix, while functionalized i-MWCNT has good dispersibility and no macroscopic agglomeration is observed. To analyze the distribution of carbon nanotubes in SMPU accurately, the fracture surfaces of pure SMPU and the composites were observed via SEM. Figure 4Bi shows that the nanoparticles agglomerate across a large area of the polymer when unmodified MWCNT-OH is added. However, such agglomeration is not observed in Figure 4B. This indicates that functionally modified i-MWCNT has better dispersion properties in the polymer matrix than its unmodified counterpart. In addition, when the i-MWCNT content of a composite is too low, the nanotubes disperse individually within the polymer and become wrapped by non-conductive SMPU, resulting in composites with no conductivity. A small amount of agglomeration occurs when the i-MWCNT content exceeds 0.5 wt%. This is a critical factor in determining whether the polymer has electrical properties (Moghim et al., 2018; Bi et al., 2020).

Conductive, electrothermal, and shape memory effects

Figure 5A shows the electrical conductivities of SMPU/i-MWCNT composites with various i-MWCNT contents. When the i-MWCNT content is 0.1 wt%, the conductivity of the resulting composite is 10^{-12} S cm^{-1}, which is similar to that of pure SMPU. Such a composite is not conductive and can be regarded as an insulator. However, when the i-MWCNT content is 0.5 wt%, the conductivity of the resulting composite exceeds 10^{-7} S cm^{-1}. This indicates the formation of a conductive path. Therefore, it can be determined that 0.5 wt% is the approximate i-MWCNT conductance threshold content. Under this condition, functionally modified i-MWCNTs exhibit enhanced adhesion to and reduce the tunneling barrier formed by the SMPU. The manner in which the temperatures of SMPU/i-MWCNT composites change under a voltage of 30 eV over time is shown in Figure 5B. When the i-MWCNT concentration exceeds 1 wt%, the sample temperature can increase beyond 60°C within 140 s (Hajializadeh et al., 2017; Sang et al., 2019).

The shape memory effect of SMPU is related to its soft and hard segments. The PCL soft phase that can be crystallized serves as the soft segment and is responsible for maintaining the temporary shape. In contrast, the hard segment mainly controls the permanent shape of the sample. Table 3 shows the shape memory properties of SMPU and several SMPU/i-MWCNT composites with various i-MWCNT contents. The shape fixation and recovery rates (at 60 °C) increase gradually as the i-MWCNT content increases. However, the SMPU/i-MWCNT composite exhibits shape recovery abilities under a voltage of 30 eV within 120 s only when the i-MWCNT content exceeds 1 wt%. The composites with i-MWCNT contents of 1 wt% and 2 wt% exhibit shape recovery rates of 81 and 85%, respectively. A SMPU/i-MWCNT composite shape strain-recovery cycle is shown in Figure 5C, and is consistent with the quantitative analysis results. The reinforced electroactive shape memory effects may be attributed to addition of i-MWCNT, which reduces the degree of microphase separation within the SMPU and effectively increases the extent of interfacial interaction with SMPU in the composites (Khasraghi et al., 2019).

To investigate the shape memory effects within the SMPU/i-MWCNT composites further, the shape memory fixation (R_f) and recovery (R_r) rates of SMPU samples without and with various

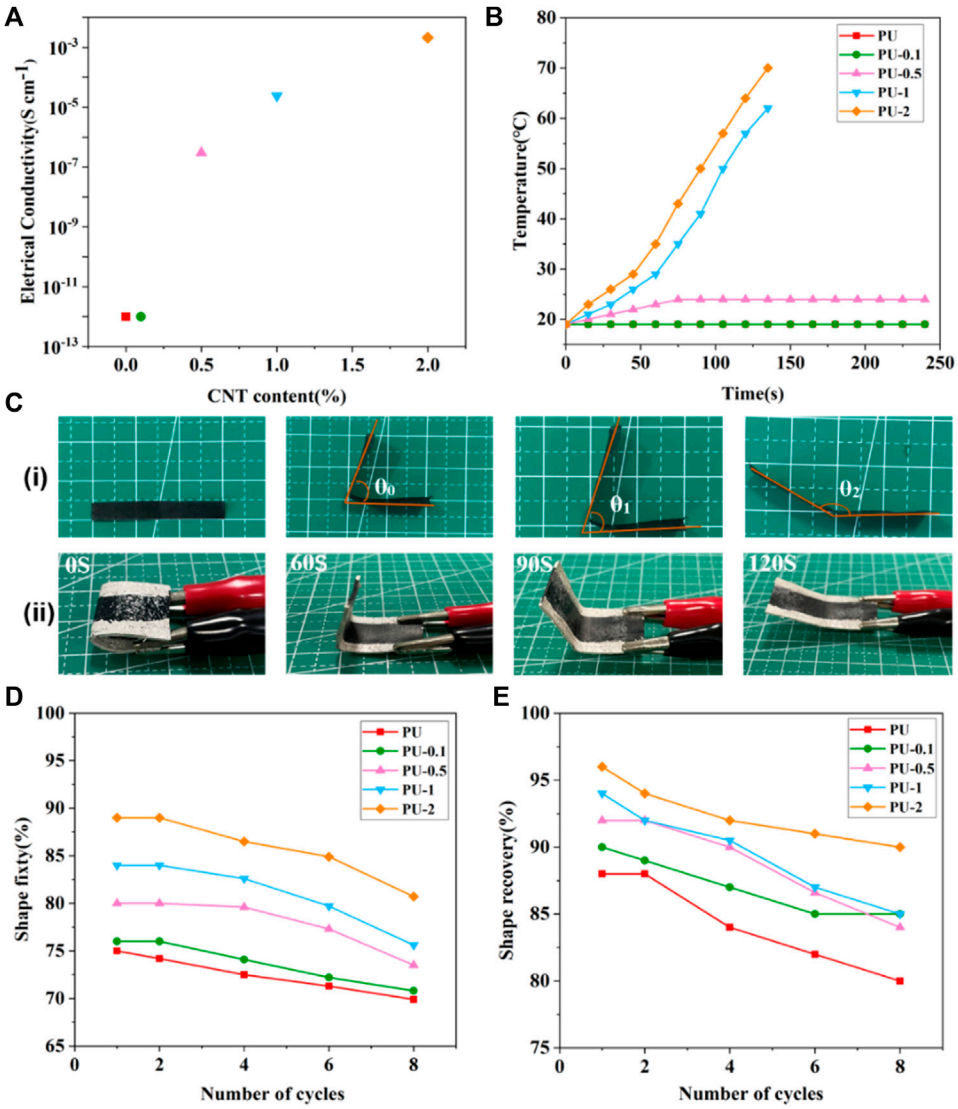

FIGURE 5
(A) Conductivity and **(B)** temperature changes among SMPU/i-MWCNT composites at a voltage of 30 eV. **(C)** Photos of (i) a shape deformation-recovery cycle and (ii) the shape recovery behaviors of SMPU/i-MWCNT composites with 1 wt% i-MWCNT content at a voltage of 30 eV. Quantitative analysis of the shape memory **(D)** fixation and **(E)** recovery rates over various shape strain-recovery cycles for SMPU/i-MWCNT composites with various i-MWCNT contents at temperatures below 60°C.

TABLE 3 Shape memory properties of SMPU and SMPU/i-MWCNT composites with various i-MWCNT contents.

Sample	R_f (%)	R_r (%) (Thermal: 60°C)	R_r (%) (Electrical: 30 eV)
PU	75	86	——
PU-0.1	76	90	——
PU-0.5	80	91	——
PU-1	84	93	81
PU-2	89	96	85

i-MWCNT contents were tested using multiple shape deformation-recovery cycles. As shown in Figures 5D,E, the shape memory fixation and recovery rates decrease in all groups. This is because the prepared SMPU is a linear polymer with intermolecular interactions that rely only on hydrogen bonding between hard and soft segments. The internal network points become damaged and thereby affect the shape memory performance after repeated shape deformation-recovery cycles. However, it is notable that the shape memory fixation and recovery rates of the composites with i-MWCNT contents greater than 1 wt% remain higher than 80 and 90%, respectively, even after up to eight shape deformation-recovery cycles.

Conclusion

In this study, hydroxylated MWCNTs were functionalized with octadecyl isocyanate to produce i-MWCNT without affecting the chemical structures of the nanotubes. The dispersion performance characteristics of the i-MWCNTs in organic reagents and the polymer matrix improved significantly. In addition, an electroactive shape memory composite (SMPU/i-MWCNT) was developed by blending i-MWCNT with shape memory polyurethane. The addition of i-MWCNT reduced the crystallinity of SMPU and decreased the hydrogen bond index and melting temperature of the SMPU soft segment while increasing the thermal decomposition temperatures of the composites. The SMPU/i-MWCNT composites exhibited substantial conductivity. This conductivity increased with the i-MWCNT content. When the i-MWCNT content exceeded 1 wt%, the temperature of the composite could increase beyond 60°C within 140 s and the temporary structure could be restored to its initial state within 120 s under a voltage of 30 eV. The shape memory effect was maintained effectively after eight cycles of testing. Therefore, the functionalized CNTs exhibit excellent potential for the development of electroactive shape memory composites, which may be used in flexible electronics and other fields.

Data availability statement

The original contributions presented in the study are included in the article/supplementary material, further inquiries can be directed to the corresponding author.

Author contributions

YS and JT performed the experiments. YS wrote the first draft of the article. YK and HM contributed to the funding supports. YK, SY, JY, HM, and ZG undertook the writing-review and editing. HM contributed to the conception and design of this study. HM and ZG contributed to the supervision. All authors contributed to article revision, read, and approved the submitted version.

Funding

The authors would like to acknowledge funding support by the Key R&D Plan of Jiangsu Province (BE2018010-3), the “Pioneer” and “Leading Goose” R&D Program of Zhejiang (2022C02023), the Fundamental Research Funds for the Provincial Universities of Zhejiang (2021TD001), and the Scientific Research Foundation for Talent Introduction of Nanjing Tech University (39803129 and 39803130).

Conflict of interest

The authors declare that the research was conducted in the absence of any commercial or financial relationships that could be construed as a potential conflict of interest.

Publisher’s note

All claims expressed in this article are solely those of the authors and do not necessarily represent those of their affiliated organizations, or those of the publisher, the editors and the reviewers. Any product that may be evaluated in this article, or claim that may be made by its manufacturer, is not guaranteed or endorsed by the publisher.

Acknowledgments

The authors gratefully acknowledge the Priority Academic Program Development of Jiangsu Higher Education Institutions (PAPD).

References

Babaie, A., Rezaei, M., and Sofla, R. L. M. (2019). Investigation of the effects of polycaprolactone molecular weight and graphene content on crystallinity, mechanical properties and shape memory behavior of polyurethane/graphene nanocomposites. *J. Mech. Behav. Biomed. Mat.* 96, 53–68. doi:10.1016/j.jmbbm.2019.04.034

Behl, M., and Lendlein, A. (2007). Shape-memory polymers. *Mater. Today* 10, 20–28. doi:10.1016/s1369-7021(07)70047-0

Bi, H., Ye, G., Yang, H., Sun, H., Ren, Z., Guo, R., et al. (2020). Near infrared-induced shape memory polymer composites with dopamine-modified multiwall

carbon nanotubes via 3D-printing. *Eur. Polym. J.* 136, 109920. doi:10.1016/j.eurpolymj.2020.109920

Chazot, C. a. C., and Hart, A. J. (2019). Understanding and control of interactions between carbon nanotubes and polymers for manufacturing of high-performance composite materials. *Compos. Sci. Technol.* 183, 107795. doi:10.1016/j.compscitech.2019.107795

Deng, J., Zhang, X., Wang, K., Zou, H., Zhang, Q., Fu, Q., et al. (2007). Synthesis and properties of poly(ether urethane) membranes filled with isophorone diisocyanate-grafted carbon nanotubes. *J. Membr. Sci.* 288, 261–267. doi:10.1016/j.memsci.2006.11.033

Du, C., Liu, J., Fikhman, D. A., Dong, K. S., and Monroe, M. B. B. (2022). Shape memory polymer foams with phenolic acid-based antioxidant and antimicrobial properties for traumatic wound healing. *Front. Bioeng. Biotechnol.* 10, 809361. doi:10.3389/fbioe.2022.809361

Eyvazzadeh Kalajahi, A., Rezaei, M., Abbasi, F., and Mir Mohamad Sadeghi, G. (2017). The effect of chain extender type on the physical, mechanical, and shape memory properties of poly(ε-caprolactone)-based polyurethane-ureas. *Polymer-Plastics Technol. Eng.* 56, 1977–1985. doi:10.1080/03602559.2017.1298797

Galindo, B., Benedito, A., Gimenez, E., and Compañ, V. (2016). Comparative study between the microwave heating efficiency of carbon nanotubes versus multilayer graphene in polypropylene nanocomposites. *Compos. Part B Eng.* 98, 330–338. doi:10.1016/j.compositesb.2016.04.082

Gao, H., Li, J., Zhang, F., Liu, Y., and Leng, J. (2019). The research status and challenges of shape memory polymer-based flexible electronics. *Mat. Horiz.* 6, 931–944. doi:10.1039/c8mh01070f

Gorbunova, M. A., Zaitsev, V., Grishchuk, A. A., and Badamshina, E. R. (2020). "Roles of phase separation and crystallization in the structure formation," in *Russian chemical bulletin*. International Edition.

Hager, M. D., Bode, S., Weber, C., and Schubert, U. S. (2015). Shape memory polymers: Past, present and future developments. *Prog. Polym. Sci.* 49-50, 3–33. doi:10.1016/j.progpolymsci.2015.04.002

Hajializadeh, S., Barikani, M., and Bellah, S. M. (2017). Synthesis and characterization of multiwall carbon nanotube/waterborne polyurethane nanocomposites. *Polym. Int.* 66, 1074–1083. doi:10.1002/pi.5362

Hardy, J. G., Palma, M., Wind, S. J., and Biggs, M. J. (2016). Responsive biomaterials: Advances in materials based on shape-memory polymers. *Adv. Mat.* 28, 5717–5724. doi:10.1002/adma.201505417

Hashmi, S. a. R., Prasad, H. C., Abishera, R., Bhargaw, H. N., and Naik, A. (2015). Improved recovery stress in multi-walled-carbon-nanotubes reinforced polyurethane. *Mater. Des.* 67, 492–500. doi:10.1016/j.matdes.2014.10.062

Hu, J., Zhu, Y., Huang, H., and Lu, J. (2012). Recent advances in shape–memory polymers: Structure, mechanism, functionality, modeling and applications. *Prog. Polym. Sci.* 37, 1720–1763. doi:10.1016/j.progpolymsci.2012.06.001

Ke, K., Solouki Bonab, V., Yuan, D., and Manas-Zloczower, I. (2018). Piezoresistive thermoplastic polyurethane nanocomposites with carbon nanostructures. *Carbon* 139, 52–58. doi:10.1016/j.carbon.2018.06.037

Khasraghi, S. S., Shojaei, A., and Sundararaj, U. (2019). Bio-based UV curable polyurethane acrylate: Morphology and shape memory behaviors. *Eur. Polym. J.* 118, 514–527. doi:10.1016/j.eurpolymj.2019.06.019

Kim, Y., Kwon, S.-M., Kim, D.-Y., Kim, H.-S., and Jin, H.-J. (2009). Dispersity and stability measurements of functionalized multiwalled carbon nanotubes in organic solvents. *Curr. Appl. Phys.* 9, e100–e103. doi:10.1016/j.cap.2008.12.039

Kim, J. T., Jeong, H. J., Park, H. C., Jeong, H. M., Bae, S. Y., Kim, B. K., et al. (2015). Electroactive shape memory performance of polyurethane/graphene nanocomposites. *React. Funct. Polym.* 88, 1–7. doi:10.1016/j.reactfunctpolym.2015.01.004

Kim, J., Ko, H. U., and Kim, H. C. (2021). Refractive index change of cellulose nanocrystal-based electroactive polyurethane by an electric field. *Front. Bioeng. Biotechnol.* 9, 606008. doi:10.3389/fbioe.2021.606008

Laza, J. M., Veloso, A., and Vilas, J. L. (2020). Tailoring new bisphenol a ethoxylated shape memory polyurethanes. *J. Appl. Polym. Sci.* 138, 49660. doi:10.1002/app.49660

Leng, J., Lan, X., Liu, Y., and Du, S. (2011). Shape-memory polymers and their composites: Stimulus methods and applications. *Prog. Mater. Sci.* 56, 1077–1135. doi:10.1016/j.pmatsci.2011.03.001

Liu, W., Zhao, Y., Wang, R., Li, J., Li, J., Luo, F., et al. (2017). Post-crosslinked polyurethanes with excellent shape memory property. *Macromol. Rapid Commun.* 38, 1700450. doi:10.1002/marc.201700450

Liu, J., Chen, Z., Hu, C., Yang, W., Wang, J., Xu, W., et al. (2021). Fluorescence visualization directly monitors microphase separation behavior of shape memory polyurethanes. *Appl. Mater. Today* 23, 100986. doi:10.1016/j.apmt.2021.100986

Lopes, M. C., Ribeiro, H., Gonçalves Santos, M. C., Seara, L. M., Queiroz Ferreira, F. L., Lavall, R. L., et al. (2017). High performance polyurethane composites with isocyanate-functionalized carbon nanotubes: Improvements in tear strength and scratch hardness. *J. Appl. Polym. Sci.* 134. doi:10.1002/app.44394

Mahapatra, S. S., Yadav, S. K., Yoo, H. J., Ramasamy, M. S., and Cho, J. W. (2014). Tailored and strong electro-responsive shape memory actuation in carbon nanotube-reinforced hyperbranched polyurethane composites. *Sensors Actuators B Chem.* 193, 384–390. doi:10.1016/j.snb.2013.12.006

Mogha, A., and Kaushik, A. (2021). Functionalized multiwall carbon nanotubes to enhance dispersion in castor oil-based polyurethane nanocomposites. *Fullerenes, Nanotub. Carbon Nanostructures* 29, 907–914. doi:10.1080/1536383x.2021.1915295

Moghim, M. H., Zebarjad, S. M., and Eqra, R. (2018). Experimental and modeling investigation of shape memory behavior of polyurethane/carbon nanotube nanocomposite. *Polym. Adv. Technol.* 29, 2496–2504. doi:10.1002/pat.4361

Nejad, S., Rezaei, M., and Bagheri, M. (2019). Polyurethane/nitrogen-doped graphene quantum dot (N-gqd) nanocomposites: Synthesis, characterization, thermal, mechanical and shape memory properties. *Polymer-Plastics Technol. Mater.* 59, 398–416. doi:10.1080/25740881.2019.1647243

Nouri, N., Rezaei, M., Mayan Sofla, R. L., and Babaie, A. (2020). Synthesis of reduced octadecyl isocyanate-functionalized graphene oxide nanosheets and investigation of their effect on physical, mechanical, and shape memory properties of polyurethane nanocomposites. *Compos. Sci. Technol.* 194, 108170. doi:10.1016/j.compscitech.2020.108170

Park, S., Moon, J., Kim, B., and Cho, M. (2021). Multi-scale coarse-grained molecular dynamics simulation to investigate the thermo-mechanical behavior of shape-memory polyurethane copolymers. *Polymer* 213, 123228. doi:10.1016/j.polymer.2020.123228

Qu, M., Wang, H., Chen, Q., Wu, L., Tang, P., Fan, M., et al. (2022). A thermally-electrically double-responsive polycaprolactone – Thermoplastic polyurethane/multi-walled carbon nanotube fiber assisted with highly effective shape memory and strain sensing performance. *Chem. Eng. J.* 427, 131648. doi:10.1016/j.cej.2021.131648

Rahmat, M., Das, K., and Hubert, P. (2011). Interaction stresses in carbon nanotube-polymer nanocomposites. *ACS Appl. Mat. Interfaces* 3, 3425–3431. doi:10.1021/am200652f

Raza, T., Qu, L., Khokhar, W. A., Andrews, B., Ali, A., Tian, M., et al. (2021). Progress of wearable and flexible electrochemical biosensors with the aid of conductive nanomaterials. *Front. Bioeng. Biotechnol.* 9, 761020. doi:10.3389/fbioe.2021.761020

Ren, D., Chen, Y., Li, H., Rehman, H. U., Cai, Y., Liu, H., et al. (2019). High-efficiency dual-responsive shape memory assisted self-healing of carbon nanotubes enhanced polycaprolactone/thermoplastic polyurethane composites. *Colloids Surfaces A Physicochem. Eng. Aspects* 580, 123731. doi:10.1016/j.colsurfa.2019.123731

Rosales, C. a. G., Duarte, M. F. G., Kim, H., Chavez, L., Hodges, D., Mandal, P., et al. (2018). 3D printing of shape memory polymer (SMP)/carbon black (CB) nanocomposites with electro-responsive toughness enhancement. *Mat. Res. Express* 5, 065704. doi:10.1088/2053-1591/aacd53

Sahoo, N. G., Rana, S., Cho, J. W., Li, L., and Chan, S. H. (2010). Polymer nanocomposites based on functionalized carbon nanotubes. *Prog. Polym. Sci.* 35, 837–867. doi:10.1016/j.progpolymsci.2010.03.002

Salam, M. A., and Burk, R. (2017). Synthesis and characterization of multi-walled carbon nanotubes modified with octadecylamine and polyethylene glycol. *Arabian J. Chem.* 10, S921–S927. doi:10.1016/j.arabjc.2012.12.028

Sang, Z., Ke, K., and Manas-Zloczower, I. (2019). Effect of carbon nanotube morphology on properties in thermoplastic elastomer composites for strain sensors. *Compos. Part A Appl. Sci. Manuf.* 121, 207–212. doi:10.1016/j.compositesa.2019.03.007

Sofla, R. M. L, Rezaei, M., Babaie, A., and Nasiri, M. (2019). Preparation of electroactive shape memory polyurethane/graphene nanocomposites and investigation of relationship between rheology, morphology and electrical properties. *Compos. Part B Eng.* 175, 107090. doi:10.1016/j.compositesb.2019.107090

Song, W.-H., Ni, Q.-P., Zheng, Z., Tian, L.-Y., and Wang, X.-L. (2009). The preparation of biodegradable polyurethane/carbon nanotube composite based onin situcross-linking. *Polym. Adv. Technol.* 20, 327–331. doi:10.1002/pat.1271

Sun, L., Gao, X., Wu, D., and Guo, Q. (2020). Advances in physiologically relevant actuation of shape memory polymers for biomedical applications. *Polym. Rev.* 61, 280–318. doi:10.1080/15583724.2020.1825487

Sun, J., Peng, B., Lu, Y., Zhang, X., Wei, J., Zhu, C., et al. (2022). A photoorganizable triple shape memory polymer for deployable devices. *Small* 18, e2106443. doi:10.1002/smll.202106443

Tamore, M. S., Ratna, D., Mishra, S., and Shimpi, N. G. (2019). Effect of functionalized multi-walled carbon nanotubes on physicomechanical properties of silicone rubber nanocomposites. *J. Compos. Mater.* 53, 3157–3168. doi:10.1177/0021998319827080

Umair, M. M., Zhang, Y., Zhang, S., Jin, X., and Tang, B. (2019). A novel flexible phase change composite with electro-driven shape memory, energy conversion/storage and motion sensing properties. *J. Mat. Chem. A Mat.* 7, 26385–26392. doi:10.1039/c9ta09088f

Ur Rehman, H., Chen, Y., Hedenqvist, M. S., Li, H., Xue, W., Guo, Y., et al. (2018). Self-Healing shape memory PUPCL copolymer with high cycle life. *Adv. Funct. Mat.* 28, 1704109. doi:10.1002/adfm.201704109

Wen, Z., Mcbride, M. K., Zhang, X., Han, X., Martinez, A. M., Shao, R., et al. (2018). Reconfigurable LC elastomers: Using a thermally programmable monodomain to access two-way free-standing multiple shape memory polymers. *Macromolecules* 51, 5812–5819. doi:10.1021/acs.macromol.8b01315

Xia, Y., He, Y., Zhang, F., Liu, Y., and Leng, J. (2021). A review of shape memory polymers and composites: Mechanisms, materials, and applications. *Adv. Mat.* 33, e2000713. doi:10.1002/adma.202000713

Xie, H., Shao, J., Ma, Y., Wang, J., Huang, H., Yang, N., et al. (2018). Biodegradable near-infrared-photoresponsive shape memory implants based on black phosphorus nanofillers. *Biomaterials* 164, 11–21. doi:10.1016/j.biomaterials.2018.02.040

Xu, X., Fan, P., Ren, J., Cheng, Y., Ren, J., Zhao, J., et al. (2018). Self-healing thermoplastic polyurethane (TPU)/polycaprolactone (PCL)/multi-wall carbon nanotubes (MWCNTs) blend as shape-memory composites. *Compos. Sci. Technol.* 168, 255–262. doi:10.1016/j.compscitech.2018.10.003

Zahedi, F., and Amraee, I. A. (2018). Carboxylated multiwalled carbon nanotubes effect on dynamic mechanical behavior of soft films composed of multilayer polymer structure. *Polymer* 151, 187–196. doi:10.1016/j.polymer.2018.07.044

Zhang, Z.-X., Dou, J.-X., He, J.-H., Xiao, C.-X., Shen, L.-Y., Yang, J.-H., et al. (2017). Electrically/infrared actuated shape memory composites based on a bio-based polyester blend and graphene nanoplatelets and their excellent self-driven ability. *J. Mat. Chem. C Mat.* 5, 4145–4158. doi:10.1039/c7tc00828g

Zhao, C., Ji, L., Liu, H., Hu, G., Zhang, S., Yang, M., et al. (2004). Functionalized carbon nanotubes containing isocyanate groups. *J. Solid State Chem.* 177, 4394–4398. doi:10.1016/j.jssc.2004.09.036

Zheng, Y., Qin, J., Shen, J., and Guo, S. (2020). Controllable distribution of conductive particles in polymer blends via a bilayer structure design: A strategy to fabricate shape-memory composites with tunable electro-responsive properties. *J. Mat. Chem. C Mat.* 8, 9593–9601. doi:10.1039/d0tc01854f

Zhu, Y., Hu, J., Choi, K.-F., Meng, Q., Chen, S., Yeung, K.-W., et al. (2008). Shape memory effect and reversible phase crystallization process in SMPU ionomer. *Polym. Adv. Technol.* 19, 328–333. doi:10.1002/pat.1001

frontiers | Frontiers in Bioengineering and Biotechnology

TYPE Original Research
PUBLISHED 11 August 2022
DOI 10.3389/fbioe.2022.959409

OPEN ACCESS

EDITED BY
Jianxun Ding,
Changchun Institute of Applied Chemistry (CAS), China

REVIEWED BY
Jayaramudu Tippabattini,
Centre of Polymer and Carbon Materials (PAN), Poland
Javier Ramon,
Institute for Bioengineering of Catalonia (IBEC), Spain
Sônia Maria Malmonge,
Federal University of ABC, Brazil
Aizheng Chen,
Huaqiao University, China

*CORRESPONDENCE
Hao Zhang,
zhanghao20201208@dlut.edu.cn
Xufeng Dong,
dongxf@dlut.edu.cn

SPECIALTY SECTION
This article was submitted to Biomaterials, a section of the journal Frontiers in Bioengineering and Biotechnology

RECEIVED 01 June 2022
ACCEPTED 11 July 2022
PUBLISHED 11 August 2022

CITATION
Liu D, Zhang H, Dong X, Sang L and Qi M (2022), Effect of viscoelastic properties of cellulose nanocrystal/collagen hydrogels on chondrocyte behaviors. *Front. Bioeng. Biotechnol.* 10:959409. doi: 10.3389/fbioe.2022.959409

Effect of viscoelastic properties of cellulose nanocrystal/collagen hydrogels on chondrocyte behaviors

Donglei Liu[1,2], Hao Zhang[2,3,4]*, Xufeng Dong[2]*, Lin Sang[5] and Min Qi[2]

[1]School of Basic Medicine, Binzhou Medical University, Yantai, China, [2]School of Materials Science and Engineering, Dalian University of Technology, Dalian, China, [3]Department of Orthopedics, Central Hospital of Dalian University of Technology, Dalian, China, [4]Changchun SinoBiomaterials Co., Ltd., Changchun, China, [5]School of Automotive Engineering, Dalian University of Technology, Dalian, China

Cartilage tissue engineering technology provides a solution for treating osteoarthritis. Based on the viscoelastic nature of articular cartilage, many viscoelastic hydrogel scaffolds have been developed for investigating the effects on chondrocyte behaviors. However, cellulose nanocrystal/collagen (CNC/COL) hydrogels have not been used as a viscoelastic microenvironment to study chondrocyte growth. Here, we prepared CNC/COL hydrogels with tunable viscoelastic properties and investigated their influences on chondrocyte behaviors. The results showed that CNC and COL within the hydrogels are bonded by hydrogen bonds. The hydrogels had a microporous structure, and the viscoelastic properties were enhanced by increasing the concentration of CNC. Moreover, enhancing the hydrogel viscoelastic properties, including stress relaxation, creep, storage modulus, and loss modulus, promoted the cell shape change, proliferation, and matrix deposition and reduced the IL-1β level. Using a principal component analysis (PCA), stress relaxation was assessed to have the strongest correlation with chondrocytes behaviors, with an authority weight value of 62.547%. More importantly, FAK and YAP were involved in the chondrocytes' response to the rapid relaxing hydrogel by immunofluorescence staining.

KEYWORDS

hydrogel, viscoelasticity, stress relaxation, creep, chondrocyte behavior

Introduction

Osteoarthritis is a common chronic disease characterized by degeneration of articular cartilage (Getgood et al., 2009). In addition, articular cartilage does not have blood vessels, nerves, and lymphatics, and it has a limited intrinsic healing capacity (Klein et al., 2010). Thus, osteoarthritis can lead to severe disability in patients if it is not treated seriously. Cartilage tissue engineering technology provides a solution for repairing cartilage defects (Lee et al., 2007). The growth status of chondrocytes in hydrogel scaffolds largely determines the quality of resulting cartilage tissue (Mauck et al., 2000; Lima et al.,

2007). Therefore, it is of great scientific significance to study the chondrocyte behaviors at the cellular level for repairing damaged cartilage.

Over the past decade, it has been demonstrated that hydrogels can serve as synthetic extracellular matrix (ECM) microenvironments and capture some features of ECM such as mechanical cues to modulate cellular behaviors significantly. Many studies have shown the correlation of stiffness with cellular behaviors such as cell adhesion, morphology, mobility, and disease progression (Discher et al., 2005; Engler et al., 2006; Solon et al., 2007; Walker et al., 2021). Walker et al. (2021) showed that nuclear mechano-sensing drove distinct chromatin signatures in persistently activated fibroblasts cultured on hydrogels with increased stiffness, which is of great significance to the study of fibrosis. To provide material platform for these studies, elastic polyacrylamide hydrogels are commonly used, but unfortunately it do not exhibit the same time-dependent and viscoelastic responses as biological tissues (Lee et al., 2019). Moreover, Bauer et al. (2017) found that elastic stress in hydrogels restricted some normal cellular process, such as shape change, proliferation, and matrix deposition.

In recent years, an increasing number of literatures have shown that hydrogels with viscoelastic properties are capable of accelerating cellular processes in comparison with stiffness. Researchers have developed various types of viscoelastic hydrogels and elucidated the interaction of cells with two-dimensional (2D) or three-dimensional (3D) hydrogels with different viscoelastic levels (Cameron et al., 2014; Chaudhuri et al., 2016; Bauer et al., 2017; Lee et al., 2017; Chester et al., 2018; Lou et al., 2018; Richardson et al., 2018). Bauer et al. (2017) prepared a set of 2D alginate hydrogels with varying initial elastic moduli and stress relaxation rates. They found that stress-relaxing hydrogel promoted myoblasts spreading and proliferation compared to the elastic with the same stiffness. With the development of highly controllable viscoelastic hydrogels and the deepening understanding of cell–ECM interactions, many works have made important advances in hydrogel viscoelasticity regulating cellular behaviors. For example, Cameron et al. (2014) found that higher loss modulus of 2D collagen/polyacrylamide hydrogel encouraged the mesenchymal stem cells (MSCs) proliferation, spread, and differentiation potential toward a smooth muscle cell (SMC) lineage. The creep-induced loss of cytoskeletal tension resulted in the increase in spread area and the increased Rac 1 activity transformed MSCs into a SMC lineage. In addition, Chester et al. (2018) showed that the difference in loss tangent of N-isopropylacrylamide microgel films could regulate fibroblast migration modes. Interestingly, it reported that faster stress relaxation of 3D alginate hydrogels enhanced fibroblast spreading, proliferation, and osteogenic differentiation of MSCs (Chaudhuri et al., 2016). The arginine–glycine–aspartic acid (RGD) ligands locally clustering, actomyosin contractility, Rho signaling pathway, and YAP nuclear localization were demonstrated to be involved in cellular responses to altered hydrogel stress relaxation. Similarly, faster stress relaxation in the hyaluronic acid/collagen hydrogels promoted cell spreading, fiber remodeling, and focal adhesion (FA) formation in 3D culture (Lou et al., 2018). Notably, Lee et al. (2017) found that faster relaxation and creep and greater loss tangent of alginate hydrogels promoted cartilage matrix formation and proposed that the chondrocytes sensed the substrate mechanical properties by cell volume confinement in 3D culture. Furthermore, hydrazone cross-linked poly(ethylene glycol) hydrogels with tunable stress relaxation times from hours to months were formulated by Richardson et al. (2018). Moreover, 4 weeks post-encapsulation of chondrocytes, the hydrogel with relaxation times of 3 days enhanced the cellularity and cartilage matrix interconnectivity.

As mentioned before, various hydrogel materials are utilized to show that cellular processes associated with their viscoelastic properties have important implications for repairing cartilage defects. However, the CNC/COL hydrogels with different viscoelastic properties have not been used to study chondrocyte behaviors. Here, we used microporous CNC/COL hydrogels as a tunable material platform for investigating the role of the viscoelastic properties in chondrocyte behaviors and elucidating the related intracellular mechano-transduction mechanism. Collagen, a natural protein, possesses inherent cytocompatibility due to the presence of cell adhesion ligand binding sites, but low Young's modulus limits its development (Zhang et al., 2014; Yang et al., 2019). To address this issue, a common strategy is to utilize composite technology to add nanoscale reinforcement additive into collagen. CNC is a kind of renewable rod-shaped nanocrystals. It possesses many desirable properties, such as no cytotoxicity, high strength, stiffness, excellent hydrophilicity, and water retention capacity due to the abundance of surface hydroxyl groups (Martha et al., 2014; Trache et al., 2017; Abitbol et al., 2018; Biswal et al., 2020). Moreover, the CNC/COL hydrogels have a wide range of viscoelastic properties by changing component concentration (Liu et al., 2020). Since the stiffness (represented by storage modulus) of the CNC/COL hydrogels is not independent, the authority weights of viscoelastic parameters such as stress relaxation, creep, storage modulus, and loss modulus on the behavior of chondrocytes were assessed using PCA by SPSS software.

Materials and methods

Materials

Cellulose microcrystal (CMC) was purchased from Hainan Yide Food Co., Ltd. (Hainan, China). Rat tail type I collagen (COL, 3 mg/ml) was bought from GIBCO Invitrogen Corporation (California, United States). Acetic acid, ethanol,

N-(3-Dimethylaminopropyl)-N′-ethylcarbodiimide hydrochloride (EDAC), and N-Hydroxysuccinimide (NHS) were purchased from Aladdin (Shanghai, China). The deionized water was provided by our laboratory. Primary chondrocytes were provided by Beijing Baiou Bowei Biotechnology Co., Ltd. (Beijing, China), and the cells were verified to be free of mycoplasma by the manufacturer. Dulbecco's modified Eagle's medium (DMEM), fetal bovine serum (FBS), and penicillin/streptomycin were bought from GIBCO Invitrogen Corporation (California, United States). L-ascorbic acid-2-phosphate was purchased from Sigma (Shanghai, China). Trypsin/EDTA solution, paraformaldehyde, sucrose, optimal cutting temperature compound (OCT), Triton X-100, goat serum (Solarbio), DAPI, Alexafluor 488 phalloidin, and papainase were bought from Beijing Solarbio Science & Technology Co., Ltd. (Beijing, China). Rabbit anti-collagen II polyclonal antibody (bs-10589R), rabbit anti-ACAN polyclonal antibody (bs-1223R), and goat anti-rabbit IgG/Cy3 (Cat. #bs-0295G-Cy3) were purchased from Beijing Biosynthesis Biotechnology Co., Ltd. (Beijing, China). FAK (focal adhesion kinase) rabbit mAb (Cat. #A11131) and YAP1 (Yes associated protein 1) rabbit pAb (Cat. #A1002) were bought from Wuhan ABclonal Biotechnology Co., Ltd. (Wuhan, China). PicoGreen assay, hydroxyproline assay, 1,9-dimethylmethylene blue (DMMB) assay, lambda phage DNA, chondroitin sulfate, and L-hydroxyproline were purchased from Genmed Scientifics Inc., United States (Shanghai, China). The rat IL-1β ELISA reagent kit and recombinant rat IL-1β were bought from Jiangsu MEIMIAN Industrial Co., Ltd. (Jiangsu, China).

Cellulose nanocrystal preparation

The CNC was prepared using the homogenization method (Liu et al., 2021). First, the 0.2 wt.% CMCs aqueous solution was sealed with a plastic wrap and swelled for 24 h at room temperature. Then the obtained CMC gel was sheared at 12,000 rpm for 5 min and centrifuged at 8,000 rpm for 20 min, and then the clear phase was collected. Finally, the collected CNCs dispersion was used for freeze-drying before use.

Cellulose nanocrystal/collagen hydrogel preparation

The CNC/COL hydrogels with different viscoelastic levels were prepared as described previously (Liu et al., 2021). In brief, COL was blended with 0.5 M acetic acid for 90 min in a cooled reaction vessel using a homogenizer at a speed of 10,000 rpm for 5 min. Cellulose nanocrystals (CNCs) were added in aliquots to the collagen solution every hour during blending to obtain the mixed solutions with a final collagen concentration of 0.5 wt.% and varying CNC concentrations of 2.5 wt.%, 5 wt.%, 10 wt.%, and 15 wt.%, respectively. The mixtures were degassed in a vacuum desiccator for 60 min. They were poured in a culture dish and froze for 4 h at −35°C. Then they were freeze-dried at −40°C and 10 Pa for 72 h to obtain dehydrated porous samples. Next, the samples were cross-linked in an ethanol solution of EDAC and NHS using a concentration of 6 mM EDAC g^{-1} of collagen, and a 5:2 M ratio of EDAC:NHS at 37°C for 72 h under oscillation, after which they were rinsed several times with deionized water. Finally, the hydrogel samples were punched into cylinders (6 mm diameter × 3 mm height) for using in following experiments.

Atomic force microscopy characterization

The CNCs height dimensions were evaluated by atomic force microscopy (AFM, Bruker Dimension 3100 SPM) in the tapping mode. Rectangular ferromagnetic resonance cantilevers with a spring constant of 2.4 N/m and a resonance frequency of 60 kHz were used to image CNCs on the mica substrates. The data was obtained in three different positions on three different images. All the measurements were done in air at room temperature.

Fourier transform infrared spectrometer characterization

The functional groups of the freeze-dried pure collagen hydrogel, CNCs dispersion, and CNC/COL hydrogels with different CNC concentrations were analyzed by using the Fourier transform infrared spectrometer (FTIR, Thermo Fisher Scientific, Nicolet 6700). A diamond crystal plate was used and the scanning wavelength ranged between 500 and 4,000 cm^{-1}, with a resolution of 4 cm^{-1}, and the number of scanning speed was 30 s^{-1}.

Scanning electron microscope characterization

The microstructures of the CNC/COL porous scaffolds were observed using a field-emission scanning electron microscope (SEM, Zeiss, SUPARR-55) at an acceleration voltage of 5 kV. The cross sections of the CNC/COL porous scaffolds were coated with gold by sputtering at 30 mA for 40 s using a sputter coater (Quorum, Q150V ES) before observation. The pore size of scaffolds was measured manually by evaluating three SEM images of three samples but with the same CNC concentration using ImageJ software (Bethesda). The detailed process includes importing the SEM image, setting scale, and measuring pore size. The results of pore size were statistically analyzed by using Origin 8.0 software (Origin Lab).

Rheological characterization

The viscoelastic properties of CNC/COL hydrogels were measured using a rotational rheometer (Anton Paar, Physica MCR 301). The hydrogel was submerged in water at 37°C during the tests. Cylindrical hydrogel was placed between parallel plates and the gap between the plates, which was adjusted using a normal force of 0.1 N in order to prevent slippage. All measurements did not run until the hydrogel relaxed to an equilibrium state. In stress relaxation test, a shear strain of 100% was applied on the hydrogel and maintained constant up to the end of the test while recording the corresponding shear stress, as a function of time. A creep test was performed by applying a constant shear stress of 100 Pa on the hydrogel and recording the shear strain over time, followed by creep recovery. A strain sweep was carried out at a frequency of 1 Hz with amplitudes ranging between 0.01% and 100% to measure the storage modulus and loss modulus as functions of strain amplitude. Each test was repeated three times.

Primary chondrocyte culture

The culture of primary chondrocytes was conducted according to a previously published method (Lou et al., 2018). In brief, the chondrocytes isolated from rat cartilage were cultured in 75 cm^2 tissue culture flasks (Thermo Fisher Scientific) in standard DMEM with an atmosphere of 5% CO_2 at 37°C. The DMEM was supplemented with 10% FBS, 0.05 mg ml^{-1} L-ascorbic acid-2-phosphate, and 1% penicillin/streptomycin. The cell culture medium was refreshed every 3 days.

Seeding chondrocytes into porous hydrogels

For cell culture use, the lyophilized hydrogels were sterilized with 70% ethanol, washed three times with deionized water, and conditioned with DMEM at 37°C for 60 min. The chondrocytes were harvested by treatment with a 0.05% trypsin/ethylene diamine tetra acetic acid solution when the cells reached a confluence of 80%. The harvested chondrocytes (P1 chondrocytes) were re-suspended in DMEM to prepare a cell suspension solution of 1×10^5 cells ml^{-1} for cell seeding. The concentration of the cells was determined using a Coulter counter (Beckman Coulter). The P1 chondrocytes were seeded into the hydrogels by adding 1 ml of the cell suspension solution (1×10^5 cells per hydrogel) to each of the cylindrical sides of the hydrogels.

Immunohistochemistry

The hydrogels containing chondrocytes cultured for 3, 7, and 14 days were fixed with 4% paraformaldehyde for 60 min and washed three times in phosphate-buffered saline (PBS). The hydrogels were placed in 30% sucrose at 4°C for 1 day and then incubated in optimal cutting temperature compound (OCT)–sucrose, a mixture of 50% OCT and 30% sucrose solution, for 5 h. They were then embedded in OCT, frozen, and sectioned. The sections were prepared with a thickness of approximately 50 μm using a cryostat (Leica CM1950) and processed using standard immunohistochemistry procedures. Sections were washed three times in PBS, permeabilized with PBS containing 0.5% Triton X-100 for 20 min, and blocked with a blocking buffer composed of 10% goat serum and 0.1% Triton X-100 in PBS for 30 min. The following antibodies and reagents were used for immunostaining: DAPI, Alexafluor 488 Phalloidin, rabbit anti-collagen II polyclonal antibody, rabbit anti-ACAN polyclonal antibody, goat anti-rabbit IgG/Cy3, FAK rabbit mAb, and YAP1 rabbit pAb. Each immunostaining was performed in six sections obtained from three hydrogels with the same CNC concentration.

Biochemical analysis

In brief, the hydrogels containing chondrocytes was cultured for 14 days were freeze-dried and their dry mass was measured. The dried samples were then digested in PBS with papainase at 60°C for 16 h. The PicoGreen assay was conducted to measure the amount of DNA in the hydrogels. Lambda phage DNA was used as the standard for DNA quantity under the assay. The proliferation rate was calculated by the measured DNA amounts divided by the DNA amounts of seeded cells. The DMMB assay was applied to measure the amounts of GAGs in the hydrogels. Chondroitin sulfate was used as the standard of GAGs amount with the DMMB assay. The hydroxyproline assay was utilized to measure the amount of the collagen matrix in the hydrogels. L-Hydroxyproline was used as the standard of hydroxyproline amount under the assay. The collagen amount was calculated by a mass ratio of hydroxyproline: collagen of 1: 7.46. The measured values of collagen, GAGs, and DNA amounts were normalized with the dry mass of the hydrogels. Three samples were used for each biochemical analysis.

IL-1β level analysis

The hydrogels containing chondrocytes were removed from culture medium after 14 days of culture and washed in PBS. They were crushed with pestles for homogenization. The crushed samples were then totally disassociated by adding 2 mM EDTA solution. The suspension was centrifuged at 10,000 r.p.m. for 2 min and the supernatant was extracted. The rat IL-1β ELISA reagent kit was utilized to quantify the protein concentration of IL-1β was quantified, and the recombinant rat IL-1β was used as a standard. The values

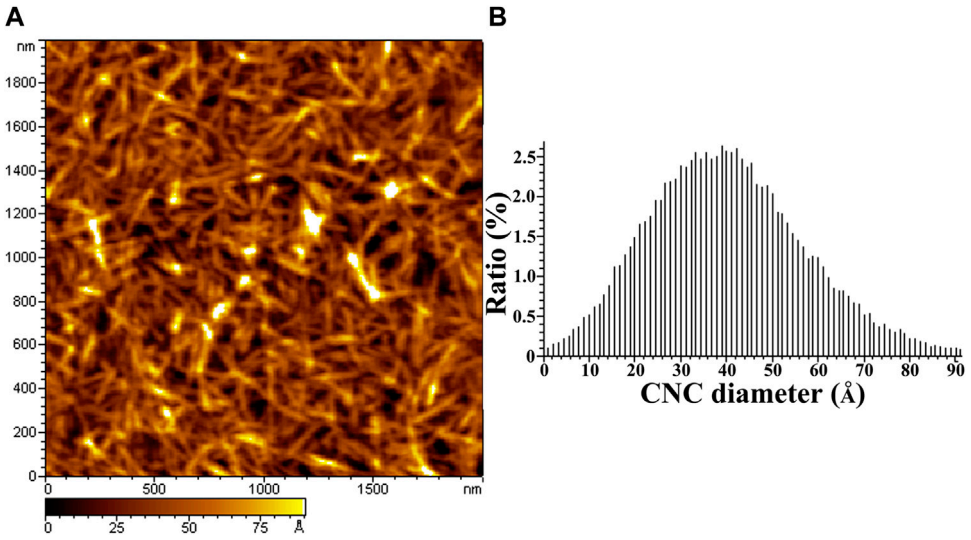

FIGURE 1
AFM height image and the diameter distribution of CNCs. **(A)** is the AFM image of CNCs, **(B)** is the diameter distribution of CNCs.

were normalized to DNA amounts in each of the hydrogels. Three samples were used for each analysis.

Image analysis

For assessing spreading, immunohistochemical staining of the hydrogel sections containing chondrocytes for DAPI/phalloidin were imaged using an inverted fluorescence microscope (Olympus, lx71). The DAPI channel was used for nuclei detection and the phalloidin channel was used for cell body detection. The area of the chondrocytes was determined using a custom routine (threshold–analyze particles) in ImageJ. The aspect ratio of the chondrocytes was measured manually by ImageJ. The cell area and aspect ratio values were obtained from four phalloidin staining images, respectively. For measurements of FAK localization in the chondrocytes, DAPI/phalloidin/FAK antibody staining of hydrogel sections was imaged. For measurements of YAP localization, DAPI/phalloidin/YAP antibody staining of hydrogel sections was imaged.

Principal component analysis

Utilizing IBM SPSS Statistics 20.0 software, principal component analysis (PCA) was used to assess the authority weight of the viscoelastic parameters, including stress relaxation time ($\tau_{1/2}$), creep time ($\gamma_{1/2}$), storage modulus (G') and loss modulus (G''), in study of chondrocyte behaviors. Specifically, the data on spreading, proliferation, and matrix

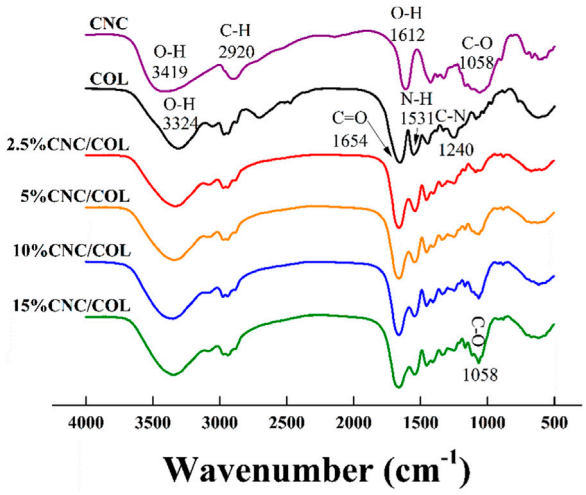

FIGURE 2
FTIR spectrogram of CNC/COL hydrogels with different CNC concentrations.

levels were all imported into the workbook to obtain the weight values.

Statistical analysis

Statistical differences were determined by analysis of variance or Student's *t* test where appropriate, with significance indicated by $p < 0.05$.

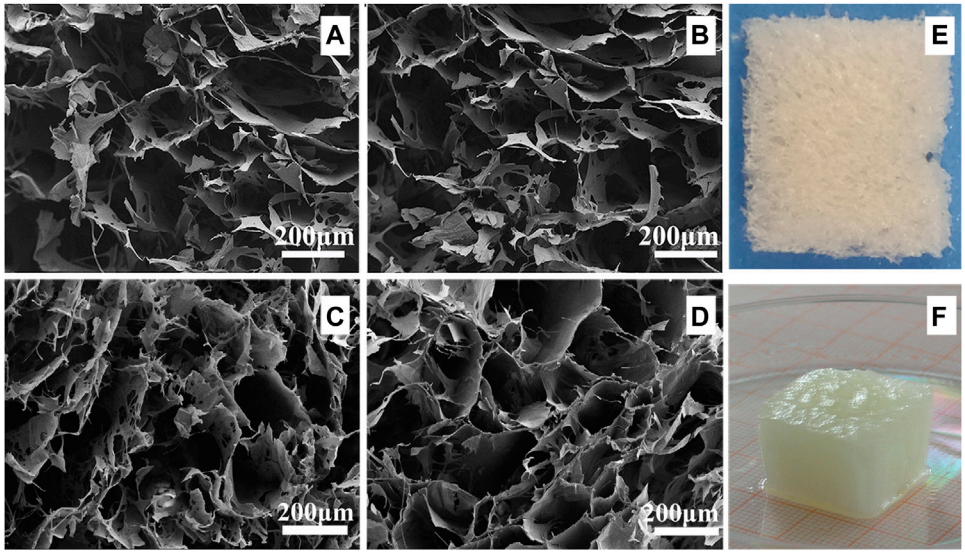

FIGURE 3
SEM images and digital photographs of CNC/COL hydrogels with different CNC concentrations. **(A)** 2.5 wt.% CNC, **(B)** 5 wt.% CNC, **(C)** 10 wt.% CNC, and **(D)** 15 wt.% CNC; **(E)** and **(F)** are the digital photographs of the cryogel and the hydrogel with 15 wt.% CNC.

Results

Atomic force microscopy analysis

Figure 1 shows the AFM image of CNC (Figure 1A) and its corresponding AFM measured height distribution (Figure 1B). CNC with length of several hundred nanometers is visible from the AFM image and the average diameter of 4 nm is found in the height statistics of the image.

Fourier transform infrared spectrometer analysis

As shown in Figure 2, some characteristic absorptions of CNC occur at 3,419, 2,920, 1,612, and 1,058 cm^{-1}, corresponding to stretching vibrations of O-H, C-H, O-H, and C-O (Martha et al., 2014; Jayaramudu et al., 2018; Jayaramudu et al., 2019; Liu et al., 2020; Liu et al., 2021). For collagen hydrogel (COL), the absorptions at 3,324, 1,654, 1,531, and 1,240 cm^{-1}, can be ascribed to stretching vibrations of the O-H in amide I, the C=O bond in amid, the N-H and C-H bonds in amide II, and the C-N bond in amide III, respectively (Zhang et al., 2014; Yang et al., 2019). Notably, the absorption peak at 3,324 cm^{-1} occurs a slight blue shift with the addition of CNC to the collagen hydrogel, which indicates that the two materials are bonded by hydrogen binding (Jayaramudu et al., 2018; Jayaramudu et al., 2019). Further, the absorption that is at 1,058 cm^{-1} becomes strong gradually with CNC concentration, which further indicates that CNC has been successfully introduced into the hydrogels.

Scanning electron microscope analysis

As shown in Figure 3, the hydrogels with varying CNC concentrations display a microporous structure. The pore size is 222 ± 29 μm, 214 ± 19 μm, 202 ± 17 μm, and 195 ± 20 μm under the CNC concentration of 2.5 wt.%, 5 wt.%, 10 wt.%, and 15 wt.%. The pore size of the hydrogel with 2.5 wt.% CNC is significantly larger than that of the hydrogel with 15 wt.% CNC (independent samples t test, $p < 0.05$). The range of pore size falls within the optimal pore diameter range of 150–250 μm, which is reported to promote the expression and production of type II collagen and aggrecan in culture of chondrocytes (Zhang et al., 2014; Andrea et al., 2018).

The viscoelastic properties of cellulose nanocrystal/collagen hydrogels

Previous studies have demonstrated that the 3D microporous CNC/COL hydrogels displayed a wide and tuneable range of viscoelastic properties (Matellan and Hernandez, 2019). This is confirmed, as it is found that by increasing CNC concentration from 2.5% to 15%, the rate of stress relaxation ($\tau_{1/2}$) and creep ($\gamma_{1/2}$), and the value of G' and G'' are enhanced markedly (Figure 4). $\tau_{1/2}$ is defined as the quantification of timescale at which the shear stress relaxes to half its total decreased value. $\gamma_{1/2}$ is the quantification of timescale at which the shear strain goes up to half its total increased value. Specifically, the $\tau_{1/2}$ value of the hydrogels ranges from ~29.2 to ~ 261 s, and the frequency at

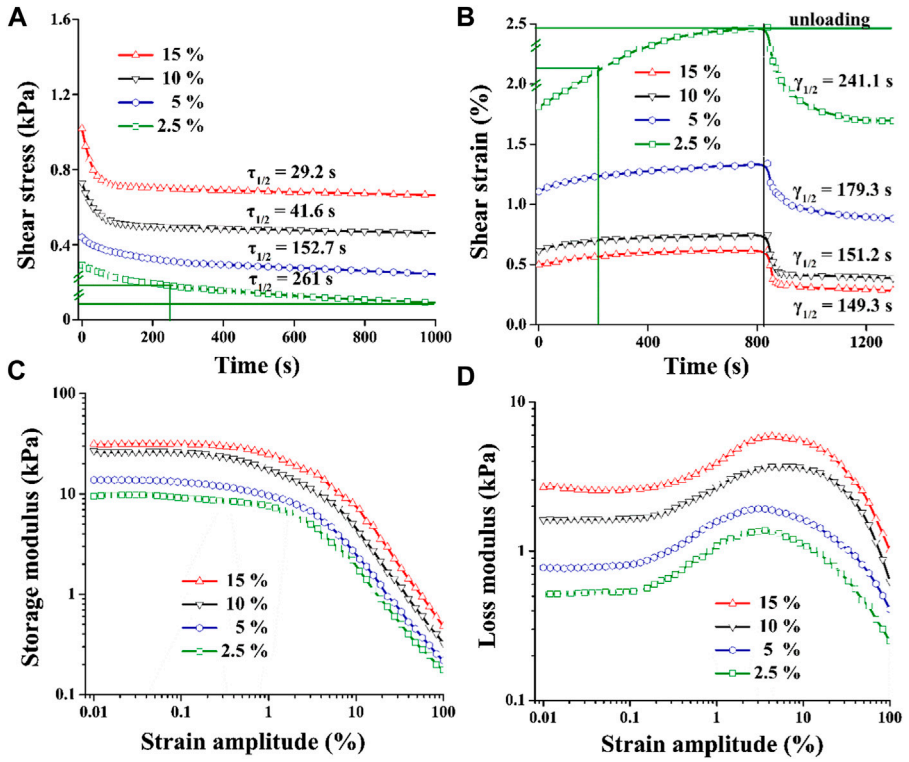

FIGURE 4
Viscoelastic properties of CNC/COL hydrogels with varying CNC concentrations. **(A)** stress relaxation, **(B)** creep, **(C)** storage modulus, and **(D)** loss modulus.

which the strain sweep measures G' and G'' is 1 Hz (Figure 4A). These timescales are related to some cellular behaviors, as cells are thought to exert traction with a timescale of minutes and respond to oscillating forces over a timescale of ~1 s (Mow et al., 1991). In addition, the G' value of the hydrogels ranges from 10 to 30 kPa in the linear viscoelastic region (Figure 4C), and it is an order of magnitude smaller than cartilage ECM which has a shear modulus of 200 ~ 500 kPa (Cameron et al., 2011; Loebel et al., 2020).

Chondrocyte spreading and proliferation

The microporous series of viscoelastic CNC/COL hydrogel scaffolds were used to culture the chondrocytes, and the effects of hydrogel viscoelasticity on cell spreading and proliferation behaviors were firstly studied. Figure 5A shows the immunofluorescence staining images of nucleus and actin skeleton of chondrocytes. After culture for 3 days, some chondrocytes in the hydrogels with higher viscoelastic properties (10% and 15% CNC), show elongated shape, while the chondrocytes in the hydrogels with lower viscoelastic properties (2.5% and 5% CNC), remain spherical shape, which is similar to the typical morphology when cell growth is inhibited in elastic hydrogel (Richardson et al., 2018). The variance in cell shape indicates that increasing hydrogel viscoelasticity can promote the morphological transformation of chondrocytes. With the prolonging of culture time (3–14 days), the chondrocytes in the hydrogels with the same viscoelastic level all show a tendency to spindle shape from spherical shape. However, at lower viscoelastic levels (2.5% and 5% CNC), the chondrocytes don't show significant shape change until 14 days of culture. In addition, the chondrocytes under the lowest viscoelastic level (2.5% CNC) emerge a spindle shaped change, but the number of cells is much lower than that under the other three viscoelastic levels (5%, 10%, and 15% CNC). These results suggest that increasing the rate of stress relaxation and creep, as well as storage modulus and loss modulus of CNC/COL hydrogels can promote chondrocyte growth.

Judging by the morphological transformation of chondrocytes, the process of cell spreading is accompanied by constantly exerting traction on the surface of hydrogel pores (Mow et al., 1991). It implies that the CNC/COL network under the pore surface is reconstructed dynamically by the chondrocytes. The mechanical reconstruction of CNC/COL network in turn provides

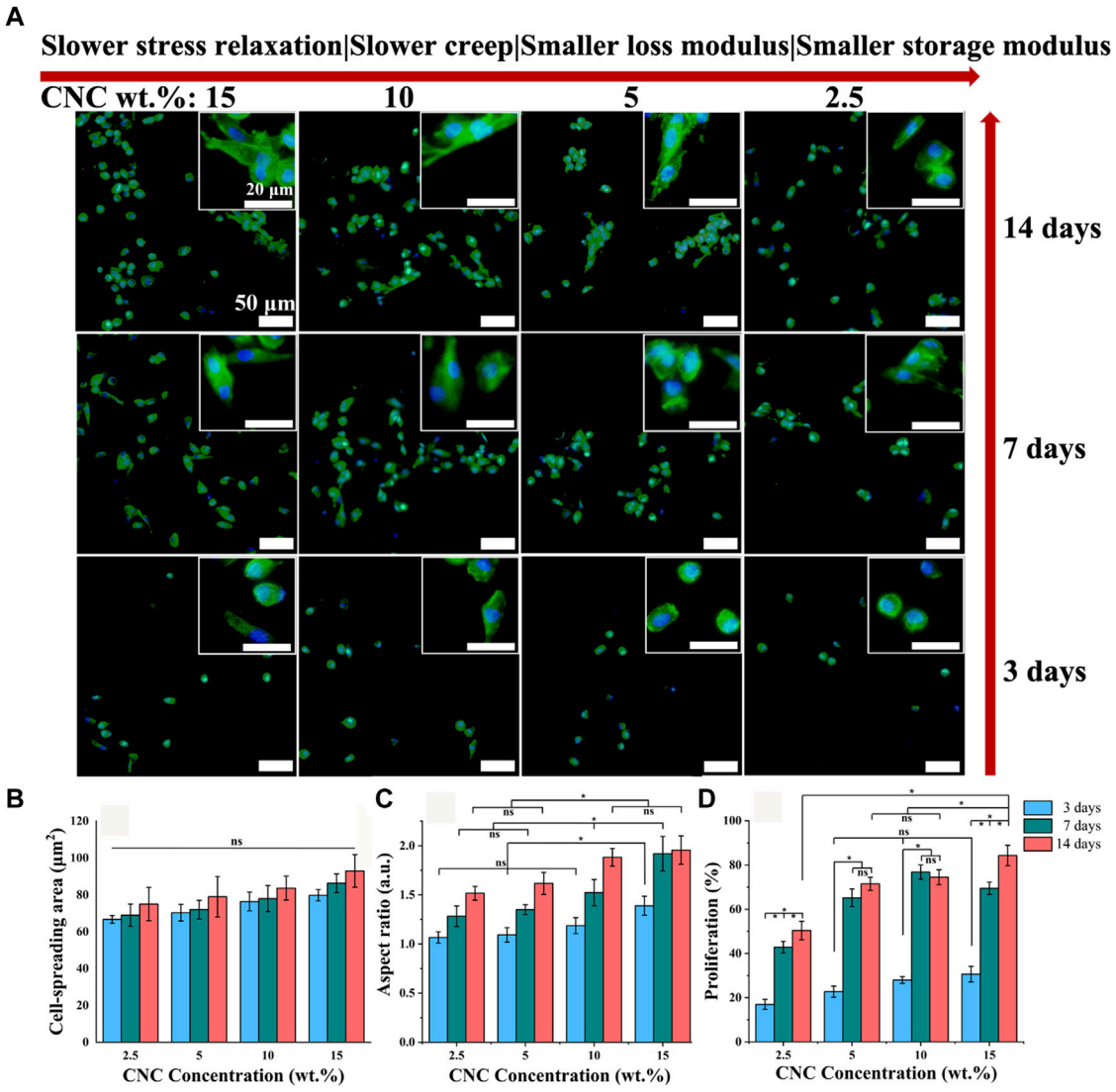

FIGURE 5
Cell spreading and proliferation for chondrocytes cultured in hydrogels with different viscoelastic properties. **(A)** Images of chondrocytes cultured in hydrogels with the indicated CNC concentration (2.5 wt.%, 5 wt.%, 10 wt.%, and 15 wt.%). Green represents actin staining and blue represents nucleus. Images were taken after 3, 7, and 14 days in culture. Scale bar is 50 μm. **(B–D)**, Spreading area, aspect ratio, and proliferation of chondrocytes (*$p < 0.05$).

larger space for cell spreading (Chaudhuri et al., 2016; Chester et al., 2018). Thus, the faster stress relaxation or creep of hydrogels will result in the higher aspect ratio of chondrocytes.

For this, the spreading and proliferation of chondrocytes cultured in the hydrogels with different viscoelastic levels are measured, and the results are shown in Figures 5B–D. With the prolonging of culture time and the increasing of viscoelastic properties, there is no significant difference in the spread area of chondrocytes, but its aspect ratio shows an increasing trend (*$p < 0.05$). At 3 days of culture, the cell aspect ratio in the hydrogel with the highest viscoelastic level (15% CNC) is significantly bigger than that in the other three viscoelastic hydrogels (*$p < 0.05$), which is consistent with the cell morphology observed in Figure 5A. At 7 and 14 days of culture, the aspect ratio in the hydrogels with higher viscoelastic levels (10% and 15% CNC) is still bigger than that in the hydrogels with lower viscoelastic levels (2.5% and 5% CNC). In addition, the proliferation rate of chondrocytes in no matter what kind of viscoelastic hydrogels presents stepped increase from 3 to 7 days of culture (Figure 5D, *$p < 0.05$). Further, the cell proliferation in the highest

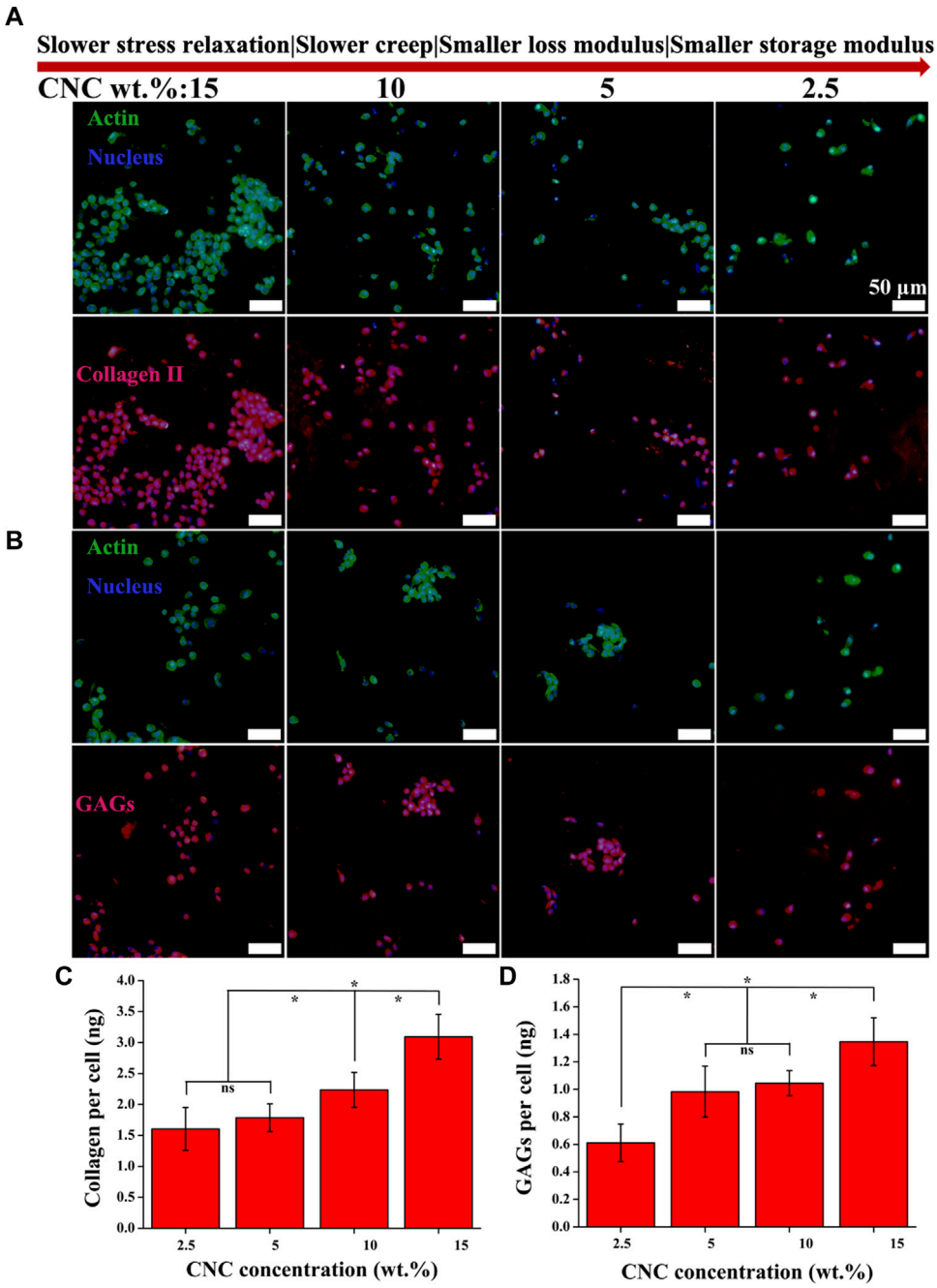

FIGURE 6
COL II and GAGs productions by chondrocytes cultured in the hydrogels with varying viscoelastic levels. **(A,B)** Images of COL II and GAGs staining for chondrocytes after 14 days of culture. **(C,D)** Quantification of the accumulated COL II and GAGs for chondrocytes after 14 days of culture (*$p < 0.05$).

viscoelastic hydrogel is larger than that in the other three viscoelastic hydrogels at 14 days of culture (*$p < 0.05$). These suggest that rapid stress relaxation and creep, as well as high storage modulus and loss modulus can promote chondrocytes growth such as elongation and proliferation.

Cartilage matrix formation

Type II collagen (COL II) and aggrecan (GAGs), critical components of cartilage matrix secreted by chondrocytes, were assessed with immunohistochemical staining after 14 days of

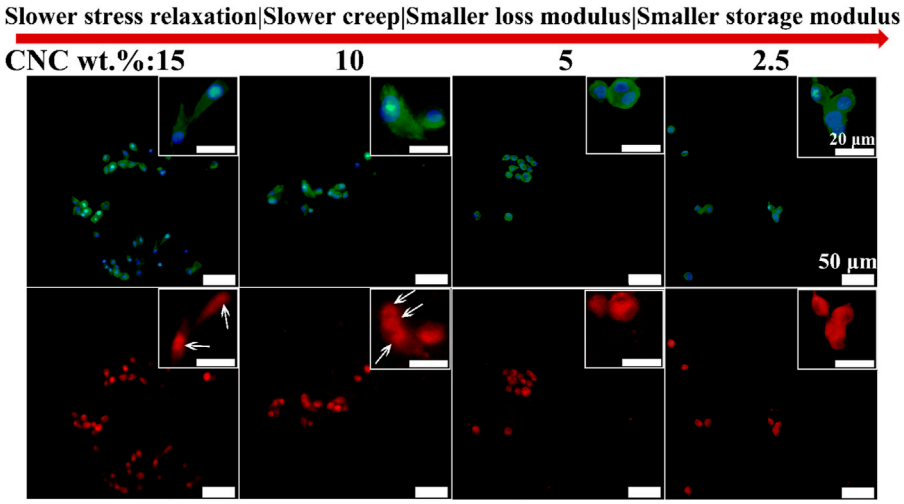

FIGURE 7
FAK staining of chondrocytes cultured in different viscoelastic hydrogels. Green represents actin staining, blue represents nucleus staining, and red represents FAK staining. Images were taken after 14 days in culture. White arrow indicates the location of FAK.

culture. As shown in Figures 6A,B, both COL II and GAGs are deposited in the region adjacent to the chondrocytes, not connected together, which is mainly attributed to the low viability of chondrocytes (Burdick and Prestwich, 2011; Loebel et al., 2020; Patel et al., 2021). With the increase of stress relaxation and creep rate, as well as storage modulus and loss modulus, the total area of COL II formation is observed to show an obvious increasing trend relative to GAGs. Further, as the hydrogels were cut into sections, greater area of cartilage matrix in the sections corresponds to greater volume of matrix in the hydrogels, i.e., the higher level of extracellular matrix secreted by the chondrocytes. To verify the inference, colorimetric method for hydroxyproline and DMMB content was used to quantitatively assess the amounts of both COL II and GAGs in the hydrogels with different viscoelastic levels. As shown in Figures 6C,D, the higher levels of both COL II and GAGs are measured in the hydrogels with faster stress relaxation and creep, as well as higher storage modulus and loss modulus ($^*p < 0.05$). In the highest viscoelastic hydrogel (15% CNC), the level of COL II (~3 ng/cell) is 2-fold higher than that of GAGs (~1.4 ng/cell).

Immunofluorescent staining of focal adhesion kinase and yes associated protein

Next, the roles of Focal Adhesion Kinase (FAK) and Yes Associated Protein (YAP) in the effect of viscoelastic properties of hydrogels on the chondrocyte behavior were investigated. FAK has been identified as a regulator in cell adhesion, migration and survival, and a critical signal transducer for cell–ECM mechanical interactions (Mitra and Schlaepfer, 2006; Brusatin et al., 2018). Figure 7 shows the immunofluorescence staining images of FAK in the chondrocytes cultured in the hydrogels with different viscoelastic levels. It can be found that FAK presents a dispersive distribution throughout the cytoplasmic region outside the nucleus in the chondrocytes cultured in the lowest viscoelastic hydrogels (2.5% CNC). As CNC concentration increases from 2.5% to 5%, FAK tends to accumulate in the cytoplasm. At the CNC concentration of 10%, FAK is observed to aggregate in the cytoplasm. As the CNC concentration increases to 15%, FAK is concentrated and localized on one side of the nucleus in some chondrocytes. These results indicate that increasing the rate of stress relaxation and creep, storage modulus and loss modulus of the hydrogels, can promote FAK localizing around the nucleus of chondrocytes.

YAP is known as a mechanosensitive transcription factor that is the key regulatory element in controlling the gene expression of cells response to mechanical cues from ECM (Daheshia and Yao, 2008; Sirio et al., 2011). Further, it is reported that FAK controlled translocation and activation of YAP in response to mechanical activation (Lachowski et al., 2017). However, the role of YAP in the chondrocyte growth under the viscoelastic stimuli has not been studied. Figure 8 shows the immunofluorescence staining images of YAP in the chondrocytes cultured in different viscoelastic hydrogels. It can be found that YAP is dispersed and distributed throughout the chondrocytes cultured in the lower viscoelastic hydrogels (2.5% and 5% CNC). With increasing the viscoelastic properties, YAP is accumulated on both sides of the nucleus (10% CNC). In the high viscoelastic hydrogel (15% CNC), YAP is found to be localized on one side of the nucleus. These results suggest that faster stress

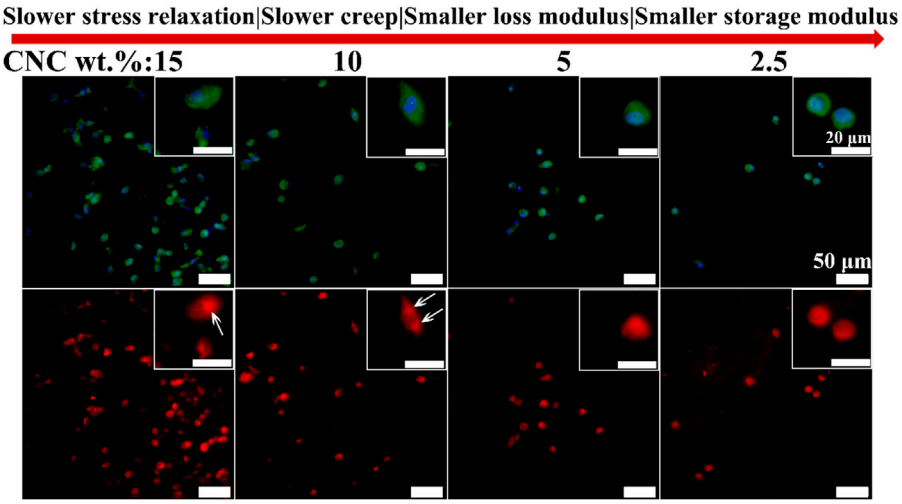

FIGURE 8
YAP staining of chondrocytes cultured in different viscoelastic hydrogels. Green represents actin staining, blue represents nucleus, and red represents YAP. White arrow indicates the location of YAP.

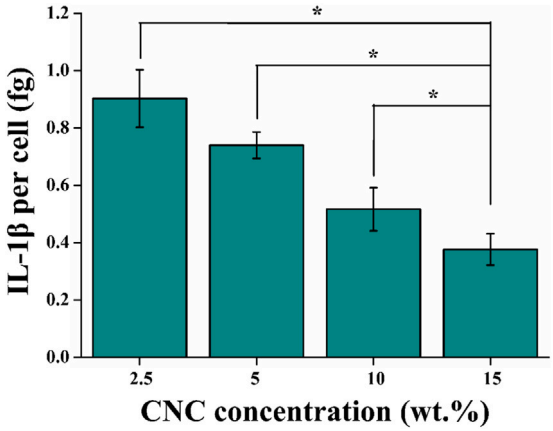

FIGURE 9
Quantification of the amount of IL-1β secreted into the different viscoelastic hydrogels after 14 days of culture (*$p < 0.05$).

relaxation and creep, higher storage modulus and loss modulus, can enhance the perinuclear translocation of YAP in the chondrocytes.

Secretion of IL-1β

Finally, the secretion of cytokine interleukin-1β (IL-1β) in different viscoelastic hydrogels were studied. IL-1β, as a major driver of osteoarthritis progression, is recognized to induce chondrocytes apoptosis in osteoarthritic cartilage (Pelletier et al., 1993). As shown in Figure 9, the level of IL-1β protein is decreased in the hydrogels with increasing the viscoelastic properties after 14 days of culture. It implies that the expression of IL-1β is related to the CNC/COL hydrogel viscoelastic properties. This matches the result previously reported in fast relaxing alginate hydrogels (Richardson et al., 2018). Thereby we speculate that the significant difference in proliferation of chondrocytes in the different viscoelastic hydrogels at 3, 7, and 14 days of culture, is primarily due to the varying levels of IL-1β secreted by chondrocytes.

Discussion

This work exhibits the role of CNC/COL hydrogel viscoelasticity in regulating chondrocytes behavior. It is worth noting that although the prepared hydrogel has a 3D porous structure, its pore size (~200 μm) is much larger than the size of chondrocytes (~20 μm) according to the SEM and chondrocyte spreading results, so the microenvironment in which the chondrocytes grew can actually be regarded as a 2D plane structure. Interestingly, the timescale of stress relaxation of the high viscoelastic hydrogel of ~29.2 s is close to that of cartilage, chondron, and chondrocytes which exhibit viscoelastic responses with a characteristic timescale of ~10 s (Figure 4) (Richardson et al., 2018). This indicates that the hydrogel may more closely mimic the viscoelasticity of native cartilage microenvironment than the other three viscoelastic hydrogels. Recent studies have used alternative material approaches, including changing

TABLE 1 Total variance explained by principal component analysis.

Chondrocyte behaviors	Kaiser–Meyer–Olkin	Viscoelastic parameters	Initial eigenvalues total	Squared loadings variance (%)
Spreading area, aspect ratio, proliferation, levels of COL II, sGAG and IL-1β	0.609	$\tau_{1/2}$	2.192	62.547
		$\gamma_{1/2}$	0.807	18.623
		G''	0.664	10.806
		G'	0.337	8.024

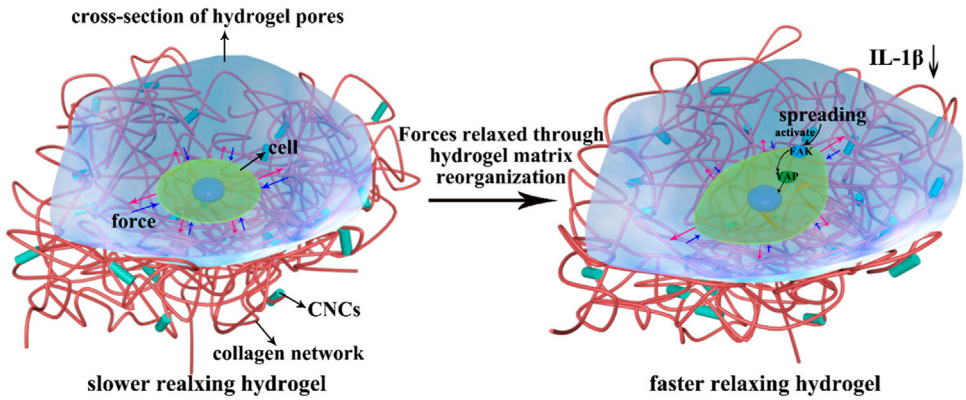

FIGURE 10
Overview of CNC/COL hydrogel stress relaxation impacting chondrocyte behavior through the mechano-transduction of FAK and YAP. Red arrow represents the force exerted by chondrocytes and blue arrow represents the resisting force applied by hydrogel substrate.

crosslinking method, modulating crosslinking density, polymer concentration, and molecular weight, to tune stress relaxation, creep, loss modulus, and storage modulus in hydrogels but hold their stiffness constant (Cameron et al., 2014; Chaudhuri et al., 2016; Bauer et al., 2017; Lee et al., 2017; Chester et al., 2018; Lou et al., 2018; Richardson et al., 2018; Lee et al., 2019). The approach described in this paper is simple and conventional so that the viscoelastic CNC/COL hydrogels do not have independent stiffness (represented by G'), but it is unfavorable for studying the effects of viscoelastic properties on chondrocyte behaviors clearly. For this, we propose to calculate the authority weight values of these viscoelastic parameters, including $\tau_{1/2}$, $\gamma_{1/2}$, G', and G'' using principal component analysis, and to provide quantifiable viscoelastic effects for probing cell–hydrogel substrate interactions (Liu et al., 2017). Table 1 shows the influence authority of each viscoelastic parameter of the CNC/COL hydrogel. The authority weight value of $\tau_{1/2}$ is 62.547%, that of $\gamma_{1/2}$ is 18.623%, that of G'' is 10.806% and that of G' is 8.024%, and thus the influence authority order is $\tau_{1/2} > \gamma_{1/2} > G'' > G'$. This result indicates that stress relaxation has the strongest correlation with chondrocyte behavior, which is consistent with the viewpoints reported in the most literatures (Cameron et al., 2014; Bauer et al., 2017; Chester et al., 2018). In addition, Kaiser–Meyer–Olkin value >0.6 indicates that this method can be used to analyze the quantized data that describe chondrocyte behavior.

Chondrocyte adhesion is the basis of cellular response to the viscoelastic CNC/COL hydrogels, as the hydrogels contain rat tail type I collagen. As described above, the results of cell shape change and proliferation indicate that the chondrocytes have adhered to the hydrogel substrates (the surface of pores within the hydrogel) successfully (Figure 5). By enhancing the concentration of CNC, the mobility of collagen chains decreases and the flowability of matrix composed of collagen network and CNCs reduces due to a steric hindrance of short rod-shaped CNCs, so that the time dependence of stress or strain occurred in the hydrogel substrates diminishes under the imposition of a defined deformation or force (applied by an adhered cell), and the behavior of the hydrogel is referred to as “stress relaxation” or “creep” (Lu and Mow, 2008; McKinnon et al., 2013; Chester et al., 2018). As adherent cells begin to exert force or deformation on a viscoelastic substrate, the substrate viscoelasticity may result in cells feeling a decreasing resistive force and an increasing resistive deformation exerted by cells they

experience when actively pulling on a substrate (Chester et al., 2018). Therefore, higher aspect ratio of the chondrocytes is observed in the faster-relaxing hydrogels because the force exerted by cells can be relaxed more quickly and thus converting its form into isotonic contraction (Chaudhuri et al., 2016). These changes in resistive force and deformation from substrate due to its viscoelastic feature, would be expected to not only activate or inhibit some signal molecules, but impact many other downstream cellular processes, such as cell spreading, proliferation, and matrix formation.

Cell spreading in turn is known to mechanically activate some signal molecules (Zhang et al., 2014; Lee et al., 2017; Richardson et al., 2018). FAK and YAP play well-known and fundamental roles in cellular mechano-sensing and mechano-transduction (Abitbol et al., 2018). It was reported that activation (phosphorylation) of FAK, a signal transducer in focal adhesions (FAs), which increased actomyosin contractility and drove actin polymerization (Mitra and Schlaepfer, 2006). Actin polymerization in turn modulated the nuclear translocation of YAP directly and started a series of cellular processes (Sirio et al., 2011; Brusatin et al., 2018). Therefore, we speculate that both FAK and YAP signal molecules participate in the growth process of chondrocytes stimulated by CNC/COL hydrogel viscoelasticity. The results of the localization of FAK and YAP in the chondrocytes cultured in different viscoelastic hydrogels, indicates that the activity of FAK and YAP mechanosensitive signal molecules are influenced by the viscoelastic properties (Figures 7, 8). Faster stress relaxation can promote the increased localization of FAK and YAP around the nucleus in the chondrocytes. Furthermore, the lower level of IL-1β is detected in the faster relaxing hydrogel, suggesting that faster stress relaxation possibly decreases the secretion of IL-1β by chondrocytes (Figure 9). This result can be attributed that faster stress relaxation promotes the growth of chondrocytes, thereby avoiding osteoarthritis (Lima et al., 2007; Klein et al., 2010).

Based on the above results, we proposed a possible molecular mechanism by which the rapid stress relaxation of 2D CNC/COL hydrogel microenvironment regulates chondrocyte behavior (Figure 10). On the surface of hydrogel pore wall where the stress relaxes slowly, the force exerted by the pore wall resists the change of chondrocyte shape over long times (Lee et al., 2017). While on the surface of hydrogel pore wall where the stress relaxes fast, the force can be relaxed or dissipated by the rearrangement of CNC/COL networks over short times so that contributes to the change of chondrocyte shape (Richardson et al., 2018). The dynamically and cyclically mechanical stimuli from the pore wall is continuously fed into the chondrocytes by actin cytoskeleton to activate FAK and YAP signal molecules and impact their activity (Mitra and Schlaepfer, 2006; Sirio et al., 2011; Brusatin et al., 2018). Further, faster mechanical stimuli facilitate the accumulation and translocation of signal molecules around the nucleus. In brief, the force interaction between developing chondrocytes and rapid relaxing CNC/COL hydrogel pore wall transduces and transforms the extracellular mechanical signals into the intracellular biochemical signals, finally facilitating the processes of chondrocytes spreading, shape change, proliferation, and matrix deposition over long timescales. Therefore, we point out FAK and YAP, as mechano-transduction signal molecules, participate in the growth of chondrocytes cultured on the 2D microenvironment constructed by a fast-relaxing CNC/COL hydrogel.

Conclusion

This work investigates the effects of viscoelastic properties of microporous CNC/COL hydrogel on chondrocyte behaviors and the related intracellular mechano-transduction mechanism. The CNC/COL hydrogels have tuneable viscoelastic properties by changing CNC concentration. The cell aspect ratio, proliferation and levels of COL II and GAGs are enhanced in the hydrogel with faster stress relaxation and creep rates, higher storage modulus and loss modulus. Particularly, the stress relaxation has the strongest correlation with the behavior of chondrocytes, and its authority weight value is as high as 62.547%. In addition, the level of IL-1β, a major driver of osteoarthritis progression, is decreased in faster relaxing hydrogel. Further, FAK and YAP play important roles in the chondrocytes' responses to the rapid relaxing hydrogel. This study contributes to understanding of how hydrogel viscoelastic properties impact chondrocyte behaviors and implicates stress relaxation as an important design parameter for preparing cartilage scaffolds.

Data availability statement

The original contributions presented in the study are included in the article/Supplementary Material; further inquiries can be directed to the corresponding authors.

Author contributions

DL: Conceptualization, methodology, data curation, writing—original draft, investigation, and visualization; HZ: Writing—review and editing, investigation, and validation; XD: Writing—review and editing, validation, resources, supervision, and project administration; LS: Methodology and validation; MQ: Validation, resources, and supervision.

Funding

This research is financial funded by the Dalian Medical Science Research Project under the grant number of

2011001 and the Fundamental Research Funds for the Central Universities of China under the grant number of DUT22YG201.

Conflict of interest

Author HZ was employed by the company ChangchunSinoBiomaterials Co., Ltd. The company provided support in the form of salaries for HZ, but did not have any additional role in the study design, data collectionand analysis, decision to publish, or preparation of the manuscript. The specific roles of these authors are articulated in the 'author contributions' section.

The remaining authors declare that the research was conducted in the absence of any commercial or financial relationships that could be construed as a potential conflict of interest.

Publisher's note

All claims expressed in this article are solely those of the authors and do not necessarily represent those of their affiliated organizations, or those of the publisher, the editors, and the reviewers. Any product that may be evaluated in this article, or claim that may be made by its manufacturer, is not guaranteed or endorsed by the publisher.

References

Abitbol, T., Kam, D., Levi-Kalisman, Y., Gray, D. G., and Shoseyov, O. (2018). Surface charge influence on the phase separation and viscosity of cellulose nanocrystals. *Langmuir* 34, 3925–3933. doi:10.1021/acs.langmuir.7b04127

Andrea, G. L., Xiomara, F. G., Ferran, V. M., Castano, A. G., Samitier, J., and Ramon-Azcon, J. (2018). Composite biomaterials as long-lasting scaffolds for 3D bioprinting of highly aligned muscle tissue. *Macromol. Biosci.* 18, 1800167. doi:10.1002/mabi.201800167

Bauer, A., Gu, L., Kwee, B., Li, W. A., Dellacherie, M., Celiz, A. D., et al. (2017). Hydrogel substrate stress-relaxation regulates the spreading and proliferation of mouse myoblasts. *Acta Biomater.* 62, 82–90. doi:10.1016/j.actbio.2017.08.041

Biswal, T., BadJena, S. K., and Pradhan, D. (2020). Sustainable biomaterials and their applications: A short review. *Mat. Today Proc.* 30, 274–282. doi:10.1016/j.matpr.2020.01.437

Brusatin, G., Panciera, T., Gandin, A., Citron, A., and Piccolo, S. (2018). Biomaterials and engineered microenvironments to control YAP/TAZ-dependent cell behaviour. *Nat. Mat.* 17, 1063–1075. doi:10.1038/s41563-018-0180-8

Burdick, J. A., and Prestwich, G. D. (2011). Hyaluronic acid hydrogels for biomedical applications. *Adv. Mat.* 23, H41–H56. H41–H56. doi:10.1002/adma.201003963

Cameron, A. R., Frith, J. E., and Cooper-White, J. J. (2011). The influence of substrate creep on mesenchymal stem cell behaviour and phenotype. *Biomaterials* 32, 5979–5993. doi:10.1016/j.biomaterials.2011.04.003

Cameron, A. R., Frith, J. E., Gomez, G. A., Yap, A. S., and Cooper-White, J. J. (2014). The effect of time dependent deformation of viscoelastic hydrogels on myogenic induction and Rac1 activity in mesenchymal stem cells. *Biomaterials* 35, 1857–1868. doi:10.1016/j.biomaterials.2013.11.023

Chaudhuri, O., Gu, L., Klumpers, D., Darnell, M., Bencherif, S. A., Weaver, J. C., et al. (2016). Hydrogels with tunable stress relaxation regulate stem cell fate and activity. *Nat. Mat.* 15, 326–334. doi:10.1038/nmat4489

Chester, D., Kathard, R., Nortey, J., Nellenbach, K., and Brown, A. C. (2018). Viscoelastic properties of microgel thin films control fibroblast modes of migration and pro-fibrotic responses. *Biomaterials* 185, 371–382. doi:10.1016/j.biomaterials.2018.09.012

Daheshia, M., and Yao, J. Q. (2008). The interleukin 1β pathway in the pathogenesis of osteoarthritis. *J. Rheumatol.* 35, 2306–2312. doi:10.3899/jrheum.080346

Discher, D. E., Janmey, P., and Wang, Y. (2005). Tissue cells feel and respond to the stiffness of their substrate. *Science* 310, 1139–1143. doi:10.1126/science.1116995

Engler, A. J., Sen, S., Sweeney, H. L., and Discher, D. E. (2006). Matrix elasticity directs stem cell lineage specification. *Cell* 126, 677–689. doi:10.1016/j.cell.2006.06.044

Getgood, A., Brooks, R., Fortier, L., and Rushton, N. (2009). Articular cartilage tissue engineering: today's research, tomorrow's practice? *J. Bone Jt. Surg. Br. volume* 91, 565–576. doi:10.1302/0301-620x.91b5.21832

Jayaramudu, T., Ko, H. U., Kim, H. C., Kim, J., Muthoka, R., and Kim, J. (2018). Electroactive hydrogels made with polyvinyl alcohol/cellulose nanocrystals. *Materials* 11 (9), 1615. doi:10.3390/ma11091615

Jayaramudu, T., Ko, H. U., Kim, H. C., Kim, J. W., and Kim, J. (2019). Swelling behavior of polyacrylamide–cellulose nanocrystal hydrogels: swelling kinetics, temperature, and pH effects. *Materials* 12 (13), 2080. doi:10.3390/ma12132080

Klein, T. J., Rizzi, S. C., Schrobback, K., Reichert, J. C., Jeon, J. E., Crawford, R. W., et al. (2010). Long-term effects of hydrogel properties on human chondrocyte behavior. *Soft Matter* 6, 5175. doi:10.1039/c0sm00229a

Lachowski, D., Cortes, E., Robinson, B., Rice, A., Rombouts, K., and Del Rio Hernandez, A. E. (2017). Fak controls the mechanical activation of yap, a transcriptional regulator required for durotaxis. *FASEB J.* 32, 1099–1107. doi:10.1096/fj.201700721r

Lee, C. D., Gleghorn, J. P., Choi, N. W., Cabodi, M., Stroock, A. D., and Bonassar, L. J. (2007). Integration of layered chondrocyte-seeded alginate hydrogel scaffolds. *Biomaterials* 28, 2987–2993. doi:10.1016/j.biomaterials.2007.02.035

Lee, H. P., Gu, L., Mooney, D. J., Levenston, M. E., and Chaudhuri, O. (2017). Mechanical confinement regulates cartilage matrix formation by chondrocytes. *Nat. Mat.* 16, 1243–1251. doi:10.1038/nmat4993

Lee, S., Stanton, A. E., Tong, X., and Yang, F. (2019). Hydrogels with enhanced protein conjugation efficiency reveal stiffness-induced yap localization in stem cells depends on biochemical cues. *Biomaterials* 202, 26–34. doi:10.1016/j.biomaterials.2019.02.021

Lima, E. G., Bian, L., Ng, K. W., Mauck, R., Byers, B., Tuan, R., et al. (2007). The beneficial effect of delayed compressive loading on tissue-engineered cartilage constructs cultured with TGF-β3. *Osteoarthr. Cartil.* 15, 1025–1033. doi:10.1016/j.joca.2007.03.008

Liu, D. L., Chen, Z. B., Du, X. Y., and Liu, Z. (2017). Study of structural parameters on the adsorption selectivity of a molecularly imprinted polymer. *J. Macromol. Sci. Part A* 54, 622–628. doi:10.1080/10601325.2017.1316670

Liu, D. L., Dong, X. F., Han, B. G., Huang, H., and Qi, M. (2020). Cellulose nanocrystal/collagen hydrogels reinforced by anisotropic structure: Shear viscoelasticity and related strengthening mechanism. *Compos. Commun.* 21, 100374. doi:10.1016/j.coco.2020.100374

Liu, D. L., Dong, X. F., Liu, H. Y., Zhao, Y., and Qi, M. (2021). Effect of pore orientation on shear viscoelasticity of cellulose nanocrystal/collagen hydrogels. *J. Appl. Polym. Sci.* 138 (7), e49856. doi:10.1002/app.49856

Loebel, C., Kwon, M. Y., Wang, C., Han, L., Mauck, R. L., and Burdick, J. A. (2020). Metabolic labeling to probe the spatiotemporal accumulation of matrix at the chondrocyte-hydrogel interface. *Adv. Funct. Mat.* 30, 1909802. doi:10.1002/adfm.201909802

Lou, J. Z., Stowers, R., Nam, S., Xia, Y., and Chaudhuri, O. (2018). Stress relaxing hyaluronic acid-collagen hydrogels promote cell spreading, fiber remodeling, and focal adhesion formation in 3D cell culture. *Biomaterials* 154, 213–222. doi:10.1016/j.biomaterials.2017.11.004

Lu, X. L., and Mow, V. C. (2008). Biomechanics of articular cartilage and determination of material properties. *Med. Sci. Sports Exerc.* 40, 193–199. doi:10.1249/mss.0b013e31815cb1fc

Martha, A. H., Mathew, A. P., and Oksman], K. (2014). Gas permeability and selectivity of cellulose nanocrystals films (layers) deposited by spin coating. *Carbohydr. Polym.* 112, 494–501. doi:10.1016/j.carbpol.2014.06.036

Matellan, C., and Hernandez, A. E. (2019). Engineering the cellular mechanical microenvironment-from bulk mechanics to the nanoscale. *J. Cell Sci.* 132, jcs229013. doi:10.1242/jcs.229013

Mauck, R. L., Soltz, M. A., Wang, C. B., Wong, D. D., Chao, P. H. G., Valhmu, W. B., et al. (2000). Functional tissue engineering of articular cartilage through dynamic loading of chondrocyte-seeded agarose gels. *J. Biomech. Eng.* 122, 252–260. doi:10.1115/1.429656

McKinnon, D. D., Domaille, D. W., Cha, J. N., and Anseth, K. S. (2013). Biophysically defined and cytocompatible covalently adaptable networks as viscoelastic 3D cell culture systems. *Adv. Mat.* 26, 865–872. doi:10.1002/adma.201303680

Mitra, S. K., and Schlaepfer, D. D. (2006). Integrin-regulated FAK-Src signaling in normal and cancer cells. *Curr. Opin. Cell Biol.* 18, 516–523. doi:10.1016/j.ceb.2006.08.011

Mow, V. C., Ratcliffe, A., and Poole, A. R. (1991). Cartilage and diarthrodial joints as paradigms for hierarchical materials and structures. *Biomaterials* 13, 67–97. doi:10.1016/0142-9612(92)90001-5

Patel, J. M., Loebel, C., Saleh, K. S., Wise, B. C., Bonnevie, E. D., Miller, L. M., et al. (2021). Stabilization of damaged articular cartilage with hydrogel-mediated reinforcement and sealing. *Adv. Healthc. Mat.* 10, e2100315. doi:10.1002/adhm.202100315

Pelletier, J. P., DiBattista, J. A., Roughley, P., McCollum, R., and Martel-Pelletier, J. (1993). Cytokines and inflammation in cartilage degradation. *Rheumatic Dis. Clin. N. Am.* 19, 545–568. doi:10.1016/s0889-857x(21)00331-8

Richardson, B. M., Wilcox, D. G., Randolph, M. A., and Anseth, K. S. (2018). Hydrazone covalent adaptable networks modulate extracellular matrix deposition for cartilage tissue engineering. *Acta. Biomater.*, 83. 71–82. doi:10.1016/j.actbio.2018.11.014

Sirio, D., Leonardo, M., Mariaceleste, A., Enzo, E., Giulitti, S., Cordenonsi, M., et al. (2011). Role of YAP/TAZ in mechanotransduction. *Nature* 474, 179–183. doi:10.1038/nature10137

Solon, J., Levental, I., Sengupta, K., Georges, P. C., and Janmey, P. A. (2007). Fibroblast adaptation and stiffness matching to soft elastic substrates. *Biophys. J.* 93, 4453–4461. doi:10.1529/biophysj.106.101386

Trache, D., Hussin, M. H., Haafiz, M., and Thakur, V. K. (2017). Recent progress in cellulose nanocrystals: sources and production. *Nanoscale* 9, 1763–1786. doi:10.1039/c6nr09494e

Walker, C. J., Crocini, C., Ramirez, D., Anouk, R. K., Joseph, C. G., Brian, A. A., et al. (2021). Author correction: nuclear mechanosensing drives chromatin remodeling in persistently activated fibroblasts. *Nat. Biomed. Eng.* 5, 1517–1518. doi:10.1038/s41551-021-00748-3

Yang, W., Zheng, Y. Y., Chen, J., Zhu, Q., Feng, L., Lan, Y., et al. (2019). Preparation and characterization of the collagen/cellulose nanocrystals/USPIO scaffolds loaded kartogenin for cartilage regeneration. *Mater. Sci. Eng. C* 99, 1362–1373. doi:10.1016/j.msec.2019.02.071

Zhang, Q., Lu, H. X., Kawazoe, N., and Chen, G. (2014). Pore size effect of collagen scaffolds on cartilage regeneration. *Acta Biomater.* 10, 2005–2013. doi:10.1016/j.actbio.2013.12.042

frontiers | Frontiers in Bioengineering and Biotechnology

TYPE Original Research
PUBLISHED 12 August 2022
DOI 10.3389/fbioe.2022.971682

OPEN ACCESS

EDITED BY
Jianxun Ding,
Changchun Institute of Applied Chemistry (CAS), China

REVIEWED BY
Dongfang Zhou,
Southern Medical University, China
Ruogu Qi,
Nanjing University of Chinese Medicine, China
Jinshan Guo,
Southern Medical University, China
Xiaowei Zeng,
Sun Yat-sen University, China
Muhammad Rizwan Younis,
Shenzhen University, China

*CORRESPONDENCE
Dalin Wu,
wudlin6@mail.sysu.edu.cn
Jun Yue,
yuejun3@mail.sysu.edu.cn

†These authors have contributed equally to this work

SPECIALTY SECTION
This article was submitted to Biomaterials, a section of the journal Frontiers in Bioengineering and Biotechnology

RECEIVED 17 June 2022
ACCEPTED 11 July 2022
PUBLISHED 12 August 2022

CITATION
Lin J, Xu L, Zheng Y, Wu D and Yue J (2022), Imitation-mussel fluorescent silicon quantum dots for selective labeling and imaging of bacteria and biofilms.
Front. Bioeng. Biotechnol. 10:971682.
doi: 10.3389/fbioe.2022.971682

Imitation-mussel fluorescent silicon quantum dots for selective labeling and imaging of bacteria and biofilms

Jiayi Lin†, Linlin Xu†, Yuling Zheng, Dalin Wu* and Jun Yue*

Key Laboratory of Sensing Technology and Biomedical Instrument of Guangdong Province, School of Biomedical Engineering, Shenzhen Campus of Sun Yat-sen University, Shenzhen, China

Selective labeling of distinct bacteria and biofilm is poised for the fundamental understanding of bacterial activities, interactions, and coupled phenomena occurring at the microscale. However, a simple and effective way to achieve selective bacterial labeling is still lacking. Herein, we report a fluorescence probe with core-shell nanostructure that has polydopamine (PDA) coating on the surface of fluorescent silicon quantum dots (SiQDs@PDA). The surface of the SiQDs@PDA can be functionalized by various molecules (2-mercaptoethylamine hydrochloride, PEG, D-alanine, glucose amide) through different strategies (Michael addition, π-π interaction, and ion–ion interaction). Importantly, the D-alanine (D-Ala)- and gluconamide (Glc)-functionalized SiQDs@PDA fluorescence probes are capable of selectively labeling gram-positive and gram-negative bacteria, as well as their biofilms. The excellent performance in universal functionalization and selective labeling and imaging of bacteria and their biofilms demonstrate that SiQDs@PDA are a promising fluorescence tool in microbe research.

KEYWORDS

selective labeling, bacteria, bacterial biofilm, fluorescence, silicon quantum dots

Introduction

Innumerable bacterial species constitute a major part of the microbial ecosystem. Some of the bacteria play a positive role in our daily lives, while a large population of bacteria are threatening to our public health due to their toxicity, high vitality, and fast propagation. Selective labeling and imaging of living bacteria can promote the understanding of cellular heterogeneity in bacterial populations and advance the fast detection of bacterial species for effective treatments (Mao et al., 2018; Kwon et al., 2019; He et al., 2020; Ye et al., 2021; Zhang et al., 2021).

Gram staining is the gold standard method to label and classify bacteria based on the structural differences in the bacterial cell wall. However, this method involves complicated procedures and can only provide average information on the bacterial population. Meanwhile, many molecular detection methods such as surface-enhanced Raman scattering (SERS) (Zhao et al., 2022), polymerase chain reaction (PCR), and DNA

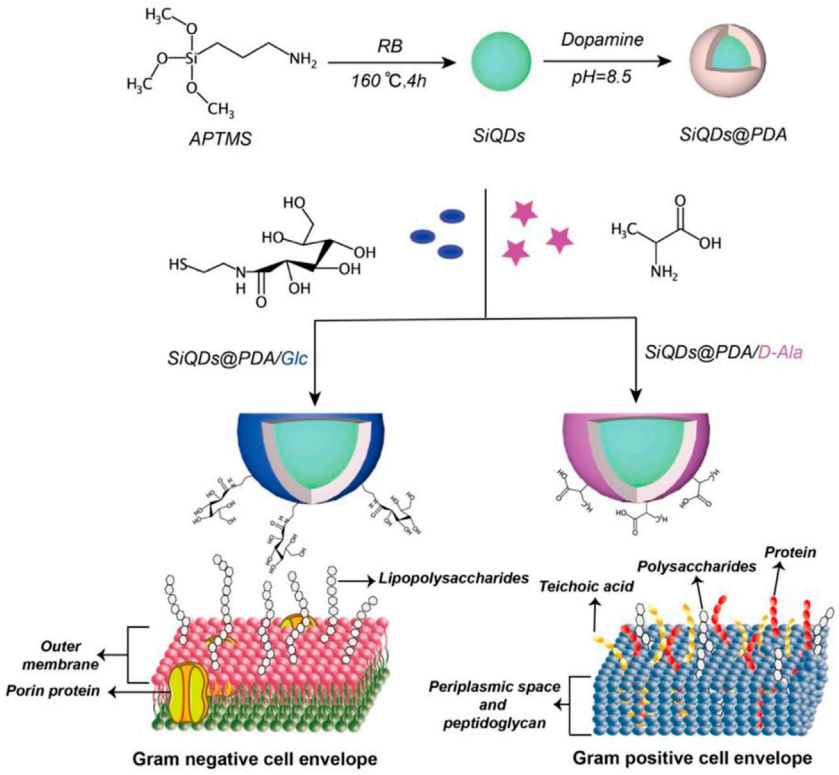

SCHEME 1
A schematic representation of the fluorescent probe preparation, surface functionalization, and selective bacterial labeling.

sequencing technology (Shendure et al., 2017) have been developed, while the application of these technologies is limited due to the need of sophisticated equipment. To date, the most widely used method for bacterial labeling and imaging is fluorescence probe–based approaches such as flow cytometry and fluorescence microscopy. Compared with other technologies, fluorescence imaging is faster, is more economical, and can provide more direct and detailed information about bacteria. To achieve selective imaging and the classification of bacteria, the applied fluorescence probe should possess the ability to recognize different species. The heterogeneity in cellular composition, metabolites, and structure of bacteria are ready to be utilized for guiding the design of the fluorescence probe. For example, Kwon et al. (2019) reported a small molecular fluorescent probe of boronic acid–functionalized BODIPY. It could selectively label and image saccharide-rich gram-positive bacteria due to the specific interaction between boronic acid and the saccharide. Nonetheless, organic fluorescence probes suffer from low stability upon long-term irradiation (Zheng and Lavis, 2017; Demchenko, 2020). The development of new types of fluorescence probes with preeminent structural stability and high fluorescence efficiency for bacteria and biofilms is thereby in great demand.

Recently, semiconductor quantum dots, carbon nanodots, and fluorescent silicon quantum dots (SiQDs) have emerged as a new generation of fluorescence materials for their excellent stability and biocompatibility (Gao et al., 2018; Kasouni et al., 2019; Sivasankarapillai et al., 2019; Huang et al., 2020; Gao et al., 2021; Li et al., 2022; Martynenko et al., 2022; Özbilgin et al., 2022; Zhao et al., 2022). Among these, zero-dimensional SiQDs with high fluorescence quantum yield and narrow emission bands have received increasing attention for the sensing of biological and bacteriologic species. For example, the Lee group applied a one-pot microwave procedure to synthesize fluorescent SiQDs with great aqueous dispersibility and robust photostability and pH stability, which exhibited excellent fluorescence stability for long-term cellular imaging (He et al., 2011). To achieve the labeling of SiQDs onto specific bacterial species, it is necessary to functionalize the surface of the SiQDs by bioactive molecules such as peptides (Jung et al., 2021), proteins (Gidwani et al., 2021), and polysaccharides (Mozetič, 2019). However, such surface functionalization is problematic due to the ultrasmall

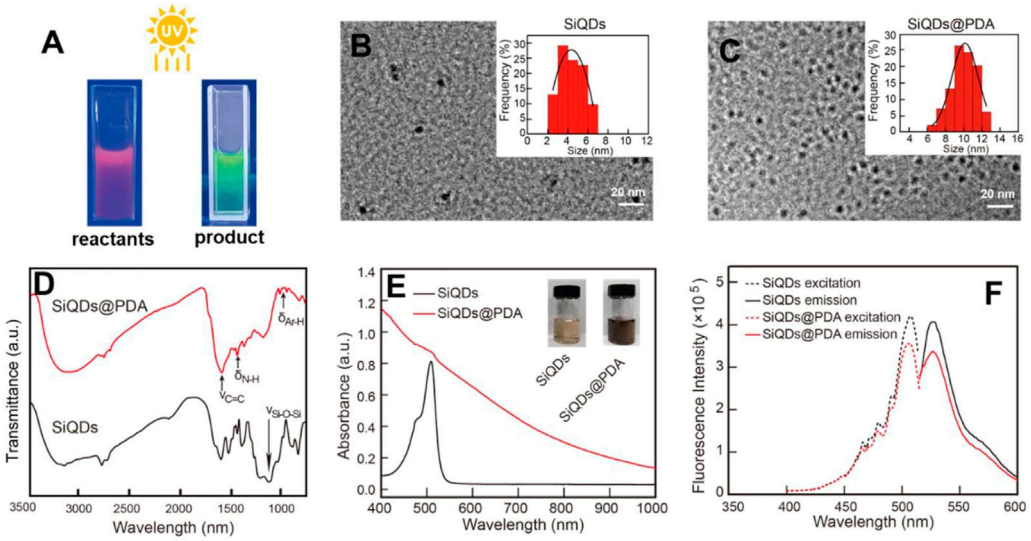

FIGURE 1
Characterization of SiQDs and SiQDs@PDA. **(A)** Digital images of the reactants in synthesizing the SiQDs fluorescent probe in aqueous solution under UV lamp irradiation; **(B,C)** TEM images with statistical analysis of average diameter; **(D)** FTIR spectra; **(E)** UV-Vis spectra; and **(F)** excitation and emission fluorescent spectra.

diameter of the SiQDs (normally less than 10 nm) and a limited number of reactive groups on the surface of the SiQDs. Therefore, it is crucial to develop a universal method to simplify the modification procedure and advance the application of the SiQDs in bacterial imaging and labeling.

Inspired by the adhesion ability of mussels, the polydopamine (PDA)-coating technique has been widely used for the universal modification of nanostructures with bioactive molecules (Tian et al., 2019; Fu and Yu, 2020; Guo et al., 2020; Jing et al., 2020; Barros et al., 2021; Chen et al., 2021; Singh et al., 2021; Tian et al., 2021). This is achieved by versatile interactions which include hydrogen bond formation, covalent bond reconstruction, and π-π stacking interaction between PDA and bioactive molecules (Barclay et al., 2017; Schanze et al., 2018; Cheng et al., 2019; Patel et al., 2019). For example, Asha et al. (2022) reported a sugar-responsive coating system based on the reversible boronic ester bonds between catechol groups of PDA and benzoxaborole pendant of zwitterionic and cationic polymers, which displayed a promising self-cleaning function. D-alanine (D-Ala), one of the main components in the cell wall of gram-positive bacteria, can be directly integrated into the bacterial cell wall during metabolism (Hu et al., 2020; Mao et al., 2020), while gluconamide (Glc) is known for its strong interaction with lipopolysaccharide on the surface of gram-negative bacteria (Capeletti et al., 2019). Therefore, we hypothesized that SiQDs decorated with D-Ala and Glc could target gram-positive and gram-negative bacteria, respectively.

Herein, we report a new type of high-performance fluorescence probe with emission wavelength of 530 nm and fluorescence quantum yield of 44.7%, by applying the PDA-coating technique on SiQDs (SiQDs@PDA). The fluorescence probe SiQDs@PDA displays excellent adaptability for the functionalization of diverse molecules through the Michael addition reaction and supramolecular interaction. More importantly, low cytometry and fluorescence microcopy investigations have demonstrated that the D-Ala–modified and Glc-modified SiQDs@PDA are capable of selectively labeling gram-positive and gram-negative bacteria, respectively, as well as their corresponding biofilms. Compared with the small molecular fluorescent dyes which are prone to photobleaching under light irradiation, SiQDs-based probes developed in this study showed excellent stability against photobleaching and are of great potential in selective bacterial imaging.

Results and discussion

Synthesis and characterization of imitation-mussel–based fluorescent silicon quantum dots

The fluorescent SiQDs were synthesized by the reduction of 3-aminopropyltrimethoxysilane (APTMS) or N-(2-aminoethyl)-3-aminopropyltrimethoxysilane (DAMO) under Rose Bengal (RB) *via* a one-step water–thermal reaction according to the published procedure (Chen et al., 2018), as shown in Scheme 1. The digital images of SiQDs aqueous solution under a UV lamp

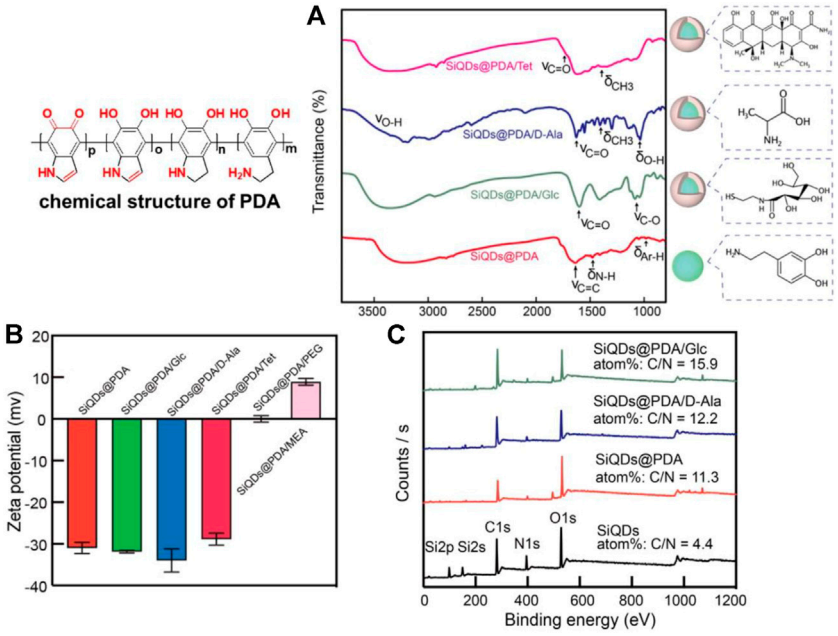

FIGURE 2
Characterization of functionalized SiQDs@PDA by various model molecules. **(A)** FTIR spectra of SiQDs@PDA after functionalization; **(B)** Zeta potential values of various model molecules–modified SiQDs@PDA in ultrapure aqueous solution; and **(C)** XPS results of D-Ala- and Glc-functionalized SiQDs@PDA.

in Figure 1A and Supplementary Figure S1A clearly show the fluorescence signal demonstrating their fluorescence characteristic. Moreover, for both APTMS-based and DAMO-based SiQDs, the maximal emission and maximal excitation wavelengths of SiQDs are at 530 and 510 nm, respectively (Supplementary Figure S1B,C). As for the quantum yield (QY), APTMS-based SiQDs showed a slightly higher fluorescence QY (44.73%) than did DAMO-based SiQDs (41.02%, Supplementary Table S1), while they were all higher than previously reported carbon quantum dots and graphene quantum dots. Therefore, APTMS-based SiQDs were chosen for further research in the following sections.

The average diameter of SiQDs is 4 ± 1.6 nm according to the statistical analysis of the TEM image shown in Figure 1B. No aggregation is detected in Figure 1B, demonstrating that the SiQDs fluorescent probe has good dispersity in aqueous solution. In addition, the presence of transmittance peak with wavenumber 1100 cm^{-1} owing to -Si-O-Si- groups shown in Figure 1D verifies that SiQDs are constituted by the siloxane structure. Several publications have reported that the crystal structure in quantum dots normally influences the fluorescence characteristic (Liu et al., 2020; Terada et al., 2020). X-ray polycrystalline diffractometer (XRD) characterization indicates that the synthesized SiQDs had a feature of an amorphous state (Supplementary Figure S1D).

Subsequently, the fluorescent SiQDs@PDA were synthesized by simply mixing SiQDs with dopamine at pH 8.5 in Tris buffer at room temperature. According to the statistical analysis of the TEM image shown in Figure 1C, the average diameter of SiQDs@PDA is 9 ± 2.2 nm with a spherical nanostructure, and the increasing diameter after polymerization of dopamine indicates that PDA was successfully coated on the surface of the SiQDs. Likewise, no aggregation was observed in the TEM image, which demonstrates good dispersity of SiQDs@PDA in aqueous solution. In addition, the FTIR result in Figure 1D clearly shows new transmittance peaks with wavenumbers 1,610 cm^{-1} and 1,470 cm^{-1} owing to the stretching vibration of the benzene ring skeleton and bending vibration of the N-H bonds, respectively, and the relative strong transmittance peak at 990 cm^{-1} is attributed to the bending vibration of the Ar-H bonds in PDA, demonstrating the successful coating of PDA on the surface of SiQDs. Also, the UV-Vis spectra result shown in Figure 1E demonstrates that the absorption peak of SiQDs at 510 nm is almost masked by PDA for the fluorescent SiQDs@PDA probe. Finally, the fluorescence performance of SiQDs@PDA was investigated in depth. The excitation wavelength (510 nm) and emission wavelength (530 nm) of SiQDs@PDA remain unchanged when compared with those of SiQDs in aqueous solution (Figure 1F). It should be noted that the fluorescence intensity of SiQDs@PDA decreased slightly when compared to that of SiQDs, but the overall decline was less

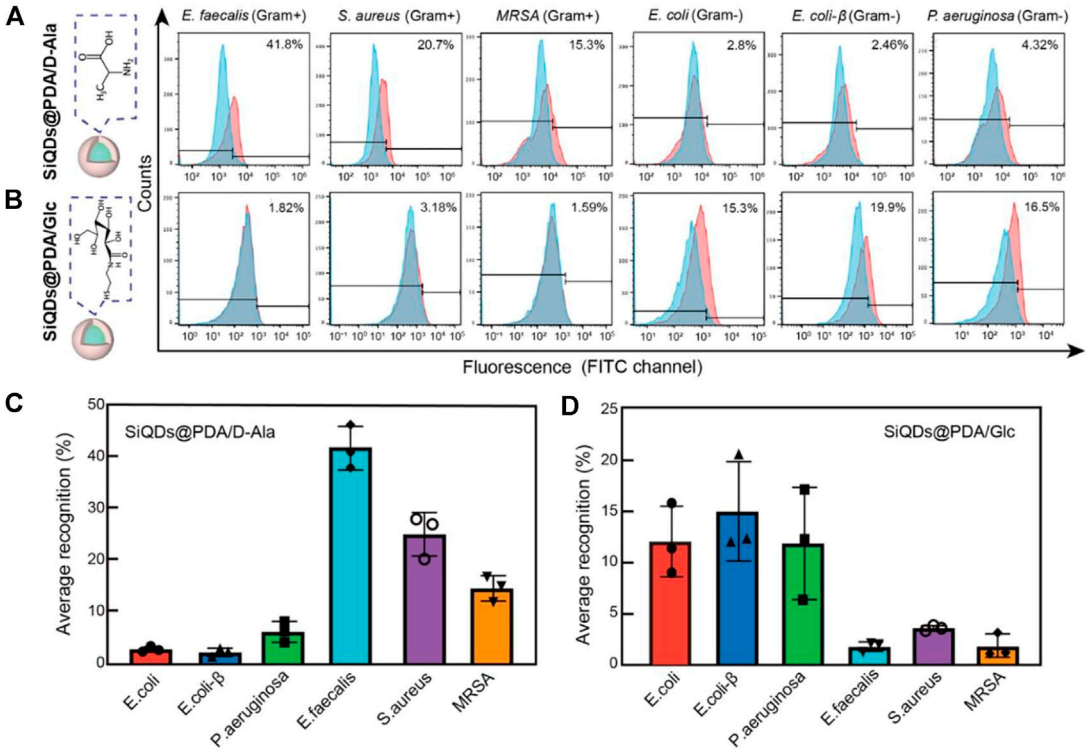

FIGURE 3
Gram-specific recognition of SiQDs@PDA/D-Ala and SiQDs@PDA/Glc. **(A,B)** Representative flow cytometry histograms collected from bacteria co-incubation with SiQDs@PDA/D-Ala and SiQDs@PDA/Glc. **(C,D)** Average recognition values for six different types of bacteria. Data = mean ± SD, $n = 3$.

pronounced, which guarantees the subsequent fluorescence signal for labeling and imaging utilization in bacteria.

Universal surface functionalization of imitation-mussel–based fluorescent silicon quantum dots

Due to the existence of amine, hydroxyl, carboxyl, vinyl groups in PDA (Yang et al., 2020) as shown in Figure 2, in principle, various molecules could be modified on PDA by suitable chemistry strategies. Moreover, the negative charges and benzene rings of PDA facilitate PDA to form ion–ion and π-π interactions with specific ligands. To validate the surface functionalization universality of synthesized SiQDs@PDA, we selected three different types of molecules to modify the surface of SiQDs@PDA. The first reagent was tetracycline (Tet) containing several benzene rings in the molecule which is capable of being modified on the surface of SiQDs@PDA through π-π interaction. The second reagent was D-alanine (D-Ala) with positive charges that can adsorb onto the negatively charged PDA surface through ion–ion interaction. The third reagent was thiol-modified gluconamide (Glc), which could be coupled onto the surface of SiQDs@PDA by the Michael addition reaction.

First of all, FTIR was utilized to characterize the surface functionalization result; the corresponding results are presented in Figure 2A. Compared with the FTIR result of SiQDs@PDA (red solid line) shown in Figure 2A, the intense peak at 1,750 cm^{-1} is attributed to the stretching vibration of the C=O bonds in Tet, while the absorption peak at 1,430 cm^{-1} is attributed to the bending vibration of the saturated C-H bonds in Tet, demonstrating the successful coating of Tet on the surface of SiQDs@PDA through π-π interaction (pink solid line). Additionally, the broad and scattered peaks at 2,500–3,300 cm^{-1} is attributed to the carboxyl group of D-Ala; the relative strong transmittance peak at 1,600 cm^{-1} is attributed to the stretching vibration of the C=O bonds in D-Ala; the transmittance peak at 1,450 cm^{-1} is attributed to the bending vibration of the saturated C-H bonds; and the transmittance peak at 1,200 cm^{-1} is attributed to the bending vibration of hydroxyl groups of D-Ala (dark blue solid line). The presence of these typical peaks demonstrates the successful modification of SiQDs@PDA by D-Ala. For Glc, the relatively strong transmittance peak at 1,580 cm^{-1} is attributed to the stretching vibration of the C=O bonds in the amide groups, and the

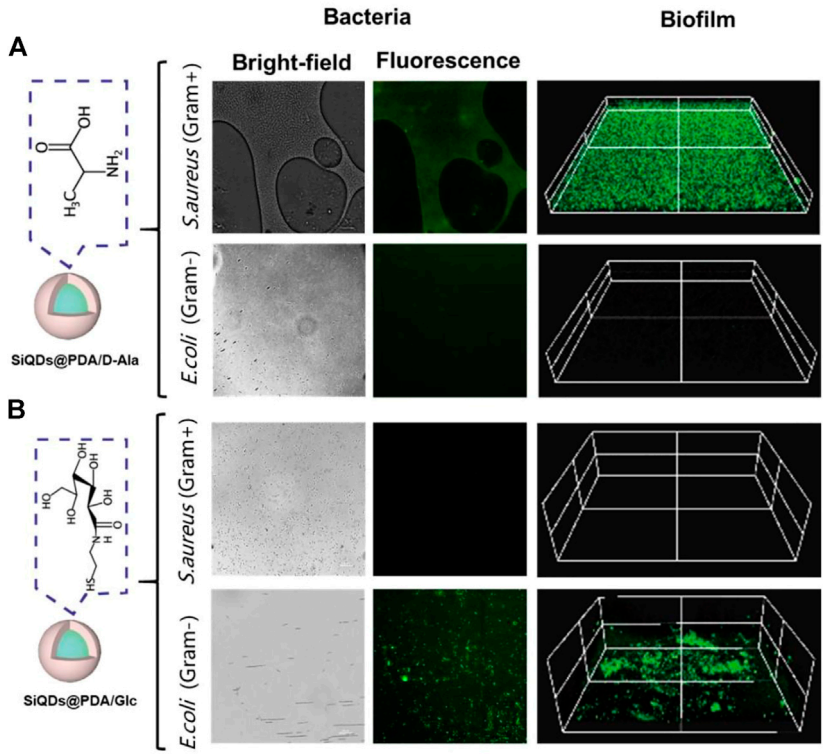

FIGURE 4
Characterization of selective imaging of bacteria and biofilms with SiQDs@PDA/D-Ala and SiQDs@PDA/Glc as fluorescent probes. **(A)** Optical and fluorescent imaging result of SiQDs@PDA/D-Ala as the probe and **(B)** optical and fluorescent imaging result of SiQDs@PDA/Glc as the probe.

transmittance peak at 1,220 cm^{-1} is attributed to the stretching vibration of the C-O bonds of Glc, indicating that Glc was successfully modified on the surface of SiQDs@PDA by the Michael addition reaction (dark green solid line). In order to evaluate the universal validity of the Michael addition reaction for SiQDs@PDA surface modification, 2-mercaptoethylamine (MEA) (M_W = 77) and polymer PEG-SH (M_W = 2000) were chosen to modify the surface of SiQDs@PDA further. According to the FTIR result shown in Supplementary Figure S2, the strong transmittance peak at 2,984 cm^{-1} from the stretching vibration of the C-H bonds, the vibration transmittance peak at 1,110 cm^{-1} owing to the stretching vibrations of the C-O-C bonds in PEG (black solid line), the wide transmittance peak appearing near 3,392 cm^{-1} attributed to the $-NH_2$ in MEA, and the transmittance peak at 1,166 cm^{-1} attributed to the stretching vibration of the C-N bonds in MEA (purple solid line) indicate that PEG and MEA were successfully coupled on the surface of SiQDs@PDA. Obviously, the Michael addition reaction in between thiol–vinyl is an effective strategy for SiQDs@PDA surface modification.

Besides FTIR, the zeta potential values of SiQDs@PDA after being functionalized by guest molecules were also systematically characterized to confirm the functionalization, and the results are presented in Figure 2B. Compared to SiQDs@PDA, the zeta potential values of Tet-, D-Ala-, and Glc-functionalized SiQDs@PDA do not change greatly and are still around −30 mV in ultrapure aqueous solution, which is attributed to the presence of many hydroxyl groups in Tet, D-Ala, and Glc. However, the zeta potential values of PEG and 2-mercapolamine (MEA) functionalized SiQDs@PDA are −0.1 mV and + 8.9 mV, respectively, indicating that the guest molecules have been successfully modified on the surface of SiQDs@PDA.

Among the above-tested molecules for surface functionalization, D-Ala belongs to bacterial metabolic activity molecules which mainly appear in gram-positive bacteria (Hu et al., 2020; Mao et al., 2020), and Glc is known for its strong interaction with lipopolysaccharide of gram-negative bacteria (Capeletti et al., 2019). We hypothesized that SiQDs@PDA after being functionalized by D-Ala and Glc could selectively label gram-positive and gram-negative bacteria, respectively. Before carrying out the selective labeling investigation, the coating results of D-Ala and Glc on the surface of SiQDs@PDA were further investigated by XPS. As shown in Figure 2C, compared with SiQDs@PDA, the ratio of C/N increased from 11.3 to 12.2 and 15.9 for SiQDs@PDA/D-Ala and SiQDs@PDA/Glc, respectively. The increase in the C/N ratio after D-Ala and

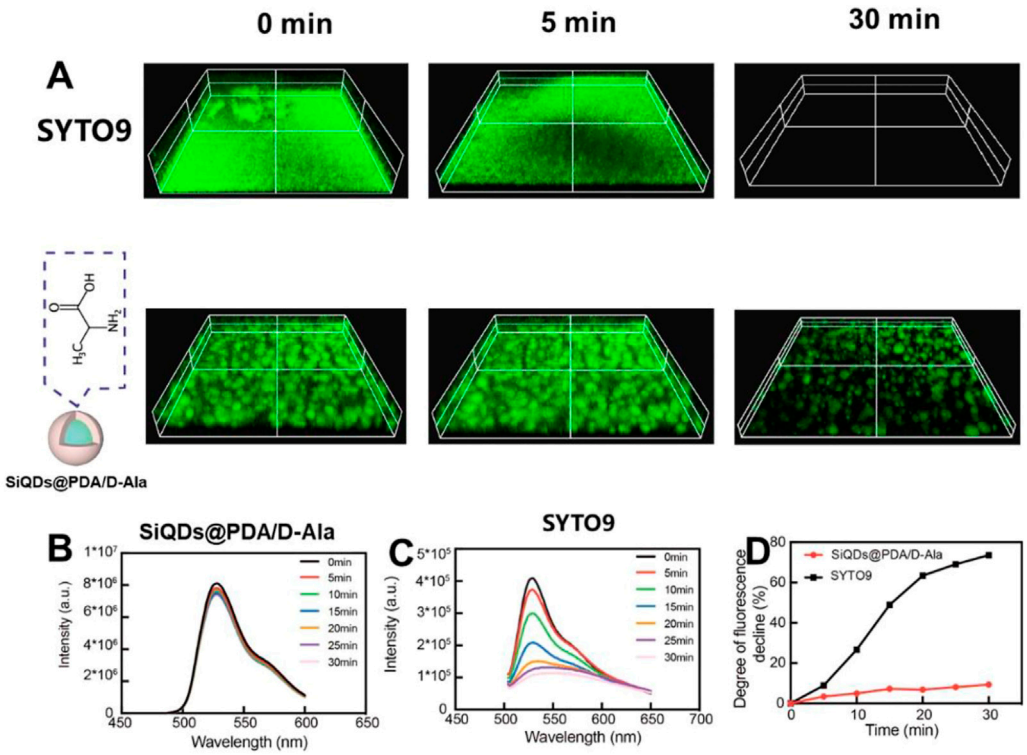

FIGURE 5
Anti-photobleaching characterizations. **(A)** Fluorescent images of SYTO 9 and SiQDs@PDA/D-Ala in *S. aureus* biofilm under white light irradiation; **(B)** fluorescent intensity of SiQDs@PDA/D-Ala under white light irradiation over time; **(C)** fluorescent intensity of SYTO 9 under white light irradiation over time; and **(D)** degree of fluorescent intensity decline of SiQDs@PDA/D-Ala and SYTO 9 under white light irradiation over time. The power of light is 2 W.

Glc modifications on SiQDs@PDA is caused by higher C/N ratio values of D-Ala and Glc. In addition, the content value of the sulfur element is 1.05% for SiQDs@PDA/Glc. The elements analyses result indicates that SiQDs@PDA/D-Ala and SiQDs@PDA/Glc for bacterial selective labeling and imaging research were successfully prepared through the universal functionalization method.

Selective labeling of SiQDs@PDA/D-Ala and SiQDs@PDA/D-Glc against bacteria

In order to verify our hypothesis that SiQDs@PDA/D-Ala and SiQDs@PDA/Glc could selectively recognize gram-positive and gram-negative bacteria, respectively, SiQDs@PDA/D-Ala and SiQDs@PDA/Glc were cultured with six types of bacteria (three types of gram-positive bacteria: *Staphylococcus aureus*, *Methicillin-resistant S. aureus*, and *Enterococcus faecalis* and three types of gram-negative bacteria: *Escherichia coli*, *E. coli*-β, *Pseudomonas aeruginosa*) for 3 h. The flow cytometry results in Figure 3A show that after the co-incubation of bacteria with SiQDs@PDA/D-Ala, the 41.8, 20.7, and 15.3% portions of *E. faecalis*, *S. aureus*, and *MRSA*, respectively, are fluorescence stained, whereas the fluorescence signals of *E. coli*, *E. coli*-β, and *P. aeruginosa* are almost identical to the control bacteria, indicating that SiQDs@PDA/D-Ala could selectively label gram-positive bacteria. The statistical analysis in Figure 3C shows that the recognition ability of SiQDs@PDA/D-Ala to gram-positive bacteria varies significantly. *E. faecalis* possesses the highest recognition ability, followed by *S. aureus* and *MRSA*, which is probably due to the different thicknesses of the peptidoglycan layers for the three of them (Alkasher and Badi, 2020).

By contrast, as shown in Figure 3B, after the co-incubation of bacteria with SiQDs@PDA/Glc, 15.3, 19.9, and 16.5% portions of *E. coli*, *E. coli*-β, and *P. aeruginosa* were fluorescence stained, respectively, whereas the fluorescence signals of *E. faecalis*, *S. aureus*, and *MRSA* were almost identical to the control bacteria, demonstrating that SiQDs@PDA/Glc could selectively label gram-negative bacteria. Moreover, the statistical analysis shown in Figure 3D demonstrates that the recognition ability of SiQDs@PDA/Glc to the three tested gram-negative bacteria do not show significant differences, which is probably caused by the similar distribution of lipopolysaccharides on the outer surface of the gram-negative bacteria (Kim et al., 2016). Obviously, by

functionalizing the surface of SiQDs@PDA by D-Ala and Glc, the selective labeling of gram-positive and gram-negative bacteria had been achieved successfully. Moreover, both SiQDs@PDA/D-Ala and SiQDs@PDA/Glc displayed negligible toxicity (Supplementary Figure S3), indicating that they are biocompatible in *in vivo* applications.

Selective imaging of bacteria and biofilms with SiQDs@PDA/D-Ala and SiQDs@PDA/Glc as fluorescent probes

The synthesized SiQDs exhibited an emission wavelength of 530 nm and 44.73% of fluorescence quantum yield. According to the flow cytometry result, SiQDs@PDA/D-Ala and SiQDs@PDA/Glc have a preference for staining gram-positive bacteria and gram-negative bacteria, respectively. As a result, SiQDs@PDA/D-Ala and SiQDs@PDA/Glc have the potential to be applied for selectively imaging gram-positive bacteria, gram-negative bacteria, and their biofilms as fluorescent probes. To verify the selective fluorescence imaging ability of SiQDs@PDA/D-Ala and SiQDs@PDA/Glc fluorescent probes, *S. aureus* and *E. coli* were chosen as model bacteria. After coculturing bacteria and their biofilms with SiQDs@PDA/D-Ala and SiQDs@PDA/Glc fluorescent probes, respectively, fluorescent microscopy was utilized to image the bacteria. As shown in Figure 4A, *S. aureus* showed strong green fluorescence, while *E. coli* had nearly no fluorescence under the same experimental procedure, which is consistent with the flow cytometry results, where SiQDs@PDA/D-Ala could selectively label gram-positive rather than gram-negative bacteria. In addition, the strong fluorescence signals in *S. aureus* biofilm and negligible fluorescence in *E. coli* biofilm indicate that SiQDs@PDA/D-Ala could not only selectively label gram-positive bacteria but also penetrate their biofilms. On the contrary, for fluorescent probe SiQDs@PDA/Glc, as shown in Figure 4B, the fluorescence signal only appears in *E. coli* and its biofilm, demonstrating that SiQDs@PDA/Glc could selectively label *E. coli* and penetrate through the biofilm unlike *S. aureus*.

Next, we investigated the anti-photobleaching capacity of SiQDs, which is an important characteristic for bacterial imaging probes. The SYTO 9 dye, a widely used green-fluorescent nuclear and chromosomal counterstain permeant dye to both prokaryotic and eukaryotic cell membranes, was utilized to be compared with SiQDs. The images of the fluorescence microscope in Figure 5A show that the fluorescent signal of SYTO 9 in gram-positive bacteria biofilm disappeared after 30 min under white light irradiation (2 W). However, under the same conditions, SiQDs@PDA/D-Ala still showed strong fluorescent signal after 30 min. In addition, the fluorescent spectra show that the fluorescence intensity of SiQDs@PDA/D-Ala only decreased by less than 10% (Figures 5B,D) within 30 min under white light irradiation (2 W). While for SYTO 9, the fluorescent intensity decreased by about 73% (Figures 5C,D) under the same irradiation condition. Obviously, the synthesized SiQDs showed better anti-photobleaching properties than did the commercial organic fluorescent dye.

Conclusion

The imitation-mussel fluorescent probe SiQDs@PDA with an emission wavelength of 530 nm and a fluorescence quantum yield of 44.7% was synthesized by *in situ* polymerization of dopamine on the surface of fluorescent silicon quantum dots. The universal functionalization ability of SiQDs@PDA was verified by successfully coupling various model molecules on its surface through π-π interaction, ion–ion interaction, and Michael addition reaction. On this basis, selective labeling and imaging of gram-positive bacteria, gram-negative bacteria, and their biofilms were achieved by modifying D-alanine and gluconamide onto the surface of SiQDs@PDA. Benefitting from the quantum confinement effect, SiQDs@PDA showed an excellent anti-photobleaching property. This imitation-mussel fluorescent SiQDs@PDA probe with excellent universal functionalization nature and anti-photobleaching performance is of great value for microbe-related research areas.

Experimental section

Materials

3-(aminopropyl)trimethoxysilane (Aladdin, ≥98%), rose bengal (Sigma-Aldrich, ≥80%), dopamine hydrochloride (Sigma-Aldrich, ≥99%), Tris base (Sigma-Aldrich, ≥99%), sulfhydryl-modified polyethylene glycol (PEG-SH) MW2000 (PEG2k-SH, Aladdin, ≥99%), 2-mercaptoethylamine hydrochloride (Sigma-Aldrich, ≥98%), tetracycline (Aladdin, ≥98%), D-alanine (Aladdin, ≥98%), tryptone soy broth (Solarbio Life Science, pH = 7.4), phosphate buffer (PBS, Gibco, pH = 7.4), sodium alginate (Aladdin, AR), gelatin (MW ~50,000–100,000, type A from porcine skin), SYTO 9 (Thermo Fisher Scientific), *E. coli* (ATCC25922), *E. coli*-β (ATCC35218), *P. aeruginosa* (ATCC27853), *S. aureus* (ATCC6538), Methicillin-resistant *Staphylococcus aureus* (MRSA, ATCC43300) and *E. faecalis* (ATCC29212) were purchased from LuWei Tech. Co., Ltd., Shanghai, China.

Synthesis of imitation-mussel florescent nanoprobe

Synthesis of SiQDs. According to the published method, SiQDs were synthesized with slight modification. The typical procedure is as follows: 20 mg of RB was dissolved in 8 ml of water first, then 2 ml 3-aminopropyltrimethoxysilane (APTMS) or N-(2-aminoethyl)-3-aminopropyltrimethoxysilane (DAMO) was added and stirred for another 5 min. The mixture was transferred to a 25-ml PTFE

hydrothermal kettle and heated at 160 C for 4 h. After the temperature returned to room temperature, the liquid was transferred to a 500-Da dialysis bag to dialyze for 2 days. After that, the solution was rapidly frozen using liquid nitrogen for freeze-drying to obtain SiQDs powder.

Synthesis of SiQDs/PDA. 5 mg of SiQDs was added into 1 ml of water. Then, 0.4 ml SiQDs water solution was added into 9.4 ml Tris buffer (pH 8.5). Afterward, a 0.2 ml dopamine water solution (5 mg/ml) was added to this Tris buffer solution. After 1 h under stirring, the solution was transferred into a 1,000-Da dialysis bag for dialysis. Finally, brown SiQDs@PDA powder was obtained after lyophilization.

Guest molecules functionalized SiQDs@PDA preparation. Tet-, D-Ala-, Glc-, PEG-SH-, and MEA-functionalized SiQDs@PDA were prepared according to a similar procedure. The specific steps are as follows: 0.4 ml SiQDs water solution (5 mg/ml) and 0.2 ml dopamine water solution (5 mg/ml) were first mixed in 9.4 ml Tris buffer (pH = 8.5). Then, 6 mg of guest molecules were added to the aforementioned solution and stirred for another 2 h. Finally, the reaction medium was collected and transferred into a 3,500-Da dialysis bag and dialyzed against water for 2 days.

Characterizations of florescent nanoprobes

TEM measurements of SiQDs and SiQDs@PDA were carried out by a JEM-2010HR instrument with an acceleration voltage of 200 kV. SiQDs and SiQDs@PDA fluorescent probes were diluted to 50 μg/ml with Millipore water. Then, 10 μl of each sample was dropped onto the copper grid and left to stand still in a ventilated dry place to dry the sample naturally. UV-Vis spectra of SiQDs and SiQDs@PDA were recorded using a UV-visible spectrophotometer (DU730) with a range of 400–1,000 nm.

The fluorescence characteristic of SiQDs was characterized by spectrofluorometer FS5. The concentration of the fluorescent probes was set at 70 μg/ml during the measurement, and the measurement temperature was set at 25 C.

Fourier transform infrared spectroscopy (FTIR) was recorded at wavenumbers between 650 cm^{-1} and 4,000 cm^{-1} on a Perkin Elmer Spectrum One Nicolet 520 spectrometer (United Kingdom) with 256 scans during the measurement. 10 mg SiQDs, SiQDs@PDA, and guest molecular functionalized SiQDs@PDA fluorescent probes were used for each measurement.

X-ray photoelectron spectroscopy (XPS) was recorded by ESCALAB 250 and Al K-Alpha X-ray as the excitation light source with a range of 0–1,200 eV and the energy level step width as 0.050 eV. The sample amount was maintained at around 10 mg per measurement.

XRD measurement was carried out by X'Pert PRO MPD instrument to investigate the crystallographic structure. The 2θ scan range was set at 30–90° under Cu Kα radiation (40 kV, 20 mA). The sample amount was maintained at around 10 mg per measurement.

The zeta potential values of different samples were measured by Malvern Zetasizer Nano ZS90. The sample concentration was set at 50 μg/ml in Millipore water, and the measurement temperature was set at 25 C.

Evaluation of the functionalized silicon quantum dots in selective labeling of bacteria

In order to assess the selective labeling effect of SiQDs@PDA/D-Ala and SiQDs@PDA/Glc against bacteria, we selected gram-negative bacteria *S. aureus* and gram-positive bacteria *E. coli* to analyze the selective labeling effect on both bacteria by targeted fluorescence silicon quantum dots by upright fluorescence microscope (NI-U) and having the quantitative fluorescence intensity evaluated by flow cytometry (Beckman CytoFLEX).

The specific experimental steps for the qualitative analysis are according to the following steps: 1) after coculturing with *S. aureus* and *E. coli* overnight in sterile tryptone soy broth (TSB), 500 μl bacteria solution was taken into a 1.5-ml sterilized centrifuge tube and mixed with 700 μl SiQDs@PDA/D-Ala (70 μg/ml) and SiQDs@PDA/Glc (70 μg/ml) for 3 hours; 2) the bacterial mixture was centrifuged as the last step at 7,000 rpm for 5 min. The supernatant was aspirated and the bacteria resuspended in 100 μl sterile PBS, then 50 μl was dropped on the cleaned glass slide. The morphology and labeling results of the bacteria were characterized by using the upright fluorescence microscope (NI-U).

The experimental steps for the quantitative analysis were similar to the qualitative analysis. Three kinds of gram-positive or gram-negative bacteria were cocultured with SiQDs@PDA/D-Ala or SiQDs@PDA/Glc for 3 hours, respectively. The mixture was centrifuged at 3,000 rpm for 3 min and the supernatant was aspirated. The mixture was then washed with sterile PBS. Finally, the mixture was suspended in 500 μl PBS, and the FITC channel was chosen to observe the bacterial labeling by flow cytometry (Beckman CytoFLEX) while the flow rate was 30 μl/min and 10,000 bacteria samples were recorded totally.

Evaluation of the functionalized silicon quantum dots in selective targeting bacterial biofilms

3D biofilm models of *E. coli* and *S. aureus* were constructed *in vitro* by using 3D bioprinting technology to further investigate the labeling of biofilms by the materials.

Firstly, 2.5% sodium alginate and 8% gelatin (Gel) were mixed in a beaker, heated at 50 C for 30 min, and then kept at 4 C for 5 min to remove air bubbles. After the heat–cool cycle had been repeated three times, the final mixture solution (Alg-Gel) was placed in a sterile syringe and incubated at 37 C for 20 min to form a complex colloidal solution.

Secondly, 10 μL of frozen *E. coli* or *S. aureus* was thawed and inoculated in 12 mL of sterile TSB medium respectively, followed by incubation in 37°C shaker overnight. The bacterial solution (OD600 = 0.3) was centrifuged at 3,000 rpm for 3 min and the supernatant was aspirated. The precipitated bacteria were resuspended in 500 μl of sterile TSB medium to obtain a concentrated bacterial suspension. The bacterial suspension was added to 10 ml of Alg-Gel solution and vortexed at 1,500 rpm for 5 min at room temperature to obtain a homogeneous bioink containing the bacteria.

Finally, the samples were printed using the EnvisionTEC 3D-Bioplotter. Before use, the bioplotter was sterilized by UV light and wiped with 75% ethanol. A sterile 10-ml syringe containing the bacterial bioink was attached to the print nozzle and loaded into the bioprinter. The bioink containing bacteria was dispensed through a needle with an internal diameter of 200 μm at a printing speed of 8–10 mm/s and an extruded air pressure of 1.2–1.4 Bar. 3D printed cubes were 15 mm in length and width and approximately 1 mm in height. After 3D printing, the constructs were cross-linked and cured in 20 mM $BaCl_2$ solution for 5 min. The cross-cured constructs were placed in a sterile 6-well culture plate and washed carefully with sterile PBS. Then, PBS was aspirated and 3 ml of sterile TSB medium was added to the wells of the plate. This was then incubated at 37 C, 100 rpm and the TSB medium changed every 1–2 days to obtain a dense 3D biofilm after 14–16 days of incubation.

Biocompatibility of silicon quantum dots, SiQDs@PDA, and ligand molecules–functionalized SiQDs@PDA

The cytotoxicity of SiQDs, SiQDs@PDA, and D-Ala- or Glc-modified SiQDs@PDA was assayed by MTT by using the A549 cell line. Briefly, 5×10^3 cells were seeded in 96-well plates with 200 μl medium per well and incubated overnight. After 6 h exposure to 70 μg/ml SiQDs, SiQDs@PDA, SiQDs@PDA/D-Ala, and SiQDs@PDA/Glc, 20 μl of 5 mg/ml MTT was added to each well and incubation was continued again for 4 h. Finally, 200 μl DMSO was added to each well and the absorption at 490 nm was measured with a microplate spectrophotometer (Synergy Mx, BioTek).

Data availability statement

The original contributions presented in the study are included in the article/Supplementary Material; further inquiries can be directed to the corresponding authors.

Author contributions

JL and LX performed most experiments. JL wrote the preliminary draft. YZ contributed to the synthesis of SiQDs. DW and JY supervised the whole project and reviewed the manuscript with editing. All authors have given approval to the final version of the manuscript.

Funding

This work was financially supported by the National Natural Science Foundation of China (22075327), the Natural Science Foundation of Guangdong Province (2019A1515010696 and 2022A1515011392), and the Science, Technology and Innovation Commission of Shenzhen Municipality (JCYJ20190807163003704).

Conflict of interest

The authors declare that the research was conducted in the absence of any commercial or financial relationships that could be construed as a potential conflict of interest.

The reviewer XZ declared a shared affiliation with the authors to the handling editor at the time of review.

Publisher's note

Supplementary material

The Supplementary Material for this article can be found online at: https://www.frontiersin.org/articles/10.3389/fbioe.2022.971682/full#supplementary-material

References

Alkasher, I., and Badi, W. (2020). *Gram-positive vs gram-negative*.

Asha, A. B., Peng, Y.-Y., Cheng, Q., Ishihara, K., Liu, Y., Narain, R., et al. (2022). Dopamine assisted self-cleaning, antifouling, and antibacterial coating via dynamic covalent interactions. *ACS Appl. Mat. Interfaces* 14, 9557–9569. doi:10.1021/acsami.1c19337

Barclay, T. G., Hegab, H. M., Clarke, S. R., and Ginic-Markovic, M. (2017). Versatile surface modification using polydopamine and related polycatecholamines: Chemistry, structure, and applications. *Adv. Mat. Interfaces* 4, 1601192. doi:10.1002/admi.201601192

Barros, N. R., Chen, Y., Hosseini, V., Wang, W., Nasiri, R., Mahmoodi, M., et al. (2021). Recent developments in mussel-inspired materials for biomedical applications. *Biomater. Sci.* 9, 6653–6672. doi:10.1039/d1bm01126j

Capeletti, L. B., De Oliveira, J. F. A., Loiola, L. M. D., Galdino, F. E., Da Silva Santos, D. E., Soares, T. A., et al. (2019). Gram-negative bacteria targeting mediated by carbohydrate–carbohydrate interactions induced by surface-modified nanoparticles. *Adv. Funct. Mat.* 29, 1904216. doi:10.1002/adfm.201904216

Chen, N., Fu, W. H., Zhou, J., Mei, L. Q., Yang, J. M., Tian, Y., et al. (2021). Mn2+-doped ZrO2@PDA nanocomposite for multimodal imaging-guided chemo-photothermal combination therapy. *Chin. Chem. Lett.* 32, 2405–2410. doi:10.1016/j.cclet.2021.02.030

Chen, X., Zhang, X., Xia, L.-Y., Wang, H.-Y., Chen, Z., Wu, F.-G., et al. (2018). One-step synthesis of ultrasmall and ultrabright organosilica nanodots with 100% photoluminescence quantum yield: Long-term lysosome imaging in living, fixed, and permeabilized cells. *Nano Lett.* 18, 1159–1167. doi:10.1021/acs.nanolett.7b04700

Cheng, W., Zeng, X., Chen, H., Li, Z., Zeng, W., Mei, L., et al. (2019). Versatile polydopamine platforms: Synthesis and promising applications for surface modification and advanced nanomedicine. *Acs Nano* 13, 8537–8565. doi:10.1021/acsnano.9b04436

Demchenko, A. P. (2020). Photobleaching of organic fluorophores: Quantitative characterization, mechanisms, protection. *Methods Appl. Fluoresc.* 8, 022001. doi:10.1088/2050-6120/ab7365

Fu, L., and Yu, A. (2020). Editorial: Polydopamine-Based nanostructures: Synthesis and biomedical applications. *Front. Chem.* 8, 206. doi:10.3389/fchem.2020.00206

Gao, G., Jiang, Y.-W., Sun, W., and Wu, F.-G. (2018). Fluorescent quantum dots for microbial imaging. *Chin. Chem. Lett.* 29, 1475–1485. doi:10.1016/j.cclet.2018.07.004

Gao, P., Xie, Z., and Zheng, M. (2021). Small nanoparticles bring big prospect: The synthesis, modification, photoluminescence and sensing applications of carbon dots. *Chin. Chem. Lett.* 33, 1659–1672. doi:10.1016/j.cclet.2021.09.085

Gidwani, B., Sahu, V., Shukla, S. S., Pandey, R., Joshi, V., Jain, V. K., et al. (2021). Quantum dots: Prospectives, toxicity, advances and applications. *J. Drug Deliv. Sci. Technol.* 61, 102308. doi:10.1016/j.jddst.2020.102308

Guo, J. S., Tian, X. G., Xie, D. H., Rahn, K., Gerhard, E., Kuzma, M. L., et al. (2020). Bone composites: Citrate-based tannin-bridged bone composites for lumbar fusion (adv. Funct. Mater. 27/2020). *Adv. Funct. Mat.* 30, 2070179. doi:10.1002/adfm.202070179

He, X., Yang, Y., Guo, Y., Lu, S., Du, Y., Li, J.-J., et al. (2020). Phage-guided targeting, discriminative imaging, and synergistic killing of bacteria by AIE bioconjugates. *J. Am. Chem. Soc.* 142, 3959–3969. doi:10.1021/jacs.9b12936

He, Y., Zhong, Y., Peng, F., Wei, X., Su, Y., Lu, Y., et al. (2011). One-pot microwave synthesis of water-dispersible, ultraphoto-and pH-stable, and highly fluorescent silicon quantum dots. *J. Am. Chem. Soc.* 133, 14192–14195. doi:10.1021/ja2048804

Hu, F., Qi, G., Mao, D., Zhou, S., Wu, M., Wu, W., et al. (2020). Visualization and *in situ* ablation of intracellular bacterial pathogens through metabolic labeling. *Angew. Chem. Int. Ed. Engl.* 59, 9374–9378. doi:10.1002/ange.201910187

Huang, B.-H., Shen, S.-S., Wei, N., Guo, X.-F., and Wang, H. (2020). Fluorescence biosensor based on silicon quantum dots and 5, 5′-dithiobis-(2-nitrobenzoic acid) for thiols in living cells. *Spectrochimica Acta Part A Mol. Biomol. Spectrosc.* 229, 117972. doi:10.1016/j.saa.2019.117972

Jing, Y., Deng, Z., Yang, X., Li, L., Gao, Y., Li, W., et al. (2020). Ultrathin two-dimensional polydopamine nanosheets for multiple free radical scavenging and wound healing. *Chem. Commun.* 56, 10875–10878. doi:10.1039/d0cc02888f

Jung, Y., Huh, Y., and Kim, D. (2021). Recent advances in surface engineering of porous silicon nanomaterials for biomedical applications. *Microporous Mesoporous Mater.* 310, 110673. doi:10.1016/j.micromeso.2020.110673

Kasouni, A., Chatzimitakos, T., and Stalikas, C. (2019). Bioimaging applications of carbon nanodots: A review. *C* 5, 19. doi:10.3390/c5020019

Kim, S., Patel, D. S., Park, S., Slusky, J., Klauda, J. B., Widmalm, G., et al. (2016). Bilayer properties of lipid A from various Gram-negative bacteria. *Biophysical J.* 111, 1750–1760. doi:10.1016/j.bpj.2016.09.001

Kwon, H. Y., Liu, X., Choi, E. G., Lee, J. Y., Choi, S. Y., Kim, J. Y., et al. (2019). Development of a universal fluorescent probe for gram-positive bacteria. *Angew. Chem. Int. Ed. Engl.* 131, 02537. doi:10.1002/ange.201902537

Li, S. Z., Ma, J. F., Zhao, X. L., Zhu, P. D., Xu, M., Niu, Y. C., et al. (2022). Highly fluorescence Ta4C3 MXene quantum dots as fluorescent nanoprobe for heavy ion detection and stress monitoring of fluorescent hydrogels. *Chin. Chem. Lett.* 33, 1850–1854. doi:10.1016/j.cclet.2021.11.020

Liu, Z., Hou, J., Wang, X., Hou, C., Ji, Z., He, Q., et al. (2020). A novel fluorescence probe for rapid and sensitive detection of tetracyclines residues based on silicon quantum dots. *Spectrochimica Acta Part A Mol. Biomol. Spectrosc.* 240, 118463. doi:10.1016/j.saa.2020.118463

Mao, D., Hu, F., Ji, S., Wu, W., Ding, D., Kong, D., et al. (2018). Antibacterial therapy: Metal-Organic-Framework-Assisted *in vivo* bacterial metabolic labeling and precise antibacterial therapy (adv. Mater. 18/2018). *Adv. Mat.* 30, 1870124. doi:10.1002/adma.201870124

Mao, D., Hu, F., KenryQi, G., Ji, S., Wu, W., Kong, D., et al. (2020). One-step *in vivo* metabolic labeling as a theranostic approach for overcoming drug-resistant bacterial infections. *Mat. Horiz.* 7, 1138–1143. doi:10.1039/c9mh01675a

Martynenko, I. V., Purcell-Milton, F., and Gun'ko, Y. K. (2022). "Quantum dots in biological imaging," in *Supramolecular chemistry in biomedical imaging*, 278–321.

Mozetič, M. (2019). *Surface modification to improve properties of materials*. Basel: Multidisciplinary Digital Publishing Institute.

ÖZbilgin, I. R. N. G., Yamazaki, T., Watanabe, J., Sun, H.-T., Hanagata, N., Shirahata, N., et al. (2022). Water-soluble silicon quantum dots toward fluorescence-guided photothermal nanotherapy. *Langmuir* 38, 5188–5196. doi:10.1021/acs.langmuir.1c02326

Patel, P., Hanini, A., Shah, A., Patel, D., Patel, S., Bhatt, P., et al. (2019). "Surface modification of nanoparticles for targeted drug delivery," in *Surface modification of nanoparticles for targeted drug delivery* (Springer), 19–31.

Schanze, K. S., Lee, H., and Messersmith, P. B. (2018). Ten years of polydopamine: Current status and future directions. *ACS Appl. Mater. Interfaces* 10 (9), 7521–7522. doi:10.1021/acsami.8b02929

Shendure, J., Balasubramanian, S., Church, G. M., Gilbert, W., Rogers, J., Schloss, J. A., et al. (2017). DNA sequencing at 40: Past, present and future. *Nature* 550, 345–353. doi:10.1038/nature24286

Singh, I., Dhawan, G., Gupta, S., and Kumar, P. (2021). Recent advances in a polydopamine-mediated antimicrobial adhesion system. *Front. Microbiol.* 11, 607099. doi:10.3389/fmicb.2020.607099

Sivasankarapillai, V. S., Jose, J., Shanavas, M. S., Marathakam, A., Uddin, M., Mathew, B., et al. (2019). Silicon quantum dots: Promising theranostic probes for the future. *Curr. Drug Targets* 20, 1255–1263. doi:10.2174/1389450120666190405152315

Terada, S., Xin, Y., and Saitow, K.-I. (2020). Cost-effective synthesis of silicon quantum dots. *Chem. Mat.* 32, 8382–8392. doi:10.1021/acs.chemmater.0c02320

Tian, Y., Wang, X. F., Zhao, S., Liao, X., Younis, M. R., Wang, S. J., et al. (2019). JQ1-Loaded polydopamine nanoplatform inhibits c-MYC/programmed cell death ligand 1 to enhance photothermal therapy for triple-negative breast cancer. *ACS Appl. Mat. Interfaces* 11, 46626–46636. doi:10.1021/acsami.9b18730

Tian, Y., Younis, M. R., Tang, Y. X., Liao, X., He, G., Wang, S. J., et al. (2021). Dye-loaded mesoporous polydopamine nanoparticles for multimodal tumor theranostics with enhanced immunogenic cell death. *J. Nanobiotechnology* 19, 365. doi:10.1186/s12951-021-01109-7

Yang, P., Zhang, S., Chen, X., Liu, X., Wang, Z., Li, Y., et al. (2020). Recent developments in polydopamine fluorescent nanomaterials. *Mat. Horiz.* 7, 746–761. doi:10.1039/c9mh01197h

Ye, X., Feng, T., Li, L., Wang, T., Li, P., Huang, W., et al. (2021). Theranostic platforms for specific discrimination and selective killing of bacteria. *Acta Biomater.* 125, 29–40. doi:10.1016/j.actbio.2021.02.010

Zhang, Y., Hu, X., Wang, Q., and Zhang, Y. (2021). Recent advances in microchip-based methods for the detection of pathogenic bacteria. *Chin. Chem. Lett.* 33, 2817–2831. doi:10.1016/j.cclet.2021.11.033

Zhao, W. B., Wang, Y., Liu, K. K., Zhou, R., and Shan, C. X. (2022a). Multicolor biomass based carbon nanodots for bacterial imaging. *Chin. Chem. Lett.* 33, 798–802. doi:10.1016/j.cclet.2021.08.084

Zhao, Y., Fang, X. X., Bai, M., Zhang, J., Yu, H. H., Chen, F., et al. (2022b). A microfluidic surface-enhanced Raman scattering (SERS) sensor for microRNA in extracellular vesicles with nucleic acid-tyramine cascade amplification. *Chin. Chem. Lett.* 33, 2101–2104. doi:10.1016/j.cclet.2021.08.047

Zheng, Q., and Lavis, L. D. (2017). Development of photostable fluorophores for molecular imaging. *Curr. Opin. Chem. Biol.* 39, 32–38. doi:10.1016/j.cbpa.2017.04.017

frontiers | Frontiers in Bioengineering and Biotechnology

ORIGINAL RESEARCH
published: 12 August 2022
doi: 10.3389/fbioe.2022.945472

Fabrication of Ginsenoside-Based Nanodrugs for Enhanced Antitumor Efficacy on Triple-Negative Breast Cancer

Shuting Zuo[1], Jing Wang[1], Xianquan An[2], Zhenyu Wang[1], Xiao Zheng[3] and Yan Zhang[1]**

[1]Department of Breast Surgery, The Second Hospital of Jilin University, Changchun, China, [2]Department of Anesthesiology, The Second Hospital of Jilin University, Changchun, China, [3]School of Biomedical Sciences and Engineering, South China University of Technology, Guangzhou, China

There is an urgent need to identify chemotherapeutic agents with improved efficacy and safety against triple-negative breast cancer (TNBC). Ginsenosides can reportedly induce tumor cell death, invasion, and metastasis; however, poor water solubility, low oral absorption rate, and rapid blood clearance limit their clinical application. Utilizing the amphiphilic property of ginsenosides as building blocks of biomaterials, we fabricated a carrier-free nanodrug composed of ginsenosides Rg3 and Rb1 using a nano-reprecipitation method without any additional carriers. After characterizing and demonstrating their uniform morphology and pH-sensitive drug release properties, we observed that Rg3-Rb1 nanoparticles (NPs) exhibited stronger antitumor and anti-invasive effects on TNBCs *in vitro* than those mediated by free ginsenosides. Consequently, Rg3-Rb1 NPs afforded superior inhibition of tumor growth and reduction of pulmonary metastasis than the Rg3 and Rb1 mixture, with no obvious systematic toxicity *in vivo*. Collectively, our results provide a proof-of-concept that self-assembled engineered ginsenoside nanodrugs may be efficient and safe for TNBC therapy.

Keywords: triple-negative breast cancer, self-assembly, nanodrug, ginsenoside, biomaterial

OPEN ACCESS

Edited by:
Mingqiang Li,
Third Affiliated Hospital of Sun Yat-sen University, China

Reviewed by:
Pengfei Wei,
Binzhou Medical University, China
Jinfeng Liao,
Sichuan University, China
He Shen,
Suzhou Institute of Nano-tech and Nano-bionics (CAS), China

****Correspondence:***
Xiao Zheng
zhengxiao129@scut.edu.cn
Yan Zhang
zhangy01@jlu.edu.cn

Specialty section:
This article was submitted to Biomaterials, a section of the journal Frontiers in Bioengineering and Biotechnology

Received: *16 May 2022*
Accepted: *10 June 2022*
Published: *12 August 2022*

Citation:
Zuo S, Wang J, An X, Wang Z, Zheng X and Zhang Y (2022) Fabrication of Ginsenoside-Based Nanodrugs for Enhanced Antitumor Efficacy on Triple-Negative Breast Cancer. Front. Bioeng. Biotechnol. 10:945472. doi: 10.3389/fbioe.2022.945472

INTRODUCTION

Triple-negative breast cancer (TNBC) is one of the most malignant tumors, exhibiting highly invasive characteristics (Cleator et al., 2007; Foulkes et al., 2010). Despite advances in chemotherapeutic, hormone-based, and combination drug therapies, the management of aggressive breast cancer, particularly TNBC, remains a formidable challenge (Podo et al., 2010; Garrido-Castro et al., 2019). As TNBC is more aggressive with a poorer prognosis and stronger metastatic rates than breast cancer, there are currently no approved targeted therapies (Collignon et al., 2015; Collignon et al., 2016). Chemotherapy, including anthracycline-, platinum-, and/or taxane-based neoadjuvant chemotherapy, remains the mainstay treatment for TNBC (Lebert et al., 2018; Nedeljkovic and Damjanovic, 2019; Jain et al., 2020). However, patients exhibit a poor response and inevitable adverse effects due to multiple drug resistance, along with chemotherapy-exacerbated tumor recurrence and metastasis (Bianchini et al., 2016). Therefore, there is an urgent need to identify chemotherapeutic agents that can demonstrate improved efficacy and safety against TNBC.

Ginsenosides are a series of bioactive compounds extracted from Panax ginseng, a Chinese translational herb in Asia that is well known for its beneficial pharmacological properties, including antitumor, antioxidant, and anti-inflammatory properties (Leung and Wong, 2010; Kim et al., 2015; Zheng M et al., 2018). The administration of ginsenosides has been shown to prevent tumor occurrence and progression and ameliorate cancer-related side effects (Jin et al., 2020). For example, ginsenoside Rg3, the main component of "Shenyi capsule," was launched as an antitumor drug by the State Food and Drug Administration of China in 2000 (Chen et al., 2014; Pan et al., 2019). Rg3 has been synergistically employed with standard chemotherapeutic agents, reportedly reducing toxicity in normal tissues (Li et al., 2017). Accumulating evidence has demonstrated that combining ginsenosides with adriamycin, cisplatin, and vincristine could reverse multidrug resistance and improve antitumor effects in several cancers (Li et al., 2014; Wang et al., 2018). In addition, ginsenosides can promote antitumor immunity by regulating signal transducers, indicating their potential for efficient and safe cancer chemotherapy (Son et al., 2016; Jiang et al., 2017).

Although advances in ginsenosides have exhibited promising potential in cancer therapy, the clinical application of the orally administered ginsenosides is limited by their poor bioavailability (<5%), given their poor water solubility, low oral absorption rate, and rapid blood clearance (Kim et al., 2018; Pan et al., 2018). Advances in nanotechnology and materials science have facilitated the development of nano-delivery systems for efficient and safe treatment of cancer and inflammatory diseases (van der Meel et al., 2019; Dawulieti et al., 2020; Shao et al., 2020; Hu et al., 2021; Wang H et al., 2021; Zhao et al., 2021; Shi et al., 2022; Tu et al., 2022). Ginsenoside nano-delivery systems have received considerable attention owing to their improved bioavailability, synergism, and detoxification (Shi et al., 2022; Tu et al., 2022). Several complex nano-delivery systems, including polymers, liposomes, metallic and inorganic particles, protein-based nanocarriers, and biomimetic nanoparticles (NPs), have been developed to improve the efficiency and safety of ginsenoside-based cancer therapy (van der Meel et al., 2019; Wahba et al., 2015; Hu et al., 2021; Wang H et al., 2021). However, most reported nano-delivery systems reportedly exhibit limited loading capacity, with additional concerns regarding their possible toxicity and biodegradation (Hong et al., 2020; Ren et al., 2020; Zhao et al., 2021; Mei et al., 2022; Xu et al., 2022).

Recently, carrier-free drug delivery systems, fabricated by self-assembly or co-assembly of pure drug molecules, have attracted substantial attention (Qin et al., 2017; Mei et al., 2022). Pure drug molecules without any chemical modification can spontaneously form uniform NPs by employing several methods (Zheng X et al., 2018; Sun et al., 2019; Zuo et al., 2021). Compared with free drugs, carrier-free nanodrugs afford improved bioavailability, prolonged blood circulation times, and superior tumor accumulation (Zheng et al., 2021). Compared with traditional nano-delivery systems, carrier-free drug delivery systems exhibit ultra-high drug loading (more than 60% or even 100%) and superior safety profiles (Huang et al., 2021). In addition, the co-delivery of dual or multiple drugs in a carrier-free form can help overcome the most intractable challenges encountered during cancer treatment (Wang M. Z et al., 2021).

In addition to their bioactive nature, ginsenosides have a potential role in stabilizing the phospholipid bilayer owing to their unique structure, comprising hydrophobic sterols and hydrophilic glycosides. The amphiphilic properties of ginsenosides can be regulated by the number of glycosides that may assemble with each other to form NPs. Based on these findings, we fabricated ginsenoside-based nanodrugs using a carrier-free method. We optimized the combination of ginsenosides Rg3 and Rb1 using self-assembly technology. The physicochemical and drug release properties of Rg3-Rb1 NPs were determined, and their therapeutic effects against TNBC were evaluated *in vitro* and *in vivo* and further compared with free ginsenosides and an Rg3/Rb1 mixture to demonstrate the advantages of carrier-free nanodrugs. Our results suggested that Rg3-Rb1 NPs can enhance antitumor efficacy for treating TNBC.

MATERIALS AND METHODS

Preparation and Characterization of Rg3-Rb1 NPs

Rg3-Rb1 NPs were prepared using a precipitation method. First, ginsenoside Rg3 was dissolved in dimethyl sulfoxide (DMSO). The final concentration of Rg3 in the DMSO solution was 5 mg/ml. Next, 1 ml of this solution and 5–25 mg of ginsenoside Rb1 powder (weight ratios of 1:1, 3:1, and 5:1, Rb1-Rg3, respectively) were mixed and stirred for 5 min at 600 rpm. Subsequently, 20 ml of deionized water was added to the mixture and stirred for 30 min at 900 rpm. The turbid mixture was dialyzed against ultrapure water for 48 h (molecular weight = 1,000) for purification. Finally, Rg3-Rb1 NPs were collected by lyophilization. The weight ratio of Rb1 to Rg3 was quantified as x:1 by high-pressure liquid chromatography (HPLC).

Drug Release

The drug release behavior of Rg3-Rb1 NPs was evaluated, as described below. Briefly, 10 mg of Rg3-Rb1 NPs (weight ratios of 1:1, 3:1, and 5:1, Rb1-Rg3, respectively) was added to a dialysis bag (1,000 Da). Subsequently, the bag was placed in a conical flask containing 100 ml of phosphate-buffered saline solution (PBS, pH: 7.4 or 5.5). The flask was sealed with a clean rubber stopper and placed on a shaking table in a 37°C incubator for 48 h. The dialysate was collected at 0, 1, 3, 6, 12, 24, and 48 h and analyzed by HPLC to determine the amount of Rb1 and Rg3.

Cytotoxicity Assay

Cells were first seeded into 96-well culture plates at a density of 5,000 cells/well and cultured overnight for full attachment to determine the cytotoxicity of Rg3-Rb1 NPs. Then, cells were treated with free Rb1, free Rg3, Rb1/Rg3 mixture, or Rg3-Rb1 NPs at different final concentrations, as displayed in **Figures**

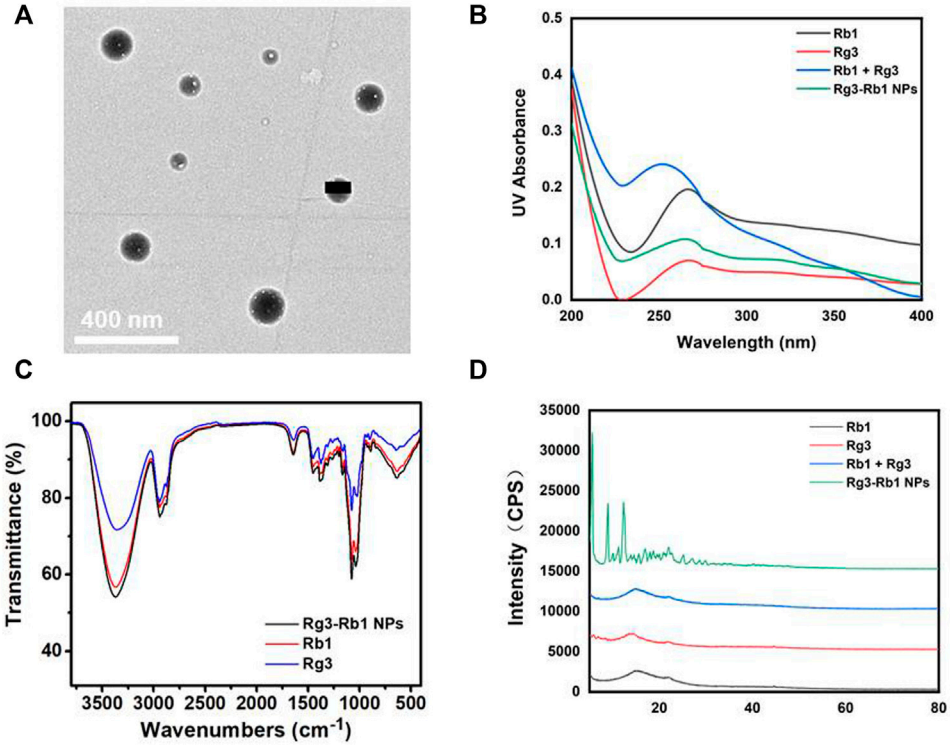

FIGURE 1 | Characterizations of Rg3-Rb1 NPs. **(A)** TEM image of Rg3-Rb1 NPs. Scale bar = 400 nm. **(B)** UV-vis of Rb1, Rg3, Rb1+Rg3, and Rg3-Rb1 NPs. **(C)** FTIR of Rb1, Rg3, and Rg3-Rb1 NPs. **(D)** XRD spectra of Rb1, Rg3, Rb1+Rg3, and Rg3-Rb1 NPs. FTIR, Fourier-transform infrared spectroscopy; NPs, nanoparticles; TEM, transmission electron microscopy; UV, ultraviolet; XRD, X-ray diffraction.

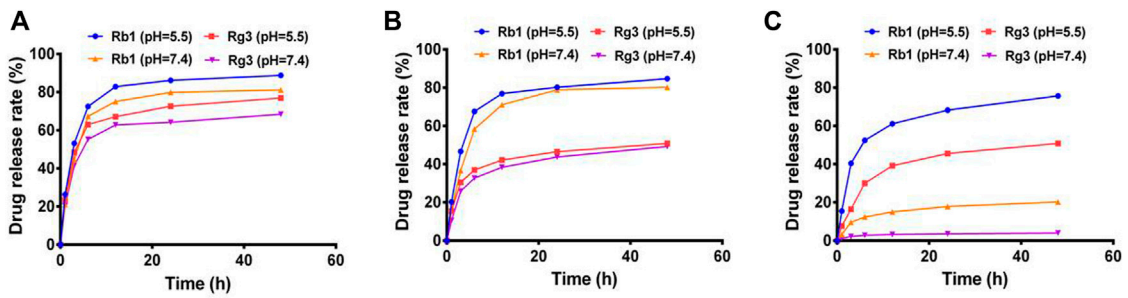

FIGURE 2 | Drug release profiles of Rg3-Rb1 NPs of different weight ratios (Rb1 to Rg3) under acidic and neutral pH conditions. **(A)** 1:1, **(B)** 3:1, and **(C)** 5:1. NPs, nanoparticles.

3A–C, respectively. Both Rb1 and Rg3 were dissolved in the cell culture medium at a high final concentration (100 μg/ml). After treatment for 48 h, cell viability was assessed using the standard SRB method. The absorbance of saline-treated cells was set at 100%. The IC50 value of each drug was calculated using GraphPad Prism software.

In Vivo Antitumor and Safety Experiments

All mice were treated in compliance with the Guide for the Care and Use of Laboratory Animals, and all procedures were approved by the Animal Care and Use Committee of Jilin University (China). Female BALB/c mice (8-week-old) were used to evaluate the *in vivo* pharmacological effects induced by Rg3-Rb1 NPs. First, equivalent volumes of 4T1 cells and Matrigel were mixed at 4°C to obtain cell suspension (10^6 cells/ml). Then, 100 μL of the suspension was injected into the second mammary fat pad of mice. Three days later, mice were randomly divided into five groups and treated with saline, Rb1 (5 mg/kg, intravenously), Rg3 (1 mg/kg, intravenously), Rb1/Rg3 mixture (5 mg/kg of Rb1 and 1 mg/kg of Rg3,

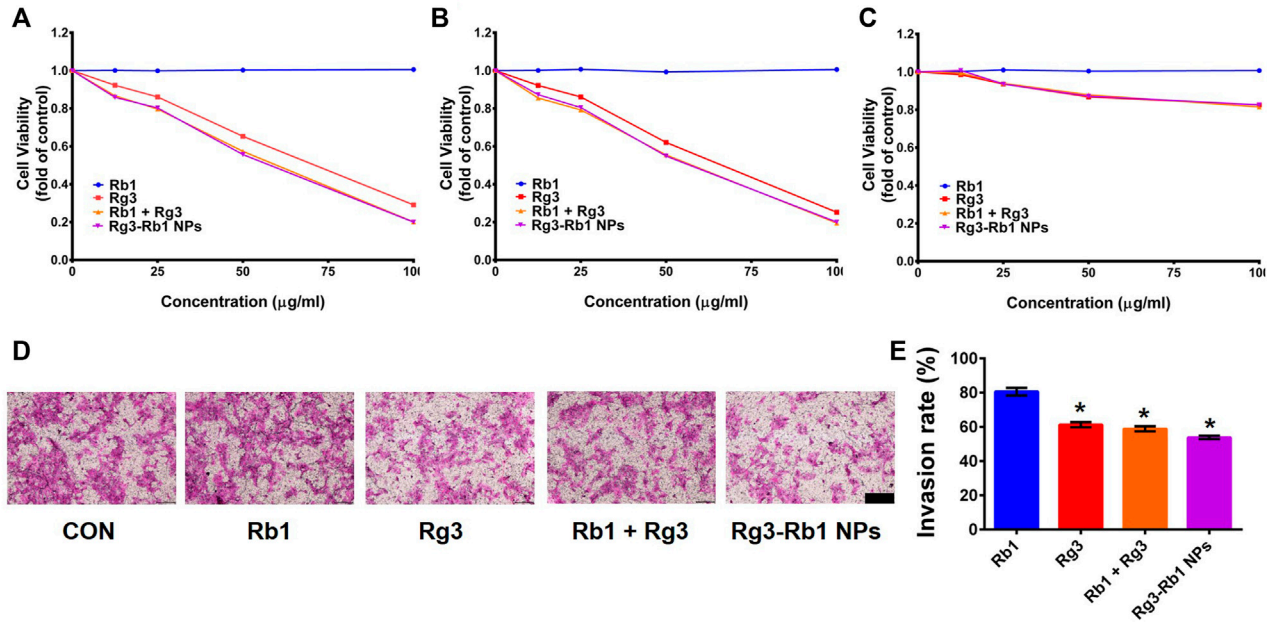

FIGURE 3 | *In vitro* pharmacological effect of Rg3-Rb1 NPs. Cell viability of **(A)** 4T1, **(B)** MDA-MB-231, and **(C)** MCF-10a cells after 48 h of treatment. **(D)** Representative images and **(E)** quantitative analysis of crystal purple-stained invasive 4T1 cells. Scale bar = 200 μm $*p < 0.05$ compared with the control group. NPs, nanoparticles.

intravenously), or Rg3-Rb1 NPs (1 mg/kg, based on the concentration of Rg3, intravenously). Drug treatment and measurements of tumor size and body weight were performed every 3 days. Tumor volume was calculated using the following formula: $V_{tumor} = 0.5 \times (\text{long diameter}) \times (\text{short diameter})^2$.

All mice were sacrificed on day 22. Major organs, including the heart, kidneys, liver, lungs, and spleen, were collected and fixed for further hematoxylin and eosin (H&E) staining, and the number of metastatic lung nodules was recorded before fixation. After H&E staining, tissue sections were photographed. The obtained images, along with body weight curves and serum biochemistry indexes, such as alanine aminotransferase (ALT), aspartate aminotransferase (AST), blood urea nitrogen (BUN), and serum creatinine (CRE), were used to evaluate the biosafety profiles of Rg3-Rb1 NPs.

RESULTS AND DISCUSSION

To fabricate Rg3-Rb1 NPs, ginsenoside Rg3-Rb1 was mixed in DMSO at different weight ratios, and the mixture was added to water under constant shaking. Transmission electron microscopy (TEM) (**Figure 1A**) revealed that Rg3-Rb1 NPs exhibited a uniform nanosized morphology (diameter: 120 ± 20 nm), indicating the successful formulation of ginsenoside nanodrugs without chemical modifications or additional carriers. To explore the assembly mechanism, the ultraviolet- (UV-) vis spectra of Rg3-Rb1 NPs were recorded and compared with those of free Rg3 and Rb1 (**Figure 1B**). Raw Rg3 and Rb1 molecules exhibited similar absorption peaks at approximately 260 nm. In contrast, Rg3-Rb1 NPs displayed a wider and red-shifted absorbance peak, indicating a robust molecular interaction during the self-assembly process. Infrared spectral analysis showed that Rg3-Rb1 NPs possessed identical groups of Rg3 and Rb1 molecules (**Figure 1C**). Additionally, the X-ray diffraction pattern of raw Rg3 and Rb1 molecules showed a wide diffraction peak, indicating an amorphous crystalline structure (**Figure 1D**). Notably, Rg3-Rb1 NPs showed characteristic high-intensity diffraction peaks at 2θ values, ranging from 5° to 20°, indicating their naturally crystalline form. This phenomenon might be explained by the crystal orientations after recrystallization, which could be solubilized more easily, enhancing the dissolution rates when compared with their respective crystalline forms. Based on these results, we concluded that the formulated Rg3-Rb1 NPs were uniform nanodrugs containing Rg3 and Rb1.

To optimize the preparation of Rg3-Rb1 NPs, we investigated the self-assembly of Rg3 and Rb1 at different weight ratios. The release profiles of the three types of Rg3-Rb1 NPs were evaluated at a pH value of 7.4 to mimic normal conditions in bodily fluids or a pH value of 5.5 to mimic the acidic tumor microenvironment. As shown in **Figures 2A–C**, Rg3 release showed a time-dependent sustainable behavior, with a slight initial burst (more than 20%, at 0–6 h) in a buffer of pH 7.4. This initial burst in the Rg3 release might be attributed to establishing a balance in equilibrium between the inside and outside release settings. However, on decreasing the pH to 5.5, Rg3 release increased substantially, reaching 50.9% over a 48 h period. The increased drug release rate at low pH may be attributed to the facilitated dissociation of ginsenosides. Collectively, Rg3-Rb1 NPs controlled drug release, which might improve the

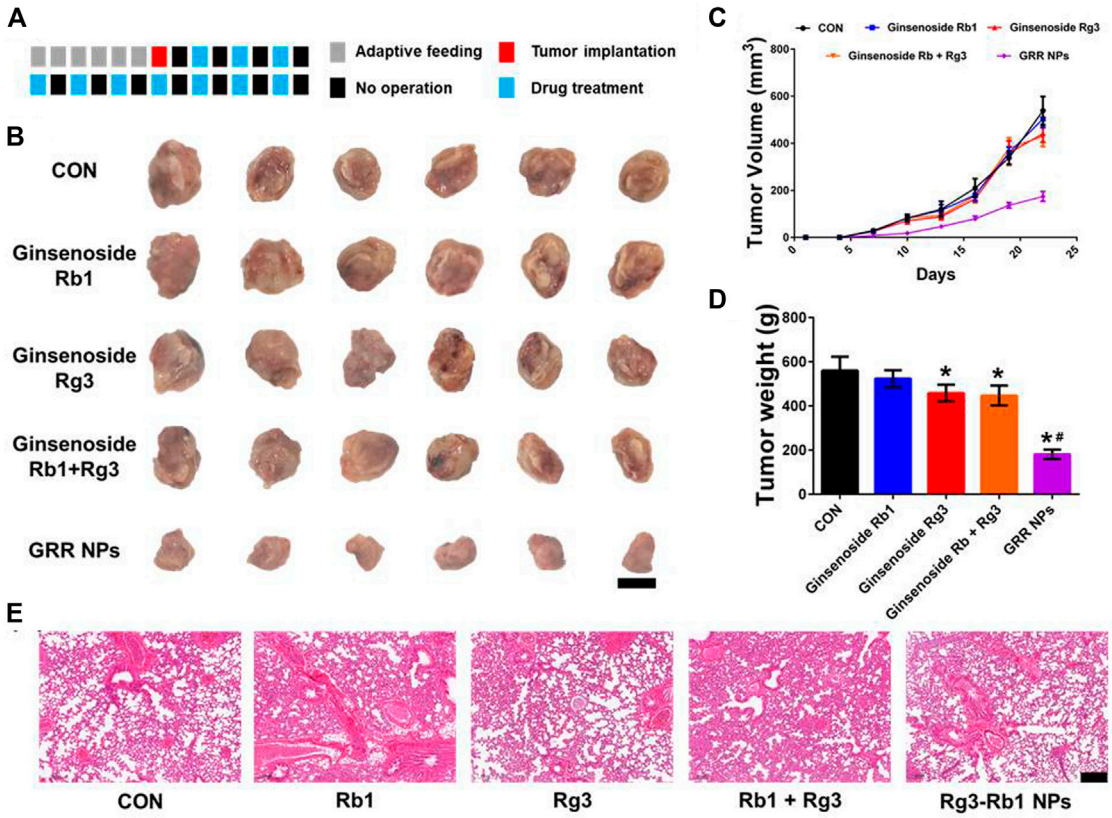

FIGURE 4 | *In vivo* pharmacological effect of Rg3-Rb1 NPs. **(A)** The dosage regimen for treating the 4T1 orthotopic mammary mouse model, each square represents 1 day, **(B)** tumor images, **(C)** tumor volume, and **(D)** tumor weight. Scale bar = 1 cm. $*p < 0.05$ compared with the control group. $\#p < 0.05$ compared with the Rg3 group. **(E)** Lung images of 4T1 orthotopic mammary mouse. Scale bar = 2 mm. NPs, nanoparticles.

bioavailability and therapeutic outcomes of ginsenosides. Based on the sustained-drug release behavior in the simulated acidic tumor microenvironment, the optimal self-assembly of Rg3-Rb1 NPs was prepared and used for subsequent experimental treatments at a mass ratio of 5:1 (Rb1:Rg3).

Next, we used the SRB assay to determine the viability of the mouse breast cancer cell line (4T1), human TNBC cell line (MDA-MB-231), and non-neoplastic breast cell line (MCF-10A) after 24 h of treatment with various concentrations of free Rg3, free Rb1, Rg3/Rb1 mixture, and Rg3-Rb1 NPs. Compared with the control group, the cell viability of all Rg3-containing groups dose-dependently decreased in 4T1 and MDA-MB-231 cells (**Figures 3A,B**), whereas free Rb1 induced minimal toxicity on breast cancer cells when compared with Rg3. The IC_{50} values in 4T1 cells were 63.87 ± 4.55 μg/ml for free Rg3, 60.14 ± 4.89 μg/ml for Rg3/Rb1 mixture, and 58.17 ± 4.14 μg/ml for Rg3-Rb1 NPs. Similarly, the IC_{50} values in MDA-MB-231 cells were greater than 100 μg/ml for the Rg3/Rb1 mix and Rg3-Rb1 NPs. These results indicated that combining Rg3 and Rb1 afforded a significantly greater decrease in toxicity than that induced by free ginsenosides, partly due to Rb1-mediated sensitization to chemotherapy. However, there were few differences between the Rg3-Rb1 NPs and Rg3+Rb1, which might be attributed to the prolonged incubation time and conditions *in vitro*. It is also worth noting that Rg3-Rb1 NPs, as well as the Rg3+Rb1 mixture, induced fewer toxic effects on normal TNBCs cells than MCF-10A cells (**Figure 3C**). The cell-protective effects of ginsenosides could explain this phenomenon. Taken together, these results indicated that the Rg3-Rb1 NPs provided a greater killing effect on TNBCs, with markedly diminished toxicity on normal breast cells. As shown in **Figures 3D,E**, Rb1-mediated sensitization to Rg3 inhibited 4T1 cell invasion (80.6%, 61.32%, 58.84%, and 53.79% for Rb1, Rg3, and Rg3/Rb1 mixture and Rg3-Rb1 NPs, respectively). In particular, Rg3-Rb1 NPs showed more efficient inhibition of invasion than Rg3+Rb1.

Based on these findings, we examined the therapeutic efficacy of Rg3-Rb1 NP-mediated TNBCs *in vivo*. Herein, 4T1 orthotopic mammary tumor-bearing mice were intravenously administered saline (control group), free Rg3, free Rb1, Rg3+Rb1 mix, and Rg3-Rb1 NPs (**Figure 4A**). Compared with the control group, we observed that free Rg3, free Rb1, Rg3/Rb1 mixture, and Rg3-Rb1 NPs decreased tumor growth and reduced tumor weights at the end of the treatment period (**Figures 4B–D**); however, free Rg3 and Rb1 did not significantly impact tumor growth. Rg3-Rb1 NPs exhibited the strongest tumor growth inhibition and the lowest number of metastatic lung nodules (**Figure 4E**; **Supplementary Figure S1**). Notably, Rg3-Rb1 NPs demonstrated superior therapeutic efficacy to the Rg3/Rb1 mixture, indicating the advantages of self-assembled nanodrugs. Consistently, *in vivo* findings revealed that Rg3-Rb1 NPs exhibit markedly robust efficacy against TNBC.

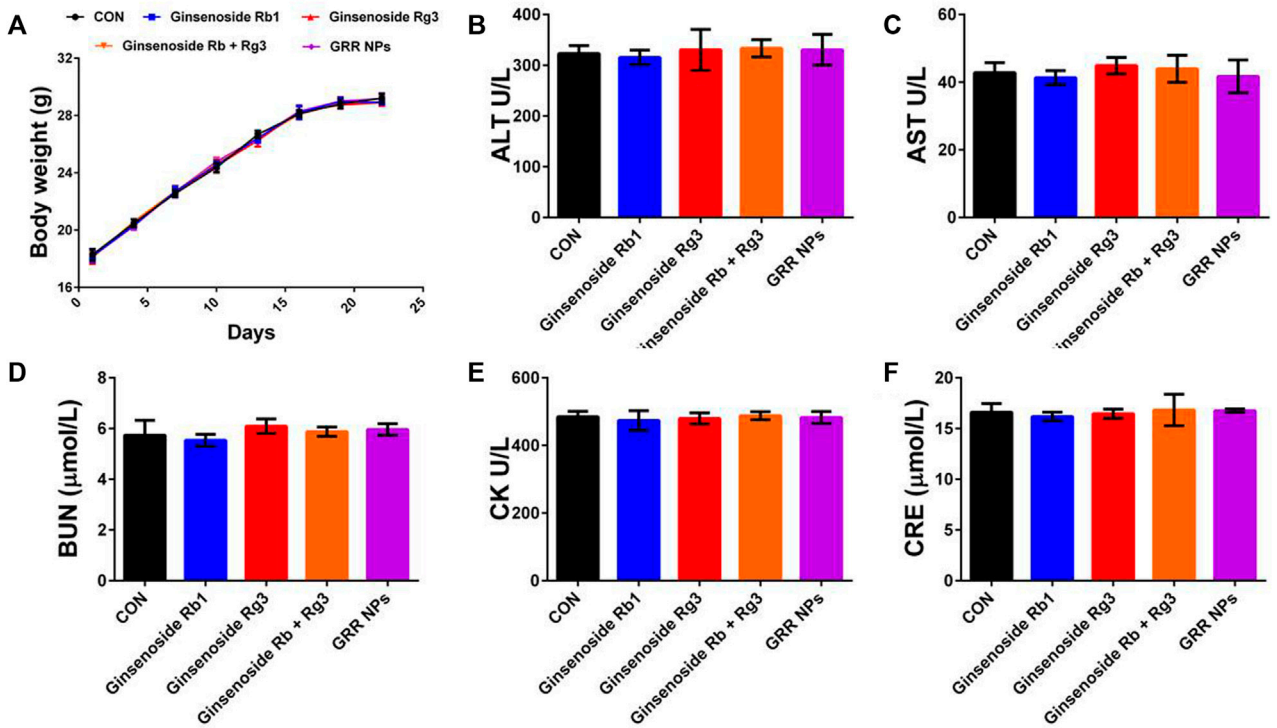

FIGURE 5 | Biosafety effect of Rg3-Rb1 NPs. **(A)** Body weight, **(B)** ALT, **(C)** AST, **(D)** BUN, **(E)** CK, and **(F)** CRE of 4T1 orthotopic mammary mouse. ALT, alanine aminotransferase; AST, aspartate aminotransferase; BUN, blood urea nitrogen; CRE, serum creatinine; NPs, nanoparticles.

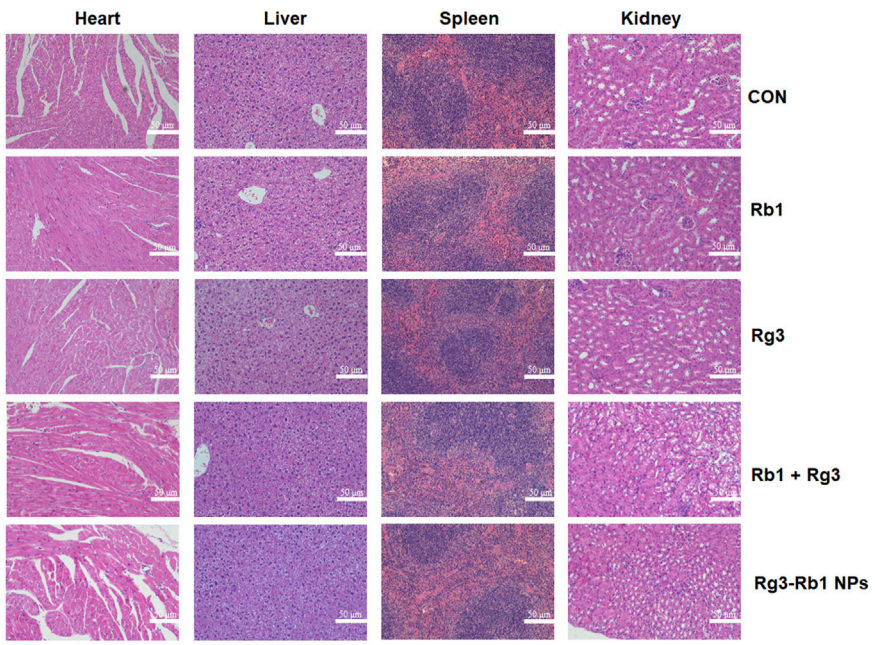

FIGURE 6 | Hematoxylin and eosin-stained image of 4T1 orthotopic mammary mouse. Scale bar = 50 μm.

Finally, we performed a toxicological evaluation to determine whether Rg3-Rb1 NPs generate toxic side effects in the body following oral administration. The weight-change curve revealed that no treated group exhibited a significant effect (**Figure 5A**). Based on serum biochemistry assays, including assays for ALT, AST, BUN, and CRE, we detected no significant differences between the ginsenoside-containing and control groups (**Figures 5B–F**). In addition, no pathological damage was observed in primary organs, including the liver, spleen, kidney, and heart, across all groups (**Figure 6**). Overall, these safety profiles suggested that Rg3-Rb1 NPs exhibit low systemic toxicity.

In summary, we developed carrier-free ginsenoside nanodrugs composed of Rg3 and Rb1 using a simple nanoprecipitation method. Rg3-Rb1 NPs demonstrated a greater antitumor and anti-invasive effect against TNBC cells (vs. free ginsenosides), along with less toxicity in normal breast cells. The *in vivo* experiments clearly revealed that Rg3-Rb1 NPs preferentially inhibited 4T1 tumor growth and lung metastasis with a good biosafety profile. Overall, the Rg3-Rb1 NPs might have superior antitumor and antimetastatic properties, which might provide insight into the development of ginsenoside nanodrugs for safe and effective TNBC management.

DATA AVAILABILITY STATEMENT

The raw data supporting the conclusion of this article will be made available by the authors, without undue reservation.

ETHICS STATEMENT

The animal study was reviewed and approved and all procedures were approved by the Animal Care and Use Committee of Jilin University (China).

AUTHOR CONTRIBUTIONS

SZ, XZ, and YZ designed the research. SZ, ZW, XA, JW, and XZ performed the research. SZ, XA, and JW analyzed the data. SZ, XZ, and YZ wrote the manuscript.

FUNDING

This study was supported by the Scientific Development Program of Jilin Province (20180201054YY), the Finance Department Program of Jilin Province (2020SCZT028), and Guangzhou Basic and Applied Basic Research Foundation (No. 202102020361).

SUPPLEMENTARY MATERIAL

The Supplementary Material for this article can be found online at: https://www.frontiersin.org/articles/10.3389/fbioe.2022.945472/full#supplementary-material

REFERENCES

Bianchini, G., Balko, J. M., Mayer, I. A., Sanders, M. E., and Gianni, L. (2016). Triple-negative Breast Cancer: Challenges and Opportunities of a Heterogeneous Disease. *Nat. Rev. Clin. Oncol.* 13 (11), 674–690. doi:10.1038/nrclinonc.2016.66

Chen, S., Wang, Z., Huang, Y., O'Barr, S. A., Wong, R. A., Yeung, S., et al. (2014). Ginseng and Anticancer Drug Combination to Improve Cancer Chemotherapy: a Critical Review. *Evidence-Based Complementary Altern. Med.* 2014, 168940. doi:10.1155/2014/168940

Cleator, S., Heller, W., and Coombes, R. C. (2007). Triple-negative Breast Cancer: Therapeutic Options. *Lancet Oncol.* 8 (3), 235–244. doi:10.1016/s1470-2045(07)70074-8

Collignon, J., Lousberg, L., Schroeder, H., and Jerusalem, G. (2016). Triple-negative Breast Cancer: Treatment Challenges and Solutions. *Breast Cancer (Dove Med. Press)* 8, 93–107. doi:10.2147/BCTT.S69488

Dawulieti, J., Sun, M., Zhao, Y., Shao, D., Yan, H., Lao, Y.-H., et al. (2020). Treatment of Severe Sepsis with Nanoparticulate Cell-free DNA Scavengers. *Sci. Adv.* 6 (22), eaay7148. doi:10.1126/sciadv.aay7148

Foulkes, W. D., Smith, I. E., and Reis-Filho, J. S. (2010). Triple-Negative Breast Cancer. *N. Engl. J. Med.* 363 (20), 1938–1948. doi:10.1056/nejmra1001389

Garrido-Castro, A. C., Lin, N. U., and Polyak, K. (2019). Insights into Molecular Classifications of Triple-Negative Breast Cancer: Improving Patient Selection for Treatment. *Cancer Discov.* 9 (2), 176–198. doi:10.1158/2159-8290.cd-18-1177

Hong, C., Liang, J., Xia, J., Zhu, Y., Guo, Y., Wang, A., et al. (2020). One Stone Four Birds: A Novel Liposomal Delivery System Multi-Functionalized with Ginsenoside Rh2 for Tumor Targeting Therapy. *Nano-Micro Lett.* 12 (1), 129. doi:10.1007/s40820-020-00472-8

Hu, H., Yang, C., Zhang, F., Li, M., Tu, Z., Mu, L., et al. (2021). A Versatile and Robust Platform for the Scalable Manufacture of Biomimetic Nanovaccines. *Adv. Sci.* 8 (15), 2002020. doi:10.1002/advs.202002020

Huang, L., Zhao, S., Fang, F., Xu, T., Lan, M., and Zhang, J. (2021). Advances and Perspectives in Carrier-free Nanodrugs for Cancer Chemo-Monotherapy and Combination Therapy. *Biomaterials* 268, 120557. doi:10.1016/j.biomaterials.2020.120557

Jain, V., Kumar, H., Anod, H. V., Chand, P., Gupta, N. V., Dey, S., et al. (2020). A Review of Nanotechnology-Based Approaches for Breast Cancer and Triple-Negative Breast Cancer. *J. Control. Release* 326, 628–647. doi:10.1016/j.jconrel.2020.07.003

Jiang, Z., Yang, Y., Yang, Y., Zhang, Y., Yue, Z., Pan, Z., et al. (2017). Ginsenoside Rg3 Attenuates Cisplatin Resistance in Lung Cancer by Downregulating PD-L1 and Resuming Immune. *Biomed. Pharmacother.* 96, 378–383. doi:10.1016/j.biopha.2017.09.129

Jin, Y., Huynh, D. T. N., Nguyen, T. L. L., Jeon, H., and Heo, K.-S. (2020). Therapeutic Effects of Ginsenosides on Breast Cancer Growth and Metastasis. *Arch. Pharm. Res.* 43 (8), 773–787. doi:10.1007/s12272-020-01265-8

Kim, Y.-J., Zhang, D., and Yang, D.-C. (2015). Biosynthesis and Biotechnological Production of Ginsenosides. *Biotechnol. Adv.* 33 (6 Pt 1), 717–735. doi:10.1016/j.biotechadv.2015.03.001

Kim, H., Lee, J. H., Kim, J. E., Kim, Y. S., Ryu, C. H., Lee, H. J., et al. (2018). Micro-/nano-sized Delivery Systems of Ginsenosides for Improved Systemic Bioavailability. *J. Ginseng Res.* 42 (3), 361–369. doi:10.1016/j.jgr.2017.12.003

Lebert, J. M., Lester, R., Powell, E., Seal, M., and McCarthy, J. (2018). Advances in the Systemic Treatment of Triple-Negative Breast Cancer. *Curr. Oncol.* 25 (Suppl. 1), 142–150. doi:10.3747/co.25.3954

Leung, K., and Wong, A. (2010). Pharmacology of Ginsenosides: a Literature Review. *Chin. Med.* 5, 20. doi:10.1186/1749-8546-5-20

Li, C., Sun, B.-Q., and Gai, X.-D. (2014). Compounds from Chinese Herbal Medicines as Reversal Agents for P-Glycoprotein-Mediated Multidrug

Resistance in Tumours. *Clin. Transl. Oncol.* 16 (7), 593–598. doi:10.1007/s12094-014-1169-7

Li, L., Ni, J., Li, M., Chen, J., Han, L., Zhu, Y., et al. (2017). Ginsenoside Rg3 Micelles Mitigate Doxorubicin-Induced Cardiotoxicity and Enhance its Anticancer Efficacy. *Drug Deliv.* 24 (1), 1617–1630. doi:10.1080/10717544.2017.1391893

Mei, H., Cai, S., Huang, D., Gao, H., Cao, J., and He, B. (2022). Carrier-free Nanodrugs with Efficient Drug Delivery and Release for Cancer Therapy: From Intrinsic Physicochemical Properties to External Modification. *Bioact. Mater.* 8, 220–240. doi:10.1016/j.bioactmat.2021.06.035

Nedeljković, M., and Damjanović, A. (2019). Mechanisms of Chemotherapy Resistance in Triple-Negative Breast Cancer-How We Can Rise to the Challenge. *Cells* 8 (9), 957. doi:10.3390/cells8090957

Pan, W., Xue, B., Yang, C., Miao, L., Zhou, L., Chen, Q., et al. (2018). Biopharmaceutical Characters and Bioavailability Improving Strategies of Ginsenosides. *Fitoterapia* 129, 272–282. doi:10.1016/j.fitote.2018.06.001

Pan, L., Zhang, T., Sun, H., and Liu, G. (2019). Ginsenoside Rg3 (Shenyi Capsule) Combined with Chemotherapy for Digestive System Cancer in China: A Meta-Analysis and Systematic Review. *Evidence-Based Complementary Altern. Med.* 2019, 2417418. doi:10.1155/2019/2417418

Podo, F., Buydens, L. M. C., Degani, H., Hilhorst, R., Klipp, E., Gribbestad, I. S., et al. (2010). Triple-negative Breast Cancer: Present Challenges and New Perspectives. *Mol. Oncol.* 4 (3), 209–229. doi:10.1016/j.molonc.2010.04.006

Qin, S.-Y., Zhang, A.-Q., Cheng, S.-X., Rong, L., and Zhang, X.-Z. (2017). Drug Self-Delivery Systems for Cancer Therapy. *Biomaterials* 112, 234–247. doi:10.1016/j.biomaterials.2016.10.016

Ren, Z., Chen, X., Hong, L., Zhao, X., Cui, G., Li, A., et al. (2020). Nanoparticle Conjugation of Ginsenoside Rg3 Inhibits Hepatocellular Carcinoma Development and Metastasis. *Small* 16 (2), 1905233. doi:10.1002/smll.201905233

Shao, D., Zhang, F., Chen, F., Zheng, X., Hu, H., Yang, C., et al. (2020). Biomimetic Diselenide-Bridged Mesoporous Organosilica Nanoparticles as an X-ray-Responsive Biodegradable Carrier for Chemo-Immunotherapy. *Adv. Mat.* 32 (50), 2004385. doi:10.1002/adma.202004385

Shi, C., Dawulieti, J., Shi, F., Yang, C., Qin, Q., Shi, T., et al. (2022). A Nanoparticulate Dual Scavenger for Targeted Therapy of Inflammatory Bowel Disease. *Sci. Adv.* 8 (4), eabj2372. doi:10.1126/sciadv.abj2372

Son, K.-j., Choi, K. r., Lee, S. J., and Lee, H. (2016). Immunogenic Cell Death Induced by Ginsenoside Rg3: Significance in Dendritic Cell-Based Anti-tumor Immunotherapy. *Immune Netw.* 16 (1), 75–84. doi:10.4110/in.2016.16.1.75

Sun, M., Zhang, Y., He, Y., Xiong, M., Huang, H., Pei, S., et al. (2019). Green Synthesis of Carrier-free Curcumin Nanodrugs for Light-Activated Breast Cancer Photodynamic Therapy. *Colloids Surfaces B Biointerfaces* 180, 313–318. doi:10.1016/j.colsurfb.2019.04.061

Tu, Z., Zhong, Y., Hu, H., Shao, D., Haag, R., Schirner, M., et al. (2022). Design of Therapeutic Biomaterials to Control Inflammation. 7 *Nat. Rev. Mater*, 1–18. doi:10.1038/s41578-022-00426-z

van der Meel, R., Sulheim, E., Shi, Y., Kiessling, F., Mulder, W. J. M., and Lammers, T. (2019). Smart Cancer Nanomedicine. *Nat. Nanotechnol.* 14 (11), 1007–1017. doi:10.1038/s41565-019-0567-y

Wahba, H. A., and El-Hadaad, H. A. (2015). Current Approaches in Treatment of Triple-Negative Breast Cancer. *Cancer Biol. Med.* 12 (2), 106–116. doi:10.7497/j.issn.2095-3941.2015.0030

Wang, J., Tian, L., Khan, M. N., Zhang, L., Chen, Q., Zhao, Y., et al. (2018). Ginsenoside Rg3 Sensitizes Hypoxic Lung Cancer Cells to Cisplatin via Blocking of NF-Kb Mediated Epithelial-Mesenchymal Transition and Stemness. *Cancer Lett.* 415, 73–85. doi:10.1016/j.canlet.2017.11.037

Wang, H., Zheng, Y., Sun, Q., Zhang, Z., Zhao, M., Peng, C., et al. (2021). Ginsenosides Emerging as Both Bifunctional Drugs and Nanocarriers for Enhanced Antitumor Therapies. *J. Nanobiotechnol* 19 (1), 322. doi:10.1186/s12951-021-01062-5

Wang, M.-Z., Xu, Y., Xie, J.-F., Jiang, Z.-H., and Peng, L.-H. (2021). Ginsenoside as a New Stabilizer Enhances the Transfection Efficiency and Biocompatibility of Cationic Liposome. *Biomater. Sci.* 9 (24), 8373–8385. doi:10.1039/d1bm01353j

Xu, Y., Zhu, B.-W., Li, X., Li, Y.-F., Ye, X.-M., and Hu, J.-N. (2022). Glycogen-based pH and Redox Sensitive Nanoparticles with Ginsenoside Rh2 for Effective Treatment of Ulcerative Colitis. *Biomaterials* 280, 121077. doi:10.1016/j.biomaterials.2021.121077

Zhao, J., Duan, Z., Ma, X., Liu, Y., and Fan, D. (2021). Recent Advances in Systemic and Local Delivery of Ginsenosides Using Nanoparticles and Nanofibers. *Chin. J. Chem. Eng.* 30, 291–300. doi:10.1016/j.cjche.2020.11.012

Zheng, X., Zhao, Y., Jia, Y., Shao, D., Zhang, F., Sun, M., et al. (2021). Biomimetic Co-assembled Nanodrug of Doxorubicin and Berberine Suppresses Chemotherapy-Exacerbated Breast Cancer Metastasis. *Biomaterials* 271, 120716. doi:10.1016/j.biomaterials.2021.120716

Zheng, M., Xin, Y., Li, Y., Xu, F., Xi, X., Guo, H., et al. (2018). Ginsenosides: A Potential Neuroprotective Agent. *BioMed Res. Int.* 2018, 8174345. doi:10.1155/2018/8174345

Zheng, X., Zhang, F., Shao, D., Zhang, Z., Cui, L., Zhang, J., et al. (2018). Gram-scale Production of Carrier-free Fluorescent Berberine Microrods for Selective Liver Cancer Therapy. *Biofactors* 44 (5), 496–502. doi:10.1002/biof.1450

Zuo, S., Wang, Z., An, X., Wang, J., Zheng, X., Shao, D., et al. (2021). Self-Assembly Engineering Nanodrugs Composed of Paclitaxel and Curcumin for the Combined Treatment of Triple Negative Breast Cancer. *Front. Bioeng. Biotechnol.* 9, 747637. doi:10.3389/fbioe.2021.747637

Conflict of Interest: The authors declare that the research was conducted in the absence of any commercial or financial relationships that could be construed as a potential conflict of interest.

Publisher's Note: All claims expressed in this article are solely those of the authors and do not necessarily represent those of their affiliated organizations or those of the publisher, the editors, and the reviewers. Any product that may be evaluated in this article, or claim that may be made by its manufacturer, is not guaranteed or endorsed by the publisher.

frontiers | Frontiers in Bioengineering and Biotechnology

TYPE Original Research
PUBLISHED 24 August 2022
DOI 10.3389/fbioe.2022.995099

OPEN ACCESS

EDITED BY
Jianxun Ding,
Changchun Institute of Applied Chemistry (CAS), China

REVIEWED BY
Guohui Liu,
Huazhong University of Science and Technology, China
Daxue Zhu,
Lanzhou University Second Hospital, China

*CORRESPONDENCE
Jianyong Zhang,
zhangjy92@126.com
Rui Tian,
tianrui17419@wchscu.cn
Liangxue Zhou,
liangxue_zhou@126.com

†These authors have contributed equally to this work

SPECIALTY SECTION
This article was submitted to Biomaterials, a section of the journal Frontiers in Bioengineering and Biotechnology

RECEIVED 15 July 2022
ACCEPTED 01 August 2022
PUBLISHED 24 August 2022

CITATION
Liu X, Zhang G, Wei P, Hao L, Zhong L, Zhong K, Liu C, Liu P, Feng Q, Wang S, Zhang J, Tian R and Zhou L (2022), 3D-printed collagen/silk fibroin/secretome derived from bFGF-pretreated HUCMSCs scaffolds enhanced therapeutic ability in canines traumatic brain injury model.
Front. Bioeng. Biotechnol. 10:995099.
doi: 10.3389/fbioe.2022.995099

3D-printed collagen/silk fibroin/secretome derived from bFGF-pretreated HUCMSCs scaffolds enhanced therapeutic ability in canines traumatic brain injury model

Xiaoyin Liu[1†], Guijun Zhang[1†], Pan Wei[2†], Lifang Hao[3], Lin Zhong[4], Kunhon Zhong[5], Chang Liu[1], Peng Liu[1], Qingbo Feng[6], Shan Wang[1], Jianyong Zhang[7]*, Rui Tian[1]* and Liangxue Zhou[1]*

[1]Department of Neurosurgery, West China Hospital, West China Medical School, Sichuan University, Chengdu, China, [2]Department of Neurosurgery, The First People's Hospital of Long Quan yi District, Chengdu, China, [3]Department of Radiology, Liao Cheng The Third People's Hospital, Liaocheng, China, [4]The First Affiliated Hospital of Chengdu Medical College, Chengdu, China, [5]State Key Laboratory of Biotherapy, West China Hospital, West China Medical School, Sichuan University, Chengdu, China, [6]Department of Liver Surgery and Liver Transplantation, State Key Laboratory of Biotherapy and Cancer Center, West China Hospital, Sichuan University, Chengdu, China, [7]Department of General Surgery, The Affiliated Hospital of Guizhou Medical University, Guiyang, China

The regeneration of brain tissue poses a great challenge because of the limited self-regenerative capabilities of neurons after traumatic brain injury (TBI). For this purpose, 3D-printed collagen/silk fibroin/secretome derived from human umbilical cord blood mesenchymal stem cells (HUCMSCs) pretreated with bFGF scaffolds (3D-CS-bFGF-ST) at a low temperature were prepared in this study. From an *in vitro* perspective, 3D-CS-bFGF-ST showed good biodegradation, appropriate mechanical properties, and good biocompatibility. In regard to vivo, during the tissue remodelling processes of TBI, the regeneration of brain tissues was obviously faster in the 3D-CS-bFGF-ST group than in the other two groups (3D-printed collagen/silk fibroin/secretome derived from human umbilical cord blood mesenchymal stem cells (3D-CS-ST) group and TBI group) by motor assay, histological analysis, and immunofluorescence assay. Satisfactory regeneration was achieved in the two 3D-printed scaffold-based groups at 6 months postsurgery, while the 3D-CS-bFGF-ST group showed a better outcome than the 3D-CS-ST group.

KEYWORDS

traumatic brain injury, secretome, human umbilical cord blood mesenchymal stem cells, bFGF, collagen, silk fibroin

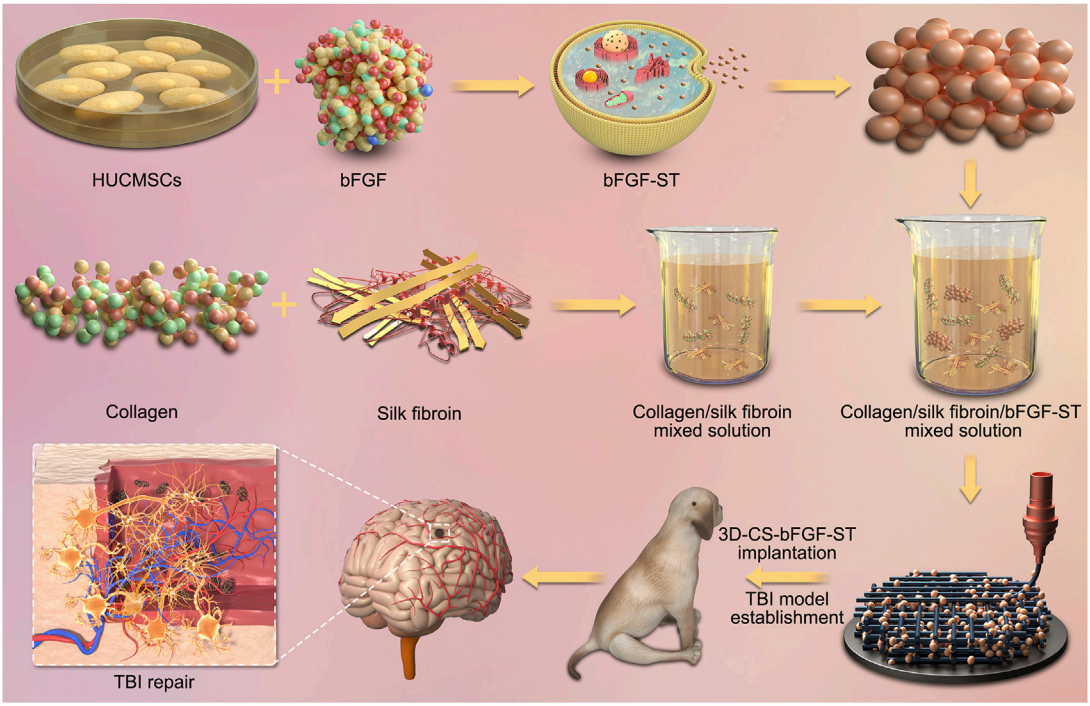

Graphical Abstract

Introduction

Considering that a growing number of the population suffers from traumatic brain injury (TBI), the incidence rate of TBI in children is 3–7%, and 1,568,346 adult patients have been diagnosed with TBI during the past eight years (Maas et al., 2017). TBI is, in accordance with the US Centers for Disease Control and Prevention, defined as a brain's normal function disruption, which is caused by bumps, blows, jolts, or penetrating head injuries (Taylor et al., 2017). Patients with TBI may suffer cognitive, emotional, and behavioral inability in their remaining lifetime (Li et al., 2021). TBI is a major cause of morbidity and mortality and attracts a wide range of public concerns. Over the last few decades, it has led to a steep rise in therapeutic strategies in TBI populations by many scholars. Current treatment strategies for TBI are prioritized for the reduction of intracranial pressure and prevention of its subsequent complications (Alexis et al., 2015). Unfortunately, the application of surgery and drugs does not result in satisfactory neuroprotection and a favorable prognosis (Nichol et al., 2015).

Stem cell therapy, in recent years, has been generally accepted to be a promising and encouraging regenerative medical treatment in basic research fields about ischemic or hemorrhagic stroke, Alzheimer's disease, and TBI(Wakai et al., 2016; Jahanbazi Jahan-Abad et al., 2018; Zhang et al., 2018; Huang et al., 2019; Bonsack et al., 2020; Han et al., 2020; Kawabori et al., 2020; Bae et al., 2021; Li and Sundström, 2022; Zhang et al., 2022). Mesenchymal stem cells (MSCs) can differentiate into various cell lineages under certain conditions: adipocytes, chondrocytes, glia, neurons, and osteoblasts. Considering its self-renewal, regenerative ability, and neuroprotective effect, MSC transplantation has been suggested as a therapeutic management strategy in animal models and clinical studies for structural and functional recovery (Tondreau et al., 2004). However, mounting evidence supports that stem cells confer a neurological benefit attributed to the corresponding secretome (ST), which exhibits similarly beneficial functions (Han et al., 2015; de Rivero Vaccari et al., 2016). It is composed of soluble factors and membrane vesicles. Soluble factors are transforming growth factors (Beer et al., 2017).

Of note, human umbilical cord blood mesenchymal stem cells (HUCMSCs) were reported to have advantages over other types of MSCs without limitations of immunological side effects or tumorigenesis as well as an aging-like nature and with easy accessibility and effective neurological protection (Bongso and Fong, 2013; Sharma et al., 2014; Pu et al., 2017; Hao et al., 2018; Sun et al., 2018). It is currently believed that ST derived from HUCMSCs harbored an ability of tissue regeneration, reducing the possibility of immune rejection. ST could be regarded as a potentially strong nanomedicine for TBI treatment, and we hypothesized that HUCMSC-ST could compensate for the

damaged neurons and neurotrophy. However, recent studies revealed that unconjugated ST was unable to be sustained in the injured area during the recovery process (Kankala et al., 2017; Metzger et al., 2017). To solve the problem of retention and stability at different storage levels, our study advocated that scaffold-based 3D printing technology could overlay HUCMSC-ST (Jiang et al., 2021).

Increasing evidence has confirmed that several biomaterials may resemble the microenvironment of the extracellular matrix, and one of the major types of tissue engineering is the use of 3-dimensional (D) scaffolds. Among these scaffolds, collagen (C), chitosan, and silk fibroin (SF), as the most valuable candidate materials for biomedical applications, are popular for cell culture, growth, and differentiation (Zhang et al., 2017). In addition, in a previous study, we found that collagen and silk fibroin (CS) had a favorable effect on a canine model of TBI(Jiang et al., 2021). Moreover, 3D bioprinting was beneficial to a more comforting placement and distribution of living cells, thereby allowing for the construction of bioactively complex microenvironments.

Basic fibroblast growth factor (bFGF) is a small peptide of a large family that regulates cell proliferation, differentiation, and migration (Xie et al., 2013). In addition, it has been reported that the production of angiogenic factors, such as bFGF and vWF, enhances the innate proangiogenic ability of MSCs(Wei et al., 2008).

With advances in tissue engineering techniques, a combination of materials and stem cells has provided promising neurogenesis results. Based on this technique, bFGF was added and supposed to increase the quality and quantity rate of cells *in vitro* and at the injury site. On the basis of the 3D-printed scaffold, we developed a novel tactic to promote the therapeutic effects of secretome derived from HUCMSCs pretreated with bFGF (bFGF-ST). We incorporated bFGF-ST into collagen/silk fibroin mixed solution to form 3D-printed collagen/silk fibroin/secretome derived from HUCMSCs pretreated with bFGF scaffolds (3D-CS-bFGF-ST), which could release bFGF-ST into the surroundings in a sustained manner.

Thus, combining these technologies, a 3D-printed platform incorporating bFGF-ST at a low temperature was described in this study. We aimed to evaluate the potential effects of 3D-CS-bFGF-ST on tissue regeneration and motor function recovery after TBI in canine models.

Materials and methods

Isolation and characterization of HUCMSCs and bFGF-ST

The umbilical cords of healthy pregnant women who gave birth naturally or by cesarean section were washed, cut and digested with collagenase and 0.25% trypsin (Liu et al., 2020). HUCMSCs were incubated in a saturated humidity of 37°C and 5% CO_2 at an inoculation density of $1 \times 10^6/cm^2$. The culture medium was changed after 24 h at the first time point and then once every 3 days. The suspension cells were passaged at a ratio of 1:1. To determine the biological characteristics of HUCMSCs. We used the immunological phenotypes CD90 (1:300, Abcam, Cambridge, UK) and CD 105 (1:400, Abcam, Cambridge, UK) based on immunofluorescence staining.

For the isolation of bFGF-ST, briefly, the primary MSCs were seeded in T75 (75-cm^2) culture flasks and maintained in DMEM with 10% fetal bovine serum for 24 h. Then, DMEM containing bFGF (PeproTech) (100 ng/ml bFGF in complete medium) was used to replace the conditioned medium. After HUCMSCs were pretreated with bFGF for 24 h, serum-free, low-glucose DMEM was used to replace the conditioned medium. Conditioned media were harvested at 24 h. The conditioned media was centrifuged once at 500×g for 10 min and then twice at 800×g for 15 min. The bFGF-ST secreted by 1×10^7 cells was concentrated into 20 μL. Two types of secretome were collected in our study: normal HUCMSCs secretome without pretreatment (ST), the HUCMSCs secretome pretreated with bFGF (bFGF-ST). A bicinchoninic acid (BCA) protein assay kit (Beyotime, China) was performed to measure the protein concentrations of ST and bFGF-ST.

Preparation of 3D-CS-bFGF-ST

Collagen was isolated from fresh bovine tendons, and purification of collagen was carried out in accordance with an established method described previously (Liu et al., 2019; Sun et al., 2019). To sufficiently improve purities, the tendons were crushed and soaked in a buffer solution (0.05 mol/L) for 24 h. The precipitate, acquired by centrifugation at 2000 rpm, was added to acetic acid solution containing pepsin to obtain the supernatant. Next, 3.5 mol/L NaCl solution was added to the supernatant for salting out. Consequently, the collagen gel was obtained by dialysis at 4°C for 5 days.

Silk fibroin was produced following the established method (Yuhui et al., 2011; Xu et al., 2016; Jiang et al., 2020). One hundred grams of silk (Jiaxing, Zhejiang, China) was prepared and boiled in a 0.5% $NaHCO_3$ (Solarbio Science & Technology Co., Ltd., Beijing, China) solution for dehydration. Subsequently, the dried silk was added to a ternary solution of $CaCl_2{\cdot}CH_3CH_2OH{\cdot}H_2O$ (Solarbio Science & Technology Co., Ltd., Beijing, China) with a molar ratio of 1:2:8 at 80°C. Through subsequent filtration, dialysis, and concentration, the SF solution was obtained and stored at 4°C.

To fabricate scaffolds, collagen and silk fibroin were evenly mixed at a mass ratio (collagen:silk fibroin = 1:10) for 3D printing preparation. Before 3D printing, 0.1 g collagen/silk fibroin mixed solution was soaked in 20 μL bFGF-ST solution (200 μg) at 4°C for 24 h, followed by stirring at 4°C for 12 h, in order to fully and uniformly mix the collagen/silk fibroin mixture and bFGF-ST

together. For low-temperature 3D printing technology, a 3D bioprinter (Regenovo Biotechnology Co., Ltd., Hangzhou, China) was designed to create constructs at −20°C. Computer aided design (CAD) to form a multihole support template. Modelling software (Solidworks software, Dassault Systèmes, Vélizy, France) was performed to use the 3D printing model for this study, followed by converting the predesigned STL 3D model into G code. The printing parameters were as follows: normal feed speed at 10 mm/s, ordinary extrusion speed at 2 mm/s, and first layer print height at 0.7 mm/s. Print layer thickness at 0.32 mm/s, print layer = 7 layers, print needle diameter at 260 μM, bottom plate molding temperature at −20°C. After 3D printing, the 3D solid model was freeze-dried and then cut into cylindrical scaffolds (2 mm diameter, 2 mm height) by using molds. The six types of scaffolds used in this study are as follows: 3D-printed collagen scaffolds (3D-C) group, 3D-printed collagen/secretome derived from HUCMSCs scaffolds (3D-C-ST) group, 3D-printed collagen/secretome derived from HUCMSCs pretreated with bFGF scaffolds (3D-C-bFGF-ST), 3D-printed collagen/silk fibroin (3D-CS), 3D-printed collagen/silk fibroin/secretome derived from HUCMSCs scaffolds (3D-CS-ST) and 3D-printed collagen/silk fibroin/secretome derived from HUCMSCs pretreated with bFGF scaffolds (3D-CS-bFGF-ST).

In vivo degradation

Thirty Sprague–Dawley (SD) rats, 2 months old and weighing approximately 300 g, were used. The scaffold degradation *in vivo* was evaluated according to the difference in their weights with 5 different mass ratios (collagen:silk fibroin = 1:2, 1:6, 1:10, 1:14, 1:18). A small incision, 3 small at approximately 1 cm in length, was made on SD rat backs after anesthesia. The three sterilized scaffolds from one group were implanted in the lesions from one rat. The final weights were recorded at predetermined time intervals of 1–6 months. Then the scaffolds were placed in 2% sodium dodecyl surface (SDS) and the 2% SDS was replaced every 12 h. After 2 days, the scaffold was placed in ultrapure water. Through sterilization by DNase-RNase I digestion fluid (Solarbio Science & Technology Co., Ltd, China) overnight and shaking at a constant temperature of 37°C for 48 h, the decellularized scaffolds were placed in 30 ml of PBS and incubated at 37°C. Percent mass remaining = (decellularized scaffold mass/initial mass) × 100%.

Characterization of the 3D-printed scaffold

Optical images and microscopic morphologies were obtained by using confocal laser scanning microscopy (CLSM, LSM 880, Zeiss), digital camera and stereomicroscope (SZX16, Olympus), respectively. The distribution and surface morphology of the scaffold were analysed by a typical HE staining procedure, which was reported previously. The physical characteristics of the scaffold, including the absorption ratio, porosity ratio, and mechanical strength, were calculated according to a previous method (Liu et al., 2021). A synchronous differentiated thermal analyser was used to analyse the phase transition temperatures of bFGF-ST, 3D-CS, and 3D-CS-bFGF-ST. The samples headed at an increase from 30 to 400°C. The scaffolds were evaluated by Braker X-ray diffraction. Its relevant parameters were as follows: tube voltage = 40 kV, tube current = 30 mA, target material was CuKα = 0.15406 nm, scanning speed = 5°C/min, step width = 0.02°, and diffraction angle range = 5–90°C. Cumulative secretome release from 3D-CC-ST was examined by using the bicinchoninic acid (BCA) reagent test kit (Beyotime) according to a previous study (Li et al., 2020; Guan et al., 2022).

Assessment of scaffold cytocompatibility

To analyse the effect of the 3D-printed scaffold on cells *in vitro*, HUCMSCs at passage 3 were dissociated into single cells and plated at a concentration of 1×10^6/ml into the scaffold, which was divided into two groups: 3D-CS-ST and 3D-CS-bFGF-ST. The proliferation of HUCMSCs on the two kinds of scaffolds was assessed by phase-contrast microscopy (Nikon, Tokyo, Japan), scanning electron microscopy (SEM) (Hitachi, Tokyo, Japan), hematoxylin and eosin (HE) staining, and MTT assay (Solarbio Science & Technology Co., Ltd) according to a previous study (Liu et al., 2021). After 7 days of coculture, through serial dehydration in ethanol, samples were dried in a CO_2 critical point dryer and then sputter-coated with gold using SEM analysis for the morphology and growth of the cells. HE staining was used to evaluate the growth status of NSCs on 3D-CS-ST and 3D-CS-bFGF-ST.

NSCs were isolated from embryonic day 14 (E14) brains (Wakai et al., 2016). The dissociated cells were cultured in a mixed medium of DMEM/F12 (1:1) (Gibco. Unitad States) supplemented with N2 (Gibco), B27 (Gibco), 20 ng/ml bFGF and 20 ng/ml epidermal growth factor (EGF) (PeproTech). These cells were incubated in a humidified incubator at 37°C and 5% CO_2. Immunofluorescence staining for Nestin, NF, GAP43 and NeuN was used to identify NSCs and assess the degree of differentiation of NSCs. NSCs were also seeded on two types of scaffolds (3D-CS-ST and 3D-CS-bFGF-ST) in a flat-bottomed 12-well plate at a density of 1×10^6/ml. The cell adhesion rate was measured at 1, 12, 24, 36, 48, 60 and 72 h. Cells were treated with MTT solution, and the absorbance was measured on days 1, 3, 5, and 7 at 490 nm with a microplate reader.

Canine TBI models and scaffold implantation

A total of 20 male canines, 1 year old and weighing 11–14 kg, were obtained. The established TBI model has been enunciated in the literature (Jiang et al., 2018). Following anesthesia, a

preconditioned traumatic cortical motor injury occurred on the right side through a craniotomy. 3D-CS-bFGF-ST and 3D-CS-ST were implanted to fill up the lesions. According to the different treatment strategies, the animals were randomly assigned to 4 groups: the Sham group (Only the skull was opened without TBI, $n = 5$), the TBI group (TBI without scaffolds implantation, $n = 5$), the 3D-CS-ST group (3D-printed collagen/silk fibroin/secretome derived from HUCMSCs scaffolds were implanted into the TBI cavity, $n = 5$), and the 3D-CS-bFGF-ST group (3D-printed collagen/silk fibroin/secretome derived from HUCMSCs pretreated with bFGF scaffolds were implanted into the TBI cavity, $n = 5$). General anesthesia was performed on each canine to minimize the pain caused by the surgery.

Evaluation of locomotor function

The neurological function assessment of all canines was performed by two independent authors at 1 day, 1 week, 2, 4, 8, 20, and 24 weeks after surgery ($n = 5$ for each group). Based on the modified GCS (mGCS) with a range from 3–18 (Platt et al., 2001), the Purdy scale with a range from 2–11 (Purdy et al., 1989), and the NDS score with a range from 0–500 (Castellá et al., 2005), they were used to comprehensively understand the behavioral level and locomotor function force measures.

Histological analysis and immunofluorescence assay

Six months after the surgery, HE staining, Bidschowsky's silver staining, Masson staining, Nissl staining, and Luxol Fast Blue (LFB) staining were used according to the manufacturer's instructions to detect cerebral cortex repair in canine brain tissue ($n = 5$ for each group) (Jiang et al., 2020; Zhu et al., 2020; Jiang et al., 2021; Zhu et al., 2022). Nissl staining using toluidine blue staining was performed to observe the distribution of dead neurons. Briefly, paraffin sections (5 μM) were prepared, dehydrated with gradient alcohol staining with toluidine blue solution, and washed with distilled water. Glacial acetic acid staining was performed on the sections. LFB, the sections were dewaxed and placed in ethanol, and following stain-filtered LFB for 2–4 h at 60°C, they were placed in ethanol, distilled water, and lithium carbonate solutions in turn. After silver staining, first, the sections were dewaxed, dehydrated in ethanol, and then placed in silver nitrate solution at 37°C for 30 min in the dark. After washing in distilled water and placing in formaldehyde solution, the slices were dehydrated and dewed with xylene. Masson staining was performed to observe glial fiber growth. The paraffin sections were dewaxed and dehydrated in descending concentrations of ethanol and then washed in leak warm running top water for 3 min. After staining in hematoxylin and rinsing with distilled water, they were placed in aniline blue dye and glacial acetic acid solution after freshly filtered phosphomolybdic acid was added. Immunofluorescence staining was based on previous reports ($n = 5$ for each group) (Jiang et al., 2020, 2021). First, after dewaxing the paraffin slices, EDTA buffer was used for antigen repair of cerebral cortex sections. Slices were then incubated with brine serum albumin (BSA (Abcam)) for 30 min to send the serum. Second, slices were incubated in a wet box overnight at 4°C with the following primary antibodies: MBP: rat anti, 1:1,000, Abcam, Cambridge, UK; NEFM: rabbit anti, 1:1,000, Proteintech, Unitad States; Syn: rabbit anti, 1:1,000, Bioss, Beijing, China; MAP-2: chicken anti, 1:1,000, Abcam, Cambridge, UK; GAP-43: chicken anti, 1:1,000, Abcam, Cambridge, UK; PSD95: rabbit anti, 1:1,000, Abcam, Cambridge, UK; Tuj-1: rabbit anti, 1:1,000, Abcam, Cambridge, UK; vWF: rabbit anti, 1:1,000, Abcam, Cambridge, UK). Secondary antibodies were added after removal of the primary antibody. They were incubated in the dark for 50 min at room temperature. Then, DAPI staining was performed and incubated at room temperature for 10 min. The slices were sealed, and the images were observed and collected through a fluorescence microscope. TUNEL staining (Promega Corporation) was performed to assess the apoptosis rate of cells in the area of TBI at 6 months after TBI according to a previous study (Zhang et al., 2021) ($n = 5$ for each group).

Enzyme-linked immunosorbent assay

ELISA (Wuhan Servicebio Technology Co., Ltd., China) was performed to analyse the relative levels of TNF-α, IL-6, and IL-10 in canine serum at the acute (1 week) and chronic stages (6 months) following the manufacturer's instructions ($n = 5$ for each group). Briefly, the samples were plotted in 24-well plates and incubated with biotinylated antibodies and termination solution analysed by ELISA.

Statistical analysis

Quantitative data in this study, from at least three biological replicates, were expressed as the mean ± standard deviation (SD). One-way ANOVA followed by connections was used to compare differences among multiple groups. Analysis was carried out with GraphPad 8.0 software. A $p < 0.05$ was considered statistically significant.

Results

Fabrication, mechanical property and degradation test of 3D-CS-bFGF-ST

Under a phase-contrast microscope, we observed a fibroblast similar to HUCMSCs (Figure 1A), and immunofluorescence staining identified HUCMSCs that strongly expressed CD90 and CD105 in our study (Figure 1B,B1). A porous

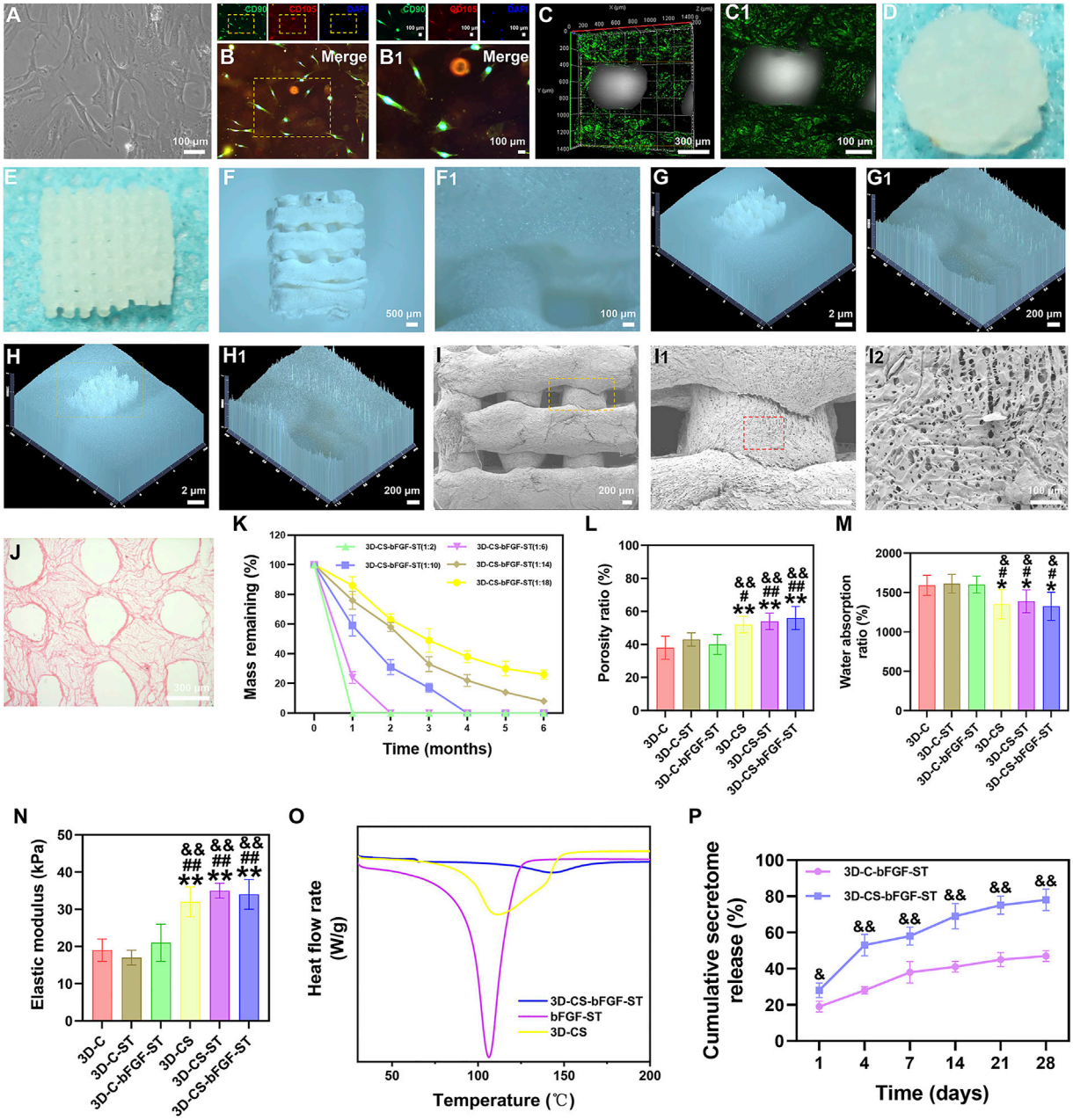

FIGURE 1
(A) HUCMSCs morphology under phase contrast microscopy. **(B–B1)** Expression of CD90 (green) and CD105 (red) in HUCMSCs under immunofluorescence. **(C–J)** Representative morphology of 3D-CS-bFGF-ST by using CLSM **(C–C1)**, digital camera **(D–E)** and stereomicroscope **(F–H1)**, SEM **(I–I2)**, and HE staining **(J)**. **(K)** The degradation test of 3D-CS-bFGF-ST. **(L–N)** Mechanical behavior of six kinds of scaffolds. The porosity ratio **(L)**, water absorption ratio **(M)**, and lastic modulus **(N)** of the six kinds of scaffolds. **(O)** DSC curves of 3D-CS, bFGF-ST and 3D-CS-bFGF-ST. **(P)** Cumulative secretome release of 3D-CS-bFGF-ST. $^{*}p < 0.05$, $^{**}p < 0.01$ vs. 3D-C. $^{\#}p < 0.05$, $^{\#\#}p < 0.01$ vs. 3D-C-ST. $^{\&}p < 0.05$, $^{\&\&}p < 0.01$ vs. 3D-C-bFGF-ST.

construct with multiple layers in a tailored size was printed using a 3D bioprinter. The surface and micromorphology of 3D-CS-bFGF-ST were obtained by using CLSM, digital camera and stereomicroscope (SZX16, Olympus), SEM, and HE staining (Figures 1C–J).

The degradation of the 3D-CS-bFGF-ST-based performance with collagen and silk fibroin was tested (Figure 1K). At one month after transplantation, 3D-CS-bFGF-ST with a mass ratio of 1:2 were totally degraded (Figure 1K). Along with the decrease in the mass ratio of collagen/silk fibroin, the degradation rate of

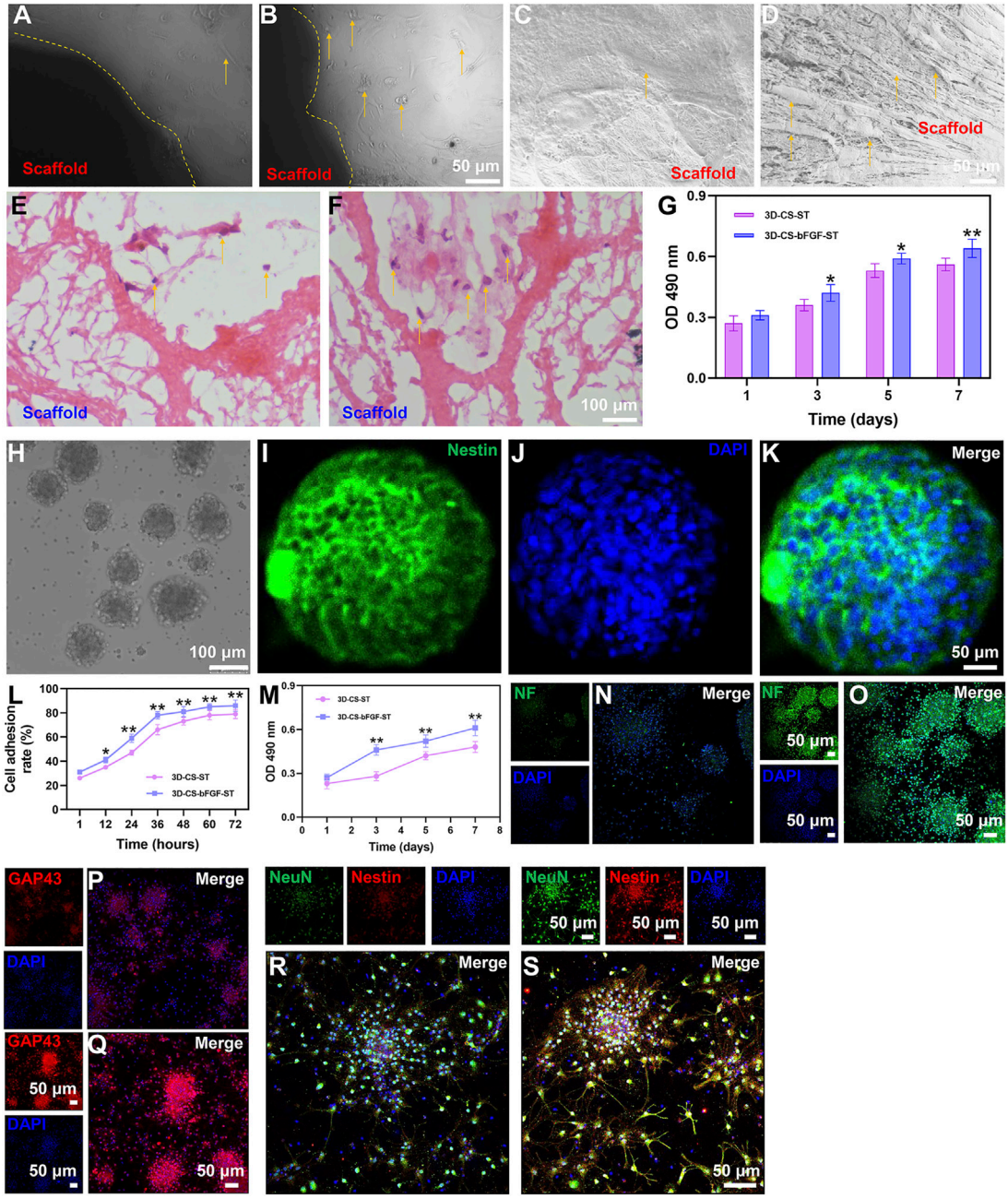

FIGURE 2
Typical morphology of cocultures of the two kinds of scaffolds (3D-CS-ST **(A,C,E)** or 3D-CS-bFGF-ST **(B,D,F)** and HUCMSCs under phase-contrast microscopy, SEM and HE staining. **(G)** MTT results of cocultures of the two kinds of scaffolds and HUCMSCs. **(H)** Typical morphology under an inverted fluorescence microscope. **(I–K)** Identification of NSCs by Nestin staining. **(L)** Cell adhesion rate of the 3D-CS-ST group and the 3D-CS-bFGF-ST group. **(M)** MTT results of cocultures of the two kinds of scaffolds and NSCs. (N–S) Expression of NF **(N–O)**, GAP43 **(P–Q)**, and NeuN **(R–S)** in NSCs after coculture. *$p < 0.05$, **$p < 0.01$ vs. 3D-CS-ST.

3D-CS-bFGF-ST increased. Approximately 74% of 3D-CS-bFGF-ST with a mass ratio of 1:18 had been degraded at half a year after transplantation (Figure 1K). Approximately 69% of 3D-CS-bFGF-ST with a mass ratio of 1:10 was degraded from the time of transplantation to 2 months after transplantation, and approximately 17% of the mass was retained at 3 months after transplantation, which indicated that 3D-CS-bFGF-ST with a mass ratio of 1:10 was a suitable mass ratio among the different scaffolds (Figure 1K). Subsequent experiments in this study selected 3D-CS-bFGF-ST with a mass ratio of 1:10.

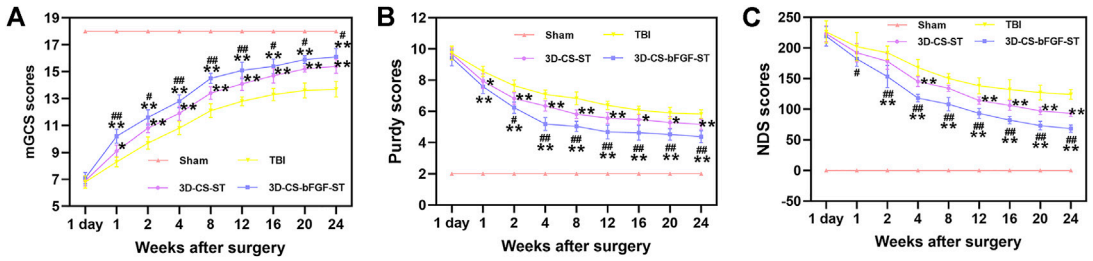

FIGURE 3
mGCS score **(A)**, Purdy score **(B)** and NDS score **(C)** of the four groups. *$p < 0.05$, **$p < 0.01$ vs. TBI. $^{\#}p < 0.05$, $^{\#\#}p < 0.01$ vs. 3D-CS-ST.

We focused on differences across the entire 3D-printed scaffold among the six groups in terms of the porosity ratio, the water absorption ratio, and the elastic modulus. Compared to 3D-C, 3D-C-ST and 3D-C-bFGF-ST, a significant increase in the porosity ratio of 3D-CS, 3D-CS-ST and 3D-CS-bFGF-ST was observed, leading to an improvement in the diffusion of nutrients as well as tissue formation ($p < 0.05$) (Figure 1L). The water absorption ratios of 3D-CS, 3D-CS-ST and 3D-CS-bFGF-ST were significantly lower than those of 3D-C, 3D-C-ST and 3D-C-bFGF-ST ($p < 0.05$) (Figure 1M). A significant increase was also observed in the elastic modulus of 3D-CS, 3D-CS-ST and 3D-CS-bFGF-ST compared with 3D-C, 3D-C-ST and 3D-C-bFGF-ST ($p < 0.01$) (Figure 1N). To further demonstrate the stability of ST, which was caused by temperature value. The Tm value of 3D-CS-bFGF-ST was significantly higher than that of bFGF-ST (Figure 1O). It should be noted that the higher the value temperature is, the better the stability. Therefore, the DSC results indicate that the combination of 3D-CS-bFGF-ST and bFGF-ST could increase the stability of bFGF-ST. We observed a significant increase in the cumulative secretome release of bFGF-ST in the 3D-CS-bFGF-ST group compared with the 3D-C-bFGF-ST group at each point (days 1, 4, 7, 14, 21, 28), indicating that the addition of silk fibroin could promote the fixation and absorption of ST to this scaffold (Figure 1P).

Influence of 3D-CS-bFGF-ST on stem cells proliferation and differentiation

3D-CS-bFGF-ST and 3D-CS-ST were examined with phase-contrast microscopy, SEM and HE staining. The 3D-CS-based scaffolds were divided into 2 different groups and then cultured for 1, 3, 5, and 7 days. On the seventh day after coculture, the results of phase-contrast microscopy, SEM and HE staining indicated that the number of HUCMSCs in the 3D-CS-bFGF-ST group was significantly higher than that in the 3D-CS-ST group (Figures 2A–F). For the results of MTT, although the significant differences did not differ between the two groups (3D-CS-ST and 3D-CS-bFGF-ST) at day 1, a larger number of cells was seen in the 3D-CS-bFGF-ST group compared to the 3D-CS-ST group at days 3, 5, and 7 ($p < 0.05$) (Figure 2G). These results suggested that the addition of ST pretreated with bFGF to 3D-printed collagen/silk fibroin scaffolds could further increase cell proliferation.

NSCs in this study exhibited typical NSCs spheroid morphology under an inverted fluorescence microscope (Figure 2H). Identification of NSCs was performed by Nestin staining (Figures 2I–K). The typical morphology of immunofluorescent staining of NSCs after 7 days of coculture with both scaffolds was shown. Next, significant differences in NSCs adhesion and proliferation were also determined. MTT indicated that the cell adhesion rate increased over time (Figure 2L). A higher level of adhesion on 3D-CS-bFGF-ST was shown compared to the 3D-CS-ST group (Figure 2L). The absorption at 490 nm was in accordance with the NSCs viability of the 3D-CS-bFGF-ST group and the 3D-CS-ST group, and good cell growth was observed in both groups (Figure 2M). The proliferation of NSCs showed a dissimilar growth trend between these two scaffolds. The cell viability in the 3D-CS-bFGF-ST group remained at a relatively slow growth rate from day 3 to day 5 but greatly increased from day 1 to day 3. The cell viability in the 3D-CS-ST group grew slowly from day 1 to day 3 and from day 5 to day 7, but it grew at a high speed from day 3 to day 5. From the first day, we did not observe any significant difference in cell growth, while significant differences between these two scaffolds were observed on days 3, 5, and 7.3D-CS-bFGF-ST had a higher optical density (OD) value than 3D-CS-ST on days 3, 5, and 7 ($p < 0.01$) (Fig. 2M). Compared to the 3D-CS-ST group, the 3D-CS-bFGF-ST group showed stronger expression of NF, GAP43, and NeuN, which suggested that 3D-CS-bFGF-ST could promote axonal growth and facilitate the formation of mature neurons (Figure 2P–S).

3D-CS-bFGF-ST ameliorated functional scores after TBI

Neurological deficits post TBI were evaluated with regard to the mGCS score, Purdy score, and NDS score, which indicated that 3D-

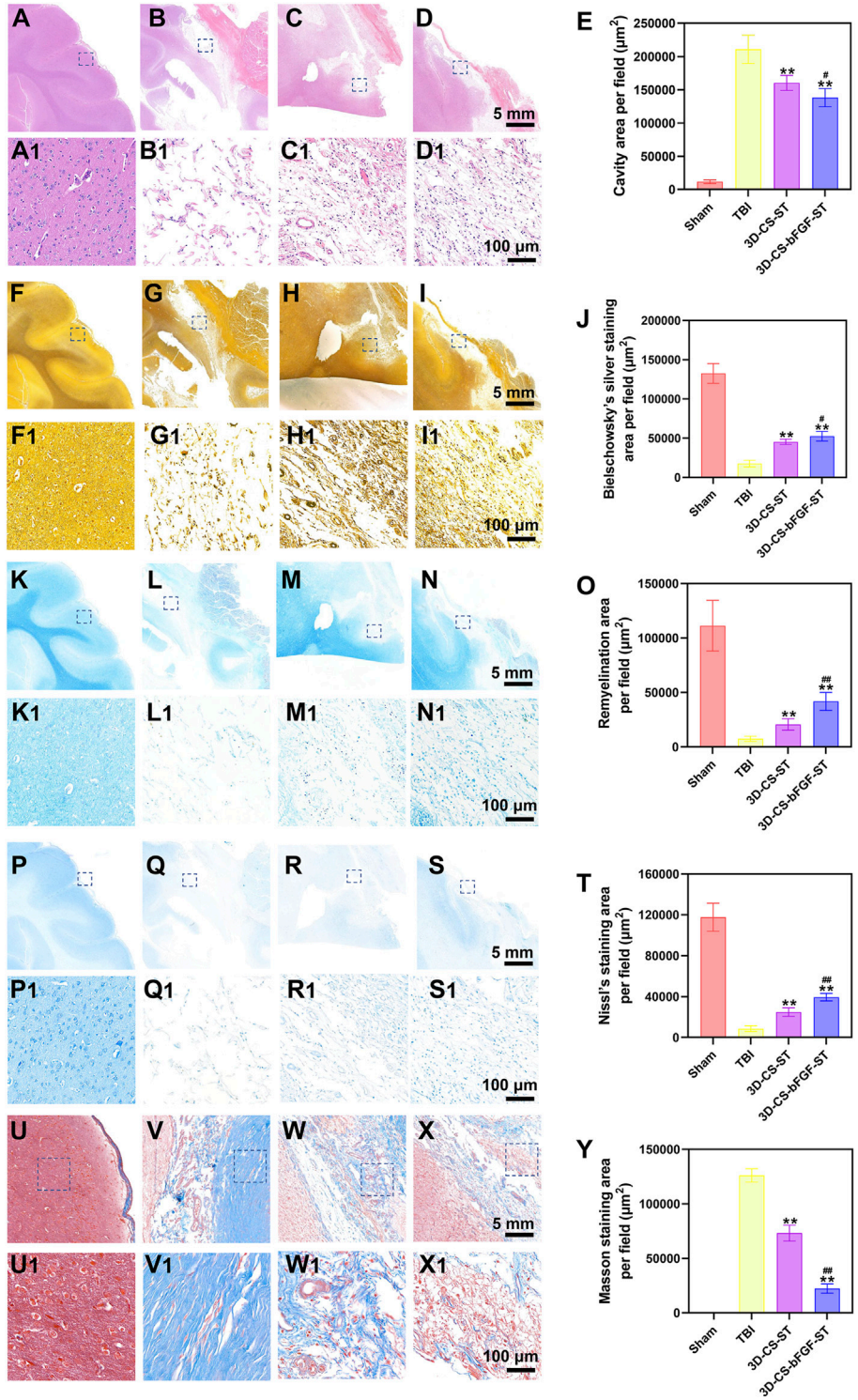

FIGURE 4
(A-E) Representative HE staining images **(A-D1)** in Sham group **(A** and **A1)**, TBI group **(B and B1)**, 3D-CS-ST group **(C and C1)**, and 3D-CS-bFGF-ST group **(D and D1)**, and their quantitative analysis **(E)**. **(F-J)** Representative Bielschowsky's silver staining images **(F-I1)** in Sham group **(F and F1)**, TBI group **(G and G1)**, 3D-CS-ST group **(H and H1)**, and 3D-CS-bFGF-ST group **(I and I1)**, and their quantitative analysis **(J)**. **(K-O)** Representative LFB staining images **(K-N1)** in Sham group **(K and K1)**, TBI group **(L and L1)**, 3D-CS-ST group **(M and M1)**, and 3D-CS-bFGF-ST group **(N and N1)**, and their quantitative analysis **(O)**. **(P-T)** Representative Nissl staining images **(P-S1)** in Sham group **(P and P1)**, TBI group **(Q and Q1)**, 3D-CS-ST group **(R and R1)**, and 3D-CS-bFGF-ST group **(S and S1)**, and their quantitative analysis **(T)**. **(U-Y)** Representative Masson staining images **(U-X1)** in Sham group **(U and U1)**, TBI group **(V and V1)**, 3D-CS-ST group **(W and W1)**, and 3D-CS-bFGF-ST group **(X and X1)**, and their quantitative analysis **(Y)**. **P < 0.01 vs TBI. #P < 0.05, ##P < 0.01 vs 3D-CS-ST.

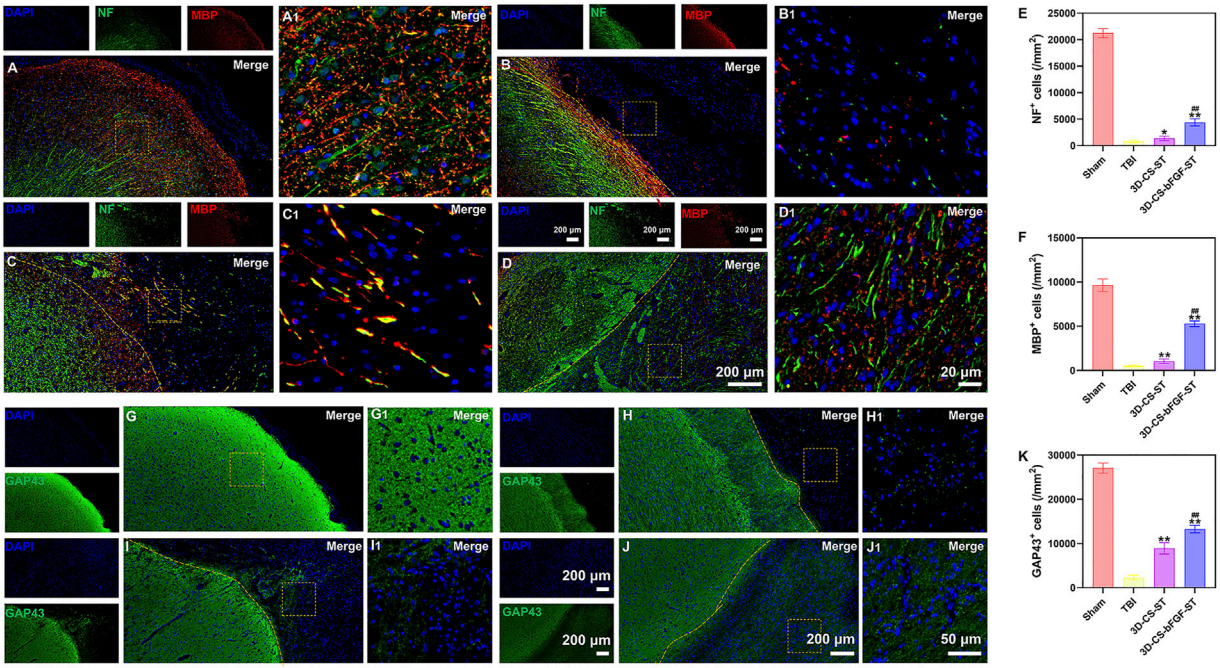

FIGURE 5
(A-D1) Typical picture of double-labelled immunofluorescence staining (NF (green) and MBP (red)) in Sham group **(A and A1)**, TBI group **(B and B1)**, 3D-CS-ST group **(C and C1)**, and 3D-CS-bFGF-ST group **(D and D1)**. **(E-F)** Quantitative analysis of NF and MBP. **(G-J1)** Typical immunofluorescence staining picture of GAP43 (green) in Sham group **(G and G1)**, TBI group **(H and H1)**, 3D-CS-ST group **(I and I1)**, and 3D-CS-bFGF-ST group **(J and J1)**. **(K)** Quantitative analysis of GAP43. *P < 0.05, **P < 0.01 vs TBI. ##P < 0.01 vs 3D-CS-ST.

CS-bFGF-ST could significantly increase the neurological score in TBI in a time-dependent manner than in the 3D-CS-ST group and the TBI group, excluding 1 day after transplantation (Figures 3A–C). A significantly higher mGCS score was found in the 3D-CS-bFGF-ST group compared to the 3D-CS-ST group and the TBI group ($p < 0.05$) (Figure 3A). The NDS score was significantly higher in the 3D-CS-bFGF-ST group than in the other two groups at each point after 2 weeks ($p < 0.05$) (Figure 3B). Significantly higher NDS scores were found in the 3D-CS-bFGF-ST group than in the TBI group and the 3D-CS-ST group ($p < 0.05$) (Figure 3C). All of these results indicate that at the same time postoperation (from 4 to 24 weeks), canines treated with 3D-CS-bFGF-ST exhibited beneficial recovery.

Implanting 3D-CS-bFGF-ST reduced the cavity area and glial scar and enhanced the formation of nerve fibers, myelin sheaths, and neurons in the TBI injury area

Histological evaluation of injured tissue was performed at 6 months after transplantation. HE staining revealed a large cavity area with a disordered structure in the TBI group (Figure 4A–D1). In contrast, a smaller cavity with a well-disordered structure was detected in the 3D-CS-bFGF-ST group and the 3D-CS-ST group (Figure 4A–D1). Compared with implantation of 3D-CS-ST, implantation of 3D-CS-bFGF-ST could significantly reduce the TBI cavity area (Figures 4A–E). In regard to Bielschowsky's silver staining, samples in the TBI-only group exhibited considerable vacuolar necrosis, without nerve fiber regeneration, while in the 3D-CS-bFGF-ST group and the 3D-CS-ST group, favorable synapse-like struck with regeneration of nerve fibers was displayed (Figures 4F–I). Larger Bielschowsky's silver staining was observed in the 3D-CS-bFGF-ST group than in the 3D-CS-ST group (Figures 4F–J). Few blue myelin sheaths were found around the damaged area by LFB staining in the TBI group, while a larger number of blue-stained myelin sheaths were found in the 3D-CS-bFGF-ST group and the 3D-CS-ST group (Figure 4K–N1). The remyelination area in the 3D-CS-bFGF-ST group was larger than that in the 3D-CS-ST group (Figure 4K–O). Nissl staining, a method for assessing the diversity of neurons that survive, was used to show the overall morphology of the injured brain in the chronic phase of TBI. An abundant loss of neurons occurred in the TBI group, while implantation of 3D-CS-bFGF-ST and 3D-CS-ST filled the cavity and prohibited neuron loss (Figure 4P–S1). Compared with implantation of 3D-CS-ST, implantation of 3D-CS-BFGF-ST could further increase the area of Nissl staining (Figure 4P–T). Masson staining showed

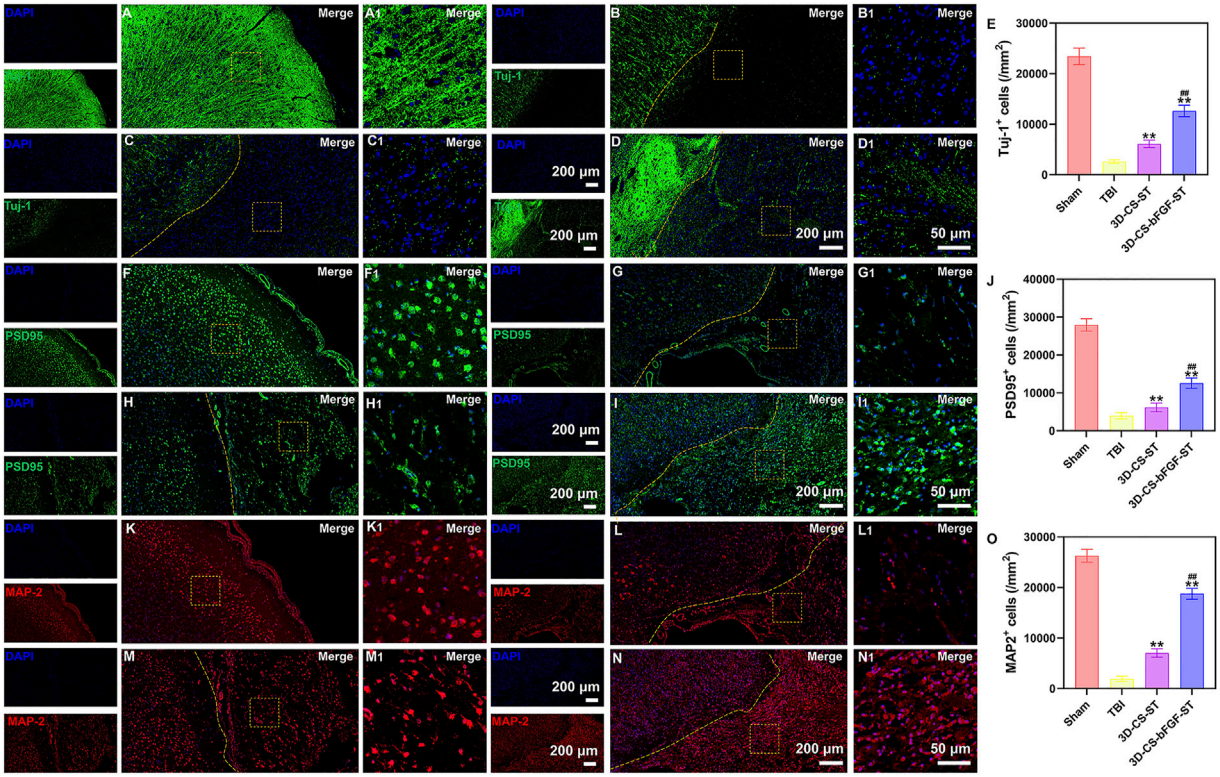

FIGURE 6
(A-D1) Typical immunofluorescence staining picture of Tuj-1 (green) in Sham group **(A and A1)**, TBI group **(B and B1)**, 3D-CS-ST group **(C and C1)**, and 3D-CS-bFGF-ST group **(D and D1)**. **(E)** Quantitative analysis of Tuj-1. **(F-I1)** Typical immunofluorescence staining picture of PSD95 (green) in Sham group **(F and F1)**, TBI group **(G and G1)**, 3D-CS-ST group **(H and H1)**, and 3D-CS-bFGF-ST group **(I and I1)**. **(J)** Quantitative analysis of Tuj-1. **(K-N)** Typical immunofluorescence staining picture of MAP-2 (red) in Sham group **(K and K1)**, TBI group **(L and L1)**, 3D-CS-ST group **(M and M1)**, and 3D-CS-bFGF-ST group **(N and N1)**. **(O)** Quantitative analysis of MAP-2. **P < 0.01 vs TBI. ##P < 0.01 vs 3D-CS-ST.

that compared with the TBI group, samples in the 3D-CS-bFGF-ST group and 3D-CS-ST group showed a significant decrease in glial fibers in the lesions (Figure 4U–X1). Notably, in regard to both treatment groups, the 3D-CS-bFGF-ST group displayed a more satisfactory outcome (Figure 4U–Y).

Implanting 3D-CS-bFGF-ST accelerated the regeneration of nerve fibers, myelin sheaths and axons *in vivo* after TBI

Double-labelled immunofluorescence staining (NF and MBP) was performed to determine neuronal regeneration in the peri-injured tissue after TBI, and the number of immunofluorescence-positive cells was counted. The 3D-CS-bFGF-ST group displayed more NF- and MBP- positive cells than the other two groups (the TBI group and the 3D-CS-ST group), which supported that local transplantation could facilitate the regeneration of nerve fibers and myelin to some degree (Figures 5A–F). In addition, compared to the 3D-CS-ST group, the regeneration-promoting effects of 3D-CS-bFGF-ST were more obvious (Figures 5A–F). Similar results were also found for the expression of GAP43, which regulates synaptic plasticity and axonal regeneration, and this effect was most obvious in the 3D-CS-bFGF-ST group among the three injury groups (Figures 5G–K).

Implanting 3D-CS-bFGF-ST improved neuron and synapse formation after TBI

Compared with the TBI group and the 3D-CS-ST group, the expression of Tuj-1 (a marker of neuronal differentiation) in the 3D-CS-bFGF-ST group had significantly more positive cells per unit area (Figures 6A–E). The levels of PSD95, a marker for synapse formation, were significantly higher in cells in the 3D-CS-bFGF-ST group and the 3D-CS-ST group (Figures 6F–J). In contrast, few cells in the TBI group exhibited synaptic transmission (Figures 6F–J). More PSD95-positive cells were observed in the 3D-CS-bFGF-ST group than in the 3D-CS-ST group (Figures 6F–J). MAP-2 plays

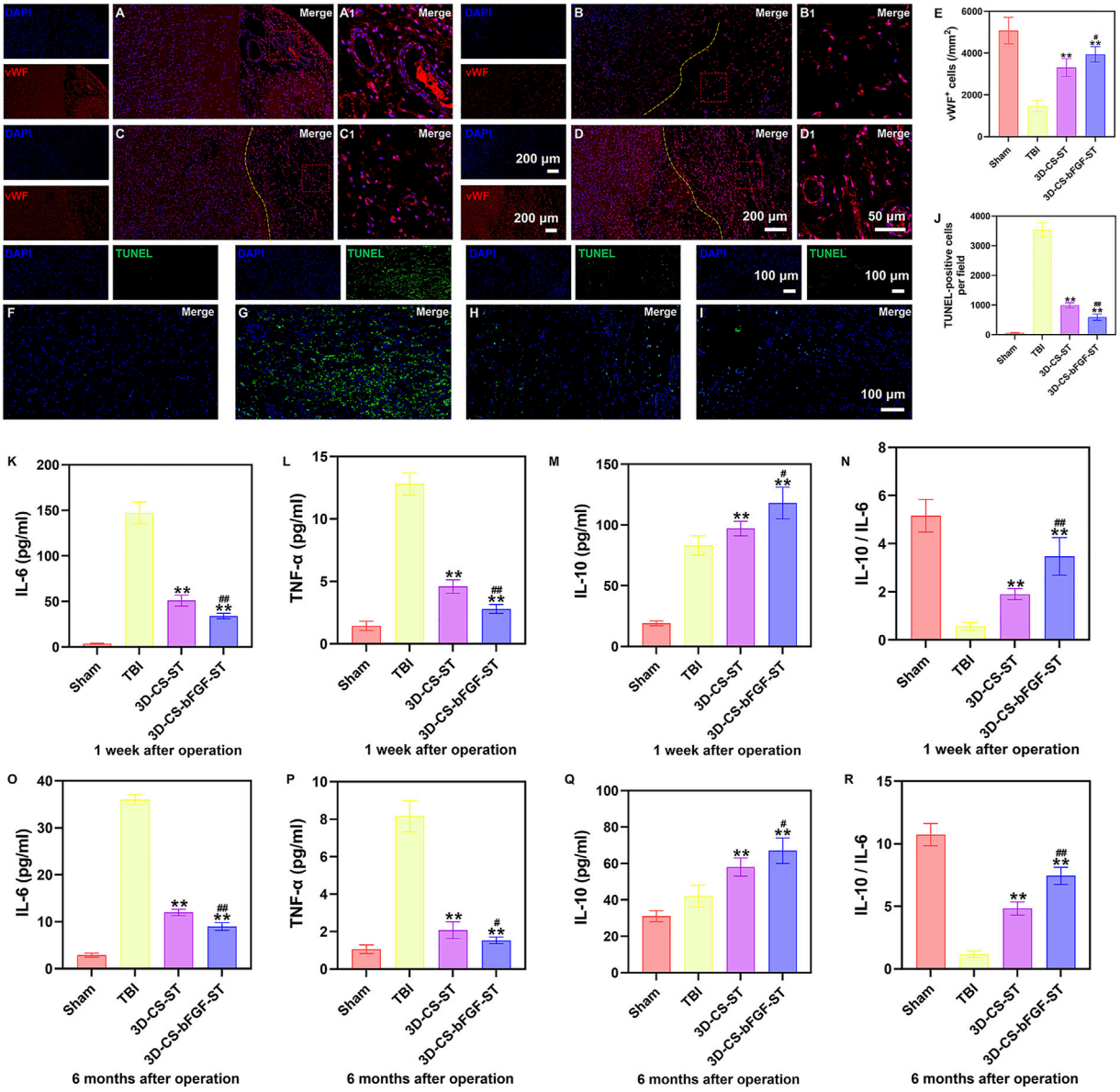

FIGURE 7
(A-D1) Typical immunofluorescence staining picture of vWF (red) in Sham group **(A and A1)**, TBI group **(B and B1)**, 3D-CS-ST group **(C and C1)**, and 3D-CS-bFGF-ST group **(D and D1)**. **(E)** Quantitative analysis of MAP-2. **(F-I)** Typical TUNEL (green) staining picture. **(J)** Quantitative analysis of TUNEL in Sham group **(F)**, TBI group **(G)**, 3D-CS-ST group **(H)**, and 3D-CS-bFGF-ST group **(I)**. **(K-N)** The expression of IL-6 **(K)**, TNF-α **(L)**, IL-10**(M)**, and IL-10/IL-6 **(N)** at 1 week after TBI. **(O-R)** The expression of IL-6 **(O)**, TNF-α **(P)**, IL-10 **(Q)**, and IL-10/IL-6 **(R)** at 6 months after TBI. **P < 0.01 vs TBI. #P < 0.05, ##P < 0.01 vs 3D-CS-ST.

important roles in neurogenesis, including stabilizing microtubules, and determining and stabilizing dendritic shape during neuronal development. The number of MAP-2 positive cells in the 3D-CS-bFGF-ST group and the 3D-CS-ST group was significantly higher than that in the TBI group (Figure 6K–O). Treatment with 3D-CS-bFGF-ST conferred a better outcome than treatment with 3D-CS-ST (Figure 6K–O).

Implanting 3D-CS-bFGF-ST could enhance angiogenesis, reduce cell apoptosis and modulate inflammatory levels after TBI

In the 3D-CS-bFGF-ST and 3D-CS-ST groups, a larger number of vWF (a marker for vessel formation)-positive cells

were captured in the perilesional area, especially in the 3D-CS-bFGF-ST group (Figures 7A–E). TUNEL staining was used to determine neuronal apoptosis in the preinjured brain. A large number of TUNEL-positive cells were found around the lesion site. Significant differences were detected between the TBI group and the 3D-CS-bFGF-ST and 3D-CS-ST groups, which indicated that treatment with 3D-CS-bFGF-ST and 3D-CS-ST could reduce cell apoptosis (Figures 7F–J). Fewer TUNEL-positive cells were found in the 3D-CS-bFGF-ST group than in the 3D-CS-ST group (Figures 7F–J). The expression of IL-6, TNF-α, and IL-10 was detected by ELISA at 1 week and 6 months after TBI. Lower IL-6 and TNF-α expression levels, higher IL-10 expression levels and higher IL-10 to IL-6 ratios were observed in the 3D-CS-bFGF-ST group than in the TBI group and 3D-CS-ST at both the chronic and acute stages, which indicated that implanting 3D-CS-bFGF-ST could modulate the level of inflammation after TBI (Figure 7K–R).

Discussion

The brain shows a limited repair ability after injury due to the lack of neural regeneration and vascularization. Stem cells are usually isolated from embryonic cells in the blastocyst or from adult tissues, with the capability of self-renewal and differentiation toward a diversity of cell types (Clevers et al., 2014; Jayarajan and Milsom, 2020). It is commonly accessible to ST from stem cells as a priority in tissue regeneration. However, how modifications assist ST in some aspects of regeneration remains disputed. bFGF is capable of witnessing neurite outgrowth (Mie et al., 2014), and its stimulation of the ST may be an appropriate cue for tissue engineering. HUCMSC-derived ST incorporated in the scaffold by transplantation into canines has been examined, but no method has yet been developed to study 3D-CS with secretome derived from HUCMSCs pretreated with bFGF *in vitro* and *in vivo*. Thus, the current study using the 3D-printed scaffold incorporating HUCMSC-ST pretreated with bFGF supported the increased benefit of this complexes.

Neuro regeneration scaffolds have attracted significant attention for improving the virtuously desirable features. Currently, for example, the collagen or silk fibroin scaffold, a type of naturally biodegradable and biocompatible polymeter, has been used in a wide range of tissue engineering applications owing to its high affinity for adherent cells (Chlapanidas et al., 2013; Kundu et al., 2013; Liu et al., 2017). Collagen appeared as an alternative to the extracellular matrix due to its most abundant, firm, fibrous, and structural protein, but its application was limited due to its poor mechanical strength and thermostability (Liu et al., 2019). Silk fibroin is extensively used to produce composite scaffolds, mainly consisting of core filament protein, which can compensate for mechanical strength and extensibility/toughness by the crystalline heavy chains and amorphous light chains (Kundu et al., 2013; Koh et al., 2015). Therefore, collagen or silk fibroin blending served as a promising candidate for improving biological and physical characteristics because of its impressive mechanical properties and its excellent cell proliferation, differentiation and matrix deposition (Ghezzi et al., 2011). The scaffold fabrication could be attributed to the 3D printing technology, but it is still challenging in porosity, water absorption and elastic modulus, and the most importantly, the suitable behavior for even distribution for bFGF-ST loading. Hence, this study developed a novel strategy using ice-templated assembly and temperature gradient-guided thermally induced phase separation.

Moreover, we identified that bFGF pretreated ST in the scaffold and regulated neuronal induction at the injury site. In general, the degradation of the fabricated scaffolds was estimated by implanting the scaffolds *in vivo* with their remaining degradation products, and desirable degradation could be obtained by modifying the mass ratio of collagen/silk fibroin. 3D-CS-bFGF-ST exhibited good mechanical strength, which is an important factor affecting cell survival, neuronal differentiation, and axon formation. Studies on the regeneration potential effects of bFGF on the neuro-regeneration of HUCMSCs or ST derived from HUCMSCs have been carried out with tissue places or 3D environments in previous research. A satisfying porous structure was observed in 3D-CS-bFGF-ST, which indirectly affects the swelling ratio, indicating the transfer of waste and nutrition in and out of the scaffold (Chowdhury et al., 2018).

We compared the influence of ST and bFGF-ST in HUCMSCs or NSCs seeded on 3D-CS scaffolds. SEM and HE assays demonstrated that our scaffold had the capability for cell adhesion and proliferation. Figure 2 revealed that there was a significant difference in the cell viability of HUCMSC-ST based on the MTT test between the 3D-CS-ST group and the 3D-CS-bFGF-ST group. In the current study, significant differences in HUCMSCs and NSCs proliferation were observed between the 3D-CS-ST group and the 3D-CS-bFGF-ST group, suggesting the superiority of bFGF. In addition, to determine whether HUCMSC-ST pretreated with bFGF also have a profound influence on the differentiation of NSCs, the relative expression, including the expression of NF, GAP43 and NeuN, was determined after 7 days of coculture. The results of confocal microscopy revealed that 3D-CS-bFGF-ST had a high synergistic differentiation property and had the potential to provide a permanent microenvironment for cell–cell communication and NSCs spreading and differentiation.

Since the complexes had good biocompatibility *in vitro*, we utilized a canine-based TBI model to explore the change in

functional recovery and neural regeneration. On the one hand, similar neuropathological changes and cerebrovascular abnormalities, such as neuronal loss, impaired neurogenesis, and cognitive decline, have been observed in both humans and canines (Giaccone et al., 1990; Uchida et al., 1990; Ellis et al., 1996; Borràs et al., 1999; Attems, 2005; Pekcec et al., 2008). To determine neurological function, we used a series of motor assays. Satisfactory locomotor recovery in TBI canines treated with 3D-CS-bFGF-induced ST was observed not only in the acute stage but also in the chronic stage.

In regard to vivo, bFGF-pretreated stem cell-based therapies for 3D-CS scaffolds represent a promising strategy for brain tissue regeneration through comprehensive regulation of the pathologically hostile microenvironment based on histological analysis. From that, we could observe the orderly arrangement with nerve regeneration in the presence of 3D-CS-bFGF-ST. In addition, we established the simultaneous effect of bFGF-ST in cell-seeded 3D-CS-bFGF-ST on increased cell regeneration by immunofluorescence; positive markers, such as NF, GAP43 and NeuN, were increased, which promoted the formation of nerve fibers, axons and mature neurons and thereby protected against cell death after injury (Choi et al., 2012). In addition, by quantitatively measuring cell proliferation and differentiation during culture in the complexes of the two types, we found that the value of the MMT assay was significantly higher in the 3D-CS-bFGF-ST group than in the 3D-CS-ST group; consistent with our results, these findings suggested that a structurally biomimetic 3D neuronal network *in vivo* was constructed fortunately that led to numerous neurons with functional connections between them. Furthermore, sufficient vascularization remains a major problem, affecting the viability of the scaffold in the long term. A higher level of vWF expression in the injured site was observed in the 3D-CS-bFGF-ST group than in the 3D-CS-ST group.

The balance between anti-inflammatory and proinflammatory cytokines might trigger secondary injury after TBI(Dekmak et al., 2018). Many studies have shown that TNF-α and IL-6 contribute to the pathogenesis and exacerbate traumatic-induced brain damage. Our data suggested that 3D-CS-bFGF-ST could inhibit the expression of TNF-α and IL-6 while increasing IL-10 protein content in the surroundings of the injured area compared with the TBI group. The 3D-CS-bFGF-ST treatment suppressed acute and chronic inflammation in the canine model.

Conclusion

In this study, the 3D-CS-based scaffold focused on the merits of blending collagen or silk fibroin. Additionally, to our knowledge, there are no published studies, indicating the effect of a combination of collagen/silk fibroin and the secretome derived from HUCMSCs pretreated with bFGF. Our study indicated the safety and efficacy profile of these complexes under manufacturing and quality control. HUCMSC-derived ST pretreated with bFGF as a substitute for cell therapy makes the clinical application of HUCMSCs possible. Implanting 3D-CS-bFGF-ST reduced the cavity area and glial scar, and enhanced the formation of nerve fibers, myelin sheaths, synapses and neurons in the TBI injury area. Furthermore, implanting 3D-CS-bFGF-ST could enhance angiogenesis, reduce cell apoptosis and modulate inflammatory levels after TBI. In future studies, more investigations are needed to provide evidence on the safety and efficacy of 3D-CS-bFGF-ST in the treatment of TBI.

Data availability statement

The original contributions presented in the study are included in the article/supplementary materials, further inquiries can be directed to the corresponding authors.

Ethics statement

The animal study was reviewed and approved by and the guidance of institutional and NIH guidelines for the care and use of research animals (approval number: SYXK (JII) 2018-017).

Author contributions

Experiment design: XL, GZ, PW, JZ, RT, and LiaZ. Experiment implementation: XL, GZ, PW, LH, LinZ, KZ, CL, PL, QF, SW, JZ, RT, and LiaZ. Data analysis: XL, GZ, PW, JZ, RT, and LiaZ. Material contribution and equipment coordination: JZ, RT, and LiaZ. Paper write: XL, GZ, and PW.

Funding

This work was supported by the National Major Scientific and Technological Special Project for Significant New Drugs Development (2015ZX09102010), National Key R&D Program of China (2018YFA0108603), and National Key R&D Program of China (2018YFA0108604).

Conflict of interest

The authors declare that the research was conducted in the absence of any commercial or financial relationships that could be construed as a potential conflict of interest.

Publisher's note

References

Alexis, I. M., Saurabha, B., and Ross, Z. (2015). Rehabilitation after traumatic brain injury. *Handb. Clin. Neurol.* 127, 411–422. doi:10.1016/B978-0-444-52892-6.00026-X

Attems, J. (2005). Sporadic cerebral amyloid angiopathy: Pathology, clinical implications, and possible pathomechanisms. *Acta Neuropathol.* 110, 345–359. doi:10.1007/s00401-005-1074-9

Bae, M., Hwang, D. W., Ko, M. K., Jin, Y., Shin, W. J., Park, W., et al. (2021). Neural stem cell delivery using brain-derived tissue-specific bioink for recovering from traumatic brain injury. *Biofabrication* 13, 044110. doi:10.1088/1758-5090/ac293f

Beer, L., Mildner, M., and Ankersmit, H. J. (2017). Cell secretome based drug substances in regenerative medicine: When regulatory affairs meet basic science. *Ann. Transl. Med.* 5, 170. doi:10.21037/atm.2017.03.50

Bongso, A., and Fong, C. Y. (2013). The therapeutic potential, challenges and future clinical directions of stem cells from the Wharton's jelly of the human umbilical cord. *Stem Cell Rev. Rep.* 9, 226–240. doi:10.1007/s12015-012-9418-z

Bonsack, B., Corey, S., Shear, A., Heyck, M., Cozene, B., Sadanandan, N., et al. (2020). Mesenchymal stem cell therapy alleviates the neuroinflammation associated with acquired brain injury. *CNS Neurosci. Ther.* 26, 603–615. doi:10.1111/cns.13378

Borràs, D., Ferrer, I., and Pumarola, M. (1999). Age-related changes in the brain of the dog. *Vet. Pathol.* 36, 202–211. doi:10.1354/vp.36-3-202

Castellá, M., Buckberg, G. D., and Tan, Z. (2005). Neurologic preservation by Na+-H+ exchange inhibition prior to 90 minutes of hypothermic circulatory arrest. *Ann. Thorac. Surg.* 79, 646–654. doi:10.1016/j.athoracsur.2004.07.007

Chlapanidas, T., Tosca, M. C., Faragò, S., Perteghella, S., Galuzzi, M., Lucconi, G., et al. (2013). Formulation and characterization of silk fibroin films as a scaffold for adipose-derived stem cells in skin tissue engineering. *Int. J. Immunopathol. Pharmacol.* 26, 43–49. doi:10.1177/03946320130260S106

Choi, D. H., Lee, K. H., Kim, J. H., Kim, M. Y., Lim, J. H., and Lee, J. (2012). Effect of 710 nm visible light irradiation on neurite outgrowth in primary rat cortical neurons following ischemic insult. *Biochem. biophysical Res. Commun.* 422, 274–279. doi:10.1016/j.bbrc.2012.04.147

Chowdhury, S. R., Mh Busra, M. F., Lokanathan, Y., Ng, M. H., Law, J. X., Cletus, U. C., et al. (2018). Collagen type I: A versatile biomaterial. *Adv. Exp. Med. Biol.* 1077, 389–414. doi:10.1007/978-981-13-0947-2_21

Clevers, H., Loh, K. M., and Nusse, R. (2014). Stem cell signaling. An integral program for tissue renewal and regeneration: Wnt signaling and stem cell control. *Sci. (New York, N.Y.)* 346, 1248012. doi:10.1126/science.1248012

de Rivero Vaccari, J. P., Brand, F., 3rd, Adamczak, S., Lee, S. W., Perez-Barcena, J., Wang, M. Y., et al. (2016). Exosome-mediated inflammasome signaling after central nervous system injury. *J. Neurochem.* 136 (1), 39–48. doi:10.1111/jnc.13036

Dekmak, A., Mantash, S., Shaito, A., Toutonji, A., Ramadan, N., Ghazale, H., et al. (2018). Stem cells and combination therapy for the treatment of traumatic brain injury. *Behav. Brain Res.* 340, 49–62. doi:10.1016/j.bbr.2016.12.039

Ellis, R. J., Olichney, J. M., Thal, L. J., Mirra, S. S., Morris, J. C., Beekly, D., et al. (1996). Cerebral amyloid angiopathy in the brains of patients with alzheimer's disease: The CERAD experience, Part XV. *Neurology* 46, 1592–1596. doi:10.1212/wnl.46.6.1592

Ghezzi, C. E., Marelli, B., Muja, N., Hirota, N., Martin, J. G., Barralet, J. E., et al. (2011). Mesenchymal stem cell-seeded multilayered dense collagen-silk fibroin hybrid for tissue engineering applications. *Biotechnol. J.* 6, 1198–1207. doi:10.1002/biot.201100127

Giaccone, G., Verga, L., Finazzi, M., Pollo, B., Tagliavini, F., Frangione, B., et al. (1990). Cerebral preamyloid deposits and congophilic angiopathy in aged dogs. *Neurosci. Lett.* 114, 178–183. doi:10.1016/0304-3940(90)90068-k

Guan, P., Liu, C., Xie, D., Mao, S., Ji, Y., Lin, Y., et al. (2022). Exosome-loaded extracellular matrix-mimic hydrogel with anti-inflammatory property Facilitates/promotes growth plate injury repair. *Bioact. Mater.* 10, 145–158. doi:10.1016/j.bioactmat.2021.09.010

Han, D., Wu, C., Xiong, Q., Zhou, L., and Tian, Y. (2015). Anti-inflammatory mechanism of bone marrow mesenchymal stem cell transplantation in rat model of spinal cord injury. *Cell biochem. Biophys.* 71, 1341–1347. doi:10.1007/s12013-014-0354-1

Han, F., Bi, J., Qiao, L., and Arancio, O. (2020). Stem cell therapy for alzheimer's disease. *Adv. Exp. Med. Biol.* 1266, 39–55. doi:10.1007/978-981-15-4370-8_4

Hao, Y., Ran, Y., Lu, B., Li, J., Zhang, J., Feng, C., et al. (2018). Therapeutic effects of human umbilical cord-derived mesenchymal stem cells on canine radiation-induced lung injury. *Int. J. Radiat. Oncology*Biology*Physics* 102, 407–416. doi:10.1016/j.ijrobp.2018.05.068

Huang, P., Freeman, W. D., Edenfield, B. H., Brott, T. G., Meschia, J. F., and Zubair, A. C. (2019). Safety and efficacy of intraventricular delivery of bone marrow-derived mesenchymal stem cells in hemorrhagic stroke model. *Sci. Rep.* 9, 5674. doi:10.1038/s41598-019-42182-1

Jahanbazi Jahan-Abad, A., Sahab Negah, S., Hosseini Ravandi, H., Ghasemi, S., Borhani-Haghighi, M., Stummer, W., et al. (2018). Human neural stem/progenitor cells derived from epileptic human brain in a self-assembling peptide nanoscaffold improve traumatic brain injury in rats. *Mol. Neurobiol.* 55, 9122–9138. doi:10.1007/s12035-018-1050-8

Jayarajan, J., and Milsom, M. D. (2020). The role of the stem cell epigenome in normal aging and rejuvenative therapy. *Hum. Mol. Genet.* 29, R236–R247. doi:10.1093/hmg/ddaa167

Jiang, J., Dai, C., Liu, X., Dai, L., Li, R., Ma, K., et al. (2021). Implantation of regenerative complexes in traumatic brain injury canine models enhances the reconstruction of neural networks and motor function recovery. *Theranostics* 11, 768–788. doi:10.7150/thno.50540

Jiang, J., Dai, C., Niu, X., Sun, H., Cheng, S., Zhang, Z., et al. (2018). Establishment of a precise novel brain trauma model in a large animal based on injury of the cerebral motor cortex. *J. Neurosci. methods* 307, 95–105. doi:10.1016/j.jneumeth.2018.06.025

Jiang, J., Liu, X., Chen, H., Dai, C., Niu, X., Dai, L., et al. (2020). 3D printing collagen/heparin sulfate scaffolds boost neural network reconstruction and motor function recovery after traumatic brain injury in canine. *Biomater. Sci.* 8, 6362–6374. doi:10.1039/d0bm01116a

Jiang, J. P., Liu, X. Y., Zhao, F., Zhu, X., Li, X. Y., Niu, X. G., et al. (2020). Three-dimensional bioprinting collagen/silk fibroin scaffold combined with neural stem cells promotes nerve regeneration after spinal cord injury. *Neural Regen. Res.* 15, 959–968. doi:10.4103/1673-5374.268974

Kankala, R. K., Zhu, K., Li, J., Wang, C. S., Wang, S. B., and Chen, A. Z. (2017). Fabrication of arbitrary 3D components in cardiac surgery: From macro-micro- to nanoscale. *Biofabrication* 9, 032002. doi:10.1088/1758-5090/aa8113

Kawabori, M., Shichinohe, H., Kuroda, S., and Houkin, K. (2020). Clinical trials of stem cell therapy for cerebral ischemic stroke. *Int. J. Mol. Sci.* 21, 7380. doi:10.3390/ijms21197380

Koh, L. D., Cheng, Y., Teng, C. P., Khin, Y. W., Loh, X. J., Tee, S. Y., et al. (2015). Structures, mechanical properties and applications of silk fibroin materials. *Prog. Polym. Sci.* 46, 86–110. doi:10.1016/j.progpolymsci.2015.02.001

Kundu, B., Rajkhowa, R., Kundu, S. C., and Wang, X. (2013). Silk fibroin biomaterials for tissue regenerations. *Adv. drug Deliv. Rev.* 65, 457–470. doi:10.1016/j.addr.2012.09.043

Li, J., Zhang, D., Guo, S., Zhao, C., Wang, L., Ma, S., et al. (2021). Dual-enzymatically cross-linked gelatin hydrogel promotes neural differentiation and neurotrophin secretion of bone marrow-derived mesenchymal stem cells for treatment of moderate traumatic brain injury. *Int. J. Biol. Macromol.* 187, 200–213. doi:10.1016/j.ijbiomac.2021.07.111

Li, L., Zhang, Y., Mu, J., Chen, J., Zhang, C., Cao, H., et al. (2020). Transplantation of human mesenchymal stem-cell-derived exosomes immobilized in an adhesive hydrogel for effective treatment of spinal cord injury. *Nano Lett.* 20, 4298–4305. doi:10.1021/acs.nanolett.0c00929

Li, X., and Sundström, E. (2022). Stem cell therapies for central nervous system trauma: The 4 Ws-what, when, where, and why. *Stem Cells Transl. Med.* 11, 14–25. doi:10.1093/stcltm/szab006

Liu, T., Dan, W., Dan, N., Liu, X., Liu, X., and Peng, X. (2017). A novel grapheme oxide-modified collagen-chitosan bio-film for controlled growth factor release in wound healing applications. *Mater. Sci. Eng. C* 77, 202–211. doi:10.1016/j.msec.2017.03.256

Liu, X. Y., Chen, C., Xu, H. H., Zhang, Y. S., Zhong, L., Hu, N., et al. (2021). Integrated printed BDNF/collagen/chitosan scaffolds with low temperature extrusion 3D printer accelerated neural regeneration after spinal cord injury. *Regen. Biomater.* 8, rbab047. doi:10.1093/rb/rbab047

Liu, X. Y., Liang, J., Wang, Y., Zhong, L., Zhao, C. Y., Wei, M. G., et al. (2019). Diffusion tensor imaging predicting neurological repair of spinal cord injury with transplanting collagen/chitosan scaffold binding bFGF. *J. Mat. Sci. Mat. Med.* 30, 123. doi:10.1007/s10856-019-6322-y

Liu, X. Y., Wei, M. G., Liang, J., Xu, H. H., Wang, J. J., Wang, J., et al. (2020). Injury-preconditioning secretome of umbilical cord mesenchymal stem cells amplified the neurogenesis and cognitive recovery after severe traumatic brain injury in rats. *J. Neurochem.* 153, 230–251. doi:10.1111/jnc.14859

Liu, X., Zheng, C., Luo, X., Wang, X., and Jiang, H. (2019). Recent advances of collagen-based biomaterials: Multi-hierarchical structure, modification and biomedical applications. *Mater. Sci. Eng. C* 99, 1509–1522. doi:10.1016/j.msec.2019.02.070

Maas, A., Menon, D. K., Adelson, P. D., Andelic, N., Bell, M. J., Belli, A., et al. (2017). Traumatic brain injury: Integrated approaches to improve prevention, clinical care, and research. *Lancet Neurol.* 16, 987–1048. doi:10.1016/S1474-4422(17)30371-X

Metzger, W., Rother, S., Pohlemann, T., Möller, S., Schnabelrauch, M., Hintze, V., et al. (2017). Evaluation of cell-surface interaction using a 3D spheroid cell culture model on artificial extracellular matrices. *Mater. Sci. Eng. C* 73, 310–318. doi:10.1016/j.msec.2016.12.087

Mie, M., Sasaki, S., and Kobatake, E. (2014). Construction of a bFGF-tethered multi-functional extracellular matrix protein through coiled-coil structures for neurite outgrowth induction. *Biomed. Mat.* 9, 015004. doi:10.1088/1748-6041/9/1/015004

Nichol, A., French, C., Little, L., Haddad, S., Presneill, J., Arabi, Y., et al. (2015). Erythropoietin in traumatic brain injury (EPO-TBI): A double-blind randomised controlled trial. *Lancet* 386, 2499–2506. doi:10.1016/S0140-6736(15)00386-4

Pekcec, A., Baumgärtner, W., Bankstahl, J. P., Stein, V. M., and Potschka, H. (2008). Effect of aging on neurogenesis in the canine brain. *Aging Cell* 7, 368–374. doi:10.1111/j.1474-9726.2008.00392.x

Platt, S. R., Radaelli, S. T., and McDonnell, J. J. (2001). The prognostic value of the modified Glasgow Coma Scale in head trauma in dogs. *J. veterinary Intern. Med.* 15, 581–584. doi:10.1111/j.1939-1676.2001.tb01594.x

Pu, L., Meng, M., Wu, J., Zhang, J., Hou, Z., Gao, H., et al. (2017). Compared to the amniotic membrane, Wharton's jelly may be a more suitable source of mesenchymal stem cells for cardiovascular tissue engineering and clinical regeneration. *Stem Cell Res. Ther.* 8, 72. doi:10.1186/s13287-017-0501-x

Purdy, P. D., Sr, D. M. D., Batjer, H. H., White, C. L., 3rd, Meyer, Y., and Samson, D. S. (1989). Microfibrillar collagen model of canine cerebral infarction. *Stroke* 20, 1361–1367. doi:10.1161/01.str.20.10.1361

Sharma, R. R., Pollock, K., Hubel, A., and McKenna, D. (2014). Mesenchymal stem or stromal cells: A review of clinical applications and manufacturing practices. *Transfusion* 54, 1418–1437. doi:10.1111/trf.12421

Sun, G., Li, G., Li, D., Huang, W., Zhang, R., Zhang, H., et al. (2018). hucMSC derived exosomes promote functional recovery in spinal cord injury mice via attenuating inflammation. *Mater. Sci. Eng. C* 89, 194–204. doi:10.1016/j.msec.2018.04.006

Sun, Y., Yang, C., Zhu, X., Wang, J. J., Liu, X. Y., Yang, X. P., et al. (2019). 3D printing collagen/chitosan scaffold ameliorated axon regeneration and neurological recovery after spinal cord injury. *J. Biomed. Mat. Res. A* 107, 1898–1908. doi:10.1002/jbm.a.36675

Taylor, C. A., Bell, J. M., Breiding, M. J., and Xu, L. (2017). Traumatic brain injury-related emergency department visits, hospitalizations, and deaths - United States, 2007 and 2013. *Surveill. Summ.* 66, 1–16. doi:10.15585/mmwr.ss6609a1

Tondreau, T., Lagneaux, L., Dejeneffe, M., Massy, M., Mortier, C., Delforge, A., et al. (2004). Bone marrow-derived mesenchymal stem cells already express specific neural proteins before any differentiation. *Differentiation* 72, 319–326. doi:10.1111/j.1432-0436.2004.07207003.x

Uchida, K., Miyauchi, Y., Nakayama, H., and Goto, N. (1990). Amyloid angiopathy with cerebral hemorrhage and senile plaque in aged dogs. *Jpn. J. Veterinary Sci.* 52, 605–611. doi:10.1292/jvms1939.52.605

Wakai, T., Narasimhan, P., Sakata, H., Wang, E., Yoshioka, H., Kinouchi, H., et al. (2016). Hypoxic preconditioning enhances neural stem cell transplantation therapy after intracerebral hemorrhage in mice. *J. Cereb. Blood Flow. Metab.* 36, 2134–2145. doi:10.1177/0271678X15613798

Wei, H. J., Chen, C. H., Lee, W. Y., Chiu, I., Hwang, S. M., Lin, W. W., et al. (2008). Bioengineered cardiac patch constructed from multilayered mesenchymal stem cells for myocardial repair. *Biomaterials* 29, 3547–3556. doi:10.1016/j.biomaterials.2008.05.009

Xie, Z., Paras, C. B., Weng, H., Punnakitikashem, P., Su, L. C., Vu, K., et al. (2013). Dual growth factor releasing multi-functional nanofibers for wound healing. *Acta biomater.* 9, 9351–9359. doi:10.1016/j.actbio.2013.07.030

Xu, Y., Zhang, Z., Chen, X., Li, R., Li, D., and Feng, S. (2016). A silk fibroin/collagen nerve scaffold seeded with a Co-culture of schwann cells and adipose-derived stem cells for sciatic nerve regeneration. *PloS one* 11, e0147184. doi:10.1371/journal.pone.0147184

Yuhui, R., Hong, L., Jinrong, Y., Chen, Z., and Shao, Z. (2011). Preparation of 3D fibroin/chitosan blend porous scaffold for tissue engineering via a simplified method. *Macromol. Biosci.* 11, 419–426. doi:10.1002/mabi.201000392

Zhang, J., Wang, R. J., Chen, M., Liu, X. Y., Ma, K., Xu, H. Y., et al. (2021). Collagen/heparan sulfate porous scaffolds loaded with neural stem cells improve neurological function in a rat model of traumatic brain injury. *Neural Regen. Res.* 16, 1068–1077. doi:10.4103/1673-5374.300458

Zhang, K., Jiang, Y., Wang, B., Li, T., Shang, D., and Zhang, X. (2022). Mesenchymal stem cell therapy: A potential treatment targeting pathological manifestations of traumatic brain injury. *Oxidative Med. Cell. Longev.* 2022, 4645021–4645111. doi:10.1155/2022/4645021

Zhang, K., Shi, Z., Zhou, J., Xing, Q., Ma, S., Li, Q., et al. (2018). Potential application of an injectable hydrogel scaffold loaded with mesenchymal stem cells for treating traumatic brain injury. *J. Mat. Chem. B* 6, 2982–2992. doi:10.1039/c7tb03213g

Zhang, W., Chen, L., Chen, J., Wang, L., Gui, X., Ran, J., et al. (2017). Silk fibroin biomaterial shows safe and effective wound healing in animal models and a randomized controlled clinical trial. *Adv. Healthc. Mat.* 6, 1700121. doi:10.1002/adhm.201700121

Zhu, T., Cui, Y., Zhang, M., Zhao, D., Liu, G., and Ding, J. (2020). Engineered three-dimensional scaffolds for enhanced bone regeneration in osteonecrosis. *Bioact. Mater.* 5, 584–601. doi:10.1016/j.bioactmat.2020.04.008

Zhu, T., Jiang, M., Zhang, M., Cui, L., Yang, X., Wang, X., et al. (2022). Biofunctionalized composite scaffold to potentiate osteoconduction, angiogenesis, and favorable metabolic microenvironment for osteonecrosis therapy. *Bioact. Mater.* 9, 446–460. doi:10.1016/j.bioactmat.2021.08.005

frontiers | Frontiers in Materials

TYPE Original Research
PUBLISHED 02 September 2022
DOI 10.3389/fmats.2022.1008704

OPEN ACCESS

EDITED BY
Jianxun Ding,
Changchun Institute of Applied Chemistry (CAS), China

REVIEWED BY
Lei Sui,
Tianjin Medical University, China
Xufeng Dong,
Dalian University of Technology, China
Ling Ren,
Institute of Metal Research (CAS), China
Qiang Wang,
China Medical University, China

*CORRESPONDENCE
Jinbao Ma,
majinbao@me.com
Jianfeng Chen,
chenjf12345678@163.com

†These authors contributed equally to this work and shared the first authorship.

SPECIALTY SECTION
This article was submitted to Biomaterials and Bio-Inspired Materials, a section of the journal Frontiers in Materials

RECEIVED 01 August 2022
ACCEPTED 15 August 2022
PUBLISHED 02 September 2022

CITATION
Liang Z, Liu Y, Jiang Y, Liu P, Zhang Y, Meng F, Liu M, Cui Z, Ma J and Chen J (2022), Effect of hot etching with HF on the surface topography and bond strength of zirconia.
Front. Mater. 9:1008704.
doi: 10.3389/fmats.2022.1008704

Effect of hot etching with HF on the surface topography and bond strength of zirconia

Zhuoran Liang†, Yang Liu†, Yulin Jiang, Pan Liu, Yannan Zhang, Fanhao Meng, Min Liu, Zhi Cui, Jinbao Ma* and Jianfeng Chen*

Department of Stomatology, First Affiliated Hospital of Dalian Medical University, Dalian, China

Zirconia has occupied an increasingly important role in oral clinical applications in recent years. However, how to achieve the ideal bonding effect of zirconia is a significant problem that needs to be solved urgently in oral clinics. Hot etching treatment of zirconia is a hot spot of current research, but it is still unclear about the optimal acid solution and the effect of hot etching on the surface topography and bond strength of zirconia. This study evaluated the effect of hot etching with HF and HCl on the surface topography, roughness, crystalline phase, zirconia/resin cement interfacial evaluation and shear bond strength of zirconia. The results showed that the hot etching groups produced completely different topographical changes on the surface of zirconia than the sandblasting group. Obvious interfacial cracks were observed in the sandblasting group. The HF hot etching group achieved the highest roughness values (78.17 ± 4.94 nm) and the highest shear bond strength (25.09 ± 4.09 MPa). Compared with HCl, hot etching with HF could achieve more uniform and dense porous morphology, greater roughness and shear bond strength. Moreover, there were no prominent zirconia/resin cement interfacial cracks and crystal phase transformations on the surface of zirconia.

KEYWORDS

zirconia ceramic, hot etching, surface topography, surface roughness, bond strength

1 Introduction

In recent years, zirconia restorations have been widely favored by doctors and patients in oral clinical treatment (Tzanakakis et al., 2020). Optimizing the cement adhesion to zirconia restorations is the key to successful prosthodontic treatment. Especially for restorations like veneers, in order to achieve an ideal clinical effect, it is more dependent on the effect of bonding (Valente et al., 2020). Before bonding to the teeth, conventional all-ceramic restorations were treated with hydrofluoric acid (HF) and silane coupling agents. However, zirconia ceramics do not contain silica components, and surface treatment with hydrofluoric acid and silane coupling agents application of zirconia ceramics is not a well-established method to achieve durable adhesion resin-based materials (Valente et al., 2020). Therefore, achieving the

ideal bonding effect of zirconia is a significant problem that urgently needs to be solved in oral clinics (Flores-Ferreyra et al., 2019). Studies have shown that zirconia includes three crystal phases: monoclinic, tetragonal and cubic phases (Sriamporn et al., 2014). When zirconia is under pressure, high temperature or humidity, it may transform from tetragonal to monoclinic (Maroun et al., 2019). However, the tetragonal to monoclinic phase transformation will affect the mechanical strength of zirconia (Allahkarami and Hanan, 2011). So the ideal treatment method for zirconia should avoid transforming its crystal phase (Jiao et al., 2018). At present, some scholars have proposed a scheme for hot etching to treat zirconia. Harb (Harb et al., 2021) indicated that hot etching treatment could improve the bond strength of zirconia restorations. Pin LV (Lv et al., 2015) not only proposed that the shear bond strength between zirconia and resin cement could be significantly increased by hot etching treatment, but also the bond strength of hot etching group was still higher than that of sandblasting group after thermocycling test. However, no consensus has been reached on the optimal type of acid solution for hot etching and the influence of hot etching on the related properties of zirconia (Wei et al., 2021). In this experiment, two acid solutions, HCl and HF, were used to conduct hot etching on zirconia, and then the related properties of zirconia were detected and analyzed. It is hoped to find an acid solution with the best effect on the hot etching of zirconia to provide a reference for future research.

2 Materials and methods

2.1 Specimen preparation

First, put the zirconia discs ($ZrO_2 \geq 99.0\%$,Y_2O_3 4.5–6.0%, $HfO_2 \leq 5.0\%$, Other oxides ≤1.0%) (Zenostar T, WIELAND, Germany) into the zirconia cutting machine (D500, Guangzhou Yihua Digital Technology Co., Ltd., China) in turn, then cut them according to the operation guide. The cut zirconia ceramic blocks into the zirconia sintering furnace (Vicce K8 Plus, Shenzhen Purong Trading Co., Ltd., China), the ceramic blocks shrink evenly during the sintering process. Then, the zirconia ceramic blocks were ground and trimmed one by one, and 24 pieces of zirconia with a size of 10 × 10 × 2 mm (type I) and 20 pieces of zirconia with a size of 3 × 3 × 2 mm (type II) were obtained. All specimens were uniformly polished on grinding and polishing machine (LABOPOL-25, Struers, Denmark) and successively used 180-, 240-, 500-, 800-, 1000-, 1200-, 1500- and 2000-grit water sandpaper for step-by-step polishing. Then these specimens were placed in a numerically controlled ultrasonic cleaner (KQ-400DE, Kunshan Ultrasound Instrument Co., Ltd., China), cleaned and shaken with deionized water for 15 min, and dried for later use.

2.2 Specimen treatment

All specimens were equally divided into 4 groups, each group including 6 types I specimens and 5 types II specimens, and proceeded according to the following groupings:

Group A. No treatment: No surface treatment procedure was applied.

Group B. Sandblasting: Airborne-particle abrasion with 50 μm Al_2O_3 particles applied for 15 s at a vertical distance of 10 mm and 0.25 MPa of air pressure.

Group C. Hot etching with HCl: Specimens and a rotor were placed in a reaction kettle filled with hot etching solution (24 ml of methanol, 6 ml of 37% HCl and 0.06 g of $FeCl_3$). Then the reaction kettle was placed in a constant temperature magnetic stirring pot (Zhengzhou Great Wall Technology Industry and Trade Co., Ltd., China), and the treatment was continued for 10 min under the conditions of 100°C and 400 rev/minute.

Group D. Hot etching with HF: Specimens and a rotor were placed in a reaction kettle filled with hot etching solution (30 ml of 9.5% HF). Then the reaction kettle was placed in a constant temperature magnetic stirring pot (Zhengzhou Great Wall Technology Industry and Trade Co., Ltd., China), and the treatment was continued for 10 min under the conditions of 100°C and 400 rev/minute.

After the treatment, each group of specimens was placed in a numerically controlled ultrasonic cleaner in turn, ultrasonically oscillated in deionized water for 15 min, and gently dried.

2.3 AFM and SEM evaluation

Three random types I specimens from each group were used for the morphological change and surface roughness analysis using atomic force microscopy (AFM, JPK NanoWizard Ultra Speed, Germany). To analyze the surface roughness of each group of specimens, a silicon AFM probe (k = 3 N/m, f = 75 kHz) was used to perform in tapping mode with a scan size of 3 × 3 μm. AFM data were generated with the JPK Data Processing software. Furthermore, the images of each group of specimens were recorded, and the average was determined as the mean Ra value. Then one type I specimen was randomly selected from each group. Each specimen was sputter-coated with gold and evaluated under a scanning electron microscope (SEM, ZEISS SUPRA 55, Germany) at ×10,000magnifications to assess changes in surface topography.

2.4 XRD evaluation

One type I specimen from each group was randomly selected to determine the crystal structures and phase transformations. Crystalline phase identification of the specimens was carried out by X-ray diffraction (XRD, PANalytical, Empyrean X, the

Netherlands) using Cu-Kα radiation operating at 60 kW and 50 mA. Scans were performed over the 2θ range of 20–70° at a scan speed of 0.02°/minute. Finally, each group of XRD patterns was analyzed to conclude.

2.5 Zirconia/resin cement interfacial evaluation

Composite discs (Paradigm MZ100, 3M ESPE, America) were cut into four composite resin blocks with a size of 10 × 10 ×2 mm by a slow-speed diamond saw (IsoMet 1000, BUEHLER, America) under constant water cooling. These composite resin blocks were ground with 180-, 240-, 500-, 800-, 1000-, 1200-, 1500- and 2000-grit water sandpaper, cleaned with deionized water and gently air-dried. One type I specimen was randomly selected from each group, and the specimen was bonded to the resin block according to the operation guide of resin cement (Panavia F, MPD-based resin cement, Kuraray, Japan). Then bonded specimens were stored in a constant temperature water bath (HWS-24, Shanghai Yiheng Scientific Instrument Co., Ltd., China) at 37°C for 24 h. Bonded specimens were sectioned perpendicularly to the interface with a slow-speed diamond saw under constant water cooling. Afterwards, each exposed zirconia/resin cement interface was polished with 180-, 240-, 500-, 800-, 1000-, 1200-, 1500- and 2000-grit water sandpaper. Then these bonded specimens were placed in the numerically controlled ultrasonic cleaner, cleaned and shaken with deionized water for 15 min, and dried. Finally, each bonded specimen was sputter-coated with gold and evaluated under the scanning electron microscope at ×1,000magnifications to assess zirconia/resin cement interfacial properties.

2.6 Shear bond strength test

The upper and mandibular premolars extracted from orthodontics were selected, and no root canal treatment was performed. There are no apparentcracks on the lip surface of the tooth crown, no large-scale caries and defects, no fluoride spots and poor mineralization. The isolated teeth were sequentially embedded in anhydrite and polished underwater sandpaper. Then the enamel with an area of no less than 3 × 3 mm was prepared. Type II specimens from each group were bonded to isolated teeth according to the operation guide of Panavia F resin cement. Then these bonded specimens were stored in the constant temperature water bath at 37°C for 24 h. A universal test machine (Instron, America) was used to complete the shear test of these bonded specimens. The vertical movement speed of the loading head was set to 1 mm/min, and the shear bond strength was calculated.

The tested specimens were placed under a stereomicroscope (NSZ-606, Yongxin, China) in turn to observe the fracture mode. The fracture mode is divided into the following types. When the fracture occurs inside the resin cement, it is a cohesive fracture; when it occurs between the zirconia and resin cement, it is the zirconia-resin interface fracture; Between the enamel and resin cement, it is the enamel-resin interface fracture; if any of the interface fractures and cohesive fractures exist at the same time, it is a mixed fracture.

2.7 Statistical analysis

The statistical analysis of surface roughness and the shear bond strength values were performed with SPSS (IBM SPSS Statistics 26, United States). Data were checked for the normal distribution and homogeneity of variance. One-way analysis of variance and most minor significant difference tests were used to analyze differences in groups ($p < 0.05$). The final results of XRD were analyzed using MDI Jade 6 combined with Origin 2019 software.

3 Results and discussions

3.1 AFM and SEM images

AFM and SEM images of each group are shown in Figure 1 and Figure 2. The surface of group A is smooth, with only a few traces of water sandpaper polishing. Rough abrasions appear on the surface of group B. The surface of the specimen exhibits a macrorough topography with grooves and scratches with sharp margins. Some scattered crater-like holes can be observed on the surface of group C. The size and shape of these holes are different. In group D, an overall homogenous and finer rough surface can be observed. Compared with group C, the surface of group D shows a more regular and dense porous topography with nanoscale irregular pores. A porous network structure with distinct peak-valley morphology is formed.

In 2009, Casucci (Casucci et al., 2009) first tried to use 37% HCl to treat zirconia at 100°C. Moreover, the findings of this study revealed that hot etching might be a feasible method for improving zirconia surface roughness. Similarly, Akay (Akay et al., 2017) found that HCl hot etching for 10 min could increase the shear bond strength of zirconia ceramics. In recent years, many scholars have begun to try to use HF for the hot etching of zirconia. Kang (Kang et al., 2020) treated zirconia with 9.5% HF at 100°Cfor 10 min and found that the bond strength of zirconia in this group was significantly higher than that in other groups. Therefore, 37% HCl and 9.5% HF were selected to treat zirconia in this experiment. Moreover, this study aimed to find the optimal acid solution for the hot etching treatment of zirconia. The images of SEM and AFM show that different treatment methods have different

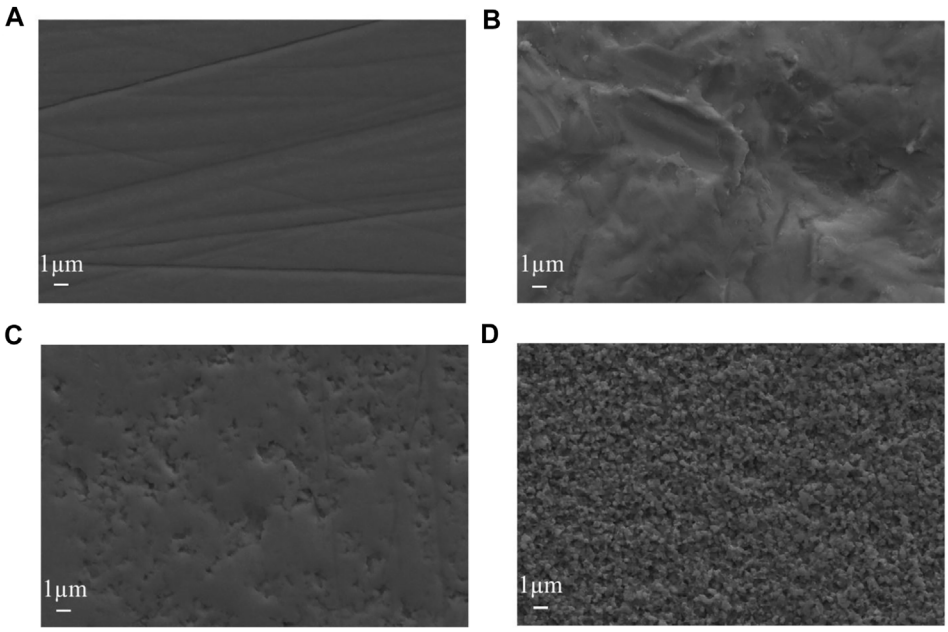

FIGURE 1
SEM observation images of zirconia specimens (×10,000 magnifications). **(A)** no treatment **(B)** sandblasting **(C)** hot etching with HCl **(D)** hot etching with HF.

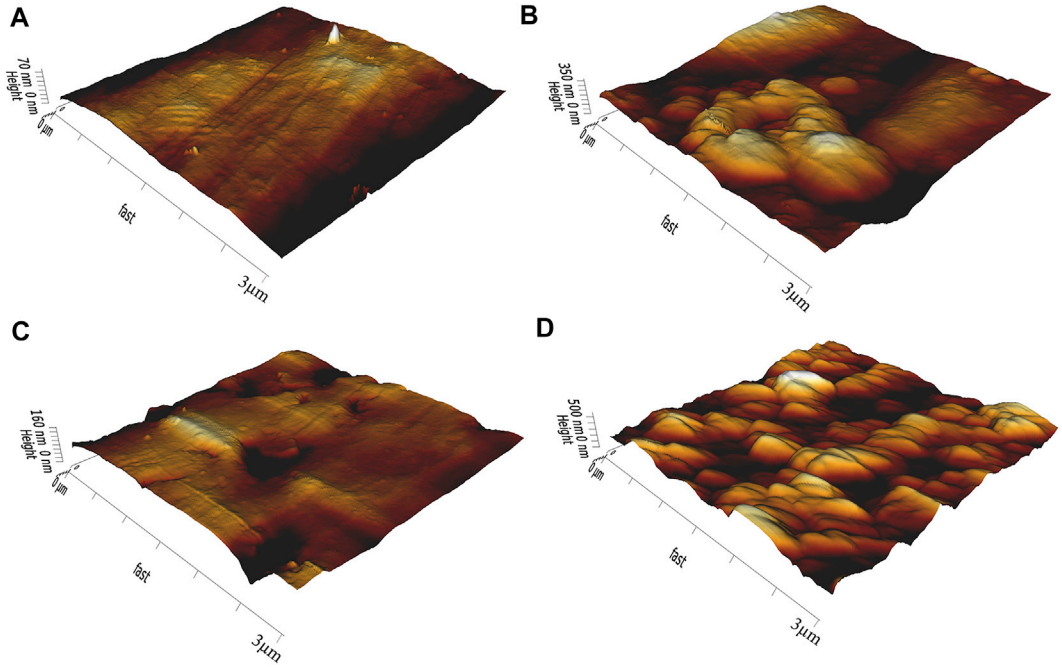

FIGURE 2
AFM observation images of zirconia specimens. **(A)** no treatment **(B)** sandblasting **(C)** hot etching with HCl **(D)** hot etching with HF.

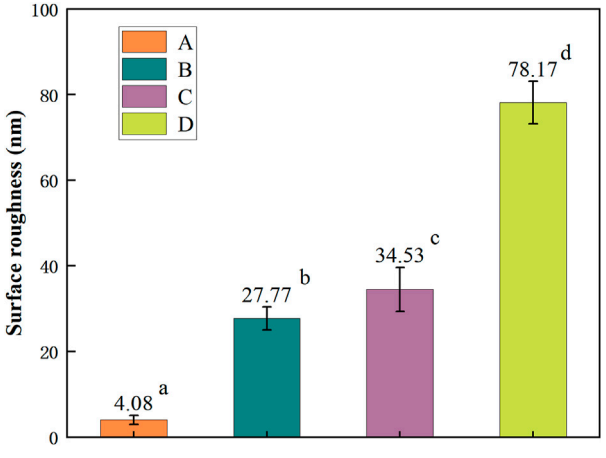

FIGURE 3
Surface roughness (Ra) values of zirconia specimens. Different superscript lowercase letters indicate statistically significant differences ($p < 0.05$).

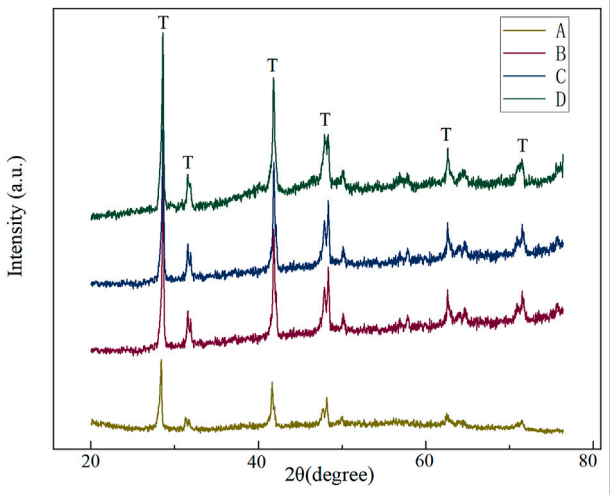

FIGURE 4
XRD patterns of zirconia specimens (T indicates the tetragonal zirconia phase).

effects on the surface topography of zirconia. During the sandblasting process, countless Al_2O_3 particles were accelerated to hit the surface of zirconia and then slid in different directions (Hallmann et al., 2016; Barreto et al., 2020). Therefore, various irregular grooves and scratches would be formed on the surface of zirconia (Saade et al., 2019). In the process of HCl hot etching, Fe^{3+} could destroy the integrity of the zirconia surface and help HCl dissolve the grain structure on the zirconia surface as an oxidizing agent, thereby causing local corrosion of zirconia (El-Korashy and El-Refai, 2014). Therefore, scattered holes could be observed on the surface of zirconia. In contrast, the surface of zirconia treated with HF hot etching shows a more uniform and dense porous topography. This is attributed to HF being more corrosive and permeable than HCl (Han et al., 2020). As the temperature increased, F gradually dissolved zirconia and yttria (Kim et al., 2020). Then reaction products such as fluoride, oxide and hydroxide complexes were produced. When these reaction products were separated from the surface of zirconia, a three-dimensional network structure with dense pores would be formed on the surface of zirconia (Lowalekar and Raghavan, 2004).

3.2 Surface roughness (Ra) values

The average surface roughness values (Ra) of each group are shown in Figure 3. Among them, D > C > B > A, the pairwise comparisons are statistically significant ($p < 0.05$). In this experiment, the zirconia treated by hot etching with two acid solutions was rougher than the sandblasting group, and this experimental finding was consistent with that of Alessio (Casucci et al., 2010). However, the experimental results of You-Jung (Kang et al., 2020) were different. He found that the surface roughness of the zirconia treated with HF hot etching was less than that of the sandblasting group. The reason may be that the concentration of HF selected in this experiment is higher than that of You-Jung's experiment. In previous studies, some scholars pointed out that the concentration of HF would affect the effect of hot etching on zirconia and found that with the increase of the concentration of HF, the surface roughness would increase accordingly (Kim et al., 2021). Moreover, this finding explains why the two experiments above have different results. However, there is no consensus on the optimal concentration selection of HF, so further exploration is needed (Seo et al., 2022). For two acid solutions, the surface roughness of the HF group was greater than that of the HCl group in this experiment, which was also attributed to the stronger corrosiveness of HF than HCl. At present, there are few comparative studies on the hot etching of zirconia with two acid solutions, so more relevant studies are needed to verify the above findings (Lv et al., 2015).

Some scholars (Ding et al., 2018) point out that with the increase of roughness, the surface irregularity of zirconia increases, and the contact area between zirconia and resin cement also increases. Numerous resins flow into the pits, which not only help the cured resin cement to lock into the zirconia surface, but also to achieve a larger chemical reaction area. The appropriate increase of the roughness has a positive significance for the excellent bond of zirconia. However, You-Jung (Kang et al., 2020) points out that the relationship between roughness and bond strength is not purely linear. When uniform nano-scale pore structure is formed by hot etching, the roughness is lower, but the bond strength is still high. It can be seen that roughness is not the only factor determining bond strength, ceramic bond surface can not be blindly pursued with ultra-high

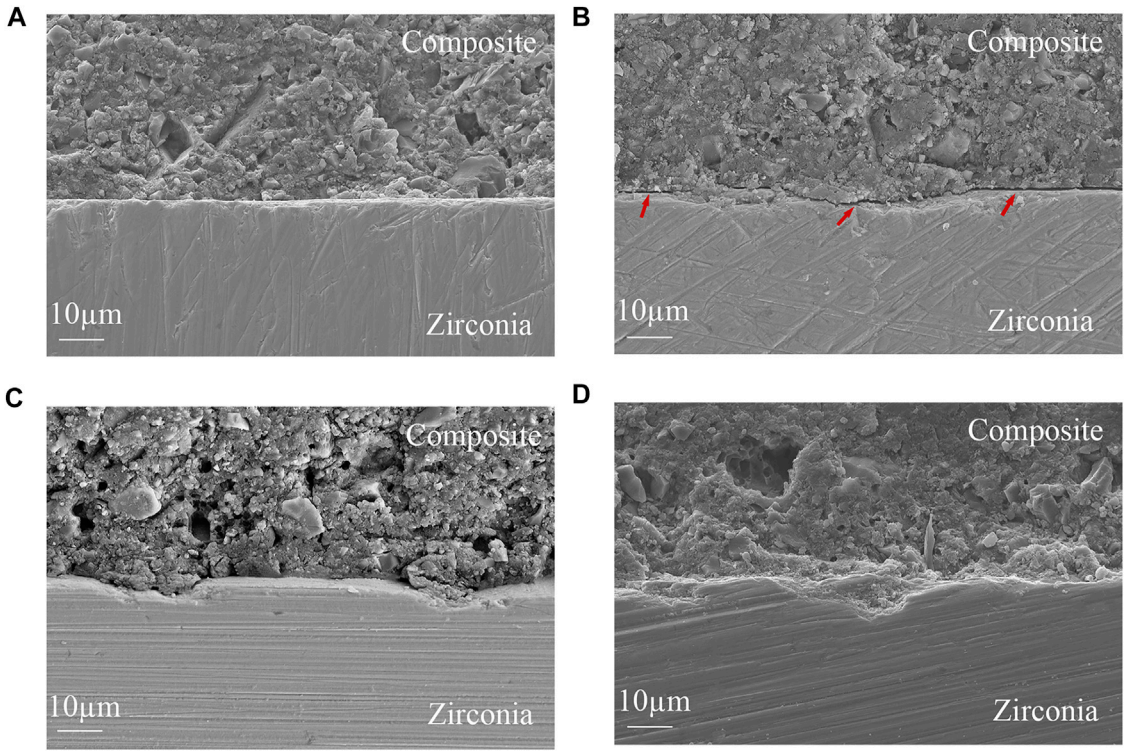

FIGURE 5
Zirconia/resin cement interfacial SEM images (x1,000 magnifications) **(A)** no treatment **(B)** sandblasting **(C)** hot etching with HCl **(D)** hot etching with HF (Interfacial cracks are visible at the red arrows).

roughness (Yu et al., 2016). However, there is no conclusion on the best range of roughness for zirconia bonding, it is still necessary to continue to bond strength testing, and then combined with the roughness to be analyzed.

3.3 X-Ray diffraction (XRD)

The X-ray diffraction patterns of each group are shown in Figure 4. Zirconia is a metastable ceramic with three crystal phase structures: monoclinic, tetragonal, and cubic phases (Sriamporn et al., 2014). When zirconia is subjected to tension and other factors, the tetragonal to monoclinic phase transformation occurs (Maroun et al., 2019). The mechanical strength of zirconia is adversely affected as the monoclinic phase increases and the tetragonal phase decreases (Allahkarami and Hanan, 2011). In this experiment, all the X-ray diffraction patterns of the Y -TZP surface treatment groups evaluated consisted of tetragonal phase (T) since detectable monoclinic peaks (M) were not observed in all surface treatment group specimens. XRD results show that the crystal structure of the treated zirconia is still stable. The occurrence of phase transformation is closely related to the selection of treatment parameters. Previous studies have proved that too large sandblasting particle size, too high hot etching concentration, and too long acid etching time will cause monoclinic phase transformation (Han et al., 2020). Saade (Saade et al., 2019) also pointed out that the occurrence of phase transformation is directly related to the particle size of sandblasting, and 50 μm causes less monoclinic phase transformation than 100 μm. Similarly, other studies have pointed out that the particle size of 50 μm, the pressure of 0.25 MPa, and the vertical distance of 10 mm are the best choices for Al_2O_3 sandblasting (Wang, 2019). Therefore, in this experiment, the above parameters were finally selected for the specimen treatment of the sandblasting group, hoping to avoid the occurrence of phase transformation and microcracks to the greatest extent. The XRD results also proved that this choice achieved the desired effect.

3.4 Zirconia/resin cement interfacial images

Zirconia/resin cement interfacial SEM images are shown in Figure 5. The top half of the images shows the resin cement

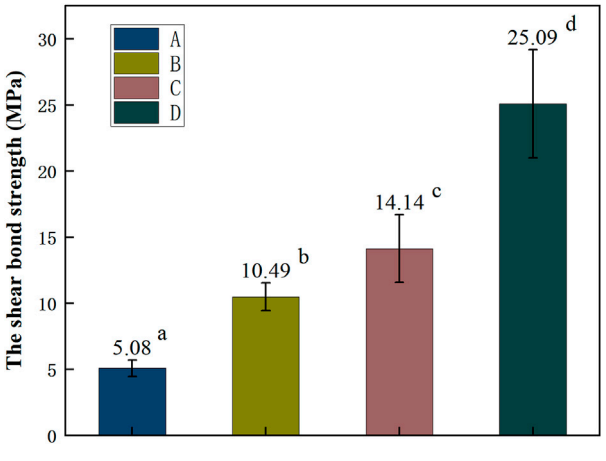

FIGURE 6
Shear bond strength of zirconia specimens. Different superscript lowercase letters indicate statistically significant differences ($p < 0.05$).

and composite resin blocks bonded together, and the bottom half is zirconia. There is a clear boundary between the resin cement and zirconia in group A, and the boundary line is straight. The two materials are independent, and neither tends to protrude into each other. Irregular depressions appear on the surface of zirconia in group B, and the boundary line is no longer straight. There is no close contact between the resin cement and zirconia, and obvious interfacial cracks can be observed (red arrows mark). There are obvious pits on the surface of the zirconia in group C, and the resin cement corresponding to the position of the pits protrudes from the surface and protrudes into the pits. There is a tendency for interlocking between zirconia and resin cement. In group D, we can observe more obvious pits on the surface of zirconia, and the resin cement protrudes into these pits. So a cross-interlocking pattern is formed between the resin cement and the zirconia. The bonding between the resin cement and zirconia is good, the contact is very close, and no cracks are observed in the entire interface.

3.5 Shear bond strength

The shear bond strength results of each group are shown in Figure 6. D > C > B > A, the data are statistically significant ($p < 0.05$). The observed results of fracture modes are summarized in Table 1. The fracture mode images are shown in Figure 7.

A large number of studies have shown that the combined application of micromechanical interlock and chemical adhesion could effectively improve the bond strength of zirconia (Comino-Garayoa et al., 2021; Babaee et al., 2022). Previous studies have shown that the chemical interaction between the P-OH group of 10-methacryloyloxydecyl dihydrogen phosphate (10-MDP) and the Zr-OH group on the zirconia surface could effectively improve the bond strength of zirconia (Serichetaphongse et al., 2022). Llerena-Icochea (Llerena-Icochea et al., 2017) proposed that useing resin cement containing 10-MDP can improve the bond strength of zirconia by about 8–72 Mpa. Phosphoric methacrylate ester has also been reported to increase the bond strength of zirconia. However, because the phosphoric methacrylate ester is prone to hydrolysis, its shear bond strength tends to be lower than that of 10-MDP (Lee et al., 2015). At the same time, Panavia F resin cement containing 10-MDP, as one of the representatives of the fifth-generation self-etch adhesive, has been widely used in clinical dental treatment. Therefore, Panavia F resin cement was selected for bonding zirconia in this experiment. The bond strength of group A is the lowest, and all the fracture modes of group A are zirconia-resin interface fractures, which fully shows that chemical adhesion between zirconia and resin cement alone cannot achieve the ideal bonding effect. Group B has obvious interfacial cracks, so the increased surface area of zirconia after roughening treatment is not effectively utilized, and the shear bond strength is lower than that of group C and group D. This finding is consistent with that of Casucci et al. (Casucci et al., 2010; Akay et al., 2017) Some studies have pointed out that small holes can provide better mechanical interlock than grooves that are relatively large and wide (Ramakrishnaiah et al., 2016). So, combined with the different morphological characteristics of the sandblasting group and the hot etching group in this experiment, it can be explained why the hot etching group achieved higher bond strength than the sandblasting group. Comparing two acid solutions, the HF hot etching group achieved higher shear bond strength than the HCl hot etching

TABLE 1 Fracture modes of zirconia specimens.

Group	Fracture mode			
	Cohesive fracture (block)	Zirconia-resin interface fracture (block)	Enamel-resin interface fracture (block)	Mixed fracture (block)
A	0	5	0	0
B	0	4	0	1
C	0	3	0	2
D	0	0	0	5

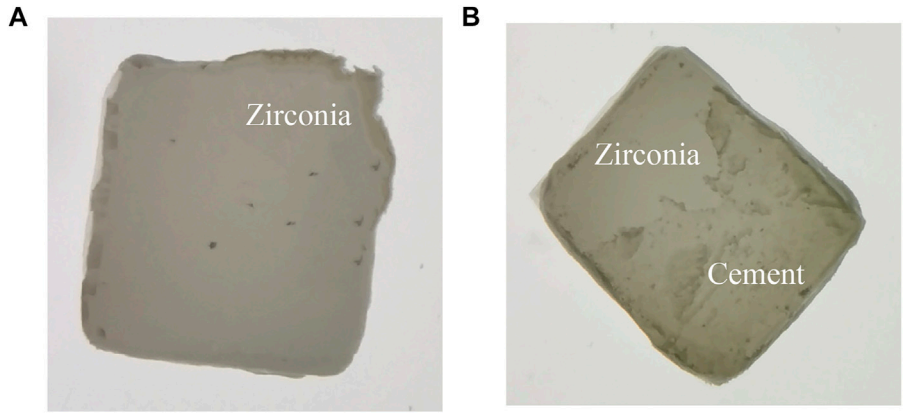

FIGURE 7
Fracture mode images of zirconia specimens. **(A)** zirconia-resin interface fracture; **(B)** mixed fracture.

group. The reason for this result is that the fluoride ion in HF has strong oxidizing power and a small radius, which leads to its strong permeability (Wei et al., 2022). Therefore, the pores formed on the surface of zirconia in the HF group are denser than those in the HCl group. The dense pores facilitate the locking of more cured resin cement on the surface of zirconia and achieve a larger chemical reaction area (Casucci et al., 2011). Finally, with the help of both micromechanical interlock and chemical adhesion, the bonding effect is guaranteed.

The observed results of fracture modes showed that HF hot etching group had less adhesive failure (zirconia-resin interface fracture) than the control and sandblasting group. This result is consistent with Shaymaa's findings. This observation confirms that sufficient micromechanical retention is important not only for establishing high bond strength but also for impeding adhesive failure (Elsaka, 2013). When there is no sufficient mechanical retention between zirconia and resin cement, the bond is mainly dependent on chemical bond, so the bond effect is not ideal. The fracture mode observed was mainly zirconia-resin interface fracture. There is less resin cement on the surface of zirconia after fracture, which indicates that the bond between zirconia and cement is not good. Therefore, a large area of residual cement can be observed on the fracture surface of zirconia in the HF hot etching group, which further shows that this treatment has a remarkable effect on improving the bond effect between zirconia and resin cement.

Attia (Attia, 2011) has stated that the minimum clinically acceptable bond strength value is approximately 13 MPa. In this experiment, the bonding effect obtained by hot etching can reach this standard, and the zirconia does not produce phase transformation, which proves the development potential of hot etching treatment of zirconia. In future research, the long-term bonding effect of zirconia after hot etching treatment needs to be further explored (Colombo et al., 2020). On the other hand, the acid solution required for the hot etching treatment is cheap, so the cost is easy to control. Moreover, the operation time of hot etching treatment is only 10 min, which can meet the high-efficiency requirements of clinical diagnosis and treatment. All of the above factors will contribute to the future promotion and application of the hot etching treatment method. However, this treatment method also has some disadvantages, including the use of the acid solution is dangerous, the equipment, such as the magnetic stirring pot, is not light and flexible enough, and so far, there is no dedicated hot etching equipment for clinical application. Therefore, it is necessary to continuously improve the flexibility of the equipment and reduce the risk of operation so that the clinical application of hot etching treatment of zirconia can be realized as soon as possible.

4 Conclusion

Within the limitations of this laboratory study, the following conclusions are drawn: The hot etching with HF and HCl would not cause phase transformation of zirconia and would not cause interfacial bond cracks like sandblasting. Compared with HCl, HF hot etching could make zirconia form a more regular and dense porous topography and achieve higher roughness and bond strength. Therefore, HF hot etching is a potential treatment method for zirconia.

Data availability statement

The original contributions presented in the study are included in the article/supplementary material, further inquiries can be directed to the corresponding authors.

Author contributions

Methodology and writing- original draft, ZL; Investigation, writing and formal analysis, YL; Conceptualization, review and editing, YJ; Investigation and editing, PL; Investigation,YZ; Resources, FM; Writing, ML; Project administration, ZC; Methodology and supervision, JM; Methodology, resources and supervision, JC; All authors have read and agreed to the published version of the manuscript.

Funding

This research was funded by Scientific Research Project of Liaoning Provincial Department of Education, grant number LZ2020034; Dalian Medical Science Research Program, grant number 2112007.

Conflict of interest

The authors declare that the research was conducted in the absence of any commercial or financial relationships that could be construed as a potential conflict of interest.

Publisher's note

All claims expressed in this article are solely those of the authors and do not necessarily represent those of their affiliated organizations, or those of the publisher, the editors and the reviewers. Any product that may be evaluated in this article, or claim that may be made by its manufacturer, is not guaranteed or endorsed by the publisher.

References

Akay, C., Çakırbay, T., and Şen, M. (2017). Effects of hot chemical etching and 10-metacryloxydecyl dihydrogen phosphate (MDP) monomer on the bond strength of zirconia ceramics to resin-based cements. *J. Prosthodont.* 26, 419–423. doi:10.1111/jopr.12435

Allahkarami, M., and Hanan, J. C. (2011). Mapping the tetragonal to monoclinic phase transformation in zirconia core dental crowns. *Dent. Mat.* 27, 1279–1284. doi:10.1016/j.dental.2011.09.004

Attia, A. (2011). Bond strength of three luting agents to zirconia ceramic-influence of surface treatment and thermocycling. *J. Appl. Oral Sci.* 19, 388–395. doi:10.1590/s1678-77572011005000015

Babaee, H. Y., Neshandar, A. H., Falahchai, M., and Sina, S. (2022). Effect of different surface treatments and orthodontic bracket type on shear bond strength of high-translucent zirconia: An *in vitro* study. *Int. J. Dent.* 2022, 1–8. doi:10.1155/2022/9884006

Barreto, S. C., Lima, R. B. W., Aguiar, F. H. B., Santos, C. T. D., Paulillo, L., and Souza, G. (2020). Mechanical properties of aged yttria-stabilized tetragonal zirconia polycrystal after abrasion with different aluminum oxide particles. *J. Prosthet. Dent.* 124 (11), 599–604. doi:10.1016/j.prosdent.2019.10.027

Casucci, A., Mazzitelli, C., Monticelli, F., Toledano, M., Osorio, R., Osorio, E., et al. (2010). Morphological analysis of three zirconium oxide ceramics: Effect of surface treatments. *Dent. Mat.* 26, 751–760. doi:10.1016/j.dental.2010.03.020

Casucci, A., Monticelli, F., Goracci, C., Mazzitelli, C., Cantoro, A., Papacchini, F., et al. (2011). Effect of surface pre-treatments on the zirconia ceramic-resin cement microtensile bond strength. *Dent. Mat.* 27, 1024–1030. doi:10.1016/j.dental.2011.07.002

Casucci, A., Osorio, E., Osorio, R., Monticelli, F., Toledano, M., Mazzitelli, C., et al. (2009). Influence of different surface treatments on surface zirconia frameworks. *J. Dent. (Shiraz).* 37, 891–897. doi:10.1016/j.jdent.2009.06.013

Colombo, M., Gallo, S., Padovan, S., Chiesa, M., Poggio, C., and Scribante, A. (2020). Influence of different surface pretreatments on shear bond strength of an adhesive resin cement to various zirconia ceramics. *Mater. (Basel)* 13 (3), 652. doi:10.3390/ma13030652

Comino-Garayoa, R., Peláez, J., Tobar, C., Rodríguez, V., and Suárez, M. J. l. (2021). Adhesion to zirconia: A systematic review of surface pretreatments and resin cements. *Materials* 14 (11), 2751. doi:10.3390/ma14112751

Ding, Q., Zhang, L., Bao, R., Zheng, G., Sun, Y., and Xie, Q. (2018). Effects of different surface treatments on the cyclic fatigue strength of one-piece CAD/CAM zirconia implants. *J. Mech. Behav. Biomed. Mat.* 84, 249–257. doi:10.1016/j.jmbbm.2018.05.002

El-Korashy, D. I., and El-Refai, D. A. (2014). Mechanical properties and bonding potential of partially stabilized zirconia treated with different chemomechanical treatments. *J. Adhes. Dent.* 16, 365–376. doi:10.3290/j.jad.a32069

Elsaka, S. E. (2013). Effect of surface treatments on the bonding strength of self-adhesive resin cements to zirconia ceramics. *Quintessence Int.* 44 (6), 407. doi:10.3290/j.qi.a29572

Flores-Ferreyra, B. I., Scougall-Vilchis, R. J., Velazquez-Enriquez, U., Garcia-Contreras, R., Aguillon-Sol, L., and Olea-Mejia, O. F. (2019). Effect of airborne-particle abrasion and, acid and alkaline treatments on shear bond strength of dental zirconia. *Dent. Mat. J.* 38 (2), 182–188. doi:10.4012/dmj.2018-078

Hallmann, L., Ulmer, P., Wille, S., Polonskyi, O., Köbel, S., Trottenberg, T., et al. (2016). Effect of surface treatments on the properties and morphological change of dental zirconia. *J. Prosthet. Dent.* 115, 341–349. doi:10.1016/j.prosdent.2015.09.007

Han, A., Tsoi, J. K. H., Lung, C. Y. K., and Matinlinna, J. P. l. (2020). An introduction of biological performance of zirconia with different surface characteristics: A review. *Dent. Mat. J.* 39, 523–530. doi:10.4012/dmj.2019-200

Harb, O., Al-Zordk, W., Özcan, M., and Sakrana, A. A. (2021). Influence of hydrofluoric and nitric acid pre-treatment and type of adhesive cement on retention of zirconia crowns. *Mater. (Basel)* 14 (4), 960. doi:10.3390/ma14040960

Jiao, Y., Wang, J. D., and Deng, J. P. (2018). Effect of different surface treatments on the crystal structure and properties of zirconia. *J. Peking Univ. Heal. Sci.* 50 (01), 49–52. doi:10.3969/j.issn.1671-167X.2018.01.008

Kang, Y. J., Shin, Y., and Kim, J. H. (2020). Effect of low-concentration hydrofluoric acid etching on shear bond strength and biaxial flexural strength after thermocycling. *Mater. (Basel)* 13 (6), 1409. doi:10.3390/ma13061409

Kim, H. E., Lim, M. J., Yu, M. K., and Lee, K. W. l. (2020). Changes in bond strength and topography for Y-tzp etched with hydrofluoric acid depending on concentration and temperature conditions. *Medicina* 56 (11), 568. doi:10.3390/medicina56110568

Kim, H. K., Yoo, K. W., Kim, S. J., and Jung, C. H. (2021). Phase transformations and subsurface changes in three dental zirconia grades after sandblasting with various Al_2O_3 particle sizes. *Mater. (Basel)* 14 (18), 5321. doi:10.3390/ma14185321

Lee, S. E., Bae, J. H., Choi, J. W., Jeon, Y. C., Jeong, C. M., Yoon, M. J., et al. (2015). Comparative shear-bond strength of six dental self-adhesive resin cements to zirconia. *Materials* 8 (06), 3306–3315. doi:10.3390/ma8063306

Llerena-Icochea, A. E., Costa, R. M., Borges, A., Bombonatti, J., and Furuse, A. Y. (2017). Bonding polycrystalline zirconia with 10-MDP-containing adhesives. *Oper. Dent.* 42, 335–341. doi:10.2341/16-156-L

Lowalekar, V., and Raghavan, S. (2004). Etching of zirconium oxide, hafnium oxide, and hafnium silicates in dilute hydrofluoric acid solutions. *J. Mat. Res.* 19, 1149–1156. doi:10.1557/JMR.2004.0149

Lv, P., Yang, X., and Jiang, T. (2015). Influence of hot-etching surface treatment on zirconia/resin shear bond strength. *Mater. (Basel)* 8, 8087–8096. doi:10.3390/ma8125409

Maroun, E. V., Guimarães, J. G. A., Miranda, W. G., Netto, L., Elias, A. B., and Silva, E. M. (2019). Bond strength stability of self-adhesive resin cement to etched vitrified yttria-stabilized tetragonal zirconia polycrystal ceramic after thermomechanical cycling. *Oper. Dent.* 44 (5), 545–555. doi:10.2341/18-131-L

Ramakrishnaiah, R., Alkheraif, A. A., Divakar, D. D., Matinlinna, J. P., and Vallittu, P. K. (2016). The effect of hydrofluoric acid etching duration on the surface

micromorphology, roughness, and wettability of dental ceramics. *Int. J. Mol. Sci.* 17 (6), 822. doi:10.3390/ijms17060822

Saade, J., Skienhe, H., Ounsi, H., Matinlinna, J. P., and Salameh, Z. l. (2019). Effect of different combinations of surface treatment on adhesion of resin composite to zirconia. *Clin. Cosmet. Investig. Dent.* 11, 119–129. doi:10.2147/CCIDE.S204986

Seo, S. H., Kim, J. E., Nam, N. E., and Moon, H. S. (2022). Effect of air abrasion, acid etching, and aging on the shear bond strength with resin cement to 3Y-TZP zirconia. *J. Mech. Behav. Biomed. Mat.* 134, 105348. doi:10.1016/j.jmbbm.2022.105348

Serichetaphongse, P., Chitsutheesiri, S., and Chengprapakorn, W. (2022). Comparison of the shear bond strength of composite resins with zirconia and titanium using different resin cements. *J. Prosthodont. Res.* 66 (1), 109–116. doi:10.2186/jpr.JPR_D_20_00299

Sriamporn, T., Thamronganankskul, N., Busabok, C., Poolthong, S., Uo, M., and Tagami, J. (2014). Dental zirconia can be etched by hydrofluoric acid. *Dent. Mat. J.* 33 (1), 79–85. doi:10.4012/dmj.2013-243

Tzanakakis, E., Kontonasaki, E., Voyiatzis, G., Andrikopoulos, K., and Tzoutzas, I. (2020). Surface characterization of monolithic zirconia submitted to different surface treatments applying optical interferometry and Raman spectrometry. *Dent. Mat. J.* 39, 111–117. doi:10.4012/dmj.2018-358

Valente, F., Mavriqi, L., and Traini, T. (2020). Effects of 10-MDP based primer on shear bond strength between zirconia and new experimental resin cement. *Mater. (Basel)* 13 (1), 235. doi:10.3390/ma13010235

Wang, C. (2019). Research progress on surface treatment methods before bonding of zirconia ceramics. *Adhesion* 40 (03), 33–36+54.

Wei, M., Zhu, H., Liang, Z. R., Jiang, Y. L., and Chen, J. F. (2022). Effect of different hot acid solution etching treatment on the bonding strength and the flexural strength of zirconia. *J. Pract. Stomatology* 5, 1–5. doi:10.3969/j.issn.1001-3733.2022.04.005

Wei, M., Zhu, H., Liang, Z. R., Jiang, Y. L., and Chen, J. F. (2021). The effect of different concentrations of hydrofluoric acid on the bonding strength of zirconia. *J. Pract. Stomatology* 37 (06), 758–761. doi:10.3969/j.issn.1001-3733.2021.06.006

Yu, P., Xue, J., Zhang, X., and Zheng, C. (2016). The influence of zirconia ceramic surface roughness on microbial attachment. *J. Prev. Treat. Stomatological Dis.* 24 (01), 20–25. doi:10.12016/j.issn.2096-1456.2016.01.004

frontiers | Frontiers in Bioengineering and Biotechnology

TYPE Original Research
PUBLISHED 08 September 2022
DOI 10.3389/fbioe.2022.989602

OPEN ACCESS

EDITED BY
Jianxun Ding,
Changchun Institute of Applied Chemistry (CAS), China

REVIEWED BY
Jun Yue,
Sun Yat-sen University, China
Lesan Yan,
Wuhan University of Technology, China

*CORRESPONDENCE
Wanguo Liu,
liuwanguo6016@jlu.edu.cn
Rui Gu,
gurui@jlu.edu.cn

SPECIALTY SECTION
This article was submitted to Biomaterials, a section of the journal Frontiers in Bioengineering and Biotechnology

RECEIVED 08 July 2022
ACCEPTED 23 August 2022
PUBLISHED 08 September 2022

CITATION
Wang Y, Luo W, Lin F, Liu W and Gu R (2022), Epigallocatechin-3-gallate selenium nanoparticles for neuroprotection by scavenging reactive oxygen species and reducing inflammation. *Front. Bioeng. Biotechnol.* 10:989602. doi: 10.3389/fbioe.2022.989602

Epigallocatechin-3-gallate selenium nanoparticles for neuroprotection by scavenging reactive oxygen species and reducing inflammation

Yiming Wang, Wenqi Luo, Feng Lin, Wanguo Liu* and Rui Gu*

Department of Orthopaedic Surgery, China-Japan Union Hospital of Jilin University, Changchun, China

Purpose: Spinal cord injury (SCI) is a severely crippling injury. Scavenging reactive oxygen species (ROS) and suppressing inflammation to ameliorate secondary injury using biomaterials has turned into a promising strategy for SCI recuperation. Herein, epigallocatechin-3-gallate selenium nanoparticles (EGCG-Se NP) that scavenge ROS and attenuate inflammation were used for neuroprotection in SCI.

Methods: EGCG-Se NP were arranged using a simple redox framework. The size, morphology, and chemical structure of the EGCG-Se NP were characterized. The protective effect of EGCG-Se NP for neuroprotection was examined in cell culture and in an SCI rat model.

Results: EGCG-Se NP could promptly scavenge excess ROS and safeguard PC12 cells against H_2O_2-induced oxidative harm *in vitro*. After intravenous delivery in SCI rats, EGCG-Se NP significantly improved locomotor capacity and diminished the injury region by safeguarding neurons and myelin sheaths. Component studies showed that the main restorative impact of EGCG-Se NP was due to their ROS-scavenging and anti-inflammatory properties.

Conclusion: This study showed the superior neuroprotective effect of EGCG-Se NP through ROS sequestration and anti-inflammatory capabilities. EGCG-Se NP could be a promising and effective treatment for SCI.

KEYWORDS

spinal cord injury, neuroprotection, epigallocatechin-3-gallate, selenium nanoparticle, reactive oxygen species, inflammation

Introduction

Spinal cord injury (SCI) can cause irreversible neurological deficits and can affect the bladder, gut, and sexual capacity, bringing about a critical decrease to quality of life, SCI is commonly induced by trauma or sudden external force, termed traumatic SCI, and is typically occurring in car accidents, high falls, sports and other accidents

(Ahuja et al., 2017b; Ropper and Ropper, 2017; Zrzavy et al., 2021). SCI includes primary injury and downstream harmful effects, referred to as "secondary injury," which exasperates the underlying effect and causes neighboring neuron death (Andrabi et al., 2020). A significant feature of secondary injury is that excess reactive oxygen species (ROS) are created in the damaged spinal cord (Kim et al., 2017; Song et al., 2019). In addition, overproduction of ROS can cause significant oxidative harm to biomolecules, including lipids, proteins, and DNA, which not only increases the infiltration of macrophages and neutrophils into the area but also activates microglia in the injured spinal cord (Ahuja et al., 2017b). These immune cells release inflammatory cytokines, like TNF-α and IL-6, in addition to ROS, thereby enhancing cell invasion into the injured spinal cord and increasing inflammation (Ahuja et al., 2017a; Desai et al., 2017; Kim et al., 2017). ROS overproduction is considered a pivotal part of the cascade of secondary injury in SCI (Kim et al., 2017; Li et al., 2019; Zhang et al., 2021). Therefore, scavenging ROS and suppressing inflammation to improve the microenvironment after injury is vital for SCI treatment (Xiao et al., 2020; Yang et al., 2020; Zhang et al., 2020; Zrzavy et al., 2021).

To this end, different kinds of antioxidative materials had been investigated for their neuroprotective properties in preclinical SCI models (Li et al., 2019; Luo et al., 2020; Zhang et al., 2021; Cui et al., 2022; Liu et al., 2022). Zhang et al. showed that lipid-polymer nanoparticles (NP) with high ROS-scavenging capacity alleviated long-haul secondary injury in a clinically applicable rodent SCI model (Zhang et al., 2021). Li et al. showed that tetramethyl pyrazine-stacked NP had significant antioxidant and anti-inflammatory properties which could forestall secondary injury and improve locomotor abilities (Li et al., 2021). In addition, release of antioxidant enzymes, which are effective ROS foragers, to the site of injury could alleviate SCI-induced oxidative pressure and tissue damage (Nukolova et al., 2018; Andrabi et al., 2020). Researchers have indicated that infusion of cerium oxide NP into the injured spinal cord of rats could decrease ROS levels, lessen irritation and apoptosis, and improve locomotor practical recovery (Kim et al., 2017). The ROS-scavenging nitroxide radical 2,2,6,6-tetramethylpiperidin-1-oxyl (TEMPO) has been attached to the side chains of polymers to control ROS levels. Zhang et al. integrated a hydrogel with TEMPO and hyaluronic acid, which furthered neuroprotection and recuperation for SCI (Zhang et al., 2020).

Selenium (Se) is a minor but significant element in human health (Rao et al., 2019). The main function of Se is through glutathione peroxidase (GPX)-associated defense against oxidative stress (Bai et al., 2017; Cong et al., 2019). Moreover, studies have recognized that Se has neuroprotective impacts in the central nervous system, with critical advantages against neurodegenerative diseases (Zhai et al., 2017; Cong et al., 2019; Rao et al., 2019). Previous investigations have also demonstrated that Se could prevent secondary pathological events in severe cases of SCI and reduce functional deficits *via* its antioxidant properties (Li et al., 2011; Zhai et al., 2017; Heller et al., 2019). Se NP has excellent antioxidant properties, low toxicity, and exceptional biocompatibility and degradability (Li et al., 2011; Zhai et al., 2017; Cong et al., 2019).

In the current study, Selenium is an essential component of the antioxidant system *in vivo*. The selenium-doped carbon quantum dots (Se-CQDs) constructed in our previous work exhibited efficacy in protecting cells from lipid peroxidation damage and inflammation regulation in an animal model of SCI (Luo et al., 2020). In light of the above-mentioned work, the present study encapsulated selenium nanoparticles by epigallocatechin-3-gallate (EGCG), which not only endowed the nanoparticles with excellent solubility and biocompatibility, but also possessed more potent antioxidant and anti-inflammatory properties, opening up a new avenue for SCI therapy (Chen et al., 2021; Lee et al., 2021; Ma et al., 2021). EGCG -Se NPs were prepared to ameliorate secondary injury by scavenging ROS and suppressing inflammation in the injured spinal cord (Figure 1). EGCG-Se NP were integrated through a simple redox response using EGCG as a stabilizer and capping agent as already reported (Zhang et al., 2010). EGCG-Se NP had great biocompatibility and exceptional ROS-scavenging properties. *In vivo* experiments, treatment with EGCG-Se NP showed promising effects on neurological capacity in terms of improvement of secondary injury, altogether presenting an effective agent for the treatment of SCI and possibly other ROS-related diseases.

Materials and methods

Materials

EGCG and selenious acid were obtained from Shanghai Macklin Biochemical (Shanghai, China), 3-(4,5-dimethylthiazol-2-yl)-2,5-diphenyl tetrazolium bromide (MTT) and 4′,6-diamidino-2-phenylindole dihydrochloride (DAPI) were obtained from Solarbio Science & Technology (Beijing, China), sodium ascorbate was obtained from Aladdin Bio-Chem Technology (Shanghai, China), and Dulbecco's modified Eagle's medium (DMEM) and fetal bovine serum were obtained from Thermo Fisher Scientific (Waltham, MA). Anti-Iba-1, anti-caspase 3, anti-NeuN, anti-GFAP, and anti-GPX 1 antibody were bought from Sigma-Aldrich (St. Louis, MO). Anti-CD68, anti-NF200, and anti-superoxide dismutase (SOD) antibodies were bought from Abcam (Cambridge, United Kingdom). Hydrogen peroxide (H_2O_2, 30 wt% in water) was bought from Shanghai Macklin Biochemical.

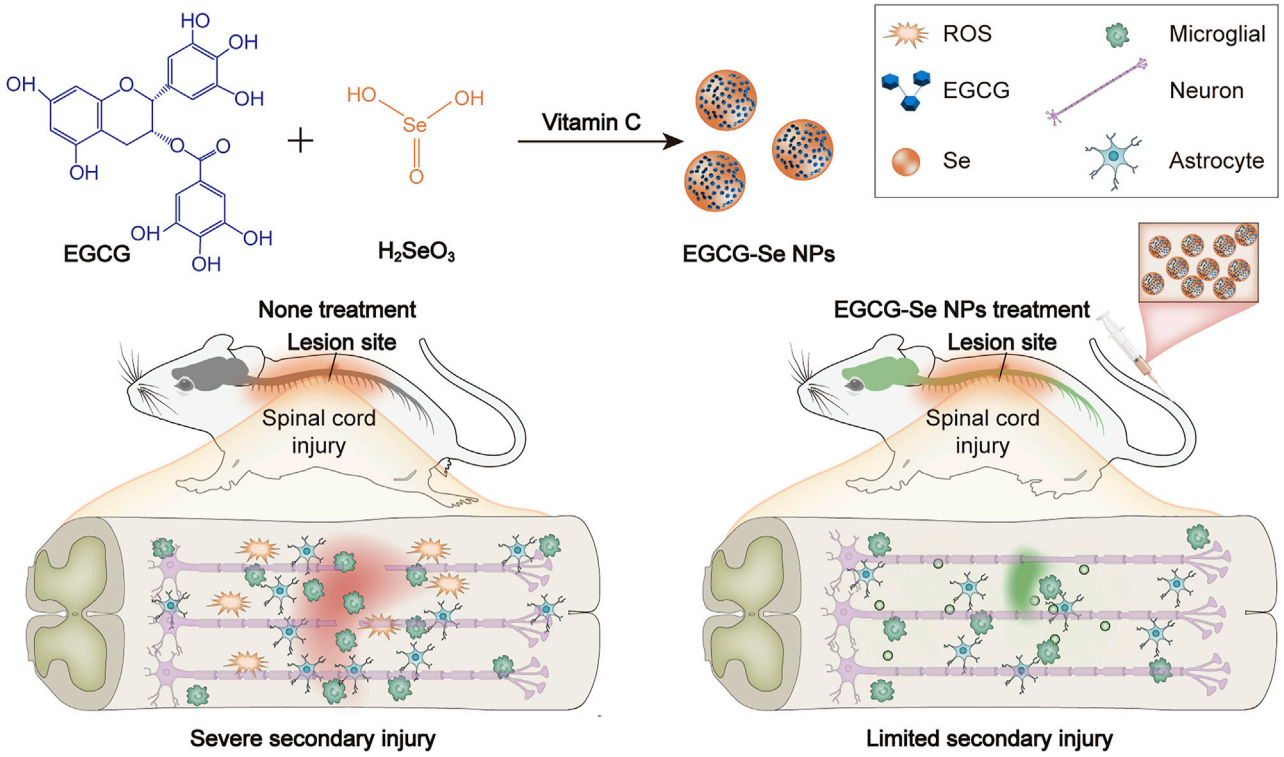

FIGURE 1
Preparation of epigallocatechin-3-gallate selenium nanoparticles (EGCG-Se NP) for treatment of spinal cord injury by scavenging reactive oxygen species (ROS) and suppressing inflammation.

EGCG-Se NP preparation and characterization

EGCG-Se NP were prepared as previously described (Zhang et al., 2010). Briefly, 2.75 g of EGCG (6 mmol) and 0.129 g of selenious acid (1 mmol) were added to 4 ml of 75% ethanol aqueous solution and stirred to completely dissolve. Then, 10 ml of sodium ascorbate solution (5 M) were dripped into the mixture, and the reaction took place overnight in a nitrogen atmosphere. After dialysis and lyophilization, EGCG-Se NP was obtained.

The size distribution of EGCG-Se NP was assessed with a ZEN3600 instrument (Malvern, Worcestershire, United Kingdom). Transmission electron microscopy (TEM) images were obtained with a JEM-1011 microscope (JEOL, Tokyo, Japan) at an accelerating voltage of 100 kV. X-ray photoelectron spectroscopy was performed with an X-ray surface photoelectron spectrometer (Thermo ESCALAB 250, United Kingdom). The Fourier transform infrared spectra (FT-IR) and ultraviolet-visible absorption spectra were acquired utilizing a Win-IR spectrometer (Bio-Rad, Hercules, CA) and a UV-Lambda365 spectrophotometer (PerkinElmer, Waltham, MA), respectively.

In Vitro antioxidant effects of EGCG-Se NP

The test configuration was listed below: control group: water (2 ml), diphenylpicrylhydrazyl (DPPH) anhydrous ethanol solution (0.4 mM, 2 ml); experimental group: EGCG-Se NP (1.25–20 μg/ml, 2 ml), DPPH anhydrous ethanol solution (0.4 mm, 2 ml); blank group: EGCG-Se NP (1.25–20 μg/ml, 2 ml), absolute ethanol (2 ml). The background was adjusted with a combination of water (2 ml) and anhydrous ethanol (2 ml). All groups were cultured in the dark for 30 min and the absorbance at 517 nm was measured with a Bio-Rad 680 microplate reader. The free radical-scavenging rate (%) was calculated by this equation: scavenging rate (%) = (1 − (absorbance value of the experimental group − absorbance value of the blank group)/absorbance value of the control) × 100.

Cytotoxicity and protection from H_2O_2-Induced oxidative stress *in vitro*

PC12 cells were obtained from the Cell Bank of the Chinese Academy of Sciences (Shanghai, China), and BV2 microglia were purchased from BNCC (Beijing, China). The cytotoxicity of

EGCG-Se NP in PC12 cells was assessed via an MTT test. Briefly, PC12 cells were cultured in 96-well plates at 7,000 cells/well and incubated overnight. Then, the medium was aspirated and 200 μL of new medium containing EGCG-Se NP with various concentrations were added. After incubating for 24 or 48 h, the MTT test was performed following the standard method. The absorbance of all was measured at 490 nm.

To investigate the protective properties of EGCG-Se NP in H_2O_2-induced oxidative stress, PC12 cells were cultured in 96-well plates at 7,000 cells/well in 180 μL of DMEM and incubated for 24 h. The media was pretreated with indicated concentrations (0–100 μg/ml) of EGCG-Se NP or phosphate-buffered saline (PBS) for 30 min. Then, the media was incubated with 500 μm H_2O_2 for 24 h. Cell viability was measured with the MTT test using a Bio-Rad 680 microplate reader and live/dead cell staining using a confocal laser scanning microscope (LSM780; Carl Zeiss Meditec, Jena, Germany). The live cell numbers were determined with ImageJ (National Institutes of Health, Bethesda, MD). The levels of ROS in PC12 cells incubated with EGCG-Se NP were quantified by estimating the fluorescence intensity with 2′,7′-dichlorofluorescein diacetate (DCFH-DA; Sigma-Aldrich) *via* confocal laser scanning microscopy.

In Vitro anti-inflammatory effects of EGCG-Se NP

The anti-inflammatory ability of EGCG-Se NP was assessed by an enzyme-linked immunosorbent assay (ELISA). BV2 cells were seeded in 6-well plates at a density of 1.5×10^5 cells per well and cultured for 24 h. After that, lipopolysaccharide (LPS) was added to stimulate cells for 30 min. Then, an equal volume of PBS or EGCG-Se NP were added to the cell culture medium (final concentration of NP, 10 μg/ml). After 24 h, the supernatant was collected and pro-inflammatory cytokines were measured by ELISA.

Rat model of SCI

Adult Sprague-Dawley rats (inbred strain, female, 200–250 g) were bought from Liaoning Changsheng Biotechnology Co., Ltd. Rats were housed with sufficient water and food in a 12-h/12-h light-dark cycle environment and under controlled temperature (23 ± 2°C). The Animal Ethics Committee of Jilin University approved the animal protocols (No. SY202103013). We used the weight-drop SCI model (Lin et al., 2022). In simple terms, rats were deeply anaesthetized with pentobarbitone sodium, and thoracic laminectomy was performed at the T10 level. The rats received a moderate contusion injury (40 g weight, 50 mm height) to expose the spinal cord at T10 using an impactor. Following a medical procedure, the rats were returned to their enclosures with plenty of water and food. Intraperitoneal injections of sodium ampicillin (80 mg/kg) were performed for 5 days (Zhang et al., 2021). The bladder was squeezed two times per day until there was no more than 0.5 ml urine per day.

Locomotor function assessment

The rats were grouped as follows: a control group without any surgery, and five groups treated with either saline, methylprednisolone sodium succinate (MP), 9.5 mg/kg EGCG, 10 mg/kg EGCG-Se (EGCG-Se high-dose group, EGCG-Se H), or 5 mg/kg EGCG-Se (EGCG-Se low-dose group, EGCG-Se L) after surgery. The restoration of hind limb motor function was assessed by the Basso, Beattie, and Bresnahan (BBB) motor rating score. The scores were finalized when both independent researchers who conducted the tests agreed. The recovery time of postoperative urinary function was also recorded.

Histological analysis and immunofluorescence

At a predetermined time, the rats were sacrificed by excessive anesthesia and perfused with 0.9% saline followed by 4% paraformaldehyde. Spinal cord tissue (2 cm fragments) and other organs were collected, embedded in paraffin, and sectioned coronally. Hematoxylin-eosin (H&E) and Luxol fast blue (LFB, 0.1%) staining were performed, and then sections were imaged under a Panoramic 1,000 optical microscope (3DHISTECH, Budapest, Hungary). The spinal cord was then dissected, cut into 1-mm^3 sheets, post-immobilized overnight in 2.5% glutaraldehyde at 4°C, transferred to osmication (90 min) and dehydration (140 min), and then uranyl acetate and lead citrate TEM (HT7700, Hitachi) was used to evaluate the restorative effect on demyelination. The number of myelin sheaths was evaluated using ImageJ. Immunofluorescence staining assays were also conducted as follows. The primary antibodies (NeuN, 1:500; NF200, 1:200; GFAP, 1:1,000; Iba-1, 1:200; CD68, 1:200; caspase 3, 1:1,000; GPX 1, 1:200; SOD, 1:200) were blocked (3% bovine serum albumin) for 1 h and then incubated overnight at 4°C. The sections were washed 3 times, then incubated in the dark with the secondary antibody for 1 h at room temperature before labeling the nucleus with DAPI. Observation of immunofluorescence sections was conducted by confocal laser scanning microscopy.

Statistical analysis

All numeric data were presented as mean ± standard deviation. Repeated-measures one-way analysis of variance or t-tests were used in GraphPad Prism (version 8.0.2; GraphPad

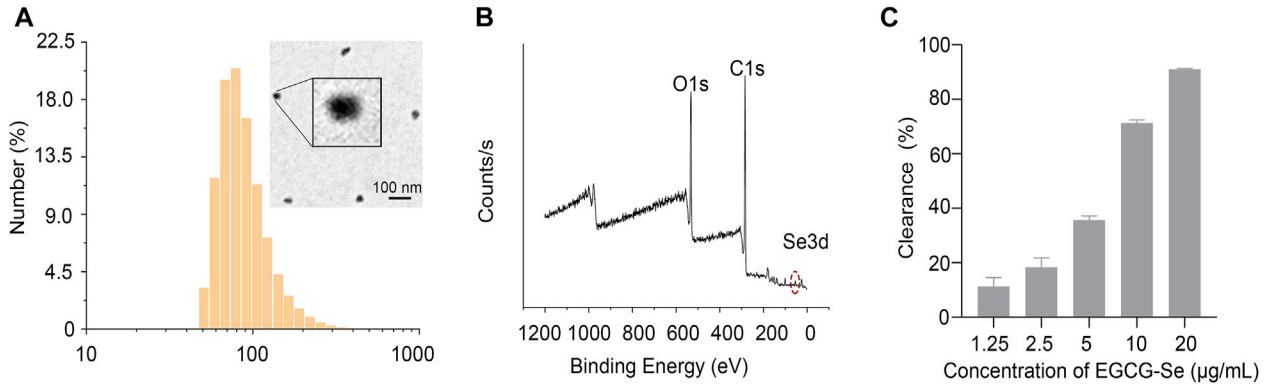

FIGURE 2
Characterization of epigallocatechin-3-gallate selenium nanoparticles (EGCG-Se NP). **(A)** EGCG-Se NP size distribution was detected by dynamic laser scattering and morphological image of an EGCG-Se NP was obtained via transmission electron microscopy. Scale bar = 100 nm. **(B)** X-ray photoelectron spectroscopy spectrum of EGCG-Se NP. **(C)** Clearance of diphenyl picrylhydrazyl by EGCG-Se NP.

Software, San Diego, CA). Significance was determined at $p < 0.05$.

Results and discussion

Preparation and characterization of EGCG-Se NP

The experimental design is described in Figure 1. First, EGCG-Se NP were prepared as per previously described (Zhang et al., 2010). The hydrodynamic particle size of the EGCG-Se NP was 91.3 ± 35.7 nm. Morphological TEM images of EGCG-Se NP show particles with a rounded shape, confirming their successful synthesis (Figure 2A). Moreover, the typical Se 3 d peak of Se (0) at 55 eV and the O1s peak of the hydroxyl group of EGCG were detected at 532 eV, indicating the successful combination of EGCG and Se (Figure 2B). According to the results of ICP-MS, the selenium content in EGCG-Se NPs is about 4.7%. FT-IR was used to further confirm this combination of EGCG and Se; the stretching vibration peaks of −OH, O=C−O, and C−O were displayed at 3,360, 1,620, and 1,150 cm^{-1}, which further confirmed that EGCG was combined with Se (Supplementary Figure S1) (Huang et al., 2019). In addition, the characteristic peak of the −OH group in EGCG alone at 3,360 cm^{-1} is higher relative to that of EGCG-Se NPs, indicating that EGCG is conjugated to the Se surface through this functional group. Together, these results indicate the successful synthesis of EGCG-Se NP. Given the inconvenient impacts of abundance ROS (Wiegman et al., 2015; Choi et al., 2019; Cong et al., 2019; Ashrafizadeh et al., 2020; Rosenkrans et al., 2020), we evaluated the ROS-scavenging capability of EGCG-Se NP *via* the DPPH test. As shown in Figure 2C and Supplementary Figure S2, EGCG-Se NP effectively removed ROS in a dose-dependent manner, thus demonstrating their potential to scavenge ROS. The effective scavenging ability of EGCG-Se NP is attributed to the oxidation of phenolic hydroxyl groups in the NP induced by ROS (Lee et al., 2021). This ROS scavenging ability enables EGCG-Se NP to protect cells against oxidative damages, which may inhibit the inflammatory response and mitigate the secondary injury in spinal cord injury.

Biocompatibility and antioxidant effect of EGCG-Se NP

To assess the biocompatibility of EGCG-Se NP, cytotoxicity tests were performed. PC12 cell viability was assessed after exposure to different concentrations of EGCG-Se NP, which exhibited no observable cytotoxicity up to a concentration of 100 μg/ml (Supplementary Figure S3). To mimic oxidative damage of cells induced by ROS, different concentrations of H_2O_2 were added to the medium and the number of dead PC12 cells were measured for each (Figure 3A). As shown in Figure 3B, EGCG-Se NP prevented PC12 cell death in a dose-dependent manner. The protective ability of EGCG-Se NP against H_2O_2-induced cell death was further affirmed by live/dead cell staining, whereby the number of viable cells significantly increased upon treatment with EGCG-Se NP (Figure 3C; Supplementary Figure S4), consistent with the cytotoxicity tests. Next, intracellular ROS levels were estimated in different treatments. As shown in Figure 3D; Supplementary Figure S5, the fluorescence intensity of dichlorofluorescein diacetate (DCF) significantly decreased with EGCG-Se NP treatment. This indicated that the ROS levels were effectively reduced by EGCG-Se NP, consistent with the results in Figures 2C, 3B. These results confirmed that EGCG-Se NP can protect PC12 cells from H_2O_2-induced damage by effectively scavenging

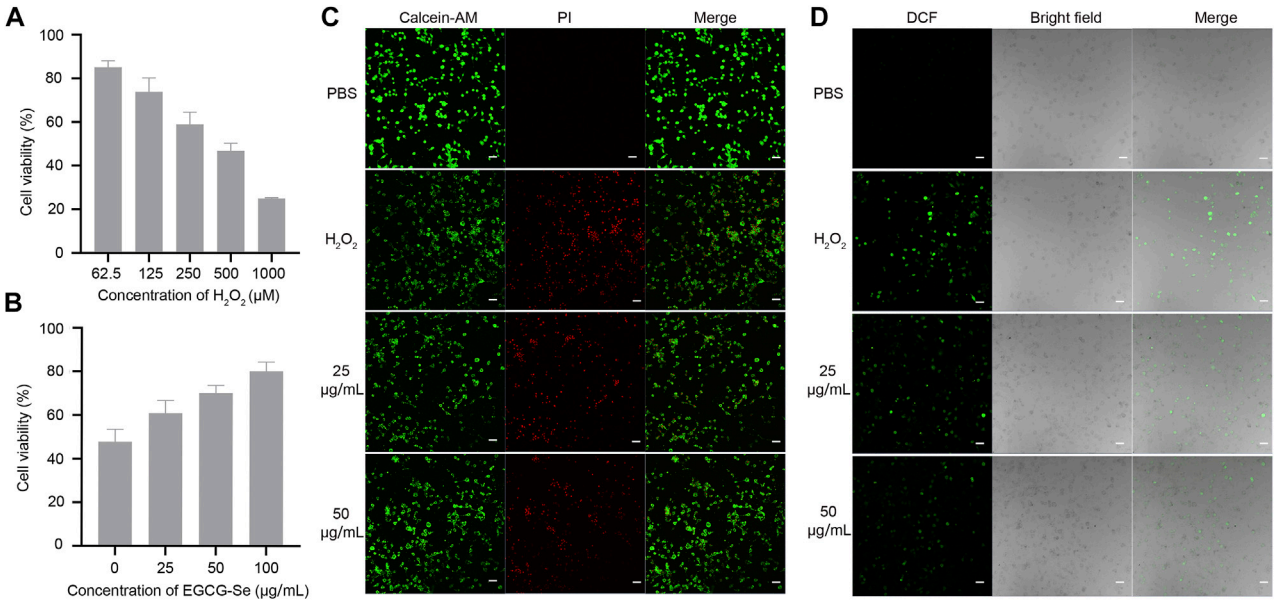

FIGURE 3
Epigallocatechin-3-gallate selenium nanoparticles (EGCG-Se NP) can protect PC12 cells from H_2O_2-induced damage. **(A)** H_2O_2-induced damage effect of PC12 cells. **(B)** EGCG-Se NP increased PC12 cell viability under 500 μm H_2O_2-induced oxidative damage in a dose-dependent manner. **(C)** Live/dead staining of PC12 cells under different conditions. Scale bar = 20 μm. **(D)** Dichlorofluorescein (DCF) diacetate staining to detect intracellular reactive oxygen species in PC12 cells. PBS, phosphate-buffered saline; PI, propidium iodide.

ROS. Furthermore, LPS-activated microglia were tested to evaluate the anti-inflammatory ability of EGCG-Se NP. TNF-α and IL-6 levels were downregulated after treatment with EGCG-Se NP compared to the LPS-treated groups (Supplementary Figure S6). The data indicated that EGCG-Se NP readily reduced the inflammatory microglial response by scavenging ROS (Kim et al., 2017).

Functional recovery of SCI rats following treatment

Considering that EGCG-Se NP can scavenge ROS and suppress inflammation *in vitro*, we examined the neuroprotective effect of EGCG-Se NP after acute SCI in a T10 contusion rat model. A locomotor function study was conducted to determine whether EGCG-Se NP could improve lower extremity motor function in injured animals. First, five or 10 mg/kg EGCG-Se NP, 0.9% saline, 9.5 mg/kg EGCG, or 30 mg/kg MP were given intravenously within 5 min after injury. According to the previous study and the ICP-MS results of EGCE-Se NP, we chose the concentration of EGCG-Se NP and EGCG was 10 mg/kg, 9.5 mg/kg, respectively (Cheng et al., 2021). The therapeutic concentration for MP is the clinically recommended therapeutic concentration for spinal cord injury (Ahuja et al., 2017b; Zhang et al., 2018). MP is one of most frequently used drug for clinical treatment of SCI, which has been routinely established as a control group in animal studies (Huang et al., 2020; Lin et al., 2022). The BBB score of rats treated with 10 mg/kg EGCG-Se NP (8.4 ± 0.5) was significantly better than that of the saline group (3.2 ± 0.4) at 8 weeks after surgery (Figure 4A). Moreover, the therapeutic effect of 10 mg/kg EGCG-Se NP was better than that of 5 mg/kg. While rats treated with saline had sweeping hind limbs without weight support, rats treated with EGCG-Se NP could frequently support their weight on their feet and occasionally showed hindlimb coordination with forelimbs (Supplementary Figure S7). In addition, the area of SCI in rats treated with EGCG-Se NP was smaller than that in rats treated with saline (Figure 4B). To comprehensively provide evidence of lower extremity motor function recovery, 3-T magnetic resonance imaging (MRI) was conducted to evaluate the spinal cord changes in each group. T2-weighted MRI demonstrated high signal intensity at the site of injury, presenting as a fluid-filled cyst. Compared with the saline-treated group, rats treated with EGCG-Se NP had better treatment effect, and a more intact spinal cord and smaller cyst volume were observed in the EGCG-Se NP group (Figure 3C). This is in accord with previous studies (Wang et al., 2019a; Wang et al., 2019b).

To understand the anatomical changes involved in the lower extremity motor function recovery, histomorphological changes of the spinal cord were detected by H&E staining at 8 weeks after

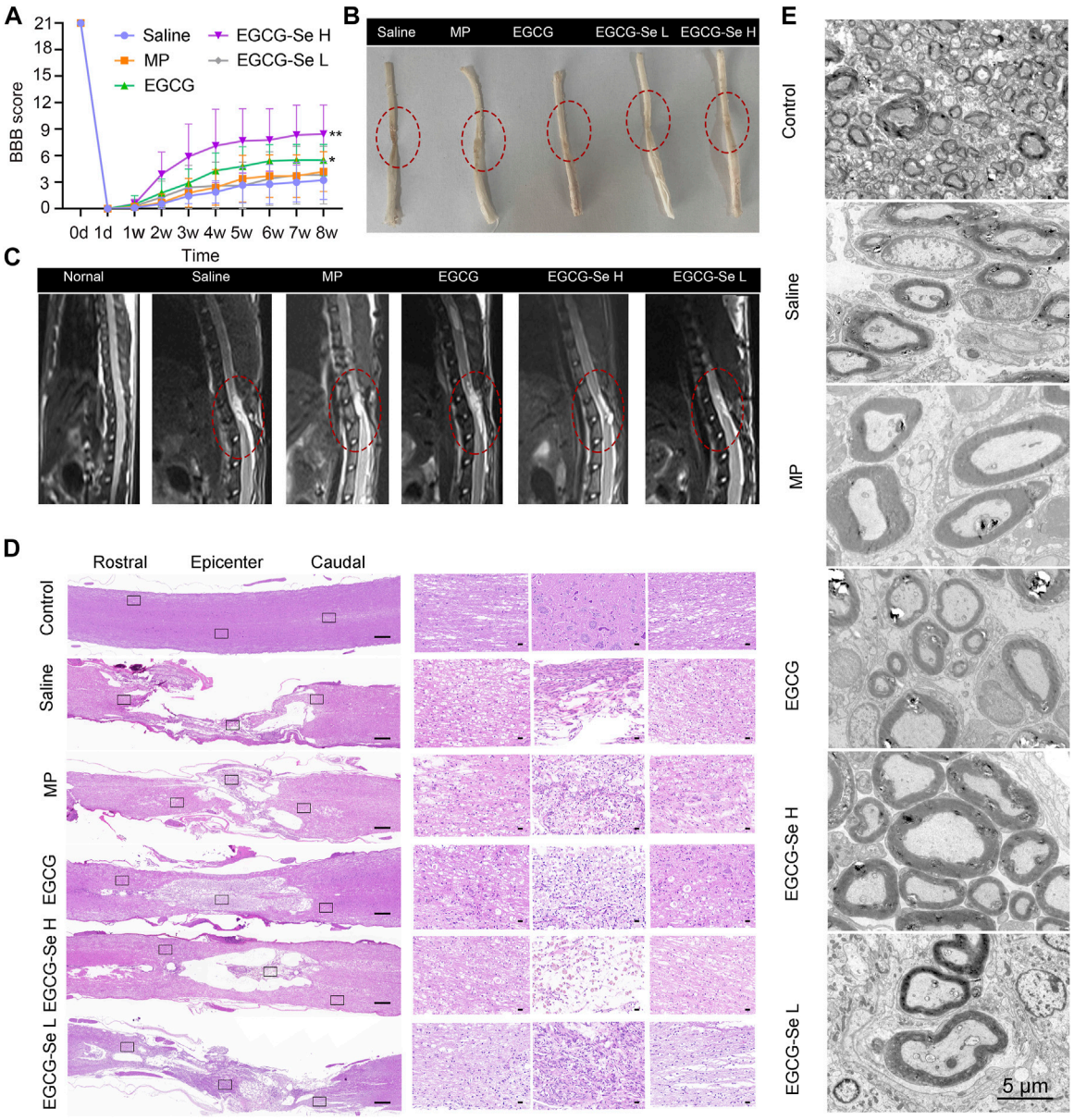

FIGURE 4
Assessment on the recovery of motor function after spinal cord injury (SCI). **(A)** Basso, Beattie, and Bresnahan (BBB) scores of SCI rats treated with saline, methylprednisolone sodium succinate, 9.5 mg/kg epigallocatechin-3-gallate (EGCG), 5 mg/kg EGCG-Se nanoparticles (NP), or 10 mg/kg EGCG-Se NP. $^{**}p < 0.01$, $^{*}p < 0.05$, in comparison with the saline group. **(B)** Images of the spinal cord in different treatment groups 8 weeks after SCI. The lesion of spinal cord injury is indicated in the red dashed circle. **(C)** T2-weighted sagittal magnetic resonance images of the spinal cord following different treatments, in which the red oval represents the injury site. **(D)** Representative hematoxylin-eosin staining images of spinal cord tissue. The black rectangle on the left shows the small image on the right after zooming in. Scale bars are 500 μm (left) and 50 μm (right), respectively. **(E)** Representative transmission electron microscopic images of myelin sheath ultrastructure. Scale bar = 5 μm.

injury. The integrality, as well as the consecutiveness of the spinal cord structure presented the worst in rats treated with saline, and glial proliferation was observed around the large cystic space (Figure 4D). In contrast, the lesion area and lumen volume were reduced in rats treated with 5 mg/kg EGCG-Se NP and MP, while the reduction was more pronounced in the 10 mg/kg EGCG-Se NP group (Figure 4D). Overall, EGCG and MP treatment significantly improved spinal cord continuity and reduced lesion voiding, with 10 mg/kg EGCG-Se NP having the most significant protective effect. SCI often results in severe axonal demyelination and myelin structure injury (Ramer et al., 2014; Silva et al., 2014; Cunha et al., 2020; Floriddia et al., 2020). Next,

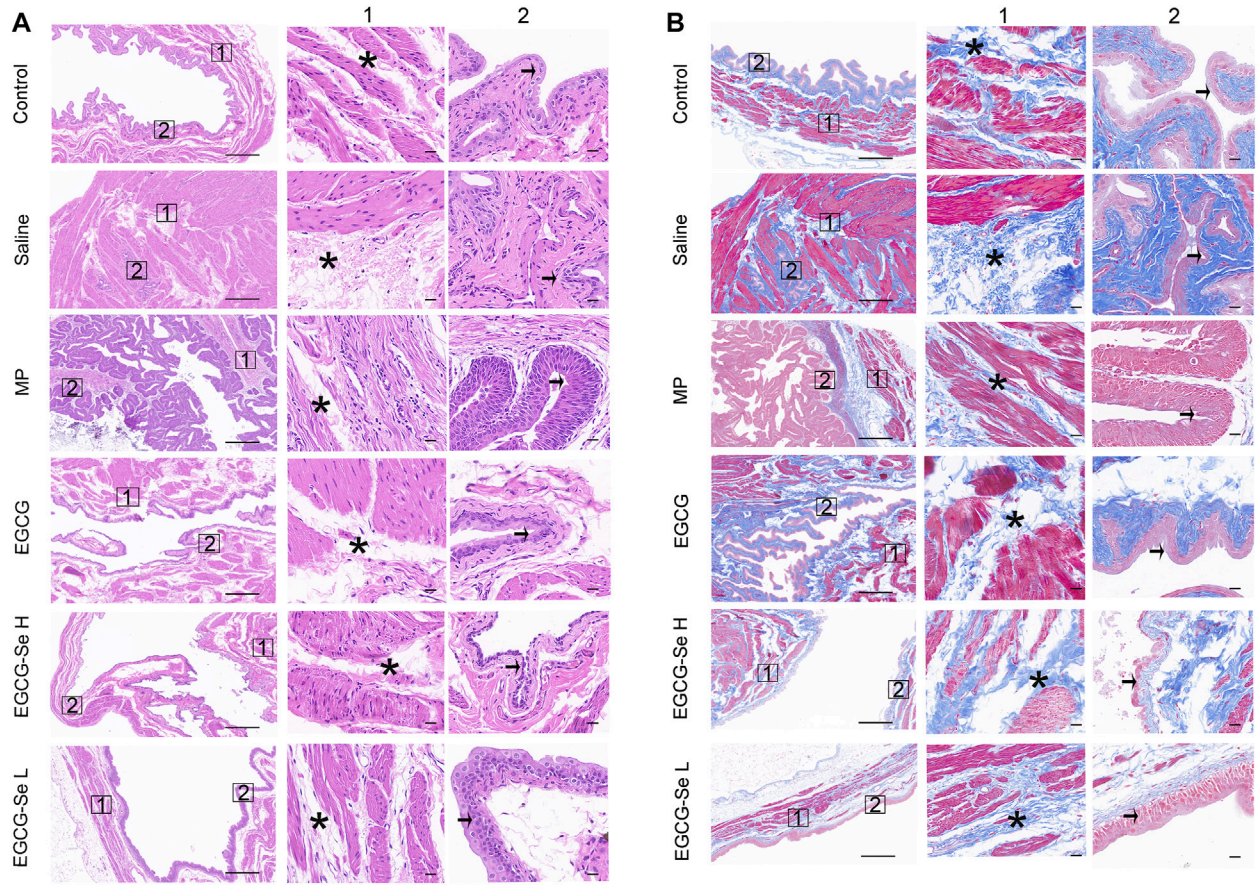

FIGURE 5
Hematoxylin-eosin (H and E) and Masson staining of bladders. **(A)** Representative bladders stained with H&E. Columns 1 and 2 are magnifications of the areas marked by the blue squares in the left column. Pathological changes of the bladder are indicated using asterisks (muscle layer) and arrows (intima). Scale bars are 500 and 50 μm, respectively. **(B)** Representative bladders stained with Masson stain. Columns 1 and 2 are magnifications of the areas marked by the blue squares in the left column. Pathological changes of the bladder are indicated using asterisks (muscle layer) and arrows (intima). Scale bars are 500 and 50 μm, respectively.

we used LFB staining and TEM to evaluate the changes of demyelination and myelin sheath ultrastructure at the lesion site (Supplementary Figure S8; Figure 4E). Compared with the control group, the saline group showed obvious demyelination with damage to the myelin sheath ultrastructure at 8 weeks after injury. Rats treated with EGCG-Se NP had more myelin sheath and more intact ultrastructure in a dose-dependent manner. Compared with the control group, the amount of myelin sheath in the saline group was significantly reduced, while it was significantly increased in the EGCG-Se NP group ($p < 0.001$) (Supplementary Figure S9). In general, the LFB staining and TEM showed that EGCG-Se NP treatment had beneficial effects on demyelination and preservation of nerve fibers in SCI models.

Neurogenic bladder is a complication of SCI the main symptoms were incomplete bladder emptying, chronic urinary retention, and increased bladder pressure lead to renal failure and the bladder will show pathological changes of bladder wall fibrosis and bladder endometriosis (Hamid et al., 2018; Li et al., 2019; Luo et al., 2020). We hypothesized that EGCG-Se NP therapy may benefit bladder tissue protection by reducing secondary injury. As shown in Supplementary Figure S10, the recovery rate of natural urination was faster in rats treated with 10 mg/kg EGCG-Se NP than in those treated with saline. Bladder tissues were stained with H&E and Masson staining to further assess bladder function recovery. In contrast to the saline group, the EGCG-Se NP group revealed significantly limited pathological damage to bladder tissue and reduced levels of bladder wall fibrosis and bladder endometriosis (Figures 5A,B). This may be due to the promoting of neurological recovery and early restoration of spontaneous urination by EGCG-Se NP.SCI results in muscle atrophy of the lower limbs due to a lack of neurotrophic factors (Sangari et al., 2019; Kutschenko et al., 2022). To detect the amyotrophic effect of EGCG-Se NP on SCI in rats, H&E staining, the muscle/weight

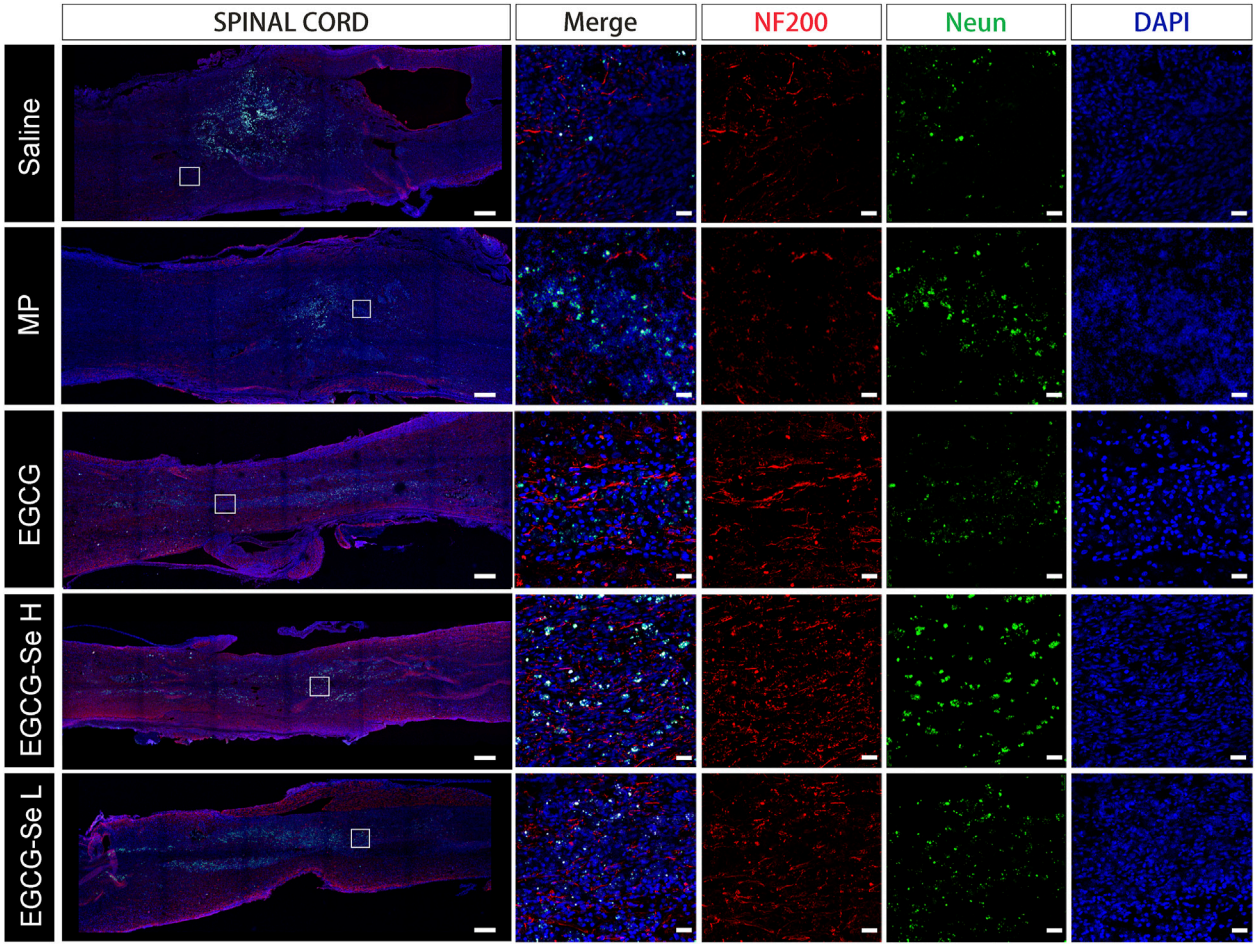

FIGURE 6
Anti-NF200 and anti-NeuN double-staining of different groups at 8 weeks post-injury. Scale bars are 400 μm in the first column and 25 μm in the other columns. MP, methylprednisolone; EGCG, epigallocatechin-3-gallate; L, 5 mg/kg EGCG-Se nanoparticles; H, 10 mg/kg EGCG-Se nanoparticles.

ratio, and Masson staining of the gastrocnemius muscle were evaluated. As shown in Supplementary Figures S11, S12, no significant differences were observed across these groups. The reason may be that the significant lower limb muscle atrophy caused by spinal cord injury occurs 8 weeks after the injury, or even longer. Therefore, the results of this experiment are negative (Koh et al., 2017).

Immunofluorescent characterization of SCI rats after EGCG-Se NP treatment

To detect the neuroprotective effect of EGCG-Se NP in SCI in rats, anti-NF200 and anti-NeuN immunofluorescent staining were performed. Compared with rats treated with 10 mg/kg EGCG-Se NP, the expression levels of NF200 and NeuN were significantly decreased in the saline group (Figure 6), NF200 is a neurofilament protein that provides structural support for axons and regulates axon diameter. NeuN is common in mature neurons. Low levels of expression indicate poor spinal cord recovery, suggesting that high concentrations of EGCG-Se NP have a neuroprotective effect, thus promoting the recovery of spinal cord function in treated animals. Previous studies have reported that scavenging ROS can inhibit the inflammatory response of SCI secondary injury (Ren et al., 2018; Zheng et al., 2019; Bai et al., 2020; Xiao et al., 2020). Thus, we investigated the inflammation suppression activity of EGCG-Se NP on days 1 and 56 *in vivo*. Immunofluorescent staining showed an increase in the number of CD68-positive cells at the injury site in saline-treated rats compared with the control group. By comparison, there were fewer CD68-positive cells in the spinal cords of rats treated with EGCG-Se NP compared with saline (Supplementary Figures S13, S15), suggesting that high concentrations of EGCG-Se NP were effective in reducing

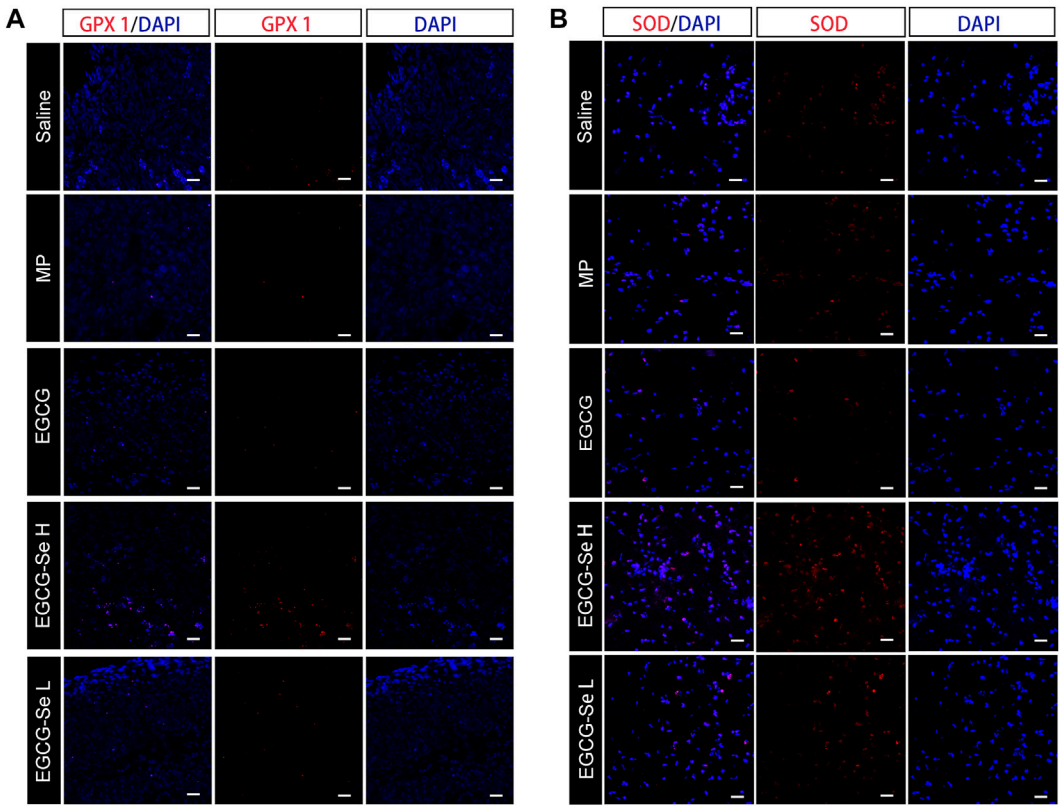

FIGURE 7
Representative immunohistochemical staining of antioxidant enzymes in the injured spinal cord. **(A)** GPX one staining at 8 weeks post-injury. **(B)** SOD staining at 1-day post-injury. Scale bars 25 μm.

inflammation at the site of injury. Studies have shown that eliminating ROS at the site of injury by antioxidant therapy is an effective neuroprotective strategy after acute SCI (Tyler et al., 2013; Wu et al., 2014; Krupa et al., 2019; Zhang et al., 2021). Therefore, to further understand the potential mechanism of the therapeutic effect of EGCG-Se NP, we measured the levels of antioxidant enzymes in rats treated with EGCG-Se NP 1 day and 56 days post-injury. Compared with the saline group, the expression levels of GPX one and SOD in rats treated with 10 mg/kg EGCG-Se NP were significantly increased (Figure 7), indicating that high concentrations of EGCG-Se NP could promote antioxidant enzymes and reduce ROS levels (Cong et al., 2019). The long-term neurological deficits after SCI are partly due to the extensive activation of neurons and oligodendrocyte apoptosis at the injury site (Springer et al., 1999; Ahuja et al., 2017b). To investigate the anti-apoptosis ability of EGCG-Se NP after SCI, cleaved caspase-3 protein expression was detected at the site injury 24 h after injury. Compared to the saline group, the cleaved caspase-3 level in the EGCG-Se NP group was significantly lower (Supplementary Figure S15). These results suggest that EGCG-Se NP have a significant anti-apoptotic effect after SCI, which may explain the effect of EGCG-Se NP on the recovery of motor function in injured rats.

To comprehensively understand the side effects of EGCG-Se NP treatment, liver and kidney functions were analyzed at days 1 and 56 after injury. There were no significant differences in alkaline phosphatase, alanine aminotransferase, blood urea nitrogen, or serum creatinine levels among all groups, suggesting that EGCG-Se NP treatment causes no side effects to the kidney or liver (Supplementary Figure S16). In addition, the biosafety of EGCG-Se NP was further evaluated by H&E staining of the heart, liver, spleen, lung, and kidney, which showed no significant changes in the EGCG-Se NP and EGCG groups (Supplementary Figure S17).

Conclusion

In this study, effective neuroprotection after acute SCI was achieved with EGCG-Se NP treatment through ROS scavenging. *In vitro* studies showed that EGCG-Se NP could effectively protect PC12 cells from oxidative stress damage as well as achieve an effective anti-inflammatory effect. Intravenous

EGCG-Se NP exert a significant anti-inflammatory and neuroprotective role and effectively promoted functional recovery in a rat model of SCI. Furthermore, this study has demonstrated a safe and prospective pathway to incorporate the merits of selenium and EGCG, thus making it a promising therapeutic for the treatment of SCI or other ROS-mediated conditions.

Data availability statement

The raw data supporting the conclusions of this article will be made available by the authors, without undue reservation.

Ethics statement

The animal study was reviewed and approved by the Animal Ethics Committee of Jilin University approval No. SY202103013.

Author contributions

YW: Visualization, Writing—Original Draft, Data Curation, Methodology, Formal analysis WLU: Writing—Original Draft, Methodology FL: Writing—Review and Editing, Resources WLI: Conceptualization, Formal analysis RG: Supervision, Project administration.

Funding

We acknowledge the financial support from the National Natural Science Foundation of China (51803072), Jilin Provincial Science and Technology Program (20200201341JC), Jilin Provincial Finance Program (2019SCZ023, 2018SCZ013, 2021SCZ07).

Acknowledgments

We thanks are due to Chunsheng Xiao with assistance for valuable guidance and proposals.

Conflict of interest

The authors declare that the research was conducted in the absence of any commercial or financial relationships that could be construed as a potential conflict of interest.

Publisher's note

All claims expressed in this article are solely those of the authors and do not necessarily represent those of their affiliated organizations, or those of the publisher, the editors and the reviewers. Any product that may be evaluated in this article, or claim that may be made by its manufacturer, is not guaranteed or endorsed by the publisher.

Supplementary material

The Supplementary Material for this article can be found online at: https://www.frontiersin.org/articles/10.3389/fbioe.2022.989602/full#supplementary-material

References

Ahuja, C. S., Nori, S., Tetreault, L., Wilson, J., Kwon, B., Harrop, J., et al. (2017b). Traumatic spinal cord injury-repair and regeneration. *Neurosurgery* 80, S9–S22. doi:10.1093/neuros/nyw080

Ahuja, C. S., Wilson, J. R., Nori, S., Kotter, M. R. N., Druschel, C., Curt, A., et al. (2017a). Traumatic spinal cord injury. *Nat. Rev. Dis. Prim.* 3, 17018. doi:10.1038/nrdp.2017.18

Andrabi, S. S., Yang, J., Gao, Y., Kuang, Y., and Labhasetwar, V. (2020). Nanoparticles with antioxidant enzymes protect injured spinal cord from neuronal cell apoptosis by attenuating mitochondrial dysfunction. *J. Control. Release* 317, 300–311. doi:10.1016/j.jconrel.2019.12.001

Ashrafizadeh, M., Mohammadinejad, R., Kailasa, S. K., Ahmadi, Z., Afshar, E. G., and Pardakhty, A. (2020). Carbon dots as versatile nanoarchitectures for the treatment of neurological disorders and their theranostic applications: A review. *Adv. Colloid Interface Sci.* 278, 102123. doi:10.1016/j.cis.2020.102123

Bai, J., Zhang, Y., Fan, Q., Xu, J., Shan, H., Gao, X., et al. (2020). Reactive oxygen species-scavenging scaffold with rapamycin for treatment of intervertebral disk degeneration. *Adv. Healthc. Mat.* 9, e1901186. doi:10.1002/adhm.201901186

Bai, K., Hong, B., Hong, Z., Sun, J., and Wang, C. (2017). Selenium nanoparticles-loaded chitosan/citrate complex and its protection against oxidative stress in D-galactose-induced aging mice. *J. Nanobiotechnology* 15, 92. doi:10.1186/s12951-017-0324-z

Chen, Z., Duan, J., Diao, Y., Chen, Y., Liang, X., Li, H., et al. (2021). ROS-responsive capsules engineered from EGCG-Zinc networks improve therapeutic angiogenesis in mouse limb ischemia. *Bioact. Mat.* 6, 1–11. doi:10.1016/j.bioactmat.2020.07.013

Cheng, C. Y., Barro, L., Tsai, S. T., Feng, T. W., Wu, X. Y., Chao, C. W., et al. (2021). Epigallocatechin-3-Gallate-Loaded liposomes favor anti-inflammation of microglia cells and promote neuroprotection. *Int. J. Mol. Sci.* 22, 3037. doi:10.3390/ijms22063037

Choi, B., Soh, M., Manandhar, Y., Kim, D., Han, S. I., Baik, S., et al. (2019). Highly selective microglial uptake of ceria-zirconia nanoparticles for enhanced analgesic treatment of neuropathic pain. *Nanoscale* 11, 19437–19447. doi:10.1039/c9nr02648g

Cong, W., Bai, R., Li, Y. F., Wang, L., and Chen, C. (2019). Selenium nanoparticles as an efficient nanomedicine for the therapy of Huntington's disease. *ACS Appl. Mat. Interfaces* 11, 34725–34735. doi:10.1021/acsami.9b12319

Cui, Z., Feng, Y., Liu, F., Jiang, L., and Yue, J. (2022). 3D bioprinting of living materials for structure-dependent production of hyaluronic acid. *ACS Macro Lett.* 11, 452–459. doi:10.1021/acsmacrolett.2c00037

Cunha, M. I., Su, M., Cantuti-Castelvetri, L., Müller, S. A., Schifferer, M., Djannatian, M., et al. (2020). Pro-inflammatory activation following demyelination is required for myelin clearance and oligodendrogenesis. *J. Exp. Med.* 217, e20191390. doi:10.1084/jem.20191390

Desai, J., Steiger, S., and Anders, H. J. (2017). Molecular pathophysiology of gout. *Trends Mol. Med.* 23, 756–768. doi:10.1016/j.molmed.2017.06.005

Floriddia, E. M., Lourenço, T., Zhang, S., van Bruggen, D., Hilscher, M. M., Kukanja, P., et al. (2020). Distinct oligodendrocyte populations have spatial preference and different responses to spinal cord injury. *Nat. Commun.* 11, 5860. doi:10.1038/s41467-020-19453-x

Hamid, R., Averbeck, M. A., Chiang, H., Garcia, A., Al Mousa, R. T., Oh, S.-J., et al. (2018). Epidemiology and pathophysiology of neurogenic bladder after spinal cord injury. *World J. Urol.* 36, 1517–1527. doi:10.1007/s00345-018-2301-z

Heller, R. A., Seelig, J., Bock, T., Haubruck, P., Grützner, P. A., Schomburg, L., et al. (2019). Relation of selenium status to neuro-regeneration after traumatic spinal cord injury. *J. Trace Elem. Med. Biol.* 51, 141–149. doi:10.1016/j.jtemb.2018.10.006

Huang, G., Lin, Y., Zhang, L., Yan, Z., Wang, Y., and Liu, Y. (2019). Synthesis of sulfur-selenium doped carbon quantum dots for biological imaging and scavenging reactive oxygen species. *Sci. Rep.* 9, 19651. doi:10.1038/s41598-019-55996-w

Huang, H., Young, W., Skaper, S., Chen, L., Moviglia, G., Saberi, H., et al. (2020). Clinical neurorestorative therapeutic guidelines for spinal cord injury (IANR/CANR version 2019). *J. Orthop. Transl.* 20, 14–24. doi:10.1016/j.jot.2019.10.006

Kim, J.-W., Mahapatra, C., Hong, J.-Y., Kim, M. S., Leong, K. W., Kim, H.-W., et al. (2017). Functional recovery of contused spinal cord in rat with the injection of optimal-dosed cerium oxide nanoparticles. *Adv. Sci. (Weinh).* 4, 1700034. doi:10.1002/advs.201700034

Koh, E. S., Kim, H. C., and Lim, J.-Y. (2017). The effects of electromyostimulation application timing on denervated skeletal muscle atrophy. *Muscle Nerve* 56, E154–E161. doi:10.1002/mus.25656

Krupa, P., Svobodova, B., Dubisova, J., Kubinova, S., Jendelova, P., and Machova Urdzikova, L. (2019). Nano-formulated curcumin (Lipodisq™) modulates the local inflammatory response, reduces glial scar and preserves the white matter after spinal cord injury in rats. *Neuropharmacology* 155, 54–64. doi:10.1016/j.neuropharm.2019.05.018

Kutschenko, A., Manig, A., Mönnich, A., Bryl, B., Alexander, C.-S., Deutschland, M., et al. (2022). Intramuscular tetanus neurotoxin reverses muscle atrophy: A randomized controlled trial in dogs with spinal cord injury. *J. Cachexia Sarcopenia Muscle* 13, 443–453. doi:10.1002/jcsm.12836

Lee, S., Lee, J., Byun, H., Kim, S. J., Joo, J., Park, H. H., et al. (2021). Evaluation of the antioxidative and ROS scavenging properties of biomaterials coated with epigallocatechin gallate for tissue engineering. *Acta Biomater.* 124, 166–178. doi:10.1016/j.actbio.2021.02.005

Li, J., Wei, J., Wan, Y., Du, X., Bai, X., Li, C., et al. (2021). TAT-modified tetramethylpyrazine-loaded nanoparticles for targeted treatment of spinal cord injury. *J. Control. Release* 335, 103–116. doi:10.1016/j.jconrel.2021.05.016

Li, L., Xiao, B., Mu, J., Zhang, Y., Zhang, C., Cao, H., et al. (2019). A MnO2 nanoparticle-dotted hydrogel promotes spinal cord repair via regulating reactive oxygen species microenvironment and synergizing with mesenchymal stem cells. *ACS Nano* 13, 14283–14293. doi:10.1021/acsnano.9b07598

Li, Y., Li, X., Wong, Y. S., Chen, T., Zhang, H., Liu, C., et al. (2011). The reversal of cisplatin-induced nephrotoxicity by selenium nanoparticles functionalized with 11-mercapto-1-undecanol by inhibition of ROS-mediated apoptosis. *Biomaterials* 32, 9068–9076. doi:10.1016/j.biomaterials.2011.08.001

Lin, F., Liu, Y., Luo, W., Liu, S., Wang, Y., Gu, R., et al. (2022). Minocycline-Loaded poly(α-lipoic acid)–methylprednisolone prodrug nanoparticles for the combined anti-inflammatory treatment of spinal cord injury. *Int. J. Nanomedicine* 17, 91–104. doi:10.2147/ijn.s344491

Liu, T., Liu, G. T., Zhang, J. H., Ding, Z. F., Li, Y. K., Sigdel, K., et al. (2022). L-Arginine based polyester amide/hyaluronic acid hybrid hydrogel with dual anti-inflammation and antioxidant functions for accelerated wound healing. *Chin. Chem. Lett.* 33, 1880–1884. doi:10.1016/j.cclet.2021.10.022

Luo, W., Wang, Y., Lin, F., Liu, Y., Gu, R., Liu, W., et al. (2020). Selenium-doped carbon quantum dots efficiently ameliorate secondary spinal cord injury via scavenging reactive oxygen species. *Int. J. Nanomedicine* 15, 10113–10125. doi:10.2147/ijn.s282985

Ma, Y., Liu, G., Tang, M., Fang, J., and Jiang, H. (2021). Epigallocatechin gallate can protect mice from acute stress induced by LPS while stabilizing gut microbes and serum metabolites levels. *Front. Immunol.* 12, 640305. doi:10.3389/fimmu.2021.640305

Nukolova, N. V., Aleksashkin, A. D., Abakumova, T. O., Morozova, A. Y., Gubskiy, I. L., Kirzhanova, E. A., et al. (2018). Multilayer polyion complex nanoformulations of superoxide dismutase 1 for acute spinal cord injury. *J. Control. Release* 270, 226–236. doi:10.1016/j.jconrel.2017.11.044

Ramer, L. M., Ramer, M. S., and Bradbury, E. J. (2014). Restoring function after spinal cord injury: Towards clinical translation of experimental strategies. *Lancet Neurol.* 13, 1241–1256. doi:10.1016/s1474-4422(14)70144-9

Rao, S., Lin, Y., Du, Y., He, L., Huang, G., Chen, B., et al. (2019). Designing multifunctionalized selenium nanoparticles to reverse oxidative stress-induced spinal cord injury by attenuating ROS overproduction and mitochondria dysfunction. *J. Mat. Chem. B* 7, 2648–2656. doi:10.1039/c8tb02520g

Ren, H., Chen, X., Tian, M., Zhou, J., Ouyang, H., and Zhang, Z. (2018). Regulation of inflammatory cytokines for spinal cord injury repair through local delivery of therapeutic agents. *Adv. Sci. (Weinh).* 5, 1800529. doi:10.1002/advs.201800529

Ropper, A. E., and Ropper, A. H. (2017). Acute spinal cord compression. *N. Engl. J. Med.* 376, 1358–1369. doi:10.1056/nejmra1516539

Rosenkrans, Z. T., Sun, T., Jiang, D., Chen, W., Barnhart, T. E., Zhang, Z., et al. (2020). Selenium-doped carbon quantum dots act as broad-spectrum antioxidants for acute kidney injury management. *Adv. Sci. (Weinh.)* 7, 2000420. doi:10.1002/advs.202000420

Sangari, S., Lundell, H., Kirshblum, S., and Perez, M. A. (2019). Residual descending motor pathways influence spasticity after spinal cord injury. *Ann. Neurol.* 86, 28–41. doi:10.1002/ana.25505

Silva, N. A., Sousa, N., Reis, R. L., and Salgado, A. J. (2014). From basics to clinical: A comprehensive review on spinal cord injury. *Prog. Neurobiol.* 114, 25–57. doi:10.1016/j.pneurobio.2013.11.002

Song, Y. H., Agrawal, N. K., Griffin, J. M., and Schmidt, C. E. (2019). Recent advances in nanotherapeutic strategies for spinal cord injury repair. *Adv. Drug Deliv. Rev.* 148, 38–59. doi:10.1016/j.addr.2018.12.011

Springer, J. E., Azbill, R. D., and Knapp, P. E. (1999). Activation of the caspase-3 apoptotic cascade in traumatic spinal cord injury. *Nat. Med.* 5, 943–946. doi:10.1038/11387

Tyler, J. Y., Xu, X. M., and Cheng, J. X. (2013). Nanomedicine for treating spinal cord injury. *Nanoscale* 5, 8821–8836. doi:10.1039/c3nr00957b

Wang, X.-J., Peng, C.-H., Zhang, S., Xu, X.-L., Shu, G.-F., Qi, J., et al. (2019b). Polysialic-acid-based micelles promote neural regeneration in spinal cord injury therapy. *Nano Lett.* 19, 829–838. doi:10.1021/acs.nanolett.8b04020

Wang, X.-J., Shu, G.-F., Xu, X.-L., Peng, C.-H., Lu, C.-Y., Cheng, X.-Y., et al. (2019a). Combinational protective therapy for spinal cord injury medicated by sialic acid-driven and polyethylene glycol based micelles. *Biomaterials* 217, 119326. doi:10.1016/j.biomaterials.2019.119326

Wiegman, C. H., Michaeloudes, C., Haji, G., Narang, P., Clark, C. J., Russell, K. E., et al. (2015). Oxidative stress-induced mitochondrial dysfunction drives inflammation and airway smooth muscle remodeling in patients with chronic obstructive pulmonary disease. *J. Allergy Clin. Immunol.* 136, 769–780. doi:10.1016/j.jaci.2015.01.046

Wu, W., Lee, S.-Y., Wu, X., Tyler, J. Y., Wang, H., Ouyang, Z., et al. (2014). Neuroprotective ferulic acid (FA)-glycol chitosan (GC) nanoparticles for functional restoration of traumatically injured spinal cord. *Biomaterials* 35, 2355–2364. doi:10.1016/j.biomaterials.2013.11.074

Xiao, L., Wei, F., Zhou, Y., Anderson, G. J., Frazer, D. M., Lim, Y. C., et al. (2020). Dihydrolipoic acid-gold nanoclusters regulate microglial polarization and have the potential to alter neurogenesis. *Nano Lett.* 20, 478–495. doi:10.1021/acs.nanolett.9b04216

Yang, L., Conley, B. M., Cerqueira, S. R., Pongkulapa, T., Wang, S., Lee, J. K., et al. (2020). Effective modulation of CNS inhibitory microenvironment using bioinspired hybrid-nanoscaffold-based therapeutic interventions. *Adv. Mat.* 32, e2002578. doi:10.1002/adma.202002578

Zhai, X., Zhang, C., Zhao, G., Stoll, S., Ren, F., and Leng, X. (2017). Antioxidant capacities of the selenium nanoparticles stabilized by chitosan. *J. Nanobiotechnology* 15, 4. doi:10.1186/s12951-016-0243-4

Zhang, S., Wang, X. J., Li, W. S., Xu, X. L., Hu, J. B., Kang, X. Q., et al. (2018). Polycaprolactone/polysialic acid hybrid, multifunctional nanofiber scaffolds for treatment of spinal cord injury. *Acta Biomater.* 77, 15–27. doi:10.1016/j.actbio.2018.06.038

Zhang, T., Lin, F., Liu, W., Liu, Y., Guo, Z., Xiao, C., et al. (2021). Reactive oxide species-scavenging lipid-polymer nanoparticles for neuroprotection after spinal cord injury. *Appl. Mat. Today* 24, 101109. doi:10.1016/j.apmt.2021.101109

Zhang, Y., Li, L., Mu, J., Chen, J., Feng, S., and Gao, J. (2020). Implantation of a functional TEMPO-hydrogel induces recovery from rat spinal cord transection through promoting nerve regeneration and protecting bladder tissue. *Biomater. Sci.* 8, 1695–1701. doi:10.1039/c9bm01530b

Zhang, Y., Wang, J., and Zhang, L. (2010). Creation of highly stable selenium nanoparticles capped with hyperbranched polysaccharide in water. *Langmuir* 26, 17617–17623. doi:10.1021/la1033959

Zheng, J., Fan, R., Wu, H., Yao, H., Yan, Y., Liu, J., et al. (2019). Directed self-assembly of herbal small molecules into sustained release hydrogels for treating neural inflammation. *Nat. Commun.* 10, 1604. doi:10.1038/s41467-019-09601-3

Zrzavy, T., Schwaiger, C., Wimmer, I., Berger, T., Bauer, J., Butovsky, O., et al. (2021). Acute and non-resolving inflammation associate with oxidative injury after human spinal cord injury. *Brain* 144, 144–161. doi:10.1093/brain/awaa360

frontiers | Frontiers in Bioengineering and Biotechnology

TYPE Review
PUBLISHED 12 September 2022
DOI 10.3389/fbioe.2022.985692

OPEN ACCESS

EDITED BY
Mingqiang Li,
Third Affiliated Hospital of Sun Yat-sen University, China

REVIEWED BY
Shuqiang Huang,
Shenzhen Institutes of Advanced Technology (CAS), China
Yao Li,
Shanghai Jiao Tong University, China
Changyong Chase Cao,
Case Western Reserve University, United States

*CORRESPONDENCE
Dianfu Li,
doctorldf@163.com
Yu Sun,
sunyu@seu.edu.cn
Zaozao Chen,
101012282@seu.edu.cn
Zhongze Gu,
Gu@seu.edu.cn

†These authors have contributed equally to this work

SPECIALTY SECTION
This article was submitted to Biomaterials, a section of the journal Frontiers in Bioengineering and Biotechnology

RECEIVED 04 July 2022
ACCEPTED 08 August 2022
PUBLISHED 12 September 2022

CITATION
Gao W, Wang C, Li Q, Zhang X, Yuan J, Li D, Sun Y, Chen Z and Gu Z (2022), Application of medical imaging methods and artificial intelligence in tissue engineering and organ-on-a-chip.
Front. Bioeng. Biotechnol. 10:985692.
doi: 10.3389/fbioe.2022.985692

Application of medical imaging methods and artificial intelligence in tissue engineering and organ-on-a-chip

Wanying Gao[1†], Chunyan Wang[2†], Qiwei Li[1], Xijing Zhang[3], Jianmin Yuan[3], Dianfu Li[4*], Yu Sun[5*], Zaozao Chen[1*] and Zhongze Gu[1*]

[1]State Key Laboratory of Bioelectronics, School of Biological Science and Medical Engineering, Southeast University, Nanjing, China, [2]State Key Laboratory of Space Medicine Fundamentals and Application, Chinese Astronaut Science Researching and Training Center, Beijing, China, [3]Central Research Institute, United Imaging Group, Shanghai, China, [4]The First Affiliated Hospital of Nanjing Medical University, Nanjing, China, [5]International Children's Medical Imaging Research Laboratory, School of Biological Science and Medical Engineering, Southeast University, Nanjing, China

Organ-on-a-chip (OOC) is a new type of biochip technology. Various types of OOC systems have been developed rapidly in the past decade and found important applications in drug screening and precision medicine. However, due to the complexity in the structure of both the chip-body itself and the engineered-tissue inside, the imaging and analysis of OOC have still been a big challenge for biomedical researchers. Considering that medical imaging is moving towards higher spatial and temporal resolution and has more applications in tissue engineering, this paper aims to review medical imaging methods, including CT, micro-CT, MRI, small animal MRI, and OCT, and introduces the application of 3D printing in tissue engineering and OOC in which medical imaging plays an important role. The achievements of medical imaging assisted tissue engineering are reviewed, and the potential applications of medical imaging in organoids and OOC are discussed. Moreover, artificial intelligence - especially deep learning - has demonstrated its excellence in the analysis of medical imaging; we will also present the application of artificial intelligence in the image analysis of 3D tissues, especially for organoids developed in novel OOC systems.

KEYWORDS

organ-on-a-chip, tissue engineering, medical imaging, artificial intelligence, deep learning

1 Introduction

About 90% of drugs could not pass the clinical trials, even they have passed cell and animal experiments. The reason is that there are species differences between animals and humans. Thus, animals cannot accurately represent and simulate the disease status, progression and following treatment that humans have (Golebiewska et al., 2020). At the

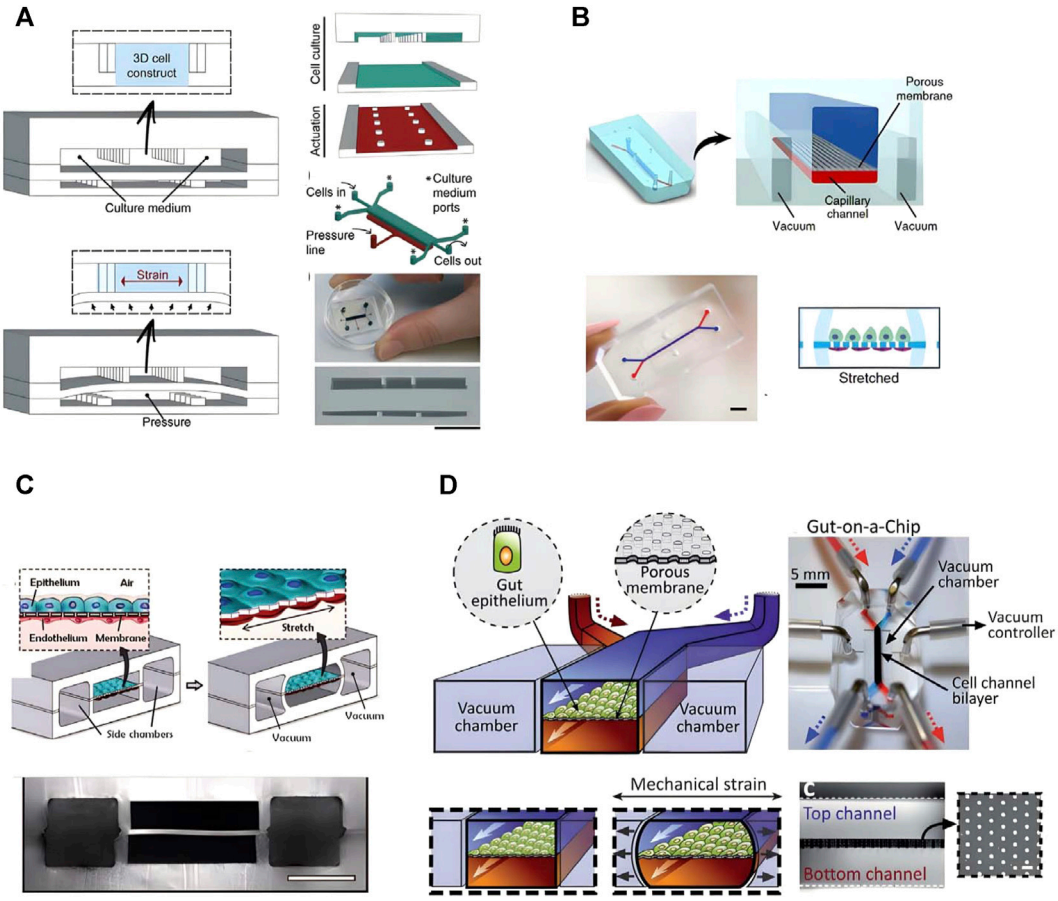

FIGURE 1
The representative chips of Organ-on-a-chip. **(A)** Heart on a chip (adapted and modified from Marsano et al., 2016). **(B)** a Glomerulus Chip (adapted and modified from Musah et al., 2018). **(C)** Lung chip (adapted and modified from Huh et al., 2010). **(D)** Intestinal chip (adapted and modified from Kim et al., 2012).

same time, the limitations of low-throughput *in vivo* animal research led to the extension of drug development life cycle and the increase of development cost. Organ-on-a-chip (OOC) is an interdisciplinary technology that combines cell biology, biomedical engineering, biomaterials, microfabrication and so on to recreate and simulate the biomedical and physical microenvironments of human organs on microfluidic chips (Wu et al., 2020; Park et al., 2019). Each unit in OOC is usually very small, so it can screen drugs with high throughput, which improves the efficiency in drug screening (Sun et al., 2019a). OOC has good potential to make up the deficiency in animal experiment, and may replace animal experiment to some extent in the future. Over the past decade, researchers have developed chips with different designs and sizes to mimic organs such as heart (Figure 1A) (Marsano et al., 2016), kidney (Figure 1B) (Musah et al., 2018), lung (Figure 1C) (Huh et al., 2010), intestine (Figure 1D) (Kim et al., 2012), and so on. OOC technology was selected as one of the top ten emerging technologies at the 2016 World Economic Forum.

Organoids are three-dimensional cell complexes with organ-specific functions and similar structures to organs induced and differentiated from stem cells by 3D *in vitro* culture technology (Artegiani and Clevers, 2018; Rossi et al., 2018). Organoids can be derived from induced pluripotent stem cells (iPSCs) and/or adult stem cells (ASCs) or even primary epithelial cells (Dutta et al., 2017), which are self-organized to form a three-dimensional structure that shares certain similarities to human organs. Currently, researchers have established dozens of organoids including organoids of intestine (Figure 2A) (Gjorevski et al., 2016), skin (Figure 2B) (Lee and Koehler, 2021), tumors (Figure 2C) (Nuciforo et al., 2018), blood vessels (Figure 2D) (Wimmer et al., 2019), etc. Organoids have a wide range of application values, which can be used for drug testing, understanding organ development and related diseases, promoting the research on tumor treatment, and

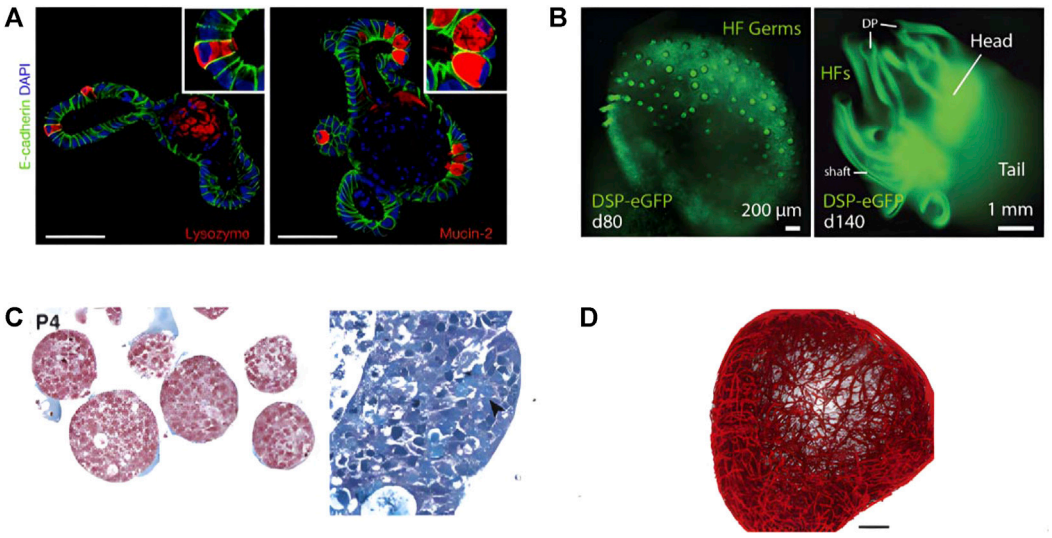

FIGURE 2
Four different types of organoids constructed by researchers. **(A)** Intestinal organoids (adapted and modified from Gjorevski et al., 2016). **(B)** Skin organoids (adapted and modified from Lee et al., 2021). **(C)** Organoid Models of Human Liver Cancers (adapted and modified from Nuciforo et al., 2018). **(D)** Human blood vessel organoids (adapted and modified from Wimmer et al., 2019).

making tissue replacement therapy possible (Lancaster and Knoblich, 2014; Bleijs et al., 2019).

While the research of organoids has made great progress, it also promotes the development of tissue engineering. The concept of tissue engineering was put forward as early as 1980. Its direct goal is to develop biological substitutes for damaged tissues or organs for clinical application. The main elements in tissue engineering include cells being seeded, supportive matrices w or w/o growth factors. The main sources of seed cells are primary tissue cells, stem cells, or progenitor cells (Berthiaume et al., 2011). Growth factors are soluble, diffusing signaling polypeptides that regulate different kinds of cell growth processes (Bakhshandeh et al., 2017). The activity and compatibility of biomaterials are also constantly improving to help regulate cell proliferation, migration, differentiation, and other behaviors (Khademhosseini and Langer, 2016). Tissue engineering has practical applications in the fields of skin replacement and cartilage repair, and significant progress has also been made in the fields of blood vessels, liver, and spinal cord (Langer and Vacanti, 2016). Researchers have already used organoid technology for *in vitro* tissue construction. Markou et al. use vascular organoids derived from human pluripotent stem cell derived mural cell phenotypes for tissue engineering (Markou et al., 2020). Reid et al. use organoids and 3D printing for consistent, reproducible culture of large-scale 3D breast structures (Reid et al., 2018). Organoid technology is expected to become a platform for tissue engineering in the future.

Though OOC and organoid have been developed and widely used in recent biological and biomedical sciences, the analyzing methodology of these models are still very limited and old-fashioned. Researchers often use very traditional paraffin-embedding with sectioning and/or cryo-sectioning to analyze slices of those tissues, while these operations are high in labor-requirement and low in efficacy. It is difficult to collect three-dimensional images due to their high in thickness and poor in light transmittance; thus, imaging with traditional light microscopy could not reach tissues in depth while having decent spatial resolution. While in the tissue engineering technology that complements and develops with organoids, medical imaging methods have been widely used and have great reference significance. Therefore, this article will review the medical imaging methods that may be used in organoid and OOC imaging, including CT/microCT, MRI/small animal MRI, OCT, etc. We will overview the pros and cons of different medical imaging methodologies, focusing on spatial resolution and image contrast analysis; the unique setup for medical imaging instruments and its applications in organoid imaging will need to be explored and specified. This article will also review the application of 3D printing combined with medical imaging technology in tissue engineering and OOC technology.

Finally, we will discuss the applications of artificial intelligence (AI) in different medical imaging methods and the image analysis of organoids, including detecting and tracking organoids, predicting the differentiation of organoids, and so on (Kegeles et al., 2020; Bian et al., 2021). The main methods reviewed in this article are mainly machine learning in

TABLE 1 Properties of different medical imaging methods.

	Spatial resolution	Temporal resolution	Soft Tissue contrast	Penetration depth	Scan time	Cost
MRI	0.5–5 mm	2–50 ms	High	Full body	Long	High
Small animal MRI	5–200 μm	20–50 ms	High	Full body	Long	High
CT	0.5–0.625 mm	60–200 ms	Low	Full body	Short	Low
Micro-CT	5 μm	50 ms	Low	Full body	Short	Medium
OCT	10–15 μm	20–50μs	Medium	About 2 mm	Short	Low

Adapted from Refs. (Lin and Alessio, 2009a; Lin and Alessio, 2009b; Cao et al., 2009; Runge, 2009; McCabe and Croce, 2012; Nam et al., 2015a; Lewis et al., 2016; Zbontar et al., 2018; Aumann et al., 2019)
MRI, magnetic resonance imaging; CT, computed tomography; OCT, optical coherence tomography.

artificial intelligence, especially deep learning. Most deep learning models are based on artificial neural networks (Gore, 2020). The artificial neural network is an algorithm inspired by human brain neuron cells, aiming to simulate the way the human brain processes problems. Therefore, deep learning is essentially a neural network with three or more layers. Deep learning can be widely used in speech recognition, image recognition, natural language processing, and other fields. At present, artificial intelligence has made significant progress in the field of medical imaging. Artificial intelligence can help provide critical diagnostic information, improve image reading efficiency, and reduce the inevitable errors of human image reading. Specific functions include but are not limited to image quality improvement, lesion detection, automatic segmentation, classification, quantification, etc. (Currie et al., 2019; Higaki et al., 2019; Zhao and Li, 2020).

2 High spatial resolution imaging method

2.1 Overview

The spatial resolution and some other properties of five medical imaging tools are listed and compared in Table 1. Each instrument has different temporal and spatial resolutions, and the corresponding use scenarios are also different.

2.2 Magnetic resonance imaging

Magnetic resonance imaging (MRI) is an important non-invasive imaging method for medical diagnosis based on the principle of nuclear magnetic resonance (Hespel and Cole, 2018). Protons precession in a strong magnetic field. When the frequency of the electromagnetic wave emitted to the proton is equal to the precession frequency, the proton will resonate and produce a transition. When the external energy pulse disappears, the proton will return from the ordered high-energy state to the disordered low-energy state and release radio waves, which can be received by the receiving coil and fall into the radio frequency range. The released energy follows the exponential decay form (Yousaf et al., 2018). The time used to release energy is called relaxation time. The relaxation time of different biological tissues is different, which is also the core principle of nuclear magnetic resonance imaging. The field strength of MRI equipment used in the clinic is mainly 1.5T and 3T. Equipment with higher field strength has a higher signal-to-noise ratio and contrast. The uMR Jupiter 5.0T has been developed for clinical whole-body scanning imaging. It shows better image quality and performance in detecting tiny details in various organs, as well as provides more precise quantitative analysis (Zhang et al., 2022). MRI is often used in the brain, blood vessels, spinal cord, abdominal and pelvic organs, musculoskeletal and so on, which can be used to study brain tumors, Parkinson's disease, mental diseases, and so on (Meijer and Goraj, 2014; Liu et al., 2020a). MRI signal needs spatial positioning (Hamilton et al., 2017), which takes longer time compared with other imaging methods. Still, it will not cause damage to human body or imaging tissue due to the use of non-ionizing electromagnetic radiation. Perfusion MRI was studied to evaluate perfusion parameters at the capillary level. It can be divided into two categories: using and not using exogenetic contrast agents (Jahng et al., 2014). Magnetic resonance spectroscopy (MRS) is a non-invasive metabolic imaging technology based on the same principle as MRI. MRS is most commonly obtained by ^{1}H. In addition, it can also be obtained by ^{13}C, ^{31}P, and other nuclei (Speyer and Baleja, 2021). Single voxel spectroscopy (SVS) is the most commonly used and easily obtained MRS technology (Zhang et al., 2018), which is limited to receiving signals from a single voxel. Multi-voxel chemical shift imaging (CSI) techniques, including 2D and 3D CSI, have a larger coverage area, which can be displayed as a single spectrum, a spectral map, or a color metabolic image (Zoccatelli et al., 2013). MRS can be used to study the metabolic changes of Alzheimer's disease, amyotrophic lateral sclerosis, brain tumor disease, etc.

MRI has also been used in organoid research. Vascular organoids are imaged to observe whether vascular tissue functions normally. The researchers construct organoid-based orthotopic mouse xenograft models, transplant the endometrial cancer organoid cultured *in vitro* into the mouse uterus, and observe the tumor growth every week with MRI (Espedal et al., 2021). Researchers have also proposed the possibility of using MRI to study brain organoids (Badai et al., 2020).

2.2.1 Small animal magnetic resonance imaging

In the process of translational research and drug development, animal models are needed for research. It is necessary to perform brain imaging of rodents, mostly rats or mice, to observe the phenotypic characteristics of the disease in order to help understand the mechanism of mental illness, especially in the research of neurological diseases (Herrmann et al., 2012; Hoyer et al., 2014). The brain structure of the animal model is tiny, reaching the sub-millimeter level (Gao et al., 2019), and the reduction of voxel volume will lead to a reduction in the signal-to-noise ratio (Boretius et al., 2009). The images produced by the human scanner are not clear on the details of the mouse brain. These demands lead to the study of high-resolution MRI for small animal imaging. Some researchers optimize T2 weighted fast spin echo MRI at 9.4 T to realize the imaging of mouse brain cell layer (Boretius et al., 2009). At present, many manufacturers have developed instruments specially used for MRI imaging of small animals. Compared with human scanners, they have higher spatial and temporal resolution, requiring the use of strong magnets, special gradient coils, and the development of special sequences for small animals (Jakob, 2011). There are also many researchers who are committed to transforming human scanners to image small animals. Some studies connect preclinical magnets and gradient coils to human scanners, making it possible to achieve high-resolution imaging (Felder et al., 2017); a surface loop array is proposed to image small animals on human scanners (Gao et al., 2019).

2.3 Computed tomography

Computed tomography (CT) is a commonly used medical image diagnosis method in clinics. It measures the attenuation of x-beams in different projection layers of the human body and finally carries out mathematical reconstruction by computer to synthesize it into three-dimensional images (du Plessis et al., 2018). The initial CT used a translational scanning system. With the advancement of technology, CT scan has gradually evolved into fan beam scanning, electron beam scanning, etc. The number of rows of detectors in CT scans is increasing, and the scanning time is getting shorter and shorter. At present, multi-slice spiral CT scans, such as 64-slice spiral CT have become the mainstream of the market because of their fast-imaging speed and clear imaging. In addition to ordinary scans, CT can also perform enhanced scans by injecting contrast agents to make the lesions appear more clearly. Lung, heart, and blood vessels are suitable for CT examination (Wiant et al., 2009; Cox and Lynch, 2015; Thillai et al., 2021).

2.3.1 Micro-computed tomography

Micro-computed tomography (micro-CT) is a cone-beam computed tomography scanning technology. The principle is the same as that of clinical CT, both of which are x-ray attenuation imaging. The difference is that the critical structure is a micro-focus x-ray tube and a high-resolution x-ray detector. Micro-CT can perform *in vitro*, *in vivo*, and *ex vivo* studies and is an essential method for preclinical imaging (Bartos, 2018). With the deepening of research, the spatial resolution of micro-CT has been continuously improved, and the imaging field of view has been reduced. Therefore, micro-CT has been applied in the fields of histomorphological analysis, bone quality assessment, small animal imaging, 3D printing and other fields that require more precision (Orhan, 2020). It enables nondestructive visualization of specimens in 2D and 3D. Tan et al. use micro-CT to analyze the microstructure of mouse calvarial bone (Tan et al., 2022). Doost et al. use iodine-enhanced micro-CT to image the mouse heart *ex vivo* (Doost et al., 2020).

2.4 Optical coherence tomography

Optical coherence tomography (OCT) is a non-invasive, high-resolution optical imaging technique that distinguishes different tissues by analyzing the difference between the incident signal and the received signal, taking advantage of the different degrees of absorption and scattering of light by different tissues (Podoleanu, 2005; Podoleanu, 2012). OCT is mainly composed of a low coherence light source, Michelson interferometer and photoelectric detection system. According to different signal acquisition units, it can be divided into time domain OCT (TD-OCT) and frequency domain OCT (FD-OCT) (Chaber et al., 2010; Mueller et al., 2010). TD-OCT developed earlier, using a mechanical reference mirror. FD-OCT improves the imaging speed and sensitivity, accelerates the development of OCT, and has become the mainstream of application. FD-OCT can be realized by spectra-domain OCT (SD-OCT) and swept-source OCT (SS-OCT) (Podoleanu, 2012). The spatial resolution of OCT is high, up to several microns, but due to the insufficient penetration of light into the tissue, the imaging depth is between 1 and 3 mm (McCabe and Croce, 2012). Therefore, OCT is suitable for precision medical fields such as intravascular imaging and ophthalmic diseases (Kim et al., 2017). In the field of intravascular imaging, the application scenarios of OCT basically overlap with that of IVUS, but it can provide more detailed intracoronary pathological features (McCabe and Croce, 2012). At the same time, OCT can also be used to evaluate

bioabsorbable vascular stents (Okamura et al., 2010; Brugaletta et al., 2012). In the field of ophthalmic diseases, OCT has become the primary imaging method. The initial imaging of the posterior end such as the retina and the optic nerve head, has progressing to the imaging of the anterior segment such as the ocular surface and the anterior segment due to the development of FD-OCT (Fu et al., 2017; Bille, 2019). The development of OCT greatly promotes the research of glaucoma, macular degeneration and other ophthalmic diseases and plays a great auxiliary role in the research of some diseases that may cause retinopathy, such as Alzheimer's disease and Parkinson's disease (Cheung et al., 2015; Zou et al., 2020). Compared with CT, MRI, and other imaging technologies commonly used in the clinic, OCT has higher spatial resolution, and higher imaging depth compared with confocal microscope and other microscopic imaging technologies. Therefore, the emergence of OCT makes up for the gap between traditional medical imaging technology and microscopic imaging technology and can provide support for the biomedical field of organoids with thicker tissue.

3 3D Printing in tissue engineering and organ-on-a-chip

3D printing and 3D bioprinting technology have introduced tissue engineering and OOC technology as a standardized culture platform, which also requires medical imaging support.

3.1 3D printing and 3D bioprinting

3D printing has made considerable progress in recent years. 3D printing creates three-dimensional objects by superimposing layers on a two-dimensional plane, which is versatile and customizable. 3D printing has been applied and improved in aerospace, manufacturing, and so on. When 3D printing is combined with medicine, it has evolved further. More and more researchers in the field of biomedical engineering take 3D printing as a transformation tool for biomedical applications. The slice data of medical images can be modeled and printed layer by layer through 3D printing to visualize simulated organs or other structures. This helps researchers study pathology, helps students learn biological structures, and helps patients better understand their own diseases.

3D bioprinting is an application of 3D printing in biomedicine and has become a promising method for tissue engineering and regenerative medicine. Compared with 3D printing, 3D bioprinting uses living cells, biological materials, etc. as "bioinks" to construct artificial multicellular tissues or organs in three dimensions (Dey and Ozbolat, 2020). It can be used to manufacture a three-dimensional framework that has a similar hierarchical structure to living tissues. Currently, popular 3D bioprinting technologies include laser-assisted bioprinting, inkjet bioprinting, and micro-extrusion bioprinting (Zhu et al., 2016). There have been 3D bioprinting studies on skin, bones, liver, nerves, blood vessels, etc. It is expected to produce transplantable biological tissues in the future to meet the demand for organ transplantation (Matai et al., 2020).

Figure 3 shows a typical process of 3D bioprinting; the main steps are imaging, 3D modeling, bioinks selection, bioprinting, post-processing, and applications. It can be seen that there is a close relationship between 3D bioprinting and medical imaging. The first step of 3D bioprinting is to image the tissue or organ to be printed through medical imaging equipment such as CT and MRI (Abdullah and Reed, 2018). The second step is that 3D modeling depends on accurate image segmentation (Squelch, 2018), which can be supported by artificial intelligence. In the final stage of application, medical images can also be used to visually inspect the tissues *in vitro* or transplanted into the body.

3.2 3D printing in tissue engineering

Conventional tissue engineering strategies employ a "top-down" approach in which cells are seeded on biodegradable polymer scaffolds (Nichol and Khademhosseini, 2009), but these approaches often fail to distribute cells rationally and provide a microenvironment for cell survival. The bottom-up modular approach has the advantage of assembling microenvironments, which is more conducive to constructing large-scale biological tissues (Mandrycky et al., 2016). Therefore, 3D printing has brought new impetus to the development of tissue engineering. 3D printing can be used in tissue engineering to rationally assemble multiple types of cells and scaffold materials for tissues. There are already impressive results using 3D printing to build skin, cartilage, blood vessels, etc. for tissue engineering. 3D printing in tissue engineering can be divided into scaffolded and scaffoldless methods. There has been tremendous progress in 3D printing methods with scaffolds. 3D printing can print precise and complex scaffolds for tissue engineering, and it is convenient to introduce computer methods to assist scaffold construction (Zaszczyńska et al., 2021). There are already 3D printed scaffolds for tissue engineering using materials such as metals, ceramics, hydrogels, etc. Wu et al. achieve 3D printing of microvascular networks using a hydrogel layer (Wu et al., 2011). Lee et al. use polycaprolactone (PCL) to create a framework for hepatocyte engineering (Lee et al., 2016). Scaffold-free approach exploits self-assembly processes in developmental biology (Richards et al., 2013). Taniguchi et al. use 3D bioprinting technology to construct a scaffold free trachea with spheroids composed of several types of cells (Taniguchi et al., 2018). Lui et al. demonstrate the enhancement of mechanical stimulation by creating scaffold-free heart tissue from hiPSC-derived cardiomyocyte spheroids (Lui et al., 2021).

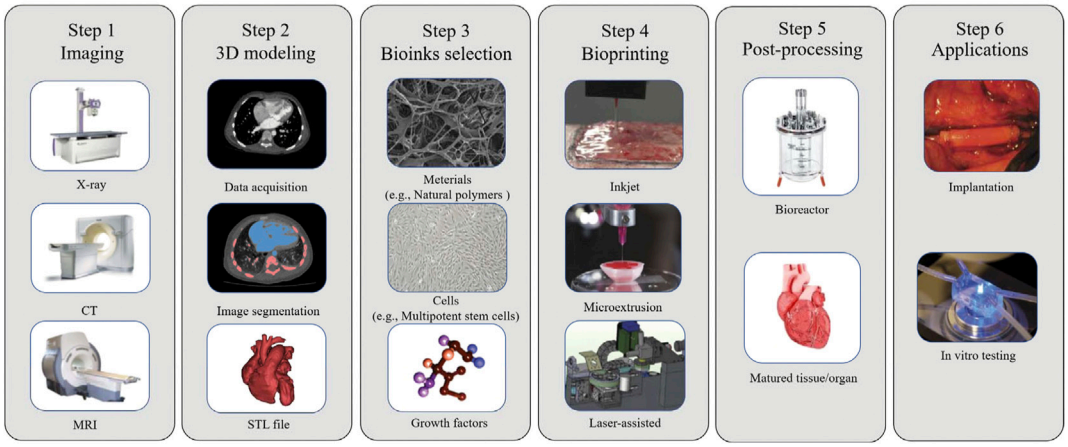

FIGURE 3
A typical process of 3D bioprinting includes 6 steps: 3D modeling, bioink selection, bioprinting, post-processing and application. (adapted and modified from Murthy et al., 2014; Vijayavenkataraman et al., 2018; Lee et al., 2021).

3.3 3D printing in organ-on-a-chip

3D printing has also been applied in the field of OOC. The microfluidic device of OOC is mainly made by using traditional manufacturing techniques. The more complex the organizational structure, the more complex and time-consuming the microfluidic device of OOC is. Since 3D printing has the advantage that complex spatial structures can be freely designed, it can change the method of fabricating microfluidic devices (Carvalho et al., 2021). The microfluidic device constructed by 3D printing has the characteristics of high accuracy and short time from design to manufacturing (Goldstein et al., 2021). Sochol et al. investigate the potential of using 3D printing to make Kidney-on-a-Chip platforms (Sochol et al., 2016). The liver chip developed by Lee et al. Using 3D printing significantly enhance liver function (Lee and Cho, 2016). The advantages of 3D printing, which is easy to design and implement, will break the technical barriers that exist in the multidisciplinary intersection of OOC, and accelerate the development and innovation of OOC (Knowlton et al., 2016).

4 Application of medical imaging in tissue engineering and artificial tissues

With the development of tissue engineering, the composition of artificial tissue has become increasingly complex, and advanced imaging techniques are required to evaluate the structure of the tissue (Nam et al., 2015b). The micro-CT, MRI, and OCT imaging techniques reviewed above can be applied to artificial tissue imaging. These advanced imaging techniques enable nondestructive visualization studies compared to some traditional tissue engineering techniques that may destroy the sample. Figure 4 shows the development trend of the number of publications combining tissue engineering and various medical imaging methods from 2006 to 2021. It can be seen that the number of publications is growing steadily, whether it is medical imaging keyword search or different medical imaging methods.

4.1 Magnetic resonance imaging in tissue engineering

MRI can image artificial tissue implanted in the body. Fujihara et al. use MRI to evaluate the maturity of cartilage tissue transplanted into the back of mice (Fujihara et al., 2016). Using small-animal MRI tracking imaging in experimental mice, Apelgren et al. demonstrate that gridded 3D bioprinted tissue allows vascular ingrowth after implantation. Harrington et al. use cellular MRI to continuously image the grafted tissue of artificial blood vessels, realizing the serial study of MRI at the cellular level of tissue engineering (Figure 5A) (Harrington et al., 2011). MRI is also an important tool for imaging tissue engineering scaffolds. Szulc et al. synthesize MnPNH2 for labeling of dECM scaffolds and visualize the scaffolds using MRI, demonstrating the potential for long-term detection of dECM-based tissue engineering (Szulc et al., 2020). Marie et al. use high-resolution 1.5-T MRI to evaluate scaffold structure and detect cell seeding (Poirier-Quinot et al., 2010). Using gadolinium-enhanced MRI to measure negative fixed-charge density in tissue-engineered cartilage *in vitro*, Miyata et al. assess its relationship to biomechanical properties (Miyata et al., 2010).

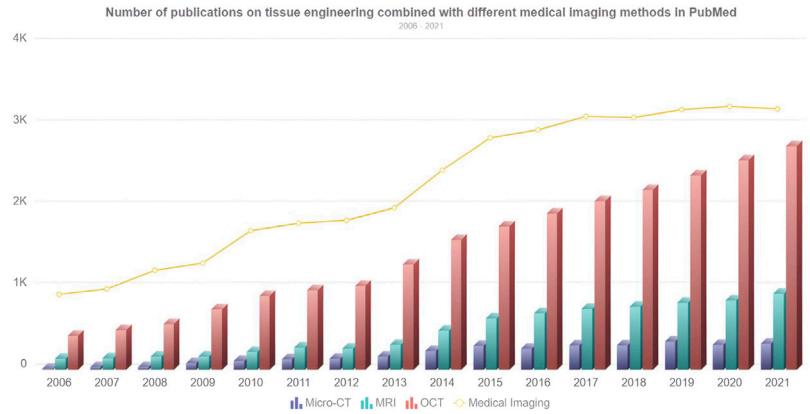

FIGURE 4
Number of publications on tissue engineering combined with different medical imaging methods in PubMed. The line chart represents the overall trend of the number of searches for medical imaging keywords, and the bar chart represents the number of searches for micro-CT, MRI, and OCT from 2006 to 2021.

4.2 Micro-computed tomography in tissue engineering

The use of micro-CT in tissue engineering has increased significantly, especially in imaging hard tissue. Martin et al. apply micro-CT to tissue engineering scaffolds aimed at bone regeneration, assessing structural changes related to hydration, complementing traditional methods that can only be studied in the dry state (Figure 5B) (Bartoš, 2018). Tim et al. model the bone tissue engineering scaffold based on micro-CT images to evaluate the structural performance (Van Cleynenbreugel et al., 2006). Wang et al. use MICROFIL perfusion and micro-CT for 3D reconstruction of rat blood vessels, helping to analyze the number, diameter, connectivity and other parameters of blood vessels as an objective assessment method for the generation of angiogenesis in tissue-engineered nerves (Wang et al., 2016). Cioffi et al. use micro-CT to construct a 3D model of a cartilage scaffold to help quantify the regulation of cartilage growth by hydrodynamic shearing (Cioffi et al., 2006). Townsend et al. use it to image tracheal tissue engineering to quantify tracheal patency for standardization in future production (Townsend et al., 2020). In addition, Papantoniou et al. use contrast-enhanced nanofocus CT for full-structure imaging of tissue engineering, which has great potential in 3D imaging and quality assessment of tissue engineering (Papantoniou et al., 2014).

4.3 Optical coherence tomography in tissue engineering

OCT is also used in tissue engineering and is especially suitable for imaging tissues with collagen matrix in tissue engineering, such as skin and tendons. Smith et al. use SS-OCT to monitor dermal rehealing of cutaneous wounds (Smith et al., 2010). Yang et al. use PS-OCT to image tissue-engineered tendon (Yang et al., 2010). Chen et al. demonstrate the effect of pulsatile stimulation on the development of engineered blood vessels using OCT for real-time imaging of tissue-engineered vascular grafts (Figure 5C) (Chen et al., 2017). Yang et al. monitor the cell contour and polylactic acid scaffold in tissue engineering by OCT (Yang et al., 2005). Levitz et al. assess the influence of atherosclerotic plaque composition on morphological features of OCT images (Levitz et al., 2007). Ishii et al. use two imaging techniques, OCT and magnetic resonance angiography to assess the patency of tissue engineered biotubes (Ishii et al., 2016). From the above, micro-CT, MRI, and OCT are developing continuously in tissue engineering and artificial tissue imaging, and are increasingly used by researchers.

5 Application of medical imaging in organoids and organ-on-a-chip

Medical imaging technology has played an important role in the construction of tissue-engineered artificial tissue. With the development and maturity of OOC technology, medical imaging technology also has the opportunity to become an imaging analysis method for OOC.

5.1 Application of medical imaging in organoids

Among the imaging methods reviewed, MRI has powerful functions and strong soft tissue contrast, which can be applied to

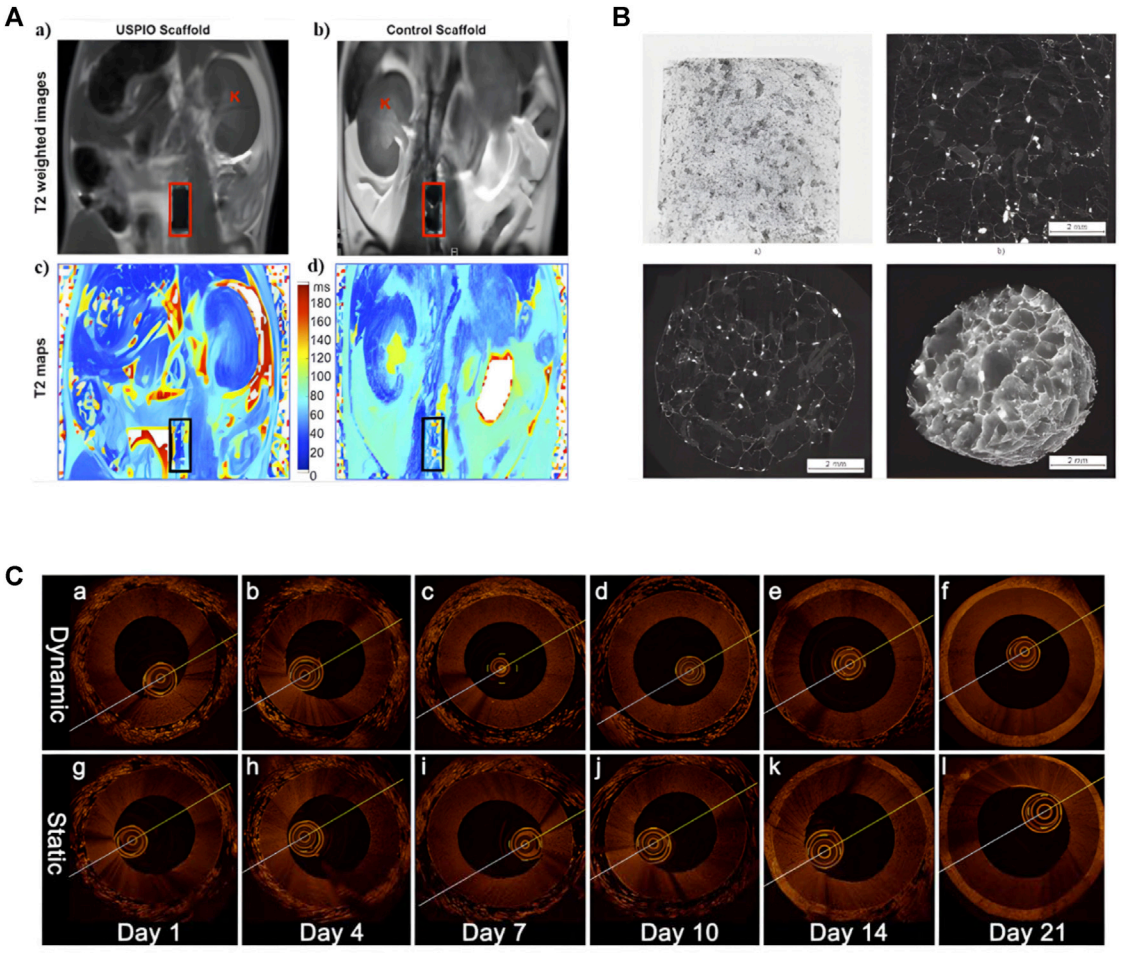

FIGURE 5
Application of Different Imaging Methods in Tissue Engineering. **(A)** Noninvasive MRI images of labeled and unlabeled stent-grafts in mice, a, b) RARE T2-weighted images of labeled (a) and unlabeled. (b) seed scaffolds after implantation. Boxes represents the location of the graft and K represents kidneys. c, d) Corresponding T2 maps of a, b) (adapted and modified from Harrington et al., 2011). **(B)** micro-CT scanning of collagen-based scaffold (adapted and modified from Bartoš et al., 2018). **(C)** OCT imaging contrasting the effects of pulsatile stimulation on tissue-engineered vascular grafts culture, (a–f) are images with arterial stimulation, (g–l) are images without arterial stimulation (adapted and modified from Chen et al., 2017).

most organoid imaging. Perfusion MRI may help provide perfusion parameters of the complex capillary network in artificial microvascular systems currently under study (Figure 6A) (Fleischer et al., 2020). The soft tissue contrast of CT or micro-CT is not as good as that of MRI, and is suitable for positional imaging of tissue that differs in density, such as imaging tumor organoids in tissue with altered density or size. The spatial resolution of OCT is high, but the contrast of soft tissue is relatively general. It is mainly used for eye, skin, and intravascular imaging in clinical practice. The same application field also serves as a reference for the application of OCT in organoids. Lee et al. construct branched tissue-engineered blood vessels to mimic early atherosclerosis (Figure 6B) (Lee et al., 2021). Skin organoids are also emerging as human models for dermatological research (Figure 2B) (Lee and Koehler, 2021). OCT is expected to play an important role in the research of artificial blood vessels and skin organoids.

5.2 Application of medical imaging in organ-on-a-chip

When using medical imaging to image OOC, it is vital to consider not only the characteristics of the organoid but also the microfluidic chip. Magnetic metals have an adverse effect on MRI, so when MRI or small animal MRI is required for OOC, metal components should be avoided early in microfluidic chip design and during processing. Additionally, if imaging with micro-CT or

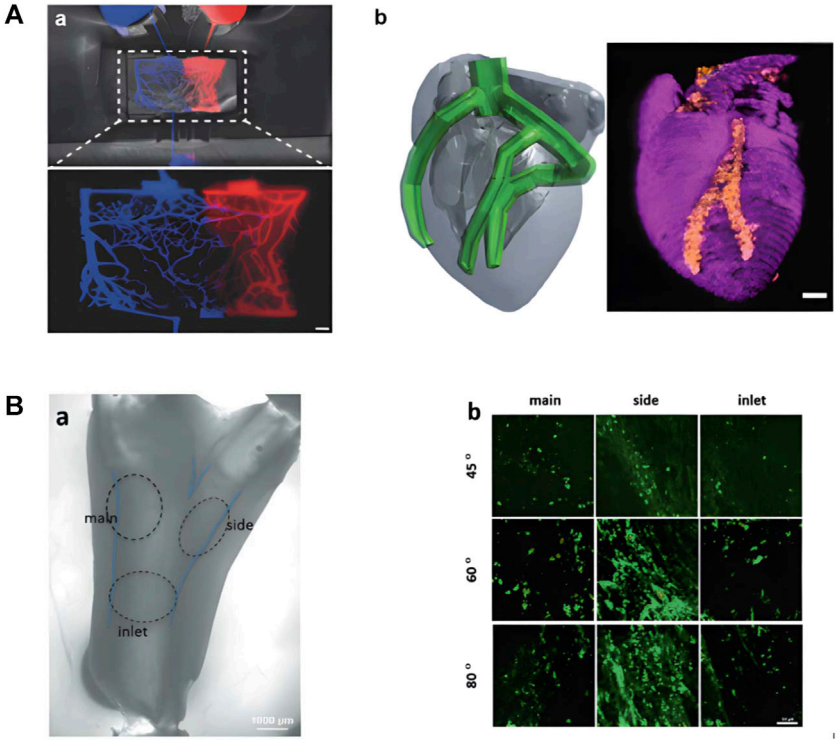

FIGURE 6
Research on artificial tissue with potential application in medical imaging. **(A)** Related research on artificial microvascular system. (a) Microvascular Networks Using Laser Patterns in Polyethylene Glycol Hydrogels. (b) 3D printed heart perfusion model (adapted and modified from Fleischer et al., 2020). **(B)** Brightfield and fluorescence images of brTEBV. (a) Brightfield image of brTEBV with a branch angle of 45° considering MC adhesion, where the dashed circles mark the inlet, side, main regions. (b) Fluorescence images of green-labeled MCs in the brTEBV region (adapted and modified from Lee et al., 2021).

CT, additional consideration should be given to possible artifacts caused by microfluidic chips, resulting in problems such as image distortion. To remove artifacts, the structure of the OOC can be skillfully laid out in the early stage, and appropriate algorithms including artificial intelligence algorithms can be used in the later stage. It is foreseeable that the application of medical imaging on OOC is not only involved in one of the links but needed to be considered comprehensively and added to the entire design process. The introduction of medical imaging into the field of OOC will help OOC to industrialize and perform large-scale imaging examinations in the future.

6 AI achievements in medical imaging and organoids

6.1 Magnetic resonance imaging combined with artificial intelligence

MRI has good soft tissue contrast, so the research and analysis of MRI images are very extensive and multifaceted. Research on MRI images has evolved from traditional methods to artificial intelligence methods. This paper mainly reviews the aspects of image reconstruction, image enhancement, object detection, image segmentation, diagnosis and prediction in the order of processing and analysis of MRI. Figure 7 takes brain MRI as an example to show the current research results of artificial intelligence methods.

6.1.1 Image reconstruction

The use of deep learning for image reconstruction is a relatively new field compared to the detection and segmentation of medical images, but it has shown better performance than traditional iterative, compressed sensing and other methods in the accelerated reconstruction of images and the improvement of reconstruction quality (Lundervold and Lundervold, 2019). The long scanning time can be an issue limiting the application of MRI in organoid researches, which may be solved by some acceleration methods like half Fourier imaging, parallel imaging and compressed sensing. However, the acceleration of these methods is quite limited and the image quality always suffers from the introduced reconstruction

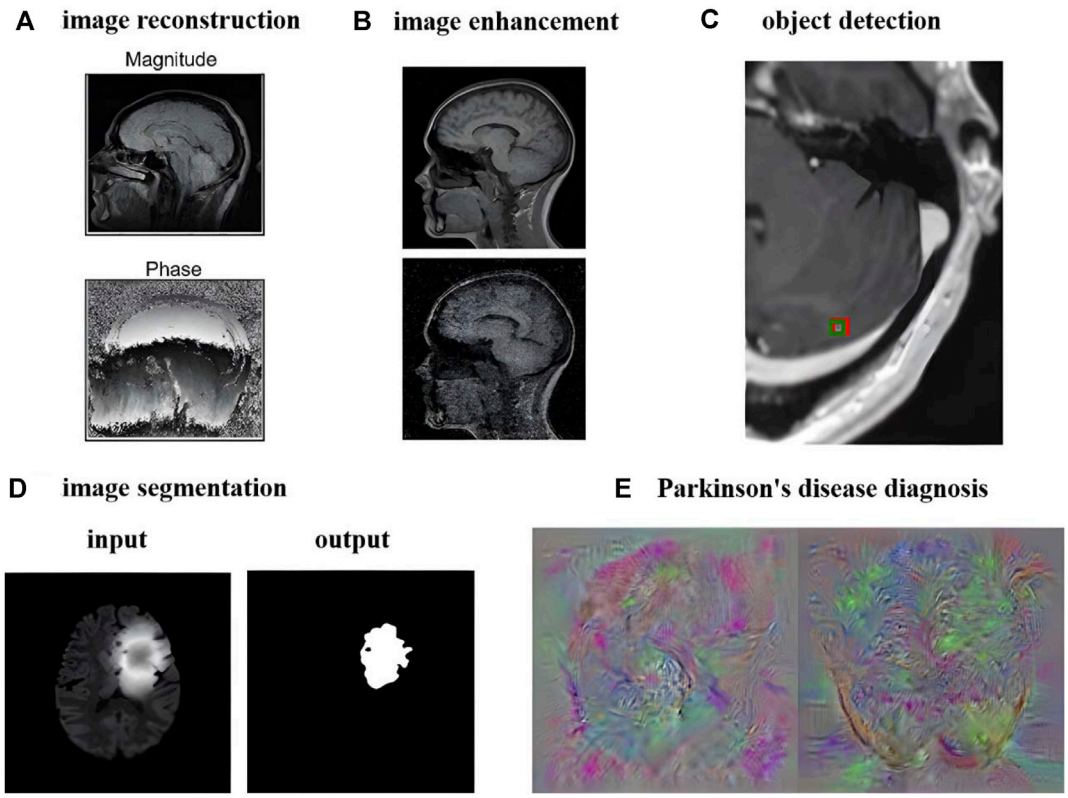

FIGURE 7
Deep Learning Image Processing and Analysis Using Brain MRI as an Example. **(A)** Image reconstruction of brain MRI (adapted and modified from Lundervold et al., 2019). **(B)** Image denoising of brain MRI (adapted and modified from Lehtinen et al., 2018). **(C)** Smallest brain metastasis detected by artificial intelligence method marked with red bounding box (adapted and modified from Zhang et al., 2020). **(D)** Brain Tumor Segmentation Using UNet++ (adapted and modified from Zhou et al., 2020). **(E)** Feature images extracted by Parkinson's diagnostic network (adapted and modified from Sivaranjini et al., 2020).

artifacts. As a potential alternative, AI-assisted compressed sensing (ACS) integrate the mentioned techniques and innovatively introduce the state-of-art deep learning neural network as the AI module into the reconstruction procedure, which lead to a superior image quality under a high acceleration factor with fewer artifacts (Wang et al., 2021a). Schlemper et al. use cascaded CNN to reconstruct the under-sampled two-dimensional cardiac MRI. It has the function of iterative algorithm to remove aliases, and it is less prone to overfitting than a single CNN network (Schlemper et al., 2018). The experimental result can reach 11 times of under-sampling, and the entire dynamic sequence can be reconstructed within 10s. Hammernik et al. propose a variational network as a variational model, which uses deep learning to learn all free parameters to accelerate MRI image reconstruction. Finally, the reconstruction time on a single graphics card is 193 ms, showing fast computing performance (Hammernik et al., 2018). Huang et al. introduce motion information into unsupervised deep learning model for dynamic MRI reconstruction for the first time (Huang et al., 2021). Kamlesh et al. combine the domain knowledge of traditional parallel imaging with U-Net for MRI reconstruction, and the reconstruction results are anti-interference and accurate (Pawar et al., 2021). Hossam et al. use a complex valued revolution network, which uses U-Net as the backbone network to join the complex valued revolution, etc. to accelerate the reconstruction of highly undersampled MRI (El-Rewaidy et al., 2020). Li et al. use 3D U-Net to construct the brain structure and adopted the recurrent convolutional network embedding LSTM to complete more detailed vector information depiction in two steps, which retains the important features of brain MRI (Figure 8A) (Li et al., 2021a). Image reconstruction is developing rapidly. Many artificial intelligence methods that combine traditional methods or directly use deep learning to complete rapid or even real-time reconstruction are still being proposed.

6.1.2 Image enhancement (de-noising, super-resolution)

Image de-noising and image super-resolution have become important research directions to improve the quality of MRI

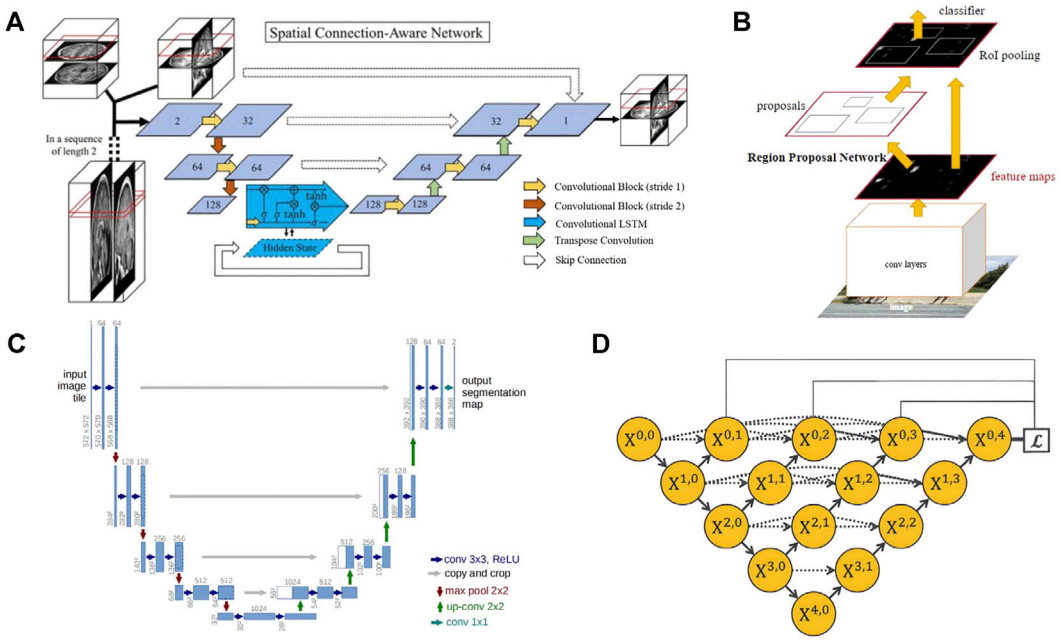

FIGURE 8
Some network frameworks applied in MRI image processing and analysis. **(A)** Spatial connectivity-aware network including LSTM blocks, exploiting sagittal information from adjacent slices. (adapted and modified from Li et al., 2019). **(B)** The Faster R-CNN network structure has two branches, the bounding box regression network and the classification network. The region proposal network is used to recommend bounding boxes that may have targets. (adapted and modified from Ren et al., 2015). **(C)** U-net is often used as a basic network. The blue boxes represent feature maps with different number of channels, the white boxes represent the copied feature maps, and the arrows represent operations such as convolution, pooling, etc. (adapted and modified from Ronneberger et al., 2015). **(D)** The UNet++ network obtained by improving U-Net, the downward arrow indicates downsampling, the upward arrow indicates down adoption, and the dot arrow indicates skip connections between feature maps. (adapted and modified from Zhou et al., 2019).

images, especially after the introduction of deep learning into this field. Despite the continuous development and innovation of medical imaging equipment, it is still inevitable to generate random noise, which will affect the speed and accuracy of doctors' judgment. Most denoising methods are based on a small range of homogeneous samples. Benou et al. study the denoising problem of dynamic contrast-enhanced MRI and construct an ensemble of expert DNNs to train different parts of the input image separately (Benou et al., 2017). Li et al. use a supervised learning network constructed by two sub-networks to learn distribution information in MRI to reduce Rician noise (Li et al., 2020a). Noise2noise, an unsupervised learning method, has also attracted widespread attention. It is characterized by the fact that the input and output of the network are all noisy pictures during training, which is very suitable for scenes such as MRI, where it is difficult to obtain clean samples. Some researchers also propose a denoising method based on a large range of multidisciplinary samples. Sharif et al. combine attention mechanism and residual learning modified by noise gate to build deep learning network, applied to radiology, microscopy, dermatology medical images (Sharif et al., 2020). The final results show good denoising effect, which also proposes a new idea for medical image denoising.

Directly generating high-resolution images using medical imaging devices is sometimes a time-consuming and expensive process, so researchers have attempted to use deep learning to perform super-resolution operation on the images for post-processing. Neonatal brain MRI and cardiac MRI images are two important application scenarios of super-resolution. Low resolution (LR) image training samples are usually obtained by downsampling the collected images. Masutani et al. build 4 CNNs to demonstrate the excellent performance of deep learning for super-resolution of Cardiac MRI images, which is expected to shorten the scanning time for image acquisition and reduce the discomfort of patients holding their breath for too long (Masutani et al., 2020). Generative Adversarial Networks (GAN) can speed up the training time, so many researchers use GAN combined with CNN to build a training network. Based on GAN, Delannoy et al. take differential low resolution (LR) images as input and simultaneously complete two tasks of neonatal brain MRI super-resolution and segmentation (Delannoy et al., 2020). Chen et al. also implement MRI super-resolution based on GAN. The generator part of GAN uses a self-designed multi-level

densely connected network (Chen et al., 2018). Zhao et al. perform parallel filtering of the original images to obtain LR images as a training set, use enhanced deep residual networks for single image super-resolution, and make different training distinctions between 2D and 3D MRI images (Zhao et al., 2020). Some researchers have also realized the joint processing of image denoising and super-resolution. Gao et al. study the super-resolution and denoising of flow MRI. They introduce physical information into the network and realize the training of the network without high-resolution labels (Gao et al., 2021).

6.1.3 Object detection

Object detection is an important link in medical image processing, usually using a square frame to mark and locate areas of interest such as lesions and organs, which is a preprocessing step for further segmentation or classification. Especially for small target lesions, locking the location of the lesions in advance and storing only the surrounding areas for semantic segmentation are conducive to reducing storage consumption and improving the accuracy of segmentation (Kern and Mastmeyer, 2021). It can be divided into detection of 2D MRI slices and 3D MRI image sets. The object detection of 2D images is to feed each slice of the MRI into the training network separately, which can obtain more training data and correspondingly more training volume than 3D object detection (Kern and Mastmeyer, 2021). But the disadvantage is that the context information will be lost. The current development trend is 3D object detection, which can make more full use of context information to improve the detection accuracy. In the research field of independent detection of 2D MRI, Zhou et al. use the transfer learning method and a special similarity function to pre-train the CNN in the pre-prepared data, and realize the use of unlabeled images of the lumbar spine to detect the vertebral position during the training process (Zhou et al., 2018). Zhang et al. use the classic Faster-RCNN (Figure 8B) to detect brain cancer metastasis, which has superior performance and application prospects (Zhang et al., 2020a). In the field of 3D detection, Alkadi et al. use 3D sliding window for prostate cancer detection (Alkadi et al., 2018). Qi et al. use a 3D CNN to detect cerebral microbleeds (CMBs), achieving a high sensitivity of 93.16% (Qi et al., 2016). Mohammed et al. use YOLO and 3D CNN to detect CMBs.

6.1.4 Image segmentation

Image segmentation aims to describe the contour of organs, tissue structures, and lesions as accurately as possible or identify the voxel set in them. Since MRI is good at depicting human soft tissues, especially the human brain, segmentation of MRI has attracted great interest from researchers. Meanwhile, the noise and artifacts of MRI images have brought challenges to segmentation (Despotović et al., 2015). Fully Convolutional Network (FCN) is the pioneer of currently popular medical image segmentation based on convolutional neural networks (CNN) (Shelhamer et al., 2017). In the multi-atlas and diffeomorphism-based encoding block, both MRI intensity profiles and expert priors from deformed atlases were encoded and fed to the proposed FCN. The MRI intensity and the expert priors from the deformation map are coded and input, and the adaptive size patches are used at the same time (Wu and Tang, 2021). The Mask RCNN framework also has a good performance in medical image segmentation. Zhang et al. use Mask RCNN to achieve tumor segmentation for breast MRI, achieving an accuracy of 0.75 on the test set (Zhang et al., 2020b) The U-Net architecture proposed by ronneberger et al. has the structure of u-encoder and decoder and the unique skip connection to help compensate for the information loss in the down sampling process (Figure 8C) (Ronneberger et al., U-Net). The design performs well in medical image segmentation and is widely used by researchers as the basic network for research. V-Net expands the segmentation method of U-Net from two-dimensional images to three-dimensional images. It uses a new loss function called dice coefficient, and replaces the pooling layer in the U-Net architecture with a convolutional layer to achieve fast (1s) and accurate (approximately 87%) volume segmentation of prostate MRI images (Milletari et al., V-Net). UNet++ (Figure 8D) is a collection of U-Net with different depths and redesigned the skip-connection in U-Net. Segmentation experiments are carried out on 6 different biomedical images, including 2D and 3D applications for brain tumor MRI image segmentation (Zhou et al., 2020). The proposal of nnUnet verify the rationality of the original U-Net framework. It only needs to adaptively set the data fingerprint and pipeline fingerprint according to different tasks. The result has won the 2020 MRI-based BraTS brain tumor segmentation competition (Isensee et al., 2021). At the same time, some researchers use recurrent neural networks (RNN) for segmentation. Rudra et al. use recurrent fully-convolutional network (RFCN) for multi-layer MRI cardiac segmentation. Recurrent networks can help extract context information from adjacent slices and improve segmentation quality (Poudel, Lamata, Montana). Andermatt et al. use RNN with multi-dimensional gated recurrent units to segment a brain MRI data set, showing a powerful segmentation ability (Andermatt et al., 2016). Transformer has begun to be applied to the field of medical image segmentation. Peiris et al. propose a U-shaped transformer architecture similar to U-Net, which specially designed the self-attention layer of the encoder and decoder, and showed promising results in MRI brain tumor segmentation (Lehtinen et al., 2018).

6.1.5 Diagnosis and prediction

With the improvement of computing level, computer-aided diagnosis has become the development trend in clinical medicine, but since decision-making must be very cautious, it

also requires high accuracy. MRI-based deep learning methods have been widely experimented and studied by researchers, and have been applied to disease diagnosis on MRI images of the brain, prostate, breast, kidney, etc. disease diagnosis can be regarded as a classification problem in neural networks, including distinguishing diseased and non-diseased patients, and subdividing the disease of diseased patients. Among them, the diagnosis of diseases based on brain MRI is the most abundant. Sivaranjini et al. use AlexNet and transfer learning network to classify Parkinson's disease patient population and refine Parkinson's disease diagnosis (Sivaranjini and Sujatha, 2020). There are also researchers apply to the diagnosis of multiple sclerosis (MS) (Shoeibi et al., 2021), Alzheimer's disease (Roy et al., 2019), identifying schizophrenia (Oh et al., 2020). Liu et al. classify prostate cancer based on 3D multi parameter MRI (Liu et al., 2017). Gravina et al. use transfer learning combined with traditional radiology experience three time points to diagnose breast cancer lesions with dynamic contrast enhanced MRI (Gravina et al., 2019). Shehata et al. create an early diagnosis of acute renal transplant rejection diagnostic system based on diffusion-weighted MRI, which can realize a fully automatic detection process from renal tissue segmentation to sample classification (Shehata et al., 2016).

Prediction of physical development and disease progression is also a hot area. Amoroso et al. use multiplex networks to accurately assess brain age (Amoroso et al., 2019). Markus et al. use CNN and tree based machine learning methods to evaluate the age of young people based on 3D knee MRI (Mauer et al., 2021). Adrian et al. use parallel convolution paths and inception networks to predict the disease progression of MS (Tousignant et al., 2019). Li et al. use an ensemble of three different 3D CNNs for survival prediction of brain tumors based on multimodal MRI (Sun et al., 2019b). There are also studies to predict the progression of Alzheimer's disease (Jo et al., 2019), amyotrophic lateral sclerosis survival prediction (van der Burgh et al., 2017), etc.

6.2 Computed tomography combined with artificial intelligence

CT and MRI are both primary imaging methods in radiology, and the problems to be solved by artificial intelligence are similar. In terms of image reconstruction, Tobias et al. map the filtered back projection algorithm to a neural network to solve the problem of limited-angle tomography, and introduce cone-beam back-projection to overcome the defect that back projection cannot complete the end-to-end network during CT reconstruction (Wurfl et al., 2018). Solomon et al. evaluate a commercial deep learning reconstruction algorithm, and the noise is greatly reduced compared to traditional methods (Solomon et al., 2020). In terms of image enhancement, low-dose CT is often used in order to reduce radiation damage to the human body, but it is accompanied by a reduction in image quality. Li et al. use improved GAN with the Wasserstein distance and a hybrid loss function including sharpness loss, adversarial loss, perceptual loss, etc. for low-dose CT image denoising (Li et al., 2021b). At the same time, low-dose CT also has the problem that the deep learning method is difficult to generalize due to different doses. In order to solve this problem, Shan et al. propose a transfer learning network cascaded by five identical networks, which does not need to be retrained with different doses (Shan et al., 2019). Yao et al. improve convolutional layers and introduce edge detection layers for denoising of micro-CT (Yao et al., 2021). To obtain high-resolution CT images, Zhao et al. construct a network with superior performance using multi-scale attention with multiple branches and information distillation (Zhao et al., 2021). Zhang et al. design a lightweight GAN, construct dense links in all residual blocks in the generator and introduce Wasserstein distance in the loss function to achieve super-resolution (Zhang et al., 2021). In the field of CT image detection, Holbrook et al. use CNN to detect lung nodules in mice based on micro-CT (Holbrook et al., 2021). Lee et al. use three CNN models for coronary artery calcium detection based on CT images. Similarly, the application of image segmentation algorithms in lung CT is more comprehensive, including lung segmentation (Yahyatabar et al., 2020), lung lobe segmentation (Gu et al., 2021), lung parenchyma segmentation (Yoo et al., 2021), lung nodule segmentation (Jain et al., 2021) and other segmentation from larger organs to smaller lesions. Shah et al. test the performance of different deep learning models for COVID-19 detection based on CT images, among which VGG-19 performs the best (Shah et al., 2021). Chen et al. construct a deep learning model with asymmetric convolution based on CT images for predicting the survival rate of non-small cell lung cancer (Chen et al., 2021a).

Currently, many researchers focus on the development of a computer-aided diagnosis (CAD) system for pulmonary nodules on chest CT. The main processes are lung segmentation, lung nodule detection, lung nodule segmentation, lung nodule classification, etc. Tan et al. perform lung segmentation using a GAN network (Figure 9A) (Tan et al., 2021). Cao et al. implement lung nodule detection using a two-stage CNNs (Figure 9B) (Cao et al., 2020). Shi et al. use aggregation U-Net Generative Adversarial Networks for lung nodule segmentation (Figure 9C) (Shi et al., 2020). Zhang et al. use ensemble learners of multiple deep CNNs to classify lung nodules (Figure 9D) (Zhang et al., 2019). More experimental details also include feature extraction and false positive removal for lung nodules. The development of pulmonary nodule CAD system can help clinicians make diagnosis, reduce the workload of doctors, and has good application value and market prospect.

6.3 Optical coherence tomography combined with artificial intelligence

Likewise, artificial intelligence has begun to develop in the field of OCT images. Since speckle noise can greatly affect the

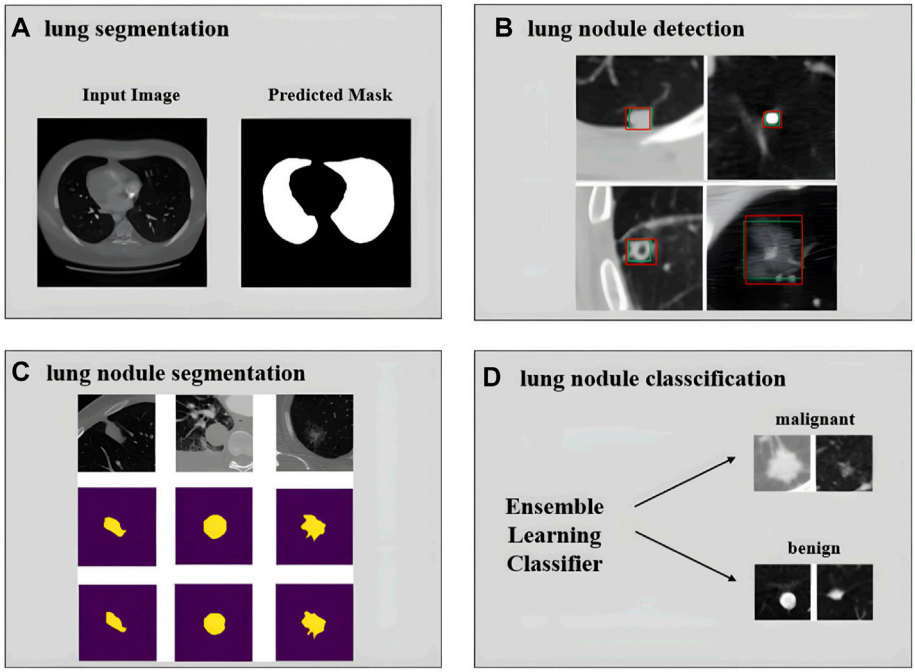

FIGURE 9
Achievements related to the realization of pulmonary nodule CAD system. **(A)** Input image and predicted mask for lung segmentation (adapted and modified from Tan et al., 2020). **(B)** Lung nodule detection results using deep learning. The green rectangle box represents ground truth and the red rectangle box represents the detection results (adapted and modified from Cao et al., 2019). **(C)** Segmentation results of large nodules, the first row is the original image, the second row is the radiologist's manual annotation results, and the third row is the result of the network prediction (adapted and modified from Shi et al., 2020). **(D)** Classification of lung nodules into malignant and benign using an ensemble learning classifier (adapted and modified from Zhang et al., 2019).

image quality of OCT, researchers seek to denoise images by using CNN and GAN. Wang et al. propose a semi-supervised learning method of GAN with fewer parameters to deal with the overfitting problem caused by too many parameters, and can use less data to complete the training (Figure 10A) (Wang et al., 2021b). Zhou et al. use CycleGAN to unify the style of images captured by different OCT instruments, and use conditional GAN for denoising (Zhou et al., 2022).

In the field of OCT intravascular imaging, researchers have applied artificial intelligence to assist in the diagnosis of atherosclerosis. Abhijit et al. propose a distribution preserving autoencoder based neural network for plaque detection in blood. To adapt to the spatiotemporal uncertainty of OCT speckle images, the model learns the representation in the data while preserving the statistical distribution of the data, and a newly proposed LogLoss function is used for error evaluation (Figure 10B) (Roy et al., 2016). To further identify vulnerable plaques, they propose to use a bag of random forests to learn tissue photon interactions (Roy et al., 2015). Asaoka et al. use deep learning to diagnose early-onset glaucoma based on macular OCT images, and use transfer learning to deal with differences in images acquired by different OCT devices (Asaoka et al., 2019). Thomas et al. construct a neural network of encoder and decoder, and complete the classification of fluid and non-fluid regions by semantic segmentation of OCT images, realizing the detection and quantification of macular fluid IRC and SRF, which is convenient for the diagnosis of exudative macular disease (Schlegl et al., 2018).

Research on automated segmentation of retinal OCT images contributes to the diagnosis of retinopathy-related diseases. Li et al. use an improved Xception65 to extract feature information, pass it into the spatial pyramid module to obtain multi-scale information, and finally used an encoder-decoder structure for retinal layer segmentation (Figure 10C) (Li et al., 2020b). Yang et al. achieve retinal layer segmentation with choroidal neovascularization, which responds to retinal morphological changes by introducing a self-attention mechanism (Yang et al., 2020). In (Roy et al., 2017), an end-to-end full CNN with encoder and decoder is constructed, realizing simultaneous segmentation of multiple retinal and fluid pockets to aid in the diagnosis of diabetic retinopathy. Artificial intelligence methods can also be combined with other methods for segmentation, Fang et al. conduct probability mapping on nine retinal layer boundaries through CNN and describe the boundary using the graph search method (Fang et al., 2017). In order to improve the segmentation accuracy, Srinivasan et al. first use

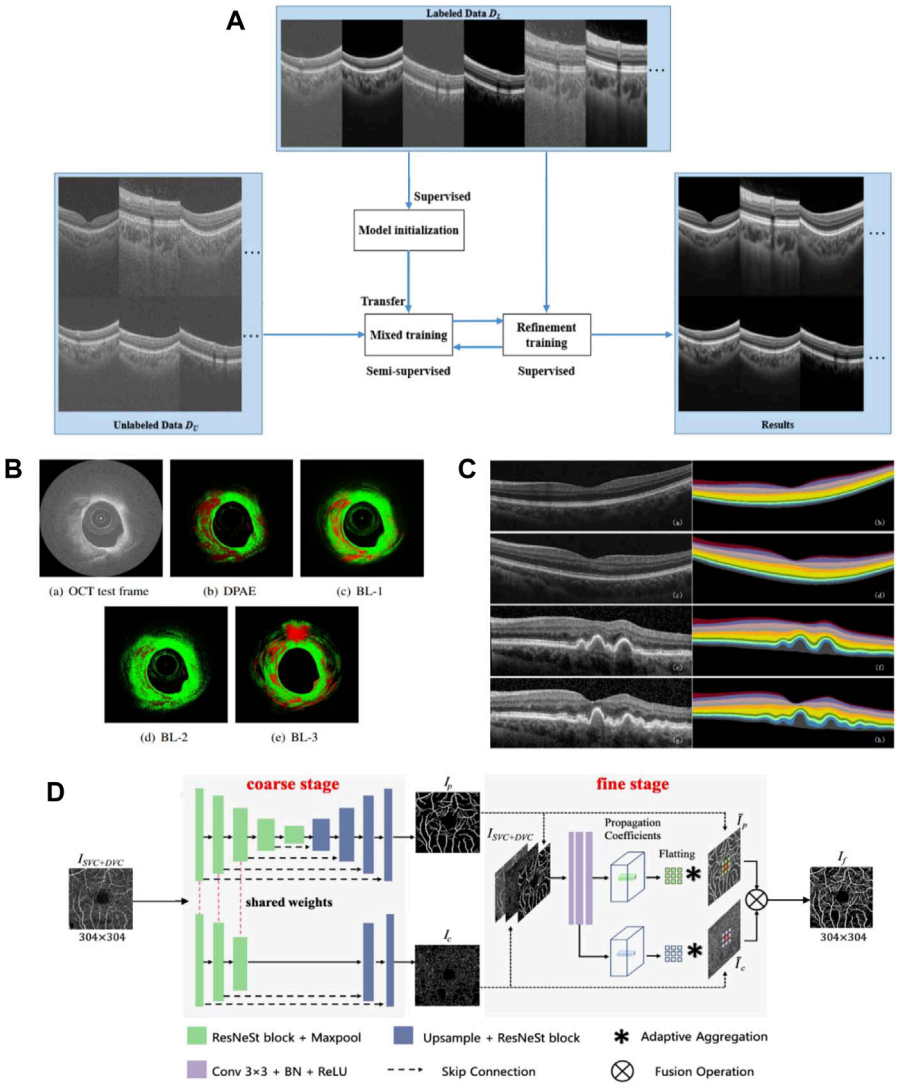

FIGURE 10
Related achievements of AI processing OCT images. **(A)** structure of the proposed semi-supervised system (adapted and modified from Wang et al., 2021). **(B)** The result of plaque detection, the red area represents the detected plaque, and the green area represents the normal tissue (adapted and modified from Roy et al., 2016). **(C)** Retinal 10-layer segmentation prediction results, The left is the original image, the right is the segmentation result (adapted and modified from Li et al., 2019). **(D)** Architecture of the proposed OCTA-Net network (adapted and modified from Ma et al., 2021).

sparsity-based image denoising, and then combine graph theory, dynamic programming and SVM to segment the ten-layer boundary of the mouse retina (Srinivasan et al., 2014).

Recently, researchers have begun to use optical coherence tomography angiography (OCTA) images to study retinal blood vessel segmentation. Compared with the more commonly used color fundus imaging techniques, OCTA can present subtle microvessels. Methods for vessel segmentation using deep learning can be roughly divided into two categories. The first category is to use multiple deep learning networks to refine the segmentation results. Ma et al. create a dataset ROSE containing 229 annotated OCTA images and propose a two-stage vessel segmentation network (OCTA-Net), where the coarse stage module is used to generate preliminary confidence maps, and the fine stage is to optimize vessel shape (Figure 10D) (Ma et al., 2021). The second is to enhance the ability of a single network to extract features. Mou et al. use U-Net as the basis and combined with self-attention mechanism to build a channel and spatial attention network, which can process various types of images from corneal confocal microscopy and OCTA (Mou et al., 2019). Li et al. propose an image projection network (IPN). The network architecture uses three-dimensional convolution and

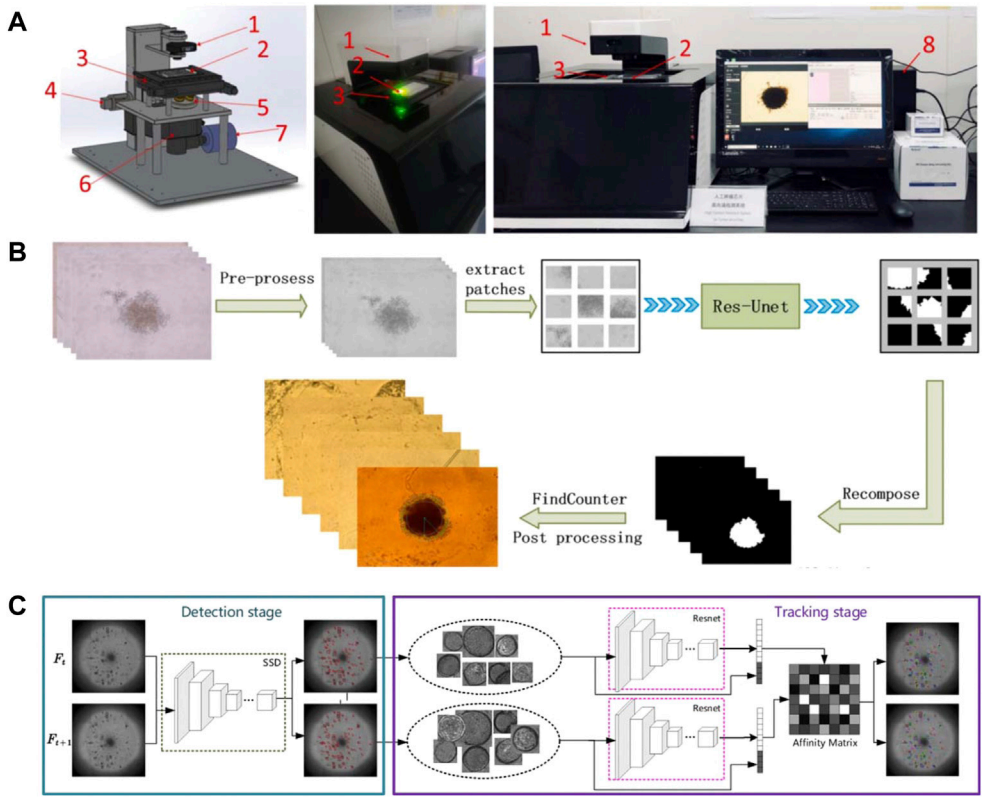

FIGURE 11
Relevant results of artificial intelligence combined with organoids. **(A–B)** System and process for edge detection of tumor spheres (adapted and modified from Chen et al., 2021b). **(A)** The SMART system for automated imaging and analysis. 1) Condenser with light source; 2) sample plate; 3) motorized x,y stage; 4) motorized Z-axis module; 5) objective wheel; 6) filter wheel; 7) CCD; 8) computer to control SMART system with developed software interface. **(B)** The process of tumor sphere edge detection. **(C)** Pipeline for organoids tracking (adapted and modified from Bian et al., 2021).

unidirectional pooling to achieve 3D-to-2D retinal vessel segmentation and foveal avascularzone segmentation (Li et al., 2020c). In (Liu et al., 2020b), unsupervised OCTA retinal vessel segmentation is proposed using encoders constructed from the same regions of different devices (Liu et al., 2020b).

6.4 Organoids combined with artificial intelligence

The development of artificial intelligence on OOC mainly focuses on the analysis of organoid images. Our team build a fully automated tumor spheres analysis system (Figure 11A) that integrates automatic identification, autofocus, and a CNN algorithm based on improved U-Net for accurate tumor boundary detection (Figure 11B). Moreover, two comprehensive parameters—the excess perimeter index and the multiscale entropy index are developed to analyze tumor invasion (Chen et al., 2021b). Bian et al. develop a deep learning model for detection and tracking of high-throughput organoid images. It is mainly implemented in two steps. The first step is to detect the organoids in the collected images of all periods, and the second step is to perform feature extraction on the detected organoids, and calculate the similarity of adjacent periods of organoids for tracking (Figure 11C) (Bian et al., 2021). Kegeles et al. use deep learning algorithms for retinal organoid differentiation, specifically using transfer learning to train a CNN for feature extraction and sample classification (Kegeles et al., 2020). Kong et al. use machine learning methods in colorectal and bladder organoid models to predict the efficacy of anti-cancer drugs in patients (Kong et al., 2020). In addition, researchers have improved deep learning methods for characterizing organoid models using augmented loss functions based on previous studies (Winkelmaier and Parvin, 2021). The development of organoids and OOC is unstoppable, and the application of artificial intelligence methods will undoubtedly bring greater vitality and impetus to the development of this field.

7 Discussion and conclusion

7.1 Discussion

1) A close combination between OOC or organoid and image-guided radiotherapy may provide extra benefits for the treatment of related diseases, especially in the field of oncology, which requires a more precise localization and efficient workflow. This challenge was overcome by a newly-designed integrated CT linear accelerator (linac) uRT-linac 506c, by achieving a diagnostic-quality visualization of anatomical structures and a seamless workflow (Yu et al., 2021). Artificial intelligence algorithm is also applied to the dose prediction of intensity-modulated radiotherapy plan generating to simply the clinical trial (Sun et al., 2022).
2) Medical imaging methods with high spatial resolution such as micro-CT, small animal MRI, and OCT are required for small-sized organoids. Some organoids with size reaching millimeter level and visible to the naked eye, such as tumor spheres, may be imaged by clinical MRI, and the instrument is easier to obtain.
3) In addition to the structural imaging mainly discussed in this article, positron emission tomography (PET) and MRS are very promising in combination with OOC to monitor biochemical changes in tissues. PET is often combined with CT or MRI. As the first total-body PET/CT scanner, the uEXPLORER can provide dynamic images with higher temporal resolution, sensitivity and signal-to-noise ratio, contributing higher feasibility to the proposed research (Marro et al., 2016; Cherry et al., 2018; Liu et al., 2021). Furthermore, benefited from the inherent advantages of MRI, PET/MR is expected to provide better soft tissue contrast compared to PET/CT. More promisingly, some previous researches show the higher sensitivity and specificity of integrated in the detection of micro lesions (Zhou et al., 2021). PET/CT and PET/MRI will provide multi-angle information for analyzing the changes and characteristics of tumor spheres.
4) In the future, as OOC enters the market, medical imaging instruments will be required to process multiple OOCs, most likely arrays of OOCs, simultaneously, and faster or even real-time imaging technology will be required. Exploring medical imaging instruments dedicated to OOC is both a challenge and an opportunity.
5) Artificial intelligence has been widely used in image analysis of medical imaging, including object detection, image segmentation, and image enhancement mentioned in this paper. In the same way, when medical imaging technology is used to image OOC, artificial intelligence will also support the development of OOC by automatically analyzing images.

7.2 Conclusion

Imaging of tissue-engineered artificial tissues and OOCs is in the ascendant. Admittedly, there are limited works utilizing medical imaging tools for tissue engineering and OOC researches. However, with the increase in the application of 3D tissue models and OOCs in drug discovery, environmental protection, and personalized medicine, we believe, in the very near future, the use of medical imaging technology to image micro-organs and use AI for analysis could be a mainstream methodology for organoid and OOC imaging. This paper reviews the research on medical imaging, artificial intelligence especially deep learning application and 3D tissue construction technology, as well as the combination of the two, which will provide relevant biomedical engineering researchers with effective imaging methods for different organoids, and lead to a more rapid development of research in this field.

Author contributions

ZC and ZG were involved in project administration. WG, CW, QL, DL helped in investigating. WG, CW, ZC were involved in writing-original draft. XZ and JY helped in instrument research. WG, QL, ZC and YS helped in writing-review & editing. ZC, ZG, and YS helped in supervision.

Funding

This work was supported by the National Key R&D Program of China (2017YFA0700500) and National Natural Science Foundation of China (Grant No. 62172202), Experiment Project of China Manned Space Program HYZHXM01019, and the Fundamental Research Funds for the Central Universities from Southeast University:3207032101C3.

Conflict of interest

Authors Xijing Zhang and Jianmin Yuan were employed by United Imaging Group.

The remaining authors declare that the research was conducted in the absence of any commercial or financial relationships that could be construed as a potential conflict of interest.

Publisher's note

References

Abdullah, K. A., and Reed, W. (2018). 3D printing in medical imaging and healthcare services. *J. Med. Radiat. Sci.* 65 (3), 237–239. doi:10.1002/jmrs.292

Alkadi, R., Taher, F., El-baz, A., and Werghi, N. (2018). A deep learning-based approach for the detection and localization of prostate cancer in T2 magnetic resonance images. *J. Digit. Imaging* 32 (5), 793–807. doi:10.1007/s10278-018-0160-1

Amoroso, N., La Rocca, M., Bellantuono, L., Diacono, D., Fanizzi, A., Lella, E., et al. (2019). Deep learning and multiplex networks for accurate modeling of brain age. *Front. Aging Neurosci.* 11, 115. doi:10.3389/fnagi.2019.00115

Andermatt, S., Pezold, S., and Cattin, P. (2016). "Multi-dimensional gated recurrent units for the segmentation of biomedical 3D-data," in 2nd International Workshop on Deep Learning in Medical Image Analysis (DLMIA)/1st International Workshop on Large-Scale Annotation of Biomedical Data and Expert Label Synthesis (LABELS) (Athens, GREECE.

Artegiani, B., and Clevers, H. (2018). Use and application of 3D-organoid technology. *Hum. Mol. Genet.* 27 (R2), R99–R107. doi:10.1093/hmg/ddy187

Asaoka, R., Murata, H., Hirasawa, K., Fujino, Y., Matsuura, M., Miki, A., et al. (2019). Using deep learning and transfer learning to accurately diagnose early-onset glaucoma from macular optical coherence tomography images. *Am. J. Ophthalmol.* 198, 136–145. doi:10.1016/j.ajo.2018.10.007

Aumann, S., Donner, S., Fischer, J., and Müller, F. (2019). Optical coherence tomography (OCT): Principle and technical realization. *High Resolut. Imaging Microsc. Ophthalmol.*, 59–85. doi:10.1007/978-3-030-16638-0_3

Badai, J., Bu, Q., and Zhang, L. (2020). Review of artificial intelligence applications and algorithms for brain organoid research. *Interdiscip. Sci. Comput. Life Sci.* 12 (4), 383–394. doi:10.1007/s12539-020-00386-4

Bakhshandeh, B., Zarrintaj, P., Oftadeh, M. O., Keramati, F., Fouladiha, H., Sohrabi-jahromi, S., et al. (2017). Tissue engineering; strategies, tissues, and biomaterials. *Biotechnol. Genet. Eng. Rev.* 33 (2), 144–172. doi:10.1080/02648725.2018.1430464

Bartos, M. (2018). MICRO-CT in tissue engineering scaffolds designed for bone regeneration: Principles and application. *Ceram. - Silik.* 62 (2), 194–199. doi:10.13168/cs.2018.0012

Bartoš, M. (2018). Micro-CT in tissue engineering scaffolds designed for bone regeneration: Principles and application. *Ceram. - Silik.* 62 (2), 194–199. doi:10.13168/cs.2018.0012

Benou, A., Veksler, R., Friedman, A., and Riklin Raviv, T. (2017). Ensemble of expert deep neural networks for spatio-temporal denoising of contrast-enhanced MRI sequences. *Med. image Anal.* 42, 145–159. doi:10.1016/j.media.2017.07.006

Berthiaume, F., Maguire, T. J., and Yarmush, M. L. (2011). Tissue engineering and regenerative medicine: History, progress, and challenges. *Annu. Rev. Chem. Biomol. Eng.* 2, 403–430. doi:10.1146/annurev-chembioeng-061010-114257

Bian, X., Li, G., Wang, C., Liu, W., Lin, X., Chen, Z., et al. (2021). A deep learning model for detection and tracking in high-throughput images of organoid. *Comput. Biol. Med.* 134, 104490. doi:10.1016/j.compbiomed.2021.104490

Bille, J. F. (2019). *High resolution imaging in microscopy and ophthalmology new Frontiers in biomedical optics*. 1st ed. ChamImprint: Springer International PublishingSpringer.

Bleijs, M., Wetering, M., Clevers, H., and Drost, J. (2019). Xenograft and organoid model systems in cancer research. *EMBO J.* 38 (15), e101654. doi:10.15252/embj.2019101654

Boretius, S., Kasper, L., Tammer, R., Michaelis, T., and Frahm, J. (2009). MRI of cellular layers in mouse brain *in vivo*. *Neuroimage* 47 (4), 1252–1260. doi:10.1016/j.neuroimage.2009.05.095

Brugaletta, S., Radu, M. D., Garcia-Garcia, H. M., Heo, J. H., Farooq, V., Girasis, C., et al. (2012). Circumferential evaluation of the neointima by optical coherence tomography after ABSORB bioresorbable vascular scaffold implantation: Can the scaffold cap the plaque? *Atherosclerosis* 221 (1), 106–112. doi:10.1016/j.atherosclerosis.2011.12.008

Cao, G., Lee, Y. Z., Peng, R., Liu, Z., Rajaram, R., Calderon-Colon, X., et al. (2009). A dynamic micro-CT scanner based on a carbon nanotube field emission x-ray source. *Phys. Med. Biol.* 54 (8), 2323–2340. doi:10.1088/0031-9155/54/8/005

Cao, H., Liu, H., Song, E., Ma, G., Jin, R., Xu, X., et al. (2020). A two-stage convolutional neural networks for lung nodule detection. *IEEE J. Biomed. Health Inf.* 24 (7), 2006–2015. doi:10.1109/jbhi.2019.2963720

Carvalho, V., Goncalves, I., Lage, T., Rodrigues, R. O., Minas, G., Teixeira, S. F. C. F., et al. (2021). 3D printing techniques and their applications to organ-on-a-chip platforms: A systematic review. *Sensors (Basel, Switz.* 21 (9), 3304. doi:10.3390/s21093304

Chaber, S., Helbig, H., and Gamulescu, M. A. (2010). Time domain OCT versus frequency domain OCT. Measuring differences of macular thickness in healthy subjects. *Ophthalmologe.* 107 (1), 36–40. doi:10.1007/s00347-009-1941-1

Chen, W., Hou, X., Hu, Y., Huang, G., Ye, X., and Nie, S. (2021). A deep learning- and CT image-based prognostic model for the prediction of survival in non-small cell lung cancer. *Med. Phys.* 48 (12), 7946–7958. doi:10.1002/mp.15302

Chen, W., Yang, J., Liao, W., Zhou, J., Zheng, J., Wu, Y., et al. (2017). *In vitro* remodeling and structural characterization of degradable polymer scaffold-based tissue-engineered vascular grafts using optical coherence tomography. *Cell. Tissue Res.* 370 (3), 417–426. doi:10.1007/s00441-017-2683-z

Chen, Y., Shi, F., Christodouloun, A. G., Xie, Y., Zhou, Z., and Li, D. (2018). "Efficient and accurate MRI super-resolution using a generative adversarial network and 3D multi-level densely connected network," in International conference on medical image computing and computer-assisted intervention (Cham: Springer), 91-99.

Chen, Z., Ma, N., Sun, X., Li, Q., Zeng, Y., Chen, F., et al. (2021). Automated evaluation of tumor spheroid behavior in 3D culture using deep learning-based recognition. *Biomaterials* 272, 120770. doi:10.1016/j.biomaterials.2021.120770

Cherry, S. R., Jones, T., Karp, J. S., Qi, J., Moses, W. W., and Badawi, R. D. (2018). Total-body PET: Maximizing sensitivity to create new opportunities for clinical research and patient care. *J. Nucl. Med.* 59 (1), 3–12. doi:10.2967/jnumed.116.184028

Cheung, C. Y. L., Ong, Y. T., Hilal, S., Ikram, M. K., Low, S., Ong, Y. L., et al. (2015). Retinal ganglion cell analysis using high-definition optical coherence tomography in patients with mild cognitive impairment and Alzheimer's disease. *J. Alzheimers Dis.* 45 (1), 45–56. doi:10.3233/jad-141659

Cioffi, M., Boschetti, F., Raimondi, M. T., and Dubini, G. (2006). Modeling evaluation of the fluid-dynamic microenvironment in tissue-engineered constructs: A micro-CT based model. *Biotechnol. Bioeng.* 93 (3), 500–510. doi:10.1002/bit.20740

Cox, C. W., and Lynch, D. A. (2015). Medical imaging in occupational and environmental lung disease. *Curr. Opin. Pulm. Med.* 21 (2), 163–170. doi:10.1097/mcp.0000000000000139

Currie, G., Hawk, K. E., Rohren, E., Vial, A., and Klein, R. (2019). Machine learning and deep learning in medical imaging: Intelligent imaging. *J. Med. Imaging Radiat. Sci.* 50 (4), 477–487. doi:10.1016/j.jmir.2019.09.005

Delannoy, Q., Pham, C. H., Cazorla, C., Tor-Diez, C., Dolle, G., Meunier, H., et al. (2020). SegSRGAN: Super-resolution and segmentation using generative adversarial networks—application to neonatal brain MRI. *Comput. Biol. Med.* 120, 103755. doi:10.1016/j.compbiomed.2020.103755

Despotović, I., Goossens, B., and Philips, W. (2015). MRI segmentation of the human brain: Challenges, methods, and applications. *Comput. Math. Methods Med.* 2015 (6), 1–23. doi:10.1155/2015/450341

Dey, M., and Ozbolat, I. T. (2020). 3D bioprinting of cells, tissues and organs. *Sci. Rep.* 10 (1), 14023. doi:10.1038/s41598-020-70086-y

Doost, A., Rangel, A., Nguyen, Q., Morahan, G., and Arnolda, L. (2020). Micro-CT scan with virtual dissection of left ventricle is a non-destructive, reproducible alternative to dissection and weighing for left ventricular size. *Sci. Rep.* 10 (1), 13853. doi:10.1038/s41598-020-70734-3

du Plessis, A., Yadroitsev, I., Yadroitsava, I., and Le Roux, S. G. X-ray microcomputed tomography in additive manufacturing: A review of the current technology and applications. 3D*Print. Addit. Manuf.*, 2018. 5(3): p. 227–247. doi:10.1089/3dp.2018.0060

Dutta, D., Heo, I., and Clevers, H. (2017). Disease modeling in stem cell-derived 3D organoid systems. *Trends Mol. Med.* 23 (5), 393–410. doi:10.1016/j.molmed.2017.02.007

El-Rewaidy, H., Neisius, U., Mancio, J., Kucukseymen, S., Rodriguez, J., Paskavitz, A., et al. (2020). Deep complex convolutional network for fast reconstruction of 3D late gadolinium enhancement cardiac MRI. *NMR Biomed.* 33 (7), e4312. doi:10.1002/nbm.4312

Espedal, H., Berg, H. F., Fonnes, T., Fasmer, K. E., Krakstad, C., and Haldorsen, I. S. (2021). Feasibility and utility of MRI and dynamic (18)F-FDG-PET in an orthotopic organoid-based patient-derived mouse model of endometrial cancer. *J. Transl. Med.* 19 (1), 406. doi:10.1186/s12967-021-03086-9

Fang, L. Y., Cunefare, D., Wang, C., Guymer, R. H., Li, S., and Farsiu, S. (2017). Automatic segmentation of nine retinal layer boundaries in OCT images of non-exudative AMD patients using deep learning and graph search. *Biomed. Opt. Express* 8 (5), 2732–2744. doi:10.1364/boe.8.002732

Felder, J., Celik, A. A., Choi, C. H., Schwan, S., and Shah, N. J. (2017). 9.4 T small animal MRI using clinical components for direct translational studies. *J. Transl. Med.* 15 (1), 264. doi:10.1186/s12967-017-1373-7

Fleischer, S., Tavakol, D. N., and Vunjak-Novakovic, G. (2020). From arteries to capillaries: Approaches to engineering human vasculature. *Adv. Funct. Mat.* 30 (37), 1910811. doi:10.1002/adfm.201910811

Fu, H., Xu, Y., Lin, S., Zhang, X., Wong, D. W. K., Liu, J., et al. (2017). Segmentation and quantification for angle-closure glaucoma assessment in anterior segment OCT. *IEEE Trans. Med. Imaging* 36 (9), 1930–1938. doi:10.1109/tmi.2017.2703147

Fujihara, Y., Nitta, N., Misawa, M., Hyodo, K., Shirasaki, Y., Hayashi, K., et al. (2016). T2 and apparent diffusion coefficient of MRI reflect maturation of tissue-engineered auricular cartilage subcutaneously transplanted in rats. *Tissue Eng. Part C. Methods* 22 (5), 429–438. doi:10.1089/ten.tec.2015.0291

Gao, H., Sun, L., and Wang, J.-X. (2021). Super-resolution and denoising of fluid flow using physics-informed convolutional neural networks without high-resolution labels. *Phys. Fluids* 33 (7), 073603. doi:10.1063/5.0054312

Gao, Y., Wang, P., Qian, M., Zhao, J., Xu, H., and Zhang, X. (2019). A surface loop array for *in vivo* small animal MRI/fMRI on 7T human scanners. *Phys. Med. Biol.* 64 (3), 035009. doi:10.1088/1361-6560/aaf9e4

Gjorevski, N., Sachs, N., Manfrin, A., Giger, S., Bragina, M. E., Ordonez-Moran, P., et al. (2016). Designer matrices for intestinal stem cell and organoid culture. *Nature* 539 (7630), 560–564. doi:10.1038/nature20168

Goldstein, Y., Spitz, S., Turjeman, K., Selinger, F., Barenholz, Y., Ertl, P., et al. (2021). Breaking the third wall: Implementing 3D-printing techniques to expand the complexity and abilities of multi-organ-on-a-chip devices. *Micromachines (Basel)* 12 (6), 627. doi:10.3390/mi12060627

Golebiewska, A., Hau, A. C., Oudin, A., Stieber, D., Yabo, Y. A., Baus, V., et al. (2020). Patient-derived organoids and orthotopic xenografts of primary and recurrent gliomas represent relevant patient avatars for precision oncology. *Acta Neuropathol.* 140 (6), 919–949. doi:10.1007/s00401-020-02226-7

Gore, J. C. (2020). Artificial intelligence in medical imaging. *Magn. Reson. Imaging* 68, A1–A4. doi:10.1016/j.mri.2019.12.006

Gravina, M., Marrone, S., Piantadosi, G., Sansone, M., and Sansone, C. (2019). Springer.3TP-CNN: Radiomics and deep learning for lesions classification in DCE-MRIInternational Conference on Image Analysis and Processing

Gu, H., Gan, W., Zhang, C., Feng, A., Wang, H., Huang, Y., et al. (2021). A 2D–3D hybrid convolutional neural network for lung lobe auto-segmentation on standard slice thickness computed tomography of patients receiving radiotherapy. *Biomed. Eng. OnLine* 20 (1), 94–13. doi:10.1186/s12938-021-00932-1

Hamilton, J., Franson, D., and Seiberlich, N. (2017). Recent advances in parallel imaging for MRI. *Prog. Nucl. Magn. Reson. Spectrosc.* 101, 71–95. doi:10.1016/j.pnmrs.2017.04.002

Hammernik, K., Klatzer, T., Kobler, E., Recht, M. P., Sodickson, D. K., and Pock, T., (2018). Learning a variational network for reconstruction of accelerated MRI data. *Magn. Reson. Med.* 79 (6), 3055–3071. doi:10.1002/mrm.26977

Harrington, J. K., Chahboune, H., Criscione, J. M., Li, A. Y., Hibino, N., Yi, T., et al. (2011). Determining the fate of seeded cells in venous tissue-engineered vascular grafts using serial MRI. *FASEB J.* 25 (12), 4150–4161. doi:10.1096/fj.11-185140

Herrmann, K. H., Schmidt, S., Kretz, A., Haenold, R., Krumbein, I., Metzler, M., et al. (2012). Possibilities and limitations for high resolution small animal MRI on a clinical whole-body 3T scanner. *Magn. Reson. Mat. Phy.* 25 (3), 233–244. doi:10.1007/s10334-011-0284-5

Hespel, A. M., and Cole, R. C. (2018). Advances in high-field MRI. *Veterinary Clin. N. Am. Small Animal Pract.* 48 (1), 11–29. doi:10.1016/j.cvsm.2017.08.002

Higaki, T., Nakamura, Y., Tatsugami, F., Nakaura, T., and Awai, K. (2019). Improvement of image quality at CT and MRI using deep learning. *Jpn. J. Radiol.* 37 (1), 73–80. doi:10.1007/s11604-018-0796-2

Holbrook, M. D., Clark, D. P., Patel, R., Qi, Y., Bassil, A. M., Mowery, Y. M., et al. (2021). Detection of lung nodules in micro-CT imaging using deep learning. *Tomography* 7 (3), 358–372. doi:10.3390/tomography7030032

Hoyer, C., Gass, N., Weber-Fahr, W., and Sartorius, A. (2014). Advantages and challenges of small animal magnetic resonance imaging as a translational tool. *Neuropsychobiology* 69 (4), 187–201. doi:10.1159/000360859

Huang, Q. Y., Xian, Y., Yang, D., Qu, H., Yi, J., Wu, P., et al. (2021). Dynamic MRI reconstruction with end-to-end motion-guided network. *Med. Image Anal.* 68, 101901. doi:10.1016/j.media.2020.101901

Huh, D., Matthews, B. D., Mammoto, A., Montoya-Zavala, M., Hsin, H. Y., and Ingber, D. E. (2010). Reconstituting organ-level lung functions on a chip. *Science* 328 (5986), 1662–1668. doi:10.1126/science.1188302

Isensee, F., Jäger, P. F., Full, P. M., Vollmuth, P., and Maier-Hein, K. H. (2021). *nnU-net for brain tumor segmentation*. ChamCham: Springer International Publishing, 118–132.

Ishii, D., Enmi, J. i., Moriwaki, T., Ishibashi-Ueda, H., Kobayashi, M., Iwana, S., et al. (2016). Development of *in vivo* tissue-engineered microvascular grafts with an ultra small diameter of 0.6 mm (MicroBiotubes): Acute phase evaluation by optical coherence tomography and magnetic resonance angiography. *J. Artif. Organs* 19 (3), 262–269. doi:10.1007/s10047-016-0894-9

Jahng, G.-H., Li, K. L., Ostergaard, L., and Calamante, F. (2014). Perfusion magnetic resonance imaging: A comprehensive update on principles and techniques. *Korean J. Radiol.* 15 (5), 554–577. doi:10.3348/kjr.2014.15.5.554

Jain, S., Indora, S., and Atal, D. K. (2021). Lung nodule segmentation using salp shuffled shepherd optimization algorithm-based generative adversarial network. *Comput. Biol. Med.* 137, 104811. doi:10.1016/j.compbiomed.2021.104811

Jakob, P. (2011). *Small animal magnetic resonance imaging: Basic principles, instrumentation and practical issue*. Berlin, Heidelberg: Springer Berlin Heidelberg.

Jo, T., Nho, K., and Saykin, A. J. (2019). Deep learning in Alzheimer's disease: Diagnostic classification and prognostic prediction using neuroimaging data. *Front. Aging Neurosci.* 11, 220. doi:10.3389/fnagi.2019.00220

Kegeles, E., Naumov, A., Karpulevich, E. A., Volchkov, P., and Baranov, P. (2020). Convolutional neural networks can predict retinal differentiation in retinal organoids. *Front. Cell. Neurosci.* 14, 171. doi:10.3389/fncel.2020.00171

Kern, D., and Mastmeyer, A. (2021). "3D bounding box detection in volumetric medical image data: A systematic literature review," in 2021 IEEE 8th International Conference on Industrial Engineering and Applications (ICIEA) (IEEE).

Khademhosseini, A., and Langer, R. (2016). A decade of progress in tissue engineering. *Nat. Protoc.* 11 (10), 1775–1781. doi:10.1038/nprot.2016.123

Kim, H. J., Huh, D., Hamilton, G., and Ingber, D. E. (2012). Human gut-on-a-chip inhabited by microbial flora that experiences intestinal peristalsis-like motions and flow. *Lab. Chip* 12 (12), 2165–2174. doi:10.1039/c2lc40074j

Kim, S. B., Lee, E. J., Han, J. C., and Kee, C. (2017). Comparison of peripapillary vessel density between preperimetric and perimetric glaucoma evaluated by OCT-angiography. *PLoS One* 12 (8), e0184297. doi:10.1371/journal.pone.0184297

Knowlton, S., Yenilmez, B., and Tasoglu, S. (2016). Towards single-step biofabrication of organs on a chip via 3D printing. *Trends Biotechnol.* 34 (9), 685–688. doi:10.1016/j.tibtech.2016.06.005

Kong, J., Lee, H., Kim, D., Han, S. K., Ha, D., Shin, K., et al. (2020). Network-based machine learning in colorectal and bladder organoid models predicts anti-cancer drug efficacy in patients. *Nat. Commun.* 11 (1), 1–13. doi:10.1038/s41467-020-19313-8

Lancaster, M. A., and Knoblich, J. A. (2014). Organogenesis in a dish: Modeling development and disease using organoid technologies. *Science* 345 (6194), 1247125. doi:10.1126/science.1247125

Langer, R., and Vacanti, J. (2016). Advances in tissue engineering. *J. Pediatr. Surg.* 51 (1), 8–12. doi:10.1016/j.jpedsurg.2015.10.022

Lee, H., and Cho, D.-W. (2016). One-step fabrication of an organ-on-a-chip with spatial heterogeneity using a 3D bioprinting technology. *Lab. Chip* 16 (14), 2618–2625. doi:10.1039/c6lc00450d

Lee, J. H., Chen, Z., He, S., Zhou, J. K., Tsai, A., Truskey, G. A., et al. (2021). Emulating early atherosclerosis in a vascular microphysiological system using branched tissue-engineered blood vessels. *Adv. Biol.* 5 (4), 2000428. doi:10.1002/adbi.202000428

Lee, J., and Koehler, K. R. (2021). Skin organoids: A new human model for developmental and translational research. *Exp. Dermatol.* 30 (4), 613–620. doi:10.1111/exd.14292

Lee, J. W., Choi, Y. J., Yong, W. J., Pati, F., Shim, J. H., Kang, K. S., et al. (2016). Development of a 3D cell printed construct considering angiogenesis for liver tissue engineering. *Biofabrication* 8 (1), 015007. doi:10.1088/1758-5090/8/1/015007

Lehtinen, J., Munkberg, J., Hasselgren, J., Laine, S., Karras, T., Aittala, M., et al. (2018). *Noise2Noise: Learning image restoration without clean data*. arXiv preprint arXiv:1803.04189..

Levitz, D., Hinds, M. T., Wang, R., Ma, Z., Hanson, S. R., and Jacques, S. L. (2007). "A tissue-engineered 3D model of light scattering in atherosclerotic plaques," in *Optics in tissue engineering and regenerative medicine*. International Society for Optics and Photonics.

Lewis, M. A., Pascoal, A., Keevil, S. F., and Lewis, C. A. (2016). Selecting a CT scanner for cardiac imaging: The heart of the matter. *Br. J. Radiol.* 89 (1065), 20160376. doi:10.1259/bjr.20160376

Li, M. C., Chen, Y., Ji, Z., Xie, K., Yuan, S., Chen, Q., et al. (2020). Image projection network: 3D to 2D image segmentation in OCTA images. *IEEE Trans. Med. Imaging* 39 (11), 3343–3354. doi:10.1109/tmi.2020.2992244

Li, Q. L., Li, S., He, Z., Guan, H., Chen, R., Xu, Y., et al. (2020). DeepRetina: Layer segmentation of retina in OCT images using deep learning. *Transl. Vis. Sci. Technol.* 9 (2), 61. doi:10.1167/tvst.9.2.61

Li, S., Zhou, J., Liang, D., and Liu, Q. (2020). MRI denoising using progressively distribution-based neural network. *Magn. Reson. Imaging* 71, 55–68. doi:10.1016/j.mri.2020.04.006

Li, Z. J., Yu, J., Wang, Y., Zhou, H., Yang, H., and Qiao, Z. (2021). DeepVolume: Brain structure and spatial connection-aware network for brain MRI super-resolution. *IEEE Trans. Cybern.* 51 (7), 3441–3454. doi:10.1109/tcyb.2019.2933633

Li, Z., Shi, W., Xing, Q., Miao, Y., He, W., Yang, H., et al. (2021). Low-dose CT image denoising with improving WGAN and hybrid loss function. *Comput. Math. Methods Med.*, 1–14. doi:10.1155/2021/2973108

Lin, E., and Alessio, A. (2009). What are the basic concepts of temporal, contrast, and spatial resolution in cardiac CT? *J. Cardiovasc. Comput. Tomogr.* 3 (6), 403–408. doi:10.1016/j.jcct.2009.07.003

Lin, E., and Alessio, A. (2009). What are the basic concepts of temporal, contrast, and spatial resolution in cardiac CT? *J. Cardiovasc. Comput. Tomogr.* 3 (6), 403–408. doi:10.1016/j.jcct.2009.07.003

Liu, G.-D., Li, Y. C., Zhang, W., and Zhang, L. (2020). A brief review of artificial intelligence applications and algorithms for psychiatric disorders. *Engineering* 6 (4), 462–467. doi:10.1016/j.eng.2019.06.008

Liu, G., Yu, H., Shi, D., Hu, P., Hu, Y., Tan, H., et al. (2021). Short-time total-body dynamic PET imaging performance in quantifying the kinetic metrics of 18F-FDG in healthy volunteers. *Eur. J. Nucl. Med. Mol. Imaging* 49, 2493–2503. doi:10.1007/s00259-021-05500-2

Liu, S., Zheng, H., Feng, Y., and Li, W. (2017). "Prostate cancer diagnosis using deep learning with 3D multiparametric MRI," in *Medical imaging 2017: Computer-aided diagnosis* (Orlando: SPIE Medical Imaging).

Liu, Y. H., Zuo, L., Carass, A., He, Y., Filippatou, A., Solomon, S. D., et al. (2020). "Variational intensity cross channel encoder for unsupervised vessel segmentation on OCT angiography," in Medical Imaging Conference - Image Processing (Houston, TX.

Lui, C., Chin, A. F., Park, S., Yeung, E., Kwon, C., Tomaselli, G., et al. (2021). Mechanical stimulation enhances development of scaffold-free, 3D-printed, engineered heart tissue grafts. *J. Tissue Eng. Regen. Med.* 15 (5), 503–512. doi:10.1002/term.3188

Lundervold, A. S., and Lundervold, A. (2019). An overview of deep learning in medical imaging focusing on MRI. *Z. fur Med. Phys.* 29 (2), 102–127. doi:10.1016/j.zemedi.2018.11.002

Ma, Y., Hao, H., Xie, J., Fu, H., Zhang, J., Yang, J., et al. (2021). Rose: A retinal OCT-angiography vessel segmentation dataset and new model. *IEEE Trans. Med. Imaging* 40 (3), 928–939. doi:10.1109/tmi.2020.3042802

Mandrycky, C., Wang, Z., Kim, K., and Kim, D. H. (2016). 3D bioprinting for engineering complex tissues. *Biotechnol. Adv.* 34 (4), 422–434. doi:10.1016/j.biotechadv.2015.12.011

Markou, M., Kouroupis, D., Badounas, F., Katsouras, A., Kyrkou, A., Fotsis, T., et al. (2020). Tissue engineering using vascular organoids from human pluripotent stem cell derived mural cell phenotypes. *Front. Bioeng. Biotechnol.* 8, 278. doi:10.3389/fbioe.2020.00278

Marro, A., Bandukwala, T., and Mak, W. (2016). Three-dimensional printing and medical imaging: A review of the methods and applications. *Curr. Probl. Diagn. Radiol.* 45 (1), 2–9. doi:10.1067/j.cpradiol.2015.07.009

Marsano, A., Conficconi, C., Lemme, M., Occhetta, P., Gaudiello, E., Votta, E., et al. (2016). Beating heart on a chip: A novel microfluidic platform to generate functional 3D cardiac microtissues. *Lab. Chip* 16 (3), 599–610. doi:10.1039/c5lc01356a

Masutani, E. M., Bahrami, N., and Hsiao, A. (2020). Deep learning single-frame and multiframe super-resolution for cardiac MRI. *Radiology* 295 (3), 552–561. doi:10.1148/radiol.2020192173

Matai, I., Kaur, G., Seyedsalehi, A., McClinton, A., and Laurencin, C. T. (2020). Progress in 3D bioprinting technology for tissue/organ regenerative engineering. *Biomaterials* 226, 119536. doi:10.1016/j.biomaterials.2019.119536

Mauer, M. A. d., Well, E. J. v., Herrmann, J., Groth, M., Morlock, M. M., Maas, R., et al. (2021). Automated age estimation of young individuals based on 3D knee MRI using deep learning. *Int. J. Leg. Med.* 135 (2), 649–663. doi:10.1007/s00414-020-02465-z

McCabe, J. M., and Croce, K. J. (2012). Optical coherence tomography. *Circulation* 126 (17), 2140–2143. doi:10.1161/circulationaha.112.117143

Meijer, F. J., and Goraj, B. (2014). Brain MRI in Parkinson's disease. *Front. Biosci.* 6, 711–719. doi:10.2741/e711

Milletari, F., Navab, N., and Ahmadi, S.-A. *V-Net: Fully convolutional neural networks for volumetric medical image segmentation*. IEEE. doi:10.1109/3dv.2016.79

Miyata, S., Homma, K., Numano, T., Tateishi, T., and Ushida, T. (2010). Evaluation of negative fixed-charge density in tissue-engineered cartilage by quantitative MRI and relationship with biomechanical properties. *J. Biomech. Eng.* 132 (7), 071014. doi:10.1115/1.4001369

Mou, L., Zhao, Y., Chen, L., Cheng, J., Gu, Z., Hao, H., et al. (2019). "CS-Net: Channel and spatial attention network for curvilinear structure segmentation," in 10th International Workshop on Machine Learning in Medical Imaging (MLMI)/22nd International Conference on Medical Image Computing and Computer-Assisted Intervention (MICCAI), Shenzhen, PEOPLES R CHINA.

Mueller, M., Schulz-Wackerbarth, C., Steven, P., Lankenau, E., Bonin, T., Mueller, H., et al. (2010). Slit-lamp-adapted fourier-domain OCT for anterior and posterior segments: Preliminary results and comparison to time-domain OCT. *Curr. Eye Res.* 35 (8), 722–732. doi:10.3109/02713683.2010.481069

Musah, S., Dimitrakakis, N., Camacho, D. M., Church, G. M., and Ingber, D. E. (2018). Directed differentiation of human induced pluripotent stem cells into mature kidney podocytes and establishment of a Glomerulus Chip. *Nat. Protoc.* 13 (7), 1662–1685. doi:10.1038/s41596-018-0007-8

Nam, S. Y., Ricles, L. M., Suggs, L. J., and Emelianov, S. Y. (2015). Imaging strategies for tissue engineering applications. *Tissue Eng. Part B Rev.* 21 (1), 88–102. doi:10.1089/ten.teb.2014.0180

Nam, S. Y., Ricles, L. M., Suggs, L. J., and Emelianov, S. Y. (2015). Imaging strategies for tissue engineering applications. *Tissue Eng. Part B Rev.* 21 (1), 88–102. doi:10.1089/ten.teb.2014.0180

Nichol, J. W., and Khademhosseini, A. (2009). Modular tissue engineering: Engineering biological tissues from the bottom up. *Soft Matter* 5 (7), 1312–1319. doi:10.1039/b814285h

Nuciforo, S., Fofana, I., Matter, M. S., Blumer, T., Calabrese, D., Boldanova, T., et al. (2018). Organoid models of human liver cancers derived from tumor needle biopsies. *Cell. Rep.* 24 (5), 1363–1376. doi:10.1016/j.celrep.2018.07.001

Oh, J., Oh, B. L., Lee, K. U., Chae, J. H., and Yun, K. (2020). Identifying schizophrenia using structural MRI with a deep learning algorithm. *Front. Psychiatry* 11, 16–2020. doi:10.3389/fpsyt.2020.00016

Okamura, T., Onuma, Y., Garcia-Garcia, H. M., Regar, E., Wykrzykowska, J. J., Koolen, J., et al. (2010). 3-Dimensional optical coherence tomography assessment of jailed side branches by bioresorbable vascular scaffolds: A proposal for classification. *JACC Cardiovasc. Interv.* 3 (8), 836–844. doi:10.1016/j.jcin.2010.05.011

Orhan, K. (2020). *Micro-computed tomography (micro-CT) in medicine and engineering*. 1st ed., 2020.

Papantoniou, I., Sonnaert, M., Geris, L., Luyten, F. P., Schrooten, J., and Kerckhofs, G. (2014). Three-dimensional characterization of tissue-engineered constructs by contrast-enhanced nanofocus computed tomography. *Tissue Eng. Part C. Methods* 20 (3), 177–187. doi:10.1089/ten.tec.2013.0041

Park, S. E., Georgescu, A., and Huh, D. (2019). Organoids-on-a-chip. *Science* 364 (6444), 960–965. doi:10.1126/science.aaw7894

Pawar, K., Egan, G. F., and Chen, Z. L. (2021). Domain knowledge augmentation of parallel MR image reconstruction using deep learning. *Comput. Med. Imaging Graph.* 92, 101968. doi:10.1016/j.compmedimag.2021.101968

Podoleanu, A. G. (2005). Optical coherence tomography. *Br. J. Radiol.* 78 (935), 976–988. doi:10.1259/bjr/55735832

Podoleanu, A. G. (2012). Optical coherence tomography. *J. Microsc.* 247 (3), 209–219. doi:10.1111/j.1365-2818.2012.03619.x

Poirier-Quinot, M., Frasca, G., Wilhelm, C., Luciani, N., Ginefri, J. C., Darrasse, L., et al. (2010). High-resolution 1.5-tesla magnetic resonance imaging for tissue-engineered constructs: A noninvasive tool to assess three-dimensional scaffold architecture and cell seeding. *Tissue Eng. Part C. Methods* 16 (2), 185–200. doi:10.1089/ten.tec.2009.0015

Poudel, R. P. K., Lamata, P., and Montana, G. *Recurrent fully convolutional neural networks for multi-slice MRI cardiac segmentation*. Cham: Cham: Springer International Publishing.

Qi, D., Chen, H., Yu, L., Zhao, L., Qin, J., Wang, D., et al. (2016). Automatic detection of cerebral microbleeds from MR images via 3D convolutional neural networks. *IEEE Trans. Med. Imaging* 35 (5), 1182–1195. doi:10.1109/tmi.2016.2528129

Reid, J. A., Mollica, P. A., Bruno, R. D., and Sachs, P. C. (2018). Consistent and reproducible cultures of large-scale 3D mammary epithelial structures using an accessible bioprinting platform. *Breast Cancer Res.* 20 (1), 122. doi:10.1186/s13058-018-1045-4

Richards, D. J., Tan, Y., Jia, J., Yao, H., and Mei, Y. (2013). 3D printing for tissue engineering. *Isr. J. Chem.* 53 (9-10), 805–814. doi:10.1002/ijch.201300086

Ronneberger, O., Fischer, P., and Brox, T.. "U-net: Convolutional networks for biomedical image segmentation,"in International conference on medical image computing and computer-assisted intervention (Cham: Springer International Publishing), 234–241.

Rossi, G., Manfrin, A., and Lutolf, M. P. (2018). Progress and potential in organoid research. *Nat. Rev. Genet.* 19 (11), 671–687. doi:10.1038/s41576-018-0051-9

Roy, A. G., Conjeti, S., Carlier, S. G., Houissa, k., Konig, A., Dutta, P. K., et al. "Multiscale distribution preserving autoencoders for plaque detection in intravascular optical coherence tomography," in 2016 IEEE 13th International Symposium on Biomedical Imaging (ISBI) (IEEE).

Roy, A. G., Conjeti, S., Carlier, S. G., Konig, A., Kastrati, A., Dutta, P. K., et al. "Bag of forests for modelling of tissue energy interaction in optical coherence tomography for atherosclerotic plaque susceptibility assessment," in 2015 IEEE 12th International Symposium on Biomedical Imaging (ISBI) (IEEE).

Roy, A. G., Conjeti, S., Karri, S. P. K., Sheet, D., Katouzian, A., Wachinger, C., et al. (2017). ReLayNet: Retinal layer and fluid segmentation of macular optical coherence tomography using fully convolutional networks. *Biomed. Opt. Express* 8 (8), 3627–3642. doi:10.1364/boe.8.003627

Roy, S. S., Sikaria, R., and Susan, A. (2019). A deep learning based CNN approach on MRI for Alzheimer's disease detection. *Intell. Decis. Technol.* 13 (4), 495–505. doi:10.3233/idt-190005

Runge, V. M. (2009). *The physics of clinical MR taught through images*. Springer.

Schlegl, T., Waldstein, S. M., Bogunovic, H., EndstraBer, F., Sadeghipour, A., Philip, A. M., et al. (2018). Fully automated detection and quantification of macular fluid in OCT using deep learning. *Ophthalmology* 125 (4), 549–558. doi:10.1016/j.ophtha.2017.10.031

Schlemper, J., Caballero, J., Hajnal, J. V., Price, A. N., and Rueckert, D. (2018). A deep cascade of convolutional neural networks for dynamic MR image reconstruction. *IEEE Trans. Med. Imaging* 37 (2), 491–503. doi:10.1109/tmi.2017.2760978

Shah, V., Keniya, R., Shridharani, A., Punjabi, M., Shah, J., and Mehendale, N. (2021). Diagnosis of COVID-19 using CT scan images and deep learning techniques. *Emerg. Radiol.* 28 (3), 497–505. doi:10.1007/s10140-020-01886-y

Shan, H., Kruger, U., and Wang, G. (2019). "A novel transfer learning framework for low-dose CT," in 15th International Meeting on Fully Three-Dimensional Image Reconstruction in Radiology and Nuclear Medicine, Philadelphia (International Society for Optics and Photonics) 11072, 513–517. SPIE

Sharif, S., Naqvi, R. A., and Biswas, M. (2020). Learning medical image denoising with deep dynamic residual attention network. *Mathematics* 8 (12), 2192. doi:10.3390/math8122192

Shehata, M., Khalifa, F., Soliman, A., Takieldeen, A., Abou El-Ghar, M., and Keynton, R. (2016). "3D diffusion MRI-based CAD system for early diagnosis of acute renal rejection," in 2016 IEEE 13th International Symposium on Biomedical Imaging (ISBI) (IEEE).

Shelhamer, E., Long, J., and Darrell, T. (2017). Fully convolutional networks for semantic segmentation. *IEEE Trans. Pattern Anal. Mach. Intell.* 39 (4), 640–651. doi:10.1109/tpami.2016.2572683

Shi, Z., Hu, Q., Yue, Y., Wang, Z., Al-Othmani, O. M. S., and Li, H. (2020). Automatic nodule segmentation method for CT images using aggregation-U-Net generative adversarial networks. *Sens. Imaging* 21 (1), 39–16. doi:10.1007/s11220-020-00304-4

Shoeibi, A., Khodatars, M., Jafari, M., Moridian, P., Rezaei, M., Alizadehsani, R., et al. (2021). Applications of deep learning techniques for automated multiple sclerosis detection using magnetic resonance imaging: A review. *Comput. Biol. Med.* 136, 104697. doi:10.1016/j.compbiomed.2021.104697

Sivaranjini, S., and Sujatha, C. (2020). Deep learning based diagnosis of Parkinson's disease using convolutional neural network. *Multimed. Tools Appl.* 79 (21), 15467–15479. doi:10.1007/s11042-019-7469-8

Smith, L., Lu, Z., Bonesi, M., Smallwood, R., Matcher, S. J., and MacNeil, S. (2010). "Using swept source optical coherence tomography to monitor wound healing in tissue engineered skin," in *Optics in tissue engineering and regenerative medicine IV*, San Francisco (SPIE). International Society for Optics and Photonics.

Sochol, R. D., Gupta, N. R., and Bonventre, J. V. (2016). A role for 3D printing in kidney-on-a-chip platforms. *Curr. Transpl. Rep.* 3 (1), 82–92. doi:10.1007/s40472-016-0085-x

Solomon, J., Lyu, P., Marin, D., and Samei, E. (2020). Noise and spatial resolution properties of a commercially available deep learning-based CT reconstruction algorithm. *Med. Phys.* 47 (9), 3961–3971. doi:10.1002/mp.14319

Speyer, C. B., and Baleja, J. D. (2021). Use of nuclear magnetic resonance spectroscopy in diagnosis of inborn errors of metabolism. *Emerg. Top. life Sci.* 5 (1), 39–48. doi:10.1042/etls20200259

Squelch, A. (2018). 3D printing and medical imaging. *J. Med. Radiat. Sci.* 65 (3), 171–172. doi:10.1002/jmrs.300

Srinivasan, P. P., Heflin, S. J., Izatt, J. A., Arshavsky, V. Y., and Farsiu, S. (2014). Automatic segmentation of up to ten layer boundaries in SD-OCT images of the mouse retina with and without missing layers due to pathology. *Biomed. Opt. Express* 5 (2), 348–365. doi:10.1364/boe.5.000348

Sun, L., Zhang, S., Chen, H., and Luo, L. (2019). Brain tumor segmentation and survival prediction using multimodal MRI scans with deep learning. *Front. Neurosci.* 13, 810. doi:10.3389/fnins.2019.00810

Sun, W., Luo, Z., Lee, J., Kim, H. J., Lee, K., Tebon, P., et al. (2019). Organ-on-a-Chip for cancer and immune organs modeling. *Adv. Healthc. Mat.* 8 (4), e1801363. doi:10.1002/adhm.201801363

Sun, Z., Xia, X., Fan, J., Zhao, J., Zhang, K., Wang, J., et al. (2022). A hybrid optimization strategy for deliverable intensity-modulated radiotherapy plan generation using deep learning-based dose prediction. *Med. Phys.* 49 (3), 1344–1356. doi:10.1002/mp.15462

Szulc, D. A., Ahmadipour, M., Aoki, F. G., Waddell, T. K., Karoubi, G., and Cheng, H. M. (2020). MRI method for labeling and imaging decellularized extracellular matrix scaffolds for tissue engineering. *Magn. Reson. Med.* 83 (6), 2138–2149. doi:10.1002/mrm.28072

Tan, J., Jing, L., Huo, Y., Li, L., Akin, O., and Tian, Y. (2021). Lgan: Lung segmentation in CT scans using generative adversarial network. *Comput. Med. Imaging Graph.* 87, 101817. doi:10.1016/j.compmedimag.2020.101817

Tan, J., Labrinidis, A., Williams, R., Mian, M., Anderson, P. J., and Ranjitkar, S. (2022). Micro-CT-based bone microarchitecture analysis of the murine skull. *Methods Mol. Biol.* 2403, 129–145. doi:10.1007/978-1-0716-1847-9_10

Taniguchi, D., Matsumoto, K., Tsuchiya, T., Machino, R., Takeoka, Y., Elgalad, A., et al. (2018). Scaffold-free trachea regeneration by tissue engineering with bio-3D printing. *Interact. Cardiovasc. Thorac. Surg.* 26 (5), 745–752. doi:10.1093/icvts/ivx444

Thillai, M., Patvardhan, C., Swietlik, E. M., McLellan, T., De Backer, J., Lanclus, M., et al. (2021). Functional respiratory imaging identifies redistribution of pulmonary blood flow in patients with COVID-19. *Thorax* 76 (2), 182–184. doi:10.1136/thoraxjnl-2020-215395

Tousignant, A., Lemaître, P., Precup, D., Arnold, D. L., and Arbel, T. (2019). "Prediction of disease progression in multiple sclerosis patients using deep learning analysis of MRI data," in International Conference on Medical Imaging with Deep Learning (San Francisco: Optics in Tissue Engineering and Regenerative Medicine).

Townsend, J. M., Weatherly, R. A., Johnson, J. K., and Detamore, M. S. (2020). Standardization of microcomputed tomography for tracheal tissue engineering analysis. *Tissue Eng. Part C. Methods* 26 (11), 590–595. doi:10.1089/ten.tec.2020.0211

Van Cleynenbreugel, T., Schrooten, J., Van Oosterwyck, H., and Vander Sloten, J. (2006). Micro-CT-based screening of biomechanical and structural properties of bone tissue engineering scaffolds. *Med. Biol. Eng. Comput.* 44 (7), 517–525. doi:10.1007/s11517-006-0071-z

van der Burgh, H. K., Schmidt, R., Westeneng, H. J., de Reus, M. A., van den Berg, L. H., and van den Heuvel, M. P. (2017). Deep learning predictions of survival based on MRI in amyotrophic lateral sclerosis. *NeuroImage Clin.* 13, 361–369. doi:10.1016/j.nicl.2016.10.008

Wang, H.-k., Wang, Y.-x., Xue, C.-b., Xue, C. b., Li, Z. m. y., Huang, J., et al. (2016). Angiogenesis in tissue-engineered nerves evaluated objectively using MICROFIL perfusion and micro-CT scanning. *Neural Regen. Res.* 11 (1), 168. doi:10.4103/1673-5374.175065

Wang, M., Zhu, W., Yu, K., Chen, Z., Shi, F., Zhou, Y., et al. (2021). Semi-supervised capsule cGAN for speckle noise reduction in retinal OCT images. *IEEE Trans. Med. Imaging* 40 (4), 1168–1183. doi:10.1109/tmi.2020.3048975

Wang, S., Cao, G., Wang, Y., Liao, S., Wang, Q., Shi, J., et al. (2021). Review and prospect: Artificial intelligence in advanced medical imaging. *Front. Radiol.* 1, 781868. doi:10.3389/fradi.2021.781868

Wiant, A., Nyberg, E., and Gilkeson, R. C. (2009). CT evaluation of congenital heart disease in adults. *Am. J. Roentgenol.* 193 (2), 388–396. doi:10.2214/ajr.08.2192

Wimmer, R. A., Leopoldi, A., Aichinger, M., Wick, N., Hantusch, B., Novatchkova, M., et al. (2019). Human blood vessel organoids as a model of diabetic vasculopathy. *Nature* 565 (7740), 505–510. doi:10.1038/s41586-018-0858-8

Winkelmaier, G., and Parvin, B. (2021). An enhanced loss function simplifies the deep learning model for characterizing the 3D organoid models. *Bioinformatics* 37 (18), 3084–3085. doi:10.1093/bioinformatics/btab120

Wu, J., and Tang, X. Y. (2021). Brain segmentation based on multi-atlas and diffeomorphism guided 3D fully convolutional network ensembles. *Pattern Recognit.*, 107904. doi:10.1016/j.patcog.2021.107904

Wu, Q., Liu, J., Wang, X., Feng, L., Wu, J., Zhu, X., et al. (2020). Organ-on-a-chip: Recent breakthroughs and future prospects. *Biomed. Eng. OnLine* 19 (1), 9. doi:10.1186/s12938-020-0752-0

Wu, W., DeConinck, A., and Lewis, J. A. (2011). Omnidirectional printing of 3D microvascular networks. *Adv. Mat.* 23 (24), H178–H183. doi:10.1002/adma.201004625

Wurfl, T., Hoffmann, M., Christlein, V., Breininger, K., Huang, Y., Unberath, M., et al. (2018). Deep learning computed tomography: Learning projection-domain weights from image domain in limited angle problems. *IEEE Trans. Med. Imaging* 37 (6), 1454–1463. doi:10.1109/tmi.2018.2833499

Yahyatabar, M., Jouvet, P., and Cheriet, F. (2020). "Dense-unet: A light model for lung fields segmentation in chest X-ray images," in 2020 42nd Annual International Conference of the IEEE Engineering in Medicine & Biology Society (EMBC) (IEEE).

Yang, X. L., Chen, X. J., and Xiang, D. H. (2020). "Attention-guided channel to pixel convolution network for retinal layer segmentation with choroidal neovascularization," in *Medical imaging conference - image processing* (Houston, TX.

Yang, Y., Bagnaninchi, P. O., Wood, M. A., El Haj, A. J., Dubois, A., and Wang, R. (2005). "Monitoring cell profile in tissue engineered constructs by OCT," in *Optical interactions with tissue and cells XVI*. International Society for Optics and Photonics.

Yang, Y., Mark, A., Ian, W., Juan, G-L., and Jim, T. (2010). "Investigation of a tissue engineered tendon model by PS-OCT," in *Optics in tissue engineering and regenerative medicine IV*. International Society for Optics and Photonics.

Yao, W., Chen, L., Wu, H., Zhao, Q., and Luo, S. (2021). Micro-CT image denoising with an asymmetric perceptual convolutional network. *Phys. Med. Biol.* 66 (13). doi:10.1088/1361-6560/ac0bd2

Yoo, S.-J., Yoon, S. H., Lee, J. H., Kim, K. H., Choi, H. I., Park, S. J., et al. (2021). Automated lung segmentation on chest computed tomography images with extensive lung parenchymal abnormalities using a deep neural network. *Korean J. Radiol.* 22 (3), 476. doi:10.3348/kjr.2020.0318

Yousaf, T., Dervenoulas, G., and Politis, M. (2018). Advances in MRI methodology. *Int. Rev. Neurobiol.* 141, 31–76. doi:10.1016/bs.irn.2018.08.008

Yu, L., Zhao, J., Zhang, Z., Wang, J., and Hu, W. (2021). Commissioning of and preliminary experience with a new fully integrated computed tomography linac. *J. Appl. Clin. Med. Phys.* 22 (7), 208–223. doi:10.1002/acm2.13313

Zaszczyńska, A., Moczulska-Heljak, M., Gradys, A., and Sajkiewicz, P. (2021). Advances in 3D printing for tissue engineering. *Mater. (Basel)* 14 (12), 3149. doi:10.3390/ma14123149

Zbontar, J., Knoll, F., Sriram, A., Murrell, T., Huang, Z., and Muckley, M. J., fastMRI: An open dataset and benchmarks for accelerated MRI. arXiv preprint arXiv:1811.08839, 2018.

Zhang, B., Qi, S., Monkam, P., Li, C., Yang, F., Yao, Y. D., et al. (2019). Ensemble learners of multiple deep CNNs for pulmonary nodules classification using CT images. *IEEE Access* 7, 110358–110371. doi:10.1109/access.2019.2933670

Zhang, M., Young, G. S., Chen, H., Li, J., Qin, L., McFaline-Figueroa, J. R., et al. (2020). Deep-learning detection of cancer metastases to the brain on MRI. *J. Magn. Reson. Imaging* 52 (4), 1227–1236. doi:10.1002/jmri.27129

Zhang, X., Feng, C., Wang, A., Yang, L., and Hao, Y. (2021). CT super-resolution using multiple dense residual block based GAN. *Signal Image Video process.* 15 (4), 725–733. doi:10.1007/s11760-020-01790-5

Zhang, Y., Chan, S., Park, V. Y., Chang, K. T., Mehta, S., Kim, M. J., et al. (2020). Automatic detection and segmentation of breast cancer on MRI using mask R-CNN trained on non-fat-sat images and tested on fat-sat images. *Acad. Radiol.* 29, S135–S144. doi:10.1016/j.acra.2020.12.001

Zhang, Y., Taub, E., Salibi, N., Uswatte, G., Maudsley, A. A., Sheriff, S., et al. (2018). Comparison of reproducibility of single voxel spectroscopy and whole-brain magnetic resonance spectroscopy imaging at 3T. *NMR Biomed.* 31 (4), e3898. doi:10.1002/nbm.3898

Zhang, Y., Yang, C., Liang, L., Shi, Z., Zhu, S., Chen, C., et al. (2022). Preliminary experience of 5.0 T higher field abdominal diffusion-weighted MRI: Agreement of apparent diffusion coefficient with 3.0 T imaging. *J. Magn. Reson Imaging*. doi:10.1002/jmri.28097

Zhao, C., Dewey, B. E., Pham, D. L., Calabresi, P. A., Reich, D. S., and Prince, J. L. (2020). Smore: A self-supervised anti-aliasing and super-resolution algorithm for MRI using deep learning. *IEEE Trans. Med. Imaging* 40 (3), 805–817. doi:10.1109/tmi.2020.3037187

Zhao, R., and Li, S. (2020). Multi-indices quantification of optic nerve head in fundus image via multitask collaborative learning. *Med. Image Anal.* 60, 101593. doi:10.1016/j.media.2019.101593

Zhao, T., Hu, L., Zhang, Y., and Fang, J. (2021). Super-resolution network with information distillation and multi-scale Attention for medical CT image. *Sensors* 21 (20), 6870. doi:10.3390/s21206870

Zhou, N., Guo, X., Sun, H., Yu, B., Zhu, H., Li, N., et al. (2021). The value of 18F-fdg PET/CT and abdominal PET/MRI as a one-stop protocol in patients with potentially resectable colorectal liver metastases. *Front. Oncol.*, 714948. doi:10.3389/fonc.2021.714948

Zhou, Y., Liu, Y., Chen, Q., Gu, G., and Sui, X. (2018). Automatic lumbar MRI detection and identification based on deep learning. *J. Digit. Imaging* 32 (3), 513–520. doi:10.1007/s10278-018-0130-7

Zhou, Y., Yu, K., Wang, M., Ma, Y., Peng, Y., Chen, Z., et al. (2022). Speckle noise reduction for OCT images based on image style transfer and conditional GAN. *IEEE J. Biomed. Health Inf.* 26 (1), 139–150. doi:10.1109/jbhi.2021.3074852

Zhou, Z., Siddiquee, M. M. R., Tajbakhsh, N., and Liang, J. (2020). UNet++: Redesigning skip connections to exploit multiscale features in image segmentation. *IEEE Trans. Med. Imaging* 39 (6), 1856–1867. doi:10.1109/tmi.2019.2959609

Zhu, W., Ma, X., Gou, M., Mei, D., Zhang, K., and Chen, S. (2016). 3D printing of functional biomaterials for tissue engineering. *Curr. Opin. Biotechnol.* 40, 103–112. doi:10.1016/j.copbio.2016.03.014

Zoccatelli, G., Alessandrini, F., Beltramello, A., and Talacchi, A. (2013). Advanced magnetic resonance imaging techniques in brain tumours surgical planning. *J. Biomed. Sci. Eng.* 06 (03), 403–417. doi:10.4236/jbise.2013.63a051

Zou, J., Liu, K., Li, F., Xu, Y., Shen, L., and Xu, H. (2020). Combination of optical coherence tomography (OCT) and OCT angiography increases diagnostic efficacy of Parkinson's disease. *Quant. Imaging Med. Surg.* 10 (10), 1930–1939. doi:10.21037/qims-20-460

frontiers | Frontiers in Bioengineering and Biotechnology

TYPE Original Research
PUBLISHED 30 September 2022
DOI 10.3389/fbioe.2022.1025138

OPEN ACCESS

EDITED BY
Jianxun Ding,
Changchun Institute of Applied Chemistry (CAS), China

REVIEWED BY
Huaqiu Zhang,
Huazhong University of Science and Technology, China
Jinrui Li,
Zhengzhou University, China
Xiao Yang,
City University of Hong Kong, Hong Kong SAR, China
Tian Weidong,
Shihezi University, China

*CORRESPONDENCE
Qingbo Feng,
fqb9175doc@163.com
Xin Wei,
weixinscu@scu.edu.cn
Liangxue Zhou,
liangxue_zhou@126.com

†These authors have contributed equally to this work

SPECIALTY SECTION
This article was submitted to Biomaterials, a section of the journal Frontiers in Bioengineering and Biotechnology

RECEIVED 22 August 2022
ACCEPTED 13 September 2022
PUBLISHED 30 September 2022

CITATION
Liu X, Wang J, Wang P, Zhong L, Wang S, Feng Q, Wei X and Zhou L (2022), Hypoxia-pretreated mesenchymal stem cell-derived exosomes-loaded low-temperature extrusion 3D-printed implants for neural regeneration after traumatic brain injury in canines. *Front. Bioeng. Biotechnol.* 10:1025138. doi: 10.3389/fbioe.2022.1025138

Hypoxia-pretreated mesenchymal stem cell-derived exosomes-loaded low-temperature extrusion 3D-printed implants for neural regeneration after traumatic brain injury in canines

Xiaoyin Liu[1,2†], Jingjing Wang[2†], Peng Wang[3†], Lin Zhong[4], Shan Wang[1], Qingbo Feng[5]*, Xin Wei[6]* and Liangxue Zhou[1]*

[1]Department of Neurosurgery, West China Hospital, West China Medical School, Sichuan University, Chengdu, Sichuan, China, [2]Tianjin Key Laboratory of Neurotrauma Repair, Institute of Neurotrauma Repair, Characteristic Medical Center of People's Armed Police Forces, Tianjin, China, [3]Department of Health Management, Tianjin Hospital, Tianjin, China, [4]The First Affiliated Hospital of Chengdu Medical College, Chengdu, Sichuan, China, [5]Department of Liver Surgery and Liver Implantation, State Key Laboratory of Biotherapy and Cancer Center, West China Hospital, Sichuan University, Chengdu, Sichuan, China, [6]Department of Urology, Institute of Urology, West China Hospital, West China Medical School, Sichuan University, Chengdu, Sichuan, China

Regenerating brain defects after traumatic brain injury (TBI) still remains a significant difficulty, which has motivated interest in 3D printing to design superior replacements for brain implantation. Collagen has been applied to deliver cells or certain neurotrophic factors for neuroregeneration. However, its fast degradation rate and poor mechanical strength prevent it from being an excellent implant material after TBI. In the present study, we prepared 3D-printed collagen/silk fibroin/hypoxia-pretreated human umbilical cord mesenchymal stem cells (HUCMSCs)-derived exosomes scaffolds (3D-CS-HMExos), which possessed favorable physical properties suitable biocompatibility and biodegradability and were attractive candidates for TBI treatment. Furthermore, inspired by exosomal alterations resulting from cells in different external microenvironments, exosomes were engineered through hypoxia stimulation of mesenchymal stem cells and were proposed as an alternative therapy for promoting neuroregeneration after TBI. We designed hypoxia-preconditioned (Hypo) exosomes derived from HUCMSCs (Hypo-MExos) and proposed them as a selective therapy to promote neuroregeneration after TBI. For the current study, 3D-CS-HMExos were prepared for implantation into the injured brains of beagle dogs. The addition of hypoxia-induced exosomes further exhibited better biocompatibility and neuroregeneration ability. Our results revealed that 3D-CS-HMExos could significantly promote neuroregeneration and angiogenesis due to the doping of hypoxia-induced exosomes. In addition, the 3D-CS-HMExos further inhibited nerve cell apoptosis and proinflammatory factor (TNF-α and IL-6) expression and promoted the expression of an

anti-inflammatory factor (IL-10), ultimately enhancing the motor functional recovery of TBI. We proposed that the 3D-CS-loaded encapsulated hypoxia-induced exosomes allowed an adaptable environment for neuroregeneration, inhibition of inflammatory factors and promotion of motor function recovery in TBI beagle dogs. These beneficial effects implied that 3D-CS-HMExos implants could serve as a favorable strategy for defect cavity repair after TBI.

KEYWORDS

traumatic brain injury, exosomes, hypoxia, 3D printing, collagen, silk fibroin

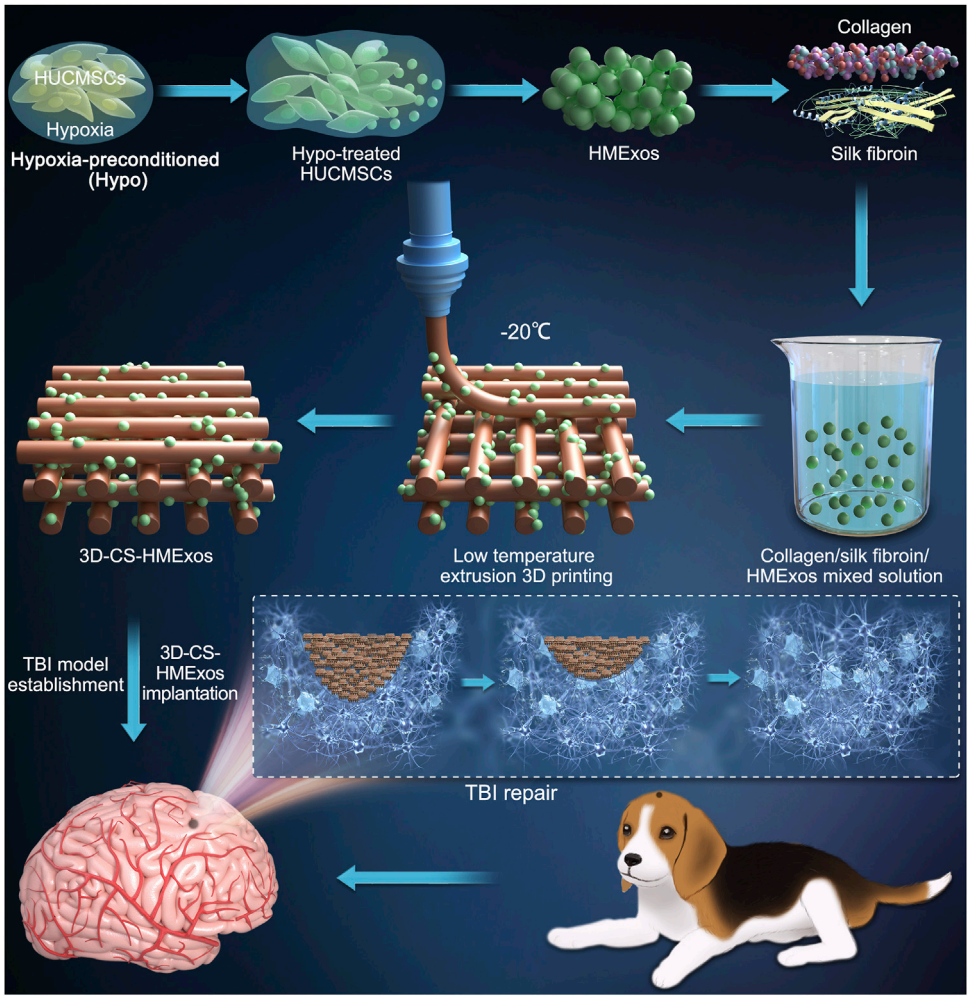

Graphical Abstract

Introduction

Currently, traumatic brain injury (TBI) is one of the key causes of unexpected death and disability in patients. The mortality rate of severe TBI is still as high as 30%, placing a heavy burden on society and families. The typical pathophysiology of TBI involves neuronal apoptosis, blood–brain barrier (BBB) disruption, and neuroinflammation (Werner and Engelhard, 2007; Kinoshita, 2016); in particular, an ischemic and hypoxic microenvironment is formed *in situ* after traumatic brain injury, which aggravates neuronal apoptosis and hinders neuroregeneration. However, despite posing a serious threat to public health, TBI generally has no effective therapy.

As a subset of extracellular vesicles released from various cell types, we considered exosomes to be great delivery vehicles due to their intrinsic biological activity and ideal nanoscale size. Exosomes play an immunomodulatory role in repairing multiple cell damage caused by CNS lesions (Branscome et al., 2020) and have emerged as a novel therapeutic agent in regenerative medicine promoting the entry of cargo complexes into the cytoplasm. It has been reported that the treatment outcomes of mesenchymal stem cells (MSCs) are mostly due to their paracrine mechanisms, primarily involving the secretion of exosomes (Veneruso et al., 2019; Ha et al., 2020). The mechanism may be that the exosomes released by MSCs play a role in promoting repair, inhibiting inflammation, and regulating immunity by regulating the immune microenvironment (Shi et al., 2018; Liu H. et al., 2020).

Under different stress environments, the exosomes released by MSCs have differences in their functions and molecular regulation mechanisms, which in turn affect regeneration and repair. In previous studies, we observed that hypoxia preconditioning could enhance the proliferation and migration activity of MSCs and maintain MSCs in an undifferentiated state (Drela et al., 2014; Zhao et al., 2018). Studies have shown that hypoxia-induced exosomes derived from MSCs can stimulate efficient angiogenesis after spinal cord injury (Mu et al., 2022). More studies have also shown that MSCs cultured *in vitro* can release more exosomes after hypoxia, and these exosomes promote angiogenesis, improving myocardial blood perfusion and cardiac function of ischemic myocardium in infarcted rats (Bian et al., 2014). Hence, given the charater of exosomes in mediating injury repair and intercellular interactions, exosomes derived by hypoxic conditions may hold great promise in regeneration, such as angiogenesis in TBI.

Recently, a growing number of engineered scaffolds materials have emerged to deliver exogenous stem cells and have confirmed the repair efficacy of the defect cavity after TBI (Wang N. et al., 2018; Zhang et al., 2018). Biomaterials such as collagen, hyaluronic acid or silk fibroin can encapsulate stem cells inside the material and can be transplanted into the TBI defect. However, in the process of exogenous stem cell implantation, some outstanding problems still exist, such as ethics, oncogenicity, and immunological rejection, which hinder its translational application. According to recent progress in 3D printing technology and exosome repair, it is urgent to develop an engineered scaffold that can play a repairing role similar to that of stem cells. As a natural extracellular matrix constituent, prominent biocompatibility, low immunogenicity and suitable biodegradability of collagen have been observed (Wang et al., 2016; Sun et al., 2019). Studies have shown that collagen has been widely applied in various tissue engineering applications. However, the restriction of collagen in mechanical properties and degradation properties hinders its popularization and application. Unlike collagen, silk fibroin has become an alternative biomaterial for soft tissue reconstruction due to its good mechanical strength, elasticity, and environmental stability despite its shortcomings (Sun et al., 2015; Chen et al., 2022). Collagen complexed with silk fibroin can make up for the deficiency of using collagen scaffolds alone. The application of collagen combined with silk fibroin can make up for the deficiency of using collagen alone.

In summary, we surmised that combining collagen/silk fibroin scaffolds with hypoxia-preconditioned exosomes derived from MSCs (HMExos) could promote neuroregeneration and angiogenesis, reduce neuronal apoptosis and inhibit inflammation, thereby promoting TBI repair. In our study, 3D-printed collagen/silk fibroin/hypoxia-pretreated human umbilical cord mesenchymal stem cells (HUCMSCs)-derived exosomes scaffolds (3D-CS-HMExos) were prepared to carry and deliver exosomes. The appropriate porosity, water absorption and degradation properties of 3D-CS-HMExos heightened the adhesion and sustained release of exosomes, which were then transplanted to the site of injury. *In vivo*, after implantation to the injury site, the 3D-CS-HMExos implants were proven to possess good biocompatibility to enhance myelinization, axonal regrowth, and angiogenesis and ultimately enhanced motor functional recovery after TBI.

Materials and methods

Experimental animals and ethical statement

Male adult (1 year old) beagles, weighing 9–11.5 kg, were obtained from the Fang Yuanyuan Experimental Animal Center (Beijing, China) for this study. All animal experiments were carried out with the consent of the Fang Yuanyuan Experimental Animal Center (the license number: SK 2018-0026). All animal procedures were carried out according to the guidelines and were approved by the Institutional Animal Care and Use Committee of the Chinese People's Armed Police Force (PAP) Medical Center and the institutional ethical and animal care committees. All experiments were approved by the Ethics Committee at the Institutional Animal Care and Use Committee of the Chinese People's Armed Police Force (PAP) Medical Center [approval number is PJHEC-2019-02 (AF)].

Establishment of a canine traumatic brain injury model and experimental grouping

The process of TBI model establishment was described previously (Jiang et al., 2018). Briefly, the beagles were anesthetized, and a bone hole approximately 3.5 cm long axis and 3 cm short axis over the right hemisphere was drilled at approximately 0.5 cm right of the midline using a hand-held cranial drill. We performed a standardized brain injury using a modified electronic cortical contusion impactor (eCCI, custom design fabrication, United States), in which the diameter of the impact probe was modified from 2 to 8 mm. Then, we set the parameters as 9.99 mm in depth, 5.34 m/s in speed and 255 ms in dwell time for the TBI model.

We randomly divided all 20 male beagles into six groups, including the Sham group (n = 5), TBI group (n = 5), 3D-CS-MExos group (n = 5), and 3D-CS-HMExos group (n = 5). Then, scaffolds with or without exosomes were implanted into the lesion immediately after the TBI model was prepared, followed by hemostasis and suturing. After the operation, the beagles were kept for recovery.

Preparation of mesenchymal stem cells and neural stem cells

According to the method described previously (Dong et al., 2018), human umbilical cord mesenchymal stem cells (HUCMSCs) were isolated from Wharton's jelly from the umbilical cord provided by the Department of Obstetrics and Gynecology of the Characteristic Medical Center of People's Armed Police Forces, and informed consent was obtained. After removing the umbilical artery and umbilical vein and their remaining blood, we cut the umbilical cord Wharton's glue into pieces approximately 1–2 mm^3 in size and then digested them with a mixed solution of 0.2% hyaluronidase and 0.2% collagenase II to extract the primary HUCMSCs. The p3-generation HUCMSCs were used for the following experiments. The morphology of HUCMSCs was captured by using a phase-contrast microscope.

Primary neural stem cells (NSCs) were isolated from embryonic (E) day 14 Sprague–Dawley rats as described in a previous study (Dai et al., 2019). In brief, the hippocampal tissue was dissociated into a cell suspension and seeded into complete growth medium containing DMEM/F12 culture medium, 20 ng/ml EGF, 20 ng/ml bFGF, 1% N2, 2% B27, and 4 mM glutamine at a density of 1×10^6/ml. After 5 days, the NSCs grew into neurospheres and were then digested mechanically for passaging. The third-generation neurospheres were collected for the subsequent experiments. For NSC identification, the NSC neurospheres were identified with an NSC-specific marker nestin antibody by immunofluorescence staining staining and observed by using a fluorescence microscope (Leica DMI4000B, Germany).

Hypoxic preconditioning treatment of mesenchymal stem cells and collection of exosomes

HUCMSCs cultured above were seeded, and FBS was depleted of exosomes by ultracentrifugation at 100,000 × g for 18 h using an XPN-100 ultracentrifuge (Beckman Coulter, United States) at 4°C. HUCMSCs were plated in T75 cell culture flasks, and hypoxia treatment was conducted after cell adhesion. HUCMSCs were incubated under normoxic conditions (21% O_2, 5% CO_2) and hypoxic conditions (1% O_2, 5% CO_2) at 37°C for a total of 24 h. After HUCMSCs reached 80% confluence, the culture supernatant was harvested for exosome isolation.

Isolation and characterization of MExos and hypo-MExos derived from human umbilical cord mesenchymal stem cells

For exosome isolation, normoxic and hypoxic exosome-containing supernatants were separated and purified by differential centrifugation. The supernatant was prepared by centrifuging at 300 × g for 10 min to remove the cell pellet; subsequently, at 2000 × g for 10 min to further remove the cell pellet; then, the sample was passed through a 0.22 μm filter (Millipore, SLGP033RB); and finally, at 10,000 × g for approximately 1 h, the precipitate was collected, which contained the crudely purified exosomes. The exosomes used in this study were further purified by centrifugation at 100,000 × g at 4°C for 18 h using a Himac CP100NX centrifuge (Hitachi, Japan). Finally, we resuspended the exosome particles in PBS. The collected exosomes were deposited at −80°C for the subsequent experiments.

We characterized the collected exosomes by using a specific surface marker, covering CD9 antibody (Proteintech, China), and CD63 antibody (Wuhan Servicebio Technology Co., Ltd., China). TEM (Tecnai G2 spirit, Thermo FEI) and nanoparticle tracking analysis (ZetaView x30, DEU) were applied to observe the morphology and size distribution of exosomes, respectively. The exosome concentration was determined and quantified by a bicinchoninic acid (BCA) protein assay kit (Beyotime, China).

Fabrication of the exosomes loaded 3D-printed collagen/silk fibroin scaffolds

A 3D-Bioplotter™ system (Regenovo, Hangzhou, China), including a personal computer, x–y–z motion nozzle and temperature controllers platform, was served for printing scaffolds. For biocompatibility and biodegradability, a blend of collagen and silk fibroin was prepared as the fabrication material as described previously (Jiang et al., 2021; Li et al., 2021; Chen et al., 2022). For collagen (Wang Y. et al., 2018; Liu et al., 2019; Jiang et al., 2020), we purchased fresh bovine tendons from a local slaughter house. After isolating aponeurosises with a thickness of 0.5 mm, we further excised the aponeurotic attachments, including connective and adipose tissue. Then, we soaked the samples in 0.05 Mtris buffer for 24 h for further purification. The supernatant was prepared by adding pepsin-containing acetic acid to the pellet. Subsequently, 3.5 mol/L NaCl was added to the supernatant for salting. Finally, purified collagen was obtained by centrifugation of the salting precipitate and dialyzed against deionized water for 5 days. Silk fibroin (Ruan et al., 2011; Xu et al., 2016) was fabricated with silkworm silk, incubated in 0.5% Na_2CO_3 solution at 100°C for 30 min and dried. Then, the $CaCl_2$ CH_3CH_2OH H_2O solution was affiliated at 70°C and stirred until dissolved. Then, a certain concentration fibrin solution is arrested after the steps of dialysis, filtration and concentration.

In the current study, collagen was blended at 1:6, 1:9, 1:12, 1:15, and 1:18 ratios with silk fibroin to investigate the optimal molding parameters of 3D printing technology. Finally, we chose a ratio of 1: 12, which is sufficient to achieve the best repair effect. To encapsulate exosomes in the 3D-printed scaffolds, 0.1 g collagen/chitosan mixed solution was mixed with 200 μg of MExos or Hypo-MExos resuspended in PBS individually. The 3D-printed scaffolds were formed at a low temperature of −20°C with the following printing parameters: nozzle diameter = 160 μm, extrusion speed = 0.17 mm/min, printing speed = 12 mm/s, and thickness = 0.3 mm per layer. There were five main types of scaffolds fabricated in our study: collagen/silk fibroin scaffolds (CS), Hypo-MExos-loaded collagen/silk fibroin scaffolds (CS-HMExos), 3D-printed collagen/silk fibroin scaffolds (3D-CS), MExos-loaded 3D-printed collagen/silk fibroin scaffolds (3D-CS-MExos), and Hypo-MExos-loaded 3D-printed collagen/silk fibroin scaffolds (3D-CS-HMExos). Next, 3D-CS scaffolds were placed at −80°C overnight and freeze-dried for 48 h. Finally, after repeatedly rinsing in deionized water, we divided the 3D-printed scaffolds into cylindrical scaffolds of 2 mm in diameter and 2 mm in height and sterilized them with Co^{60} radiation. To prove the distribution of exosomes in 3D-CS-HMExos, exosomes microscopy and adhesion were observed with scanning electron microscopy (SEM, Hitachi, Tokyo, Japan) and confocal laser scanning microscopy (CLSM, LSM 880, Zeiss). 3D-CS-MExos and 3D-CS-HMExos were incubated with D-Hank's solution for 30 min. We implanted 3D-CS-MExos and 3D-CS-HMExos into the canine lesion site after incubation.

Scanning electron microscopy and TEM assay

3D-CS-HMExos were investigated with SEM. Briefly, we prepared 3D-CS scaffolds with or without exosomes. The crosslinked construct was fixed with 70% ethanol for 90 min and then 100% ethanol for 30 min. Immediately thereafter, the fixed samples were freeze-dried in a freeze dryer for 2 days and then coated with platinum for SEM imaging. For the TEM assay, exosomes were prepared as described above. After rinsing the mesh copper grids, the samples were placed on the grids and incubated for 30 min. The excess-free sample droplets were absorbed into a tissue to ride off the remaining particles. Finally, the samples were stained with 2% uranyl acetate for 10 min. The morphology of exosomes was observed by TEM.

Evaluation of physical properties

Scaffolds were prepared as mentioned above and placed in phosphate buffered saline (PBS, pH 7.4) at 37°C. *In vivo* degradation experiments of scaffolds at 1, 2, 3, 4, 5, and 6 months after scaffolds implantation were performed according to previously published study (Jiang et al., 2020). The water absorption was determined by examining the wet weight of each scaffold after a certain time (Zeng et al., 2015). The estimation formula of the water absorption rate is Ws/Wo × 100%, where Wo and Ws represent the wet weight of the initial stent on day 0 and the wet weight of the swollen stent at a certain time point, respectively. The porosity of the scaffolds was obtained according to the established formula: Porosity ratio (%) = (V1 − V3)/(V2 − V3) × 100%. A BCA protein assay kit (Beyotime, China) was performed to evaluate cumulative release profile of exosomes from 3D-CS-HMExos and CS-HMExos at 2, 4, 6, 8, 10, 12, and 14 days according to the published literature (Guan et al., 2022).

Fluorescence staining and cellular uptake of exosomes by human umbilical vein endothelial cells and neural stem cells

The red fluorescent dye PKH 26 (Sigma–Aldrich, United States) was used for exosome staining according to the instructions. The remaining dye solution was subjected to repeated ultracentrifugation at 100,000 × g for 70 min at 4°C. For cellular uptake, HUVECs and MSCs were incubated with labelled exosome suspension (30 μg/ml) for 4 h at 37°C. Subsequently, F-actin was stained with phalloidin (Beyotime, China) before being observed.

Cell proliferation and adhesion evaluation

To carry out the cell proliferation test, 1×10^6 HUCMSCs or NSCs were cocultured with 3D-CS-MExos and 3D-CS-HMExos for 1, 3, 5, and 7 days. The culture medium was replaced with CCK-8 solution (Solarbio) and incubated for 3 h. Then, the absorbance of the supernatant was measured at 450 nm with a microplate analyser (BioTech). The adhesion of NSCs to the scaffold was tested by the following method. Briefly, NSCs at a density of 1 × 105 per well were cocultured with 3D-CS-MExos and 3D-CS-HMExos for 3 days, fixed with 4% paraformaldehyde, and stained with F-actin and DAPI, and the morphology of the NSCs was detected by CLSM.

Neurological examination

As described in our previous study (Liu et al., 2022), a modified Galasne score system (mGCS) was prepared and evaluated by two individuals blinded to the experimental groups at 1, 2, 4, 8, 12, 16, 20, and 24 weeks after surgery. The mGCS score scale (Platt et al., 2001) (total score range from 3 to 18) evaluates the recovery of brain neurological function according to the level of scores, of which 3 scores indicate brain damage and 18 scores represent healthy brain.

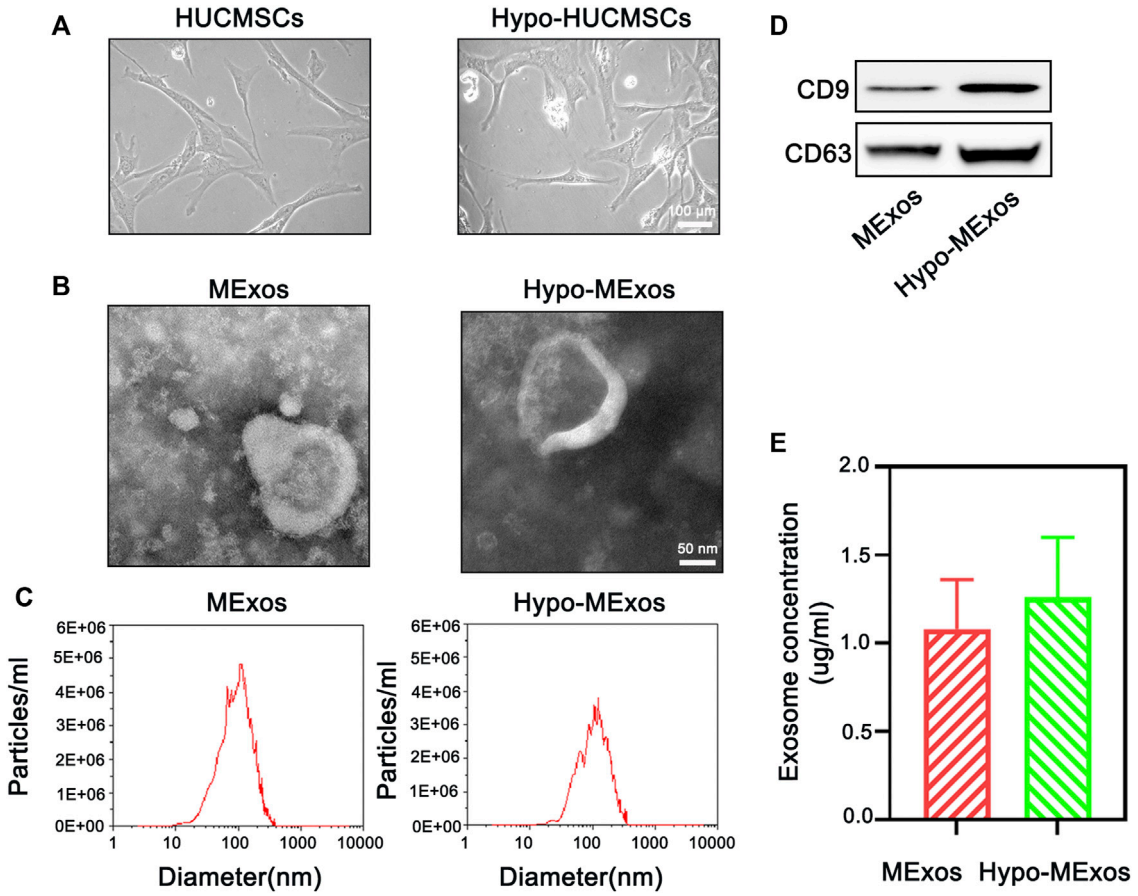

FIGURE 1
Characterization of HUCMSC-derived exosomes under normoxic conditions (MExos) and hypoxic conditions (Hypo-MExos). **(A)** Morphology of HUCMSCs and Hypo-HUCMSCs observed under a phase-contrast microscope. **(B)** TEM images of MExos and Hypo-MExos. **(C)** Particle size distributions of exosomes detected by NTA. **(D)** Western blot illustrating the characteristic surface markers of exosomes, CD9 and CD63. **(E)** Exosome concentration was determined by BCA quantification.

Meanwhile, NDS scores (Castellá et al., 2005) and Purdy scores (Wu and Zhong, 2010) were calculated at the same time point as the above mGCS score to further verify the recovery of neurological function. On the NDS scale, 0 scores represent healthy brains, and 500 scores suggest brain damage, while on the Purdy scale, a score of 2 indicates healthy brains, and a score of 11 suggests coma or death (n = 5 for each group).

Immunofluorescence staining and TUNEL assay

After cardiac perfusion, the beagles were sacrificed. The harvested brains encompassing the lesion site were fixed in 4% paraformaldehyde (PFA) and then prepared for frozen sections. Specific surface markers for neurogenesis (MAP-2: microtubule-associated protein 2, Tuj-1: neuronal class III β-Tubulin and NF: neurofilament protein), angiogenesis (vWF: von Willebrand factor), myelination (MBP: myelin basic protein), axon membrane protein formation (GAP43: growth-associated protein-43), and synapse formation (PSD95: postsynaptic dense protein 95 and Syn: synapsin) were detected. Primary antibodies against NF (Proteintech, China), MBP (Abcam, United Kingdom), GAP43(Proteintech, China), Tuj-1 (Abcam, United Kingdom), Syn (Bioss, China), MAP-2 (Abcam, United Kingdom), PSD95 (Proteintech, China), and vWF (Abcam, United Kingdom) were used and incubated with the slices overnight at 4°C. Subsequently, secondary antibodies (Life Technologies, United States) were incubated at 37°C for 1 h. Nuclei were stained with DAPI (Sigma, United States). Finally, the sections were observed under a fluorescence microscope (DMI4000B, Leica, Germany).

TUNEL staining (Promega Corporation) was used to detect the apoptotic cells in the lesion in each group at

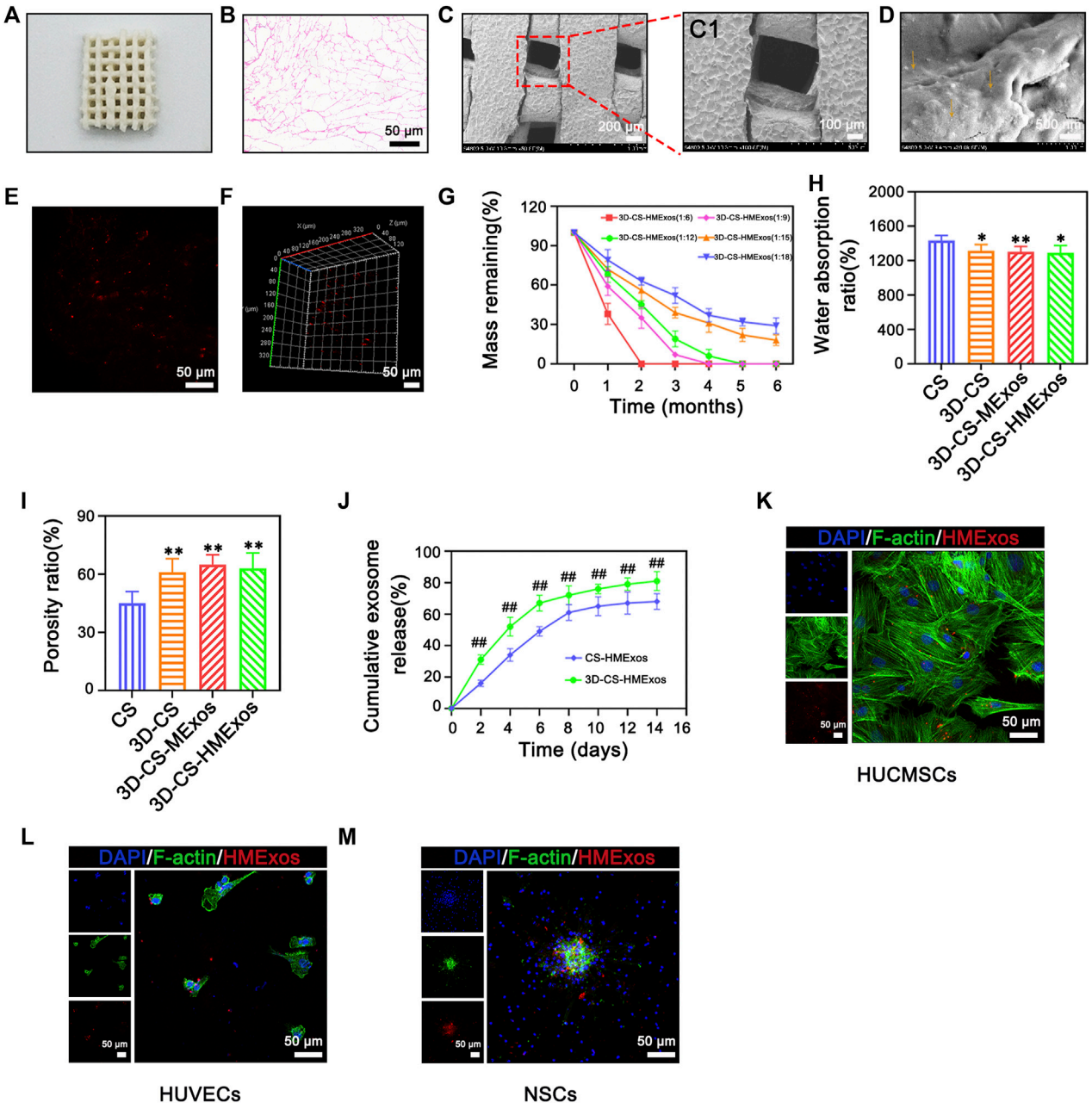

FIGURE 2
Characteristics of 3D-CS-HMExos. **(A)** General structure of 3D-CS-HMExos. **(B)** HE staining revealed the internal structure of 3D-CS-HMExos. **(C)** SEM micrographs of 3D-CS-HMExos. C1 is an enlarged view in the dashed box. **(D)** SEM image of 3D-CS-HMExos. The yellow arrow showed exosomes loaded on 3D-CS-HMExos. **(E)** Image of exosomes labelled with PKH26 in 3D-CS-HMExos. **(F)** 3D immunofluorescence staining images revealed the distribution of Exos in 3D-CS-HMExos **(G)** Degradation rate of 3D-CS-HMExos with different ratios of collagen and silk fibroin within 6 months. **(H)** Water absorption of scaffolds. **(I)** Porosity ratio analysis of the four groups. High porosity can increase the scaffold surface area/volume ratio, which is beneficial for exosome adhesion. **(J)** Cumulative release profile of exosomes from 3D-CS-HMExos and CS-HMExos. **(K–M)** Representative immunofluorescence staining images showed that the exosomes released from the scaffold could be phagocytized by HUCMSCs **(K)**, HUVECs **(L)** and NSCs **(M)** *in vitro*. Nuclei were stained with DAPI (blue), exosomes were stained with PKH26 (red), and the cytoskeleton was stained with F-actin (green). $^{*}p < 0.05$, $^{**}p < 0.01$ vs. CS. $^{\#}p < 0.05$, $^{\#\#}p < 0.01$ vs. CS-HMExos.

6 months as described previously (Zhang J. et al., 2021). The numbers of TUNEL-positive neurons were recorded in five fields that were randomly selected under the microscope at ×200 magnification. The ratio of apoptotic neurons was calculated by the following equation: TUNEL-positive neurons/total neurons) ×100%.

Measurement of plasma inflammatory factors

After the serum of each group was harvested at 1 week and 6 months, the levels of IL-10, IL-6, and TNF-a were detected by an ELISA kit (Wuhan Servicebio Technology Co., Ltd., China).

Statistical analysis

All data are expressed as the mean ± SD. Statistical analyses were processed by SPSS 22.0. Statistical differences between groups were compared by one-way ANOVA. Statistical significance was defined as $^{**}p < 0.01$, $^{*}p < 0.05$, $^{\#\#}p < 0.01$, and $^{\#}p < 0.05$.

Results

Preparation and characterization of MExos and Hypo-MExos

MExos and Hypo-MExos were isolated from the culture medium supernatant of normoxic and hypoxia-stimulated MSCs. Then, the free cell debris and large vesicles were removed by ultracentrifugation. The MExos and hypo-Mexos were characterized by NTA, TEM, and Western blotting. The macromorphology of the isolated MSCs was observed using a phase contrast optical microscope (Figure 1A), which showed no significant changes in either the HUCMSCs group or the Hypo-HUCMSCs group. The micromorphology of the extracted exosomes was observed by TEM, which showed typical cup-shaped and smooth double-layer structures (Figure 1B). The integrity of the original morphology of exosomes was maintained after hypoxic pretreatment. The NTA results showed that the peak particle sizes of MExos and Hypo-MExos were 113.1 and 129.1 nm, respectively, while the median diameters of both MExos and Hypo-MExos were 136.5 and 149.0 nm, respectively (Figure 1C). Western blotting results indicated that representative markers of exosomes, including CD9 and CD63, were expressed in the MExos and Hypo-MExos (Figure 1D). The exosome concentration of the Hypo-MExos group was quantified by bicinchoninic acid (BCA) protein assay, which showed an increasing trend but was not significantly different from that of the MExos group (Figure 1E). The results showed that after hypoxic pretreatment, the characterization of exosomes conformed to the identification standard of exosomes.

Synthesis, characterization, and assessment of 3D-printed scaffolds

3D-CS-HMExos were synthesized by mixing Hypo-MExos into collagen/silk fibroin, wherein its porous structure supplies conditions for the adsorption and the sustained release of Hypo-MExos (Figure 2A). Its porous interconnected structures within the scaffolds suitable for cargo delivery were also observed with HE staining (Figure 2B). The porous structure inside 3D-CS-HMExos was displayed by SEM (Figures 2C,C1). The surface morphology of the scaffolds imaged a continuous and interconnected porous 3-dimensional network structure. SEM images also showed that Hypo-MExos can be firmly embedded and adsorbed on 3D-CS-HMExos (Figure 2D). The distribution of PKH 26-labelled Hypo-MExos on 3D-CS-HMExos was observed under CLSM (Figure 2E), and the 3D reconstruction image indicated the even distribution of PKH 26-labelled Hypo-MExos in 3D-CS-HMExos (Figure 2F). To develop an appropriate mixing ratio of the scaffolds, we selected collagen of different proportions with silk fibroin at 1:6, 1:9, 1:12, 1:15, and 1:18 mass ratios to detect the degradation ratio. The degradation ratio of scaffolds was measured at 1, 2, 3, 4, 5, and 6 months (Figure 2G). The ratio of the 1:12 group degraded 30% at 2 months and completely degraded at 5 months, which was suitable for the TBI repair process in this study. Therefore, the scaffold with 3D-CS-MExos and 3D-CS-HMExos with a mass ratio of 1:12 was used in the next experiment. The water absorption in PBS (pH 7.4) was shown in Figure 2H. These 3D-CS scaffolds exhibited a lower water absorption rate compared to CS (Figure 2H). The porosity of 3D-CS, 3D-CS-MExos, and 3D-CS-HMExos was significantly different from that of CS (Figure 2I). In addition, we immersed the fabricated CS-HMExos and 3D-CS-HMExos in PBS and detected exosomes released into PBS at different time points by BCA to calculate the release profile of exosomes (Figure 2J). HMExos loaded in the 3D-CS-HMExos exhibited continuous release for up to 14 days. The cellular uptake of hypo-MExos by cells was demonstrated in HUCMSCs, HUVECs and NSCs (Figures 2K–M). The results showed that PKH-26-labelled HMExos were scattered around the nuclei, indicating that exosomes can be normally phagocytized by HUCMSCs, HUVECs and NSCs at 1 day after incubation. In this study, 3D-CS-HMExos sustained the release of exosomes as a graft support, which further guaranteed their potential repair function in TBI.

In vitro evaluation of the scaffolds

In vitro assessments were applicable to evaluate the cell compatibility of scaffolds and to detect whether the scaffolds offered a conducive microenvironment for NSC differentiation. To analyse the biocompatibility and regenerative capability in response to exosomes, 3D-CS-MExos and 3D-CS-HMExos were incubated with HUCMSCs and NSCs, respectively. Subsequently, the specimens were imaged using a phase contrast microscope (Figure 3A). The morphology images showed no significant

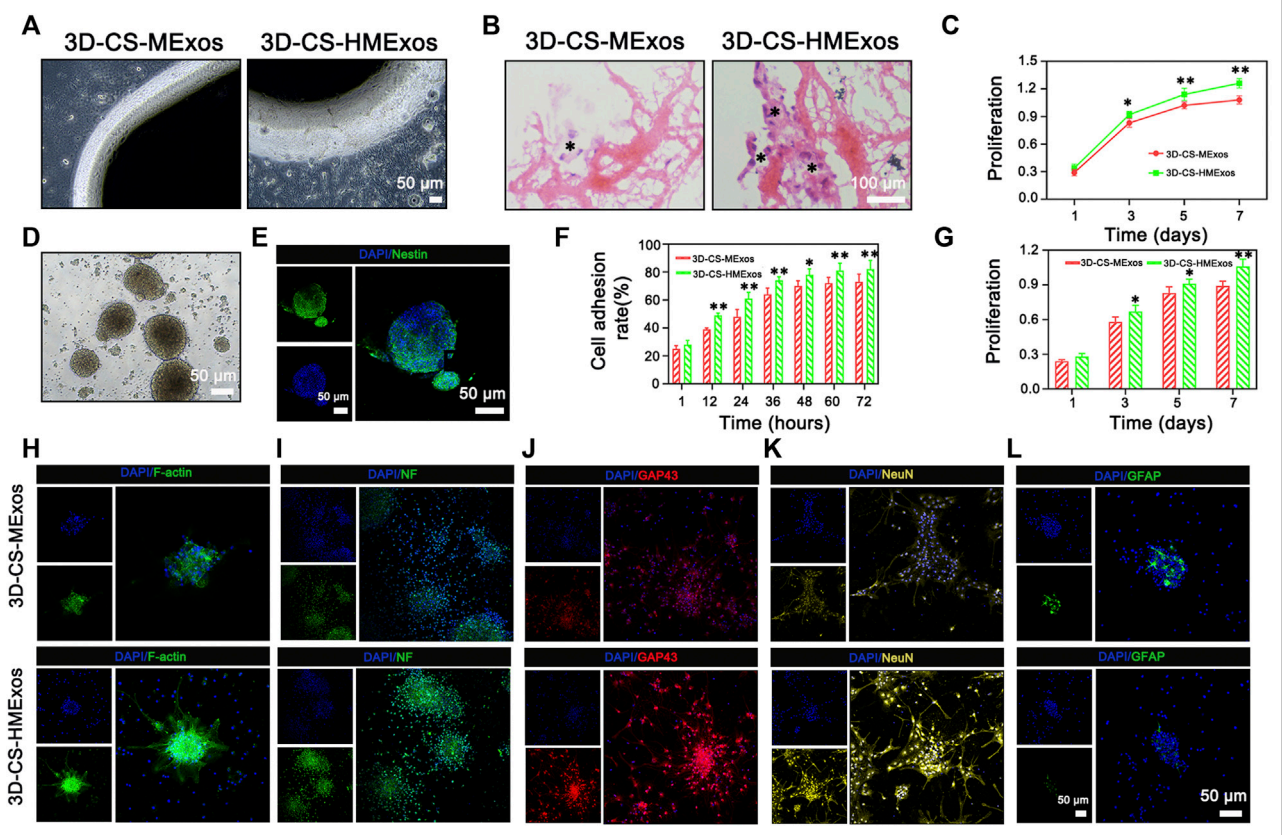

FIGURE 3
In vitro biological response of NSCs and HUCMSCs to 3D-CS-MExos or 3D-CS-HMExos. **(A)** Representative images of HUCMSCs coincubated with 3D-CS loaded with MExos or HMExos under a phase contrast microscope. **(B)** The morphology of 3D-CS-MExos and 3D-CS-HMExos after 7 days of coincubation with HUCMSCs assessed by HE staining. **(C)** Cell proliferation evaluated by CCK-8 assay after 1, 3, 5, and 7 days of culture in the scaffolds. **(D)** Representative images of NSCs under a phase contrast microscope after culture for 7 days. **(E)** Immunofluorescence staining identification verifies NSCs. Green and blue represent Nestin and DAPI, respectively. **(F)** Quantification analysis of the NSC adhesion rate of the 3D-CS-MExos/HMExos scaffold. **(H)** Cell adhesion analysis of NSCs was evaluated by cytoskeleton staining. Green: F-actin; blue: DAPI. **(G)** CCK-8 analysis of NSCs was also used to evaluate the biocompatibility of scaffolds *in vitro*. The proliferation rate of NSCs on the 3D-CS-HMExos scaffold was significantly higher than that on the 3D-CS-MExos scaffold. **(I–L)** Immunofluorescence staining analysis to verify the differentiation of NSCs after 7 days of incubation in scaffolds with NF, GAP43, NeuN, and GFAP antibodies. *$p < 0.05$, **$p < 0.01$ vs. 3D-CS-MExos.

changes in the coincubation of 3D-CS-MExos or 3D-CS-HMExos with HUCMSCs. Additionally, HE staining showed excellent biocompatibility of 3D-CS-HMExos cocultured with HUCMSCs, with relatively large amounts of cell proliferation and deposition in the 3C-CS-HMExos group (Figure 3B). The proliferation of HUCMSCs coincubated in 3D-CS-MExos or 3D-CS-HMExos was demonstrated by CCK8 assay (Figure 3C). The proliferation increased slightly on the 3D-CS-MExos scaffold but rapidly increased on the 3D-CS-HMExos scaffold.

To further explore the effect of the HMExos on NSCs, NSCs were isolated (Figure 3D) and identified using immunofluorescence staining (Figure 3E). The results showed that the protein expression of the surface marker of NSCs, nestin, was abundantly expressed. Since the cellular morphology and behavior of NSCs depend partly on the proper organization of actin filaments, we performed cellular assays to examine cell adhesion and morphology, which are critical to assessing exosome function in the adhesion, proliferation, and differentiation of NSCs. As expected, the cell adhesion ability of the NSCs on 3D-CS-HMExos was significantly increased compared with that on 3D-CS-MExos (Figures 3F,H), indicating that hypoxia-induced exosomes might play important roles in mediating NSC function. The proliferation of NSCs cocultured with 3D-CS-MExos or 3D-CS-HMExos scaffolds is shown in Figure 3G. NSCs were observed to significantly proliferate in both 3D-CS scaffolds incubated with MExos and HMExos within 7 days of culture. The numbers of NSCs in the 3D-CS-HMExos scaffold were higher than those in the 3D-CS-MExos scaffold at 3, 5, and 7 days (Figure 3G). The NSC viability at 3, 5, and 7 days was consistent with the results obtained for HUCMSCs. In our study, we verified markers of neural

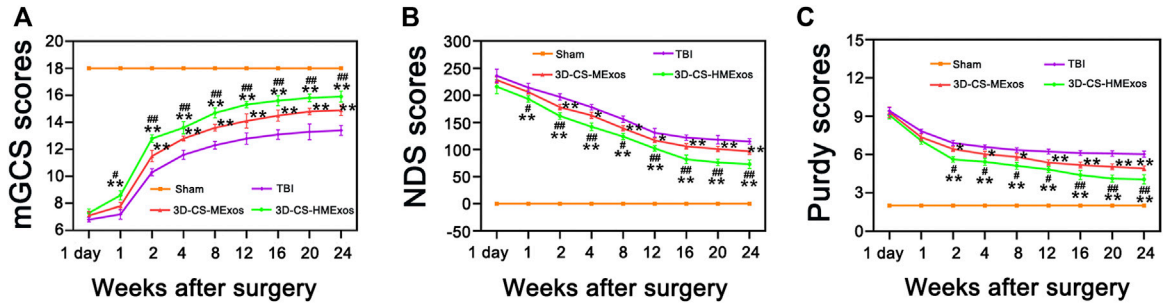

FIGURE 4
Hypoxia-induced exosomes combined with 3D-printed collagen and silk fibroin scaffolds improved locomotor function after TBI. mGCS scores **(A)**, NDS scores **(B)**, and purdy scores **(C)** were evaluated and analysed at 1 day and 1, 2, 4, 8, 12, 16, 20, and 24 weeks after TBI. $^{*}p < 0.05$, $^{**}p < 0.01$ vs. TBI group. $^{\#}p < 0.05$, $^{\#\#}p < 0.01$ vs. 3D-CS-MExos group, $n = 5$.

differentiation after 7 days of culture with immunofluorescence staining staining analysis, focusing on differentiated axons, nerve fibers, neurons, and astrocytes. Among the protein expression levels, NF, GAP43, NeuN, and GFAP indicated mature differentiated nerve fibers, axonal neurons, and astrocytes, respectively (Figures 3I–L). The immunofluorescence staining results showed that the NSCs cocultured with the 3D-CS-HMExos scaffold expressed relatively high mature neuronal differentiation intensity and axonal proteins compared with those cocultured with the 3D-CS-MExos scaffold. However, the exact opposite result of astrocyte expression was observed in the two groups. Taken together, these findings support the ability of the 3D-CS-HMExos scaffold to enhance the neural differentiation potential of NSCs.

Neurological function evaluation of MExos-loaded 3D-printed collagen/silk fibroin scaffolds and Hypo-MExos-loaded 3D-printed collagen/silk fibroin scaffolds implants in traumatic brain injury beagle dogs

The efficiency of 3D-CS-MExos and 3D-CS-HMExos in promoting locomotor function repair was further evaluated using the TBI beagle dog model. The mGCS, NDS and Purdy scores were recorded and quantitated to evaluate the recovery of motor function in TBI dogs implanted with 3D-CS-MExos and 3D-CS-HMExos (Figures 4A–C). Each group exhibited a similar neurological impairment on the first day after TBI. Consistent with the NDS scores, the Purdy scores suggested tremendous behavioral function recovery in the treatment group compared to the TBI group, which was also observed in the mGCS scores after implantation of 3D-CS-MExos and 3D-CS-HMExos for 7 days. As shown in Figure 4, significant differences in mGCS, NDS and Purdy scores were detected in the 3D-CS-HMExos group compared to the TBI group and 3D-CS-MExos group at each time point after 2 weeks. Generally, the TBI beagles implanted with 3D-CS-HMExos revealed the best locomotor functional recovery. This finding suggests that 3D-CS-HMExos could further promote the locomotor functional recovery of beagles with TBI to a certain extent.

Regeneration of nerve fibers, myelin sheath, and axon regeneration after hypoxia-induced human umbilical cord mesenchymal stem cells-exosomes loaded 3D-printed scaffolds implantation

To verify nerve fiber regeneration, myelination, axonal outgrowth and after TBI, NF, MBP, and GAP43 were further investigated by immunofluorescence staining. Nerve fiber regeneration was additionally evaluated with the nerve fibers marker neurofilaments (NF). Along with axonal extension, newly generated myelination emerged at the periphery of regenerated axons (Figures 5A–D,F). As shown, immunofluorescence staining of NF and MBP indicated significant nerve fiber regeneration and remyelination associated with the 3D-CS-HMExos scaffold implanted at the brain lesion site (Figures 5A–F). There were more GAP43-positive cells at the lesion site in the 3D-CS-HMExos group than in the TBI and 3D-CS-MExos groups (Figures 5G–K). These results suggest that implantation of hypoxia-induced exosomes associated with 3D-CS scaffolds could provide a suitable microenvironment for neuroregeneration and further enhance axon formation and myelination at the injury site.

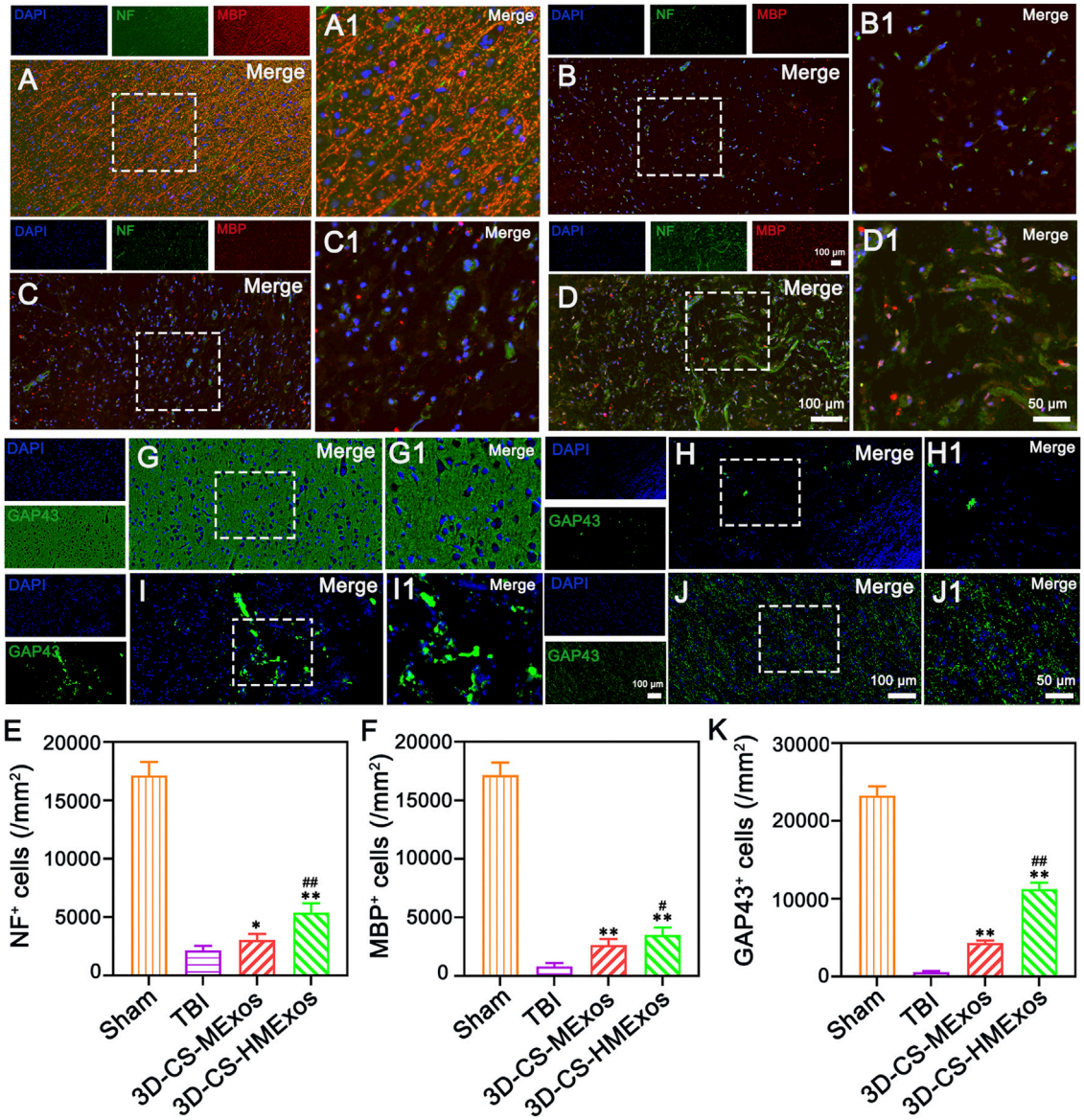

FIGURE 5
Nerve fiber regeneration, myelination, and axonal outgrowth after TBI. **(A–D)** 6 months after TBI, the NF, and MBP staining results identified regenerated nerve fibers that had undergone myelination. **(E,F)** Quantification of the relative density of NF- and MBP-positive cells in each group. **(G–J)** Axonal regeneration (GAP43⁺) was detected in lesion sites of canines treated with a hypoxia-modified exosome scaffold (3D-CS-HMExos). **(K)** Quantification of newborn axons in the lesion area of dogs among each group. The amplification views of the injured sites, in which the signals of NF, MBP, and GAP43 in regions between the black dotted bordered rectangle are presented in (A1), (B1), (C1), and (D1), respectively. The image on the right is an enlarged image of the image in the white box of the image on the left. $^{*}p < 0.05$, $^{**}p < 0.01$ vs. TBI group. $^{\#}p < 0.05$, $^{\#\#}p < 0.01$ vs. 3D-CS-MExos group, $n = 5$.

Establishment of synaptic connections after hypoxia-induced human umbilical cord mesenchymal stem cells-exosomes loaded 3D-printed collagen/silk fibroin scaffold implantation

The neuronal marker Tuj-1 was used to assess the condition of neurons in the injured area after TBI. Implantation of 3D-CS-HMExos further increased the number of Tuj-1 positive cells in the injured area after TBI compared with implantation of 3D-CS-MExos, indicating that hypoxia-induced HUCMSCs-exosomes are beneficial for increasing the number of neurons in the injured area after TBI (Figures 6A–E). Synaptic connection formation was further investigated by immunofluorescence staining staining of the synaptic connection markers synaptophysin

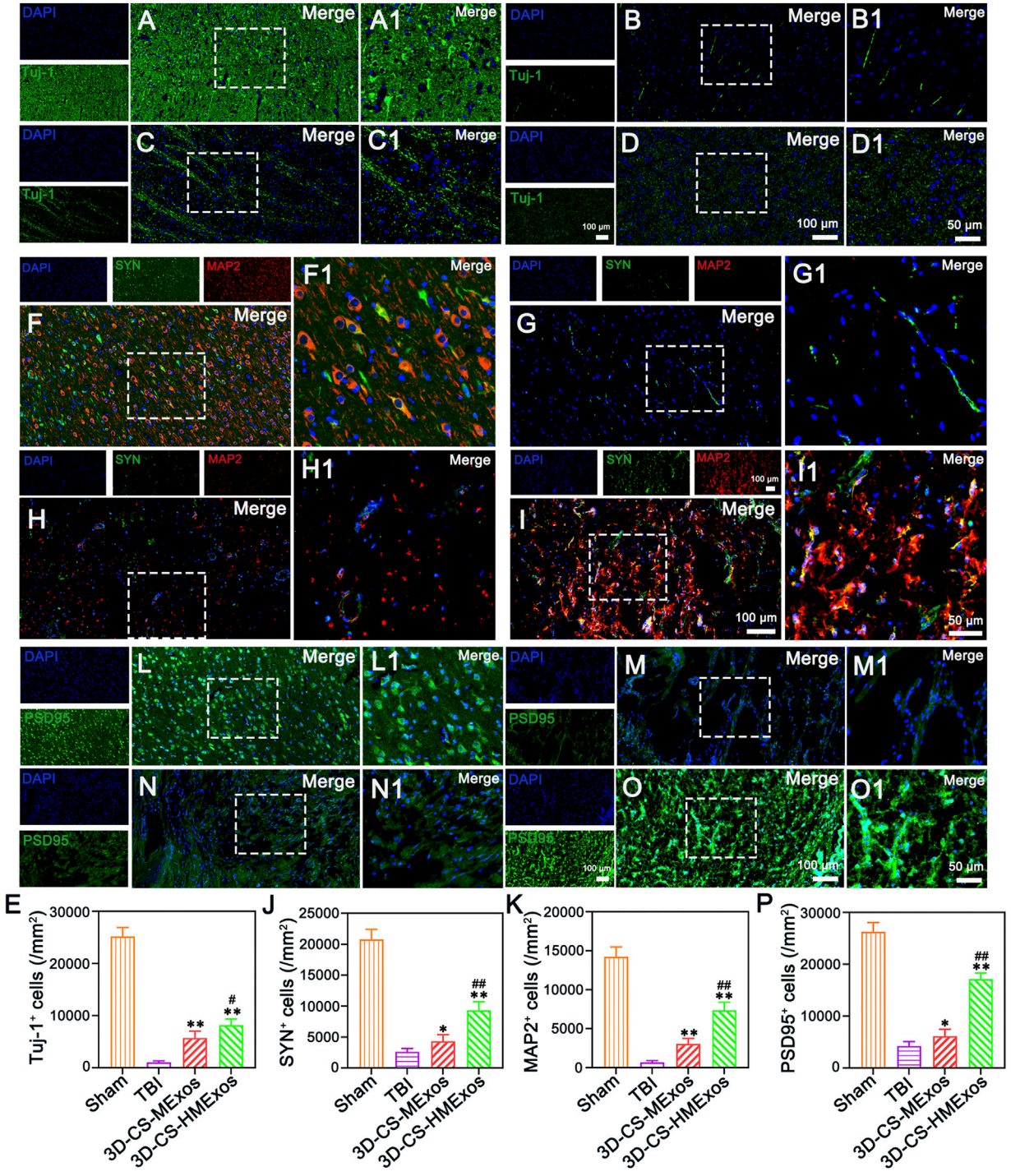

FIGURE 6
Regenerated neurons and synaptic connection formation at 6 months after TBI. **(A–D)** Representative images of Tuj-1-positive neurons in the lesion site of beagles in each group. **(E)** Quantitative analysis of Tuj-1 in injured brain tissues in the Sham, TBI, 3D-CS-MExos, and 3D-CS-HMExos groups. **(F–I)** Double-labelling of SYN and MAP2 immunofluorescence staining staining images of synapse formation at the lesion site, green: SYN; red: MAP-2. **(J,K)** SYN- and MAP-2-positive cells in the four groups at 6 months after the operation. **(L–O)** Representative immunofluorescence staining images showed another hallmark protein of synapses, PSD95, which serves as an important surface marker in neuronal excitatory postsynaptic membranes. **(P)** Quantitative analysis of PSD95-positive signals in the four groups, indicating that hypoxia-pretreated HUCMSCs-exosomes combined with 3D-printed collagen/fibroin scaffolds could further promote the formation of synaptic connections after TBI. The image on the right is an enlarged image of the image in the white box of the image on the left. $^{*}p < 0.05$, $^{**}p < 0.01$ vs. TBI group. $^{\#}p < 0.05$, $^{\#\#}p < 0.01$ vs. 3D-CS-MExos group, $n = 5$.

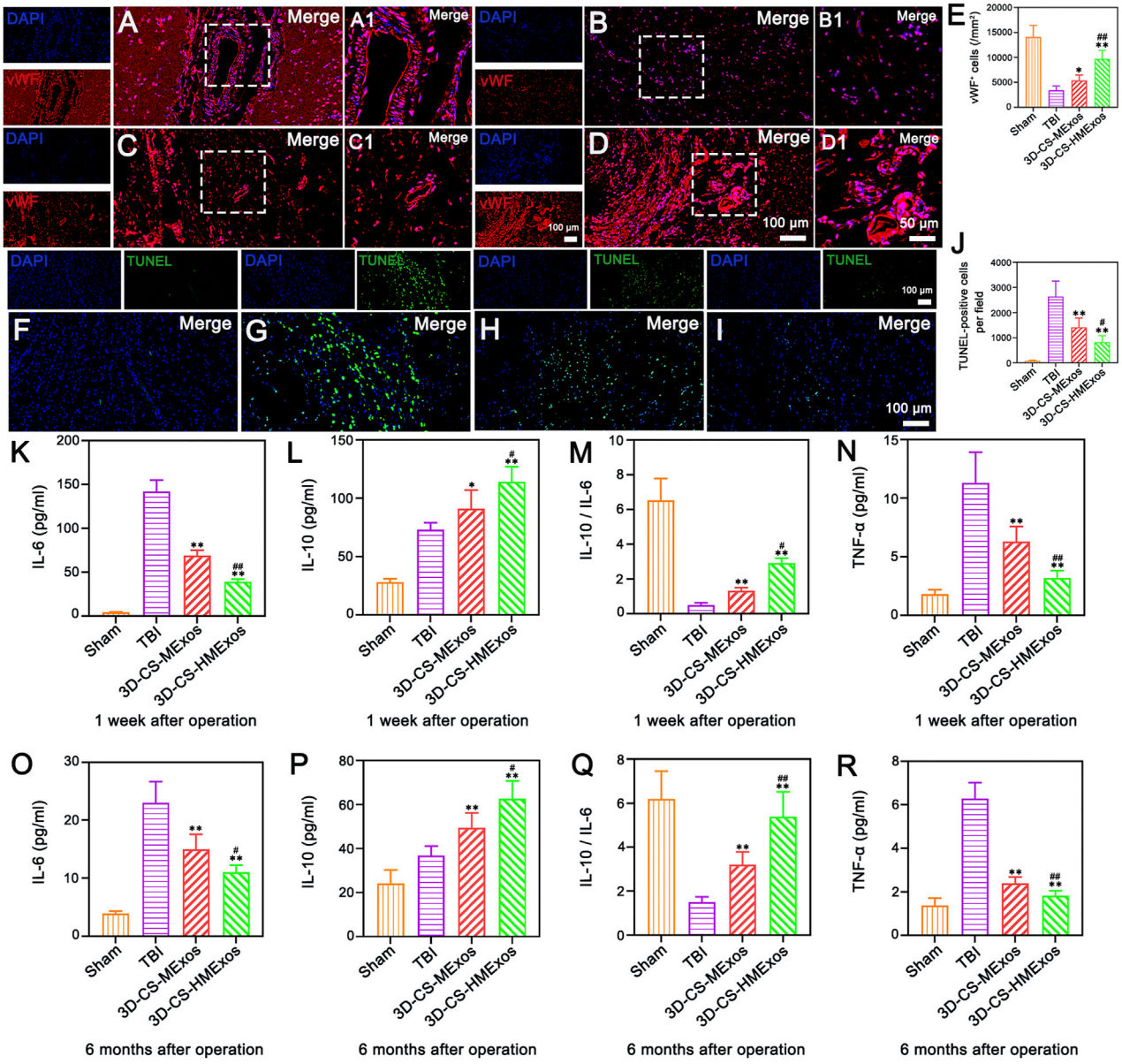

FIGURE 7
Hypoxia-induced exosomes combined with 3D-printed collagen and silk fibroin scaffolds significantly enhanced angiogenesis, inhibited apoptosis, and alleviated inflammation after TBI. **(A–D)** Representative image of vWF immunofluorescence staining (red) in the lesion area. **(A–D)** show the full view of the injured area, with the boxed adjacent and lesion areas magnified in A1, B1, C1 and D1, respectively. Nuclei were stained with DAPI (blue). **(E)** Quantitative analysis of vWF-positive cells in the lesion area in the four groups. **(F–I)** Representative images revealing TUNEL-positive cells (green) indicative of cell apoptosis within the injured area at 6 months after TBI. Note that the 3D-CS-HMExos group showed fewer apoptotic cells than the TBI and 3D-CS-MExos groups at 6 months after TBI. **(J)** Quantitative analysis of TUNEL-positive cells. **(K–R)** Graphs showing the expression of the inflammatory factors IL-6 **(K,O)**, IL-10 **(L,P)**, IL-10/IL-6 **(M,Q)**, and TGF-α **(N,R)** in the acute (1 week) and chronic phases (6 months) after the operation. Note that lower levels of IL-6 and TGF-α and higher levels of IL-10 were observed in the 3D-CS-HMExos group than in the 3D-CS-MExos group at 1 week and 6 months after the operation. In general, 3D-CS-HMExos diminished proinflammatory cytokine (IL-6, TGF-α) release but enhanced anti-inflammatory cytokine (IL-10) release after TBI. The image on the right is an enlarged image of the image in the white box of the image on the left. $^{*}p < 0.05$, $^{**}p < 0.01$ vs. TBI group. $^{\#}p < 0.05$, $^{\#\#}p < 0.01$ vs. 3D-CS-MExos group, $n = 5$.

(SYN) and postsynaptic density protein-95 (PSD95) and microtubule associated protein 2 (MAP2), which represent synaptic reconstruction and reflect the compensatory regeneration of nerve fibers, myelin sheaths, and axons. As the results showed, immunofluorescence staining of SYN, PSD95, and MAP2 in the lesion area revealed the superior

synaptic regenerative capacity of HUCMSCs-exosomes combined with the 3D-CS scaffold (Figures 6F–P). Notwithstanding, the therapeutic effect of the 3D-CS-HMExos scaffold was significantly better than that of the 3D-CS-MExos scaffold (Figures 6F–P). In particular, the images illustrated that tighter synaptic connections were formed in the 3D-CS-HMExos group in the injury area than in the TBI and 3D-CS-MExos groups (Figures 6F–P). The evaluation showed consistent results with locomotor function recovery trends for subsequent assessments, demonstrating the effective neuroregenerative capacity of the 3D-CS-HMExos scaffold.

Proangiogenic functions of hypoxia-stimulated human umbilical cord mesenchymal stem cells-exosomes *in vivo*

Vascularization effects were further evaluated to investigate the alleviation of the microenvironment after TBI by hypoxia-induced HUCMSCs-exosomes. The distribution of von Willebrand factor (vWF)-positive staining was present in the damaged brain tissue of each group (Figures 7A–D). In comparison, the 3D-CS-HMExos group exhibited a larger amount of blood vessel structures. The vWF-positive structures were quantified and shown to be closely associated with 3D-CS-HMExos engraftment (Figure 7E). In contrast to the TBI and 3D-CS-MExos groups, the 3D-CS-HMExos group significantly further increased vWF expression at the center of the lesion, implying that HMExos regulated angiogenesis at the implantation site.

The effect of hypo-MExos-loaded 3D-printed collagen/silk fibroin scaffolds on apoptosis after traumatic brain injury

To further investigate whether the implantation of 3D-CS-HMExos could ameliorate neuron survival, TUNEL staining was performed at 6 months after TBI. Fewer TUNEL-positive cells were observed in the 3D-CS-HMExos group than in the TBI group and the 3D-CS-MExos group (Figures 7F–J). These findings demonstrated that the 3D-CS-HMExos scaffold has the best utility of significantly inhibiting apoptosis after TBI. Since plasma inflammatory factors are the primary mediators of inflammation after injury, we studied the expression of TNF-a, IL-6, and IL-10 at 1 week and 6 months in peripheral venous blood plasma to confirm whether the 3D-CS-HMExos scaffold can alter the expression of these plasma inflammatory factors (Figures 7K–R). Consistent with the results of the analysis at 1 week, the expression of IL-6 and TNF-a was lower in the 3D-CS-HMExos group than in the TBI and 3D-CS-MExos groups, while the expression of IL-10 in the 3D-CS-HMExos group was higher at 6 months after the operation (Figures 7K–R). Together, these results indicate that the implantation of 3D-CS-HMExos could further inhibit apoptosis and reduce inflammation after TBI.

Discussion

Some previous studies have only assessed the influence of 3D-CS implants on regeneration after TBI. The effect of exosomes with or without hypoxia combined with 3D-CS scaffolds on large animals remains unclear. Therefore, in the current study, the influence of hypoxia-induced HUCMSCs-exosomes (HMExos) combined with 3D-CS (3D-CS-HMExos) scaffolds on post-TBI regenerative ability was explored. In this study, a TBI model of beagles was established by a modified electrically controlled cortical impactor approach. A 3D printing technique was used to fabricate scaffolds to pad the brain cavity of TBI beagles. The biocompatibility of 3D-CS-HMExos loaded with HMExos was verified by coincubation with HUCMSCs and NSCs, the most commonly employed cell sources for brain tissue engineering. The results of our experiments confirmed that 3D-CS-HMExos could serve as a novel strategy based on exosomes and biomaterials for brain tissue regeneration.

A defect cavity forming *in situ* after TBI is one of the devastating problems restricting its nerve repair. Current tissue engineering repair strategies are altering to try to raise this challenge, with innovative strategies from simple scaffold implantation to scaffold-carrying stem cell or growth factor delivery. Natural biomaterials were ideal scaffolding materials to fill brain defect cavities and supported the ingrowth and integration of cells (Liu Y. et al., 2020). For example, the utility of chitosan derived from chitin has been demonstrated to have beneficial effects on enhanced regeneration in rats, holding safety *in vivo* applications (Mo et al., 2010; Skop et al., 2014).

Multiple studies have been implemented to demonstrate the effect of 3D printing scaffolds for neuroregeneration. Therefore, there is an urgent need to develop composite natural biomaterials that can better repair brain injury. As one of the constituents of the extracellular matrix, collagen has several attractive features, such as biodegradability, biocompatibility, and low immunogenicity for neural repair (Zhang L. et al., 2021), but it still has many shortcomings that need to be further improved to afford a beneficial microenvironment for TBI repair. Silk fibroin, a biomaterial obtained from silkworm cocoons, has been widely investigated due to its favorable biocompatibility. Nevertheless, some defects of silk fibroin, such as frangibility and high solubility, restrict its application (Li et al., 2018). To adapt to different repair needs and overcome their own limitations, blending silk fibroin with other biomaterials has attracted increasing attention. In the current study, as a biodegradable

mixture, the collagen/silk fibroin composite overcame the defects of pure collagen and silk fibroin and showed remarkable biocompatibility, appropriate biodegradability, and mechanical properties. Therefore, it could be a promising tissue engineering material for TBI. In this study, 3D-CS-HMExos implants were developed with the incorporation of exosomes into scaffolds. One of the benefits of 3D-CS-HMExos was their inherent porous structure, consisting of pore size, network connection and size distribution, which have been shown to have significant effects on tissue regeneration (Duan et al., 2016; Bae et al., 2021). Another advantage was its biocompatibility and biodegradability, ensuring that scaffolds induce minimal inflammatory responses after implantation *in vivo*. Compared with similar articles related to collagen/fibroin scaffolds. The scaffolds in our study prepared by 3D printing technology have more uniform internal pore size and are more suitable for cytokine intercommunication than scaffolds prepared by simple mixing of collagen and silk fibroin alone. Moreover, collagen/silk fibroin scaffolds equipped with natural exosomes have better biocompatibility and repair effect than scaffolds reported in other literatures.

As important mediators of cell–cell communication, exosomes can regulate immunity, which plays a key role in neuroregeneration. Numerous studies have reported the effect of exosome therapy on the repair of TBI. The exosomes derived from MSCs promote TBI repair by regulating paracrine mechanisms. The exosomes derived from MSCs carry soluble factors, nucleic acids, lipids, and proteins that may enhance neural regeneration and thus improve neurological recovery. Alterations in the microenvironment usually influence the cargo packaging of exosomes and may shift the therapeutic functions of exosomes. Oxygen concentration was an important factor affecting the cell biology of MSCs (Mohyeldin et al., 2010), and hypoxia stimulation makes MSCs in an activated/stressed state, which could secrete a large number of exosomes (Gonzalez-King et al., 2017). The measurement of hypoxia handling for the production of enhanced exosomes is critical in this strategy, which can trigger angiogenesis and enhance cell tolerance to hypoxia. In this study, hypoxia-induced exosomes derived from HUCMSCs loaded 3D-CS-HMExos were applied to explore the therapeutic effect on nerve regeneration and motor function recovery after TBI.

Sufficient exchange of trophic factors and metabolites in biomaterials facilitates the survival and regeneration of surrounding nerve cells. For that, a porous structure is required for the 3D-printed scaffold. The results of HE staining and SEM proved that 3D-CS-HMExos presented a porous network structure and that the exosomes were bound to the inner surface of 3D-CS-HMExos. The above results verified that exosomes could be successfully loaded onto 3D-CS-HMExos. Additionally, the exosomes loaded on 3D-CS-HMExos could be released continuously by more than 80% in 14 days, ensuring an uninterrupted repair of nerve damage.

The degradation rate of transplanted carriers affects the efficacy of delivered exosomes. Moreover, the suitable degradation rate is crucial for the integration of transplanted carriers into the host tissue. To select the best degradation profile of the 3D-CS-HMExos scaffold, printed constructs for different ratios of collagen and silk fibroin (1:6, 1:9, 1:12, 1:15, and 1:18) were incubated in PBS at 37°C, having similar ionic and temperature conditions to *in vivo* conditions. The results showed that the scaffold was completely degraded at 5 months at a ratio of 1:12 collagen to silk fibroin, which best matched the time point set in this study.

Cell proliferation and adhesion were important to determine the biological properties of grafted biomaterials for neuronal regeneration (Unal et al., 2019). We performed cytoskeleton staining and metabolite analysis with CCK-8 at specific time points to verify the cytotoxicity on each scaffold. Cytoskeleton staining images showed the encapsulated cell proliferation of HUCMSCs or NSCs within 7 days. However, proliferation increased slightly on 3D-CS-MExos but rapidly increased on 3D-CS-HMExos. Cytoskeleton imaging revealed that the NSCs in each group had a better range of expansion area, further indicating that the 3D-CS-HMExos had beneficial adhesion for NSCs. Cell differentiation is essential for posttraumatic nerve repair. Therefore, we examined the effect of 3D-CS-HMExos scaffolds on the differentiation of NSCs *in vitro*. During morphology imaging of immunofluorescence staining on each scaffold, the cells on the 3D-CS-HMExos groups at 7 days after coculture showed the greatest number of nerve fibers, axons and neurons and the lowest number of astrocytes compared to the 3D-CS-MExos group on the same date. NSCs can highly proliferate during the self-renewal period, whereas the proliferation rate rapidly decreases during neuronal differentiation (Homem et al., 2015). This result may shed light on the role of hypoxia-induced exosome loading on 3D-CS scaffolds in regulating the proliferation of NSCs and differentiation into neurons.

Insufficient vessel growth associated with injury remains an unresolved issue, restricting neuroregeneration after TBI. The hypoxic microenvironment has been reported to upregulate the expression of proangiogenic factors in MSCs and enhance their wound-healing ability (Tong et al., 2016; Mu et al., 2022). According to reports, exosomes derived from hypoxia-induced MSCs have proven to be effective in treating femoral head osteonecrosis by promoting angiogenesis (Yuan et al., 2021). In addition, studies have shown that exosomes from hypoxia-preconditioned human umbilical vein endothelial cells (HUVECs) promote MSC angiogenic function after spinal cord injury (Li et al., 2022). The present work attempted to investigate whether exosomes derived from HUCMSCs upon hypoxia stimulation could mediate angiogenesis. The results showed that hypoxia-induced exosomes promoted angiogenesis *in vivo*, particularly at 6 months after TBI. The immunofluorescence staining results of vWF, an angiogenesis

marker, were significantly higher on 3D-CS-HMExos than on 3D-CS-MExos. These findings provide new insights into the exosome-mediated promotion of neurodegeneration and the surface design of biomaterials from the perspective of angiogenesis.

The ultimate goal of hypoxia-induced exosomes loaded 3D-CS-HMExos delivery was to enhance the neuroregeneration of the damaged brain. We next investigated the *in vivo* behavior of grafted HMExos within 3D-CS-HMExos in TBI beagle models by directly implanting 3D-CS-HMExos into the injury area of the beagles brain. In this study, we verified markers of nerve fibers at 6 months after implantation with immunofluorescence staining analysis, focusing on the regeneration of functional nerve fibers, axon, myelination, regeneration of neurons and the establishment of synaptic connections under higher magnification. Immunofluorescence staining quantitative analysis showed that the protein expression of the nerve fibers, myelination, axons, neurons, and synapse formation markers NF/MBP, GAP43, Tuj-1, SYN/MAP2, and PSD95 was higher on 3D-CS-HMExos than on 3D-CS-MExos.

We generally recognize that apoptosis at the injury site is closely associated with neurological function impairments. Hence, we analysed apoptosis using TUNEL staining. The results indicated that 3D-CS-HMExos significantly inhibited apoptosis after TBI. Neuroinflammation was a key component of the pathological environment during TBI pathogenesis (Johnson et al., 2013). In response to TBI, a large number of proinflammatory and anti-inflammatory cytokines were released (Loane and Kumar, 2016). The balance between inflammation and antiinflammation could be measured by the levels and ratios of IL-6 and IL-10 (Jiang et al., 2021). In our study, we found that 3D-CS-HMExos implants could lessen neuroinflammation, manifested by downregulating the expression of the proinflammatory factors IL-6 and TNF-α and increasing the level of the anti-inflammatory factor IL-10.

To verify the feasibility of using 3D-CS-HMExos in terms of motor function recovery, mGCS scores, NDS scores, and Purdy scores were used. The results indicated that implantation of 3D-CS-HMExos facilitated recovery of motor function after TBI, which might be related to regeneration of nerve fibers, axons and neurons, remyelination, and synaptic connection establishment at the injury site after TBI.

Conclusion

In summary, our approach demonstrated that hypoxia-induced exosome carriers with a 3D-printed collagen/silk fibroin scaffold promoted neuroregeneration and motor function recovery after TBI. Moreover, the method allowed suppression of prolonged neuroinflammation and inhibition of nerve cell apoptosis after TBI. The combined use of the 3D-CS scaffold and hypoxia-induced exosomes increased the effectiveness of implantation after TBI by supporting angiogenesis and nerve regeneration at the lesion while suppressing chronic neuroinflammation and nerve cell apoptosis. This study provides a novel treatment for TBI based on exosome-based therapy.

Data availability statement

The original contributions presented in the study are included in the article/supplementary material, further inquiries can be directed to the corresponding authors.

Ethics statement

All animal experiments were carried out with the consent of the Fang Yuanyuan Experimental Animal Center (the license number: SK 2018-0026). All animal procedures were carried out according to the guidelines and were approved by the Institutional Animal Care and Use Committee of the Chinese People's Armed Police Force (PAP) Medical Center and the institutional ethical and animal care committees. All experiments were approved by the Ethics Committee at the Institutional Animal Care and Use Committee of the Chinese People's Armed Police Force (PAP) Medical Center -[approval number is PJHEC-2019-02 (AF)].

Author contributions

Experiment design: XL, JW, PW, QF, XW, and LZ. Experiment implementation: XL, JW, PW, LZ, SW, QF, XW, and LiaZ. Data analysis: XL, JW, PW, XW, and LiaZ. Material contribution and equipment coordination: XW and LiaZ. Paper write: XL, JW, and PW.

Funding

This work was supported by the National Major Scientific and Technological Special Project for Significant New Drugs Development (2015ZX09102010).

Conflict of interest

The authors declare that the research was conducted in the absence of any commercial or financial relationships that could be construed as a potential conflict of interest.

Publisher's note

References

Bae, M., Hwang, D. W., Ko, M. K., Jin, Y., Shin, W. J., Park, W., et al. (2021). Neural stem cell delivery using brain-derived tissue-specific bioink for recovering from traumatic brain injury. *Biofabrication* 13 (4), 044110. doi:10.1088/1758-5090/ac293f

Bian, S., Zhang, L., Duan, L., Wang, X., Min, Y., and Yu, H. (2014). Extracellular vesicles derived from human bone marrow mesenchymal stem cells promote angiogenesis in a rat myocardial infarction model. *J. Mol. Med.* 92 (4), 387–397. doi:10.1007/s00109-013-1110-5

Branscome, H., Paul, S., Yin, D., El-Hage, N., Agbottah, E. T., Zadeh, M. A., et al. (2020). Use of stem cell extracellular vesicles as a "holistic" approach to CNS repair. *Front. Cell. Dev. Biol.* 8, 455. doi:10.3389/fcell.2020.00455

Castellá, M., Buckberg, G. D., and Tan, Z. (2005). Neurologic preservation by Na+-H+ exchange inhibition prior to 90 minutes of hypothermic circulatory arrest. *Ann. Thorac. Surg.* 79 (2), 646–654. discussion 646-54. doi:10.1016/j.athoracsur.2004.07.007

Chen, C., Xu, H. H., Liu, X. Y., Zhang, Y. S., Zhong, L., Wang, Y. W., et al. (2022). 3D printed collagen/silk fibroin scaffolds carrying the secretome of human umbilical mesenchymal stem cells ameliorated neurological dysfunction after spinal cord injury in rats. *Regen. Biomater.* 9, rbac014. doi:10.1093/rb/rbac014

Dai, Y., Sun, F., Zhu, H., Liu, Q., Xu, X., Gong, P., et al. (2019). Effects and mechanism of action of neonatal versus adult astrocytes on neural stem cell proliferation after traumatic brain injury. *Stem Cells* 37 (10), 1344–1356. doi:10.1002/stem.3060

Dong, H. J., Zhao, M. L., Li, X. H., Chen, Y. S., Wang, J., Chen, M. B., et al. (2018). Hypothermia-modulating matrix elasticity of injured brain promoted neural lineage specification of mesenchymal stem cells. *Neuroscience* 377, 1–11. doi:10.1016/j.neuroscience.2018.02.013

Drela, K., Sarnowska, A., Siedlecka, P., Szablowska-Gadomska, I., Wielgos, M., Jurga, M., et al. (2014). Low oxygen atmosphere facilitates proliferation and maintains undifferentiated state of umbilical cord mesenchymal stem cells in an hypoxia inducible factor-dependent manner. *Cytotherapy* 16 (7), 881–892. doi:10.1016/j.jcyt.2014.02.009

Duan, H., Li, X., Wang, C., Hao, P., Song, W., Li, M., et al. (2016). Functional hyaluronate collagen scaffolds induce NSCs differentiation into functional neurons in repairing the traumatic brain injury. *Acta Biomater.* 45, 182–195. doi:10.1016/j.actbio.2016.08.043

Gonzalez-King, H., García, N. A., Ontoria-Oviedo, I., Ciria, M., Montero, J. A., and Sepúlveda, P. (2017). Hypoxia inducible factor-1α potentiates jagged 1-mediated angiogenesis by mesenchymal stem cell-derived exosomes. *Stem Cells* 35 (7), 1747–1759. doi:10.1002/stem.2618

Guan, P., Liu, C., Xie, D., Mao, S., Ji, Y., Lin, Y., et al. (2022). Exosome-loaded extracellular matrix-mimic hydrogel with anti-inflammatory property Facilitates/promotes growth plate injury repair. *Bioact. Mater.* 10, 145–158. doi:10.1016/j.bioactmat.2021.09.010

Ha, D. H., Kim, H. K., Lee, J., Kwon, H. H., Park, G. H., Yang, S. H., et al. (2020). Mesenchymal stem/stromal cell-derived exosomes for immunomodulatory therapeutics and skin regeneration. *Cells* 9 (5), 1157. doi:10.3390/cells9051157

Homem, C. C., Repic, M., and Knoblich, J. A. (2015). Proliferation control in neural stem and progenitor cells. *Nat. Rev. Neurosci.* 16 (11), 647–659. doi:10.1038/nrn4021

Jiang, J., Dai, C., Liu, X., Dai, L., Li, R., Ma, K., et al. (2021). Implantation of regenerative complexes in traumatic brain injury canine models enhances the reconstruction of neural networks and motor function recovery. *Theranostics* 11 (2), 768–788. doi:10.7150/thno.50540

Jiang, J., Dai, C., Niu, X., Sun, H., Cheng, S., Zhang, Z., et al. (2018). Establishment of a precise novel brain trauma model in a large animal based on injury of the cerebral motor cortex. *J. Neurosci. Methods* 307, 95–105. doi:10.1016/j.jneumeth.2018.06.025

Jiang, J., Liu, X., Chen, H., Dai, C., Niu, X., Dai, L., et al. (2020a). 3D printing collagen/heparin sulfate scaffolds boost neural network reconstruction and motor function recovery after traumatic brain injury in canine. *Biomater. Sci.* 8, 6362–6374. doi:10.1039/d0bm01116a

Jiang, J. P., Liu, X. Y., Zhao, F., Zhu, X., Li, X. Y., Niu, X. G., et al. (2020b). Three-dimensional bioprinting collagen/silk fibroin scaffold combined with neural stem cells promotes nerve regeneration after spinal cord injury. *Neural Regen. Res.* 15 (5), 959–968. doi:10.4103/1673-5374.268974

Johnson, V. E., Stewart, J. E., Begbie, F. D., Trojanowski, J. Q., Smith, D. H., and Stewart, W. (2013). Inflammation and white matter degeneration persist for years after a single traumatic brain injury. *Brain* 136, 28–42. doi:10.1093/brain/aws322

Kinoshita, K. (2016). Traumatic brain injury: Pathophysiology for neurocritical care. *J. intensive care* 4, 29. doi:10.1186/s40560-016-0138-3

Li, D. W., He, J., He, F. L., Liu, Y. L., Liu, Y. Y., Ye, Y. J., et al. (2018). Silk fibroin/chitosan thin film promotes osteogenic and adipogenic differentiation of rat bone marrow-derived mesenchymal stem cells. *J. Biomater. Appl.* 32 (9), 1164–1173. doi:10.1177/0885328218757767

Li, L., Mu, J., Zhang, Y., Zhang, C., Ma, T., Chen, L., et al. (2022). Stimulation by exosomes from hypoxia preconditioned human umbilical vein endothelial cells facilitates mesenchymal stem cells angiogenic function for spinal cord repair. *ACS Nano* 16, 10811–10823. doi:10.1021/acsnano.2c02898

Li, X. H., Zhu, X., Liu, X. Y., Xu, H. H., Jiang, W., Wang, J. J., et al. (2021). The corticospinal tract structure of collagen/silk fibroin scaffold implants using 3D printing promotes functional recovery after complete spinal cord transection in rats. *J. Mat. Sci. Mat. Med.* 32 (4), 31. doi:10.1007/s10856-021-06500-2

Liu, H., Li, R., Liu, T., Yang, L., Yin, G., and Xie, Q. (2020). Immunomodulatory effects of mesenchymal stem cells and mesenchymal stem cell-derived extracellular vesicles in rheumatoid arthritis. *Front. Immunol.* 11, 1912. doi:10.3389/fimmu.2020.01912

Liu, X., Zhang, G., Wei, P., Zhong, L., Chen, Y., Zhang, J., et al. (2022). Three-dimensional-printed collagen/chitosan/secretome derived from HUCMSCs scaffolds for efficient neural network reconstruction in canines with traumatic brain injury. *Regen. Biomater.* 9, rbac043. doi:10.1093/rb/rbac043

Liu, X. Y., Liang, J., Wang, Y., Zhong, L., Zhao, C. Y., Wei, M. G., et al. (2019). Diffusion tensor imaging predicting neurological repair of spinal cord injury with transplanting collagen/chitosan scaffold binding bFGF. *J. Mat. Sci. Mat. Med.* 30 (11), 123. doi:10.1007/s10856-019-6322-y

Liu, Y., Hsu, Y. H., Huang, A. P., and Hsu, S. H. (2020). Semi-interpenetrating polymer network of hyaluronan and chitosan self-healing hydrogels for central nervous system repair. *ACS Appl. Mat. Interfaces* 12 (36), 40108–40120. doi:10.1021/acsami.0c11433

Loane, D. J., and Kumar, A. (2016). Microglia in the TBI brain: The good, the bad, and the dysregulated. *Exp. Neurol.* 275 Pt 3, 316–327. doi:10.1016/j.expneurol.2015.08.018

Mo, L., Yang, Z., Zhang, A., and Li, X. (2010). The repair of the injured adult rat hippocampus with NT-3-chitosan carriers. *Biomaterials* 31 (8), 2184–2192. doi:10.1016/j.biomaterials.2009.11.078

Mohyeldin, A., Garzón-Muvdi, T., and Quiñones-Hinojosa, A. (2010). Oxygen in stem cell biology: A critical component of the stem cell niche. *Cell. Stem Cell.* 7 (2), 150–161. doi:10.1016/j.stem.2010.07.007

Mu, J., Li, L., Wu, J., Huang, T., Zhang, Y., Cao, J., et al. (2022). Hypoxia-stimulated mesenchymal stem cell-derived exosomes loaded by adhesive hydrogel for effective angiogenic treatment of spinal cord injury. *Biomater. Sci.* 10 (7), 1803–1811. doi:10.1039/d1bm01722e

Platt, S. R., Radaelli, S. T., and McDonnell, J. J. (2001). The prognostic value of the modified Glasgow Coma Scale in head trauma in dogs. *J. Vet. Intern. Med.* 15 (6), 581–584. doi:10.1111/j.1939-1676.2001.tb01594.x

Ruan, Y., Lin, H., Yao, J., Chen, Z., and Shao, Z. (2011). Preparation of 3D fibroin/chitosan blend porous scaffold for tissue engineering via a simplified method. *Macromol. Biosci.* 11 (3), 419–426. doi:10.1002/mabi.201000392

Shi, Y., Wang, Y., Li, Q., Liu, K., Hou, J., Shao, C., et al. (2018). Immunoregulatory mechanisms of mesenchymal stem and stromal cells in inflammatory diseases. *Nat. Rev. Nephrol.* 14 (8), 493–507. doi:10.1038/s41581-018-0023-5

Skop, N. B., Calderon, F., Cho, C. H., Gandhi, C. D., and Levison, S. W. (2014). Improvements in biomaterial matrices for neural precursor cell transplantation. *Mol. Cell. Ther.* 2, 19. doi:10.1186/2052-8426-2-19

Sun, K., Li, H., Li, R., Nian, Z., Li, D., and Xu, C. (2015). Silk fibroin/collagen and silk fibroin/chitosan blended three-dimensional scaffolds for tissue engineering. *Eur. J. Orthop. Surg. Traumatol.* 25 (2), 243–249. doi:10.1007/s00590-014-1515-z

Sun, Y., Yang, C., Zhu, X., Wang, J., Liu, X., Yang, X., et al. (2019). 3D printing collagen/chitosan scaffold ameliorated axon regeneration and neurological recovery after spinal cord injury. *J. Biomed. Mat. Res. A* 107 (9), 1898–1908. doi:10.1002/jbm.a.36675

Tong, C., Hao, H., Xia, L., Liu, J., Ti, D., Dong, L., et al. (2016). Hypoxia pretreatment of bone marrow-derived mesenchymal stem cells seeded in a collagen-chitosan sponge scaffold promotes skin wound healing in diabetic rats with hindlimb ischemia. *Wound Repair Regen.* 24 (1), 45–56. doi:10.1111/wrr.12369

Unal, D. B., Caliari, S. R., and Lampe, K. J. (2019). Engineering biomaterial microenvironments to promote myelination in the central nervous system. *Brain Res. Bull.* 152, 159–174. doi:10.1016/j.brainresbull.2019.07.013

Veneruso, V., Rossi, F., Villella, A., Bena, A., Forloni, G., and Veglianese, P. (2019). Stem cell paracrine effect and delivery strategies for spinal cord injury regeneration. *J. Control. Release* 300, 141–153. doi:10.1016/j.jconrel.2019.02.038

Wang, J., Yang, Q., Cheng, N., Tao, X., Zhang, Z., Sun, X., et al. (2016). Collagen/silk fibroin composite scaffold incorporated with PLGA microsphere for cartilage repair. *Mater. Sci. Eng. C* 61, 705–711. doi:10.1016/j.msec.2015.12.097

Wang, N., Xiao, Z., Zhao, Y., Wang, B., Li, X., Li, J., et al. (2018). Collagen scaffold combined with human umbilical cord-derived mesenchymal stem cells promote functional recovery after scar resection in rats with chronic spinal cord injury. *J. Tissue Eng. Regen. Med.* 12 (2), e1154–e1163. doi:10.1002/term.2450

Wang, Y., Tan, H., and Hui, X. (2018). Biomaterial scaffolds in regenerative therapy of the central nervous system. *Biomed. Res. Int.* 2018, 7848901–7848919. doi:10.1155/2018/7848901

Werner, C., and Engelhard, K. (2007). Pathophysiology of traumatic brain injury. *Br. J. Anaesth.* 99 (1), 4–9. doi:10.1093/bja/aem131

Wu, G., and Zhong, W. (2010). Effect of minimally invasive surgery for cerebral hematoma evacuation in different stages on motor evoked potential and thrombin in dog model of intracranial hemorrhage. *Neurol. Res.* 32 (2), 127–133. doi:10.1179/016164109x12478302362617

Xu, Y., Zhang, Z., Chen, X., Li, R., Li, D., and Feng, S. (2016). A silk fibroin/collagen nerve scaffold seeded with a Co-culture of schwann cells and adipose-derived stem cells for sciatic nerve regeneration. *PLoS One* 11 (1), e0147184. doi:10.1371/journal.pone.0147184

Yuan, N., Ge, Z., Ji, W., and Li, J. (2021). Exosomes secreted from hypoxia-preconditioned mesenchymal stem cells prevent steroid-induced osteonecrosis of the femoral head by promoting angiogenesis in rats. *Biomed. Res. Int.* 2021, 1–13. doi:10.1155/2021/6655225

Zeng, S., Liu, L., Shi, Y., Qiu, J., Fang, W., Rong, M., et al. (2015). Characterization of silk fibroin/chitosan 3D porous scaffold and *in vitro* cytology. *PloS one* 10, e0128658. doi:10.1371/journal.pone.0128658

Zhang, J., Wang, R. J., Chen, M., Liu, X. Y., Ma, K., Xu, H. Y., et al. (2021). Collagen/heparan sulfate porous scaffolds loaded with neural stem cells improve neurological function in a rat model of traumatic brain injury. *Neural Regen. Res.* 16 (6), 1068–1077. doi:10.4103/1673-5374.300458

Zhang, K., Shi, Z., Zhou, J., Xing, Q., Ma, S., Li, Q., et al. (2018). Potential application of an injectable hydrogel scaffold loaded with mesenchymal stem cells for treating traumatic brain injury. *J. Mat. Chem. B* 6 (19), 2982–2992. doi:10.1039/c7tb03213g

Zhang, L., Fan, C., Hao, W., Zhuang, Y., Liu, X., Zhao, Y., et al. (2021). Spinal cord injury repair: NSCs migration promoted and drug delivered exosomes-collagen scaffold via a bio-specific peptide for one-step spinal cord injury repair (adv. Healthcare mater. 8/2021). *Adv. Healthc. Mat.* 10 (8), 2170034. doi:10.1002/adhm.202170034

Zhao, D., Liu, L., Chen, Q., Wang, F., Li, Q., Zeng, Q., et al. (2018). Hypoxia with Wharton's jelly mesenchymal stem cell coculture maintains stemness of umbilical cord blood-derived CD34(+) cells. *Stem Cell. Res. Ther.* 9, 158. doi:10.1186/s13287-018-0902-5

frontiers | Frontiers in Bioengineering and Biotechnology

TYPE Original Research
PUBLISHED 17 October 2022
DOI 10.3389/fbioe.2022.1038829

OPEN ACCESS

EDITED BY
Mingqiang Li,
Third Affiliated Hospital of Sun Yat-Sen University, China

REVIEWED BY
Xinyu Yu,
Huazhong University of Science and Technology, China
Wooram Um,
Pukyong National University, South Korea
Shengcai Yang,
Jilin University, China

*CORRESPONDENCE
Ji Wu,
gxnnwuji@163.com

†These authors have contributed equally to this work

SPECIALTY SECTION
This article was submitted to Biomaterials, a section of the journal Frontiers in Bioengineering and Biotechnology

RECEIVED 07 September 2022
ACCEPTED 26 September 2022
PUBLISHED 17 October 2022

CITATION
Li J, Zhang X, Mo Y, Huang T, Rao H, Tan Z, Huang L, Zeng D, Jiang C, Zhong Y, Cai Y, Liang B and Wu J (2022), Urokinase-loaded cyclic RGD-decorated liposome targeted therapy for in-situ thrombus of pulmonary arteriole of pulmonary hypertension. *Front. Bioeng. Biotechnol.* 10:1038829. doi: 10.3389/fbioe.2022.1038829

Urokinase-loaded cyclic RGD-decorated liposome targeted therapy for *in-situ* thrombus of pulmonary arteriole of pulmonary hypertension

Jingtao Li[1†], Xiaofeng Zhang[1†], Yingying Mo[1], Tongtong Huang[1], Huaqing Rao[1], Zhenyuan Tan[2], Liuliu Huang[3], Decai Zeng[1], Chunlan Jiang[1], Yanfen Zhong[1], Yongzhi Cai[1], Binbin Liang[1] and Ji Wu[1]*

[1]Department of Ultrasound, The First Affiliated Hospital of Guangxi Medical University, Nanning, China, [2]Pharmaceutical College, Guangxi Medical University, Nanning, China, [3]Department of Cardiothoracic Surgery, The First Affiliated Hospital of Guangxi Medical University, Nanning, China

Background: *In-situ* thrombosis is a significant pathophysiological basis for the development of pulmonary hypertension (PH). However, thrombolytic therapy for *in-situ* thrombus in PH was often hampered by the apparent side effects and the low bioavailability of common thrombolytic medications. Nanoscale cyclic RGD (cRGD)-decorated liposomes have received much attention thanks to their thrombus-targeting and biodegradability properties. As a result, we synthesized urokinase-loaded cRGD-decorated liposome (UK-cRGD-Liposome) for therapy of *in-situ* thrombosis as an exploration of pulmonary hypertensive novel therapeutic approaches.

Purpose: To evaluate the utilize of UK-cRGD-Liposome for targeted thrombolysis of *in-situ* thrombus in PH and to explore the potential mechanisms of *in-situ* thrombus involved in the development of PH.

Methods: UK-cRGD-Liposome nanoscale drug delivery system was prepared using combined methods of thin-film hydration and sonication. Induced PH *via* subcutaneous injection of monocrotaline (MCT). Fibrin staining (modified MSB method) was applied to detect the number of vessels within-situ thrombi in PH. Echocardiography, hematoxylin-eosin (H & E) staining, and Masson's trichrome staining were used to analyze right ventricular (RV) function, pulmonary vascular remodeling, as well as RV remodeling.

Results: The number of vessels with *in-situ* thrombi revealed that UK-cRGD-Liposome could actively target urokinase to *in-situ* thrombi and release its payload in a controlled manner in the *in vivo* environment, thereby enhancing the thrombolytic effect of urokinase. Pulmonary artery hemodynamics and echocardiography indicated a dramatical decrease in pulmonary artery pressure and a significant improvement in RV function post targeted thrombolytic therapy. Moreover, pulmonary vascular remodeling and RV remodeling were significantly restricted post targeted thrombolytic therapy.

Conclusion: UK-cRGD-Liposome can restrict the progression of PH and improve RV function by targeting the dissolution of pulmonary hypertensive *in-situ* thrombi, which may provide promising therapeutic approaches for PH.

KEYWORDS

cyclic RGD peptide, liposome, *in-situ* thrombus, targeted thrombolysis, pulmonary hypertension, right ventricular function

Introduction

PH is a life-threatening chronic disease characterized by pulmonary vasoconstriction, pulmonary vascular remodeling, and *in-situ* thrombosis that induces a progressive increase in pulmonary vascular resistance, ultimately leading to right heart failure and death (Vonk-Noordegraaf et al., 2013; Paulin et al., 2015). Currently, pharmacological therapies for PH focus on the imbalance between vasoconstriction and vasodilation, which mainly includes drugs such as prostacyclin receptor agonists, endothelin receptor antagonists (ERAs), and phosphodiesterase type 5 inhibitors (PDE-5is) (Velayati et al., 2016; Sommer et al., 2021). Although such therapies have improved the vascular function of the patient, the survival rate is still unsatisfactory (Boucly et al., 2017; Jalce and Guignabert, 2020). Clinical therapies for *in-situ* thrombosis of PH are mainly concentrated on anticoagulant therapy, but forceful clinical evidence to verify its usefulness and efficacy is lacked (Olschewski and Rich, 2018; Cullivan et al., 2021; Rawal et al., 2021). Previous studies have reported that *in-situ* thrombi of pulmonary arterioles in idiopathic pulmonary hypertension and experimental pulmonary hypertension were micro-thrombotic composed of aggregated activated platelets and deposited fibrin (Figure 1) (Fan et al., 2019). Since micro-thrombosis is very tiny (micron scale) and relatively stable, conventional thrombolytic therapy has little effect on its treatment. In addition, *in-situ*

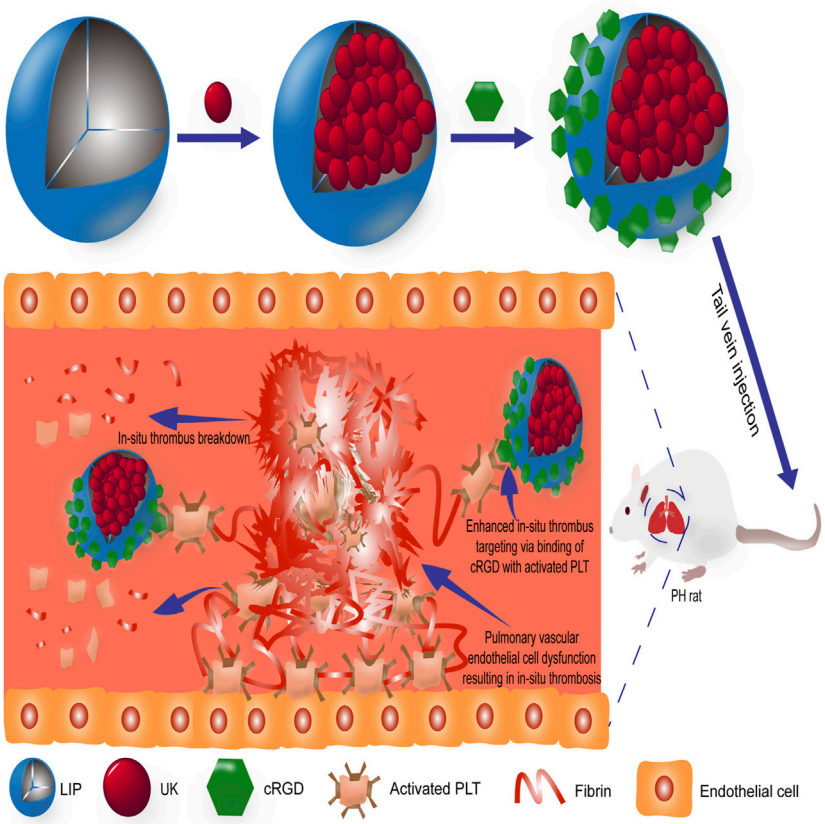

FIGURE 1
Schematic illustration of the mechanism of targeted therapy of *in-situ* thrombus in PH with UK-cRGD-Liposome nanoparticles. Abbreviations: PH, pulmonary hypertension; cRGD, Cyclic RGD; UK, urokinase; PLT, platelet.

thrombosis of pulmonary arteriole could lead to more severe PH (White et al., 2007; Fernandez et al., 2012). Therefore, it is of great importance to develop a novel targeted therapy method for curing pulmonary arteriole *in-situ* thrombus in PH.

Thrombolytic therapy is so far the main method used clinically to dissolve blood clots and restore vessel patency (Vaidya et al., 2012; Zhou et al., 2021). A variety of thrombolytic drugs, such as urokinase, streptokinase, and tissue-type fibrinogen activators, which can convert fibrinolytic zymogen to fibrinolytic enzymes and thus degrade the thrombus backbone fibrin (Liu et al., 2007; Hu et al., 2019), these thrombolytic drugs for a short plasma clearance half-life and the lack of thrombus targeting, large drug doses are required for effective thrombolysis. However, heavy use of thrombolytic drugs can over-activate the systemic fibrinolytic system, resulting in severe hemorrhagic side effects (Koudelka et al., 2016; Altaf et al., 2021). Furthermore, incomplete thrombolysis could lead to embolism of the distal vascular vessels. Consequently, how to improve thrombolytic drugs' bioavailability, plasma clearance half-life, and at the same time reduce systemic side effects are key to thrombolytic therapy.

Liposomes have numerous advantages, such as good biocompatibility, biodegradability, low cytotoxicity, and easy surface modification (Akbarzadeh et al., 2013; Khan et al., 2020). Meanwhile, PEGylated liposome is an ideal drug carrier due to inhibiting the clearance of the mononuclear macrophage system and improving liposome stability and *in vivo* circulation time (Sercombe et al., 2015). Integrin αIIbβ3 (also called GPIIb/IIIa) is a glycoprotein on the surface of activated platelets that promotes platelet aggregation and thrombosis (Guo et al., 2015). GPIIb/IIIa on the surface of activated platelets could be specifically recognized by RGD peptides (Pawlowski et al., 2017). cRGD peptides have higher affinity and enzymatic stability with GPIIb/IIIa glycoproteins than linear RGD peptides, which are ideal ligands for targeting the thrombus where activated platelets are gathering (Huang et al., 2008). Previous studies by Zhang et al. (2018), as well as our research group (Rao, 2020; Rao et al., 2021), have demonstrated that UK-cRGD-Liposome has the advantages of targeting activated platelets (Figure 1), improving the plasma clearance half-life of thrombolytic drugs, and reducing hemorrhagic side effects.

Integrin αvβ3, which is highly expressed in a variety of tumor cells and tumor vascular endothelial cells, could be specifically bound with RGD peptide (Pan et al., 2019). Several *in vivo* targeting results have also showed that RGD peptide was able to target tumor cells of many cancer types, including breast, colon, gastric, and lung cancers, etc (Garcia Ribeiro et al., 2019; Chen et al., 2021; Liu et al., 2022). In contrast, UK-cRGD-Liposome has only been studied *in vivo* in target-seeking studies of acutely formed micro thrombus (Zhang et al., 2018). Its *in vivo* target-seeking studies of chronically formed pulmonary arteriole *in-situ* thrombus in PH are still blank, and whether its treatment effect is better than conventional thrombolytic drugs or anticoagulant in chronically formed pulmonary arteriole *in-situ* thrombus is also still unclear.

Thus, the goal of this study was to establish an animal model of PH in order to explore the thrombolytic efficacy of UK-cRGD-Liposome in pulmonary arteriole *in-situ* thrombus in PH as well as the relationship between pulmonary arteriole *in-situ* thrombus and the process of PH, which could lead to new ideas and basic research evidence for the targeted therapy of PH.

Material and methods

Material and animals

Monocrotaline (MCT) and sodium pentobarbital were purchased from Sigma, USA. Beijing Solarbio Science & Technology Co. supplied 1,2-dipalmitoyl-sn-glycero-3-hosphocholine (DPPC), cholesterol, fibrin staining solution, and Masson's trichrome staining kits. 1,2-distearoyl-sn-phosphoethanolamine-N-[methoxy (polyethylene glycol)-2000] (DSPE-mPEG-2000) and 1,2-distearoyl-sn-phosphoethanolamine-N-[methoxy (polyethylene glycol)-2000]-cRGD (DSPE-mPEG2000-cRGD) were synthesized by Hunan Huateng Pharmaceutical Co. Urokinase for injection (250,000U) was acquired from the First Affiliated Hospital of Guangxi Medical University's central pharmacy.

Eighty-five pathogen-free inbred 8-weeks-old male Sprague-Dawley (SD) rats were purchased from the Animal Experiment Center of Guangxi Medical University (certificate number: SCXK GUI 2020-0003).

Preparation of UK-cRGD-liposome

UK-cRGD-Liposome was prepared using integrated methods of thin-film hydration and sonication (Zhang et al., 2018; Rao, 2020). DPPC, Cholesterol, DSPE-mPEG2000, and DSPE-mPEG2000-cRGD (ratio of 12 mg: 6 mg: 2 mg: 1 mg) were dissolved in chloroform. The solution dissolved all the solutes in a water bath sonicator and was preliminarily dried using a rotary evaporator (Yarong Biochemical Instrument Factory, China) to form a thin film of cRGD liposome. The cRGD liposome film was then dried in a vacuum dryer overnight to evaporate the organic solvent. The next day, lysis of cRGD liposome film membranes with the phosphate buffer solution (PBS) of urokinase (5 ml, 50,000 U/ml) combined with a water bath sonicator. The ultrasonic cell disruption instrument (4°C, 5/5 s, on/off, 320w) was used to reduce the size of UK-cRGD-Liposome for 10 min and then centrifuge for 5 min (4°C, 3,000 rpm) to produce a limpid suspension of UK-cRGD-Liposome. The suspension was transferred to a dialysis bag (molecular weight cut off 300 kDa) and dialyzed with 2 L of PBS buffer for 6 h to remove unencapsulated urokinase.

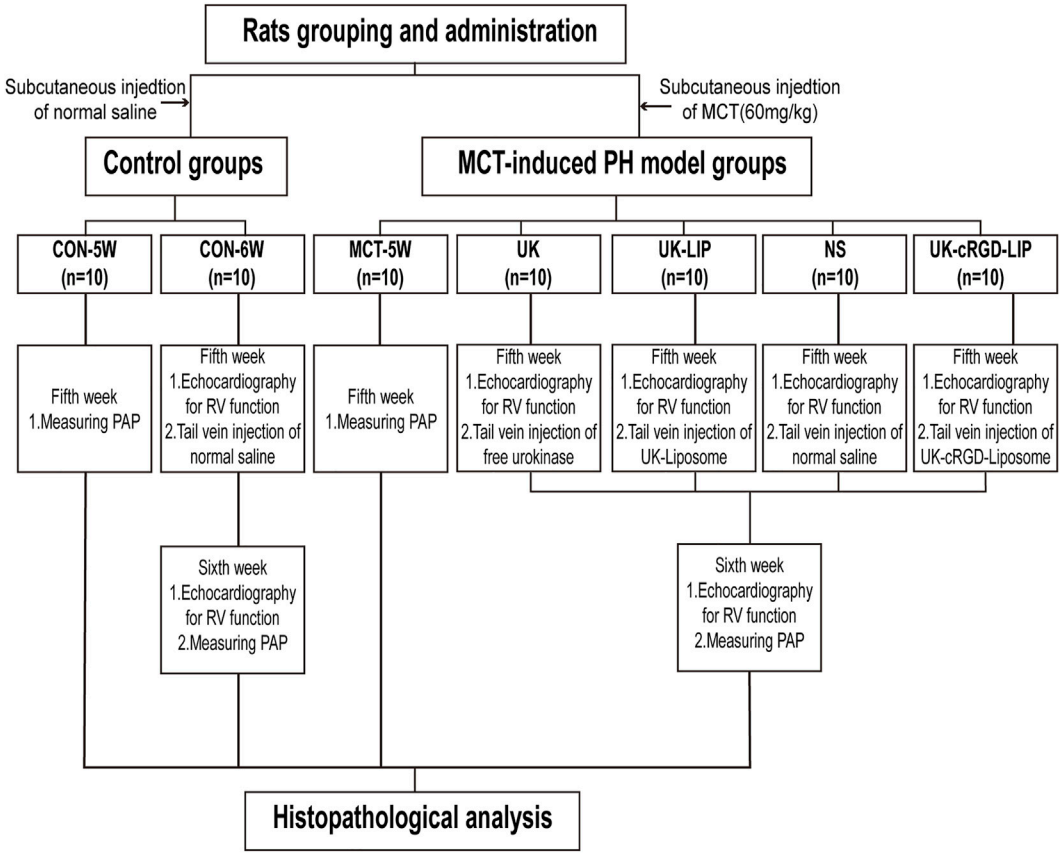

FIGURE 2
Flowchart of grouping and administration of rats in each group. Abbreviations: MCT, monocrotaline; RV, right ventricular; PAP, pulmonary artery pressure; UK-Liposome, urokinase-loaded liposome; UK-cRGD-Liposome, urokinase-loaded cycle RGD-decorated liposome.

DPPC, Cholesterol, and DSPE-mPEG2000 (ratio of 12 mg: 6 mg: 3 mg) were dissolved in chloroform, and the remaining steps were performed as above to obtain urokinase-loaded liposome (UK-Liposome).

Animal grouping and administration

The temperature of the rat rearing environment was regulated at 20 ± 2°C, the humidity was kept at 60 ± 5%, and a 12-h:12-h light-dark cycle was used. Previous studies have shown that MCT-induced PH rats develop *in-situ* thrombosis at week three (Fan et al., 2019) and right heart failure at week five or six (Paulin et al., 2015; Deng et al., 2017). Therefore, this study proposed administering thrombolytic therapy at week five after MCT injection and monitoring it for 1 week. Seventy SD rats were randomly divided to MCT (n = 50) or control (n = 20) groups (Figure 2). The MCT group received a single subcutaneous injection of MCT (60 mg/kg), while the control group received an equivalent volume of saline. Each group of rats was further subdivided according to duration after MCT injection (5, 6 weeks) and thrombolytic treatment modality (normal saline, free urokinase, UK-Liposome, UK-cRGD-Liposome). These subgroups were referred to as MCT-5W (n = 10), NS (n = 10), UK (n = 10), UK-LIP (n = 10), UK-cRGD-LIP (n = 10), and CON-5W (n = 10), CON-6W (n = 10), respectively. In the fifth week after MCT injection, rats in the MCT-5W and CON-5W groups measured pulmonary artery pressure *via* echocardiography-guided transthoracic puncture. Following invasive hemodynamic analysis, the heart and lung tissues of rats were pathologically examined to determine the degree of pulmonary vascular remodeling and RV remodeling and whether *in-situ* thrombi in pulmonary arterioles were formed. Five weeks after MCT injection, echocardiography was performed on rats in the CON-6W, NS, UK, UK-LIP, and UK-cRGD-LIP groups. Then, rats in the NS, UK (100 U/g), UK-LIP (100 U/g), and UK-cRGD-LIP (100 U/g) groups were injected with appropriate amounts of thrombolytic medicines *via* the tail vein. One week after thrombolytic therapy, echocardiography was performed again in rats in the CON-

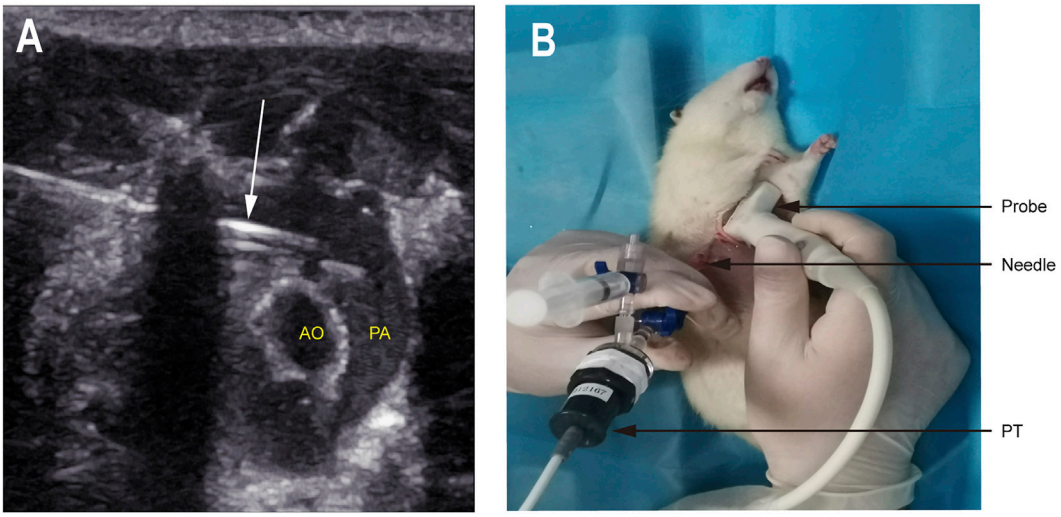

FIGURE 3
Echocardiography guided transthoracic puncture measurement of pulmonary artery pressure. **(A)** The puncture needle tip (white arrow) was located in the PA. **(B)** The actual operation of PA puncture by echocardiography was guided. Abbreviations: PA, pulmonary artery; AO, aorta; PT, pressure transducer.

6W, NS, UK, UK-LIP, and UK-cRGD-LIP groups. The heart and lung tissues were removed for pathological examination after an echocardiography-guided transthoracic puncture to evaluate pulmonary artery pressure.

Fifteen SD rats were randomly divided into three groups: a blank control group (Control, n = 5); an UK-cRGD-Liposome group (n = 5); and an UK-Liposome (n = 5). The Control group received saline treatment, and the UK-cRGD-Liposome and UK-Liposome groups were administered with appropriate medicines injected *via* the tail vein. Pathological evaluation of heart, liver, spleen, lung, and kidney tissues was performed 1 week following treatment.

Echocardiography

The rats were anesthetized *via* intraperitoneal administration of 2% sodium pentobarbital (50 mg/kg) and subjected to transthoracic echocardiography using a GE Vivid E95 ultrasound diagnostic machine (General Electric Company, USA) with an 18.0 MHz ultrasound probe (L8-18I-D). RV anterior wall thickness (RVAWT) was measured in a left ventricular long-axis view. Pulmonary artery acceleration time (PAAT) was assessed by Pulse-wave Doppler in short-axis views of the parasternal. RV end-diastolic transverse diameter (RVEDD), RV end-diastolic volume (RVEDV), RV end-systolic volume (RVESV), RV end-diastolic area (RVEDA), and RV end-systolic area (RVESA) were measured in apical four-chamber views. RV ejection fraction (RVEF%) = (RVEDV-RVESV)/RVEDV×100%, RV area change fraction (RVFAC%) = (RVEDA-RVESA)/RVEDA×100%. Tricuspid annular plane systolic excursion (TAPSE) was measured by M-mode echocardiography. The tricuspid annular movement was detected using tissue Doppler imaging in the apical cardiac four-chamber view, then to obtain isovolumic contraction time (ICT), isovolumic relaxation time (IRT), and ejection time (ET). RV myocardial work index (RV Tei index) = (ICT + IRT)/ET. RVEF, RVFAC, TAPSE, and RV Tei index were used to evaluate RV systolic function. RVEDD and RVAWT were used to assess right ventricular morphology. All examinations were performed by a sonographer who was blinded to the groups, and each parameter was measured three times and averaged.

Invasive pulmonary artery hemodynamic measurements

The puncture needle was connected to the pressure transducer (PT) through a tee tube, and a syringe was connected to the tee tube and injected with heparin saline (100 U/mL) to maintain pressure (Figure 3B). Under the guidance of real-time echocardiography, the surgeon carefully inserted the puncture needle into the right ventricular outflow tract in the parasternal short-axis view (Figure 3A). After the right ventricular pressure curve appeared on the BL-420 F Biosignal Acquisition and Analysis System (Chengdu Taimeng Software Co., Ltd.), the puncture needle continued to be slowly advanced to the main pulmonary artery and recorded the pulmonary artery pressure curve.

Histopathological analysis

After completion of pulmonary artery pressure detection, the rats were euthanized with an overdose of sodium pentobarbital. The thoracic cavity was opened quickly, and saline was injected steadily and slowly from the RV outflow tract (at the puncture hole) to flush the Cardiac and lung tissue, which could prevent excess blood and blood cells from remaining in the cardiac cavity or pulmonary vessels. Right ventricular hypertrophy index (RVHI) was calculated using the formula: RVHI (%) = RV/(LV + IVS) × 100%. RV hypertrophy was evaluated by RVHI (Yang et al., 2014). RV myocardial tissue and lung tissue were fixed with 4% paraformaldehyde for 48 h, routinely dehydrated, paraffin-embedded, and sectioned (5 μm).

Hematoxylin-eosin (H & E) staining: H & E staining was performed on lung tissue sections. Images were captured using an EVOS new inverted microscope imaging system (Life Technologies, United States). Using ImageJ image analysis software to measured vertical vessel external diameter (ED), vertical vessel inner diameter (ID), vessel total area (TA), and vessel lumen area (LA). Pulmonary arteriole morphology was assessed using the quantitative analysis methods proposed by Price et al. (2011), and Wu et al. (2016). with the calculation formulas pulmonary arteriole wall thickness percentage (wt %) = (ED-ID)/ED X 100% and pulmonary arteriole wall area percentage (WA%) = (TA-LA)/TA X 100%. Ten pulmonary arterioles (20–100 μm in diameter) were randomly selected for measurement in each section.

Fibrin staining (modified MSB method): Fibrin staining was performed on lung tissue sections according to the kit instructions. After staining, fibrin in the vessel was red, and red blood cells were yellow. 100 pulmonary arterioles (20–100 μm in diameter) were randomly observed and tallied as the number of vessels with residual *in-situ* thrombus for each rat in the MCT group. Right ventricular myocardial fibrosis was observed by Masson's trichrome staining. After staining, the collagen fibers were blue, and the myocardial tissue was red. Collagen volume fraction (CVF) was obtained by measuring the percentage of blue collagen fibers in myocardial tissues using ImageJ image analysis software (Guo et al., 2014). Ten slices of RV myocardial tissue were taken from each group of rats for evaluation.

Statistical analysis

Statistical Product and Service Solutions software Version 26.0 (SPSS, IBM, USA) was used for statistical analysis. All values were expressed as Mean ± SD (standard deviation). An unpaired Student's t-test was used to compare the data of two groups. For comparisons among multiple-group, the data with normal distribution and homogeneity of variance were compared by one-way ANOVA, otherwise by Kruskal–Wallis test. $p < 0.05$ was considered statistically significant.

Results

MCT-induced PH

MCT rats showed clinical signs of right heart failure such as shortness of breath, pleural fluid, ascites, and decreased physical activity in the fifth week after MCT injection, which was consistent with previously reported (Paulin et al., 2015; Deng et al., 2017). During the induction period, the mortality rates of rats in the MCT-5W, NS, UK, UK-LIP, and UK-cRGD-LIP groups were 10% (1/10), 20% (2/10), 20% (2/10), 20% (2/10), and 10% (1/10), respectively. In contrast, rats in the CON-5W and CON-6W groups all survived. No rats died in the NS, UK, UK-LIP, and UK-cRGD-LIP groups during the thrombolytic therapy period.

Compared with the CON-5W group, both pulmonary artery systolic pressure (PASP) (Figures 4A,B) and mean pulmonary artery pressure (mPAP) (Figures 4A,C) were significantly higher in the MCT-5W group rats. H& E staining of lung tissue sections revealed significant pulmonary vascular remodeling in the MCT-5W rats (Figures 4D–F). Furthermore, RV myocardial fibrosis (Figures 4G,H) and RV remodeling were also significantly aggravated (Figure 4I). These histopathological results further validated the pulmonary artery hemodynamic findings. In addition, fibrin staining (modified MSB method) of lung tissue sections also confirmed the presence of *in situ* thrombus dominated by fibrin deposition in pulmonary arteriole in the MCT-5W group of rats (Figure 4).

UK-cRGD-liposome for *in-situ* thrombus

UK-cRGD-Liposome could target dissolve of pulmonary arteriole *in-situ* thrombus in PH. As known by fibrin staining (modified MSB method) of lung tissue sections, the number of vessels with *in-situ* thrombi in rats in the UK-cRGD-LIP group was clearly less than that in the NS, UK, and UK-LIP groups (Table 1 and Figure 5). In addition, we found that the number of vessels with *in-situ* thrombi was further increased in the UK and UK-LIP groups compared with the MCT-5W group, whereas it was markedly decreased in the UK-cRGD-LIP group (Table 1). The above data suggest that UK-cRGD-Liposome improves the thrombolytic efficacy of urokinase by actively targeting urokinase delivery to *in-situ* thrombus.

Pulmonary vascular remodeling, RV remodeling and RV function

To get a flavor of the role of pulmonary arteriole *in situ* thrombosis in PH, we observed pulmonary artery pressure as well as cardiac and pulmonary pathological tissues in MCT rats. PASP (Figure 6A and Figure 7A) and mPAP (Figure 6B and Figure 7B)

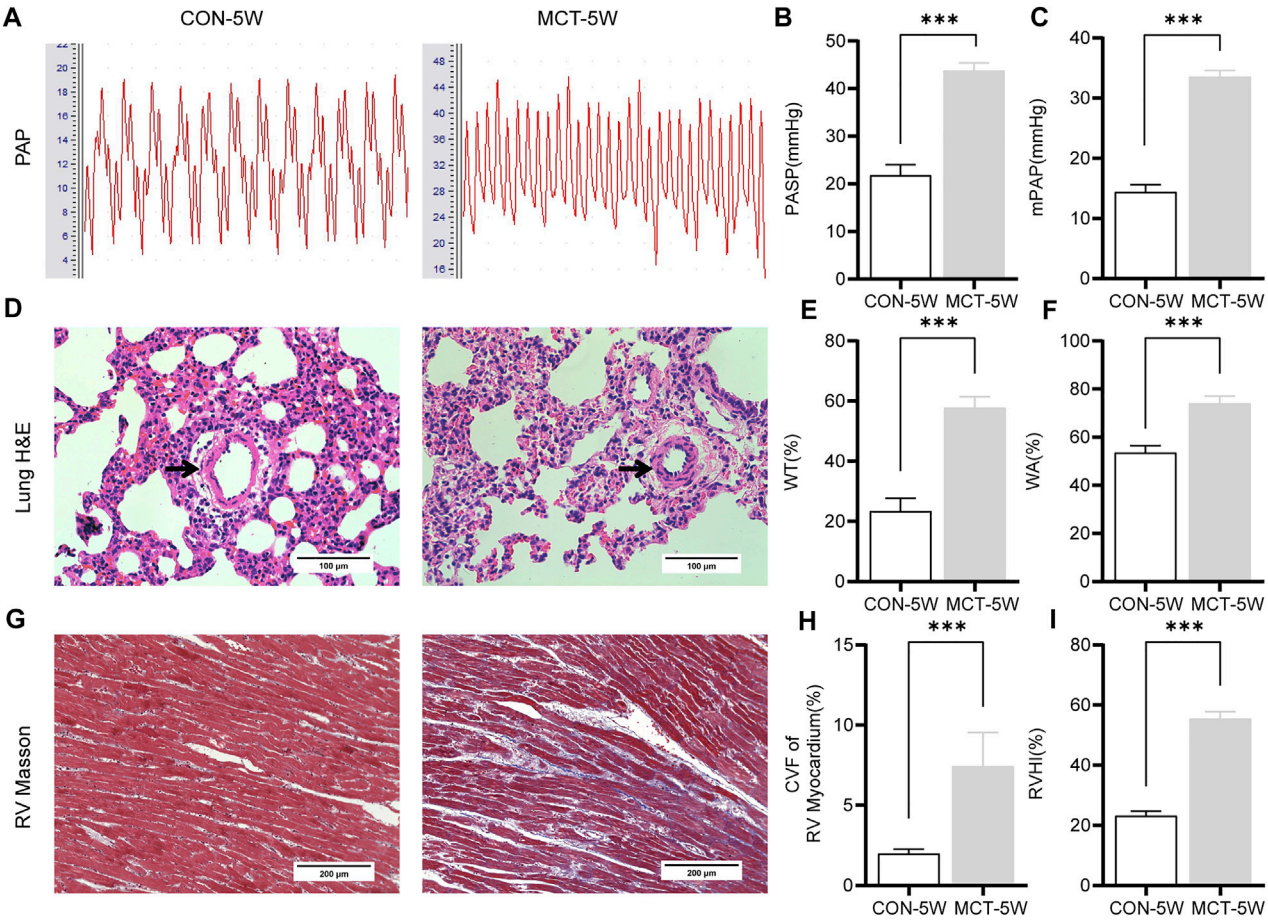

FIGURE 4
MCT-induced PH in rats. **(A)** Representative pulmonary artery pressure wavaforms obtained from CON-5W and MCT-5W rats. **(B)** Pulmonary artery systolic pressure was measured in CON-5W and MCT-5W rats. **(C)** Mean pulmonary artery pressure was measured in CON-5W and MCT-5W rats. **(D)** Representative images (×400 original magnification) of H & E staining of lung tissues from CON-5W and MCT-5W rats. Black arrow points to pulmonary arteriole (20–100 μm in diameter). **(E)** Quantitative analysis of vascular wall thickness **(F)** Quantitative analysis of vascular wall area **(G)** Representative images (×200 original magnification) of Masson's trichrome staining of RV tissues from CON-5W and MCT-5W rats. Red indicates muscle fibers; blue indicates collagen fibers. **(H)** Quantitative analysis of fibrotic area **(I)** Quantitative analysis of right ventricular hypertrophy index. Values are presented as Mean ± SD. Data (CON-5W, $n = 10$; MCT-5W, $n = 9$) were analyzed by unpaired Student's t-test. ***$p < 0.001$. Abbreviations: PASP, pulmonary artery systolic pressure; mPAP, mean pulmonary artery pressure; H & E, hematoxylin-eosin; WT, pulmonary arteriole wall thickness; WA, pulmonary arteriole wall area; CVF, collagen volume fraction; RVHI, right ventricular hypertrophy index.

TABLE 1 The number of vessels with residual in-situ thrombus.

Group	N	Vessels
MCT-5W	9	30.6 ± 2.3
UK	8	36.4 ± 3.2**
UK-LIP	8	35.5 ± 3.0*
NS	8	41.5 ± 4.1**#
UK-cRGD-LIP	9	19.7 ± 3.2**##▲▲

Notes: 100 pulmonary arterioles (20–100 μm in diameter) were randomly observed. Values were presented as Mean ± SD. Data were analyzed by one-way ANOVA. *$p < 0.05$ and **$p < 0.01$ vs. MCT-5W. #$p < 0.05$ and ##$p < 0.01$ vs. UK or UK-LIP; ▲▲$p < 0.01$ vs. NS.

were notably lower in rats in the UK-cRGD-LIP group compared with the MCT-5W, NS, UK, and UK-LIP groups. Compared with the UK-cRGD-LIP group, the results of RVHI (Figure 7C), WT (Figure 6B and Figure 7D), WA (Figure 6B and Figure 7E), and CVF of RV myocardium (Figure 6C and Figure 7F) suggested that RV myocardial remodeling and pulmonary vascular remodeling were further aggravated in the NS, UK, and UK-LIP groups. Surprisingly, RVHI, WT, WA, and CVF of RV myocardium in the MCT-5W group were not significantly different from those in the UK-cRGD-LIP group (Figures 7C–F). The above outcomes demonstrate that *in-situ* thrombi of pulmonary arterioles by targeted therapy can significantly

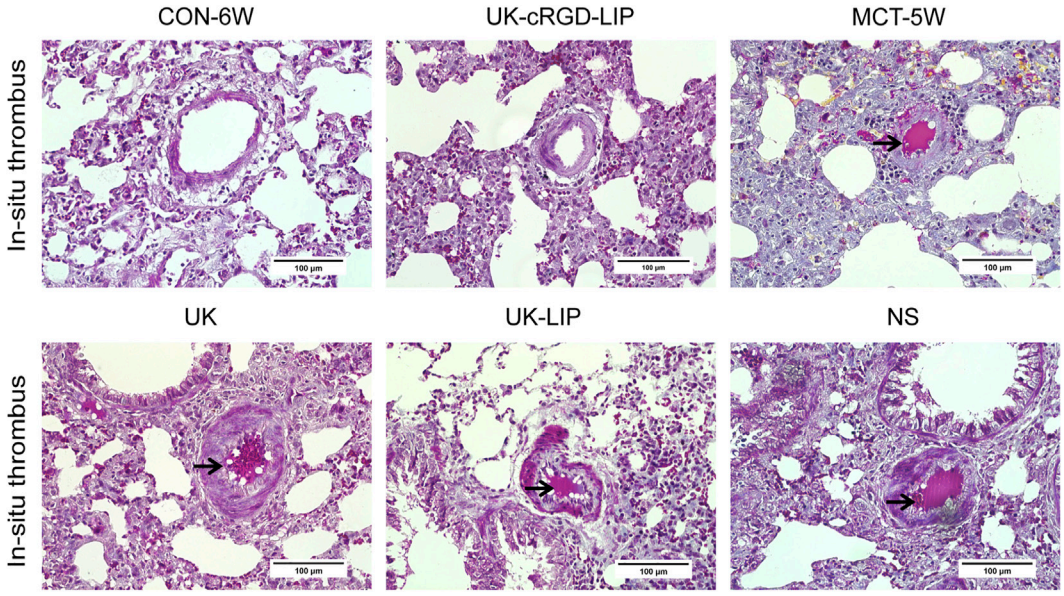

FIGURE 5
Representative images (×400 original magnification) of fibrin staining (modified MSB method) of lung tissues from CON-6W, MCT-5W, UK, UK-LIP, NS, and UK-cRGD-LIP rats. Red indicates fibrin deposition; yellow indicates erythrocyte accumulation. Black arrow points to intravascular *in-situ* thrombus.

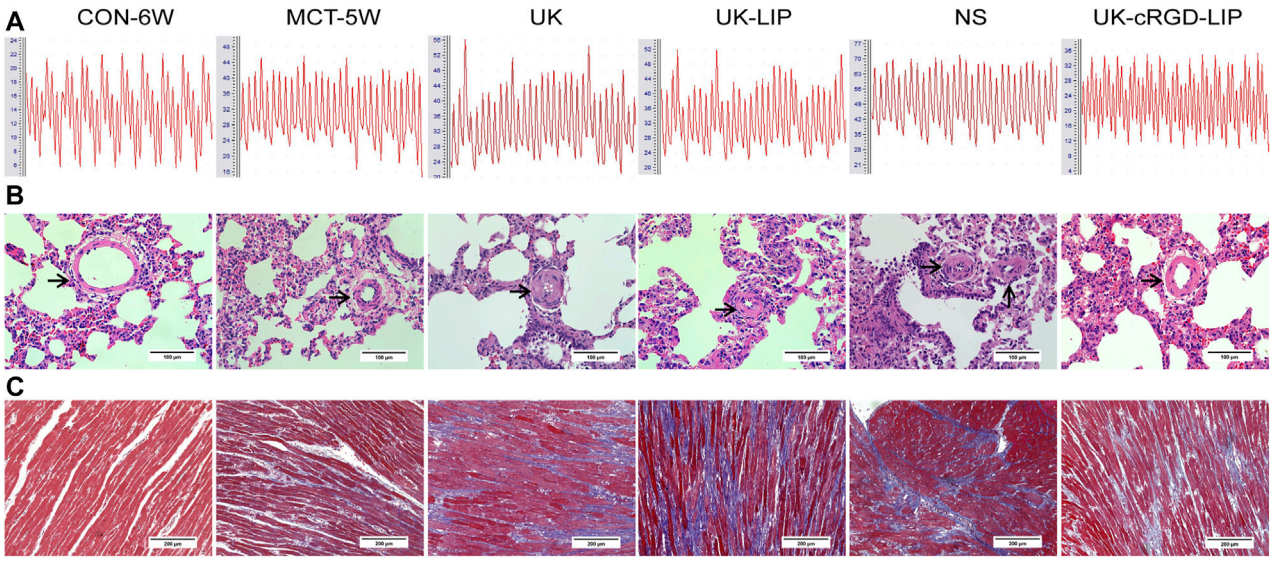

FIGURE 6
(A) Representative pulmonary artery pressure wavaforms obtained from CON-6W, MCT-5W, UK, UK-LIP, NS, and UK-cRGD-LIP rats. **(B)** Representative images (×400 original magnification) of H & E staining of lung tissues from CON-6W, MCT-5W, UK, UK-LIP, NS, and UK-cRGD-LIP rats. Black arrow points to pulmonary arteriole (20–100 μm diameter). **(C)** Representative images (×200 original magnification) of Masson's trichrome staining of RV tissues from CON-6W, MCT-5W, UK, UK-LIP, NS and UK-cRGD-LIP rats. Red indicates muscle fibers; blue indicates collagen fibers.

10.3389/fbioe.2022.1038829

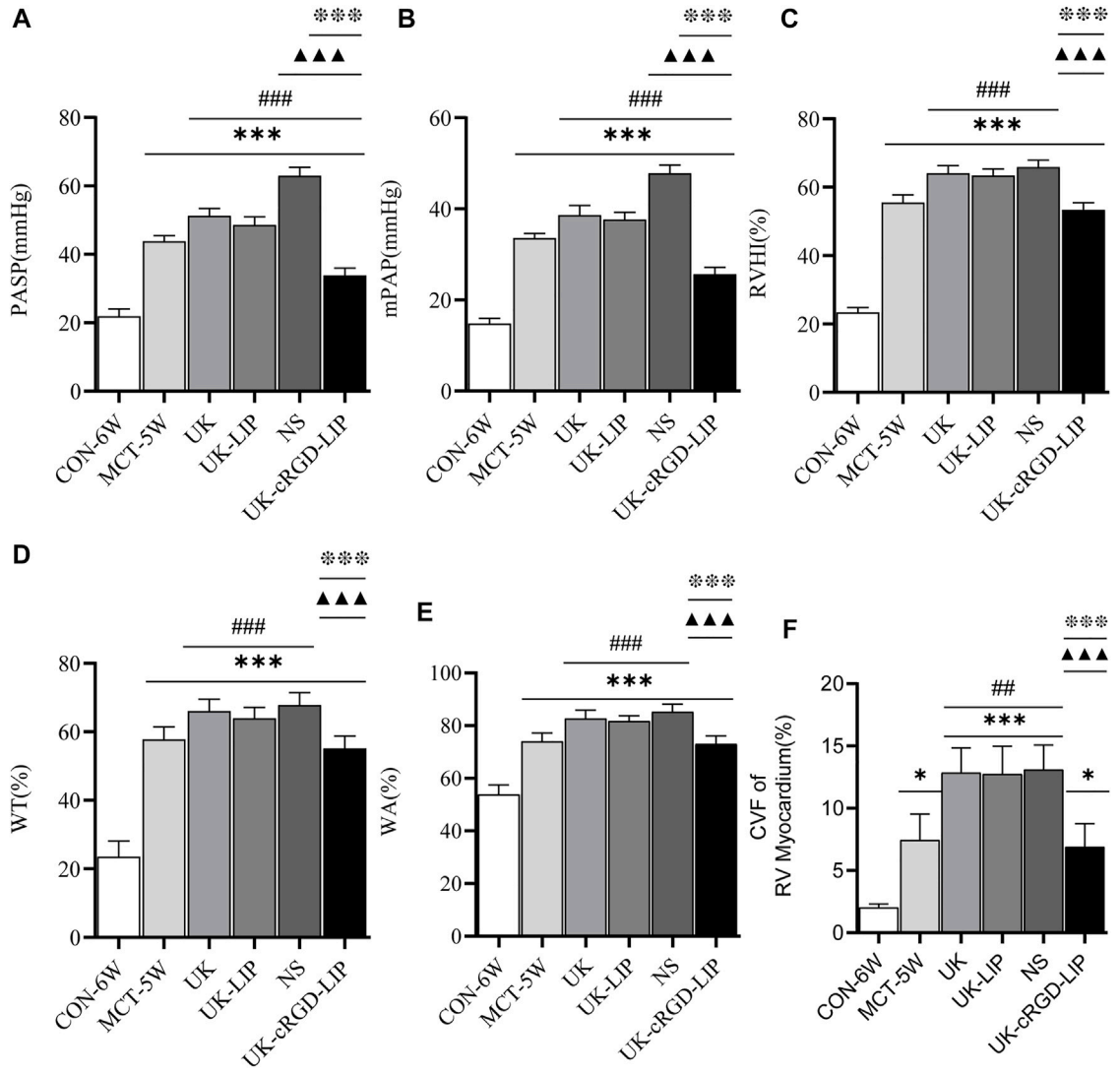

FIGURE 7
Reduction of *in-situ* thrombi in pulmonary arterioles alleviates the progression of MCT-induced PH in rats. **(A)** Pulmonary artery systolic pressure was measured in CON-6W, MCT-5W, UK, UK-LIP, NS, and UK-cRGD-LIP rats. **(B)** Mean pulmonary artery pressure was measured in CON-6W, MCT-5W, UK, UK-LIP, NS, and UK-cRGD-LIP rats. **(C)** Quantitative analysis of right ventricular hypertrophy index. **(D)** Quantitative analysis of vascular wall thickness. **(E)** Quantitative analysis of vascular wall area. **(F)** Quantitative analysis of fibrotic area. Values were presented as Mean ± SD. Data (CON-6W, $n = 10$; MCT-5W, $n = 9$; UK, $n = 8$; UK-LIP, $n = 8$; NS, $n = 8$; UK-cRGD-LIP, $n = 9$) were analyzed by one-way ANOVA **(A–E)** or Kruskal–Wallis test **(F)**. $^{*}p < 0.05$ and $^{***}p < 0.001$ vs. CON-6W; $^{\#\#}p < 0.01$ and $^{\#\#\#}$fn$^{\#\#\#}p < 0.001$ vs. MCT-5W; $^{\blacktriangle\blacktriangle\blacktriangle}p < 0.001$ vs. UK or UK-LIP; $^{***}p < 0.001$ vs. NS.

reduce pulmonary arterial pressure and thus limit the pathological development of PH.

To investigate whether targeted thrombolytic therapy for PH ameliorates RV function, we performed echocardiography in rats in the CON-6W and NS, UK, UK-LIP, and UK-cRGD-LIP groups pre and post thrombolytic treatment. In MCT rats, PAAT displayed mid-systolic notching, a characteristic echocardiographic feature of elevated pulmonary artery pressure (Figure 8 and Figure 9A). Compared with pre thrombolytic treatment, the rats in the NS, UK, and UK-LIP groups' echocardiography values indicated further deterioration of right ventricular function and morphology post thrombolytic treatment (increased RVEDD; decreased TAPSE, RVEF, and RVFAC; ascended RV Tei index; thickened RVAWT) (Figure 8 and Figures 9B–G). In contrast, the RV systolic function was significantly improved in the UK-cRGD-LIP group post thrombolytic treatment. There was no significant difference in echocardiography values pre and post treatment in the CON-6W group. In the MCT-induced rat model of PH, RVEF <40%, RV FAC <35%, and TASPE<1.75 mm have been

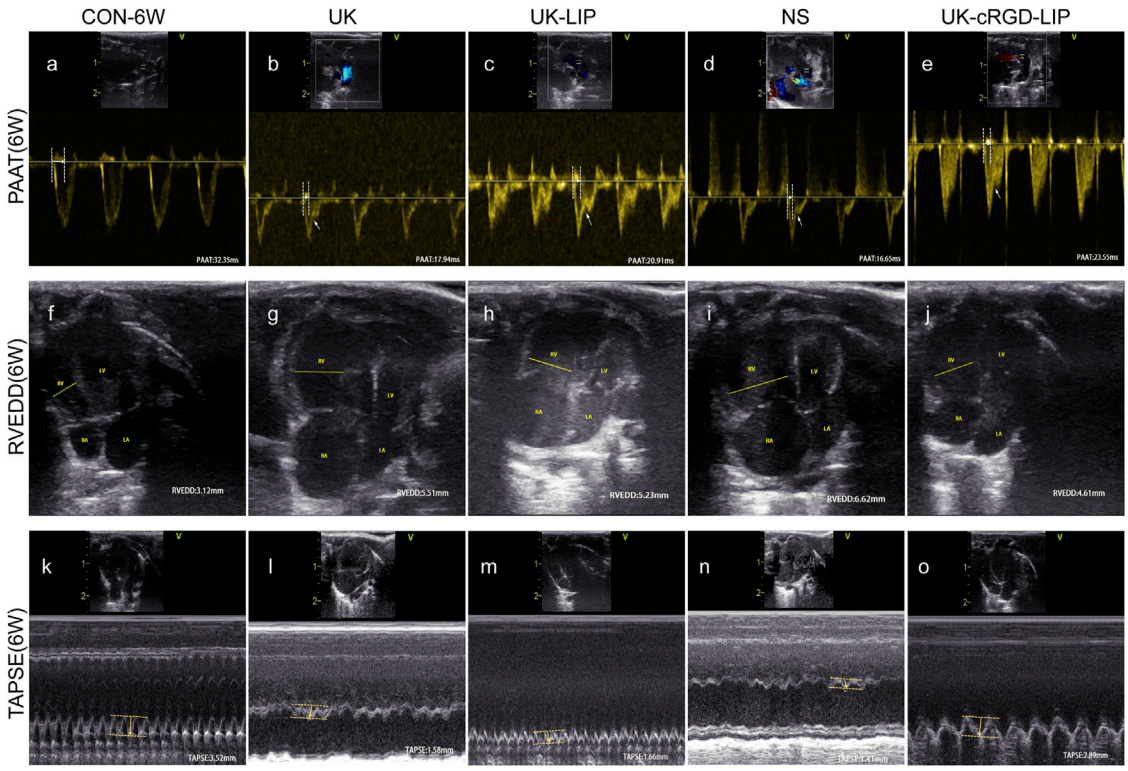

FIGURE 8
Representative echocardiography images of CON-6W, UK, UK-LIP, NS and UK-cRGD-LIP rats. **(A–E)** PAAT: Pulse-wave Doppler of views at the parasternal short-axis section. White arrow pointed to midsystolic notching. **(F–J)** RVEDD: Apical four-chamber view. Yellow line highlighted right ventricle internal diameter during diastole. **(K–O)** TAPSE: Tricuspid annular plane systolic excursion was recorded by M-mode echocardiography. Yellow arrow represented distance. Abbreviations: RV, right ventricular; LV, left ventricular; RA, right atrium; LA, left atrium.

widely used as ultrasonographic value gauges for right heart failure (Mariano-Goulart et al., 2003; Hardziyenka et al., 2006; Rudski et al., 2010). RVEF (Figure 9E), RVFAC (Figure 9F), and TAPSE (Figure 8 and Figure 9B) in rats in the NS, UK, and UK-LIP groups reached above cut-off values post conventional thrombolytic treatment. These results suggest that effective targeted dissolution of pulmonary arterioles *in-situ* thrombi in PH can improve RV function markedly.

In vivo safety evaluation

Since MCT rats could suffer some degree of damage to their major organs, healthy SD rats were reselected for histological examination to investigate the possible toxic effects of nanoscale drug carriers *in vivo*. During the treatment period, all groups of rats survived. In addition, no abnormal clinical behaviors or signs were observed in any of the groups. The H&E staining results of the heart, liver, spleen, lung, and kidney tissue sections showed that no significant injuries or pathophysiological changes were observed in the major organs of the rats in each group (Figure 10). Therefore, the cRGD-modified nanoscale active targeting drug delivery vehicle has good biocompatibility.

Discussion

To the best of our knowledge, this is the first research to show that UK-cRGD-Liposome can target the dissolution of chronically formed pulmonary arterioles *in-situ* thrombi in PH. Furthermore, we also found that pulmonary arterioles *in-situ* thrombi in PH with targeted therapy can considerably enhance RV function and alleviate the progression of PH. These findings demonstrate that micro-thrombi formed *in-situ* in pulmonary arterioles play a critical role in the progression of PH.

Animal models of PH

Currently, typical experimental PH models include the MCT-induced PH model, the chronic hypoxia-induced PH model, and the surgically established body-pulmonary circulation shunt-induced

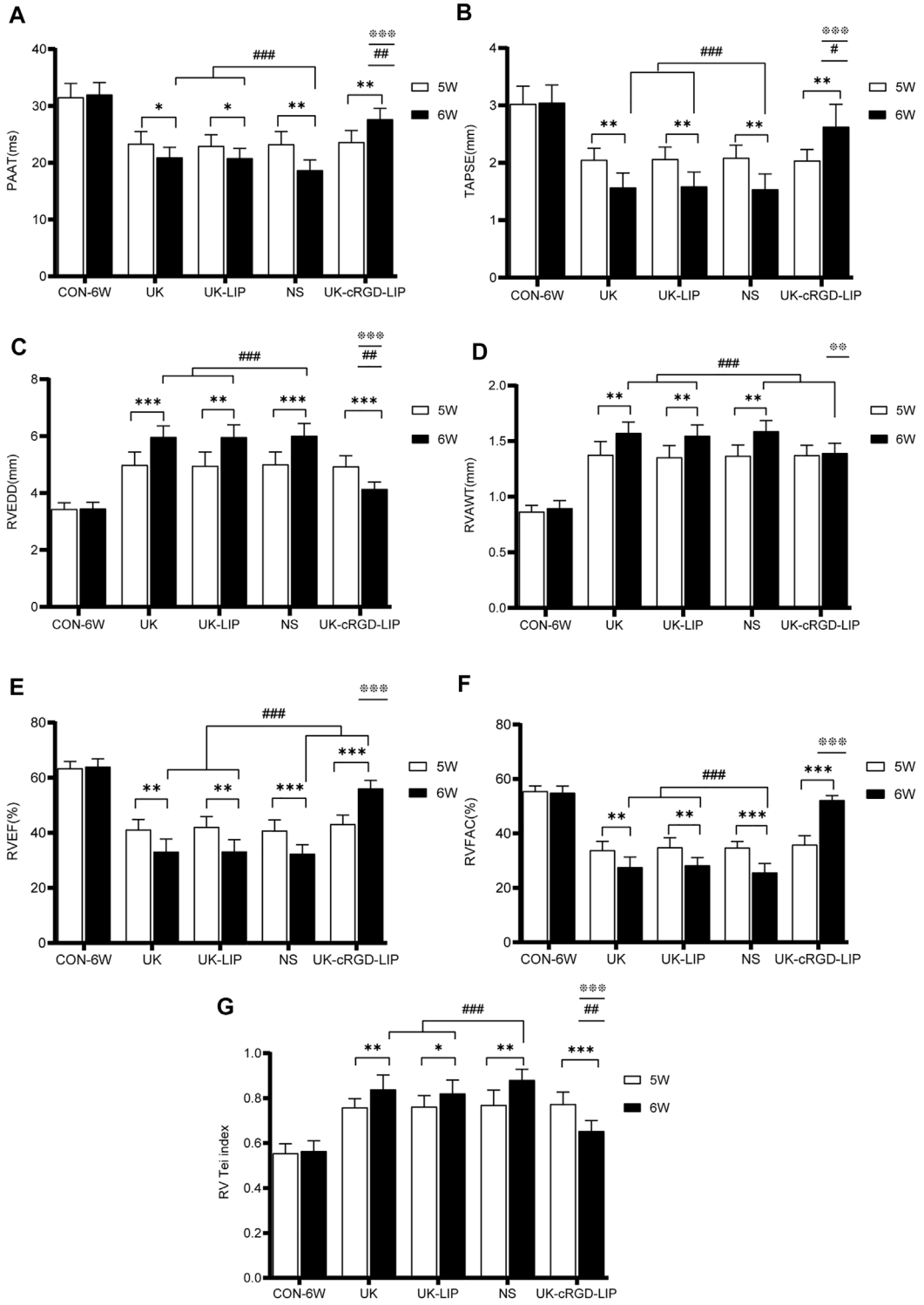

FIGURE 9
Echocardiography parameters of right ventricular function and morphology. **(A–G)** Analysis of PAAT, TAPSE, RVEDD, RVAWT, RVEF, RVFAC, RV Tei index from CON-6W, UK, UK-LIP, NS, and UK-cRGD-LIP rats. Values were presented as Mean ± SD. Data (CON-6W, $n = 10$; UK, $n = 8$; UK-LIP, $n = 8$; NS, $n = 8$; UK-cRGD-LIP, $n = 9$) were analyzed by unpaired Student's t-test or one-way ANOVA. $^{*}p < 0.05$, $^{**}p < 0.01$, and $^{***}p < 0.001$. $^{\#}p < 0.05$, $^{\#\#}p < 0.01$, and $^{\#\#\#}p < 0.001$ vs. CON-6W (6W). $^{*}p < 0.05$, $^{**}p < 0.01$, and $^{***}p < 0.001$ vs. UK(6W), UK-LIP(6W), or NS(6W). Abbreviations: 5W, pre thrombolytic therapy; 6W, post thrombolytic therapy; PAAT, pulmonary artery acceleration time; RVEDD, right ventricular end-diastolic transverse diameter; TAPSE, tricuspid annular plane systolic excursion; RVEF, right ventricular ejection fraction; RVFAC, right ventricular area change fraction; RV Tei index, right ventricular myocardial work index; RVAWT, right ventricular anterior wall thickness.

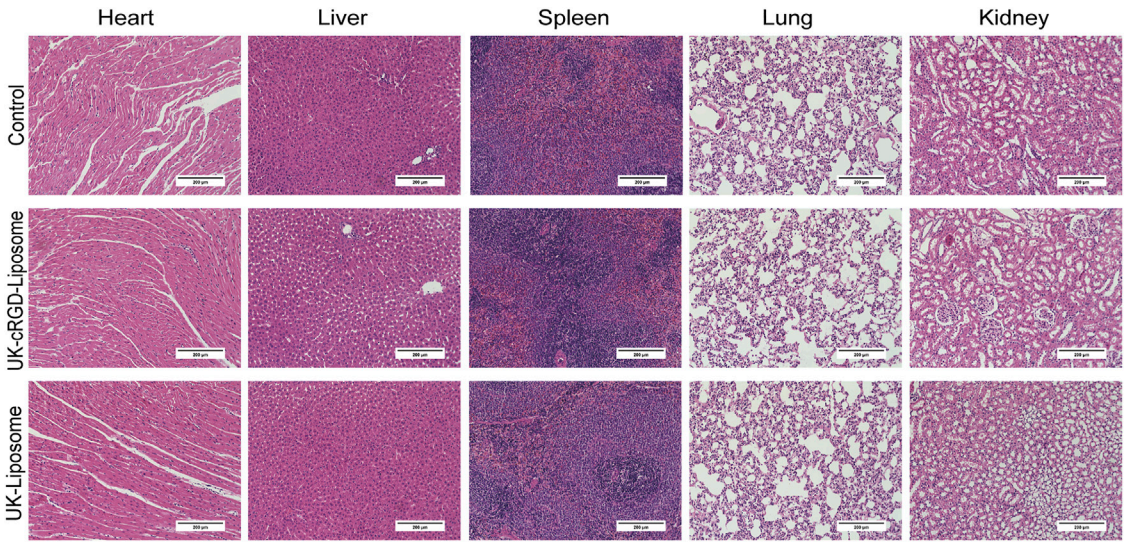

FIGURE 10
H & E staining of the major organs collected from healthy SD rats 1 week after tail vein injection of UK-cRGD-Liposome, UK-Liposome or normal saline (Control). Abbreviations: UK-cRGD-Liposome, urokinase-loaded cycle RGD-decorated liposome; UK-Liposome, urokinase-loaded liposome.

PH model (Wu et al., 2015; Kawai et al., 2022). MCT is a pyrrolizidine alkaloid extracted from the seeds of the Crotalaria spectabilis (Benoist et al., 2014). The MCT alkaloid selectively injures pulmonary vascular endothelial cells through activated monocrotaline pyrrole (MCTP) by cytochrome P450 in the liver, thereby inducing an increase in pulmonary artery pressure (Li et al., 2016). Fibrinogen-like protein two expressed in pulmonary arterioles in PH can directly activate the coagulation system and cause massive fibrin deposition, and the activated coagulation system and damaged vascular endothelial cells cause activated platelet aggregation. These processes result in *in-situ* thrombosis in pulmonary arterioles (Fan et al., 2019). Furthermore, neonate rat lungs exhibit alveolar and capillary surface development similar to that of humans (Zoetis and Hurtt, 2003). Therefore, this study selected the method of subcutaneous injection of MCT to establish an experimental PH model. In our study, the presence of *in situ* thrombi composed of deposited fibrin was observed in the pulmonary arterioles of MCT rats by fibrin staining (modified MSB method) (Figure 5), which not only further confirmed the previous study but also provided an experimental model for the thrombolytic study of UK-cRGD-Liposome in pulmonary arteriole *in-situ* thrombus.

The efficacy of targeted thrombolysis in PH

The RGD peptide not only specifically binds the GPIIb/IIIa receptor on the surface of activated platelets but also inhibits the GPIIb/IIIa receptor from binding to fibrinogen, thus preventing platelet aggregation (Figure 1) (Pawlowski et al., 2017; Rima et al., 2018). Moreover, PEGylated liposomes could accumulate *in vivo via* enhanced permeability and retention (EPR) effect (Sercombe et al., 2015). Pharmacokinetic study of FITC-cRGD liposome showed that the plasma clearance half-life of cRGD liposome was 2.5 h, which was several times that of free urokinase. The tail bleeding assay in mice implied that the cRGD liposome could significantly reduce the bleeding side effects of urokinase (Zhang et al., 2018). Based on the Zhang et al. (2018) study, ourselves successfully prepared UK-cRGD-Liposome with smaller particle size (176.8 nm), higher encapsulation efficiency (58.83%), higher drug loading capacity (40.64%), and more stable release capacity (most of the urokinase could be released stably and continuously in first 8 h) (Rao, 2020). In this study, the results of the thrombolysis experimental demonstrated that UK-cRGD-Liposome was four times more efficient at thrombolysis than that of the same dose of urokinase (Table 1). These results not only demonstrate that UK-cRGD-Liposome can effectively deliver urokinase to chronically formed pulmonary arterioles *in-situ* thrombi but also further improve the basic research of cRGD peptide targeting activated platelets. Furthermore, liposomes have been widely used as nanoscale drug delivery vehicles in clinical settings, such as daunorubicin citrate liposomes and vincristine liposomes have been licensed for enhancing the efficacy of chemotherapeutics and for overcoming drug resistance by the US Food and Drug Administration (FDA) (Janko et al., 2019). The RGD sequence-based antiplatelet medication tirofiban also has been widely used in clinical (Suntravat et al., 2013). As a

consequence, UK-cRGD-Liposome is safe and efficient nano-drug delivery systems that are expected to be novel targeted thrombolytic medications.

Guidelines for the diagnosis and treatment of pulmonary hypertension have classified PH into five groups on the basis of pathophysiology, etiology, and hemodynamics (Humbert et al., 2022). Group 1: Pulmonary arterial hypertension (PAH), including idiopathic PH, hereditary PH, and drug or toxin-induced PH. MCT-induced PH belongs to PAH (Group 1); in PAH patients, improvement in RV function was critical to lowering mortality (Potus et al., 2015; Clapham et al., 2020). PAH induces an increase in RV afterload, which eventually results in fibrosis of RV myocardial tissue and RV dysfunction when the afterload exceeds RV compensatory capacity (Vang et al., 2021). In our study, rats in the UK-cRGD-LIP group had considerably improved RV systolic function and RV pumping efficiency (Figures 9B,E–G) post targeted thrombolytic therapy. More notably, pulmonary artery pressure was reduced in the UK, UK-LIP, and UK-cRGD-LIP groups compared to the NS group. Meanwhile, pulmonary artery pressure in the UK-cRGD-LIP group was also significantly lower than that in the MCT-5W group (Figure 6A and Figures 7A,B). This finding supports the hypothesis that *in-situ* thrombus in PH can cause a significant increase in pulmonary artery pressure by increasing mechanical obstruction of the pulmonary vascular system, which can lead to further worsening in PH. Additionally, we also observed that CVF and WT, WA were no longer further elevated in the post targeted thrombolytic therapy (Figures 6B,C and Figures 7D–F). These results suggest that reducing *in-situ* thrombosis can significantly restrict the progression of pulmonary vascular remodeling and RV remodeling in PH. In summary, targeted thrombolytic therapy can clearly lower pulmonary artery pressure in PH, leading to improved right ventricle-pulmonary artery coupling and RV function.

Limitation

In this study, albeit targeted thrombolytic therapy improved RV function, it failed to reverse pulmonary vascular remodeling and RV remodeling, which may be related to the short therapy time point and observation period. Hence, it is worthy of further study to grasp the therapy time point of pulmonary arteriole *in-situ* thrombus in pulmonary hypertension as well as to utilize UK-cRGD-Liposome more effectively and to improve the production process of UK-cRGD-Liposome.

Conclusion

In conclusion, our study demonstrates that this biocompatible UK-cRGD-Liposome could targeted therapy the chronically formed pulmonary arterioles *in-situ* thrombi in PH. Furthermore, the most intriguing finding from our study is that reducing *in-situ* thrombosis of pulmonary arterioles can alleviate the progression of PH and improve RV function, which could be a beneficial exploration of the potential mechanisms of *in-situ* thrombus involved in the development of PH. In summary, UK-cRGD-Liposome offers a promising target drug-delivery system for thrombolytic therapy as well as a beneficial reference for the targeted therapy of *in-situ* thrombus in PH.

Data availability statement

All datasets presented in this study are included in the article, further inquiries can be directed to the corresponding author.

Ethics statement

The animal study was reviewed and approved by The Animal Experiment Ethics Committee of Guangxi Medical University.

Author contributions

JW designed the research. HR, ZT performed drug synthesis, JL, XZ, YM, TH, LH, DZ, CJ, YC, and BL conducted the animal experiments, JW, JL, and XZ analyzed the data, JL and XZ wrote the manuscript. All authors have read and approved the final submitted manuscript.

Funding

This study was supported by the National Natural Science Foundation of China (Grant No. 81760314), and the Guangxi Medical “139” Project for Training High-level Backbone Talents (Grant No. G201903014).

Conflict of interest

The authors declare that the research was conducted in the absence of any commercial or financial relationships that could be construed as a potential conflict of interest.

Publisher’s note

References

Akbarzadeh, A., Rezaei-Sadabady, R., Davaran, S., Joo, S. W., Zarghami, N., Hanifehpour, Y., et al. (2013). Liposome: Classification, preparation, and applications. *Nanoscale Res. Lett.* 8 (1), 102. doi:10.1186/1556-276x-8-102

Altaf, F., Wu, S., and Kasim, V. (2021). Role of fibrinolytic enzymes in anti-thrombosis therapy. *Front. Mol. Biosci.* 8, 680397. doi:10.3389/fmolb.2021.680397

Benoist, D., Stones, R., Benson, A. P., Fowler, E. D., Drinkhill, M. J., Hardy, M. E., et al. (2014). Systems approach to the study of stretch and arrhythmias in right ventricular failure induced in rats by monocrotaline. *Prog. Biophys. Mol. Biol.* 115 (2-3), 162–172. doi:10.1016/j.pbiomolbio.2014.06.008

Boucly, A., Weatherald, J., Savale, L., Jaïs, X., Cottin, V., Prevot, G., et al. (2017). Risk assessment, prognosis and guideline implementation in pulmonary arterial hypertension. *Eur. Respir. J.* 50 (2), 1700889. doi:10.1183/13993003.00889-2017

Chen, R., Ni, S., Chen, W., Liu, M., Feng, J., and Hu, K. (2021). Improved anti-triple negative breast cancer effects of docetaxel by RGD-modified lipid-core micelles. *Int. J. Nanomedicine* 16, 5265–5279. doi:10.2147/ijn.S313166

Clapham, K. R., Highland, K. B., Rao, Y., and Fares, W. H. (2020). Reduced RVSWI is associated with increased mortality in connective tissue disease associated pulmonary arterial hypertension. *Front. Cardiovasc. Med.* 7, 77. doi:10.3389/fcvm.2020.00077

Cullivan, S., Murphy, C. A., Weiss, L., Comer, S. P., Kevane, B., McCullagh, B., et al. (2021). Platelets, extracellular vesicles and coagulation in pulmonary arterial hypertension. *Pulm. Circ.* 11 (3), 1–9. doi:10.1177/20458940211021036

Deng, Y., Wu, W., Guo, S., Chen, Y., Liu, C., Gao, X., et al. (2017). Altered mTOR and Beclin-1 mediated autophagic activation during right ventricular remodeling in monocrotaline-induced pulmonary hypertension. *Respir. Res.* 18 (1), 53. doi:10.1186/s12931-017-0536-7

Fan, C., Wang, J., Mao, C., Li, W., Liu, K., and Wang, Z. (2019). The FGL2 prothrombinase contributes to the pathological process of experimental pulmonary hypertension. *J. Appl. Physiol. (1985).* 127 (6), 1677–1687. doi:10.1152/japplphysiol.00396.2019

Fernandez, R. A., Sundivakkam, P., Smith, K. A., Zeifman, A. S., Drennan, A. R., and Yuan, J. X. (2012). Pathogenic role of store-operated and receptor-operated Ca2+ channels in pulmonary arterial hypertension. *J. Signal Transduct.* 2012, 1–16. doi:10.1155/2012/951497

Garcia Ribeiro, R. S., Belderbos, S., Danhier, P., Gallo, J., Manshian, B. B., Gallez, B., et al. (2019). Targeting tumor cells and neovascularization using RGD-functionalized magnetoliposomes. *Int. J. Nanomedicine* 14, 5911–5924. doi:10.2147/ijn.S214041

Guo, Y., Wu, J., Jia, H., Chen, W., Shao, C., Zhao, L., et al. (2015). Balancing the expression and production of a heterodimeric protein: Recombinant agkisacutacin as a novel antithrombotic drug candidate. *Sci. Rep.* 5, 11730. doi:10.1038/srep11730

Guo, Y., Wu, W., Cen, Z., Li, X., Kong, Q., and Zhou, Q. (2014). IL-22-producing Th22 cells play a protective role in CVB3-induced chronic myocarditis and dilated cardiomyopathy by inhibiting myocardial fibrosis. *Virol. J.* 11, 230. doi:10.1186/s12985-014-0230-z

Hardziyenka, M., Campian, M. E., de Bruin-Bon, H. A., Michel, M. C., and Tan, H. L. (2006). Sequence of echocardiographic changes during development of right ventricular failure in rat. *J. Am. Soc. Echocardiogr.* 19 (10), 1272–1279. doi:10.1016/j.echo.2006.04.036

Hu, Y., Yu, D., Wang, Z., Hou, J., Tyagi, R., Liang, Y., et al. (2019). Purification and characterization of a novel, highly potent fibrinolytic enzyme from Bacillus subtilis DC27 screened from Douchi, a traditional Chinese fermented soybean food. *Sci. Rep.* 9 (1), 9235. doi:10.1038/s41598-019-45686-y

Huang, G., Zhou, Z., Srinivasan, R., Penn, M. S., Kottke-Marchant, K., Marchant, R. E., et al. (2008). Affinity manipulation of surface-conjugated RGD peptide to modulate binding of liposomes to activated platelets. *Biomaterials* 29 (11), 1676–1685. doi:10.1016/j.biomaterials.2007.12.015

Humbert, M., Kovacs, G., Hoeper, M. M., Badagliacca, R., Berger, R. M. F., Brida, M., et al. (2022). 2022 ESC/ERS Guidelines for the diagnosis and treatment of pulmonary hypertension. *Eur. Heart J.* 00, 1–114. doi:10.1093/eurheartj/ehac237

Jalce, G., and Guignabert, C. (2020). Multiple roles of macrophage migration inhibitory factor in pulmonary hypertension. *Am. J. Physiology-Lung Cell. Mol. Physiology* 318 (1), L1–l9. doi:10.1152/ajplung.00234.2019

Janko, C., Ratschker, T., Nguyen, K., Zschiesche, L., Tietze, R., Lyer, S., et al. (2019). Functionalized superparamagnetic iron oxide nanoparticles (SPIONs) as platform for the targeted multimodal tumor therapy. *Front. Oncol.* 9, 59. doi:10.3389/fonc.2019.00059

Kawai, M., Zhang, E., Kabwe, J. C., Okada, A., Maruyama, J., Sawada, H., et al. (2022). Lung damage created by high tidal volume ventilation in rats with monocrotaline-induced pulmonary hypertension. *BMC Pulm. Med.* 22 (1), 78. doi:10.1186/s12890-022-01867-6

Khan, A. A., Allemailem, K. S., Almatroodi, S. A., Almatroudi, A., and Rahmani, A. H. (2020). Recent strategies towards the surface modification of liposomes: An innovative approach for different clinical applications. *3 Biotech.* 10 (4), 163. doi:10.1007/s13205-020-2144-3

Koudelka, S., Mikulik, R., Mašek, J., Raška, M., Turánek Knotigová, P., Miller, A. D., et al. (2016). Liposomal nanocarriers for plasminogen activators. *J. Control. Release* 227, 45–57. doi:10.1016/j.jconrel.2016.02.019

Li, L. S., Luo, Y. M., Liu, J., Zhang, Y., Fu, X. X., and Yang, D. L. (2016). Icariin inhibits pulmonary hypertension induced by monocrotaline through enhancement of NO/cGMP signaling pathway in rats. *Evidence-Based Complementary Altern. Med.* 2016, 1–10. doi:10.1155/2016/7915415

Liu, H., Zhang, R., Zhang, D., Zhang, C., Zhang, Z., Fu, X., et al. (2022). Cyclic RGD-decorated liposomal gossypol AT-101 targeting for enhanced antitumor effect. *Int. J. Nanomedicine* 17, 227–244. doi:10.2147/ijn.S341824

Liu, M., Wu, B., Wang, W. Z., Lee, L. M., Zhang, S. H., and Kong, L. Z. (2007). Stroke in China: Epidemiology, prevention, and management strategies. *Lancet Neurol.* 6 (5), 456–464. doi:10.1016/s1474-4422(07)70004-2

Mariano-Goulart, D., Eberlé, M. C., Boudousq, V., Hejazi-Moughari, A., Piot, C., Caderas de Kerleau, C., et al. (2003). Major increase in brain natriuretic peptide indicates right ventricular systolic dysfunction in patients with heart failure. *Eur. J. Heart Fail.* 5 (4), 481–488. doi:10.1016/s1388-9842(03)00041-2

Olschewski, H., and Rich, S. (2018). Are anticoagulants still indicated in pulmonary arterial hypertension? *Pulm. Circ.* 8 (4), 2045894018807681–2045894018807685. doi:10.1177/2045894018807681

Pan, Q., Zhang, J., Li, X., Zou, Q., Zhang, P., Luo, Y., et al. (2019). Construction of novel multifunctional luminescent nanoparticles based on DNA bridging and their inhibitory effect on tumor growth. *RSC Adv.* 9 (26), 15042–15052. doi:10.1039/c9ra01381d

Paulin, R., Sutendra, G., Gurtu, V., Dromparis, P., Haromy, A., Provencher, S., et al. (2015). A miR-208-Mef2 axis drives the decompensation of right ventricular function in pulmonary hypertension. *Circ. Res.* 116 (1), 56–69. doi:10.1161/circresaha.115.303910

Pawlowski, C. L., Li, W., Sun, M., Ravichandran, K., Hickman, D., Kos, C., et al. (2017). Platelet microparticle-inspired clot-responsive nanomedicine for targeted fibrinolysis. *Biomaterials* 128, 94–108. doi:10.1016/j.biomaterials.2017.03.012

Potus, F., Ruffenach, G., Dahou, A., Thebault, C., Breuils-Bonnet, S., Tremblay, È., et al. (2015). Downregulation of MicroRNA-126 contributes to the failing right ventricle in pulmonary arterial hypertension. *Circulation* 132 (10), 932–943. doi:10.1161/circulationaha.115.016382

Price, L. C., Montani, D., Tcherakian, C., Dorfmüller, P., Souza, R., Gambaryan, N., et al. (2011). Dexamethasone reverses monocrotaline-induced pulmonary arterial hypertension in rats. *Eur. Respir. J.* 37 (4), 813–822. doi:10.1183/09031936.00028310

Rao, H., Che, X., Pan, X., Huang, G., Chen, X., and Wu, J. (2021). A comparative study on physicochemical properties of two kinds of targeting thrombus urokinase-loaded microbubbles. *Chongqing Med.* 50 (05), 845–849. doi:10.3969/j.issn.1671-8348.2021.05.001

Rao, H. (2020). Nanning, China: Guangxi Medical University. Master's Thesis. doi:10.27038/d.cnki.ggxyu.2020.000454Experimental study on the preparation and physicochemical properties of urokinase-loaded cyclic RGD-modified liposomes

Rawal, H., Suman, A., Bhoite, R. R., Kanwal, A., Young, R. K., Aronow, W. S., et al. (2021). Anticoagulation in pulmonary arterial hypertension: Do we know the answer? *Curr. Probl. Cardiol.* 46 (3), 100738. doi:10.1016/j.cpcardiol.2020.100738

Rima, M., Alavi Naini, S. M., Karam, M., Sadek, R., Sabatier, J. M., and Fajloun, Z. (2018). Vipers of the Middle East: A Rich source of bioactive molecules. *Molecules* 23 (10), 2721. doi:10.3390/molecules23102721

Rudski, L. G., Lai, W. W., Afilalo, J., Hua, L., Handschumacher, M. D., Chandrasekaran, K., et al. (2010). Guidelines for the echocardiographic assessment of the right heart in adults: A report from the American society of echocardiography. *J. Am. Soc. Echocardiogr.* 23 (7), 685–713. quiz 786-688. doi:10.1016/j.echo.2010.05.010

Sercombe, L., Veerati, T., Moheimani, F., Wu, S. Y., Sood, A. K., and Hua, S. (2015). Advances and challenges of liposome assisted drug delivery. *Front. Pharmacol.* 6, 286. doi:10.3389/fphar.2015.00286

Sommer, N., Ghofrani, H. A., Pak, O., Bonnet, S., Provencher, S., Sitbon, O., et al. (2021). Current and future treatments of pulmonary arterial hypertension. *Br. J. Pharmacol.* 178 (1), 6–30. doi:10.1111/bph.15016

Suntravat, M., Jia, Y., Lucena, S. E., Sánchez, E. E., and Pérez, J. C. (2013). cDNA cloning of a snake venom metalloproteinase from the eastern diamondback rattlesnake (*Crotalus adamanteus*), and the expression of its disintegrin domain with anti-platelet effects. *Toxicon* 64, 43–54. doi:10.1016/j.toxicon.2012.12.025

Vaidya, B., Agrawal, G. P., and Vyas, S. P. (2012). Functionalized carriers for the improved delivery of plasminogen activators. *Int. J. Pharm. X.* 424 (1-2), 1–11. doi:10.1016/j.ijpharm.2011.12.032

Vang, A., da Silva Gonçalves Bos, D., Fernandez-Nicolas, A., Zhang, P., Morrison, A. R., Mancini, T. J., et al. (2021). α7 Nicotinic acetylcholine receptor mediates right ventricular fibrosis and diastolic dysfunction in pulmonary hypertension. *JCI Insight* 6 (12), 142945. doi:10.1172/jci.insight.142945

Velayati, A., Valerio, M. G., Shen, M., Tariq, S., Lanier, G. M., and Aronow, W. S. (2016). Update on pulmonary arterial hypertension pharmacotherapy. *Postgrad. Med.* 128 (5), 460–473. doi:10.1080/00325481.2016.1188664

Vonk-Noordegraaf, A., Haddad, F., Chin, K. M., Forfia, P. R., Kawut, S. M., Lumens, J., et al. (2013). Right heart adaptation to pulmonary arterial hypertension: Physiology and pathobiology. *J. Am. Coll. Cardiol.* 62 (25), D22–D33. doi:10.1016/j.jacc.2013.10.027

White, R. J., Meoli, D. F., Swarthout, R. F., Kallop, D. Y., GalariaII, Harvey, J. L., et al. (2007). Plexiform-like lesions and increased tissue factor expression in a rat model of severe pulmonary arterial hypertension. *Am. J. Physiology-Lung Cell. Mol. Physiology* 293 (3), L583–L590. doi:10.1152/ajplung.00321.2006

Wu, J., Luo, X., Huang, Y., He, Y., and Li, Z. (2015). Hemodynamics and right-ventricle functional characteristics of a swine carotid artery-jugular vein shunt model of pulmonary arterial hypertension: An 18-month experimental study. *Exp. Biol. Med. (Maywood).* 240 (10), 1362–1372. doi:10.1177/1535370214566561

Wu, Y., Adi, D., Long, M., Wang, J., Liu, F., Gai, M. T., et al. (2016). 4-Phenylbutyric acid induces protection against pulmonary arterial hypertension in rats. *PLoS One* 11 (6), e0157538. doi:10.1371/journal.pone.0157538

Yang, P. S., Kim, D. H., Lee, Y. J., Lee, S. E., Kang, W. J., Chang, H. J., et al. (2014). Glycyrrhizin, inhibitor of high mobility group box-1, attenuates monocrotaline-induced pulmonary hypertension and vascular remodeling in rats. *Respir. Res.* 15, 148. doi:10.1186/s12931-014-0148-4

Zhang, N., Li, C., Zhou, D., Ding, C., Jin, Y., Tian, Q., et al. (2018). Cyclic RGD functionalized liposomes encapsulating urokinase for thrombolysis. *Acta Biomater.* 70, 227–236. doi:10.1016/j.actbio.2018.01.038

Zhou, X., Wang, Z., Xu, B., Ji, N., Meng, P., Gu, L., et al. (2021). Long non-coding RNA NORAD protects against cerebral ischemia/reperfusion injury induced brain damage, cell apoptosis, oxidative stress and inflammation by regulating miR-30a-5p/YWHAG. *Bioengineered* 12 (2), 9174–9188. doi:10.1080/21655979.2021.1995115

Zoetis, T., and Hurtt, M. E. (2003). Species comparison of lung development. *Birth Defect. Res. B* 68 (2), 121–124. doi:10.1002/bdrb.10014

frontiers | Frontiers in Bioengineering and Biotechnology

TYPE Review
PUBLISHED 14 November 2022
DOI 10.3389/fbioe.2022.1058251

OPEN ACCESS

EDITED BY
Mingqiang Li,
Third Affiliated Hospital of Sun Yat-sen University, China

REVIEWED BY
Yilong Cheng,
Xi'an Jiaotong University, China
Tairong Kuang,
Zhejiang University of Technology, China
Chao Zhao,
University of Alabama, United States

*CORRESPONDENCE
Changfeng Fu,
fucf@jlu.edu.cn

SPECIALTY SECTION
This article was submitted to Biomaterials, a section of the journal Frontiers in Bioengineering and Biotechnology

RECEIVED 30 September 2022
ACCEPTED 01 November 2022
PUBLISHED 14 November 2022

CITATION
Liu Z and Fu C (2022), Application of single and cooperative different delivery systems for the treatment of intervertebral disc degeneration. *Front. Bioeng. Biotechnol.* 10:1058251. doi: 10.3389/fbioe.2022.1058251

Application of single and cooperative different delivery systems for the treatment of intervertebral disc degeneration

Zongtai Liu[1] and Changfeng Fu[2]*

[1]Department of Orthopedics, Affiliated Hospital of Beihua University, Jilin, China, [2]Department of Spine Surgery, First Hospital of Jilin University, Changchun, China

Intervertebral disc (IVD) degeneration (IDD) is the most universal pathogenesis of low back pain (LBP), a prevalent and costly medical problem across the world. Persistent low back pain can seriously affect a patient's quality of life and even lead to disability. Furthermore, the corresponding medical expenses create a serious economic burden to both individuals and society. Intervertebral disc degeneration is commonly thought to be related to age, injury, obesity, genetic susceptibility, and other risk factors. Nonetheless, its specific pathological process has not been completely elucidated; the current mainstream view considers that this condition arises from the interaction of multiple mechanisms. With the development of medical concepts and technology, clinicians and scientists tend to intervene in the early or middle stages of intervertebral disc degeneration to avoid further aggravation. However, with the aid of modern delivery systems, it is now possible to intervene in the process of intervertebral disc at the cellular and molecular levels. This review aims to provide an overview of the main mechanisms associated with intervertebral disc degeneration and the delivery systems that can help us to improve the efficacy of intervertebral disc degeneration treatment.

KEYWORDS

delivery system, intervertebral disc degeneration, biomaterial, nanometer materials, low back pain

Introduction

Low back pain (LBP) is a widespread health problem characterized by a long duration and high disability rate that is a cause of widespread concern (Katz, 2006). LBP seriously affects the quality of life and is one of the top three causes of disability in developed countries (Murray et al., 2012; Hartvigsen et al., 2018). According to past statistics, it is estimated that LBP affects almost 700 million people worldwide, although this number is increasing (GBD 2017 Disease and Injury Incidence and Prevalence Collaborators, 2017; Jin et al., 2020). LBP also imposes a significant burden on society and the economy. LBP is responsible for more than 30% of work absences and its directly related costs are as high as $90 billion annually in the United States alone (Dieleman et al., 2016; Hartvigsen et al., 2018).

The etiology of LBP is complex and has yet to be fully elucidated. The current consensus is that LBP is caused by multiple factors, including biological, psychological and social factors (Vlaeyen et al., 2018). Despite many cognitive limitations, Intervertebral disc (IVD) degeneration (IDD) is definitely an important cause of LBP (Cheung et al., 2009; Mohd Isa et al., 2022). Interestingly, not all patients with IDD develop LBP. A previous study estimated that between 26% and 42% of IDD patients experience significant LBP (Peng, 2013; Mohd Isa et al., 2022). There are two main possible reasons for such pain, one is the sagittal imbalance of the spine due to disc height reduction which may lead to soreness from exertion of the surrounding muscles; the other reason is the inflammation caused by damage to the disc and its adjacent tissues.

The three-joint structure between adjacent vertebral bodies plays an important role in motion, weight-bearing, maintaining flexibility and protecting vulnerable tissues. IVDs are a crucial fibrocartilage component of this structure and regulate the amounts of bound water to ensure that the intrinsic intradiscal pressure is within the appropriate range (Urban and McMullin, 1988; Vergroesen et al., 2014). The intradiscal pressure is approximately 0.1 MPa–2.3 MPa according to its loading (Sato et al., 1999; Wilke et al., 1999). The ability to retain water under stress decreases in degenerating IVDs; this is reflected by the reduction of disc high and intradiscal pressure (Iatridis et al., 2013; Lee et al., 2013; Vergroesen et al., 2014). At the same time, the reduced intradiscal pressure increases the shear stress concentrations in IVDs, thus leading to subsequent complications such as herniation (Adams et al., 1996; Andersson et al., 2006). The main anatomical structure of an IVD consists of three parts, the nucleus pulposus (NP), the annulus fibrosus (AF) and the cartilaginous endplates (CEP). The healthy NP is a highly hydrated tissue that is rich in proteoglycans and generates an intradiscal pressure and evenly distributes pressure on the adjacent endplates (Iatridis et al., 2013; Vergroesen et al., 2014). The AF is composed of collagen fibers, which together with lamellae and proteoglycans, form a multilayered concentric structure (Nerurkar et al., 2010). The AF is tensioned by intradiscal pressure and also plays a role in protecting and constraining the NP inside it (Iatridis et al., 2013). It is worth noting that the majority of the AF is avascular and nerve-free, thus making its renewal and healing highly dependent on sparsely distributed cell populations. At the same time, fragile blood supply and nutritional support mean that once damaged, the AF experiences difficulty in repairing itself (Holm et al., 1981). In a healthy state, the endplate is composed of homogeneous hyaline cartilage of uniform thickness (Rutges et al., 2013). Almost all nutrients are transported to the IVD via the CEPs (Malandrino et al., 2014; Bowles and Setton, 2017). Cartilage damage is an important characteristic of IDD, and is a similar condition to osteoarthritis (Wang et al., 2012; Zhu et al., 2022b; Francisco et al., 2022). Mineralized endplates may hinder nutrient transport to the IVD, and insufficient nutrient supply has been considered as one of the causes of IDD (Roberts et al., 1996; Benneker et al., 2014; Huang et al., 2014; Malandrino et al., 2014). Collectively, the IVD components can affect each other and any single site of injury or degeneration can lead to overall IDD.

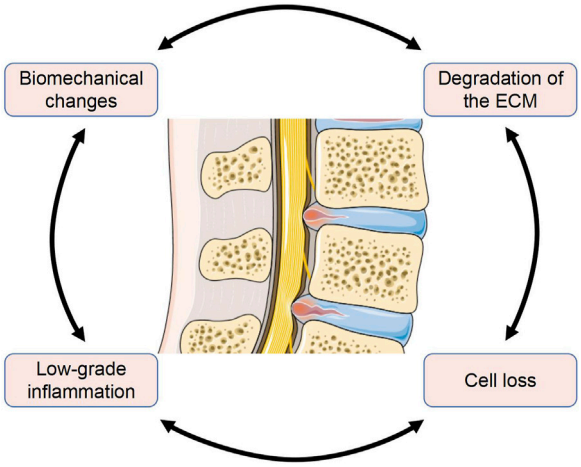

FIGURE 1
Several major pathological mechanisms in IDD are interconnected (The Figure was partly generated using Servier Medical Art, provided by Servier, licensed under a Creative Commons Attribution 3.0 unported license).

In clinical work, magnetic resonance imaging (MRI) of the spine is the most commonly used method to detect IDD. There are some IDD classification methods based on T2-weighted MRI. Pfirrmann divided IDD into five grades (grade I to grade V) according to structural heterogeneity, the degree of differentiation between the NP and AF, disc height and signal density (Pfirrmann et al., 2001). In 2007, Griffith made an adjustment based on the previous classification by classifying IDD into eight grades (grade I to VIII). Unfortunately, T2-weighted MRI has irreparable limitations in detecting the early stage of IDD. Bruno et al. (Zobel et al., 2012) used T1ρ to identify early IDD and found that this system achieved good discrimination performance. In addition, more advanced equipment, along with the development of artificial intelligence (AI) technology, provide new directions for the detection of IDD (Sher et al., 2019; Gao et al., 2021). At present, there are three main approaches to treating LBP caused by IDD, including pharmacological therapies, physical and psychological therapies, and surgical interventions (Foster et al., 2018). Nevertheless, all of these approaches are remedial for patients with IDD who already have obvious symptoms. Blocking disease progression at an early stage can further reduce symptoms and complications and improve quality of life. Benefiting from the rapid development of modern biotechnology, an increasing number of biomarkers have been

detected, thus making it possible for us to intervene in the development of IDD. However, an inevitable problem is how to deliver the required substances to the appropriate location to achieve effective intervention. Therefore, in the present study, we review the mainstream understanding of IDD-related pathological mechanisms and summarize the delivery systems that could effectively intervene in these mechanisms. Furthermore, we analyzed the classification, application and clinical application prospects of these systems.

The pathophysiology of intervertebral disc degeneration

The pathophysiology of IDD is intricate and has yet to be explained fully. Several pathological changes of IVD are thought to be related to IDD. These pathological mechanisms involve almost all levels of the IVD, from the microscopic level such as gene and cytokine expression to the macroscopic level such as structural loading and composition changes. These changes are interconnected and create a vicious cycle (Figure 1). Enhancing our understanding of the pathological processes involved will provide new opportunities and challenges for the treatment of IDD.

Biomechanical changes in local structures

The instability of the mechanical structure of the IVD is an important cause of complications such as annulus rupture, herniation and nerve extrusion (Adams and Roughley, 2006; Vergroesen et al., 2014; Desmoulin et al., 2020). In recent years, biomechanical changes have been progressively considered as one of the pathological processes of IDD; this is closely related to metabolism, cell renewal and the inflammatory response of IVD tissues (Chan et al., 2011; Neidlinger-Wilke et al., 2012; Desmoulin et al., 2020). Because the IVD is avascular, diffusion is the main transport mechanism used to move nutrients and oxygen (Desmoulin et al., 2020). In addition, due to low oxygen content, IVD cells perform anaerobic respiration which consumes more glucose and produces more metabolic toxicity than aerobic respiration (Bartels et al., 1998). Previous studies have confirmed that excessive loading not only obstructs the diffusion of nutrients and oxygen but also leads to lactic acid accumulation in the NP and AF regions, accompanied by local PH reduction (Huang and Gu, 2008; Wang et al., 2013). Two *in vitro* experiments using human tissues revealed that the diffusion of glucose by AF and CEP diminished with increasing loading (Jackson et al., 2012; Wu et al., 2016). This may be related to the narrowing of the microscopic pore size due to compression. Unfortunately, these results have not yet been verified with *in vivo* data due to a lack of *in vivo* measurement techniques (Desmoulin et al., 2020; Shalash et al., 2021; McDonnell and Buckley, 2022).

Biomechanics also affect cells and their extracellular matrix (ECM). Biomechanical changes affect cellular homeostasis by regulating the expression of several substances, such as matrix metalloproteinases (MMP), cytokines and growth factors (Phillips et al., 2013a; Vo et al., 2013; Neidlinger-Wilke et al., 2014). These substances are bound up with the degradation of the ECM, activation of the inflammatory response and cell loss. Previous studies have shown that tensile strain can cause IVD cells to reduce the expression of proteoglycan and collagen II; these are important for maintaining normal disc performance (Court et al., 2001; Hutton et al., 2002). Svenja et al. (Illien-Jünger et al., 2010) reported that high-frequency loading resulted in cell death and an increase in MMP-13 expression. An *in vivo* study in a mouse model indicated that excessive load exposure resulted in a reduction in tissue inhibitor of matrix metalloproteinase-3 (TIMP-3) and an increase in a disintegrin and a metalloproteinase with thrombospondin motifs-4 (ADAMTS-4); this could relate to an early stage of IDD (Wuertz et al., 2009). It is important to note that a moderate dynamic compressive load is beneficial for IVDs (Walsh and Lotz, 2004; Wang et al., 2007; Paul et al., 2012). In addition, a distinct compressive force on the IVD can cause inflammatory responses; this has been verified in both *in vivo* and *in vitro* models (Wang et al., 2007; Paul et al., 2013; Gawri et al., 2014). Structural deficits in IVDs, such as herniation, can cause immune cell activation and infiltration; these cells include macrophages, neutrophils and T cells (Kokubo et al., 2008; Risbud and Shapiro, 2014). Meanwhile, the loss of intradiscal pressure significantly elevates the release of inflammatory cytokines such as interleukin (IL)-1 and-6 (Dudli et al., 2014). Interestingly, the migration of immune cells into the disc is accompanied by the appearance of nerve fibers arising from the dorsal root ganglion (DRG) (Martínez-Lavín, 2021). These changes are thought to contribute to the sensation of pain. Of note, almost all astronauts experience LBP when the gravity environment changes dramatically, again demonstrating the importance of biomechanics in IVD (Bailey et al., 2018; Lazzari et al., 2021).

Degradation of the extracellular matrix

Degradation, rebuilding and composition changes are crucial characteristics of IDD pathology. In fact, it is quite common to induce IDD animal models by damaging the ECM, thus demonstrating the importance of the ECM in maintaining IVD stability. The normal ECM consists of two main substances. One is proteoglycans; aggrecan is the most abundant proteoglycan in the NP (Roughley et al., 2006). The polyanionic proteoglycans provide the normal physiological osmotic pressure within the NP, which is crucial in maintaining tissue hydration and buffering compressive forces during daily activities. The water content of the IVD increases from the outer layer of AF to the NP located in the center, as does

the concentration of proteoglycans (Feng et al., 2006). In IDD, aggrecan is cleaved from the hyaluronic acid backbone; this reduces its ability to bind water (Yurube et al., 2012; Iatridis et al., 2011). Another main substance in ECM is collagen. Type I and II collagen are the most abundant collagens in the disc (approximately 80%). The collagen framework of the disc is crucial for preserving normal architecture and function (Roughley et al., 2006). AF cells possess mostly type I while NP cells possess mostly type II collagen. From an anatomical structure viewpoint, from the inside to the outside of the IVD, the content of type II collagen gradually decreases and the content of type I collagen increases (Scott et al., 1994). Previous studies have observed the gradual transformation of notochordal cells into chondrocyte-like cells with increasing age; this reduces the expression of type II collagen and proteoglycans (Scott et al., 1994; Antoniou et al., 1996; Boos et al., 2002; Zhao et al., 2007). Type II collagen has better mechanical compliance than type I; thus, a reduction in type II collagen results in an uneven distribution of stress across the IVD. In addition, the loss of water-binding potential is reflected in the reduction of IVD height (Iatridis et al., 2013; Vergroesen et al., 2014). Collectively, these changes further deteriorate the mechanical environment of the IVD.

Like other substances in the body, normal ECM is in a delicate balance between anabolism and catabolism. Disruption of this balance will undoubtedly lead to the impairment of function. NP cells perform a central role in regulating the anabolism and catabolism of the ECM by regulating the MMP and ADAMTS families of enzymes (Weiler et al., 2002; Vo et al., 2013). Both the excessive activation of MMP and ADAMTS are mainly reflected in the catabolism of ECM. A previous study included 41 specimens of patients who had undergone operations for lumbar disc herniation and analyzed the relationship between the degree of degeneration and the expression of MMP-1 (Xu et al., 2014a). As the degree of degeneration increased, the expression of MMP-1 increased notably. Tang et al. (Tang et al., 2014) used microarray analysis to show that MMP-2 was overexpressed in IDD tissue. The increased expression of MMP-3 was also reported in different animal models (Sobajima et al., 2005; Wei et al., 2014). Furthermore, the upregulation of MMP-7, -8, -10, -12, -13 and-14 were also reported in previous studies (Bachmeier et al., 2009; Richardson et al., 2009; Phillips et al., 2013b; Gruber et al., 2014b; Xu et al., 2014b; Iwata et al., 2015). Similar to MMP, the upregulation of several types of ADAMTS has been reported in degenerated discs (Pockert et al., 2009; Zhang et al., 2012). Of note, Patel et al. (Patel et al., 2007) reported that the amount of ADAMTS-5 in the NP and AF shows no significant difference in different degeneration grades. However, Chen et al. (Chen et al., 2014) reported the upregulation of ADAMTS-5 in the CEPs of IDD patients. Interestingly, ADAMTS-3 and ADAMTS-10 were found to be significantly downregulated in degenerated discs (Gruber et al., 2011). Thus, different tissues may tend to express ADAMTS differently. In addition, the upregulation of inflammatory cytokines, such as IL-1 and tumor necrosis factor (TNF)-α, is closely related to the regulation of MMP and ADAMTS. The upregulation of a variety of catabolic mediators by cytokines, including ADAMTS −4/5, MMP −1, −2, −3, −13 and −14 has been reported in many previous studies (Le Maitre et al., 2005; Séguin et al., 2005; Wang et al., 2011; Shi et al., 2019). The emergence of so many biomarkers makes it possible to better explain the pathological process of IDD and block its pathological progress at an early stage.

Chronic state of low-grade inflammation

The inflammatory response of IVD tissue and the corresponding release of proinflammatory cytokines are considered important hallmarks of IDD. A prominent feature is the IL-1β and TNF-α secreted by the disc cells (Kadow et al., 2015). These cytokines trigger a range of pathogenic responses, such as amplifying the inflammatory cascade, apoptosis, cellular senescence, pyroptosis and degradation of ECM. Kepler et al. (Kepler et al., 2013b) showed that exposing human NP and AF cells to IL-1β or TNF-α can upregulate the expression of substance P. The contents of other inflammatory factors such as IL-6 and IL-8 were further significantly increased by substance P. In addition, the expression of some other inflammatory molecules was also upregulated by exposure to IL-1β, such as nitric oxide (NO), cyclooxygenase (COX)-2 and prostaglandin E (PGE)-2 (Wang et al., 2019b; Jin et al., 2019). Similarly, the upregulation of IL-17, NO, and PGE-2 in NP and AF cells exposed to TNF-α have also been reported in previous studies (Gabr et al., 2011; Gruber et al., 2013). IL-1β and TNF-α can also regulate chemokine expression in IVD. In a previous study using IVD samples from LBP patients, the expression of C-C motif ligand (CCL)-5 and IL-1β was significantly enhanced in painful IVDs; furthermore, the correlated expression of CCL-5 with IL-1β expression was also indicated (Kepler et al., 2013a). In subsequent *in vitro* experiments, disc cells exposed to both IL-1β and TNF-α upregulated CCL-5 expression, and interestingly, TNF-α promoted higher levels of CCL-5 (Gruber et al., 2014a). Phillips et al. (Phillips et al., 2015) reported that the expression of CCL −2, −3, −4, −5, −6, −7 and C-X-C motif chemokine ligand (CXCL) −1, −8, −9 and −10 was increased by the stimulation of IL-1β. A bioinformatics study reported that the gene expression levels of CCL −3, −20, CXCL −2 and −5 were increased in disc cells under TNF-α stimulation. In addition, IL-1β and TNF-α are closely related to mechanical loading (Elfervig et al., 2001; Wang et al., 2007).

IL-1β and TNF-α also play crucial roles in the regulation of the cell cycle. Yang et al. (Yang et al., 2019) reported that IL-1β stimulated the expression of senescence associated-β-galactosidase (SA-β-Gal), which is considered as a dependable

marker of cell senescence. Chen et al. (Chen et al., 2020b) subsequently indicated that IL-1β promoted the progression of IDD, with significantly increased expression of type I collagen, p16, p53 and SA-β-Gal, as well as the reduced expression of type II collagen and aggrecan. Similarly, a previous study from Xie et al. (Xie et al., 2018) indicated that TNF-α could also promote NP cell senescence, reflected by the elevation of SA-β-Gal, p16 and p53 expression. Although apoptosis is important for maintaining cell renewal, once out of balance, excessive apoptosis can lead to the depletion of IVD cells and result in IDD. Jiang et al. (Jiang et al., 2019) demonstrated that IL-1β significantly increased caspase-3 activity, NP cell apoptosis ratio and the expression of Bax, caspase-3, cleaved caspase-3 and cleaved PARP. Similarly, Yu et al. (Yu et al., 2018) reported that TNF-α stimulation markedly improved cell apoptosis ratio, caspase-3 activity, expression of Bcl-2, Bax, and caspase-3, reactive oxygen species (ROS) content, and the activity of the NF-κB pathway.

Pyroptosis is a newfound type of cell death mediated by inflammation. The pyroptosis of cells is often accompanied by an increased number of the NLRP3 inflammasome (He et al., 2015; He et al., 2016). Zhao et al. (Zhao et al., 2021b) reported that an increase in pyroptosis was accompanied by an increase in IL-1β and NLRP3 inflammasome activation. In addition, the disc becomes vascularized and innervated; this has been recognized as an important pathological change of IDD (Karamouzian et al., 2010; Miyagi et al., 2014). The overexpression of vascular endothelial growth factor (VGEF) and neurotrophic factors, such as nerve growth factor (NGF) and brain-derived neurotrophic factor (BDNF), result in vascularization and innervation of the IVD (Liu et al., 2013; Moon et al., 2014; Zhu et al., 2018). Lee et al. (Lee et al., 2011) indicated that IL-1β and TNF-α stimulated the gene expression of VGEF, NGF and BDNF in NP cells; furthermore, they also indicated a positive inter-relationship between IL-1β and VEGF/NGF/BDNF expression using the immunohistochemical method. A deeper understanding of the inflammatory mechanism in IDD will undoubtedly help us to block pathological processes in a timelier manner.

Cell loss

A sufficient number of cells is undoubtedly necessary to maintain material renewal and the functional maintenance of IVD. Degenerative discs show higher rates of senescence, apoptosis and pyroptosis, thus leading to fewer functioning cells. The most prominent feature of cellular senescence is the irreversible cessation of cell proliferation, which can be identified by the expression of a senescence-associated secretory phenotype (SASP) (McCarthy et al., 2013; Childs et al., 2015; Su et al., 2019). Although multiple molecular signaling pathways are involved in cellular senescence, these all converge on the p53/p21/retinoblastoma (RB) and p16/RB pathways (Chicas et al., 2010; Muñoz-Espín and Serrano, 2014). Because IVD is avascular, this limits the clearance of metabolic waste and immune mediation to cause abnormal accumulation (de Magalhães and Passos, 2018). Previous studies indicated that oxidative stress (OS) and epigenomic perturbations accelerated the cellular senescence of IDD (Campisi et al., 2019). The use of antioxidant drugs to reduce cellular senescence in IDD has been reported in previous studies (Larrañaga et al., 2018; Liu et al., 2018). In addition, genome-wide analysis of DNA methylation profiles revealed significant differences in DNA methylation profiles of NP cells at different stages of IDD. Ikuno et al. (Ikuno et al., 2019) reported 220 differently methylated loci. Unfortunately, differential methylation was found mainly in genes located upstream, which hindered their further clinical application (Ikuno et al., 2019). As key regulators of gene expression, miRNAs have also attracted attention in recent years. Notably, some of these, such as miRNA-338-3p and miRNA-24-3p, are reported to be upregulated in degenerative NP cells (Chen et al., 2020a; Jiang et al., 2021).

Apoptosis and pyroptosis are common modes of programmed cell death and play critical roles in immune regulation. An imperative characteristic of apoptosis is the release of cytochrome-c from mitochondria (Fraser and Evan, 1996). At present, it is commonly accepted that apoptosis mainly includes intrinsic and extrinsic pathways. The dysregulation of intracellular homeostasis by toxic agents or DNA damage triggers the intrinsic pathway; this is characterized by mitochondrial outer membrane permeabilization (MOMP). Under the joint action of MOMP and cytochrome-c, the activity of caspase-3 is upregulated; this is broadly considered the point of no return in apoptotic death (Liu et al., 1996). The activation of cell surface receptors, such as the TNF-related apoptosis-including ligand receptors R1 and R2 triggers the extrinsic pathway (Schneider et al., 1997). Upon activation by their ligands, the intrinsic pathway is finally activated through a complex signaling network (Bertheloot et al., 2021). In the simplified pathway of pyroptosis, caspase-1 is activated by inflammasomes; then, gasdermin-D (GSDMD) is cleaved to GSDMD C-terminal and GSDMD N-terminal. The GSDMD N-terminal can puncture the cell membrane, thus resulting in pyroptosis (Boucher et al., 2018; Wang et al., 2020b). Recent studies demonstrated that (*P. acnes*) is a microbial pathogenic factor of IDD (Berjano et al., 2019). He et al. (He et al., 2020) reported that the expression of NLRP3, caspase -1, caspase -5, and IL-1β were upregulated in NP cells co-cultured with *P. acnes*, thus suggesting the activation of pyroptosis. Tang et al. (Tang et al., 2021a) demonstrated that *P. acnes* activated the pyroptosis of NP cells via the ROS-NLRP3 pathway. The complex relationship between cell loss and other pathological factors makes our understanding of IDD even more challenging, but also provides more directions for subsequent interventions.

The application of different transmission systems

Our increasing understanding of IDD pathology has led to more therapeutic approaches. Current treatment covers almost all scales of disc tissue from macro to micro levels, such as gene therapy, cell replenishment and surgical treatment (Debono et al., 2018; Li et al., 2021; Roh et al., 2021). Limited by many factors such as ethics, biocompatibility and persistence, IDD therapy, which regulates the metabolism and repairment of cells and tissues, appears to be more popular. Many previous studies have focused on IDD-related drugs, regulatory molecules and gene targets (Chao-Yang et al., 2021; Kamali et al., 2021). Because most of these biologics are fragile and easily decomposed, it is very important to select suitable delivery systems. Nevertheless, comparatively few studies have focused on delivery systems. Here, we exemplify the design principles and application scenarios of delivery systems on different scales.

Virus vectors

The continuous discovery of IDD-related gene targets makes it possible to intervene in the pathological progress of IDD at the gene level (Cazzanelli and Wuertz-Kozak, 2020). In addition, due to its avascular structure, which makes drug delivery through the blood more difficult, the targeted therapy of IVD cells is a more promising treatment method. As a type of targeted therapy, gene therapy can delay or even reverse IDD by regulating the expression of IDD-related substances in cells (Roh et al., 2021). The method of delivering the proper gene to the target cells is the first issue to be considered. Because of the natural advantages of viruses in delivering genetic information to host cells, viral vectors have attracted extensive attention.

Retroviruses were the first to be considered. Wehling et al. (Wehling et al., 1997) successfully transfected a target gene by retroviruses into chondrocytes from bovine CEP *in vitro*. Unfortunately, the effect of retroviruses on cells with a low-dividing rate is restricted, thus limiting the use of retroviruses in IDD (Bartels et al., 1998; Desmoulin et al., 2020). Subsequently, researchers turned to adenoviruses because of their higher transduction efficiency, notably in quiescent or slow-dividing cells (Moon et al., 2000). Many previous studies have demonstrated that adenovirus delivery systems play a significant role in regulating inflammation and improving ECM metabolism (Liang et al., 2010; Luo et al., 2016; Zheng et al., 2018). However, the potential infectivity and immunogenicity of adenoviral vectors cannot be ignored. In 1999, the first case of lethal systemic inflammation after the intra-arterial injection of an adenovirus vector was reported. This has forced researchers to stop the rapid development of adenoviral vectors and reassess their safety. In a safety assessment of gene transfer for the treatment of IVD, Wallach et al. (Wallach et al., 2006) indicated that improperly dosed or direct gene delivery to disc tissue may result in adverse complications. Driesse et al. (Driesse et al., 2000) reported that recombinant adenovirus may cause infection of the central nervous system. In fact, there has been a significant decline in the number of articles investigating adenoviral vectors over recent years; these have been replaced by adeno-associated viruses (AAVs). Compared with adenoviruses, AAVs have lower immunogenicity and safety has been confirmed (Levicoff et al., 2008; Mern et al., 2017). In 2015, Mern et al. (Mern and Thomé, 2015) identified NP cell-specific AAV serotypes by transfecting human NP cells with diverse AAV serotypes. This study makes AAVs more promising in the treatment of IDD. Kim et al. (Kim et al., 2022) reported that AAV6 could provide superb transduction efficiency with limited cytotoxicity *in vivo* (Figure 2). Although some AAV-based therapeutics gained regulatory approval in Europe or the United States, their use in IDD has been limited by their high price and difficulties in guaranteeing homogeneity between different batches (Wang et al., 2019a). Lentiviruses have become popular vectors in recent years, mainly due to their ability to transduce non-dividing cells. Wu et al. (Wu et al., 2014) reported that lentiviral vector-mediated gene expression lasted nearly twice as long as AAV in human NP cells. The regulation of IDD-related factors such as inflammation, ECM and apoptosis by lentiviral vectors has been reported (Farhang et al., 2019; Lin et al., 2021; Lu et al., 2021; Lu and Lin, 2021).

Although virus vectors have great potential, the high development cost, the need for rigorous toxicology tests, safety verification, the lack of standardization, and inherent batch-to-batch differences are all difficulties that need to be overcome.

Physical methods

Rather than using a virus as a transit point, physically delivering the target material into a cell seems to be a more straightforward solution. The main options at present are ultrasound exposure and electroporation. In 2006, Nishida et al. (Nishida et al., 2006) established a novel gene therapy technique for IVD cells using ultrasound. The target gene was wrapped in microbubbles, and these microbubbles were injected into IVDs. Immediately after injection, ultrasound was irradiated on the surface of the injected discs, thus resulting in the breaking of the microbubbles and transient holes in the cell surface (Nishida et al., 2006). Electroporation is a method that uses short electrical pulses to disturb cell membranes and momentarily creates holes in the membranes that allow genetic material to pass through. Once the optimal conditions for electroporation are determined, it is possible to transfer many

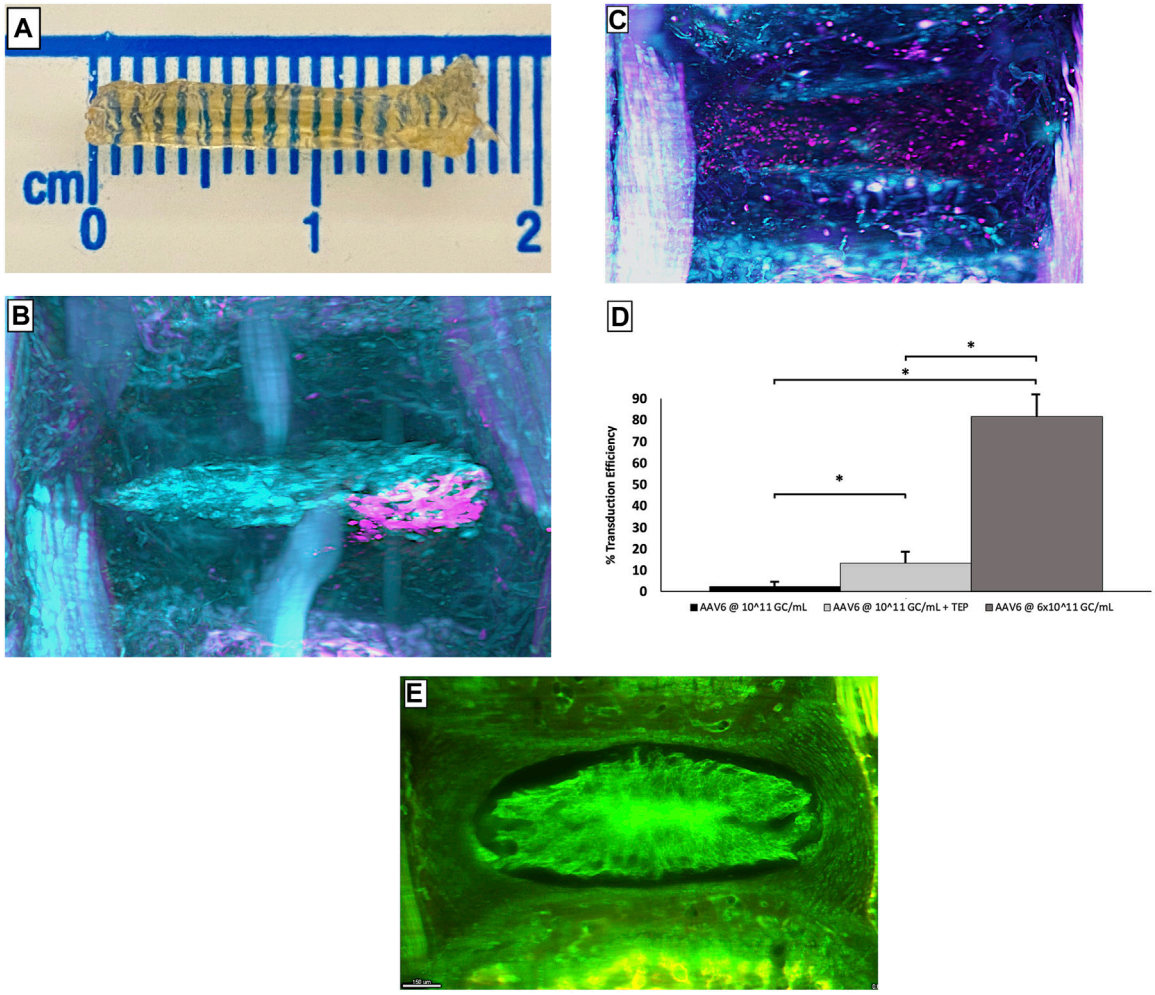

FIGURE 2
Complete mice caudal spines obtained using the PEGASOS method **(A)**. The images of the caudal tissues transferred by AAV6 alone **(B)** and AAV6+cell-permeable peptide **(C)** are viewed using 3D lightsheet microscopy, pink represents cells that transduced successfully, and cyan represents cells that transduced failed. Statistical analysis of the number of NP cells successfully transduced under each condition **(D)**. The representative image of IVD tissue without punctured **(E)**. Error bars show SEM. '*' means $p < 0.05$, indicating a statistical difference. Reprinted permission by CC BY license (Kim et al., 2022). https://creativecommons.org/licenses/by-nc-nd/4.0/.

cells in a short period. May et al. (May et al., 2017) indicated that two pulses of 1400 V for 20 ms resulted in favorable and reproducible results for both human and bovine IVD cells. Tang et al. (Tang et al., 2021c) used the electroporation method to deliver forkhead-box F1 mRNA to degenerated NP cells in human disc tissue and significantly reduced the secretion of IL-1β and MMP-13 (Figure 3). In addition, laser-mediated transfection and magnetofection are also used in other diseases (Antkowiak et al., 2013; Sizikov et al., 2021). Despite physical methods that can deliver genetic materials directly into target cells, there are non-negligible drawbacks, such as lower transfection rates, potential cell damage, and difficulty in determining the appropriate stimulation intensity.

Hydrogel-based delivery systems

Hydrogel is a three-dimensional mesh polymer with a hydrophilic structure that is able to bound large amounts of water. A microenvironment with ideal water content is beneficial to maintain the metabolism of IVD tissue and promote regeneration. Besides water, hydrogels can also provide mechanical support for cell proliferation. Hydrogels are highly manipulable because their mechanical strength, degradability, gelation time/temperature and other characteristics can be modified. Due to these advantages, hydrogels have been widely used to intervene with the pathological development of IDD.

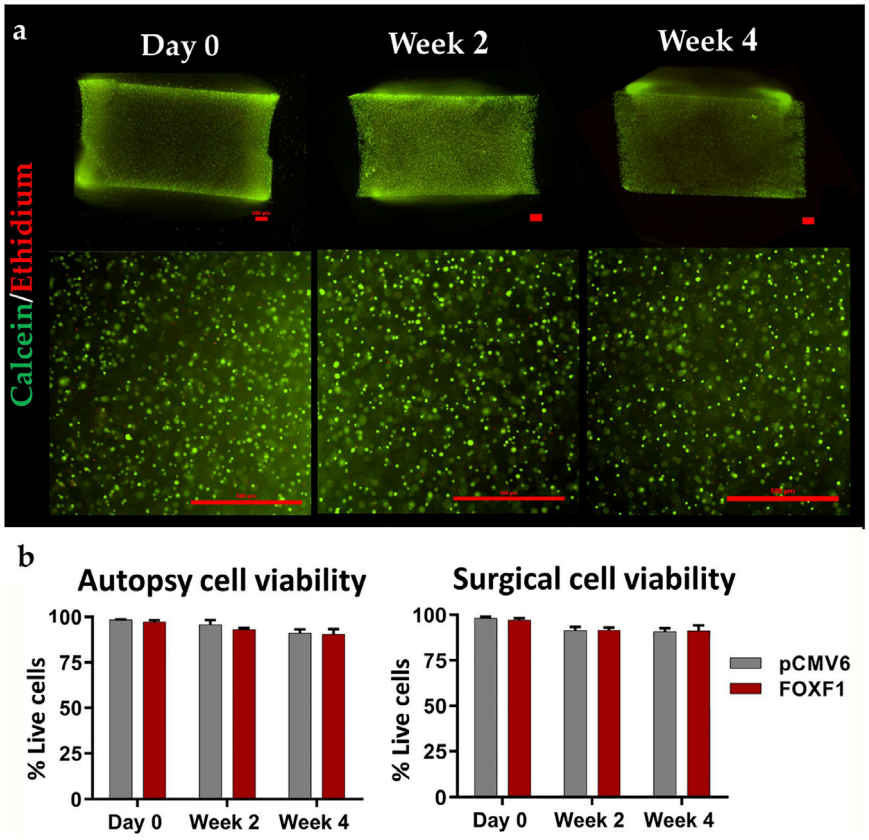

FIGURE 3
Representative 4 × (top) and 10 × (bottom) stained images (scale bar: 500 μm) of gel sagittal frozen sections containing human NP cells at day 0, week 2 and 4 weeks in culture **(A)**; green represents cells that survived after electroporation transduction, and red represents cells that died after electroporation. The live rate of cells transfected with FOXF1 and pCMV6 by electroporation in the autopsy group and surgery group were quantified **(B)**. Reprinted permission by CC BY license (Tang et al., 2021c). https://creativecommons.org/licenses/by-sa/4.0/.

There are various methods to arrange hydrogels into different subclasses. At the most fundamental level, natural hydrogels and synthetic hydrogels are classified according to their source composition. Natural hydrogels such as cellulose, alginate and hyaluronic acid always have favorable biocompatibility and low toxicity. However, most natural hydrogels can barely meet the mechanical stress requirements needed in human IVD tissue, thus severely limiting their application (Growney Kalaf et al., 2017; Alinejad et al., 2019). Compared with natural hydrogels, synthetic hydrogels generally have less variability and greater flexibility in mechanical properties, although their potential toxicity to cells cannot be ignored (Klein et al., 2009). As the name suggests, composite hydrogels are composed of at least two components and seem to overcome defects caused by a traditional single component. According to the cross-linking form, composite hydrogels can be classified into chemical and physical hydrogels. Chemical hydrogels are linked by covalent bonds, making the cross-linking irreversible, while physical hydrogels are connected by molecular entanglement and secondary forces and the transformations are reversible (Hoffman, 2002). Nevertheless, in the clinical transformation of hydrogels, it is difficult to implant gelatiniform hydrogels *in vivo* due to the deep target location and complex anatomy.

It is worth noting that traditional *in situ*-forming bulk hydrogels have relatively low efficiency in exchanging substances with tissues. In fact, exchanges with the target microenvironment are limited to the hydrogel/tissue interface. In recent years, stimulus-responsive composite hydrogels have been developed rapidly. Because stimulus-responsive composite hydrogels can solidify rapidly only after receiving the corresponding stimulus, they can be injected into the damaged area in a sol-gel state, thus making the hydrogels fit the tissue well. There are various types of stimuli, such as physical, chemical and biological (Koetting et al., 2015; Choi et al., 2019). Considering the changes in the pH microenvironment caused by inflammation

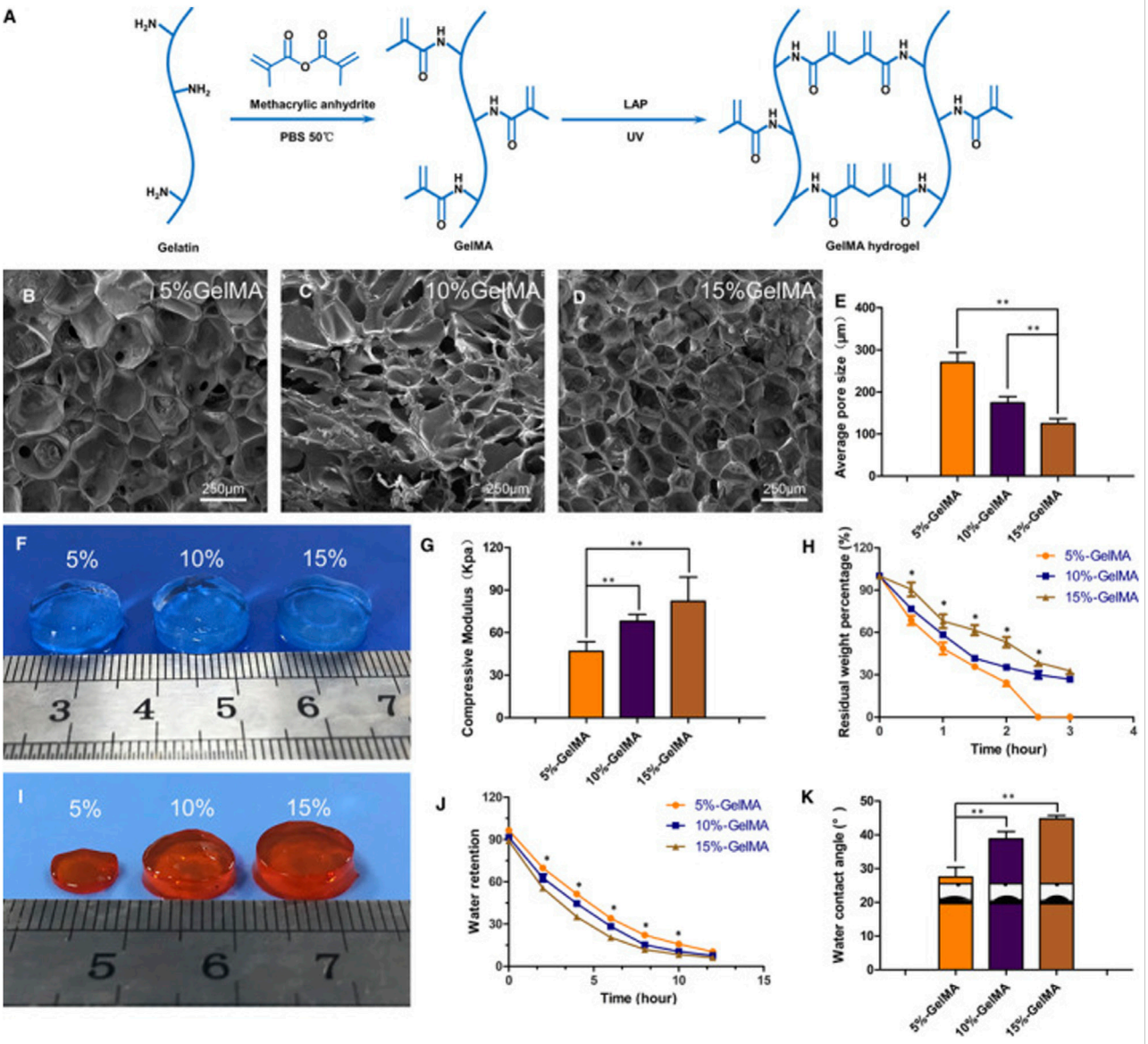

FIGURE 4
Schematic diagram of synthetic molecules of GelMA hydrogels **(A)**. Scanning electron microscopy was used to observe the microstructure of GelMA hydrogels with different concentrations **(B–D)**. Comparison of the pore size of hydrogels with different concentrations **(E)**. Comparison of the appearance of three different concentrations of hydrogels **(F)**. Comparison of mechanical properties of three different concentrations of hydrogels **(G)**. Degradation of hydrogels with different concentrations over time *in vitro* **(H)**. The appearance of hydrogel after 2 h *in vitro* degradation **(I)**. Comparison of water binding capacity of hydrogels with different concentrations **(J)**. Comparison of water content angle of hydrogels with different concentrations **(K)**. (*$p < 0.05$, **$p < 0.01$). Reproduced with permission from (Xu et al., 2021).

and dysregulation of cellular metabolism, pH-sensitive composite hydrogels seem to have ideal prospects. The ionizable pendant groups in the backbone of the hydrogel are responsible for its pH-sensitive behavior (Gupta et al., 2002). According to pendant group ionization, pH-sensitive composite hydrogels can be classified into anionic hydrogels and cationic hydrogels. The generation of an electrostatic repulsive force leads to the swelling and deswelling of the hydrogel; this is accompanied by the absorption and expulsion of water (Gupta et al., 2002). Nguyen et al. (Nguyen et al., 2019) reported the synthesis of a type of poly (ethylene glycol) (PEG)-based hydrogel with adjustable mechanical strength via ring-opening reactions; cytotoxicity tests showed that human NP cells remained a high survival rate after 8 days. In another previous study, Zhang et al. (Zhang et al., 2022b) adjusted the ratio between components to reach a balance of

histocompatibility and mechanical stability of poly (acrylic acid) (PAA) hydrogels. Collectively, the most common monomers that can be used to introduce pH-sensitive properties include methacrylic acid (MMA), acrylic acid (AA) and dimethylaminoethyl methacrylate (DMAEMA) (Koetting et al., 2015). In addition, some natural hydrogels can also exhibit pH-sensitive properties, such as albumin and alginate (Zheng and Du, 2021). Considering the constant temperature inside the body compared to outside, temperature-sensitive composite hydrogels have also attracted the attention of researchers. Temperature-sensitive composite hydrogels can be divided into two fundamental subtypes: positively and negatively responsive hydrogels. Common monomers with temperature sensitivity include cellulose derivatives, chitosan, PEG and poly (N-isopropyl acrylamide) (pNiPAAm) (Klouda and Mikos, 2008). Schmitt et al. (Schmitt et al., 2021) reported the long-term evaluation of an injectable chitosan carboxymethyl cellulose hydrogel in an ovine model. Compared with the untreated group, the intervertebral disc was stabilized, and the progression of degeneration was significantly slower in the treated group after 12 months. Furthermore, due to its low cytotoxicity and excellent biocompatibility, PEG has been widely used in medical applications such as promoting the healing of surgical incisions or drug delivery (Tan et al., 2019; Chen et al., 2022).

A significant advantage of photosensitive composite hydrogels is easy to access to light stimulation and the precise control of stimulation. Thus far, three types of photosensitive monomers have attracted a lot of attention, including gelatin methacrylate (GelMA), photopolymerized polyethylene glycol diacrylate (PEGDA) and hyaluronic acid methacrylate (HAMA) (Burdick and Prestwich, 2011; Clark et al., 2017; Kurian et al., 2022). Xu et al. (Xu et al., 2021) combined collagen hydrolysate and GelMA to make a photosensitive composite hydrogel that could encapsulate NP cells *in vitro* (Figure 4). Unfortunately, the debilitating effect of IVD tissue on light stimulation prevents the application of photosensitive composite hydrogels *in vivo*. Considering that there are some upregulated enzymes in IDD, such as MMP, some enzyme-sensitive composite hydrogels focusing on IDD-related enzymes have been developed in recent years, although more *in vivo* experiments are needed (Skaalure et al., 2015; Amer and Bryant, 2016; Schneider et al., 2020). Due to the special mechanical and metabolic environment of the degenerated disc, pressure-sensitive composite hydrogels and ion-sensitive composite hydrogels are expected to play a role in IDD treatment; however, few relevant studies have been reported.

There has been promising progress in stimulus-responsive composite hydrogels, although the advances in biological material and tissue engineering technologies have led researchers to focus on more microscopic structures. A better understanding of microstructure would allow us to better manipulate the properties of materials.

Microsphere-based delivery systems

Just as stimulus-responsive composite hydrogels solve the problem of tissue fitting when compared to *in situ* gels, injectable microsphere-based delivery systems can provide superior substance exchange efficiency. Microspheres are a class of three-dimensional spherical structures with a mean particle diameter of 1–1,000 μm (Gupta et al., 2017). According to the distribution of therapeutic substances in microspheres, microspheres can be divided into microcapsules and micromatrices. Microcapsules take the therapeutic substance as the core, while micromatrices are formed when the therapeutic substance is dispersed or embedded in the entire material matrix (Kulchar et al., 2021). Due to its good delivery capacity and biocompatibility, the microsphere system has significant application potential as a cell, drug and biological factor delivery system in IVD therapy. Common natural ingredients include collagen, chitosan, gelatin and alginate. Indeed, gelatin- and collagen-based microsphere systems are already commercially available (Chen et al., 2013).

Poly (lactic-co-glycolic acid) (PLGA) copolymer is one of the most widely used biomaterials at present due to its excellent biodegradation and biocompatibility (Zhao et al., 2021a; Zhu et al., 2022a). PLGA is synthesized by lactic acid (LA) and glycolic (GA) through random polymerization (Su et al., 2021). Hodgkinson et al. (Hodgkinson et al., 2019) reported that recombinant human growth difference factor (rhGDF-6) was loaded in PLGA-PEG-PLGA microspheres and induced the differentiation of adipose stem cells (ASCs) to NP cells and aggrecan production (Figure 5). Huang et al. (Huang et al., 2021) used PEG-PLGA-PGE as a drug carrier and showed that this microsphere system had ideal biocompatibility and low cytotoxicity. In a recent study, Lim et al. (Lim et al., 2022) encapsulated ABT263, a senolytic drug, in PLGA microspheres which were intradiscally administered into injury-induced IDD rat models. Analysis showed the selective clearance of senescent cells from degenerative IVD tissue, the downregulated expression of proinflammatory cytokines and the restoration of the IVD structure. However, considering the more complex anatomical structure and mechanical environment of the human spine, the application of PLGA microspheres in human IVD still needs to be demonstrated in further experiments.

Poly (ε-caprolactone) (PCL) is a polymer with very low glasses transition temperature and melting point. Due to its good biocompatibility, PCL has been widely used in medicine; for example, as surgical sutures (Wei et al., 2009). Jang et al. (Jang et al., 2020) embedded hyaluronic acid (HA) in PCL/HA hybrid microspheres, and the results indicated that the PCL/HA hybrid microspheres provided a proper environment for the proliferation and differentiation of human periosteum-derived cells *in vitro*. Zhou et al. (Zhou et al., 2020) presented a simple method that combined poly (vinyl alcohol) (PVA) hydrogels

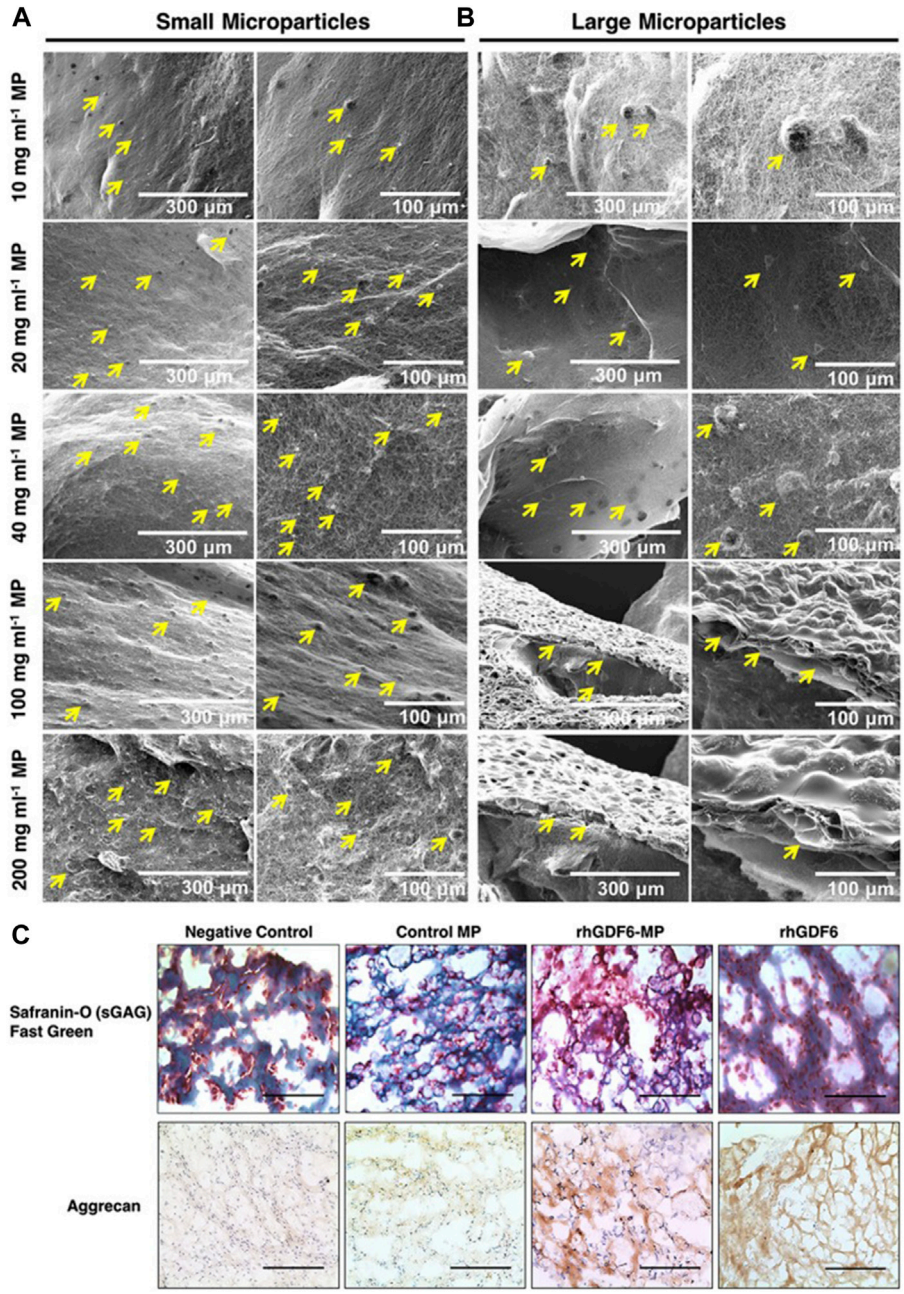

FIGURE 5
The binding ability of different concentrations of small **(A)** and large **(B)** microspheres to collagen gel under scanning electron microscopy. After 14 days of culture, the microspheres containing rhGDF-6 showed more ideal target substances expression in both histological and immunohistochemical staining **(C)**. Scale bars = 300 μm. Reproduced with permission from (Hodgkinson et al., 2019).

with PCL and reflected a new type of microsphere with a PVA core and PCL shell. Unfortunately, due to its slow decomposition *in vivo*, PCL is mainly used as a scaffold material to repair AF or osteonecrosis, and its use as a microsphere-based delivery system in IDD has been rarely reported (Shamsah et al., 2019; Zhang et al., 2022a).

Since its release properties can be modified by adjusting physical and chemical parameters, researchers can better regulate the release of therapeutic substances by microsphere hydrogels. Chang et al. (Chang et al., 2022b) reported a circRNA silencing-hydrogel microsphere by grafting silencing genes loaded on HAMA microspheres. The results indicated that HAMA

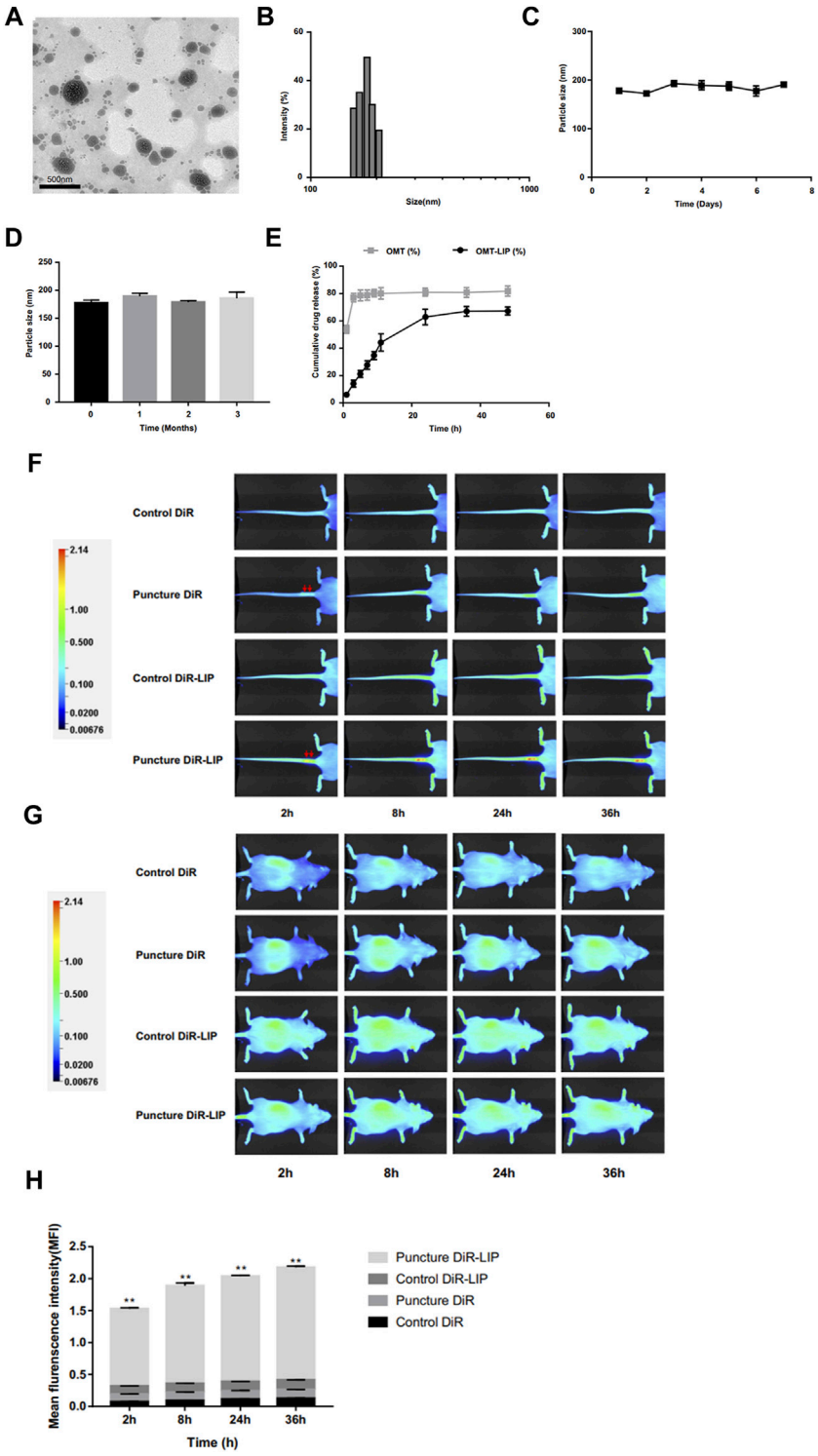

FIGURE 6
Image of oxymatrine liposome staining under the transmission electron microscope **(A)**. The particle size distribution of oxymatrine liposome **(B)**. The particle size changes of oxymatrine liposome during storage for 7°days **(C)** and 3°months **(D)** at 4°C. The curve of oxymatrine liposome releasing oxymatrine *in vitro* **(E)**. The NIFR images of the liposome delivery system biodistribution in tails **(F)** and whole bodies **(G)** at different timepoints (2, 8, 24, and 36 h). Red arrows indicate puncture sites. Statistical analysis of fluorescence intensity at the degenerative discs **(H)**. (**$p < 0.01$). Reproduced with permission from (207). https://creativecommons.org/licenses/by-nc/3.0/.

microspheres had ideal degradability and that silencing genes can be significantly released for 27 days. Platelet-rich plasma (PRP) is the product of whole blood centrifugation and can relieve IDD symptoms in humans (Tuakli-Wosornu et al., 2016). In another previous study, Miran et al. (Choi et al., 2020) reported that loading powdered PRP into PEG microspheres could significantly prolong the degradation and protein release time of microspheres. In short, the development of microsphere hydrogels brings us one step closer to the single injection of drugs that could provide long-term intervention for IDD processes.

As a common delivery system, the microsphere-based delivery system has a broad clinical application prospect for IDD. However, rigorous safety audits must be carried out and the performance degradation caused by the complex physical and chemical environment in the human body must be considered. In addition, the parameters that are more suitable for IVD tissue also require extensive preliminary experiments.

Nano-scale delivery systems

Besides microspheres, many nanomaterials are also used for drug delivery because they are more easily taken up by cells. Therapeutic substances can be immobilized on or encapsulated by such nanomaterials. Nanomaterials that can be degraded *in situ* are generally considered to have excellent biocompatibility and low immunogenicity (Mitchell et al., 2021). Common nanomaterials used for nanocarriers include lipids, polymers and inorganic compounds.

Lipid-based delivery systems have many inherent advantages, such as simple composition, good biocompatibility, low toxicity and self-assembly (Sercombe et al., 2015). Liposomes are the most well know lipid-based delivery systems. In addition, some artificial liposomes also show promising therapeutic prospects. Banala et al. (Banala et al., 2019) were able to reduce the expression of caspase-3 and ADAMTS-5 via liposomes loaded with siDNA. In 2020, Wang et al. (Wang et al., 2020a) used liposomes to deliver oxymatrine and found that the degeneration of IDD was slowed down both *in vitro* and *in vivo* (Figure 6). It is worth noting that liposomes are susceptible to the interference of complex environments *in vivo*, thus limiting their clinical application. Extracellular vesicles (EVs) can break through the limitations of mesenchymal stem cells (MSCs) in the treatment of IDD, of which exosomes have received widespread attention over recent years. Kang et al. (Lu et al., 2017) reported that exosomes act as a critical transport agent in information communication between MSCs and NP cells. Luo et al. (Luo et al., 2021) confirmed that CEP delayed the progression of IDD via exosomes. Similarly, Sun et al. (Sun et al., 2021b) reported that the endothelial cell migration and inflammation response could be controlled by AF cell-derived exosomes. EV-based therapies are also developing rapidly. Liao et al. (Liao et al., 2021) achieved a high uptake of EVs loaded with antioxidant proteins in TNF-α-treated NP cells by gene-editing parental MSCs; this resulted in reduced cell death and lower progression of IDD. In a subsequent study, Qian et al. (Qian et al., 2022) reported that the application of PRP-derived exosomes could alleviate IDD-associated inflammation. At present, the optimal dose and mode of administration of exosomes are not clear, and due to their cell origin, they may receive a more stringent ethical review.

Polymeric nanoparticles can be classified into three types: polymersomes, micelles and dendrimers. Similar to liposomes, polymersomes have membranes made by amphiphilic block copolymers. Polymersomes are generally more stable and less permeable than liposomes, but many factors can affect these properties, such as the diameter of the polymeric vesicle and the inherent properties of the material (Rideau et al., 2018). Polymersomes have been extensively studied in the fields of anti-inflammation and tumors and their application in IDD is worth considering. Polymeric micelles have a hydrophilic core and a hydrophobic coating and have been used in the clinical treatment of ovarian cancer (Lee et al., 2018). Zhang et al. (Chang et al., 2022a) used polymeric micelles loaded with mRNA to improve the synthesis of ECM. Dendrimers are branched polymers, and their size, mass, and shape can be tightly controlled (Mitchell et al., 2021). Dendrimers have been widely used in many clinical applications, such as contrast media and topical gels (Kannan et al., 2014; Palmerston Mendes et al., 2017). However, the further use of polymeric nanoparticles in human bodies requires strict safety reviews.

Inorganic materials such as carbon and silicon can also be used to establish nano-scale delivery systems. Carbon nanotubes are hollow graphitic structures made of a layer of graphene; therefore, they have a high surface area and excellent electrical conductivity (Negri et al., 2020). Carbon nanotubes have an excellent ability to penetrate cell membranes and bind therapeutic substances. Carbon nanotubes have significant potential in the diagnosis and treatment of cancer and neurodegeneration (John et al., 2015; Tang et al., 2021b). In addition, carbon nanotubes modified with hydrogels have better mechanical, physical and biological features (Vashist et al., 2018). All of these findings provide a reference for the application of carbon nanotubes in IDD. However, the clinical application of carbon nanotubes still is still associated with difficulties that need to be overcome, such as poor water solubility, low biodegradation and dispersion. There have been a number of studies focusing on the use of mesoporous silica nanoparticles in cancer-related drug systems (Li et al., 2019). Mesoporous silica nanoparticles exhibit many advantages such as a large surface area, a high pore volume, tunable pore size and excellent stability. Wang et al. (Wang et al., 2020c) reported the synthesis of mesoporous silica nanoparticles with a cell-targeting function. Although mesoporous silica

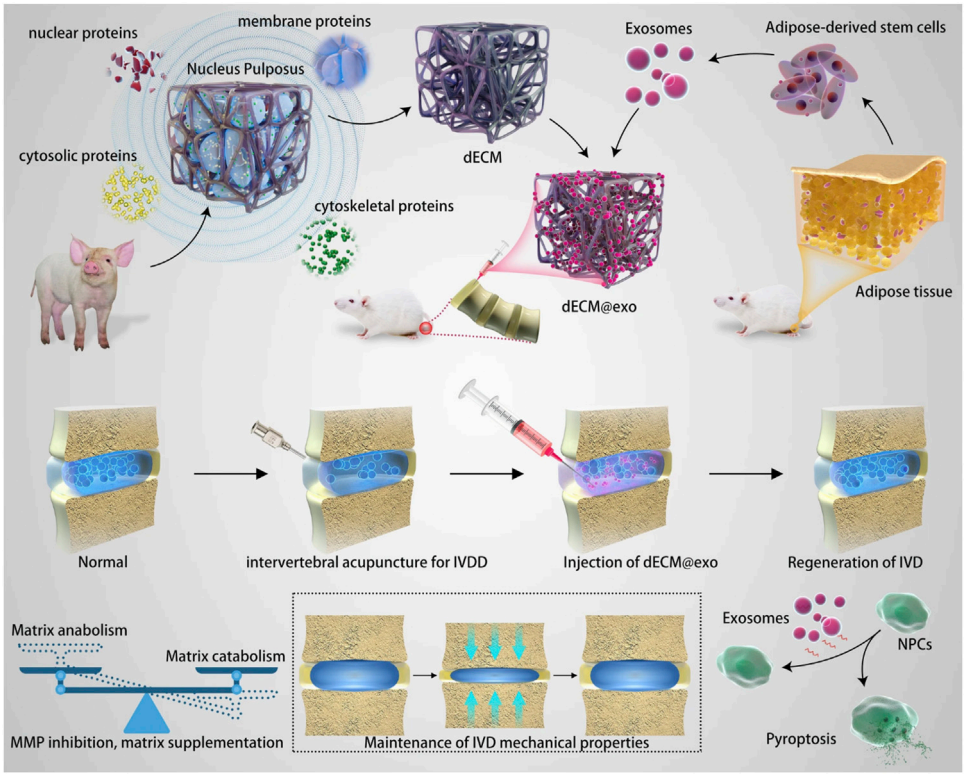

FIGURE 7
Schematic diagram of the mechanisms of one kind of multiscale drug delivery system combining thermosensitive acellular ECM hydrogels and adipose-derived MSC exosomes for IVD treatment. Reproduced with permission from (Xing et al., 2021).

nanoparticles have broad application prospects, it is necessary to adjust parameters such as hollow structure, surface chemistry and pore size based on IVD tissue and corresponding drug properties; this requires a large amount of *in vivo* and *in vitro* experiments.

The application of nanotechnology provides a new solution for the treatment of IDD but still needs to be personalized and adjusted according to the local complex microenvironment in the spine. In addition, the potential cytotoxicity requires further attention.

Multiscale delivery systems

With the rapid development of new technologies such as gene programming and bio-3D printing, the boundaries between biology, materials science, pharmacy and other related disciplines are gradually becoming blurred (Cui et al., 2020; Zhu et al., 2020). Multi-disciplinary and multi-scale technology exchanges make up for the shortcomings of a traditional single technology, which undoubtedly brings new hope for the treatment of IDD. Multi-scale delivery systems do not only include the multiscale aspect; here, we prefer to extend this concept to the temporal scale in which this type of system could show difference performance in different disease stages.

The pathological process of IDD is a multi-scale process from the gene to the local anatomical structure, which makes it difficult to obtain satisfactory results by intervening with a single factor; therefore, the establishment of a multi-scale delivery system has good prospects. Ligorio et al. (Ligorio et al., 2019) reported a new hybrid injectable 3D-scaffold that used graphene oxide (GO) as a nanofiller; results indicated that the 3D-scaffold had similar mechanical properties as health NP tissue and promotes metabolic activity. In addition to its potential to deliver NP cells, researchers explored the possibility of using the 3D-scaffold as a transporter that modulated the sequestration and delivery of transforming growth factor beta-3 (TGF-β3) (Ligorio et al., 2021). In their latest study, these authors extended the use of the 3D-scaffold as a versatile pH-tunable platform for cell encapsulation (Ligorio et al., 2022). Instead of using one system to interfere with pathological processes at different levels, it seems more convenient to combine two systems that work at different levels as one. Due to the instability of exosomes *in vivo*, their clinical application has stalled. Zhou et al. (Xing et al., 2021) reported the combination of thermosensitive acellular ECM hydrogels and adipose-derived MSC exosomes.

TABLE 1 A brief comparison of various delivery systems.

Feature	Delivery palace	Substance carried	Major advantages	Major disadvantages
Virus vector				
retroviruses	intracellular	genetic information	Wide range of sources, simple to operate and easy to build	Weak effect on low-dividing rate cells
adenoviruses	intracellular	genetic information	Higher transduction efficiency in quiescent slow-dividing cells	Potential infectivity and immunogenicity
adeno-associated viruses	intracellular	genetic information	Biocompatible, low immunogenicity	Costly and difficult to ensure homogeneity between batches
lentiviruses	intracellular	genetic information	Ability to transduce nondividing cells	Costly, low manufacturing capacity and complex bioprocessing
Physical method				
ultrasound	intracellular	genetic information/ drug molecular	Simple procedure and no immunogenicity	Potential damage to cells
electroporation	intracellular	genetic information/ drug molecular	Ability to transfer a large number of cells in a short period	Potential damage to cells and difficulty in determining the appropriate stimulation intensity
Hydrogel-based delivery system				
natural polymers	extracellular	genetic information/ drug molecular/cell	Good biocompatibility, biodegradable, some are biological functional	*In vivo* performance is difficult to meet the requirements, easy to decompose
synthetic polymers	extracellular	genetic information/ drug molecular/cell	Better mechanical properties and easy to ensure stable performance between batches	Possible cytotoxicity and low biocompatibility
stimulus-responsive composite hydrogel	extracellular	genetic information/ drug molecular/cell	Adjust performance parameters based on requirements	Potential cytotoxicity, design difficulties and extensive pre-testing for ideal parameter
Microsphere-based delivery system				
microcapsule	Intracellular/ extracelluar	genetic information/ drug molecular/cell	Superior substance exchange efficiency, the parameters can be adjusted, targeted drug delivery	Complicated fabrication methods, have some requirements for the loading
micromatrice	Intracellular/ extracelluar	genetic information/ drug molecular/cell	Better compatibility with different loading, higher encapsulation rate, targeted drug delivery	Ideal parameters require extensive per-testing, complicated to design
Nano-scale delivery system				
Lipid-based delivery system	Intracellular/ extracelluar	genetic information/ drug molecular	Simple composition, good biocompatibility, low toxicity, and some are self-assembly	Susceptible to the interference of complex environment *in vivo*
Polymeric nanoparticles	Intracellular/ extracelluar	genetic information/ drug molecular	Good stability, adjustable parameters	Require rigorous safety assessment, complicated to design
Inorganic material	Intracellular/ extracelluar	genetic information/ drug molecular	Good stability, biocompatibility, and low toxicity	Difficult to decompose, ideal parameters require extensive per-testing
Multiscale delivery system	Intracellular/ extracelluar	genetic information/ drug molecular/cell	Multiscale intervention, more lasting and effective treatment	High cost, complicated to design

This hydrogel system can provide both gelation for ECM leakage and a suitable environment for the growth of NP cells (Figure 7). In addition, sustained released exosomes significantly downregulated the expression of MMP and mitigated the inflammatory response *in vitro*.

Bio-3D printing is an emerging technology platform that uses computational methods to precisely manipulate the distribution of biomaterials, biological factors and cells. Due to its flexible, precise, and personalized features, bio-3D printing can meet people's needs more accurately than traditional manufacturing methods (Kang et al., 2016). Because printing different materials requires different parameters, it is difficult to integrate biomaterials, biological factors and cells into one system. Sun et al. (Sun et al., 2021a) designed a new scaffold with biomaterials, cells and biological factors. The replica NP component was printed from MSCs and TGF-β3 hydrogel while the replica AF part was printed by MSCs and connective tissue growth factor hydrogel. In addition, the framework of the whole scaffold was printed by PCL to provide necessary mechanical support (Sun et al., 2021a). Zhu et al. (Zhu et al., 2021) conceived another method to solve this problem by using poly lactide (PLA) to print an IVD frame structure; AF and NP are modeled by oriented porous poly (L-lactide)/octa-armed polyhedral oligomeric silsesquioxanes fiber bundles and gellan gum/ PEGDA hydrogel loaded with MSCs, respectively. Both

scaffolds exhibited good mechanical properties *in vitro*, maintained high cell activity and produced new ECM *in vivo*.

A sequential delivery system that can deliver corresponding drugs at different pathological stages in the temporal dimension is also remarkable. Bayer et al. (Bayer et al., 2017) established a delivery system that achieved the sequential release of platelet-derived growth factor (PDGF) and bone morphogenetic protein-2 (BMP-2) by combing alginate matrices with calcium phosphate scaffolding. In a subsequent study, Leslie et al. (Frapin et al., 2020) developed a delivery system based on pullulan microbeads. This sequential delivery system first released CCL-5 to recruit stem cells to NP, followed by the release of TGF-β1 and growth/differentiation factor (GDF)-5 to upregulate the expression of type II collagen and aggrecan.

New technologies and multidisciplinary communication have accelerated the development of multi-scale delivery systems, but long-term safety assessment and adequate *in vivo* experiments on large mammals still need to be carried out. In addition, the clinical experience and the need for detailed evaluation also need to be considered.

Conclusion

IDD is an important health problem that has a significant effect on a patient's quality of life. In today's aging society, this problem should be given increased levels of attention. Although we are still exploring the detailed pathological process of IDD, we have reviewed several widely accepted mechanisms in the development of IDD; these mechanisms are interconnected and form a vicious loop. Treatment methods for these mechanisms are also developing rapidly, covering almost every time stage and physical scale of IDD development. Although significant levels of attention have been paid to specific targets and effective drugs, an equally important question tends to be overlooked: how do we get these therapeutic substances to where they should be and in the way that people expect them to be? In this review, we summarized the pathological mechanisms associated with IDD and described the delivery systems at various scales. We emphasized the multi-scale delivery systems brought about by multidisciplinary communication as a new direction for delivery systems. However, there are still many difficulties to be overcome in the selection of suitable carriers. Cytotoxicity, degradability, and biocompatibility are unavoidable problems for all implants. In addition, the technical difficulty and cost of materials are also practical problems that need to be considered. The choice is often a trade-off between various performances, and it is difficult to meet all the expectations at the beginning of the design.

When the delivery system is considered for clinical application, it is necessary to discuss the practical aspects; various delivery systems are briefly evaluated in Table 1. The mechanisms responsible for IDD and LBP remain unclear and some IDD patients do not receive special examinations before the onset of symptoms. How we screen early-stage IDD patients and persuade them to accept treatment is the first problem that clinicians need to address. The next problem is the personalization of therapeutic strategies and how to select the appropriate system according to the specific condition of patients; this requires more research. Finally, any material implanted into the body should undergo rigorous safety assessments and pre-clinical validation.

In conclusion, we should design delivery systems with better theoretical performance through multidisciplinary and advanced technology. Furthermore, we should adjust the parameters and components of these systems according to the specific situation of patients. Although a significant amount of research is still needed, we still expect that multi-scale delivery systems will bring new opportunities for IDD treatment.

Author contributions

ZL: Conception of the work; Drafted the manuscript; Revision of the manuscript. CF: Supervised the direction of manuscript; Design of the work; Revision of the manuscript.

Acknowledgments

The authors would like to express their gratitude to EditSprings (https://www.editsprings.cn) for the expert linguistic services provided.

Conflict of interest

The authors declare that the research was conducted in the absence of any commercial or financial relationships that could be construed as a potential conflict of interest.

Publisher's note

References

Adams, M. A., Mcmillan, D. W., Green, T. P., and Dolan, P. (1996). Sustained loading generates stress concentrations in lumbar intervertebral discs. *Spine (Phila Pa 1976)* 21, 434–438. doi:10.1097/00007632-199602150-00006

Adams, M. A., and Roughley, P. J. (2006). What is intervertebral disc degeneration, and what causes it? *Spine (Phila Pa 1976)* 31, 2151–2161. doi:10.1097/01.brs.0000231761.73859.2c

Alinejad, Y., Adoungotchodo, A., Grant, M. P., Epure, L. M., Antoniou, J., Mwale, F., et al. (2019). Injectable chitosan hydrogels with enhanced mechanical properties for nucleus pulposus regeneration. *Tissue Eng. Part A* 25, 303–313. doi:10.1089/ten.tea.2018.0170

Amer, L. D., and Bryant, S. J. (2016). The *in vitro* and *in vivo* response to MMP-sensitive poly(ethylene glycol) hydrogels. *Ann. Biomed. Eng.* 44, 1959–1969. doi:10.1007/s10439-016-1608-4

Andersson, G. B., An, H. S., Oegema, T. R., and Setton, L. A. (2006). Directions for future research. *J. Bone Jt. Surg.* 88 (2), 110–114. doi:10.2106/jbjs.f.00030

Antkowiak, M., Torres-Mapa, M. L., Stevenson, D. J., Dholakia, K., and Gunn-Moore, F. J. (2013). Femtosecond optical transfection of individual mammalian cells. *Nat. Protoc.* 8, 1216–1233. doi:10.1038/nprot.2013.071

Antoniou, J., Steffen, T., Nelson, F., Winterbottom, N., Hollander, A. P., Poole, R. A., et al. (1996). The human lumbar intervertebral disc: Evidence for changes in the biosynthesis and denaturation of the extracellular matrix with growth, maturation, ageing, and degeneration. *J. Clin. Invest.* 98, 996–1003. doi:10.1172/jci118884

Bachmeier, B. E., Nerlich, A., Mittermaier, N., Weiler, C., Lumenta, C., Wuertz, K., et al. (2009). Matrix metalloproteinase expression levels suggest distinct enzyme roles during lumbar disc herniation and degeneration. *Eur. Spine J.* 18, 1573–1586. doi:10.1007/s00586-009-1031-8

Bailey, J. F., Miller, S. L., Khieu, K., O'Neill, C. W., Healey, R. M., Coughlin, D. G., et al. (2018). From the international space station to the clinic: How prolonged unloading may disrupt lumbar spine stability. *Spine J.* 18, 7–14. doi:10.1016/j.spinee.2017.08.261

Banala, R. R., Vemuri, S. K., Dar, G. H., Palanisamy, V., Penkulinti, M., Surekha, M. V., et al. (2019). Efficiency of dual siRNA-mediated gene therapy for intervertebral disc degeneration (IVDD). *Spine J.* 19, 896–904. doi:10.1016/j.spinee.2018.10.016

Bartels, E. M., Fairbank, J. C., Winlove, C. P., and Urban, J. P. (1998). Oxygen and lactate concentrations measured *in vivo* in the intervertebral discs of patients with scoliosis and back pain. *Spine (Phila Pa 1976)* 23, 1–7. discussion 8. doi:10.1097/00007632-199801010-00001

Bayer, E. A., Jordan, J., Roy, A., Gottardi, R., Fedorchak, M. V., Kumta, P. N., et al. (2017). <sup/>Programmed platelet-derived growth factor-BB and bone morphogenetic protein-2 delivery from a hybrid calcium phosphate/alginate scaffold. *Tissue Eng. Part A* 23, 1382–1393. doi:10.1089/ten.tea.2017.0027

Benneker, L. M., Andersson, G., Iatridis, J. C., Sakai, D., HäRTL, R., Ito, K., et al. (2014). Cell therapy for intervertebral disc repair: Advancing cell therapy from bench to clinics. *Eur. Cell. Mat.* 27, 5–11. doi:10.22203/ecm.v027sa02

Berjano, P., VillafañE, J. H., Lo Re, D., Ismael, M., Damilano, M., Bertozzi, L., et al. (2019). Is Propionibacterium acnes related to disc degeneration in adults? A systematic review. *J. Neurosurg. Sci.* 63, 216–223. doi:10.23736/s0390-5616.16.03842-x

Bertheloot, D., Latz, E., and Franklin, B. S. (2021). Necroptosis, pyroptosis and apoptosis: An intricate game of cell death. *Cell. Mol. Immunol.* 18, 1106–1121. doi:10.1038/s41423-020-00630-3

Boos, N., Weissbach, S., Rohrbach, H., Weiler, C., Spratt, K. F., and Nerlich, A. G. (2002). Classification of age-related changes in lumbar intervertebral discs: 2002 volvo award in basic science. *Spine (Phila Pa 1976)* 27, 2631–2644. doi:10.1097/00007632-200212010-00002

Boucher, D., Monteleone, M., Coll, R. C., Chen, K. W., Ross, C. M., Teo, J. L., et al. (2018). Caspase-1 self-cleavage is an intrinsic mechanism to terminate inflammasome activity. *J. Exp. Med.* 215, 827–840. doi:10.1084/jem.20172222

Bowles, R. D., and Setton, L. A. (2017). Biomaterials for intervertebral disc regeneration and repair. *Biomaterials* 129, 54–67. doi:10.1016/j.biomaterials.2017.03.013

Burdick, J. A., and Prestwich, G. D. (2011). Hyaluronic acid hydrogels for biomedical applications. *Adv. Mat.* 23, H41–H56. doi:10.1002/adma.201003963

Campisi, J., Kapahi, P., Lithgow, G. J., Melov, S., Newman, J. C., and Verdin, E. (2019). From discoveries in ageing research to therapeutics for healthy ageing. *Nature* 571, 183–192. doi:10.1038/s41586-019-1365-2

Cazzanelli, P., and Wuertz-Kozak, K. (2020). MicroRNAs in intervertebral disc degeneration, apoptosis, inflammation, and mechanobiology. *Int. J. Mol. Sci.* 21, 3601. doi:10.3390/ijms21103601

Chan, S. C., Ferguson, S. J., and Gantenbein-Ritter, B. (2011). The effects of dynamic loading on the intervertebral disc. *Eur. Spine J.* 20, 1796–1812. doi:10.1007/s00586-011-1827-1

Chang, C. C., Tsou, H. K., Chang, H. H., Chan, L. Y., Zhuo, G. Y., Maeda, T., et al. (2022a). Runx1 messenger RNA delivered by polyplex nanomicelles alleviate spinal disc hydration loss in a rat disc degeneration model. *Int. J. Mol. Sci.* 23, 565. doi:10.3390/ijms23010565

Chang, H., Cai, F., Zhang, Y., Jiang, M., Yang, X., Qi, J., et al. (2022b). Silencing gene-engineered injectable hydrogel microsphere for regulation of extracellular matrix metabolism balance. *Small Methods* 6, e2101201. doi:10.1002/smtd.202101201

Chao-Yang, G., Peng, C., and Hai-Hong, Z. (2021). Roles of NLRP3 inflammasome in intervertebral disc degeneration. *Osteoarthr. Cartil.* 29, 793–801. doi:10.1016/j.joca.2021.02.204

Chen, A. K., Reuveny, S., and Oh, S. K. (2013). Application of human mesenchymal and pluripotent stem cell microcarrier cultures in cellular therapy: Achievements and future direction. *Biotechnol. Adv.* 31, 1032–1046. doi:10.1016/j.biotechadv.2013.03.006

Chen, S., Huang, Y., Zhou, Z. J., Hu, Z. J., Wang, J. Y., Xu, W. B., et al. (2014). Upregulation of tumor necrosis factor α and ADAMTS-5, but not ADAMTS-4, in human intervertebral cartilage endplate with modic changes. *Spine (Phila Pa 1976)* 39, E817–E825. doi:10.1097/brs.0000000000000362

Chen, T., Wang, Y., Xie, J., Qu, X., and Liu, C. (2022). Lysozyme amyloid fibril-integrated PEG injectable hydrogel adhesive with improved antiswelling and antibacterial capabilities. *Biomacromolecules* 23, 1376–1391. doi:10.1021/acs.biomac.1c01597

Chen, Z. B., Yu, Y. B., Wa, Q. B., Zhou, J. W., He, M., and Cen, Y. (2020b). The role of quinazoline in ameliorating intervertebral disc degeneration by inhibiting oxidative stress and anti-inflammation via NF-κB/MAPKs signaling pathway. *Eur. Rev. Med. Pharmacol. Sci.* 24, 2077–2086. doi:10.26355/eurrev_202002_20387

Chen, Z., Liu, M., Zhang, W., Deng, M., Zhou, Y., and Li, Y. (2020a). miR-24-3p induces human intervertebral disc degeneration by targeting insulin-like growth factor binding protein 5 and the ERK signaling pathway. *Life Sci.* 243, 117288. doi:10.1016/j.lfs.2020.117288

Cheung, K. M., Karppinen, J., Chan, D., Ho, D. W., Song, Y. Q., Sham, P., et al. (2009). Prevalence and pattern of lumbar magnetic resonance imaging changes in a population study of one thousand forty-three individuals. *Spine (Phila Pa 1976)* 34, 934–940. doi:10.1097/brs.0b013e3181a01b3f

Chicas, A., Wang, X., Zhang, C., Mccurrach, M., Zhao, Z., Mert, O., et al. (2010). Dissecting the unique role of the retinoblastoma tumor suppressor during cellular senescence. *Cancer Cell* 17, 376–387. doi:10.1016/j.ccr.2010.01.023

Childs, B. G., Durik, M., Baker, D. J., and Van Deursen, J. M. (2015). Cellular senescence in aging and age-related disease: From mechanisms to therapy. *Nat. Med.* 21, 1424–1435. doi:10.1038/nm.4000

Choi, J. R., Yong, K. W., Choi, J. Y., and Cowie, A. C. (2019). Recent advances in photo-crosslinkable hydrogels for biomedical applications. *Biotechniques* 66, 40–53. doi:10.2144/btn-2018-0083

Choi, M. H., Blanco, A., Stealey, S., Duan, X., Case, N., Sell, S. A., et al. (2020). *Micro-clotting of platelet-rich plasma upon loading in hydrogel microspheres leads to prolonged protein release and slower microsphere degradation*. Basel: Polymers, 12.

Clark, E. A., Alexander, M. R., Irvine, D. J., Roberts, C. J., Wallace, M. J., Sharpe, S., et al. (2017). 3D printing of tablets using inkjet with UV photoinitiation. *Int. J. Pharm. X.* 529, 523–530. doi:10.1016/j.ijpharm.2017.06.085

Court, C., Colliou, O. K., Chin, J. R., Liebenberg, E., Bradford, D. S., and Lotz, J. C. (2001). The effect of static *in vivo* bending on the murine intervertebral disc. *Spine J.* 1, 239–245. doi:10.1016/s1529-9430(01)00056-0

Cui, L., Zhang, J., Zou, J., Yang, X., Guo, H., Tian, H., et al. (2020). Electroactive composite scaffold with locally expressed osteoinductive factor for synergistic bone repair upon electrical stimulation. *Biomaterials* 230, 119617. doi:10.1016/j.biomaterials.2019.119617

De MagalhãES, J. P., and Passos, J. F. (2018). Stress, cell senescence and organismal ageing. *Mech. Ageing Dev.* 170, 2–9. doi:10.1016/j.mad.2017.07.001

Debono, B., Lonjon, G., Galovich, L. A., Kerever, S., Guiot, B., Eicker, S. O., et al. (2018). Indication variability in degenerative lumbar spine surgery: A four-nation survey. *Spine (Phila Pa 1976)* 43, 185–192. doi:10.1097/brs.0000000000002272

Desmoulin, G. T., Pradhan, V., and Milner, T. E. (2020). Mechanical aspects of intervertebral disc injury and implications on biomechanics. *Spine (Phila Pa 1976)* 45, E457–e464. doi:10.1097/brs.0000000000003291

Dieleman, J. L., Baral, R., Birger, M., Bui, A. L., Bulchis, A., Chapin, A., et al. (2016). US spending on personal health care and public health. *Jama* 316, 2627–2646. doi:10.1001/jama.2016.16885

Driesse, M. J., Esandi, M. C., Kros, J. M., Avezaat, C. J., Vecht, C., Zurcher, C., et al. (2000). Intra-CSF administered recombinant adenovirus causes an immune response-mediated toxicity. *Gene Ther.* 7, 1401–1409. doi:10.1038/sj.gt.3301250

Dudli, S., Ferguson, S. J., and Haschtmann, D. (2014). Severity and pattern of post-traumatic intervertebral disc degeneration depend on the type of injury. *Spine J.* 14, 1256–1264. doi:10.1016/j.spinee.2013.07.488

Elfervig, M. K., Minchew, J. T., Francke, E., Tsuzaki, M., and Banes, A. J. (2001). IL-1beta sensitizes intervertebral disc annulus cells to fluid-induced shear stress. *J. Cell. Biochem.* 82, 290–298. doi:10.1002/jcb.1153

Farhang, N., Ginley-Hidinger, M., Berrett, K. C., Gertz, J., Lawrence, B., and Bowles, R. D. (2019). Lentiviral CRISPR epigenome editing of inflammatory receptors as a gene therapy strategy for disc degeneration. *Hum. Gene Ther.* 30, 1161–1175. doi:10.1089/hum.2019.005

Feng, H., Danfelter, M., StröMQVIST, B., and HeinegåRD, D. (2006). Extracellular matrix in disc degeneration. *J. Bone Jt. Surg.* 88 (2), 25–29. doi:10.2106/jbjs.e.01341

Foster, N. E., Anema, J. R., Cherkin, D., Chou, R., Cohen, S. P., Gross, D. P., et al. (2018). Prevention and treatment of low back pain: Evidence, challenges, and promising directions. *Lancet* 391, 2368–2383. doi:10.1016/s0140-6736(18)30489-6

Francisco, V., Pino, J., GonzáLEZ-Gay, M., Lago, F., Karppinen, J., Tervonen, O., et al. (2022). A new immunometabolic perspective of intervertebral disc degeneration. *Nat. Rev. Rheumatol.* 18, 47–60. doi:10.1038/s41584-021-00713-z

Frapin, L., Clouet, J., ChéDEVILLE, C., Moraru, C., Samarut, E., Henry, N., et al. (2020). Controlled release of biological factors for endogenous progenitor cell migration and intervertebral disc extracellular matrix remodelling. *Biomaterials* 253, 120107. doi:10.1016/j.biomaterials.2020.120107

Fraser, A., and Evan, G. (1996). A license to kill. *Cell* 85, 781–784. doi:10.1016/s0092-8674(00)81005-3

Gabr, M. A., Jing, L., Helbling, A. R., Sinclair, S. M., Allen, K. D., Shamji, M. F., et al. (2011). Interleukin-17 synergizes with IFNγ or TNFα to promote inflammatory mediator release and intercellular adhesion molecule-1 (ICAM-1) expression in human intervertebral disc cells. *J. Orthop. Res.* 29, 1–7. doi:10.1002/jor.21206

Gao, F., Liu, S., Zhang, X., Wang, X., and Zhang, J. (2021). Automated grading of lumbar disc degeneration using a push-pull regularization network based on MRI. *J. Magn. Reson. Imaging* 53, 799–806. doi:10.1002/jmri.27400

Gawri, R., Rosenzweig, D. H., Krock, E., Ouellet, J. A., Stone, L. S., Quinn, T. M., et al. (2014). High mechanical strain of primary intervertebral disc cells promotes secretion of inflammatory factors associated with disc degeneration and pain. *Arthritis Res. Ther.* 16, R21. doi:10.1186/ar4449

GBD 2017 Disease and Injury Incidence and Prevalence Collaborators (2017). Global, regional, and national incidence, prevalence, and years lived with disability for 354 diseases and injuries for 195 countries and territories, 1990-2017: A systematic analysis for the global burden of disease study 2017. *Lancet* 392, 1789–1858. doi:10.1016/S0140-6736(18)32279-7

Growney Kalaf, E. A., Pendyala, M., Bledsoe, J. G., and Sell, S. A. (2017). Characterization and restoration of degenerated IVD function with an injectable, *in situ* gelling alginate hydrogel: An *in vitro* and *ex vivo* study. *J. Mech. Behav. Biomed. Mat.* 72, 229–240. doi:10.1016/j.jmbbm.2017.05.014

Gruber, H. E., Hoelscher, G. L., Ingram, J. A., Bethea, S., Norton, H. J., and Hanley, E. N. (2014a). Production and expression of RANTES (CCL5) by human disc cells and modulation by IL-1-β and TNF-α in 3D culture. *Exp. Mol. Pathol.* 96, 133–138. doi:10.1016/j.yexmp.2014.01.002

Gruber, H. E., Hoelscher, G. L., Ingram, J. A., Bethea, S., Zinchenko, N., and Hanley, E. N. (2011). Variations in aggrecan localization and gene expression patterns characterize increasing stages of human intervertebral disk degeneration. *Exp. Mol. Pathol.* 91, 534–539. doi:10.1016/j.yexmp.2011.06.001

Gruber, H. E., Hoelscher, G. L., Ingram, J. A., Norton, H. J., and Hanley, E. N. (2013). Increased IL-17 expression in degenerated human discs and increased production in cultured annulus cells exposed to IL-1ß and TNF-α. *Biotech. Histochem.* 88, 302–310. doi:10.3109/10520295.2013.783235

Gruber, H. E., Ingram, J. A., Cox, M. D., and Hanley, E. N. (2014b). Matrix metalloproteinase-12 immunolocalization in the degenerating human intervertebral disc and sand rat spine: Biologic implications. *Exp. Mol. Pathol.* 97, 1–5. doi:10.1016/j.yexmp.2014.04.007

Gupta, P., Vermani, K., and Garg, S. (2002). Hydrogels: From controlled release to pH-responsive drug delivery. *Drug Discov. Today* 7, 569–579. doi:10.1016/s1359-6446(02)02255-9

Gupta, V., Khan, Y., Berkland, C. J., Laurencin, C. T., and Detamore, M. S. (2017). Microsphere-based scaffolds in regenerative engineering. *Annu. Rev. Biomed. Eng.* 19, 135–161. doi:10.1146/annurev-bioeng-071516-044712

Hartvigsen, J., Hancock, M. J., Kongsted, A., Louw, Q., Ferreira, M. L., Genevay, S., et al. (2018). What low back pain is and why we need to pay attention. *Lancet* 391, 2356–2367. doi:10.1016/s0140-6736(18)30480-x

He, D., Zhou, M., Bai, Z., Wen, Y., Shen, J., and Hu, Z. (2020). Propionibacterium acnes induces intervertebral disc degeneration by promoting nucleus pulposus cell pyroptosis via NLRP3-dependent pathway. *Biochem. Biophys. Res. Commun.* 526, 772–779. doi:10.1016/j.bbrc.2020.03.161

He, W. T., Wan, H., Hu, L., Chen, P., Wang, X., Huang, Z., et al. (2015). Gasdermin D is an executor of pyroptosis and required for interleukin-1β secretion. *Cell Res.* 25, 1285–1298. doi:10.1038/cr.2015.139

He, Y., Hara, H., and NúñEZ, G. (2016). Mechanism and regulation of NLRP3 inflammasome activation. *Trends biochem. Sci.* 41, 1012–1021. doi:10.1016/j.tibs.2016.09.002

Hodgkinson, T., Stening, J. Z., White, L. J., Shakesheff, K. M., Hoyland, J. A., and Richardson, S. M. (2019). Microparticles for controlled growth differentiation factor 6 delivery to direct adipose stem cell-based nucleus pulposus regeneration. *J. Tissue Eng. Regen. Med.* 13, 1406–1417. doi:10.1002/term.2882

Hoffman, A. S. (2002). Hydrogels for biomedical applications. *Adv. Drug Deliv. Rev.* 54, 3–12. doi:10.1016/s0169-409x(01)00239-3

Holm, S., Maroudas, A., Urban, J. P., Selstam, G., and Nachemson, A. (1981). Nutrition of the intervertebral disc: Solute transport and metabolism. *Connect. Tissue Res.* 8, 101–119. doi:10.3109/03008208109152130

Huang, C. Y., and Gu, W. Y. (2008). Effects of mechanical compression on metabolism and distribution of oxygen and lactate in intervertebral disc. *J. Biomech.* 41, 1184–1196. doi:10.1016/j.jbiomech.2008.02.002

Huang, X., He, W., Wang, W., Fan, Q., Ye, X., Wu, Z., et al. (2021). Toxicology and pharmacokinetics study of intradiscal injection of simvastatin in rabbits. *Front. Pharmacol.* 12, 582309. doi:10.3389/fphar.2021.582309

Huang, Y. C., Urban, J. P., and Luk, K. D. (2014). Intervertebral disc regeneration: Do nutrients lead the way? *Nat. Rev. Rheumatol.* 10, 561–566. doi:10.1038/nrrheum.2014.91

Hutton, W. C., Yoon, S. T., Elmer, W. A., Li, J., Murakami, H., Minamide, A., et al. (2002). Effect of tail suspension (or simulated weightlessness) on the lumbar intervertebral disc: Study of proteoglycans and collagen. *Spine (Phila Pa 1976)* 27, 1286–1290. doi:10.1097/00007632-200206150-00008

Iatridis, J. C., Nicoll, S. B., Michalek, A. J., Walter, B. A., and Gupta, M. S. (2013). Role of biomechanics in intervertebral disc degeneration and regenerative therapies: What needs repairing in the disc and what are promising biomaterials for its repair? *Spine J.* 13, 243–262. doi:10.1016/j.spinee.2012.12.002

Ikuno, A., Akeda, K., Takebayashi, S. I., Shimaoka, M., Okumura, K., and Sudo, A. (2019). Genome-wide analysis of DNA methylation profile identifies differentially methylated loci associated with human intervertebral disc degeneration. *PLoS One* 14, e0222188. doi:10.1371/journal.pone.0222188

Illien-JüNGER, S., Gantenbein-Ritter, B., Grad, S., Lezuo, P., Ferguson, S. J., Alini, M., et al. (2010). The combined effects of limited nutrition and high-frequency loading on intervertebral discs with endplates. *Spine (Phila Pa 1976)* 35, 1744–1752. doi:10.1097/brs.0b013e3181c48019

Iwata, M., Aikawa, T., Hakozaki, T., Arai, K., Ochi, H., Haro, H., et al. (2015). Enhancement of Runx2 expression is potentially linked to β-catenin accumulation in canine intervertebral disc degeneration. *J. Cell. Physiol.* 230, 180–190. doi:10.1002/jcp.24697

Jackson, A. R., Yuan, T. Y., Huang, C. Y., Brown, M. D., and Gu, W. Y. (2012). Nutrient transport in human annulus fibrosus is affected by compressive strain and anisotropy. *Ann. Biomed. Eng.* 40, 2551–2558. doi:10.1007/s10439-012-0606-4

Jang, H. Y., Shin, J. Y., Oh, S. H., Byun, J. H., and Lee, J. H. (2020). PCL/HA hybrid microspheres for effective osteogenic differentiation and bone regeneration. *ACS Biomater. Sci. Eng.* 6, 5172–5180. doi:10.1021/acsbiomaterials.0c00550

Jiang, H., Moro, A., Wang, J., Meng, D., Zhan, X., and Wei, Q. (2021). MicroRNA-338-3p as a novel therapeutic target for intervertebral disc degeneration. *Exp. Mol. Med.* 53, 1356–1365. doi:10.1038/s12276-021-00662-3

Jiang, Y., Xie, Z., Yu, J., and Fu, L. (2019). Resveratrol inhibits IL-1β-mediated nucleus pulposus cell apoptosis through regulating the PI3K/Akt pathway. *Biosci. Rep.* 39, BSR20190043. doi:10.1042/bsr20190043

Jin, H., Wang, Q., Wu, J., Han, X., Qian, T., Zhang, Z., et al. (2019). Baicalein inhibits the IL-1β-induced inflammatory response in nucleus pulposus cells and

attenuates disc degeneration *in vivo*. *Inflammation* 42, 1032–1044. doi:10.1007/s10753-019-00965-8

Jin, Z., Wang, D., Zhang, H., Liang, J., Feng, X., Zhao, J., et al. (2020). Incidence trend of five common musculoskeletal disorders from 1990 to 2017 at the global, regional and national level: Results from the global burden of disease study 2017. *Ann. Rheum. Dis.* 79, 1014–1022. doi:10.1136/annrheumdis-2020-217050

John, A. A., Subramanian, A. P., Vellayappan, M. V., Balaji, A., Mohandas, H., and Jaganathan, S. K. (2015). Carbon nanotubes and graphene as emerging candidates in neuroregeneration and neurodrug delivery. *Int. J. Nanomedicine* 10, 4267–4277. doi:10.2147/ijn.s83777

Kadow, T., Sowa, G., Vo, N., and Kang, J. D. (2015). Molecular basis of intervertebral disc degeneration and herniations: What are the important translational questions? *Clin. Orthop. Relat. Res.* 473, 1903–1912. doi:10.1007/s11999-014-3774-8

Kamali, A., Ziadlou, R., Lang, G., Pfannkuche, J., Cui, S., Li, Z., et al. (2021). Small molecule-based treatment approaches for intervertebral disc degeneration: Current options and future directions. *Theranostics* 11, 27–47. doi:10.7150/thno.48987

Kang, H. W., Lee, S. J., Ko, I. K., Kengla, C., Yoo, J. J., and Atala, A. (2016). A 3D bioprinting system to produce human-scale tissue constructs with structural integrity. *Nat. Biotechnol.* 34, 312–319. doi:10.1038/nbt.3413

Kannan, R. M., Nance, E., Kannan, S., and Tomalia, D. A. (2014). Emerging concepts in dendrimer-based nanomedicine: From design principles to clinical applications. *J. Intern. Med.* 276, 579–617. doi:10.1111/joim.12280

Karamouzian, S., Eskandary, H., Faramarzee, M., Saba, M., Safizade, H., Ghadipasha, M., et al. (2010). Frequency of lumbar intervertebral disc calcification and angiogenesis, and their correlation with clinical, surgical, and magnetic resonance imaging findings. *Spine (Phila Pa 1976)* 35, 881–886. doi:10.1097/brs.0b013e3181b9c986

Katz, J. N. (2006). Lumbar disc disorders and low-back pain: Socioeconomic factors and consequences. *J. Bone Jt. Surg.* 88 (2), 21–24. doi:10.2106/jbjs.e.01273

Kepler, C. K., Markova, D. Z., Dibra, F., Yadla, S., Vaccaro, A. R., Risbud, M. V., et al. (2013a). Expression and relationship of proinflammatory chemokine RANTES/CCL5 and cytokine IL-1β in painful human intervertebral discs. *Spine (Phila Pa 1976)* 38, 873–880. doi:10.1097/brs.0b013e318285ae08

Kepler, C. K., Markova, D. Z., Hilibrand, A. S., Vaccaro, A. R., Risbud, M. V., Albert, T. J., et al. (2013b). Substance P stimulates production of inflammatory cytokines in human disc cells. *Spine (Phila Pa 1976)* 38, E1291–E1299. doi:10.1097/brs.0b013e3182a42bc2

Kim, C. H., Oliver, C., Dar, H., Drissi, H., and Presciutti, S. M. (2022). AAV6 as an effective gene delivery vector for prolonged transgene expression in intervertebral disc cells *in vivo*. *Genes Dis.* 9, 1074–1085. doi:10.1016/j.gendis.2020.12.009

Klein, T. J., Malda, J., Sah, R. L., and Hutmacher, D. W. (2009). Tissue engineering of articular cartilage with biomimetic zones. *Tissue Eng. Part B Rev.* 15, 143–157. doi:10.1089/ten.teb.2008.0563

Klouda, L., and Mikos, A. G. (2008). Thermoresponsive hydrogels in biomedical applications. *Eur. J. Pharm. Biopharm.* 68, 34–45. doi:10.1016/j.ejpb.2007.02.025

Koetting, M. C., Peters, J. T., Steichen, S. D., and Peppas, N. A. (2015). Stimulus-responsive hydrogels: Theory, modern advances, and applications. *Mater. Sci. Eng. R Rep.* 93, 1–49. doi:10.1016/j.mser.2015.04.001

Kokubo, Y., Uchida, K., Kobayashi, S., Yayama, T., Sato, R., Nakajima, H., et al. (2008). Herniated and spondylotic intervertebral discs of the human cervical spine: Histological and immunohistological findings in 500 *en bloc* surgical samples. Laboratory investigation. *J. Neurosurg. Spine* 9, 285–295. doi:10.3171/spi/2008/9/9/285

Kulchar, R. J., Denzer, B. R., Chavre, B. M., Takegami, M., and Patterson, J. (2021). A review of the use of microparticles for cartilage tissue engineering. *Int. J. Mol. Sci.* 22, 10292. doi:10.3390/ijms221910292

Kurian, A. G., Singh, R. K., Patel, K. D., Lee, J. H., and Kim, H. W. (2022). Multifunctional GelMA platforms with nanomaterials for advanced tissue therapeutics. *Bioact. Mat.* 8, 267–295. doi:10.1016/j.bioactmat.2021.06.027

LarrañAGA, A., Isa, I. L. M., Patil, V., Thamboo, S., Lomora, M., FernáNDEZ-Yague, M. A., et al. (2018). Antioxidant functionalized polymer capsules to prevent oxidative stress. *Acta Biomater.* 67, 21–31. doi:10.1016/j.actbio.2017.12.014

Latridis, J. C., Godburn, K., Wuertz, K., Alini, M., and Roughley, P. J. (2011). Region-dependent aggrecan degradation patterns in the rat intervertebral disc are affected by mechanical loading *in vivo*. *Spine (Phila Pa 1976)* 36, 203–209. doi:10.1097/brs.0b013e3181cec247

Lazzari, Z. T., Aria, K. M., and Menger, R. (2021). Neurosurgery and spinal adaptations in spaceflight: A literature review. *Clin. Neurol. Neurosurg.* 207, 106755. doi:10.1016/j.clineuro.2021.106755

Le Maitre, C. L., Freemont, A. J., and Hoyland, J. A. (2005). The role of interleukin-1 in the pathogenesis of human intervertebral disc degeneration. *Arthritis Res. Ther.* 7, R732–R745. doi:10.1186/ar1732

Lee, H. Y., Han, L., Roughley, P. J., Grodzinsky, A. J., and Ortiz, C. (2013). Age-related nanostructural and nanomechanical changes of individual human cartilage aggrecan monomers and their glycosaminoglycan side chains. *J. Struct. Biol. X.* 181, 264–273. doi:10.1016/j.jsb.2012.12.008

Lee, J. M., Song, J. Y., Baek, M., Jung, H. Y., Kang, H., Han, I. B., et al. (2011). Interleukin-1β induces angiogenesis and innervation in human intervertebral disc degeneration. *J. Orthop. Res.* 29, 265–269. doi:10.1002/jor.21210

Lee, S. W., Kim, Y. M., Cho, C. H., Kim, Y. T., Kim, S. M., Hur, S. Y., et al. (2018). An open-label, randomized, parallel, phase II trial to evaluate the efficacy and safety of a cremophor-free polymeric micelle formulation of paclitaxel as first-line treatment for ovarian cancer: A Korean gynecologic oncology group study (KGOG-3021). *Cancer Res. Treat.* 50, 195–203. doi:10.4143/crt.2016.376

Levicoff, E. A., Kim, J. S., Sobajima, S., Wallach, C. J., Larson, J. W., 3R. D., Robbins, P. D., et al. (2008). Safety assessment of intradiscal gene therapy II: Effect of dosing and vector choice. *Spine (Phila Pa 1976)* 33, 1509–1516. doi:10.1097/brs.0b013e318178866c

Li, B., Yang, Y., Wang, L., and Liu, G. (2021). Stem cell therapy and exercise for treatment of intervertebral disc degeneration. *Stem Cells Int.* 2021, 1–10. doi:10.1155/2021/7982333

Li, T., Shi, S., Goel, S., Shen, X., Xie, X., Chen, Z., et al. (2019). Recent advancements in mesoporous silica nanoparticles towards therapeutic applications for cancer. *Acta Biomater.* 89, 1–13. doi:10.1016/j.actbio.2019.02.031

Liang, H., Ma, S. Y., Feng, G., Shen, F. H., and Joshua Li, X. (2010). Therapeutic effects of adenovirus-mediated growth and differentiation factor-5 in a mice disc degeneration model induced by annulus needle puncture. *Spine J.* 10, 32–41. doi:10.1016/j.spinee.2009.10.006

Liao, Z., Liu, H., Ma, L., Lei, J., Tong, B., Li, G., et al. (2021). Engineering extracellular vesicles restore the impaired cellular uptake and attenuate intervertebral disc degeneration. *ACS Nano* 15, 14709–14724. doi:10.1021/acsnano.1c04514

Ligorio, C., O'Brien, M., Hodson, N. W., Mironov, A., Iliut, M., Miller, A. F., et al. (2021). TGF-β3-loaded graphene oxide - self-assembling peptide hybrid hydrogels as functional 3D scaffolds for the regeneration of the nucleus pulposus. *Acta Biomater.* 127, 116–130. doi:10.1016/j.actbio.2021.03.077

Ligorio, C., Vijayaraghavan, A., Hoyland, J. A., and Saiani, A. (2022). Acidic and basic self-assembling peptide and peptide-graphene oxide hydrogels: Characterisation and effect on encapsulated nucleus pulposus cells. *Acta Biomater.* 143, 145–158. doi:10.1016/j.actbio.2022.02.022

Ligorio, C., Zhou, M., Wychowaniec, J. K., Zhu, X., Bartlam, C., Miller, A. F., et al. (2019). Graphene oxide containing self-assembling peptide hybrid hydrogels as a potential 3D injectable cell delivery platform for intervertebral disc repair applications. *Acta Biomater.* 92, 92–103. doi:10.1016/j.actbio.2019.05.004

Lim, S., An, S. B., Jung, M., Joshi, H. P., Kumar, H., Kim, C., et al. (2022). Local delivery of senolytic drug inhibits intervertebral disc degeneration and restores intervertebral disc structure. *Adv. Healthc. Mat.* 11, e2101483. doi:10.1002/adhm.202101483

Lin, J., Zheng, X., Zhang, Z., Zhuge, J., Shao, Z., Huang, C., et al. (2021). Inhibition of LRRK2 restores parkin-mediated mitophagy and attenuates intervertebral disc degeneration. *Osteoarthr. Cartil.* 29, 579–591. doi:10.1016/j.joca.2021.01.002

Liu, H., Kang, H., Song, C., Lei, Z., Li, L., Guo, J., et al. (2018). Urolithin A inhibits the catabolic effect of TNFα on nucleus pulposus cell and alleviates intervertebral disc degeneration *in vivo*. *Front. Pharmacol.* 9, 1043. doi:10.3389/fphar.2018.01043

Liu, X., Kim, C. N., Yang, J., Jemmerson, R., and Wang, X. (1996). Induction of apoptotic program in cell-free extracts: Requirement for dATP and cytochrome c. *Cell* 86, 147–157. doi:10.1016/s0092-8674(00)80085-9

Liu, X. W., Kang, J., Fan, X. D., and Sun, L. F. (2013). Expression and significance of VEGF and p53 in rat degenerated intervertebral disc tissues. *Asian pac. J. Trop. Med.* 6, 404–406. doi:10.1016/s1995-7645(13)60047-4

Lu, K., Li, H. Y., Yang, K., Wu, J. L., Cai, X. W., Zhou, Y., et al. (2017). Exosomes as potential alternatives to stem cell therapy for intervertebral disc degeneration: *In-vitro* study on exosomes in interaction of nucleus pulposus cells and bone marrow mesenchymal stem cells. *Stem Cell Res. Ther.* 8, 108. doi:10.1186/s13287-017-0563-9

Lu, S., and Lin, C. W. (2021). Lentivirus-mediated transfer of gene encoding fibroblast growth factor-18 inhibits intervertebral disc degeneration. *Exp. Ther. Med.* 22, 856. doi:10.3892/etm.2021.10288

Lu, S., Song, Y., Luo, R., Li, S., Li, G., Wang, K., et al. (2021). Ferroportin-dependent iron homeostasis protects against oxidative stress-induced nucleus pulposus cell ferroptosis and ameliorates intervertebral disc degeneration *in vivo*. *Oxid. Med. Cell. Longev.* 2021, 1–18. doi:10.1155/2021/6670497

Luo, L., Jian, X., Sun, H., Qin, J., Wang, Y., Zhang, J., et al. (2021). Cartilage endplate stem cells inhibit intervertebral disc degeneration by releasing exosomes to nucleus pulposus cells to activate Akt/autophagy. *Stem Cells* 39, 467–481. doi:10.1002/stem.3322

Luo, X. W., Liu, K., Chen, Z., Zhao, M., Han, X. W., Bai, Y. G., et al. (2016). Adenovirus-mediated GDF-5 promotes the extracellular matrix expression in degenerative nucleus pulposus cells. *J. Zhejiang Univ. Sci. B* 17, 30–42. doi:10.1631/jzus.b1500182

Malandrino, A., Lacroix, D., Hellmich, C., Ito, K., Ferguson, S. J., and Noailly, J. (2014). The role of endplate poromechanical properties on the nutrient availability in the intervertebral disc. *Osteoarthr. Cartil.* 22, 1053–1060. doi:10.1016/j.joca.2014.05.005

MartíNEZ-LavíN, M. (2021). Dorsal root ganglia: Fibromyalgia pain factory? *Clin. Rheumatol.* 40, 783–787. doi:10.1007/s10067-020-05528-z

May, R. D., Tekari, A., Frauchiger, D. A., Krismer, A., Benneker, L. M., and Gantenbein, B. (2017). Efficient nonviral transfection of primary intervertebral disc cells by electroporation for tissue engineering application. *Tissue Eng. Part C. Methods* 23, 30–37. doi:10.1089/ten.tec.2016.0355

Mccarthy, D. A., Clark, R. R., Bartling, T. R., Trebak, M., and Melendez, J. A. (2013). Redox control of the senescence regulator interleukin-1α and the secretory phenotype. *J. Biol. Chem.* 288, 32149–32159. doi:10.1074/jbc.m113.493841

Mcdonnell, E. E., and Buckley, C. T. (2022). Consolidating and re-evaluating the human disc nutrient microenvironment. *JOR Spine* 5, e1192. doi:10.1002/jsp2.1192

Mern, D. S., and Thomé, C. (2015). Identification and characterization of human nucleus pulposus cell specific serotypes of adeno-associated virus for gene therapeutic approaches of intervertebral disc disorders. *BMC Musculoskelet. Disord.* 16, 341. doi:10.1186/s12891-015-0799-4

Mern, D. S., Tschugg, A., Hartmann, S., and Thomé, C. (2017). Self-complementary adeno-associated virus serotype 6 mediated knockdown of ADAMTS4 induces long-term and effective enhancement of aggrecan in degenerative human nucleus pulposus cells: A new therapeutic approach for intervertebral disc disorders. *PLoS One* 12, e0172181. doi:10.1371/journal.pone.0172181

Mitchell, M. J., Billingsley, M. M., Haley, R. M., Wechsler, M. E., Peppas, N. A., and Langer, R. (2021). Engineering precision nanoparticles for drug delivery. *Nat. Rev. Drug Discov.* 20, 101–124. doi:10.1038/s41573-020-0090-8

Miyagi, M., Millecamps, M., Danco, A. T., Ohtori, S., Takahashi, K., and Stone, L. S. (2014). ISSLS Prize winner: Increased innervation and sensory nervous system plasticity in a mouse model of low back pain due to intervertebral disc degeneration. *Spine (Phila Pa 1976)* 39, 1345–1354. doi:10.1097/brs.0000000000000334

Mohd Isa, I. L., Mokhtar, S. A., Abbah, S. A., Fauzi, M. B., Devitt, A., and Pandit, A. (2022). Intervertebral disc degeneration: Biomaterials and tissue engineering strategies toward precision medicine. *Adv. Healthc. Mat.* 11, e2102530. doi:10.1002/adhm.202102530

Moon, H. J., Yurube, T., Lozito, T. P., Pohl, P., Hartman, R. A., Sowa, G. A., et al. (2014). Effects of secreted factors in culture medium of annulus fibrosus cells on microvascular endothelial cells: Elucidating the possible pathomechanisms of matrix degradation and nerve in-growth in disc degeneration. *Osteoarthr. Cartil.* 22, 344–354. doi:10.1016/j.joca.2013.12.008

Moon, S. H., Gilbertson, L. G., Nishida, K., Knaub, M., Muzzonigro, T., Robbins, P. D., et al. (2000). Human intervertebral disc cells are genetically modifiable by adenovirus-mediated gene transfer: Implications for the clinical management of intervertebral disc disorders. *Spine (Phila Pa 1976)* 25, 2573–2579. doi:10.1097/00007632-200010150-00006

MuñOZ-EspíN, D., and Serrano, M. (2014). Cellular senescence: From physiology to pathology. *Nat. Rev. Mol. Cell Biol.* 15, 482–496. doi:10.1038/nrm3823

Murray, C. J., Vos, T., Lozano, R., Naghavi, M., Flaxman, A. D., Michaud, C., et al. (2012). Disability-adjusted life years (DALYs) for 291 diseases and injuries in 21 regions, 1990-2010: A systematic analysis for the global burden of disease study 2010. *Lancet* 380, 2197–2223. doi:10.1016/s0140-6736(12)61689-4

Negri, V., Pacheco-Torres, J., Calle, D., and LóPEZ-Larrubia, P. (2020). Carbon nanotubes in biomedicine. *Top. Curr. Chem. (Cham).* 378, 15. doi:10.1007/s41061-019-0278-8

Neidlinger-Wilke, C., Galbusera, F., Pratsinis, H., Mavrogonatou, E., Mietsch, A., Kletsas, D., et al. (2014). Mechanical loading of the intervertebral disc: From the macroscopic to the cellular level. *Eur. Spine J.* 23 (3), S333–S343. doi:10.1007/s00586-013-2855-9

Neidlinger-Wilke, C., Mietsch, A., Rinkler, C., Wilke, H. J., Ignatius, A., and Urban, J. (2012). Interactions of environmental conditions and mechanical loads have influence on matrix turnover by nucleus pulposus cells. *J. Orthop. Res.* 30, 112–121. doi:10.1002/jor.21481

Nerurkar, N. L., Elliott, D. M., and Mauck, R. L. (2010). Mechanical design criteria for intervertebral disc tissue engineering. *J. Biomech.* 43, 1017–1030. doi:10.1016/j.jbiomech.2009.12.001

Nguyen, N. T., Milani, A. H., Jennings, J., Adlam, D. J., Freemont, A. J., Hoyland, J. A., et al. (2019). Highly compressive and stretchable poly(ethylene glycol) based hydrogels synthesised using pH-responsive nanogels without free-radical chemistry. *Nanoscale* 11, 7921–7930. doi:10.1039/c9nr01535c

Nishida, K., Doita, M., Takada, T., Kakutani, K., Miyamoto, H., Shimomura, T., et al. (2006). Sustained transgene expression in intervertebral disc cells *in vivo* mediated by microbubble-enhanced ultrasound gene therapy. *Spine (Phila Pa 1976)* 31, 1415–1419. doi:10.1097/01.brs.0000219945.70675.dd

Palmerston Mendes, L., Pan, J., and Torchilin, V. P. (2017). Dendrimers as nanocarriers for nucleic acid and drug delivery in cancer therapy. *Molecules* 22, 1401. doi:10.3390/molecules22091401

Patel, K. P., Sandy, J. D., Akeda, K., Miyamoto, K., Chujo, T., An, H. S., et al. (2007). Aggrecanases and aggrecanase-generated fragments in the human intervertebral disc at early and advanced stages of disc degeneration. *Spine (Phila Pa 1976)* 32, 2596–2603. doi:10.1097/brs.0b013e318158cb85

Paul, C. P., Schoorl, T., Zuiderbaan, H. A., Zandieh Doulabi, B., Van Der Veen, A. J., Van De Ven, P. M., et al. (2013). Dynamic and static overloading induce early degenerative processes in caprine lumbar intervertebral discs. *PLoS One* 8, e62411. doi:10.1371/journal.pone.0062411

Paul, C. P., Zuiderbaan, H. A., Zandieh Doulabi, B., Van Der Veen, A. J., Van De Ven, P. M., Smit, T. H., et al. (2012). Simulated-physiological loading conditions preserve biological and mechanical properties of caprine lumbar intervertebral discs in *ex vivo* culture. *PLoS One* 7, e33147. doi:10.1371/journal.pone.0033147

Peng, B. G. (2013). Pathophysiology, diagnosis, and treatment of discogenic low back pain. *World J. Orthop.* 4, 42–52. doi:10.5312/wjo.v4.i2.42

Pfirrmann, C. W., Metzdorf, A., Zanetti, M., Hodler, J., and Boos, N. (2001). Magnetic resonance classification of lumbar intervertebral disc degeneration. *Spine (Phila Pa 1976)* 26, 1873–1878. doi:10.1097/00007632-200109010-00011

Phillips, K. L., Chiverton, N., Michael, A. L., Cole, A. A., Breakwell, L. M., Haddock, G., et al. (2013a). The cytokine and chemokine expression profile of nucleus pulposus cells: Implications for degeneration and regeneration of the intervertebral disc. *Arthritis Res. Ther.* 15, R213. doi:10.1186/ar4408

Phillips, K. L., Cullen, K., Chiverton, N., Michael, A. L., Cole, A. A., Breakwell, L. M., et al. (2015). Potential roles of cytokines and chemokines in human intervertebral disc degeneration: interleukin-1 is a master regulator of catabolic processes. *Osteoarthr. Cartil.* 23, 1165–1177. doi:10.1016/j.joca.2015.02.017

Phillips, K. L., Jordan-Mahy, N., Nicklin, M. J., and Le Maitre, C. L. (2013b). Interleukin-1 receptor antagonist deficient mice provide insights into pathogenesis of human intervertebral disc degeneration. *Ann. Rheum. Dis.* 72, 1860–1867. doi:10.1136/annrheumdis-2012-202266

Pockert, A. J., Richardson, S. M., Le Maitre, C. L., Lyon, M., Deakin, J. A., Buttle, D. J., et al. (2009). Modified expression of the ADAMTS enzymes and tissue inhibitor of metalloproteinases 3 during human intervertebral disc degeneration. *Arthritis Rheum.* 60, 482–491. doi:10.1002/art.24291

Qian, J., Wang, X., Su, G., Shu, X., Huang, Z., Jiang, H., et al. (2022). Platelet-rich plasma-derived exosomes attenuate intervertebral disc degeneration by promoting NLRP3 autophagic degradation in macrophages. *Int. Immunopharmacol.* 110, 108962. doi:10.1016/j.intimp.2022.108962

Richardson, S. M., Doyle, P., Minogue, B. M., Gnanalingham, K., and Hoyland, J. A. (2009). Increased expression of matrix metalloproteinase-10, nerve growth factor and substance P in the painful degenerate intervertebral disc. *Arthritis Res. Ther.* 11, R126. doi:10.1186/ar2793

Rideau, E., Dimova, R., Schwille, P., Wurm, F. R., and Landfester, K. (2018). Liposomes and polymersomes: A comparative review towards cell mimicking. *Chem. Soc. Rev.* 47, 8572–8610. doi:10.1039/c8cs00162f

Risbud, M. V., and Shapiro, I. M. (2014). Role of cytokines in intervertebral disc degeneration: Pain and disc content. *Nat. Rev. Rheumatol.* 10, 44–56. doi:10.1038/nrrheum.2013.160

Roberts, S., Urban, J. P., Evans, H., and Eisenstein, S. M. (1996). Transport properties of the human cartilage endplate in relation to its composition and calcification. *Spine (Phila Pa 1976)* 21, 415–420. doi:10.1097/00007632-199602150-00003

Roh, E. J., Darai, A., Kyung, J. W., Choi, H., Kwon, S. Y., Bhujel, B., et al. (2021). Genetic therapy for intervertebral disc degeneration. *Int. J. Mol. Sci.* 22, 1579. doi:10.3390/ijms22041579

Roughley, P. J., Melching, L. I., Heathfield, T. F., Pearce, R. H., and Mort, J. S. (2006). The structure and degradation of aggrecan in human intervertebral disc. *Eur. Spine J.* 15 (3), S326–S332. doi:10.1007/s00586-006-0127-7

Rutges, J. P., Duit, R. A., Kummer, J. A., Bekkers, J. E., Oner, F. C., Castelein, R. M., et al. (2013). A validated new histological classification for intervertebral disc degeneration. *Osteoarthr. Cartil.* 21, 2039–2047. doi:10.1016/j.joca.2013.10.001

Sato, K., Kikuchi, S., and Yonezawa, T. (1999). *In vivo* intradiscal pressure measurement in healthy individuals and in patients with ongoing back problems. *Spine (Phila Pa 1976)* 24, 2468–2474. doi:10.1097/00007632-199912010-00008

Schmitt, C., Radetzki, F., Stirnweiss, A., Mendel, T., Ludtka, C., Friedmann, A., et al. (2021). Long-term pre-clinical evaluation of an injectable chitosan nanocellulose hydrogel with encapsulated adipose-derived stem cells in an ovine model for IVD regeneration. *J. Tissue Eng. Regen. Med.* 15, 660–673. doi:10.1002/term.3216

Schneider, M. C., Lalitha Sridhar, S., Vernerey, F. J., and Bryant, S. J. (2020). Spatiotemporal neocartilage growth in matrix-metalloproteinase-sensitive poly(ethylene glycol) hydrogels under dynamic compressive loading: An experimental and computational approach. *J. Mat. Chem. B* 8, 2775–2791. doi:10.1039/c9tb02963j

Schneider, P., Thome, M., Burns, K., Bodmer, J. L., Hofmann, K., Kataoka, T., et al. (1997). TRAIL receptors 1 (DR4) and 2 (DR5) signal FADD-dependent apoptosis and activate NF-κB. *Immunity* 7, 831–836. doi:10.1016/s1074-7613(00)80401-x

Scott, J. E., Bosworth, T. R., Cribb, A. M., and Taylor, J. R. (1994). The chemical morphology of age-related changes in human intervertebral disc glycosaminoglycans from cervical, thoracic and lumbar nucleus pulposus and annulus fibrosus. *J. Anat.* 184 (1), 73–82.

SéGUIN, C. A., Pilliar, R. M., Roughley, P. J., and Kandel, R. A. (2005). Tumor necrosis factor-alpha modulates matrix production and catabolism in nucleus pulposus tissue. *Spine (Phila Pa 1976)* 30, 1940–1948. doi:10.1097/01.brs.0000176188.40263.f9

Sercombe, L., Veerati, T., Moheimani, F., Wu, S. Y., Sood, A. K., and Hua, S. (2015). Advances and challenges of liposome assisted drug delivery. *Front. Pharmacol.* 6, 286. doi:10.3389/fphar.2015.00286

Shalash, W., Ahrens, S. R., Bardonova, L. A., Byvaltsev, V. A., and Giers, M. B. (2021). Patient-specific apparent diffusion maps used to model nutrient availability in degenerated intervertebral discs. *JOR Spine* 4, e1179. doi:10.1002/jsp2.1179

Shamsah, A. H., Cartmell, S. H., Richardson, S. M., and Bosworth, L. A. (2019). Mimicking the annulus fibrosus using electrospun polyester blended scaffolds. *Nanomater. (Basel)* 9, 537. doi:10.3390/nano9040537

Sher, I., Daly, C., Oehme, D., Chandra, R. V., Sher, M., Ghosh, P., et al. (2019). Novel application of the pfirrmann disc degeneration grading system to 9.4T MRI: Higher reliability compared to 3T MRI. *Spine (Phila Pa 1976)* 44, E766–e773. doi:10.1097/brs.0000000000002967

Shi, C., Wu, L., Lin, W., Cai, Y., Zhang, Y., Hu, B., et al. (2019). MiR-202-3p regulates interleukin-1β-induced expression of matrix metalloproteinase 1 in human nucleus pulposus. *Gene* 687, 156–165. doi:10.1016/j.gene.2018.11.056

Sizikov, A. A., Kharlamova, M. V., Nikitin, M. P., Nikitin, P. I., and Kolychev, E. L. (2021). Nonviral locally injected magnetic vectors for *in vivo* gene delivery: A review of studies on magnetofection. *Nanomater. (Basel)* 11 (5), 1078. doi:10.3390/nano11051078

Skaalure, S. C., Chu, S., and Bryant, S. J. (2015). An enzyme-sensitive PEG hydrogel based on aggrecan catabolism for cartilage tissue engineering. *Adv. Healthc. Mat.* 4, 420–431. doi:10.1002/adhm.201400277

Sobajima, S., Shimer, A. L., Chadderdon, R. C., Kompel, J. F., Kim, J. S., Gilbertson, L. G., et al. (2005). Quantitative analysis of gene expression in a rabbit model of intervertebral disc degeneration by real-time polymerase chain reaction. *Spine J.* 5, 14–23. doi:10.1016/j.spinee.2004.05.251

Su, Y., Xu, C., Sun, Z., Liang, Y., Li, G., Tong, T., et al. (2019). S100A13 promotes senescence-associated secretory phenotype and cellular senescence via modulation of non-classical secretion of IL-1α. *Aging (Albany NY)* 11, 549–572. doi:10.18632/aging.101760

Su, Y., Zhang, B., Sun, R., Liu, W., Zhu, Q., Zhang, X., et al. (2021). PLGA-Based biodegradable microspheres in drug delivery: Recent advances in research and application. *Drug Deliv. (Lond).* 28, 1397–1418. doi:10.1080/10717544.2021.1938756

Sun, B., Lian, M., Han, Y., Mo, X., Jiang, W., Qiao, Z., et al. (2021a). A 3D-Bioprinted dual growth factor-releasing intervertebral disc scaffold induces nucleus pulposus and annulus fibrosus reconstruction. *Bioact. Mat.* 6, 179–190. doi:10.1016/j.bioactmat.2020.06.022

Sun, Z., Zhao, H., Liu, B., Gao, Y., Tang, W. H., Liu, Z. H., et al. (2021b). AF cell derived exosomes regulate endothelial cell migration and inflammation: Implications for vascularization in intervertebral disc degeneration. *Life Sci.* 265, 118778. doi:10.1016/j.lfs.2020.118778

Tan, H., Jin, D., Qu, X., Liu, H., Chen, X., Yin, M., et al. (2019). A PEG-Lysozyme hydrogel harvests multiple functions as a fit-to-shape tissue sealant for internal-use of body. *Biomaterials* 192, 392–404. doi:10.1016/j.biomaterials.2018.10.047

Tang, G., Han, X., Lin, Z., Qian, H., Chen, B., Zhou, C., et al. (2021a). Propionibacterium acnes accelerates intervertebral disc degeneration by inducing pyroptosis of nucleus pulposus cells via the ROS-NLRP3 pathway. *Oxid. Med. Cell. Longev.* 2021, 1–12. doi:10.1155/2021/4657014

Tang, L., Xiao, Q., Mei, Y., He, S., Zhang, Z., Wang, R., et al. (2021b). Insights on functionalized carbon nanotubes for cancer theranostics. *J. Nanobiotechnology* 19, 423. doi:10.1186/s12951-021-01174-y

Tang, S., Salazar-Puerta, A., Richards, J., Khan, S., Hoyland, J. A., Gallego-Perez, D., et al. (2021c). Non-viral reprogramming of human nucleus pulposus cells with FOXF1 via extracellular vesicle delivery: An *in vitro* and *in vivo* study. *Eur. Cell. Mat.* 41, 90–107. doi:10.22203/ecm.v041a07

Tang, Y., Wang, S., Liu, Y., and Wang, X. (2014). Microarray analysis of genes and gene functions in disc degeneration. *Exp. Ther. Med.* 7, 343–348. doi:10.3892/etm.2013.1421

Tuakli-Wosornu, Y. A., Terry, A., Boachie-Adjei, K., Harrison, J. R., Gribbin, C. K., Lasalle, E. E., et al. (2016). Lumbar intradiskal platelet-rich plasma (PRP) injections: A prospective, double-blind, randomized controlled study. *PM&R.* 8, 1–10. quiz 10. doi:10.1016/j.pmrj.2015.08.010

Urban, J. P., and Mcmullin, J. F. (1988). Swelling pressure of the lumbar intervertebral discs: Influence of age, spinal level, composition, and degeneration. *Spine (Phila Pa 1976)* 13, 179–187. doi:10.1097/00007632-198802000-00009

Vashist, A., Kaushik, A., Vashist, A., Sagar, V., Ghosal, A., Gupta, Y. K., et al. (2018). Advances in carbon nanotubes-hydrogel hybrids in nanomedicine for therapeutics. *Adv. Healthc. Mat.* 7, e1701213. doi:10.1002/adhm.201701213

Vergroesen, P. P., Van Der Veen, A. J., Van Royen, B. J., Kingma, I., and Smit, T. H. (2014). Intradiscal pressure depends on recent loading and correlates with disc height and compressive stiffness. *Eur. Spine J.* 23, 2359–2368. doi:10.1007/s00586-014-3450-4

Vlaeyen, J. W. S., Maher, C. G., Wiech, K., Van Zundert, J., Meloto, C. B., Diatchenko, L., et al. (2018). Low back pain. *Nat. Rev. Dis. Prim.* 4, 52. doi:10.1038/s41572-018-0052-1

Vo, N. V., Hartman, R. A., Yurube, T., Jacobs, L. J., Sowa, G. A., and Kang, J. D. (2013). Expression and regulation of metalloproteinases and their inhibitors in intervertebral disc aging and degeneration. *Spine J.* 13, 331–341. doi:10.1016/j.spinee.2012.02.027

Wallach, C. J., Kim, J. S., Sobajima, S., Lattermann, C., Oxner, W. M., Mcfadden, K., et al. (2006). Safety assessment of intradiscal gene transfer: A pilot study. *Spine J.* 6, 107–112. doi:10.1016/j.spinee.2005.05.002

Walsh, A. J., and Lotz, J. C. (2004). Biological response of the intervertebral disc to dynamic loading. *J. Biomech.* 37, 329–337. doi:10.1016/s0021-9290(03)00290-2

Wang, C., Gonzales, S., Levene, H., Gu, W., and Huang, C. Y. (2013). Energy metabolism of intervertebral disc under mechanical loading. *J. Orthop. Res.* 31, 1733–1738. doi:10.1002/jor.22436

Wang, D. L., Jiang, S. D., and Dai, L. Y. (2007). Biologic response of the intervertebral disc to static and dynamic compression *in vitro*. *Spine (Phila Pa 1976)* 32, 2521–2528. doi:10.1097/brs.0b013e318158cb61

Wang, D., Tai, P. W. L., and Gao, G. (2019a). Adeno-associated virus vector as a platform for gene therapy delivery. *Nat. Rev. Drug Discov.* 18, 358–378. doi:10.1038/s41573-019-0012-9

Wang, H., Ding, Y., Zhang, W., Wei, K., Pei, Y., Zou, C., et al. (2020a). <p>Oxymatrine liposomes for intervertebral disc treatment: Formulation, *in vitro* and vivo assessments</p>. *Drug Des. devel. Ther.* 14, 921–931. doi:10.2147/dddt.s242493

Wang, J., Markova, D., Anderson, D. G., Zheng, Z., Shapiro, I. M., and Risbud, M. V. (2011). TNF-α and IL-1β promote a disintegrin-like and metalloprotease with thrombospondin type I motif-5-mediated aggrecan degradation through syndecan-4 in intervertebral disc. *J. Biol. Chem.* 286, 39738–39749. doi:10.1074/jbc.m111.264549

Wang, K., Chen, T., Ying, X., Zhang, Z., Shao, Z., Lin, J., et al. (2019b). Ligustilide alleviated IL-1β induced apoptosis and extracellular matrix degradation of nucleus pulposus cells and attenuates intervertebral disc degeneration *in vivo*. *Int. Immunopharmacol.* 69, 398–407. doi:10.1016/j.intimp.2019.01.004

Wang, K., Sun, Q., Zhong, X., Zeng, M., Zeng, H., Shi, X., et al. (2020b). Structural mechanism for GSDMD targeting by autoprocessed caspases in pyroptosis. *Cell* 180, 941–955.e20. e20. doi:10.1016/j.cell.2020.02.002

Wang, L., Niu, X., Song, Q., Jia, J., Hao, Y., Zheng, C., et al. (2020c). A two-step precise targeting nanoplatform for tumor therapy via the alkyl radicals activated by

the microenvironment of organelles. *J. Control. Release* 318, 197–209. doi:10.1016/j.jconrel.2019.10.017

Wang, Y., Videman, T., and Battié, M. C. (2012). Lumbar vertebral endplate lesions: Prevalence, classification, and association with age. *Spine (Phila Pa 1976)* 37, 1432–1439. doi:10.1097/brs.0b013e31824dd20a

Wehling, P., Schulitz, K. P., Robbins, P. D., Evans, C. H., and Reinecke, J. A. (1997). Transfer of genes to chondrocytic cells of the lumbar spine. Proposal for a treatment strategy of spinal disorders by local gene therapy. *Spine (Phila Pa 1976)* 22, 1092–1097. doi:10.1097/00007632-199705150-00008

Wei, F., Zhong, R., Zhou, Z., Wang, L., Pan, X., Cui, S., et al. (2014). *In vivo* experimental intervertebral disc degeneration induced by bleomycin in the rhesus monkey. *BMC Musculoskelet. Disord.* 15, 340. doi:10.1186/1471-2474-15-340

Wei, X., Gong, C., Gou, M., Fu, S., Guo, Q., Shi, S., et al. (2009). Biodegradable poly(ε-caprolactone)–poly(ethylene glycol) copolymers as drug delivery system. *Int. J. Pharm. X.* 381, 1–18. doi:10.1016/j.ijpharm.2009.07.033

Weiler, C., Nerlich, A. G., Zipperer, J., Bachmeier, B. E., and Boos, N. (2002). 2002 SSE award competition in basic science: Expression of major matrix metalloproteinases is associated with intervertebral disc degradation and resorption. *Eur. Spine J.* 11, 308–320. doi:10.1007/s00586-002-0472-0

Wilke, H. J., Neef, P., Caimi, M., Hoogland, T., and Claes, L. E. (1999). New *in vivo* measurements of pressures in the intervertebral disc in daily life. *Spine (Phila Pa 1976)* 24, 755–762. doi:10.1097/00007632-199904150-00005

Wu, J., Wang, D., Ruan, D., He, Q., Zhang, Y., Wang, C., et al. (2014). Prolonged expansion of human nucleus pulposus cells expressing human telomerase reverse transcriptase mediated by lentiviral vector. *J. Orthop. Res.* 32, 159–166. doi:10.1002/jor.22474

Wu, Y., Cisewski, S. E., Wegner, N., Zhao, S., Pellegrini, V. D., Slate, E. H., et al. (2016). Region and strain-dependent diffusivities of glucose and lactate in healthy human cartilage endplate. *J. Biomech.* 49, 2756–2762. doi:10.1016/j.jbiomech.2016.06.008

Wuertz, K., Godburn, K., Maclean, J. J., Barbir, A., Donnelly, J. S., Roughley, P. J., et al. (2009). *In vivo* remodeling of intervertebral discs in response to short- and long-term dynamic compression. *J. Orthop. Res.* 27, 1235–1242. doi:10.1002/jor.20867

Xie, J., Li, B., Zhang, P., Wang, L., Lu, H., and Song, X. (2018). Osteogenic protein-1 attenuates the inflammatory cytokine-induced NP cell senescence through regulating the ROS/NF-κB pathway. *Biomed. Pharmacother.* 99, 431–437. doi:10.1016/j.biopha.2018.01.053

Xing, H., Zhang, Z., Mao, Q., Wang, C., Zhou, Y., Zhou, X., et al. (2021). Injectable exosome-functionalized extracellular matrix hydrogel for metabolism balance and pyroptosis regulation in intervertebral disc degeneration. *J. Nanobiotechnology* 19, 264. doi:10.1186/s12951-021-00991-5

Xu, H., Mei, Q., He, J., Liu, G., Zhao, J., and Xu, B. (2014a). Correlation of matrix metalloproteinases-1 and tissue inhibitor of metalloproteinases-1 with patient age and grade of lumbar disk herniation. *Cell biochem. Biophys.* 69, 439–444. doi:10.1007/s12013-014-9815-9

Xu, H., Mei, Q., Xu, B., Liu, G., and Zhao, J. (2014b). Expression of matrix metalloproteinases is positively related to the severity of disc degeneration and growing age in the East Asian lumbar disc herniation patients. *Cell biochem. Biophys.* 70, 1219–1225. doi:10.1007/s12013-014-0045-y

Xu, P., Guan, J., Chen, Y., Xiao, H., Yang, T., Sun, H., et al. (2021). Stiffness of photocrosslinkable gelatin hydrogel influences nucleus pulposus cell properties*in vitro*. *J. Cell. Mol. Med.* 25, 880–891. doi:10.1111/jcmm.16141

Yang, M., Peng, Y., Liu, W., Zhou, M., Meng, Q., and Yuan, C. (2019). Sirtuin 2 expression suppresses oxidative stress and senescence of nucleus pulposus cells through inhibition of the p53/p21 pathway. *Biochem. Biophys. Res. Commun.* 513, 616–622. doi:10.1016/j.bbrc.2019.03.200

Yu, W., Fu, J., Liu, Y., Wu, Y., and Jiang, D. (2018). Osteogenic protein-1 inhibits nucleus pulposus cell apoptosis through regulating the NF-κB/ROS pathway in an inflammation environment. *Biosci. Rep.* 38, BSR20181530. doi:10.1042/bsr20181530

Yurube, T., Takada, T., Suzuki, T., Kakutani, K., Maeno, K., Doita, M., et al. (2012). Rat tail static compression model mimics extracellular matrix metabolic imbalances of matrix metalloproteinases, aggrecanases, and tissue inhibitors of metalloproteinases in intervertebral disc degeneration. *Arthritis Res. Ther.* 14, R51. doi:10.1186/ar3764

Zhang, J., Tong, D., Song, H., Ruan, R., Sun, Y., Lin, Y., et al. (2022a). Osteoimmunity-regulating biomimetically hierarchical scaffold for augmented bone regeneration. *Adv. Mat.* 34, e2202044. doi:10.1002/adma.202202044

Zhang, Q., Huang, M., Wang, X., Xu, X., Ni, M., and Wang, Y. (2012). Negative effects of ADAMTS-7 and ADAMTS-12 on endplate cartilage differentiation. *J. Orthop. Res.* 30, 1238–1243. doi:10.1002/jor.22069

Zhang, X., Wan, H., Lan, W., Miao, F., Qin, M., Wei, Y., et al. (2022b). Fabrication of adhesive hydrogels based on poly (acrylic acid) and modified hyaluronic acid. *J. Mech. Behav. Biomed. Mat.* 126, 105044. doi:10.1016/j.jmbbm.2021.105044

Zhao, C. Q., Wang, L. M., Jiang, L. S., and Dai, L. Y. (2007). The cell biology of intervertebral disc aging and degeneration. *Ageing Res. Rev.* 6, 247–261. doi:10.1016/j.arr.2007.08.001

Zhao, D., Zhu, T., Li, J., Cui, L., Zhang, Z., Zhuang, X., et al. (2021a). Poly(lactic-co-glycolic acid)-based composite bone-substitute materials. *Bioact. Mat.* 6, 346–360. doi:10.1016/j.bioactmat.2020.08.016

Zhao, K., An, R., Xiang, Q., Li, G., Wang, K., Song, Y., et al. (2021b). Acid-sensing ion channels regulate nucleus pulposus cell inflammation and pyroptosis via the NLRP3 inflammasome in intervertebral disc degeneration. *Cell Prolif.* 54, e12941. doi:10.1111/cpr.12941

Zheng, K., and Du, D. (2021). Recent advances of hydrogel-based biomaterials for intervertebral disc tissue treatment: A literature review. *J. Tissue Eng. Regen. Med.* 15, 299–321. doi:10.1002/term.3172

Zheng, Y., Liu, C., Ni, L., Liu, Z., Mirando, A. J., Lin, J., et al. (2018). Cell type-specific effects of Notch signaling activation on intervertebral discs: Implications for intervertebral disc degeneration. *J. Cell. Physiol.* 233, 5431–5440. doi:10.1002/jcp.26385

Zhou, X., Hou, C., Chang, T. L., Zhang, Q., and Liang, J. F. (2020). Controlled released of drug from doubled-walled PVA hydrogel/PCL microspheres prepared by single needle electrospraying method. *Colloids Surfaces B Biointerfaces* 187, 110645. doi:10.1016/j.colsurfb.2019.110645

Zhu, M., Tan, J., Liu, L., Tian, J., Li, L., Luo, B., et al. (2021). Construction of biomimetic artificial intervertebral disc scaffold via 3D printing and electrospinning. *Mater. Sci. Eng. C* 128, 112310. doi:10.1016/j.msec.2021.112310

Zhu, T., Cui, Y., Zhang, M., Zhao, D., Liu, G., and Ding, J. (2020). Engineered three-dimensional scaffolds for enhanced bone regeneration in osteonecrosis. *Bioact. Mat.* 5, 584–601. doi:10.1016/j.bioactmat.2020.04.008

Zhu, T., Jiang, M., Zhang, M., Cui, L., Yang, X., Wang, X., et al. (2022a). Biofunctionalized composite scaffold to potentiate osteoconduction, angiogenesis, and favorable metabolic microenvironment for osteonecrosis therapy. *Bioact. Mat.* 9, 446–460. doi:10.1016/j.bioactmat.2021.08.005

Zhu, T., Jiang, M., Zhang, M., Cui, L., Yang, X., Wang, X., et al. (2022b). Construction and validation of steroid-induced rabbit osteonecrosis model. *MethodsX* 9, 101713. doi:10.1016/j.mex.2022.101713

Zhu, Y., Jia, H., Li, J., Ren, S., Huang, Z., Li, F., et al. (2018). Associations between variants in BDNF/BDNFOS gene and lumbar disc herniation risk among han Chinese people. *Sci. Rep.* 8, 12782. doi:10.1038/s41598-018-31146-6

Zobel, B. B., Vadalà, G., Del Vescovo, R., Battisti, S., Martina, F. M., Stellato, L., et al. (2012). T1ρ magnetic resonance imaging quantification of early lumbar intervertebral disc degeneration in healthy young adults. *Spine (Phila Pa 1976)* 37, 1224–1230. doi:10.1097/brs.0b013e31824b2450

frontiers | Frontiers in Bioengineering and Biotechnology

TYPE Original Research
PUBLISHED 14 November 2022
DOI 10.3389/fbioe.2022.1067111

OPEN ACCESS

EDITED BY
Mingqiang Li,
Third Affiliated Hospital of Sun Yat-sen University, China

REVIEWED BY
Lele Li,
Baylor College of Medicine, United States
Yi Xu,
The University of Texas Health Science Center at San Antonio, United States
Xiaonan Deng,
Georgia State University, United States

*CORRESPONDENCE
Meiyan Sun,
sunmy990@163.com
Jieqiong Lin,
linjieqiong@ccut.edu.cn

†These authors have contributed equally to this work

SPECIALTY SECTION
This article was submitted to Biomaterials, a section of the journal Frontiers in Bioengineering and Biotechnology

RECEIVED 11 October 2022
ACCEPTED 31 October 2022
PUBLISHED 14 November 2022

CITATION
Fu H, Yu B, Wang H, Tong H, Jiang L, Zhang Y, Meng G, Sun M and Lin J (2022), Knowledge domain and hotspots concerning photosensitive hydrogels for tissue engineering applications: A bibliometric and visualized analysis (1996-2022). *Front. Bioeng. Biotechnol.* 10:1067111. doi: 10.3389/fbioe.2022.1067111

Knowledge domain and hotspots concerning photosensitive hydrogels for tissue engineering applications: A bibliometric and visualized analysis (1996-2022)

Hongxun Fu[1†], Baojun Yu[1], Hao Wang[2], Haibin Tong[3], Lin Jiang[2], Yupeng Zhang[4], Guixian Meng[2], Meiyan Sun[2*] and Jieqiong Lin[1*]

[1]Key Laboratory of Micro/Nano and Ultra-precision Manufacturing, Jilin Province, School of Mechatronic Engineering, Changchun University of Technology, Changchun, China, [2]College of Laboratory Medicine, Jilin Medical University, Jilin, China, [3]College of Life and Environmental Science, Wenzhou University, Wenzhou, China, [4]Affiliated Hospital of Beihua University, Jilin, China

Objective: The aim of tissue engineering (TE) is to replace the damaged tissues or failed organs, or restore their missing functions. The important means to achieve this aim is to integrate biomaterials and life elements. Hydrogels are very attractive biomaterials in the field of TE. In particular, engineering extracellular matrices (ECMs) formed by photosensitive hydrogels have captivated much attention, because photopolymerization has many advantages over traditional polymerization approaches, such as rapidity of reaction, spatiotemporal controllability of polymerization process, and operability at physiological temperature, especially it can realize the fabrications of engineering ECMs in the presence of living cells. There have been many excellent reviews on the applications of photosensitive hydrogels in TE in recent years, however, it is inevitable that researchers may have left out many important facts due to exploring the literature from one or a few aspects. It is also a great challenge for researchers to explore the internal relationships among countries, institutions, authors, and references from a large number of literatures in related fields. Therefore, bibliometrics may be a powerful tool to solve the above problems. A bibliometric and visualized analysis of publications concerning the photosensitive hydrogels for TE applications was performed, and the knowledge domain, research hotspots and frontiers in this topic were identified according to the analysis results.

Methods: We identified and retrieved the publications regarding the photosensitive hydrogels for TE applications between 1996 and 2022 from Web of Science Core Collection (WoSCC). Bibliometric and visualized analysis employing CiteSpace software and R-language package Bibliometrix were performed in this study.

Results: 778 publications meeting the eligibility criteria were identified and retrieved from WoSCC. Among those, 2844 authors worldwide participated in the studies in this field, accompanied by an average annual article growth rate of

15.35%. The articles were co-authored by 800 institutions from 46 countries/regions, and the United States published the most, followed by China and South Korea. As the two countries that published the most papers, the United States and China could further strengthen cooperation in this field. Univ Colorado published the most articles (*n* = 150), accounting for 19.28% of the total. The articles were distributed in 112 journals, among which Biomaterials (*n* = 66) published the most articles, followed by Acta Biomaterialia (*n* = 54) and Journal of Biomedical Materials Research Part A (*n* = 42). The top 10 journals published 47.8% of the 778 articles. The most prolific author was Anseth K (*n* = 33), followed by Khademhosseini A (*n* = 29) and Bryant S (*n* = 22). A total of 1443 keywords were extracted from the 778 articles and the keyword with the highest centrality was "extracellular matrix" (centrality: 0.12). The keywords appeared recently with strong citation bursts were "gelatin", "3d printing" and "3d bioprinting", representing the current research hotspots in this field. "Gelma", "3d printing" and "thiol-ene" were the research frontiers in recent years.

Conclusion: This bibliometric and visualized study offered a comprehensive understanding of publications regarding the photosensitive hydrogels for TE applications from 1996 to 2022, including the knowledge domain, research hotspots and frontiers in this filed. The outcome of this study would provide insights for scholars in the related research filed.

KEYWORDS

photosensitive hydrogels, tissue engineering, bibliometrics, bibliometrix, citespace

Introduction

The aim of tissue engineering (TE) is to replace the damaged tissues or failed organs, or restore their missing functions (Mooney and Langer 2000; Ratner and Bryant, 2004). The important means to achieve this aim is to integrate biomaterials and life elements (seed cells and growth factor) (Mikos et al., 2006; Qin et al., 2014). The tissue substitutes, wound dressings, or substrates for TE all put forward various requirements for biomaterials. In particular, the engineering extracellular matrices (ECMs), or the mimics of the microenvironment for cell growth, and 3D cell culture models, are usually called the tissue engineering scaffolds, which interact with cells as ECMs before forming new tissues (Yao et al., 2013; Jafari et al., 2017; Jing et al., 2022). TE scaffold is the crux to achieve the goal of TE (Langer and Vacanti 1993; Wu et al., 2020). In order to provide engineering ECMs for cells to produce new tissues, scaffolds have to possess biocompatibility, proper degradability, reasonable mechanical properties, and sufficient porosity and pore connectivity (Zhang et al., 2019). In addition, integrating different functions such as hydrophilicity, biological and physical cues could promote the formation of new tissues (Jing et al., 2022). Hydrogels are three-dimensional (3D) natural or synthetic crosslinked networks composed of polymerization chains formed by hydrophilic monomers or macromers (Qin et al., 2014; Gholamali and Yadollahi 2021). Due to the ability to simulate many properties of natural ECMs, hydrogels have been widely used in biomedical fields, such as drug delivery and tissue engineering (Fu et al., 2022; Jing et al., 2022). Especially for TE, hydrogel scaffolds have captivated much attention because they provide cells with not only the mechanical supports but also the interconnected pores for permeating nutrients, oxygen and metabolite (Qin et al., 2014). In addition, the physical properties of hydrogels can be adjusted and they can be functionalized to meet the requirements of different tissues (Qin et al., 2014; Zhao et al., 2020). Hydrogels can be obtained by many polymerization strategies such as heat and redox, however, photochemistry is the most interesting to researchers in this field (Qin et al., 2014; Zhang et al., 2019). Photoinitiator(PI) molecules in the photosensitive hydrogel precursors absorb photons to produce free radicals, which then initiate radical polymerization and constitute crosslinked hydrogel networks. Photon absorption of PIs can be either single photon or multi photons (Jing et al., 2022). Photopolymerization has many advantages over traditional polymerization approaches, such as rapidity of reaction, spatiotemporal controllability of polymerization process, operability at physiological temperature, etc., especially it can realize scaffold fabrications in the presence of living cells (Qin et al., 2014).

Since the photosensitive hydrogels applied in TE were first described in 1996, they have shown a very promising potential in this field. There have been many excellent reviews on the applications of photosensitive hydrogels in TE in recent years, however, it is inevitable that researchers may have left out many important facts due to exploring the literature from one or a few aspects. It is also a great challenge for researchers to explore the internal relationships among countries, institutions, authors, and

references from a large number of literatures in related fields. Therefore, bibliometrics may be a powerful tool to solve the above problems.

As a statistical method combining quantitative and qualitative analysis, bibliometrics explores literature from multiple aspects, such as countries, institutions, journals, authors, keywords and cited literature, to identify the knowledge base, hotspots, frontiers, development trends of related research fields, and relationships between specific research areas. (Chen 2004; Chen 2017; Zhang et al., 2021; Fu et al., 2022). With the continuous development of this discipline, bibliometrics has creatively visualized the information regarding the publications to form network maps, which assist researchers in intuitively grasping the important connotation and denotation implied in the literature (Ellegaard and Wallin 2015; Gonzalez-Alcaide et al., 2017). Bibliometrics has extended to analyze a multitude of scientific research fields, and has obtained a lot of achievements (Ugolini et al., 2010; Wei et al., 2016; Ke et al., 2020; Gu et al., 2021; Shi et al., 2021). However, the bibliometric study for photosensitive hydrogels is still lacking, especially their applications in TE.

In this article, we conducted bibliometric and visualized study using bibliometrics software CiteSpace and the R-language package Bibliometrix to analyze the retrieved publications worldwide regarding the applications of photosensitive hydrogels for TE, and the knowledge domain, research hotspots and frontiers in this topic were identified according to the analysis results.

Materials and methods

Data source and search strategy

We performed a targeted search of literature in Web of Science Core Collection (WoSCC) in the field of photosensitive hydrogels applications for TE from 1 January 1996 (the first year photosensitive hydrogels for TE were reported) to 1 October 2022 (end date of the search). WoSCC is a very commonly used database for bibliometric analysis. Following concepts were used to conduct the queries: (((TS= (photopolymeriz* hydrogel*)) OR TS= (photocrosslink* hydrogel*)) OR TS= (photosensitive hydrogel*)) AND TS= ("tissue engineer*") and the English literature types were filtered as "article". The qualified literature was selected for further bibliometric analysis, and the exported record content was "full record and cited references". After removing duplicates, topics were screened for any mention of photosensitive hydrogels for TE applications by independent reviewers. All literature search and information extraction work were completed continuously within one day to avoid data deviation due to date change.

Statistical analysis

CiteSpace (version 6.1. R3), and the R-language package Bibliometrix 4.2.1 were used to conduct the bibliometric and visualized analysis in this study. Information was extracted and analyzed by automatic algorithm and machine intelligence of bibliometrics software.

Bibliometrix is an R-language tool for comprehensive science mapping analysis. It has superior flexibility and can be facilely upgraded and operated (Aria and Cuccurullo, 2017). Using Bibliometrix, we obtained the data of overall information, trend topics, cited references, landmark literature regarding the publications of the research field, and conducted countries analysis, journals analysis, institutions analysis and authors productivity analysis.

CiteSpace is an analysis software developed for bibliometrics, which can be utilized to analyze the knowledge base, research content, hotpots and frontiers of specific research fields by visualizing network maps (Chen 2004; Chen and Leydesdorff 2014). In this article, CiteSpace was used to obtain dual-map overlay of citations and perform the analysis for keywords, references, clusters, and the collaboration relationships among countries and institutions. It is noteworthy to mention that modularity Q and mean silhouette value are two vital evaluation indicators regarding clustering analysis. When the values of these two indicators are greater than 0.3 and 0.5 respectively, the clustering results are considered to be reliable and significant.

Results

Overall information of publications

We identified and retrieved 778 publications in total met the eligibility criteria from WoSCC. Figure 1A shows the main information of the publications regarding the applications of photosensitive hydrogels for TE. As can be seen from this figure, 2844 authors worldwide participated in the studies in this field we analyzed, accompanied by an average annual article growth rate of 15.35%. Meanwhile, we could confirm that photosensitive hydrogels applications for TE is a relatively new research field due to the 7.79 years of publication average age. As shown in Figure 1B, the number of annual publications generally increased in a time-dependent manner since 1996 which peaked in year 2021. Especially in the past decade, the number of publications in this field showed a rapid growth trend, accounting for 63.75% of the total. The annual scientific production map (Figure 1B) shows that 60 articles were expected to be published in 2022.

FIGURE 1
Main information **(A)** and annual scientific production **(B)** of publications concerning the photosensitive hydrogels for TE applications.

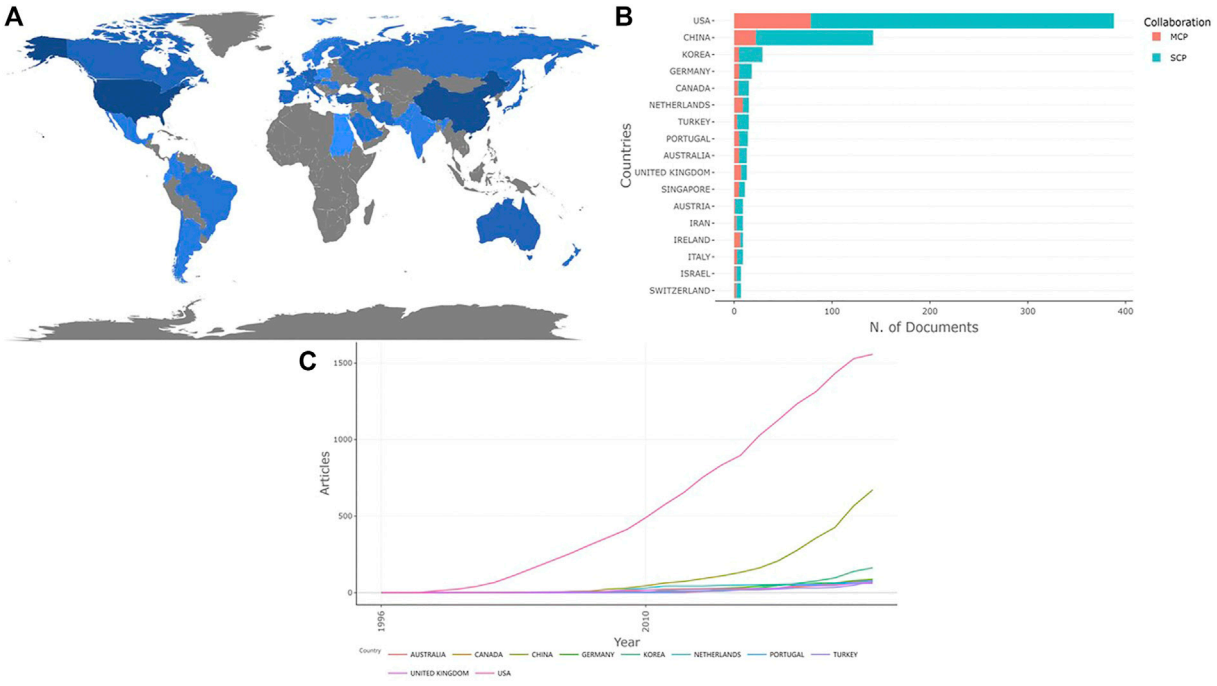

FIGURE 2
Contributions of different countries related to the research of photosensitive hydrogels for TE applications. **(A)** Global country scientific production contributions (The depth of color represents the number of articles published); **(B)** Top 10 countries with the most artilcles related to photosensitive hydrogels for TE applications (based on the countries where the corresponding authors come from); **(C)** Production of the top 10 countries with the highest productivity over time.

TABLE 1 Top 10 countries with the most publications related to photosensitive hydrogels for TE applications (based on the countries where the corresponding authors come from).

Country	Articles	SCP	MCP	Freq	MCP Ratio	Average article citations
USA	388	310	78	0.499	0.201	101.99
CHINA	142	120	22	0.183	0.155	29.92
KOREA	29	24	5	0.037	0.172	33.31
GERMANY	18	13	5	0.023	0.278	54.56
CANADA	15	11	4	0.019	0.267	45.13
NETHERLANDS	15	6	9	0.019	0.6	117.67
TURKEY	15	12	3	0.019	0.2	26.20
PORTUGAL	14	9	5	0.018	0.357	34.57
AUSTRALIA	13	8	5	0.017	0.385	57.00
UNITED KINGDOM	13	6	7	0.017	0.538	38.23
SINGAPORE	11	6	5	0.014	0.455	37.91
AUSTRIA	9	8	1	0.012	0.111	57.67
IRAN	9	7	2	0.012	0.222	24.00
IRELAND	9	3	6	0.012	0.667	25.56
ITALY	9	6	3	0.012	0.333	46.00
ISRAEL	7	5	2	0.009	0.286	71.299
SWITZERLAND	7	5	2	0.009	0.286	123.43

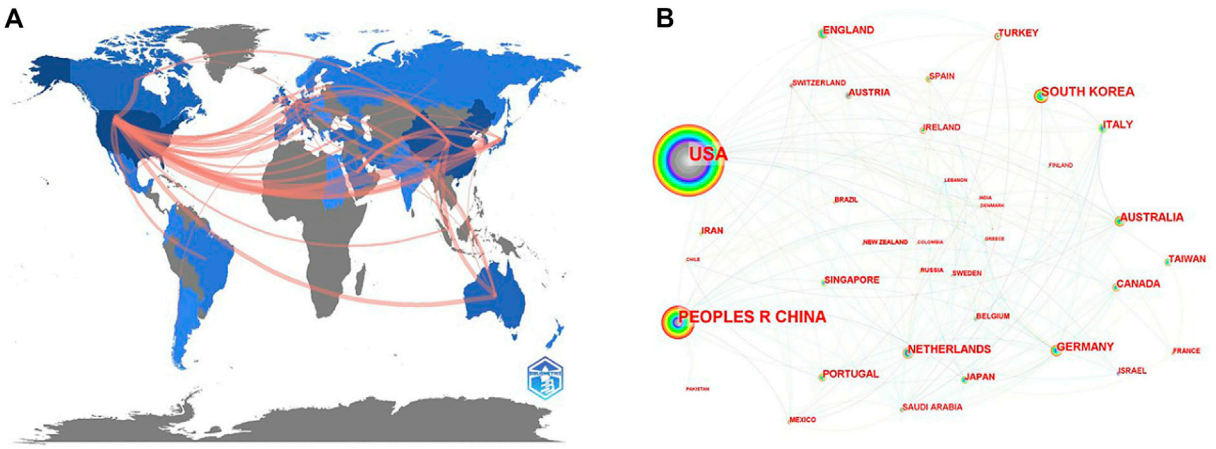

FIGURE 3
Cooperation of countries regarding the photosensitive hydrogels for TE applications. **(A)** The network map of collaboration relations between countries generated with R-Bibliometrix; **(B)** Visualized network map of collaboration relations between countries generated with CiteSpace.

Analysis of countries/regions and institutions

The publications we retrieved were co-authored by 800 institutions from 46 countries/regions. The global distribution of country scientific production regarding the field is shown in Figure 2A. The top 10 countries with the highest number of publications come from four continents, including one country in Oceania (Australia), two in Asia (China and South Korea), two in North America (the USA and Canada) and five in Europe (Germany, Portugal, Turkey, Netherlands and the UK), all of them are developed countries except China and Turkey. Figure 2B and Table 1 show the ranking of the publications number based on the countries where the corresponding authors come from. Among the top 10 countries, the USA published the most articles, followed by

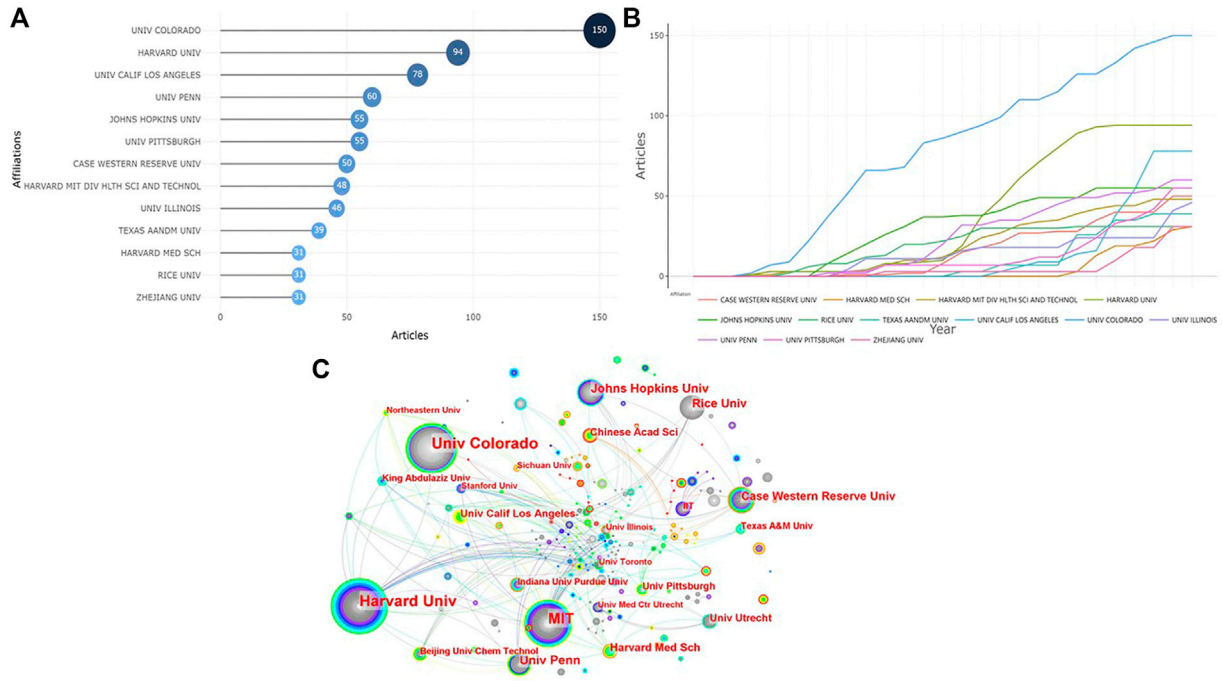

FIGURE 4
Visualized analysis of institutions concerning the publications of photosensitive hydrogels for TE applications. **(A)** The top 10 institutions with the most published articles; **(B)** Production of the top 10 institutions with the highest productivity over time. **(C)** The network map of collaboration relations between institutions.

China and South Korea. In addition, the United States is not only the first country to engage in the study of photosensitive hydrogels for TE, but also had an absolute advantage in the number of papers increased and published compared with other countries (Figure 2C).In addition, The average citation rate of articles from the top 10 countries with the most published articles shows that the United States not only ranked first in the number of articles, but also had a relatively high citation rate, indicating that its articles are of good quality.

The visualized international collaboration relation maps were generated by Bibliometrix and CiteSpzce (Figures 3A,B). In these two network maps, there is quite close collaboration between different countries/regions, among which the top 10 countries that published the most articles also have the top 10 largest nodes, indicating that cooperation between countries is conducive to the output of research results. At the same time, we could find that, although the United States and China were the top 2 countries with the most publications, the cooperation between them was not close.

Figure 4A demonstrates the top 10 institutions with the highest number of articles regarding the photosensitive hydrogels for TE. Except one of the top 10 institutions comes from China (Zhejiang Univ, ranked 10th), all institutions are located in the United States, of which the Univ Colorado published the most articles (n = 150), accounting for 19.28% of the total. Univ Colorado began to study photosensitive hydrogels for TE applications in 1998, and had maintained a high output in the number of publications (Figure 4B). The research in this field did not start in Zhejiang Univ from China until 2006, but the number of articles published by this institution increased relatively rapidly (Figure 4B). As shown in Figure 4C, academic institutions in the United States universally had larger nodes, indicating that they had very close cooperation with other institutions. Several research institutions in China (Chinese Acad Sci, BeiJing Univ Chem Technol and SiChuan Univ) also had relatively large nodes, indicating a relatively significant degree of institutional cooperation. However, there was not much cooperation between them and American research institutions.

Analysis of authors and journals

Figure 5A shows that 2844 researchers co-authored the 778 articles, 13 of whom published more than 10 paper. The most prolific author was Anseth K (n = 33), followed by Khademhosseini A(n = 29) and Bryant S (n = 22). In the network map of author collaboration relations (Figure 5B),

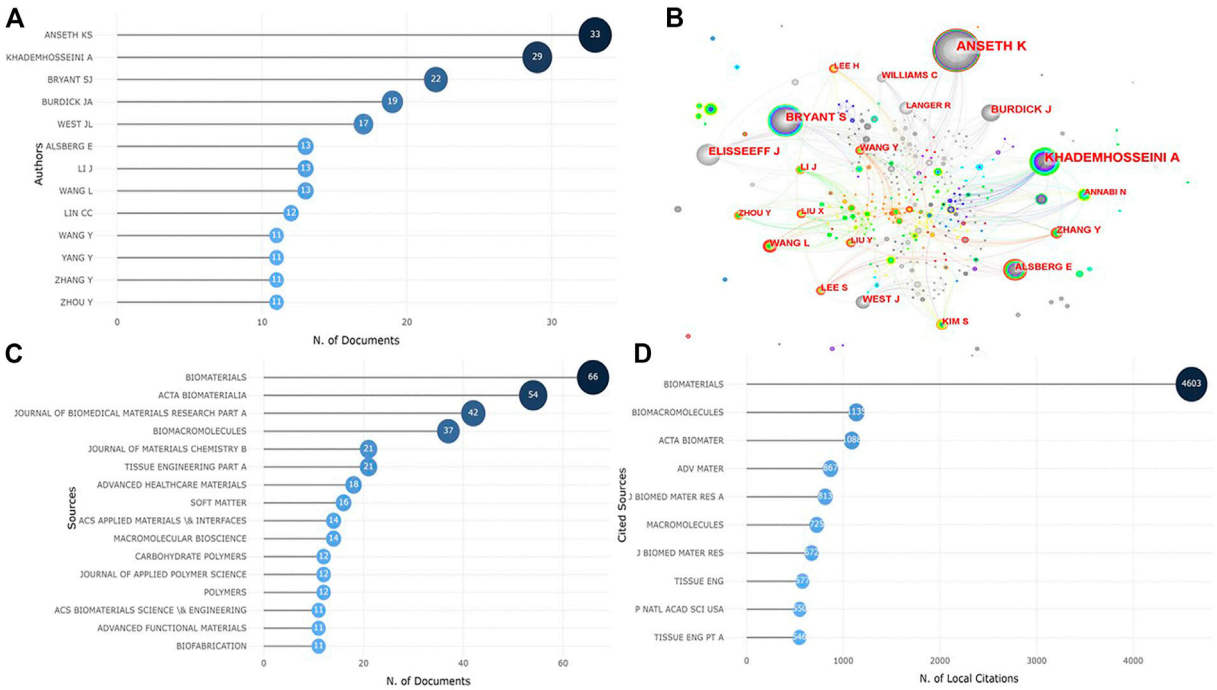

FIGURE 5
Visualized analysis of authors and journals concerning publications of photosensitive hydrogels for TE applications. **(A)** The top 10 authors with the most published articles; **(B)** The network map of collaboration relations between authors. **(C)** The top 10 most productive journals; **(D)** The top 10 journals with the most local cited publications.

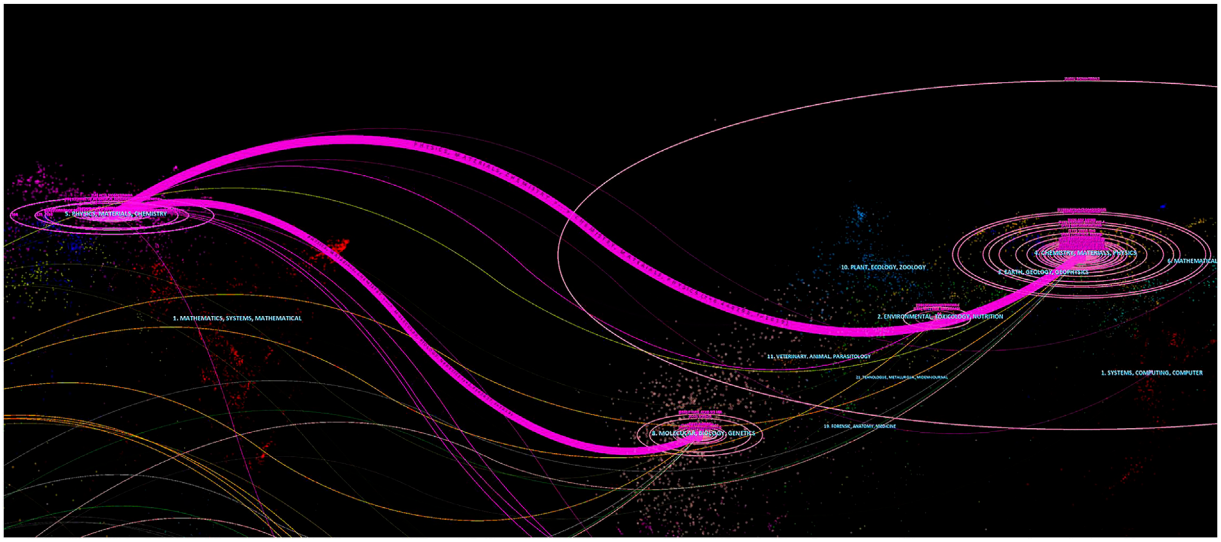

FIGURE 6
Part of dual-map overlay for journals related to the photosensitive hydrogels for TE applications.

TABLE 2 Some typical keywords about the publications related to the photosensitive hydrogels for TE applications.

Rank	keywords	Count	Keywords	Centrality
1	Scaffold	189	Extracellular matrix	0.12
2	Tissue engineering	163	*in vitro*	0.11
3	Hydrogel	154	Cartilage	0.11
4	*in vitro*	111	Alginate	0.11
5	Mechanical property	103	Hydrogel	0.10
6	Tissue	93	Tissue engineering	0.09
7	Biomaterial	93	Tissue	0.09
8	Differentiation	89	Articular cartilage	0.09
9	Photopolymerization	87	Design	0.09
10	Delivery	83	Behavior	0.09

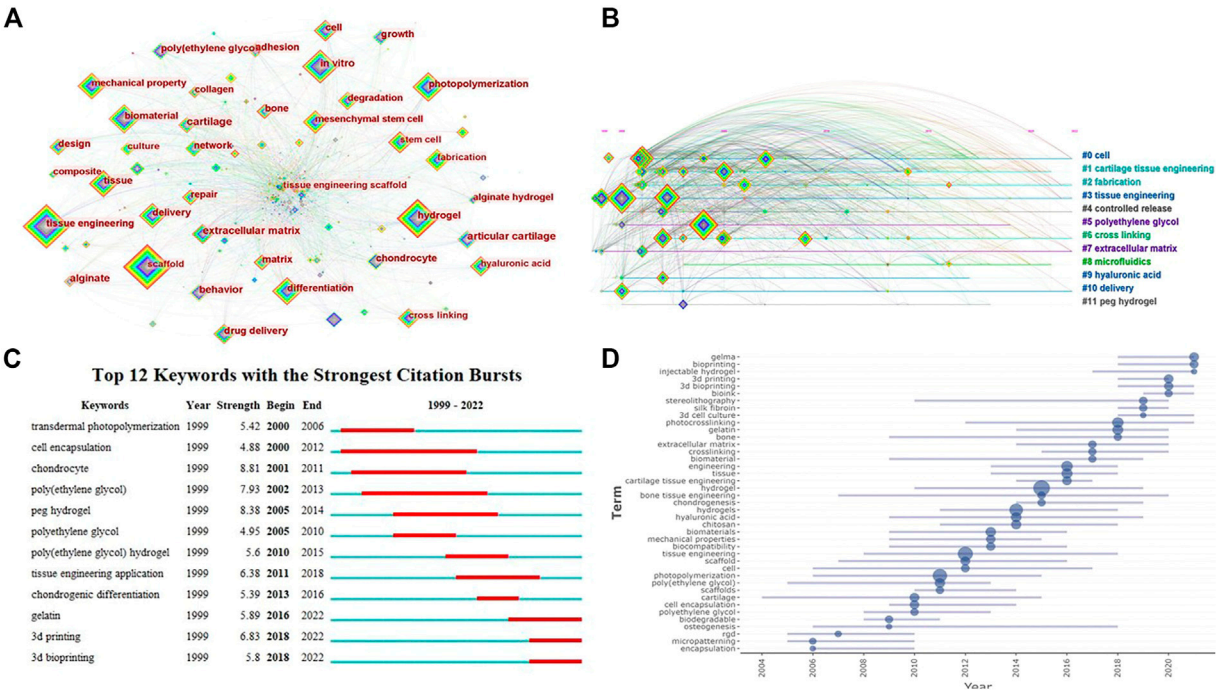

FIGURE 7
Visualized analysis of keywords regarding the publications on the applications of photosensitive hydrogels for TE. **(A)** The keywords co-occurrence network; **(B)** The timeline of clustering for keywords; **(C)** Keywords burst analysis indicated by the map of "Top 12 Keywords with the Strongest Citation Bursts"; **(D)** Map of keywords trend topics.

the large nodes owned by high-yield authors also imply that cooperation contributes to the output of research results.

The publications we analyzed were distributed in 112 journals, among which Biomaterials (n = 66) published the most articles, followed by Acta Biomaterialia (n = 54) and Journal of Biomedical Materials Research Part A (n = 42) (Figure 5C). The top 10 journals published 47.8% of the 778 articles, or 372 articles. In addition, we analyzed the most local cited sources using bibliometrix. Figure 5D shows that the top 3 journals most locally cited were Biomaterials, Biomacromolecules and Acta Biomaterialia.

Another unique function of CiteSpace is to generate dual-map, which can show the topic distribution of journals in specific research fields (Chen 2017). In dual-map, the color stripes in the

middle connect the two ends of the paths, and the left ends trace the citing journals, the right ends trace the cited journals. There are two main paths in Figure 6, indicating that the publications regarding photosensitive hydrogels for TE applications were mainly involved in Physics/Materials/Chemistry journals, while the cited documents were usually distributed in Chemistry/Materials/Physics and MOLECULAR/BIOLOGY/GENETICS journals.

Analysis of keywords

A total of 1443 keywords were extracted from the 778 articles. Some top keywords with high frequency and centrality are shown in Table 2. The keyword with the highest centrality was "extracellular matrix" (centrality: 0.12), indicating that it was an important content in this research field. Other significant keywords included "*in vitro*" (frequency:111, centrality: 0.11), "scaffold" (frequency:189, centrality: 0.04), "cartilage" (centrality: 0.11) and "alginate" (centrality: 0.11). The network map of keywords co-occurrence (Figure 7A) shows that "(tissue engineering) scaffold", "extracellular matrix", "*in vitro*", "(mesenchymal) stem cell", "mechanical property", "differentiation", "hyaluronic acid" and "poly(ethylene) glycol" were all remarkable keywords, indicating the main research contents or specific issues in this field. It is worth mentioning here that stem cells, which are special cells that are expected to provide unlimited amounts of cells for transplantation, have been the focus of TE and regenerative medicine in recent years (Akhmanova et al., 2015). Stem cells reside in stem cell niches that are specialized microstructures to control stem cell growth and differentiation by imparting biochemical and biophysical cues (Jing et al., 2022). Using photosensitive hydrogels to fabricate stem cell niches to study cell behaviors *in vitro* is an important content in this field. Alginate, hyaluronic acid and poly(ethylene) glycol are commonly used biomaterials to synthesize photosensitive hydrogels, which are widely used in biomedical fields including TE.

Further, the keywords were clustered and a network map of clustering timeline was formed (Figure 7B). From the network map, we found "PEG hydrogel", "poly(ethylene) glycol" and "cartilage tissue engineering" were once the research topics in this field, and "cell" and "extracellular matrix" had always been the focuses of research in this field. In addition, although beyond the research content of this article, the applications of photosensitive hydrogels for drug delivery may be another topic, because "delivery" was also a cluster of the keywords. It should be pointed out here that, the mean silhouette value of the cluster was 0.6973 and the modularity Q was 0.3939, showing the clustering is meaningful and reasonable.

Keywords with citation bursts were extracted and Figure 7C shows the top 12 keywords with the strongest citation bursts. "Chondrocyte" was once the most concerned hotspot, due to its strongest citation bursts. In addition, "Poly(ethylene) glycol" and "PEG hydrogel" were all hotspots in this field. The keywords appeared recently with strong citation bursts were "gelatin", "3d printing" and "3d bioprinting", representing the current research hotspots in this field. At the same time, we could find from trends of keyword occurrences map (Figure 7D) that "gelma" which is a gelatin derivative with photopolymerizable function, and "bioprinting" were the latest research hotspots in this filed, indicating the potential research direction in the future, which was consistent with the results of keyword bursts analysis.

Analysis of references

According to the number of citations, the top 10 of 23124 local cited references related to the publications we analyzed are listed in Table 3. An article with 135 citations entitled "Cell-laden microengineered gelatin methacrylate hydrogels" published in the journal of Biomaterials ranked first (29). This paper demonstrated gelatin methacrylate (GelMA) as a hydrogel platform for fabricating cell-responsive microtissues in the presence of living cells, proving GelMA is a kind of cell-responsive microengineered photosensitive hydrogels. The second and third most locally cited references were "Photopolymerizable hydrogels for tissue engineering applications" published in the journal of Biomaterials (Nguyen and West, 2002) and Cytocompatibility of UV and visible light photoinitiating systems on cultured NIH/3T3 fibroblasts *in vitro*" published in Journal of Biomaterials Science (Bryant et al., 2000).

As presented in Figure 8A, the top 3 co-cited references were (Yue et al., 2015), (Nichol et al., 2010) and (Bryant et al., 2000), of which (Nichol et al., 2010) and (Bryant et al., 2000) were also in the top 3 references with the most local citations. (Yue et al., 2015). is a review focusing on the synthesis and characterization of GelMA and its composites, as well as the fabrication and applications of GelMA-based materials. Moreover, the references were clustered and formed into 19 clusters for clustering analysis. The modularity Q was 0.7962, and the mean silhouette value was 0.8873. The map of clustering timeline (Figure 8B) shows that, "two-photon polymerization", "regenerative medicine" and "tropoelastin", etc. were early research areas, while "gelma", "3d printing" and "thiol-ene" were the research frontiers in recent years. Finally, the references with strong citation bursts were extracted by CiteSpace (Figure 8C). The three publications recently appeared in the top 19 references with the strongest citation bursts were "Photocrosslinkable Gelatin Hydrogel for Epidermal Tissue Engineering" (Zhao et al., 2016), "Gelatin-Methacryloyl Hydrogels: Towards Biofabrication-Based Tissue Repair" (Klotz et al., 2016) and "Functionalization, preparation and use of cell-laden gelatin methacryloyl–based hydrogels as modular tissue culture platforms" (Loessner et al., 2016). These three papers are all reviews discussing the applications of (photopolymerizable) gelatin derivatives for TE, indicating the

TABLE 3 Top 10 local cited references of publications regarding the photosensitive hydrogels for TE applications.

Rank	Cited references	Citations
1	NICHOL JW, 2010, BIOMATERIALS, V31, P5536, DOI 10.1016/J.BIOMATERIALS. 2010.03.064	135
2	NGUYEN KT, 2002, BIOMATERIALS, V23, P4307, DOI 10.1016/S0142-9612(02)00175-8	111
3	BRYANT SJ, 2000, J BIOMAT SCI-POLYM E, V11, P439, DOI 10.1163/156856200743805	90
4	ENGLER AJ, 2006, CELL, V126, P677, DOI 10.1016/J.CELL.2006.06.044	77
5	VAN DEN BULCKE AI, 2000, BIOMACROMOLECULES, V1, P31, DOI 10.1021/BM990017D	75
5	YUE K, 2015, BIOMATERIALS, V73, P254, DOI 10.1016/J.BIOMATERIALS. 2015.08.045	75
6	ELISSEEFF J, 1999, P NATL ACAD SCI USA, V96, P3104, DOI 10.1073/PNAS.96.6.3104	69
7	FAIRBANKS BD, 2009, BIOMATERIALS, V30, P6702, DOI 10.1016/J.BIOMATERIALS. 2009.08.055	68
8	SAWHNEY AS, 1993, MACROMOLECULES, V26, P581, DOI 10.1021/MA00056A005	66
9	DRURY JL, 2003, BIOMATERIALS, V24, P4337, DOI 10.1016/S0142-9612(03)00340-5	65
9	LEE KY, 2001, CHEM REV, V101, P1869, DOI 10.1021/CR000108X	65
10	BURDICK JA, 2002, BIOMATERIALS, V23, P4315, DOI 10.1016/S0142-9612(02)00176-X	64

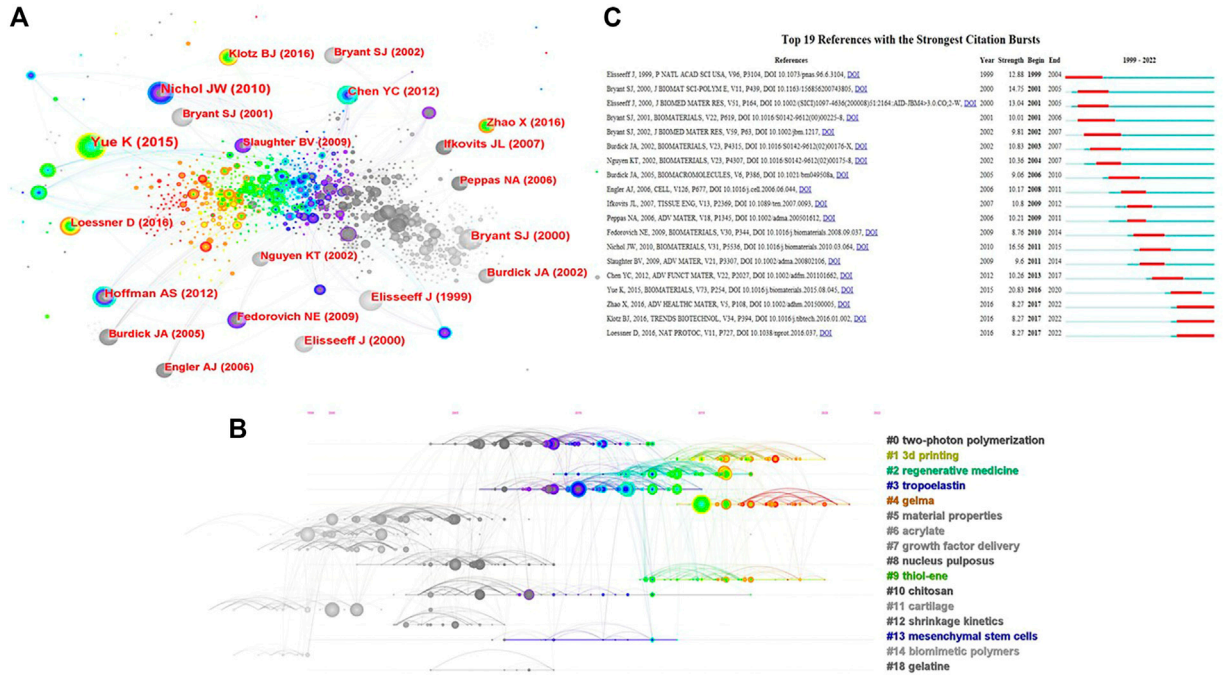

FIGURE 8
The analysis of references regarding the publications on the applications of photosensitive hydrogels for TE. **(A,B)** The visualized network map and clustering timeline of the co-cited references; **(C)** Top 16 References with the Strongest Citation Bursts.

current research hot spot regarding the photosensitive hydrogels for TE applications.

Discussion

In this article, we retrieved and conducted analysis on 778 publications that scoped on the photosensitive hydrogels for TE applications. Some landmark literature was also extracted (Figure 9; Table 4). Since the first paper on the applications of photosensitive hydrogels for TE was published in 1996 (Hubbell et al., 1996), the research field has attracted the attention from scholars. For example, in 1999, a groundbreaking work described the poly (ethylene oxide)-based injectable hydrogels used for TE by transdermal photopolymerization (Elisseeff et al., 1999). Subsequently, Bryant et al. used

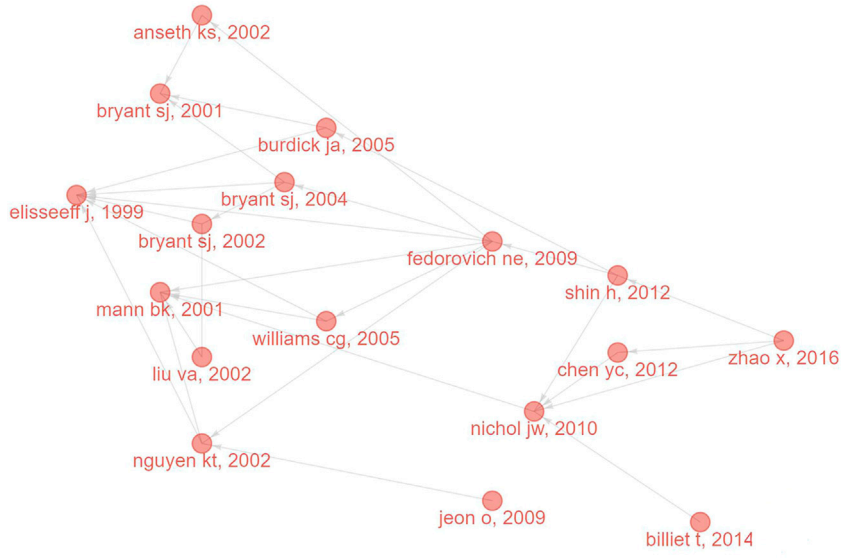

FIGURE 9
Landmark articles related to the photosensitive hydrogels for TE applications.

TABLE 4 Landmark papers concerning publications related to the photosensitive hydrogels for TE applications.

Paper	Year	LCS	GCS
ELISSEEFF J, 1999, PLAST RECONSTR SURG DOI 10.1097/00006534-199909040-00017	1999	35	165
MANN BK, 2001, BIOMATERIALS DOI 10.1016/S0142-9612(01)00051-5	2001	55	546
BRYANT SJ, 2001, BIOMATERIALS DOI 10.1016/S0142-9612(00)00225-8	2001	25	231
ANSETH KS, 2002, J CONTROL RELEASE DOI 10.1016/S0168-3659(01)00500-4	2002	29	363
NGUYEN KT, 2002, BIOMATERIALS DOI 10.1016/S0142-9612(02)00175-8	2002	111	1205
LIU VA, 2002, BIOMED MICRODEVICES DOI 10.1023/A:1020932105236	2002	26	322
BRYANT SJ, 2002, J BIOMED MATER RES DOI 10.1002/JBM.1217	2002	53	616
BRYANT SJ, 2004, J ORTHOP RES DOI 10.1016/J.ORTHRES.2004.02.001	2004	26	146
BURDICK JA, 2005, BIOMACROMOLECULES DOI 10.1021/BM049508A	2005	57	561
WILLIAMS CG, 2005, BIOMATERIALS DOI 10.1016/J.BIOMATERIALS.2004.04.024	2005	60	622
FEDOROVICH NE, 2009, BIOMATERIALS DOI 10.1016/J.BIOMATERIALS.2008.09.037	2009	43	287
JEON O, 2009, BIOMATERIALS DOI 10.1016/J.BIOMATERIALS.2009.01.034	2009	36	399
NICHOL JW, 2010, BIOMATERIALS DOI 10.1016/J.BIOMATERIALS.2010.03.064	2010	135	1396
CHEN YC, 2012, ADV FUNCT MATER DOI 10.1002/ADFM.201101662	2012	49	467
SHIN H, 2012, BIOMATERIALS DOI 10.1016/J.BIOMATERIALS.2011.12.050	2012	36	272
BILLIET T, 2014, BIOMATERIALS DOI 10.1016/J.BIOMATERIALS.2013.09.078	2014	24	610
ZHAO X, 2016, ADV HEALTHC MATER DOI 10.1002/ADHM.201500005	2016	25	447

photocrosslinked poly(ethylene oxide) hydrogels to fabricated tissue engineered cartilage scaffolds encapsulating cells and studied the effects of scaffold thickness on the engineered cartilage (Bryant and Anseth, 2001). With the continuous development of this research field, different types of photosensitive hydrogels have been studied and applied to TE, such as PEG-based hydrogels (Mann et al., 2001), alginate hydrogels (Jeon et al., 2009), gelatin-based hydrogels (Billiet et al., 2014), hyaluronic acid hydrogels (Zerobin et al., 2020) and silk fibroin hydrogels (Hong et al., 2020). The application of photosensitive hydrogels has brought unprecedented promising for the TE and regenerative medicine.

In general, although it fluctuated in some years, the publications concerning photosensitive hydrogels for TE applications showed a steady upward trend as a whole. In terms of the number of publications, the United States was undoubtedly the leading country, with more articles published than the other 9 countries in the top 10 combined. Univ Colorado in the United States was the institution that published the most articles, and Anseth K from this institution was the most prolific author. An early article published by Anseth K group describing the applications of degradable photosensitive hydrogels based on poly(ethylene glycol) and poly(vinyl alcohol) in TE is also one of the landmark articles we extracted above(Anseth et al., 2002). Recently, the research group of Univ Colorado demonstrated the electrospun PEG fibrous hydrogels formed by thiol-ene photoclick chemistry and studied the effects of different process parameters on their properties (Sharma et al., 2021). Meanwhile, we could find that although China started this research not early, the growth rate of publications was relatively rapid, with Zhejiang Univ as its representative. In 2006, the research team from Zhejiang Univ developed a water-soluble chitosan hydrogel with photo crosslinking potential for the first time (Hong et al., 2006). Since then, the university has been committed to the study of photosensitive hydrogels for TE applications. Recently, the research group of Ouyang from Zhejiang Univ developed a biomimetic joint paint containing GelMA with hyaluronic acid which can be rapidly activated by light for the treatment of cartilage defect (Wei et al., 2021). However, as the two countries that published the most papers, the United States and China did not cooperate closely in this field. As we know, cooperation is an important means to promote the output of research results, whether between authors, institutions or countries. Therefore, China and the United States could collaborate more closely in photosensitive hydrogels for TE applications to promote the development of this research field. In addition, there was still a significant gap between developing countries and developed countries in this field, indicating that developing countries could invest more in this field and seek more opportunities for cooperation with developed countries.

In terms of the number of articles, the journal of Biomaterials had the most publications in this field by now, and it also published the most local cited references. For instance, the journal recently reported a Fluorescently LAbelled Sensitive Hydrogel (FLASH) generated by GelMA covalently bound to the FITC fluorophore, which can not only be fabricated into TE scaffolds by photo crosslinking, but also be used as a sensor to detect the degradation of the scaffolds during the process of new tissue formation (Onofrillo et al., 2021). The top 2 articles with the highest number of local citations and co-citations were all published in this journal. In addition, based on the analysis results of the journals publishing the articles, the journals publishing the cited documents, and the dual-map, we could know that the research topics in this field were mainly involved in (bio)materials science, chemistry, biology and medicine, and the application of photosensitive hydrogels for TE is an interdisciplinary field.

The keyword with the highest centrality was “extracellular matrix”, indicating the engineering ECM was the most important research content in this field. In addition, from the significant keywords and co-occurrence keywords in the above analysis we could know that, the main research scope in this field was to apply photosensitive hydrogels such as “alginate”-based, “hyaluronic acid”-based and “poly(ethylene) glycol”-based hydrogels to fabricate “tissue engineering scaffolds” (engineering ECMs) that meet the requirements, including the proper “mechanical property”, to study cell behaviors *in vitro*, such as the “differentiation” of “(mesenchymal) stem cell”. According to the results of keywords analysis, we could also identify that, “PEG hydrogel” and “poly(ethylene) glycol” were once the main research topics in this field. PEG-based photosensitive hydrogel is one of the most commonly used photopolymerizable synthetic materials and is widely used for TE and drug delivery applications (Yao et al., 2013; Qin et al., 2014; Jing et al., 2022; Liu et al., 2022). The analysis of keywords with citation bursts indicated that “gelatin” was a current research hotspot in this field, which is consistent with the results shown in trends of keyword occurrences map and the map of references clustering timeline. Gelatin is derived from type 1 collagen, which is the main component of mammalian ECMs (Van Hoorick et al., 2019). GelMA possessing photopolymerizable functionalities is formed by reacting the primary amines of hydroxylysine, lysine and ornithine with methacrylic anhydride. As a naturally-derived material, GelMA containing tripeptide arginine-glycine-aspartic acid (RGD) and matrix metalloproteinase (MMP) sequences has high bioactivity and biodegradability (Piao et al., 2021). As a hotspot in TE applications of photosensitive hydrogels in recent years, GelMA has attracted extensive study. For example, recently, Kumar et al. studied the effect of different GelMA synthesis parameters on the performance of the resulting bioink used in TE. Other research results on GelMA for TE applications are also numerous (Ovsianikov et al., 2011; Tytgat et al., 2018; Ying et al., 2018; Zhou et al., 2018; Kumar et al., 2021). Accordingly, the three publications recently appeared in the top 19 references with the strongest citation bursts are all reviews discussing the GelMA for TE applications.

It is worth noting that, “thiol-ene” was a research frontier in recent years, which is indicated in the map of references clustering timeline. As we all know, free-radical chain polymerization is a facile and easy-to-handle polymerization mechanism. However, chain growth has its inherent disadvantages, including 1) the multiple kinetic chains generating more heterogeneous networks; 2) the complex kinetic profile of polymerizations damaging the control of the reacted functionalities; 3) the oxygen inhibition resulting in longer processing times (Hoyle and Bowman 2010; Pereira and Bártolo, 2015; Tytgat et al., 2020). In contrast, thiol–ene

click chemistry can form crosslinked polymer networks with a high degree of homogeneous structures at a very high reaction rate. Radical-mediated thiol-ene photo-click chemistry, which leads to step-growth polymerization for networks, is based on the extremely efficient reaction of thiols with non-homopolymerizable C=C double bonds, and it can surmount the disadvantages of chain-growth polymerization (Jing et al., 2022). Recently, Bilgik et al. demonstrated a clickable polyacrylamide hydrogel synthesized by photopolymerization using acrylamide and propargyl acrylate (Bilgic et al., 2014). Another article reported the synthesis and orthogonal crosslinking of poly(γ-glutamic acid)-norbornene photosensitive hydrogels and assesses the effect of the mechanical cues of hydrogels on the monocyte phenotype(Kim and Lin, 2021). It is noteworthy that the research groups of Vienna University of Technology and Ghent University has done a lot of research on thiol-ene hydrogels and processed them using two-photon polymerization technology to obtain homogeneous and high-resolution 3D structures for TE (Qin et al., 2013; Baudis et al., 2016; Van Hoorick et al., 2020). It is necessary to discuss the two-photon polymerization (TPP) technique here. Different from the traditional single photon polymerization, TPP uses a photoinitiator molecule in the photosensitive hydrogels to absorb two photons at the same time to initiate polymerization. The spatial resolution of the structures manufactured by TPP can reach below 100 nm. At present, it is the only technology capable of manufacturing complex 3D structures with precisely adjusted geometric shapes on a sub-cellular scale and is used to process engineering ECM (Fu et al., 2022).

The limitations of this study still exist. Firstly, analysis based on computer software would inevitably result in insufficient manual intervention. Secondly, although WoSCC is the most commonly used database for bibliometric analysis, it does not cover all articles in this field. Besides, articles after 1 October 2022 (the search end date) are excluded from this analysis. It should be pointed out here that there are other bibliometrics software based on different algorithms, such as VOSviewer, HistCite, *etc.* They can analyze scientific publications from different key directions. The software used in this article is powerful, but not perfect.

Conclusion

This bibliometric and visualized study identifies the investigative information that are associated with photosensitive hydrogels for TE applications 1996-2022, using the bibliometric visualized tools CiteSpace and R-bibliometrix. Based off our analysis, we found that photosensitive hydrogels for TE applications is an interdisciplinary field widely studied, and its research achievements are expected to continue to grow steadily. The United States had absolute advantages in this field, and developing countries could seek opportunities for cooperation with it. The journal of Biomaterials published the most articles in this field, and Anseth K, Khademhosseini A and Bryant S had published lots of articles. Academic cooperation between authors, institutions and countries moves the development of this research field forward. Gelatin photosensitive hydrogels, especially GelMA-based hydrogels, have become a research hotspot in recent years, which is expected to last until the next years. In addition, as a research frontier, thiol–ene chemistry applied in photosensitive hydrogels for TE applications is expected to attract more researchers' attention. The results of this study would provide scholars in relevant research fields with a profound understanding and insight into the applications of photosensitive hydrogels for TE.

Data availability statement

The original contributions presented in the study are included in the article/Supplementary material, further inquiries can be directed to the corresponding authors.

Author contributions

JL and MS conceived the idea for the study, provided a retrieval strategy. HF performed the analysis and wrote the first draft of the manuscript that was iteratively improved by BY, HW, HT, LJ, YZ, and GM.

Funding

This study was supported by the grant of the Science and Technology Planning Project of Jilin Province, China (No. YDZJ202201ZYTS193), and Jilin province science and technology project of traditional Chinese medicine (2022088).

Conflict of interest

The authors declare that the research was conducted in the absence of any commercial or financial relationships that could be construed as a potential conflict of interest.

Publisher's note

References

Akhmanova, M., Osidak, E., Domogatsky, S., Rodin, S., and Domogatskaya, A. (2015). Physical, spatial, and molecular aspects of extracellular matrix of *in vivo* niches and artificial scaffolds relevant to stem cells research. *Stem Cells Int.* 2015, 1–35. doi:10.1155/2015/167025

Anseth, K. S., Metters, A. T., Bryant, S. J., Martens, P. J., Elisseeff, J. H., and Bowman, C. N. (2002). *In situ* forming degradable networks and their application in tissue engineering and drug delivery. *J. Control. Release* 78 (1-3), 199–209. doi:10.1016/S0168-3659(01)00500-4

Aria, M., and Cuccurullo, C. (2017). Bibliometrix : An R-tool for comprehensive science mapping analysis. *J. Inf.* 11 (4), 959–975. doi:10.1016/j.joi.2017.08.007

Baudis, S., Bomze, D., Markovic, M., Gruber, P., Ovsianikov, A., and Liska, R. (2016). Modular material system for the microfabrication of biocompatible hydrogels based on thiol-ene-modified poly(vinyl alcohol). *J. Polym. Sci. Part A Polym. Chem.* 54 (13), 2060–2070. doi:10.1002/pola.28073

Billiet, T., Gevaert, E., De Schryver, T., Cornelissen, M., and Dubruel, P. (2014). The 3D printing of gelatin methacrylamide cell-laden tissue-engineered constructs with high cell viability. *Biomaterials* 35 (1), 49–62. doi:10.1016/j.biomaterials.2013.09.078

Bryant, S. J., Nuttelman, C. R., and Anseth, K. S. (2000). Cytocompatibility of UV and visible light photoinitiating systems on cultured NIH/3T3 fibroblasts *in vitro*. *J. Biomaterials Sci. Polym. Ed.* 11 (5), 439–457. doi:10.1163/156856200743805

Chen, C., and Leydesdorff, L. (2014). Patterns of connections and movements in dual-map overlays: A new method of publication portfolio analysis. *J. Assoc. Inf. Sci. Technol.* 65 (2), 334–351. doi:10.1002/asi.22968

Chen, C. (2017). Science mapping: A systematic review of the literature. *J. Data Inf. Sci.* 2 (2), 1–40. doi:10.1515/jdis-2017-0006

Chen, C. (2004). Searching for intellectual turning points: Progressive knowledge domain visualization. *Proc. Natl. Acad. Sci. U. S. A.* 101, 5303–5310. doi:10.1073/pnas.0307513100

Elisseeff, J., Anseth, K., Sims, D., McIntosh, W., Randolph, M., Yaremchuk, M., et al. (1999). Transdermal photopolymerization of poly(ethylene oxide)-based injectable hydrogels for tissue-engineered cartilage. *Plastic Reconstr. Surg.* 104 (4), 1014–1022. doi:10.1097/00006534-199909020-00018

Ellegaard, O., and Wallin, J. A. (2015). The bibliometric analysis of scholarly production: How great is the impact? *Scientometrics* 105 (3), 1809–1831. doi:10.1007/s11192-015-1645-z

Fu, H., Jing, X., Lin, J., Wang, L., Jiang, H., Yu, B., et al. (2022). Knowledge domain and hotspots analysis concerning applications of two-photon polymerization in biomedical field: A bibliometric and visualized study. *Front. Bioeng. Biotechnol.* 10, 1030377. doi:10.3389/fbioe.2022.1030377

Gholamali, I., and Yadollahi, M. (2021). Bio-nanocomposite polymer hydrogels containing nanoparticles for drug delivery: A review. *Regen. Eng. Transl. Med.* 7 (2), 129–146. doi:10.1007/s40883-021-00207-0

Gonzalez-Alcaide, G., Peris, J., and Ramos, J. M. (2017). Areas of research and clinical approaches to the study of liver abscess. *World J. Gastroenterol.* 23 (2), 357–365. doi:10.3748/wjg.v23.i2.357

Gu, J., Hu, M., Gu, Z., Yu, J., Ji, Y., Li, L., et al. (2021). Bibliometric analysis reveals a 20-year research trend for chemotherapy-induced peripheral neuropathy. *Front. Neurol.* 12, 793663. doi:10.3389/fneur.2021.793663

Hong, H., Seo, Y. B., Kim, D. Y., Lee, J. S., Lee, Y. J., Lee, H., et al. (2020). Digital light processing 3D printed silk fibroin hydrogel for cartilage tissue engineering. *Biomaterials* 232, 119679. doi:10.1016/j.biomaterials.2019.119679

Hong, Y., Mao, Z., Wang, H., Gao, C., and Shen, J. (2006). Covalently crosslinked chitosan hydrogel formed at neutral pH and body temperature. *J. Biomed. Mat. Res. A* 79 (4), 913–922. doi:10.1002/jbm.a.30837

Hoyle, C. E., and Bowman, C. N. (2010). Thiol-ene click chemistry. *Angew. Chem. Int. Ed.* 49 (9), 1540–1573. doi:10.1002/anie.200903924

Hubbell, J. A. (1996). *In situ* material transformations in tissue engineering. *MRS Bull.* 21 (11), 33–35. doi:10.1557/S0883769400031821

Jafari, M., Paknejad, Z., Rad, M. R., Motamedian, S. R., Eghbal, M. J., Nadjmi, N., et al. (2017). Polymeric scaffolds in tissue engineering: A literature review. *J. Biomed. Mat. Res.* 105 (2), 431–459. doi:10.1002/jbm.b.33547

Jeon, O., Bouhadir, K. H., Mansour, J. M., and Alsberg, E. (2009). Photocrosslinked alginate hydrogels with tunable biodegradation rates and mechanical properties. *Biomaterials* 30 (14), 2724–2734. doi:10.1016/j.biomaterials.2009.01.034

Jing, X., Fu, H., Yu, B., Sun, M., and Wang, L. (2022). Two-photon polymerization for 3D biomedical scaffolds: Overview and updates. *Front. Bioeng. Biotechnol.* 10, 994355. doi:10.3389/fbioe.2022.994355

Kim, M. H., and Lin, C. C. (2021). Assessing monocyte phenotype in poly(γ-glutamic acid) hydrogels formed by orthogonal thiol-norbornene chemistry. *Biomed. Mat.* 16 (4), 045027. doi:10.1088/1748-605X/ac01b0

Klotz, B. J., Gawlitta, D., Rosenberg, A., Malda, J., and Melchels, F. P. W. (2016). Gelatin-methacryloyl hydrogels: Towards biofabrication-based tissue Repair. *Trends Biotechnol.* 34 (5), 394–407. doi:10.1016/j.tibtech.2016.01.002

Kumar, H., Sakthivel, K., Mohamed, M. G. A., Boras, E., Shin, S. R., and Kim, K. (2021). Designing gelatin methacryloyl (GelMA)-Based bioinks for visible light stereolithographic 3D biofabrication. *Macromol. Biosci.* 21 (1), e2000317. doi:10.1002/mabi.202000317

Langer, R., and Vacanti, J. P. (1993). Tissue engineering. *Science* 260 (5110), 920–926. doi:10.1126/science.8493529

Liu, J., Bao, X., Kolesnik, I., Jia, B., Yu, Z., Xing, C., et al. (2022). Enhancing the *in vivo* stability of polycation gene carriers by using PEGylated hyaluronic acid as a shielding system. *BIO Integr.* 3, 103–111. doi:10.15212/bioi-2021-0033

Loessner, D., Meinert, C., Kaemmerer, E., Martine, L. C., Yue, K., Levett, P. A., et al. (2016). Functionalization, preparation and use of cell-laden gelatin methacryloyl-based hydrogels as modular tissue culture platforms. *Nat. Protoc.* 11 (4), 727–746. doi:10.1038/nprot.2016.037

Mann, B. K., Gobin, A. S., Tsai, A. T., Schmedlen, R. H., and West, J. L. (2001). Smooth muscle cell growth in photopolymerized hydrogels with cell adhesive and proteolytically degradable domains: Synthetic ECM analogs for tissue engineering. *Biomaterials* 22 (22), 3045–3051. doi:10.1016/s0142-9612(01)00051-5

Mikos, A. G., Herring, S. W., Ochareon, P., Elisseeff, J., Lu, H. H., Kandel, R., et al. (2006). Engineering complex tissues. *Tissue Eng.* 12 (12), 3307–3339. doi:10.1089/ten.2006.12.3307

Mooney, D., and Langer, R. (2000). "Engineering biomaterials for tissue engineering: The 10–100 micron size scale," in *The biomedical engineering handbook*. 2nd edition (Bronzino: CRC Press LLC).

Nguyen, K. T., and West, J. L. (2002). Photopolymerizable hydrogels for tissue engineering applications. *Biomaterials* 23 (22), 4307–4314. doi:10.1016/s0142-9612(02)00175-8

Nichol, J. W., Koshy, S. T., Bae, H., Hwang, C. M., Yamanlar, S., and Khademhosseini, A. (2010). Cell-laden microengineered gelatin methacrylate hydrogels. *Biomaterials* 31 (21), 5536–5544. doi:10.1016/j.biomaterials.2010.03.064

Onofrillo, C., Duchi, S., Francis, S., O'Connell, C. D., Caballero Aguilar, L. M., Doyle, S., et al. (2021). Flash: Fluorescently LAbelled Sensitive Hydrogel to monitor bioscaffolds degradation during neocartilage generation. *Biomaterials* 264, 120383. doi:10.1016/j.biomaterials.2020.120383

Ovsianikov, A., Deiwick, A., Van Vlierberghe, S., Dubruel, P., Moller, L., Drager, G., et al. (2011). Laser fabrication of three-dimensional CAD scaffolds from photosensitive gelatin for applications in tissue engineering. *Biomacromolecules* 12 (4), 851–858. doi:10.1021/bm1015305

Pereira, R. F., and Bártolo, P. J. (2015). 3D bioprinting of photocrosslinkable hydrogel constructs. *J. Appl. Polym. Sci.* 132 (48). doi:10.1002/app.42458

Piao, Y., You, H., Xu, T., Bei, H.-P., Piwko, I. Z., Kwan, Y. Y., et al. (2021). Biomedical applications of gelatin methacryloyl hydrogels. *Eng. Regen.* 2, 47–56. doi:10.1016/j.engreg.2021.03.002

Qin, X.-H., Ovsianikov, A., Stampfl, J., and Liska, R. (2014). Additive manufacturing of photosensitive hydrogels for tissue engineering applications. *BioNanoMaterials* 15, 3–4. doi:10.1515/bnm-2014-0008

Qin, X.-H., Torgersen, J., Saf, R., Mühleder, S., Pucher, N., Ligon, S. C., et al. (2013). Three-dimensional microfabrication of protein hydrogels via two-photon-excited thiol-vinyl ester photopolymerization. *J. Polym. Sci. Part A Polym. Chem.* 51 (22), 4799–4810. doi:10.1002/pola.26903

Ratner, B. D., and Bryant, S. J. (2004). Biomaterials: Where we have been and where we are going. *Annu. Rev. Biomed. Eng.* 6, 41–75. doi:10.1146/annurev.bioeng.6.040803.140027

Sharma, S., Monteleone, N., Kopyeva, I., and Bryant, S. J. (2021). The effects of processing variables on electrospun poly(ethylene glycol) fibrous hydrogels formed from the thiol-norborneneclick reaction. *J. Appl. Polym. Sci.* 138 (32), 50786. doi:10.1002/app.50786

Shi, J., Gao, Y., Ming, L., Yang, K., Sun, Y., Chen, J., et al. (2021). A bibliometric analysis of global research output on network meta-analysis. *BMC Med. Inf. Decis. Mak.* 21 (1), 144. doi:10.1186/s12911-021-01470-5

Stephanie, J. B., and Anseth, K. S. (2001). The effects of scaffold thickness on tissue engineered cartilage in photocrosslinked poly(ethylene oxide) hydrogels. *Biomaterials* 22 (6), 619–626. doi:10.1016/s0142-9612(00)00225-8

Tytgat, L., Dobos, A., Markovic, M., Van Damme, L., Van Hoorick, J., Bray, F., et al. (2020). High-resolution 3D bioprinting of photo-cross-linkable recombinant collagen to serve tissue engineering applications. *Biomacromolecules* 21 (10), 3997–4007. doi:10.1021/acs.biomac.0c00386

Tytgat, L., Vagenende, M., Declercq, H., Martins, J. C., Thienpont, H., Ottevaere, H., et al. (2018). Synergistic effect of kappa-carrageenan and gelatin blends towards adipose tissue engineering. *Carbohydr. Polym.* 189, 1–9. doi:10.1016/j.carbpol.2018.02.002

Ugolini, D., Neri, M., Casilli, C., Ceppi, M., Canessa, P. A., Ivaldi, G. P., et al. (2010). A bibliometric analysis of scientific production in mesothelioma research. *Lung Cancer* 70 (2), 129–135. doi:10.1016/j.lungcan.2010.01.013

Van Hoorick, J., Dobos, A., Markovic, M., Gheysens, T., Van Damme, L., Gruber, P., et al. (2020). Thiol-norbornene gelatin hydrogels: Influence of thiolated crosslinker on network properties and high definition 3D printing. *Biofabrication* 13 (1), 015017. doi:10.1088/1758-5090/abc95f

Van Hoorick, J., Tytgat, L., Dobos, A., Ottevaere, H., Van Erps, J., Thienpont, H., et al. (2019). (Photo-)crosslinkable gelatin derivatives for biofabrication applications. *Acta Biomater.* 97, 46–73. doi:10.1016/j.actbio.2019.07.035

Wei, M., Wang, W., and Zhuang, Y. (2016). Worldwide research productivity in the field of spine surgery: A 10-year bibliometric analysis. *Eur. Spine J.* 25 (4), 976–982. doi:10.1007/s00586-016-4442-3

Wei, W., Ma, Y., Zhang, X., Zhou, W., Wu, H., Zhang, J., et al. (2021). Biomimetic joint paint for efficient cartilage Repair by simultaneously regulating cartilage degeneration and regeneration in pigs. *ACS Appl. Mat. Interfaces* 13 (46), 54801–54816. doi:10.1021/acsami.1c17629

Wu, L., Li, X., Guan, T., Chen, Y., and Qi, C. (2020). 3D bioprinting of tissue engineering scaffold for cell culture. *Rapid Prototyp. J.* 26 (5), 835–840. doi:10.1108/rpj-10-2018-0264

Yao, X., Peng, R., and Ding, J. (2013). Cell-material interactions revealed via material techniques of surface patterning. *Adv. Mat.* 25 (37), 5257–5286. doi:10.1002/adma.201301762

Ying, G., Jiang, N., Yu, C., and Zhang, Y. S. (2018). Three-dimensional bioprinting of gelatin methacryloyl (GelMA). *Biodes. Manuf.* 1 (4), 215–224. doi:10.1007/s42242-018-0028-8

Yue, K., Trujillo-de Santiago, G., Alvarez, M. M., Tamayol, A., Annabi, N., and Khademhosseini, A. (2015). Synthesis, properties, and biomedical applications of gelatin methacryloyl (GelMA) hydrogels. *Biomaterials* 73, 254–271. doi:10.1016/j.biomaterials.2015.08.045

Zerobin, E., Markovic, M., Tomášiková, Z., Qin, X. H., Ret, D., Steinbauer, P., et al. (2020). Hyaluronic acid vinyl esters: A toolbox toward controlling mechanical properties of hydrogels for 3D microfabrication. *J. Polym. Sci.* 58 (9), 1288–1298. doi:10.1002/pol.20200073

Zhang, B., Rahmatullah, B., Wang, S. L., Zhang, G., Wang, H., and Ebrahim, N. A. (2021). A bibliometric of publication trends in medical image segmentation: Quantitative and qualitative analysis. *J. Appl. Clin. Med. Phys.* 22 (10), 45–65. doi:10.1002/acm2.13394

Zhang, S., Vijayavenkataraman, S., Lu, W. F., and Fuh, J. Y. H. (2019). A review on the use of computational methods to characterize, design, and optimize tissue engineering scaffolds, with a potential in 3D printing fabrication. *J. Biomed. Mat. Res.* 107 (5), 1329–1351. doi:10.1002/jbm.b.34226

Zhao, H., Liu, M., Zhang, Y., Yin, J., and Pei, R. (2020). Nanocomposite hydrogels for tissue engineering applications. *Nanoscale* 12 (28), 14976–14995. doi:10.1039/d0nr03785k

Zhao, X., Lang, Q., Yildirimer, L., Lin, Z. Y., Cui, W., Annabi, N., et al. (2016). Photocrosslinkable gelatin hydrogel for epidermal tissue engineering. *Adv. Healthc. Mat.* 5 (1), 108–118. doi:10.1002/adhm.201500005

Zhou, X., Cui, H., Nowicki, M., Miao, S., Lee, S. J., Masood, F., et al. (2018). Three-dimensional-bioprinted dopamine-based matrix for promoting neural regeneration. *ACS Appl. Mat. Interfaces* 10 (10), 8993–9001. doi:10.1021/acsami.7b18197

frontiers | Frontiers in Bioengineering and Biotechnology

TYPE Review
PUBLISHED 07 December 2022
DOI 10.3389/fbioe.2022.1091360

OPEN ACCESS

EDITED BY
Jianxun Ding,
Changchun Institute of Applied Chemistry (CAS), China

REVIEWED BY
Shiyu Liu,
Fourth Military Medical University, China
Qianli Ma,
University of Oslo, Norway
Mingming Yang,
Northwest A&F University, China

*CORRESPONDENCE
Ye Li,
lisa.l0309@163.com
Dandan Pei,
peidandan@xjtu.edu.cn

SPECIALTY SECTION
This article was submitted to Biomaterials, a section of the journal Frontiers in Bioengineering and Biotechnology

RECEIVED 07 November 2022
ACCEPTED 28 November 2022
PUBLISHED 07 December 2022

CITATION
Ma S, Zhang Y, Li S, Li A, Li Y and Pei D (2022), Engineering exosomes for bone defect repair.
Front. Bioeng. Biotechnol. 10:1091360.
doi: 10.3389/fbioe.2022.1091360

Engineering exosomes for bone defect repair

Shaoyang Ma, Yuchen Zhang, Sijia Li, Ang Li, Ye Li* and Dandan Pei*

Key Laboratory of Shaanxi Province for Craniofacial Precision Medicine Research, College of Stomatology, Xi'an Jiaotong University, Xi'an, Shaanxi, China

Currently, bone defect repair is still an intractable clinical problem. Numerous treatments have been performed, but their clinical results are unsatisfactory. As a key element of cell-free therapy, exosome is becoming a promising tool of bone regeneration in recent decades, because of its promoting osteogenesis and osteogenic differentiation function *in vivo* and *in vitro*. However, low yield, weak activity, inefficient targeting ability, and unpredictable side effects of natural exosomes have limited the clinical application. To overcome the weakness, various approaches have been applied to produce engineering exosomes by regulating their production and function at present. In this review, we will focus on the engineering exosomes for bone defect repair. By summarizing the exosomal cargos affecting osteogenesis, the strategies of engineering exosomes and properties of exosome-integrated biomaterials, this work will provide novel insights into exploring advanced engineering exosome-based cell-free therapy for bone defect repair.

KEYWORDS

bone regeneration, engineering exosomes, exosomal cargos, exosome-integrated biomaterials, osteogenesis

1 Introduction

Bone is the central element in skeletal tissues of the human body, and provides a framework for attachment of muscles and other tissues, enables body movements, provides protection of internal organs from injury, promotes blood cells production, and balances calcium and acid/base homeostasis (Elefteriou, 2018). However, the regeneration of critical-size bone defects is still a major clinical challenge and globally costs up to $45 billion per year (Mauffrey et al., 2015; Bharadwaz and Jayasuriya, 2020). Recently, stem cell therapy is considered as a potential strategy for bone defect regeneration (Tan SHS. et al., 2020), and several clinical studies have demonstrated mesenchymal stromal/stem cells (MSCs) to be safe and efficacious for the treatment of bone defects and diseases (Liebergall et al., 2013; Chen et al., 2016; Castillo-Cardiel et al., 2017; Hernigou et al., 2018a; Hernigou et al., 2018b). Nevertheless, cellular therapies incur significant costs and challenges as they require stringently monitored manufacturing, handling, and storage to ensure optimal viability and potency of cells needed for transplantation (Tan et al., 2021). More importantly, accumulating evidence indicates that the positive effect of MSCs on tissue repair is to stimulate the activity of tissue-resident recipient cells through paracrine, such as exosomes,

rather than directly differentiate into parenchymal cells to repair or replace damaged tissue (Liang et al., 2014; Zhang et al., 2016). Such concerns have driven the search for alternate therapeutic strategies and cell-free therapies based on exosomes have become strongly established in the landscape of regenerative medicine.

Exosome is a subclass of membrane-coated extracellular vesicles with sizes of 30–150 nm (Tkach and Thery, 2016). As one of the most revolutionary contributions to cell biology in the past 30 years (Wang Y. et al., 2019), exosomes can exert multiple biological functions by targeting recipient cells and inducing signaling *via* receptor-ligand interactions, endocytosis and/or phagocytosis (Bobrie et al., 2012; Colombo et al., 2014; Hoshino et al., 2015; Shang et al., 2021). Exosomes have been experimented with many animal models for the regeneration of bone, osteochondral, and cartilage injury/diseases such as osteoarthritis (OA), osteoporosis, osteonecrosis, and inflammatory bone loss in periodontitis with enhanced tissue formation and integration (Kuang et al., 2019; Kim et al., 2020; Lei et al., 2022). Furthermore, several exosome-based clinical experiments of orthopedic diseases have been performed based on US-NIH clinical trial database (https://clinicaltrials.gov/). However, there still are several constraints to exosome clinical applications for bone defect repair: 1) unclear mechanism of promoting bone tissue regeneration; 2) poor retention and targeting ability of exosome at the bone defect site; 3) low extraction rate and complex separation process.

In view of the shortcomings of natural exosomes, a growing number of studies are aiming to develop engineering exosomes based on modifying exosomal cargos or/and incorporating biomaterials (Bei et al., 2021; Lathwal et al., 2021; Liang et al., 2021). Here we will review the recent research of engineering exosome used in bone defect repair, and highlight the bioactive cargos and construction strategies. Additionally, we will also summarize the application of biomaterials to impregnate exosome and focus on how the properties of biomaterials assist exosome to promote bone regeneration. By reviewing currently available knowledge, this present review will contribute to the clinical knowledge and may have implications for the engineering design of exosomes used in bone defect repair.

2 Osteogenic cargos in exosomes

In the past decade, numerous exosomal bioactive cargos have been revealed (Kalluri and LeBleu, 2020). Exosomal cargos are dependent on the parent cell type and vary between different physiological or pathological conditions (Meng et al., 2019). The vesicular structure of exosome provides an enclosed space to protect exosomal cargos against degradation. In return, exosomal cargos are the foundation to endow exosomes with various biological functions. In this section we will review recent research about exosomes in bone regeneration and focus on the functions of exosomal cargos and their molecular mechanisms (Figure 1).

2.1 Non-Coding RNA

Non-coding RNAs (ncRNAs) refer to the RNAs that lack protein-coding regions, and have the potential to regulate gene expression at transcriptional, post-transcriptional, and translational levels, thereby modulating associated signaling networks (Bhat et al., 2020). NcRNAs have become a hot topic of increasing concern after the completion of the Human Genome Project (Lander et al., 2001), which showed only 1.2% of genes in the genome could encode proteins, whereas the rest were considered as “non-coding”. Accumulating evidence demonstrates that a variety of ncRNAs can be encapsulated and transported by exosomes, among which exosomal microRNAs (miRNAs), long non-coding RNAs (lncRNAs), and circular RNAs (circRNAs) are the most attractive subclasses in the field of bone regeneration.

2.1.1 miRNAs

MiRNAs are small, highly conserved ncRNAs with ~22 nt length (Prattichizzo et al., 2021). The biogenesis of miRNAs involves the processing of larger primary miRNAs (pri-miRNAs) into shorter pre-miRNAs, and the maturation of pre-miRNA to produce active miRNAs (Ha and Kim, 2014). MiRNAs mediate post-transcriptional gene silencing by binding to the target mRNAs 3′-untranslated region (UTR) or open reading frames (ORFs) to regulate the translational process in a wide range of physiological processes (Yang et al., 2017).

Since the first observation of exosomal miRNAs in 2007 (Valadi et al., 2007), miRNAs have become the most studied cargos in exosome. Recently, a massive number of studies have demonstrated that miRNAs in natural exosomes derived from multiple cell types can promote osteogenesis (Table 1). These studies confirmed miRNAs from exosomes of different cellular origin can enter recipient cells with the help of exosome internalization, and then regulate the expressions of genes associated with osteogenic at the translational level to regulate bone regeneration.

2.1.2 lncRNAs

As a heterogeneous group of non-protein-coding transcripts with length of greater than 200 nucleotides, lncRNAs are emerging regulators involved in diverse physiological and pathological processes (Kopp and Mendell, 2018; Nair et al., 2020). Notably, lncRNAs can be selectively packaged into exosomes (Valadi et al., 2007), which enable them as biomarkers of certain disease. For instance, the expressions of lncRNAs in serum exosomes from persons with or without osteoporosis showed significant differences (Teng et al., 2020).

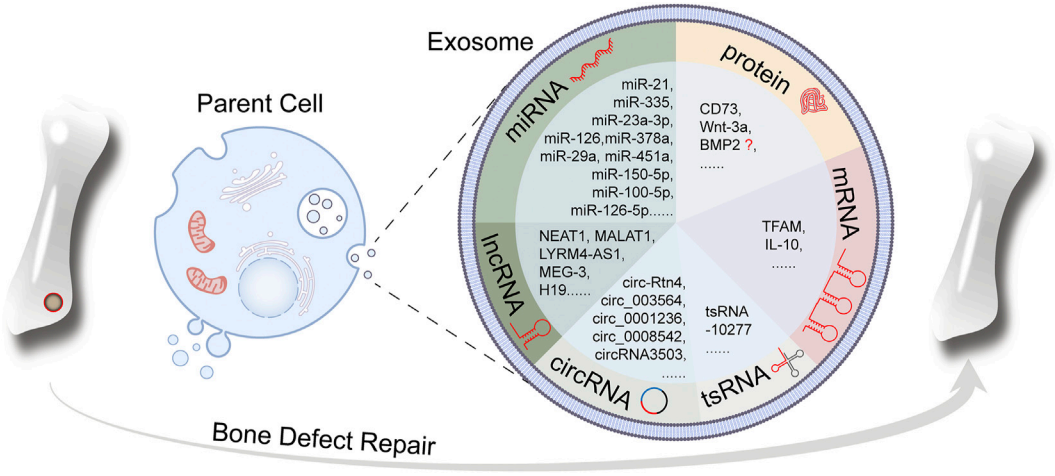

FIGURE 1
Schematic of exosomal cargos (miRNA, lncRNA, circRNA, tsRNA, mRNA and protein) with the function of promoting bone regeneration.

Beyond as molecular markers, lncRNAs can sponge miRNAs and regulate the expression of downstream genes, called competing endogenous RNA (ceRNA) mechanism (Salmena et al., 2011). Accumulating evidence showed that lncRNAs from multiple cells-derived exosomes can enter the receptor cells and have the potential to regulate bone regeneration (Table 1).

2.1.3 circRNAs

CircRNA, a special subclass of lncRNAs with a circular structure, has recently gained interest because of their extraordinary stability, much longer half-life and diverse biological functions (Jeck and Sharpless, 2014; Liu and Chen, 2022). CircRNAs can be selectively packaged into exosomes similar to lncRNAs (Ma et al., 2021). Additionally, exosomal circRNA also has the potential to regulate gene expression by ceRNA mechanism (Zhi et al., 2021; Du et al., 2022). Number of studies have revealed the regulatory function of exosomal circRNA in bone regeneration (Table 1). Interestingly, the effect of exosomal circRNAs in regulating bone regeneration, it seems, is a double-edged sword. For example, Zhi et al. (2021) reported that serum exosomal hsa_circ_0006859 was upregulated in patients with osteoporosis, and suppressed osteogenesis and promoted adipogenesis. Therefore, the regulatory functions of exosomal circRNAs are still unclear, which needs further studies.

2.1.4 tsRNAs

Transfer RNA (tRNA)-derived small RNA (tsRNA) is a class of small ncRNAs generated from precursor or mature tRNAs, which has recently received considerable attention (Zhu et al., 2018; Zhu et al., 2019). With the deepening of research, tsRNAs have been reported to regulate stem cell maintenance (Blanco et al., 2016), cancer (Balatti et al., 2017), viral infection (Nunes et al., 2020), neurological diseases (Zhang et al., 2020), epigenetic inheritance (Zhang Y. et al., 2018), and symbiosis (Ren et al., 2019). The mechanisms of action of tsRNAs include playing as mimicry/replacement of tRNAs with sequence/structure effects, associating with ribonucleoproteins and binding to the target genes like miRNAs (Chen et al., 2021). Although the function of exosomal tsRNAs is an emerging field with a paucity of research, Fang et al. (2020) explored the osteogenic effect of exosomal tsRNA (Table 1). They found tsRNA-10277 in the exosome derived from BMSCs could enhance osteogenic differentiation ability of dexamethasone-induced BMSCs.

2.2 mRNAs

As the Central Dogma of molecular biology presented mRNA as the fundamental ingredient in genetic translational machinery (Crick, 1970), it seemed that transferring mRNA *via* exosomes to affect the biological processes of recipient cells would be a more simple and efficient method compared with transferring ncRNAs. However, there has been remarkably little work about exosomal mRNA. This is probably because miRNAs and lncRNAs are the vast majority of exosomal RNAs (Hergenreider et al., 2012; Zhang et al., 2015; Zhang et al., 2017), and exosomal mRNAs were classically thought to be in the form of fragments, but not their intact forms (Valadi et al., 2007; Wei et al., 2017). With further research, it was estimated that on average, one intact mRNA can be found within every 1,000 exosomes produced endogenously without external stimulation (Yang Z. et al., 2020). Therefore, it is essential to confirm the integrity, high expression and regulatory function of mRNAs in the research based on exosomal mRNAs. In recent

TABLE 1 The exosomal cargos involved in bone regeneration.

Cargos	Sources	Target cell	Function	References
ncRNA				
miRNA				
miR-23a-3p	UCMSCs	Chondrocytes BMSCs	Promoting the migration, proliferation and differentiation of chondrocytes and BMSCs	Hu et al. (2020)
miR-21	UCMSCs	EPCs	Enhancing angiogenesis	Zhang et al. (2021c)
miR-378a	M2 polarized macrophages	MSCs	Inducing osteogenic differentiation	Kang et al. (2020)
miR-100-5p	IPFP-MSCs	Chondrocytes	Enhancing the autophagy level of chondrocytes	Wu et al. (2019)
miR-335	Mature DCs	BMSCs	Promoting the proliferation and osteogenic differentiation of BMSCs	Cao et al. (2021)
miR-126	EPCs	Endothelial cells	Enhancing the proliferation, migration, and angiogenic capacity of endothelial cells	Jia et al. (2019)
miR-451a	ADSCs	Macrophages	Inhibiting inflammation and promoting the polarization of M1 macrophages to M2 macrophages	Li et al. (2022)
miR-126–5p	SCAP	HUVECs	Promoting angiogenesis	Jing et al. (2022)
miR-150–5p		MC3T3-E1	Promoting osteogenesis	
miR-29a	BMSCs	HUVECs	Promoting angiogenesis	Lu et al. (2020)
lncRNA				
NEAT1	Prostate cancer cells	BMSCs	Inducing osteogenic differentiation	Mo et al. (2021)
MALAT1	EPCs	Bone marrow-derived macrophages	Enhancing recruitment and differentiation of osteoclast precursors	Cui et al. (2019)
MALAT1	BMSCs	hFOB1.19	Enhancing osteoblast activity	Yang et al. (2019)
MEG-3	BMSCs	Chondrocytes	Reducing senescence and apoptosis	Jin et al. (2021)
LYRM4-AS1	BMSCs	Chondrocytes	Regulating the growth of chondrocytes	Wang et al. (2021c)
H19	BMSCs	$CD31^+$ ECs and BMSCs	Promoting endothelial angiogenesis and BMSCs osteogenesis	Behera et al. (2021)
		BMSCs	Affecting osteogenic differentiation	Wang et al. (2021d)
circRNA				
circLPAR1	Osteogenic-induced DPSCs	DPSCs	Promoting osteogenic differentiation of the recipient DPSCs	Xie et al. (2020)
circRNA_0001236	BMSCs	BMSCs	Promoting chondrogenic differentiation	Mao et al. (2021)
circ_003564	BMSCs	Primary neurons and PC-12 cells	Attenuating inflammasome-related pyroptosis	Zhao et al. (2022)
circ-Rtn4	BMSCs	MC3T3-E1 cells	Attenuating TNF-α-induced cytotoxicity and apoptosis	Cao et al. (2020)
circ_0008542	MC3T3-E1 cells	Osteoclast	Promoting osteoclast differentiation and bone resorption	Wang et al. (2021b)
circRNA3503	SMSCs	Chondrocytes	Promoting chondrocyte renewal to alleviate the progressive loss of chondrocytes	Tao et al. (2021)
cirHmbox1	Osteoclasts	Osteoclasts and osteoblasts	Regulating osteoclasts differentiation and osteoblasts differentiation	Liu et al. (2020)
tsRNA				
tsRNA-10277	BMSCs	Dexamethasone-induced BMSCs	Enhancing osteogenic differentiation ability	Fang et al. (2020)
mRNA				
TFAM	SHED	DPSCs	Promoting osteogenic differentiation	Guo et al. (2022)
IL-10	M2 polarized macrophages	BMSCs	Regulating cell differentiation and bone metabolism	Chen et al. (2022)
Protein				
CD73	MSCs	Chondrocytes	Suppressing inflammation and restoring matrix homeostasis	Zhang et al. (2019)
Wnt-3a	ADSCs	Primary osteoblastic cells	Promoting the proliferation and osteogenic differentiation	Lu et al. (2017)

(Continued on following page)

TABLE 1 (*Continued*) The exosomal cargos involved in bone regeneration.

Cargos	Sources	Target cell	Function	References
Mutant HIF-1α	BMSCs	BMSCs HUVECs	Promoting osteogenic differentiation capacity and angiogenesis	Li et al. (2017)
BMP2	BMSCs	BMSCs	Promoting tendon bone healing in rotator cuff tear	Han et al. (2022a)

UCMSCs, umbilical cord-derived mesenchymal stem cells; IPFP-MSCs, infrapatellar fat pad mesenchymal stem cells; DCs, dendritic cells; EPCs, endothelial progenitor cells; ADSCs, adipose-derived stem cells; SCAP, stem cells from apical papilla; BMSCs, bone marrow mesenchymal stem cells; ECs, endothelial cells; DPSCs, dental pulp stem cells; SMSCs, synovium mesenchymal stem cells; SHED, stem cells from human exfoliated deciduous teeth; DPSCs, dental pulp stem cells; MSCs, mesenchymal stem cells; HUVECs, human umbilical vein endothelial cells.

research, the regulatory function of exosomal mRNA in bone regeneration have been revealed (Table 1). These studies showed exosomal mRNAs also could be a useful tool to aid the healing of bone defects, as long as improving the loading efficiency of intrinsically encapsulate transcribed mRNA into secreted exosomes.

2.3 Protein

A variety of proteins have been observed in exosomes, including cytoskeletal proteins, tetraspanins (CD9, CD63, CD81, and CD82), ESCRT-associated components (Alix and TSG101), heat shock proteins (HSP60, HSP70, and HSP90), antigen presentation proteins (MHC I and MHC II), and integrins (Kalluri and LeBleu, 2020; Zhu et al., 2020). As the main executor of life activities, proteins are not only the markers of exosomes but also endow exosomes with many biofunctions including regulating bone regeneration (Table 1).

Despite above research drawn inspiring conclusions, the controversy about the function of exosomal protein in bone regeneration persists. Take BMP2, an important regulator of osteogenesis, as an example. Han L. et al. (2022) reported that BMP2 in BMSC-derived exosomes could promote tendon bone healing in rotator cuff tear by activating Smad/RUNX2 signaling pathway. Conversely, in another study, exosomes derived from MSCs overexpressing *BMP2* did not contain BMP2 protein, and the function of promoting bone regeneration was possibly due to the changes of exosomal miRNA composition (Huang et al., 2020). Additionally, Furuta et al. (2016) found MSC exosomes could promote mice fracture healing, but the levels of SDF-1, MCP-1, and MCP-3, essential factors in the initial phase of fracture healing (Kitaori et al., 2009; Toupadakis et al., 2012; Ando et al., 2014; Ishikawa et al., 2014), in MSC exosomes were significantly lower, suggesting that bone regeneration may be mediated by other exosome components (such as miRNAs) but not exosomal proteins. The controversy above suggests that the mechanisms by which exosomal proteins work may be complex and remain to be determined.

To sum up, the function of various exosomal cargos makes exosomes have the ability to regulate bone regeneration in different ways. Predictably, more and more exosomal cargos would be revealed to function in bone regeneration by conventional or novel mechanism in the near future. Meanwhile, the explorations of mechanism inspired investigators to design engineering exosomes for bone regeneration by modifying the exosomal cargos, which will be discussed in the next section.

3 Strategies of engineering exosomes for bone defect repair

Although numerous exosomal cargos have been revealed to function in promoting osteogenic differentiation in the past decade, the clinical application of exosome in bone regeneration is still facing major challenges. The reason may be the low exosome yield, low content of functional exosomal cargos and low targeting efficiency of native exosomes (Song et al., 2022).

To improve the yield of exosomes, it is necessary to simplify the exosome extraction procedure. Until now, six classes of exosome separation strategies have been reported, including ultra-speed centrifugation, ultrafiltration, immunoaffinity capture, charge neutralization-based polymer precipitation, size-exclusion chromatograph, and microfluidic techniques, with unique sets of advantages and disadvantages for each technique (Yang D. et al., 2020). These rapid development in separation technology has in a large extent solved the problem of exosome isolation.

In order to enrich the exosomal cargo and increase exosome targeting efficiency, engineering exosome is rapidly expanding in the past decade. Engineering exosomes are the exosomes created through changing parent cells or directly on exosomes by biochemical or physical treatment (Kojima et al., 2018; Yerneni et al., 2019). In this section, we summarized the three strategies of engineering exosomes for bone regeneration (Figure 2): 1) direct modification of exosomes, 2) chemical or physical treatment of parent cells, and 3) genetic modification of parent cells.

3.1 Direct modification of exosomes

The direct modification of exosomes means decorating the surface proteins to improve the targeting ability of exosomes; or

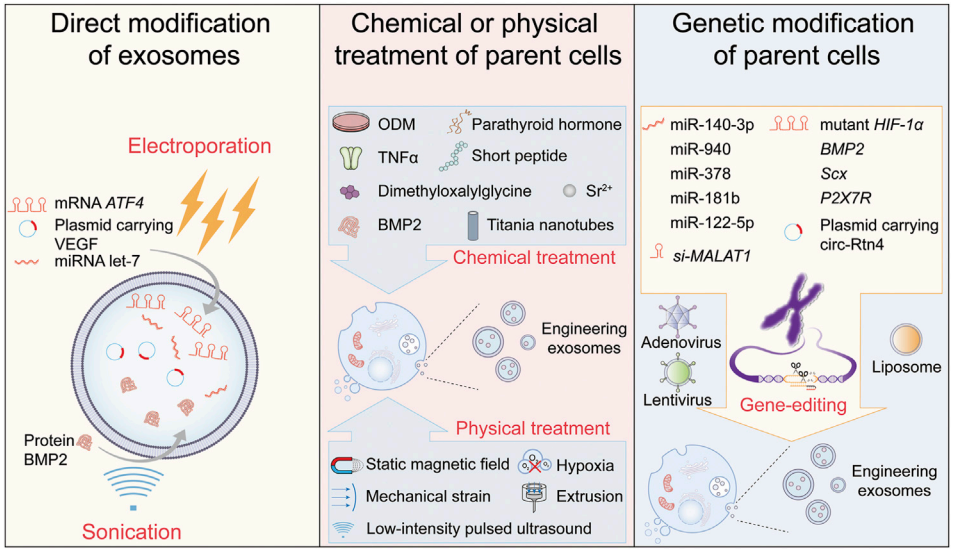

FIGURE 2
Three strategies of engineering exosomes for bone regeneration. ODM: osteogenic differentiation medium.

embellishing exosomal cargos or exogenous bioactive molecules to enhance the regulatory function through chemical methods (conjugation of peptides to exosomal surface (Gao X. et al., 2018)) or physical methods (electroporation (Tian et al., 2014) or sonication (Wang P. et al., 2019)) directly. This strategy has been extensively used to enhance the targeting ability and/or deliver specific cargo to the lesion region in numerous diseases, such as cancers (Gilligan and Dwyer, 2017; Zhang and Yu, 2019; Zhou et al., 2021), acute lung injury/acute respiratory distress syndrome (Zoulikha et al., 2022), inflammatory bowel disease (Ocansey et al., 2020) and Alzheimer's disease (Alvarez-Erviti et al., 2011).

In bone regeneration, several studies have revealed the enhanced function of exosomes modified by electroporation and sonication. For example, Wang et al. (2021e) used electroporation to introduce activating transcription factor 4 (*ATF4*) mRNA into mice serum exosomes, and found the *ATF4*-overloading exosomes could promote chondrocyte autophagy and inhibit chondrocyte apoptosis, which in turn protected cartilage and alleviated osteoarthritic progression. Zha et al. (2021) encapsulated plasmid carrying the vascular endothelial growth factor (*VEGF*) into exosomes *via* electroporation, and the gene-activated engineering exosomes could effectively induce the bulk of vascularized bone regeneration. Choi et al. (2019) inactivated pre-osteoblast exosomal let-7, a critical miRNA regulating osteogenesis regulation, by transfecting let-7 inhibitor into exosomes *via* electroporation, and found these exosomes lost the ability to recover osteogenic differentiation, which confirmed the availability of direct modification of exosomes strategy from the opposite. Additionally, although data are scarce, sonication is another method to load hydrophilic molecules into exosomes, which is considered much more efficient than electroporation (Kim et al., 2016). In several studies, the mixture of BMP2 protein and exosomes was sonicated on ice to construct BMP2-loaded exosomes (Haney et al., 2015; Yerneni et al., 2021; Yerneni et al., 2022), and these engineering exosomes could enhance the osteogenic potential of MC3T3-E1 cells (Yerneni et al., 2022).

Direct modification of exosomes seems a simple and useful approach to obtain engineering exosomes, but the application of this strategy is still facing several challenges. The loading efficiency of electroporation is largely suppressed when transferring oligonucleotides with more than 750 bp length into exosomes (Lamichhane et al., 2015). Another important point to consider is that sonication is reported to be the most damaging technique for exosomal membrane integrity (Donoso-Quezada et al., 2020). Besides, the size and zeta potential were reported to affect the efficiency of exosome internalization (Caponnetto et al., 2017; Patel et al., 2019), which should be taken into consideration in the further research. Therefore, when using this strategy to product engineering exosomes, it must be carefully designed to increase loading and internalization efficiency and avoid exosome rupture.

3.2 Chemical or physical treatment of parent cells

Directly treating parent cells with chemical or physical factors is an available strategy for engineering exosomes. As originated from parent cells, the characteristics of exosomes will be reflected by the

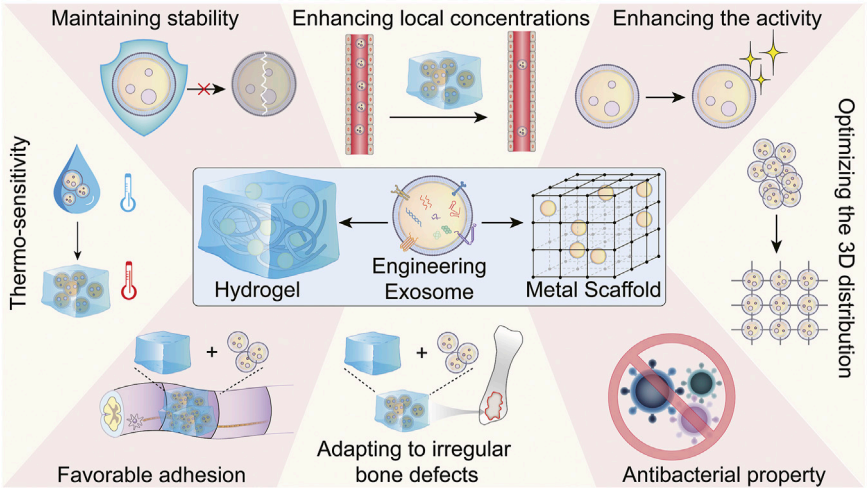

FIGURE 3
The properties of biomaterial (hydrogel and metal scaffold) help exosomes to promote bone regeneration.

physiological and biochemical alterations of parent cells. Numerous studies have confirmed that the preconditioning of stem cells *via* hypoxia, pharmacological agents, chemical agents, trophic factors, cytokines, and physical factors could improve stem cells' function *in vitro* and *in vivo* (Liu et al., 2011; Ferrer et al., 2013; Yang et al., 2016; Kheirandish et al., 2017; Yin et al., 2017; Hu and Li, 2018).

Chemical agents and metal ions are the two main treatment modalities of producing engineering exosomes by chemical treatment. Culturing parent cells in the osteogenic differentiation medium (ODM) is the most common method. Liu A. et al. (2021) isolated exosomes from BMSCs after osteoinductive culturing and found these engineering exosomes enhanced the bone forming capacity and induced rapid initiation of bone regeneration. In other research, umbilical cord mesenchymal stem cells (Ge and Wang, 2021) and dental pulp stem cells (Xie et al., 2020) were cultured in the ODM to produce engineering exosomes, which could enhance osteogenesis. Besides the ODM, many other chemical agents, TNF-α (Lu et al., 2017), short peptide (Zhao W. et al., 2021), parathyroid hormone (Shao et al., 2022), dimethyloxalylglycine (Liang et al., 2019) and BMP2 (Wei et al., 2019), were also used to produce engineering exosomes for bone defect repair. The metal ions treatment of parent cells can also endow exosomes with the ability to enhance bone regeneration. The exosomes derived from BMSCs stimulated by strontium-substituted calcium silicate ceramics could regulate osteogenesis and angiogenesis of human umbilical vein endothelial cells (Liu et al., 2021c). Similarly, macrophage-derived exosomes upon stimulation with titania nanotubes simultaneously enhanced osteogenesis and angiogenesis (Wang et al., 2022d).

Moreover, various physical modifications of parent cells also could yield engineering exosomes. Wu et al. (2021a) collected exosomes from BMSCs stimulated by magnetic nanoparticles and a static magnetic field and found these exosomes could improve osteogenesis and angiogenesis. As oxygen concentration plays a crucial role in proliferation (Silván et al., 2009), Shen et al. (2022) found exosomes derived from hypoxia preconditioned MSCs promote cartilage regeneration *via* the miR-205–5p/PTEN/AKT pathway. The mechanical force is an essential factor to regulate the differentiation of stem cells (Halder et al., 2012). Lv et al. (2020) found exosomes derived from osteocyte induced by mechanical strain could promote the proliferation and osteogenic differentiation of human periodontal ligament stem cell. Low yield is one of the main challenges for the application of engineering exosomes. To overcome this, Fan et al. (2020) employed an extrusion approach to amass exosome mimetics (EMs) from human MSCs, and the EMs demonstrated robust bone regeneration. In other studies, low-intensity pulsed ultrasound not only promoted BMSC-exosome release, but enhances the effects of BMSC-exosomes on cartilage regeneration in osteoarthritis (Liao et al., 2021; Xia et al., 2022).

According to above research, chemical or physical treatment of parent cells indeed is an effective strategy to produce engineering exosomes for bone regeneration. It is worthwhile to mention that the function of the engineering exosomes produced by this strategy still relies on the exosomal cargos in substantially all these studies. Therefore, modifying the nucleic acids of parent cells to produce engineering exosomes with bioactive cargos seems another ideal strategy, which will be elaborated on below.

3.3 Genetic modification of parent cells

With advances in molecular biological techniques, gene-editing has become one of the most commonly used methodologies in molecular research. Consequently,

TABLE 2 The properties of exosome-integrated biomaterials for bone defect repair.

Properties	Biomaterials	References
Maintaining exosomes stability	Nanocomposite hydrogels	Li et al. (2021b)
Enhancing local concentrations of exosomes	Acellular extracellular matrix hydrogel	Xing et al. (2021)
	Injectable hyaluronic acid hydrogel	Zhang et al. (2021c)
	Gelatin methacrylate/nanoclay hydrogel	Hu et al. (2020)
	3D matrix hydrogels	Holkar et al. (2021)
	Injectable thermosensitive hydrogel	Ma et al. (2022)
Enhancing exosomes activity	3D matrix hydrogels	Yu et al. (2022b)
	Alginate hydrogel	Holkar et al. (2021)
Optimizing the 3D distribution	ABM/P-15 CMC-hydrogel	Matos et al. (2012)
	3D-printed porous bone scaffolds	Zha et al. (2021)
Antibacterial property	Food-grade probiotic-modified implant	Tan et al. (2020a)
	Multifunctional HA hydrogel	Liu et al. (2022)
		Yu et al. (2022a)
	Natural polymer HA hydrogel	Mi et al. (2022)
	Chitosan hydrogel	Shen et al. (2020)
Adapting to irregular bone defects	Injectable thermosensitive hydrogel	Xing et al. (2021)
	PDLLA-PEG-PDLLA triblock copolymer gels	Tao et al. (2021)
	Chitosan hydrogel	Fan et al. (2020)
		Wu et al. (2021b)
	Nanocomposite hydrogel based on gelatin and Laponite	Liu et al. (2021b)
	PG/TCP	Zhang et al. (2021a)
	HA hydrogel	Yu et al. (2022a)
	Alginate	Huang et al. (2020)
		Holkar et al. (2021)
	Gel-ADH	Lin et al. (2022)
	Silk fibroin	Shen et al. (2022)
	Hyaluronic acid	Sang et al. (2022)
		Yang et al. (2020b)
	SIS-CA hydrogel	Ma et al. (2022)
Favorable adhesion	Crosslinked network of alginate-dopamine, chondroitin sulfate, and regenerated silk fibroin	Zhang et al. (2021b)
	HA hydrogel modified with the PPFLMLLKGSTR peptide	Li et al. (2020)
Thermo-sensitivity	SIS-CA hydrogel	Ma et al. (2022)

ABM/P-15, CMC-hydrogel: bovine-derived mineral bound to a P-15 carboxymethyl cellulose-hydrogel; HA, hyaluronic acid; PDLLA-PEG-PDLLA, poly (D, L-lactide)-b-poly (ethylene glycol)-b-poly (D, L-lactide); PG/TCP, poly ethylene glycol maleate citrate with β-TCP; Gel-ADH, hydrazide grafted gelatin; SIS-CA, small intestinal submucosa with propionic acid.

engineering exosomes with more or totally new bioactive molecules can be performed by editing certain genes in parent cells. As described previously, cargos are the basis of exosomes function, and numerous exosomal cargos (mRNAs, miRNAs, lncRNAs, circRNAs and proteins) have been confirmed to promote bone regeneration, which enlightened researchers to produce engineering exosomes by genetic modification of the parent cells.

As the most extensively studied exosomal cargos, miRNAs with the function of promoting bone regeneration received tremendous attention, and a vast variety of studies have attempted to enhance the biofunction of exosomes by gene-editing of parent cells' miRNAs. Wang N. et al. (2022) transfected BMSCs with lentivirus to obtain exosomes overexpressing miR-140–3p, and found these exosomes promoted bone defect remodeling. A lentiviral infection system was also used to overexpress miR-940 in MDA-MB-231 cells to attain engineering exosomes, which could promote the osteogenic differentiation of human MSCs (Hashimoto et al., 2018). Transferring parent cells with miRNAs by Lipofectamine reagent is another genetic modification method. By this way, exosomes overexpressing miR-378 (Nan et al., 2021), miR-181b (Liu W. et al., 2021) and miR-122–5p (Liao et al., 2019) have been demonstrated to promote osteogenic differentiation.

The mRNA is also an important target for this strategy. Li et al. (2017) transfected adenovirus carrying mutant *HIF-1α* into BMSCs, and found the mutant protein was highly expressed in BMSCs exosomes, which markedly accelerated the bone regeneration and angiogenesis. Interestingly, in several other

studies, exosomes derived from parent cells with gene-editing of *BMP2* (Huang et al., 2020), *Scx* (Feng et al., 2021) and *P2X7R* (Xu et al., 2020) performed the enhanced osteogenic ability. However, this modulating function was due to the changes of exosomal miRNA rather than the transfection of these genes. This might be due to two reasons: firstly, the cellular components are selectively packaged into exosomes to be exosomal cargos (Ma et al., 2021), and gene-editing of certain genes may not inevitably result in their expression change in exosome; secondly, miRNAs are the most abundant exosomal cargos, which may be more sensitive to the gene-editing modification.

Several studies revealed the effect of genetic modification on other exosomal bioactive molecules (lncRNAs and circRNAs). Cui et al. (2019) inhibited lncRNA-MALAT1 expression in endothelial progenitor cells-derived exosomes by transfecting lncRNA-MALAT1-targeting siRNA, which disrupted bone regeneration. Cao et al. (2020) subcloned the full sequence of circ-Rtn4 into the pcDNA-3.1 vector and transfected the vector into BMSCs using Lipofectamine 2000 to overexpress exosomal circ-Rtn4. Nevertheless, to date, the research in this field has remained limited for the technical reason. Take upregulating circRNAs as an example, it is difficult to deplete or generate the circular form without affecting the linear counterpart of circRNA (Nielsen et al., 2022). In addition, low cyclization efficacy and accuracy also limited the modification of circRNAs by gene-editing. Therefore, investigation into novel and high-efficiency genetic modification technologies is required to combat these problems.

4 Properties of exosome-integrated biomaterials essential for bone defect repair

Although the strategies of engineering exosomes could enhance exosome yield and biofunction, exosomes used for clinical bone defect treatment are still limited (van der Meel et al., 2014; Lener et al., 2015). Currently, the major modes of exosome application are direct injection or carrier loading, which is mainly aimed at systemic diseases, such as osteoporosis (Song et al., 2019), hematological malignancies (De Luca et al., 2017), and myocardial ischemia-reperfusion injury (Zhao et al., 2019). Nevertheless, it has been reported that no significant effect was observed with free exosomes treatment by direct injection, because of its rapid excretion from the site of application (Zhang Z. et al., 2018; Wang C. et al., 2019; Xing et al., 2022), suggeting the medand for exosome-integrated biomaterials. Currently, more and more biomaterials have been designed and applied in bone regeneration (Cui et al., 2020; Zhao D. et al., 2021; Zhu et al., 2022a; Zhu et al., 2022b; Wang et al., 2022c; Zhang et al., 2022). Therefore, the selection of available biomaterials with appropriate stability and integrity to load and release exosomes at the bone defect site to increase their retention and stability may be necessary for bone regeneration.

Several excellent and informative reviews have addressed the types, synthetic procedure and/or encapsulation approaches of biomaterials used to carry exosomes (Riau et al., 2019; Pishavar et al., 2021; Wang D. et al., 2022; Sun et al., 2022). Instead, we propose to streamline the properties of biomaterial to dissect how and by what mechanisms the biomaterials help exosomes to promote bone regeneration (Figure 3; Table 2). By summarizing the previous studies, we expected to represent a promising strategy for the use of engineering exosomes in combination with biomaterials for clinical bone regeneration.

4.1 Maintaining the exosome stability

The first consideration is how to maintain the stability of exosomes. Despite the bilayer membrane structures making exosomes resist degradation to some extent, exosomes are unstable and maintain for less 48 h at room temperature (Chew et al., 2019). The time will be even shorter at 37°C, at which exposed functional substances (proteins and RNA) will be rapidly degraded and metabolized. In fact, stability is an important but often overlooked point in the research of biomaterials loading exosomes, which should be given sufficient attention in the further. Hydrogel encapsulated exosomes was reported to protect them without degradation and supply therapeutic effects with persistent exosomes delivery (Riau et al., 2019). Li et al. (2021b) used the gelatin and laponite to prepare nanocomposite hydrogels as a carrier for exosomes to extend the time of BMSC-exosomes in the periodontal pocket and enhance their osteoinductive function.

4.2 Enhancing local concentrations of exosomes

The therapeutic effect of exosomes depends strongly on the local concentrations. However, it is demanding to produce exosomes in large quantities with high quality and purity, making clinical applications of exosomes more expensive. Additionally, free exosomes diffused out from the defect rapidly, resulting in no exertion of exosomal cargo activity (Riau et al., 2019). According to the research of Lai et al. (2012), biodistribution proceeds in the stages of liver and lungs for 30 min after direct injection of exosomes, and exosomes are removed within 1 h–6 h after administration *via* liver and kidney treatment. Thus, much research was performed with the aim of enhancing the retention and sustained-releasing of exosomes at the defect site. Xing et al. (2021) synthesized an acellular extracellular matrix hydrogel coupled with adipose-derived mesenchymal stem cell exosomes to regulate the intervertebral disc microenvironment for the treatment of intervertebral disc degeneration. The decomposition of the hydrogel was slowed down, allowing exosomes to remain in

the disc for up to 28 days Zhang Y. et al. (2021) fabricated an injectable hyaluronic acid hydrogel encapsulated with umbilical MSC-derived exosomes through three-dimensional (3D) printing technology, and the hydrogel showed good sustained-releasing features in the rat critical-size cranial defect model. Hu et al. (2020) fabricated Gelatin methacrylate/nanoclay hydrogel for sustained release of exosomes. The hydrogels with a 3D matrix prevent the dispersion of exosomes and maintained their local concentration, which enable the controlled release of exosomes at bone defect sites (Holkar et al., 2021). In another study, exosomes were incorporated into an injectable thermosensitive hydrogel by constructing fusion peptides, which also enhanced the retention of exosomes and improved the biological activity of exosomes (Ma et al., 2022). Generally, the consensus has been achieved that it is essential to enhance local exosome concentrations at the bone defect site, and the biomaterials loading exosomes should possess the property of enhancing the retention and sustained-releasing of exosomes.

4.3 Enhancing exosomes activity

The hydrogel with 3D microenvironment can enhance exosome activity and affect the interaction of integrin membrane protein between cells and the cell matrix, which promotes cell proliferation and differentiation in a bone regeneration environment. Yu W. et al. (2022) encapsulated exosomes derived from periodontal ligament stem cells into a hydrogel with 3D microenvironment, which enhanced osteoinductive ability and significantly promoted bone defect repair in rats. Another study demonstrated alginate hydrogels combined with exosomes promoted osteogenesis by increasing cell-exosomes interactions, cell aggregation, and long-term viability (Holkar et al., 2021).

4.4 Optimizing the 3D distribution of exosomes

Biomaterials with a highly porous and 3D structure mimic the porosity, pore size, and interconnectedness of native bone ideally. In bone defects repair, bioactive materials with good mechanical properties not only provide temporary mechanical support for the bone at the implant site, but also modulate extracellular matrix formation, facilitate better cell-cell and cell-matrix interactions, retain the cell morphology, provide mechanical stimulations, and support cell growth and exosomes secretion, the features which are akin to *in vivo* systems (Tibbitt and Anseth, 2009). Matos et al. (2012) showed that the lyophilized biomaterials created a more homogenous interparticle spacing, allowed a more suitable particle distribution and stabilization, then promoting a faster bone regeneration with relevant clinical benefits. Similarly, biocompatible 3D porous biomaterials ensured a uniform spacing and stable distribution of MSC-exosomes compared with compacted materials (Zha et al., 2021).

4.5 Antibacterial property

During bone defect healing, the bacterial infection is one of the risk factors (Blair et al., 2015). Therefore, antibacterial property of biomaterials should also be taken into consideration. Tan L. et al. (2020) developed a food-grade probiotic-modified implant to prevent methicillin-resistant *Staphylococcus aureus* infection and accelerated bone integration. Liu et al. (2022) designed a multifunctional hyaluronic acid (HA) hydrogel with antibacterial property. Then, this group loaded plasma exosomes to this hydrogel for promoting infected fracture healing (Yu C. et al., 2022). Mi et al. (2022) combined engineered exosomes and a natural polymer HA hydrogel, which performed an anti-inflammatory and antibacterial function on fracture repair acceleration. As a cationic natural polymer biomaterial, chitosan has anti-microbial property (Dai et al., 2011), and many reports have shown cationic loaded engineering exosomes could promote bone regeneration (Fan et al., 2020; Shen et al., 2020; Wang et al., 2020; Wu et al., 2021b; Bahar et al., 2022; Nikhil and Kumar, 2022), although some of them did not look at the antibacterial property. The biomaterials with antibacterial property have been designed in some studies, but these materials are still rarely used for bone defect repair, which merits further investigation.

4.6 Adapting to irregular bone defects

Clinical bone defects caused by trauma, neoplasia, infection or corrective osteotomies are always irregular. Hence, biomaterials should have the injectable property to fill irregular defects and promote *in situ* bone tissue regeneration. Xing et al. (2021) constructed an injectable thermosensitive hydrogel system *via* a coordinative crossing of ADSC-derived exosomes and acellular extracellular matrix hydrogels to effectively protect nucleus pulposus cells from pyroptosis after intervertebral disc degeneration. By taking advantage of injectable, reversible, and thermosensitive abilities, Tao et al. (2021) used PDLLA-PEG-PDLLA triblock copolymer gels as a carrier of synovium mesenchymal stem cells-derived exosomes for intra-articular injection to prevent osteoarthritis progression. Additionally, multiple biomaterials, including chitosan hydrogel (Fan et al., 2020; Wu et al., 2021b), nanocomposite hydrogel (based on gelatin and Laponite) (Liu et al., 2021b), PG/TCP (PEGMC with β-TCP) (Zhang B. et al., 2021), HA hydrogel (Yu C. et al., 2022), alginate (Huang et al., 2020; Holkar et al., 2021), Gel-ADH (hydrazide grafted gelatin) (Lin et al., 2022), silk fibroin (Shen et al., 2022), hyaluronic acid (Yang S. et al., 2020; Sang et al., 2022)

and SIS-CA (small intestinal submucosa (SIS) with propionic acid (CA)) hydrogel (Ma et al., 2022) were reported to adapt irregular bone defects and were used to carry exosomes for skeletal regeneration. Generally, although local injection therapy is not suitable for certain types of bone regeneration, such as spinal cord repair (Han M. et al., 2022), injectable biomaterials loading engineering exosomes have been used extensively to repair irregular bone defects.

4.7 Other properties

In a moist environment, the favorable adhesion of biomaterials is essential for *in situ* bone regeneration (Hasani-Sadrabadi et al., 2020; Li et al., 2020; Zhang FX. et al., 2021). Inspired by mussel materials, which exhibit underwater robust adhesion (Gao Z. et al., 2018), Zhang and the colleague (2021b) prepared a hydrogel with high bonding strength to the wet surface using a crosslinked network of alginate-dopamine, chondroitin sulfate, and regenerated silk fibroin, which promote cartilage defect regeneration by combining with BMSCs-exosomes. Peptide-modification is another strategy for enhancing biomaterial adhesion. Li et al. (2020) prepared a biomaterial with high adhesion by modifying HA hydrogel with the PPFLMLLKGSTR peptide, which could locally deliver human placenta amniotic membrane mesenchymal stem cell-derived exosomes in spinal cord tissue.

Biomaterials with thermo-sensitivity are also of particular concern for their property, changing between a liquid state and a solid-state based on the ambient temperature (López-Noriega et al., 2014; Ni et al., 2014). Several thermo-sensitive biomaterials have been used in bone defect repair (Fu et al., 2012; Kim et al., 2018; Yu et al., 2020; Wang QS. et al., 2021). Further, Ma et al. (2022) designed a novel thermo-sensitive biomaterial by loading BMSCs-exosomes with SIS-CA hydrogel to regulate bone regeneration.

Collectively, the bio-functional materials not only provide a scaffold or carrier for engineering exosomes, but also play an essential role by their own variety properties. Along with major advancements in chemical engineering techniques, more and more novel biomaterials with various properties have been synthesized for bone regeneration. In the future, selection of appropriate biomaterials to integrate engineering exosomes should be one of the leading focuses of bone defect repair.

5 Conclusion and perspective

Coexistence of challenges and opportunities have greatly stimulated the study of engineering exosomes for bone regeneration in the past 10 years. In the present review, we mainly addressed the molecular basis of exosomal cargos, the strategies of engineering exosomes and the properties of exosome-integrated biomaterials required for bone regeneration. The research about engineering exosomes for bone defect repair is undeniably in its infancy. The rapid development of engineering exosomes is impeded by several key challenges, especially the consistency of exosomes production. As a result, these difficulties inspired the development of new and cutting-edge approaches, often distinct from those in the conventional study of cells, to address both exosome production and function. Refining the isolation, purification and storage techniques of exosomes may be an effective means of improving the consistency of exosomes production (Colao et al., 2018; Zeng et al., 2022). Additionally, excellent biomaterials emerged continuously, which greatly promoted research self-renewal. The effective combination of engineering exosomes and biomaterials will be greater than the sum of their parts and exhibit synergy effects in bone regeneration. We optimistically foresee that novel biomaterials will be constructed and more sophisticated engineering exosomes will be implemented for bone tissue regeneration. This huge progress is sure to benefit both biomedical research and therapeutic modalities in the field of bone regeneration.

Author contributions

Conceptualization, SM, YL, and DP; writing—original draft preparation, SM, YZ, and SL; writing—review and editing, SM, AL, and DP; visualization, SM and YZ; funding acquisition, DP, YL, and SM. All authors have read and agreed to the published version of the manuscript.

Funding

This work was supported by National Natural Science Foundation of China (No. 81870798 and 82170927) and the Fundamental Research Funds for the Central Universities, Xi'an Jiaotong University (xzy012021066).

Conflict of interest

The authors declare that the research was conducted in the absence of any commercial or financial relationships that could be construed as a potential conflict of interest.

Publisher's note

References

Alvarez-Erviti, L., Seow, Y., Yin, H., Betts, C., Lakhal, S., and Wood, M. J. (2011). Delivery of siRNA to the mouse brain by systemic injection of targeted exosomes. *Nat. Biotechnol.* 29, 341–345. [PubMed: 341]. doi:10.1038/nbt.1807

Ando, Y., Matsubara, K., Ishikawa, J., Fujio, M., Shohara, R., Hibi, H., et al. (2014). Stem cell-conditioned medium accelerates distraction osteogenesis through multiple regenerative mechanisms. *Bone* 61, 82–90. [PubMed: 82]. doi:10.1016/j.bone.2013.12.029

Bahar, D., Gonen, Z. B., Gumusderelioglu, M., Onger, M. E., Tokak, E. K., Ozturk-Kup, F., et al. (2022). Repair of rat calvarial bone defect by using exosomes of umbilical cord-derived mesenchymal stromal cells embedded in chitosan/hydroxyapatite scaffolds. *Int. J. Oral Maxillofac. Implants* 37, 943–950. [PubMed: 943]. doi:10.11607/jomi.9515

Balatti, V., Nigita, G., Veneziano, D., Drusco, A., Stein, G. S., Messier, T. L., et al. (2017). tsRNA signatures in cancer. *Proc. Natl. Acad. Sci. U. S. A.* 114, 8071–8076. [PubMed: 28696308]. doi:10.1073/pnas.1706908114

Behera, J., Kumar, A., Voor, M. J., and Tyagi, N. (2021). Exosomal lncRNA-H19 promotes osteogenesis and angiogenesis through mediating Angpt1/Tie2-NO signaling in CBS-heterozygous mice. *Theranostics* 11, 7715–7734. [PubMed: 34335960]. doi:10.7150/thno.58410

Bei, H. P., Hung, P. M., Yeung, H. L., Wang, S., and Zhao, X. (2021). Bone-a-Petite: Engineering exosomes towards bone, osteochondral, and cartilage repair. *Small* 17, e2101741. [PubMed: 34288410]. doi:10.1002/smll.202101741

Bharadwaz, A., and Jayasuriya, A. C. (2020). Recent trends in the application of widely used natural and synthetic polymer nanocomposites in bone tissue regeneration. *Mater. Sci. Eng. C* 110, 110698. [PubMed: 32204012]. doi:10.1016/j.msec.2020.110698

Bhat, A. A., Younes, S. N., Raza, S. S., Zarif, L., Nisar, S., Ahmed, I., et al. (2020). Role of non-coding RNA networks in leukemia progression, metastasis and drug resistance. *Mol. Cancer* 19, 57. [PubMed: 32164715]. doi:10.1186/s12943-020-01175-9

Blair, J. M., Webber, M. A., Baylay, A. J., Ogbolu, D. O., and Piddock, L. J. (2015)., 13. PubMed, 4242–4251. doi:10.1038/nrmicro3380Molecular mechanisms of antibiotic resistance*Nat. Rev. Microbiol.*

Blanco, S., Bandiera, R., Popis, M., Hussain, S., Lombard, P., Aleksic, J., et al. (2016). Stem cell function and stress response are controlled by protein synthesis. *Nature* 534, 335–340. [PubMed: 27306184]. doi:10.1038/nature18282

Bobrie, A., Krumeich, S., Reyal, F., Recchi, C., Moita, L. F., Seabra, M. C., et al. (2012). Rab27a supports exosome-dependent and -independent mechanisms that modify the tumor microenvironment and can promote tumor progression. *Cancer Res.* 72, 4920–4930. [PubMed: 4920]. doi:10.1158/0008-5472.Can-12-0925

Cao, G., Meng, X., Han, X., and Li, J. (2020). Exosomes derived from circRNA Rtn4-modified BMSCs attenuate TNF-α-induced cytotoxicity and apoptosis in murine MC3T3-E1 cells by sponging miR-146a. *Biosci. Rep.* 40, BSR20193436. [PubMed: 32400849]. doi:10.1042/bsr20193436

Cao, Z., Wu, Y., Yu, L., Zou, L., Yang, L., Lin, S., et al. (2021). Exosomal miR-335 derived from mature dendritic cells enhanced mesenchymal stem cell-mediated bone regeneration of bone defects in athymic rats. *Mol. Med.* 27, 20. [PubMed: 33637046]. doi:10.1186/s10020-021-00268-5

Caponnetto, F., Manini, I., Skrap, M., Palmai-Pallag, T., Di Loreto, C., Beltrami, A. P., et al. (2017). Size-dependent cellular uptake of exosomes. *Nanomedicine Nanotechnol. Biol. Med.* 13 (3), 1011–1020. [PMID: 27993726]. doi:10.1016/j.nano.2016.12.009

Castillo-Cardiel, G., López-Echaury, A. C., Saucedo-Ortiz, J. A., Fuentes-Orozco, C., Michel-Espinoza, L. R., Irusteta-Jiménez, L., et al. (2017). Bone regeneration in mandibular fractures after the application of autologous mesenchymal stem cells, a randomized clinical trial. *Dent. Traumatol.* 33, 38–44. [PubMed: 27513920]. doi:10.1111/edt.12303

Chen, C., Qu, Z., Yin, X., Shang, C., Ao, Q., Gu, Y., et al. (2016). Efficacy of umbilical cord-derived mesenchymal stem cell-based therapy for osteonecrosis of the femoral head: A three-year follow-up study. *Mol. Med. Rep.* 14, 4209–4215. [PubMed: 27634376]. doi:10.3892/mmr.2016.5745

Chen, Q., Zhang, X., Shi, J., Yan, M., and Zhou, T. (2021). Origins and evolving functionalities of tRNA-derived small RNAs. *Trends Biochem. Sci.* 46, 790–804. [PubMed: 790]. doi:10.1016/j.tibs.2021.05.001

Chen, X., Wan, Z., Yang, L., Song, S., Fu, Z., Tang, K., et al. (2022). Exosomes derived from reparative M2-like macrophages prevent bone loss in murine periodontitis models via IL-10 mRNA. *J. Nanobiotechnol.* 20, 110. [PubMed: 35248085]. doi:10.1186/s12951-022-01314-y

Chew, J. R. J., Chuah, S. J., Teo, K. Y. W., Zhang, S., Lai, R. C., Fu, J. H., et al. (2019). Mesenchymal stem cell exosomes enhance periodontal ligament cell functions and promote periodontal regeneration. *Acta Biomater.* 89, 252–264. [PubMed: 252]. doi:10.1016/j.actbio.2019.03.021

Choi, S. Y., Han, E. C., Hong, S. H., Kwon, T. G., Lee, Y., and Lee, H. J. (2019). Regulating osteogenic differentiation by suppression of exosomal microRNAs. *Tissue Eng. Part A* 25, 1146–1154. [PubMed: 1146]. doi:10.1089/ten.TEA.2018.0257

Colao, I. L., Corteling, R., Bracewell, D., and Wall, I. (2018). Manufacturing exosomes: A promising therapeutic platform. *Trends Mol. Med.* 24 (3), 242–256. [PMID: 29449149]. doi:10.1016/j.molmed.2018.01.006

Colombo, M., Raposo, G., and Thery, C. (2014). Biogenesis, secretion, and intercellular interactions of exosomes and other extracellular vesicles. *Annu. Rev. Cell Dev. Biol.* 30, 255–289. [PubMed: 25288114]. doi:10.1146/annurev-cellbio-101512-122326

Crick, F. (1970)., 227. PubMed, 561561–561563. doi:10.1038/227561a0Central dogma of molecular biology*Nature*

Cui, L., Zhang, J., Zou, J., Yang, X., Guo, H., Tian, H., et al. (2020). Electroactive composite scaffold with locally expressed osteoinductive factor for synergistic bone repair upon electrical stimulation. *Biomaterials* 230, 119617. [PubMed: 31771859. doi:10.1016/j.biomaterials.2019.119617

Cui, Y., Fu, S., Sun, D., Xing, J., Hou, T., and Wu, X. (2019)., 23. PubMed, 38433843–38433854. doi:10.1111/jcmm.14228EPC-derived exosomes promote osteoclastogenesis through LncRNA-MALAT1*J. Cell. Mol. Med.*

Dai, T., Tanaka, M., Huang, Y. Y., and Hamblin, M. R. (2011). Chitosan preparations for wounds and burns: Antimicrobial and wound-healing effects. *Expert Rev. Anti-infective Ther.* 9, 857–879. [PubMed: 21810057]. doi:10.1586/eri.11.59

De Luca, L., Trino, S., Laurenzana, I., Lamorte, D., Caivano, A., Del Vecchio, L., et al. (2017). Mesenchymal stem cell derived extracellular vesicles: A role in hematopoietic transplantation? *Int. J. Mol. Sci.* 18, 1022. [PubMed: 1022. doi:10.3390/ijms18051022

Donoso-Quezada, J., Ayala-Mar, S., and González-Valdez, J. (2020). State-of-the-art exosome loading and functionalization techniques for enhanced therapeutics: A review. *Crit. Rev. Biotechnol.* 40, 804–820. [PubMed: 804]. doi:10.1080/07388551.2020.1785385

Du, Z., Yuan, J., Wu, Z., Chen, Q., Liu, X., and Jia, J. (2022). Circulating exosomal circRNA_0063476 impairs expression of markers of bone growth via the miR-518c-3p/DDX6 Axis in ISS. *Endocrinology* 163, bqac138. [PubMed: 35974445]. doi:10.1210/endocr/bqac138

Elefteriou, F. (2018). Impact of the autonomic nervous system on the skeleton. *Physiol. Rev.* 98, 1083–1112. [PubMed: 1083]. doi:10.1152/physrev.00014.2017

Fan, J., Lee, C. S., Kim, S., Chen, C., Aghaloo, T., and Lee, M. (2020). Generation of small rna-modulated exosome mimetics for bone regeneration. *ACS Nano* 14, 11973–11984. [PubMed: 11973]. doi:10.1021/acsnano.0c05122

Fang, S., He, T., Jiang, J., Li, Y., and Chen, P. (2020). <p>Osteogenic effect of tsRNA-10277-loaded exosome derived from bone mesenchymal stem cells on steroid-induced osteonecrosis of the femoral head</p>. *Drug Des. Devel Ther.* 14, 4579–4591. [PubMed: 4579]. doi:10.2147/dddt.S258024

Feng, W., Jin, Q., Ming-Yu, Y., Yang, H., Xu, T., You-Xing, S., et al. (2021). MiR-6924-5p-rich exosomes derived from genetically modified Scleraxis-overexpressing PDGFRα(+) BMMSCs as novel nanotherapeutics for treating osteolysis during tendon-bone healing and improving healing strength. *Biomaterials* 279, 121242. [PubMed: 34768151]. doi:10.1016/j.biomaterials.2021.121242

Ferrer, R. A., Wobus, M., List, C., Wehner, R., Schönefeldt, C., Brocard, B., et al. (2013). Mesenchymal stromal cells from patients with myelodyplastic syndrome display distinct functional alterations that are modulated by lenalidomide. *Haematologica* 98, 1677–1685. [PubMed: 1677]. doi:10.3324/haematol.2013.083972

Fu, S., Ni, P., Wang, B., Chu, B., Zheng, L., Luo, F., et al. (2012). Injectable and thermo-sensitive PEG-PCL-PEG copolymer/collagen/n-HA hydrogel composite for guided bone regeneration. *Biomaterials* 33, 4801–4809. [PubMed: 4801]. doi:10.1016/j.biomaterials.2012.03.040

Furuta, T., Miyaki, S., Ishitobi, H., Ogura, T., Kato, Y., Kamei, N., et al. (2016). Mesenchymal stem cell-derived exosomes promote fracture healing in a mouse model. *Stem Cells Transl. Med.* 5, 1620–1630. [PubMed: 27460850]. doi:10.5966/sctm.2015-0285

Gao, X., Ran, N., Dong, X., Zuo, B., Yang, R., Zhou, Q., et al. (2018a). Anchor peptide captures, targets, and loads exosomes of diverse origins for diagnostics and therapy. *Sci. Transl. Med.* 10, eaat0195. [PubMed: 29875202]. doi:10.1126/scitranslmed.aat0195

Gao, Z., Duan, L., Yang, Y., Hu, W., and Gao, G. (2018b). Mussel-inspired tough hydrogels with self-repairing and tissue adhesion. *Appl. Surf. Sci.* 427, 74–82. doi:10.1016/j.apsusc.2017.08.157

Ge, Y., and Wang, X. (2021). The role and mechanism of exosomes from umbilical cord mesenchymal stem cells in inducing osteogenesis and preventing osteoporosis. *Cell Transpl.* 30, 096368972110574. [PubMed: 34814742]. doi:10.1177/09636897211057465

Gilligan, K. E., and Dwyer, R. M. (2017). Engineering exosomes for cancer therapy. *Int. J. Mol. Sci.* 18, 1122. [PubMed: 28538671]. doi:10.3390/ijms18061122

Guo, J., Zhou, F., Liu, Z., Cao, Y., Zhao, W., Zhang, Z., et al. (2022). Exosome-shuttled mitochondrial transcription factor A mRNA promotes the osteogenesis of dental pulp stem cells through mitochondrial oxidative phosphorylation activation. *Cell Prolif.*, e13324. [PubMed: 36054692]. doi:10.1111/cpr.13324

Ha, M., and Kim, V. N. (2014). Regulation of microRNA biogenesis. *Nat. Rev. Mol. Cell Biol.* 15, 509–524. [PubMed: 25027649]. doi:10.1038/nrm3838

Halder, G., Dupont, S., and Piccolo, S. (2012). Transduction of mechanical and cytoskeletal cues by YAP and TAZ. *Nat. Rev. Mol. Cell Biol.* 13, 591–600. [PubMed: 591. doi:10.1038/nrm3416

Han, L., Liu, H., Fu, H., Hu, Y., Fang, W., and Liu, J. (2022a). Exosome-delivered BMP-2 and polyaspartic acid promotes tendon bone healing in rotator cuff tear via Smad/RUNX2 signaling pathway. *Bioengineered* 13, 1459–1475. [PubMed: 1459]. doi:10.1080/21655979.2021.2019871

Han, M., Yang, H., Lu, X., Li, Y., Liu, Z., Li, F., et al. (2022b). Three-dimensional-cultured MSC-derived exosome-hydrogel hybrid microneedle array patch for spinal cord repair. *Nano Lett.* 22, 6391–6401. [PubMed: 35876503]. doi:10.1021/acs.nanolett.2c02259

Haney, M. J., Klyachko, N. L., Zhao, Y., Gupta, R., Plotnikova, E. G., He, Z., et al. (2015)., 207. PubMed, 1818–1830. doi:10.1016/j.jconrel.2015.03.033Exosomes as drug delivery vehicles for Parkinson's disease therapy*J. Control. Release*

Hasani-Sadrabadi, M. M., Sarrion, P., Pouraghaei, S., Chau, Y., Ansari, S., Li, S., et al. (2020). An engineered cell-laden adhesive hydrogel promotes craniofacial bone tissue regeneration in rats. *Sci. Transl. Med.* 12, eaay6853. [PubMed: eaay6853]. doi:10.1126/scitranslmed.aay6853

Hashimoto, K., Ochi, H., Sunamura, S., Kosaka, N., Mabuchi, Y., Fukuda, T., et al. (2018). Cancer-secreted hsa-miR-940 induces an osteoblastic phenotype in the bone metastatic microenvironment via targeting ARHGAP1 and FAM134A. *Proc. Natl. Acad. Sci. U. S. A.* 115, 2204–2209. [PubMed: 29440427]. doi:10.1073/pnas.1717363115

Hergenreider, E., Heydt, S., Tréguer, K., Boettger, T., Horrevoets, A. J., Zeiher, A. M., et al. (2012). Atheroprotective communication between endothelial cells and smooth muscle cells through miRNAs. *Nat. Cell Biol.* 14, 249–256. [PubMed: 249]. doi:10.1038/ncb2441

Hernigou, P., Auregan, J. C., Dubory, A., Flouzat-Lachaniette, C. H., Chevallier, N., and Rouard, H. (2018a). Subchondral stem cell therapy versus contralateral total knee arthroplasty for osteoarthritis following secondary osteonecrosis of the knee. *Int. Orthop.* 42, 2563–2571. [PubMed: 29589086]. doi:10.1007/s00264-018-3916-9

Hernigou, P., Dubory, A., Homma, Y., Guissou, I., Flouzat Lachaniette, C. H., Chevallier, N., et al. (2018b). Cell therapy versus simultaneous contralateral decompression in symptomatic corticosteroid osteonecrosis: A thirty year follow-up prospective randomized study of one hundred and twenty five adult patients. *Int. Orthop.* 42, 1639–1649. [PubMed: 29744647]. doi:10.1007/s00264-018-3941-8

Holkar, K., Kale, V., and Ingavle, G. (2021). Hydrogel-Assisted 3D model to investigate the osteoinductive potential of mc3t3-derived extracellular vesicles. *ACS Biomater. Sci. Eng.* 7, 2687–2700. [PubMed: 34018721]. doi:10.1021/acsbiomaterials.1c00386

Hoshino, A., Costa-Silva, B., Shen, T. L., Rodrigues, G., Hashimoto, A., Tesic Mark, M., et al. (2015). Tumour exosome integrins determine organotropic metastasis. *Nature* 527, 329–335. [PubMed: 26524530]. doi:10.1038/nature15756

Hu, C., and Li, L. (2018). Preconditioning influences mesenchymal stem cell properties *in vitro* and *in vivo*. *J. Cell. Mol. Med.* 22, 1428–1442. [PubMed: 1428]. doi:10.1111/jcmm.13492

Hu, H., Dong, L., Bu, Z., Shen, Y., Luo, J., Zhang, H., et al. (2020). miR-23a-3p-abundant small extracellular vesicles released from Gelma/nanoclay hydrogel for cartilage regeneration. *J. Extracell. Vesicles* 9, 1778883. [PubMed: 32939233]. doi:10.1080/20013078.2020.1778883

Huang, C. C., Kang, M., Lu, Y., Shirazi, S., Diaz, J. I., Cooper, L. F., et al. (2020). Functionally engineered extracellular vesicles improve bone regeneration. *Acta Biomater.* 109, 182–194. [PubMed: 182]. doi:10.1016/j.actbio.2020.04.017

Ishikawa, M., Ito, H., Kitaori, T., Murata, K., Shibuya, H., Furu, M., et al. (2014). MCP/CCR2 signaling is essential for recruitment of mesenchymal progenitor cells during the early phase of fracture healing. *PLoS One* 9, e104954. [PubMed: 25133509][. doi:10.1371/journal.pone.0104954

Jeck, W. R., and Sharpless, N. E. (2014). Detecting and characterizing circular RNAs. *Nat. Biotechnol.* 32, 453–461. [PubMed: 453]. doi:10.1038/nbt.2890

Jia, Y., Zhu, Y., Qiu, S., Xu, J., and Chai, Y. (2019). Exosomes secreted by endothelial progenitor cells accelerate bone regeneration during distraction osteogenesis by stimulating angiogenesis. *Stem Cell Res. Ther.* 10, 12. [PubMed: 30635031]. doi:10.1186/s13287-018-1115-7

Jin, Y., Xu, M., Zhu, H., Dong, C., Ji, J., Liu, Y., et al. (2021). Therapeutic effects of bone marrow mesenchymal stem cells-derived exosomes on osteoarthritis. *J. Cell. Mol. Med.* 25, 9281–9294. [PubMed: 34448527]. doi:10.1111/jcmm.16860

Jing, X., Wang, S., Tang, H., Li, D., Zhou, F., Xin, L., et al. (2022). Dynamically bioresponsive DNA hydrogel incorporated with dual-functional stem cells from apical papilla-derived exosomes promotes diabetic bone regeneration. *ACS Appl. Mat. Interfaces* 14, 16082–16099. [PubMed: 35344325]. doi:10.1021/acsami.2c02278

Kalluri, R., and LeBleu, V. S. (2020). The biology, function, and biomedical applications of exosomes. *Science* 367. [PubMed: eaau6977]. doi:10.1126/science.aau6977

Kang, M., Huang, C. C., Lu, Y., Shirazi, S., Gajendrareddy, P., Ravindran, S., et al. (2020). Bone regeneration is mediated by macrophage extracellular vesicles. *Bone* 141, 115627. [PubMed: 32891867]. doi:10.1016/j.bone.2020.115627

Kheirandish, M., Gavgani, S. P., and Samiee, S. (2017). The effect of hypoxia preconditioning on the neural and stemness genes expression profiling in human umbilical cord blood mesenchymal stem cells. *Transfus. Apher. Sci.* 56, 392–399. [PubMed: 392]. doi:10.1016/j.transci.2017.03.015

Kim, M. H., Kim, B. S., Park, H., Lee, J., and Park, W. H. (2018). Injectable methylcellulose hydrogel containing calcium phosphate nanoparticles for bone regeneration. *Int. J. Biol. Macromol.* 109, 57–64. [PubMed: 57]. doi:10.1016/j.ijbiomac.2017.12.068

Kim, M. S., Haney, M. J., Zhao, Y., Mahajan, V., Deygen, I., Klyachko, N. L., et al. (2016). Development of exosome-encapsulated paclitaxel to overcome MDR in cancer cells. *Nanomedicine Nanotechnol. Biol. Med.* 12, 655–664. [PubMed: 655]. doi:10.1016/j.nano.2015.10.012

Kim, Y. G., Choi, J., and Kim, K. (2020). Mesenchymal stem cell-derived exosomes for effective cartilage tissue repair and treatment of osteoarthritis. *Biotechnol. J.* 15, 2000082. [PubMed: 32559340]. doi:10.1002/biot.202000082

Kitaori, T., Ito, H., Schwarz, E. M., Tsutsumi, R., Yoshitomi, H., Oishi, S., et al. (2009). Stromal cell-derived factor 1/CXCR4 signaling is critical for the recruitment of mesenchymal stem cells to the fracture site during skeletal repair in a mouse model. *Arthritis Rheum.* 60, 813–823. [PubMed: 19248097]. doi:10.1002/art.24330

Kojima, R., Bojar, D., Rizzi, G., Hamri, G. C., El-Baba, M. D., Saxena, P., et al. (2018). Designer exosomes produced by implanted cells intracerebrally deliver therapeutic cargo for Parkinson's disease treatment. *Nat. Commun.* 9, 1305. [PubMed:29610454]. doi:10.1038/s41467-018-03733-8

Kopp, F., and Mendell, J. T. (2018). Functional classification and experimental dissection of long noncoding RNAs. *Cell* 172, 393–407. [PubMed: 393]. doi:10.1016/j.cell.2018.01.011

Kuang, M. J., Huang, Y., Zhao, X. G., Zhang, R., Ma, J. X., Wang, D. C., et al. (2019). Exosomes derived from Wharton's jelly of human umbilical cord mesenchymal stem cells reduce osteocyte apoptosis in glucocorticoid-induced osteonecrosis of the femoral head in rats via the miR-21-PTEN-AKT signalling pathway. *Int. J. Biol. Sci.* 15, 1861–1871. [PubMed: 1861]. doi:10.7150/ijbs.32262

Lai, R. C., Tan, S. S., Teh, B. J., Sze, S. K., Arslan, F., de Kleijn, D. P., et al. (2012). Proteolytic potential of the msc exosome proteome: Implications for an exosome-mediated delivery of therapeutic proteasome. *Int. J. Proteomics* 2012, 1–14. [PubMed: 22852084]. doi:10.1155/2012/971907

Lamichhane, T. N., Raiker, R. S., and Jay, S. M. (2015). Exogenous DNA loading into extracellular vesicles via electroporation is size-dependent and enables limited gene delivery. *Mol. Pharm.* 12, 3650–3657. [PubMed: 3650]. doi:10.1021/acs.molpharmaceut.5b00364

Lander, E. S., Linton, L. M., Birren, B., Nusbaum, C., Zody, M. C., Baldwin, J., et al. (2001). Initial sequencing and analysis of the human genome. *Nature* 409, 860–921. [PubMed: 860]. doi:10.1038/35057062

Lathwal, S., Yerneni, S. S., Boye, S., Muza, U. L., Takahashi, S., Sugimoto, N., et al. (2021). Engineering exosome polymer hybrids by atom transfer radical polymerization. *Proc. Natl. Acad. Sci. U. S. A.* 118, e2020241118. [PubMed: 33384328]. doi:10.1073/pnas.2020241118

Lei, F., Li, M., Lin, T., Zhou, H., Wang, F., and Su, X. (2022). Treatment of inflammatory bone loss in periodontitis by stem cell-derived exosomes. *Acta Biomater.* 141, 333–343. [PubMed: 333]. doi:10.1016/j.actbio.2021.12.035

Lener, T., Gimona, M., Aigner, L., Börger, V., Buzas, E., Camussi, G., et al. (2015). Applying extracellular vesicles based therapeutics in clinical trials - an ISEV position paper. *J. Extracell. Vesicles* 4, 30087. [PubMed: 26725829]. doi:10.3402/jev.v4.30087

Li, H., Liu, D., Li, C., Zhou, S., Tian, D., Xiao, D., et al. (2017). Exosomes secreted from mutant-HIF-1α-modified bone-marrow-derived mesenchymal stem cells

attenuate early steroid-induced avascular necrosis of femoral head in rabbit. *Cell Biol. Int.* 41, 1379–1390. [PubMed:28877384]. doi:10.1002/cbin.10869

Li, L., Zhang, Y., Mu, J., Chen, J., Zhang, C., Cao, H., et al. (2020). Transplantation of human mesenchymal stem-cell-derived exosomes immobilized in an adhesive hydrogel for effective treatment of spinal cord injury. *Nano Lett.* 20, 4298–4305. [PubMed: 4298]. doi:10.1021/acs.nanolett.0c00929

Li, R., Li, D., Wang, H., Chen, K., Wang, S., Xu, J., et al. (2022). Exosomes from adipose-derived stem cells regulate M1/M2 macrophage phenotypic polarization to promote bone healing via miR-451a/MIF. *Stem Cell Res. Ther.* 13, 149. [PubMed: 35395782]. doi:10.1186/s13287-022-02823-1

Liang, B., Liang, J. M., Ding, J. N., Xu, J., Xu, J. G., and Chai, Y. M. (2019). Dimethyloxaloylglycine-stimulated human bone marrow mesenchymal stem cell-derived exosomes enhance bone regeneration through angiogenesis by targeting the AKT/mTOR pathway. *Stem Cell Res. Ther.* 10, 335. [PubMed: 31747933]. doi:10.1186/s13287-019-1410-y

Liang, X., Ding, Y., Zhang, Y., Tse, H. F., and Lian, Q. (2014). Paracrine mechanisms of mesenchymal stem cell-based therapy: Current status and perspectives. *Cell Transpl.* 23, 1045–1059. [PubMed: 23676629]. doi:10.3727/096368913x667709

Liang, Y., Duan, L., Lu, J., and Xia, J. (2021). Engineering exosomes for targeted drug delivery. *Theranostics* 11, 3183–3195. [PubMed: 3183]. doi:10.7150/thno.52570

Liao, Q., Li, B. J., Li, Y., Xiao, Y., Zeng, H., Liu, J. M., et al. (2021). Low-intensity pulsed ultrasound promotes osteoarthritic cartilage regeneration by BMSC-derived exosomes via modulating the NF-κB signaling pathway. *Int. Immunopharmacol.* 97, 107824. PubMed: 34102487]. doi:10.1016/j.intimp.2021.107824

Liao, W., Ning, Y., Xu, H. J., Zou, W. Z., Hu, J., Liu, X. Z., et al. (2019). BMSC-derived exosomes carrying microRNA-122-5p promote proliferation of osteoblasts in osteonecrosis of the femoral head. *Clin. Sci. (Lond)* 133, 1955–1975. [PubMed: 1955]. doi:10.1042/cs20181064

Liebergall, M., Schroeder, J., Mosheiff, R., Gazit, Z., Yoram, Z., Rasooly, L., et al. (2013). Stem cell-based therapy for prevention of delayed fracture union: A randomized and prospective preliminary study. *Mol. Ther.* 21, 1631–1638. [PubMed: 23732992]. doi:10.1038/mt.2013.109

Lin, Z., Xiong, Y., Meng, W., Hu, Y., Chen, L., Chen, L., et al. (2022)., 13. PubMed, 300300–300311. doi:10.1016/j.bioactmat.2021.10.042Exosomal PD-L1 induces osteogenic differentiation and promotes fracture healing by acting as an immunosuppressant*Bioact. Mater.*

Liu, A., Lin, D., Zhao, H., Chen, L., Cai, B., Lin, K., et al. (2021a). Optimized BMSC-derived osteoinductive exosomes immobilized in hierarchical scaffold via lyophilization for bone repair through Bmpr2/Acvr2b competitive receptor-activated Smad pathway. *Biomaterials* 272, 120718. [PubMed: 33838528]. doi:10.1016/j.biomaterials.2021.120718

Liu, C. X., and Chen, L. L. (2022). Circular RNAs: Characterization, cellular roles, and applications. *Cell* 185, 2016–2034. [PubMed: 2016]. doi:10.1016/j.cell.2022.04.021

Liu, L., Guo, S., Shi, W., Liu, Q., Huo, F., Wu, Y., et al. (2021b). Bone marrow mesenchymal stem cell-derived small extracellular vesicles promote periodontal regeneration. *Tissue Eng. Part A* 27, 962–976. [PubMed: 962]. doi:10.1089/ten.TEA.2020.0141

Liu, L., Yu, F., Li, L., Zhou, L., Zhou, T., Xu, Y., et al. (2021c). Bone marrow stromal cells stimulated by strontium-substituted calcium silicate ceramics: Release of exosomal miR-146a regulates osteogenesis and angiogenesis. *Acta Biomater.* 119, 444–457. [PubMed: 444]. doi:10.1016/j.actbio.2020.10.038

Liu, P., Xiong, Y., Chen, L., Lin, C., Yang, Y., Lin, Z., et al. (2022). Angiogenesis-based diabetic skin reconstruction through multifunctional hydrogel with sustained releasing of M2 Macrophage-derived exosome. *Chem. Eng. J.* 431, 132413. doi:10.1016/j.cej.2021.132413

Liu, W., Yu, M., Chen, F., Wang, L., Ye, C., Chen, Q., et al. (2021d). A novel delivery nanobiotechnology: Engineered miR-181b exosomes improved osteointegration by regulating macrophage polarization. *J. Nanobiotechnol.* 19, 269. [PubMed: 34493305]. doi:10.1186/s12951-021-01015-y

Liu, X., Duan, B., Cheng, Z., Jia, X., Mao, L., Fu, H., et al. (2011). SDF-1/CXCR4 axis modulates bone marrow mesenchymal stem cell apoptosis, migration and cytokine secretion. *Protein Cell* 2, 845–854. [PubMed: 22058039]. doi:10.1007/s13238-011-1097-z

Liu, Z., Li, C., Huang, P., Hu, F., Jiang, M., Xu, X., et al. (2020). CircHmbox1 targeting miRNA-1247-5p is involved in the regulation of bone metabolism by TNF-α in postmenopausal osteoporosis. *Front. Cell Dev. Biol.* 8, 594785. [PubMed: 33425899]. doi:10.3389/fcell.2020.594785

López-Noriega, A., Ruiz-Hernández, E., Quinlan, E., Storm, G., Hennink, W. E., and O'Brien, F. J. (2014). Thermally triggered release of a pro-osteogenic peptide from a functionalized collagen-based scaffold using thermosensitive liposomes. *J. Control. Release* 187, 158–166. [PubMed: 158]. doi:10.1016/j.jconrel.2014.05.043

Lu, G. D., Cheng, P., Liu, T., and Wang, Z. (2020). BMSC-derived exosomal miR-29a promotes angiogenesis and osteogenesis. *Front. Cell Dev. Biol.* 8, 608521. [PubMed: 33363169]. doi:10.3389/fcell.2020.608521

Lu, Z., Chen, Y., Dunstan, C., Roohani-Esfahani, S., and Zreiqat, H. (2017). Priming adipose stem cells with tumor necrosis factor-alpha preconditioning potentiates their exosome efficacy for bone regeneration. *Tissue Eng. Part A* 23, 1212–1220. [PubMed: 1212]. doi:10.1089/ten.tea.2016.0548

Lv, P. Y., Gao, P. F., Tian, G. J., Yang, Y. Y., Mo, F. F., Wang, Z. H., et al. (2020). Osteocyte-derived exosomes induced by mechanical strain promote human periodontal ligament stem cell proliferation and osteogenic differentiation via the miR-181b-5p/PTEN/AKT signaling pathway. *Stem Cell Res. Ther.* 11, 295. [PubMed: 32680565]. doi:10.1186/s13287-020-01815-3

Ma, S., Niu, M., Hao, Z., Liu, M., Tong, C., and Zhao, X. (2021). Selective packaged circular RNAs in milk extracellular vesicles during *Staphylococcus aureus* infection may have potential against bacterial infection. *RNA Biol.* 18, 818–831. [PubMed: 818]. doi:10.1080/15476286.2020.1853975

Ma, S., Wu, J., Hu, H., Mu, Y., Zhang, L., Zhao, Y., et al. (2022). Novel fusion peptides deliver exosomes to modify injectable thermo-sensitive hydrogels for bone regeneration. *Mater. Today Bio* 13, 100195. [PubMed: 35024598]. doi:10.1016/j.mtbio.2021.100195

Mao, G., Xu, Y., Long, D., Sun, H., Li, H., Xin, R., et al. (2021). Exosome-transported circRNA_0001236 enhances chondrogenesis and suppress cartilage degradation via the miR-3677-3p/Sox9 axis. *Stem Cell Res. Ther.* 12, 389. [PubMed: 34256841]. doi:10.1186/s13287-021-02431-5

Matos, S., Guerra, F., Krauser, J. T., Figueiredo, H., Marcelino, J. P., and Sanz, M. (2012). Evaluation of an anorganic bovine-derived mineral with P-15 hydrogel bone graft: Preliminary study in a rabbit cranial bone model. *Clin. Oral Implants Res.* 23, 698–705. [PubMed: 698]. doi:10.1111/j.1600-0501.2011.02179.x

Mauffrey, C., Barlow, B. T., and Smith, W. (2015). Management of segmental bone defects. *J. Am. Acad. Orthop. Surg.* 23, 143–153. [PubMed: 25716002]. doi:10.5435/jaaos-d-14-00018

Meng, W., Hao, Y., He, C., Li, L., and Zhu, G. (2019). Exosome-orchestrated hypoxic tumor microenvironment. *Mol. Cancer* 18, 57. [PubMed: 30925935]. doi:10.1186/s12943-019-0982-6

Mi, B., Chen, L., Xiong, Y., Yang, Y., Panayi, A. C., Xue, H., et al. (2022). Osteoblast/osteoclast and immune cocktail therapy of an exosome/drug delivery multifunctional hydrogel accelerates fracture repair. *ACS Nano* 16, 771–782. [PubMed: 771]782. doi:10.1021/acsnano.1c08284

Mo, C., Huang, B., Zhuang, J., Jiang, S., Guo, S., and Mao, X. (2021). LncRNA nuclear-enriched abundant transcript 1 shuttled by prostate cancer cells-secreted exosomes initiates osteoblastic phenotypes in the bone metastatic microenvironment via miR-205-5p/runt-related transcription factor 2/splicing factor proline- and glutamine-rich/polypyrimidine tract-binding protein 2 axis. *Clin. Transl. Med.* 11, e493. [PubMed: 34459124]. doi:10.1002/ctm2.493

Nair, L., Chung, H., and Basu, U. (2020). Regulation of long non-coding RNAs and genome dynamics by the RNA surveillance machinery. *Nat. Rev. Mol. Cell Biol.* 21, 123–136. [PubMed: 32020081]. doi:10.1038/s41580-019-0209-0

Nan, K., Zhang, Y., Zhang, X., Li, D., Zhao, Y., Jing, Z., et al. (2021). Exosomes from miRNA-378-modified adipose-derived stem cells prevent glucocorticoid-induced osteonecrosis of the femoral head by enhancing angiogenesis and osteogenesis via targeting miR-378 negatively regulated suppressor of fused (Sufu). *Stem Cell Res. Ther.* 12, 331. [PubMed: 34099038]. doi:10.1186/s13287-021-02390-x

Ni, P., Ding, Q., Fan, M., Liao, J., Qian, Z., Luo, J., et al. (2014). Injectable thermosensitive PEG-PCL-PEG hydrogel/acellular bone matrix composite for bone regeneration in cranial defects. *Biomaterials* 35, 236–248. [PubMed: 236]. doi:10.1016/j.biomaterials.2013.10.016

Nielsen, A. F., Bindereif, A., Bozzoni, I., Hanan, M., Hansen, T. B., Irimia, M., et al. (2022). Best practice standards for circular RNA research. *Nat. Methods* 19, 1208–1220. [PubMed: 35618955]. doi:10.1038/s41592-022-01487-2

Nikhil, A., and Kumar, A. (2022). Evaluating potential of tissue-engineered cryogels and chondrocyte derived exosomes in articular cartilage repair. *Biotech. Bioeng.* 119, 605–625. [PubMed: 34723385]. doi:10.1002/bit.27982

Nunes, A., Ribeiro, D. R., Marques, M., Santos, M. A. S., Ribeiro, D., and Soares, A. R. (2020). Emerging roles of tRNAs in RNA virus infections. *Trends Biochem. Sci.* 45, 794–805. [PubMed: 794]. doi:10.1016/j.tibs.2020.05.007

Ocansey, D. K. W., Zhang, L., Wang, Y., Yan, Y., Qian, H., Zhang, X., et al. (2020). Exosome-mediated effects and applications in inflammatory bowel disease. *Biol. Rev.* 95, 1287–1307. [PubMed: 1287]. doi:10.1111/brv.12608

Patel, G. K., Khan, M. A., Zubair, H., Srivastava, S. K., Khushman, M., Singh, S., et al. (2019). Comparative analysis of exosome isolation methods using culture

supernatant for optimum yield, purity and downstream applications. *Sci. Rep.* 9 (1), 5335. [PMID: 30926864]. doi:10.1038/s41598-019-41800-2

Pishavar, E., Luo, H., Naserifar, M., Hashemi, M., Toosi, S., Atala, A., et al. (2021). Advanced hydrogels as exosome delivery systems for osteogenic differentiation of MSCs: Application in bone regeneration. *Int. J. Mol. Sci.* 22. [PubMed: 6203]. doi:10.3390/ijms22126203

Prattichizzo, F., Matacchione, G., Giuliani, A., Sabbatinelli, J., Olivieri, F., de Candia, P., et al. (2021). Extracellular vesicle-shuttled miRNAs: A critical appraisal of their potential as nano-diagnostics and nano-therapeutics in type 2 diabetes mellitus and its cardiovascular complications. *Theranostics* 11, 1031–1045. [PubMed: 1031]. doi:10.7150/thno.51605

Ren, B., Wang, X., Duan, J., and Ma, J. (2019). Rhizobial tRNA-derived small RNAs are signal molecules regulating plant nodulation. *Science* 365, 919–922. [PubMed: 919]. doi:10.1126/science.aav8907

Riau, A. K., Ong, H. S., Yam, G. H. F., and Mehta, J. S. (2019). Sustained delivery system for stem cell-derived exosomes. *Front. Pharmacol.* 10, 1368. [PubMed: 1368]. doi:10.3389/fphar.2019.01368

Salmena, L., Poliseno, L., Tay, Y., Kats, L., and Pandolfi, P. P. (2011). A ceRNA hypothesis: The rosetta stone of a hidden RNA language? *Cell* 146, 353–358. [PubMed: 353]. doi:10.1016/j.cell.2011.07.014

Sang, X., Zhao, X., Yan, L., Jin, X., Wang, X., Wang, J., et al. (2022). Thermosensitive hydrogel loaded with primary chondrocyte-derived exosomes promotes cartilage repair by regulating macrophage polarization in osteoarthritis. *Tissue Eng. Regen. Med.* 19, 629–642. [PubMed: 35435577]. doi:10.1007/s13770-022-00437-5

Shang, F., Yu, Y., Liu, S., Ming, L., Zhang, Y., Zhou, Z., et al. (2021). Advancing application of mesenchymal stem cell-based bone tissue regeneration. *Bioact. Mater.* 6, 666–683. [PubMed: 33005830]. doi:10.1016/j.bioactmat.2020.08.014

Shao, L. T., Luo, L., Qiu, J. H., and Deng, D. Y. B. (2022). PTH (1-34) enhances the therapeutic effect of bone marrow mesenchymal stem cell-derived exosomes by inhibiting proinflammatory cytokines expression on OA chondrocyte repair *in vitro*. *Arthritis Res. Ther.* 24, 96. [PubMed: 35488245]. doi:10.1186/s13075-022-02778-x

Shen, K., Duan, A., Cheng, J., Yuan, T., Zhou, J., Song, H., et al. (2022). Exosomes derived from hypoxia preconditioned mesenchymal stem cells laden in a silk hydrogel promote cartilage regeneration via the miR-205-5p/PTEN/AKT pathway. *Acta Biomater.* 143, 173–188. [PubMed:35202856]. doi:10.1016/j.actbio.2022.02.026

Shen, Z., Kuang, S., Zhang, Y., Yang, M., Qin, W., Shi, X., et al. (2020). Chitosan hydrogel incorporated with dental pulp stem cell-derived exosomes alleviates periodontitis in mice via a macrophage-dependent mechanism. *Bioact. Mater.* 5, 1113–1126. [PubMed: 32743122]. doi:10.1016/j.bioactmat.2020.07.002

Silván, U., Díez-Torre, A., Arluzea, J., Andrade, R., Silió, M., and Aréchaga, J. (2009). Hypoxia and pluripotency in embryonic and embryonal carcinoma stem cell biology. *Differentiation* 78, 159–168. [PubMed: 159]. doi:10.1016/j.diff.2009.06.002

Song, H., Chen, X., Hao, Y., Wang, J., Xie, Q., and Wang, X. (2022). Nanoengineering facilitating the target mission: Targeted extracellular vesicles delivery systems design. *J. Nanobiotechnol.* 20, 431. [PubMed: 36175866][. doi:10.1186/s12951-022-01638-9

Song, H., Li, X., Zhao, Z., Qian, J., Wang, Y., Cui, J., et al. (2019). Reversal of osteoporotic activity by endothelial cell-secreted bone targeting and biocompatible exosomes. *Nano Lett.* 19, 3040–3048. [PubMed: 3040]. doi:10.1021/acs.nanolett.9b00287

Sun, J., Yin, Z., Wang, X., and Su, J. (2022). Exosome-laden hydrogels: A novel cell-free strategy for *in-situ* bone tissue regeneration. *Front. Bioeng. Biotechnol.* 10, 866208. [PubMed: 35433664]. doi:10.3389/fbioe.2022.866208

Tan, L., Fu, J., Feng, F., Liu, X., Cui, Z., Li, B., et al. (2020a). Engineered probiotics biofilm enhances osseointegration via immunoregulation and anti-infection. *Sci. Adv.* 6. [PubMed: eaba5723]. doi:10.1126/sciadv.aba5723

Tan, S. H. S., Wong, J. R. Y., Sim, S. J. Y., Tjio, C. K. E., Wong, K. L., Chew, J. R. J., et al. (2020b). Mesenchymal stem cell exosomes in bone regenerative strategies-a systematic review of preclinical studies. *Mater. Today Bio* 7, 100067. [PubMed: 32695985]. doi:10.1016/j.mtbio.2020.100067

Tan, S. S. H., Tjio, C. K. E., Wong, J. R. Y., Wong, K. L., Chew, J. R. J., Hui, J. H. P., et al. (2021). Mesenchymal stem cell exosomes for cartilage regeneration: A systematic review of preclinical *in vivo* studies. *Tissue Eng. Part B Rev.* 27, 1–13. [PubMed: 1]. doi:10.1089/ten.TEB.2019.0326

Tao, S. C., Huang, J. Y., Gao, Y., Li, Z. X., Wei, Z. Y., Dawes, H., et al. (2021). Small extracellular vesicles in combination with sleep-related circRNA3503: A targeted therapeutic agent with injectable thermosensitive hydrogel to prevent osteoarthritis. *Bioact. Mater.* 6, 4455–4469. [PubMed: 4455]. doi:10.1016/j.bioactmat.2021.04.031

Teng, Z., Zhu, Y., Zhang, X., Teng, Y., and Lu, S. (2020). Osteoporosis is characterized by altered expression of exosomal long non-coding RNAs. *Front. Genet.* 11, 566959. [PubMed: 33281871]. doi:10.3389/fgene.2020.566959

Tian, Y., Li, S., Song, J., Ji, T., Zhu, M., Anderson, G. J., et al. (2014). A doxorubicin delivery platform using engineered natural membrane vesicle exosomes for targeted tumor therapy. *Biomaterials* 35, 2383–2390. [PubMed: 2383]. doi:10.1016/j.biomaterials.2013.11.083

Tibbitt, M. W., and Anseth, K. S. (2009). Hydrogels as extracellular matrix mimics for 3D cell culture. *Biotechnol. Bioeng.* 103, 655–663. [PubMed: 19472329]. doi:10.1002/bit.22361

Tkach, M., and Thery, C. (2016). Communication by extracellular vesicles: Where we are and where we need to go. *Cell* 164, 1226–1232. [PubMed: 1226]. doi:10.1016/j.cell.2016.01.043

Toupadakis, C. A., Wong, A., Genetos, D. C., Chung, D. J., Murugesh, D., Anderson, M. J., et al. (2012). Long-term administration of AMD3100, an antagonist of SDF-1/CXCR4 signaling, alters fracture repair. *J. Orthop. Res.* 30, 1853–1859. [PubMed: 1853]. doi:10.1002/jor.22145

Valadi, H., Ekström, K., Bossios, A., Sjöstrand, M., Lee, J. J., and Lötvall, J. O. (2007). Exosome-mediated transfer of mRNAs and microRNAs is a novel mechanism of genetic exchange between cells. *Nat. Cell Biol.* 9, 654–659. [PubMed: 654]. doi:10.1038/ncb1596

van der Meel, R., Fens, M. H., Vader, P., van Solinge, W. W., Eniola-Adefeso, O., and Schiffelers, R. M. (2014). Extracellular vesicles as drug delivery systems: Lessons from the liposome field. *J. Control. Release* 195, 72–85. [PubMed: 72]. doi:10.1016/j.jconrel.2014.07.049

Wang, C., Wang, M., Xu, T., Zhang, X., Lin, C., Gao, W., et al. (2019a). Engineering bioactive self-healing antibacterial exosomes hydrogel for promoting chronic diabetic wound healing and complete skin regeneration. *Theranostics* 9, 65–76. [PubMed: 65]. doi:10.7150/thno.29766

Wang, D., Cao, H., Hua, W., Gao, L., Yuan, Y., Zhou, X., et al. (2022a). Mesenchymal stem cell-derived extracellular vesicles for bone defect repair. *Membr. (Basel)* 12, 716. [PubMed:35877919]. doi:10.3390/membranes12070716

Wang, L., Wang, J., Zhou, X., Sun, J., Zhu, B., Duan, C., et al. (2020). A new self-healing hydrogel containing hucmsc-derived exosomes promotes bone regeneration. *Front. Bioeng. Biotechnol.* 8, 564731. [PubMed: 33042966]. doi:10.3389/fbioe.2020.564731

Wang, N., Liu, X., Tang, Z., Wei, X., Dong, H., Liu, Y., et al. (2022b). Increased BMSC exosomal miR-140-3p alleviates bone degradation and promotes bone restoration by targeting Plxnb1 in diabetic rats. *J. Nanobiotechnol.* 20, 97. [PubMed: 35236339]. doi:10.1186/s12951-022-01267-2

Wang, P., Wang, H., Huang, Q., Peng, C., Yao, L., Chen, H., et al. (2019b). Exosomes from M1-polarized macrophages enhance paclitaxel antitumor activity by activating macrophages-mediated inflammation. *Theranostics* 9, 1714–1727. [PubMed: 1714]. doi:10.7150/thno.30716

Wang, Q. S., Xu, B. X., Fan, K. J., Fan, Y. S., Teng, H., and Wang, T. Y. (2021a). Dexamethasone-loaded thermo-sensitive hydrogel attenuates osteoarthritis by protecting cartilage and providing effective pain relief. *Ann. Transl. Med.* 9, 1120. [PubMed:34430561]. doi:10.21037/atm-21-684

Wang, W., Qiao, S. C., Wu, X. B., Sun, B., Yang, J. G., Li, X., et al. (2021b). Circ_0008542 in osteoblast exosomes promotes osteoclast-induced bone resorption through m6A methylation. *Cell Death Dis.* 12, 628. [PubMed: 34145224]. doi:10.1038/s41419-021-03915-1

Wang, X., Li, Z., Cui, Y., Cui, X., Chen, C., and Wang, Z. (2021c). Exosomes isolated from bone marrow mesenchymal stem cells exert a protective effect on osteoarthritis via lncRNA LYRM4-AS1-GRPR-miR-6515-5p. *Front. Cell Dev. Biol.* 9, 644380. [PubMed: 34124036]. doi:10.3389/fcell.2021.644380

Wang, Y., Chen, W., Zhao, L., Li, Y., Liu, Z., Gao, H., et al. (2021d). Obesity regulates miR-467/HoxA10 axis on osteogenic differentiation and fracture healing by BMSC-derived exosome LncRNA H19. *J. Cell. Mol. Med.* 25, 1712–1724. [PubMed: 1712]. doi:10.1111/jcmm.16273

Wang, Y., He, S. H., Liang, X., Zhang, X. X., Li, S. S., and Li, T. F. (2021e)., 73. PubMed, 146146–146158. doi:10.1002/iub.2414ATF4-modified serum exosomes derived from osteoarthritic mice inhibit osteoarthritis by inducing autophagy*IUBMB Life*

Wang, Y., Liu, J., Ma, J., Sun, T., Zhou, Q., Wang, W., et al. (2019c). Exosomal circRNAs: Biogenesis, effect and application in human diseases. *Mol. Cancer* 18, 116. [PubMed: 31277663]. doi:10.1186/s12943-019-1041-z

Wang, Z., Le, H., Wang, Y., Liu, H., Li, Z., Yang, X., et al. (2022c). Instructive cartilage regeneration modalities with advanced therapeutic implantations under abnormal conditions. *Bioact. Mater.* 11, 317–338. [PubMed: 34977434]. doi:10.1016/j.bioactmat.2021.10.002

Wang, Z., Zhao, F., Zhao, Y., Bai, L., and Hang, R. (2022d). Simultaneously enhanced osteogenesis and angiogenesis via macrophage-derived exosomes upon

stimulation with titania nanotubes. *Biomater. Adv.* 134, 112708. [PubMed: 35581093]. doi:10.1016/j.msec.2022.112708

Wei, F., Li, M., Crawford, R., Zhou, Y., and Xiao, Y. (2019). Exosome-integrated titanium oxide nanotubes for targeted bone regeneration. *Acta Biomater.* 86, 480–492. [PubMed: 480]. doi:10.1016/j.actbio.2019.01.006

Wei, Z., Batagov, A. O., Schinelli, S., Wang, J., Wang, Y., El Fatimy, R., et al. (2017). Coding and noncoding landscape of extracellular RNA released by human glioma stem cells. *Nat. Commun.* 8, 1145. [PubMed: 29074968]. doi:10.1038/s41467-017-01196-x

Wu, D., Chang, X., Tian, J., Kang, L., Wu, Y., Liu, J., et al. (2021a). Bone mesenchymal stem cells stimulation by magnetic nanoparticles and a static magnetic field: Release of exosomal miR-1260a improves osteogenesis and angiogenesis. *J. Nanobiotechnol.* 19, 209. [PubMed: 34256779]. doi:10.1186/s12951-021-00958-6

Wu, D., Qin, H., Wang, Z., Yu, M., Liu, Z., Peng, H., et al. (2021b). Bone mesenchymal stem cell-derived sEV-encapsulated thermosensitive hydrogels accelerate osteogenesis and angiogenesis by release of exosomal miR-21. *Front. Bioeng. Biotechnol.* 9, 829136. [PubMed: 35127680]. doi:10.3389/fbioe.2021.829136

Wu, J., Kuang, L., Chen, C., Yang, J., Zeng, W. N., Li, T., et al. (2019). miR-100-5p-abundant exosomes derived from infrapatellar fat pad MSCs protect articular cartilage and ameliorate gait abnormalities via inhibition of mTOR in osteoarthritis. *Biomaterials* 206, 87–100. [PubMed: 87]. doi:10.1016/j.biomaterials.2019.03.022

Xia, P., Wang, Q., Song, J., Wang, X., Wang, X., Lin, Q., et al. (2022). Low-intensity pulsed ultrasound enhances the efficacy of bone marrow-derived MSCs in osteoarthritis cartilage repair by regulating autophagy-mediated exosome release. *Cartilage* 13, 194760352210930. [PubMed: 35438034]. doi:10.1177/19476035221093060

Xie, L., Guan, Z., Zhang, M., Lyu, S., Thuaksuban, N., Kamolmattayakul, S., et al. (2020). Exosomal circLPAR1 promoted osteogenic differentiation of homotypic dental pulp stem cells by competitively binding to hsa-miR-31. *BioMed Res. Int.* 2020, 1–13. [PubMed:33062690]. doi:10.1155/2020/6319395

Xing, H., Zhang, Z., Mao, Q., Wang, C., Zhou, Y., Zhou, X., et al. (2021). Injectable exosome-functionalized extracellular matrix hydrogel for metabolism balance and pyroptosis regulation in intervertebral disc degeneration. *J. Nanobiotechnol.* 19, 264. [PubMed:34488795]. doi:10.1186/s12951-021-00991-5

Xing, Y., Yerneni, S. S., Wang, W., Taylor, R. E., Campbell, P. G., and Ren, X. (2022). Engineering pro-angiogenic biomaterials via chemoselective extracellular vesicle immobilization. *Biomaterials* 281, 121357. [PubMed: 34999538]. doi:10.1016/j.biomaterials.2021.121357

Xu, X. Y., Tian, B. M., Xia, Y., Xia, Y. L., Li, X., Zhou, H., et al. (2020). Exosomes derived from P2X7 receptor gene-modified cells rescue inflammation-compromised periodontal ligament stem cells from dysfunction. *Stem Cells Transl. Med.* 9, 1414–1430. [PubMed:32597574]. doi:10.1002/sctm.19-0418

Yang, D., Zhang, W., Zhang, H., Zhang, F., Chen, L., Ma, L., et al. (2020a). Progress, opportunity, and perspective on exosome isolation - efforts for efficient exosome-based theranostics. *Theranostics* 1910 (8), 3684–3707. [PMID: 32206116]. doi:10.7150/thno.41580

Yang, F., Ning, Z., Ma, L., Liu, W., Shao, C., Shu, Y., et al. (2017). Exosomal miRNAs and miRNA dysregulation in cancer-associated fibroblasts. *Mol. Cancer* 16, 148. [PubMed: 28851377]. doi:10.1186/s12943-017-0718-4

Yang, S., Zhu, B., Yin, P., Zhao, L., Wang, Y., Fu, Z., et al. (2020b). Integration of human umbilical cord mesenchymal stem cells-derived exosomes with hydroxyapatite-embedded hyaluronic acid-alginate hydrogel for bone regeneration. *ACS Biomater. Sci. Eng.* 6, 1590–1602. [PubMed: 33455380]. doi:10.1021/acsbiomaterials.9b01363

Yang, X., Yang, J., Lei, P., and Wen, T. (2019). LncRNA MALAT1 shuttled by bone marrow-derived mesenchymal stem cells-secreted exosomes alleviates osteoporosis through mediating microRNA-34c/SATB2 axis. *Aging (Albany NY)* 11, 8777–8791. [PubMed: 8777]. doi:10.18632/aging.102264

Yang, Y., Choi, H., Seon, M., Cho, D., and Bang, S. I. (2016). LL-37 stimulates the functions of adipose-derived stromal/stem cells via early growth response 1 and the MAPK pathway. *Stem Cell Res. Ther.* 7, 58. [PubMed: 27095351]. doi:10.1186/s13287-016-0313-4

Yang, Z., Shi, J., Xie, J., Wang, Y., Sun, J., Liu, T., et al. (2020c). Large-scale generation of functional mRNA-encapsulating exosomes via cellular nanoporation. *Nat. Biomed. Eng.* 4, 69–83. [PubMed: 31844155]. doi:10.1038/s41551-019-0485-1

Yerneni, S. S., Adamik, J., Weiss, L. E., and Campbell, P. G. (2021). Cell trafficking and regulation of osteoblastogenesis by extracellular vesicle associated bone morphogenetic protein 2. *J. Extracell. Vesicles* 10, e12155. [PubMed: 34669267]. doi:10.1002/jev2.12155

Yerneni, S. S., Lathwal, S., Cuthbert, J., Kapil, K., Szczepaniak, G., Jeong, J., et al. (2022). Controlled release of exosomes using atom transfer radical polymerization-based hydrogels. *Biomacromolecules* 23, 1713–1722. [PubMed: 35302760]. doi:10.1021/acs.biomac.1c01636

Yerneni, S. S., Lathwal, S., Shrestha, P., Shirwan, H., Matyjaszewski, K., Weiss, L., et al. (2019). Rapid on-demand extracellular vesicle augmentation with versatile oligonucleotide tethers. *ACS Nano* 13, 10555–10565. [PubMed: 10555]. doi:10.1021/acsnano.9b04651

Yin, K., Zhu, R., Wang, S., and Zhao, R. C. (2017). Low-level laser effect on proliferation, migration, and antiapoptosis of mesenchymal stem cells. *Stem Cells Dev.* 26, 762–775. [PubMed: 762]. doi:10.1089/scd.2016.0332

Yu, C., Chen, L., Zhou, W., Hu, L., Xie, X., Lin, Z., et al. (2022a). Injectable bacteria-sensitive hydrogel promotes repair of infected fractures via sustained release of miRNA antagonist. *ACS Appl. Mat. Interfaces* 14, 34427–34442. [PubMed:35866896]. doi:10.1021/acsami.2c08491

Yu, P., Xie, J., Chen, Y., Liu, J., Liu, Y., Bi, B., et al. (2020). A thermo-sensitive injectable hydroxypropyl chitin hydrogel for sustained salmon calcitonin release with enhanced osteogenesis and hypocalcemic effects. *J. Mat. Chem. B* 8, 270–281. [PubMed:31802093]. doi:10.1039/c9tb02049g

Yu, W., Li, S., Guan, X., Zhang, N., Xie, X., Zhang, K., et al. (2022b). Higher yield and enhanced therapeutic effects of exosomes derived from MSCs in hydrogel-assisted 3D culture system for bone regeneration. *Biomater. Adv.* 133, 112646. [PubMed: 35067433]. doi:10.1016/j.msec.2022.112646

Zeng, Y., Qiu, Y., Jiang, W., Shen, J., Yao, X., He, X., et al. (2022). Biological features of extracellular vesicles and challenges. *Front. Cell Dev. Biol.* 10, 816698. [PMID: 35813192]. doi:10.3389/fcell.2022.816698

Zha, Y., Li, Y., Lin, T., Chen, J., Zhang, S., and Wang, J. (2021). Progenitor cell-derived exosomes endowed with VEGF plasmids enhance osteogenic induction and vascular remodeling in large segmental bone defects. *Theranostics* 11, 397–409. [PubMed: 397]. doi:10.7150/thno.50741

Zhang, B., Huang, J., Liu, J., Lin, F., Ding, Z., and Xu, J. (2021a). Injectable composite hydrogel promotes osteogenesis and angiogenesis in spinal fusion by optimizing the bone marrow mesenchymal stem cell microenvironment and exosomes secretion. *Mater. Sci. Eng. C* 123, 111782. [PubMed: 33812569]. doi:10.1016/j.msec.2020.111782

Zhang, F. X., Liu, P., Ding, W., Meng, Q. B., Su, D. H., Zhang, Q. C., et al. (2021b). Injectable Mussel-Inspired highly adhesive hydrogel with exosomes for endogenous cell recruitment and cartilage defect regeneration. *Biomaterials* 278, 121169. [PubMed: 34626937][. doi:10.1016/j.biomaterials.2021.121169

Zhang, J., Liu, X., Li, H., Chen, C., Hu, B., Niu, X., et al. (2016). Exosomes/tricalcium phosphate combination scaffolds can enhance bone regeneration by activating the PI3K/Akt signaling pathway. *Stem Cell Res. Ther.* 7, 136. [PubMed: 27650895]. doi:10.1186/s13287-016-0391-3

Zhang, J., Tong, D., Song, H., Ruan, R., Sun, Y., Lin, Y., et al. (2022). Osteoimmunity-regulating biomimetically hierarchical scaffold for augmented bone regeneration. *Adv. Mater.* 34, e2202044. [PubMed: 35785450]. doi:10.1002/adma.202202044

Zhang, L., and Yu, D. (2019). Exosomes in cancer development, metastasis, and immunity. *Biochimica Biophysica Acta - Rev. Cancer* 1871, 455–468. [PubMed: 455]. doi:10.1016/j.bbcan.2019.04.004

Zhang, L., Zhang, S., Yao, J., Lowery, F. J., Zhang, Q., Huang, W. C., et al. (2015). Microenvironment-induced PTEN loss by exosomal microRNA primes brain metastasis outgrowth. *Nature* 527, 100–104. [PubMed: 100]. doi:10.1038/nature15376

Zhang, S., Teo, K. Y. W., Chuah, S. J., Lai, R. C., Lim, S. K., and Toh, W. S. (2019). MSC exosomes alleviate temporomandibular joint osteoarthritis by attenuating inflammation and restoring matrix homeostasis. *Biomaterials* 200, 35–47. [PubMed: 35]. doi:10.1016/j.biomaterials.2019.02.006

Zhang, X., Trebak, F., Souza, L. A. C., Shi, J., Zhou, T., Kehoe, P. G., et al. (2020). Small RNA modifications in Alzheimer's disease. *Neurobiol. Dis.* 145, 105058. [PubMed:32835860]. doi:10.1016/j.nbd.2020.105058

Zhang, Y., Kim, M. S., Jia, B., Yan, J., Zuniga-Hertz, J. P., Han, C., et al. (2017). Hypothalamic stem cells control ageing speed partly through exosomal miRNAs. *Nature* 548, 52–57. [PubMed: 28746310]. doi:10.1038/nature23282

Zhang, Y., Xie, Y., Hao, Z., Zhou, P., Wang, P., Fang, S., et al. (2021c). Umbilical mesenchymal stem cell-derived exosome-encapsulated hydrogels accelerate bone repair by enhancing angiogenesis. *ACS Appl. Mat. Interfaces* 13, 18472–18487. [PubMed:33856781]. doi:10.1021/acsami.0c22671

Zhang, Y., Zhang, X., Shi, J., Tuorto, F., Li, X., Liu, Y., et al. (2018a). Dnmt2 mediates intergenerational transmission of paternally acquired metabolic disorders through sperm small non-coding RNAs. *Nat. Cell Biol.* 20, 535–540. [PubMed: 29695786]. doi:10.1038/s41556-018-0087-2

Zhang, Z., Wang, X., Wang, Y., and Hao, J. (2018b). Rapid-forming and self-healing agarose-based hydrogels for tissue adhesives and potential wound dressings. *Biomacromolecules* 19, 980–988. [PubMed: 980]. doi:10.1021/acs.biomac.7b01764

Zhao, D., Zhu, T., Li, J., Cui, L., Zhang, Z., Zhuang, X., et al. (2021a). Poly(lactic-co-glycolic acid)-based composite bone-substitute materials. *Bioact. Mater.* 6, 346–360. [PubMed: 346]. doi:10.1016/j.bioactmat.2020.08.016

Zhao, J., Li, X., Hu, J., Chen, F., Qiao, S., Sun, X., et al. (2019). Mesenchymal stromal cell-derived exosomes attenuate myocardial ischaemia-reperfusion injury through miR-182-regulated macrophage polarization. *Cardiovasc Res.* 115, 1205–1216. [PubMed:30753344]. doi:10.1093/cvr/cvz040

Zhao, W., Hu, J., and He, Q. (2021b). The effect of the WKYMVm peptide on promoting mBMSC secretion of exosomes to induce M2 macrophage polarization through the FPR2 pathway. *J. Orthop. Surg. Res.* 16, 171. [PubMed: 33658070]. doi:10.1186/s13018-021-02321-9

Zhao, Y., Chen, Y., Wang, Z., Xu, C., Qiao, S., Liu, T., et al. (2022). Bone marrow mesenchymal stem cell exosome attenuates inflammasome-related pyroptosis via delivering circ_003564 to improve the recovery of spinal cord injury. *Mol. Neurobiol.* 59, 6771–6789. [PubMed: 36038697]. doi:10.1007/s12035-022-03006-y

Zhi, F., Ding, Y., Wang, R., Yang, Y., Luo, K., and Hua, F. (2021). Exosomal hsa_circ_0006859 is a potential biomarker for postmenopausal osteoporosis and enhances adipogenic versus osteogenic differentiation in human bone marrow mesenchymal stem cells by sponging miR-431-5p. *Stem Cell Res. Ther.* 12, 157. [PubMed: 33648601]. doi:10.1186/s13287-021-02214-y

Zhou, W., Zhou, Y., Chen, X., Ning, T., Chen, H., Guo, Q., et al. (2021). Pancreatic cancer-targeting exosomes for enhancing immunotherapy and reprogramming tumor microenvironment. *Biomaterials* 268, 120546. [PubMed: 33253966]. doi:10.1016/j.biomaterials.2020.120546

Zhu, L., Li, J., Gong, Y., Wu, Q., Tan, S., Sun, D., et al. (2019). Exosomal tRNA-derived small RNA as a promising biomarker for cancer diagnosis. *Mol. Cancer* 18, 74. [PubMed: 30940133]. doi:10.1186/s12943-019-1000-8

Zhu, L., Liu, X., Pu, W., and Peng, Y. (2018). tRNA-derived small non-coding RNAs in human disease. *Cancer Lett.* 419, 1–7. [PubMed: 1]. doi:10.1016/j.canlet.2018.01.015

Zhu, L., Sun, H. T., Wang, S., Huang, S. L., Zheng, Y., Wang, C. Q., et al. (2020). Isolation and characterization of exosomes for cancer research. *J. Hematol. Oncol.* 13, 152. [PubMed: 33168028]. doi:10.1186/s13045-020-00987-y

Zhu, T., Jiang, M., Zhang, M., Cui, L., Yang, X., Wang, X., et al. (2022a). Biofunctionalized composite scaffold to potentiate osteoconduction, angiogenesis, and favorable metabolic microenvironment for osteonecrosis therapy. *Bioact. Mater.* 9, 446–460. [PubMed: 34820582]. doi:10.1016/j.bioactmat.2021.08.005

Zhu, T., Jiang, M., Zhang, M., Cui, L., Yang, X., Wang, X., et al. (2022b). Construction and validation of steroid-induced rabbit osteonecrosis model. *MethodsX* 9, 101713. [PubMed: 35601954]. doi:10.1016/j.mex.2022.101713

Zoulikha, M., Xiao, Q., Boafo, G. F., Sallam, M. A., Chen, Z., and He, W. (2022). Pulmonary delivery of siRNA against acute lung injury/acute respiratory distress syndrome. *Acta Pharm. Sin. B* 12, 600–620. [PubMed: 600]. doi:10.1016/j.apsb.2021.08.009

Frontiers in
Bioengineering and Biotechnology

Accelerates the development of therapies, devices, and technologies to improve our lives

A multidisciplinary journal that accelerates the development of biological therapies, devices, processes and technologies to improve our lives by bridging the gap between discoveries and their application.

Discover the latest Research Topics

See more →

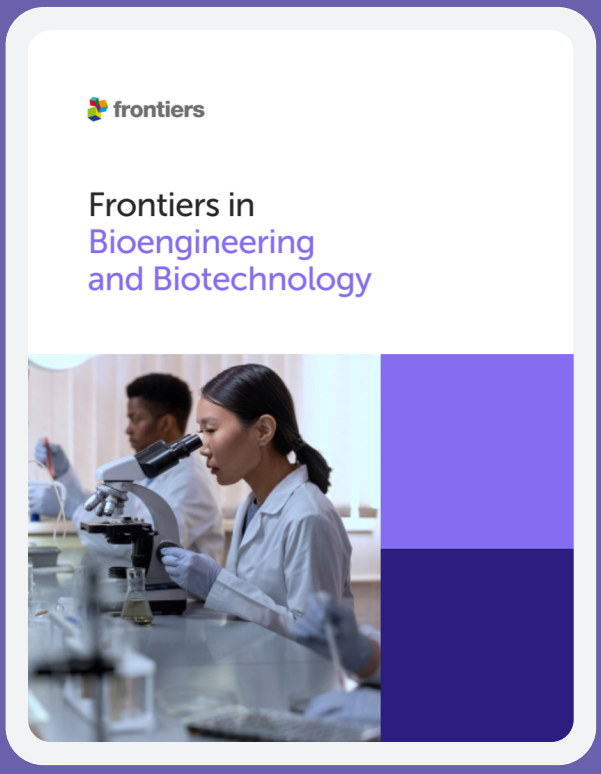

Frontiers

Avenue du Tribunal-Fédéral 34
1005 Lausanne, Switzerland
frontiersin.org

Contact us

+41 (0)21 510 17 00
frontiersin.org/about/contact